



STAB 2012

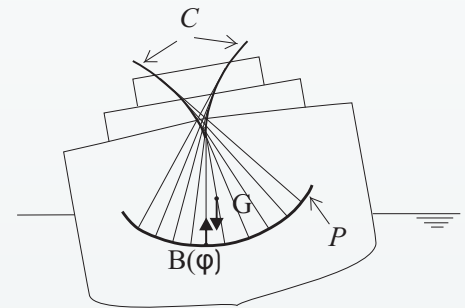


Stability of Ships *and* Ocean Vehicles


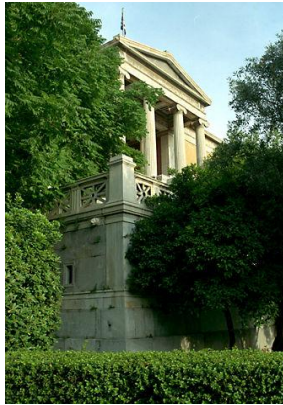
11th International Conference
Athens, 23-28 September 2012

Proceedings

Edited by:
K.J. Spyrou
N. Themelis
A.D. Papanikolaou



National Technical
University of Athens



STAB 2012

Stability of Ships *and* Ocean Vehicles

11th International Conference
Athens, 23-28 September 2012

Proceedings

Edited by:

K.J. Spyrou, N. Themelis, A.D. Papanikolaou

Hosted by:

School of Naval Architecture
and Marine Engineering



National Technical
University of Athens

Pictures of front cover:

1. *Acropolis, Athens, Greece, 2000. Photograph by James Stanfield, shot for the National Geographic magazine. Obtained from:*
http://photography.nationalgeographic.com/photography/enlarge/acropolis-athens-greece_pod_image.html
2. *Archimedes: Detail of an engraving by M. Weber of a painting by Niccolò Barabino. The painting can be found in the Revoltella Museum in Trieste, Italy. Obtained from:*
<http://www.math.nyu.edu/~crrorres/Archimedes/Pictures/ArchimedesPictures.html>
3. *The curve of metacentre. Obtained from the notes of a dynamic stability course taught at NTUA, K. Spyrou.*

By the time of print, the following organizations were committed to supporting STAB 2012:

Golden Sponsor



Silver sponsors



Sponsors

STAB 2012 is supported by the
Royal Institution of Naval Architects



The opinions expressed in the papers of the current Proceedings are those of the authors and do not necessarily reflect the views of any organizations with which these authors are associated.

ISBN: 978-618-80163-0-9

Printed in Greece by A. Eliopoulos, Paraskevopoulou 120, Athens, Greece, eliopoulos-1@otenet.gr.

PREFACE

In the present volume are contained the Proceedings of the 11th International Conference on the Stability of Ships and Ocean Vehicles (STAB 2012). With a history of nearly 40 years, the STAB Conferences and the affiliated Workshops are the meeting points for world's maritime researchers and professionals who are interested in problems of stability of marine vehicles. It is not an exaggerated claim that all important advances realized over several years in the field, referring to better understanding of extreme vessel dynamics, improved mathematical modelling, new stability regulations, understanding of the effect on stability of new design trends, technological solutions for enhancing stability; have been debated at a STAB Meeting. Held recently triennially, the STAB Conferences are based on fully refereed contributions. Between consecutive Conferences take place annual Stability Workshops having a more informal protocol and fostering in depth discussions on novel ideas and on promising, but untried, solutions.

As a topic of investigation ship stability enjoys a long and celebrated history, whose beginning is seemingly defined by Archimedes's spectacular investigations on the tilt and stability of a floating segment of paraboloid. Eminent scientists including Huygens, Bouguer, Euler and the "Bernoullis" were intrigued by what makes a ship stable or unstable, in effect creating the foundation of modern approaches. In spite of unrelenting research effort, new trends in ship design and the unfathomable nature of ship dynamics incessantly supply fresh scientific and technological challenges. Stability is always a prime driver for the art and the science of naval architecture. It should not be coincidental that the first risk - based approach to ship design had used "damage" stability as raw model. "Intact" and "damage" stability regulations are at the forefront of current interests at IMO.

This prestigious event comes, at last, to Athens, hosted by the School of Naval Architecture and Marine Engineering of the National Technical University of Athens. About 85 papers from 22 countries have been selected for presentation, classified in 16 themes: ship dynamic stability in rough seas, damage stability of passenger and cargo ships, probabilistic and risk based assessment of stability, decision support and operational guidance, stability of floating platforms, fishing vessel safety, naval vessel stability, nonlinear dynamics of extreme behaviour, design safety integration, stability of high - speed craft and unconventional problems, modelling of environmental excitations, sloshing and cargo shift, second generation intact stability criteria, implication of stability regulations for design, roll damping, ship stability accident investigation.

Several people have vitally contributed to the organization of STAB 2012. Above all are thanked the authors whose works have made this Conference worthwhile. Very special thanks go also to our expert reviewers. Working on a purely voluntary basis, they enable us to believe that a sound technical programme has been produced. We are indebted to our sponsors whose support allowed us to endeavour offer an attractive social programme too. The Chairman of the International Standing Committee Dr. J.O. de Kat and the Members of this Committee are thanked for their trust and support during the 3 years of preparation.

Deepest appreciation is expressed to the tireless STAB 2012 Secretariat, namely Dr. N. Themelis, Dr. E. Eliopoulou, Mrs. E. Alissafaki, Mr. E. Angelou and Mrs. A. Trikalioti. We thank NTUA's Network Management Centre for hosting and supporting the STAB 2012 site, as also ConfTool GmbH for offering their conference management software. Our smooth collaboration with our Agent, SBOKOS S.A. is acknowledged. I personally thank the Co - Chairman Prof. A. Papanikolaou and all the National Committee Members who were never short of offering their amplest support to our collective undertaking.

Let STAB 2012 be a fruitful event whose works will contribute towards safer marine vehicles.

Kostas J. Spyrou *for the National Committee of STAB 2012*

THE STAB SERIES OF CONFERENCES AND WORKSHOPS

PURPOSE

The STAB Conferences and Workshops are organized to meet the following objectives:

- to promote the exchange of ideas and methodologies addressing the stability of ships and ocean vehicles;
- to provide opportunity for professional naval architects, stability researchers, regulatory agencies, inspection and certifying authorities, ship and platform owners, consultants and operators; to present, discuss and be informed about improvements in the assessment of stability for all types and sizes of floating bodies.

HISTORY

The STAB Conferences were initiated in Glasgow in 1975 by Prof. Chengi Kuo. They were subsequently held in Tokyo (1982), Gdansk (1987), Naples (1990), Melbourne, Florida (1994), Varna (1997), Launceston, Tasmania (2000), Madrid (2003), Rio de Janeiro (2006) and St Petersburg (2009). The Stability Workshops were initiated also in Glasgow, in 1995, by Prof. D. Vassalos. Similar events were held later in Osaka (1996), Hersonissos, Crete (1997), St. John's Newfoundland (1998), Trieste (2001), New York (2002), Shanghai (2004), Istanbul (2005), Hamburg (2007), Daejeon (2008), Wageningen (2010) and Washington D.C. (2011).

MANAGEMENT

The STAB Conferences and Workshops are run by an International Standing Committee (ISC) comprised by about 15 internationally recognized and active stability specialists who elect their own Chair. The ISC oversees that half of its members are elected during each STAB Conference, by all delegates to that Conference. In the selection of the ISC members, regional aspects are considered. Existing Members may stand for re-election. The Chair may not stand more than once for re-election.

The ISC appoints an International Advisory Board (IAB) consisted of eminent persons in the field, some of whom may have served earlier in the ISC. The ISC co-opts the Chair of the IAB.

A Research and Development Committee (RDC) is also appointed by the ISC, whose members are young professionals active in the field. During their assembly at a STAB Conference, RDC members elect their own Chair on the basis of a short list of nominees provided by the ISC. He represents them at the ISC, with no voting rights.

The IAB and RDC assist with any task assigned by the ISC. The ISC is responsible for deciding the location of STAB Conferences and their frequency.

The organization of a STAB event is entrusted upon the National Committee (NC) that works under guidelines provided by the ISC. The NC Chair is nominated by the ISC at the previous STAB. The ISC offers suggestions and agrees the make-up of the NC. In consultation with the NC, the ISC sets out NC's terms of reference, including the event's broad technical content. The NC specifies the detailed content of the forthcoming STAB Conference and is responsible for all the arrangements [location, dates, travel, conference and exhibitions (if included), proceedings, visits], for deciding on the submitted abstracts and papers; and for the finances. The ISC are supportive by way of assisting in the selection of papers and of suggesting speakers/exhibitors. The ISC have a consultative role in setting of fees for the conference.

THE STAB PRIZES

As an act of highest recognition for outstanding lifetime contributors to the field of stability of marine vehicles, the ISC established the presentation, normally during the STAB Conference, of the “STAB Prize”. Until now, recipients of this prestigious award have been: Prof. R. Pauling (University of California at Berkeley), Prof. K. Motora (University of Tokyo), Prof. M. Hamamoto (University of Osaka), Prof. C. Kuo (University of Strathclyde), Prof. Y. Nechaev (St. Petersburg State Marine Technical University) and Prof. L. Kobylinski (Technical University of Gdansk). Furthermore, the ISC decided that, during STAB 2012, the Prize to be awarded posthumously to Late Prof. Y. Odabashi (University of Istanbul).

CURRENT MEMBERSHIP OF INTERNATIONAL STANDING COMMITTEE (ISC)

Dr. Jan O. de Kat (Chair)	<i>A.P. Maersk, Denmark</i>
Dr. Vadim Belenky	<i>David Taylor Model Basin, USA</i>
Mr. Henrik Bruhns	<i>Herbert Engineering, USA</i>
Prof. Alexander Degtyarev	<i>University of St. Petersburg, Russia</i>
Prof. Alberto Francescutto	<i>University of Trieste, Italy</i>
Prof. Yoshiho Ikeda	<i>University of Osaka Prefecture, Japan</i>
Prof. Marcelo A.S. Neves	<i>Federal University of Rio de Janeiro, Brazil</i>
Prof. Apostolos Papanikolaou	<i>National Technical University of Athens, Greece</i>
Prof. Maciej Pawlowski	<i>Technical University of Gdansk, Poland</i>
Prof. Luis Perez - Rojas	<i>Universidad Politécnica de Madrid, Spain</i>
Prof. Martin Renilson	<i>Higher Colleges of Technology, UAE</i>
Prof. Kostas Spyrou	<i>National Technical University of Athens, Greece</i>
Prof. Naoya Umeda	<i>Osaka University, Japan</i>
Prof. Dracos Vassalos	<i>University of Strathclyde, United Kingdom</i>
Dr. Frans van Walree	<i>Maritime Research Institute, Netherlands</i>

STAB 2012 NATIONAL COMMITTEE (NC)

Prof. Kostas Spyrou (Chair)	<i>National Technical University of Athens</i>
Prof. Apostolos Papanikolaou (Co-Chair)	<i>National Technical University of Athens</i>
Prof. Gerassimos Athanassoulis	<i>National Technical University of Athens</i>
Dr. Eleftheria Eliopoulou	<i>National Technical University of Athens</i>
Mr. Dimitrios Floros	<i>Ministry of Shipping</i>
Mr. Panagiotis Giannoulis	<i>Hellenic Institute of Marine Technology</i>
Dr. Georgios Gratsos	<i>Nautical Chamber of Greece</i>
Dr. Ioannis Kokkarakis	<i>Hellenic Institute of Marine Technology</i>
Mr. Ioannis Kouimanis	<i>Hellenic Institute of Marine Technology</i>
Dr. Dimitrios Spanos	<i>National Technical University of Athens</i>
Dr. Nikolaos Themelis	<i>National Technical University of Athens</i>
Prof. Georgios Tsabiras	<i>National Technical University of Athens</i>
Mr. Nikolaos Varvates	<i>Mediterranean Cargo Vessels Shipowners</i>
Prof. Dracos Vassalos	<i>University of Strathclyde, United Kingdom</i>
Prof. Georgios Zaraphonitis	<i>National Technical University of Athens</i>

Table of Contents

Probabilistic and risk - based assessment of ship stability

Development of a new methodology to predict the capsize risk of ships <i>Egbert Ypma, Eelco Harmsen</i>	1
Critical wave groups vs. direct Monte-Carlo simulations for typical stability failure modes of a container ship <i>Vladimir Shigunov, Nikos Themelis, Kostas J. Spyrou</i>	11
Application of stochastic dynamical system to nonlinear ship rolling problems <i>Jeffrey Falzarano, Zhiyong Su, Arada Jamnongpipatkul</i>	21
Evaluation of the probability of surf-riding in irregular waves with the time-split method <i>Vadim Belenky, Kostas J. Spyrou, Kenneth M. Weems</i>	29
Total stability failure probability of a ship in beam wind and waves: model experiment and numerical simulation <i>Takumi Kubo, Naoya Umeda, Satoshi Izawa, Akihiko Matsuda</i>	39
Quantitative analysis of parametric roll and operational guidance <i>KangHyun Song, YongHwan Kim</i>	47
Dependence of roll and roll rate in nonlinear ship motions in following and stern quartering seas <i>Vadim Belenky, Kenneth M. Weems</i>	57
A probabilistic analysis of stability regulations for river-sea ships <i>Igor Bačkalov</i>	67
Steady state probabilistic response of a half oscillator under colored, Gaussian or non-Gaussian excitation <i>Gerassimos A. Athanassoulis, Ivi C. Tsantili, Zacharias G. Kapelonis</i>	79

Second generation intact stability criteria

Stability criteria-50 years of experience and future prospects <i>Lech Kobylinski</i>	91
Approaches to ship motion simulation acceptance criteria <i>Timothy Smith</i>	101
On regulatory framework for direct stability assessment <i>William S. Peters, Vadim Belenky, Arthur M. Reed</i>	115

Test application of second generation IMO intact stability criteria on a large sample of ships <i>Clève Wandji, Philippe Corrigan</i>	129
Validation of a numerical simulation model for parametric rolling prediction using a PCTC <i>Hirotsada Hashimoto, Naoya Umeda</i>	141
Vulnerability assessment for the loss of stability in waves: some application cases for a further insight into the problem <i>Andrea Coraddu, Paola Gualeni, Diego Villa</i>	151
Ship dynamic stability in rough seas	
Study on parametric roll and its rudder stabilization based on unified seakeeping and maneuvering model <i>Liwei Yu, Ning Ma, Xiechong Gu</i>	159
Study of system-based mathematical model using system identification methods with experimental, CFD and system-based free-running trials in waves <i>Motoki Araki, Hamid Sadat-Hosseini, Yugo Sanada, Naoya Umeda, Frederick Stern</i>	171
Roll motion of a ship with low metacentric height in bi-chromatic beam waves <i>Gabriele Bulian, Alberto Francescutto, Marco Sinibaldi</i>	187
Roll stabilization by vertical thrust-producing flapping wings using active pitch control <i>Kostas A. Belibassakis, Gerassimos K. Politis</i>	201
Numerical simulations of maneuvering and dynamic stability of a containership in waves <i>Sungeun (Peter) Kim, Young Jae Sung</i>	215
Model characteristics and validation approach for a simulation tool supporting direct stability assessment <i>William F. Belknap, Arthur M. Reed, Michael J. Hughes</i>	227
Statistical extrapolation for direct stability assessment <i>Vadim Belenky, Bradley Campbell</i>	243
Parameter estimation of a mathematical model used for ship motions in following seas based on the data assimilation <i>Daisuke Terada, Hirotsada Hashimoto, Akihiko Matsuda, Naoya Umeda, Tomohiro Furukawa</i>	257
Catastrophe theory: a modern approach for the interpretation of ship dynamics in irregular waves <i>Yury Nechaev</i>	267

An experimental study on characteristics of rolling in head waves for a vessel with non-linear GZ-curve <i>Toru Katayama, Shugo Miyamoto, Hirotada Hashimoto, Yoshifumi Tai</i>	281
Ship roll motion in irregular waves during a turning circle maneuver <i>Jerzy Matusiak, Claus Stigler</i>	291
Design requirements for stability and minimal motions in a storm <i>Vasily N. Khramushin</i>	299
 Nonlinear dynamics of extreme behaviour	
Stability of ships in parametric roll resonance under time-varying heading and speed <i>Dominik A. Breu, Christian Holden, Thor I. Fossen</i>	305
The unstable boundary of large amplitude rolling of a ship in waves <i>Ju Fan, Renchuan Zhu, Guoping Miao, Xianglu Huang</i>	315
Conditions of surf-riding in an irregular seaway <i>Kostas J. Spyrou, Vadim Belenky, Nikos Themelis, Kenneth M. Weems</i>	323
Continuation analysis of surf-riding and periodic responses of a ship in steep quartering seas <i>Ioannis G. Tigkas, Kostas J. Spyrou</i>	337
Bifurcation from fluttering to autorotation of an hinged vertical flat plate submitted to a uniform current <i>Antonio C. Fernandes, Sina M. Sefat</i>	351
Effectiveness of chaotic system measures for the validation of ship dynamics simulations <i>Michele D. Cooper, Leigh S. McCue</i>	363
 Damage stability of passenger and cargo ships	
Damaged Ro-Pax vessel time to capsize <i>Heng Ran, Ingvar Rask, Carl-Erik Janson</i>	373
Study on the evaluation for performance of the crossflooding arrangements by means of the Computational Fluid Dynamics <i>Kunihide Ohashi, Yoshitaka Ogawa, Koichiro Shiraishi</i>	381
Flooding prediction onboard a damaged ship <i>Pekka Ruponen, Markku Larmela, Petri Pennanen</i>	391
Time dependent survivability against flooding of passenger ships in collision damages <i>Dimitris Spanos, Apostolos Papanikolaou</i>	401

An explicit progressive flooding simulation method <i>Hendrik Dankowski</i>	411
CFD and EFD study of damaged ship stability in calm water and regular waves <i>Hamid Sadat-Hosseini, Dong Hwan Kim, Sung Kyun Lee, Shin Hyung Rhee, Pablo Carrica, Frederick Stern, Key-Pyo Rhee</i>	425
A study for the harmonized probabilistic approach for damage stability taking account of the difference between Collision and Grounding <i>Koichiro Shiraishi, Yoshitaka Ogawa</i>	453
Developing the p-factor for the case of grounding <i>Maciej Pawłowski, Dagmara Głowacka</i>	461
The numerical study of hydrodynamic coefficients by RANS <i>Qiuxin Gao, Dracos Vassalos</i>	471
 Sloshing and cargo shift	
Numerical simulation method for coupling of tank fluid and ship roll motions <i>Hirotsada Hashimoto, Yuto Ito, Nagisa Kawakami, Makoto Sueyoshi</i>	477
3D GPU SPH analysis of coupled sloshing and roll motion <i>Luis Pérez-Rojas, José L. Cercós-Pita</i>	487
Use of granular material dynamics simulation for the study of cargo shift of ships <i>Christos C. Spandonidis, Kostas J. Spyrou</i>	497
 Stability of floating platforms	
Investigation on parametrically excited motions of Spar platforms in waves <i>Claudio A. Rodriguez, Marcelo A. S. Neves</i>	509
A study on unstable motions of a tension leg platform in close proximity to a large FPSO <i>Luis Alberto Rivera, Marcelo A. S. Neves, Roberto E Cruz, Paulo de Tarso T Esperança</i>	519
The hydrodynamics of submerged prolate spheroidal bodies in infinite water depth <i>Ioannis K. Chatjigeorgiou, Spyros A. Mavrakos, Thomas P. Mazarakos</i>	533
 Stability of high-speed craft and unconventional problems	
Dynamic transverse stability for high speed craft <i>Carolyn Q. Judge</i>	545
Bow diving of semi-swath vessel in following seas and fins stabilizer effect <i>Adi Maimun, Rahimuddin, Muhamad Pauzi Abdul Ghani, Andi Haris Muhammad</i>	557

FLO/FLO Heavy lift critical stability phases 569
Paul Handler, Vincent Jarecki, Hendrik Bruhns

Naval vessel stability

Operability of French naval ships over 50 years 575
Brice Beaupuy, Nicolas Stachelhausen, Jean-Yves Billard, Emmanuel Mogenicato, Pierre Vonier et Jean-François Leguen.

Development and validation of a time domain seakeeping code for a destroyer hull form operating in extreme sea states 583
Frans van Walree

An investigation on stability under dead ship condition of a tumblehome hull 593
Min Gu, Jiang Lu, Tianhua Wang

Mathieu instability of surfacing submarine 599
Sergei Karlinskiy, Andrei Efimov

Naval landing craft stability – simulation of extreme roll motions and shipping of water into the well deck 607
Peter Hayes, Warren Smith, Martin Renilson, Stuart Cannon

An investigation on parametric rolling of a tumblehome hull 617
Jiang Lu, Min Gu

Fishing vessel safety

Experimental parametric roll resonance characterization of a stern trawler in head seas 625
Marcos Míguez-González, Vicente Díaz-Casás, Fernando López-Peña, Luis Pérez-Rojas

The safest catch program - fishermen taking ownership of safety 635
Gina McKay, John Krgovich, Barbara Howe

Small fishing vessels study and modelling for the improvement of the behaviour in extreme seas 643
Antoine Pagès, Jean-Jacques Maisonneuve, Clève Wandji, Philippe Corrignan, Benoît Vincent

Decision support and operational guidance

Operational guidance with respect to pure loss of stability and parametric rolling 655
Erik Ovegård, Anders Rosén, Mikael Palmquist, Mikael Huss

Analysis of onboard ship stability and loading instruments from developer's perspective <i>Metin Taylan, Bulent Sener, Yasar Gul, Dirim Sener, Cemal Sahin</i>	669
Putting vessel motion research into the hands of operators <i>Leigh McCue</i>	679
Spend less, save more (Lives) <i>Barry Deakin</i>	689
Nonlinear observer design for parametric roll resonance <i>Dennis J.W. Belleter, Dominik A. Breu, Thor I. Fossen, Henk Nijmeijer</i>	699
Monitoring of dynamic stability via ship's motion responses <i>Hossein Enshaei, Richard Birmingham</i>	707
Blind estimation of wave state from ship motions in navigation <i>Jiang Lin, Li Ji-de</i>	719
System identification for wave measurements using ship as a buoy <i>Alexander Degtyarev, Ilya Busko, Yury Nechaev</i>	725
Ship stability accident investigation	
Capsizing and sinking of the dredger Rozgwiazda <i>Zbigniew Szozda</i>	735
Numerical investigations of the capsizing sequence of SS Heraklion <i>Stefan Krüger, Hendrik Dankowski, Caroline Teuscher</i>	743
Investigation into the sinking of the RO-RO passenger ferry S.S Heraklion <i>Apostolos Papanikolaou, Evangelos Boulougouris, Aleksandros Sklavenitis</i>	755
Implication of stability regulation for design	
Influence of lower cargo deck longitudinal subdivision of SOLAS 90/2004 on Ro-Pax vessels over attained damage stability indices as 2006 amendments SOLAS per MSC 216(82) <i>Fernando Junco, Juan M.Marcote, Vicente Día, Marcos Míguez</i>	767
Damage stability of passenger ships - notions and truths <i>Dracos Vassalos</i>	775
Effect of Revised Damage Survivability Formulation upon Ship Design <i>Romanas Puisa, Przemek Zagorski, Dracos Vassalos</i>	791

Design safety integration

Coupling of progressive structural failure and loss of stability in the safe return to port framework 807
Seungmin Kwon, Qi Chen, George Mermiris, Dracos Vassalos

FLOODSTAND – overview of achievements 819
Risto Jalonen, Pekka Ruponen, Andrzej Jasionowski, Pierre Maurier, Markku Kajosaari, Apostolos Papanikolaou

Multiobjective optimization of ROPAX ships considering the SOLAS 2009 and GOALDS damage stability formulations 831
George Zaraphonitis, Sotiris Skoupas, Apostolos Papanikolaou, Mike Cardinale

Modelling of environmental excitations

Evaluation of hydrodynamic pressures for autoregression model of irregular waves 841
Alexander Degtyarev, Ivan Gankevich

Application of computing hydrodynamic forces and moments on a vessel without Bernoulli's equation 853
Arthur M. Reed

Captive model test and numerical simulation on the maneuvering forces in waves 865
Young Jae Sung, Hyun-ho Lee, Tae-il Lee, Sungeun Kim

Roll damping

Assessment of ship roll damping through full scale and model scale experiments and semi-empirical methods 877
Carl-Johan Söder, Anders Rosén, Sofia Werner, Mikael Huss, Jakob Kutteneuler

Roll damping of twin-screw vessels: comparison of RANSE with established methods 887
Sven Handschel, Nikolai Köllisch, Moustafa Abdel-Maksoud

Industry's views of stability and safety - Keynote addresses

Improvement of ship safety through stability research and innovations 899
Fai Cheng, Spyros Hirdaris



Development of a New Methodology to Predict the Capsize Risk of Ships

Egbert Ypma, *MARIN, the Netherlands*, e.ypma@marin.nl

Eelco Harmsen, *DMO, the Netherlands*, e.harmsen@mindef.nl

ABSTRACT

The paper describes the choices & decisions that were made between different methodologies and implementations to determine an exceedance probability of a rare event (capsize). Out of this comparison it was concluded that a Envelope Peak-Over-Threshold (EPOT) approach required the least simulation time to determine a sufficiently accurate exceedance probability. Secondly, the paper discusses the practical implementation of the method and the rationale behind some of the choices that were made during this process. Thirdly, it describes the development of a software application that automatically distributes a large number of simulations over a office computer network, processes all the results and translates these to an overall capsize risk.

KEYWORDS: *capsize probability, peak over threshold, time domain simulation*

1. INTRODUCTION

Nowadays, large amplitude ship motion simulation software can be used to study the capsize behaviour of ships. One way this may be done is by computing a limited number of conditions and comparing the behaviour of a certain ship with the behaviour of other ships. The consequence of such an approach is that only a limited part of all conditions are tested. To have a good indication of the safety of a ship, simulations should be done for all conditions (combinations of wave systems, speeds, headings and loading conditions) that a ship may encounter during its life. While this is possible, it requires an automatic handling of both the execution of the actual simulations and the analysis of the results.

The Cooperative Research Navies (CRNav) group (consisting of representatives from the British, Canadian, French, Dutch, Australian Navies, and the USCG, MARIN, QinetiQ, DRDC, DGA and DSTO) developed such a system 10 years ago and it was used for a number of studies. The experience gained through these studies indicates that careful attention must be paid to establishing the validity and robustness of the results. This lead

to a thorough review of the existing methodology, its design and its implementation.

2. OVERVIEW

2.1 FREDYN

The 6DoF large ship motion simulation program FREDYN (de Kat & McTaggart, [2000]) has a long development and validation history. Its development started 20 years ago as an integrated seakeeping and manoeuvring simulation program for (mainly) frigates. Over the years it was refined, extended and improved. Recently, the implementation was rebuilt up from the ground to form the sound, flexible and modular basis for the time simulations done at MARIN.

Currently, the major usage of FREDYN is as a ship dynamic stability assessment tool for intact and damaged ships.

The strip theory based SHIPMO tool is used as a pre-processor to calculate the frequency dependent added mass, added damping, diffraction and radiation coefficients.



A panelled hull form is used to calculate the Froude Krylov forces acting on the instantaneous wetted hull. The roll damping can be tuned when (speed dependent) roll decay data is available. The default frigate manoeuvring model can be tuned or even replaced when so desired. The internal flooding of a ship can be simulated using the flooding module and this component will play a large role in the future damaged stability simulations. A growing range of simulation components is available such as fixed pitch propellers, controllable pitch propellers, rudders, skegs, bilgekeels, waterjets etc. The forces calculated by these components are partly empirical based. A simple PID controller is used to control the vessels' trajectory.

One of the recent additions to improve the assessment of the capsizing probability at extreme roll angles is the addition of a module that calculates the 'water on deck' forces. It takes the instantaneous wave profile close to the hull into account to calculate the amount of water on the deck and the forces exerted by the water on the ship itself. The wave profile contains corrections for diffraction and forward speed. This feature was validated using dedicated model tests.

The application is capable of simulating the following mechanisms that can potentially lead to a capsizing:

- Broaching
- Static loss of stability (e.g. on a wave crest)
- Dynamic loss of stability (e.g. parametric roll)

2.2 Environment

The ship's environment is characterised by wind and waves and can be modelled by choosing and configuring one of the available spectra. Using these, a random wave height sequence and varying wind speed and direction will be generated.

The Bales North-Atlantic wave scatter diagram was used to determine the combinations of wave height, peak period and their probability of occurrence for all capsizing probability studies conducted to date. In the latest study, however, the full diagram was not used. All significant wave heights lower than 4.5 meter were ignored as the capsizing probability during these conditions is extremely low. In addition to that the conditions with a mean wave period above 17 seconds were also excluded, but for a different reason. Under these conditions, the real ship will be following the wave profile resulting in a relatively low capsizing probability. As these conditions have a low probability of occurrence, it was thought wise to exclude them. The fact that they were observed (and hence included in the scatter diagram) was accounted for in the probability of occurrence of each H_s , T_1 combination. The Pierson-Moskowitz spectrum was used to generate a 80 component wave sequence. Care is taken that the wave sequence does not repeat itself during a single simulation.

FREDYN uses a linear relationship based on a wind speed – significant wave height scatter diagram from ANEP 11, see Bales et al. [1981].

$$V_{wind @ 10m} = 2.88 + 1.652 \cdot H_s \quad (1)$$

This relation is corrected for the wind speed reference height used in FREDYN. The wind coefficients take the above water part of the hull and the superstructure into account.

Up to FREDYN version 9 the wind coefficients were based on a paper of McTaggart [1994]. Comparisons with wind tunnel test data for four RNN ships showed that these values may be exaggerating the wind forces and the FREDYN settings were reduced accordingly.

The randomness of the generated wave sequence is guaranteed by using random number generators for the wave phase angle.

2.3 Deck Edge immersion

In 2006 it was observed from model test video recordings, that in FREDYN simulations the amount of water on deck was much larger than in the model tests. As the Froude-Krylov wave pressure that is applied to panels on the deck contribute to the heeling moment, this could be an explanation for the fact that FREDYN seemed to predict more capsizes than model tests, resulting in a higher overall capsize probability. These findings were confirmed by other comparisons.

In the paper from van Walree (2010) an attempt was made to have a better correlation between the actual wave profile along the hull and the water profile in FREDYN. Until recently, FREDYN only used the undisturbed wave profile. The improvements of the ‘water-on-deck’ immersion method include:

- The static wave due to forward speed;
- The diffracted wave;
- The radiated wave (zero speed only).

The input data for these calculations comes from databases computed beforehand by SHIPMO (for the diffracted and radiated wave) and DAWSON, a MARIN in-house 3D linear panel code used to compute the forward speed wave profile, see Raven [1988]. The effects of the ‘deck-edge-immersion’ method on the wave height along the hull, the roll peak distribution and the number of capsizes were compared with dedicated model tests with the pre-design DDG-51 destroyer (European version). As the radiated wave gave some problems due to the missing forward speed effects, only the static and diffracted waves are included.

The results of the comparison showed that the new method had significant influence on the tail of the roll angle distribution; in general the probability of an extreme roll angle is lower with the new method as is shown in Figure 1. Naturally, this has its effects on the capsizes counted in the simulations. However, a direct comparison of the capsize counts in the model

tests and the simulations could not be made as the duration of each condition in the model tests was too short to gather reliable statistics of these extreme events.

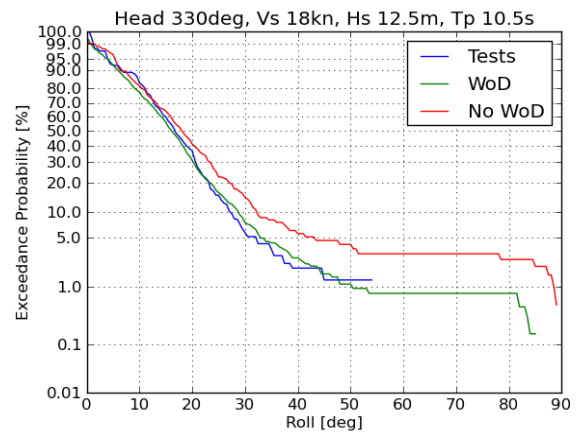


Figure 1: Cumulative roll exceedance probabilities

The ‘deck-edge-immersion’ method is implemented and has been used in the capsize probability simulations.

2.4 Ship model

Each ship - loading condition combination is considered as a ‘case’. The loading condition is defined in FREDYN by specifying the initial draft, trim and vertical centre of gravity. Each ship has its own set of moments of inertia, which are constant over all loading conditions.

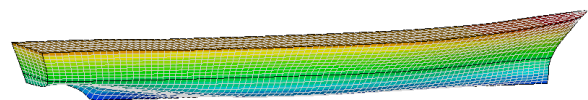


Figure 2: Typical panelized hull

When applicable, the bilge keels, static stabilizing fins and skegs were modelled. The skeg is modelled as a panelled part of the hull as well as a lifting surface. The bilge keels were discretised at least 4 locations along its length.

The roll damping is obviously an important



characteristic for these simulations. The FDS model is used to calculate the roll damping for all ships, see Blok [1991]. No tuning was done for any of the ships.

2.5 Speed Control

For each ship calm water runs were performed to determine the rpm / pitch setting for the required calm water speed. The calm water resistance is modelled by a single resistance curve for all loading conditions. Hence, the rpm / pitch settings were the same for the loading conditions of each ship. No speed control was used during the simulations. This implies that the actual speed of the ships in the simulations might vary considerably due to wind and wave forces. The reduced speed will have the consequence that the ship will have more difficulties to keep its heading and large deviations from the desired heading might be the result. This will influence the capsize probability for that particular heading.

FREDYN has the option to control the vessel speed. It can change the rpm and / or pitch setting in such a way that the ships' speed is maintained in varying conditions. Using it would have the following (dis)advantages:

- The average speeds of each wave condition are closer to each other, making them more comparable.
- In extreme conditions the ships might be better in keeping their heading.
- Under real circumstances the speed will be adapted to the environmental circumstances (probably by the operator).
- The average speeds might be quite different from the average speeds in earlier simulations which makes comparison more difficult.
- Using speed control might introduce unexpected effects.

Mainly for the last two reasons it was decided not to use speed control for the simulations.

2.6 Heading Control

The FREDYN heading control is based on a PID type controller where each ship has its own controller settings. The integration action was not used to avoid saturation of the rudder(s) in extreme conditions. In addition, the steering machinery can be modelled by specifying a maximum rudder rate.

The settings for the heading control and steering machinery were the same as had been used in earlier phases of the simulations.

2.7 Simulation Setup

All the choices made in the simulation and model set-up result in an almost real time performance of FREDYN. In view of the high number of simulations that was anticipated a lot of effort was spent to reduce these in an intelligent way. Reducing the number of irrelevant conditions (as discussed in §2.2) is just a first step. Predicting extreme events in a reliable way unfortunately requires a large amount of reliable data which in this case has to be collected by doing a large number of simulations. To make this possible use was made of Condor[®] which allows simulations to be done on idle workstation CPU's in the MARIN network. At the moment a maximum of approximately 600 nodes are available. To be able to use this grid efficiently the simulations should not be too long; if they are interrupted they have to be rescheduled again.

Initial studies on the application of the EPOT method for capsize probability assessment showed that to obtain an estimated uncertainty of approximately 5% 300~400 simulation hours were needed for a single operational condition (a single combination of wave height, wave period, ship speed and ship heading). Giving a realistic heavy weather duration of 3 hours this would have resulted in 100 runs per operational condition. Considering the number of cases (43) this

would have resulted in almost 2×10^6 3 hour simulations. To reduce this rather high value the duration of each simulation was reduced to 1 hour unavoidably resulting in a higher uncertainty of the final capsizing probability result.

Initially 10 simulations of 1 hour are done with different seed values to collect sufficient data for a single operational condition. Using the results from these simulations the hourly capsizing probability is calculated. If this value is above a preset limit then another 10 simulations are added for this operational condition until a maximum of 100 is reached. The rationale is that, if the capsizing probability is very low after doing a number of simulations, then it will not give a significant contribution to the overall value: hence no further simulations are needed. The preset limit value is rather arbitrary and is based upon results from earlier simulations.

3. CAPSIZE PROBABILITY & STATISTICS

3.1 EPOT method

Various methods were investigated to predict the capsizing probability for a single condition (speed, heading, wave height and period combination). Out of these methods, the Envelope Peaks-Over-Threshold (EPOT) proved to be most effective in the sense that it needed the least number of simulations for reliable results. The main benefit of the method is that it uses all extremes from a time series and not just the single maximum from a simulation. The workflow is as follows:

1. All the envelope peaks of the combined simulations for one operational condition are ranked resulting in a distribution free estimate for the cumulative distribution function.

$$\hat{F} x_i = \frac{i}{N_s + 1} \quad (2)$$

2. All but one envelope peaks exceeding

the Fredyn stop angle are removed (see §3.4 for details).

3. The threshold angle is determined by taking the 50th highest sample (see §3.3).
4. The distribution function's parameters σ and ξ (scale and shape) are estimated by fitting the data above the threshold to the Generalised Pareto Distribution (GPD) with a minimum error method. There is a third parameter, the location μ . This value is fixed by the selected threshold.

The GPD is given by:

$$F_{\sigma, \xi} x = \begin{cases} 1 - \left(1 + \xi \cdot \frac{x}{\sigma}\right)^{-\frac{1}{\xi}}, & \xi \neq 0 \\ 1 - \frac{1}{\sigma} e^{-\frac{x}{\sigma}}, & \xi = 0 \end{cases} \quad (3)$$

It is called 'generalised' because it is able to represent a whole class of distribution functions (depending on the parameters). The idea is to focus on the tail (values above the threshold) of the distribution. The distribution of extremes above a certain threshold μ can be given by:

$$F_{\mu} y = P(X - \mu \leq y | X > \mu) \quad (4)$$

$$0 \leq y \leq x_F - \mu$$

where μ is the threshold value, X the stochastic variable (in this case the envelope peaks), $F_{\mu}(y)$ the conditional probability that the value exceeds a threshold μ by at most y and x_F the right endpoint of the function $F_{\mu} y$. Pickands [1975] showed that for a large class of distributions functions (including Normal, Log-Normal, Chi-Squared, Student, F, Gamma) the conditional excess function $F_{\mu} y$ is well approximated by the GPD.

Using Bayes theorem on conditional probability and some math, see McNeil et al, [1999] results in an expression to be used with the estimated distribution parameters:



$$\hat{P}(X > z) = \frac{N_{obs>\mu}}{n_{obs}} \left(1 + \xi \frac{z - \mu}{\hat{\sigma}} \right)^{-\frac{1}{\xi}} \quad (5)$$

$$z > \mu$$

$\hat{P}(X > z)$ is the estimated probability that X is higher than the value z (the capsize probability), given that z is higher than the threshold μ . $N_{obs>\mu}$ is the number of observations (envelope peaks) above the threshold μ , $n_{obs>\mu}$ is the total number of observed envelope peaks and z is (in this application) the angle defining capsize (see §3.4)

3.2 Roll envelope peak determination

The EPOT method assumes independence of all used (roll) extremes. However, due to the strong non-linear behaviour an extreme roll angle is likely to be influenced by a previous extreme making these two extremes statistically dependent. An attempt to overcome these dependencies was to select the extreme of the envelope of roll amplitudes. The maxima of two successive envelope peaks are assumed to be statistically independent. The envelope is based on the absolute value of the roll signal, so it includes both the negative and positive extremes, see Figure 3. To further increase the independencies of the roll angle extremes the envelope of the envelope is calculated. The peaks of it are used in the EPOT calculation.

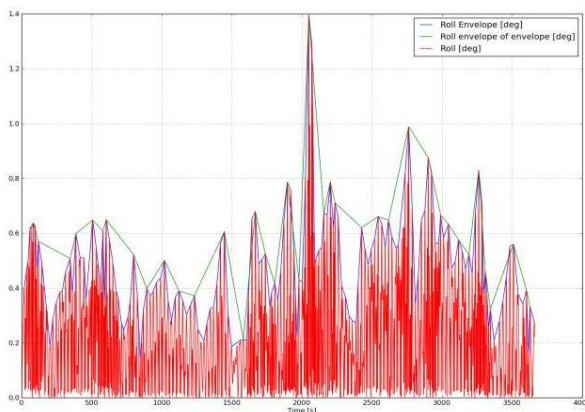


Figure 3: Envelope Peaks example

The EPOT probability distribution now provides the exceedance probability of a peak in the roll envelope. The average time span of such a roll envelope will be different for each condition and should therefore be normalized. For this CRNav work all capsize probabilities are normalised to a probability per hour. The probability found with the EPOT distribution must be transferred to an hourly time frame with :

$$P_{cap, hour} = 1 - P_{EPOT} \left(\frac{n_{peaks, env}}{T_{simulations}} * 3600 \right) \quad (6)$$

where $P_{cap, hour}$ is the hourly capsize risk, P_{EPOT} the exceedance probability derived from the EPOT fitting, $n_{peaks, env}$ the total number of roll envelopes in the simulations for this condition and $T_{simulations}$ the total simulation time for the condition in seconds. The formula scales the probability of capsize from the average envelope peak period to one hour.

3.3 Threshold selection

The selection of the threshold value of the EPOT method is very important as it determines the data set that is used to construct the fitting curve. Within the CRNav group the feeling exists that the selection may be linked to the angle at which certain non-linearity's start to become important and thus depend on certain physical features of the ship.

A logical choice could be the angle of maximum GZ as after that angle the spring term for roll changes rapidly. However, for a moving ship in large waves, this angle may be different from the static GZ-curve angle.

As at the moment virtually nothing is known about the relations between the ship or stability characteristics and the optimum threshold, it was decided to abandon this path for the time being as the available time was too limited for thorough research in this area.

Brabson [2000] suggested that the best threshold should be selected based on the

number of points beyond that threshold. If the number of points is too large the fitting curve is too much driven by the lower values so that the tail of the curve may not be represented well. If the number of points is too small the reliability of the fitting curve becomes too small.

This assumption was tested for four different sea states for a single ship - loading condition combination. The capsize probability was determined using the EPOT method for a systematically varied threshold value. The relation between the threshold angle and predicted capsize probability is shown in Figure 4.

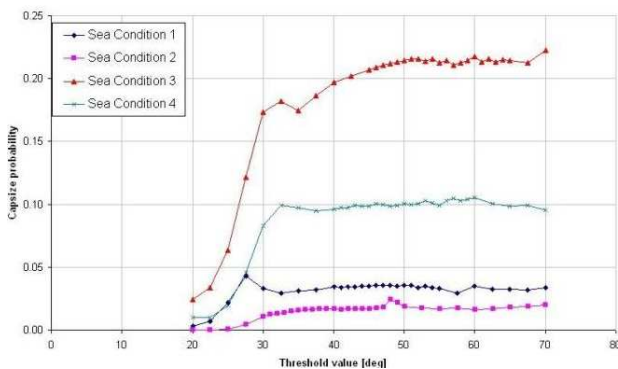


Figure 4: Threshold angle versus capsize probability

It can be seen that the capsize probability grows towards a more or less steady value, but if the angle becomes too large, the capsize probability starts to fluctuate. From the four examples it seems that the “optimal” threshold angle is larger if the capsize probability is larger.

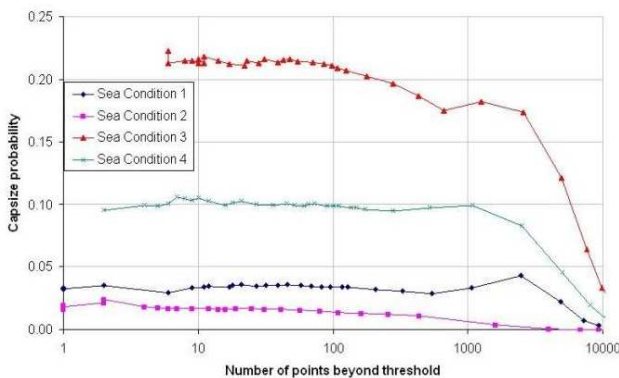


Figure 5: Number of point beyond threshold versus capsize probability

To further check the recommendations of Brabson [2000], the number of points beyond the threshold angle was plotted against the capsize probability in Figure 5 (note the log-scale in the horizontal axis).

For a low threshold angle, the number of points is high and it can be seen that the fitted curve is too much driven by the lower values so that the fat tail is not represented well. For a low number of points the prediction starts to fluctuate. The figure shows that the most stable part is found when there are approximately 50 points beyond the threshold angle. This number is used for the EPOT fitting as the number of points above the threshold.

3.4 Capsize vs. Stop Angle

As was explained earlier, the shape of the fitting curve can be negatively influenced if there is a number of extreme roll angles reaching the FREDYN stopping angle (angle at which FREDYN simulations are stopped). In reality at least some of these roll extremes would be larger than this stopping angle (some may be much larger if the angle of vanishing stability is reached). Using these extremes for the fitting curve would pull the tail of this curve to lower values, resulting in a lower capsize probability.

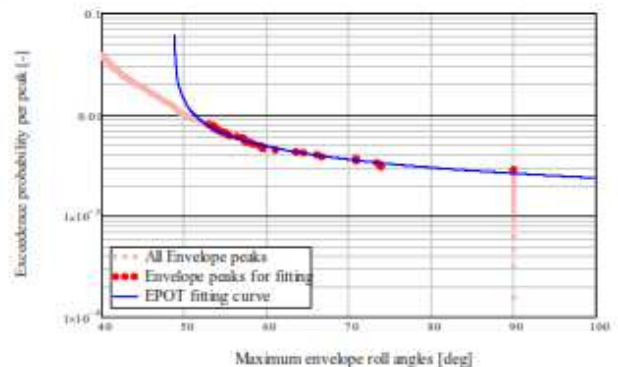


Figure 6: Elimination of FREDYN stop-angles

Eliminating all but one points that have reached the FREDYN stopping angle from the data set that is used for the fitting can solve this issue: see Figure 6.



The angle defining a capsize is set at a lower value of 70 degrees for all cases, while the stop angle was set at 90 degrees.

4. OVERALL CAPSIZE PROBABILITY

The overall capsize probability of a vessel should also include the probability of occurrence of the operational and environmental conditions. The probability of occurrence of the wave conditions is completely determined by the scatter-diagram (see §2.2). The occurring wind-speed is dependent on the wave condition, the wind direction is always coincident with the waves.

The probability of occurrence of the vessel speed is determined by the number of speeds defined by the user and is not directly linked to the operational profile of a ship. The same applies to the probability of occurrence of each heading, although the symmetry of the ship can be taken into account.

$$P_{total} \varphi > \varphi_{cap} = \sum_{i,j,k} P_{H_{S_i}, T_{P_i}, \beta_j, V_{S_k}} \cdot P_{cap, hour} \varphi > \varphi_{cap} | H_{S_i}, T_{P_i}, \beta_j, V_{S_k} \quad (7)$$

where $P_{cap, hour} \varphi > \varphi_{cap} | H_{S_i}, T_{P_i}, \beta_j, V_{S_k}$ is the conditional probability that the capsize angle is exceeded. It is determined using formula (5) and (6).

The probability of occurrence of a loading condition during the lifetime of a ship is not taken into account at the moment. This would be an additional refinement provided this information is available.

5. CAPSIZE SIMULATIONS

For the first set of simulations 11 frigate type hull forms were used. The designs varied from WWII designs (Farragut & Fletcher, see Friedman [1982] and Ross [1988]) to more recent designs. The WWII designs were

included to be able to link the capsize probabilities directly to the ships and loading conditions that were used to base the Sarchin & Goldberg criteria on. In total 43 cases were modelled: for each case the hull needed to be modelled to take changes in draft and trim into account.

6. DISCUSSION & CONCLUSIONS

A new method is proposed and implemented to determine the capsize probability of a ship in a seaway taking into account the physical properties of a ship, the loading condition and the environmental conditionals.

The method uses time-domain simulations to collect the peaks of the roll envelope and fits the values that are above a threshold to a Generalised Pareto Distribution. The resulting function is used to estimate the probability of exceedance of the capsize angle and hence the capsize probability.

It is important to realise that the proposed method results in relative and no absolute probabilities. To determine absolute probabilities is a much more complex undertaking. For example, the influence of the operator will have a major impact on the probability of occurrence of speeds and headings in relation to the environmental conditions. In addition, an operator can also take the wrong decisions. This level of complexity is not included in this method.

To keep the method practical, the implementation aims to reduce the number of simulations as much as possible. A number of pragmatic choices had to be made but with the combined CRNav experience gained in 10 years, it is believed that the current results are representative for the cases that were included in the project.

The method described in this paper has been implemented in a simulation handling and post-processing tool called „Lorelei“, see



Figure 7. It uses Condor[®] to submit simulations over a computer network. It does all the probability calculations and adds simulations when necessary. The final answer is an hourly capsize probability for a single ship-loading condition.

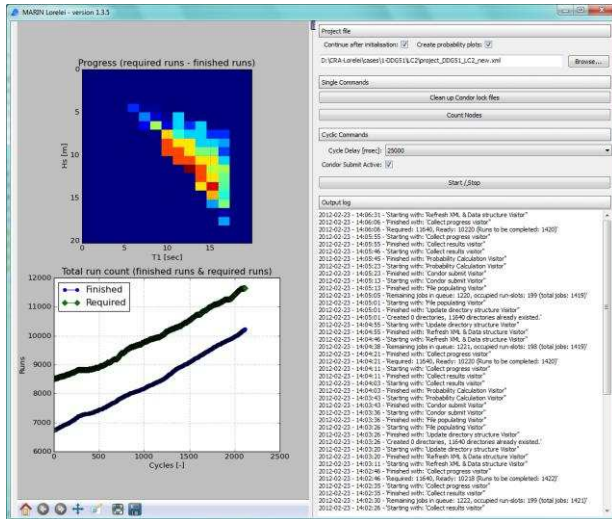


Figure 7: Lorelei in action

The first simulation project is completed and incorporated 11 frigate / destroyer type ships and a total of 43 ship-loading condition combinations. A total of approximately 300,000 simulations of one hour (or shorter in case of a capsize) were done to collect the data and to compute the overall capsize probability of these 43 cases.

The results of the simulations have been used in a regression study to find relations between characteristic ship parameters and the capsize probabilities. The objective of that study is to find simple relations that can be used early in the design process to compare the capsize probability of new ship designs to the values of existing designs.

The results are encouraging and will be used in an analysis to find a relation between the capsize probability and the driving (hydrostatic) ship properties. More details can be found in Perrault [2012] and Harmsen [2012], see Figure 8 for the typical results of a single operational condition.

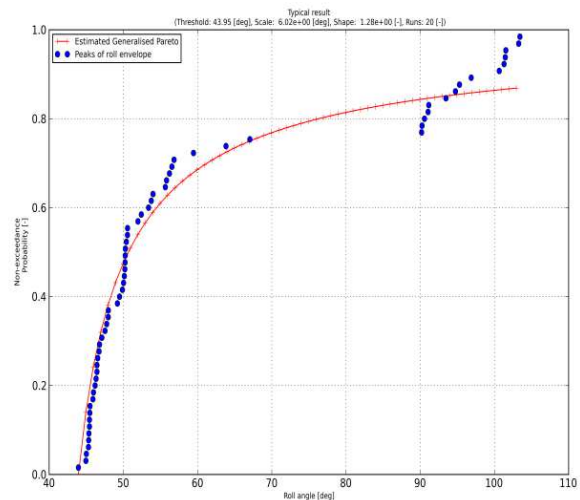


Figure 8: Typical result of a fitted GPD

In the near future more ship-loading condition combinations and different ship types will be added to a database. This will make the data accessible for certified users and make data mining possible.

7. REFERENCES

Bales, S.L., Lee, W.T., Voelker, J.M., July 1981, Standardized wave and wind environments for NATO operational areas, ANEP 11, David W. Taylor Naval Ship Research and Development Center, DTNSRDC/SPD-0919-01

Campbell, B., Belenky, V., June 2010, Assessment of Short-Term Risk with Monte-Carlo Method, Proceedings of the 11th International Ship Stability Workshop.

McTaggart, K., Savage, M., November 1994, Wind heeling loads on a naval frigate, Proceedings of the fifth International Conference on Stability of Ships and Ocean Vehicles STAB '94, Melbourne, Florida.

Brabson, B.B., Palutikof, J.P., September 2000, Tests of the Generalised Pareto Distribution for Predicting Extreme



Wind Speeds, American Meteorological Society.

Friedman, N., 1982, U.S. Destroyers – An illustrated design history, Naval Institute Press, ISBN 0-87021-733-X.

Ross, A., 1988, Anatomy of the ship – The destroyer the Sullivans, Conway Maritime Press Ltd., ISBN 0 85177 476 8,

van Walree, F., Carette, N., Oct. 2010, “Validation of Time Domain Seakeeping Codes for a Destroyer Hull Form Operating in Steep Stern-quartering Seas”, ITTC Workshop on Seakeeping, Seoul, Korea

Blok J.J. and Aalbers A.B., 1991, "Roll damping due to lift effects on high speed monohulls", 1st International Conference of High Speed Sea Transportation, FAST'91, Trondheim, Norway.

McNeil, A.J. et al, 1999, Extreme Value theory for Risk Managers, Department Mathematik, ETH Zentrum, Zurich, Switzerland.

Pickands, J., 1975, 2Statistical Inference using extreme value theory. Annals of Statistics, number 3, page 119-131

Harmsen, E., Marshall, S., Deriving Intact Stability Criteria from the Capsize Risk of Naval Frigates, STAB 2012, Athens, Greece

Raven, H.C.; "Variations on a theme by DAWSON", Proceedings of 17th Symposium on Naval Hydrodynamics, The Hague, Netherlands, 1988.

De Kat, J.O., McTaggart, K., 2000, Capsize Risk of Intact Frigates in Irregular Seas”, Transactions SNAME, Vol. 108, pp.147-177



Critical Wave Groups vs. Direct Monte-Carlo Simulations for Typical Stability Failure Modes of a Container Ship

Vladimir Shigunov, *Germanischer Lloyd SE, Hamburg, Germany*, vladimir.shigunov@gl-group.com

Nikos Themelis, *Department of Naval Architecture and Marine Engineering, National Technical University of Athens, Athens, Greece*, nthemelis@naval.ntua.gr

Kostas J. Spyrou, *Department of Naval Architecture and Marine Engineering, National Technical University of Athens, Athens, Greece*, k.spyrou@central.ntua.gr

ABSTRACT

In the new generation intact stability criteria currently debated at IMO, the process of direct assessment of stability is interlaced with a requirement of performing several numerical simulations. However, extreme responses that are generally behind stability failures are rare events, usually based on the non-Gaussian roll response stochastic process. A practical approach discussed recently exploits the idea that extreme events occur due to the encountering of extreme wave groups (critical wave episodes). This could alleviate the need for a large number of simulations by focusing on the systematic identification of those deterministic wave sequences that generate unacceptable roll responses. Taking a first step towards a systematic validation process of the wave groups method, the present study compares the exceedance probabilities of 40 deg roll angle and of $g/2$ lateral acceleration, computed by the critical wave groups method for a large containership, with Monte-Carlo simulations. The nonlinear seakeeping code *rolls* is used as mathematical model of ship motion. Typical loading conditions where various stability failure modes can occur are examined.

Keywords: Numerical Simulations; Monte Carlo Method; Critical Wave Groups

1. NOMENCLATURE

B_{wl}	waterline breadth	p	probability
GM	initial metacentric height	r	exceedance rate
g	acceleration due to gravity	T_m	mean draft
H	wave height	T_w	wave period
\mathbf{H}	vector of wave heights in a wave group	T_z	zero upcrossing period of the seaway
H_{cr}	threshold wave height	T_ϕ	linear natural roll period
\mathbf{H}_{cr}	vector of critical wave heights	T_1	mean seaway period
h_s	significant wave height	v	ship speed
KG	centre of gravity height above keel	μ	mean seaway direction (0 and 180° for following and head seas, respectively)
L_{pp}	length between perpendiculars	ω_ϕ	linear natural roll frequency



2. INTRODUCTION

Application of numerical simulations for direct stability assessment is currently discussed at IMO as an important part of the new generation intact stability criteria. This requires both sufficiently accurate mathematical models of nonlinear ship dynamics, and rational probabilistic procedures able of predicting probabilities of rare extreme motion events for non-Gaussian processes.

A practical solution for the latter problem proposed by Themelis & Spyrou (2007) exploits the idea that extreme events occur due to the encountering of extreme wave groups (critical wave episodes). The identification of the critical wave groups in terms of height, period and duration is then possible on the basis of nonlinear deterministic ship motion analysis, while the probability of encountering specific wave groups is based on statistical seaway models.

The method is by its nature approximative in its consideration of the ship-wave encounter, because, at its current stage of development, certain regular wave profiles are examined. On the other hand, the method is very versatile, combining arbitrarily sophisticated nonlinear analysis of ship dynamics (and thus any stability failure mode captured by the method used for motion analysis) with accurate probabilistic analysis of the seaway.

The present study is a step towards the comparison of this method with the direct stability assessment through numerical simulations with the nonlinear seakeeping code *rolls*, for typical stability failure modes of a modern post-panamax container ship in a range of practically relevant initial *GM* values. Short-term average exceedance rates of the maximum (over the ship) lateral acceleration value $g/2$, as well as of roll angle 40 deg, are determined from Monte-Carlo simulations. They are compared against the exceedance rate obtained by using the critical wave groups approach.

3. CRITICAL WAVE GROUPS

According to the principle of this method, the ship can be assumed as performing initially ordinary (linear) oscillatory motion of small to moderate amplitude in the considered mode(s). Then extreme behavior is realised due to the encounter of a wave group. Thus the critical wave groups identification process supplies in fact the threshold excitation that generates undesirable ship behavior. Such wave groups are identified for frequencies spanning the usual range of wave frequencies. Each group is characterised by its run length, period and height. However, the choice of fixed height does not imply that groups physically display such a property. Instead, it specifies the critical height above which ship behavior exhibits at least one unacceptable characteristic. As for the discrete period, it should be seen as a representative of the small range of periods around it. It is important to note that, in the implementation of this method, all wave groups that result in undesirable dynamic response are extracted beforehand. Then, probabilities can be determined for encountering conditions “worse” than the critical, for the seaway situations that exist in the considered area of ship operation.

The process of consecutive waves is modeled as a first order “autoregressive model” which is in fact equivalent to assuming the Markov chain property for the waves, a well established characteristic of sea waves. However, it is essential that no similar assumption is necessary concerning roll response. The targeted probability is calculated as the product of (1) the conditional probability $p(T|H > H_{cr})$ of encountering n successive waves with periods T , lying in a specific range, and heights above a threshold level H_{cr} , and (2) the probability $p(H > H_{cr})$ that n successive waves have heights exceeding this critical threshold¹. For

¹ The slightly unorthodox inequality in the above means that each component of vector \mathbf{H} obtains greater value than the corresponding value in vector \mathbf{H}_{cr} . However, in the current implementation, all entries of vector \mathbf{H}_{cr} receive the same value H_{cr} .

the calculation of the first probability, the conditional multivariate normal probability density function (pdf) is used (Wist et al., 2004), combined with Tayfun (1993) work on the joint probability density function (pdf) of large wave height and its associated period. On the other hand, the calculation of $p(H > H_{cr})$ is based on the bivariate Rayleigh pdf of two successive wave heights, Battjes & Van Vledder (1984), combined with the Markov chain property. This modelling approach can handle efficiently both the period and the height of successive waves and represents a key step beyond the Kimura-type modelling of wave groups that is not sensitive to the period, Kimura (1980).

4. SHIP AND LOADING CONDITIONS

A modern 8000 TEU container ship was selected for the study. Such vessels are presently the work horses of east-bound container shipping routes, and many of them might be employed in west-bound routes with more harsh weather conditions after the modernisation of Panama channel. Many years of full-scale measurements onboard several vessels of this size are available, thus their loading and speed profiles are well known. Moreover, roll damping parameters are known from model tests.

The selected vessel has a length between perpendiculars of about 320.0 m, waterline breadth of about 43.0 m and design speed of about 25.0 knots. Vessels of this size operate most frequently in partial loading conditions with GM from about 2.5 to about 4.5 m; such loading conditions are relatively safe with respect to both parametric and synchronous resonance. Therefore, a wider range of loading conditions was studied, Table 1, including (1) nearly full load with GM of 1.2 m, which might be vulnerable to parametric roll, (2) a “typical” loading condition with GM of 3.8 m and (3)

Table 1: Loading conditions

T_m [m]	14.44	12.84	11.36
GM [m]	1.2	3.8	7.5
T_ϕ [s]	30.1	18.5	12.6

ballast loading condition with a very high GM of 7.5 m, expected to lead to large lateral accelerations due to synchronous roll.

5. SELECTION OF SPEEDS AND SEAWAY PARAMETERS

Synchronous roll is most relevant in beam waves, where the added resistance is rather low and thus forward speed can be rather high, see case 01 in Table 2. The corresponding critical seaway parameters for this loading condition are shown with a black point in Figure 1.

Table 2: Selected conditions

Case	GM [m]	Fr [-]	μ [°]	T_1 [s]
01	7.50	0.16	98.0	11.5
02	1.26	0.09	50.0	10.0
03	1.26	0.12	49.0	9.2
04	1.26	0.04	180.0	13.4
05	3.80	0.16	60.0	12.7

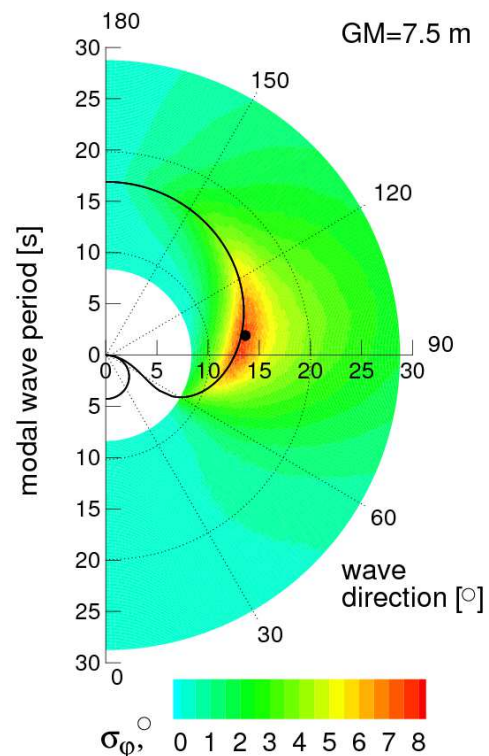


Figure 1: Calculated rms of roll angle for the loading condition with $GM=7.5$ m at $Fr=0.16$ in irregular waves vs. modal wave period and wave direction (radial and circumferential coordinates, respectively). Black line indicates resonance condition.



Principal parametric resonance occurs typically at low GM in following waves (at low forward speeds) to quartering waves (at higher forward speeds, which are more realistic in waves from the stern directions), Shigunov et al. (2009). Cases 02 and 03 in Table 2 represent this failure mode, and Figure 2 shows these cases on polar plots; two cases are selected to study the influence of the ship speed.

Principal parametric resonance also occurs at low GM in head waves at low forward speeds, which are realistic in high head waves; case 04 in Table 2 and Figure 3 illustrate the selected seaway conditions and the ship forward speed.

Finally, case 05 in Table 2 and Figure 4 represent direct excitation case for a “typical” loading condition.

6. MONTE-CARLO SIMULATIONS

To study the influence of the significant wave height on the accuracy of the critical wave groups method, significant wave height was systematically varied with a small step for each of the selected combinations 01 to 05 of wave direction, wave period and ship speed. Simulations were performed in long-crested seaways described by JONSWAP spectrum with the peak parameter $\gamma=3.3$. For each combination of ship speed and seaway parameters, 50 to 500 simulations were carried out with different initial phases of seaway components, until maximum over the ship lateral acceleration exceeded the value $g/2$. In the other series of simulations (denoted as cases 01a to 05a, with the conditions corresponding to those in cases 01 to 05), exceedance of the roll angle of 40 deg was considered as the extreme event. The average exceedance period was calculated by averaging over all exceedance periods. Numerical simulation method *rolls*, proposed by Söding (1982), was used for simulations (see Petey, 1986, for details of the method and Shigunov et al., 2009, for validation examples).

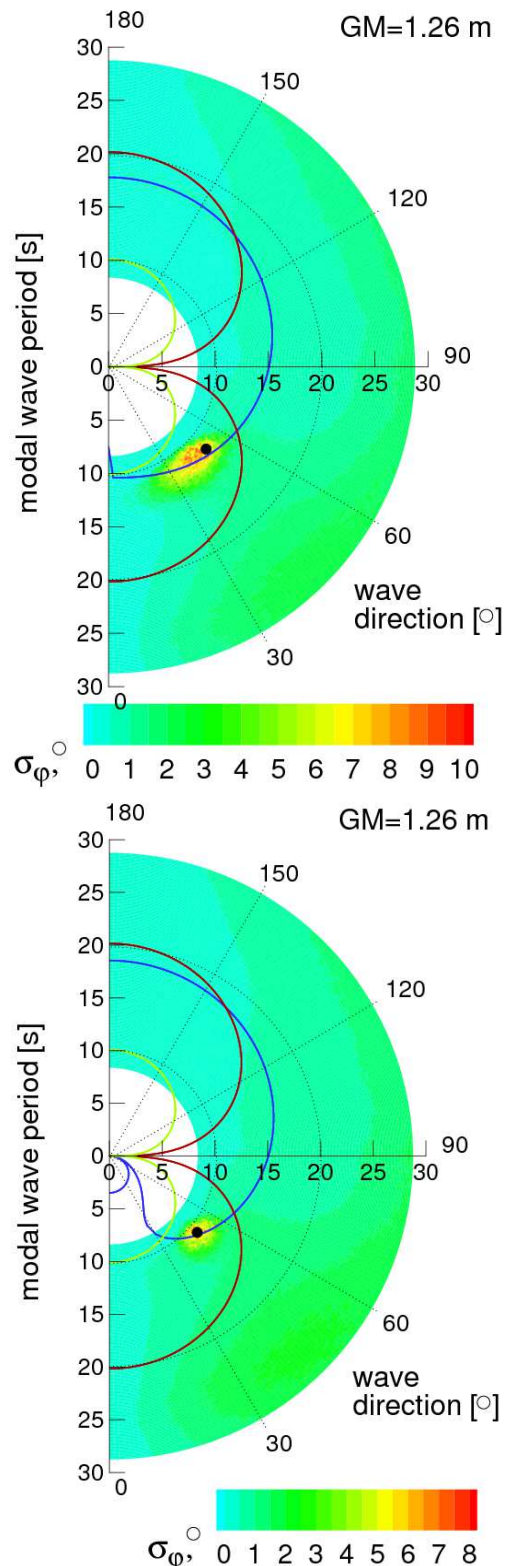


Figure 2: Calculated rms of roll angle for $GM=1.2$ m at $Fr=0.09$ (top) and 0.12 (bottom); the black points indicate representative scenarios for parametric resonance in quartering waves; blue line indicates resonance condition while yellow and green lines limit the area of suitable wave lengths.

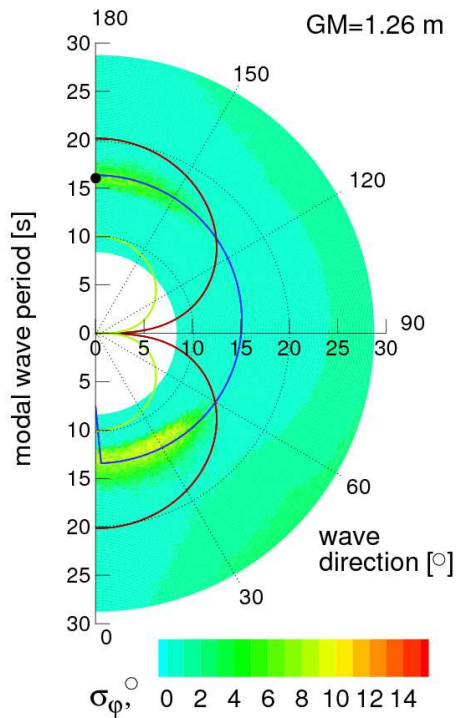


Figure 3: Calculated rms of roll angle for GM of 1.2 m and Fr of 0.04 in irregular waves. Black point indicates selected case for parametric resonance in bow waves; blue line indicates resonance condition, yellow and green lines limit the area of suitable wave lengths.

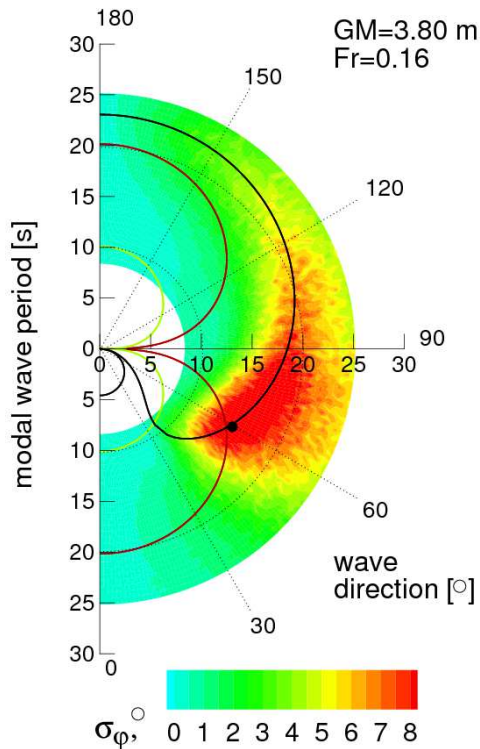


Figure 4: Calculated rms of roll angle for $GM=3.8$ m at $Fr=0.16$ in irregular waves.

7. CALCULATION OF HYDRODYNAMIC DATABASE

For each of cases 01 to 05 (and 01a to 05a, respectively), a corresponding hydrodynamic database of roll responses in regular waves was computed. The period of regular waves was varied in a broad range with a step of 0.5 s, and GM , forward speed and wave direction were kept constant. The same simulation method *rolls* was used for the computation of the hydrodynamic database. The initial condition was an upright ship with zero roll velocity.

Time histories of responses (maximum over the ship lateral acceleration or roll angle) are processed to obtain response maxima, i.e. $\max(a_n, -a_{n^*})$, Figure 5, per cycle of oscillation. Figure 5 explains the definitions used: the reaction period n from the start of simulation and $*$ for negative peaks. Post-processing considered 9 roll cycles. The wave height was varied until the response maximum in each response period exceeded the threshold ($g/2$ for lateral acceleration or 40 deg for roll amplitude). In this way, nine “critical” wave height values $H_{cr}(T, n)$, $n=1, \dots, 9$ were identified, each of which leads to a response amplitude equal to, or greater than, the threshold during the corresponding wave encounter.

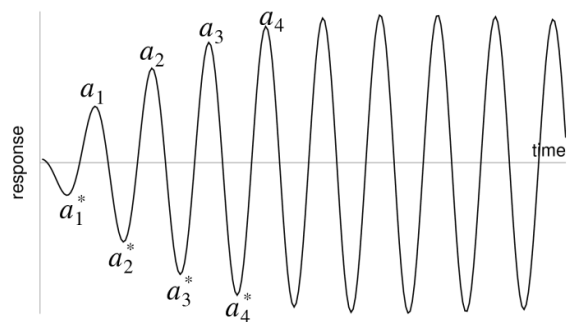


Figure 5: Post-processing of responses in regular waves.

Figures 6 and 7 present examples of the identified critical wave heights. The corresponding scenario and the threshold are also indicated. The shown curves were obtained for the wave group period equal to the mean period of the seaway, Table 2.

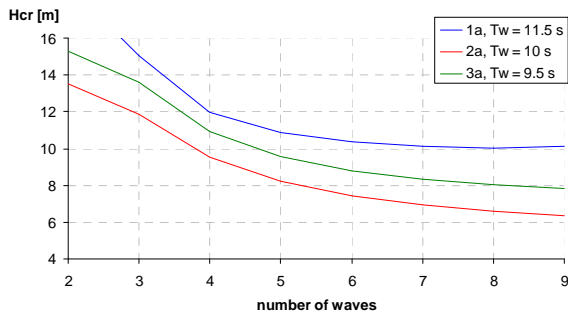


Figure 6: Characteristics of critical wave groups for 40 deg roll angle exceedance.

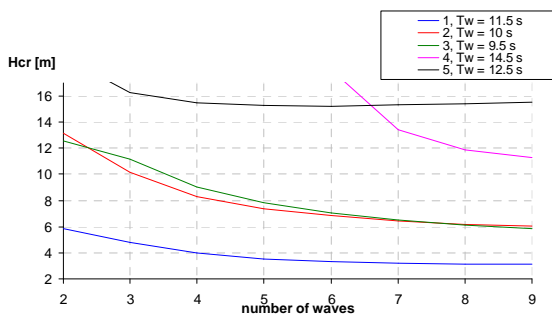


Figure 7: Characteristics of critical wave groups for $g/2$ lateral acceleration exceedance.

In general, exceedance of 40 deg roll angle requires higher waves than those required to exceed $g/2$ lateral acceleration. Figure 6 also indicates that higher waves are required for 40 deg roll angle exceedance in beam seas (case 01a) compared to quartering seas parametric roll (at a low forward speed with $Fr=0.09$ – case 02a, and at a higher forward speed with $Fr=0.12$ – case 03a). Figure 7 indicates that the exceedance of acceleration threshold in beam seas is realised in lower waves (case 01) compared to the two quartering sea parametric roll scenarios 02 and 03.

The critical heights for case 04 (parametric rolling in head seas at low speed) and case 05 (direct excitation in a typical loading condition) are much higher than those in cases 01, 02 and 03. Note that the identified critical wave heights for cases 04a and 05a (these correspond to the 40 deg roll angle threshold) were found to be extremely high even for high run length (they are not shown in Figure 6), and thus their encounter probability should be very low.

8. EXCEEDANCE RATE AND HOURLY PROBABILITY OF EXCEEDANCE

To calculate the exceedance rate by the critical wave groups approach, the same JONSWAP spectrum was used as in the Monte-Carlo simulations. Figures 8 and 9 show the calculated exceedance rates per case and threshold (roll angle and lateral acceleration) obtained by the two methodologies, as a function of the inverse significant wave height squared.

For the 40 deg roll angle threshold (Figure 8), case 02a presents the best example of agreement between the two approaches. For case 03a, the results are in a satisfactory

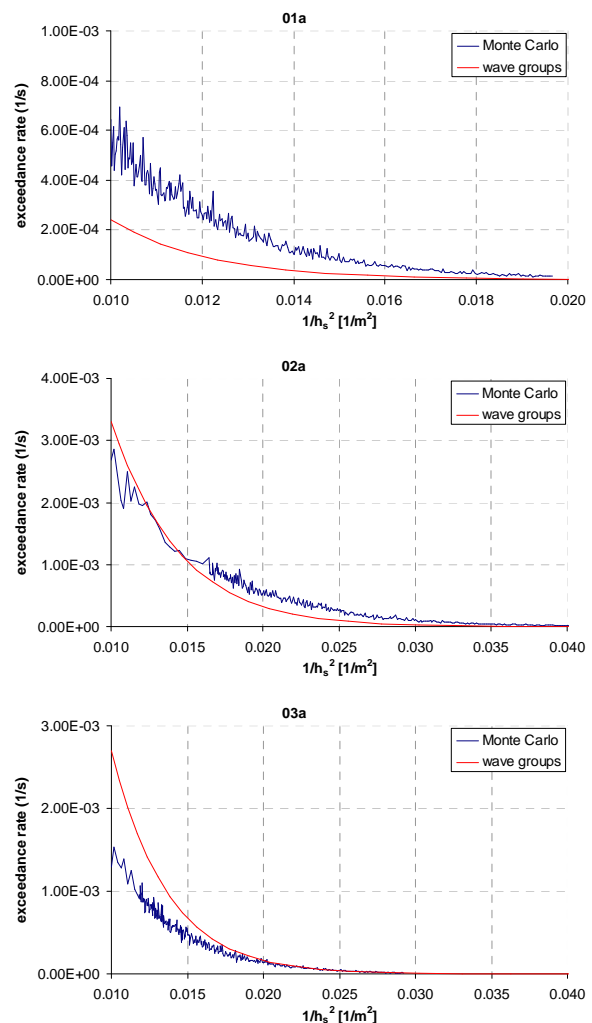


Figure 8: Comparison of exceedance rate of 40 deg roll angle between Monte-Carlo simulations and wave groups approach.

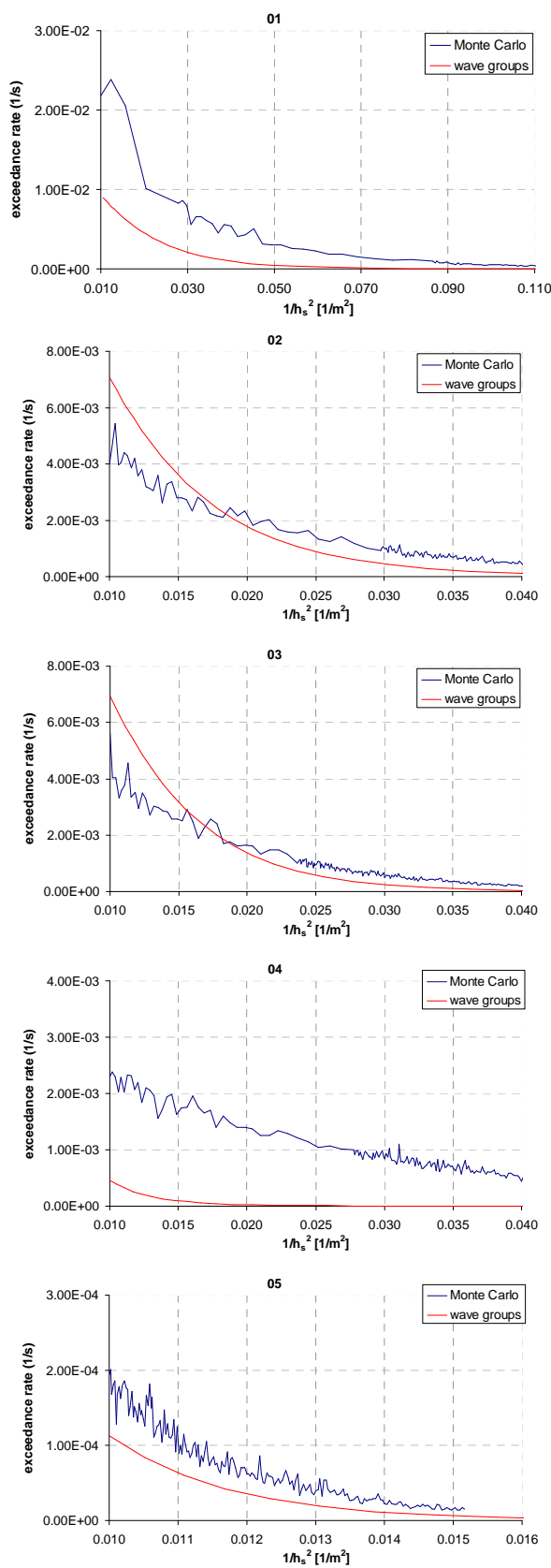


Figure 9: Comparison of exceedance rate of $g/2$ lateral acceleration between Monte-Carlo simulations and critical wave groups approach.

agreement for $1/h_s^2$ larger than 0.015 1/m^2 , but for the smaller values, the wave groups approach predicts higher rates. On the other hand, the exceedance rates obtained with Monte-Carlo simulations for case 01a are consistently higher than those of wave groups approach.

Figure 9 shows the results related to the acceleration threshold (cases 01 to 05). Case 05 demonstrates the best agreement here, and cases 02 and 03 agree well on average. Moreover it is observed that, for the more severe sea states examined, the “wave groups” approach predicts more frequent exceedances for cases 02 and 03. The largest discrepancies arise for cases 01 and 04, where Monte Carlo simulations predict far more frequent exceedances in the whole range of wave heights.

Knowing the exceedance rate r , the probability of exceedance during a given exposure time T (e.g. one hour) can be calculated using Poisson law for the flow of the exceedance events. Both exceedance rate and probability of exceedance per given time have advantages, and offer different comparison viewpoints on the results. The next formula can be used:

$$p(T) = 1 - e^{-rT} \quad (1)$$

The applicability of the Poisson flow assumption depends upon the validity of certain assumptions, namely that

- only one event can happen at a given time
- the probability of event happening at a particular time instant is infinitely small
- events are independent of each other.

While the first two conditions are satisfied for roll motion and related processes, the last condition is not, because exceedance events of a certain large roll angle tend to appear in groups. In order to cancel the influence of this strong auto-correlation of roll motion, average estimates of the exceedance time period, derived from multiple realisations of the same



seaway, were used in the Monte-Carlo simulations, as proposed by Söding (1987), see Shigunov (2009) for application. Each simulation was continued only until the first exceedance event; then the ship was returned to the upright position, and the simulation was repeated in the same seaway with the new set of random phases, frequencies and directions of seaway components until the next exceedance event. The estimation of the expected exceedance period is found as the average of the exceedance periods obtained in all simulations.

Figure 10 shows the respective results for the 40 deg threshold for each stability failure case. Case 03a seems to show the best agreement between the two approaches in terms of the hourly probability. Larger deviation of the rate occurs at the smaller values of $1/h_s^2$ than 0.015 1/m^2 , where the hourly probability is close to 1.0 anyway. Cases 01a and 02a could be also considered as adequately close. The average relative difference between the two methods in terms of h_s corresponding to the same exceedance probability is 9.4% and 7.8% for cases 01a and 02a, respectively.

Figure 11 shows results for the $g/2$ lateral acceleration threshold. Case 05 demonstrates the best agreement between the two methods, similarly to what was observed for the exceedance rate. Relative differences between the two methods in terms of h_s corresponding to the same hourly exceedance probability are 15.6% and 10.45% for cases 02 and 03, respectively.

On the contrary, there is a significant disagreement in the exceedance of acceleration threshold for the beam-sea scenario (case 01) and for the head-sea scenario (case 04). Specifically, for the beam-sea scenario, the 90% exceedance probability within one hour exposure corresponds to significant wave heights 3.31 and 4.78 m for the Monte-Carlo simulations and wave groups method, respectively. For the head-sea scenario, the corresponding wave heights are 5.2 and 10.6 m, respectively. Table 3 shows the significant wave heights cor-

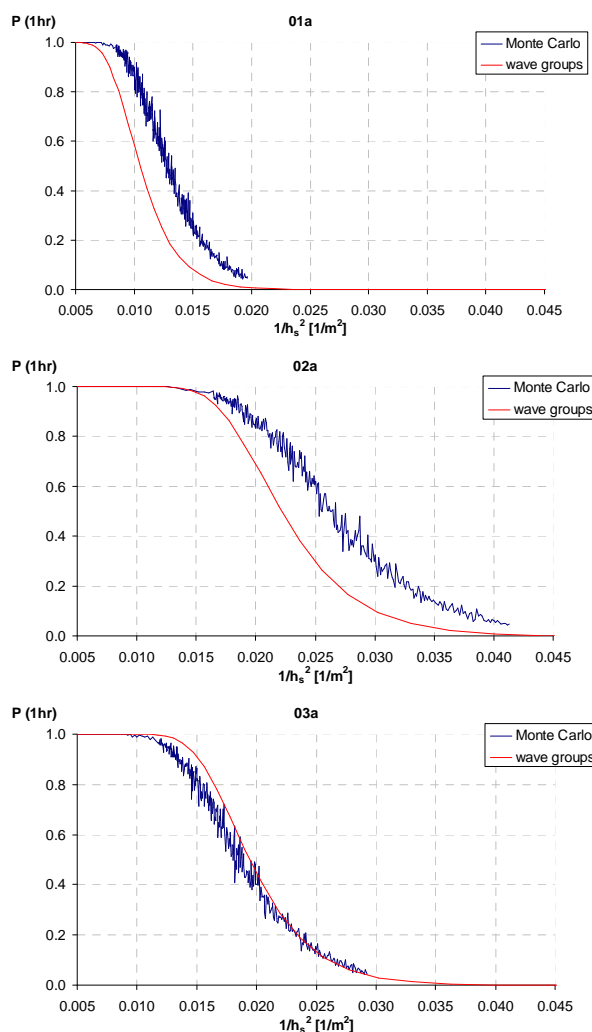


Figure 10: Comparison of exceedance probability per hour of roll angle 40 deg between Monte-Carlo simulations and critical wave groups approach.

responding to 90% hourly probability of exceedance for all examined cases.

The order of the magnitude of probabilities seems to be the same between the two approaches, with the exception, however, of case 04 related to the acceleration threshold in reference to head-sea parametric rolling. Further work will be required in order to identify the reason of the differences in this case.

However it is recalled that a Monte-Carlo method captures the statistic of a process without identifying the phenomenon, whilst the wave groups methods addresses each specific phenomenon individually.

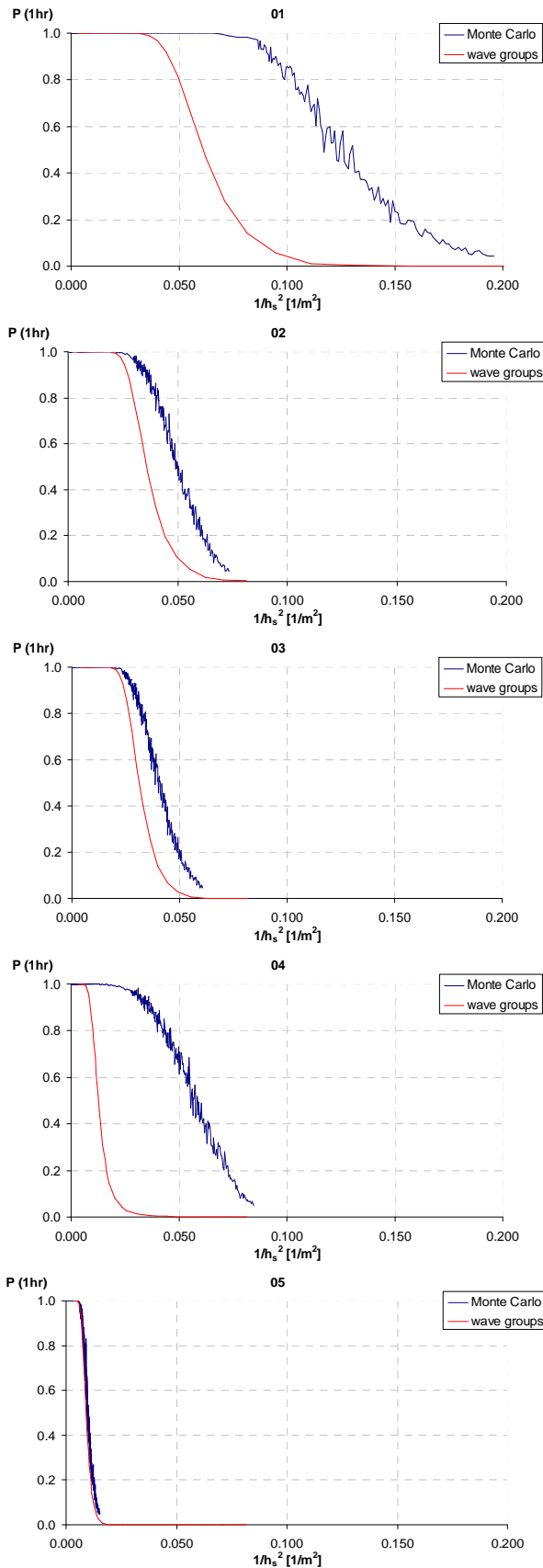


Figure 11: Exceedance probability per hour of $g/2$ lateral acceleration from Monte-Carlo simulations and wave groups approach.

Table 3: Significant wave heights required for 90% hourly probability of exceedance.

case	Monte-Carlo	wave groups	relative difference
01a	10.11	11.25	10.13%
02a	7.10	7.63	6.89%
03a	8.50	8.13	-4.62%
01	3.31	4.63	28.43%
02	5.30	6.13	13.47%
03	5.70	6.30	9.52%
04	5.20	10.60	50.94%
05	11.75	11.90	1.26%

For the 40 deg roll angle exceedance criterion, case 02a appears to produce the most frequent exceedances, while case 01a the least frequent. On the other hand, both approaches indicate that case 01 is the most critical for the acceleration threshold, followed by cases 02 and 03. These trends follow the trend of the required wave heights in Figures 6 and 7.

9. CONCLUSIONS

A comparison of exceedance rates and probabilities obtained by Monte-Carlo simulations and the critical wave groups approach has been carried out. Typical stability failure modes have been studied. Thresholds were set in terms of the roll angle and the lateral acceleration. In some cases satisfactory agreement was shown, e.g. for parametric rolling in quartering seas (cases 02 and 03) and direct excitation (case 05), but in some other cases, such as head seas parametric rolling, the difference was not negligible. A factor that can be governing certain discrepancies, especially when these are within an order of magnitude, is the different initial phasing, because in the wave groups method, the ship is assumed initially upright and with a fixed phase with respect to the first wave crest. An assessment of the effect of the initial phase on the results of the wave groups method can be found in Themelis & Spyrou (2008). On the other hand, the average exceedance rate in Monte-Carlo simulations was derived by averaging over a large number of



realisations, in each of which the ship was assumed initially upright, but the phases of wave realisations changed randomly.

A source of large quantitative differences, however, can be the fact that Monte-Carlo simulations do not discriminate between phenomena and record threshold exceedance events irrespectively of the underlying causes, which could, in principle, be more than one per realisation. On the other hand, the wave groups method is implemented for each scenario with one specific phenomenon in mind.

A further factor that could produce higher exceedance rate in Monte-Carlo simulations is the possible non-monotonic increase of roll amplitude with time, which can occur due to the passage of a wave group having an intermediate wave with height below the critical one. The critical wave group approach as used in this paper excludes such events, as it sets the same value for the heights of the waves in the group (vector **H** mentioned in section 3). A further study taking into account intermediate variation of the heights of the groups and their associated probabilities of occurrence will consider this effect.

10. REFERENCES

- Battjes, J. A., and van Vledder, G. Ph., 1984, "Verification of Kimura's theory for wave group statistics", Proceedings of the 10th Int. Conf. on Coastal Engineering, pp. 642-648.
- Kimura, A., 1980, "Statistical properties of random wave groups", Proceedings of the 17th Int. Conf. on Coastal Engineering, Sydney, Australia, pp. 2955-73.
- Petey, F., 1986, "Forces and moments due to fluid motions in tanks and damaged compartments", Proceedings of the 3rd Int. Conf. on Stability of Ships and Ocean Vehicles STAB'86, Gdansk.
- Tayfun, M. A., 1993, "Joint distributions of large wave heights and associated periods", Journal of Waterway, Port, Coastal and Ocean Engineering, Vol. 119, pp. 261-273.
- Themelis, N., and Spyrou, K. J., 2007 "Probabilistic assessment of ship stability", SNAME Transactions, Vol. 115, pp. 181-204.
- Themelis, N., and Spyrou, K. J., 2008, "Probabilistic assessment of ship stability based on the concept of critical wave groups." Proceedings of the 10th International Ship Stability Workshop, Daejeon, Korea.
- Shigunov, V., el Moctar, O., and Rathje, H., 2009, "Conditions of parametric roll", Proceedings of the 10th Int. Conf. on Stability of Ships and Ocean Vehicles STAB 2009, St. Petersburg.
- Shigunov, V., 2009, "Operational Guidance for Prevention of Container Loss", Proceedings of the 10th Int. Conf. on Stability of Ships and Ocean Vehicles STAB 2009, St. Petersburg.
- Söding, H., 1982, "Leckstabilität im Seegang", Report No. 429, Institut für Schiffbau, Hamburg.
- Söding, H., 1987, "Ermittlung der Kentergefahr aus Bewegungssimulationen", Schiffstechnik, Vol. 34, pp. 28-39.
- Wist, H., Myrhaug, D., and Rue, H., 2004, "Statistical properties of successive wave heights and successive wave periods", Applied Ocean Research, Vol. 26, pp. 114-136.



Application of Stochastic Dynamical System to Nonlinear Ship Rolling Problems

Jeffrey Falzarano, *Texas A & M University*, jfalzarano@civil.tamu.edu

Zhiyong Su, *Texas A & M University*, lincsu@neo.tamu.edu

Arada Jamnongpipatkul, *Texas A & M University*, plummy23@neo.tamu.edu

ABSTRACT

The stochastic nonlinear dynamic behaviour and probability density function of ship rolling are studied using the dynamical systems approach and probability theory. Two different methods are applied to the nonlinear ship rolling problems in this paper: Moment Equation and Path Integral Method. The moment equation is generated from a six state space rolling model with a fourth order linear filter using the Itô differential rule. By considering the excitation as a harmonic force with white noise disturbance, the probability density function of the rolling response is evaluated through solving the Fokker Planck Equation by path integral method.

Keywords: *Nonlinear Rolling; Random Waves; Filtered white noise; Non Gaussian Cumulant Neglect Method; Path integral method; Capsizing Probability; Fokker Planck Equation.*

1. INTRODUCTION

Safety against capsizing in heavy sea is one of the major concerns of ship operators and designers. Dynamical behaviours of ship have been of interest to many researchers and engineers, particularly in stability of roll motion. Prior to capsizing, ships will undergo severe roll motion. The motion is believed to be chaotic. Identifying the chaotic motion and its critical condition are important for both predicting ships' capsizing and studying the capsize mechanism.

Large amplitude ship rolling motion under random beam sea has been approached several times by different research groups, including Markov methods and non-Markov methods. Non-Markov methods include statistical equivalent linearization (Roberts and Spanos, 2003), perturbation methods, Monte Carlo methods and Melnikov methods (Falzarano et al., 1992; Hsieh et al., 1994; Jiang et al., 1996; Jiang et al., 2000) and Vakakis methods (Vishnubhotla et al., 2000; Falzarano et al., 2004; Falzarano et al., 2005; Vishnubhotla and

Falzarano, 2009; Falzarano et al., 2010). Markov methods include the stochastic averaging method (Roberts and Vasta, 2000), moment closure and the direct solution of the Fokker-Planck-Kolmogorov (FPK) equation (Naess and Moe, 2000). The FPK equation is limited to the Markov assumption and ideal white noise excitation or filtered white noise. Since wave excitation spectrum normally have a central peak and limited bandwidth, a method of transformation between ideal white noise and colored noise has been developed using filter technology. Using linear filters, any type of excitation can be handled by the Fokker-Planck-Kolmogorov equation.

The cumulant neglect method which discards cumulants higher than a particular order N is adopted in this paper to close the moment equations. If N equals 2, then the method is defined as Gaussian closure, otherwise the method is non-Gaussian closure. By setting the higher order cumulants to zero, the higher order moment can be expressed by the lower order moments. For the ship rolling problems, most previous papers about moment



equations only consider Gaussian cumulant closure due to the difficulty in tracking the higher order closure (Francescutto, 1990; Francescutto and Naito, 2004). This is especially for higher order systems which include a linear filter. The cumulant neglect becomes tedious and untraceable when increasing the neglect order. This tedium is the motivation to develop an automatic tool to address the difficulty to handle the higher dimensional state space stochastic models and higher order closure.

In order to apply path integral method to understand the rolling problem, the wave excitation was treated as regular waves perturbed by Gaussian white noise (Lin and Yim, 1995). The ship may experience stochastic chaotic motion. Some initial research about the effects of noise on chaotic behaviour of nonlinear systems has been conducted in ship dynamics and also other engineering fields. Lin & Yim (Lin and Yim, 1995; Yim and Lin, 2001) studied the stochastic chaotic motion of ship under periodic excitation with the disturbance approximated by Gaussian white noise from a probability perspective. The joint probability density functions of roll angle and roll angular velocity was calculated by applying the path integral method to solve the stochastic differential equations governing ship rolling motion. Lin and Yim found that the steady-state joint probability density functions can reflect the existing chaotic attractor on the Poincaré section and also the roll response in the heteroclinic region can be related to the capsizing through the joint probability density functions. To examine the chaotic characteristic of nonlinear roll motion in an unpredictable sea state, one cannot avoid dealing with the probabilistic approaches.

Gaussian white noise has become an important factor in these studies. The response of a dynamical system, roll angle and roll angular velocity in ship rolling study, under periodic excitation and Gaussian white noise can be modeled as a Markov process whose transition probability density function is

governed by a partial differential equation called the Fokker-Planck equation. Solving the Fokker-Planck equation would provide an alternative mean to express the evolution of the probability density function.

2. NONLINEAR SHIP ROLLING ANALYSIS USING STOCHASTIC DYNAMICAL SYSTEM

2.1 Application of Gaussian and Non-Gaussian Closure of Moment Equation Using Cumulant Neglect Method

Since the moment equations are derived from the Fokker Planck equation, which is based on the theory of diffusion process, the excitation force for the Itô system has to be pure white noise. However, the random excitation term of rolling motion cannot be modelled as white noise. One method to handle the non-white excitation is to use a shaping filter, which is driven by Gaussian white noise. For a Linear constant-coefficient differential equation (LCCDE system) as follows (Stark and Woods, 2002).

$$a_N Y^N(t) + a_{N-1} Y^{N-1}(t) + \dots + a_0 Y^0(t) = b_M X^M(t) + b_{M-1} X^{M-1}(t) + \dots + b_0 X^0(t) \quad -\infty < t < +\infty \quad (1)$$

The frequency response function or transfer function for this linear system above is:

$$H(\omega) = B(\omega) / A(\omega), \quad \text{with } a_0 \neq 0 \quad (2)$$

where $B(\omega) = \sum_{m=0}^M b_m(j\omega)^m$, $A(\omega) = \sum_{n=0}^N a_n(j\omega)^n$

where j represent the imaginary unit, and the relationship between input excitation $X(t)$ and output response $Y(t)$ spectrums:

$$S_{YY}(\omega) = |H(\omega)|^2 S_{XX}(\omega) \quad (3)$$

The bandwidth, characteristic frequency, etc, can be easily adjusted by changing the coefficient of the linear filter. Three filters were introduced in this paper following Francescutto (Francescutto and Naito, 2004):

$$\ddot{Y}(t) + \alpha_1 \dot{Y}(t) + \beta_1 Y(t) = \gamma_1 W(t) \quad (4)$$

$$\ddot{Y}(t) + \alpha_2 \dot{Y}(t) + \beta_2 Y(t) = \gamma_2 \dot{W}(t) \quad (5)$$

$$\ddot{Y}(t) + \lambda_3 \ddot{Y}(t) + \lambda_2 \dot{Y}(t) + \lambda_1 Y(t) = \gamma_3 \ddot{W}(t) \quad (6)$$

Where $W(t)$ is the Gaussian white noise input or excitation of the dynamical system and $Y(t)$ is the response of this linear dynamical system. The response of this filter system is actually the input excitation to the ship roll system. The frequency response function is defined by equation (2). A fourth order linear differential equation could be designed as a higher order filter. This filter can also be viewed as a cascade of two linear filters (Spanos, 1983; Francescutto and Naito, 2004).

All coefficients of the filter are determined through a non linear curve fitting method after setting $S_{ff} = S_{YY}$, where the S_{ff} is the wave excitation force spectrum. Fitting results are shown in Figure 1. The original curve represents the target spectrum S_{ff} , and filter1, filter2, filter3 represents S_{YY} using various fitting coefficients of equations (4), (5) and (6).

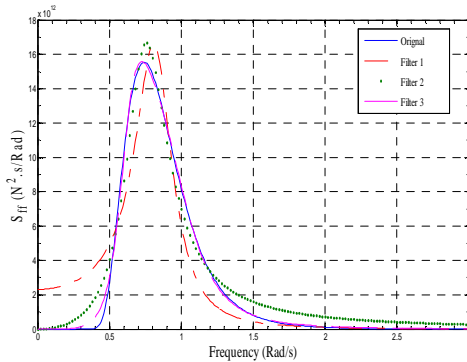


Figure 1: Comparison of original force spectrum with filtered spectrum

By combining filter equation (6) and classical nonlinear rolling model, rolling motion in random seas can be modelled in a high dimensional state space form, e.g. equation (7). Any excitation spectrum can be reproduced by some designed filter.

Where $x_3 = f$ and $W(t)$ represents the Gaussian white noise. With the Markov assumption, equation (7) forms an Itô's differential equations, e.g. equation (8).

$$\begin{cases} \dot{x}_1 = x_2 \\ \dot{x}_2 = -2\mu x_2 - \delta x_2^3 - \omega_0^2 x_1 - \alpha_3 x_1^3 + \varepsilon x_3(t) \\ \dot{x}_3 = x_4 - \lambda_3 x_3 \\ \dot{x}_4 = x_5 - \lambda_2 x_3 + \gamma_3 W(t) \\ \dot{x}_5 = x_6 - \lambda_1 x_3 \\ \dot{x}_6 = -\lambda_0 x_3 \end{cases} \quad (7)$$

$$dX = F(X, t)dt + G(X, t)dB \quad (8)$$

Following Itô's differential rule (Itô, 1951), the moment equation can be formed as below,

$$\frac{\partial E(\varphi)}{\partial t} = E\left(\sum_{i=1}^N F^{(i)} \frac{\partial \varphi}{\partial x_i}\right) + \frac{1}{2} \sum_{i=1}^N \sum_{j=1}^N E((GQGT)_{ij}) \frac{\partial^2 \varphi}{\partial x_i \partial x_j} \quad (9)$$

The moment equations will form a closed system of equations after application of the closure of the cumulant. To apply the Gaussian Cumulant neglect method, 27 moment equations up to second order are derived by (9) for system, equation (7) and analyzed by neglecting cumulants higher than second order. Figure 2, Figure 3 and Figure 4 express the effect of nonlinear damping coefficient, nonlinear stiffness and linear damping on the rolling response with Gaussian cumulant neglect.

In order to better understand the nonlinear effect, the authors have developed an automatic cumulant neglect tool using characteristic function to investigate the non-Gaussian response up to 4th order cumulant neglect (Su and Falzarano, 2011; Su and Falzarano, 2011). The automatic cumulant neglect tool takes advantages of two different representation of characteristic function of random variables to automatically neglect higher order cumulant. The higher order moments could be derived directly by applying higher order neglect.



2.2 Application of Path Integral Method

The perturbed waveforms may be modeled as regular waves with Gaussian white noise as the external disturbance as in equation (10). With some noise intensity, the response appears random as shown in the Poincaré map of Figure 5.

$$\ddot{x}(t) + \mu\dot{x}(t) + \delta\dot{x}^3(t) + x(t) - \alpha x^3(t) = H / 2 \cos \omega t + \sqrt{D}N(t) \quad (10)$$

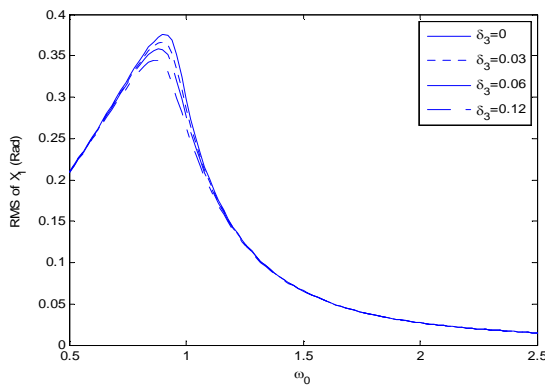


Figure 2: Effect of Nonlinear Damping Coefficient on the Root Mean Square (RMS) of Rolling Displacement

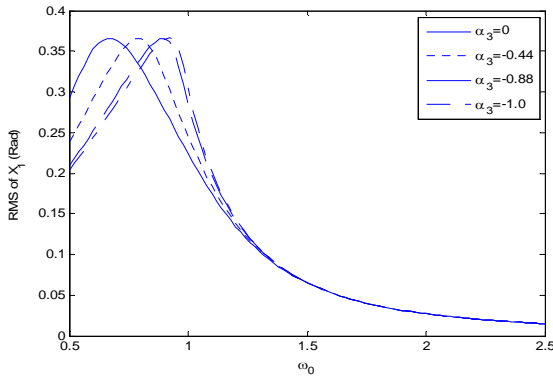


Figure 3: Effect of Nonlinear Stiffness Coefficient on the Root Mean Square (RMS) of Rolling Displacement

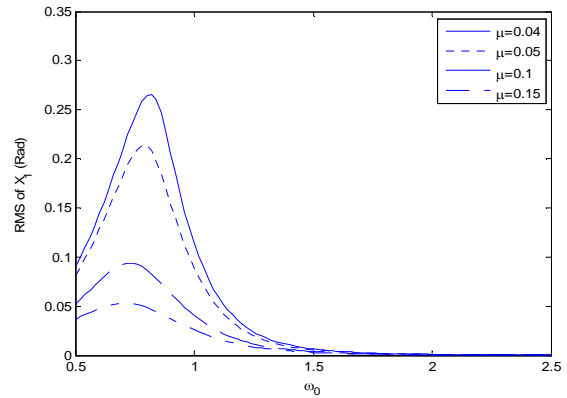


Figure 4: Effect of Linear Damping Coefficient on the Root Mean Square (RMS) of Rolling Displacement

The evolution of the probability density function is another way to describe the behaviour of the nonlinear roll motion in random waves. The behaviour of the noisy forced ship roll motion under periodic excitation with Gaussian white noise can be modelled as a Markov process. The probability density function of a Markov process satisfies Fokker-Planck equation. The associated Fokker-Planck equation governing the evolution of the probability density function of the roll motion is derived and numerically solved by the path integral method based on Gauss-Legendre interpolation to obtain joint probability density functions in state space (Jamnongpipatkul et al., 2011).

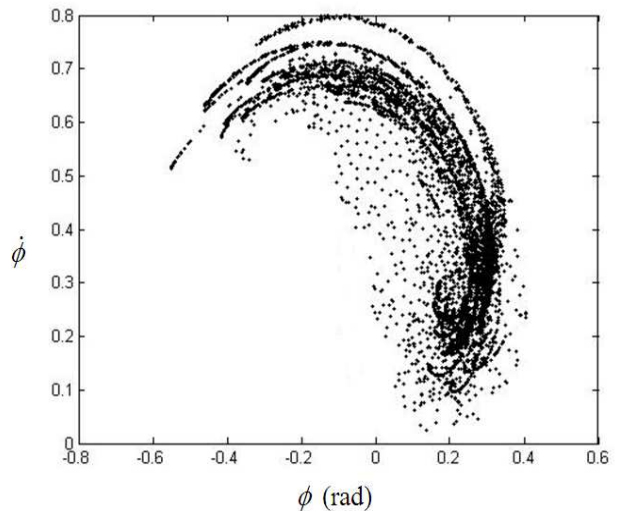


Figure 5: The Poincaré map with noise intensity

In the presence of a small random disturbance to the external period excitation, the imprint of the Poincaré map is preserved and can be identified via the joint probability density function on the Poincaré section as shown in Figure 6, Figure 7 and Figure 8. The probability density function indicates the preferred locations of the trajectories in the average sense.

The time-dependent probability of ship rolling restricted within the safe domain is provided in Figure 9. It is found that the probability decreases as time progresses and it decreases much more quickly for the high intensity of the white noise. At $t = 45.32$ s, the probability is about 45% when $D = 0.01$. It is about 20% when $D = 0.05$, and it is only about 2% when $D = 0.1$. The ship will finally leave the safe domain and capsize in the probability's view.

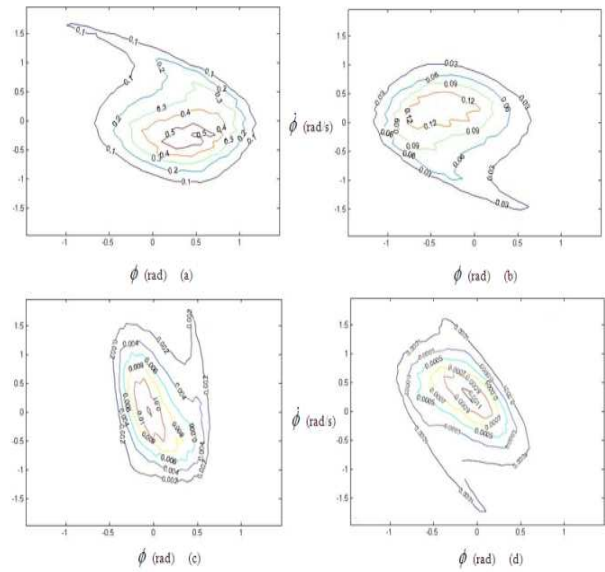


Figure 7: Evolution of contour plot of the joint probability density function with $(H, D, \omega) = (0.3, 0.05, 0.97)$ at time (a) $t = 12.95$ s (b) $t = 29.13$ s (c) $t = 45.32$ s (d) $t = 74.45$ s

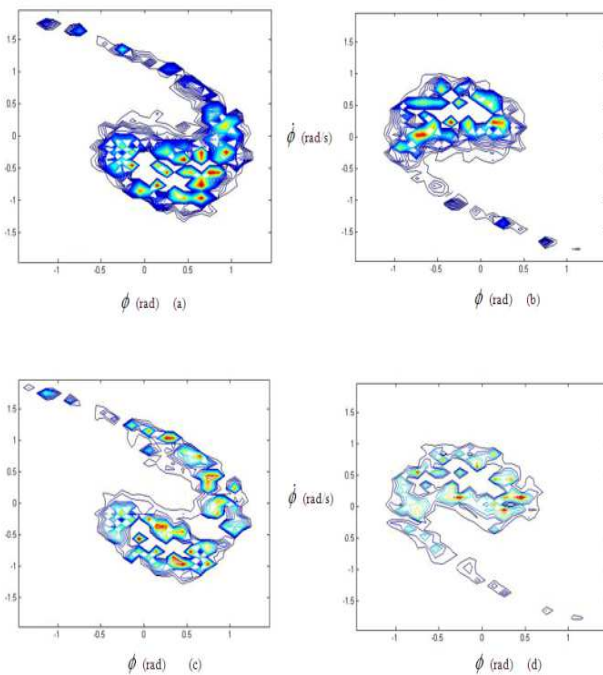


Figure 6: Evolution of contour plot of the joint probability density function with $(H, D, \omega) = (0.3, 0.01, 0.97)$ at time (a) $t = 12.95$ s (b) $t = 29.13$ s (c) $t = 45.32$ s (d) $t = 74.45$ s

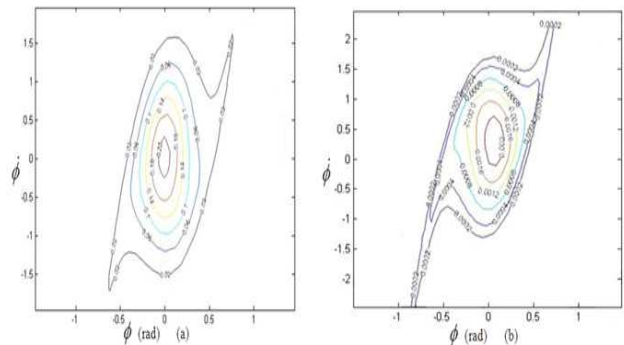


Figure 8: Evolution of contour plot of the joint probability density function with $(H, D, \omega) = (0.3, 0.1, 0.97)$ at time (a) $t = 12.95$ s (b) $t = 29.13$ s

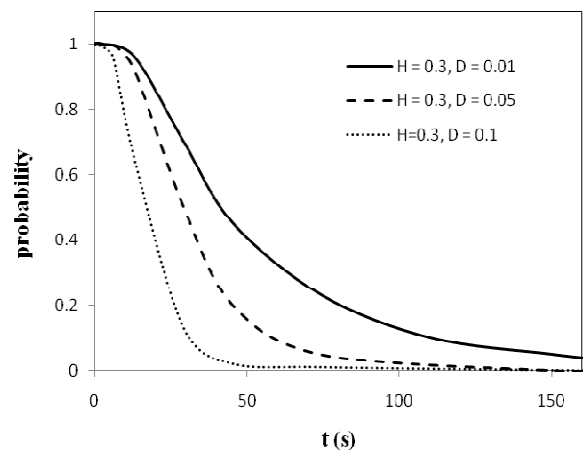


Figure 9: Probability of the ship rolling within the safe domain when $\omega = 0.97$ rad/s



3. CONCLUSIONS

This paper represents an attempt to study the qualitative behaviour of the ship roll motion in the probability space. The stochastic nonlinear dynamic behaviours and the probability density function of ship rolling in the random beam waves are studied. Moment equations are applied to the high dimensional dynamical system with filtered colored noise using both Gaussian and Non Gaussian cumulant neglect method. The probability density function for the response of the system is obtained numerically for all excitation types and with varying amount of noise. The probability density function of rolling response is evaluated and the time-dependent probability of ship rolling restricted within the safe domain is provided. It is found that the value of joint probability density decreases gradually as time progresses. And it decreases much more quickly for the high intensity of white noise. The ship will leave the safe domain with enough time and capsize from a probabilistic point of view.

Moment equation method could be applied to real colored noise given any wave excitation. We are able to get response statistics with appropriate assumption through cumulant neglect method, etc. But it is difficult to find any bifurcation phenomena and probability density function. However, path integral method provides the transient response probability density function, when considering only harmonic wave with disturbance noise. It is still a challenging work and still need more effort to solve the high dimensional Fokker Planck Equation, although some work has been done in the past years.

4. ACKNOWLEDGMENTS

The work has been funded by the Office of Naval Research (ONR) T-Craft Tools development program ONR Grant N00014-07-1-1067 with program manager Kelly Cooper

5. REFERENCES

- Falzarano, J., Shaw, S. W. and Troesch, A. W., 1992. Application of global methods for analyzing dynamical systems to ship rolling motion and capsizing. International Journal of Bifurcation and Chaos 2(1): 101-115.
- Falzarano, J., Vishnubhotla, S. and Cheng, J., 2004. Nonlinear dynamic analysis of ship capsizing in random waves. Proceedings of the Fourteenth (2004) International Offshore and Polar Engineering Conference, Vol 3: 479-484.
- Falzarano, J. M., Vishnubhotla, S. and Juckett, S. E., 2005. Combined steady state and transient analysis of a patrol vessel as affected by varying amounts of damping and periodic and random wave excitation. Proceedings of the 24th International Conference on Offshore Mechanics and Arctic Engineering - 2005 - Vol 1, Pts A and B: 1081-1085.
- Falzarano, J. M., Vishnubhotla, S. and Juckett, S. E., 2010. Combined Steady State and Transient Analysis of a Patrol Vessel as Affecteds by Varying Amounts of Damping and Periodic and Random Wave Excitation. Journal of Offshore Mechanics and Arctic Engineering-Transactions of the Asme 132(1): -.
- Francescutto, A., 1990. On the Nonlinear Motions of Ships and Structures in Narrow Band Sea. Proceedings of the IUTAM Symp. on Dynamics of Marine Vehicles and Structures in Waves. London, Elsevier Publishing: 291-304.



- Francescutto, A. and Naito, S., 2004. Large amplitude rolling in a realistic sea. International Shipbuilding Progress **51**(2): 221-235.
- Hsieh, S.-R., Troesch, A. W. and Shaw, S. W., 1994. A Nonlinear Probabilistic Method for Predicting Vessel Capsizing in Random Beam Seas. Proceedings: Mathematical and Physical Sciences **446**(1926): 195-211.
- Itô, K., 1951. On a formula concerning stochastic differentials. Nagoya Math Journal **3**: 55-65.
- Jamnongpipatkul, A., Su, Z. and Falzarano, J. M., 2011. Nonlinear ship rolling motion subjected to noise excitation. Ocean Systems Engineering **1**(3).
- Jiang, C., Troesch, A. W. and Shaw, S. W., 2000. Capsize criteria for ship models with memory-dependent hydrodynamics and random excitation. Philosophical Transactions of the Royal Society of London Series a-Mathematical Physical and Engineering Sciences **358**(1771): 1761-1791.
- Jiang, C. B., Troesch, A. W. and Shaw, S. W., 1996. Highly nonlinear rolling motion of biased ships in random beam seas. Journal of Ship Research **40**(2): 125-135.
- Lin, H. A. and Yim, S. C. S., 1995. Chaotic roll motion and capsize of ships under periodic excitation with random noise. Applied Ocean Research **17**(3): 185-204.
- Naess, A. and Moe, V., 2000. Efficient path integration methods for nonlinear dynamic systems. Probabilistic Engineering Mechanics **15**(2): 221-231.
- Roberts, J. B. and Spanos, P. D., 2003. Random vibration and statistical linearization. Mineola, NY, Dover Publications.
- Roberts, J. B. and Vasta, M., 2000. Markov modelling and stochastic identification for nonlinear ship rolling in random waves. Philosophical Transactions of the Royal Society of London Series a-Mathematical Physical and Engineering Sciences **358**(1771): 1917-1941.
- Spanos, P. T. D., 1983. ARMA Algorithms for Ocean Wave Modeling. Journal of Energy Resources Technology **105**(3): 300-309.
- Stark, H. and Woods, J. W., 2002. Probability and random processes with applications to signal processing. Upper Saddle River, N.J., Prentice Hall.
- Su, Z. and Falzarano, J. M., 2011. Gaussian and non-Gaussian cumulant neglect application to large amplitude rolling in random waves. International Shipbuilding Progress **58**(2): 97-113.
- Su, Z. and Falzarano, J. M., 2011. Gaussian and non Gaussian response of ship rolling in random beam waves. 12th International Ship Stability Workshop, Washington D.C., USA.
- Vishnubhotla, S. and Falzarano, J., 2009. Effect of More Accurate Hydrodynamic Modeling on Calculating Critical Nonlinear Ship Rolling Response. Vibro-Impact Dynamics of Ocean Systems and Related Problems **44**: 269-274.
- Vishnubhotla, S., Falzarano, J. and Vakakis, A., 2000. A new method to predict vessel/platform critical dynamics in a realistic seaway. Philosophical Transactions of the Royal Society of London Series a-Mathematical Physical and Engineering Sciences **358**(1771): 1967-1981.
- Yim, S. C. S. and Lin, H., 2001. Unified analysis of complex nonlinear motions via densities. Nonlinear Dynamics **24**(1): 103-127.





Evaluation of the Probability of Surf-Riding in Irregular Waves with the Time-Split Method

Vadim Belenky, *David Taylor Model Basin (NSWCCD)*, vadim.belenky@navy.mil

Kostas J. Spyrou, *National Technical University of Athens*, k.spyrou@central.ntua.gr

Kenneth M. Weems, *Science Applications International Corporation*, kenneth.m.weems@saic.com

ABSTRACT

Surf-riding is an important phenomenon for the evaluation of ship dynamic stability, as it is related to one of the principal mechanisms of broaching-to, and the evaluation of the probability of surf-riding in irregular waves is a necessary step toward determining the probability of broaching-to after surf-riding. The concept of wave celerity in irregular waves introduces the possibility of developing a probabilistic description of surf-riding. The phenomenon of surf-riding can then be treated as a problem of the exceedance (or upcrossing) of the wave celerity by the instantaneous surging velocity.

To facilitate the probabilistic study of surf-riding, a simple model of surging and surf-riding in irregular waves of variable bandwidth is introduced. This model can be used to identify patterns of surf-riding in irregular waves and to determine the relationship between surf-riding and the appearances and disappearances of the surf-riding equilibria.

Keywords: *Surf-riding, Broaching-to, Split-time method*

1. INTRODUCTION

The paper focuses on the basic study of surf-riding in irregular waves, and continues from the work presented at the most recent International Ship Stability Workshop (Belenky *et al.*, 2011). The study is oriented toward building a description of surf-riding in irregular waves through which the probabilistic assessment methods discussed above could be effectively applied. A key element of this description is the definition of wave celerity in irregular waves, which is detailed in a separate paper submitted to this conference (Spyrou *et al.*, 2012). The overall objective of this work is to develop a procedure for probabilistic assessment of surf-riding and broaching using the split-time method.

The split-time method has been developed to provide a practical method for assessing the probability of capsizing for an intact ship, and was originally implemented for capsizing in beam seas (Belenky *et al.*, 2008). To handle the extreme rarity of capsizing, the problem was separated into two problems. The first problem (“non-rare”) is formulated as an assessment of upcrossing of some intermediate level usually associated with the angle of maximum of the roll restoring (GZ) curve. The second problem (“rare”) is the determination of conditions that lead to capsizing given that an upcrossing has occurred, and is associated with exceeding some critical roll rate at the instant of upcrossing. The method is being extended for stern quartering seas where the variation of stability in waves is significant and can lead to a “pure loss of stability” event (Belenky *et al.*,



2010). A key advantage of the split-time method over more customary probabilistic methods is that it can be effectively applied to a finite volume of time-domain data, which allows it to be efficiently used with advanced hydrodynamic simulation codes such as LAMP, the Large Amplitude Motion Program (Shin *et al.*, 2003, Spyrou, *et al.*, 2009). This advantage is shared by other methods that use different logic to separate the dynamic problem into parts, such as the “critical wave groups” method (Themelis and Spyrou, 2007). The strength of the wave group method is its flexibility in terms of the selected level of rigor, thus allowing simplicity. The split-time method, however, may be more robust in terms of reflecting the statistics of initial conditions. Since the methods share the same philosophy of handling rarity (Belenky *et al.*, 2012), they have a potential to complement each other.

Capsizing or large roll angle in stern quartering and following seas may also be caused by broaching-to, which is defined as a violent uncontrollable turn in spite of maximum steering effort applied. One of the possible scenarios of broaching-to is related to surf-riding and realized as a directional instability of one of the surf-riding equilibria (Spyrou, 1996). The application of the “critical wave groups” method would entail finding a set or sets of wave (or wave group) characteristics that lead to broaching-to and then finding the probability of encountering such a wave or wave group.

2. SURGING AND SURF-RIDING IN IRREGULAR FOLLOWING WAVES

2.1 Equation of Motion

The simplest mathematical model for surging and surf-riding in following irregular waves is a single degree of freedom equation of motion along the x-axis:

$$(M + A_{11})\ddot{\xi}_G + R(\dot{\xi}_G) - T(\dot{\xi}_G, n) + F_X(t, \xi_G) = 0 \quad (1)$$

Here M is the ship mass, A_{11} is longitudinal added mass, R is resistance in calm water, T is the thrust in calm water, n is the number of propeller revolutions, F_X is the Froude-Krylov incident wave force, and ξ_G is longitudinal position of the ship’s center of gravity in an Earth-fixed coordinate system. The dot above the position indicates a temporal derivative.

For compatibility with Spyrou (2006), polynomial presentations are used for the resistance and thrust in calm water:

$$\begin{aligned} R(U) &= r_1 U + r_2 U^2 + r_3 U^3 \\ T(U, n) &= \tau_1 n^2 + \tau_2 n U + \tau_3 U^2 \end{aligned} \quad (2)$$

Since the Earth-fixed coordinate system is used, the irregular waves are presented as a spatial-temporal stochastic process using the standard Longuet-Higgins model:

$$\zeta_w(t, \xi) = \sum_{i=1}^N a_i \cos(k_i \xi - \omega_i t + \varphi_i) \quad (3)$$

Here a_i is the amplitude, k_i is the wave number, ω_i is the frequency, and φ_i is a random, uniformly distributed phase shift of the wave component i .

As the model is meant at this stage to be qualitative, a linear wave-body formulation is appropriate. Therefore:

$$F_X(t, \xi_G) = \sum_{i=1}^N A_{Xi} \cos(k_i \xi - \omega_i t + \varphi_i + \gamma_i) \quad (4)$$

Here A_{Xi} is the amplitude of the component of the surging force, while γ_i is the phase shift between the wave and the force components. Details of the surging force calculation can be found in Belenky *et al.* (2011).

2.2 Surf-Riding

The physical mechanism of surf-riding includes the appearance of dynamical equilibria and a ship's attraction to the stable equilibrium. The equilibria appear when the wave surging force becomes large enough to offset the difference between the ship's thrust and its resistance at wave celerity. The equilibrium points are the positions of the ship on the wave where the forces balance exactly.

To illustrate this, consider surf-riding in regular waves and plot the variation in the wave-induced surging force as a function of the ship's position on the waves; see Figure 1. In this plot, the horizontal axis is the position of the ship's center of gravity ahead of the wave crest, the dashed blue line is the wave profile, and the red line is the wave surging force, with a negative value indicating a forward (accelerating) force. The largest forward surging force (most negative on this plot) occurs when the ship is running down the wave face, while the magnitude of surging force is a function of wave amplitude.

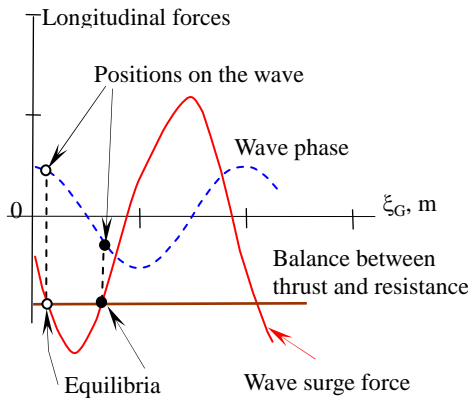


Figure 1: On appearance of dynamic equilibria

Since the commanded speed is insufficient to propel the ship with wave celerity in calm water, additional wave force is necessary to drive the ship at wave celerity. If the amplitude of the wave surging force exceeds the absolute value of the balance between thrust and resistance, two intersection points appear, as shown in Figure 1. Those will be called “surf-riding equilibria” (knowing that this is not an

exact condition of equilibrium); one shows stability features (black point, located around the wave trough) and the other behaves as unstable (empty point, located around wave crest).

While these considerations are well-established in the field, they were repeated here to highlight the difference between the regular and irregular waves. If Figure 1 is considered as a snapshot an irregular wave, all the elements of the surf-riding problem can be readily transferred from regular waves into irregular, except for wave celerity. How can celerity be defined in irregular waves?

2.3 Celerity of Irregular Waves

The very definition of celerity in irregular waves is actually a very deep problem and is given full consideration in Spyrou *et al.*, (2012), which discusses the formulation of a practical definition of wave celerity and the implementation of schemes for evaluating it for theoretical and numerical analysis. An extremely simplified version of the approach is used here, in which the local celerity is defined by identifying the three profile zero-crossing points that are closest to the ship and tracking their movement from time step to time step, as illustrated in Figure 2.

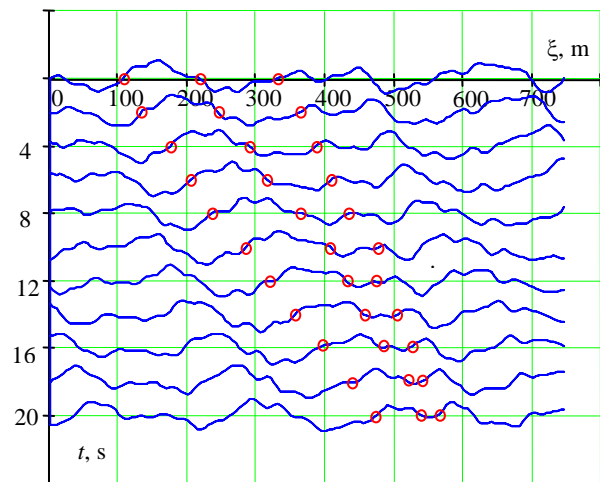


Figure 2: Zero-crossing points in space and time



Such a definition attempts to provide the speed associated with a particular wave face. Since the zero crossing points, like other individual waves and wave features, have a finite time of existence, the celerity calculated by this approach is not continuous. Nevertheless, it is sufficient for this paper's objectives.

3. NUMERICAL STUDY

3.1 Objectives

The previous numerical study (Belenky *et al.*, 2011) has shown some sort of surf-riding behavior in irregular waves, which was most pronounced for cases using "filtered" irregular waves with limited bandwidth. Since the principal objective of this numerical study is to see the relation between the visible surf-riding behavior and appearance of equilibrium, irregular waves with a very limited bandwidth – two and three frequency components – are used.

3.2 Two-Component Wave Model

Figure 3 shows a spectrum for the two-component waves used in the study. While these waves look nearly regular to the naked eye (see Figure 4), the duration of surf-riding in these waves is no longer unlimited as for regular waves.

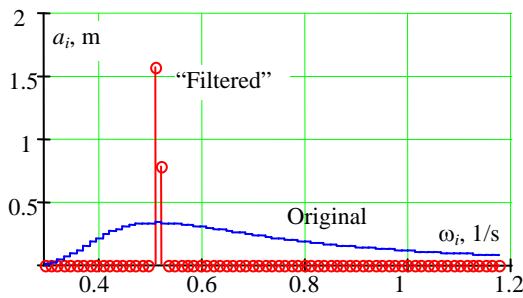


Figure 3: Two-component wave spectrum

As shown in Belenky *et al.*, (2011), a ship "caught" by the wave at certain time is later

"released." To see how this is related with the appearance and disappearance of the surf-riding equilibria, the wave celerity has been estimated by tracking the zero crossing points as described above and illustrated in Figure 4.

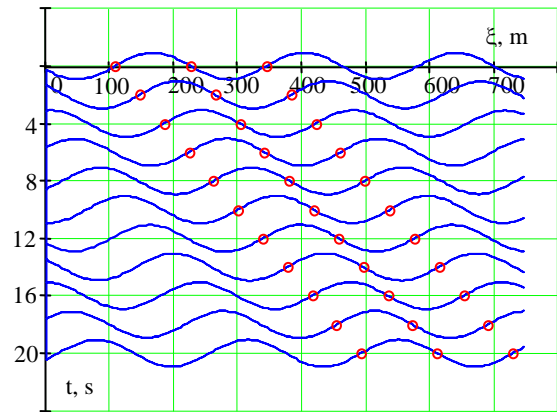


Figure 4: Zero-crossing points of two-component wave

The time history of the celerity of the wave tracked in Figure 4 is shown in Figure 5 along with values calculated for the previous and the next wave. The change of the celerity over time has a magnitude of about 0.6 m/s. The celerities of the previous and next waves experience similar changes, but at different times.

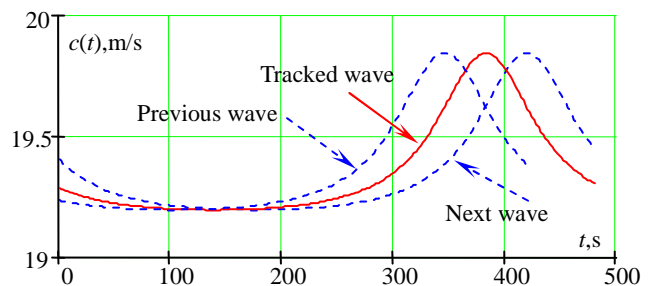


Figure 5: Celerity of the two-component wave tracked in Figure 4, along with the celerities of the previous and next waves

Figure 6c shows a time history of the instantaneous ship speed and the estimated wave celerity for a ship modeled using Equations (1) through (4) and running in this two-component wave. While the thrust is set so that calm water speed is below wave celerity,

the initial speed was set to wave celerity, so the ship is immediately captured.

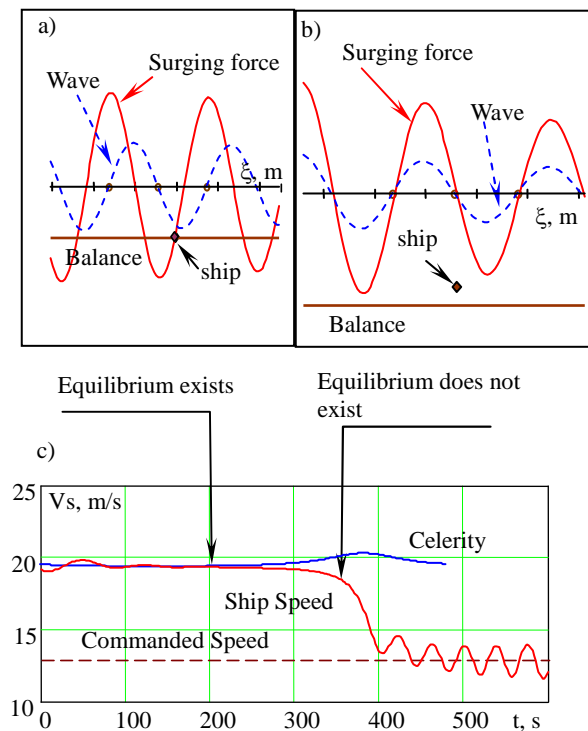


Figure 6: Release from surf-riding in two-component waves:

- (a) “spatial snapshot” at 200 s;
- (b) “spatial snapshot” at 340 s;
- (c) time history

Some decaying oscillations are observed during the first 100 seconds, which is typical for an attraction to the equilibrium. The “spatial snapshot” in Figure 6a shows the existence of the equilibria and the ship located close to one of them. This is, indeed, the stable equilibrium, which is located near the wave trough, as can be seen from the spatial wave profile superimposed on the plot.

At around 250 s, the time histories of the wave celerity and instantaneous ship speed diverge, after which the ship is released from surf-riding and experiences periodic surging. The reason of the release is, most likely, the increase of the wave celerity observed in Figure 5. As seen from the “spatial snapshot” in Figure 6b, the surf-riding equilibria do not exist at this time because the wave can no

longer generate a large enough surge force to propel the ship at celerity. The higher wave celerity increased the resistance and the level of balance between the resistance and thrust went down.

Note that the estimated wave celerity is *not* part of the surging / surf-riding calculations. It has been evaluated independently from the same wave field that was used for motion calculations. The indications of the equilibria’s appearance and disappearance are therefore independent interpretations of the observed phenomena. At the same time, the interpretation based on the estimate of celerity and observed behavior of the dynamical system are consistent. This consistency suggests that that estimate of the celerity is, to some degree, valid (Spyrou *et al.*, 2012).

3.3 Three-Component Wave Model

Figure 7 shows the spectrum for a three-component model of the irregular wave. While still very simplistic, simulations using this wave and the same simplified ship surging model show three transitions – two captures and one release – over the passing of six waves. The time histories of the celerities of these six waves are shown in Figure 8.

Along with larger (about 1 m/s magnitude) changes in wave celerity, there are quite dramatic peaks with three secondary peaks on the top. These secondary peaks may be artifacts of the simplified wave tracking scheme and/or results of waves overtaking one another. Further studies of this and similar effects are described in Spyrou *et al.*, (2012).

Figure 9a shows the time history of the instantaneous ship speed and the wave celerity of the “current” wave, the wave closest to the ship, at any given time. One can see that the celerity curve at Figure 9a is a combination of all six time histories in Figure 8, and can be discontinuous as the current wave changes.

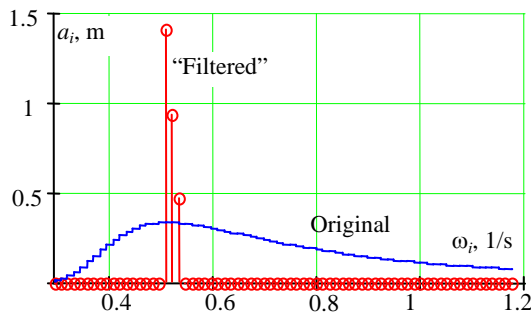


Figure 7: Three-component wave spectrum

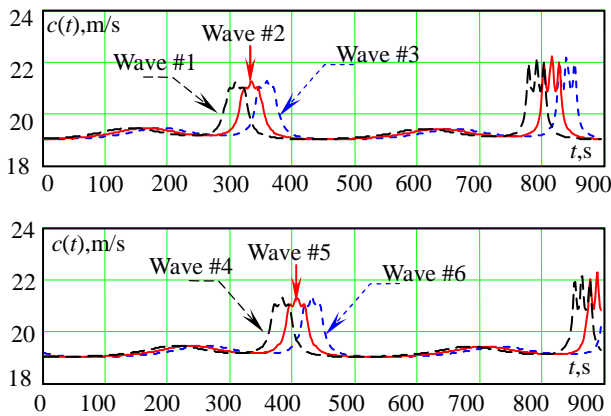


Figure 8: Time histories of wave celerities

Figure 9a also shows the temporal boundaries for waves. During periodic surge motion, they coincide with downcrossing the commanded speed line. Figures 9b through 9r are the “spatial snapshots” corresponding to specific instant of time as noted in the captions. These instances of time are identified in Figure 9a with lettered arrows referring to the respective “spatial snapshot.”

On each “spatial snapshot” plot, the blue line shows the wave profile around the ship, with the horizontal position of the diamond marking the ship’s position relative to the wave. The circles on the wave profile mark three zero-crossing points that are tracked to estimate wave celerity, of which the outermost circles define the spatial boundary of the “current” wave. The direction of the ship (and wave) motion is to the right.

The vertical position of the diamond indicates the ship speed, while the middle line (0 wave) marks the commanded speed (calm water) and higher speeds are down.

Each special snapshot also contains a plot for surging wave force (red curve) and the balance between the available thrust and resistance at the current wave celerity in the same scale (lower line).

The first spatial snapshot, Figure 9b, corresponds to the initial conditions, with the instantaneous speed equal to the commanded speed. The ship has just encountered wave #1 and is located just within its boundary. The surf-riding equilibria exist, since the surging force crosses the line corresponding to the balance between the thrust and resistance.

The stable surf-riding equilibrium attracts the dynamical system and one oscillation period is seen in Figure 9a until approximately $t=100$ s. The next two spatial snapshots, Figures 9c and 9d, correspond to the positive and negative peaks during this transition, respectively. The transition is completed and the dynamical system reaches the stable equilibrium at around $t=150$ s, in Figure 9e.

Looking at Figures 9b through 9e, one can see that the amplitude of the surging force is decreasing due to lower wave amplitude. This tendency leads to the disappearance of the surf-riding equilibria around $t=256$ s and to the release of the ship from surf-riding (Figure 9f).

The ship slows down (Figure 9g), the wave #1 overtakes her, and wave #2 is encountered at around $t=325$ s (Figure 9h). The ship experiences the first almost periodic surge with the positive peak corresponding to the spatial snapshot in Figure 9i. As expected, wave #2 overtakes the ship quite quickly and wave #3 is encountered around $t=380$ s (Figure 9j).

The modulation of wave amplitude and surging force then reverses and they begin to increase. This is may be already seen in Figure 9h, but becomes quite apparent in Figures 9i and 9j. New surf-riding equilibria appear around $t=398$ s (Figure 9k).

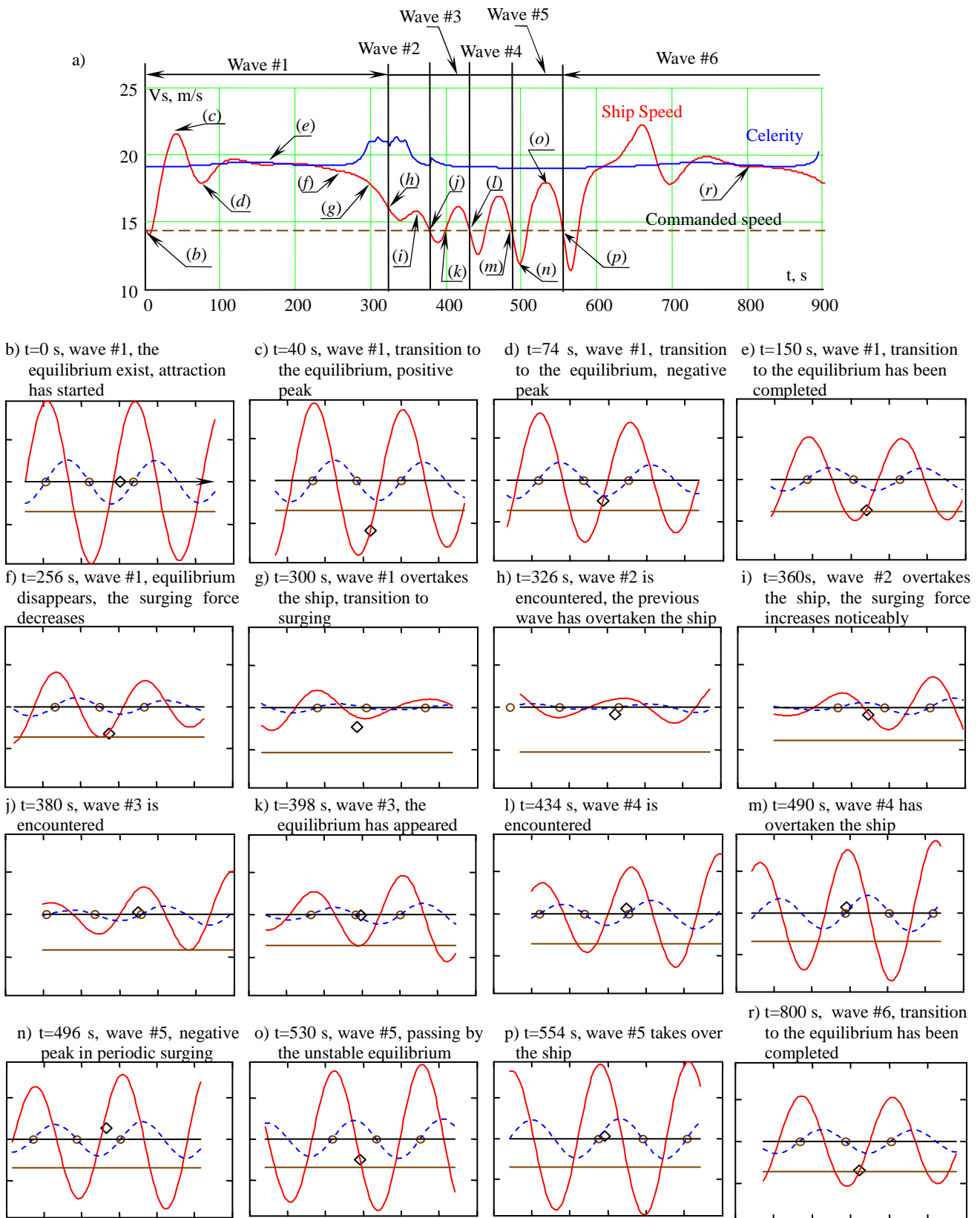


Figure 9: Two captures and one release from surf-riding in a three-component irregular wave; time history (a) and “spatial snapshots” (b-r)



The existence of the surf-riding equilibria has an immediate influence on the surge motions, which become asymmetric with wider positive peaks and sharper negative ones (Spyrou, 2006). Symmetry is observed during the passing of waves #4 and #5, during which the surf-riding equilibria exists continuously (Figures 9l through 9o). Figure 9o shows how the dynamical system passed near the unstable surf-riding equilibrium, but the ship is not yet “caught” and wave #5 takes over (Figure 9p). The ship is finally “caught” by wave #6 and at around $t=800$ again reaches the stable surf-riding equilibrium (Figure 9r).

3.4 Conclusion of Numerical Study

In the analysis of the numerical simulations of surf-riding using a 1 DOF surge equation, an evaluation of wave celerity based on the tracking of wave zero-crossing points was successfully used to reveal the existence or non-existence of surf-riding equilibrium, which was then able to explain the ship’s transition into and out of surf-riding in irregular seas. This ability to characterize the behavior of the dynamical system from these equilibria allows consideration of a probabilistic formulation for surf-riding in irregular waves.

4. POSSIBLE FORMULATION FOR THE NON-RARE PROBLEM

This numerical study demonstrated the possibility of quantifying surf-riding equilibria in irregular waves by considering the estimated celerity of a local wave feature and the variation of wave forces for the spatial domain within the boundaries of a “current wave.” The existence of the surf-riding equilibrium can then be formulated as an upcrossing problem of the following process:

$$X(t) = F_x(\xi_G(t)) - R(c(t)) \quad (5)$$

The level of upcrossing is defined by the commanded speed defined through the number of propeller revolutions and expressed through the thrust in calm water.

The existence of the surf-riding equilibria is a necessary, but not sufficient condition of surf-riding. Similarly, surf-riding is necessary, but not sufficient condition of the considered type of broaching. Furthermore, the act of broaching-to following surf-riding may or may not induce a dangerous roll angle. It is therefore reasonable to expect that the split-time method may include several rare problems: surf-riding if the equilibria exist, broaching if surf-riding occurs, and then large roll angle or capsizing if broaching occurs. Formulation of these problems belongs to future work.

5. CONCLUSIONS

The work presented in this paper is aimed towards developing an understanding of surf-riding behavior in multi-frequency waves, understanding that could enable the application of the split-time and critical wave group methods for evaluating the probability of capsizing (or large roll angle) due to broaching-to following surf-riding.

The attempt to describe surf-riding in a probabilistic framework has led to the necessity of defining wave celerity in irregular waves. The formulation of a viable definition of wave celerity in irregular waves and the development of robust methods for evaluating it in numerical theoretic analysis is a quite substantial task and represents its own area of research. For the present study, a simple definition was adopted, in which the wave celerity was defined as a speed of zero-crossing points of a wave and evaluated using a point tracking scheme.

This approximate definition of wave celerity in irregular waves nevertheless allowed the characterization of the surf-riding equilibria



(or the lack thereof) for numerical case studies involving irregular waves with two and three components. These numerical studies showed that an almost complete explanation of the dynamical behavior of surf-riding can be presented in terms of the surf-riding equilibria.

Based on these results and considerations, a non-rare problem has been postulated for the appearance of surf-riding equilibria in irregular waves that can be related to an upcrossing of a process of the difference between wave surging force and the ship resistance at the speed equal to the wave celerity in irregular waves. The non-rare problem can be considered as the first step in the development of a split-time method for the probability of capsizing after broaching-to following surf-riding.

6. ACKNOWLEDGMENTS

The work described in this paper has been funded by the Office of Naval Research (ONR) under Dr. Patrick Purtell and by ONR Global under Dr. Richard Vogelsong.

7. REFERENCES

- Belenky, V., Weems, K.M., and Lin, W.-M., 2008, "Numerical Procedure for Evaluation of Capsizing Probability with Split Time Method," Proceedings of 27th Symposium on Naval Hydrodynamics, Seoul.
- Belenky, V.L., Weems, K.M., Lin, W.M., and Spyrou, K.J., 2010, "Numerical Evaluation of Capsizing Probability in Quartering Seas with Split Time Method," Proceedings of 28th Symposium on Naval Hydrodynamics, Pasadena, California.
- Belenky, V., Spyrou, K. J., and Weems, K. M., 2011, "Split-Time Method for Surf-Riding and Broaching-To," Proceedings of 12th International Ship Stability Workshop, (ISSW 2011), Washington DC, pp.163-168.
- Belenky, V., Weems, K.M., Bassler, C.C., Dipper, M.J., Campbell, B., and Spyrou, K.J., 2012, "Approaches to Rare Events in Stochastic Dynamics of Ships," Probabilistic Engineering Mechanics Vol. 28, pp. 30–38.
- Shin, Y.S, Belenky, V., Lin, W.M., Weems, K., and Engle, A.H., 2003, "Nonlinear time domain simulation technology for seakeeping and wave-load analysis for modern ship design," Transactions, SNAME, Vol. 111, pp. 557-578.
- Spyrou, K.J., 1996, "Dynamic Instability in Quartering Seas: The Behavior of a Ship During Broaching," Journal of Ship Research, Vol. 40, No. 1.
- Spyrou, K.J., 2006, "Asymmetric Surging of Ships in Following Seas and its Repercussions for Safety," Nonlinear Dynamics, Vol. 43, pp. 149-172.
- Spyrou, K.J, Weems, K.M., and Belenky, V., 2009, "Patterns of Surf-Riding and Broaching-to Captured by Advanced Hydrodynamic Modelling," Proceedings of 10th International Conference on Stability of Ships and Ocean Vehicles (STAB2009), St. Petersburg, Russia.
- Spyrou, K.J., Belenky, V., Themelis, N., and Weems, K., 2012, "Conditions of Surf-riding in an Irregular Seaway", Proceedings of 11th International Conference on Stability of Ships and Ocean Vehicles (STAB 2012), Athens, Greece.
- Themelis, N., and Spyrou, K.J., 2007, "Probabilistic assessment of ship stability," Transactions, SNAME, Vol. 115, pp. 181-206.





Total Stability Failure Probability of a Ship in Irregular Beam Wind and Waves: Model Experiment and Numerical Simulation

Takumi Kubo, *Osaka University*, takumi_kubo@naoe.eng.osaka-u.ac.jp

Naoya Umeda, *Osaka University*, umeda@naoe.eng.osaka-u.ac.jp

Satoshi Izawa, *Osaka University*, tg5012is@docomo.ne.jp

Akihiko Matsuda, *National Research Institute of Fisheries Engineering*, amatsuda@fra.affrc.go.jp

ABSTRACT

For establishing the second generation intact stability criteria, the International Maritime Organization (IMO) requires experimentally validated numerical simulation models for stability under dead ship condition. Here it is expected to select a beam wind and wave condition as a worst scenario and to quantify total stability failure probability. The authors developed a coupled sway-heave-roll-pitch numerical model and compared it with physical experiments of a ship model in artificial irregular beam waves and fluctuating beam wind. The results indicate that the probability of total stability failure estimated by the simulation exists within the confidential interval of those estimated by the experiment.

Keywords: *capsizing, IMO, intact stability, dead ship, fluctuating wind*

1. INTRODUCTION

At the IMO (2012), the second generation intact stability criteria are now under development. They are requested to prevent total stability failure (capsizing) and partial stability failure (cargo shift and so on) due to pure loss of stability, parametric rolling, broaching, excessive acceleration and harmonic resonance under dead ship condition with physics-based approaches. They will consist of two layered vulnerability criteria and direct assessment for each failure mode and a ship is requested to comply with at least one of them. This is because the use of expensive numerical simulation as direct assessment should be minimised for realising feasible application of new scheme. It is also essential that numerical simulation used for the direct assessment shall be validated with physical model experiments.

Other than harmonic resonance under dead ship condition, it is agreed to allow a ship failing to comply with all three levels to operate with operational guidance based on method used for higher level criterion. This is because these failure modes can be avoided with appropriate operation. The dead ship condition is their exception because it assumes all propulsive power is lost so that no operational means such as the propeller revolution and the rudder deflection, are available for avoiding danger. In other words, it is crucial to guarantee stability safety under the dead ship condition because a ship shall have at least one safe option to escape from all other failure modes by operational means.

If a ship is almost longitudinally symmetrical and wind direction is the same as the wave direction, the ship without any propulsive power suffers beam wind and waves.



This can be regarded as the worst scenario in case of dead ship condition. It was theoretically confirmed by one of the authors (Umeda et al., 2007). If we allow a ship to yaw, the ship could escape from the worst scenario due to wind-induced yaw moment and/or second-order wave-induced yaw moment (Umeda et al., 2007). For the vulnerability criterion, at the IMO, it was already agreed that the current weather criterion but with extended wave steepness table is used for its level 1 criterion and analytical calculation of stability failure probability under stochastic wind and wave excitation with uncoupled roll model is used for the level 2 (IMO, 2012). In case of the IMO weather criterion, random wind is modelled with a gusty wind with assumed occurrence probability (IMO, 2008). Thus, it is necessary for the level 2 criterion to directly use fluctuating wind for overcoming the drawback of the level 1 criterion. For direct stability assessment, many numerical simulation techniques are reported so far (for example, Vassalos et al., 2004) but no numerical models are authorised at the IMO.

One of its reasons is that model experiments of capsizing of a ship in artificial random beam wind and waves were not available so far for this purpose within the knowledge of the authors. For example, Shaughnessy et al. (1994) and Ogawa et al. (2006) executed model experiments of ships in beam wind and irregular waves under moored and drifting conditions, respectively. They, however, used non-fluctuating wind for their experiments. In the field of offshore structure, model experiments with random wind were reported but without waves (Kajita and Tanaka, 1986). Indeed, generation of fluctuating wind is a challenge for tank testing.

Responding to this situation, some of the authors (Umeda et al., 2011) were executed physical model experiments of ship capsizing in irregular beam waves but with non-fluctuating wind. Thus the authors upgraded a wind blower for realising fluctuating wind and

conducted experiments of ship capsizing under random environment of both waves and wind.

Furthermore, a coupled sway-heave-roll-pitch numerical model was newly developed for a use of direct stability assessment under dead ship condition. Using the above mentioned our experimental data, the numerical simulation model was attempted to be validated.

2. NUMERICAL SIMULATION MODELS

2.1 Uncoupled roll model

The roll motion is modelled with the following nonlinear and uncoupled equation of absolute rolling angle of a ship under a stochastic wave excitation and steady wind moment (Kubo et al., 2010). Usually the ship motions in beam seas are modelled with equations of coupled motions in sway and roll with wave radiation forces and diffraction forces. Watanabe (1938), however, proposed a one-degree of freedom equation of roll angle, as follows:

$$(I + J)\ddot{\phi} + D(\dot{\phi}) + WGZ(\phi) = M_{wind}(t) + M_{wave}(t) \quad (1)$$

where ϕ : the absolute roll angle, I : the roll moment of inertia of a ship, J : the added roll moment of inertia, D : the roll damping moment, W : the ship weight, GZ : the righting arm and a dot indicates differentiation with respect to time. $M_{wave}(t)$ is the wave induced moment consisting of the steady and fluctuating wind moment and $M_{wind}(t)$ is the wave exciting moment based on the Froude-Krylov assumption. This is because the roll diffraction moment and roll radiation moment due to sway can cancel out when the wavelength is sufficiently longer than the ship breadth. (Tasai, 1965)



The uncoupled equation of the absolute roll motion can be rewritten by dividing by the virtual moment of inertia as follows:

$$\ddot{\phi} + d(\dot{\phi}) + \omega_0^2 \cdot kf(\phi) = \omega_0^2 \cdot (m_{wind}(t) + m_{wave}(t)) \quad (2)$$

where

$$d(\dot{\phi}) = \frac{D(\dot{\phi})}{I + J} \quad (3)$$

$$\omega_0 = \sqrt{\frac{W \cdot GM}{I + J}} \quad (4)$$

$$kf(\phi) = \frac{GZ(\phi)}{GM} \quad (5)$$

$$m_{wind}(t) = \frac{M_{wind}(t)}{W \cdot GM} \quad (6)$$

$$m_{wave}(t) = \frac{M_{wave}(t)}{W \cdot GM} \quad (7)$$

and GM is the metacentric height.

The wind induced roll moment is modelled as follows:

$$M_{wind}(t) = 0.5 \rho_{air} C_m(\phi) \{U_{w0} + U_w(t)\}^2 A_L(\phi) H_c(\phi) \quad (8)$$

where ρ_{air} : the air density, U_{w0} : mean wind velocity, U_w : fluctuating wind velocity component, A_L : lateral windage area, H_c : height of centre of lateral windage area and C_m : aerodynamic drag coefficient. The fluctuating wind velocity is determined by the following equation:

$$U(t) = \sum_{i=1}^{N_w} b_i \sin(\sigma_i t + \psi_i) \quad (9)$$

where

$$b_i = \sqrt{2S_{wind}(\sigma_i) d\sigma} \quad (10)$$

The wind velocity in metres per second is modelled by the Davenport spectrum as follows:

$$S_{wind}(\sigma_i) = 4K \frac{U_{w0}}{\sigma_i} \frac{X_D}{(1 + X_D^2)^{4/3}} \quad (11)$$

where

$$K = 0.003 \quad (12)$$

$$X_D = 600 \frac{\sigma_i}{\pi U_{w0}} \quad (13)$$

The wave exciting moment is modeled as follows:

$$M_{wave}(t) = WGM \gamma \Theta(t) \quad (14)$$

where $\gamma \Theta(t)$ is the effective wave slope, which can be calculated with a strip theory. Similar to the fluctuating wind velocity, the wave slope is calculated as follows:

$$\Theta(t) = \sum_{i=1}^{N_w} \frac{\omega_i^2}{g} a_i \sin(\omega_i t + \varphi_i) \quad (15)$$

where

$$a_i = \sqrt{2S_{wave}(\omega_i) \delta\omega} \quad (16)$$

The sea elevation in metres is modelled using the spectrum recommended by the 15th International Towing Tank Conference (ITTC) as follows:

$$S_{wave}(\omega_i) = \frac{A}{\omega_i^5} \exp\left(\frac{-B}{\omega_i^4}\right) \quad (17)$$

where

$$A = 172.75 \frac{H_{1/3}^2}{T_{01}^4} \quad (18)$$

$$B = \frac{691}{T_{01}^4} \quad (19)$$

$H_{1/3}$ is the significant wave height (m) and T_{01} is the mean wave period (s).

2.2 Coupled sway-heave-roll-pitch model

More rigorous approach is modelling a six degrees-of-freedom motion as a rigid body in a three dimensional space. If surge and yaw motion is constrained for realising a beam sea condition in model experiments, sway-heave-roll and pitch motions should be modelled. The body-fixed coordinate system, $G-x,y,z$, of



which the origin is situated at the centre of ship gravity, the x axis pointing towards the bow, the y axis to starboard and the z axis downwards, and the inertia coordinate system, $O-\xi, \eta, \zeta$, which moves with a constant lateral speed in the direction of wind and waves, are used. The ξ axis is the direction of wave travel and the ζ axis points downwards.

The equations of coupled motion is given by

$$\begin{aligned} m\ddot{x}_2 &= F_2(x_2, x_3, x_4, x_5, \dot{x}_2, \dot{x}_3, \dot{x}_4, \dot{x}_5, \ddot{x}_2, \ddot{x}_3, \ddot{x}_4, \ddot{x}_5, t) \\ m\ddot{x}_3 &= F_3(x_2, x_3, x_4, x_5, \dot{x}_2, \dot{x}_3, \dot{x}_4, \dot{x}_5, \ddot{x}_2, \ddot{x}_3, \ddot{x}_4, \ddot{x}_5, t) \\ I_{44}\ddot{x}_4 &= F_4(x_2, x_3, x_4, x_5, \dot{x}_2, \dot{x}_3, \dot{x}_4, \dot{x}_5, \ddot{x}_2, \ddot{x}_3, \ddot{x}_4, \ddot{x}_5, t) \\ I_{55}\ddot{x}_5 &= F_5(x_2, x_3, x_4, x_5, \dot{x}_2, \dot{x}_3, \dot{x}_4, \dot{x}_5, \ddot{x}_2, \ddot{x}_3, \ddot{x}_4, \ddot{x}_5, t) \end{aligned} \quad (20)$$

where the suffices 2, 3, 4 and 5 denote sway, heave, roll and pitch motions measured from $O-\xi, \eta, \zeta$. The ship mass is indicated by m and the moment of inertia due to i th ($i=1, \dots, 6$) direction is I_{ij} . The external forces or moments in the i th direction, F_i , are assumed to consist of buoyancy (B), the Froude-Krylov (FK), radiation (R), diffraction (D), gravity (G), wind (WD) and hydrodynamic reaction (HR) components as follows:

$$F_i = F_i^B + F_i^{FK} + F_i^R + F_i^D + F_i^G + F_i^{WD} + F_i^{HR} \quad (21)$$

where

$$F_i^B = \rho g \int_{AE}^{FE} dx \int_{S_H(x_2, x_3, x_4, x_5)} (-zn_i) ds \quad (22)$$

$$\begin{aligned} F_i^{FK} &= -\rho g \int_{AE}^{FE} dx \int_{S_H(x_2, x_3, x_4, x_5)} \sum_{k=1}^{N_w} a_k \exp\left(-\frac{\omega_k^2}{g} \zeta\right) \\ &\quad \cos\left(-\frac{\omega_k^2}{g} \xi - \omega_k t + \varphi_k\right) n_i ds \end{aligned} \quad (23)$$

$$F_i^R = \sum_{j=2}^5 (-A_{ij}(x_4) \ddot{x}_j - B_{ij}(x_4) \dot{x}_j) \quad (24)$$

$$F_i^D = \sum_{k=1}^{N_w} a_k f_{ki}^D(x_4) \cos(-\omega_k t - \varepsilon_{ki}^D(x_4) + \varphi_k)$$

$$\begin{aligned} F_3^G &= mg \\ F_2^G &= F_4^G = F_5^G = 0 \\ F_2^{WD} &= \frac{1}{2} \rho \{U_{w0} + U(t)\}^2 A_L(\phi) C_m(\phi) \\ F_4^{WD} &= \frac{1}{2} \rho \{U_{w0} + U(t)\}^2 A_L(\phi) H_c(\phi) C_m(\phi) \\ F_3^{WD} &= F_5^{WD} = 0 \end{aligned} \quad (25)$$

(26)

AE : ship aft end, FE : ship fore end, n_j : the directional cosine of hull surface, S_H : the wetted surface, A_{ij} : the added mass due to the j th motion in the direction of the i th motion, B_{ij} : the wave making damping coefficient due to the j th motion in the direction of the i th motion, f_{ki}^D : amplitude of the wave diffraction force in the i th direction with the k th frequency and ε_{kj}^D : phase difference of the wave diffraction force in the i th direction with the k th frequency. The hydrodynamic reaction force is added to keep the mean position of the sway direction.

In this numerical model, the radiation force coefficients are estimated with a strip theory (Lee and Kim, 1982) using the natural roll frequency for sway and the peak wave frequency of heave and pitch. The roll radiation coefficients were estimated with the roll decay model tests. The diffraction forces are calculated with the strip theory (Salvesen et al., 1970). The roll restoring moment is obtained by a conventional manner. The aerodynamic coefficient is estimated with an empirical method (Fujiwara et al., 1998) and its heel effect is calculated by a momentum theory.

3. MODEL EXPERIMENT

Model experiments of a ship model in beam wind and waves were conducted in a seakeeping and manoeuvring basin of National Research Institute of Fisheries Engineering (NRIFE). The subject ship used here is a hypothetical ship known as CEHIPAR2792. Its principal particulars and restoring arm curves

are shown in Table 1 and Fig. 1, respectively. Its 1/70 scaled model has a flat plate on the upper deck for realising the windage area and its area centre height of the super structure but without additional buoyancy. The ship model was not equipped with bilge keels, propellers, shaft brackets and rudders. An optical fibre gyroscope inside the model is used for detecting the roll, pitch and yaw angles.

Table1: Principal particulars of the CEHIPAR2792 ship

Displacement	24585.7	Ton
Length between perpendicular	205.7	m
Breadth	32	m
Draught	6.6	m
Metacentric height: GM	2	m
Natural roll period	18.36	s

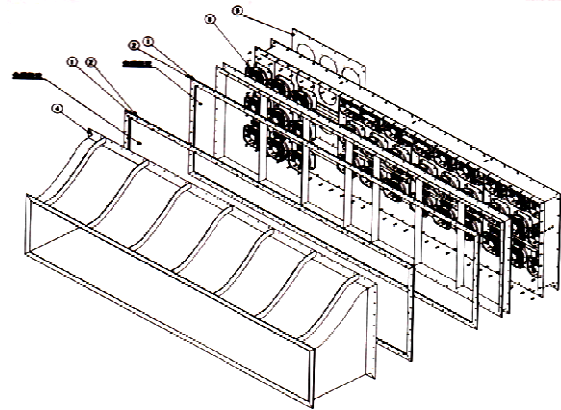


Figure 3: Wind blower

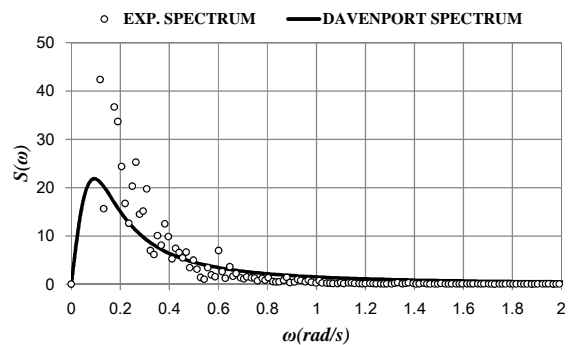


Figure 4: Wind velocity spectrum

Irregular water waves were generated by plunger-type wave makers with the ITTC spectrum. As shown in Fig. 2, the specified spectrum was satisfactorily realised. Fluctuating wind was generated by a wind blower in the wave direction. The wind blower, as shown in Fig. 3, consists of 36 axial flow fans and is controlled by invertors with a v/f control law. The relationship between the frequency for this control and the wind velocity was adjusted by measuring steady heel angle of the ship model under non-fluctuating wind with the equation (8). The wind velocity spectrum is designed with the Davenport one. The measured spectrum agrees with the specified one in the region around the ship natural roll frequency, i.e. 0.34 rad/s, as shown in Fig.4.

The model was kept to be orthogonal to the wind and wave direction by a wire system, which softly restrains drift and yaw. Here the

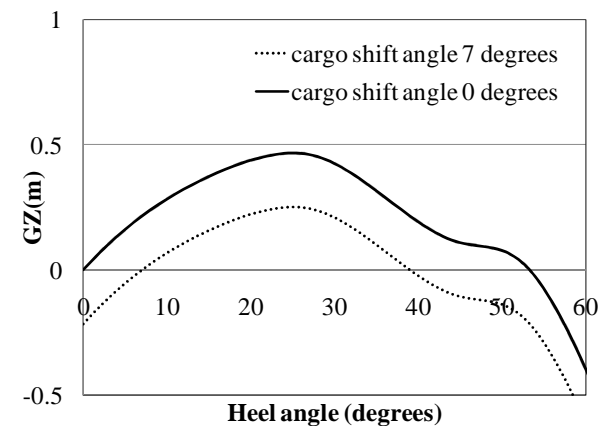


Figure 1: GZ curves of the CEHIPAR2792 ship

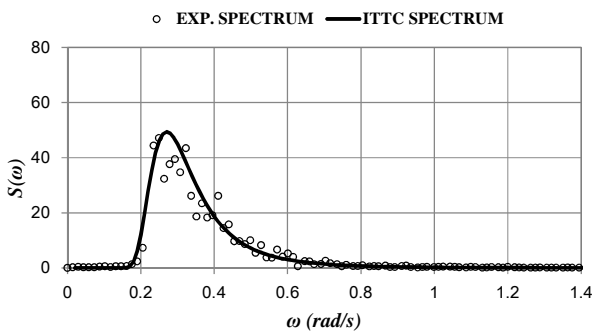


Figure 2: Wave spectrum



wire system was connected to the ship model at bow and stern where the height was set to be equal to calm water surface based on measured hydrodynamic reaction force and moment in a captive model test of the subject ship. The mean of fluid dynamic force in the sway direction was cancelled out by a counter weight as shown in Fig. 5.

The experimental condition in full scale was specified as the wind velocity of 30 metres per second, the significant wave height of 11.04 metres, the mean wave period of 16.48 seconds and the duration of 1 hour. Furthermore, for simulating cargo shifts, three different constant heel angles, i.e. six, eight and ten degrees, were added due to lateral shifts of weights on board. The wave elevation was measured by a servo needle-type wave probe and the wind velocity was measured by a hot wire sensor. Instantaneous model position relative to the basin was measured by a total station system. This system consists of a theodolite, an optical distance measuring device, and a prism which is on the model.

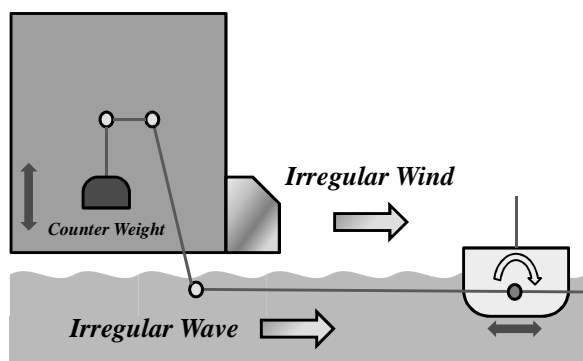


Figure 5: Layout of experimental set-ups

Many realisations were repeated and then capsizing probability was estimated as the ratio of the number of capsizing to that of realizations. The confidence interval was estimated assuming the binomial distribution.

4. COMPARISON BETWEEN EXPERIMENT AND CALCULATION

The results of comparison between the experiment and the calculations with these confidence intervals of 95 per cents are shown in Fig. 6. Here the number of realisations of 1 degrees-of-freedom (DoF) model and 4 DoF model for each heel angle are 1000 and 300, respectively. As a result, their confidence intervals are very small. On the other hand, the number of realisation of the experiment for each heel angle is 25 or less so that the confidence interval is not so small. As a whole, when the heel angle due to cargo shift increases, the total stability failure increases. The 1 DoF model roughly agrees with the experiment but in case of the heel angle of 8 degrees the confidence interval of the 1 DoF model and that of the experiment is not overlapped. In contrast, the confidence interval of the 4 DoF model and that of the experiment is completely overlapped for all three cases. Thus, it can be concluded that agreement between the experiment and 4 DoF model is satisfactory and the 4 DoF model slightly overestimates the experiment. This means the 4 DoF simulation model used here provides a conservative prediction at least for this subject ship and the tested environmental condition.

To investigate the reason of discrepancy between the experiment and the simulation models, the roll spectra are calculated as shown in Fig. 7. The results indicate that the roll spectral density of the simulation models are larger than that of the experiment in the region of the frequency ranging from 0.25 to 0.3 rad/s. The difference between the two simulation models is not so significant. Thus, it can be presumed that roll damping moment could depend on frequency although both the models use the roll damping at the natural roll frequency. It might be desirable to model the effect of frequency on the roll damping in future.

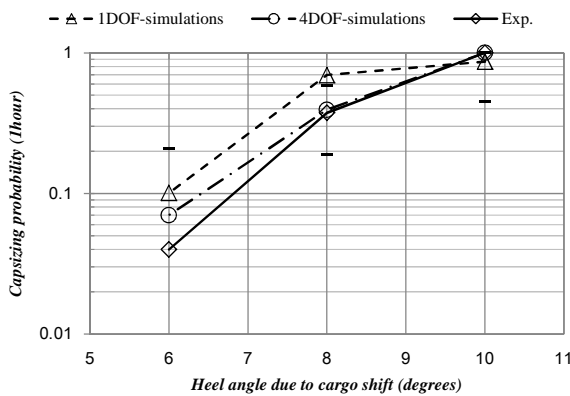


Figure 6: Estimated Probability of total stability failure for one hour with the confidence intervals. Here the wind velocity of 24.5(m/s), the significant wave height of 11.04(m) and the mean wave period of 16.48(s)

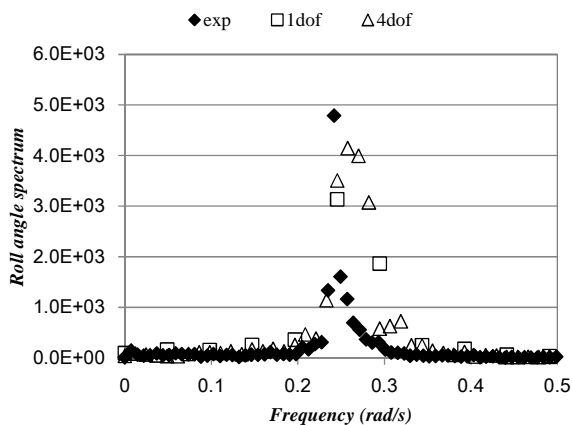


Figure 7: Roll spectra. Here the cargo shift angle of 8 degrees, the wind velocity of 24.5(m/s), the significant wave height of 11.04(m) and the mean wave period of 16.48(s)

Furthermore, the phase difference between the roll angle and sway velocity is estimated with the cross spectrum of these variables as shown in Fig. 8. The phase difference between the two is generally small but not exactly zero as we assume in the derivation of the 1 DoF model. This could be the reason why the 4 DoF model outcomes improve the 1 DoF ones but it should be discussed with the accuracy of spectral analysis in future.

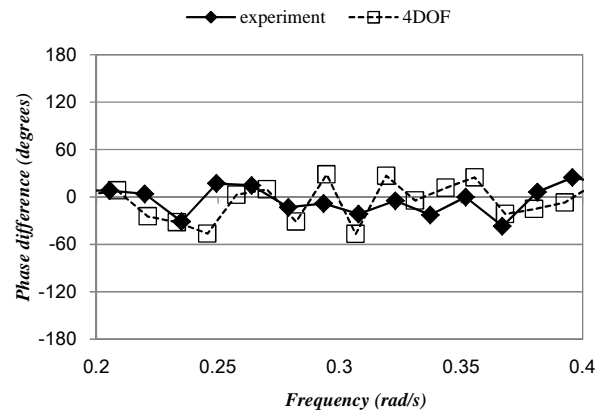


Figure 8: Phase difference between the roll angle and sway velocity. Here the cargo shift angle of 6 degrees, the wind velocity of 24.5(m/s), the significant wave height of 11.04(m) and the mean wave period of 16.48(s)

5. CONCLUDING REMARKS

A coupled sway-heave-roll-pitch model in irregular beam wind and waves based on a potential flow theory is presented for quantifying total stability failure probability by the Monte Carlo simulation. The physical model experiment was executed under stochastic wind and waves. The comparison among the existing and present simulation models and the experiment indicates that the probability of total stability failure estimated by the present simulation model exists within the confidential interval of those estimated by the experiment. The existing uncoupled model does not show similar agreements as the present model.

6. ACKNOWLEDGEMENTS

This work was supported by a Grant-in Aid for Scientific Research of the Japan Society for Promotion of Science (No. 21360427). It was partly carried out as a research activity of Stability Project of Japan Ship Technology Research Association in the fiscal year of 2011, funded by the Nippon Foundation. The authors sincerely thank these organisations. The



authors also appreciate Prof. Alberto Francescutto and Dr. Gabriele Bulian from the University of Trieste for kindly providing data of the subject ship. The authors are grateful to Dr. Daisuke Terada from NRIFE, Mr. Keisuke Yamane, Mses. Hisako Kubo, Ayumi Morimoto and Fuka Yoshiyama from Osaka University for their assistance in the experiments.

7. REFERENCES

- Fujiwara, T., Ueno, M. and Nimura, T. (1998). "Estimation of Wind Forces and Moments Acting on Ships", Journal of Society of Naval Architects of Japan, Vol. 183, pp. 77-90, (in Japanese).
- IMO, 2008, "Explanatory Notes to the International Code on Intact Stability", MSC.1/Circ. 1281, London.
- IMO, 2012, "Development of Second Generation Intact Stability Criteria - Report of the Working Group (part I)", SLF 54/WP.3, London.
- Kajita, E and Tanaka, K., 1986, "Experimental Techniques for Behaviors of Offshore Structures Under Extreme Environmental Conditions", Proceedings of the 3rd Marine Dynamics Symposium, The Society of Naval Architects of Japan, pp. 375-395, (in Japanese).
- Kubo, T., Maeda, E. and Umeda, N., 2010, "Theoretical Methodology for Quantifying Probability of Stability Failure for a Ship in Beam Wind and Waves and its Numerical Validation", Proceedings of 4th International Maritime Conference on Design for Safety, Trieste, pp.1-8.
- Lee, C.M. and Kim, K.H., 1982, "Prediction of Ships in Damaged Condition in Waves", Proceedings of the 2nd International Conference on Stability of Ships and Ocean Vehicles, Tokyo, pp. 287-301,
- Ogawa, Y., de Kat, J.O. and Ishida, S., 2006, "Analytical Study of the Effect of Drift Motion on the Capsizing Probability under Dead Ship Condition", Proceedings of the 9th International Conference on Stability of Ships and Ocean Vehicles, Rio de Janeiro, Vol. 1, pp. 29-36.
- Salvesen, N., Tuck E.O. and Faltinsen O. 1970, "Ship Motions and Sea Load", Transaction of the Society of Naval Architects and Marine Engineers, Vol.78, pp.250-287.
- Shaughnessy, J., Nehrling, B.C. and Compton, R.H., 1994, "Some Observations on Experimental Techniques for Modeling Ship Stability in Wind and Waves", Proceedings of the 5th International Conference on Stability of Ships and Ocean Vehicles, Melbourne, Vol. 3, pp. 21-37.
- Tasai, F., 1965, "On the Equation of Rolling of a Ship", Bulletin of Research Institute for Applied Mechanics, Kyushu University, Vol. 26, pp. 51-57. (in Japanese).
- Umeda, N., Koga, S., Ueda, J., Maeda, E., Tsukamoto, I. and Paroka, D., 2007, "Methodology for Calculating Capsizing Probability for a Ship under Dead Ship Condition", Proceedings of the 9th International Ship Stability Workshop, Hamburg, pp. 1.2.1-1.2.19.
- Umeda, N., Izawa, S., Sano, H., Kubo, H. and Yamane, K., 2011, "Validation Attempts on Draft New Generation Intact Stability Criteria", Proceedings of the 12th International Ship Stability Workshop, Washington D.C., pp.19-26.
- Vassalos, D., Jasionowski, A. and Cichowicz, J. (2004). "Issues Related to the Weather Criterion", International Shipbuilding Progress, Vol. 51, No. 2/3, pp. 251-271.
- Watanabe, Y. 1938, "Some Contributions of the Theory of Rolling." Transactions of Institution of Naval Architects, Vol. 80, pp.408 – 432.



Quantitative Analysis of Parametric Roll and Operational Guidance

KangHyun Song, *Korean Register of Shipping*, khsong@krs.co.kr

YongHwan Kim, *Seoul National University*, yhwhankim@snu.ac.kr

ABSTRACT

This paper addresses huge number of numerical simulations is needed to get a stable long-term prediction of parametric roll in consideration of actual wave scatter diagram and loading conditions, because parametric roll is highly non-ergodic process. To this end, a very fast and effective numerical tool is proposed by transfer functions of GM mean and amplitude and approximated GZ curve based on assumption of linearity. The effects of the GM mean and amplitude on parametric roll are discussed in regular wave cases. Some factors which influence the probability density function are discussed such as number of realizations, run length and initial roll angle in irregular waves. Using this model, the long-term predictions of parametric roll are carried out for typical post-Panamax container ships such as 6500, 8000, 10000 TEU carriers and a VLCC using Monte Carlo Method. The results are analyzed based on effect of GM variation and each ship type.

As a countermeasure, development of operational guidance and relevant procedure are shown based on IRF method. The guidance show clear and enough information for ship crew's decision supporting even if the results are calculated qualitatively because of limitation of computation time. The dangerous situations in real sea are discussed based on the results.

Keywords: *parametric roll, quantitative analysis, GZ approximation, GM RAO, operational guidance*

1. INTRODUCTION

The primary difficulty in quantifying parametric roll is that this phenomenon is a non-ergodic process (Belenky et al., 2001), because parametric roll motion is not a linear system due to nonlinear restoring moment and damping. If the process is not ergodic, a number of realizations are necessary to get a stable probability density function. More number of realizations will give more stable results and the proper number of realization will depends on the degree of non-ergodicity (Belenky, 2003).

Considering many sea states in wave scatter diagram, the total number of realizations to get a stable longterm prediction significantly increases. Therefore very fast and effective

numerical tool is needed for quantitative analysis under some simplification of real physics.

The influence of roll motion on heave and pitch motions is not significant (Paulling, 1959). Therefore it is not strongly needed to solve a fully coupled heave-roll-pitch equation, but the 1-DOF roll motion should include explicitly the influence of heave and pitch motions. This means that the pre-computed heave and pitch motions can be used in solving roll motion equation.

GM change, the main source of parametric roll, mainly comes from the wave elevation and heave and pitch motion. Fortunately, these processes can be assumed as linear system, Gaussian distribution and ergodic process. It



means that one long realization is enough to get constant statistical parameters such as mean value and standard deviation and consequently probability distribution.

The GM fluctuation can be expressed by Fourier series. The mean value and first component are very important and these values are quite linear for post-Panamax container carrier. Under this assumption, transfer function of mean and first component can be used as GM variation in irregular seas.

Simplification of righting arm using still water GZ curve and above GM variation can make it possible to carry out a huge number of numerical realizations by Monte Carlo Method. Using this simplified method, the vulnerability of parametric roll will be measured quantitatively for a post-Panamax container ship with several GM values considering all seas states in North Atlantic seas. This kind of quantitative results can be useful for ship design and validation of safety level to decide a proper criteria and standard.

If the ship design is not satisfied with a standard of parametric roll corresponding to certain safety level, the severe parametric roll should be avoided in operational stage by means of provision of a proper guidance. The guidance should be developed using state of art tools as far as possible to support ship crew's proper decision making in urgent situation according to 'Framework of New Generation of Intact Stability Criteria' (IMO, 2010).

The impulse-response-function (IRF) approach formulated by Cummins (1962) can be a good candidate to compromise the accuracy and efficiency of numerical computation. This approach solves the equation of ship motion by using pre-computed hydrodynamic coefficients. Using this advantage, Spanos and Papanikolaou (2007) have applied the IRF approach in the parametric roll analysis of a fishing vessel.

2. MATHEMATICAL MODEL

2.1 Roll motion equation

Let's consider the following 1-DOF equation of roll motion in order to describe parametric roll in longitudinal waves:

$$(I_{44} + A_{44})\ddot{\phi} + \delta_1\dot{\phi} + \delta_2\phi|\dot{\phi}| + \Delta \cdot GZ(\phi, z, \theta, \zeta, t) = 0 \quad (1)$$

ϕ is the roll angle, and I_{44} , A_{44} , Δ are the roll moment of inertia, the roll added moment inertia, and ship displacement, respectively. δ_1 and δ_2 are linear and quadratic damping coefficients. The restoring lever GZ is affected mostly by the change of water-plan area which is dictated by roll angle ϕ , displacement of heave z , pitch angle θ and wave elevation ζ .

Taking the advantage that the influence of roll motion on heave and pitch motions is not significant, pre-computed heave and pitch motions can be used to compute GZ . In the computational viewpoint, this provides the significant reduction of computational effort.

Better computational efficiency can be achieved if a proper approximation for GZ can be introduced. In the analysis of above equation, GZ is an instantaneous quantity which can be obtained by the integration of external pressure on the wetted ship surface. Such instantaneous direct pressure integration can require a significant computation time, particularly when long simulation is considered in irregular waves. Therefore, if GZ can be accurately approximated to a simple manner, a significant reduction of computation time can be expected.

2.2 GM fluctuation

The GZ curve is quite linear up to certain heeling angle before the side of a deck is immersed into water for many ship types. The linear region of GZ curve is almost up to 30

degrees for container ships and even larger in case of tankers. This is still true for a ship in waves. The Figure 1 shows the GZ curves in every time steps when the crest of a wave moves forward along the ship length for typical post-Panamax container ship. The wave length is equal to the ship length and wave height is 12 meter. The bold line stands for still water GZ curve. Therefore, the slope of GZ curve or GM is very important to predict the initial occurrence of parametric roll and its growth to some extent before the roll is bounded to a steady angle due to nonlinear components of GZ curve.

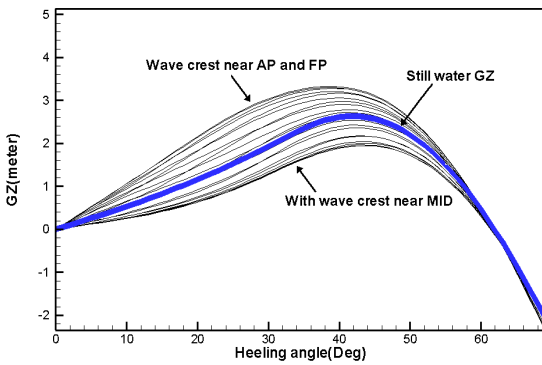


Figure 1: GZ curves for typical post-Panamax containership

Figure 2 shows the GM variation of a post-Panamax container ship, accounting for wave, heave, pitch and geometrically nonlinear hull shape. When the wave crest is in midship region, the parallel middle body is immersed and the water plane area is a little bit smaller than that of still water and the variation of water plane area is quite small as the crest passes along the long parallel body. On other hand, when the wave crest is near bow and stern, the water plane area is much larger and the variation of water plane area is quite big because the overhanging transom and bow flare are immersed and wetted area is rapidly changed.

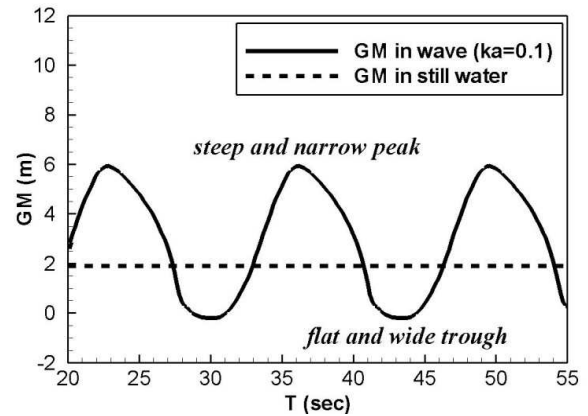


Figure 2: GM fluctuation for typical post-Panamax containership

$GM(t)$ can be decomposed into a fluctuation term $GM_f(t)$ and a still-water term GM_{still} and the $GM_f(t)$ can be also expressed by Fourier series as follows.

$$GM(t) = GM_f(t) + GM_{still} \quad (2)$$

$$GM_f(t) = GM_0 + \sum_{n=1}^{\infty} GM_n \cos(n\omega t + \alpha_n) \quad (3)$$

Figures 3 to Figure 5 show transfer functions of GM_0 , GM_1 , and GM_2 which are mean value, the first and second harmonic amplitudes of $GM_f(t)$ respectively. It shows that GM_0 is always positive as already expected by geometrical shape and the value of VLCC is smaller than those of container ships.

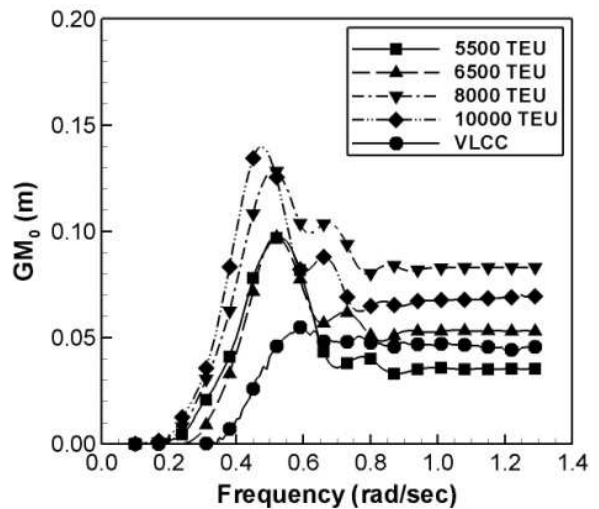


Figure 3: Transfer function of GM_0

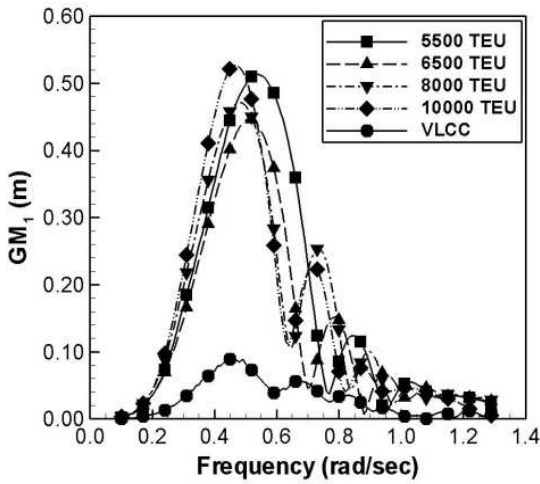


Figure 4: Transfer function of GM_1

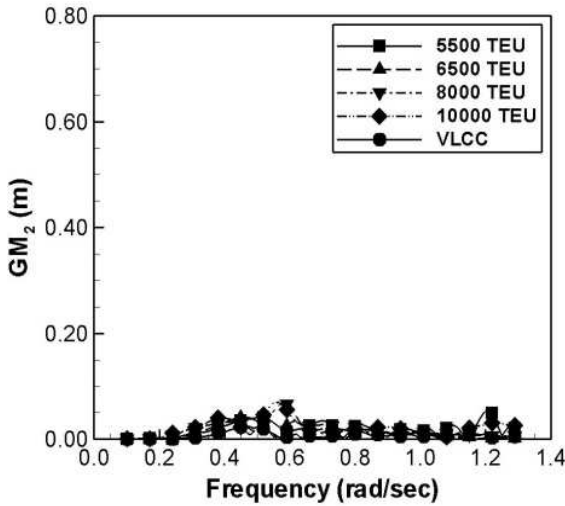


Figure 5: Transfer function of GM_2

The role of GM_0 and GM_1 is obvious to check vulnerability of parametric roll by means of Matieu equation (ABS, 2004). The GM_0 and GM_1 are induced by geometrical nonlinearity but Figure 6 and Figure 7 show that both of values are quite linear up to very high wave amplitude before the deck is immersed. This kind of linearity is dependent on hull shape and can be verified only numerically. Considering severe geometrical nonlinearity of container ships, this assumption can be applied to most of ship types in general.

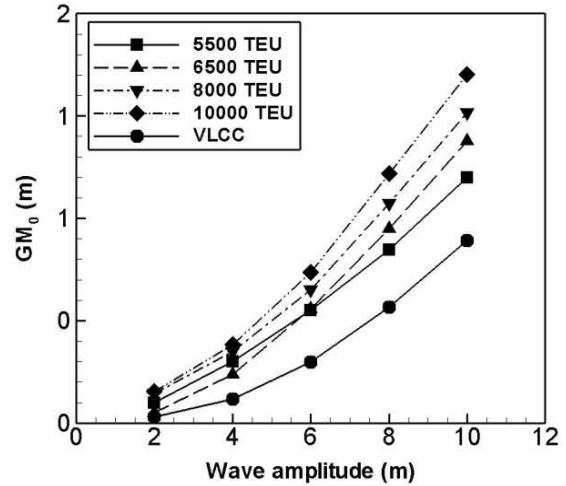


Figure 6: Variation of GM_0 for wave heights

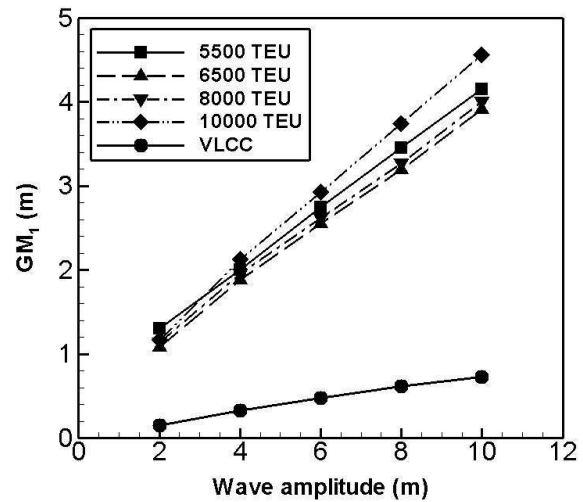


Figure 7: variation of GM_1 for wave heights

The assumption of linearity of GM_1 in container ship can be also validated in irregular waves. If GM_1 is linear, the response spectrum of GM_1 $S(GM_1, \omega)$ can be obtained by RAO of GM_1 $RAO_{GM_1}(\omega)$ and wave spectrum $S(\omega)$.

$$S(GM_1, \omega) = RAO_{GM_1}(\omega)^2 S(\omega) \quad (4)$$

Figure 8 shows the comparison between the response spectrum GM_1 and Fourier transform results from numerical time simulations of GM .

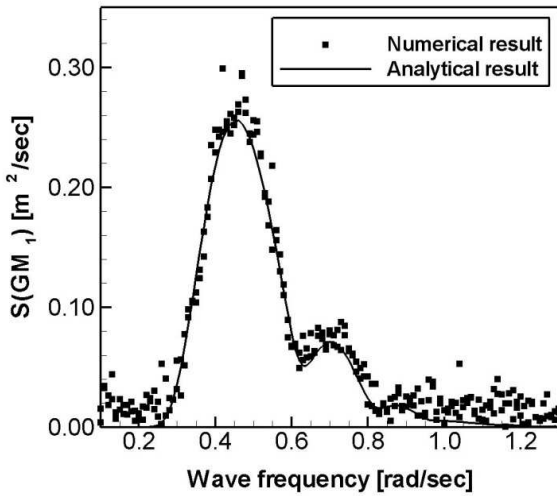


Figure 8: Comparison of Response spectrum of GM_1 between numerical and analytical approach.

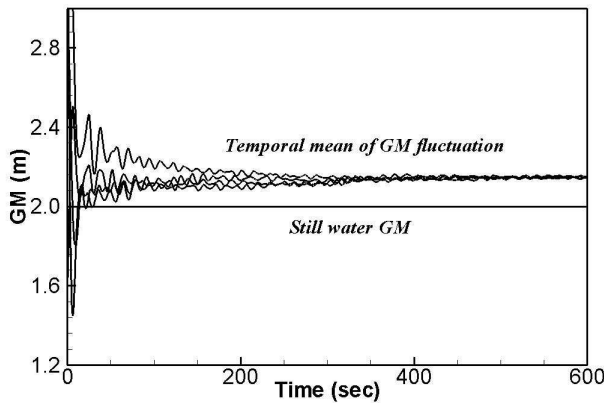


Figure 9: GM mean variation for several numerical realizations.

Figure 9 shows also the temporal means of GM variations by several numerical tests. It shows that temporal means of GM variation is asymptotically converged to certain value and its value is positive like a regular wave case. The shift of GM_0 in irregular wave can be obtained by following equation under the assumption of linearity and Rayleigh distribution of GM_0 .

2.3 Approximation of GZ curve

The approximation of GZ curve is essential to reduce computation cost. Even if there are several approaches to calculate GZ curves (Vidic-Perunovic, 2010) the approximation of

GZ curve by still water GZ curve and GM variation (IMO, 2010) is very useful to reduce computation cost with keeping an acceptable accuracy. Figure 1 shows that the angles corresponding zero restoring moment are not changed according to the position of wave crest. It is easily understood that the variation of water plane area in a wave is small when a ship is inclined to severe roll angle.

The GZ curve in waves is fitted using still water GZ curve $GZ_{still}(\phi)$ and roll angle ϕ where GZ curve is zero.

$$GZ(\phi, t) = GZ_{still}(\phi) + \{GM(t) - GM_{still}\} \times \{\sin(\phi) - \sin(\phi)^3 / \sin(\phi)^2\} \quad (5)$$

2.4 1 DOF roll motion equation

The $GM(t)$ in (6) can be obtained for an irregular wave with significant wave height H_s and zero crossing period by following equation.

$$GM(t) = GM_{still} + GM_0(H_s, T_z) + \sum \zeta_i \cdot RAO_{GM1}(\omega_i) \cdot \cos(\omega_i t + \alpha_i) \quad (6)$$

ω_i and α_i are encounter frequency and random phase angle of each regular wave component respectively. The wave height ζ_i can be calculated from following equation using wave spectrum $S(H_s, T_z, \omega_i)$.

$$\zeta_i = \sqrt{2 \cdot S(H_s, T_z, \omega_i) d\omega} \quad (7)$$

The substitution of (6) and (7) into (1) leads to following roll equation in an irregular wave.

$$(I_{44} + A_{44})\ddot{\phi} + \delta_1 \dot{\phi} + \delta_2 \phi + \Delta \cdot [GZ_{still}(\phi) + \{GM_0(H_s, T_z) + \sum \zeta_i \cdot RAO_{GM1}(\omega_i) \cdot \cos(\omega_i t + \alpha_i)\} \cdot \{\sin(\phi) - \sin(\phi)^3 / \sin(\phi)^3 / \sin(\phi_{max})^2\}] = 0 \quad (8)$$

$$m_0 = \int S(H_s, T_z, \omega) RAO_{GM0}(\omega)^2 d\omega \quad (9)$$

$$GM_o(H_s, T_z) = 1.25 \sqrt{m_0} \quad (10)$$



3. NUMERICAL CALCULATION

3.1 Irregular wave case

Figure 10 shows the number of parametric roll occurrence during 100 times of numerical realizations for each sea state. Parametric roll never occurs in sea state A and C and always occurs in sea state B. Figure 14 shows response spectrum of GM_1 for point A, B and C. In point B, the response spectrum of GM_1 are maximized and the energy are concentrated near the resonance frequency(0.48) while the spectrum are spread and low at point B and C. It means the distance between the modal frequency of response spectrum of GM_1 and resonance frequency and the area near resonance frequency can be a good index for parametric roll occurrence in irregular waves.

3.2 Long-term prediction

Long-term predictions to quantify the vulnerability to parametric roll are carried out for following typical modern container ships and a VLCC. North Atlantic Wave data are used for occurrence probability of each sea state.

1000 times of numerical simulation are carried out for each short-term sea state and each simulation takes 40 minutes and first half are cut off. The initial roll angle is 15 degrees with zero velocity. Zero ship speed is considered. The probability of exceeding roll angle ϕ is calculated as following equations.

$$P(x > \phi) = \sum \sum P(x > \phi, H_{s_i}, T_{z_j}) * P(H_{s_i}, T_{z_j}) \quad (11)$$

$P(H_{s_i}, T_{z_j})$ is occurrence probability of sea state with i th significant wave height H_{s_i} and j th zero crossing period T_{z_j} .

Figure 12 shows long-term predictions of roll angle for various GM values. Each graph starts from certain probability level because parametric roll are not observed in mild sea states or the modal wave frequency is far from the resonance frequency. Lager GM gives low exceeding probability in general. However, the

exceeding probability with GM 0.5 is smaller than that of 1.0 and 1.5. In this case, the resonance frequency is shifted to lower frequency where exciting energy is smaller. There is a certain threshold value of GM where parametric roll never occurs. For this container ship, the threshold GM value is between 3 and 4. The angle from which the curve is kept constant stands for total stability failure angle. Large GM results in large roll acceleration, and total stability failure starts from smaller angle due to large inertia forces.

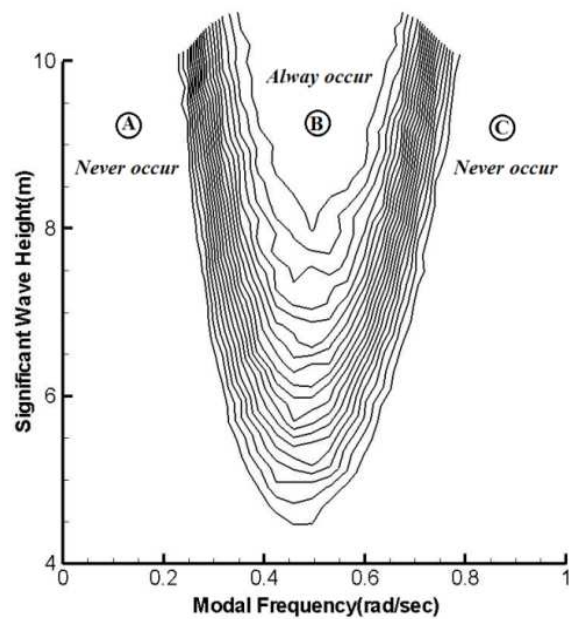


Figure 10: Map of parametric roll occurrence for irregular waves.

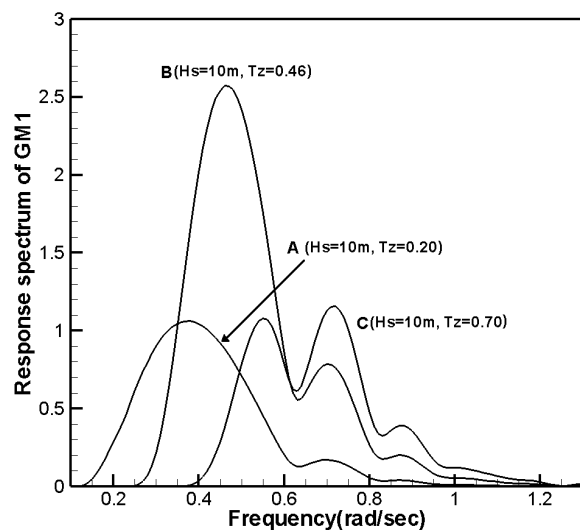


Figure 11: Map of parametric roll occurrence for irregular waves.

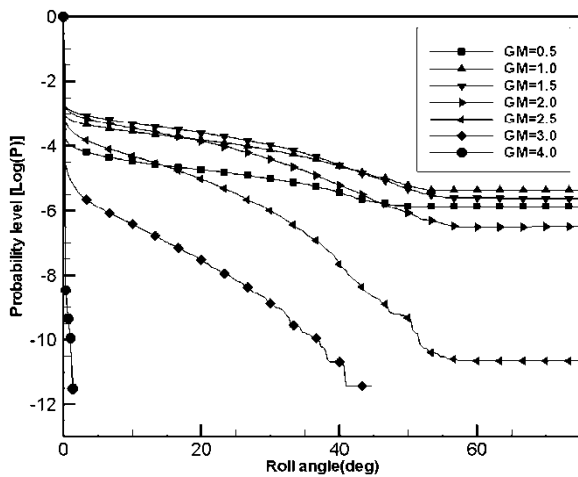


Figure 12: Long-term prediction of parametric roll for GM_{still} variation.

Figure 13 also shows long-term predictions of roll angle for typical container ships. The shapes of curves are very similar and the vulnerability to parametric roll is clearly determined. Based on the 10,000 TEU container ship is most vulnerable to parametric roll. The vulnerability of Even though GM_1 transfer function of 5500 TEU is larger than that of 8000 TEU, 8000 TEU is more vulnerable to parametric roll because the sea states of which length is near effective ship length is different. Therefore, the vulnerability is dependent on not only GM_1 transfer function but also ship length.

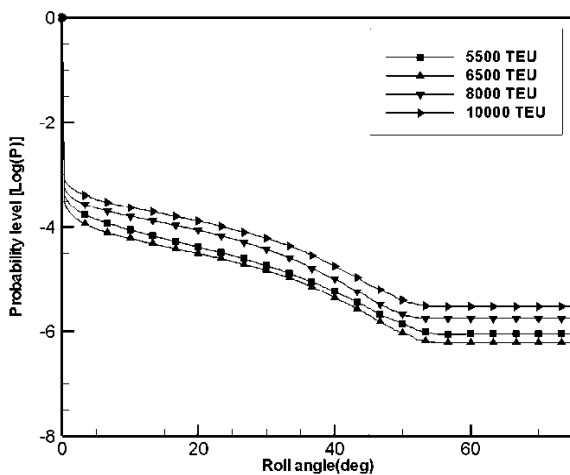


Figure 13: Long-term prediction of parametric roll for typical container ships.

Based on above results, the parametric roll occurs under the two conditions. The first

condition is that GM should be quite low so the wave energy near resonance frequency is sufficiently large. The other condition is the variation of water plane area or self - exciting energy is large enough to overcome threshold value.

4. OPERATIONAL GUIDANCE

The change of ship design as a counter measure of parametric roll is limited for both of ship designers and owners because it increases the shipbuilding cost and may sacrifice cargo capacity by reducing flare angle and long transom stern. Increase of GM value results in excessive transverse acceleration and reinforcement of cargo securing system. To install roll damping devices may be a good choice but still expensive.

The best way to solve this problem in the view of economic efficiency is to provide operational guidance to ship crew to avoid very dangerous situations. If the ship can be avoided from severe environmental and operational conditions for parametric roll, the exceeding probability can be let down dramatically to satisfy above criteria. This kind of operational guidance should be made by using state of art tools which can deal with 6 DOF freedom, arbitrary heading angle and ship speed. However we should consider so many cases to deal with many GM s, speeds, heading angles and sea states to develop the operational guidance which is precise enough to support decision making.

In this paper, the impulse-response-function (IRF) approach is used to develop operational guidance, keeping the accuracy and efficiency of numerical computation. This approach solves the equation of ship motion by using pre-computed hydrodynamic coefficients that helps to reduce the computation times. Therefore, IRF method is applied to develop the operational guidance for 10,000 TEU container ship.



Table 1 shows the calculation conditions to develop operational guidance for 10000TEU. The occurrence map shown in Figure 14 is developed with respect to ship speeds and heading angles which are controllable by ship crews under given external condition such as wave heights and periods and GM s .

Only one realization is carried out for one sea state. The roll value stands for the mean value of one third maximum rolls. The figure shows very clear indication of danger zone and safe zone even if one realization is performed. Considering the purpose of operational guidance is not to give exact roll angle but to indicate the degree of danger, it can be acceptable.

The most dangerous region is more than 10 knots in following sea with wave length near 200m and very low GM . In this region, the ship is very vulnerable to parametric roll because the encounter modal frequency is near resonance one in that speed and the response spectrum is very narrow-banded and wave energy is concentrated on resonance frequency. When the wave length is near the ship length, both of following sea and head sea are dangerous for all speed ranges.

Table 1 Calculation condition for operational guidance.

Parameter	Value
Ship Type	10,000 TEU Container carrier
L, B, D(m)	334, 45.6, 27.3
Hs(m)	6, 7, 8
H. Ang.(deg)	0 ~ 360 (15 increment)
Tz(sec)	25, 18, 14, 10, 8
GM(m)	0.73, 1.2, 1.8
Speed(knots)	0 ~ 15(1.5 increment)

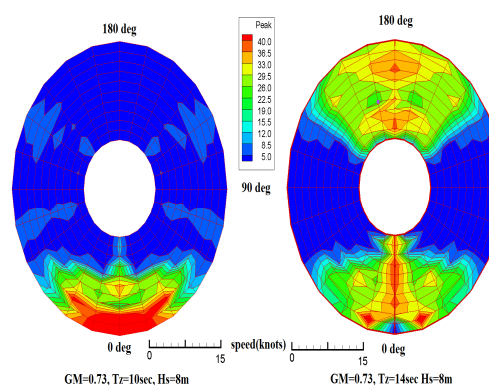


Figure 14: Occurrence maps for parametric roll

5. CONCLUSIONS

The linearity of mean and first harmonic amplitudes of GM fluctuation is valid for Post-Panamax container ship. The mean and first harmonic amplitudes are dominant to the occurrence of parametric roll. The second harmonic components can result in parametric roll in a very high regular wave but it is impossible in a real sea case. The roll may decrease as wave height increase due to change of resonance frequency induced by shift of mean value.

The GZ can be approximated by mean and first harmonic amplitudes of GM fluctuation and also by still water GZ curve. It gives very fast computation keeping some degree of accuracy.

1 DOF roll equation based on above assumption and approximation is proposed and tested for both of regular and irregular waves. This method is very useful to get a stable longterm prediction accounting for a large number of numerical realizations by Monte Carlo Method.

Using the method, the vulnerabilities to parametric roll can be quantified in a practically short time. The vulnerability to parametric roll of Post-Panamax ship is governed by GM value and if the GM is over certain critical value the parametric roll never occurs.



The operational guidance can be developed successively based on IRF method, giving ship operators enough information to avoid severe roll angle even if one realization is carried out. These results can give ship operator qualitative information such as very danger zone, danger zone, cautious zone and safe zone.

6. REFERENCES

- ABS, 2004, "Guide for the Assessment of Parametric Roll Resonance in the design of Container Carriers", Houston, Texas
- Cummins, W.E., 1962, "The impulse response function and ship motions," Schiffstechnik, Vol 47, No 9, pp101-109
- Dunwoody, A.B., 1989, "Roll of a ship in astern Seas – Metacentric height spectra," Journal of Ship Research, Vol 33, No 3, pp 221-228
- Gabriele Bulian, 2006, "Theoretical, numerical and experimental study on the problem of ergodicity and 'practical ergodicity' with an application to parametric roll", Ocean Engineering 33, , pp. 1007-1043
- IMO SLF 52/INF.2, 2010, "Development of New Generation Intact Stability Criteria", IMO document, London.
- IMO SLF 52/WP.1, 2010, "Development of New Generation Intact Stability Criteria", IMO document, London.
- Kim, Y.H., 2011, "Time-domain analysis of nonlinear motion responses and structural loads on ships and offshore structures: development of WISH programs", International Journal of Naval Architecture and Ocean Engineering, Vol 3, No1, pp 37-52
- Spanos, D., 2007, "Numerical simulation of parametric roll in head seas," International Shipbuilding Progress 54, pp 249-267
- V. L. Belenky, 2003, "Prababilistic analysis of roll parametric resonance in head seas", Proc. 8th International Conference on the Stability of Ships and Ocean Vehicles, Madrid
- Vidic-Perunovic, 2011, "Influence of the GZ calculation method on parametric roll prediction", Ocean Engineering 38, , pp. 295-303.





Dependence of Roll and Roll Rate in Nonlinear Ship Motions in Following and Stern Quartering Seas

Vadim Belenky, *David Taylor Model Basin (NSWCCD)*, vadim.belenky@navy.mil

Kenneth M. Weems, *Science Applications International Corporation*, kenneth.m.weems@saic.com

ABSTRACT

The changing stability of a ship in waves may have a significant influence on the probabilistic properties of roll in irregular following and quartering seas. In particular, nonlinear effects may lead to dependence between roll angles and rates, which will have significant repercussions on the application of the theory of upcrossings for evaluating the probability of a stability failure related to roll motion such as capsizing. The roll response of a ship in a stationary seaway is a stationary stochastic process. For such a process, the roll angle and its first derivative are, by definition, not correlated and are often assumed to be independent. However, this independence can only be assumed *a priori* for normal processes, and it has been shown that the nonlinearity of large-amplitude roll motions can lead to a deviation from normal distribution. In the present work, the independence of roll angles and rates is studied using the results of numerical simulations from the Large Amplitude Motion Program (LAMP), which includes a general body-nonlinear calculation of the Froude-Krylov and hydrostatic restoring forces. These simulations show that for the considered case, the independence of roll and roll rates can be assumed in beam seas even though the distribution of the roll response is not normal, but cannot be assumed in stern quartering seas.

Keywords: *Independence, Correlation, Roll Motions, Stern Quartering Seas*

1. INTRODUCTION

The problem of dependence between roll and roll rate appeared during the extension of the split-time method to following and stern quartering seas (Belenky, *et al.*, 2010). The split-time method is intended for estimating the probability of capsizing from the results of advanced numerical simulation, and is being implemented using the Large Amplitude Motion Program – LAMP (Shin, *et al.*, 2003).

The method is based on the principle of separation, in which the problem of evaluating the probability for an extremely rare event in an extremely nonlinear dynamical system is separated into two problems related to events that are less rare (Belenky *et al.*, 2012). The first problem is to find the upcrossing rate for an intermediate level of roll, which is typically selected to be around the maximum of the roll

restoring (GZ) curve. The second problem is to evaluate the probability of capsizing if upcrossing occurs.

The method was initially implemented for the probability of capsizing in beam seas in dead ship conditions (Belenky, *et al.*, 2008). The number of upcrossings was intended to be calculated by fitting the distributions of roll angles and rates and then using the following theoretical formula:

$$\xi = f(\phi_{m0}) \int_0^{\infty} \dot{\phi} f(\dot{\phi}) d\dot{\phi}, \quad (1)$$

where ϕ is the roll angle, ϕ_{m0} is the intermediate threshold, a dot above a symbol means a temporal derivative, and $f()$ is a probability density function (PDF).



Formula (1) assumes independence between the roll angles and roll rate (Kramer and Leadbetter, 1967). The applicability of this assumption for roll motions and rates in stern quartering seas is the main subject of this paper.

2. DEPENDENCE AND CORRELATION

When the stochastic processes of roll and roll rate are independent, the following formula is correct:

$$f(\phi, \dot{\phi}) = f(\dot{\phi})f(\phi) \quad (2)$$

Correlation is one measure of dependence. It is defined through the joint second moment M , which is known as covariance, or the correlation coefficient r :

$$M_{\phi, \dot{\phi}} = \int_{-\infty}^{\infty} (\phi - m_{\phi}) \dot{\phi} f(\phi, \dot{\phi}) d\phi d\dot{\phi} \quad (3)$$

$$r_{\phi, \dot{\phi}} = \frac{M_{\phi, \dot{\phi}}}{\sqrt{V_{\phi} \cdot V_r}} \quad (4)$$

where V_{ϕ} and V_r are the variances of roll and roll rate, respectively, and m_{ϕ} is the mean value of the roll angle. For simplicity, m_{ϕ} is assumed to be zero in much of the subsequent discussion, although it is equally applicable to a case with a non-zero mean. One can substitute Equation (2) into Formula (3), and see that both the covariance and correlation coefficient equal zero if the processes are independent.

In general, the opposite is not necessarily true. If the processes are dependent, they may still be uncorrelated. The joint normal distribution is the only exception. If two random values or stochastic processes have normal distribution and are uncorrelated, they

are independent. Consider two-dimensional normal distribution:

$$f(\phi, \dot{\phi}) = \frac{1}{2\pi\sigma_{\phi}\sigma_r\sqrt{1-r^2}} \times \exp\left(-\frac{1}{2(1-r^2)}\left(\frac{\phi^2}{\sigma_{\phi}^2} + \frac{\dot{\phi}^2}{\sigma_r^2} - \frac{2\phi\dot{\phi}r}{\sigma_{\phi}\sigma_r}\right)\right) \quad (5)$$

Here σ_{ϕ} and σ_r are the standard deviations of roll and roll rates, respectively. If the correlation coefficient r equals zero, the joint distribution (5) becomes simply the product of two Gaussian distributions, which indicates independence according to Formula (2).

Since roll rate is a derivative of roll, the roll angles and rates are uncorrelated. If roll motion is a stationary ergodic stochastic process and it is represented with a record of sufficient length, it can be expressed with a Fourier series:

$$\phi(t) = \sum_i a_{\phi i} \cos(\omega_i t + \varphi_{\phi i}) \quad (6)$$

Here $a_{\phi i}$ and $\varphi_{\phi i}$ are the amplitude and phase angle for frequency ω_i . If roll does not follow a Gaussian distribution, the amplitude and phase are just coefficients of the Fourier series calculated for a particular time history of roll motions. The roll rates can then be expressed as:

$$\dot{\phi}(t) = -\sum_i a_{\phi i} \omega_i \sin(\omega_i t + \varphi_{\phi i}) \quad (7)$$

Consider an estimate of the correlation coefficient in the time domain (the superscript asterisk indicates an estimate):

$$M_{\phi, \dot{\phi}}^* = \frac{1}{T} \int_0^T \phi \dot{\phi} dt \quad (8)$$

Substitution of Fourier series (6) and (7) into Formula (8) yields a frequency domain expression for covariance:



$$M_{\phi, \dot{\phi}}^* = -\frac{1}{2} \sum_i a_{\phi_i}^2 \omega_i \cos(0.5\pi) \equiv 0 \quad (9)$$

Formula (9) can be also considered as exact, by carrying out a limit transformation:

$$M_{\phi, \dot{\phi}} = \lim_{\substack{T \rightarrow \infty \\ \Delta\omega \rightarrow 0_i}} M_{\phi, \dot{\phi}}^* \equiv 0 \quad (10)$$

Therefore, the dependence between roll and roll rate (if any) is only evident in joint moments of higher order. Here, the fourth joint moment represented by $M2$ is used:

$$M2_{\phi, \dot{\phi}} = \int_{-\infty}^{\infty} \phi^2 \dot{\phi}^2 f(\phi, \dot{\phi}) d\phi d\dot{\phi} \quad (11)$$

One can see that if the processes are independent, this moment is equal to the product of variances. The corresponding non-dimensional coefficient (represented by $r2$) is expressed as:

$$r2_{\phi, \dot{\phi}} = \frac{M2_{\phi, \dot{\phi}}}{V_{\phi} \cdot V_r} \quad (12)$$

If roll and roll rates are independent, then:

$$r2_{\phi, \dot{\phi}} = 1 \quad (13)$$

3. NUMERICAL STUDY

3.1 Numerical Simulations

The numerical simulations for the present study, which are described in Belenky, *et al.* (2010), consist of three series of calculations performed for the Tumblehome configuration

of the ONR Topside series (Bishop, *et al.*, 2005): zero speed with a wave heading angle of 90° (beam seas), 15 knots with a wave heading of 45° (stern quartering seas), and 14 knots with a wave heading of 40°. Long-crested irregular seas were generated using a Bretschneider spectrum with a significant wave height 7.5 m and a modal period of 15 seconds. The waves were discretized using 790 frequency components, which provides a wave representation free of self-repeat and other artifacts for 40 minutes. Each set consisted of 200 records corresponding to independent realizations of the seaway. The ship motion calculations used LAMP's blended body-nonlinear formulation in which the hydrostatic and Froude-Krylov forces were computed on the instantaneous wetted hull surface, while the wave-body disturbance forces, which include forward speed, diffraction and radiation effects, were computed using a 3-D potential-flow panel method over the mean wetted surface. The ship was free to move in heave, roll, and pitch but constrained in surge (constant speed), sway, and yaw. An empirical model was used for roll damping.

In addition to the ship-motion data, this irregular wave representation was used to evaluate the incident wave elevation and its derivatives at a fixed or constant speed point in order to provide a corresponding data set that is known to be Gaussian.

3.2 Model of Probability Distribution

Formula (1) for the theoretical rate of upcrossings requires a probability distribution. Roll motion is the response of a nonlinear system to Gaussian excitation, so it may not follow a normal distribution. Several methods to approximate the distribution have been considered, as described in Belenky, *et al.* (2008) and Belenky and Weems (2011). In the present work, the moving average model from the latter reference is used.

The moving average allows smoothing of the histogram, and possesses sufficient flexibility to represent the unusual features of



the PDF of a significantly nonlinear response. It has been shown to be flexible enough to be applied to parametric roll (Belenky and Weems, 2011). In the present work, this method has been extended for the joint distribution, because the calculation of the upcrossing rates without the assumption of independence requires a joint PDF for roll and roll rates:

$$\xi = \int_0^{\infty} \dot{\phi} f(\phi = \phi_{m0}, \dot{\phi}) d\dot{\phi}. \quad (14)$$

The calculation starts with estimates of the conditional variances of roll angle for a series of values of roll rate. A series of conditional histograms for roll are then computed using Scott's (1979) formula for the width of a bin of the histogram:

$$W(\dot{\phi}) = \frac{3.5\sqrt{V_{\phi}(\dot{\phi})}}{\sqrt[3]{N(\dot{\phi})}}, \quad (15)$$

where V_{ϕ} is the conditional variance of roll estimated for a particular value of roll rate and N is the total number of points from the conditional histogram for this value of roll rate. The moving average is then applied to each of the conditional histograms:

$$H_i = \frac{1}{n} \sum_{j=1}^n H0_{j+i}, \quad (16)$$

where $H0$ is an original histogram and n is a number of neighboring bins used for averaging. The averaged points, H are used with linear interpolation to create a continuous piecewise linear function, which is then corrected to meet the normalization condition as well as equality to the conditional variance.

Figure 1 shows examples of these conditional distributions for the incident wave data set and illustrates how the method is

capable of recovering the shape of the normal distribution. Once the conditional distributions are completed, the procedure is applied once more for the marginal distributions of the derivatives. The joint distribution can then be approximated as a product of two piecewise linear functions:

$$f^*(\phi, \dot{\phi}) = f^*(\phi | \dot{\phi}) f^*(\dot{\phi}) \quad (17)$$

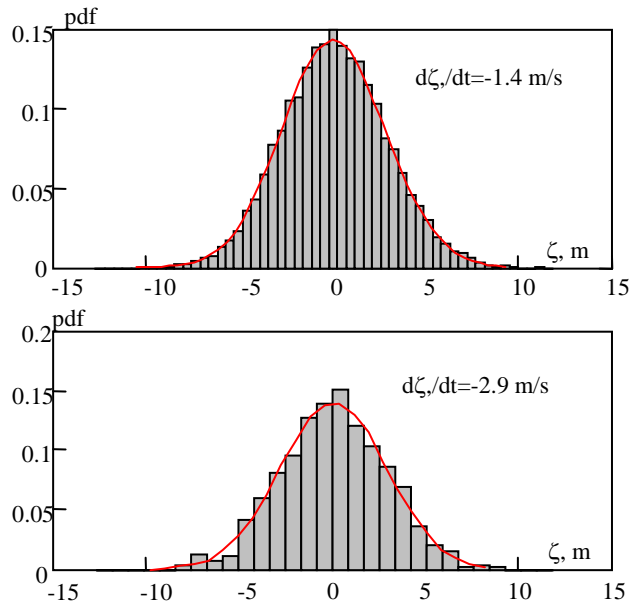


Figure 1: Conditional Distribution of Wave Elevations for Two Particular Values of the Time Derivative.

The resultant joint distribution and its horizontal sections are shown in Figure 2. Visually, both shapes are very close to a joint normal distribution.

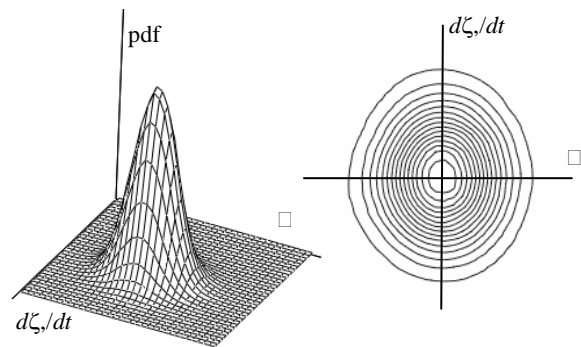


Figure 2: Joint PDF of Wave Elevations and Their Temporal Derivatives and Horizontal Section.

3.3 Statistics of Upcrossing

Upcrossing statistics were evaluated for the three ship motion data sets: beam seas, zero speed (Figure 3); 45° heading at 15 knots (Figure 4); and 40° heading at 14 knots (Figure 5). A level for upcrossing was chosen in order to keep the sample size around 300. The calculation of the confidence interval for the statistical estimate of the upcrossing rate was described in Belenky, *et al.* (2008). A normal distribution was assumed for the estimate of the upcrossing rate and its variance was calculated as:

$$V(\xi^*) = \frac{\xi^* T}{N_r} (1 - \xi^* \cdot \Delta t) \quad (18)$$

Here ξ^* is an estimate of the upcrossing rate, Δt is the time step of the data records, T is the time duration of a single record, and N_r is a number of records in the sample. Belenky and Campbell (2011) have proposed an alternative way to calculate the confidence interval, based directly on the binomial distribution. However, the difference seems to not be significant. Confidence probability was set equal to 95%.

In addition to the statistical estimate of the upcrossing rate, two calculated values are included; the first assumes independence and uses Formula (1), while the second does not assume independence and uses Formula (14).

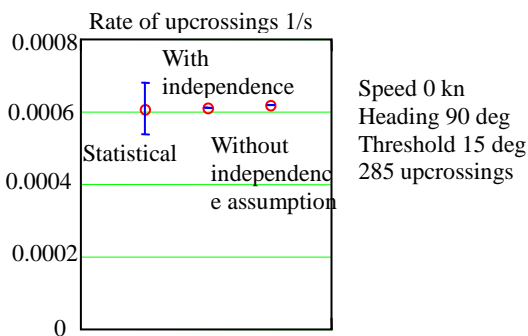


Figure 3: Upcrossing Statistics of Roll Angles for Beam Seas Case.

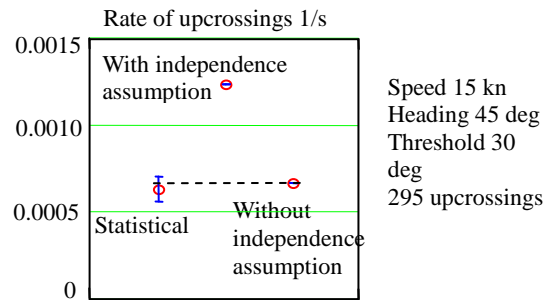


Figure 4: Upcrossing Statistics of Roll Angles for Stern Quartering Seas Case, Heading 45°.

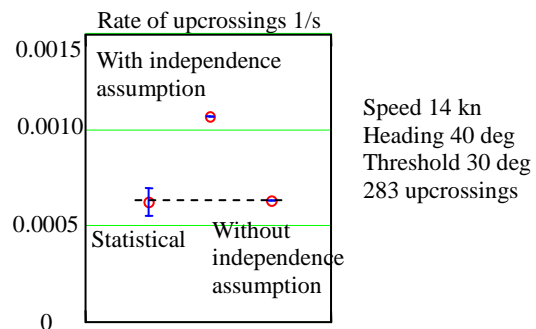


Figure 5: Upcrossing Statistics of Roll Angles for Stern Quartering Seas Case, Heading 40°.

Strictly speaking, both of the calculated upcrossing rates are also random numbers and should be presented with their own confidence interval. However, the very large amount of data used in approximating the distributions should mean that the variances of these numbers are small relative to the variance of the statistical estimates of the upcrossing rate. Nevertheless, the calculation of the confidence interval for these estimates remains for future work.

Figures 3 through 5 clearly show that the independence assumption may be applicable in beam seas and but not in the two stern quartering sea cases. The upcrossing rate calculated with the independence assumption in stern quartering seas overestimates the upcrossing rate significantly. This is a sign of possible dependence of roll and roll rate in stern quartering seas.



3.4 Statistics of the Correlation

The absence of correlation between a stationary process and its first derivative is a well established fact. Nevertheless, it is important to see if the techniques applied in this numerical study recover this result for the sample data; if they do not, this method may be not applicable here. The estimate of the covariance of two processes, presented as an ensemble of N_r records with N_t data points in each record, is expressed as:

$$M_{\phi, \dot{\phi}}^* = \frac{\sum_{j=1}^{N_r} \sum_{i=1}^{N_t} (\phi_{i,j} - m_{\phi}^*) \dot{\phi}_{i,j}}{N_t N_r} \quad (19)$$

Note that the mean value estimate m_{ϕ}^* , which had been assumed to be zero in much of the preceding discussion, has been reinstated because the roll motion in oblique seas actually have a small mean value (because the waves act on the ship from one side, it makes a difference in terms of diffraction forces).

The estimate of covariance (20) is a random number; therefore its confidence interval must be evaluated if a comparison with theory is needed. For two random numbers x and y , the variance of covariance is known (Priestly, 1981):

$$V(M_{XY}^*) = \frac{1}{N-1} \left((M_{XY}^*)^2 + V_X^* V_Y^* \right), \quad (20)$$

where M_{XY} is the covariance of two random variables x and y , and V_X and V_Y are their respective variances, the superscript asterisk indicates an estimate, and N is the size of the sample.

Formula (21), however, is not applicable for stochastic processes other than white noise because the consecutive values of x are assumed independent of each other. The same assumption is made for the values y . The roll motion of a ship possesses certain inertia, so consecutive values of the roll angle are

dependent on each other. This dependence is measured with an autocorrelation function, the decay of which is the measure of inertia of the motions. The same can be said for the stochastic process of roll rates. The full description of correlation between two processes is given by the covariance function, defined as

$$R_{\phi, \dot{\phi}}(\tau) = \int_{-\infty}^{\infty} (\phi(t) - m_{\phi}) \dot{\phi}(t + \tau) \times f(\phi(t), \dot{\phi}(t + \tau)) d\phi d\dot{\phi} \quad (21)$$

The covariance is the initial value of the covariance function. The covariance function can be estimated for the ensemble of records as

$$R_{\phi, \dot{\phi}}^*(\tau_k) = \frac{\sum_{j=1}^{N_r} \sum_{i=1}^{N_t-k} (\phi_{i,j} - m_{\phi}^*) \dot{\phi}_{i+k,j}}{N_r(N_t - k)} \quad (22)$$

The covariance function is formally defined for time $\tau \in (-\infty; +\infty)$, while the time series is available only for positive time. To account for the negative time, the following property of the covariance function is used:

$$R_{\phi, \dot{\phi}}(-\tau) = R_{\dot{\phi}, \phi}(\tau) \quad (23)$$

Therefore, changing of the sign the time is equivalent to switching the order of processes in the covariance function:

$$R_{\phi, \dot{\phi}}^*(\tau_k) = \frac{\sum_{j=1}^{N_r} \sum_{i=1}^{N_t-k} \dot{\phi}_{i,j} (\phi_{i+k,j} - m_{\phi}^*)}{N_r(N_t - k)} \quad (24)$$

Priestly (1981) gives the following formula for the variance of the covariance function estimated over one record:

$$V_R(R_{\phi, \dot{\phi}}^*, \tau_k) = \frac{1}{N_t - k} \sum_{i=-N_t+k+1}^{N_t-k-1} \left(1 - \frac{|i|}{N_t}\right) \times (R_{\phi}^*(t_{|i|})R_{\dot{\phi}}^*(t_{|i|}) + R_{\phi, \dot{\phi}}^*(t_i + \tau_k)R_{\phi, \dot{\phi}}^*(\tau_k - t_i)) \quad (25)$$

The autocorrelation functions for the roll angles and roll rates are included in Formula (25) in order to account for the dependence between consecutive values of roll angle and roll rate. The autocorrelation functions for the same samples can be estimated as:

$$R_{\phi}^*(\tau_k) = \frac{\sum_{j=1}^{N_r} \sum_{i=1}^{N_t-k} (\phi_{i+k,j} - m_{\phi}^*)(\phi_{i,j} - m_{\phi}^*)}{N_r(N_t - k)} \quad (26)$$

$$R_{\dot{\phi}}^*(\tau_k) = \frac{\sum_{j=1}^{N_r} \sum_{i=1}^{N_t-k} \dot{\phi}_{i,j} \dot{\phi}_{i+k,j}}{N_r(N_t - k)}. \quad (27)$$

The autocorrelation functions also can be computed from the corresponding spectra, if available. The variance of the covariance estimate for one record can then be obtained from (25) simply by letting $\tau_k=0$, taking into account Equation (24)

$$V_R(M_{\phi, \dot{\phi}}^*) = \frac{1}{N_t - k} \sum_{i=-N_t+k+1}^{N_t-k-1} \left(1 - \frac{|i|}{N_t}\right) \times (R_{\phi}^*(t_{|i|})R_{\dot{\phi}}^*(t_{|i|}) + R_{\phi, \dot{\phi}}^*(t_i)R_{\phi, \dot{\phi}}^*(t_i)). \quad (28)$$

The variance of the ensemble estimate of the covariance can be calculated as sum of the above variances of independent values, because the different records are meant to be independent:

$$V_R(M_{\phi, \dot{\phi}}^*) = \frac{1}{N_R^2} \sum_{j=1}^{N_R} V_{R_j}(M_{\phi, \dot{\phi}}^*). \quad (29)$$

The large number of data points used in these calculations justifies the assumption that the estimate of the covariance has a normal distribution. For the same reason, the bias of

the estimate can be neglected and its mean value can be taken equal to the estimate itself.

Figure 6 shows the correlation coefficients between the processes and their derivatives for the LAMP roll motion and wave elevations. All of the confidence intervals contain zero, so the statistical technique is not rejected by the theory.

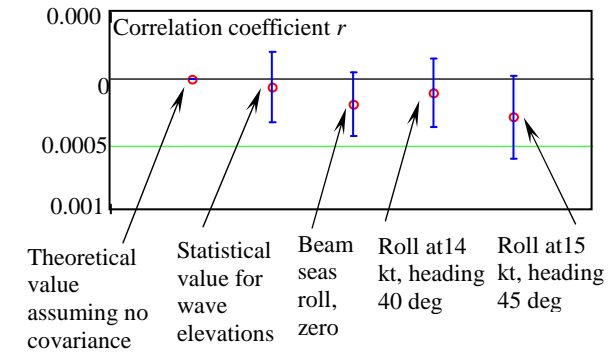


Figure 6: Estimates of Correlation Coefficients between the Processes and Derivatives.

3.5 Visual Inspection

Correlation between two values can be seen in the joint distribution of the values as a “rotation of axis,” as shown in Figure 7, which plots theoretical Gaussian distributions with and without correlation.

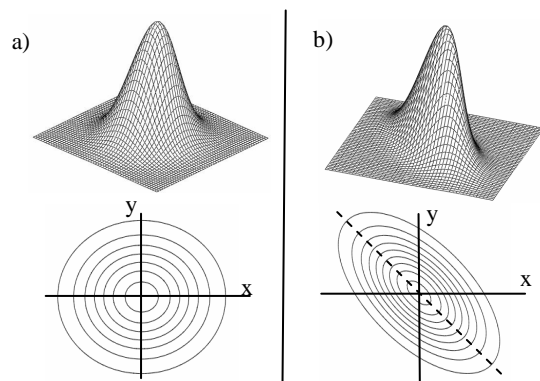


Figure 7: Theoretical Gaussian Joint Distributions of Two Random Variables (a) without Correlation and (b) with Correlation.

This “rotation of the axes” can be most clearly seen in the lower plot of a series of horizontal cross-sections of the joint distributions. The correlation leads to



asymmetry relative the axis. Figures 8, 9, and 10 contain similar plots for the roll motions and rates from the LAMP simulations. These joint distributions were smoothed with the moving average method described earlier in the paper.

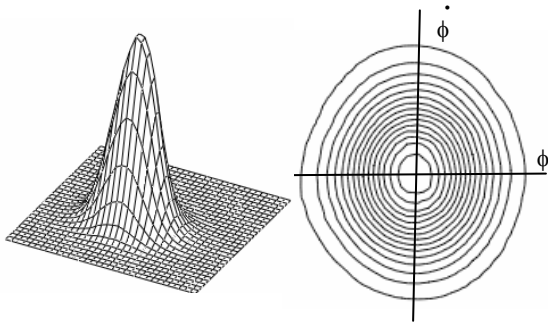


Figure 8: Joint Distribution for Beam Seas (Heading 90°) at Zero Speed.

All three plots retain symmetry relative to the horizontal axis, taking into account that the plots are based on moving average method. Nevertheless, the horizontal sections for the stern quartering seas appear to be “squeezed,” resulting in a somewhat rhomboidal pattern. This may be a sign of dependence without correlation.

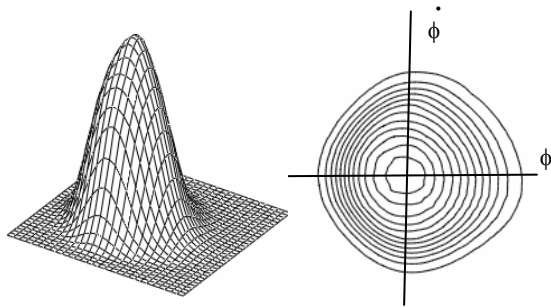


Figure 9: Joint Distribution of Roll Angles and Rates for Heading 45° at 15 Knots.

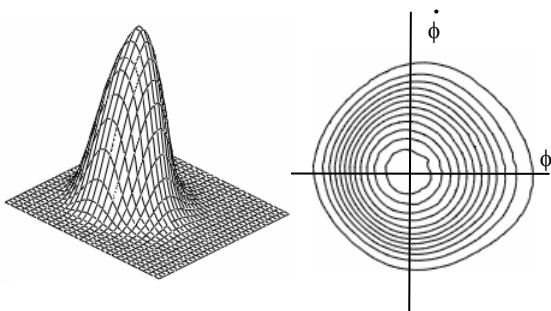


Figure 10: Joint Distribution of Roll Angles and Rates for Heading 40° at 14 Knots.

3.6 High-order Correlation

The second-order covariance can be estimated from an ensemble of records as

$$M 2_{\phi, \dot{\phi}}^* = \frac{\sum_{j=1}^{N_r} \sum_{i=1}^{N_t} (\phi_{i,j} - m_{\phi}^*)^2 (\dot{\phi}_{i,j})^2}{N_t N_r} \quad (30)$$

To find the variance of the second order covariance, consider a covariance of the centered squares of roll and roll rates:

$$\phi 2 = (\phi - m_{\phi})^2 ; \quad \dot{\phi} 2 = \dot{\phi}^2 \quad (31)$$

By definition, the mean values of these quantities are the variances of roll and roll rates, respectively. The estimate of the covariance between the centered squares of the roll and roll rates can then be expressed as:

$$\begin{aligned} M_{\phi 2, \dot{\phi} 2}^* &= \frac{1}{N_t N_r} \sum_{j=1}^{N_r} \sum_{i=1}^{N_t} (\phi 2_{i,j} - V_{\phi}^*)^2 \\ &\quad \times (\dot{\phi} 2_{i,j} - V_{\dot{\phi}}^*)^2 \\ &= M 2_{\phi, \dot{\phi}}^* - V_{\phi}^* V_{\dot{\phi}}^* \end{aligned} \quad (32)$$

The second-order covariance can be expressed through the covariance between the centered squares:

$$M 2_{\phi, \dot{\phi}}^* = M_{\phi 2, \dot{\phi} 2}^* + V_{\phi}^* V_{\dot{\phi}}^* \quad (33)$$

A complete statistical study the variance of the second-order covariance needs to be found.

Assuming that all the estimates are independent and using the well-known formula for the variance of a product of independent random variables, it can be seen that:

$$\begin{aligned}
 V(M_{\phi, \dot{\phi}}^*) &= V(M_{\phi 2, \dot{\phi} 2}^*) + V(V_{\phi}^* V_{\dot{\phi}}^*) \\
 &= V(M_{\phi 2, \dot{\phi} 2}^*) + V(V_{\phi}^*) \cdot V(V_{\dot{\phi}}^*) \\
 &\quad - (V_{\phi}^*)^2 \cdot V(V_{\dot{\phi}}^*) - (V_{\dot{\phi}}^*)^2 \cdot V(V_{\phi}^*).
 \end{aligned} \quad (34)$$

The variance of the covariance of the centered squares can be computed using Formulae (28) and (29). The autocorrelation and the covariance functions of centered squares can be estimated from the ensemble. A formula for the variance of the variance estimates is known, from Priestly (1981):

$$\begin{aligned}
 V(V_{\phi}^*) &= \frac{1}{(N_t - k)N_r^2} \sum_{j=1}^{N_r} \sum_{i=-N_t+k+1}^{N_t-k-1} \left(1 - \frac{|i|}{N_t}\right) \\
 &\quad \times (R_{\phi}^*(t_{|i|}))^2
 \end{aligned} \quad (35)$$

$$\begin{aligned}
 V(V_{\dot{\phi}}^*) &= \frac{1}{(N_t - k)N_r^2} \sum_{j=1}^{N_r} \sum_{i=-N_t+k+1}^{N_t-k-1} \left(1 - \frac{|i|}{N_t}\right) \\
 &\quad \times (R_{\dot{\phi}}^*(t_{|i|}))^2
 \end{aligned} \quad (36)$$

The results of these calculations (for the cases presently shown in Figure 6) are shown in Figure 11. As with the previous case, all estimates are assumed to be un-biased and a normal distribution is taken for the estimates on the basis of the large number of points, the confidence probability is still 95%. The second order correlation coefficient for the wave elevation and its temporal derivative show how the dependence is indicated by the high-order measure. This result is expected and does not reject the validity of the calculation technique.

All estimates of the second-order roll and roll rate correlation show a dependence of motions and rates because the theoretical value indicating the absence of this dependence, 1.0 in this case, is not contained in the confidence intervals. Contrary to the situation with correlation, the indication of dependence in the second-order coefficient is sufficient proof of the existence of such dependence. The degree

of this dependence is obviously different for different headings.

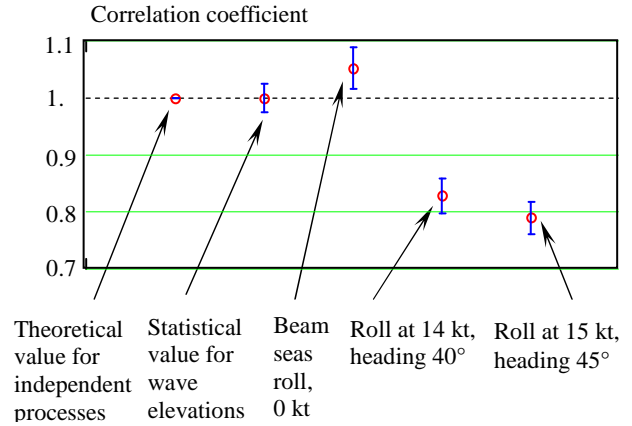


Figure 11: Estimates of Second-Order Correlation Coefficient between the Processes and Derivatives.

For the case of beam seas, the value around 1.051 and the lower bound almost touches unity at the value 1.014. Based on the upcrossing statistics shown in Figure 3, one can conclude that such a degree of dependence is small enough to use the independence assumption. No obvious signs of the changing shape of the horizontal sections of the joint distribution can be seen in Figure 8.

The situation is different in stern quartering seas. The upper bound of the confidence intervals are quite far from the unity (0.82 and 0.86), the upcrossing statistics shows clear differences in Figure 4 and 5, and the shape of the joint distribution is visually distorted in Figures 9 and 10. Such dependence must be recognized as strong enough to render the assumption of independence inapplicable in stern quartering seas.

4. SUMMARY

The absence of correlation between roll and roll rates does not mean that they are independent for all cases. The independence of roll and rates is completely justified only for a linear system where a normal distribution is applicable. It is an assumption for all other cases; in the case studied for beam seas this



assumption seems to be applicable, while in stern quartering wave it may lead to significant errors. This dependence without correlation can be seen in horizontal sections of the joint distribution as some sort of “squeezing.” The second-order correlation coefficient can be used to quantify the dependence without correlation. The covariance function between the centered squares of roll and roll rate can be employed to evaluate the confidence interval of the second order correlation coefficient.

5. ACKNOWLEDGMENTS

The work described in this paper has been funded by the Office of Naval Research (ONR) under Dr. Patrick Purtell. The authors are grateful and happy to recognize contributions from their colleagues: Prof. M. Collette (formerly of SAIC, currently University of Michigan) discovered problems predicting the upcrossing rate with independence assumption, Prof. M. R. Leadbetter (University of North Carolina) pointed out the possibility of dependence without correlation and hinted towards use of squares, and Prof. P. Spanos (Rice University) motivated the authors to pursue this issue and has contributed to a series of fruitful discussions. The authors also would like to thank Dr. A. Reed (NSWCCD) for his editing that has improved readability of the paper.

6. REFERENCES

- Belenky, V., and Campbell, B., 2011, “Evaluation of the Exceedance Rate of a Stationary Stochastic Process by Statistical Extrapolation Using the Envelope Peaks over Threshold (EPOT) Method,” Report NSWCCD-50-TR-2011/032.
- Belenky, V., Weems, K.M., Bassler, C.C., Dipper, M.J., Campbell, B., and Spyrou, K.J., 2012, “Approaches to Rare Events in Stochastic Dynamics of Ships,” Probabilistic Engineering Mechanics, Vol. 28, pp. 30–38.
- Belenky, V., and Weems, K.M., 2011, “On the Distribution of Parametric Roll,” Proceedings of the 12th Int. Ship Stability Workshop, Washington, DC, USA, pp. 205–212.
- Belenky, V., Weems, K.M., and Lin, W.-M., 2008, “Numerical Procedure for Evaluation of Capsizing Probability with Split Time Method,” Proceedings of 27th Symposium on Naval Hydrodynamics, Seoul, Korea.
- Belenky, V.L., Weems, K.M., Lin, W.M., and Spyrou, K.J., 2010, “Numerical Evaluation of Capsizing Probability in Quartering Seas with Split Time Method,” Proceedings of 28th Symposium on Naval Hydrodynamics, Pasadena, California, USA.
- Bishop, B., Belknap, W., Turner, C., Simon, B., Kim, J., 2005, “Parametric Investigation on the Influence of GM, Roll Damping, and Above-Water Form on the Roll Response of Model 5613,” Report NSWCCD-50-TR-2005/027.
- Kramer, H., and Leadbetter, M.R., 1967, Stationary and Related Stochastic Processes, John Wiley, New York.
- Priestley, M. B., 1981, Spectral Analysis and Time Series, Vol. 1, Academic Press, New York.
- Scott, D.W., 1979, “On Optimal and Data-based Histograms,” Biometrika, 66(3):605–610.
- Shin, Y.S, Belenky, V., Lin, W.M., Weems, K., and Engle, A.H., 2003, “Nonlinear Time Domain Simulation Technology for Seakeeping and Wave-load Analysis for Modern Ship Design,” Transactions, SNAME, Vol. 111, pp. 557-578.



A Probabilistic Analysis of Stability Regulations for River-Sea Ships

Igor Bačkalov, *University of Belgrade, Faculty of Mechanical Engineering, Department of Naval Architecture, ibackalov@mas.bg.ac.rs*

ABSTRACT

The present paper focuses on the recent developments in the field of stability regulations for the river-sea ships in Europe. The river-sea ships are primarily inland vessels that operate on the coastal sea routes on a regular basis. Due to their particular service and design, the river-sea ships are subject to special stability requirements that incorporate seakeeping considerations to an extent. In the present analysis, some of the existing stability regulations (Russian River Register and UNECE Resolution No. 61) intended for the river-sea ships are evaluated from the probabilistic point of view. It is demonstrated that these regulations are, in some cases, insufficient and not strict enough. Critical analysis is followed by some guidelines for possible improvement of regulations and the development of new intact stability criteria for river-sea ships.

Keywords: *River-sea ships; Probabilistic analysis; Intact stability criteria; Nonlinear rolling; Lateral accelerations.*

1. INTRODUCTION

In the recent years, several initiatives for improvement of safety of river-sea ships were launched on both the national and international level. As a consequence, in some countries, such as Belgium and France, new regulations already came into force. It is expected that international (European) regulatory framework, i.e. United Nations Economic Commission for Europe (UNECE) Resolution No. 61 (2006) would be updated with the provisions for stability of river-sea ships in the near future as well. Present paper will provide an overview of the afore-mentioned developments, with special emphasis on the requirements set forth in the Russian River Register (2008). The principal reason for this particular focus is the fact that the criteria (deterministic in nature) originally established by the Russian classification societies (River and Maritime Register) serve as the basis for development of the river-sea ships stability regulations on the European level.

The stability requirements imposed by the Russian River Register (2008) as well as the regulations proposed by UNECE (2010) were analyzed by means of probabilistic tools, previously described in e.g. Hofman & Bačkalov (2005). Probability of partial stability failure (flooding through unsecured openings) and lateral acceleration in the working areas positioned furthest from the rolling axis were calculated in a series of numerical experiments performed on the sample ships, whose main particulars are typical for river-sea navigation in Europe.

Numerical tests reveal that level of safety attained by present stability standards considerably varies depending of ship characteristics. Furthermore, it was found that vessels satisfying examined regulations could not be considered as safe from the probabilistic point of view in a number of cases. Nevertheless, stability considerations of Russian River Register ("acceleration criterion") constitute a solid basis for development of the next generation of intact stability criteria.



It should be noted that the paper presents results of an independent analysis, as the author is affiliated with neither UNECE nor Russian River Register.

2. STABILITY REGULATIONS FOR THE RIVER-SEA SHIPS: STATE-OF-THE ART AND PROSPECTS

The terms “river-sea ship” and “sea-river ship” are sometimes used to describe the same vessel type. On the other hand, either of the terms may also be used to refer to very dissimilar ship types. Here, however, a principal distinction would be made between the two. The term “sea-river ship” would be used for a sea-going vessel which also operates on inland waterways. Unlike that, “river-sea ship” would represent primarily an inland vessel that, under certain conditions, performs sea voyages on a regular basis.

Clearly, an inland vessel is not designed for the maritime environment; therefore, additional safety measures, including special stability provisions, are required. So far, process for improvement of river-sea ships safety resulted in new regulations applicable on the local level (Belgium, France), while the European regulations are underway.

2.1 Belgium

In 2007, following the research carried out by the Ghent University (see Truijens et al., 2006), Belgian Federal Authorities launched safety regulations intended for the so called estuary ships. Estuary ships are basically inland navigation vessels which are allowed to operate on the sea routes between Belgian deep-sea ports and the West Scheldt estuary. The regulations, which are published in the Belgisch Staatsblad / Moniteur Belge (2007), impose several probabilistic requirements related to slamming, bow diving, shipping of green water, rolling, habitability and ship strength. Sufficient safety should be demonstrated by direct calculations. Wave loads are obtained from

measured directional spectra. By incorporating classical seakeeping considerations (regardless of certain simplifications mainly related to the wind effects) Belgian regulations introduced an advanced approach to ship stability. Furthermore, for the first time, probabilistic calculations and risk analysis became an integral part of the intact ship stability regulatory framework (see for instance Vantorre et al., 2012). These regulations were thoroughly analyzed by Bačkalov (2010).

2.2 France

“Port 2000” is the new container terminal in the Le Havre seaport, designed to facilitate the largest container ships. Le Havre is situated near the river Seine estuary, which enables waterborne transport connections between the major maritime port and the hinterland, in particular with the Greater Paris area. During 2007, in order to provide access of inland container vessels to the new container terminal, French transport authorities have issued two decrees dealing with safety of inland vessels in maritime environment. Inland container vessels using the North access to the Port 2000 (involving a short sea trip) are required to prove sufficient stability in waves, for a number of loading conditions, speeds and wave headings, by means of model experiments or computer simulations approved by a classification society. Standard wave spectra (Pierson-Moskowitz, JONSWAP or Bretschneider) should be used. Navigation is limited to wave height up to 1.2m and wind speed up to 21kn. The regulations are published in *Journal officiel de la République Française* (2007).

Belgian experiences with estuary navigation and specific navigation requirements in the port of Le Havre have motivated Permanent International Association of Navigation Congresses (PIANC) to appoint an expert group on “Direct Access of Maritime Ports by Inland Waterway Vessels” in 2011, which clearly indicates a necessity to thoroughly investigate the problem of river-sea ships safety.

2.3 Europe

On the European level, consideration of safety requirements for the river-sea ships took a different course. The appropriate regulations are to be introduced through the UNECE Resolution No. 61 (2006) which represents a step towards the Europe-wide harmonization of technical regulations for inland vessels. Chapter 20 of the Resolution No. 61, dedicated to special provisions for sea-going ships, was originally left void. In 2006, upon invitation by UNECE Inland Transport Committee, Russian Federation (which has a large number of registered ships for river-sea navigation and appropriate experience) submitted the basic document on technical requirements for the river-sea ships (UNECE, 2006b). In this document, the regulations used in Russian Federation, including ship stability requirements, were indicated as the starting point for development of the appropriate European rules.

During 2010 and 2011, the Group of Volunteers submitted the draft versions of Chapter 20B: Special provisions applicable to river-sea navigation vessels, to the UNECE bodies in charge¹. It is expected that the draft of Chapter 20B could be finalized in spring 2012. The first draft of the Chapter 20B (UNECE, 2010) submitted in the 36th session of SC.3/WP.3, was used as the reference document in the present analysis.

UNECE (2010) defines a river-sea navigation vessel as a “vessel intended for navigation on inland waterways and suitable for restricted navigation at sea”. River-sea vessels are divided in classes by “navigation areas” they are allowed to operate on:

- Class RS 6.0, in waves up to $H_{3\%} = 6\text{m}$;
- Class RS 4.5, in waves up to $H_{3\%} = 4.5\text{m}$;
- Class RS 3.5, in waves up to $H_{3\%} = 3.5\text{m}$;
- Class RS 3.0, in waves up to $H_{3\%} = 3\text{m}$;
- Class RS 2.0, in waves up to $H_{3\%} = 2\text{m}$.

¹ Working Party on the Standardization of Technical and Safety Requirements in Inland Navigation (SC.3/WP.3)

Stability should be verified for a number of loading conditions. Stability is deemed as sufficient if the ship satisfies the following: minimal metacentric height, parameters of static stability diagram, weather criterion (corresponding to wind speed of 18m/s) as well as supplementary provisions for specific ship types. The latter include “dry bulk cargo ships” whose stability is additionally checked by the “acceleration criterion”. Acceleration criterion determines limiting operational conditions of a river-sea ship, i.e. permitted wave heights that would secure safe navigation. Estimated acceleration a_{est} in transverse direction should not be larger than 0.3, in g -fractions.

$$k^* = \frac{0.3}{a_{est}} \geq 1. \quad (1)$$

Estimated acceleration is calculated as:

$$a_{est} = 1.1 \cdot 10^{-3} \cdot B \cdot X_l^2 \cdot \theta_r, \quad (2)$$

where X_l and roll amplitude θ_r are determined in compliance with the Intact Stability Code. In case that $k^* < 1$, Administration may permit a vessel to operate with wave height restrictions, “upon well-grounded presentation by the owner”. Permitted wave heights, as a function of the k^* value, are given in the Table 1.

Table 1: Wave heights limitations based on acceleration criterion, UNECE (2010).

k^*	<0.5	0.5÷1	1÷1.5	1.5÷2	>2
$H_{3\%}$ [m]	2	3	3.5	4.5	6

2.4 Russian Federation

As outlined before, approach based on the acceleration criterion, proposed by the UNECE (2010) is adopted from the Russian stability regulations for the river-sea ships. There are two classification societies in Russian Federation, concerned with the safety of ships for combined navigation: Russian River Register (RRR) and Russian Maritime Register of Shipping (RS). Stability assessment of the river-sea



ships in both registers includes the “acceleration criterion”, i.e. a condition similar to the formula (1). Although both registers refer to the “river-sea ships”, classes assigned by RRR and RS as well as associated navigation areas are substantially different and so are the formulas and related coefficients. Using the terminology adopted in this paper, RS in fact deals with the sea-river ships. The river-sea vessels, as defined by UNECE (2010), are within the scope of the RRR.

Russian Maritime Register (2005) specifies two classes of ships for combined navigation:

- Class IICII, in waves up to $H_{3\%} = 6\text{m}$;
- Class IIICII, in waves up to $H_{3\%} = 3.5\text{m}$.

Russian River Register (2008) indicates three classes of ships for combined navigation:

- Class M-CII, in waves up to $H_{3\%} = 3.5\text{m}$;
- Class M-III, in waves up to $H_{3\%} = 2.5\text{m}$;
- Class O-III, in waves up to $H_{3\%} = 2\text{m}$.

In addition to prescribed minimal metacentric height, static stability diagram parameters and weather criterion, dry bulk cargo river-sea ships of class M-CII are required to satisfy the acceleration criterion $a_{est} \leq 0.3g$. Estimated acceleration is calculated as:

$$a_{est} = 1.1 \cdot 10^{-3} \cdot B \cdot m_l^2 \cdot \theta_m \quad (3)$$

The coefficient m_l is derived based on the natural frequency of the ship, while θ_m represents the resonant roll amplitude. Again, wave height restrictions apply when $k^* < 1$ (Table 2). According to Lesyukov (1974), a_{est} should correspond to the estimated acceleration in the working spaces furthest positioned from the rolling axis, such as bridge. Nevertheless, estimated accelerations (as defined by RRR and UNECE) do not depend on the bridge height. Instead, the wheelhouse position (or another appropriate location) typical for standard ships of the specified class is incorporated in coefficients contained in formulas (2) and (3).

Table 2: Wave heights limitations based on acceleration criterion, RRR (2008).

k^*	<0.5	0.5÷1	>1
$H_{3\%}$ [m]	2.5	3	3.5

Although formulas (2) and (3), given by UNECE (2010) and Russian River Register (2008) respectively, are quite alike, the results obtained by their application on the same vessel may be very dissimilar, as it is going to be demonstrated later in the paper.

3. PROBABILISTIC ANALYSIS

Probabilistic analysis used in the present investigation is a two-phase approach. In the first phase, the roll motion of the sample vessels in the “dead-ship” condition, subjected to simultaneous action of wind and waves, is derived. The time history of roll motion is subsequently statistically analyzed, in an aim to estimate the probability of an event considered as critical for the safety of the examined vessel. The method was previously described in detail elsewhere, e.g. in Hofman & Bačkalov (2005), Bačkalov et al. (2010).

3.1 Sample Ships

Following the UNECE (2010) definition of the river-sea ships, the selected sample ships are standard European inland vessels with main particulars typical for combined navigation, except for the freeboards (Table 3). Sample ships *V* and *ST* have minimal freeboards in accordance with the UNECE (2010) and Russian River Register (2008) requirements, while in practice, river-sea ships may have higher freeboards than required. A typical inland vessel is given in Figure 1.

Table 3: Sample ships

Name	L [m]	B [m]	d [m]	D [m]
<i>V</i>	136	16.5	3.5	5.7
<i>ST</i>	83.6	12	2.9	3.9

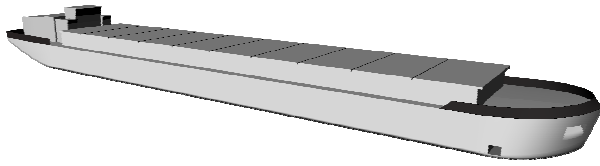


Figure 1: Typical inland dry cargo vessel.

3.2 Numerical Experiments Setup

Numerical experiments should indicate whether sample ships, which fulfil stability requirements prescribed by the regulations, may be considered as safe from the probabilistic point of view, in waves determined based on the acceleration criteria (Tables 1 and 2) and mean wind specified by class notation.

In the present analysis, roll motion of the sample ships, subjected to stochastic action of beam wind and waves, is modelled using the 1DOF nonlinear differential equation of roll.

$$\begin{aligned} (J_x + m_\varphi) \cdot \ddot{\varphi} + M_{damp}(\dot{\varphi}) + M_{st}(\varphi) = \\ = M_{wave}(t) + M_{wind}(t) \end{aligned} \quad (4)$$

The wind speed v_w is not constant, but consists of the mean wind speed and wind speed fluctuations:

$$v_w(t) = \bar{v}_w + \sum_{n=1}^N A_n \cos(\omega_n t + \alpha_n). \quad (5)$$

Gusting wind amplitudes are obtained from the semi-empirical Davenport wind spectrum S_D :

$$A_n = \sqrt{2S_D(\omega_n) \cdot d\omega},$$

where:

$$S_D = \frac{4K \cdot \bar{v}_w^2 X_D^2}{\omega(1 + X_D^2)^3}, \quad X_D = \frac{600\omega}{\pi \cdot \bar{v}_w}.$$

In the present analysis, wave amplitudes are acquired from the Bretschneider wave spectrum S_B :

$$B_n = \sqrt{2S_B(\omega_n) \cdot d\omega},$$

Righting moment is the restoring term in equation (4):

$$\begin{aligned} M_{st}(\varphi) &= g\Delta \cdot h(\varphi) = \\ &= g\Delta \cdot [h'(\varphi) + GM \sin \varphi] \end{aligned} \quad (6)$$

Residual stability lever of the vessel was approximated by a high order odd polynomial:

$$h'(\varphi) \approx \sum a_{2n+1} \varphi^{2n+1}.$$

The roll damping moment is nonlinear, consisting of the quadratic term:

$$M_{damp}(\dot{\varphi}) = \beta \cdot \dot{\varphi} |\dot{\varphi}|. \quad (7)$$

Since the roll damping significantly affects calculated roll motion and, consequently, ship safety considerations, proper assessment of roll damping coefficients is an important and a delicate matter. This is particularly true for inland vessels, as the available experimental data for typical inland forms are scarce. This difficulty was highlighted in several papers so far (see for instance Bačkalov et al., 2010). In the present analysis, nonlinear roll damping was assessed using the recommendation given by Basin & Anfimov (1961), Figure 2. Quadratic roll damping coefficient β is expressed as a function of m_θ (Fig. 2), where:

$$m_\theta = \left(\frac{r_s}{\rho_{xx}} \right)^2 \frac{GM}{B}.$$

Quadratic coefficient β was derived based on the results of model tests with single- and twin-screw inland vessels and sea-going ships, without the influence of forward speed and bilge keels.

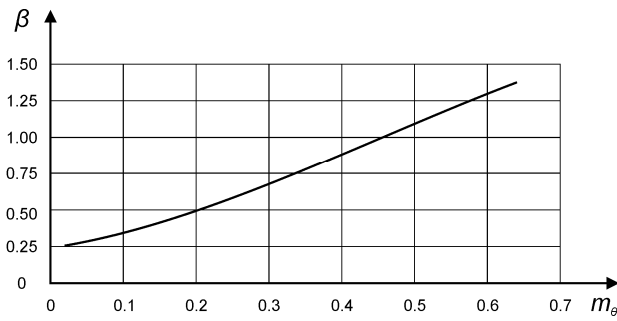


Figure 2: Quadratic coefficient of roll damping.

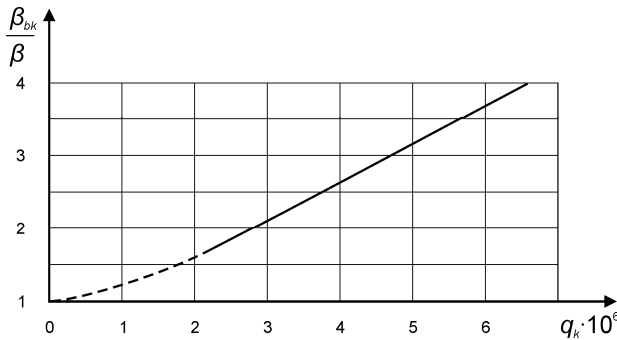


Figure 3: Increase of quadratic roll damping coefficient due to bilge keels.

Assuming that the river-sea vessels are normally equipped with bilge keels, the following recommendation (also based on the model experiments, see Basin & Anfimov, 1961) for quadratic damping coefficient of the ship with bilge keels, is adopted (Fig. 3), whereby:

$$\frac{\beta_{bk}}{\beta} = f(q_k), \quad q_k = \frac{s_K}{LB} \left(\frac{d_{bk}}{B} \right)^3 \frac{GK}{d} \cdot 10^{-3}.$$

Equation (4) is solved numerically using Runge-Kutta method, in order to obtain time record of roll. In the second phase of analysis, time history of roll is statistically analyzed in order to acquire mean angle of roll $\bar{\phi}$ and standard deviation of roll s_ϕ . Using these statistical values, as it was demonstrated by Bulian & Francescutto (2004) the probability that the vessel would heel to a critical angle ϕ in a given period of time t_s , is determined as:

$$P = 1 - \exp \left\{ -N_c \exp \left[-\frac{1}{2} \left(\frac{\phi - \bar{\phi}}{s_\phi} \right)^2 \right] \right\}. \quad (8)$$

In the present investigation, critical angle ϕ is the angle of flooding through unsecured openings, defined as the angle at which the top of hatch coaming immerses the water. Probabilistic criterion of stability used in present paper permits probability of flooding $P_{fl} = O(10^{-4})$ in two hours of specified weather conditions. This criterion was adopted in Bačkalov (2010) assuming that flooding through unsecured openings may occur once in a lifetime of a coastal ship (which typically makes 300 round trips a year during 20 years of operation) and it was preserved in the present paper for the sake of comparison. Clearly, the choice of an appropriate safety level is a sensitive issue, open to discussion.

Furthermore, it should be noted that the formula (8) is used assuming that the ship roll is Gaussian and ergodic process. These approximations enable assessment of important safety-related quantities; hence they are utilized in a number of comprehensive studies dealing with probabilistic approach to ship stability in realistic weather conditions (see e.g. Bulian & Francescutto, 2004, Vassalos et al., 2004).

3.3 Discussion of results

Probability of flooding in weather conditions defined by the Russian River Register (2008) ($\bar{v}_w = 24\text{m/s}$, wave height based on the acceleration criterion, see Table 2) for examined sample vessels *ST* and *V* is given in Fig. 4 (full lines).

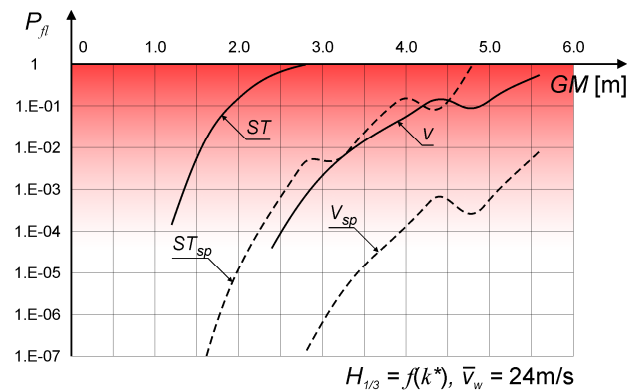


Figure 4: Probability of cargo hold flooding of the examined river-sea ships.

Although the application of acceleration criterion should secure sufficient safety in given conditions over the range of realistic metacentric heights (if all the other stability criteria of RRR are fulfilled), obviously this is not the case. For a large span of GM , the sample vessels fail to fulfil the probabilistic criterion, although they meet the terms of the acceleration criterion.

According to available data (see comprehensive study of Egorov, 2007) dynamic stability related accidents do not seem to be as frequent as probabilistic analysis indicates. Nevertheless, river-sea ships are highly susceptible to wave climate: in some 70 accidents analyzed by Egorov (2007), almost half occurred when class-prescribed wave height limitations were exceeded (either intentionally or due to forecast errors). In addition, in over 30% of cases, a violation of ICLL requirements for construction of hatch covers, coamings, air pipes and watertight doors (i.e. possible points of water ingress) was reported. So, is there really a disagreement between numerical experiments and daily reality?

In an attempt to resolve this dilemma, a new series of numerical experiments was performed on sample vessels whose characteristics were in accordance with the current shipbuilding practice. For instance, V-type vessels may have exceptionally high hatch coaming, up to 3.5m; ST-type vessels, on the other hand, commonly have freeboards much higher than minimal, i.e. $D = 6\text{m}$ instead of 3.9m (see e.g. Egorov, 2007). Probabilistic results obtained for such vessels are also given in Fig. 4 (dashed lines V_{sp} and ST_{sp}). Obviously, these vessels may be considered as much safer from the probabilistic point of view. The ships that are known to perform well in terms of stability in class-defined weather conditions, satisfy the probabilistic criterion as well, for a reasonable span of metacentric heights. However, the higher safety is not a consequence of stability regulations. In case of vessel V_{sp} , for instance, high coamings represent strong structural elements which contribute to overall longitudinal

strength by increasing hull section modulus (see Egorov & Initskiy, 2006).

The goal of the next series of numerical tests was to calculate the wave heights that would yield probability of flooding of the same level (i.e. $O(10^{-4})$) for any GM in the examined range. Assumed mean wind speed was 24m/s, as required by the RRR. Using the probabilistic analysis, the upper boundary of weather conditions in which a sample vessel of particular characteristics (metacentric height, angle of flooding) could safely operate, was defined. Wave height limitations obtained by application of: the probabilistic criterion, RRR and UNECE requirements are compared in Fig. 5. In general, present regulations would allow sailing in wave heights higher than those permitted by the adopted probabilistic condition.

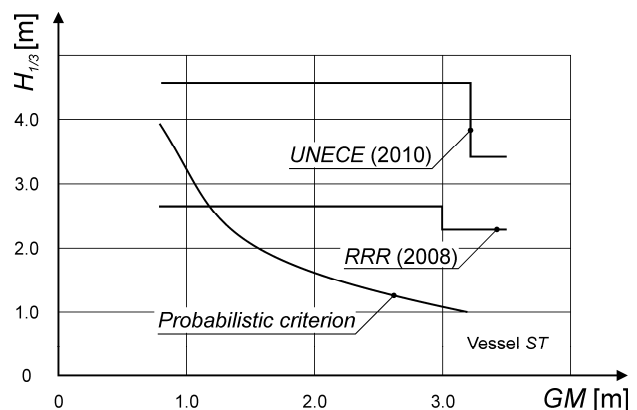


Figure 5: Permitted wave heights according to the present rules and the probabilistic criterion.

Following the RRR safety concept, each numerical test included the calculation of time history of lateral acceleration in the helmsman position in the wheelhouse, in the centreline of the ship, divided by gravity acceleration g :

$$a_T = \frac{l \cdot \ddot{\varphi}}{g},$$

where l represents the distance of the bridge from the rolling axis. Probability that limiting value $a_T = 0.3$ would be attained in the specified point on the ship was also derived for a range of metacentric heights. This probability,



denoted as $P(a_T > 0.3)$, should be restricted based on the assessment of impact of high lateral accelerations on ship safety (which, however, falls out of the scope of present research). Other limiting values for lateral accelerations could be considered, see for instance Shigunov et al. (2011) and Ross (2009). For the purposes of present analysis, it will be assumed that $P(a_T > 0.3) = O(10^{-3})$ may be permitted. Thus, an additional safety requirement, “modified acceleration criterion” could be introduced. The safety assessment of a river-sea ship may be carried out in the following manner (Fig. 6). Probability of flooding is considered as the basic safety criterion. Consequently, the first step would be to calculate the upper limit of permitted significant wave heights based on the condition $P_{fl} = O(10^{-4})$. This is carried out for a range of metacentric heights (curve $H_{1/3}$). Then, for obtained wave heights, the probability that acceleration $0.3g$ would be attained in helmsman’s position is estimated, for the same range of GM s. In given example, modified acceleration criterion is exceeded in waves corresponding to acceptable probability of flooding if $GM \geq 4.2m$ (indicated with a dot); permitted wave heights, therefore, should be lowered accordingly.

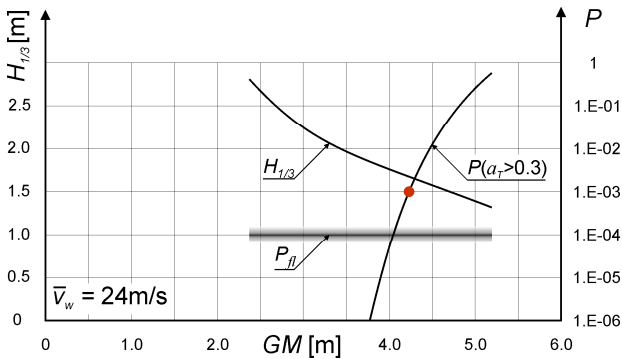


Figure 6: Safety assessment of the sample vessel V, using modified acceleration criterion.

In Fig. 7, modified acceleration criterion is used to compare two designs of the same length, breadth and draft but different freeboard. Due to a relatively high freeboard, probabilities of cargo hold flooding of the sample vessel ST_{sp} are much lower than corresponding values for the vessel ST , that is, ST_{sp} could

safely operate in higher sea states than ST , in some cases even higher than prescribed by RRR. However, higher freeboard also implies that the bridge on the vessel ST_{sp} is located farther from the rolling axis within the same range of metacentric heights. As a consequence, considerably higher lateral accelerations are attained in the wheelhouse.

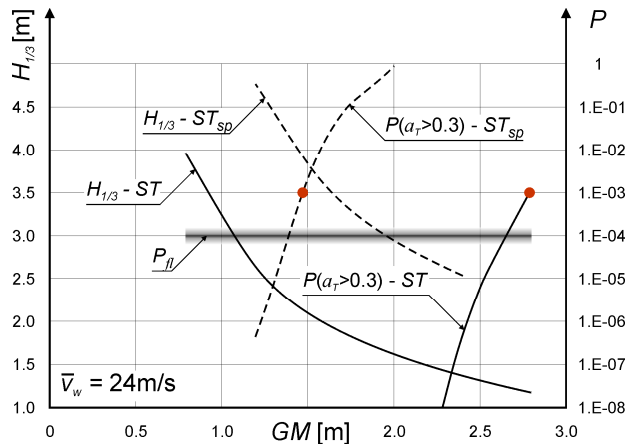


Figure 7: Comparison of two designs using modified acceleration criterion.

So, although vessel ST_{sp} may be regarded as safer from one point of view (as far as the flooding through unsecured openings is concerned), its crew would experience ship motion induced disturbance that could lead to navigation errors and ultimately affect the safety of the vessel. In order to diminish these effects, following the modified acceleration criterion, vessel ST_{sp} would have to sail in wave heights lower than determined by probabilistic criterion of flooding, in case that GM exceeds $\approx 1.5m$.

So far, the analysis focused on the stability requirements of the Russian River Register (2008). UNECE (2010) proposal generally prescribes higher wave heights, as it was demonstrated in Fig. 5. Therefore, in the next series of experiments, P_{fl} in weather conditions defined by UNECE (2010) was estimated for the “safer” sample vessels V_{sp} and ST_{sp} (Fig. 8). UNECE (2010) clearly overestimates the safety of vessels in waves. Though this could be the subject of a separate analysis, possible reasons could be the following. UNECE (2010) proposal covers the complete wave height range

otherwise considered by the Russian River and Maritime Register together. This could represent an effort of the authors of UNECE (2010) to extend the operation of the river-sea ships to the higher sea states, or perhaps to integrate the rules for sea-river and river-sea ships in one document.

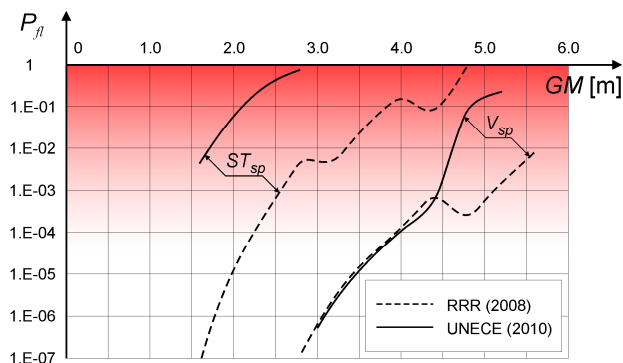


Figure 8: Probability of cargo hold flooding of the examined river-sea ships.

However, Russian classification societies use different calculation procedures to treat these two ship types, taking into account their specific features. A uniform, deterministic approach used in UNECE (2010) apparently fails to encompass both types.

4. CONCLUSIONS

The goal of the current paper was to present an overview and an analysis of the recent developments in the field of stability regulations for river-sea ships. Since the rules of the classification societies of Russian Federation are used as the basis for development of new safety requirements for the river-sea ships on the European level (Chapter 20B of the UNECE Resolution No. 61), a probabilistic investigation of the stability requirements laid down by Russian River Register (2008) was carried out. The author was not involved in development of the analyzed regulations; hence the paper presents an independent, personal view.

It should be noted that Russian classification societies recognized the perils of excessive accelerations and incorporated a seakeeping

approach as a remedy. However, present analysis demonstrated that deterministic acceleration criterion, which is used to define operational limits of river-sea ships, failed to provide sufficient safety, from the probabilistic point of view, in a number of realistic cases. In performed numerical tests, wave heights permitted by Russian River Register (2008) and particularly UNECE (2010) generated high probability of flooding of cargo hold for sample vessels which fulfilled stability criteria laid down by regulations. Vessels with high freeboards and hatch coaming heights, common in shipbuilding practice, performed much better in tests, which may explain the low rate of accidents related to dynamic stability of river-sea ships in waves.

As it was correctly pointed out by Shigunov et al. (2011), physical and mental fatigue, induced by ship motions, may influence the crew performance and lead to increase of errors, which in turn adversely affect safety. Numerical examples given in this paper, related to accelerations on the bridges of analyzed river-sea ships (Fig. 7) demonstrated that safety assessment is a complex and multifaceted task. Although ship ST_{sp} , designed according to current shipbuilding practices, may be safe from heeling to a critical angle in a number of realistic cases, high accelerations on the bridge could trigger an accident. Indeed, navigation errors were noticed in about 10% of river-sea ship accidents examined by Egorov (2007).

Criticism of a particular “chapter” in regulations (such as stability requirements) which constitute a part of a larger set of (classification) rules, may seem as incomplete without taking into account other rules that may also affect safety (e.g. structural requirements or guidelines for navigation in a specific area). However, the author believes that sufficient stability in given weather conditions should be targeted and accomplished by stability regulations themselves. Presently, as it was demonstrated in the paper, it may be an unintentional consequence of application of another (unrelated) rule.



5. ACKNOWLEDGMENTS

The paper is part of the project “Development of Next Generation of Safe, Efficient, Ecological (SE-ECO) Ships” executed by Department of Naval Architecture, Faculty of Mechanical Engineering University of Belgrade. The project is partly financed by Serbian Ministry of Education and Science, Contract No. TR35009.

6. REFERENCES

- Bačkalov, I., 2010, “Probabilistic safety of estuary vessels based on nonlinear rolling in wind and waves”, Transactions RINA, International Journal of Maritime Engineering, Vol. 152, Part A1, pp 1-8.
- Bačkalov, I., Kalajdžić, M., Hofman, M., 2010, “Inland vessel rolling due to severe beam wind: A step towards a realistic model”, Probabilistic Engineering Mechanics, Vol. 25, No. 1, pp 18-25.
- Basin, A.M., Anfimov, V.N., 1961, “Ship Hydrodynamics” (In Russian), Rechnoy Transport, Leningrad.
- Belgisch Staatsblad / Moniteur Belge, 2007, “Royal Decree concerning inland vessels also used for non-international sea voyages” (In Flemish and French), 16.03.2007, N. 2007 - 1187, pp. 14699-14711.
- Bulian, G., Francescutto, A., 2004, “A simplified modular approach for the prediction of the roll motion due to the combined action of wind and waves”, Proc. Inst. Mech. Eng. Vol. 218, Part M, Journal of Engineering for the Maritime Environment, pp. 189-212.
- Egorov, G. V., 2007, “Risk-based design of ships for restricted navigation areas” (In Russian), Sudostroenie, Saint-Petersburg.
- Egorov, G. V., Ilnitsky, I.A., 2006, “New generation of the Russian dry-cargo vessels of river-sea navigation ‘Volgo-Don MAX type’”, Proceedings of the 2nd Conference on Coastal Ships & Inland Waterways, RINA, London.
- Hofman, M., Bačkalov, I., 2005, “Weather Criterion for Seagoing and Inland Vessels – Some New Proposals”, Proceedings of International Conference on Marine Research and Transportation, University of Naples “Federico II”, pp 53-62.
- Journal officiel de la République Française, 2007, “Arrêté du 10 janvier 2007 relatif à la navigation de bateaux fluviaux en mer pour la desserte de Port 2000”, 27.01.2007, Texte 18 sur 122.
- Lesyukov, V. A., 1974, “Theory and design of inland vessels” (In Russian), Transport, Moscow.
- Ross, J. M., 2009, “Human Factors for Naval Marine Vehicle Design and Operation”, Ashgate Publishing Limited.
- Russian Maritime Register of Shipping, 2005, “Rules for classification and construction of sea-going ships”, Saint-Petersburg.
- Russian River Register, 2008, “Rules for classification of ships for inland and combined (river-sea) navigation” (In Russian), Moscow.
- Shigunov, V., Rathje, H., El Moctar, O., Altmayer, B., 2011, “On the Consideration of Lateral Accelerations in Ship Design Rules”, Proceedings of the 12th International Ship Stability Workshop, Washington D.C., pp 27-35.
- Truijens, P., Vantorre, M., Van der Werff, T., 2006, “On the Design of Ships for Estuary Service”, Transactions RINA, International Journal of Maritime Engineering, Vol. 148, Part A2, pp. 25-39.



United Nations Economic Commission for Europe (UNECE), 2006, “Resolution No. 61, Recommendations on Europe-Wide Technical Requirements for Inland Navigation Vessels”, New York and Geneva.

United Nations Economic Commission for Europe (UNECE), 2006b, “Drafting of ECE technical requirements for sea-river vessels”, Submitted by Russian Federation, ECE/TRANS/SC.3/2006/8, Geneva.

United Nations Economic Commission for Europe (UNECE), 2010, Draft proposal on Chapter 20B “Special provisions applicable to river-sea navigation vessels”, Submitted by the group of volunteers on Resolution No. 61, ECE/TRANS/SC.3/WP.3/2010/6, ECE/TRANS/SC.3/WP.3/2010/6/Add.1, Geneva.

Vantorre, M., Eloit, K., Delefortrie, G., 2012, “Probabilistic Regulation for Inland Vessels Operating at Sea as an Alternative Hinterland Connection for Coastal Harbours“, European Journal of Transport and Infrastructure Research, Vol. 12, Issue 1, pp 111-131.

Vassalos, D., Jasionowski, A., Cichowicz, J., 2004, “Issues Related to the Weather Criterion“ International Shipbuilding Progress, 51, no. 2/3, pp 251-271.

$H_{3\%}$ wave height with 3% probability of over-topping (m)
 h total stability lever (m)
 h' residuary stability lever (m)
 J_x moment of inertia for x axes (tm²)
 L vessel length (m)
 M_{st} righting (stability) moment (kNm)
 M_{wave} exciting wave moment (kNm)
 M_{wind} exciting wind moment (kNm)
 m_φ added mass of roll (tm²)
 N_c number of cycles (-)
 P probability (-)
 P_{fl} probability of flooding (-)
 s_K total area of bilge keels (m²)
 \bar{v}_w absolute mean wind speed (m/s)
 α_n phase shift of n -th wind component (-)
 Δ vessel displacement (t)
 ρ_{xx} radius of inertia (m)
 φ roll angle, heel (rad,°)
 $\bar{\varphi}$ mean value of roll (rad)
 ω_n frequency of n -th component (rad/s)

ICLL International Convention on Load Lines

7. NOMENCLATURE

A_n n -th wind-gust amplitude (m/s)
 B vessel breadth (m)
 B_n n -th wave amplitude (m)
 GK vertical position of vessel’s centre of gravity (m)
 GM metacentric height (m)
 D vessel depth (m)
 d vessel draft (m)
 d_{bk} distance of bilge keels from vessel’s rolling axis (m)
 $H_{1/3}$ significant wave height (m)





Steady State Probabilistic Response of a Half Oscillator Under Colored, Gaussian or non-Gaussian Excitation

Gerassimos A. Athanassoulis, *National Technical University of Athens (NTUA), School of Naval*

Architecture and Marine Engineering (SNAME), mathan@central.ntua.gr

Ivi C. Tsantili, *NTUA, SNAME, ivits@central.ntua.gr*

Zacharias G. Kapelonis, *NTUA, SNAME, zkapel@central.ntua.gr*

ABSTRACT

In the present work the probabilistic characteristics of the long-time (when dynamic statistical equilibrium has been reached), steady-state response of a half oscillator, subject to a colored, asymptotically stationary, Gaussian or non Gaussian (cubic Gaussian) excitation, are derived by means of the Response-Excitation (RE) theory, first introduced by Athanassoulis & Sapsis (2006). RE theory permits us to derive an evolution equation for the joint Response-Excitation Probability Density Function (REPDF) of any dynamical system with polynomial nonlinearities under arbitrary stochastic excitation. This evolution equation is derived by projecting an exact, infinite dimensional, Functional Differential Equation, for the joint response-excitation characteristic functional, to finite dimensions. Application of this theory to the ship roll motion has been presented by Athanassoulis *et al* (2009). The joint REPDF evolution equation is a peculiar equation, involving two times (one for the excitation and one for the response), and two sets of probability arguments (one for the excitation variables, and another one for the response variables), and partial derivatives only with respect to the response time and the response probability arguments. In general it is not uniquely solvable and, thus, it needs to be completed by an appropriate closure scheme. In this paper we present a closure technique via localized linear problems, and a numerical solution to the steady-state case, providing the long-time, statistical equilibrium PDFs. The method of numerical solution is based on a representation of the sought-for REPDF by means of kernel density functions, and a Galerkin-type numerical scheme. The obtained PDFs are compared with results from Monte Carlo simulation for the same problem. The method can be extended to treat full nonlinear oscillators, with polynomial nonlinearities, subjected to Gaussian or non Gaussian excitation.

Keywords: *Probabilistic characterization of responses, non markovian responses, non gaussian excitation, stochastic modeling of non-linear systems, half oscillator.*

1. INTRODUCTION

Wave loads on ships are generally modelled as colored (smoothly-correlated) stochastic processes (in contrast to delta-correlated processes, which are commonly used in stochastic dynamic analysis; see e.g., Naess (2000), Iourtchenko (2003), Pirrotta (2007)). Thus, ship responses are also smoothly-correlated stochastic processes, lacking to obey the Markovian property, which essentially simplifies the analysis of stochastic systems. The determination of probability density functions (PDFs) associ-

ated with ship responses is straightforward as far as the assumption of linearity is (approximately) valid, and the excitation can be simplified as Gaussian. When strong nonlinearities are present, and the excitation cannot be considered neither Gaussian nor delta correlated, as in the case of roll motion, the classical theory of diffusion processes and the **Fokker-Planck-Kolmogorov (FPK) equation** is not applicable (see e.g. Neves *et al*, 2011, for a comprehensive review on issues involving dynamic behaviour and probabilistic nature of extreme events in a seaway). In such cases, the proba-



bilistic characterization of the responses is a difficult problem, calling for specific modelling techniques and advanced mathematical tools.

In cases where the correlation time of the excitation is small, in comparison with the relaxation time of the dynamical system, it is possible to reformulate the problem as an averaged Ito SDE and advance to the corresponding averaged FPK. This technique, known as **the stochastic averaging method**, was first introduced by Stratonovitch (1963) and made rigorous by Khasminkii (1966). Variants of this methodology have been applied to the ship rolling problem by Roberts (1982), Roberts and Vasta (2000), where also an extensive survey of the previous works is presented, Kreuzer and Sichertmann (2007).

An approach which can resolve the non-Markovian character of the response, keeping a close connection with the standard treatment of stochastic differential equations, is the **filtering approach**. This method is implemented by making the colored excitation to be the output of an appropriate linear filter, coupled with the original dynamic system. In this way, an augmented stochastic system is obtained, which can be treated by means of a FPK equation involving the state-space variables of the original system and the filter (Spanos, 1986, Muscolino, 1995, Pugachev and Sinitsyn, 2001). The method has been applied to the ship roll motion by Francescutto and Naito (2004) and others. It is rather general and effective as far as the excitation is Gaussian and the appropriate filter is of low order. Hybrid techniques, combining some of the above methods have also been developed (Di Paola & Floris, 2008).

Another generic approach, applicable to quite general dynamical systems under colored stochastic excitation, introduced in 2006 (Athansoulis & Sapsis, 2006), further developed in Sapsis & Athansoulis (2008) (hereafter referred to as [1]), and applied to ship rolling motion by Athansoulis *et al* (2009) (hereafter referred to as [2]). This approach is based on the use of the joint,

response-excitation characteristic functional, which is an infinite-dimensional mathematical object modelling the complete probabilistic structure of the involved stochastic processes, without any simplifying assumptions. See Hopf (1952), who introduced the characteristic functional for the study of turbulent flows, and its extensions to other stochastic dynamical problems presented by Beran (1968). A Hopf-type functional differential equation (FDE) governing the evolution of the joint, response-excitation characteristic functional for quite general stochastic differential equations is easy to obtain. Since, however, the numerical solution of infinite-dimensional FDEs is not feasible (at least, for the time being), the goal of this approach is to come back to probabilistic equations for finite-dimensional PDFs, by appropriate projections of the FDE. For example, if we assume that the ship roll motion obeys the following dynamical equation (see, e.g., Belenky & Sevastianov, 2003).

$$(I + A)\ddot{x}(t) + b_1\dot{x}(t) + b_3\dot{x}^3(t) + K_1x(t) + K_3x^3(t) = Y(t) \quad (1)$$

where $Y(t)$ is the external stochastic excitation, the Response-Excitation (RE) theory developed in [1,2] leads to the following evolution equation for the joint Response-Excitation, Probability Density Function (REPDF) $f_{x_1(t)x_2(t)y(s)}(\alpha_1, \alpha_2, \beta)$ ($x_1(t) = x(t)$, $x_2(t) = \dot{x}(t)$; see [2] for a detailed description of all coefficients appearing in equ. (1)):

$$\begin{aligned} & \frac{\partial}{\partial t} f_{x_1(t)x_2(t)y(s)}(\alpha_1, \alpha_2, \beta) \Big|_{s \rightarrow t} + \\ & + \mathbf{L}_{\alpha_1\alpha_2} f_{x_1(t)x_2(t)y(s)}(\alpha_1, \alpha_2, \beta) + \\ & + \beta \frac{\partial f_{x_1(t)x_2(t)y(s)}(\alpha_1, \alpha_2, \beta)}{\partial \alpha_2} = 0 \end{aligned} \quad (2a)$$

supplemented by the marginal compatibility condition

$$\begin{aligned} f_{y(s)}(\beta) &= \iint_{\mathbb{R}^2} f_{x_1(t)x_2(t)y(s)}(\alpha_1, \alpha_2, \beta) d\alpha_1 d\alpha_2 = \\ &= \text{known density function}, \quad \forall s \geq t_0 \end{aligned} \quad (2b)$$

and the initial condition.

$$f_{x_1(t_0)x_2(t_0)}(\alpha_1, \alpha_2) = \text{known density function} \quad (2c)$$

$\mathbb{L}_{\alpha_1 \alpha_2}(\cdot)$, appearing in (2a), is a linear differential operator given by

$$\begin{aligned} \mathbb{L}_{\alpha_1 \alpha_2}(\cdot) = & \left[-\frac{1}{I+A} \left(b_1 + 3b_3 \alpha_2^2 - \alpha_2 \frac{\partial}{\partial \alpha_1} + \right. \right. \\ & + K_1 \alpha_1 \frac{\partial}{\partial \alpha_2} + K_3 \alpha_1^3 \frac{\partial}{\partial \alpha_2} + b_1 \alpha_2 \frac{\partial}{\partial \alpha_2} + \\ & \left. \left. + b_3 \alpha_2^3 \frac{\partial}{\partial \alpha_2} + b_1 \alpha_2 \frac{\partial}{\partial \alpha_2} + b_3 \alpha_2^3 \frac{\partial}{\partial \alpha_2} \right) \right] (\cdot) \quad (3) \end{aligned}$$

Equ. (2a) is a peculiar equation, involving two times and three probability arguments (one for the excitation, one for the motion and one for the velocity), and partial derivatives only with respect to one (response) time and two (motion-velocity) probability arguments. This peculiarity gives rise to fundamental questions regarding both the well-posedness of the problem (2a,b,c) and the methods of its numerical solution. Recently, our approach re-examined by Venturi *et al* (2012), using a different (but essentially equivalent) method. They confirmed the validity of equation derived in [1] (and, thus, indirectly, of equation (2a), derived in [2]), and answered in negative the question regarding the well-posedness of problem (2), by presenting a simple example in which our equation is valid but it does not ensure uniqueness. Accordingly, it becomes clear that a kind of completion of problem (2) is necessary. The type of completion proposed by Venturi *et al* (2012) results in a much more complicated equation, including the entire history of the response process in a functional integral form, which cannot be considered as an attractive alternative.

The crucial problem with the equ. (2a) is that the joint-REPDF $f_{x_1(t)x_2(t)y(s)}(\alpha_1, \alpha_2, \beta)$ is differentiated only with respect to the response time t . However, since the function $f_{x_1(t)x_2(t)y(s)}(\alpha_1, \alpha_2, \beta)$ is unknown, the partial-time (called hereafter *half-time*) derivative $\partial f_{x_1(t)x_2(t)y(s)}(\alpha_1, \alpha_2, \beta) / \partial t$ cannot be properly

evaluated, because there is no way to separate the effect of the response time t from the effect of the excitation time s , without knowing the specific form of $f_{x_1(t)x_2(t)y(s)}(\alpha_1, \alpha_2, \beta)$. This fact calls for a kind of *a priori* approximation of the term $\lim_{s \rightarrow t} \partial f_{x_1(t)x_2(t)y(s)}(\alpha_1, \alpha_2, \beta) / \partial t$, before any attempt to formulate a numerical scheme for solving.

In the present paper we develop an *a priori* closure technique, for the long-time, steady-state REPDF evolution equation, by formulating and using localized linear problems. Up to now, this, improved, response-excitation theory has been developed only for first-order dynamical systems, that is, half-oscillators, under Gaussian excitation. (Athanasoulis *et al*, 2012). Accordingly, we shall present herewith the method of closure, the scheme of the numerical solution, and numerical results for a half-oscillator of the form:

$$\dot{x}(t; \theta) = H(x(t; \theta)) + \Psi(y(t; \theta)) \quad (4a)$$

$$x(0; \theta) = x_0(\theta) \quad (4b)$$

where θ is the stochastic argument (the sample-point indicator), $H(\cdot)$ and $\Psi(\cdot)$ are polynomial functions, and $y(t; \theta)$ is a given, smoothly correlated, asymptotically stationary, Gaussian stochastic process (regular colored noise). Accordingly, the polynomial excitation $\Psi(y(t; \theta))$ can model (strongly) non-Gaussian processes. We shall focus on the long-time, steady-state response of equ. (4), assuming that the Gaussian process $y(t; \theta)$, shaping the excitation, becomes quickly stationary, as $t \rightarrow \infty$. Then, the evolution equation for the long time steady state REPDF $f_{x(t)y(s)}(\alpha, \beta)$, which is valid in the limit $s \rightarrow t$ (for s and t in the long-time regime) and for every point $(\alpha, \beta) \in \mathbb{R}^2$ of the RE phase space, reads as follows:

$$\begin{aligned} & \left. \frac{\partial}{\partial t} f_{x(t)y(s)}(\alpha, \beta) \right|_{s \rightarrow t} + \\ & + \frac{\partial}{\partial \alpha} \left[(H(\alpha) + \Psi(\beta)) \cdot f_{x(t)y(s)}(\alpha, \beta) \right]_{s \rightarrow t} = 0 \end{aligned} \quad (5a)$$



supplemented by the marginal-compatibility constraint,

$$\int_{\alpha \in \mathbb{R}} f_{x(t)y(s)}(\alpha, \beta) d\alpha = f_{y(s)}(\beta) = \text{a known pdf} \quad (5b)$$

ensuring that $f_{x(t)y(s)}(\alpha, \beta)$ complies with the given marginal, as well as by the conditions:

$$f_{x(t)y(s)}(\alpha, \beta) \geq 0, \quad (5c)$$

$$\int_{\beta \in \mathbb{R}} \int_{\alpha \in \mathbb{R}} f_{x(t)y(s)}(\alpha, \beta) d\beta d\alpha = 1. \quad (5d)$$

No initial condition needs to be assumed, since in the long-time statistical equilibrium system's response is no longer dependent on the initial conditions.

2. LOCAL DESCRIPTION OF THE RESPONSE-EXCITATION CORRELATION STRUCTURE

In order to implement our *a priori* closure scheme for equ. (5a), we define and solve localized linear problems, providing us with information concerning the local RE-correlation structure. Focusing on a (any) specific point y_0 of the excitation state space, we find the corresponding (deterministic) long-time equilibrium point x_0 in the response state space, by solving the equation $H(x_0) = -\Psi(y_0)$. Introducing a localized, around the point (x_0, y_0) , linear approximation of the right-hand side of equ.(4a), we get:

$$\dot{x}(t; \theta) \approx H'(x_0) \cdot (x(t; \theta) - x_0) + \Psi'(y_0) \cdot (y(t; \theta) - y_0) \quad (6)$$

and formulate the following **localized version** of equ. (4a):

$$\dot{x}_{loc}(t; \theta) = H'(x_0) \cdot (x_{loc}(t; \theta) - x_0) + \Psi'(y_0) \cdot (y_{loc}(t; \theta) - y_0) \quad (7)$$

To ensure stability we always assume that $H'(x_0) < 0$. The localized excitation $y_{loc}(t; \theta)$ is considered Gaussian (as $y(t; \theta)$), with mean value $m_{y_{loc}} = y_0$ and an appropriate autocovariance function $C_{y_{loc}y_{loc}}(t; s)$. Since we are interested in the long-time regime, we choose a scaled version of the long-time limit of the global autocovariance function $C_{yy}^{(\infty)}(t-s)$, that is $C_{y_{loc}y_{loc}}(t-s) = \sigma_{y_{loc}}^2 \cdot C_{yy}^{(\infty)}(t-s) / \sigma_y^2$. However, the long-time correlation matrix of the local linear problem is scaled uniformly by $\sigma_{y_{loc}}^2 / \sigma_y^2$, and we can assume $\sigma_{y_{loc}}^2 = \sigma_y^2$ and introduce the scaling later on.

The localized, linear, stochastic differential equation (7) is readily solved analytically. The long-time covariances $C_{x_{loc}y_{loc}}^{(\infty)}(w)$ and $C_{x_{loc}x_{loc}}^{(\infty)}(w)$ are given by the formulae:

$$\begin{aligned} C_{x_{loc}y_{loc}}^{(\infty)}(w) &= \lim_{\substack{t \rightarrow \infty \\ w = \text{const.}}} C_{x_{loc}y_{loc}}(t, t-w) = \\ &= \Psi'(y_0) \cdot \int_{-w}^{\infty} e^{H'(x_0) \cdot (u+w)} \cdot C_{y_{loc}y_{loc}}(u) du, \end{aligned} \quad (8)$$

and

$$\begin{aligned} C_{x_{loc}x_{loc}}^{(\infty)}(w) &= \frac{(\Psi'(y_0))^2}{2(-H'(x_0))} \times \\ &\times \int_{v=-\infty}^{v=+\infty} C_{y_{loc}y_{loc}}(v) \cdot e^{H'(x_0) \cdot |v-w|} dv \end{aligned} \quad (9)$$

We shall now specialize the results (8) and (9) for the covariance function

$$\begin{aligned} C_{y_{loc}y_{loc}}(t-s) &= C_{yy}^{(\infty)}(t-s) = \\ &= \sigma_y^2 \cdot \exp(-a(t-s)^2) \end{aligned} \quad (10)$$

The integrals appearing in the right-hand side of eqs. (8) and (9) can be calculated explicitly. The results read as follows:

$$C_{x_{loc} y_{loc}}^{(\infty)}(t-s) = \frac{\sqrt{\pi}}{2\sqrt{a}} \cdot \sigma_y^2 \cdot \Psi'(y_0) \times \exp\left(\frac{(H'(x_0))^2}{4 \cdot a} + H'(x_0) \cdot (t-s)\right) \times \left\{ \operatorname{erf}\left(\sqrt{a} \cdot (t-s) + \frac{H'(x_0)}{2 \cdot \sqrt{a}}\right) + 1 \right\} \quad (11)$$

$$C_{x_{loc} x_{loc}}^{(\infty)}(t-s) = \frac{\Psi'(y_0)}{-H'(x_0)} \cdot \frac{1}{2} \times \left\{ C_{x_{loc} y_{loc}}^{(\infty)}(t-s) + C_{x_{loc} y_{loc}}^{(\infty)}(s-t) \right\} \quad (12)$$

Using equ. (11) we are able to determine the partial-time derivative of $C_{x_{loc} y_{loc}}^{(\infty)}(t-s)$ with respect to the excitation time t . After some algebraic manipulations, the final result reads as follows:

$$\frac{\partial C_{x_{loc} y_{loc}}^{(\infty)}(t-s)}{\partial t} = H'(x_0) \cdot C_{x_{loc} y_{loc}}^{(\infty)}(t-s) + \Psi'(y_0) \cdot C_{y_{loc} y_{loc}}^{(\infty)}(t-s) \quad (13)$$

The derived auxiliary conditions (11)-(13), provide the local correlation structure between $x(t; \theta)$ and $y(s; \theta)$, as $s \rightarrow t$, in the vicinity of the RE phase space point $(\alpha, \beta) = (x_0, y_0)$. This information will be exploited in the next section, in order to implement the long time limit $\lim_{s \rightarrow t} \partial f_{x(t)y(s)}(\alpha, \beta) / \partial t$.

3. KERNEL DENSITY REPRESENTATION FOR THE JOINT RESPONSE-EXCITATION AND MARGINAL PDFS

The target of the numerical solution to equ. (5a), supplemented by all appropriate auxiliary conditions (already discussed), is to find the time-independent (statistical equilibrium) joint REPDF $f_{xy}(\alpha, \beta) = f_{x(t)y(t)}(\alpha, \beta)$. However, in order to cope with the appearance of the unusual, response-time (half-time) derivative in equ. (5a), a representation of the lag-time dependent joint REPDF $f_{x(t)y(s)}(\alpha, \beta)$ capable

of embedding the acquired local conditions shall be introduced. On the basis of the above and previous (successful) experience in representing PDFs by superposition of kernel density functions (Athanasoulis and Belibassakis 2002, Athanasoulis and Gavriladis 2002), the following Kernel Density Representation (KDR) is adopted:

$$f_{x(t)y(s)}(\alpha, \beta) = \sum_{i,j} p_{ij} \cdot K(\alpha, \beta; \alpha_i, \beta_j, \Sigma_{\alpha_i, \beta_j}(t-s)) \quad (14)$$

where $(\alpha_i, \beta_j), (i, j) \in \mathbb{Z} \times \mathbb{Z}$, is a grid of points in the state space $\mathbb{R} \times \mathbb{R}$, each (α_i, β_j) serving as the center of the **Gaussian kernel density function** $K(\alpha, \beta; \cdot, \cdot, \cdot)$, while

$$\Sigma_{\alpha_i, \beta_j}(t-s) = \begin{pmatrix} C_{\alpha_i \alpha_i}(0) & C_{\alpha_i \beta_j}(t-s) \\ C_{\alpha_i \beta_j}(t-s) & C_{\beta_j \beta_j}(0) \end{pmatrix} \quad (15)$$

is the covariance matrix of $K(\alpha, \beta; \cdot, \cdot, \cdot)$. To ensure that (14) is a legitimate PDF, the following constraints need to be imposed on the unknown coefficients $p_{ij}, (i, j) \in \mathbb{Z} \times \mathbb{Z}$:

$$0 \leq p_{ij} \quad \text{and} \quad \sum_{i,j} p_{ij} = 1. \quad (16a,b)$$

In principle, $f_{x(t)y(t)}(\alpha, \beta)$ is supported on the whole plane $\mathbb{R} \times \mathbb{R}$. For computational reasons, we focus on its form in its essential support D_{ess} , conventionally defined as the subset of $\mathbb{R} \times \mathbb{R}$ where $f_{xy}(\alpha, \beta) > \varepsilon \approx 10^{-3} \cdot \max\{f_{xy}(\alpha, \beta)\}$. This choice, restricts the approximation in a compact subdomain $D_{\alpha\beta} = [\alpha_{\min}, \alpha_{\max}] \times [\beta_{\min}, \beta_{\max}]$, of $\mathbb{R} \times \mathbb{R}$, such that $D_{ess} \subseteq D_{\alpha\beta}$ (tail questions are not considered herewith), and the indices (i, j) run over the finite set $\mathcal{N}(I) \times \mathcal{N}(J)$, where $\mathcal{N}(I) = \{1, 2, \dots, I\}$ and $\mathcal{N}(J)$ is similarly defined. Since D_{ess} is not known a priori some preliminary information is necessary in order to choose the computational domain $D_{\alpha\beta}$. This information is provided by the essential support of the known excitation $f_y(\beta)$, in conjunction



with an estimate of the total response variance, approximated by solving a global moment problem using Gaussian closure.

Introducing the KDR in equs. (5a) (the constitutive conditions, equs. (5c,d) are automatically satisfied thanks to the defining properties of the KDR), we obtain the following reformulation of problem (5a,c,d):

$$\sum_{i,j} p_{ij} \left[\frac{\partial}{\partial t} K(\alpha, \beta; \alpha_i, \beta_j, \Sigma_{\alpha_i, \beta_j}(t-s)) \Big|_{s \rightarrow t} + \frac{\partial}{\partial \alpha} \left\{ (H(\alpha) + \Psi(\beta)) \times K(\alpha, \beta; \alpha_i, \beta_j, \Sigma_{\alpha_i, \beta_j}(0)) \Big|_{s \rightarrow t} \right\} \right] = 0 \quad (17a)$$

under the marginal compatibility constraint

$$\sum_{i,j} p_{ij} K_{\beta_{j(i)}}(\beta; \beta_{j(i)}, \sigma_{\beta_{j(i)}}) - f_y(\beta) = 0 \quad (17b)$$

where $K_{\beta_{j(i)}}(\beta; \beta_{j(i)}, \sigma_{\beta_{j(i)}}) =$

$$= \int_{\alpha \in \mathbb{R}} K(\alpha, \beta; \alpha_i, \beta_j, \Sigma_{\alpha_i, \beta_j}(t-s)) d\alpha$$

Note that, the half-time derivative $\partial K(\dots, \Sigma_{\alpha_i, \beta_j}(t-s)) / \partial t$, appearing in equ. (17a), is now reduced to the corresponding derivative of the covariance matrix $\Sigma_{\alpha_i, \beta_j}(t-s)$, which is a priori estimated by means of the results of the previous section.

4. GALERKIN TYPE DISCRETIZATION OF THE PROBLEM

On the basis of the KDR, equ. (14), the determination of the sought-for joint REPDF has been reduced to the determination of the coefficients p_{ij} , $(i, j) \in \mathcal{N}(I) \times \mathcal{N}(J)$, from the system of equs. (17a,b). This problem can be solved using a Galerkin type, weighted-residual method (Kantorovich and Krylov, 1964, Zeidler, 1990) to find a discrete system of equations, approximately equivalent to equs. (17a,b). Using Gaussian Galerkin Kernels

$\Lambda_{\kappa, \lambda}(\alpha, \beta)$ and $\tilde{\Lambda}_{\tilde{\lambda}}(\beta)$ (see Athanassoulis *et al* 2012) we obtain the following linear system for p_{ij} coefficients:

$$\sum_{i,j} p_{ij} \cdot G_{ij, \kappa \lambda} = 0, \quad \forall (\kappa, \lambda) \in \mathcal{N}(K) \times \mathcal{N}(L),$$

$$\sum_{i,j} p_{ij} \cdot \tilde{G}_{j(i), \tilde{\lambda}} = g_{\tilde{\lambda}_{\tilde{\lambda}}}(f_y), \quad \forall \tilde{\lambda} \in \mathcal{N}(\tilde{L}) \quad (18a,b)$$

where $G_{ij, \kappa \lambda}$, $\tilde{G}_{j(i), \tilde{\lambda}}$ are integrals of Gaussian functions (calculated analytically) and

$$g_{\tilde{\lambda}_{\tilde{\lambda}}}(f_y) = \int_{\mathbb{R}} f_y(\beta) \cdot \tilde{\Lambda}_{\tilde{\lambda}}(\beta) d\beta.$$

On the basis of the above discussion, the problem of calculating the expansion coefficients p_{ij} of the joint-REPDF takes the following form:

Problem P : Find p_{ij} , $(i, j) \in \mathcal{N}(I) \times \mathcal{N}(J)$, satisfying the homogeneous equation (18a), under the marginal compatibility constraint (18b) and the constitutive constraints (16a,b).

5. RESULTS - SOLUTION OF THE HALF-OSCILLATOR PROBLEM

In this section numerical results will be presented for the special case of equ. (4a), describing a cubic half-oscillator under cubic excitation:

$$\dot{x}(t; \theta) = (\mu_1 + \mu_2 \cdot x(t; \theta)^2) \cdot x(t; \theta) + (\kappa_1 + \kappa_2 \cdot y(t; \theta)^2) \cdot y(t; \theta) \quad (19)$$

where $y(t; \theta)$ is a Gaussian stochastic process, with long-time correlation function given by equ. (10). Two cases have been considered: the case of a linear half-oscillator under non Gaussian (cubic) excitation, with parameter values $\mu_1 = -1$, $\mu_2 = 0$, $\kappa_1 = 0$, $\kappa_2 = 1$, (hereby called **Case 1**) and the case of a non-linear half-oscillator under Gaussian excitation, with parameter values $\mu_1 = \mu_2 = -1$, $\kappa_1 = 1$, $\kappa_2 = 0$ (hereby called **Case 2**). The correlation time of the Gaussian excitation process $y(t; \theta)$

is given, by $\tau_{\text{corr}}^{(y)} = \int_0^\infty C_{yy}(\tau) d\tau / C_{yy}(0) = 0.5\sqrt{\pi/a}$, while the relaxation time of the system is estimated by the linear relaxation time $\tau_{\text{relax}}^{(\text{lin})} = 1$ (which is an overestimation regarding Case 2). Two methods have been used for the derivation of the joint REPDF $f_{xy}(\alpha, \beta)$ and the marginal PDF $f_x(\alpha)$. The numerical solution of the constraint optimization problem **P** (hereby referred to as **RE solution**), and a conventional Monte Carlo scheme (hereby referred to as **MC simulation**). Systematic comparisons of the results obtained by the two methods are also presented.

In the context of the RE theory, Problem **P** is solved numerically in three steps. In the **first step**, representation kernels and Galerkin kernels are identified. Their centers α_i, β_j , $i \in \mathcal{N}(I)$, $j \in \mathcal{N}(J)$, are placed on a regularly spaced grid over the computational domain $D_{\alpha\beta}$. The kernel variances $C_{\alpha_i\alpha_i}, C_{\beta_j\beta_j}$ are adjusted to $D_{\alpha\beta}$ and the resolution of the grid, aiming at a certain degree of overlapping between contiguous kernels. The kernel covariances $C_{\alpha_i\beta_j}$, are defined by means of the formula $C_{\alpha_i\beta_j} = \rho_{\text{loc}}^{(\infty)}(0) \cdot \sqrt{C_{\alpha_i\alpha_i}} \cdot \sqrt{C_{\beta_j\beta_j}}$, where the local correlation coefficient $\rho_{\text{loc}}^{(\infty)}(0)$ is calculated from the localized linear problem. The long-time limit of the half-time derivative $\partial C_{\alpha_i\beta_j} = \lim_{s \rightarrow t} \partial C_{\alpha_i\beta_j}(t-s) / \partial t$, necessary in order to fully specify the coefficients $G_{ij, \kappa\lambda}$, is estimated from the localized approximation, equ. (13). The Galerkin kernels have been selected to be Gaussian kernels, identical with the representation ones. With these choices all coefficients of eqs. (18) are fully specified and thus we can proceed to the **second step**, namely, the numerical solution of problem **P**. This is performed using LSQLIN, the constrained least squares MATLAB® function. The solution yields p_{ij} , from which a first estimate of the joint-REPDF is obtained. In the **third step** the solution obtained in the second

step is exploited in order to estimate the essential support D_{ess} , to redistribute the kernels, and redefine the kernel parameters. Within usually one or two iterations of step 3, the essential support converges, and the final solution $f_{xy}(\alpha, \beta)$ is extracted.

The Monte Carlo simulation is obtained by generating 4000 samples of the excitation process $y(t; \theta)$, using the 1-D random-phase model. Equ. (19) (with zero initial condition) is solved using ODE45, a MATLAB® implementation of the Dormant-Prince method (Dormand and Prince 1980), based on an explicit Runge-Kutta (4,5) formula. The MC PDF estimations are computed using the kernel density estimation via diffusion, introduced by Botev *et al* (2010) and coded in MATLAB® functions by the same author.

Results are presented for two different values of parameter a , namely $a = 3$ and 7 , corresponding to excitation correlation time: $\tau_{\text{corr}}^{(y)} = 0.51$ and 0.33 respectively. Since the nonlinearity of equ. (19) contributes to damping terms, the relaxation time of Case 2 is smaller than that of Case 1, for which $\tau_{\text{relax}}^{(\text{lin})} = 1$. Thus, the values $a = 3$ and 7 correspond to $\lambda = \tau_{\text{corr}}^{(y)} / \tau_{\text{relax}}^{(\text{lin})} = 0.51, 0.33$. In all cases $\sigma_y^2 = 1$.

In Figures 1 and 5, the joint REPDF is shown, as calculated by the MC simulation for Case 1 and 2 respectively. The corresponding calculations using RE theory are illustrated in Figures 2 and 6. The latter Figures also depict the marginals obtained by the two methods. The absolute difference between the MC and RE method is shown in Figure 3 for Case 1, and Figure 7 for case 2. This difference is, in general, less than 5% in both Cases, except for the high probability areas in the strongly colored examples ($a = 3$), where it locally reaches a maximum of 20%. The latter, local, high mismatch should be associated with the local steepness of the corresponding PDFs. In general, the PDFs shapes, as obtained by the



two methods, are very similar, as can be seen from Figs. 1, 2 and 5, 6. In addition, the response marginal PDFs calculated by the two

methods, compare very satisfactorily in both Cases, regardless of the color strength

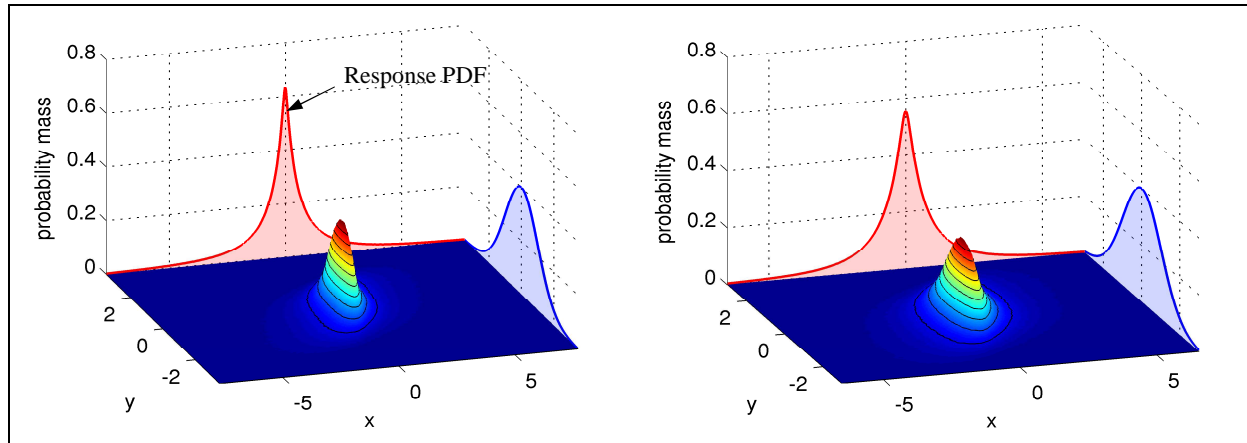


Figure 1: (Color online). REPDFs as calculated via MC solution for Case 1 and $a = 3, 7$. The projections depict the marginal PDFs.

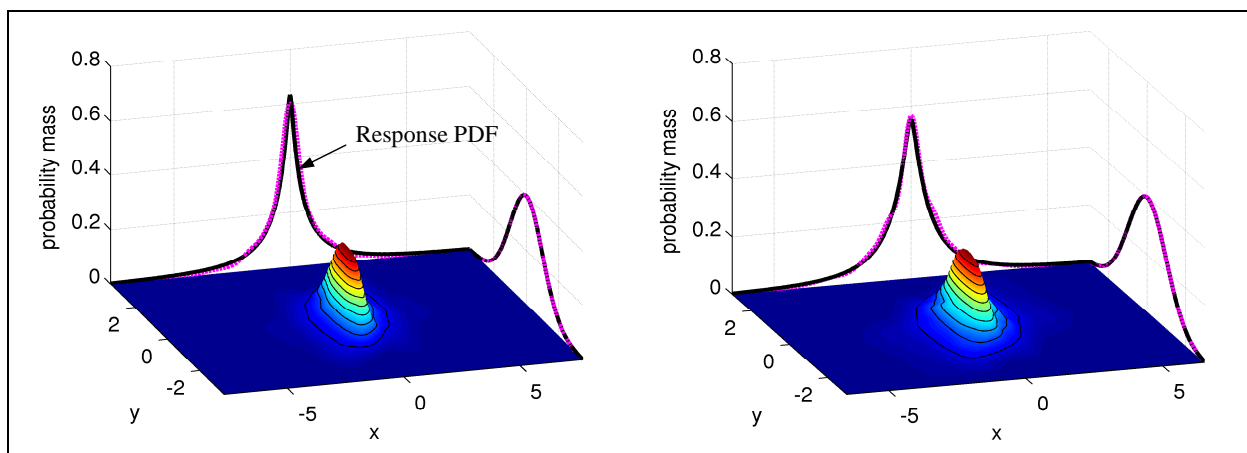


Figure 2: (Color online). REPDFs as calculated using the RE solution for Case 1 and $a = 3, 7$. The marginal projections depict both MC (solid lines) and RE solutions (dashed lines).

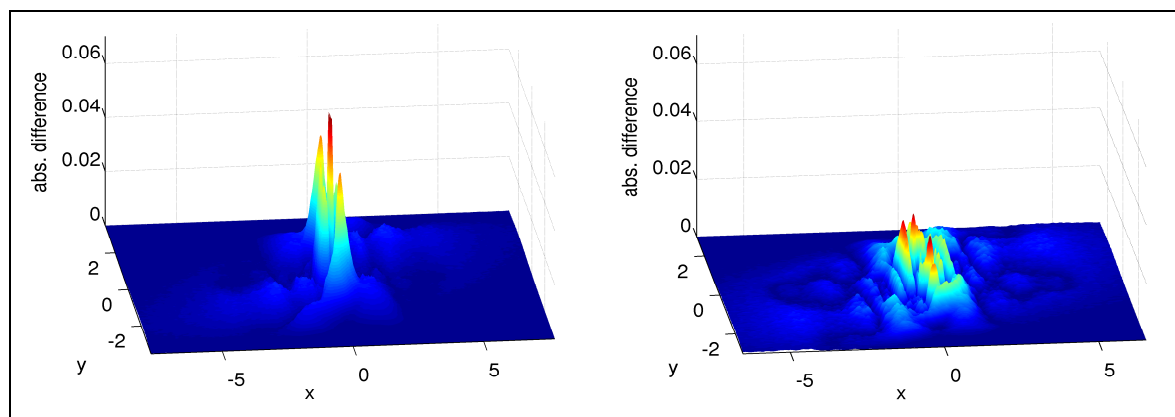


Figure 3: (Color online). The absolute difference between RE and MC solutions: Case 1, $a = 3, 7$.

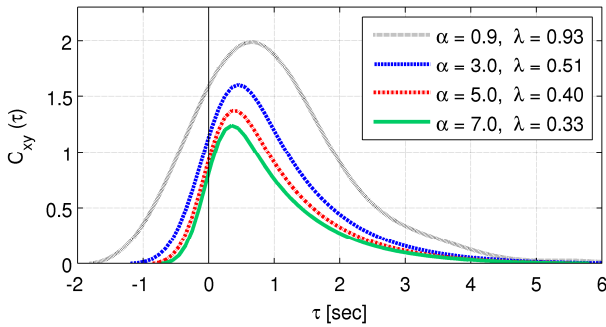


Figure 4: (Color online). The RE covariance function for Case 1.

It is interesting to notice the strong deviations of the calculated PDFs from the “equivalent” 2D Gaussian distributions, for both examined cases. The same also holds for the response densities, as intuitively expected. Apart from the examples shown here, the RE solution is also applicable for higher values of ratio λ , as shown in recent work (Athanasoulis *et al*, 2012), where the joint REPDF

becomes bi-modal, although the examined system is mono-stable (regarding the bi-modality of bi-stable systems see also Grigolini *et al*, 1988, Jung & Risken, 1985).

In Figs. 4 and 8, the response-excitation covariance $C_{xy}(\tau)$ for Cases 1 and 2 is plotted, as obtained by MC simulation. $\tau < 0$ corresponds to future lag values (excitation in advance of response). In contrast to cases of delta-correlated excitation, there is a correlation between the current response value and the future excitation. It is interesting to point out that, after a rescaling, $C_{xy}(\tau)$ has a very similar shape for both examined cases, when a values are equal.

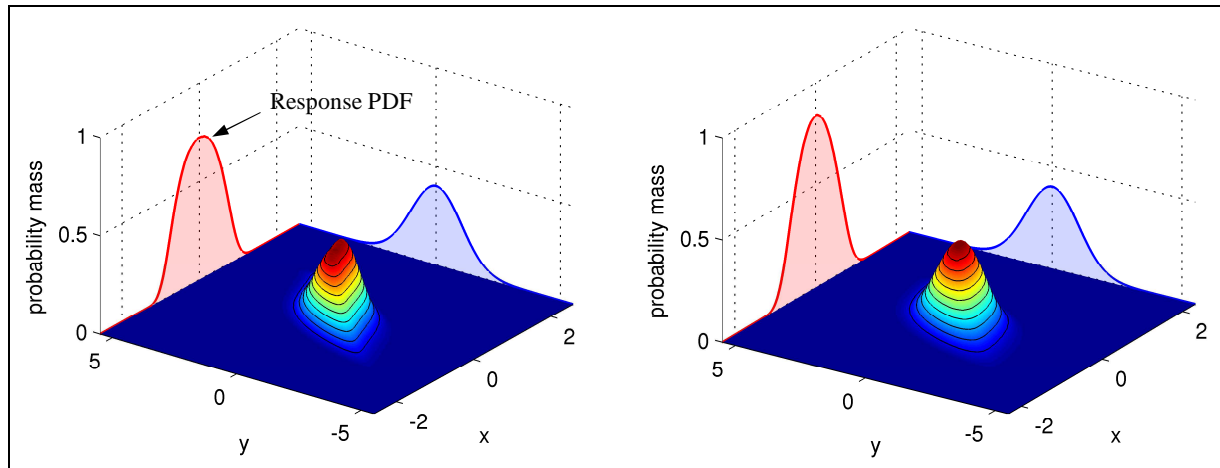


Figure 5: (Color online). REPDFs as calculated via MC solution for Case 2 and $a = 3, 7$. The projections depict the marginal PDFs.

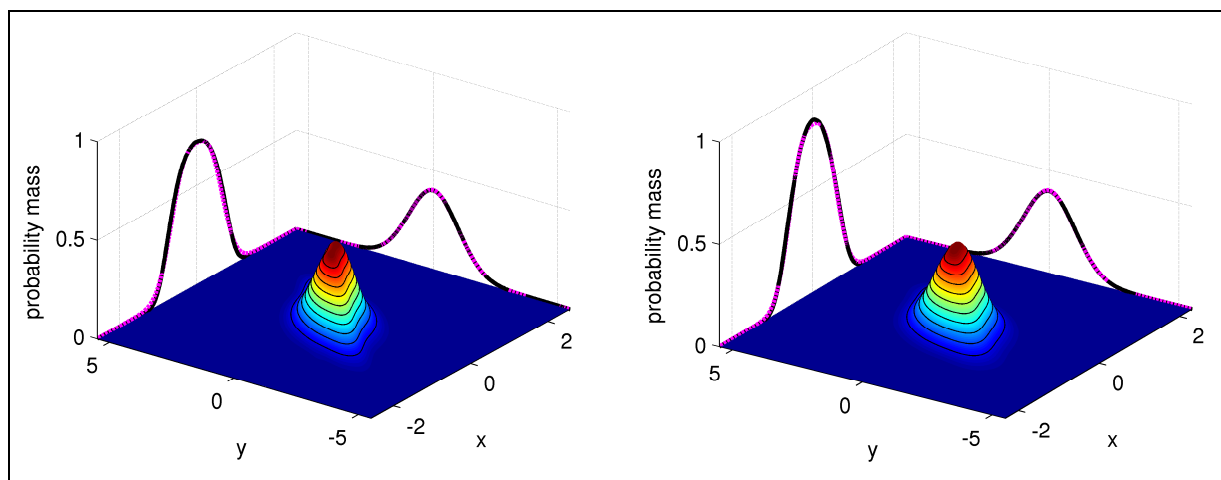


Figure 6: (Color online). REPDFs as calculated using the RE solution for Case 2 and $a = 3, 7$. The marginal projections depict both MC (solid lines) and RE solutions (dashed lines).

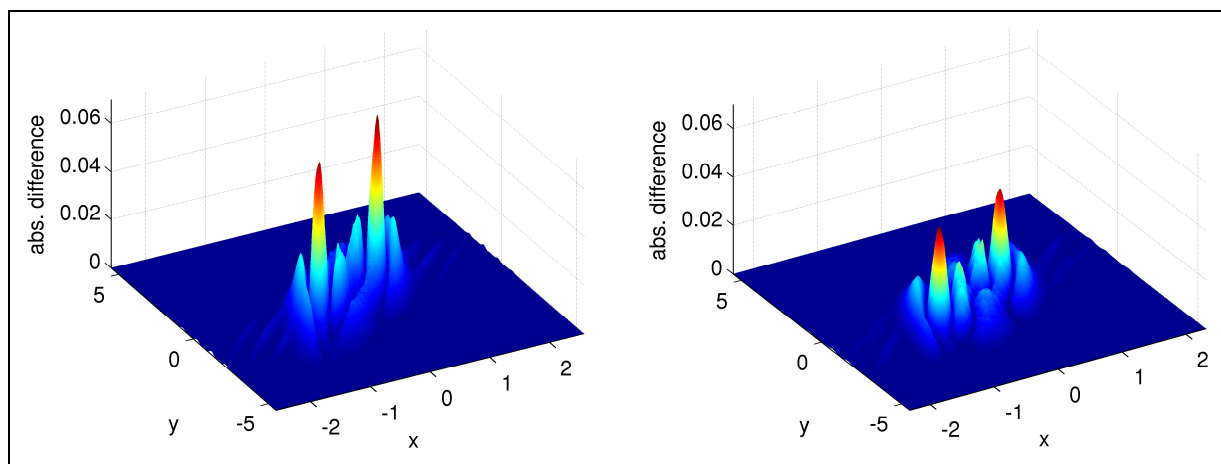


Figure 7: (Color online). The absolute difference between RE and MC solutions: Case 2, $a = 3, 7$.

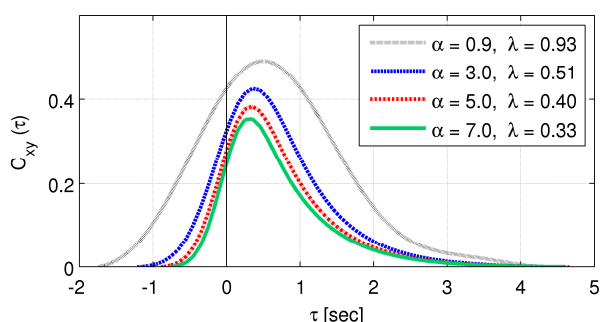


Figure 8: (Color online). The RE covariance function for Case 2.

6. CONCLUSIONS

In this paper we present, for the first time, an *a priori* closure scheme, and a method for numerical solution of the joint REPDF evolution equation, introduced in [1] and applied to ship rolling motion in [2]. The method is used to solve numerically two examples, a linear half-oscillator excited by a non-Gaussian random process, and a non-linear half-oscillator excited by Gaussian noise (see also Athanasoulis *et al*, 2012). The numerical results obtained have been confirmed via MC simulation. It is clear that the present method can be



extended straightforwardly to the general case of equ. (19) (nonlinear half-oscillator under non Gaussian excitation), covering both monostable and bistable cases. The extension of the presented methodology to full (2D) oscillators (e.g., to the 2nd-order ship roll motion equ. (1)), is currently under investigation.

7. ACKNOWLEDGMENTS

Ivi C. Tsantili and Zacharias G. Kapelonis are PhD candidates at SNAME, NTUA, supported by NTUA scholarships.

8. REFERENCES

- Athanassoulis, G.A., Belibassakis, K.A., 2002, "Probabilistic description of metocean parameters by means of Kernel density models. Part 1: Theoretical background and first results", Applied Ocean Research, Vol. 24, pp. 1-20.
- Athanassoulis, G.A., Gavriliadis, P.N., 2002, "The truncated Hausdorff moment problem solved by using kernel density functions", Probab. Eng. Mech., Vol. 17, pp. 273-291.
- Athanassoulis, G.A., Sapsis, Th.P., 2006, "New partial differential equations governing the response-excitation joint probability distributions of nonlinear systems under general stochastic excitation I: Derivation", 5th Conference on Computation Stochastic Mechanics, Rhodes Island, Greece. In Deodatis, G, Spanos, P.D., Eds. (2007).
- Athanassoulis, G.A., Tsantili, I.C., Kapelonis, Z.G., 2012, "The joint Response-Excitation PDF evolution equation. Numerical solutions for the long-time, steady-state response of a half oscillator", Proceedings of the 11th ASCE Joint Specialty Conference on Probabilistic Mechanics and Structural Reliability, Notre Dame, Indiana, USA.
- Athanassoulis, G.A., Tsantili, I.-S.C. and Sapsis, Th.P., 2009a, [2] "New Equations for the Probabilistic Prediction of Ship Roll Motion in a Realistic Stochastic Seaway", Proceedings of the 10th International Conference on Stability of Ships and Ocean Vehicles, St. Petersburg, Russia, pp. 661 – 672.
- Belenky, V.L., and Sevastianov N.B., 2003, "Stability and Safety of Ships, Vol. 2: Risk of Capsizing" Elsevier Ocean Engineering Books, Vol. 10, Amsterdam.
- Beran, M.J., 1968, "Statistical continuum theories", Interscience Publishers, New York.
- Botev, Z.I., Grotowski, J.F., Kroese, D.P., 2010, "Kernel density estimation via diffusion", Annals of Statistics, Vol. 38, pp. 2916–2957.
- Deodatis G., Spanos P.D., Eds., 2007, "Proceedings of 5th Conference on Computation Stochastic Mechanics", Millpress, Rotterdam.
- Di Paola, M., Floris, C., 2008, "Iterative closure method for non-linear systems driven by polynomials of Gaussian filtered processes", Computers and Structures, Vol. 86, pp. 1285–1296.
- Dormand, J.R., Prince, P.J., 1980, "A family of embedded Runge-Kutta formulae", J. Comp. Appl. Math., Vol. 6, pp. 19-26.
- Francescutto, A., Naito, S., 2004, "Large amplitude realistic sea", Int. Shipb. Progress, Vol. 51, pp. 221-235.
- Grigolini, P., Lugiato, L. A., Mannella, R., McClintock, P. V. E., Merri, M., Pernigo, M., 1988, "Fokker-Planck description of stochastic processes with colored noise", Phys. Rev. A, Vol. 38, pp. 1966–1978.
- Hopf, E., 1952, "Statistical hydromechanics



- and functional calculus”, J. of Rat. Mech. and Analysis, Vol. 1, pp. 87–123.
- Iourtchenko, I.V., 2003, “Response spectral density of linear systems with external and parametric non-Gaussian, delta-correlated excitation” Probab. Eng. Mech., Vol. 18, pp. 31–36.
- Jung, P., Risken, H., 1985, “Motion in a Double-Well Potential with Additive Colored Gaussian Noise”, Z. Phys. B Condensed Matter, Vol. 61, pp. 367-379.
- Kantorovich, L.V., Krylov, V.I., 1964, “Approximate methods of higher analysis”, Interscience, New York.
- Khasminskii, R.Z., 1966, “A limit theorem for the solutions of differential equations with random right-hand sides”, Theory Probability App, Vol. 11, pp. 390-405.
- Kreuzer, E., Sichermann, W., 2007, “On unpredictable Ship Rolling in Irregular Seas”, Nonlinear Dyn, Vol. 47, pp. 105-113.
- Muscolino, G., 1995, “Linear systems excited by polynomial forms of non-Gaussian filtered processes”, Probab. Eng. Mech., Vol. 10, pp. 35–44.
- Naess, A., 2000, “Chaos and nonlinear stochastic dynamics”, Probab. Eng. Mech., Vol. 15, pp. 37–47.
- Neves, M.A.S., Belenky, V.L., de Kat, J.-O., Spyrou, K., Umeda, N., editors, 2011, “Contemporary Ideas on Ship Stability and Capsizing in Waves”, Fluid Mechanics and its Applications, Vol. 56, Springer, New York.
- Pirrotta, A., 2007, “Multiplicative cases from additive cases: Extension of Kolmogorov–Feller equation to parametric Poisson white noise processes”, Probab. Eng. Mech., Vol. 22, pp. 127–135.
- Pugachev, V.S., Sinitzyn, I.N., 2001. “Stochastic systems. Theory and applications”, World Scientific, New Jersey.
- Roberts, J.B., 1982, “Effect of Parametric Excitation on Ship Rolling Motion in Random Waves”, J. Ship Res, Vol. 26, pp. 246-253.
- Roberts, J.B., Vasta, M., (2000), “Markov Modelling and Stochastic Identification for Nonlinear Ship Rolling in Random Waves”, Phil. Trans. R. Soc. London, Series A, Vol. 358, pp. 1917-1941.
- Sapsis, Th.P., Athanassoulis, G.A., 2008 [1], “New Partial Differential Equations Governing the Joint, Response-Excitation, Probability Distributions of Nonlinear Systems Under General Stochastic Excitation”, Probab. Eng. Mech., Vol. 23, pp. 289-306.
- Spanos, P.T., 1986, “Filter Approaches to Wave Kinematics Approximation”, Applied Ocean Research, Vol. 8, pp. 2-7.
- Stratonovitch, R.L., 1963, “Topics in the Theory of Random Noise, Vols 1 and 2”, Gordon and Breach, New York.
- Venturi, D., Sapsis, T. P., Cho, H., Karniadakis, G. E., 2012, “A computable evolution equation for the joint response-excitation probability density function of stochastic dynamical systems”, Proc. R. Soc. A, Vol. 468, pp. 759-783.
- Zeidler, E., 1990, “Nonlinear functional analysis and its applications”, Springer-Verlag, New York.



Stability Criteria - 50 Years of Experience and Future Prospects

Lech Kobylinski, *Foundation for Safety of Navigation and Environment Protection, Poland*

lechk@portilawa.com

ABSTRACT

50 years passed from the time of the first meeting of the IMO STAB Subcommittee that started work on developing international stability criteria. The paper gives account briefly of the history of development of the criteria up to the present time. It underlines the different ways of approach to the development of criteria at certain points of time and ideas presented and considered at those times. Some of the ideas presented are still of value as well as critical remarks to the criteria at some stages are still important. Although progress in development of rational stability criteria is remarkable there is still a need for discussion of the future approach to international and universal stability requirements that take into account all factors that may have impact on safety against stability accidents.

Keywords: *safety of ships, stability criteria, risk analysis*

1. INTRODUCTION

This year exactly 50 years have passed from the time when the first session of the IMCO (IMO) Sub-committee on Subdivision and Stability Problems (STAB Sub-committee – now called SLF Sub-committee) started its work on development of international stability requirements. This was actually the result of recommendation No.7 of the International Conference on Safety of Life at Sea 1960 that recommended the Organization (IMCO) *inter alia* to: "...initiate studies ...of (a) intact stability of passenger ships (b) intact stability of cargo ships, (c) intact stability of fishing vessels and (d) standards of stability information...".

The first meeting of the STAB Subcommittee that was charged with the task mentioned, was attended by the group of prominent specialists on stability problems and there was an extensive discussion on the way how to develop stability criteria.

General opinion was that international stability criteria should be based on physics of ship motions and capsizing of ships in a seaway. On the other hand at this early stage specialists on stability were fully aware of the complexity of the problem and realized that drafting such requirements in short time may be a hopeless task.

The Subcommittee was, however, under pressure that something has to be done quickly. Therefore at this session the pragmatical approach was chosen and the decision was taken to develop stability criteria (or rather stability requirements or norms) on the basis of statistics by comparing stability characteristics of ships that suffered stability failures with those that were considered safe.

This was possibly a very wise decision and it was taken univocally. At the same meeting working group on stability problems was created (IS group) that during the next few years met twice a year and accomplished the



bulk of the work of developing first internationally accepted stability criteria.

2. FIRST IMCO (IMO) RESOLUTIONS CONCERNING STABILITY CRITERIA

Subsequently to the decision of the Sub-committee all its members were invited to submit as many as possible data on stability casualties and, on the other hand, on stability characteristics of ships that were considered safe. The request to submit data on casualties and on ships considered safe from the point of view of stability met with good response and during the next year about 166 casualties were reported, most of them, however, related to ships of the length less than 100m. Also data on about 110 vessels considered safe in operation were also made available.

During the next few years statistical data were collated and two delegations, Federal Republic of Germany and Poland agreed to analyse the data submitted and propose stability criteria on this basis. The way how it has been done is well described in many sources e.g.(Kobylnski and Kastner 2003) and is not repeated here. It is only worth mentioning that the delegation of Federal Republic of Germany adopted in the analysis the method being modification of the method used by Rahola in his work whether the delegation of Poland adopted the method based on discrimination analysis. Actually both methods provided almost identical results. Finally the criteria were drafted by the IS group, approved by the STAB Sub-committee and adopted in 1968 by Assembly resolutions A167(ES.IV) for passenger and cargo ships under 100 meters in length and in A.168(ES.IV) for fishing vessels.

In mid eighties of the last century the analysis of additional statistical data was repeated by the delegation of Poland (IMO 1985), with the conclusion reached, however, that there was no need to amend previous results. In spite of their simplicity and obvious

deficiencies the criteria developed at that time are still in force and, the maritime world seems to be satisfied with them. Moreover, they are quite recently made compulsory by incorporating them via reference to SOLAS Convention.

The statistical criteria are burdened by many imperfections. There is no place for detailed consideration of those imperfections there, (reference is made in this context to the papers (Bird and Odabasi, 1975 and Kuo and Welaya, 1981), but it is obvious that criteria of Resolution A.167 and A.168 were based on insufficient statistics and the statistical analysis was not the rigorous one.

Bearing aware that stability criteria developed are not perfect IMO STAB Sub-committee in late sixties included in the 1967 (IMO 1967) statement that there is a need to continue studies on ships' stability, paying particular attention to the effect of external forces and of variation of displacement on stability with the view to develop improved (or so called „rational”) stability criteria.

3. CONCEPT OF „RATIONAL” STABILITY CRITERIA

During the development stage of the above resolutions the Sub-committee clearly stated, however, that the criteria recommended should not be treated as a final solution. Members of the Sub-committee stressed the point that they of rather of preliminary character and they cannot safeguard ships against stability failure adequately.

The idea of developing of “rational “ criteria was advanced and for some time the Sub-committee discussed on the basis of several papers submitted the problem of how to develop those “rational” criteria. During the discussion the point was raised that there is a necessity to develop so called “rational” criteria that must take into account forces of the sea acting on the ship. The need to take into account loss of stability on wave crest,



parametrical resonance and broaching-to phenomena was underlined. It was also stressed that safety of a ship at sea depends strongly on proper operation of the ship and good seamanship. These opinions are actually reflected in the preamble to the above mentioned recommendations.

The concept what really „rational” criteria may mean was not entirely clear. Different persons understood the word „rational” differently. („Rational”, according to Oxford Dictionary is: endowed with reason, sensible, based on reason or reasoning). Some members of the IMO Sub-committee understood rational criteria as those, which are based on balancing external heeling and righting moments in the deterministic way; others understood them more widely, as criteria based on the probability of capsizing. Those differences in understanding of the essence of rational criteria caused lack of determination regarding future programme of work, which was discussed during several sessions with no final agreement concerning work programme reached. Nevertheless several valuable proposals were advanced at that time, details of which could be found in the Reports of the Working Group on Intact Stability of IMO and which still should be taken into consideration in any work programme aimed at development of future stability criteria. Looking at the past it may be concluded that experts on stability were fully aware of the need of developing future improved stability criteria although they were unable to specify how to achieve this goal.

The group stressed the point that the problem of developing safety criteria for stability of ships in a seaway is so complicated that it would be impossible to solve it once and for all. Establishment of stability criteria, which have to assure safety of a ship against capsizing, poses tremendous difficulties and constitutes probably one of the most difficult problems in ship hydrodynamics. This is because there does not exist simple relation between ship's parameters and its ability to survive all possible dangerous situations, which it may meet during its lifetime.

The Working Group when considering various proposals for the programme aimed at development of rational stability criteria was of the opinion that any such attempt will require installation of the long term programme of research involving theoretical as well experimental investigations including also measurements onboard ships and therefore it would be unrealistic to expect to achieve results in short time. In general, it was stated that the present state of knowledge regarding physics of capsizing is insufficient and therefore scientists should be encouraged to induce research on better understanding of ship motions in confused seas and capsizing phenomena and on identification of those ship parameters which influence capsizing. At the later stage the Group also stressed the importance of probabilistic approach to the development of stability criteria. Ultimately, however, the Group limited itself in this respect to specifying recommendations of the very general nature only.

One result of these deliberations was that subsequently in several countries research programmes were installed that include theoretical investigations as well as model tests.

With apparently no practical results achieved towards development of „rational” criteria and with apparent lack of interest in introducing any substantial changes into already existing stability requirements, bearing in mind, however, that ships complying with those criteria could capsize, the important question arises: what direction has to be taken in further work on enhancing safety at sea from the point of view of stability?

The task of developing rational criteria after discussion during several sessions was finally abandoned with no final agreement concerning the future programme of developing stability criteria. The main reason of the failure of specifying future programme was lack of suitable tools for simulating different dangerous situations for ships in rough sea.



4. WEATHER CRITERION

Being actually unable to formulate a definite programme of development of “rational” stability criteria the Sub-committee, taking into account that resolution A.167 was applicable only to ships of the length of not more than 100 meters, decided to aim at improving safety against stability failure and to develop requirement for the situation where the ship is exposed to beam wind when rolling on the wave. This situation was chosen because at that time (late seventies) in several countries national regulations or recommendations on stability already included this situation (USSR, China, Japan, The Netherlands, Poland and some others). Therefore some experience with the application of criterion taking account of this situation was already available. In comparative short time the requirement was developed and checked against large population of existing vessels and is now known under the name “weather criterion”. Weather criterion was adopted by resolutions A.562(14) for passenger and cargo vessels and A.685(17) for fishing vessels and its application was not limited to ships under 100 meters in length.

However, physical model adopted finally in the weather criterion is far from being rigorous one. In all stages of calculations far reaching simplifications were made. Those include the calculation of dynamical wind heeling model, simplified calculation of the rolling angle, negligence of coupling effects etc. The most important parameter, wind pressure was selected arbitrarily in such a way that average ship considered safe must satisfy this criterion. The same applies to the other important parameter, that is, the amplitude of rolling. This was done on the basis of calculations of maximum KG values that are allowed to satisfy this criterion for a large population of existing ships considered safe.

Therefore calculation of the weather criterion, as it is now, is not related to the actual wind force that the ship may encounter.

Introduction of the weather criterion was in fact a large step forward towards improving safety against capsizing. Comparison of maximum allowable KG values meeting weather criterion or meeting statistical criteria as in resolution A.167(ES.IV) did show that many ships meeting weather criterion may not meet statistical criteria and *vice versa*. Meeting both types of criteria at the same time would make ships safer. Recently, however, it was found that the weather criterion may be not fully applicable to certain types of ships, in particular to ships with large B/D ratio and therefore alternative assessment of the weather criterion was included by MSC.1/Circ.1200.

5. IS CODE AND SECOND GENERATION CRITERIA

In late eighties and early nineties of the last century the Sub-committee being unable to develop any entirely new set of stability criteria concentrated its effort on the harmonization and review of already existing stability requirements consisting of criteria of resolutions A.167(ES.IV) and 168.(ES.IV) and weather criterion. Several recommendations developed and adopted in the meantime including additional or modified criteria applicable to certain types of ships such as for example for passenger vessels, ships carrying timber deck cargo, high speed craft, fishing vessels etc. were also included into one instrument in an orderly and systematic manner in order to facilitate its use.

This effort materialized in development of the Intact Stability Code, first edition of which was adopted in 1993 by resolution A.749(18). Current version of the IS Code 2008 was adopted about 15 years later by resolution MSC.267(85).

IS Code preserved basic stability criteria, statistical as well as weather criterion virtually unchanged from their original versions, the only important difference being that the basic statistical criteria and weather criterion were made compulsory by way of reference in the



SOLAS Convention to part A of the IS Code 2008. Weather criterion was actually amended by introduction of the alternative assessment of the weather criterion (MSC.1Circ.1200)

After completion of the development of IS CODE 2008 the project consisting of the so called Second Generation stability criteria was initiated and currently this task is well advanced with the view of its finalization in near future. Details of this project are not discussed in detail because in general they are well known, however it may necessary to mention that the second generation stability criteria were meant to be initially included in future in the Part B (recommended) of the IS Code.

The essence of the Second Generation Stability Criteria is the three layers lay-out of assessing vulnerability of a ship to some hazards posed by forces of the sea that include the following dangerous phenomena:

- Loss of stability on wave crest
- Parametric resonance
- Surf riding and broaching –to
- Dead ship condition.

In the course of work on second generation stability criteria the excessive accelerations was added as the fifth dangerous situations. It is worth mentioning that those phenomena are virtually the same as those considered by the Sub-committee when discussing rational criteria forty years ago. Layer one of the criteria should include simple vulnerability criteria, whether layer two will include more accurate judgment about the risk involved with the above mentioned phenomena and layer three will include so called direct stability assessment where full simulation of the behaviour of the ship should be performed. It is expected, that by doption of the above criteria ships that may be vulnerable to the above mentioned hazards will be safer.

6. GENERAL COMMENTS REGARDING PRESENT SITUATION REGARDING STABILITY CRITERIA

The criteria included currently in the IS Code are design criteria, addressed mainly to ship designers. This was the result of the opinion that safety against capsizing has to be assured by the design measures. However, if a ship satisfies the criteria it does not mean automatically that she is safe. Actually no ship can be built which is 100 per cent safe and which cannot be capsized by negligence or mishandling. To design a foolproof ship is totally unrealistic. It is well known that in about 80% of all casualties at sea operational factor as well as and human factor play predominant part. Therefore stress should be put to improve all aspects of ship operation, in particular to ship handling in confused seas. Resolution A.167(ES.IV) in the preamble included clear statement in this respect stressing the importance of good seamanship.

In spite of the fact that the existing criteria are not perfect the maritime world seems to be satisfied with them at present at least for so called conventional ships, although improved future stability requirements are still included in the long-term plan of action of IMO. Serious stability casualties with heavy toll of life are rare and fortunately such accident did not happen recently. But it may happen any time and history of seafaring is very educational in this respect. If such accident would happen then all organizations responsible for safety at sea raise alarm and stars looking for new regulations. So better be prepared for that. It must be stressed, that many stability casualties still happen every year, mostly, however with small ships. Those accidents do not create strong reaction of the public opinion as some casualties with large ships do.

The existing compulsory and recommended requirements as in the IS Code and also the second generation stability criteria under the development may improve the situation in some respects but they are not the ultimate solution. They were initially intended to be



applied to non-conventional vessels only, but it is not clear how to define non-conventional vessels in this respect.

First of all the criteria under the development are design criteria that do not take into account most important operational aspects and human factor. Secondly, they are of prescriptive nature which is in a way convenient for approving authorities and designers but they are in contradiction to modern understanding of the design process

At present to solve similar problems risk-based approach is usually adopted and actually IMO recommended to use this approach under the name Formal Safety Assessment (FSA) to the rule making process. (IMO 2002). However this approach apart of few trials was not generally accepted with regard to stability problems, although there are available now results of application of risk analysis to ship design, in particular to ship subdivision and damage stability (e.g. Papanicolaou 2009).

Current criteria as well as second generation criteria of the level 1 and 2 are basically deterministic. They include the concept of checking the vulnerability of ship to some dangerous situations. Vulnerability in essence is hazard. However hazards in risk analysis procedure is probabilistic quantity whether vulnerability is deterministic and binary quantity (yes or no) (Peters et al 2011).

Lever three, direct stability assessment on the other hand is supposed to be based on probability of stability failure. Probabilistic approach to stability criteria was recommended at the early stage of criteria development, when rational criteria were discussed. Tribute in this respect must be paid to professor Sevastyanov who discussed this problem long time ago systematically possibly for the first time. (Sevastyanov 1970).

To apply probabilistic approach to estimate safety level against stability failure is not, however, an easy task because capsizing is a very rare event and usual statistical methods

used in investigation of frequency of accidents are not applicable. The more so risk analysis methods may be recommended.

It is not clear how to draft prescriptive criteria on the basis of probability of capsizing. Probability of capsizing, whether calculated on the basis of long term or short term concept or on the basis of model tests, cannot be used directly as a criterion of safety. First of all this is a very small quantity beyond the accuracy of calculated quantity. Secondly the calculated probability does not take into account all factors affecting stability, for example helmsman behaviour. Certainly some important conclusions may be drawn from the simulations, for example eliminating revealing obviously badly designed ships with very high probability of capsizing. But if calculated probability of capsizing is small, but above the established criterion, then it would be not at all certain that the ship is dangerous. As far I see it, the solution would be the application of risk analysis. This is uncertain situation and risk analysis is meant to be used in uncertain world.

7. RISK BASED APPROACH

It is obvious that even when second generation stability criteria will be developed this does not solve the problem of safety against stability failure or capsizing. Although some improvement in safety level may be expected, but there are still many uncertainties and factors, let us say, such as human factor, that are not taken into account. So accidents may happen.

We are living in uncertain world. One way to take account of uncertainty in planning and accomplishing enterprises in the uncertain world is to perform risk analysis. (Aven 2003). The basic dichotomy in the conception of safety requirements consists of prescriptive approach and risk-based approach.

Traditional regulations were of prescriptive nature and usually were based on deterministic calculations. They are formulated in the way

where a ship dimension or other characteristic (e.g. metacentric height) must be greater (or smaller) than certain prescribed quantity. Prescriptive regulations could be developed on the basis of experience (experts opinions) statistics, analytical methods, computer simulation, model tests and full-scale trials. Deterministic or probabilistic calculations may be employed when developing the criteria, although, as a rule, deterministic approach is used in most cases.

The main shortcoming of prescriptive regulations is that they are bounding designers and they do not allow introduction of novel design solutions. They are based on experience gained with existing objects and they are not suitable for novel types. Usually they were amended after serious casualties happened. The risk involved with the application of prescriptive regulations is not known.

At the opposite of the prescriptive regulations, there is risk-based approach. In the risk-based approach, the regulations specify objectives to be reached, which are safe performance of an object. Risk-based approach could be described as a goal-oriented performance based approach utilizing, as a rule, probabilistic calculations. However, it is possible to imagine risk-based approach utilizing deterministic calculations as well. The same tools could be used as when developing prescriptive regulations.

The prescriptive criteria could be supplemented by the substitution rules allowing application of alternative measures. If the formulation of this provision (rather often used in IMO instruments) is such, that the objectives are specified, it opens the way to application of the risk-based approach (Chantelave 2005).

The advantages of risk-based approach are obvious. They may take into account all factors that contribute to safety of the enterprise. They give free hand for the designer to develop new solutions, they actually allow taking optimal decisions from the point of view of economy

and safety, and the risk to the public and to the environment is assessed and accepted.

All existing stability regulations are of the prescriptive nature. At present, however, the need to apply risk-based approach is recognized. The Marine Safety Committee of IMO recommended this approach as Formal Safety Assessment (FSA) (IMO 2002). Risk-based approach is widely used in many fields of technology.

The schematic representation of the above classification is shown in figure.1.

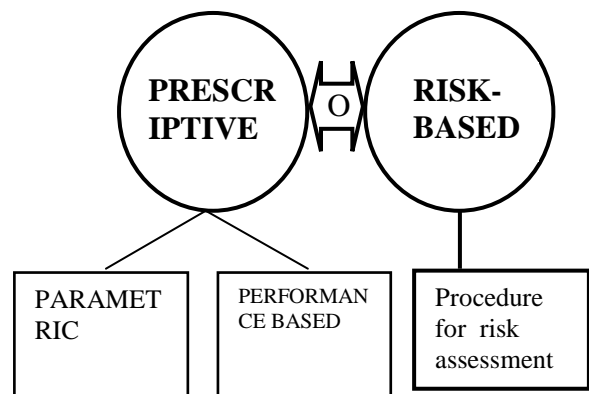


Figure 1: Prescriptive versus risk based criteria

The most recent concept of safety regulations is goal-based approach. Goal based regulations does not specify the means of achieving compliance but sets goals that allow alternative ways of achieving compliance (Hoppe 2006). Goal-based standards are for some time considered at IMO and appraised by some authors (Vassalos 2002, Chantelave 2005), and they were introduced in some areas, albeit not in the systematic manner. Marine Safety Committee of IMO commenced in 2004 at MSCC 78 its work on goal-based standards in relation to ship construction adopting five-tier system. (Hoppe 2006).

IMO MSC committee agreed in principle on the following tier I goals to be met in order to build and operate safe and environmentally friendly ships: “Ships are to be designed and constructed for a specific design life to be safe and environmentally friendly, when properly



operated and maintained under specified operating and environmental conditions, in intact and specified damage conditions, throughout their life”.

8. POSSIBLE FUTURE SOLUTION

It seems that the future alternative criteria should be based on the above principle. With this in mind the block diagram of the future system of stability requirements may be developed as shown as in fig.2 and in table 1. Left hand side of the diagram in fig.2 refers to conventional ships, whether the right hand part refers to non-conventional ships. Shaded part is actually completed and the practical problem consists of how to develop requirements for non-conventional ships. The diagram shows, that it could be done using SOLAS clause allowing using alternative means of assuring safety.

Table 1: Method of safety assurance

Ships	Method of stability safety assessment
Conventional, not sophisticated	Prescriptive criteria as in the IS Code
Novel types, large sophisticated ships	Risk analysis under the provision allowing application of alternative means of assuring safety

Clarification is needed regarding the definition of conventional and non-conventional ships. Traditionally under the term “non-conventional ships”, ships revealing novel design features are understood. However this is very vague definition because of the difficulty which features may be classified as “novel”. For example, almost all vessels are susceptible to parametric resonance in certain situations, even small fishing boats, but they are hardly to be classified as non-conventional

It seems that the best way to classify ships as non-conventional would be to include in this category all ships to which by way of hazards identification requirements of the existing IS

Code are considered non applicable in the view of designers, ship owners or administrations. The other solution may be not to make any distinction between conventional and non-conventional ships.

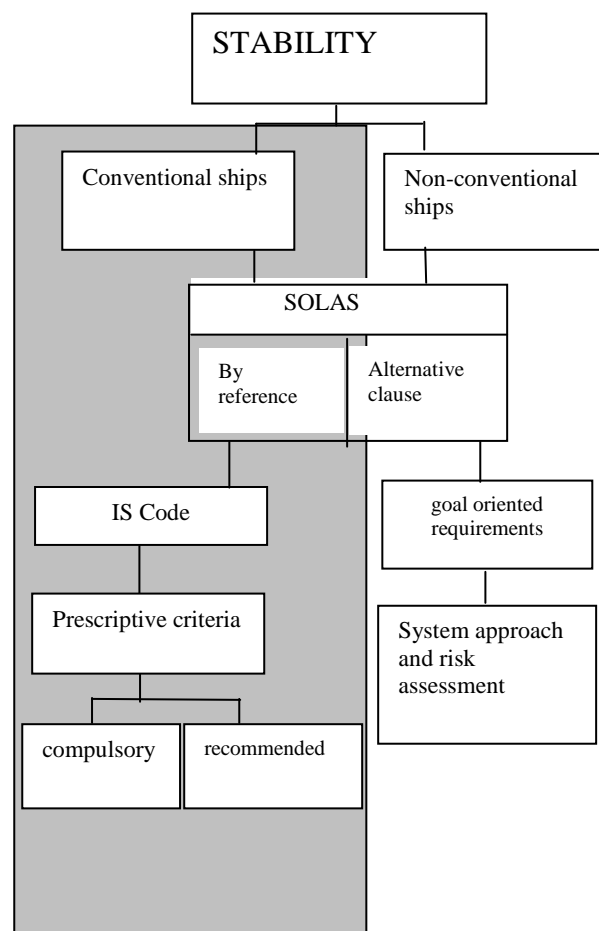


Figure 2: Proposed system of stability requirement

9. HAZARD IDENTIFICATION

The crucial problem in safety assessment analysis is proper identification of various hazards to which a ship may be subjected. according to the definition, hazard is “*a potential to threaten human life, health, property or the environment*” (IMO 2002). In the goal oriented approach and when performing risk analysis all relevant types of hazards must be taken into consideration – environmental, technical, operational and managerial. and the frequency (probability) of



occurrence of those hazards should be assessed. Human factor must be taken also into consideration. Belenky et al (2008) proposed to apply “vulnerability criteria” within the system of future criteria. those criteria are, in fact, hazards. however, the vulnerability criteria are meant as considered in a binary mode, whether hazards are inherently connected with probability.

Hazard identification is carried-out using hazard identification and ranking procedure (HAZID). Hazards could be identified using several different methods.

IMO resolution included general guidance on the methodology of hazard identification. with respect to stability. Hazard identification could be achieved using standard methods involving evaluation of available data in the context of functions and systems relevant to the type of ship and mode of its operation. Stability is considered assuming that the ship is intact and accident evaluated is stability failure that means taking by the ship position upside down, but also covering a situation where amplitudes of rolling motion or heel exceed a limit that makes operation or handling the ship impossible for various reasons, e.g. loss of power, loss of manoeuvrability, necessity to abandon the ship etc. It does not necessary mean the total loss of the ship.

According to general recommendation the method of hazard identification comprised mixture of creative and analytical techniques. Creative element was necessary in order to ascertain that the process is proactive and is not limited to hazards that happened in the past.

In general HAZID involves several possibilities used separately or in combination:

- statistical data concerning causes of accidents
- historical data including detailed description of accidents
- conclusions resulting from model tests of ships in waves
- conclusions resulting from computer simulation of capsizing

- event and fault trees method
- analysis of accidents scenarios using (e.g. TRIPOD method (ter Bekke et al 2006))
- organized opinions of experts (e.g. according to DELPHI method)

10. CONCLUSIONS

The review of 50 years of history of developing stability criteria by IMO shows that the ideas discussed then are still of value. It is still, however, not certain what should be the ultimate solution in respect of the requirements assuring safety against stability failure, although important progress has been achieved in safety of ships of all types.

11. REFERENCES

- Aven T. (2003): Foundations of risk analysis. J.Wiley
- Belenky V., de Kat J.O., Umeda N. (2008): “Towards performance-based criteria for intact stability”, Marine Technology, Vol 45(2), p.101-105
- Bird H., Odabasi A. Y. (1975) “A state of art: past, present and future”, Proc of STAB’75 1st International Conference on Stability of Ships and Ocean Vehicles, Glasgow
- Chantelauve, G. (2005) “On the use of risk analysis in maritime certification and classification”, Advances in Safety and Reliability ESREL 2005, Vol. I p.329.
- Hoppe H. (2006) “Goal based standards – a new approach to the international regulations of ship construction”, IMO News, Issue 1.
- IMO. (1967) Report of the Sub-Committee on Subdivision and Stability. Doc. STAB VII/11,
- IMO (1984): Intact Stability. Report of the ad hoc working group. Doc. SLF29/WP.7.
- IMO (1985) Analysis of intact stability casualty records. Submitted by Poland. Docs. SLF
- IMO (2002) Guidelines for Formal Safety Assessment (FSA) for use in the IMO rule-making process. Doc. MSC/Circ.1023; MEPC/Circ.392.



- Kobyliński L., Kastner S. (2003): Safety and Stability of Ships, Vol.1, Elsevier
- Kuo C., Welaya Y. (1981) "A review of intact stability research and criteria", Ocean Engineering, p.65
- Papanicolaou A. (Editor) (2009) Risk-based ship design. Methods, tools and applications. Springer
- Peters W., Belenky V., Bassler C., Spyrou K., Umeda N., Bulian G., Altmayer B. (2011). The Society of Naval Architects and Marine Engineers. Annual Meeting Paper.
- Sevastyanov N.B. (1970) Stability of fishing vessels. Sudostroyenye. (in Russian)
- ter Bekke E.C.A., van Daalen E.F.G., Willeboordse E.J., Boonstra H., Keizer E.W.H., Ale, B. (2006) "Integrated safety assessment of small container ships", 8th Intern. Conference on Probabilistic Safety Assessment and Management, New Orleans.
- Vassalos D. (2002) Total ship safety – a life-cycle risk-based DOR for safety. The Stability Research Centre, Universities of Glasgow and Strathclyde, May 2002.



Approaches to Ship Motion Simulation Acceptance Criteria

Timothy C. Smith, *Naval Surface Warfare Center, Carderock Division,*
timothy.c.smith1@navy.mil

ABSTRACT

Direct assessment of stability in irregular waves for regulatory purposes requires a validated tool for numerical simulation. Motion simulation acceptance criteria are a key part of the simulation validation process. The acceptance criteria need to reflect the specific intended uses (that is, mode(s) of stability failure) of the simulation as well as taking into consideration available validation data and levels of uncertainty. The paper presents desired characteristics for acceptance criteria in terms of self-consistency, completeness, quantifiable accuracy, and type of comparison — statistical or time history. A number of approaches to acceptance criteria are proposed that can be applied to elemental force modules to total simulations. These approaches range from engineering judgment to mathematically rigorous statistical comparisons to an uncertainty approach with a sum of known errors to a mixed approach acceptance criteria. These approaches are discussed in the context of the desired characteristics, and providing an overall simulation tool acceptance determination.

Keywords: *validation, acceptance criteria, seakeeping*

1. INTRODUCTION

For many years, numerical simulation of ship motions has been used to determine relative performance of various design options (Bales, 1980) with idealized wave spectra. The state of numerical simulation of ship motion, maneuvering and seakeeping, is approaching the point of predicting performance as a replacement for model and full-scale testing. Granted numerical simulations have been used instead of model or full-scale testing, but there have been many caveats and conditions on their use. Similarly, numerical simulations have been compared to model test data as part of the theory and simulation development process. To limit the difference between the model test and the theory being examined, previous comparisons to model testing have been for

very controlled model test data, such as motion transfer functions. The use of simulation for direct assessment of stability in irregular waves for regulatory purposes requires a rigorous and comprehensive approach to validation and accreditation.

The simulation community uses the following loose definitions for verification, validation, and accreditation. Verification deals with the correct implementation of the theory or math model. Validation deals with the simulation code's accuracy compared to benchmark data. Accreditation deals with the applicability of the simulation for a specific use. The 26th International Towing Tank Conference (ITTC, 2011) recognized the need for verification and validation of seakeeping computer codes and prepared guidelines. The ITTC guidelines clearly lay out verification



and validation tasks and activities going so far as listing what to consider at a component level.

When comparing simulation data to benchmark data, Belknap (2011) makes the distinction between qualitative and quantitative validation. Qualitative data comparisons are made by examining trends and expected behavior often at a component or force model level, such as roll damping or Froude-Krylov force. Additionally, it is often difficult to determine quantitatively how much a specific component affects the final or total answer. In these cases, benchmark data are often highly constrained to focus on one particular element, such as roll decay tests. Favorable qualitative comparisons give the user confidence in the simulation, but cannot replace quantitative acceptance criteria.

Quantitative validation is a direct comparison of simulation and benchmark data with some defined metric of accuracy. There is a difference between acceptance criteria for validation and for accreditation. In both cases, the simulation is compared against benchmark data to ascertain its accuracy. However, for validation the purpose is diagnostic, to identify areas requiring improvement with the goal of improving the overall accuracy of the simulation. This can focus on specific aspects or elements of the simulation. For accreditation, the acceptance criteria are a quantification of acceptable accuracy for Specific Intended Uses (SIUs).

The SIUs serve to limit the scope of the validation to a reasonable and useful domain. The SIUs define the operational and environmental conditions and type of response and statistics where the simulation is applicable. For instance, a typical linear seakeeping simulation would have a SIU such as “The simulation will be applied for all speeds and heading for Sea States 5 and less to produced significant single amplitude statistics.” This limits simulation applicability to an expected linear response

domain and precludes using the simulation for extreme events and non-linear behavior.

To be used for a particular application, such as, direct assessment of parametric rolling, the validated simulation needs to be accredited for use. The first step is to selection a simulation code with the desired simulation capability. Once a simulation code is selected, the accreditation process clearly defines the boundary of where the simulation may be used and not used. The boundary is defined in the SIUs. (Belknap et. al., 2012, Navy Guides) As part of this, there are acceptance criteria to determine if a simulation is accurate enough for use. Depending upon simulation use, “accurate enough” can range from similar motion properties (qualitative) or random behavior to matching a set of time histories to a specified accuracy (quantitative). If a simulation code passes the acceptance criteria, it can be accredited for use in the region defined by the SIUs. It is possible, though hopefully unlikely, that a validated simulation code would not accredit for a set of SIUs.

This raises the issue of actually applying the acceptance criteria. Many different motions or parameters can be measured for a specific condition or group of seaway, speed, heading, and mass properties (loading condition). A benchmark data set contains many conditions for comparison. To validate or accredit a simulation, it must pass acceptance criteria at the parameter, condition, and set levels. These different acceptance criteria are often related and inter-related, but are typically different at each level.

This paper discusses the desired characteristics to be found in acceptance criteria and possible forms of acceptance criteria. Examples will be shown for the application each of the acceptance criteria approaches. The paper will discuss the inter-relationship of acceptance criteria for the parameter, condition, and set.



2. DESIRED CHARACTERISTICS

As a key part of the accreditation process, the acceptance criteria should be clearly laid out as to what is acceptable and what is not. Even when the accuracy requirements are relatively low, such as, general behavior, the acceptance criteria need to specify what the general behavior is, how the simulations are made, how the comparisons are made, how many comparisons are made, and how many comparisons have to pass. As the accuracy level increases, so does the complexity of the acceptance criteria. For a specified level of accuracy, the means of determining that accuracy, even the calculation method, also needs to be specified. Due to the complex interactions between the acceptance criteria levels, it is possible to have surprising outcomes from the accreditation process. As such, there are desired characteristics for the acceptance criteria.

The acceptance criteria should have quantifiable accuracy. For a single comparison, this can be done by specifying the accuracy, such as, an overlap of 95% confidence intervals. However, often more than one comparison is made and the acceptance is some passing percentage of all the comparisons made. Now the overall accuracy is the aggregate of the accuracy of the individual comparisons, not necessarily the specified passing percentage of conditions.

Typically, the acceptance criteria will specify at least two levels of acceptance – individual parameter comparison and overall. An individual parameter would be a specific response, such as roll. The overall level would consider all the roll comparisons made. There may also be an acceptance level for the intermediate condition level. The condition level would be speed-heading-wave condition where multiple responses (individual parameters) would be evaluated.

At this point, care needs to be taken to understand the relation between these the

individual and overall comparison. If the overall accuracy is set very high, this forces the individual comparison pass rates to be very high as well; perhaps higher than can reasonably be expected. Additionally, more complex, or multi-level comparison methods may have interactions that result in unintended weighting of certain motions or conditions. The acceptance levels need to be checked to make sure they are behaving as expected and are self-consistent.

The acceptance criteria need to be complete. This appears to be an obvious statement. It bears repeating as the acceptance criteria can become complex and it is easy to overlook key parts. The acceptance criteria needs to specify the manner of comparison for individual conditions and desired pass rate for overall acceptance. The acceptance criteria should cover and account for all sources of difference in the comparisons. This includes random response, variation in simulation input, and non-ergodic processes. These set a maximum level of accuracy for a given data set and process. The simulation accuracy can only be validated to the level of the benchmark data set.

The acceptance criteria need to encompass the requirements of the SIUs, the benchmark data available and the analysis capability compatible with the data. For instance, it will be difficult to apply criteria if the SIUs specify statistical values in Sea State 5 at all speeds and headings, but only limited transfer function benchmark data are available.

The acceptance criteria for validation efforts should be multi-level to validate the specific motion theories and numerical approaches. This will involve various requirements for different force components, individual motions, and all six degrees-of-freedom. To the extent this is possible depends on the available data. For force components, comparison with other simulations may be enough to validate a simulation's implementation of a given



theory. The integration of the various components needs to be validated as well. This is often done by comparing model test and simulations for all six degrees-of-freedom motions.

Finally, the acceptance criteria should be evaluated with a sensitivity study to confirm its behavior with respect to accuracy and other desired traits. The acceptance criteria are varied in what-if scenarios to reveal limiting motions, conditions, or criteria, such as, 90% confidence intervals instead of 95% confidence interval. As a further check, the data can be compared with themselves to ensure the acceptance criteria pass data that are indeed the same. Additionally, the data can be compared with the same data that has been randomly varied with a specified error. Using this with a Monte Carlo approach, it is possible to determine the maximum amount of error allowed in order to pass the acceptance criteria. These various studies of the acceptance criteria will ensure they are behaving as expected. As the acceptance criteria become more complex, it is easy to end up with unrealistic or unattainable levels of required accuracy.

3. COMPARISON

The comparison between benchmark and simulation data is either a comparison of time histories or some processed data from the time histories, such as, standard deviation. Time history comparisons are often made for roll decay or bow slamming or forced motion tests. In these instances, time dependent details are important. A processed data comparisons are often made on significant single amplitude of motion response to validate “general” behavior. Though processed data comparisons need not be limited to that as histograms or extreme event mean crossing rates could also be compared.

The comparison of time histories requires accurate initial conditions for the numerical

simulation. Otherwise, the motion phase with respect to the wave may be different which leads to increasing differences as time increases. It is possible to use ranges of initial conditions to approximate the actual initial conditions and determine the effect of initial conditions. Typically, the comparison of time histories is of a qualitative nature where general behavior or phenomenon is of concern. In maneuvering comparisons, overlaid track plots are common for qualitative purposes, but the values compared are processed data from the track. Ray, *et. al.* (2008) give examples of more quantitative means of comparing time histories.

Usually, a quantitative comparison is required between the benchmark and simulation data. In these cases, the points of comparison are processed data from the time histories, such as, steady turning diameter. The processed data can be motion transfer function characteristics (values, peak amplitude, peak frequency), statistical properties, and extreme value distributions. Typically, the data points can be considered acceptable if the benchmark and simulation uncertainty bands overlap. The uncertainty bars can be assigned as a set percentage or based on some other analysis. Oberkampf and Blottner (1997) suggest an approach similar to standard uncertainty analysis where each of the possible uncertainties is quantified and vector summed to find a total value. Belenky (2011) describes the calculation of confidence interval for variance. Special care is needed for non-ergodic processes where the uncertainty needs to be determined through repeated simulations (Reed, 2011).

As model test data for motion transfer functions are usually much sparser than simulation data, a curve to curve comparison is not helpful. Rather comparison of certain features in the transfer function, such as peak location and magnitude and low/high frequency asymptotic behavior, is more useful. These features should have both frequency and magnitude uncertainty bars associated with them.



Statistical properties, such as, standard deviation, are compared based on an overlap of uncertainty bars.

4. THREE TIER CRITERIA

Validating a simulation for a single degree of freedom and single condition, while possible, is not very useful. A simulation code is typically validated and accredited for multiple degrees of freedom and conditions to determine an overall acceptance. A proposed three tier acceptance criteria covers the typical case of parameter, condition, and set acceptance.

Parameter acceptance criteria deal with the comparison of single degrees of freedom. The condition and set acceptance criteria reflect a validation or accreditation philosophy rather than a strict comparison of data. It is at these levels that subjectivism is most apparent, and perhaps most needed as requiring 100% matching of all conditions in the entire set is likely impossible.

4.1. Parameter Criteria

In addition to capturing the SIUs, there are various approaches to the parameter acceptance criteria — ranging from engineering judgment to rigorous uncertainty analysis. This is the level that has received the most attention to date. The approach selected depends on the completeness of the benchmark data set as well as the maturity of simulation method.

Engineering Judgment

Engineering judgment is used when there is historical experience as to what is acceptable, but the quantification of the uncertainty is difficult or impossible. The uncertainty bands are simply set as some percentage of the values being compared or an acceptable difference, such as, 2 degrees. The advantage is that it is relatively quick and simple to implement, and the results are easily understandable. The disadvantage is possibly

accepting simulations which are incorrect due to arbitrarily large uncertainty bands. Some calibration with a generally accepted simulation code is warranted when using with a new simulation code.

It is also possible to use this approach with a purely subjective or qualitative assessment of acceptance using a panel of Subject Matter Experts (SMEs) that vote on each parameter. In this case, the vote tally becomes the quantitative measure of acceptance. The acceptance criterion is then surpassing a specified percentage of “yes” votes. Hopefully, the more SMEs that vote, the better the assessment of acceptance.

Statistical Hypothesis Testing. With statistical data, statistical hypothesis testing is an obvious and well-documented alternative (Bendat and Piersol, 1966, Priestly, 1981). The objective of these tests is to determine if two estimates could come from two samples belonging to the same general population. The test is based on calculation of the probability that the observed difference between the estimates is caused by random reasons, due to the finite size of both samples. If this probability is finite, the hypothesis that both samples belong to the same general population is not rejected. In practice, a significance level is set (typically 0.01 or 0.05); the exceedance of which constitutes the finite probability and acceptance of the hypothesis.

There are several standard methods available, namely Student’s t test and Fisher F-test. However, they are applicable for independent data points and need to be modified for continuous processes of ship motions (Smith, 2011). Brief review of assumptions associated with tests is given below.

Student’s t Test

Consider a random variable x with normal distribution, unity variance and zero mean value. Consider a sample of n independent realizations of the random variable x . The



estimate of the mean value, the random variable T , has Student's t distribution with $d = n - 1$ degrees of freedom. It is expressed by the following formula:

$$f_t(T) = \frac{\Gamma\left(\frac{d+1}{2}\right)}{\Gamma\left(\frac{d}{2}\right) \cdot \sqrt{\pi d}} \left(1 + \frac{T^2}{d}\right)^{-\frac{d+1}{2}} \quad (1)$$

The mean value estimate is proportional to a sum of identically distributed random numbers. Therefore an increase in the number of degrees of freedom makes Student's t distribution asymptotically converge to the normal distribution (per the Central Limit Theorem). Figure 1 shows that the visual difference between the Student's t and normal distribution visually disappears for $d=30$. That is why the Student's t distribution is considered to be more appropriate a for relatively small volume of a sample.

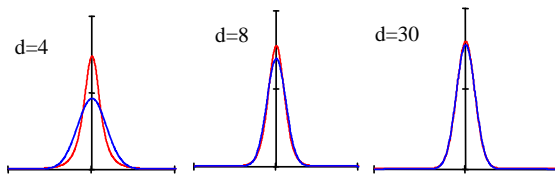


Figure 1: Tendency of Student's t distribution (red) with increasing number of statistical degrees of freedom to the normal distribution (blue)

The T-test uses the Student's t distribution for the difference between the estimates of mean values of two samples: experiment m_1^* and simulation m_2^* . The volume of samples may be different (say n_1 and n_2), but the variance is assumed the same, since the hypotheses is that the simulations and experiment yielded the same result and the difference between them is just a result of finite volume of samples. The random variable expressing the difference between the estimates and having the Student's t distribution is expressed as

$$T = \frac{m_1^* - m_2^*}{\sigma^* \sqrt{n_1^{-1} + n_2^{-1}}} \quad (2)$$

Where σ^* is the standard deviation estimated over the both samples together. The number of degrees of freedom is defined as

$$d = n_1 + n_2 - 2 \quad (3)$$

Fisher's F-Test

Consider a random variable x with normal distribution, unity variance and zero mean value. Consider a sample of n independent realizations of the random variable x . The estimate of the variance, the random variable U , has chi-squared distribution with $d = n - 1$ degrees of freedom. It is expressed by the following formula:

$$f(x) = \frac{x^{0.5d-1} \exp(-0.5x)}{2^{0.5d} \Gamma(0.5d)}; \quad x > 0 \quad (4)$$

The chi-squared distribution also tends towards a normal distribution (per the Central Limit Theorem) with a non-zero mean value, see Figure 2.

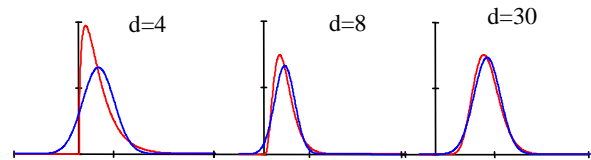


Figure 2: Tendency of chi-square distribution (red) with increasing of the number of statistical degrees of freedom to the normal distribution (blue)

The F-test uses the ratio of the two variance estimates to check the difference between them. This requires introduction of yet another distribution describing the ratio of two chi-squared distributed random variables, U_1 and U_2 , with d_1 and d_2 degrees of freedom, respectively:

$$Z = \frac{U_1/d_1}{U_2/d_2} \quad (5)$$

The F-distribution is expressed as:

$$f(Z) = \frac{Z^{0.5d_1-1}}{B(0.5d_1, 0.5d_2)} \left(\frac{d_1}{d_2}\right)^{0.5d_1} \times \left(1 + \frac{d_1}{d_2}Z\right)^{-0.5(d_1+d_2)} \quad (6)$$

Here B is beta function defined as:

$$B(p, q) = \int_0^1 z^{p-1} (1-z)^{q-1} dz \quad (7)$$

If the arguments p and q are integers, the beta function can be expressed as:

$$B(p, q) = \frac{(p-1)!(q-1)!}{(p+q-1)!} = \frac{\Gamma(p)\Gamma(q)}{\Gamma(p+q)} \quad (8)$$

The mean value and variance of the F-distribution are expressed as follows

$$m = \frac{d_2}{d_2 - 2} \quad \text{for } d_2 > 2 \quad (9)$$

$$V = \frac{2d_2^2(d_1 + d_2 - 2)}{d_1(d_2 - 2)^2(d_2 - 4)} \quad \text{for } d_2 > 4 \quad (10)$$

The F-distribution is asymmetric, however, increasing number of degrees of freedom, makes it less asymmetric and closer to the normal distribution, see Figure 3 and 4.

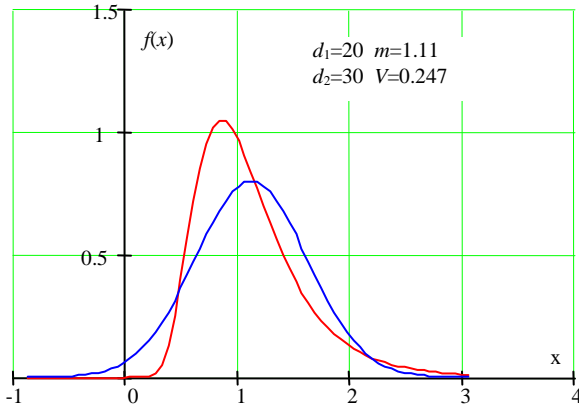


Figure 3: Appearance of F-distribution (red) in comparison with normal distribution (blue) for a moderate number degrees of freedom.

Since the actual F-test involves the calculation of probabilities, the Cumulative Distribution Function (CDF) is more convenient for calculations:

$$F(Z) = I_{\frac{d_1 Z}{d_1 Z + d_2}}(0.5d_1, 0.5d_2) \quad (11)$$

Here $I_y(p, q)$ is the regularized Beta function expressed as:

$$I_y(p, q) = \sum_{j=p}^{p+q-1} \frac{(a+q-1)!}{j!(p+q-1-j)!} \times y^j (1-y)^{p+q-1-j} \quad (12)$$

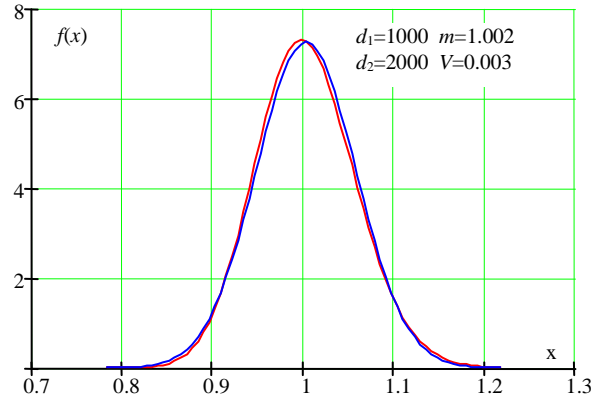


Figure 4: Appearance of F-distribution (red) in comparison with normal distribution (blue) for a large number degrees of freedom.

Statistical Tests for Processes

The use of statistical tests requires the data to meet various assumptions. Specifically, the data are random, normally distributed, and independent. Ship motion data are dependent due to inertial properties of the waves and the ship as well hydrodynamic memory effects caused by wavemaking, that is, the retardation function.

Also, the number of degrees of freedom cannot simply equal the number of points, since the actual measure of the volume of sample depends on the duration of the record and cannot be defined by the time step / sampling rate. Smith (2011) proposed a concept of equivalent number of equivalent degrees of freedom. It is the number of degrees of freedom for a chi squared distribution that has the same confidence interval as the data. If the number of degrees of freedom d is known, the confidence interval boundaries of the variance estimate is:



$$V_{Low}^*(d) = \frac{d \cdot V^*}{\chi_{low}^2(d)}; \quad V_{Up}^*(d) = \frac{d \cdot V^*}{\chi_{low}^2(d)} \quad (13)$$

The lower and upper values for chi-square are found using the CDF of chi-squared distribution.

$$F_{\chi^2}(\chi_{low}^2; d) = \frac{1 - P_\beta}{2};$$

$$F_{\chi^2}(\chi_{up}^2; d) = 1 - \frac{1 - P_\beta}{2}; \quad (14)$$

Where P_β is the given confidence interval.

At the same time, if the number of degrees of freedom is high enough (see Figure 2), the boundaries of the confidence interval of the variance estimate can be found using the normal distribution.

$$V_{Low}^{**} = V_\phi^* - k_\beta \sqrt{V(V_\phi^*)}$$

$$V_{up}^{**} = V_\phi^* + k_\beta \sqrt{V(V_\phi^*)} \quad (15)$$

Here $V(V_\phi^*)$ is the variance of the variance estimate and k_β is defined by the given confidence probability:

$$F_N(k_\beta) = 1 - \frac{1 - P_\beta}{2} \quad (16)$$

Here F_N is the CDF of the normal distribution with zero mean and unity variance.

The variance of the variance of an ensemble of N_r records is evaluated as (Priestley, 1981):

$$V(V_\phi^*) = \frac{2}{N_{total}^2} \sum_{j=1}^{N_r} N_{t_j} \sum_{i=-N_{t_j}+1}^{N_{t_j}-1} \left(1 - \frac{|i|}{N_{t_j}}\right) \times (R_\phi^*(t_{|i|}))^2 \quad (17)$$

Here N_{total} is the total number of data points, N_{t_j} is the number of data points in record j and R_ϕ is the autocorrelation function, which can be estimated from the time series that accounts for data dependency. The

autocorrelation function determines when data are no longer correlated. If the spectrum estimate is available, the autocorrelation function can be exactly calculated from spectrum using

$$R(\tau_i) = \sum_{j=1}^{N_\omega} S(\omega_j) \cos(\omega_j \tau_i) \quad (18)$$

and can be estimated from the time series using:

$$R_\phi^*(\tau_k) = \frac{\sum_{j=1}^{N_r} \sum_{i=1}^{N_t-k} (\phi_{i+k,j} - m_\phi^*)(\phi_{i,j} - m_\phi^*)}{N_r(N_t - k)} \quad (19)$$

Once the boundaries of the confidence interval (15) are calculated, the equivalent number of degrees of freedom can be found by minimizing the following expression

$$\max \left(\frac{|V_{Low}^{**} - V_{Low}^*(d)|}{V_{Low}^{**}}, \frac{|V_{up}^{**} - V_{up}^*(d)|}{V_{up}^{**}} \right) \quad (20)$$

Smith (2011) uses this in an approach to determine an equivalent number of independent data samples for a given set of dependent data. With an equivalent number of independent data samples or degrees of freedom and variance of variance, it is possible to apply the standard statistical significant tests such as Student's t, or F-test.

Besides data independency, the data are assumed to be normally distributed. This is a standard seakeeping assumption for wave elevation or small-to-moderate amplitude ship motions. While the F-test test is known to sensitive to non-normality, it may be not so much of a problem for ship motion records of sufficient length. Large equivalent number of degrees of freedom is likely make the chi-squared distribution very close to normal, so non-normality of the processes itself may be not that important for the F-test. Nevertheless, this issue needs to be studied as there are other statistical tests available for comparing variance estimates



The disadvantage of a purely statistical approach is the assumption that all the uncertainty is stochastic in nature, either variance for mean or variance of variance for variance. Previous results using this approach have been inconsistent, suggesting there may be other factors at work. These factors need to be included in the analysis

Sum of Errors. Stern, *et. al.* (1999) suggests a weighted vector sum of the uncertainties in a manner similar to standard uncertainty analysis. The simulation is considered acceptable when its uncertainty bar overlaps the benchmark uncertainty bar. The simulation uncertainty sources are: grid density, time step size, initial condition variation, random process variation, and theory maturity. This approach has the advantage of capturing potentially all the dissimilar sources of uncertainty on both the benchmark and simulation data sets. The main disadvantage is quantifying the uncertainty from the various uncertainty sources.

It is possible to use this approach with a sub-set of the potential uncertainty sources. In this case, the assumption is either the uncertainty sources neglected are negligible relative to those used or the uncertainty from the neglected uncertainty sources are comparable between the simulation and benchmark data.

This is essentially the approach favored by ITTC — “The only guiding criterion that could be stated is that the discrepancy of the code under consideration over some benchmark data should not exceed the combined uncertainty of that model and the one used to produce the benchmark data.”

Many fluid simulation validation efforts have focused on computational fluid dynamics (CFD) looking at steady state phenomenon (ASME, 2009; Oberkampf and Blottner, 1997; Stern, *et. al.*, 1999; Stern, *et. al.*, 2005). Ship motion is typically not steady

state, but random. This adds a level of complexity to the validation effort.

Mixed. A mixed acceptance criteria approach is a combination of other methods. This is an attempt to use to best elements of the other approaches, while balancing or eliminating the disadvantages. An obvious mixed acceptance criterion is using engineering judgment to set some minimum level concern and overlapping uncertainty bars above that level of concern. This approach can become quite elaborate as more considerations are included. Care needs to be taken to ensure the interaction between the different pieces does not result in an undesirable cumulative acceptance criterion, even though all individual pieces seem reasonable.

4.2. Condition Criteria

Acceptance criteria for a condition are generally based upon having a specified number of parameters/motions/components passing based on individual motion/component acceptance criteria. The SIUs specify which motions to include in the criteria. As mentioned in Belknap, *et. al.* (2011), when considering the total simulation, it is desired that all the motions be acceptable simultaneously. This precludes considering the simulation acceptable when matching vertical acceleration, but not matching speed or heading at which the vertical acceleration is calculated.

However, motions are not uniformly sensitive to variations in speed, heading, wave height, modal period, or wave spreading. Requiring all motions, including speed and heading, to pass simultaneously may penalize the simulation unduly. This can be accounted for by adjusting the parameter acceptance criteria to different accuracy levels depending upon sensitivity.

Alternatively, requiring a certain number or mix of motions, but not all motions, is a potential compromise provided there is not a



consistently failing motion. The presence of a consistently failing motion indicates a theory or implementation problem with the simulation.

4.3. Set Criterion

The set or overall criterion deals with acceptance of the total simulation or component rather than just a specific condition or case. This can be simply characterized as a passing percentage of all cases examined or even a weighted sum of the passing cases based on importance. For instance, if beam seas performance was most important, then those conditions could be weighted more than other cases. This would ensure the simulation performed adequately where it was most important. The benchmark data set also provides a *de facto* weighting, which should be evaluated against the desired weighting.

It should be noted that setting an overall acceptance criterion also sets a required pass rate for the individual parameter/motion/components. Intuitively, it is apparent the higher the required condition passing requirement (overall criterion), the higher the individual motion or component pass rate that is required to meet the overall criterion. What can be overlooked is that requiring the simultaneous passing of multiple individual parameters, motions, or components quickly leads to not passing the overall acceptance criterion despite relatively high individual motion or component pass rates. From simple probability theory, the conditional probability of acceptance requiring N independent parameters to pass is the product of the N individual pass rates. For instance as seen in Figure 5, requiring 8 motions to pass simultaneously, each with a pass rate of 80%, has an overall pass rate of 0.8^8 or 16.7%. An overall condition pass rate of 70% requires the 8 motions to have pass rates on the order of 96%.

5. EXAMPLE ACCEPTANCE CRITERIA APPROACHES

Some common acceptance criteria approaches will be examined using numerical examples. The data used for the numerical example are linear seakeeping predictions that have been randomly modified. The data modification process is described in Appendix A.

The data set has 4 wave heights, 6 modal periods, 6 speeds, and 24 relative wave headings. There are a total of 4,032 conditions. The 13 motions compared are: heave, roll, pitch, yaw, roll rate, pitch rate, yaw rate, center of gravity acceleration (longitudinal, transverse, vertical), and off center stern location acceleration (longitudinal, transverse, vertical).

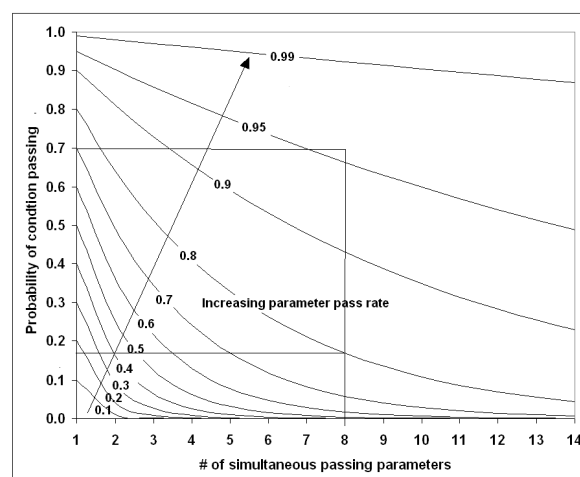


Figure 5: Probability of a condition passing based on parameter pass rate and simultaneous passing of parameters.

For this example, the set acceptance criterion is passing 80% of the conditions. The two condition acceptance criteria are: all motions passing and roll, pitch, yaw rate, and either CG or stern location acceleration (longitudinal, transverse, vertical) passing. The second criterion, referred to as “sub-set motion,” requires six motions to pass simultaneously, but the passing accelerations can be from either point. The parameter acceptance criteria will use “engineering judgment,” statistical testing, and sum of



errors. The mixed acceptance criteria results can be deduced from the others. The results, Table 1, show how the different tier criteria affect each other.

With “engineering judgment,” the motion is considered acceptable if the absolute difference between the two data sets is less than a threshold. The different thresholds were selected to ensure some failures. In practice, the difference thresholds are set by a “close enough” judgment. In this case, the differences for all the accelerations, yaw, and yaw rate are all less than the threshold as shown by the 100% motion pass rate. That may not necessarily be true for a different set of random data. The remaining motions have an average pass rate of 85%.

Still only 51% of the conditions passed as “all the motions to pass” to pass a condition. This can be seen on Figure 5 using five motions to pass (others have 100% pass rate and do not affect condition passing) with a motion pass rate of 85%. The “sub-set

motion” criterion pass rate is the product of the roll and pitch pass rates; the motions that did not have 100% pass rates.

The hypothesis testing example used the F-test to compare variances following Smith (2011) with a 95% confidence. The individual motion pass rates are uniformly in the mid-70 percentile. This is a function of how the simulation data were generated – uniformly random distribution with a $\pm 25\%$ change. Actual data would be less consistent. Other hypothesis tests, such as, Student’s *t* test, could be used following the same principles depending on the data being compared.

Despite all the motions having a 74-77% pass rate, the “all motions” condition pass rate is only 3%. This can be seen on Figure 5, which is more than double the expected 0.75 to the sixth power (18%). The increase is due to the “or” in the acceleration acceptance.

Table 1: Comparison of parameter and condition acceptance criteria approaches.

		Engineering Judgment		Hypothesis Test	Sum of Errors
Motion	Units	Difference Threshold	Motion Pass Rate	Motion Pass Rate	Motion Pass Rate
Heave	m	0.076	79%	75%	92%
Roll	deg	0.500	90%	76%	85%
Pitch	deg	0.250	93%	77%	98%
Yaw	deg	3.000	100%	75%	99%
Roll Rate	deg/sec	0.150	76%	75%	96%
Pitch Rate	deg/sec	0.150	85%	76%	98%
Yaw Rate	deg/sec	0.150	100%	75%	99%
CG Lon Acc	g's	0.025	100%	74%	100%
CG Lat Acc	g's	0.025	100%	76%	100%
CG Vrt Acc	g's	0.025	100%	76%	100%
Pt1 Lon Acc	g's	0.025	100%	75%	100%
Pt1 Lat Acc	g's	0.025	100%	74%	100%
Pt1 Vrt Acc	g's	0.025	100%	74%	99%
All Motions (13)			51%	3%	70%
Sub-Set Motions (6)			84%	38%	82%



The sum of errors example only used stochastic uncertainty, though other error estimates could be added. The motion pass rates are very high; only roll being less than 90%. This is most likely a function of data generation method; actual data are expected to have lower motion pass rates. Requiring “all motions to pass” a condition has a condition pass rate of 70%. This is close to the expected value from Figure 5 for eight motions and 97% pass rate (72%). The sum of errors results for the “sub-set motions” criterion are very similar to the engineering judgment results and for the same reasons.

None of the parameter approaches with “all motions” condition criterion passed the set acceptance criterion of 80% condition pass rate, despite having very high pass rates for the sum of errors approach. Using the “sub-set motion” criterion with engineering judgment or sum of errors passed the set acceptance criterion.

6. CONCLUSION

At this time there does not appear a universal answer to acceptance criteria approach. This paper discusses quantitative acceptance criteria for validation and accreditation of seakeeping simulation codes. The concept of parameter, condition, and set acceptance criteria were introduced to ensure a definitive statement could be made of the simulation’s applicability. The desired traits of acceptance criteria were specified as quantifiable error, self consistency, completeness, multi-leveled, and having a known sensitivity. Four approaches to parameter acceptance criteria were explored: engineering judgment, statistical hypothesis testing, sum of errors, and mixed.

The example cases using randomly modified linear simulation data showed the application of the different approaches. The examples also show the interaction of acceptance criteria at the different levels. Specifying the simultaneous passing of parameters for a condition forces the

individual parameter pass rates to be high in order to pass the condition. Most of the focus of acceptance criteria is at the parameter level as that is more easily understood. However, to validate or accredit a simulation requires a condition and set acceptance criteria.

The methodology described here does not address required levels of accuracy, merely how to make the comparison. Determining the required levels of accuracy is left to certification bodies.

7. APPENDIX A - SAMPLE DATA

The data used for the example cases are purely for demonstration purposes. Both the simulation and benchmark data are from SMP95 (Conrad, 2008) results for a small, double chine research vessel. SMP95 was run for a range of speeds, significant wave heights, and modal periods to represent variation in input, forming a condition input group. The significant wave heights were 0.9, 1.8, 2.7, and 3.6 meters. There were 6 modal periods from 7.9 to 15.0 seconds. Relative wave heading is fixed within SMP95 at 15 degree increments. There were 4032 conditions.

The simulation data were generated by randomly altering the SMP95 benchmark data set by up to $\pm 25\%$ of the benchmark value as seen in Equation 21 where RMS is root mean squared and \check{R} is a random number between 0 and 1.

$$RMS_{sim} = RMS_{bench} (1 - (\check{R} - 0.5)/2) \quad (21)$$

Motions that had zero motions in head and following seas used a value equal to up 50% of the value at the nearest heading.

As SMP95 is a frequency domain code, variance of variance ($V(V^*)$) and confidence intervals are technically zero. Furthermore, there are no data samples to apply statistical hypothesis testing to. The data required for these calculations were generated using Equation 22 for variance of variance where V



is the variance. The resulting values were of typical magnitude.

$$V(V^*) = \begin{cases} 0.1 * V^* \check{R} & \text{if } V > 1 \\ 0.1 * V^* V^* \check{R} & \text{if } V < 1 \end{cases} \quad (22)$$

The number of equivalent independent variables was taken as a random value between 35 and 95.

The confidence interval is calculated using: $\text{var} \pm \text{fact} \sqrt{\text{VoV}}$, where *fact* is determined from the confidence level. Variance confidence intervals can be nonsensical if the $V(V^*)$ is large compared to the variance. In these cases, the lower confidence bound can be negative and variance cannot be less than zero. When this occurred, the lower confidence bound was set to zero. The value using the sum of errors approach was half the difference between the upper and lower confidence bounds.

8. ACKNOWLEDGEMENTS

The author would like to thank Dr. Vadim Belenky for his many discussions on autocorrelation and ensemble methods, and providing the text for the Student's *t* and F-test descriptions.

The author also thanks Dr. Patrick Purtell of the Office of Naval Research for funding this effort.

9. REFERENCES

ASME, 2009, "Standard for Verification and Validation in Computational Fluid Dynamics and Heat Transfer," American Society of Mechanical Engineers, New York.

Bales, N.K., 1980, "Optimizing the Seakeeping Performance of Destroyer-Type Hulls," 13th ONR Symposium on Naval Hydrodynamics, Tokyo.

Belenky, V.L. (2011) "On Self-Repeating Effect in Reconstruction of Irregular Waves" Chapter 33 of "Contemporary Ideas on Ship Stability", Neves, M.A.S., Belenky, V., de Kat, J.O., Spyrou, K., Umeda, N. (eds),

Springer, ISBN 978-94-007-1481-6 pp. 589-598

Belknap, W.F., Smith, T.C., and Campbell, B.L., 2011, "Addressing Challenges in the Validation of Dynamic Stability Simulation Tools," Proc. of the 12th International Ship Stability Workshop, Washington DC.

Bendat, J. and Piersol, 1966, "Measurement and Analysis of Random Data," John Wiley & Sons.

Conrad, R.E., 2005, "Standard Ship Motion Program (SMP95) User's Manual," NSWCCD-50-TR-029/2005 .

Elele, J. N., 2008, "Assessing Risk Level of Verification, Validation, and Accreditation of Models and Simulations," ITEA Journal, Vol:29: 190-200.

ITTC, 2011, "Loads and Responses Seakeeping Verification and Validation of Linear and Weakly Nonlinear Seakeeping Computer Codes," 26th ITTC Seakeeping Committee Procedure 7.5 – 02 07-02.5 rev 1.

Oberkampf, W., Blottner, F., 1997, "Issues in Computational Fluid Dynamics Code Verification and Validation," Sandia National Laboratories Report SAND95-1352.

Priestley, M. B., 1981, "Spectral Analysis and Time Series," Vol. 1, Academic Press, New York.

Ray, M. H., Anghileri, M., and Mongiardini, M., 2008, "Comparison of Validation Metrics Using Repeated Full-scale Automobile Crash Tests," Proc. of 8th World Congress on Computational Mechanics, Venice, Italy.

Reed, A. M., 2008, "Comments to Belenky, V. de Kat, J.O. and Umeda, N. Towards Performance-Based Criteria for Intact Stability," Marine Technology 45(2): 101-123.

Reed, A. M., 2011, "26th ITTC Parametric Roll Benchmark Study," Proc. of the 12th International Ship Stability Workshop, Washington DC.



Smith, T.C., 2011, "Statistical Data Set Comparison for Continuous, Dependent Data," Proc. of the 12th International Ship Stability Workshop, Washington DC.

Stern, F., Wilson, R., Coleman, H., Paterson, E., 1999, "Verification and Validation of CFD Simulations," Iowa Institute of Hydraulic Research Report No. 407.

Stern, F., Wilson, R., and Shao, J., 2005, "Quantitative V&V of CFD Simulations and Certification of CFD Codes," Int. J. Numer. Meth. Fluid Vol 50: pp1335-1355.



On Regulatory Framework of Direct Stability Assessment

William S. Peters, *US Coast Guard, Office of Design and Engineering Standards* william.s.peters@uscg.mil

Vadim Belenky, *David Taylor Model Basin (NSWCCD)*, vadim.belenky@navy.mil

Arthur M. Reed, *David Taylor Model Basin (NSWCCD)* arthur.reed@navy.mil

ABSTRACT

Direct assessment of stability, including model tests and numerical simulations, is the ultimate way to evaluate the risk of stability failure for an unconventional vessel. That is why direct assessment is considered to be the highest tier of the second generation of intact-stability criteria, that are being developed by IMO. Direct assessment procedures for stability failure are intended to employ the most advanced state-of-the-art technology available, yet be sufficiently practical so as to be uniformly applied, verified, validated, and approved using currently available infrastructure. This paper addresses several principal issues related to the application of numerical simulation in the IMO regulatory framework, including possible requirements for a method that adequately replicates ship motions in waves, validation of such a method, actual assessment procedures and their validation.

Keywords: Direct assessment, intact stability, numerical simulations

1. INTRODUCTION

The concept of direct stability assessment has evolved from the idea of performance-based intact-stability criteria during development of second generation intact stability criteria by IMO (Belenky, *et al.*, 2008). The principal motivation for developing direct assessment is to reduce the level of empiricism and be prepared for the assessment of novel designs. These new designs may be well outside of the population of ships used for development of the first generation of the intact-stability criteria codified in the 2008 IS Code.

Accurate computational reproduction of an intact-stability failure in irregular seas is a challenging technical task because the dynamical system describing ship motions in waves is characterized by significant nonlinearities. On the other hand- and fortunately-, intact-stability failures are very

rare. This combination of nonlinearity and rarity makes simulation a challenge.

Multi-tiered structure of the second-generation-stability criteria was adopted to make sure that costly numerical assessment procedures are only applied when it is absolutely necessary, *i.e.*, when vulnerability to dynamical stability failures has been established “beyond reasonable doubt” (Peters, *et al.*, 2011).

Application of advanced numerical simulations for regulatory purposes and operational advice is relatively new. Several examples are: the ABS Parametric Roll Guide (ABS, 2004a), Themelis & Spyrou (2007) and Shigunov (2009). As a part of optional class notation ABS (2004a) requires numerical simulations to be carried out to develop an operational guidance system to avoid parametric roll. Themelis & Spyrou (2007) described a numerical simulation of a typical



voyage to assess the probability of stability failure using the wave-group method. Shigunov (2009) reported application of advanced numerical simulations to develop operational guidance to reduce loss of containers from container ships.

Mathematical methods and software for numerical simulation of ship motions in waves have been developed during the last three decades (Beck & Reed, 2001). However, computational efficiency issues with rigorous physics-based models have been identified by (Belknap & Reed, 2010). Hybrid codes combining potential flow hydrodynamics with simple models for other forces seems to be the practical way to approach dynamic stability assessment. Examples of this are represented by Shin, *et al.*, (2003); Brunswig & Pereira, (2006). The most difficult issue, however, is related to the validation of the numerical codes (Reed, 2008, 2009; Smith, 2012). Another challenge is presented by the rarity of stability failures, a fact that requires application of special extrapolation procedures (see review by Belenky, *et al.*, 2012).

One of the first attempts to formulate requirements to direct assessment of stability has been presented in Annex 21 of SLF 54/INF.12, followed by the comments and discussion in Annex 22. This paper presents a review and further discussion of this subject.

2. POSSIBLE STRUCTURE OF REQUIREMENTS

Up to now there are only a few cases in which numerical simulations of ship motions were applied to parametric roll and then recognized by classification societies. However, the history of application and recognition of advanced numerical methods in classification society practice is much longer, since finite element analysis is considered as a standard tool today (see, *e.g.*, ABS 2004b). Following this long-term experience, the requirements for direct assessment of intact stability have to be formulated in terms of the

method itself and the procedure of its application. These requirements also have to include the conditions for recognition and acceptance by flag administration (or by an organization acting on behalf of the administration) of the method and procedure.

Since direct stability assessment is meant to be a state-of-the art method, it has to be applied to the most realistic model of the wave environment, *i.e.*, irregular waves. Since intact-stability failure is a very rare event, a sample record of sufficient volume cannot be obtained by numerical simulation alone. Therefore, any statistical extrapolation method will be based on a set of assumptions that will also need validation.

Based on the above considerations, the possible structure of the requirements for direct stability assessment can be envisioned as consisting of the followings:

- A method that adequately replicates ship motions in waves
- A prescribed procedure that identifies the process by which input values are obtained for the assessment, how the output values are processed, and how the results are evaluated.
- Conditions of acceptance and requirements for verification and validation of the method for ship motion replication.
- Conditions of acceptance and requirements for verification and validation of the extrapolation procedure.

3. METHOD FOR REPLICATION OF SHIP MOTIONS

3.1 Mathematical Model of Waves

Mathematical modeling of irregular waves is more than just a representation of a stochastic process of wave elevations.

Calculations of potential hydrodynamic forces (including hydrostatic, Froude-Krylov, diffraction and radiation) require evaluating the pressures around the instantaneous position of the hull relative to the water surface. Therefore, the modeling of irregular waves involves presentation of a large number of dependent stochastic processes. Fourier series have been traditionally used as a method to present these stochastic processes. Wave elevations (as a function of time and space), for example, are presented as

$$\zeta_w(x, t) = \sum_{i=1}^N r_i \cos(k_i x - \omega_i t + \varphi_i) \quad (1)$$

where r_i is an amplitude of a component, calculated from a wave spectrum; φ_i is a random initial phase (uniformly distributed from 0 to 2π); and k_i and ω_i are wave number and frequency of a component. They are related through the well-known Dispersion Equation, that expresses the assumption of small waves according to the Airy theory in deep water:

$$k_i = \frac{\omega_i^2}{g} \quad (2)$$

where g is the gravitational acceleration. Inclusion of the dispersion relation into the presentation of the stochastic process makes this wave model hydro-dynamically valid within the Airy theory.

While this model remains the mainstay of numerical simulations of ship motions, it incurs a computational cost when a large sample size is needed. This problem comes from the so-called “self-repeating effect” that is caused by an insufficient number of components for the required record length (Belenky, 2011). The presence of the self-repeating effect in a particular frequency set can be revealed by an autocorrelation function calculated from the wave spectrum when using the method of rectangles.

$$R(\tau) = \int_0^{\infty} s(\omega) \cos(\omega\tau) d\omega \quad (3)$$

$$= \sum_{i=1}^N s(\omega_i) \cos(\omega_i \tau) \Delta\omega_i$$

here $s(\omega_i)$ is the spectral density and $\Delta\omega_i$ is the frequency increment around the i -th component.

Figure 1 shows the autocorrelation function (3) indicating the self-repeating effect. The repetition of the pattern may be different if the variable-frequency step is used. An increase of the autocorrelation function after the initial decay is a result of numerical error and indicates the limits of the duration of the record length. For example, in Figure 1 the valid duration is about 180 seconds.

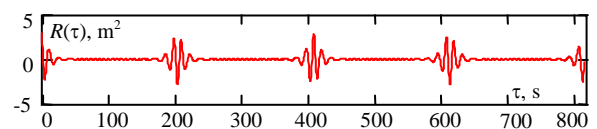


Figure 1: Example of the Self-Repeating Effect.

To extend the length of the record, the number of components needs to be increased, which leads to an increase in computational costs. One way to deal with a problem of increased computational costs is increase the number of records instead on number of frequencies.

A promising alternative to the Fourier series representation is the Autoregression Method.

$$\zeta(x, t) = \sum_{i=1}^{N_t} \sum_{j=1}^{N_x} \Phi_{i,j} \zeta(t_i, x_j) + \varepsilon(x, t) \quad (4)$$

here Φ is the autoregressive parameter, and ε is white noise. Hydrodynamical validity of the method has been recently address by Degtyarev & Reed (2011), while further development of autoregressive method is focused on predicting the pressures needed to computes forces and moments (Degtyarev & Gankevich, 2012).



3.2 Mathematical Model of Roll Damping and Hull Forces

Using a hybrid approach for reproducing ship motions is computationally efficient, but the cost for this efficiency is potential inconsistency in the modeling of forces with significant vortex components. Roll damping is the best example of such potential inconsistency. The potential solver of a hybrid code internally reproduces the wave component of roll damping. An empirical evaluation of roll damping that is obtained from a model test or CFD also contains a wave component. As a result the simple addition an empirical to a potential flow model will inevitably lead to “double counting” of the wave component of roll damping.

To deal with this problem, the ABS Guide (2004a) requires that the empirical part of roll damping be “calibrated” such that the resultant damping is close to that measured in a roll decay test. This approach was first successfully applied during a parametric-roll-accident investigation (France, *et al.*, 2003). A detailed description is available in Belenky, *et al.*, (2011b). The procedure can be expressed in the form of a system of two nonlinear algebraic equations.

$$(k, f) - D(B_1(f), B_2(k)) = 0 \quad (5)$$

here, D is a symbolic expression for a run of numerical simulations followed by a standard procedure for roll-decay processing, k is the slope, and f is the intercept of the fitted line; functions $B_1(f)$ and $B_2(k)$ are expressions, respectively, of the linear-roll-damping coefficient which depends on the intercept and the quadratic-roll- damping coefficient witch depends on the slope. This equation can be solved with any appropriate numerical method Practical experience has shown that, on the average, calculations converge after five to six iterations.

A similar approach has been developed and verified for maneuvering hull forces (Yen, *et al.*, 2010). The maneuvering coefficients were “calibrated” to allow a hybride code to reproduce a model test done with the Planar Motion Mechanism (PMM) in calm water. It was shown that this procedure offers a reasonable performance when simulating maneuvers in waves.

3.3 Parametric Roll

Since early 2000, when the problem of parametric roll of container ships came into focus, there have been some positive results from numerical simulations of parametric roll. Stability variations in waves are modeled as a part of a body-exact formulation for the Froude-Krylov and hydrostatic forces. As described above, calibration of roll damping is known to work well for modeling parametric roll (France, *et al.*, 2003).

Planning numerical simulations in irregular waves requires special care (Reed, 2011). The parametrically excited motions in irregular waves “come and go” which leads to practical non-ergodicity (Belenky, *et al.*, 2011a). Here, ergodicity refers to the ability to estimate statistics from a single “long-enough” record. While the process of roll motions formally remains ergodic, the required length of a record may be impractically long. However, the use of a collection of independent records mitigates the problem (see Figure 2)

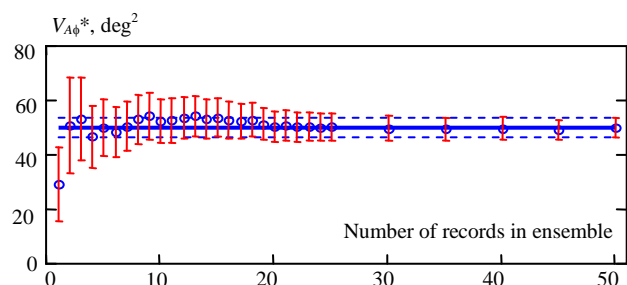


Figure 2: Convergence of Ensemble Estimate of Variance (Belenky & Weems 2011)



3.4 Pure Loss of Stability

The phenomenon of pure loss of stability is caused by the degradation of roll restoring near a wave crest. The body-exact formulation for hydrostatic and Froude-Krylov forces is the best way to predict loss of stability. The main difference with parametric roll is the importance of the time duration of reduced stability around a wave crest. This is one reason why numerical simulations of a ship's motion may need to include surging. As shown by Umeda & Yamakoshi (1993), surging may influence the timing of reduced stability due to specific phase shifts between the processes of surge motions and stability variation.

3.5 Surf-riding and Broaching-to

Contemporary mathematical models describing surf-riding and broaching-to include at least four degrees of freedom: surge, sway, roll and yaw. These models were developed in the early 1990's (Umeda & Renilson, 1992) and were used for developing the modern dynamical theory of broaching-to (Spyrou, 1996). Previously, all the predictions for surf-riding and broaching-to were described by ordinary differential equations (ODE). While ODE are still considered acceptable (SLF 53/3/8), work is underway to simulate surf-riding and broaching-to using hybrid codes (Spyrou, *et al.*, 2009; Belknap & Reed, 2010; Yen, *et al.*, 2010) and CFD (Sadat-Hosseini, *et al.*, 2011). Because the computational costs of the CFD remains high, its role may only be as a source of coefficients for the ODE and hybrid codes. However, at this point, a model test remains the main source of coefficients.

3.6 Dead-Ship Conditions

Within the framework of IMO regulations, capsizing in dead-ship conditions was the first situation in which direct stability assessment was considered (MSC.1/Circ.1200 & 1227). The assessment was done using model tests; however, in the future, the use of numerical

simulations for predicting capsizing in dead-ship conditions cannot be ruled out.

To provide consistency with the existing weather criteria, a code for predicting behavior in dead ship conditions should be able to reproduce the responses of a ship under the action of waves and experiencing a wind gust. Although this hypothetical situation is classic, its numerical simulation may be not simple. There are several issues to discuss: beam seas assumption, hydrodynamic drift force and influence of water on deck.

Beam Seas Assumption

Stability regulations were first formulated in the steamship era (Rahola, 1939). The prevailing architecture of those ships included a superstructure located amidships with the topside as well as the hull volume more or less longitudinally symmetric about amidships. In a dead-ship condition, that type of vessel would be turned by the wind into a beam seas orientation. Fleets today are characterized by a much larger variety of architectural types: the superstructure located aft (containerships, bulk carriers and tankers); the superstructure located forward (offshore supply vessels); the superstructure occupying most of ship length (car carriers, RoPax, cruise ships). Thus, today a vessel in dead-ship conditions may not be turned to a beam seas orientation.

Umeda, *et al.*, (2007) developed a method to predict the orientation of a vessel in waves and wind under dead-ship conditions, which was based on a system of ODE describing sway, surge, roll and yaw motions to predict the orientation.

Because the heeling moment from the wind is maximum in this orientation, the beam position is still considered the most dangerous in Annex 22 of SLF 54/INF.12. The issue identified here is: when carrying out numerical simulations in dead-ship conditions, should a ship be fixed in beam position even in the



presence of significant aerodynamic yawing moment?

The answer to this may depend on how quickly aerodynamic forces can turn a ship. The actual orientation may be a more realistic scenario to consider if the turn toward quasi-equilibrium position can be completed quickly, *i.e.*, before the hydrodynamic drift reaction is fully developed. If the turn takes a long time, then it may be reasonable to ignore the aerodynamic turning moment and consider beam seas only.

Hydrodynamic Drift Force

The challenge of modeling this force is in the complexity of flow around the hull with non-stationary vortices. Thus, model testing remains the main source of data for this force and its moment. Review of some of the experimental data is available from Belenky & Sevastianov, 2007. CFD calculations may be a practical way to get the coefficients of force for the direct stability assessment.

Presence of Water on Deck

If a ship has a relatively low free board, water may be shipped on deck after the first semi-period of roll oscillations. This may significantly change the dynamics of further motions. Water on the deck may play the role of additional damping, resulting in the heeling motion growing slower, and causing the ship to capsize after the second or third period (see Figure 3).

The dynamics of a ship with water on the deck can be simulated with a hybrid code (Belenky, *et al.*, 2003), which showed that the inertia of water may have significant influence on ship motions. The scenario of water on the deck shown in Figure 3 is only one possibility; another one is shown in Figure 4. It corresponds to the “deck-in-water” situation when the water on the deck is connected with the outside fluid domain. The hydrodynamic force created by the deck-in-water scenario may create a significant additional heeling moment (Grochowalski, *et al.*, 1998).

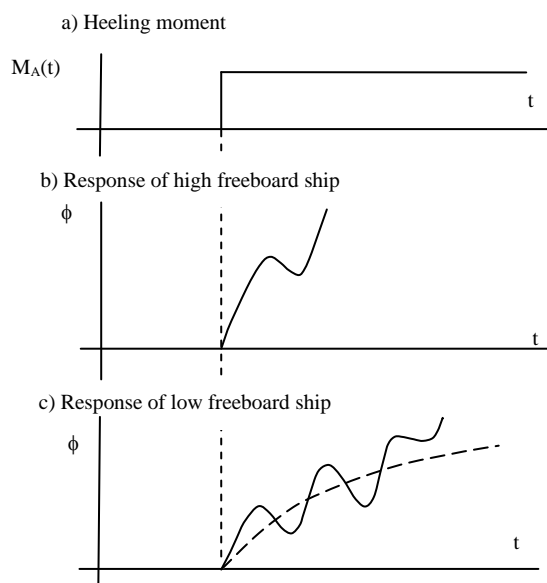


Figure 3: Difference in Response to a Sudden Wind Gust (Belenky & Sevastianov, 2007).

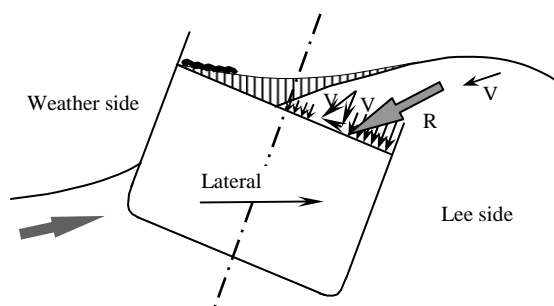


Figure 4: Hydrodynamic Reaction on Submerged Part of the Deck (Grochowalski, *et al.*, 1998).

Water on the deck is not only a modeling issue, but raises the question of consistency because water on deck / deck-in-water considerations are not included in the vulnerability criteria development at this time. One possible solution is to consider inclusion of these effects only when they are not dominating factors in the dynamics of heeling and capsizing in dead-ship conditions. The literature on stability in dead ship conditions is quite comprehensive, with the most recent review on this topic available from Ogawa, *et al.* (2008).

4. VALIDATION OF NUMERICAL TOOLS

In general, the problem of validation of numerical tools is not new. A standard already exists for numerical fluid dynamics (ASME, 2009). However, the field of dynamic stability is much wider, because it includes fluid dynamics and rigid body dynamics, as well as statistical problems.

Possible regulatory use of software for numerical simulation of ship motions makes the validation problem even more difficult. The first question to ask is if the ship motion software reproduces the physical phenomenon “responsible” for a particular stability failure. Thus, the first step is a qualitative validation.

Qualitative validation can be seen as a series of test runs of simulation software for a formal proof that a particular physical phenomenon is actually modeled. For example, from the preceding discussion, it is evident that a tool based on the mathematical model of linear roll is inadmissible for direct stability assessment. Then, how does one demonstrate that roll nonlinearity is actually present in the code? The answer can be found in the application of the methods of nonlinear dynamics. Figure 5 shows a response curve (calculated with Large Amplitude Motion Program - LAMP), compared with a simple 1 DOF-roll equation.

Qualitative validation requires showing that the numerical code is capable of reproducing known nonlinear effects, *i.e.*, demonstrates the “proper nonlinearity.” The example from Shin, *et al.* (2003) includes a calculation of the response curve with LAMP. Calculations are done for a series of regular waves of the same height with systematically changing frequencies. Simulations are run until the steady-state mode is achieved. Then the frequency is slightly changed, while the initial conditions are taken from the steady-state mode of the previous run. There are two series of such runs: from the lower frequencies to the

higher and back to the lower. The expected known nonlinear behavior is a hysteresis effect; which results in the existence of a frequency range with two stable solutions. The ability of the code to reproduce this effect is especially important because the same effect was observed experimentally (Francescutto, *et al.*, 1994).

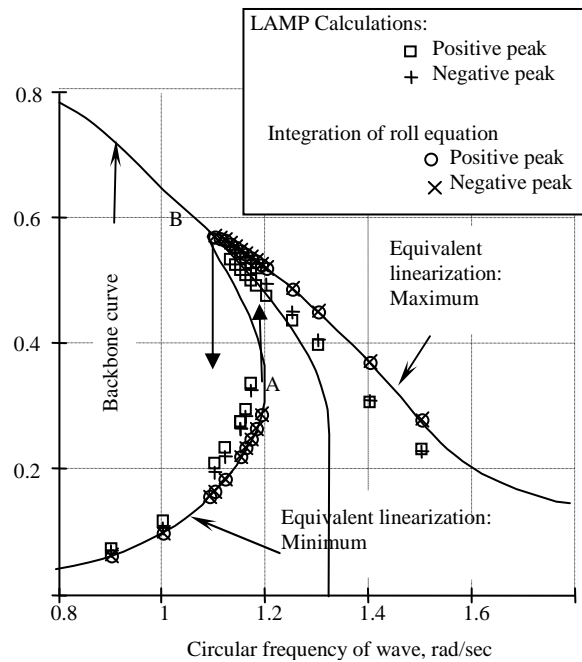


Figure 5: Response Curve of Roll based on LAMP Calculation, Numerical Integration of Nonlinear Roll Equation and Equivalent Linearization (Shin, *et al.*, 2003).

The hysteresis effect in roll motions is associated with fold bifurcation. Motion stability analysis can be used for further proof that observed hysteresis is, indeed, fold bifurcation, for which motion stability analysis shows that the eigenvalues of the Jacobean leave the unit circle in a positive direction (See Figure 6a).

$$J = \begin{pmatrix} \frac{\partial \phi(t_0 + T)}{\partial \phi(t_0)} & \frac{\partial \phi(t_0 + T)}{\partial \dot{\phi}(t_0)} \\ \frac{\partial \dot{\phi}(t_0 + T)}{\partial \phi(t_0)} & \frac{\partial \dot{\phi}(t_0 + T)}{\partial \dot{\phi}(t_0)} \end{pmatrix} \quad (6)$$

here ϕ is the roll angle, the dot above the symbol means a temporal derivative, T stands



for the period of steady-state-roll motions, t_0 is the initial instant in time for determining motion stability.

Computation of the Jacobean consists of a series of short simulations starting at t_0 when the motion, or its derivative, is given a small perturbation (on the order of a quarter or half a degree). Then, the simulation is carried out for one period. The value of the motion displacement is recovered and used to evaluate the derivatives in Equation (6). From this the eigenvalues of the Jacobean can be computed. The above eigenvalues calculations are repeated for each frequency. Comparing the tendency of eigenvalues based on a LAMP solution (Figure 6b) with a theoretical plot (Figure 6a), one can see that they are similar, i.e., do not contradict each other.

The eigenvalues from the numerical simulation cannot reach the axis, as on the theoretical plot because the numerical simulation can only reproduce a stable solution. A similar picture can be seen in Figure 6c where the same method is applied to the ordinary differential equation that describes roll motions.

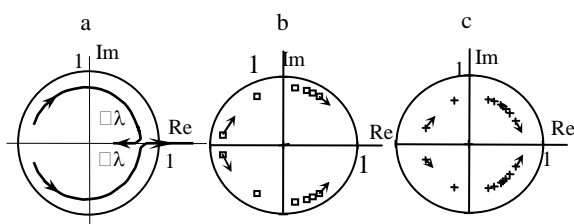


Figure 6: Eigenvalues of Jacobean Matrix for (a) LAMP Calculation, (b) Nonlinear Roll Equation (c) Theoretical (Shin, *et al.*, 2003).

In general, most of methods of ODE analysis seem to be applicable to the hydrodynamic codes. Spyrou, *et al.* (2009) demonstrated that the continuation method can be used together with LAMP and even find unstable equilibria. Therefore, more interesting results can be expected from “merging” nonlinear dynamics with numerical hydrodynamics.

Available techniques allow a comprehensive qualitative analysis of ship-motion simulation software. Annex 21 of SLF 54/INF.12 contains a table that summarizes these possibilities, and is reproduced here in Table 1 for easy reference. The second row in that table contains requirement for the analysis that was shown in Figures 5 and 6 as an example. Unfortunately, providing sample analyses for other lines in Table 1 is not within the scope of this paper.

The next validation step is a quantitative validation, and the question to be answered is, “How well are the forces modeled?” Belknap, *et al.* (2011) addressed key challenges in this area. One of the challenges is formulating metrics or an acceptance criterion (*e.g.*, how much difference is still acceptable?). A realistic approach to this problem, however, shows that a numerical tool has to be valid only for the particular problem for which it is intended to be used. This issue is considered in detail by Smith (2012). The concept of “intended use” allows limiting the scope of the validation problem to a more manageable size.

In addition to the force components, a numerical tool should reproduce a response reasonably close to the true values (assuming that a model test can provide such). There are two distinct problems to consider. The first is physical uncertainty (Belknap, *et al.*, 2011), the second is statistical uncertainty, which is relevant to irregular waves (Smith, 2011, 2012).

The problem physical uncertainty is addressed by comparisons between the characteristics of roll motions in regular waves. Annex 21 of SLF 54/INF.12 proposes considering the response curves for synchronous and parametric resonance. The acceptance criteria can be based on amplitude for synchronous resonance, and on both amplitude and frequency for parametric resonance. Accounting for significant nonlinearity by relaxing accuracy requirements for large amplitudes makes sense.



Table 1: Possible Requirements for Qualitative Validation

Item	Required for:	Objective:	Acceptance criteria:
Periodic Properties of Roll Oscillator	software where hydrostatic and Froude-Krylov forces are calculated with body exact formulation.	demonstration of consistency between calculated roll backbone curve (dependence of roll frequency in calm water on initial roll amplitude) and GZ curve in calm water.	shape of calculated backbone curve. The backbone curve must follow the trend of instantaneous GM with increasing heel angle
Response Curve of Roll Oscillator	software where hydrostatic and Froude-Krylov forces are calculated with body exact formulation.	demonstration of consistency between the calculated roll backbone curve and the calculated roll response curve (dependence of amplitude of excited roll motion on the frequency of excitation)	shape of the roll response curve. The roll response curve must “fold around” the backbone curve and show hysteresis when magnitude of excitation is increased
Change of Stability in Waves	software where hydrostatic and Froude-Krylov forces are calculated with body exact formulation. Additional capability to track the instantaneous GZ curve in waves may be required.	demonstration of capability to reproduce wave pass effect.	decrease of stability when the wave crests is located around midship section (within the quarter of length) and increase when the wave trough is located around midship section (within the quarter of length)
Principal Parametric Resonance	software where hydrostatic and Froude-Krylov forces are calculated with a body exact formulation	demonstration of capability to reproduce principal parametric resonance	observing increase and stabilization of amplitude of roll oscillation in exact following or head seas when encounter frequency is about twice of natural roll frequency.
Surf-riding Equilibrium	software for numerical simulation of surf-riding and broaching.	demonstrate capability to reproduce surf-riding; & turn off yaw motions.	observing sailing with the speed equal to wave celerity when the propeller RPM is set for the speed in calm water is less than the wave celerity. Center of gravity is expected to be located near wave trough
Heel during Turn	software for numerical simulation of surf-riding and broaching.	demonstrate capability to reproduce heel caused by turn	observing development of heel angle during the turn.
Turn in Waves	software for numerical simulation of surf-riding and broaching	demonstrate correct modeling of maneuvering forces in waves	same direction of drift that was observed in a model test
Heel caused by Drift and Wind	software for numerical simulation of ship motions in dead ship condition	demonstrate capability to reproduce heel caused by a moment created by aerodynamic load and drag caused by drift	observed slowly developed heel angle after applying aerodynamic load



Turning and zig-zag maneuvers in calm water may be used as a background for validation of horizontal-plane motions.

Wave conditions (height and length) and ship speed, where broaching is observed, provides another basis for comparison.

Statistical uncertainty is encountered when carrying out validation in irregular waves. In this case two random variables must be compared. Smith (2011, 2012) describes a number of statistical tests that may be used to judge the validity of the numerical tools under consideration.

5. PROCEDURES

Validated numerical tools are necessary, but not sufficient by themselves to complete a direct- stability assessment. There should be a prescribed procedure of applications of the tools, and following such a procedure, multiple applications should reach the same conclusions on the subject vessel. Obviously, the procedure should prescribe how to choose loading and environmental conditions. Beyond the choice of input parameters, the procedure can be seen as instructions on “how to get there from here”. The following objectives of the procedure are formulated in Annex 21 of SLF 54/INF.12:

- Confirmation of the vulnerability to a particular mode of stability failure, established with Level 2 vulnerability criteria.
- Evaluation of the safety level and showing the adequacy of the assessment if the likelihood of stability failure for that failure mode is acceptable.
- Development ship-specific operational guidance, if necessary.

The measure of likelihood of stability failure is one of the main results of direct-

stability assessment. The long-term-averaged rate of failure events (λ_a), one of the best candidates for this measure, was proposed by Sevastianov (1963). (For an English version see Sevastianov, 1994; or Belenky & Sevastianov, 2007). There are several important properties of this value that are briefly reviewed below.

The long-term-averaged rate of events is related with a life-time probability of failure as

$$P(T_L) = \exp(-\lambda_a T_L) \quad (7)$$

where T_L is the expected life time of a vessel. In principle this allows comparison of the estimated probability of failure with the achieved safety level. The latter can be evaluated using the same direct stability assessment procedure on an older vessel with a good stability-safety record. The long-term-averaged rate of events is expressed as:

$$\lambda_a = \sum_i W_i \lambda_i \quad (8)$$

here, λ_i is the rate of events (stability failures) in a particular hypothetical situation characterized by a given sea state, and ship speed and heading; and W_i is a statistical weight corresponding to a life-time exposure to such conditions. Determining the sources of data for the statistical weights also is the part of the procedure. Usually data of this type are obtainable from operational statistics of a prototype. An additional advantage of this approach is that the probability (7) can be re-evaluated if the mode of operation changes in the future.

In principle, the rate of events, λ_i , can be estimated simply by direct counting of large roll angles or capsizes during the numerical simulations. However, because of the rarity of stability failures and the complexity of using numerical tools, direct counting is not very practical. This problem is already recognized



in various IMO documents as the “problem of rarity” (Belenky, *et al.*, 2008).

A solution of the problem of rarity is sought by the application of special extrapolation methods to the output of numerical simulations, which produce the rate of events, λ_i . These methods can take into account extreme nonlinearities of the intact-stability problem. A state-of-the-art review of these special extrapolation methods can be found in (Belenky, *et al.*, 2012).

Although these methods are based on physical considerations of the mechanisms of stability failures, they are not free from assumptions and therefore must be validated. Validation of the extrapolation methods also presents a challenge because of the same problem of rarity.

How can an extrapolation method be validated in principle? Extrapolation methods require several hours of numerical simulations of ship motions to predict a probability of stability failure with the average time of occurrence much longer than the simulation time. If a large statistical sample (with a sufficient number of stability failures) is available, a portion of the statistical sample can be used to run the extrapolation method, and then the results can be compared with direct counting. However, producing a data sample of such a large size may be neither possible nor practical because of the “problem of rarity” and the computational cost associated with it.

There are two approaches to solve this problem: the first is to use more severe conditions and the second is to use a less complex mode. In the first approach, a validated model is used to produce a large data sample can be produced under conditions that are more severe than normal conditions. Thus the stability failures may become more frequent and computational costs will be reduced to a more manageable level. This method is used in reliability engineering, *e.g.*, when the reliability of an electronic component

is tested using temperatures much higher than the normal operating temperatures. Then the data which have been obtained are recalculated for normal operating conditions (Meeker & Escobar, 1998).

In the second approach, the “problem of rarity” is resolved by using less complex models of ship motions. Such models must possess all of the primary qualitative similarities of the validated numerical tool, but may be significantly less accurate. If the computational costs of running the reduced-complexity model are reasonably low, an extrapolation method can be validated under more or less realistic conditions.

6. CONCLUSIONS

Direct-stability assessment is intended the third tier of the second-generation IMO intact stability criteria under development. Although it is to be the newest state-of-the-art stability-assessment method, its use is envisioned only in exceptional cases of novel and unconventional ship designs. Notwithstanding the above, the maritime industry has experience with the application of advanced numerical methods in the regulatory and classification framework, *i.e.*, finite element analysis of ship structures.

Successful application of direct-stability assessment within the regulatory framework requires addressing the following issues: 1) requirements for numerical tools, 2) validation of numerical tools, 3) extrapolation procedures, 4) validation of extrapolation procedures.

Based on the current state-of-the-art of numerical hydrodynamics, it seems that hybrid codes represent the best combination of fidelity and performance. However, numerical tools based on a system of ordinary differential equations are also useful for more complex problems related to stability failures due to broaching-to. In general, the requirement for a tool should be specific to the mode of stability



failure. Requirements for validation of numerical tools are also dependent on the mode of stability failure and consist of both qualitative and quantitative validation.

The way in which the procedures are applied is an important part of direct-stability assessment process because it prescribes the origin of the input, the post-processing methodology and the interpretation of output. It is also necessary to include extrapolation procedures to handle the “problem or rarity”. Extrapolation procedures must also be validated.

7. ACKNOWLEDGMENTS

The authors are grateful to the following colleagues for their fruitful discussions and helpful comments: W. Belknap, B. Campbell, and T. Smith (David Taylor Model Basin, NSWCDD); K. Weems (SAIC); K. Spyrou (National Technical University of Athens); and N. Umeda (Osaka University).

The authors are grateful to Ms. Suzanne Reed for her detailed editing that has greatly improved clarity and readability of the text.

8. REFERENCES

- ABS (2004a) “Guide for the Assessment of Parametric Roll Resonance in the Design of Container Carriers.” American Bureau of Shipping, Houston, TX, 70 p.
- ABS (2004b) “Guidance Notes on Safehull Finite Element Analysis of Hull Structures.” American Bureau of Shipping, Houston, TX, 52 p.
- ASME, (2009) “Standard for Verification and Validation in Computational Fluid Dynamics and Heat Transfer.” V V 20 2009, Amer. Soc. Mech. Engin., New York.
- Beck, R. F. & A. M. Reed, (2001). Modern computational methods for ships in seaway. Trans. SNAME, 109:1–48.
- Belenky, V. L. (2011) “On Self-Repeating Effect in Reconstruction of Irregular Waves” in Contemporary Ideas on Ship Stability, Neves, M. A. S., *et al.* (eds), Springer, pp. 589–598.
- Belenky V., J. O. de Kat & N. Umeda (2008) “Towards Performance-Based Criteria for Intact Stability.” Marine Tech., 45(2):101–123.
- Belenky, V. L., D. Liut, K. M. Weems & Y. S. Shin (2003) Nonlinear roll with water-on-deck: numerical approach, Proc. 8th Int’l Conf. Stability of Ships & Ocean Vehicles (STAB ’03), Madrid, Spain.
- Belenky, V. L & N. B. Sevastianov (2007) Stability and Safety of Ships: Risk of Capsizing. (2nd ed) SNAME, Jersey City.
- Belenky, V. & K. M. Weems (2011), “Probabilistic Properties of Parametric Roll.” Chapter 6 of Parametric Resonance in Dynamical Systems, Fossen, T. I. & H. Nijmeijer (Eds.) Springer, NY.
- Belenky, V., K. M. Weems, C. C. Bassler, M. J. Dipper, B. Campbell & K. Spyrou (2012) “Approaches to Rare Events in Stochastic Dynamics of Ships.” Probabilistic Engineering Mechanics, 28:30–38.
- Belenky, V., K. M. Weems, W. M. Lin & J. R. Paulling (2011a) Probabilistic Analysis of Roll Parametric Resonance in Head Seas Contemporary Ideas on Ship Stability, Neves, M. A. S., *et al.* (eds), Springer, pp. 555–572
- Belenky, V., H. Yu & K. M. Weems (2011b) “Numerical Procedures and Practical Experience of Assessment of Parametric Roll of Container Carriers.” in Contemporary Ideas on Ship Stability, Neves, M. A. S., *et al.* (eds), Springer, pp. 295–305.
- Brunswig, J. & R. Pereira (2006) Validation of Parametric Roll Motion Predictions for a Modern Containership Design. Proc. 9th Int’l Conf. Stability Ships & Ocean Vehicles (STAB ’06), Vol. 1, Rio de Janeiro, Brazil, pp. 157–168.
- Belknap, W. F. & A. M. Reed (2010) TEMPEST — A New Computationally



- Efficient Dynamic Stability Prediction Tool. Proc. 11th Int'l Ship Stability Workshop, Wageningen, the Netherlands, pp. 185–197.
- Belknap, W. F., T. C. Smith & B. Campbell (2011) Addressing Challenges in the Validation of Dynamic Stability Simulation Tools, Proc. 12th Int'l Ship Stability Workshop, Washington, DC, USA, pp. 81–90.
- Degtyarev A. B. & I. Gankevich (2012) Evaluation of Hydrodynamic Pressures for Autoregression Model of Irregular Waves, Proc. 11th Int'l Conf. Stability of Ships & Ocean Vehicles (STAB '12), Athens, Greece.
- Degtyarev, A. B. & A. M. Reed (2011) Modeling of Incident Waves near the Ship's Hull (Application of Autoregressive Approach in Problems of Simulation of Rough Seas) Proc. 12th Int'l Ship Stability Workshop, Washington, D.C., pp 175–188.
- France, W. M., M. Levadou, T. W. Treacle, J. R. Paulling, K. Michel & C. Moore (2003). An Investigation of Head-Sea Parametric Rolling and its Influence on Container Lashing Systems, Marine Tech., 40(1):1–19.
- Francescutto, A., G. Contento & R. Penna (1994) Experimental Evidence of Strong Nonlinear Effects in the Rolling Motion of the Destroyer in Beam Seas, Proc. 5th Int'l Conf. Stability of Ships and Ocean Vehicles (STAB '94), Vol. 1, Melbourne, Florida, USA.
- Grochowalski, S., C. C. Hsiung, Z. J. Huang & L. Z. Cong (1998). Theoretical Modelling of Ship Motions and Capsizing in Large and Steep Waves Trans. SNAME, 106:241–267.
- IMO MSC.1/Circ.1227 (2007) Explanatory Notes to the Interim Guidelines for Alternative Assessment of the Weather Criterion, London, UK, 23 p
- IMO SLF 53/3/8 (2010) “Comments on Proposed Criteria for Surf-riding and Broaching.” submitted by Japan and the United States, London, 2010
- IMO SLF 54/INF.12 (2011) Information Collected by the Correspondence Group on Intact Stability, Submitted by Japan, London, UK, 147 p.
- Meeker, W. O. & L. A. Escobar (1998) Statistical Methods for Reliability Data. Wiley, New York, 680 p.
- Ogawa, Y., N. Umeda, D. Paroka, H. Taguchi, S. Ishida, A. Matsuda, H. Hashimoto & G. Bulian (2008) “Prediction Methods for Capsizing under Dead Ship Condition and Obtained Safety Level — Final Report of SCAPE Committee (Part 4)”, Proc. Osaka Colloquium on Seakeeping and Stability of Ships, Osaka, Japan, pp. 253–265
- Peters, W., V. Belenky, C. Bassler, K. Spyrou, N. Umeda, G. Bulian & B. Altmayer (2011) “The Second Generation of Intact Stability Criteria An Overview of Development.” Trans SNAME, Vol. 119.
- Rahola, J. (1939) “The Judging of the Stability of Ships and the Determination of the Minimum Amount of Stability Especially Considering the Vessel Navigating Finnish Waters.” PhD Thesis, Technical University of Finland, Helsinki, viii+232 p.
- Reed, A. M. (2008) Discussion of: Belenky, V., J. O. de Kat & N. Umeda (2008) “Towards Performance-Based Criteria for Intact Stability.” Marine Tech., 45(2):122–123.
- Reed, A. M. (2009) A Naval Perspective on Ship stability, Proc. 10th Int'l Conf. Stability of Ships & Ocean Vehicles (STAB '09), St. Petersburg, Russia, pp. 21–43.
- Reed, A. M. (2011) 26th ITTC Parametric Roll Benchmark Study, Proc. 12th Int'l Ship Stability Workshop, Washington DC, USA, pp. 195–204.
- Sadat-Hosseini, H., P. Carrica, F. Stern, N. Umeda, H. Hashimoto, S. Yamamura & A. Mastuda (2011) CFD, system-based and EFD study of ship dynamic instability events: Surf-riding, periodic motion, and broaching. Ocean Engineering, 38:88–110.
- Shigunov, V. (2009) Operational Guidance for Prevention of Container Loss. Proc. 10th Int'l Conf. Stability of Ships & Ocean



- Vehicles (STAB '09), St. Petersburg, Russia, pp. 473–482.
- Shin, Y. S., V. L. Belenky, W. M. Lin, K. M. Weems & A. H. Engle (2003) “Nonlinear time domain simulation technology for sea-keeping and wave-load analysis for modern ship design.” Trans SNAME, 111:557–578.
- Smith, T. C. (2011) Statistical Data Set Comparison for Continuous, Dependent Data, Proc. 12th Int’l Ship Stability Workshop, Washington, DC, USA pp. 75–80.
- Smith, T. C. (2012) Approaches to Ship Motion Simulation Acceptance Criteria, Proc. 11th Int’l Conf. Stability of Ships & Ocean Vehicles (STAB '12), Athens, Greece.
- Sevastianov, N. B. (1963). “On probabilistic approach to stability standards.” Trans. Kaliningrad Institute of Technology, 18:3–12. (in Russian)
- Sevastianov, N. B. (1994). “An algorithm of probabilistic stability assessment and standards” Proc. 5th Int’l Conf. Stability of Ships & Ocean Vehicles (STAB '94), Vol. 5, Melbourne, Florida, USA
- Spyrou, K. (1996). “Dynamic instability in quartering seas: the behaviour of a ship during broaching.” J. Ship Research, 40(1):46–59.
- Spyrou, K., K. Weems & V. Belenky (2009) Patterns of Surf-Riding and Broaching-to Captured by Advanced Hydrodynamic Modeling Proc. 10th Int’l Conf. Stability of Ships & Ocean Vehicles, St. Petersburg, Russia.
- Themelis, N. & K. J. Spyrou (2007) Probabilistic Assessment of Ship Stability. Trans. SNAME, 117:181–206.
- Umeda, N., S. Koga, J. Ueda, E. Maeda, I. Tsukamoto & D. Paroka (2007) Methodology for Calculating Capsizing Probability for a Ship under Dead Ship Condition, Proc. 9th Int’l Ship Stability Workshop, Hamburg, pp. 1.2.1–1.2.19
- Umeda, N. & M. R. Renilson (1992). “Broaching — a dynamic behaviour of a vessel in following and quartering seas.” in Manoeuvring and Control of Marine Craft, Wilson, P. A. (editor), Computational Mechanics Publication, Southampton, pp. 533–543.
- Umeda, N. & Y. Yamakoshi (1993). Probability of Ship Capsizing Due to Pure Loss of Stability in Irregular Quartering Seas, Naval Architecture and Ocean Engineering, Vol. 30.
- Yen T. G., S. Zhang, K. Weems & W-M. Lin (2010) Development and Validation of Numerical Simulations for Ship Maneuvering in Calm Water and in Waves, Proc. 28th Symp. Naval Hydro., Pasadena, California.



Test Application of Second Generation IMO Intact Stability Criteria on a Large Sample of Ships

Clève Wandji, *Bureau Veritas*, cleve.wandji@bureauveritas.com

Philippe Corrigan, *Bureau Veritas*, philippe.corrigan@bureauveritas.com

ABSTRACT

This paper describes the application of level 1 and level 2 vulnerability criteria, as outlined in the current state of development, by the International Maritime Organisation (IMO), of the second generation of intact stability criteria. In order to understand the functionality of the proposed level 1 and 2 criteria for problems related to righting lever variation (pure loss of stability and parametric roll) and surf-riding, numerical tools have been developed and tested on a large number of ships, covering a wide range of ship type, size and speed. In addition, an investigation has been started to identify groups of ships/ship characteristics which appear to be particularly vulnerable to the stability failure modes, according to these criteria. Comments on the applicability of these criteria from a regulatory/approval perspective, are presented.

Keywords: *dynamic stability, vulnerability criteria, pure loss of stability, parametric roll, surf-riding/broaching*

1. INTRODUCTION

The first part of the long work undertaken for the revision of the IMO Intact Stability Code in 2001 with the establishment of an ad-hoc Working Group (ISWG) operating during the Sessions of the Sub-Committee on Stability, Load Lines and on Fishing Vessel Safety (SLF) and intersessionally between them, has been completed in 2008 (Francescutto & Umeda 2010). This part of the ISWG activity was mostly devoted to restructuring the previous Intact Stability Code (IMO Res. A.749(18)) in several parts and making Part A of the new "International Code on Intact Stability, 2008 (2008 IS Code)" (IMO, 2009) mandatory under the provisions of both SOLAS and ILLC Conventions. Notwithstanding the importance of this work, the most important part of the initial scope of the revision, i.e. the formulation and implementation of a second generation performance-based intact stability criteria is still under development (Bulian et al. 2009).

The scope of second generation intact stability criteria is to provide methods to assess

ships which may be vulnerable to particular failures modes not adequately assessed by the existing criteria. For this it was decided that the following four dangerous situations (called "failure modes") should be individually addressed:

- Righting lever variation: any ship exhibiting large righting lever variations between wave crest conditions may experience parametric roll, or pure loss of stability.
- Resonant roll in dead ship condition: ship without propulsion or steering ability may be endangered by resonant roll while drifting freely.
- Broaching and other manoeuvring related phenomena: ship in following and quartering seas may not be able to keep constant course despite maximum steering efforts, which may lead to extreme heel angles.
- Excessive accelerations: any ship, having a large metacentric height may experience excessive accelerations.

The second generation intact stability criteria are based on a multi-tiered assessment approach structured in three levels: vulnerability



first level, vulnerability second level, direct assessment. Specific Operational Guidelines should be developed, in the acknowledgement that not all dangerous situations can be avoided only by design prescriptions, and this is an expected outcome of the direct assessment. For each ship the level $i+1$ assessment is performed only if the level i fails (Francescutto & Umeda 2010).

Hard work was done intersessionally between SLF51, SLF52, SLF53 and SLF54 with the active participation of many delegations. As a result, several methodologies have been submitted. During SLF 54 session in January 2012, significant work was done to harmonize draft vulnerability criteria of level 1 and 2 for some failure modes (parametric roll, pure loss of stability and surf-riding/broaching). The next sections of this paper describe briefly the development of numerical tools for the calculation of level 1 and level 2 criteria for these failure modes, their application to a large number of ships, an investigation of ships types/ships characteristics that appear to be vulnerable to stability failure modes and, finally, some comments on the applicability of these criteria from a regulatory/approval perspective.

2. SAMPLE SHIPS POPULATION

This study is performed on 36 ships of different characteristics and types with length between 20.35 and 349.5 meters; their main particulars are given in table 1. This sample population has been examined using the proposed methods for vulnerability assessment (levels 1 and 2), for three of the identified intact stability failure modes (parametric roll, pure loss of stability and broaching). Only three ships of this sample were used to perform the level 2 vulnerability criterion for surf-riding and broaching due to the lack of information regarding propulsion and resistance data. 28 ships (i.e. 75%) in this population are existing ships, with well-defined geometry and load case. The remaining 8 samples are vessels made available in the correspondence group (ISCG), and for

some of these ships, it is known to what stability failure mode they are vulnerable.

Table1: Ship types and general characteristics

Ship type	L/B	B/T	C _B
Military 1	7.979	3.418	0.535
Military 2	7.450	3.099	0.507
Fishing vessel 1	4.539	3.040	0.597
Fishing vessel 2	5.406	2.156	0.470
Fishing vessel 3	2.891	2.347	0.560
General cargo 1	7.007	2.496	0.700
General cargo 2	5.083	3.579	0.785
Chemical Tanker 1	5.686	2.550	0.760
Chemical Tanker 2	5.677	3.263	0.756
Tanker 1	4.891	2.875	0.893
Tanker 2	5.700	2.597	0.799
Tanker 3	6.429	2.333	0.771
Tanker 4	5.371	2.255	0.772
Containership 1	6.550	3.118	0.562
Containership 2	5.515	3.200	0.667
Containership 3	9.167	2.913	0.554
Containership 4	6.826	3.303	0.699
Containership 5	6.084	3.079	0.607
Containership 6	5.846	2.957	0.666
Containership 7	7.046	3.078	0.697
Containership 8	6.142	2.745	0.635
Containership 9	8.261	2.382	0.652
Containership 10	7.000	2.400	0.635
Passenger ship 1	6.627	4.237	0.658
Passenger ship 2	7.011	3.750	0.628
Ropax 1	5.590	4.391	0.628
Ropax 2	5.659	4.300	0.553
Ropax 3	5.316	4.537	0.572
Ropax 4	5.511	4.296	0.582
Ropax 5	5.680	3.745	0.635
Supply 1	4.288	3.000	0.758
Bulk carrier 1	6.727	2.272	0.846
Bulk carrier 2	6.267	2.727	0.880
Bulk carrier 3	6.143	2.726	0.800
LNG Carrier 1	6.323	3.440	0.750
LNG Carrier 2	6.355	2.406	0.742

In the following these acronyms will be used for each group of ships: M for military



ship, FS for fishing vessel, GC for general cargo ship, CT for chemical tanker, T for tanker ship, CS for containership, PS for passenger ship, RP for Ropax vessel, S for supply vessel, BC for bulk carrier and LNG for LNG carrier.

3. PARAMETRIC ROLL

Let's assume that a ship is sailing exactly in longitudinal regular waves. Once she reaches the wave crest, if a transverse heeling moment is applied, this causes an initial roll angle and/or roll velocity. When the ship is at the position "wave crest amidships", her stability is decreased. As the restoring moment is less, the ship will roll further than she would in calm water. When the wave trough reaches the midship, the stability increases. The larger restoring moment means a larger acceleration and the ship returns to zero angle with the velocity larger than she would in calm water (Belenky and Sevastianov 2007).

Environmental conditions. In this work we used the Japanese environment proposal because the proposal takes into account the ship size and the proposal is complete i.e. the levels 1 and 2 environmental conditions for vulnerability criteria of parametric roll and pure loss of stability are given. A brief description of the proposal is given below.

After selecting a wave scatter diagram (e.g. IACS Rec.34) the effective significant wave height ($H_{1/3}^{eff}$) for all stationary sea states defined by period of zero crossing (T_z) and significant wave height (H_s) presented in the scatter diagram are computed as a function of the ship length. The effect of ship size is taken into account by using the Grim's effective significant wave concept and the ITTC spectrum (ISCG 2012).

The level 1 vulnerability calculations for parametric roll are carried out by using the following conservative value for the wave steepness parameter: for the wave height by using

the maximum effective significant wave height and for wave length by using ship length between perpendiculars.

The level 2 vulnerability calculations for parametric roll are carried out by using the following wave height: for each period of zero crossing of the scatter diagram, by using the maximum effective significant wave height if lower than 10% of the ship length; otherwise the wave height is set to 10% of the ship length.

3.1 Level 1 vulnerability criteria

Short description of the criterion. The criterion is based on simplified formulation of the GM variation in wave. Therefore only the difference between the waterline area moments of inertia in wave crest and trough conditions in simplified form is calculated. The moment of inertia for the wave crest condition is calculated with a horizontal water line positioned at the height equal to the lowest draught of the wave condition. The moment of inertia for the wave trough condition is calculated with a horizontal water line at the height equal to the highest draught of the wave condition. If the ship has tumblehome topside, the variation of metacentric height is to be calculated with the true water line (sinusoidal water line) i.e. considering that the ship is situated on a wave.

If the ratio of GM variation to GM in calm water is greater than 0.34, the vessel is considered vulnerable to parametric roll. Note that the value of the standard is under definition in the correspondence group (ISCG), and the value of 0.34 used in this paper is the smallest value which would correspond to the ship without bilge keels.

Application and results. The criterion has been applied to the sample ships. In this work the GM and GZ evaluations in waves were performed using the USA simplified method described in the paper SLF 52/INF.2, annex 6. The area at each station and its moment relative



to the vertical axis are expressed as function of the local draft and taking into account sinkage and trim. Therefore, the local draft at each station comes from the formula, describing wave elevations along the hull, and depends on sinkage and trim. The wave profile along the ship hull is evaluated by satisfying equilibrium conditions. Once sinkage and trim are found, the wave profile is found and the moment of inertia of the waterplane and other hydrostatic terms are computed. Finally the value of GM in waves is computed as a function of the position of the wave crest.

The results of the level 1 vulnerability criterion assessment of the sample ships are presented in table 2.

All the bulk carriers were judged as non-vulnerable to parametric roll according, to this criterion. Four tankers in this group were found vulnerable (chemical tanker 2, tanker 4 and the two LNG carriers), although the expectation was to found this kind of vessel as conventional (non-vulnerable to the first level criterion). The biggest fishing vessel of this group (fishing vessel 2) was judged as non-vulnerable. Ten container vessels were investigated, and only one vessel was judged as non-vulnerable to parametric roll according to this criterion. All the passenger ships and Ropax were found to be vulnerable to parametric roll.

3.2 Level 2 vulnerability criteria

Short description of the criterion. The second level criterion consists of two checks. The first check requires calculations of GM variations for a series of waves. The value for the criterion is calculated as a weighted average of a binary condition obtained by GM variations from a set of specified waves (see SLF 54/WP.3 for more details). The weighting factors are obtained from a look-up table based on a scatter diagram. The ship is considered vulnerable to parametric roll if the criterion is greater than a threshold value.

If the ship was found to be vulnerable based on the first check, the second check is to be carried out. The second check is based on roll response in head or following waves evaluated for the range of operational ship speed. In absence of roll decay test data, roll damping may be modelled, using either simplified Ikeda's method or type-specific empirical data if appropriate. Calculation of stability in waves is expected to account for the influence of pitch and heave quasi statically. For the second check, in this work we used the Japanese method described in SLF 53/INF.10, annex 2. In this method the parametric roll amplitude is calculated using an averaging method which is applied on an uncoupled roll model. The amplitude of steady state parametric rolling can be obtained by solving a twelfth order algebraic equation.

Application and results. The criteria have been applied to all the ships of the sample. The damping coefficients were determined by Ikeda simplified method. Since no standard was proposed, the result of the containership 1 (C11 class containership) was used to set the standard, which was set to a threshold value of 0.4 for the first check, and for the second check the threshold was set to 25°. Results obtained for the two checks, as well as the value of the speed used for the calculations are given in table 2.

Table 2: Calculations results for the levels 1 and 2 vulnerability criteria for parametric roll

Ship type	V [kts]	GM [m]	Level 1 Δ GM/GM	Level 2 1 st check	Level 2 2 nd check
M 1	30.0	1.500	0.677	0.978	18
M 2	30.0	1.950	1.601	0.000	12
FS 1	18.0	1.000	0.946	1.000	22
FS 2	17.7	0.665	0.309	0.873	6
FS 3	10.0	0.520	1.575	0.976	19
GC 1	18.0	0.665	0.453	0.978	16
GC 2	12.0	1.298	0.512	0.873	13
CT 1	13.5	1.800	0.070	0.000	7
CT 2	15.0	3.345	0.393	0.000	9
T 1	15.0	5.624	0.047	0.000	4
T 2	14.0	1.912	0.175	0.966	8

T 3	15.0	3.137	0.168	0.000	7
T 4	13.0	0.552	0.578	0.941	22
CS 1	25.0	1.911	1.861	0.977	57
CS 2	23.0	1.010	2.084	1.000	45
CS 3	35.0	2.904	1.005	0.999	>60
CS 4	24.0	2.816	0.923	0.885	38
CS 5	19.0	0.829	0.183	0.977	29
CS 6	19.0	0.908	1.988	0.998	>60
CS 7	19.0	0.599	2.356	1.000	>60
CS 8	21.0	0.675	2.918	0.998	>60
CS 9	24.0	1.421	1.332	0.977	55
CS 10	23.0	0.755	2.506	0.998	>60
PS 1	20.0	1.910	2.169	0.998	55
PS 2	16.0	1.381	0.978	1.000	49
RP 1	15.0	1.540	2.981	1.000	>60
RP 2	20.0	3.647	1.363	1.000	>60
RP 3	24.0	3.651	1.558	0.998	55
RP 4	23.0	4.292	1.184	0.000	16
RP 5	15.0	1.313	1.840	1.000	37
S 1	13.0	2.464	0.261	0.987	13
BC 1	14.0	2.358	0.151	0.000	8
BC 2	14.0	4.734	0.079	0.000	11
BC 3	14.0	3.245	0.162	0.000	9
LNG 1	20.0	2.386	0.534	0.000	6
LNG 2	16.0	0.943	0.658	0.000	12

All the bulk carriers, tankers, fishing vessels, general cargo and the supply vessel were judged as non-vulnerable. All the container-ships were found to be vulnerable to parametric roll according to this criterion. For the supply vessel, containership 5, fishing vessel 2 and tanker 2, the result of the first check of the second level criterion contradicts the result of the first level criterion.

3.3 Conclusions

The results are consistent; all the ships found as to be non-vulnerable on the level 1 criterion as shown in figure 1, have been found as to be non-vulnerable for on the level 2, except for the containership 5. The levels 1 and 2 vulnerability criteria can separate a bulk carrier or a tanker from a containership (figure 1). In

this regard they reflect the general naval architects experience. It is interesting to note that, in the Ropax group, some vessels are vulnerable and others not. Vulnerability is not necessarily associated with a ship type.

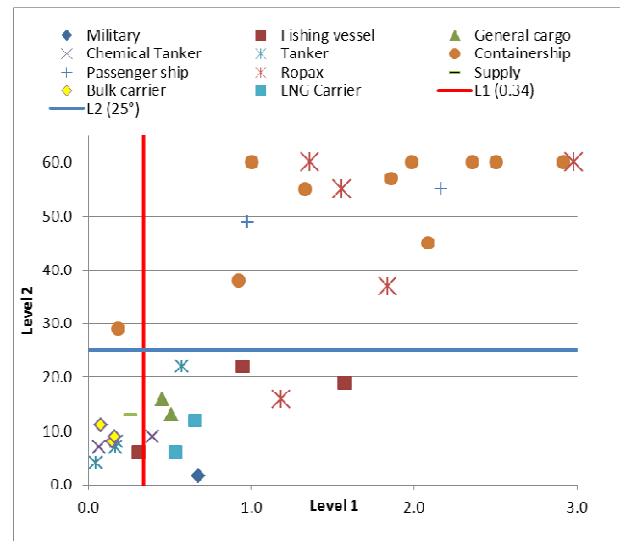


Figure 1: Levels 1 and 2 vulnerability criteria results for parametric roll

4. PURE LOSS OF STABILITY

As the roll restoring moment may be significantly decreased while the wave is located about the midship section, a vessel may suffer large roll angles or even capsize, if she spends long enough time in this situation of decreased stability; this phenomenon is known as pure loss of stability (Belenky and Sevastianov 2007).

Environmental conditions. The procedure to determine wave characteristics to use for the levels 1 and 2 vulnerability criteria for pure loss of stability is the same as that of parametric roll, except that instead of using the effective significant wave height, the effective 3% largest wave height is used in all calculations (ISCG 2012, to be submitted to SLF 55).



4.1 Level 1 vulnerability criteria

Short description of the criterion. The criterion will be applied only if the Froude number based on service speed exceeds 0.2. The criterion is based on an approximation of the minimum metacentric height in waves. It evaluates the stability on wave crest with the same simplification as for the level 1 criterion for parametric roll.

The ship is considered vulnerable to pure loss of stability if the minimum metacentric height is less than 0.05 m.

Application and results. The criterion was applied to the 36 sample ships. Results are shown for the two checks (speed and stability checks), together with the value of the Froude number used for the calculations in table 3.

All ships having service Froude number less than 0.2 were judged as non-vulnerable by the level 1 vulnerability criterion. Two tankers were judged as vulnerable (tanker 4 and LNG carrier 2). All the containerships, passenger ships, Ropax and fishing vessels were found to be vulnerable to pure loss of stability according to this criterion. This seems to result from large changes of the water-plane area for these ships. This latter result depends also to the level of the lower draught.

4.2 Level 2 vulnerability criteria

Short description of the criterion. The vulnerability check requires calculations of GZ curve variations for a series of waves. The GZ variations are evaluated with three criteria representing a weighted average from the specified waves. The first criterion compares the GM value calculated on wave with a critical value of GM; the second criterion calculates the loll angle and compares it with a standard, and the third criterion calculates the maximum of the GZ curve on wave and compares it with a standard (see SLF 54/WP.3 for more details).

The ship is considered vulnerable to pure loss of stability if the maximum of the three criteria is greater than a standard that is not defined yet by SLF.

Application and results. The criteria have been applied to the sample ships. The standard for the first criterion (critical GM) was set to 0.15 m (value of the minimum GM required in the IS 2008 code), the standard for the second criterion (critical loll angle) was set to 25°, and the standard for the third criterion (GZmax) was set to 0.05 m. Since no standard was proposed for the final criterion (maximum of three criteria), the result of the fishing vessel 1 (purse seiner) and military 1 (ONR tumblehome) were used to set the standard, which was set to a threshold value of 0.9. The results of the assessment are shown in table 3.

Table 3: Calculations results for the levels 1 and 2 vulnerability criteria for pure loss of stability

Ship type	Lpp [m]	F _n	Level1	Level2
M 1	150.00	0.402	-2.681	0.977
M 2	142.00	0.248	-2.308	0.000
FS 1	34.50	0.503	-1.225	1.000
FS 2	74.60	0.337	-1.113	0.000
FS 3	20.35	0.364	-0.542	0.000
GC 1	121.92	0.223	0.034	0.199
GC 2	69.12	0.237	0.285	0.962
CT 1	116.00	0.206	0.661	0.000
CT 2	176.00	0.188	1.043	0.000
T 1	225.00	0.164	1.058	0.000
T 2	114.00	0.215	1.229	0.966
T 3	180.00	0.184	2.415	0.000
T 4	99.90	0.225	-0.065	0.000
CS 1	262.00	0.252	-5.279	0.885
CS 2	150.00	0.308	-1.248	0.000
CS 3	275.00	0.228	-1.783	0.999
CS 4	349.50	0.211	-2.338	0.000
CS 5	142.37	0.266	-2.613	0.977
CS 6	159.00	0.247	-2.021	0.953
CS 7	167.00	0.251	-1.966	0.998
CS 8	185.50	0.259	-2.354	0.999

CS 9	266.00	0.242	-2.269	0.000
CS 10	210.00	0.261	-3.053	0.978
PS 1	213.40	0.225	-5.128	0.978
PS 2	126.20	0.234	-2.205	0.999
RP 1	135.00	0.297	-2.883	0.000
RP 2	146.00	0.272	-2.743	0.978
RP 3	161.60	0.310	-4.350	0.000
RP 4	168.10	0.303	-3.903	0.000
RP 5	117.00	0.228	-2.736	0.999
S 1	70.76	0.254	0.976	0.986
BC 1	217.00	0.162	1.525	0.000
BC 2	282.00	0.137	4.001	0.000
BC 3	172.00	0.182	2.015	0.000
LNG 1	274.10	0.203	0.284	0.000
LNG 2	146.80	0.218	-0.773	0.000

All the bulk carriers, LNG carriers were judged as non-vulnerable. In the group of tankers, one vessel was found to be vulnerable (tanker 2). This criterion confirms the vulnerability of Military 1 and fishing vessel 1, which are two ships known for their vulnerability to pure loss of stability (Hashimoto 2009). 40% of the containerships were judged as non-vulnerable to pure loss of stability according to this criterion.

4.3 Conclusions

More vessels were judged as non-vulnerable to the second level criterion than to the first level criterion. But some contradictions remain; the results of general cargo 2, tanker 2 and the supply vessel contradict the outcome of the first level assessments as shown in figure 2. These differences could be explained by the value of the critical GM which was set to 0.15 m for all the vessels (may be this value is too high), because in these three cases the maximum of the three criteria were given, by the outcome of the first criterion (critical GM). One should note that the GZ curve was calculated with a simplified method, and this approximation seems to be more conservative than the real GZ curve in waves (SLF 52/INF.2 Annex 6). This fact could also ex-

plain the observed inconsistency for the three vessels above. Bulk carrier could clearly be classified as a conventional vessel regarding pure loss of stability according to the results of these criteria.

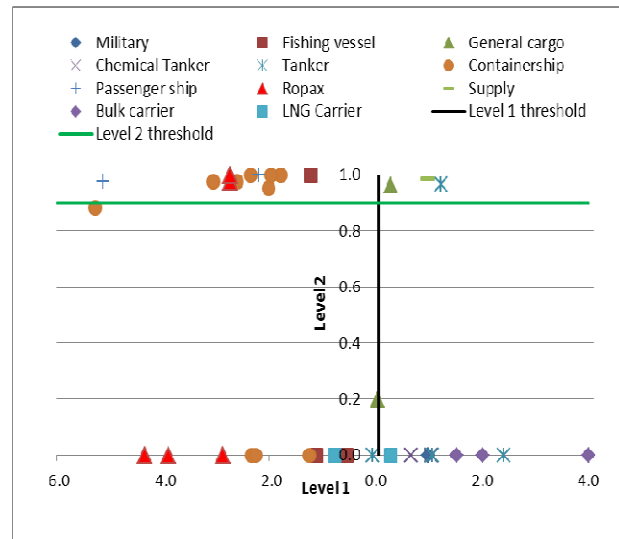


Figure 2: Levels 1 and 2 vulnerability criteria results for pure loss of stability

5. SURF-RIDING AND BROACHING

Surf-riding is a phenomenon where a ship is captured by a wave and is forced to run with it. This phenomenon occasionally occurs when a ship runs in following to quartering seas with relatively high forward speed. Once surf-riding occurs, a ship may be involved in violent uncontrollable turn despite of maximum steering effort, known as broaching-to, and the centrifugal forces due to broaching-to may lead to stability failure.

5.1 Level 1 vulnerability criteria

Short description of the criterion. The criterion is based on a phase analysis of uncoupled surging motions that leads to a condition on the ship speed (SLF 53 /INF.10 Annex 5); in order to reflect the ship dimension, an additional condition referring to ship length is introduced. The ship is considered vulnerable if her length between perpendiculars is smaller than 200 m



and her operational Froude number is larger than 0.3.

Application and results. The criteria were applied to the sample ships. Results are shown together with the value of the operational Froude number in table 4.

The two military ships, the three fishing vessels, one containership (containership 2) and two Ropax vessels (Ropax 3 and 4) were found to be vulnerable to surf-riding and broaching according to this criterion.

5.2 Level 2 vulnerability criteria

Short description of the criterion. The vulnerability to surf-riding is measured by the percentage of waves capable of generating surf-riding equilibria. The irregular seaway is modelled as a sequence of sinusoidal waves with random amplitude and length. For each wave of given length and amplitude, associated with a wave spectrum, the speed of the ship is compared with the speed corresponding to the second threshold for surf-riding, that is to be calculated either with Melnikov's method or by a direct numerical bifurcation analysis (Umeda and al., 2010, Belenky and al., 2011). The long-term version of the criterion can be formulated by averaging the short-term probabilities over the values of significant wave heights and mean zero crossing period using entries of scatter diagrams as weights.

The ship is judged vulnerable for broaching, if the long-term probability for surf-riding is greater than 10^{-6} .

Application and results. The criterion has been applied to the three ships of the sample for which necessary resistance and propulsion information were available: the fishing vessel 1 and the military ships 1 and 2. The sea state used for the second level criterion is characterized by the following values of significant wave height and mean zero crossing period: $H_s=2.5$ m and $T_z=8.5$ s. Table 4 presents the

results of calculations carried out on these three vessels.

Table 4: Calculations results for the levels 1 and 2 vulnerability criterion for surf-riding and broaching

Ship type	Lpp [m]	Fn	Level 1	Level 2
M 1	150.00	0.40	Yes	0.224
M 2	150.00	0.40	Yes	0.221
FS 1	34.50	0.50	Yes	0.291
FS 2	74.60	0.34	Yes	N.A
FS 3	20.35	0.36	Yes	N.A
GC 1	121.92	0.28	No	N.A
GC 2	69.12	0.24	No	N.A
CT 1	116.00	0.21	No	N.A
CT 2	176.00	0.19	No	N.A
T 1	225.00	0.16	No	N.A
T 2	114.00	0.22	No	N.A
T 3	180.00	0.18	No	N.A
T 4	99.90	0.23	No	N.A
CS 1	262.00	0.25	No	N.A
CS 2	150.00	0.31	Yes	N.A
CS 3	275.00	0.35	No	N.A
CS 4	349.50	0.21	No	N.A
CS 5	142.37	0.27	No	N.A
CS 6	159.00	0.25	No	N.A
CS 7	167.00	0.25	No	N.A
CS 8	185.50	0.26	No	N.A
CS 9	266.00	0.24	No	N.A
CS 10	210.00	0.26	No	N.A
PS 1	213.40	0.22	No	N.A
PS 2	126.20	0.23	No	N.A
RP 1	135.00	0.21	No	N.A
RP 2	146.00	0.27	No	N.A
RP 3	161.60	0.31	Yes	N.A
RP 4	168.10	0.30	Yes	N.A
RP 5	117.00	0.23	No	N.A
S 1	70.76	0.25	No	N.A
BC 1	217.00	0.16	No	N.A
BC 2	282.00	0.14	No	N.A
BC 3	172.00	0.18	No	N.A
LNG 1	274.10	0.20	No	N.A
LNG 2	146.80	0.22	No	N.A



In the table 4, N.A means not available. The three vessels were found to be vulnerable to surf-riding and broaching.

5.3 Conclusions

For the three vessels used for the assessment of the second level criterion, the results are consistent with the first level vulnerability assessment. Fishing vessel 1 (Japanese purse seiner) and military ship 1 (ONR tumblehome) are known for their vulnerability to this phenomenon (Umeda et al. 1999). All ships with length greater than 200 m, or with an operational Froude number less than 0.3, are conventional to surf-riding and broaching. The second level criterion was applied only on three sample ships, because it was difficult to collect reliable data regarding propulsion and resistance.

6. RESULTS INVESTIGATIONS AND CRITERIA APPLICABILITY

6.1 Results investigations

Thirty six vessels have been investigated for the first and second level vulnerability criteria of parametric roll, pure loss of stability and for the first level vulnerability criteria of surf-riding and broaching. Three of these ships were used for the second level vulnerability criteria for surf-riding and broaching. The environmental conditions used to compute parametric roll and pure loss of stability vulnerability criteria were the Japan proposal to the Intact Stability Working Group (ISCG). Early trends observed for the different stability failure modes are commented in this section.

Parametric roll. Selected bulkers and tankers are found to be not vulnerable to this phenomenon. Parametric roll development is observed for containerships, passenger ships and Ropax vessels. Fishing vessels and general cargo ships are between these two groups of ships. While the three fishing vessels in the

above table (see table 2) did not indicate vulnerability to parametric roll, fishing vessels, in principle, are known to be susceptible to this phenomenon (Neves et al., 2009). General cargo ships, can reveal parametric roll in following seas (Paulling et al., 1975).

Pure loss of stability. The criteria judged bulk carriers and tankers as non-vulnerable. Possible vulnerability was detected for containerships, Ropax vessels and passenger ships. Fishing vessels and military ships could also suffer from this phenomenon.

Surf-riding and broaching. Vessels which could be vulnerable to this phenomenon are “not large enough” (length less than 200 m) and “fast enough” (Froude number greater than 0.3). Fishing vessels and military vessels could be vulnerable to surf-riding and broaching. The three vessels (one fishing vessel and both military ships) tested with the second level criterion were judged as vulnerable.

6.2 Criteria applicability

The first level criteria for phenomena related to righting lever variations in waves (parametric roll and pure loss of stability) are simple to apply, as all the values can be directly obtained from the vessel’s hydrostatic curves.

The first level vulnerability criterion for surf-riding and broaching is very simple and can be evaluated without calculations, knowing only the ship length and its service speed.

The second level criteria for phenomena related to righting lever variations in waves require the calculations of the instantaneous GM in waves. While these calculations are straight forward, they need computer software and time for preparation of the geometric input. These calculations are time consuming because the instantaneous GM in waves needs to be evaluated for at least ten positions of the wave crest along the ship length, and these calculations are



to be repeated for all the wave cases (sixteen in this work).

In general the outcome of second level criterion for pure loss of stability and the first check for parametric roll is obtained by a weighted average of binary conditions. Their do not take into account how the criterion is above or below the standard, e.g. for a given wave, a ship with GM of 0.1 m and another with GM of -0.6 m are considered in the same way because they are less than 0.15 m (level 2 of pure loss of stability – first criterion). Therefore they are assigned the same weight. This does not reflect the experience of the naval architect, because it is known that a ship with GM of 0.1 m is “safer” or more “stable” than the one with GM of -0.6 m. One can also note in figure 2 that the values of the level 2 results for the considered ships are very close either to 0 or to 1. There are no intermediates values.

The second level criterion for surf-riding and broaching based on the second threshold of surf-riding and evaluated with Melnikov’s method is straight forward although requiring computer software calculations and time for preparation of the geometric input to compute the surge induced wave force. The main foreseen obstacle for the application of the criterion is the difficulty to obtain reliable information about resistance and propulsion. Simplified generic resistance models, such as Holtrop-Mennen, exist, but the influence of their uncertainty on the criterion assessment should be investigated before being applied. It should also be noted that such simplified models require many input parameters which are delicate and long to collect from ship drawings.

Generally speaking, for most of the criteria, the standards are not fixed and for some not proposed, yet. The standards need to be set carefully, to ensure the consistency between the first and the second level, and also be sure that a vulnerable vessel cannot be judged as non-vulnerable. The environmental conditions are also not fixed; their definitions are currently in progress in the correspondence group (ISCG).

7. CONCLUSIONS

This paper presents the application of level 1 and level 2 vulnerability criteria, as outlined in the current state of development, by the International Maritime Organisation (IMO), of the second generation intact stability criteria. Calculations results for a sample population of 36 ships were examined for phenomena related to righting lever variation in waves and surf-riding and broaching. An investigation to identify groups of ships/ship characteristics which appear to be particularly vulnerable to the stability failure modes, according to these criteria was done. Moreover comments on the applicability of these criteria from a regulatory/approval point of view were presented. However additional work remains to determine possible standards for these criteria and their environmental conditions.

8. REFERENCES

- Belenky, V.N., Bassler, C.C., and Spyrou, K.J., 2011, “Development of Second Generation Intact Stability Criteria”, Naval Surface Warfare Center Carderock Division, Hydromechanics Department Report, pp. 95 – 107.
- Belenky, V.,N. and Sevastianov, N., B., 2007, “Stability and safety of ships – Risk of Capsizing”, 2nd edition, SNAME, Jersey City, pp. 195 – 198.
- Bulian, G., Francescutto, A., and Zotti, I., 2009, “The new international regulations for intact stability, subdivision and damage stability of ships”, Proceeding International Conference on Transport Science – ICTS 2009 – Transport Science, Profession and Practice, Portoroz, pp. 1-8.
- Francescutto, A. and Umeda, N., 2010, “Current Status of New Generation Intact Stability Criteria Development”, Proceeding of 11th International Ship Stability Workshop, pp. 1-4.



- Hashimoto, H., 2009, "Pure loss of stability of a Tumblehome Hull in Following Seas", Proceeding on the 19th International Off-shore and Polar Engineering Conference, Osaka, Japan.
- IMO, 2009, "International code on intact stability, 2008 Third Edition", IMO (London)
- IMO SLF 52/INF.2, "Information collected by the intersectional Correspondence Group on Intact Stability", Submitted by USA (Annex 6 submitted by the United States), London 2009.
- IMO SLF 53/INF.10, "Information collected by the intersectional Correspondence Group on Intact Stability". Submitted by Japan (Annex 5 submitted by the United States), London 2010.
- IMO SLF 54/WP.3, "Development of Second Generation on Intact Stability", Report of the working group, London, 2012
- ISCG (2012), "Comments on proposal from Italy on the "selection of reference environmental conditions for vulnerability criteria for parametric roll and pure loss of stability" as well as proposal from the USA", submitted by Japan
- Neves, M.A.S., Vivanco, J.E.M., Rodriguez, C.A., "Nonlinear Dynamics on Parametric Rolling of Ships in Head Seas", Proceeding of 10th International Conference on Stability of Ships and Ocean Vehicles, St. Petersburg, Russia, pp. 509 – 520.
- Paulling, J.R., Oakley, O.H., and Wood, P.D., 1975, "Ships capsizing in heavy seas: the correlation of theory and experiments", Proceeding of 1st International Conference on Stability of Ships and Ocean Vehicles, Glasgow, Scotland.
- Umeda, N., Matsuda, N.A., Hamamoto, M., and Suzuki, S., (1999), "Stability Assessment for Intact Ships in the Light of Model Experiments", J. Mar. Sci. Technol., 4, pp. 45 – 57.
- Umeda, N., Maki, A., Renilson, M. and Ueta, T., (2010), "Analytical formulae for predicting the surf-riding threshold for a ship in following seas", J. Mar. Sci. Technol., pp. 1 – 11.





Validation of a Numerical Simulation Model for Parametric Rolling Prediction Using a PCTC

Hirota Hashimoto, *Osaka University*, h_hashi@naoe.eng.osaka-u.ac.jp

Naoya Umeda, *Osaka University*, umeda@naoe.eng.osaka-u.ac.jp

ABSTRACT

The authors developed a numerical simulation model based on a nonlinear strip method for parametric rolling prediction in regular/irregular head waves. Although this model was already validated with several containerships, further validation studies are requested for its practical use. In this study a pure car and truck carrier (PCTC) is selected as a subject ship, and the numerical simulation model is compared with the existing model experiments in regular/irregular head waves. Through the comparisons between the model experiments and the numerical simulations in statistical properties, the validity of the numerical model is demonstrated.

Keywords: *Parametric Rolling, Direct Stability Assessment, Statistical Properties, PCTC*

1. INTRODUCTION

In recent years, it has been well recognized that containerships prone to suffer severe parametric rolling. Car carriers are also considered as high-risk ships which could suffer severe parametric rolling as well as containerships, and there was an accident report of the PCTC AIDA which experienced almost 50 degrees of parametric rolling in 2003. She suffered parametric rolling again next year and about 20 degrees of rolling was recorded [Hua et al., 2006]. Parametric rolling is a phenomenon treated as a part of roll restoring variation problems in the second generation intact stability criteria under development at the International Maritime Organization (IMO). Numerical simulation codes used as the direct stability assessment tool are required to accurately predict the occurrence of parametric rolling and its maximum roll angle at actual sea to assess the achievement of safety levels. For this purpose, every numerical simulation models should be intensively validated through the comparisons with sufficient numbers of model experiments. The authors developed a numerical simulation model for parametric

rolling prediction in regular/irregular longitudinal waves based on a nonlinear strip method. Although this model was already applied to predict parametric rolling of several containerships and compared with the model experiments, further validation studies are requested for its practical use.

In this study a PCTC is selected as a subject ship, and the numerical simulation results are compared with the model experiments in regular/irregular head waves to discuss the reliability of the numerical model. Regarding the regular wave, the changes of amplitude of parametric rolling with Froude number, wave length and wave height are well predicted by the proposed model. Regarding the irregular wave, direct evaluation of the numerical model using one long record is difficult because of practical non-ergodicity [Belenky, 2004] [Bulian et al., 2008]. Therefore relatively short-time simulations in irregular waves with a huge number of realizations are repeated to evaluate the numerical simulation model in terms of statistical properties, e.g. dispersion of maximum roll angles and standard deviations,



confidence interval of standard deviations, probability density functions of roll. Through the comparisons between the model experiments and the numerical simulations in statistical properties, the validity of the numerical model as a direct stability assessment tool for parametric rolling is demonstrated.

2. MATHEMATICAL MODEL

The coupled heave-roll-pitch mathematical model, i.e. 3 degrees-of-freedom (DOF), based on the nonlinear strip method was developed for quantitative prediction of parametric rolling in regular and irregular longitudinal waves [Hashimoto and Umeda, 2010] [Hashimoto et al., 2011]. This model is named as OU-PR (Osaka University - simulation programme for Parametric Rolling). In this model, ship motions are predicted by time integration of the differential equations of a ship motion with the fourth-order Runge-Kutta method.

2.1 Regular Wave

Nonlinear Froude-Krylov forces are calculated by integrating wave pressure up to the wave surface. Radiation and diffraction forces are calculated for the instantaneous submerged hull by considering the time-dependent roll angle. Two-dimensional hydrodynamic forces are calculated by solving the boundary integral equation for the velocity potential. Diffraction forces are calculated by the STF (Salvesen–Tuck–Faltinsen) method [Salvesen et al., 1970]. Hydrodynamic forces for the heave and diffraction modes are calculated with the encounter frequency and those for the roll mode are done with half the encounter frequency assuming the principal parametric rolling. In calculations of the radiation forces, so called the end term effect is included because a hydrodynamic lift effect on roll moment cannot be neglected when a ship has advance speed. Linear and quadratic roll damping coefficients are used in the mathematical model, which are determined from an experimental result of roll decay tests

if it is available. Otherwise, they are determined by the Ikeda's semi-empirical method [Ikeda, 2004]. The coupled 3DOF equations for the prediction of parametric rolling in regular waves are expressed as Eqs.(1)-(3).

$$\begin{aligned} & (m + A_{33}(\phi))\ddot{\zeta} + B_{33}(\phi)\dot{\zeta} + A_{34}(\phi)\ddot{\phi} \\ & + B_{34}(\phi)\dot{\phi} + A_{35}(\phi)\ddot{\theta} + B_{35}(\phi)\dot{\theta} \\ & = F_3^{FK+B}(\zeta_G / \lambda, \zeta, \phi, \theta) + F_3^{DF}(\phi) \end{aligned} \quad (1)$$

$$\begin{aligned} & (I_{xx} + A_{44}(\phi))\ddot{\phi} + N_{\phi}\dot{\phi} + N_{\phi\zeta}\dot{\zeta} + A_{43}(\phi)\ddot{\zeta} \\ & + B_{43}(\phi)\dot{\zeta} + A_{45}(\phi)\ddot{\theta} + B_{45}(\phi)\dot{\theta} \\ & = F_4^{FK+B}(\zeta_G / \lambda, \zeta, \phi, \theta) + F_4^{DF}(\phi) \end{aligned} \quad (2)$$

$$\begin{aligned} & (I_{yy} + A_{55}(\phi))\ddot{\theta} + B_{55}(\phi)\dot{\theta} + A_{53}(\phi)\ddot{\zeta} \\ & + B_{53}(\phi)\dot{\zeta} + A_{54}(\phi)\ddot{\phi} + B_{54}(\phi)\dot{\phi} \\ & = F_5^{FK+B}(\zeta_G / \lambda, \zeta, \phi, \theta) + F_5^{DF}(\phi) \end{aligned} \quad (3)$$

2.2 Irregular Wave

Nonlinear Froude-Krylov forces are directly calculated by integrating wave pressure up to the irregular wave surface profile. The wave pressure used for the Froude-Krylov calculation and the diffraction forces are calculated with the linear superposition principle. In default, the number of elementary waves is 200 and their frequencies are determined from the ITTC wave spectra. Here the unequally divided frequencies, having the same area in each division, are used to avoid the self-repeating effect. Diffraction forces are calculated by the STF method, and transfer functions with respect to a frequency and a heel angle are prepared in advance. Radiation forces in roll are calculated for the natural roll frequency and those in heave and pitch are done for the peak of mean wave frequency. The coupled 3DOF equations for the prediction of parametric rolling in irregular waves are expressed as Eqs.(4)-(6).

$$\begin{aligned}
 & (m + A_{33}(\phi))\ddot{\zeta} + B_{33}(\phi)\dot{\zeta} + A_{34}(\phi)\ddot{\phi} \\
 & + B_{34}(\phi)\dot{\phi} + A_{35}(\phi)\ddot{\theta} + B_{35}(\phi)\dot{\theta} \\
 & = F_3^{FK}(t, \zeta, \phi, \theta) + F_3^{DF}(t, \phi)
 \end{aligned} \quad (4)$$

$$\begin{aligned}
 & (I_{xx} + A_{44}(\phi))\ddot{\phi} + N_{\phi}\dot{\phi} + N_{\phi\zeta}\dot{\zeta} + A_{43}(\phi)\ddot{\zeta} \\
 & + B_{43}(\phi)\dot{\zeta} + A_{45}(\phi)\ddot{\theta} + B_{45}(\phi)\dot{\theta} \\
 & = F_4^{FK}(t, \zeta, \phi, \theta) + F_4^{DF}(t, \phi)
 \end{aligned} \quad (5)$$

$$\begin{aligned}
 & (I_{yy} + A_{55}(\phi))\ddot{\theta} + B_{55}(\phi)\dot{\theta} + A_{53}(\phi)\ddot{\zeta} \\
 & + B_{53}(\phi)\dot{\zeta} + A_{54}(\phi)\ddot{\phi} + B_{54}(\phi)\dot{\phi} \\
 & = F_5^{FK}(t, \zeta, \phi, \theta) + F_5^{DF}(t, \phi)
 \end{aligned} \quad (6)$$

3. SUBJECT SHIP

The principal particulars of a PCTC used in this research are shown in Table 1 and the GZ curve is done in Fig.1. She has the similar dimensions as the PCTC AIDA [Hua et al., 2006].

Table 1 Principal particulars of the PCTC

Item	value
length: L_{PP}	192.0 m
breadth:	32.26 m
depth: D	37.0 m
mean draught: T	8.18 m
block coefficient: C_b	0.54
longitudinal position of centre of gravity from the midship: x_{CG}	4.67 m aft
metacentric height: GM	1.25 m
natural roll period: T_ϕ	22.0 s

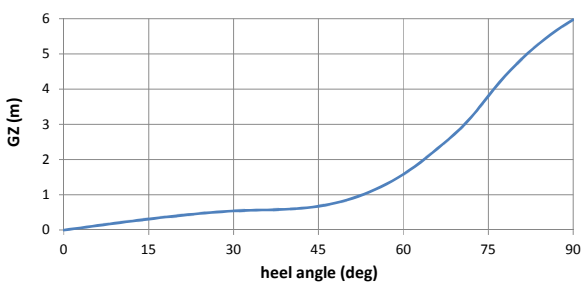


Figure 1: GZ curve of the PCTC.

4. PARAMETRIC ROLLING IN REGULAR HEAD WAVES

In order to evaluate the numerical model, numerical simulations in regular head waves are compared with the existing experimental results [Hashimoto et al, 2007]. The model experiments were conducted at the towing tank of Osaka University with a 1/64 scaled model. A ship model was towed by soft elastic ropes connected to the bow. Numerical simulations were executed for the same conditions of wave length, wave height, and Froude number as the model experiment. As shown in Fig.2, the general trend of the experiment is that the roll amplitude decreases as the Froude number increases, and when the wavelength increases the occurrence region shifts to higher Froude number. The numerical prediction quantitatively agrees with the model experiment in the maximum roll amplitude and the occurrence region of parametric rolling for four wave lengths which cover almost the occurrence region of parametric rolling.

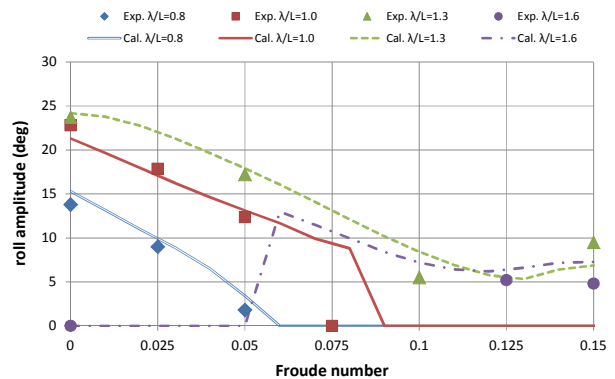


Figure 2: Comparison of the steady amplitude of parametric rolling with H=3.2m.

Figs.3-5 show the comparisons of the roll amplitude between the experiment and the simulation with various wave heights for three different wave lengths to ship length ratio of $\lambda/L=1.0, 1.3$ and 1.6 . Here the numerical model well predicts the nonlinear relationship between parametric rolling and the wave steepness. Some discrepancies near the onset of parametric roll could be explained as a local bifurcation, in other words initial condition



dependence. These comparisons demonstrate that the 3DOF coupled model of heave-roll-pitch based on the nonlinear strip method (OU-PR) almost realizes the quantitative prediction of parametric rolling in regular head waves.

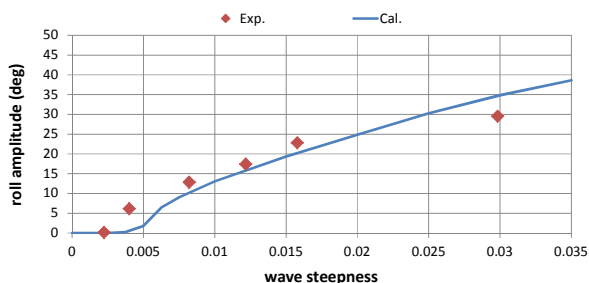


Figure 3: Comparison of the steady amplitude of parametric rolling with $\lambda/L=1.0$ and $F_n=0.0$.

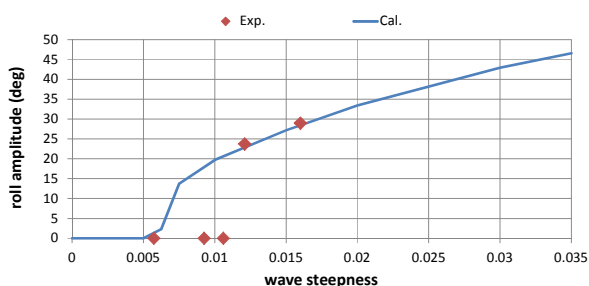


Figure 4: Comparison of the steady amplitude of parametric rolling with $\lambda/L=1.3$ and $F_n=0.0$.

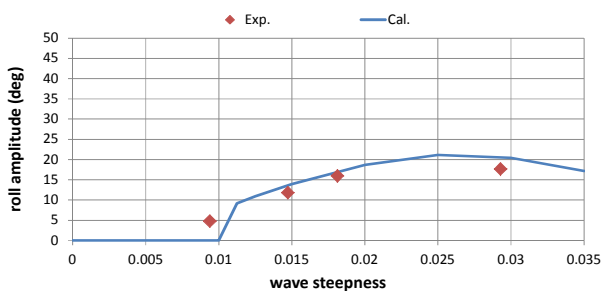


Figure 5: Comparison of the steady amplitude of parametric rolling with $\lambda/L=1.6$ and $F_n=0.15$.

5. PARAMETRIC ROLLING IN IRREGULAR HEAD WAVES

5.1 Maximum Roll Angle

Numerical simulations of parametric rolling in long-crested irregular head waves are compared with the existing experimental results [Umeda et al, 2011]. The model experiments were conducted at the towing tank of Osaka University with the same model as the regular wave study. Following the assumed condition where the PCTC Aida encountered, 5.31m of significant wave height and 9.76 seconds of wave mean period where the peak period corresponds to the wave period of the regular wave whose length is 1.3 times as long as the ship length were used. 2.655m of significant wave height, which is half the 5.31m, is also used. Since parametric rolling in irregular waves is considered as non-ergodic in practical, model runs in irregular waves were repeated 30 and 25 times with different phase sets of the ingredient waves for significant wave height of 5.31m and 2.655m, respectively. The time duration in the model experiments was 100 minutes in full scale for each run. Numerical simulations are executed for the same conditions of wave mean period, significant wave height, number of realisation, and time duration as the model experiment. In the numerical simulations, 5 degrees of roll angle and 0 deg/sec of roll angular velocity are used as the initial condition.

Firstly examples of measured and simulated time histories of parametric rolling are shown in Figs.6-7. The repetition of appearance and disappearance of parametric rolling is qualitatively reproduced by the numerical simulation, and the occurrence frequency of parametric rolling seems to be similar with the model experiment for both significant wave heights. The comparisons of maximum roll angle between the model experiment and the numerical simulation for $H_{1/3}=5.31\text{m}$ and 2.655m are shown in Figs.8-9. The scattering of the maximum roll angle among the realizations is clearly found in both the experiment and the simulation nevertheless of the long-time duration. More significant

scattering can be found for the $H_{1/3}=2.655\text{m}$ because it is closer to the threshold of parametric rolling. The numerical simulation well reproduces the scattering of maximum roll angle due to practical non-ergodicity. The ensemble mean and the confidence interval of maximum roll angles of parametric rolling are shown in Fig.10. The ensemble mean of the maximum roll angles of the simulation for $H_{1/3}=5.31\text{m}$ is slightly larger than that of the experiment while the ensemble mean and the 95% confidence interval of the simulation for $H_{1/3}=2.655\text{m}$ agree well with the experiment. Since the minimum value of confidence interval agrees with each other, one of reasons could be explained as the limitation of the roll damping estimation from roll decay tests. When a maximum roll angle of parametric rolling is much larger than an initial heel angle of roll decay test, the extrapolation with linear and quadratic terms, which is an ordinary way to fit a roll decaying curve, could provide unreliable roll damping due to higher order nonlinear effects. The influence of the curve fittings of roll decaying curve on the maximum roll angle of parametric rolling in irregular waves was pointed out [Hashimoto et al., 2011]. Therefore the roll damping estimation in an accurate manner for large amplitudes is necessary in the future for the validation study of significant parametric rolling.

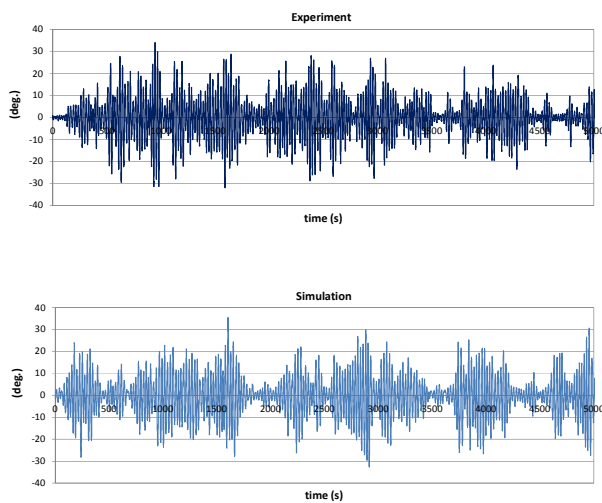


Figure 6: Typical time-series of the measured and the calculated roll motion with $H_{1/3}=5.31\text{m}$, $T_{01}=9.76\text{s}$ and $F_n=0.0$

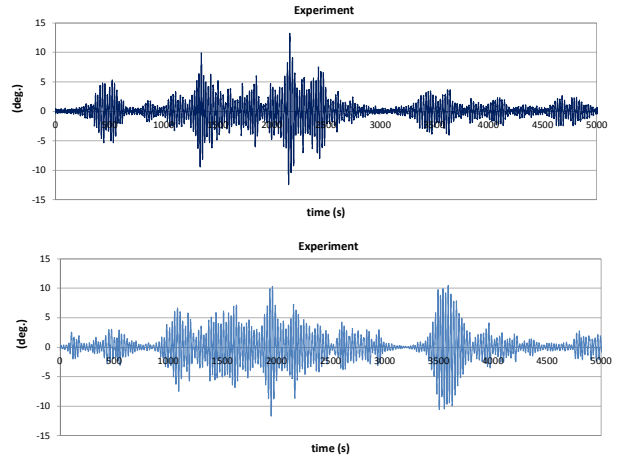


Figure 7: Typical time-series of the measured and the calculated roll motion with $H_{1/3}=2.655\text{ m}$, $T_{01}=9.76\text{s}$ and $F_n=0.0$

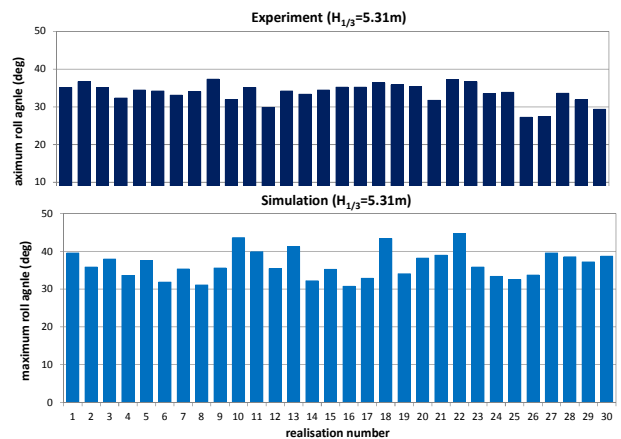


Figure 8: Comparison of the maximum roll angle for 30 realizations with $H_{1/3}=5.31\text{m}$, $T_{01}=9.76\text{s}$ and $F_n=0.0$

The probability density functions (PDF) of roll angle are plotted in Figs. 11-12. In the figures, Gaussian distribution is also drawn. As it has been pointed out with numerical results [Belenky et al., 2003] and experimental results [Hashimoto et al., 2006], the PDF of parametric rolling does not follow the Gaussian distribution particularly near the upright and large roll angle regions. This is because parametric rolling only develops when an encounter wave group satisfies the occurrence condition, and rapidly disappears when they do not. The numerical results qualitatively capture



the nature of non-Gaussian parametric rolling in irregular waves.

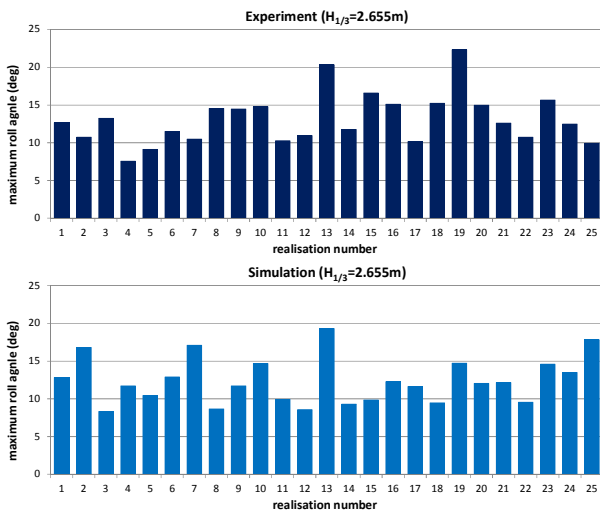


Figure 9: Comparison of the maximum roll angle for 25 realizations with $H_{1/3}=2.655\text{m}$, $T_{01}=9.76\text{s}$ and $F_n=0.0$

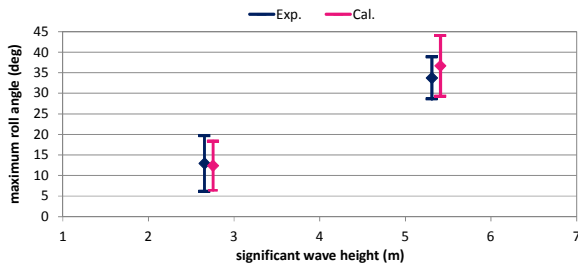


Figure 10: Comparison of the 95% confidence interval of maximum roll angle

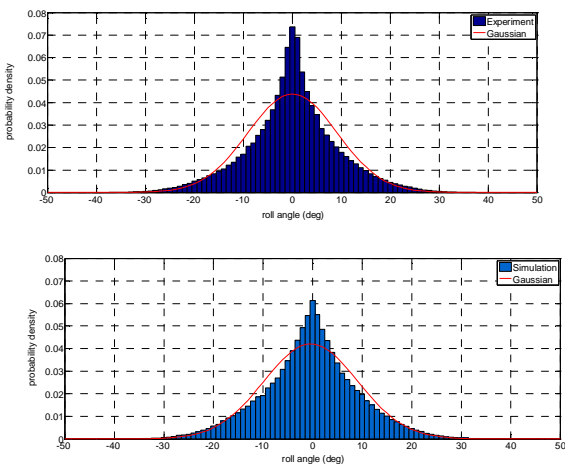


Figure 11: Comparison of the probability density function of roll angle with $H_{1/3}=5.31\text{m}$, $T_{01}=9.76\text{s}$ and $F_n=0.0$

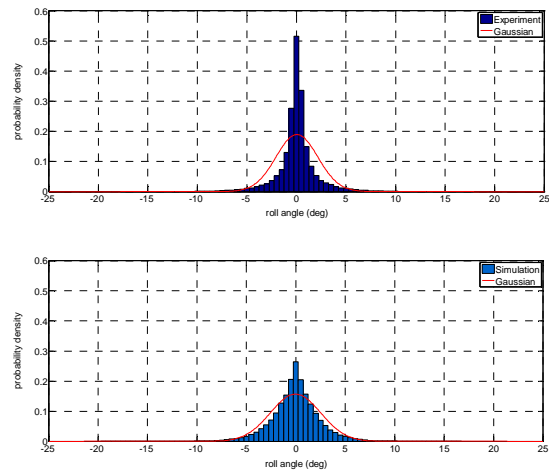


Figure 12: Comparison of the probability density function of roll angle with $H_{1/3}=2.655\text{m}$, $T_{01}=9.76\text{s}$ and $F_n=0.0$

5.2 Standard Deviation

As mentioned, the outcomes of parametric rolling significantly change depending on the difference of wave samples even with the same mean wave period and significant wave height. Therefore the large scattering among each realization cannot be avoided by simply lengthening the time duration. Therefore we attempt to investigate the validity of the numerical model by comparing results focusing on standard deviations.

The standard deviations of roll angle are calculated with $H_{1/3}=5.31\text{m}$ and 2.655m , and plotted in Figs.13-14. The standard deviation of roll angle scatters significantly due to practical non-ergodicity, as well as the maximum roll angle. The variations of standard deviation are well reproduced by the numerical simulation. The mean values of the standard deviations in numerical simulations are slightly larger than those of the experiment. Next the 95% confidence intervals of the standard deviation are obtained by calculating the variance of variance. [Reed, 2011] Here the selected three samples of realizations have the minimum, mean, maximum of the standard deviations among all trials. In Figs.13-14, the calculated 95% confidence intervals for the three samples are shown. In the case with $H_{1/3}=5.31\text{m}$, each

confidence interval is overlapped in both the experiment and simulation because the significant wave height is sufficiently large as compared to the threshold. In the experimental result with $H_{1/3}=2.665\text{m}$, however, the confidence intervals of realization no.19 (maximum) and that of no.4 (minimum) are not overlapped at all nevertheless the time duration is quite long. This fact clearly indicates the scatters of standard deviations come from practical non-ergodicity. Therefore it is hard to represent the population's characteristic with a single trial when a wave condition is comparable to the threshold of parametric rolling. Since the calculated outcome is almost similar to the experimental one, it is concluded the numerical model fully reproduced non-ergodicity of parametric rolling in terms of the maximum roll angle and standard deviation.

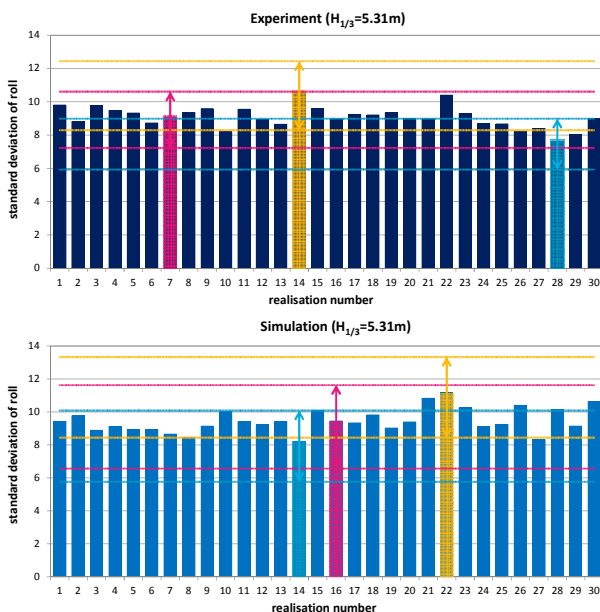


Figure 13: Comparison of the standard deviation and the 95% confidence interval with $H_{1/3}=5.31\text{m}$, $T_{01}=9.76\text{s}$ and $F_n=0.0$.

Through the intensive comparisons with the model experiments, the time-domain numerical simulation code based on the nonlinear strip method is validated. As a result, it is demonstrated the OU-PR reproduces parametric rolling in irregular head waves, having the equivalent statistical properties as the model experiments. Therefore it could be

applicable for a direct stability assessment of parametric rolling in the second generation intact stability criteria at least for irregular head waves.

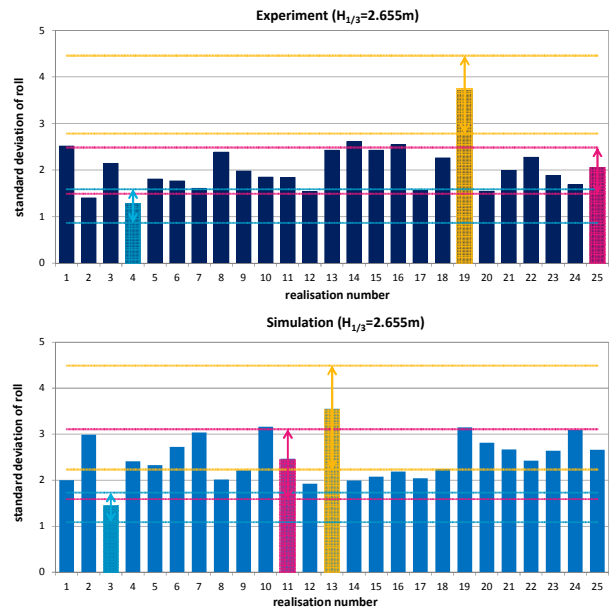


Figure 14: Comparison of the standard deviation and the 95% confidence interval with $H_{1/3}=2.655\text{m}$, $T_{01}=9.76\text{s}$ and $F_n=0.0$

5.3 Relationship between Maximum Roll Angle and Standard Deviation

Although the mathematical model developed for parametric rolling prediction in irregular waves has been validated in terms of the scattering of standard deviations due to practical non-ergodicity, the safety assessment in final should be performed using the maximum rolling angle, which is responsible for cargo shifts. From this viewpoint, the relation between the standard deviation and the maximum roll angle in each trial is plotted in Fig.15. Here, the additional experimental and numerical data is added which are obtained with $H_{1/3}=3.98\text{m}$ and 1.991m . When we look the experimental results, there is an almost proportional relation between the standard deviation and the mean value of maximum roll angles. The numerical result has the almost same slope and the envelope band as the experimental ones for the wide range of standard deviation. If such a corresponding



distribution is calculated in advance, a possible maximum roll angle of parametric rolling could be roughly estimated even from a small number of model trials. This procedure seems to be a reasonable way for the direct stability assessment utilizing the advantages of physical model experiments and numerical simulations. The similar attempts to examine the relationship between a maximum roll angle and a standard deviation are required for different forward speeds as a future task.

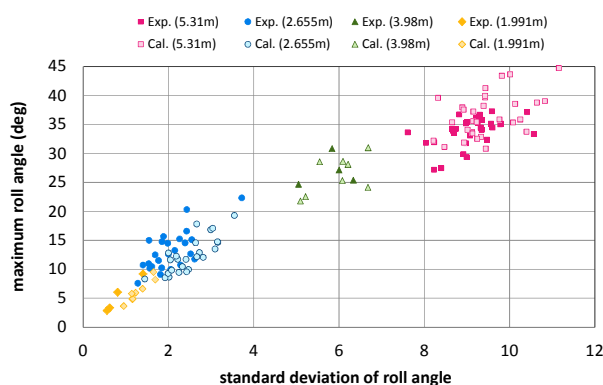


Figure 15: Maximum roll angle vs standard deviation of roll with several significant wave heights.

6. CONCLUSIONS

In order to develop a numerical simulation tool supplied for the direct stability assessment of parametric rolling in the second generation intact stability criteria, the heave-roll-pitch coupled mathematical model is evaluated by comparing the numerical results with the existing model experiments in regular/irregular head waves. Through the systematic comparisons between the model experiments and the numerical simulations, the following conclusions are obtained.

- The coupled heave-roll-pitch mathematical model based on the nonlinear strip method (OU-PR) provides the quantitative prediction of parametric rolling in regular head waves.
- The OU-PR predicts the maximum roll angles and the standard deviations of

parametric rolling in irregular head waves with sufficient accuracy.

- The OU-PR reproduces almost the same statistical properties due to non-ergodicity of parametric rolling in irregular waves as the model experiments.
- Further extension of the mathematical model is necessary to be applied for irregular oblique waves to establish as a direct stability assessment tool which can provide an operational guidance to avoid significant parametric rolling.

7. ACKNOWLEDGMENTS

This work was supported by a Grant-in Aid for Scientific Research of the Japan Society for Promotion of Science (No. 21360427).

8. REFERENCES

- Belenky, V.L., 2004, "On Risk Evaluation at Extreme Seas", Proceedings of the 7th International Ship Stability Workshop, Shanghai, pp.188-202.
- Belenky, V.L., Weems, K.M., Lin, W.M. and Paulling, J.R., 2003, "Probabilistic Analysis of Roll Parametric Resonance in Head Seas", Proceedings of the 8th International conference on Stability of Ships and Ocean Vehicles, pp.325-340
- Bulian, G., Francescutto, A., Umeda, N. and Hashimoto, H., 2008, "Qualitative and Quantitative Characteristics of Parametric Ship Rolling in Random Waves in the Light of Physical Model Experiments", Ocean Engineering, Vol.35, Nos. 17-18, pp. 1661-1675.
- Hashimoto, H. and Umeda, N., 2010, "A Study on Quantitative Prediction of Parametric Roll in Regular Waves", Proceedings of the 11th International Ship Stability Workshop, Wageningen, pp.295-301.



Hashimoto, H., Umeda, N., Matsuda, A. and Nakamura, S., “Experimental and numerical study on parametric roll of a post-panamax container ship in irregular waves”, Proceedings of the 9th International conference on Stability of Ships and Ocean Vehicles, Rio de Janeiro, Vol.1, pp. 181-190.

Hashimoto, H., Umeda, N. and Sakamoto, G., 2007, “Head-Sea Parametric Rolling of a Car Carrier”, Proceedings of the 9th International Ship Stability Workshop, Hamburg, CD.

Hashimoto, H., Umeda, N. and Sogawa, Y., 2011, “Prediction of Parametric Rolling in Irregular Head Waves”, Proceedings of the 12th International Ship Stability Workshop, Washington D.C., pp.213-218.

Hua, J., Palmquist, M. and Lindgren, G., 2006, “An Analysis of the Parametric Roll Events Measured Onboard the PCTC AIDA”, Proceedings of the 9th International conference on Stability of Ships and Ocean Vehicles, Rio de Janeiro, Vol.1, pp. 109-118.

Ikeda, Y., 2004, “Prediction Methods of Roll Damping of Ships and Their Application to Determine Optimum Stabilization Devices”, Marine Technology, Vol.41, No.2, PP.89-93.

Reed, A.M., 2011, “26th ITTC Parametric Roll Benchmark Study”, Proceedings of the 12th International Ship Stability Workshop, Washington D.C., pp.195-204.

Salvesen, N., Tuck, E.O. and Faltinsen, O., 1970, “Ship Motions and Sea Load”, TSNAME, Vol.78.

Umeda, N., Hashimoto, H., Tsukamoto, I. and Sogawa, Y., 2011, “Estimation of Parametric Resonance in Random Waves”, Parametric Resonance in Dynamical Systems (T. Fossen and H. Nijmeijer, eds.), Springer, pp.45-62.

9. NOMENCLATURE

A_{ij}	added mass/added moment of inertia
B_{ij}	damping coefficient
F_i^{DF}	diffraction force
F_i^{FK+B}	Froude-Krylov force and buoyancy
I_{xx}	moment of inertia in roll
I_{yy}	moment of inertia in pitch
m	ship mass
N	roll damping coefficient
t	time
ϕ	roll angle
λ	wave length
θ	pitch angle
ω_e	encounter frequency
ξ_G	longitudinal position of centre of gravity from a wave trough
ζ	heave displacement





Vulnerability Assessment for the Loss of Stability in Waves: Some Application Cases for a Further Insight into the Problem

Andrea Coraddu, *University of Genoa*, andrea.coraddu@unige.it

Paola Gualeni, *University of Genoa*, paola.gualeni@unige.it

Diego Villa, *University of Genoa*, diego.villa@unige.it

ABSTRACT

During IMO activity about “second generation intact stability criteria” attention is given, among other issues, to the restoring moment variation in waves. Several studies are available and, at present, the challenge is to formulate the proper vulnerability assessment procedures organized into two consistent and harmonized levels.

For the purpose of this paper, an in-house developed numerical tool is applied to investigate some issues of the criteria currently in progress for the loss of stability failure mode; attention is paid to the wave profile effect not only on the metacentric height GM but also on the righting arm GZ, with wave crest at different positions along the ship length. The effect of design modification to the main scantlings of a Ro-Ro passenger ship, in terms of breadth, is analysed and for a specific case results are going to be observed as a function of time, in relation with different Froude numbers.

Keywords: *vulnerability criteria, intact stability, righting lever variation in waves*

1. INTRODUCTION

Vulnerability assessment for loss of stability in waves is focussed on the wave profile effect in terms of ship metacentric height and righting arm variations. This is a rather classic issue (Helas, 1982; Blume, 1990; Vermeer, 1990) that has known an increasing interest in the recent years (Bulian, 2010, Belenky & Sevastainov, 2007) due to the IMO activity about the renewal of the intact stability criteria that has produced the present Intact Stability Code 2008 (IMO, 2008). In the Code it is recognized that a further attention is needed for some ships that are more at risk of encountering critical situations in waves. At

present an item named “Second generation intact stability criteria” is constantly put on agenda of SLF sub-committee and an inter-sessional correspondence group is regularly established to carry on the activity.

One of the main implications of this activity is the development of the so called vulnerability criteria i.e. procedures able to assess the ship tendency to specific failure modes that have been focussed in: dead ship condition, parametric roll, surf-riding, broaching, pure loss of stability, this last being the main topic of this paper.



The logical and procedural interaction among IS Code, vulnerability levels, direct stability assessment and operational guidance are framed in a flow chart presented for example in SLF 53/WP.4 Annex 3. Recently the new failure mode of “excessive acceleration” has been introduced and draft criteria for two levels of vulnerability are proposed (SLF 54/WP.3 Annex 2).

An intense activity is required now to harmonize, verify, validate and test draft vulnerability criteria (levels 1 and 2) that identify the possible susceptibility of a ship to stability failure. At the same time, it is important that vulnerability criteria are really rational and efficient in supporting the design team, starting from the very early stage of the design process.

At present a summary of the draft methodologies for the second generation stability criteria available is presented in SLF 54/WP.3 Annex 3, as a result of a intense effort of several Administrations engaged at IMO on the matter. In this paper we are going to consider the present proposals for the first and the second vulnerability level for pure loss of stability. In particular we are going to calculate the metacentric height GM and the righting lever GZ with a computational tool and we are going to make some observations especially in relation to the approximation for the estimation of transversal metacentric radius BM_T and to GZ results expressed in terms of Froude number.

2. THE COMPUTATIONAL TOOL

A computational tool has been developed at the University of Genoa, dealing with evaluation of ship geometrical characteristics at upright condition and at large heel angles, in still water and in longitudinal waves. It is possible to select the sinusoidal as well as the trochoidal wave formulation. It is well-known that several commercial codes are available for this kind of calculations but we decided to

develop an in-house tool in order to have a more direct control on its calculation modality and with the aim to integrate it in a much wider architecture for the assessment of ship vulnerability.

It can be described as made of three parts: one for input conditions regarding both the ship and the wave (i.e. ship geometry, mean draft and VCG or wave length and steepness); the second part reads and elaborates the geometry of the ship and for example is able to give the hydrostatic results with and without wave profile; in the third part there is the evaluation of the GZ curves with the static balance of heave and pitch.

The ship geometry is defined in terms of points in space coordinates stored in a matricial form. A technique relying on shifting of points, in relation with the wave profile, is applied to facilitate the calculation of intersection between the ship and the free surface, in order to identify the immersed geometry of the ship. Calculation about geometrical characteristics are performed by transversal sections and integration on the longitudinal axis.

For the calculation of GZ righting arms, an iterative procedure is performed to guarantee heave and pitch static balance in waves, which is recognized to be significant and in fact it has a considerable impact on the results. Further details on the computational tool are given in Coraddu et al. (2011).

3. APPLICATIONS

The analysis has been performed considering five different ship typologies, more or less vulnerable as far as loss of stability is concerned. Results and detailed geometries are given in the just above mentioned reference. In this paper only results relevant to the most interesting ship typologies are reported i.e. a tumblehome vessel, a Ro-Ro passenger ship and a containership; their main characteristics are recalled in Table 1.

For the Ro-Ro passenger ship, some other configurations are investigated, derived from the increment/decrement of 3 m in beam, starting from the base breadth given in Table 1. For the investigation of cases generated in this way, it has been assumed that the draft and the vertical centre of gravity VCG do not change.

Table 1: Recapture of main characteristics for the investigated ships.

		Tumblehome	Ro-Ro pax	Containership
V	[m ³]	8552	25226	138366
L _{pp}	[m]	154	186.21	317.21
B	[m]	18.80	30.40	45.32
D	[m]	16.61	15.50	24.60
T	[m]	5.50	7.45	14.50
VCG	[m]	5.50	13.38	19.50

The following characteristics for the wave profile are taken into consideration: sinusoidal wave, wave length λ equal to ship length between perpendiculars L_{BP} and wave height H equal to $H\alpha=0,25T$ and $H\beta=0,5T$, where T is the ship design draft. The consequent wave steepness values are reported in Table 2 for reference purposes.

It is well known that loss of stability phenomenon is the result of interaction between ship geometry and wave characteristics. If the first aspect is in principle dependant on naval architects competence, the second should be properly selected as a representative environmental situation in the safety rule. An intense activity has been developed in the matter by several Administrations and the values taken into consideration for this application are in line with the proposed wave steepness values expressed in SLF 54/INF.12, annex 14, Table 5

(originally in SLF 53/INF.10, annex 1, table A2.1).

It can be observed, moreover, that the so determined wave height and relevant wave steepness are lower in comparison of those values calculated by the formula:

$$H(\lambda)=0,1351 \lambda^{0,7056} \quad (1)$$

proposed in Krueger (2005). The formula was derived by regression from the North Atlantic Wave Spectrum as a 90% quantil.

Besides, also the time of exposure, i.e. the duration of the ship stability alteration, is recognized to be a significant issue to frame the danger of a situation and this is dependant on the ship speed in relation with the wave celerity. In the following paragraph an application is described in order to put in evidence this aspect.

For all the above mentioned ship typologies the hydrostatics tables are calculated, with reference to the traditional even keel waterlines and to the intersection of ship hull with parallel wave profiles. The wave crest is amidships, while calculating hydrostatics. For some of the analysis about the GZ curves, the longitudinal position of the wave crest, x_{crest} , has also been varied along the ship length between perpendiculars L_{BP} , with increment step of $x_{crest}/L_{BP}=0,1$.

Table 2: Information about the wave geometry applied for the performed analysis.

		Tumblehome	Ro-Ro pax	Containership
$H\alpha=0,25T$	[m]	1,375	1,863	3,625
$H\beta=0,5T$	[m]	2,75	3,725	7,25
$H\alpha/L$	-	0,009	0,010	0,011
$H\beta/L$	-	0,018	0,020	0,023



4. COMMENTS TO RESULTS

Hydrostatic tables with and without waves for the above mentioned ships and conditions are reported in the following Fig. 1, 2 and 3. All the classic geometrical properties that can be found in hydrostatics tables have been calculated but only an extract is presented. In particular we show values relevant to immersed volumes and transversal metacentric radius BM_T for the tumblehome hull, the Ro-Ro passenger ship and the containership. In the vertical axis there is draft T that, for curves referring to cases with wave profile, represents the vertical position of the sinusoidal wave axis. From the curves describing the behavior of volume, it is possible to observe the importance of a vertical shift of the wave axis in order to guarantee the same volume of the still water condition. In the same figures, there is also the representation of the approximated BM_T defined by the draft proposal for the first level vulnerability criteria in case of loss of stability (SLF 54/WP.3). In the proposal, the evaluation of the metacentric height GM is formulated as follows:

$$GM_{min} = KB(d) + \frac{I_L}{V(d)} - KG \quad (2)$$

Where d is the draft corresponding to the loading condition and I_L is a transversal moment of inertia of the waterplane corresponding to a lower draft determined as $d_L = d - \delta d_L$.

In figures 1, 2 and 3 the term $I_L/V(d)$ is indicated as “BMT-1st level” since it is to be used for the 1st level vulnerability criteria. In this graphical form, it is possible to observe the margin due to this simplified approach, in comparison with the actual value calculated with the wave profile. In order to assess the margin, we compared the BMT – 1st level calculated at $d_L = d - \delta d_L(\alpha)$ and $d_L = d - \delta d_L(\beta)$ where the meaning of α and β can be derived from table 2 and the value as well. For sake of clearness, the value δd_L corresponds to the wave amplitude. The equivalent actual values

for BM_T are to be read on the relevant curves for the two wave profiles. Nevertheless this reading is to be performed for the draft that guarantees the conservation of the initial immersed volume.

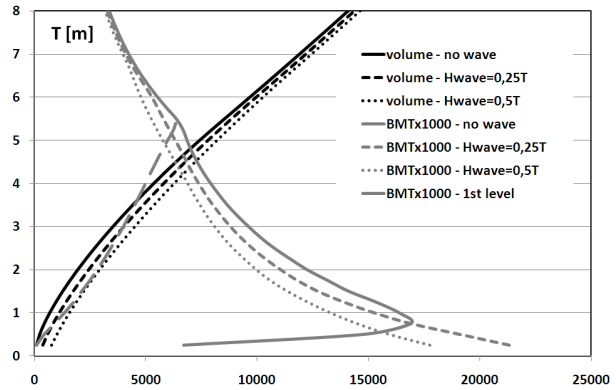


Figure 1: The behaviour of volume and transversal metacentric radius BM_T with and without wave profile for the tumblehome hull.

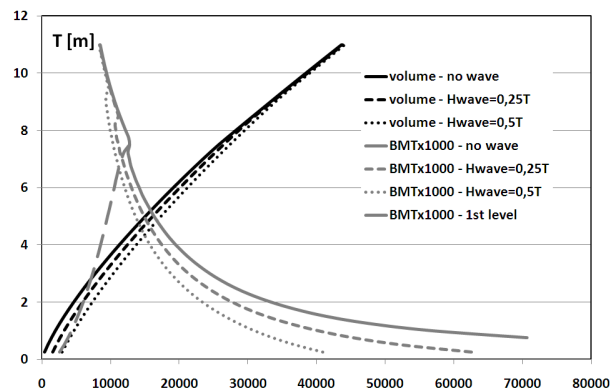


Figure 2: The behaviour of volume and transversal metacentric radius BM_T with and without wave profile for the Ro-Ro pax ship hull.

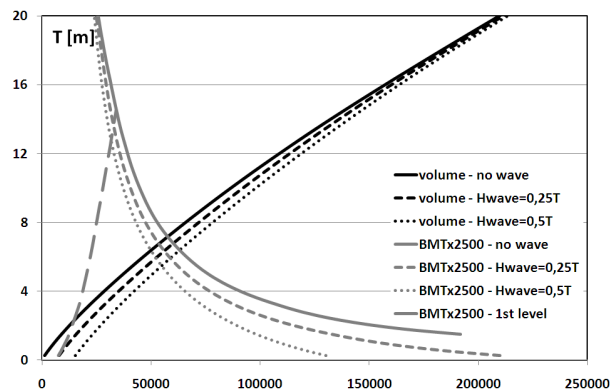


Figure 3: The behaviour of volume and transversal metacentric radius BM_T with and without wave profile for the containership hull.

In the following figures 4 and 5 a graphical representation of the comparison procedure is given for the containership, that is the most significant case.

It is evident that the approach proposed for the first level of vulnerability guarantees a certain margin, but in a reasonable way. The gap in fact is not so large, especially for the case of the lower wave height ($H\alpha$).

For the other investigated ship typologies it can be confirmed the same observation i.e. that the approximated approach is conservative but in a reasonable way and that the actual and the approximated values are very near especially for the case of $H_{wave} = 0,25T$.

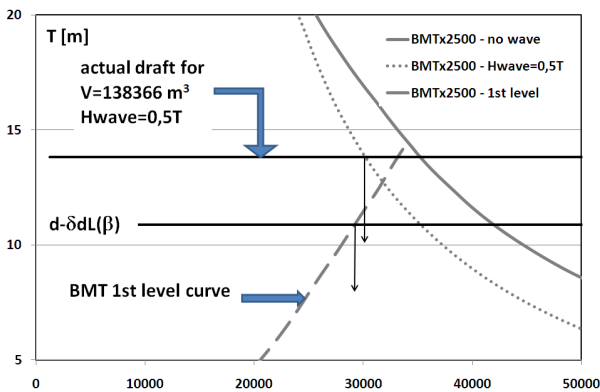


Figure 4: A comparison between the value of BMT- 1st level calculated with the approximated procedure and the actual value for the container ship and $H_{wave}=0,5T$.

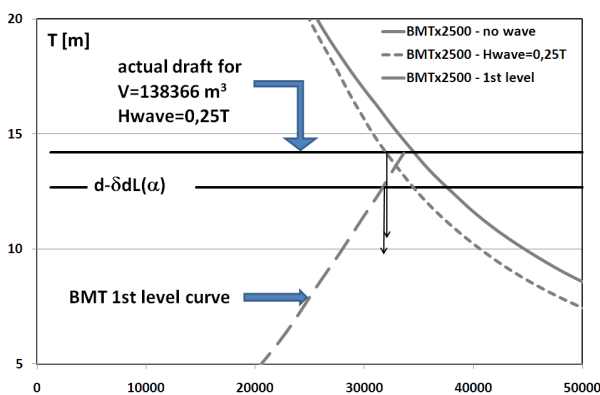


Figure 5: A comparison between the value of BMT- 1st level calculated with the approximate procedure and the actual value for the container ship and $H_{wave}=0,25T$.

The criterion for the 2nd level of vulnerability requires the analysis of the righting arm. The assessment is rather articulated and requires calculations of GZ variations for a series of waves. Then a weighting procedure is applied with three criteria.

In the application performed in this paper, only some partial aspects of the criterion are taken into consideration and in particular the investigation has been performed in a design perspective. In fact, it is interesting to observe the outcomes in case of a design modification of the ship. To this aim the Ro-Ro passenger ship has been transformed in terms of breadth. Calculations have been performed both in terms of hydrostatics and GZ (only with $H_{wave}=0,5T$).

GZ results are shown, for the ship with “base breadth $B - 3$ m” and “base breadth $B + 3$ m”, together with the “base condition” in figure 6. GZ curves are reported with wave crest at different positions along the ship length (in fig. 6 a selection among all cases of x_{crest}/L_{BP} from 0 to 1, i.e. the wave crest position from the afterward perpendicular to the forward perpendicular).

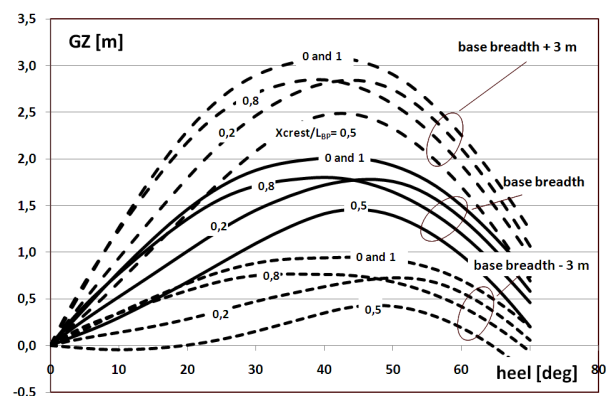


Figure 6: GZ curves for the base design case and two modifications in terms of breadth for the Ro-Ro passenger ship.

It seems that the breadth reduction of 3 m (comparable to a cargo line width, on a garage deck) is a critical modification for the design: the typical non-dimensional ratios between



ship main scantlings are still in a classic range, (i.e. for example after modification $B/T = 3,68$, $L/B = 6,8$) but the stability performance seems to show a vulnerability, for the influence of the wave profile. Just for sake of completeness, this vulnerability would be pointed out by the 1st-level criterion: by the approximated approach proposed by SLF. 54/WP.3, the result is $GM_{min} = -0,87$ m, while the actual value calculated with the computational tool is $GM = -0,26$ m. For same values for the “base case”, are respectively $GM_{min} = 0,95$ and $GM = 2,18$ m.

Another more complete representation of the GZ curves, for the design option “base breadth $B = 3$ m” is given in figure 7.

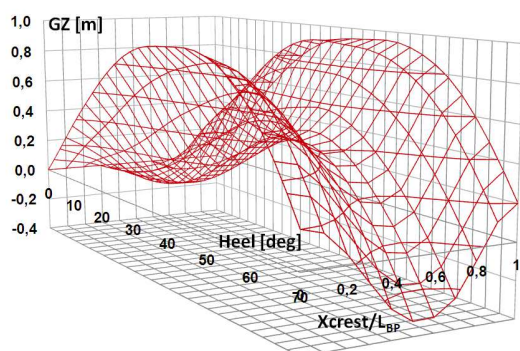


Figure 7: The complete set of GZ curves for the Ro-Ro passenger ship with “base breadth $B = 3$ m” and wave crest shifting for afterward perpendicular to forward perpendicular.

The same information of figure 7 is elaborated taking into account the wave celerity in relation with the ship speed, in following waves: $F_n=0,20-0,24-0,35$ have been considered and results are shown in figure 8 and 9.

As already mentioned, the wave length is equal to the ship length. Two ship speeds are selected as reasonable lower and upper extremes of a possible operational speed for a Ro-Ro passenger ship (i.e. 20 kn and 29 kn). These are equivalent to $F_n=0.24$ and $F_n=0.35$ respectively. For the lower speed, the potentially vulnerable largest time window is

of around ten seconds, while for the upper value the critical range is nearly thirty-five seconds.

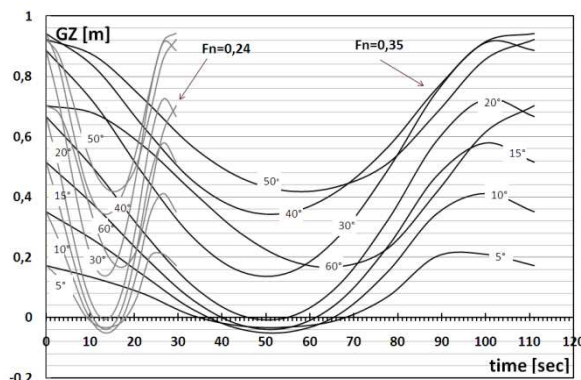


Figure 8: GZ curves for the Ro-Ro passenger ship (“base breadth- 3 m”) as a function of time for two different ship F_n (0,24 and 0,35).

In case it is decided that the speed entry level threshold for the vulnerability assessment requirement is $F_n=0,2$, for the Ro-Ro passenger ship under investigation this would be translated in 17 kn in terms of speed. The relevant presentation of results is given in figure 9.

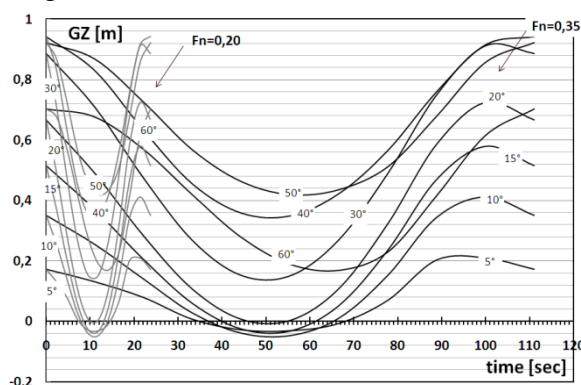


Figure 9: GZ curves for the Ro-Ro passenger ship (“base breadth- 3 m”) as a function of time for two different ship F_n (0,20 and 0,35).

In this case the exposure at risk is very short being of nearly five seconds. This exercise is useful to put in evidence the effect of relative speed between ship and wave, in parallel with the attention to the general characteristics of the critical righting arm curves, like GM , loll angle and GZ_{max} .



5. CONCLUSIONS

A computational tool developed in-house at University of Genoa has been applied to assess the effect of wave profile on ship stability in the general frame of the first and second level vulnerability criteria for the “loss of stability” in waves at present under development at IMO. One of the investigated issues was the magnitude of the margin introduced by the approximated methodology for GM calculation in the 1st level vulnerability criterion as proposed in document SLF 54/WP.3. In relation with the actual value the approximated GM resulted lower, as expected, but in a reasonable way. In the case of the containership results were nearly comparable. In the paper some design modifications of the main scantlings for the Ro-Ro passenger ship have been taken into consideration. The beam reduction has implied the expression of a vulnerability in terms of loss of stability. For this case GZ results have been presented, calculated at different wave crest positions along the ship length. This has permitted to model the ship exposure to risk in terms of time, comparing the ship speed with the wave celerity. All the calculations have been performed with the sinusoidal wave profile and the trochoidal formulation. These results have not been presented since they are nearly identical with a perceptible difference only for considerable wave height.

6. REFERENCES

- Belenky V.L. & Sevastianov N.B., 2007. *Stability and Safety of Ships*. Bhattacharyya and Mc Cormic Editors –SNAME.
- Blume, P., 1990 “On the Influence of the Variation of Righting Levers in Waves on Stability Requirements” , Proceedings of the 4th International Conference on Stability of Ships and Ocean Vehicles (STAB90), Napoli, pp. 452–459.
- Coraddu, A., Gualeni, P., and Villa, D., 2011
- “Investigation about wave profile effects on ship stability”, Proceeding of the 13th International congress of the International Maritime Association of the Mediterranean – IMAM2011, Genoa 12-16 Sept. 2011.
- Helas, G., 1982. “Intact stability of ships in following waves” , Proceedings of the 2nd International Conference on Stability of Ships and Ocean Vehicles (STAB82), Tokyo, pp. 689–699.
- IMO, 2008, “Adoption of the International Code On Intact Stability”, Resolution MSC.267(85) MSC85/26/Add.1. London.
- Krueger S., 2005 “Dynamic Intact Stability Criteria” Institut für Entwerfen von Schiffen und Schiffssicherheit - Hamburg University of Technology (TUHH).
- SLF 53/WP.4, 2011. “Development Of Second Generation Intact Stability Criteria - Report of the working group (part 1)”. IMO, London.
- SLF 53/INF.10, 2010. “Development Of Second Generation Intact Stability Criteria - Information collected by the Correspondence Group”. IMO, London.
- SLF 54/WP.3, 2012. “Development of Second Generation Intact Stability Criteria Any Other Business - Report of the working group (part 1)”. IMO, London.
- SLF 54/INF.12, 2011. “Development of Second Generation Intact Stability Criteria Information collected by the intersessional Correspondence Group on Intact Stability” IMO, London.
- Vermeer, H., 1990 “Loss of stability of ships in following waves in relation to their design characteristics”, Proceedings of the 4th International Conference on Stability of Ships and Ocean Vehicles (STAB90), Napoli, pp. 369–377.





Study on Parametric Roll and Its Rudder Stabilization Based on Unified Seakeeping and Maneuvering Model

Liwei Yu, *Graduate School, Shanghai Jiao Tong University*, liwyu55@sjtu.edu.cn

Ning Ma, *State Key Laboratory of Ocean Engineering, SJTU*, ningma@sjtu.edu.cn

Xiechong Gu, *State Key Laboratory of Ocean Engineering, SJTU*, xcgu@sjtu.edu.cn

ABSTRACT

This paper presents a model for the simulation and stabilization of parametric roll considering ship sea-keeping, manoeuvring and control in regular head seas. In the real-time simulation, the frequency-domain potential terms calculated by strip theory are transferred to time-domain, and the restoring forces are calculated non-linearly through pressure integration on instantaneous wetted surfaces. Meanwhile, propeller and rudder are incorporated in the model to investigate the influence of time-varying ship speed and effectiveness of rudder roll stabilization on parametric roll. The 6-DOF model is applied to simulate parametric roll motion of three container ships with different main particulars. Results show that rudder anti-roll moment can stabilize parametric roll motion especially when control system is triggered on during the onset stage of parametric roll.

Keywords: *parametric roll, 6 degree-of-freedom, rudder roll stabilization, PID*

1. INTRODUCTION

Parametric roll occurs when a ship sails in heavy head or following seas. Due to large variations of water plane area and roll restoring characteristics, transversely symmetrical ships may experience extreme self-resonant roll motion when wave passage passes along the hull. This phenomenon is most likely to happen under the following circumstances: the wave length is close to ship length, encounter frequency is almost twice the roll natural frequency, and wave height is greater than a threshold which depends on the ship GM variation in wave. Normally parametric roll happens on small fishing vessels (Neves et al., 1999) and large container ships (France et al., 2003). It can cause severe cargo loss and damage as investigated by France et al. (2003).

As a typical self-resonant problem, parametric roll was studied theoretically based on Mathieu equation (Pauling & Rosenberg, 1959, Nayfeh, 1988). The metacentric height,

GM, was assumed to be varying harmonically when solving the Mathieu equation, and results showed the possibility of large roll motion in head or following waves. At the same time, a few numerical simulation codes were developed taking into account the nonlinear restoring force and the influence of other degree of ship motions in time domain. Umeda et al. (2004) simulated parametric roll based on a 1-DOF model with realistic modeling of restoring moment as a nonlinear function of wave steepness. Bulian (2005) proposed a 1.5-DOF numerical model whereas the additional half DOF indicates the coupling with heave and pitch by means of hydrostatic calculations regardless of dynamic effects. Meanwhile, a coupled 3-DOF model incorporated with heave and pitch motion was presented by Neves et al. (1999). Matusiak (2003) applied a two-stage approach to solve the nonlinear problem involved in parametric roll. Spanos and Papanikolaou (2007) conducted parametric roll simulations of a fishing vessel and a RoRo ship using a 6-DOF code based on the IRF approach.



Results showed the importance of roll-pitch motion coupling and non-linear restoring forces. Shin et al. (2004) applied 3D Rankine Panel Method in parametric roll simulation, which has more accurate calculation on motion and force, but longer computation time. To capture complete rational viscous flow effects, Sadat-Hosseini et al. (2010) conducted a parametric roll study of a surface combatant based on CFD code. And CFD showed remarkably close agreement with EFD for forward-speed parametric roll in head waves.

Recently in order to further investigate the non-linearity of parametric roll and validate the effectiveness of existing parametric roll simulation codes, two benchmark studies were conducted by ITTC Stability In Waves Committee (ITTC, 2011) and E.C. research project SAFEDOR (Spanos & Papanikolaou, 2009). Results showed poor coherence between different simulation programs and model test results, especially in large amplitude waves. In irregular waves, different realisations of the same condition showed different statistical results. However, longer records or several combined short records can produce identical convergent results (Belenky and Weems, 2011). Due to the uncertainty and incoherence of current simulation programs, more and more researches focus on the factors that concerns with the highly non-linearity of parametric roll, such as non-linear restoring forces (Vidic-Perunovic et al., 2009), roll damping (Hashimoto and Umeda, 2010), surge and sway motion (Vidic-Perunovic et al., 2009, Ahmed et al., 2010), large amplitude wave dynamics (Ahmed et al., 2010) and uncertainty in irregular waves (Belenky and Weems, 2011, Kim et al., 2011).

Roll motion stabilisation has been an important issue among naval architects for a long time. However there are few researches on the reduction of parametric roll. Umeda et al. (2008) assessed the effectiveness of using sponsons or ART to prevent parametric rolling experimentally. Results demonstrated that both sponson and ART were effective in preventing

parametric rolling. Meanwhile Holden et al. (2009) applied an active u-tank to stabilize parametric roll using Lyapunov theory. And the results are very encouraging. Except for sponsons and ART which aren't normally installed on ships, rudder can also be used to prevent parametric roll.

In the present numerical analysis, a 6-DOF unified model for the simulation of parametric roll in regular head seas is developed based on the IRF approach formulated by Cummins (1962). This approach can compromise the accuracy and efficiency of numerical computation. The required hydrodynamic coefficients are calculated through strip theory. The non-linear restoring forces are calculated through pressure integration on instantaneous wetted surfaces. In this study, ship sea-keeping, manoeuvring and control, coupling between roll and other motion are considered. Thus, the influence of manoeuvring motion like sway and time-varying speed can be discussed. In manoeuvring equations, the propeller thrust has been estimated through the propeller characteristics and hull resistance, while rudder forces are calculated based on an empirical formulae.

To validate the present model, simulation results are compared with limited experiment results which are obtained from a normal sea-keeping experiment of a 3100teu containership conducted in SJTU. Then the model is applied to simulate parametric roll motion of three different containerships: C11 containership, a 3100TEU container ship and a 320m long containership. Although the model is capable of coupling all six degrees of freedom, results in these simulations were performed using 3-DOF, namely heave-roll-pitch, for simplicity. Additionally a thorough investigation into the influence of the inclusion of surge motion in the simulation of parametric roll is conducted using the fully coupled 6-DOF model. Finally based on the 6-DOF sea-keeping and manoeuvring model, rudder is used to stabilize parametric roll while at the same time keeping the ship's course. The controller is designed using traditional PID method.

2. MATHEMATICAL MODEL FOR PARAMETRIC ROLL

In the present numerical model, a combined seakeeping and manoeuvring analysis is carried out by the unified model presented by Skejic and Faltinsen (2006). Based on the unified theory, the manoeuvring analysis is divided into two time scales, slowly and rapidly varying ones. The slowly varying one is associated with manoeuvring analysis, while the rapidly varying one concerns with seakeeping analysis conducted in a mean forward speed without feedback from the slowly varying one. Based on this assumption, the 6-DOF mathematical model for parametric roll is developed.

2.1 Coordinate System

Three coordinate systems are used for describing ship motion, namely the earth fixed coordinate $O_e-x_e y_e z_e$, the body fixed coordinate $O-xyz$ and the horizontal body axes coordinate $O-x_h y_h z_h$. The coordinate $O-x_h y_h z_h$ moves along with ship with its axes parallel to the axes of the Earth-fixed co-ordinate, as presented in Figure 1.

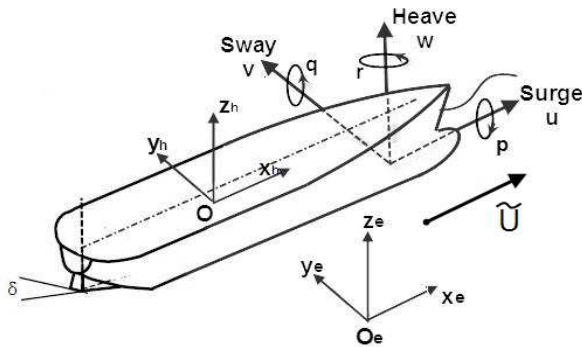


Figure 1: Definition of coordinate system and ship motions.

The ship is moving forward with speed \tilde{U} . The position, velocity and force vectors are defined as:

$$\begin{aligned} \boldsymbol{\eta} &= [x, y, z, \phi, \theta, \psi]^T \\ \mathbf{v} &= [u, v, w, p, q, r]^T \\ \mathbf{f} &= [X, Y, Z, K, M, N]^T \end{aligned} \quad (1)$$

The velocity vector \mathbf{v} which is defined in body-fixed coordinate will be transferred to earth-fixed coordinate:

$$\dot{\boldsymbol{\eta}} = \begin{bmatrix} \mathbf{R}_{3 \times 3} & \mathbf{0}_{3 \times 3} \\ \mathbf{0}_{3 \times 3} & \mathbf{Q}_{3 \times 3} \end{bmatrix} \mathbf{v} \quad (2)$$

where

$$\mathbf{R}_{3 \times 3} = \begin{bmatrix} \cos \psi \cos \theta & -\sin \psi \cos \phi + \sin \psi \sin \phi + \cos \psi \sin \theta \sin \phi & \cos \psi \sin \theta \cos \phi \\ \sin \psi \cos \theta & \cos \psi \cos \phi + \sin \psi \sin \theta \sin \phi & -\cos \psi \sin \phi + \sin \psi \sin \theta \cos \phi \\ -\sin \theta & \cos \theta \sin \phi & \cos \theta \cos \phi \end{bmatrix}$$

$$\mathbf{Q}_{3 \times 3} = \begin{bmatrix} 1 & \sin \phi \tan \theta & \cos \phi \tan \theta \\ 0 & \cos \phi & -\sin \phi \\ 0 & \sin \phi / \cos \theta & \cos \phi / \cos \theta \end{bmatrix} \quad \mathbf{0}_{3 \times 3} = \begin{bmatrix} 0 & 0 & 0 \\ 0 & 0 & 0 \\ 0 & 0 & 0 \end{bmatrix}$$

Then the mathematical model for parametric roll is set up according to these coordinate systems

2.2 Manoeuvring and Seakeeping Model

In the unified model, the manoeuvring motion is simulated through a 3-DOF surge-sway-yaw manoeuvring model, proposed by Japanese research group: Manoeuvring Mathematical Modelling Group (MMG).

$$\begin{bmatrix} m - X_{\dot{U}} & 0 & 0 \\ 0 & m - Y_{\dot{V}} & mx_G - Y_{\dot{R}} \\ 0 & mx_G - N_{\dot{V}} & I_z - N_{\dot{R}} \end{bmatrix} \begin{bmatrix} \dot{U} \\ \dot{V} \\ \dot{R} \end{bmatrix} + \begin{bmatrix} 0 & -mR & 0 \\ 0 & -Y_V & mU - Y_R \\ 0 & -N_V & mx_G U - N_R \end{bmatrix} \begin{bmatrix} U \\ V \\ R \end{bmatrix} = \begin{bmatrix} X_{\delta} \\ Y_{\delta} \\ N_{\delta} \end{bmatrix} \delta + \begin{bmatrix} -R(\dot{U}) \\ +(1-t)T(\dot{U}) \\ 0 \\ 0 \end{bmatrix} \quad (3)$$

where m and I represent the ship mass and moment of inertia, (x_G, y_G, z_G) is the location of centre of gravity referring to the body fixed coordinate, and $(X_{\delta}, Y_{\delta}, Z_{\delta})$, R and T are defined as rudder force, resistance and propeller thrust respectively. And the velocity vector in Eq. (3) is defined as:

$$[U, V, W]^T = [\dot{x}, \dot{y}, \dot{z}]^T = \mathbf{R}_{3 \times 3} [u, v, r]^T \quad (4)$$



In the MMG manoeuvring model, forces and moments acting on the ship are separated into hull hydrodynamic forces, rudder forces and propeller forces from the viewpoint of the physical meaning. In this paper, the hydrodynamic coefficients are estimated using the empirical formula proposed by Kijima et al. (1990). The propeller thrust is equal to the calm water resistance when ship is sailing at speed \tilde{U} . The rudder forces are calculated:

$$\begin{cases} X_R = -0.5(1-t_R)\rho A_R U_R^2 C_N \sin \alpha_R \sin \delta \\ Y_R = -0.5(1+a_H)\rho A_R U_R^2 C_N \sin \alpha_R \cos \delta \\ N_R = -0.5(GR_L + a_H x_H)\rho A_R U_R^2 C_N \sin \alpha_R \cos \delta \\ K_R = -GR Y_R \end{cases} \quad (5)$$

where A_R , U_R , GR , GR_L are the rudder area, the advance speed of rudder, the vertical and longitudinal distance between centre of gravity and point of rudder force. And the rudder force coefficient C_N is determined empirically. K_R indicates the force that rudder imposed on roll motion, which is added on the 6-DOF seakeeping model and is used for the stabilization of parametric roll.

The rapidly varying motion, namely the sea-keeping motion, is simulated by a 6-DOF model based on the IRF approach (Cummins, 1962). And the equation of motion can be written as:

$$\sum_{j=1}^6 \left[(m_{ij} + a_{ij}(\infty)) \dot{v}_j(t) + \int_0^t R_{ij}(t-\tau) v_j(\tau) d\tau + F_i^{res}(t) \right] \quad (6)$$

$$= F_i^{FK}(t) + F_i^{dif}(t)$$

where m_{ij} and $a_{ij}(\infty)$ stand for the ship mass and the infinite-frequency added mass. And the nonlinear restoring forces, incident wave forces and diffraction forces are denoted as $F_i^{res}(t)$, $F_i^{FK}(t)$, $F_i^{dif}(t)$. According to the IRF approach, the radiation forces are given by:

$$F_i^{rad}(t) = \sum_{j=1}^6 \int_0^t R_{ij}(t-\tau) v_j(\tau) d\tau \quad (7)$$

where the retardation function can be derived from either added mass or damping coefficients calculated by the 2-D strip theory:

$$\begin{aligned} R_{ij}(t) &= \frac{2}{\pi} \int_0^\infty b_{ij}(\omega_e) \cos(\omega_e t) d\omega_e \\ &= -\frac{2}{\pi} \int_0^\infty \omega_e [a_{ij}(\omega_e) - a_{ij}(\infty)] \sin(\omega_e t) d\omega_e \end{aligned} \quad (8)$$

And the diffraction forces are also derived based on the IRF approach:

$$F_i^{dif}(t) = \int_{-\infty}^t Q_i(t-\tau) \alpha(\tau) d\tau \quad (9)$$

$\alpha(\tau)$ is the wave elevation, and the retardation function can be derived from the frequency domain diffraction forces calculated by the strip theory:

$$\begin{aligned} Q_{ij}(t) &= \\ \frac{1}{\pi} \int_0^\infty & [d_{ij}^R(\omega_e) \cos(\omega_e t) - d_{ij}^I(\omega_e) \sin(\omega_e t)] d\omega_e \end{aligned} \quad (10)$$

The restoring and Froude-Krylov forces are calculated nonlinearly through pressure integration on instantaneous wetted surfaces.

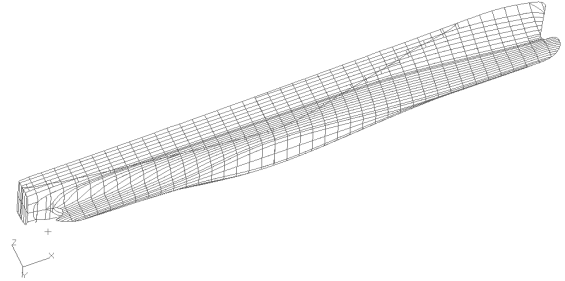


Figure 2: Hull NURBS Surfaces

The hull and upper deck consist of several NURBS surfaces. Each surface has an area of A_i , a central point $r_i=(x_i, y_i, z_i)$ with a normal vector $n_i=(n_{xi}, n_{yi}, n_{zi})$ in body-fixed axis. And the restoring forces and incident wave forces:

$$F_3^{FK\&res} = \sum_{i=1}^N A_i P(r_i^*) n_{zi}^* - mg \cos \theta \cos \phi \quad (11)$$

$$F_i^{FK\&res} = \sum_{i=1}^N A_i P(r_i^*) n_i^* \times (r_G - r_i^*), (i=4,5) \quad (12)$$

where the pressure are given by:

$$\begin{aligned} P(r_i^*) &= \rho g (d(x_i^*) - z_i^*) \\ &+ A \rho g e^{k(z_i^* - d(x_i^*))} \cos(kx_i^* - \omega_e t) \end{aligned} \quad (13)$$

and the superscript (*) indicates vectors in earth fixed coordinate system. For surge, sway and yaw motion, the concept of soft spring is adopted to prevent the monotonously changing motion. The spring stiffness can be calculated as follows:

$$C_{ij} = (m_{ij} + a_{ij}(\infty)) \times \left(\frac{2\pi}{T_i} \right)^2, i = 1, 2, 6 \quad (14)$$

The viscous roll damping coefficient is estimated by using free rolling test results for the 3100teu containership and semi-empirical formulae (Ikeda et al., 1978) for the others.

2.3 The Unified Model

In the unified model, the manoeuvring and seakeeping models described above are solved in different time scale. As a slowly varying motion, the manoeuvring motion is simulated using larger time step than the seakeeping motion. In this paper, the time step of the manoeuvring model is set as ten times that of the seakeeping model. And for the seakeeping simulation which is done within one time step of the manoeuvring simulation, the slowly varying motion $\boldsymbol{\eta}$ is assumed to be constant. Then the total motion of the ship is calculated by combining the two motions referring to different coordinate system together:

$$\begin{aligned} [X, Y, Z, \Phi, \Theta, \Psi] &= [x^0, y^0, z^0, \phi^0, \theta^0, \psi^0] \\ &+ \left[\int_0^t U dt, \int_0^t V dt, \int_0^t W dt, \int_0^t \Phi dt, \int_0^t \Theta dt, \int_0^t \Psi dt \right] \end{aligned} \quad (15)$$

where superscript 0 means the initial value for time $t = 0$, and the seakeeping velocity in earth-fixed coordinate:

$$[U, V, W, \Phi, \Theta, \Psi]^T = \begin{bmatrix} \mathbf{R}_{3 \times 3} & \mathbf{0}_{3 \times 3} \\ \mathbf{0}_{3 \times 3} & \mathbf{Q}_{3 \times 3} \end{bmatrix} [u, v, w, p, q, r]^T \quad (16)$$

Thus the sea-keeping and manoeuvring computations are interconnected in the unified model.

3. PROGRAM VALIDATION

To validate the present mathematical model, the variation of restoring characteristics in wave and the motion RAOs of a C11 containership are observed.

Table 1: Main particulars of C11 containership

Length between perpendiculars, L_{pp}	262	m
Breadth, B	40	m
Depth, D	24.45	m
Fore draft, d_f	11.5	m
Aft draft, d_a	11.5	m
Displacement	69196	t
Metacentric height, GM	1.928	m
Block coefficient, C_B	0.56	m
Radius of gyration, roll k_{xx}	16.095	m
Radius of gyration, pitch/yaw k_{yy}/k_{zz}	62.88	m
Roll natural period, T_R	24.68	s
Speed, V	2.572	m/s

When the wave passage passes along ship hull, large variation of water plane area will

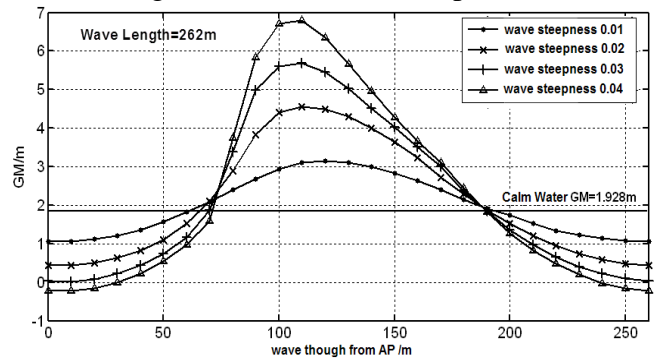


Figure 3: GM fluctuation

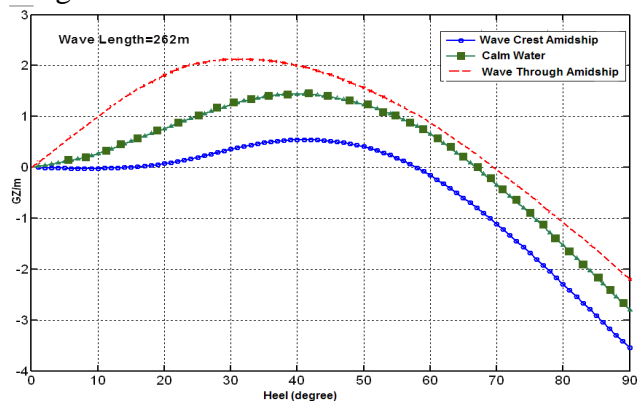


Figure 4: GZ curve in calm water, wave crest amid ship and wave through amid ship.



result in huge fluctuation in GM. And the variation can be calculated by using the code for pressure integration on instantaneous wetted surfaces, as shown in Fig. 3. It shows that the larger wave steepness is, the larger GM variation becomes. Moreover GM decreases as wave crest moves close to mid ship, increases as wave trough moves close to mid ship. This result can also be confirmed from Fig. 4, showing GZ curves in calm water, wave crest amid ship and wave trough amid ship.

To validate the seakeeping model, the heave and pitch RAOs of the containership are obtained using 2-D strip theory, and the corresponding time domain motions are computed based on the seakeeping model with a wave height of 1m. Then the motion RAOs derived from the Fourier transform of the time signals are compared with the one obtained from strip theory, as shown in Fig.5.

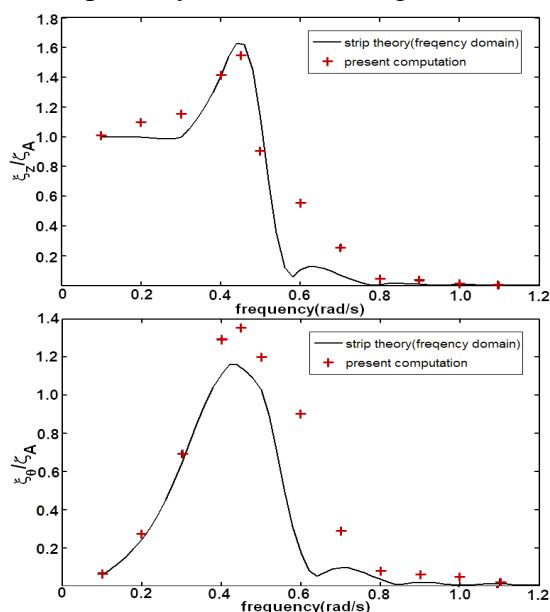


Figure 5: Heave and pitch RAOs in head sea

The agreement between two approaches is generally fine, except for some points. And the discrepancy maybe cause by the nonlinear restoring forces which are not considered in the strip theory results.

Experimental data for parametric roll is very limited. However a set of experiment results is obtained from a normal sea-keeping experiment of a 1:68.694 containership model

conducted in SJTU. Parametric roll happened in the case with a wave height of 9.348cm and frequency of 0.66Hz. The model speed was 0.35m/s. The present computational code is utilized to simulate the parametric roll of the 3100TEU containership with the same loading condition and wave as experiment. The viscous roll damping is estimated by using free rolling test data. The resulting motions are compared with those recorded in the experiment, as shown in Fig. 6.

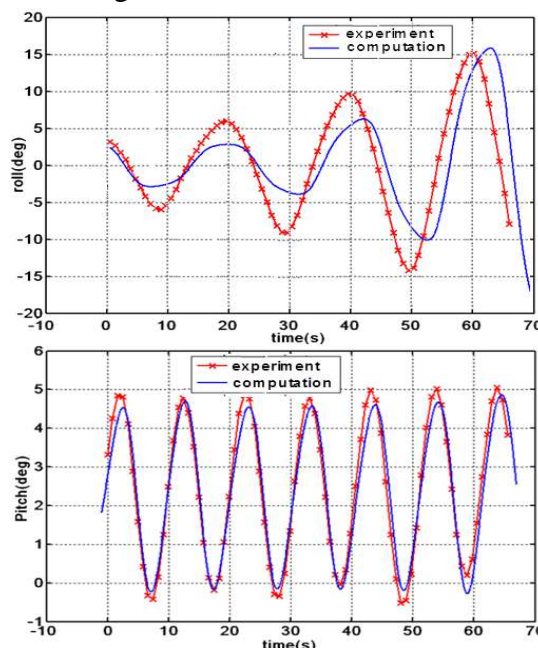


Figure 6: Comparison with experiment data

Due to the limitation of the experimental setup, only short time roll and pitch motions are recorded during the onset stage of parametric roll. However, the comparison shows good agreement for pitch motion, while roll motion does not agree very well. And through further investigation on the experiment video, it is found that the regular wave profile is largely deformed due to the severe roll motion, which is not considered in present mathematical model. Meanwhile without considering other non-linear effects and speed loss, the simulated roll motion is still quite ideal.

Through all the validations, the present mathematical model is proved to be effective in simulating parametric roll motion, although it looks quite ideal without considering the fully nonlinear condition.

4. SAMPLE SHIP CALCULATION

Because container ship has relatively thin aft and fore body which cause large water plane area fluctuations under different wave position, three container ships are chosen as sample ships. The three ships include the C11 container-ship mentioned in the last chapter, a 3100teu containership and a 320m long containership with two different loading conditions. Main particulars are shown in the following table:

Table 2: Main particulars of sample ships

	3100 TEU	320m L.C.I	320m L.C.II
Length between per-pendiculars, $L_{pp}(m)$	214.2	320	320
Breadth, $B(m)$	32.2	42.8	42.8
Depth, $D(m)$	18.8	24.8	24.8
Fore draft, $d_f(m)$	11.49	14.53	13.60
Aft draft, $d_a(m)$	12.31	14.74	14.28
Displacement(t)	55633	137255	129288
Metacentric height, $GM(m)$	0.85	0.95	0.53
Block coefficient, C_B	0.668	0.643	0.640
Radius of gyration, roll, $k_{xx}(m)$	7.09	14.27	14.27
Radius of gyration, pitch/yaw, $k_{yy}/k_{zz}(m)$	53.6	80	80
Roll natural period, $T_R(s)$	18.85	32.17	43.06
Speed, $V(m/s)$	11.57	0	0

In order to evaluate their vulnerability for parametric roll, the ship motion is simulated in regular head waves with 180° heading angle and length equal to each ship length, using the simulation program with 3-DOF, heave-roll-pitch. And the wave steepness varies from 0 to 0.05. The viscous roll damping coefficient is estimated using semi-empirical methods (Ikeda et al., 1978). During the calculation, the initial rolling angle is set to 0.2 degree acting as the small disturbance which causes parametric roll.

Results show that parametric roll happens on every ship except for the 320m long containership loading condition II. The motion time history of some cases where parametric roll occurs is presented in the following figures:

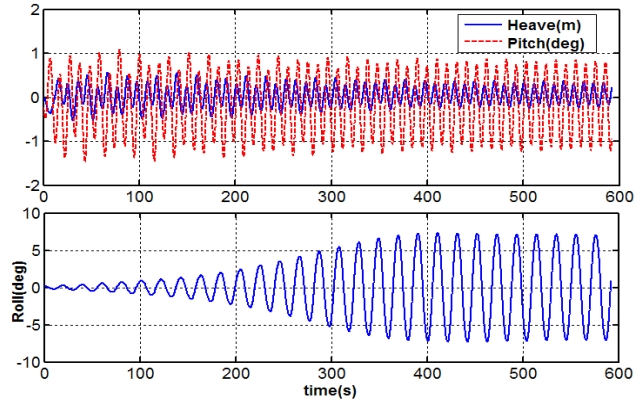


Figure 7: 3100TEU, wave steepness 0.005

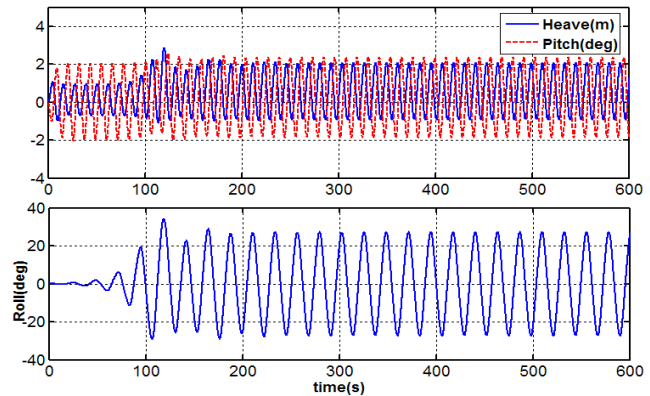


Figure 8: C11 containership, wave steepness 0.02

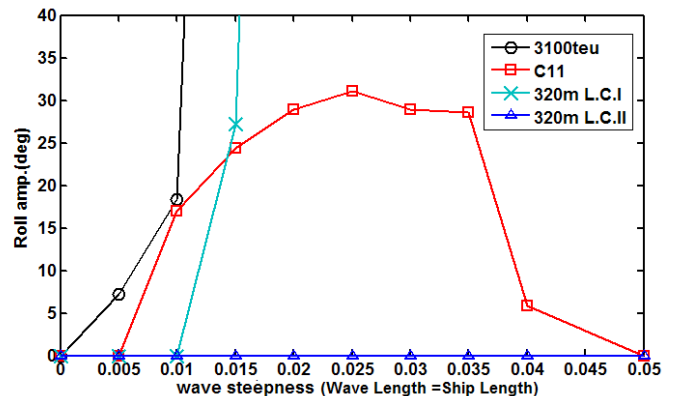


Figure 9: Roll amplitude of different ships

And the roll amplitude of each case is demonstrated in Fig.9. Results indicate large difference in parametric roll resonance for different ships and loading conditions.

For the 320m long ship, loading condition II doesn't experience parametric roll even in heavy waves, while loading condition I



encounters severe parametric roll and even capsizes. Above all, two loading conditions have different GM, which causes the difference on natural roll period. With the same encounter period 14.32s, loading condition I has the natural roll period close to twice of the encounter period, while loading condition II doesn't. Therefore parametric roll doesn't happen on loading condition II. According to the simulation results, 3100teu and 320m long (L.C. I) containerships capsized (roll angle > 40degrees) at wave height 2.3m (steepness 0.0108) and 4.9m (steepness 0.0154) respectively. However, the capsizing criteria wave height could be higher due to the restoring force from the water-tight superstructure and other non-linear effects, which are neglected here.

Comparing to other ships, the C11 container-ship doesn't capsize in heavy waves but has large roll amplitudes. Although, large GM variation and small block coefficient make it vulnerable for parametric roll in head waves. The C11 containership has a large bow flare which provide extra roll restoring moment in large roll angle and lower the possibility of capsizing.

Furthermore with a complete set of rudder and propeller data, the 3100teu containership is also used to simulate parametric roll base on the unified model coupling both maneuvering

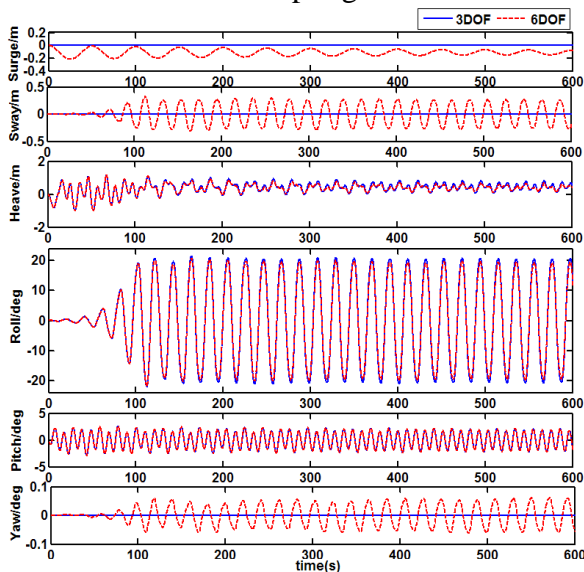


Figure 10: Comparison between 3-DOF model and 6-DOF unified model

and seakeeping. Thus the influence of surge, sway and yaw motion on parametric roll is investigated by comparing the results with that of the 3-DOF program, as presented in Fig. 9:

Through the comparison, it is found that there is no significant difference in roll, heave and pitch motion results between the two models in head sea. So at least in this simulation condition, surge, sway and yaw motion has little influence on parametric roll simulation. But the maneuvering model is important especially when applying rudder to stabilize parametric roll while keeping ship's course and considering speed loss due to waves.

5. RUDDER PARAMETRIC ROLL STABILIZATION

Due to the vertical height between rudder force center and center of gravity, rudder can generate roll moment, which can be considered for the purpose of stabilization of parametric roll. But rudder's ability in keeping ship's course should not be affected. So it's crucial and indispensable to study rudder parametric roll stabilization based on the unified model presented in this paper which considers both maneuvering and seakeeping.

In the present study, rudder is utilized to prevent and stabilize parametric roll motion of the 3100TEU containership described in the last chapter based on the unified model. And the PD control scheme is implemented on rudder to control roll and yaw motion. The rudder characteristics are shown in Table 3:

Table 3: Rudder Characteristics

Area, A_R	42.58	m^2
Longitudinal distance between Rudder force centre and ship centre of gravity, GR_L	106.93	m
Vertical distance between Rudder force centre and ship centre of gravity, GR	8.95	m
Rudder Height, h	9.6	m
Aspect Ratio, λ	2.12	

5.1 PD Control Scheme

Based on the traditional PD control method, the controller output, namely rudder angle is determined by input error, namely roll angle and yaw angle:

$$\begin{aligned} \delta_{roll} &= G_1 p + G_2 \phi \\ \delta_{yaw} &= G_3 r + G_4 (\psi - \psi_0) \end{aligned} \quad (17)$$

where ψ_0 is the initial heading angle, and the coefficients G_1, G_2, G_3, G_4 are determined theoretically and adjusted during simulation.

maximum rudder angle is set to 8 degree per second and 35 degree respectively.

5.2 Simulation Results

According to the last chapter, parametric roll occurs on the 3100TEU containership in certain wave (wave length= L_{pp} , wave steepness=0.01). Then the PD rudder controller is applied to stabilize the parametric roll. Results are presented in Fig.11.

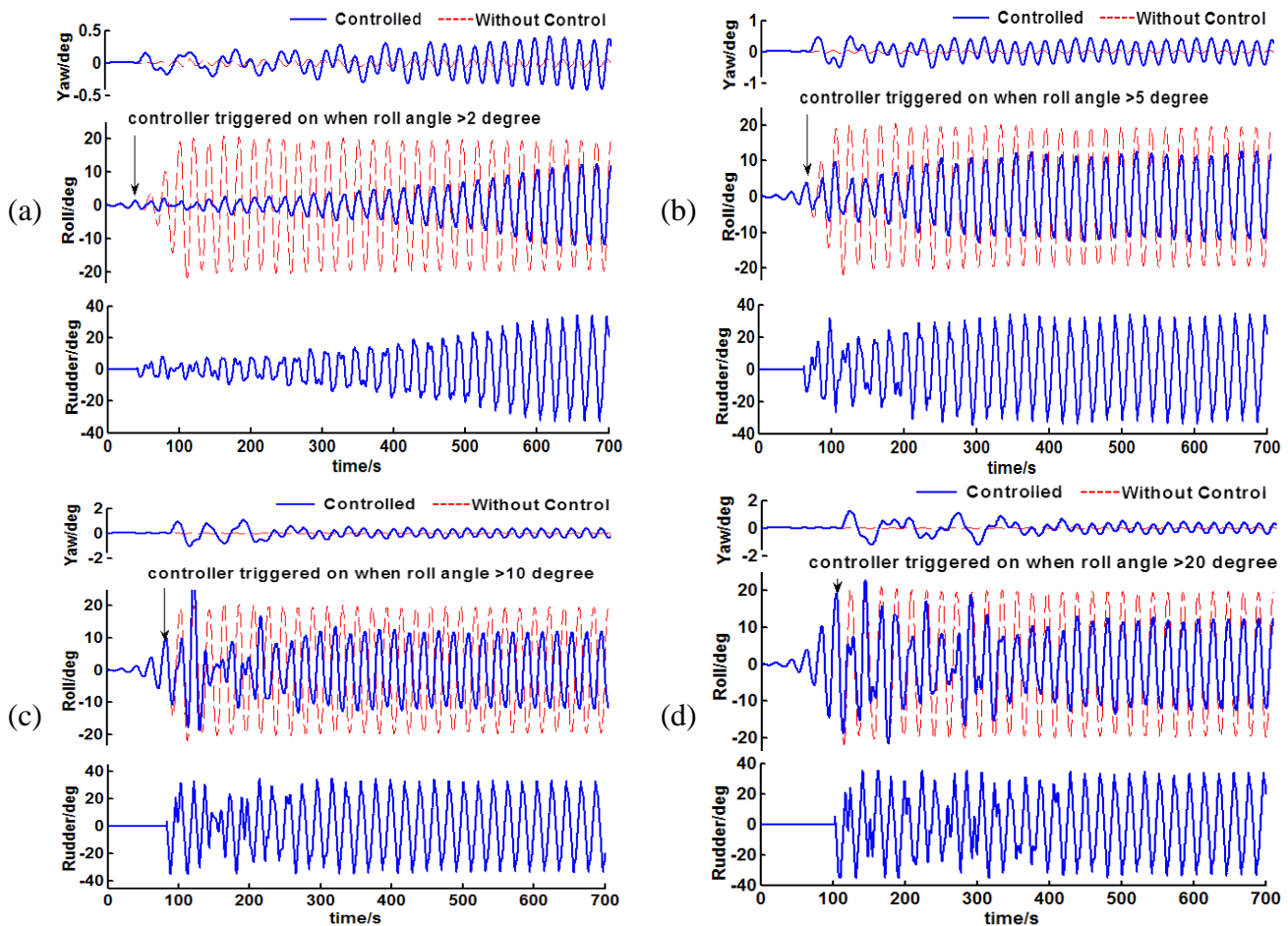


Figure 11: Simulation results of rudder parametric roll stabilization with different controller trigger time

To achieve a better roll reduction effect, the PD course keeping controller and PD roll stabilization controller were activated individually. When the yaw angle variation exceeds 3 degree, the roll stabilization controller will be shut down and course keeping controller will be triggered on, vice versa. According to the mechanism of rudder, the maximum turning rate of rudder and

Comparing to roll motion without roll stabilization (dot line), results show that rudder roll stabilization is quite efficient in reducing parametric roll amplitude. But it will also increase yaw motion significantly. And rudder angle changes frequently.

In the simulation, the PD controller can be triggered on when roll angle exceed a certain value or roll amplitude changing rate is large.



As shown in Fig.11, the controller is triggered on when roll angle exceed four different values. Then results with different controller trigger time are acquired. It seems that rudder roll stabilization based on PD control method can't prevent parametric roll from happening, no matter when the controller is triggered on. However, it appears that early controller trigger time can postpone the occurrence of parametric roll. And the final steady roll amplitude is almost the same and does not affect by different controller trigger time.

In general, rudder anti-roll moment can stabilize parametric roll motion effectively with the maximum reduction of about 50% of the original roll amplitude for the target ship.

6. CONCLUSIONS

In this paper, a time domain 6-DOF unified model for the simulation and stabilization of parametric roll considering ship sea-keeping, manoeuvring and control in regular head seas is presented. The model is validated by comparing the simulation results with limited experiment results, 3-DOF method and strip method.

The parametric roll simulation of three containerships is conducted using the 3-DOF model. From the results, significant difference in parametric roll resonance for different ships and loading conditions is observed. Through the comparison of different ships, GM and block coefficient are important factors for the occurrence of parametric roll.

The influence of surge, sway and yaw motion on parametric roll is investigated by using the 6-DOF model, and the results are compared with that of the 3-DOF program. Results indicate that in head sea condition, surge, sway and yaw motion has little influence on parametric roll simulation.

Utilization of rudder is attempted to stabilize parametric roll motion while keeping

the ship's course based on the unified model. And rudder roll stabilization using PD control scheme can reduce the amplitude of parametric roll, but can't prevent it from happening. Moreover, early controller trigger time can postpone the occurrence of parametric roll, but doesn't affect the final steady roll amplitude.

7. REFERENCES

- Ahmed, T.M., Hudson, D.A., and Temarel, P., 2010, "An investigation into parametric roll resonance in regular waves using a partly non-linear numerical model", Ocean Engineering, Vol. 37, No. 14/15, pp. 1307–1320.
- Belenky, V., and Weems, K., 2011, "Probabilistic Properties of Parametric Roll", Proc. Workshop on Parametric Resonance in Dynamical Systems, Spitsbergen, Norway, 21 p.
- Bulian, G., 2005, "Nonlinear parametric rolling in regular waves-a general procedure for the analytical approximation of the GZ curve and its use in time domain simulations", Ocean Engineering, pp. 309-330.
- Cummins, W.E., 1962. "The impulse response function and ship motions", Schiffstechnik, 47(9), pp. 101-109.
- France, W.N., Levadou, M., Treacle, T.W., Paulling, J.R., Michel, R.K., Moore, C., 2003. "An Investigation of head sea parametric rolling and its influence on container lashing systems", Marine Technology 40 (1), 1–19.
- Hashimoto H., and Umeda N., 2010, "A study on Quantitative Prediction of Parametric Roll in Regular Waves", Proc. 11th Int'l Ship Stability Workshop, Wageningen, Netherlands, 7p.
- Holden C., Galeazzi R., Fossen T. I., Perez T., 2009, "Stabilization of Parametric Roll



- Resonance with Active U-Tanks via Lyapunov Control Design”, Proceedings of the European Control Conference, Budapest, Hungary.
- Ikeda, Y., and Himeno, Y., “Report of the Department of Naval Architecture University of Osaka Prefecture, A Prediction Method for ship Roll Damping”, report number 00405, 1978
- ITTC, The Specialist Committee on Stability in Waves, Final Report and Recommendations to the 26th ITTC, Proceedings of the 26th ITTC, Vol. II, pp.534-542, 2011.
- Kijima K., Toshiyuku K., Yasuaki N., Yoshitaka F., 1990, “On the manoeuvring performance of ship with the parameter of loading condition”, Journal of The society of Naval Architects of Japan, pp141-148
- Kim, Y., Park, D.M., Kim, T.Y., Song, K.H., 2011, “On uncertainty of in numerical analysis of parametric roll”, Proc. Int. Workshop on Ship Stability, Washington DC, USA.
- Matusiak, J., 2003, “On the Effects of Wave Amplitude, Damping and Initial Conditions On the Parametric Roll Resonance”, 8th International Conference on the Stability of Ships and Ocean Vehicles, pp. 341-347.
- Nayfeh, A.H., 1988. “On the undesirable roll characteristics of ships in regular seas”, Journal of Ship Research, 32(2), pp. 89-103.
- Neves, M.A.S., Perez, N., Valerio, L., 1999. “Stability of small fishing vessels in longitudinal waves”, Ocean Engineering 26, 1389-1419.
- Pauling, J.R. and Rosenberg, R.M., 1959. “On unstable ship motions resulting from nonlinear coupling”, Journal of Ship Research, 3(1), pp. 36-46.
- Sadat-Hosseini, H., Stern, F., Olivieri, A., Campana, E., Hashimoto, H., Umeda, N., Bulian, G., Francescutto, A., 2010. “Head-waves parametric rolling of surface combatant”, Ocean Engineering, 37(10), pp. 859-878
- Shin, Y.S. Belenky, V.L Pauling, J.R. Weems, K.M. and Lin W.M., 2004. “Criteria for parametric roll of large container ships in longitudinal seas”, SNAME Annual Meeting, Washington DC.
- Spanos, D. and Papanikolaou, A., 2007. “Numerical simulation of parametric roll in head seas”, International Shipbuilding Progress, 54, pp. 249-267.
- Spanos, D. and Papanikolaou, A., 2009, “Benchmark Study on Numerical Simulation Methods for the Prediction of Parametric Roll of Ships in Waves”, Proc. 10th Int’l Conf. Stability of Ships & Ocean Vehicles, St Petersburg, Russia.
- Skejic, R., Faltinsen, O. M., 2006, “A unified seakeeping and maneuvering analysis of a monohull in regular incident waves”, Proceedings of the 7th international conference on hydrodynamics, Ischia, pp 97–104
- Umeda, N., Hashimoto, H., Vassalos, D., Urano, S. and Okou, K. 2004, “Nonlinear Dynamics on a Parametric Roll Resonance with Realistic Numerical Modelling”, International Shipbuilding Progress, Vol.51, No.2/3, pp.205-220.
- Umeda, N., Hashimoto, H., Minegaki, S., and Matsuda, A., 2008, “An investigation of different methods for the prevention of parametric rolling”, Journal of Marine Science and Technology, 13, pp. 16-23.
- Vidic-Perunovic, J. and Juncher J.J., 2009, “Parametric roll due to hull instantaneous volumetric changes and speed variations”, Ocean Engineering, Vol. 36 No. 12/13, pp.891–899.





Study of System-based Mathematical Model Using System Identification Technique with Experimental, CFD, and System-Based Free Running Trials in Following Waves

Motoki Araki¹, Hamid Sadat-Hosseini², Yugo Sanada¹, Naoya Umeda¹, Frederick Stern²

¹*Department of Naval Architecture & Ocean Engineering, Osaka University, Japan*
motoki_araki@naoe.eng.osaka-u.ac.jp

²*IHR – Hydrosience & Engineering, The University of Iowa, Iowa City, USA*
frederick-stern@uiowa.edu

ABSTRACT

Predicting ship maneuverability and stability in following and quartering waves are one of the most important topics to prevent broaching; however system-based (SB) simulations have quantitative errors with the experimental free running results while CFD simulations show quantitative agreement which is promising to improve the mathematical model employed in system-based. Here system identification technique is applied to improve maneuvering coefficients in the SB model and wave correction parameters are used to improve the wave model in the SB model using CFD outputs. From turning circle and zigzag calm water CFD free running data, the maneuvering coefficients are estimated. Also, the wave correction parameters are found from a few forced and free running CFD simulations in waves. The SB simulations using the estimated parameters shows much better agreement with experiments in calm water and waves than the original SB simulations. The original SB simulations were conducted using maneuvering coefficients estimated from several captive tests and wave forces calculated from linear Froude-Krylov forces and diffraction forces based on a slender ship theory.

Keywords: *System identification, constrained least square method, Wave model, Seakeeping*

1. INTRODUCTION

Ship stability and maneuverability in waves are one of the most important topics for ship safety. Especially, in following and quartering waves, it is necessary to discuss about maneuverability in waves to prevent dangerous phenomena like broaching.

System-based (SB) and recently computational fluid dynamic (CFD) methods are used to predict ship stability and maneuverability in calm water and waves. The

SB approach in this paper means an approach consisting of two layered sub systems. In the lower layer, hydrodynamic forces mainly due to potential flow are calculated by solving partial differential equations of potential flow and hydrodynamic forces mainly due to viscosity flow are estimated with captive model experiments or empirical formulas. In the upper layer, ship motions are calculated by solving ordinary differential equations with initial conditions. Since short computational time is required to sweep out dangerous maneuvering and wave conditions from huge number of



suspect conditions, the SB method shows superior ability to the CFD; SB needs less than a minute for one free running simulation using personal computer while CFD needs a few weeks or a month using very expensive supercomputer. Meanwhile it is also very expensive and time consuming to predict maneuvering and rudder coefficients from captive model tests which is necessary for SB method while CFD just needs ship geometry and propeller characteristics. The SB free running simulations in calm water showed that the SB model was very sensitive to the accuracy of the maneuvering coefficients such that the scatter in the SB predictions were substantial for a SB model with coefficients estimated from different captive tests (Stern et al., 2011). Also, SB showed only qualitative agreement with experimental fluid dynamics (EFD) free running results in following and quartering waves while CFD shows quantitative agreement (Sadat-Hosseini et al., 2011). Since CFD free running simulation can provide not only ship motion but also total forces/moments acting on the ship which are unknown during EFD free running, it could give a chance to modify and tune the SB model to reduce the disagreement with EFD free running results in calm water and waves.

For calm water maneuvers, several researches showed system identification (SI) techniques are available to predict maneuvering coefficients from free running results. EFD (Abkowitz, 1980) or SB simulation results (Rhee, 1999) are often used to reconstruct the coefficients. The authors used CFD outputs to improve the SB predictions in calm water (Araki et al., 2012). Hydrodynamic and rudder maneuvering coefficients included in a SB model were estimated from turning circle and zigzag CFD free running simulations trial data. The SB simulations using the predicted coefficients showed much better agreement with EFD free running than those using coefficients estimated from captive model experiments and empirical prediction. Hence, several CFD free running simulations could replace the many number of captive model

experiments needed to estimate the maneuvering coefficients for the SB model.

For maneuvering in waves, the hydrodynamic maneuvering coefficients estimated from EFD captive test in calm water are often used in SB model. Also, the wave forces are considered as summation of Froude-Krylov and diffraction forces. These result in discrepancy between SB prediction and EFD as maneuvering coefficients variations due to waves and wave drift forces are important for SB prediction in waves (Son and Hamamoto, 1982).

The objective of the present work is to employ the SI technique with CFD outputs to improve SB predictions in following and quartering waves by tuning the maneuvering coefficients and wave forces. The wave forces/effects are found from CFD simulations. First CFD free running simulations in waves are executed. Second, CFD forced motion simulations in calm water are performed with imposing exactly same motions as the free running simulation. The wave forces/effects are estimated as the difference between the total force of the first and second simulations. The CFD wave forces/effects are compared with the conventional SB wave model based on slender body theory and used to tune SB wave forces/effects by the SI technique. The SI technique along with CFD outputs can improve the SB simulation in waves and provide opportunity for SB to have quantitative broaching prediction in following and quartering waves. The improved SB and CFD free running simulation results are compared with that of EFD. Here it should be pointed out that the SB and CFD simulations are done before the EFD data are available.

2. EFD, CFD, AND SB METHODS

2.1 Subject Ship

The 1/49 scaled model of ONR tumblehome (ONRTH), was developed at Naval Surface Warfare Center (Bishop et al., 2005), appended with skeg, bilge keels, rudders, shafts with

propeller shaft brackets and twin propellers was used for the free running experiments. The main particulars of the ONRTH ship are listed in Table 1. The details of the body plan and the model are shown in Fig. 1 and 2.

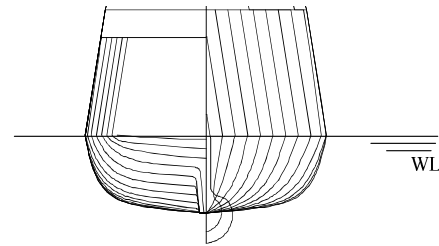


Figure 1: Body plan of the ONRTH model.

Table 1: Principal particulars of the ONRTH.

	Model scale
Length: L	3.147 m
Breadth: B	0.384 m
Depth: D	0.266 m
Draft: d	0.112 m
Displacement: W	72.6 kg
Metacentric height: GM	0.0424 m
Natural roll period: T_ϕ	1.644 s
Rudder area: A_R	$0.012 \text{ m}^2 \times 2$
Block coefficient: C_b	0.535
Vertical position of CoG from waterline (downward positive): OG	$-0.392 \times d$
Radius of gyration in pitch: κ_{yy}	$0.25 \times L$
Maximum rudder angle: δ_{\max}	$\pm 35^\circ$



Figure 2: Bow and stern of the ONRTH model: (a) bow; (b) stern.

2.2 EFD Method

All EFD free running data was acquired in IIHR wave basin. The wave basin has dimensions of 40×20 square meters with 3 meters water depth and is designed to test captive or radio-controlled model scale ships.

The model launch system enables specification and replication of the free running trial initial conditions. Roll, pitch and yaw angles of the model ship were measured by a fiber optical gyroscope. Meanwhile, the plane trajectory of model was recorded by the tracking system, which uses two-camera vision.



The tracking cameras capture two LED lights placed on the deck of model. In order to increase the reliability and accuracy of the 5DOF (Degree of Freedom) measurement and to enable measurement for all 6DOF of the free running model, i.e. the heave motion, a 6DOF visual motion capture system was added to the tracking system. A detailed description of the wave basin and wavemakers, carriage model tracking, 6DOF visual motion capture and free running 6DOF systems, model geometry and ballasting, and free running trials tests in calm water and waves is provided by Sanada et al. (2012).

The experimental procedure was as follows. First the model ship was fixed on the launch

system by electromagnetics while heave, roll and pitch are free. After the propeller starts to rotate, the model was accelerated by the launch system to reach the target speed. Since the towing system acts as the hard spring there would be small oscillations for the surge motion of the towed ship. After the ship was at the target speed the model was towed for more distance until the bow was located on the wave crest. Then the model was released and the rudder controller was activated after few seconds to start maneuvering. The propeller rate was kept constant during free running. The EFD and CFD trial conditions are shown in Table 2.

Table 2: EFD and CFD free running test matrice.

		Test	Nominal Fr	δ (deg)	ψ_c^* (deg)	H/ λ	λ/L_{pp}
EFD	Calm water	Turning circle	0.1, 0.2	25, 35	NA		
		Zigzag	0.1, 0.2	10,20,35	10,20,35		
		Large angle zigzag	0.2	35	90		
	Wave	Zigzag	0.1, 0.2	20	20	0.02,0.03	1.0
		Straight running	0.1, 0.2	NA	NA	0.02,0.03	1.0
		Course keeping	0.1, 0.2	Proportional control, P=1	20	0.02,0.03	1.0
CFD	Calm water	Turning circle	0.2	25	NA		
		Zigzag	0.2	20	20		
		Large angle zigzag	0.2	35	90		
	Wave	Zigzag	0.2	20	20	0.02,0.03	1.0
		Straight running	0.2	NA	NA	0.02,0.03	1.0
		Course keeping	0.2	Proportional control, P=1	20	0.02,0.03	1.0

ψ_c^* : target yaw angle

2.3 CFD Method

The code CFDSHIP-IOWA v4 (Carrica et al., 2010) is used for the CFD computations. The CFDSHIP-IOWA is an overset, block structured CFD solver designed for ship applications using either absolute or relative inertial non-orthogonal curvilinear coordinate system for arbitrary moving but non-deforming control volumes. Turbulence models include blended k- ϵ /k- ω based isotropic and anisotropic Reynolds Averaged Navier Stokes (RANS),

and (detached eddy simulations) DES approaches with near-wall or wall functions. A simplified body force model is used for the propeller which prescribes axisymmetric body force with axial and tangential components.

The propeller model requires the open water curves and advance coefficients as input and provides the torque and thrust forces. The open water curves are defined as a second order polynomial fit of the experimental $K_T(J)$ and $K_Q(J)$ curves. The advance coefficient is computed using ship speed with neglecting the

wake effects. Herein, two PID controllers are used. The heading controller acting on the rudders are responsible to turn the rudders to keep the ship in the desired direction. The speed controller acting on the body force propeller model is responsible to rotate the propellers at appropriate propeller rate to keep the ship at the desired speed. The heading controller uses $P=1$ for the proportional gain and zero for both the integral and derivative gains mimicking EFD setup.

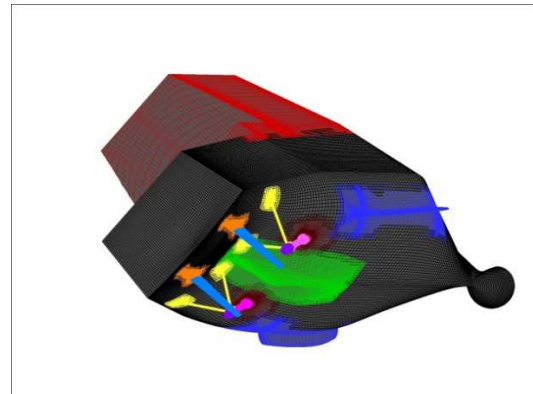


Figure 3: CFD overset grids for ONRTH hull and appendages.

Table 3: Grids for free model simulations.

Name	Size (grid points)	# of procs	Type
Hull S/P*	199x61x104 (1.26 M x2)	12 (x2)	Double O
Skeg S/P	61x49x40 (0.12 M x2)	1 (x2)	O
Bilge Keel S/P	99x45x50 (0.23 M x2)	2 (x2)	H
Rudder Root Collar S/P	121x35x28 (0.12 M x2)	1 (x2)	O
Rudder Root Gap S/P	121x51x19 (0.12 M x2)	2 (x2)	Conformal to Collar
Rudder Outer S/P	61x36x55 (0.12 M x2)	1 (x2)	Double O
Rudder Inner S/P	61x36x55 (0.12 M x2)	1 (x2)	Double O
Rudder Gap S/P	121x51x19 (0.12 M x2)	2 (x2)	Conformal to Inner and Outer
Shaft Collar S/P	39x50x57 (0.11 M x2)	1 (x2)	O
Shaft Proper S/P	74x41x37 (0.11 M x2)	1 (x2)	O
Shaft Tip S/P	110x117x100 (1.29 M x2)	12 (x2)	O with end pole
Strut Outer S/P	69x34x50 (0.12 M x2)	1 (x2)	O
Strut Inner S/P	69x34x50 (0.12 M x2)	1 (x2)	O
Superstructure	165x61x85 (0.86 M)	8	Wrap
Refinement	145x81x113 (1.33 M)	12	Cartesian
Background	213x84x113 (2.02 M)	20	O
Total	(12.1 M)	116	

* S/P: Starboard/Port

The CFD initial condition is different with EFD in several ways. The CFD model was accelerated with infinite rate to the target speed unlike EFD. Then the model was towed at target speed which was constant while the model was only free to heave and pitch and not roll until the wave trough was located at midship. After that, the model was released and

rudder controller was activated immediately to start maneuvering. The differences between EFD and CFD setup might cause some discrepancies between EFD and CFD results.

The free model is appended with skeg, bilge keels, superstructure, rudders, rudder roots, shafts, and propeller brackets same as the EFD model but not appended with actual propellers.



The computational grids are overset with independent grids for the hull, superstructure, appendages, refinement and background, and then assembled together to generate the total grid. The total number of grid points is 12.1 M for free model simulations. Details of the grids are shown in Table 3 and Fig. 3. The free running in waves and calm water verification studies have been done (Sadat-Hosseini et al., 2011, and Araki et al., 2012) which showed quantitative agreement with EFD results.

2.4 SB Method

4DOF maneuvering mathematical model was used for the SB simulations as shown in Eq. (1)-(5). The low encounter frequency model (Umeda et al, 2008) is 4DOF surge-sway-roll-yaw model and is modified especially for surge equation and rudder model (Araki et al, 2012). The model is developed in horizontal body axes which are shown in Fig. 4.

$$(m + m_x)\ddot{u} - (m + m_y)vr = T(u; n) - R(u; n) + X_{vv}(u)v^2 + X_{vr}(u)vr + X_{rr}(u)r^2 + X_R(\delta, u, v, r) + X_W \quad (1)$$

$$(m + m_y)\dot{v} + (m + m_x)ur = Y_v(u)v + Y_r(u)r + Y_\phi(u)\phi + Y_{vv}(u)v^3 + Y_{vr}(u)v^2r + Y_{rr}(u)r^2v + Y_{rrr}(u)r^3 + Y_R(\delta, u, v, r) + Y_W \quad (2)$$

$$(I_{xx} + J_{xx})\dot{p} = m_x z_H ur + K_v(u)v + K_r(u)r + K_p(u)p + K_\phi(u)\phi - mgGZ(\phi) + K_{vv}(u)v^3 + K_{vr}(u)v^2r + K_{rr}(u)r^2v + K_{rrr}(u)r^3 + K_R(\delta, u, v, r) + K_W \quad (3)$$

$$(I_{zz} + J_{zz})\dot{r} = N_v(u)v + N_r(u)r + N_\phi(u)\phi + N_{vv}(u)v^3 + N_{vr}(u)v^2r + N_{rr}(u)r^2v + N_{rrr}(u)r^3 + N_R(\delta, \phi, u, v, r) + N_W \quad (4)$$

here

$$[K_v \ K_r \ K_{vv} \ K_{vr} \ K_{rr} \ K_{rrr}]^T = z_H [Y_v \ Y_r \ Y_{vv} \ Y_{vr} \ Y_{rr} \ Y_{rrr}]^T \quad (5).$$

In the mathematical model, resistance is estimated from a captive model experiment and the thrust is estimated from propeller open water tests in calm water as described in Umeda et al (2008). Roll restoring moment ($mgGZ$) is estimated from hydrostatic calculations in calm water. Maneuvering coefficients including heel-induced hydrodynamic derivatives are estimated from calm water captive model experiments (Hashimoto et al., 2008). Roll damping is estimated from roll decay model tests (Umeda

et al. 2008). For the ONRTH, the values of correction coefficients for rudder are empirically developed from other model experiments (Kose et al., 1981). The empirical values are also used for the interaction force coefficients induced on the hull by rudder nominal force. All maneuvering and rudder coefficients are listed in Table 4. In wave cases, the wave forces X_w , Y_w , K_w , and N_w are calculated from linear Froude-Krylov forces and diffraction forces based on slender ship theory for zero encounter frequency. It is known that the wave particle velocity affects the rudder and propeller inflow speed which is important for the maneuverability in waves. Therefore the effects of wave particle velocity to propeller thrust and rudder force are taken into account.

However the SB simulations using these coefficients and wave model show some discrepancy with the EFD free running in calm water and waves. The authors tuned the calm water maneuvering and rudder coefficients values using the SI with CFD free running results in calm water. The results showed better agreement with the EFD calm water data (Araki et al., 2012). The values of tuned coefficients are shown in Table 4. Herein, the wave model is tuned using the SI technique with CFD free running and captive results in waves.

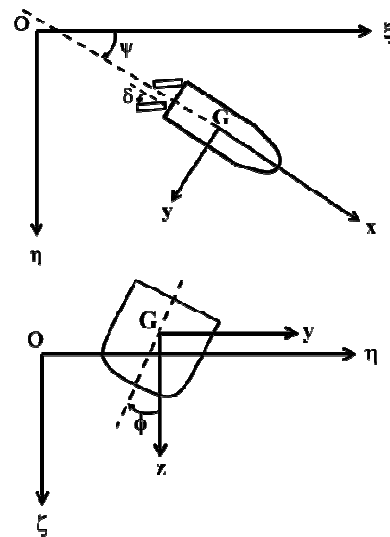


Figure 4: Coordinate system for 4DOF SB model.

3. SI METHOD AND THE RESULTS

A constrained least square (CLS) method using generalized reduced gradient algorithm (Lasdon et al., 1978) is used for SI. The CLS method provided reasonable maneuvering coefficients from CFD calm water maneuvers (Araki et al., 2012). To predict wave forces/effects, it is necessary to extract the wave forces/effects from total hydrodynamic forces. To achieve this purpose, first 6DOF CFD free running simulations in waves are executed. Second, CFD forced motion simulations in calm water are performed with imposing exactly same motions as the free running simulation. Thus the wave forces/effects are estimated as the difference between the total force of the first and second simulations.

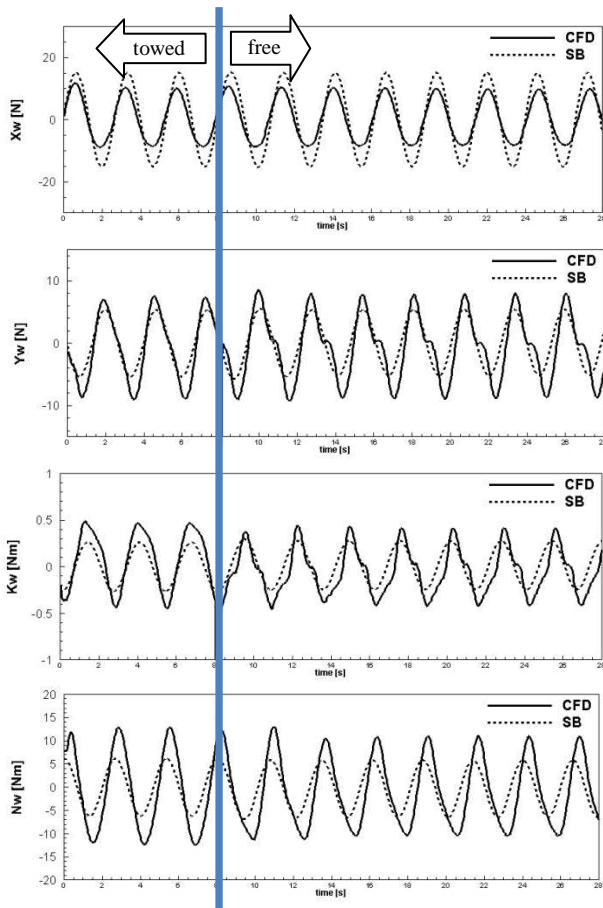


Figure 5: Wave forces during $\psi_C=20\text{deg}$ course keeping maneuver in following waves with nominal $Fr=0.20$, wave steepness 1/50 and wave length to ship length ratio 1.0.

Table 4: Values of original and SI-calm maneuvering and rudder coefficients used in 4-DOF nonlinear SB model.

Coef.	Original	SI-calm	Coef.	Original	SI-calm
ϵ	1.0	0.75	Y_{vrr}	-0.80	0.32
γ_R	0.70	0.55	Y_{rrr}	0.174	0.080
l_R/L	-1.00	-0.95	Y_ϕ	-5.1E-04	-6.5E-04
t_R	0.30	0.10	J_{xx}	4.1E-05	0.0001
a_H	0.25	0.23	z_H	0.852	1.08
z_{HR}/d	0.854	0.802	K_p	-0.243	-0.203
x_H/L	-0.45	-0.52	K_ϕ	6.3E-04	1.0E-03
m_x	0.0131	0.0	J_{zz}	0.0079	0.0059
X_{vv}	-0.0858	-0.070	N_v	-0.0932	-0.0851
X_{vr}	0.0522	0.065	N_r	-0.0549	-0.0395
X_{rr}	-0.0213	-0.025	N_{vvv}	-0.532	-0.492
m_y	0.109	-0.070	N_{vvr}	-0.629	-0.805
Y_v	-0.30	-0.20	N_{vrr}	-0.139	-0.121
Y_r	-0.0832	0.07	N_{rrr}	-0.00446	-0.0065
Y_{vvv}	-1.77	-2.0	N_ϕ	-0.00511	-0.00989
Y_{vvr}	0.262	0.32			

Figure 5 shows the extracted CFD wave forces/effects during $\psi_C=20\text{deg}$ course keeping maneuver in quartering waves with nominal $Fr=0.20$, wave steepness 1/50 and wave length to ship length ratio 1.0. During the free running, the model is imposed with constant forward speed $Fr=0.20$ and constant yaw angle 20deg until 8.02 seconds then released to start course keeping maneuvers. Here the “SB” is the wave forces computed by SB wave model.

It is shown that SB overestimates surge wave force and underestimates sway, roll, and yaw wave forces. Although definitions of wave forces are different, these tendencies are found in previous research by Hashimoto et al (2011) as well where they compared SB and captive EFD wave exciting forces for ONRTH. Moreover the SB waveforms seem to be different from CFD waveforms especially after the model is released. This could be because that SB wave model merely includes the Froude-Krylov and diffraction forces while CFD wave force includes all wave effects not just Froude-Krylov and diffraction forces but also wave



drift forces and maneuvering coefficients variations due to waves. According to CFD extracted wave forces/effects, the wave correction parameters are estimated by SI methods to tune SB wave model based on Eq. (6)-(8).

$$\begin{aligned}
 X_w &= a_1 X_w^{FK} + k \zeta_w (a_2 \sin(k \xi_G + \varepsilon_{a2}) \cdot X_{vv} \cdot v^2 \\
 &+ a_3 \sin(k \xi_G + \varepsilon_{a3}) \cdot X_{vr} \cdot vr + a_4 \sin(k \xi_G + \varepsilon_{a4}) \cdot X_{rr} \cdot r^2) + W_{CX} \\
 Y_w &= b_1 Y_w^{FK} + b_2 Y_w^{Dij} + k \zeta_w (b_3 \sin(k \xi_G + \varepsilon_{b3}) \cdot Y_v \cdot v \\
 &+ b_4 \sin(k \xi_G + \varepsilon_{b4}) \cdot Y_r \cdot r) + W_{CY} \\
 K_w &= c_1 K_w^{FK} + c_2 K_w^{Dij} + k \zeta_w (c_3 \sin(k \xi_G + \varepsilon_{c3}) \cdot K_v \cdot v + c_4 \sin(k \xi_G + \varepsilon_{c4}) \cdot K_r \cdot r) \\
 N_w &= d_1 N_w^{FK} + d_2 N_w^{Dij} + k \zeta_w (d_3 \sin(k \xi_G + \varepsilon_{d3}) \cdot N_v \cdot v \\
 &+ d_4 \sin(k \xi_G + \varepsilon_{d4}) \cdot N_r \cdot r) + W_{CN}
 \end{aligned} \tag{6}$$

where

$$W_{CX} = \rho g \zeta_w^2 B^2 / L \cdot \sin(\psi / 2 + \psi_0) \cdot (1 - e^{-10Fr}) \cdot C_X(T_w) \tag{7}$$

$$W_{CY} = \rho g \zeta_w^2 B^2 / L \cdot \sin \psi \cdot C_Y(T_w)$$

$$W_{CN} = \rho g \zeta_w^2 B^2 \cdot \sin \psi \cdot C_N(T_w)$$

$$C_{X,Y,N}(T_w) = \alpha_{X,Y,N} \cdot \left(\frac{m}{\eta}\right) \left(\frac{T_w}{\eta}\right)^{m-1} \exp\left[-\left(\frac{T_w}{\eta}\right)^m\right] \tag{8}$$

$$u_w = \beta_1 \cdot \zeta_w \omega \cos \psi e^{-kz} \cos(k \xi_G + kx \cos \psi) \tag{9}$$

$$v_w = -\beta_2 \cdot \zeta_w \omega \sin \psi e^{-kz} \cos(k \xi_G + kx \cos \psi)$$

Table 5: Original wave correction coefficients and the coefficients estimated by SI using extracted CFD wave forces/effects data.

Coef.	Orig	SI-wave	Coef.	Orig	SI-wave
a_1	1.0	0.758	c_1	1.0	1.26
a_2	0.0	16.33	c_2	1.0	0.355
a_3	0.0	0.855	c_3	0.0	0.510
a_4	0.0	0.132	c_4	0.0	0.195
ε_{a2}	0.0	0.391	ε_{c3}	0.0	-0.99
ε_{a3}	0.0	3.21	ε_{c4}	0.0	1.03
ε_{a4}	0.0	0.0	d_1	1.0	1.43
α_X	0.0	-46.3	d_2	1.0	0.403
b_1	1.0	1.35	d_3	0.0	1.01
b_2	1.0	0.423	d_4	0.0	0.213
b_3	0.0	2.18	ε_{d3}	0.0	0.982
b_4	0.0	0.496	ε_{d4}	0.0	-0.99
ε_{b3}	0.0	-0.552	α_N	0.0	-2.50
ε_{b4}	0.0	0.810	ψ_0	0.0	0.301
α_Y	0.0	-106.2	β_1	1.0	0.643
			β_2	1.0	0.425

The new wave model includes the major maneuvering coefficients variations and wave drift forces. For the simplification the wave drift coefficients shown in Eq. (8) are expressed as the Weibull distribution respect to

wave periods. The shape and scale parameter m , η of Eq. (8) are determined from the Yasukawa's research (2006). Also the normal force of CFD rudder is used to tune the wave particle velocity effects to propeller and rudder as shown in Eq. (9).

Here a , b , c , d , ε in Eq. (6), ψ_0 in Eq. (7), α in Eq. (8), and β in Eq. (9) are tuned by the SI. These SI procedures are repeated to the other cases: straight running and 20/20 zigzag with nominal $Fr=0.20$, wave steepness 1/50 and wave length to ship length ratio 1.0. The original wave correction coefficients and the tuned coefficients are shown in Table 5.

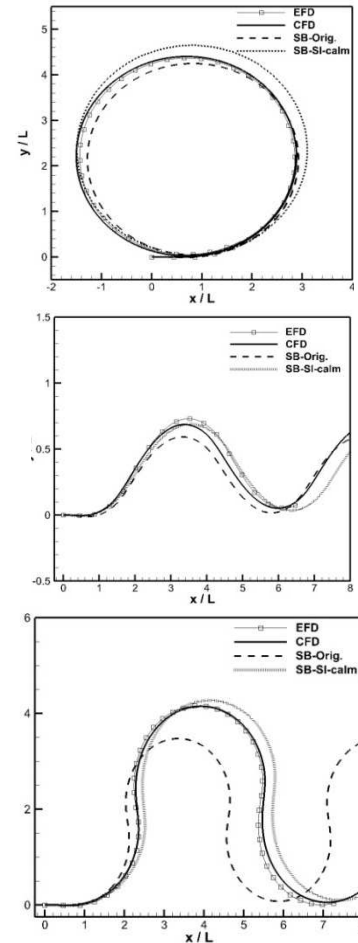


Figure 6: Trajectories of EFD, CFD, SB-Orig., and SB-SI free running in calm water: (a) $\delta=25$ deg turning circle; (b) 20/20 zigzag; (c) 90/35 large angle zigzag.

4. COMPARISON BETWEEN EFD, CFD, AND SB FREE RUNNINGS

4.1 Maneuvering in Calm Water

Comparison between EFD, CFD, “SB-Orig.”, and “SB-SI-calm” trajectories are shown in Fig. 6. Here “SB-Orig.” indicates the SB simulation using the maneuvering coefficients estimated from captive model test and rudder coefficients predicted from empirical charts (Kose et al., 1981). “SB-SI-calm” indicates SB simulation using maneuvering and rudder coefficients estimated by SI using CFD calm water maneuvering data (Araki et al., 2012). Figure 6a shows the trajectories of turning circle tests ($\delta=25\text{deg}$, $Fr=0.20$), Figure 6b shows zigzag tests ($\psi_c/\delta=20/20$, $Fr=0.20$) trajectories, and Fig.6c shows large angle zigzag tests ($\psi_c/\delta=90/35$, $Fr=0.20$).

The steady state variables and turning parameters for turning circle and 1st, 2nd overshoot angles and K_s , T_s , N_s steering quality indices for zigzag cases (ABS, 2006) for both CFD and SB predictions are compared against EFD ones and the overall errors are plotted in Fig.7. The steering quality indices are computed from nonlinear first order Nomoto’s model (Norrbin, 1963) shown in Eq.(10). As shown in Fig.6 and 7, the errors of SB-SI-calm are much smaller than that of SB-Orig.

$$T_s \dot{r} + N_s r^3 + r = K_s \delta \quad (10)$$

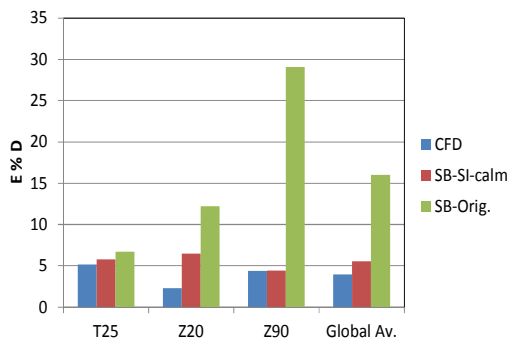


Figure 7: Errors from EFD free running results: “T25” $\delta=25\text{deg}$ turning circle; “Z20” 20/20 zigzag; “Z90” 90/35 zigzag; “Global Av.” average of T25, Z20, and Z90 errors.

4.2 Straight Running in Following Waves

Figure 8 shows the comparison between CFD, SB-SI-calm and SB-SI-wave straight running in following waves with nominal $Fr=0.20$, wave steepness 1/50 and wave length to ship length ratio 1.0. Here “SB-SI-calm” indicates SB simulation using maneuvering and rudder coefficients estimated by SI from CFD calm water maneuvering data (Araki et al., 2012) with original wave model. “SB-SI-wave” indicates SB simulations using same maneuvering and rudder coefficients with “SB-SI-calm” but with new wave model shown in Eq. (6) which is the improved wave forces using CFD wave forces/effects data.

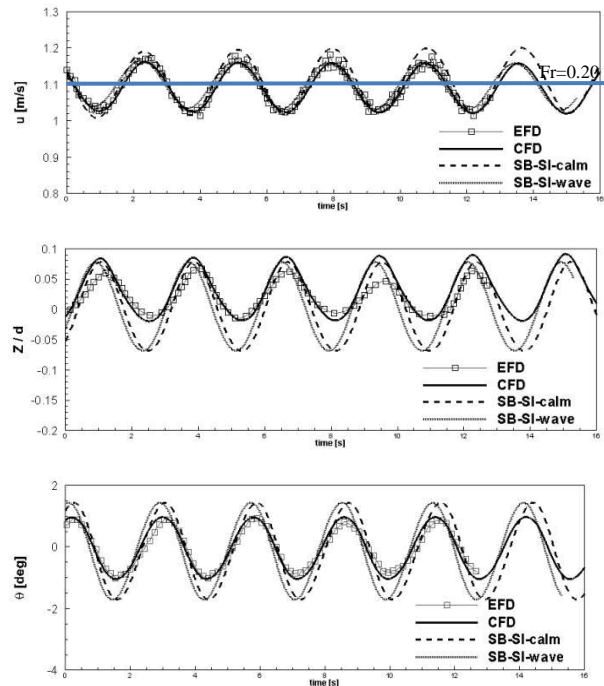


Figure 8: Straight running in following waves with nominal $Fr=0.20$, wave steepness 1/50, and wave length to ship length ratio 1.0.

In Fig.8, CFD shows remarkable agreement with EFD especially for the surge and pitch motions. It is showing possibility to replace EFD free running test with CFD simulations even in wave conditions. Here heave and pitch motions for the 4DOF (surge-sway-yaw-roll) SB model are assumed to be the same as the static equilibrium positions of the ship in waves. SB shows larger heave and pitch



motion than those of CFD and EFD which indicates that 6DOF model could be desirable. In surge motion, CFD successfully reproduce the nominal speed loss due to waves. The SB-SI-calm fails to express the nominal speed loss and the surging amplitudes are larger than that of CFD and EFD. The SB-SI-calm cannot represent nominal speed loss because the wave drift terms are not included in the SB-SI-calm model. Meanwhile SB-SI-wave successfully predicts nominal speed loss and surging amplitude within high degree of accuracy.

4.3 Course Keeping and Zigzag in Following and Quartering Waves

Course keeping and zigzag simulations in wave conditions are shown in this section. The simulation procedure is as follows. First the model is accelerated to the target ship speed with 2DOF (heave and pitch). After the model reaches to the speed, the model is towed with constant speed for a while and released when the bow is located on the wave crest. The rudder control starts just after the model is released. In the EFD, it should be noted that the towing time was very short because of the limitation of the facility's size. Moreover it was 3DOF (heave, pitch and roll) during towing in EFD.

Figure 9 shows the comparison between CFD and SB-SI-calm $\psi_C=20\text{deg}$ course keeping in quartering waves with nominal $Fr=0.20$, wave steepness $1/50$ and wave length to ship length ratio 1.0 . Here the EFD and CFD rudder control start just after the model is released at a wave trough.

In the trajectory, CFD course deviation shows good agreement with EFD which indicates that CFD well predicts the wave drift force. Although the EFD shows wobbly trajectory compared to CFD due to large oscillations for sway motions. Due to the sway motion error, the roll motions show some difference between EFD and CFD while the error is much smaller than that of sway motion. However CFD successfully predicts the surge

and yaw motions in quartering waves. Paying attention to CFD and SB results, SB-SI-calm shows small course deviation compared to that of CFD.

From the state variables comparisons, it is clear that SB-SI-calm has some discrepancy on the wave forces and wave drift effects compared to CFD and EFD. SB-SI-calm's wave model overestimates the surge wave force and underestimates the sway, roll, and yaw wave forces. The SB-SI-wave shows better agreement with CFD than SB-SI-calm for state variables and the trajectory. The wave drift effects can be seen in sway motion prediction which improves the prediction of the course deviation.

Figure 10 shows the comparison between EFD, CFD and SB 20/20 zigzag in following and quartering waves with nominal $Fr=0.20$, wave steepness $1/50$ and wave length to ship length ratio 1.0 . The CFD results show good agreement with shifted EFD for trajectory, surge, and yaw motions. In sway motion, CFD seems underestimating the wave force compared to EFD which could explain the discrepancy of the roll motions. SB-SI-calm shows qualitative agreement with EFD maneuver but not quantitative. SB-SI-calm overestimates surge wave force and underestimates sway, and yaw wave forces. The SB-SI-calm prediction of the zigzag trajectory is very close to the one predicted in calm water shown in Fig.6b. This is due to the fact that the maneuvering coefficients oscillations and drift forces induced by waves are neglected in SB-SI-calm. The SB-SI-wave improves the prediction as it shows the oscillations on the state variables induced by the waves. Also, the speed loss is predicted well in SB-SI-wave such that the trajectory shows good agreement with CFD and EFD ones.

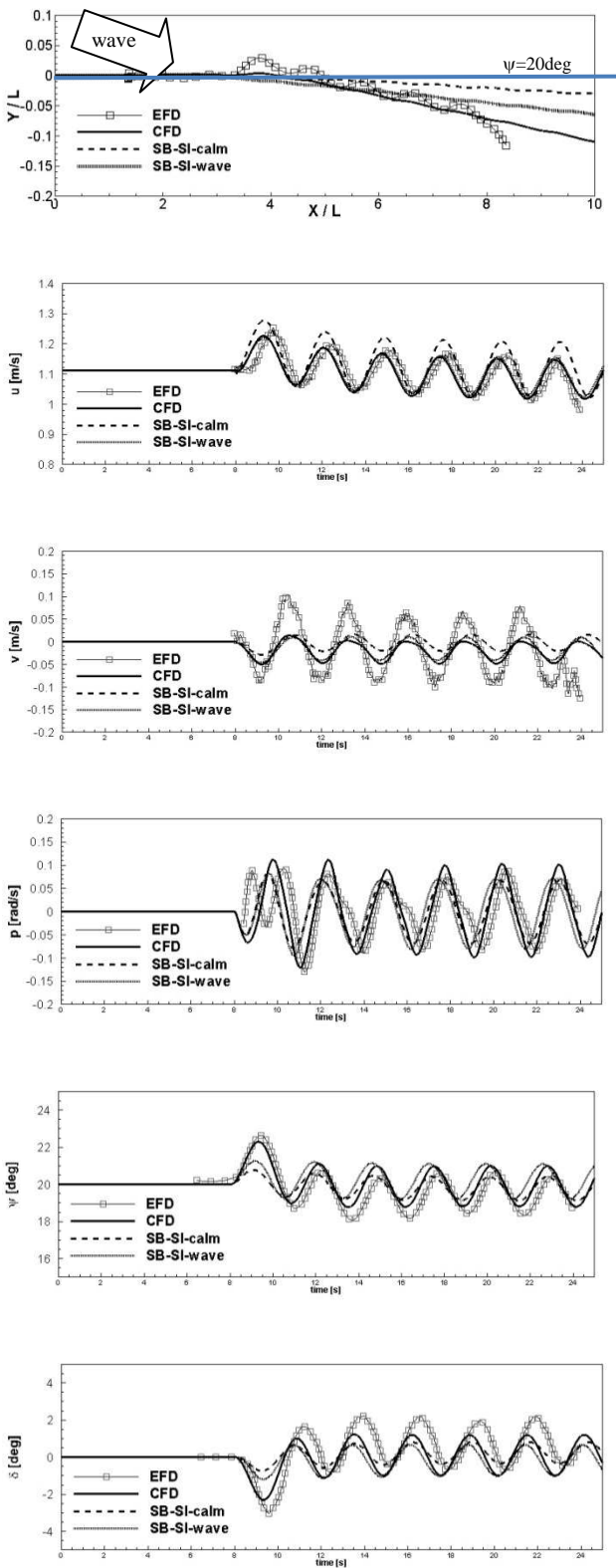


Figure 9: $\psi_C=20\text{deg}$ course keeping maneuver in quartering waves with nominal $Fr=0.20$, wave steepness $1/50$, and wave length to ship length ratio 1.0.

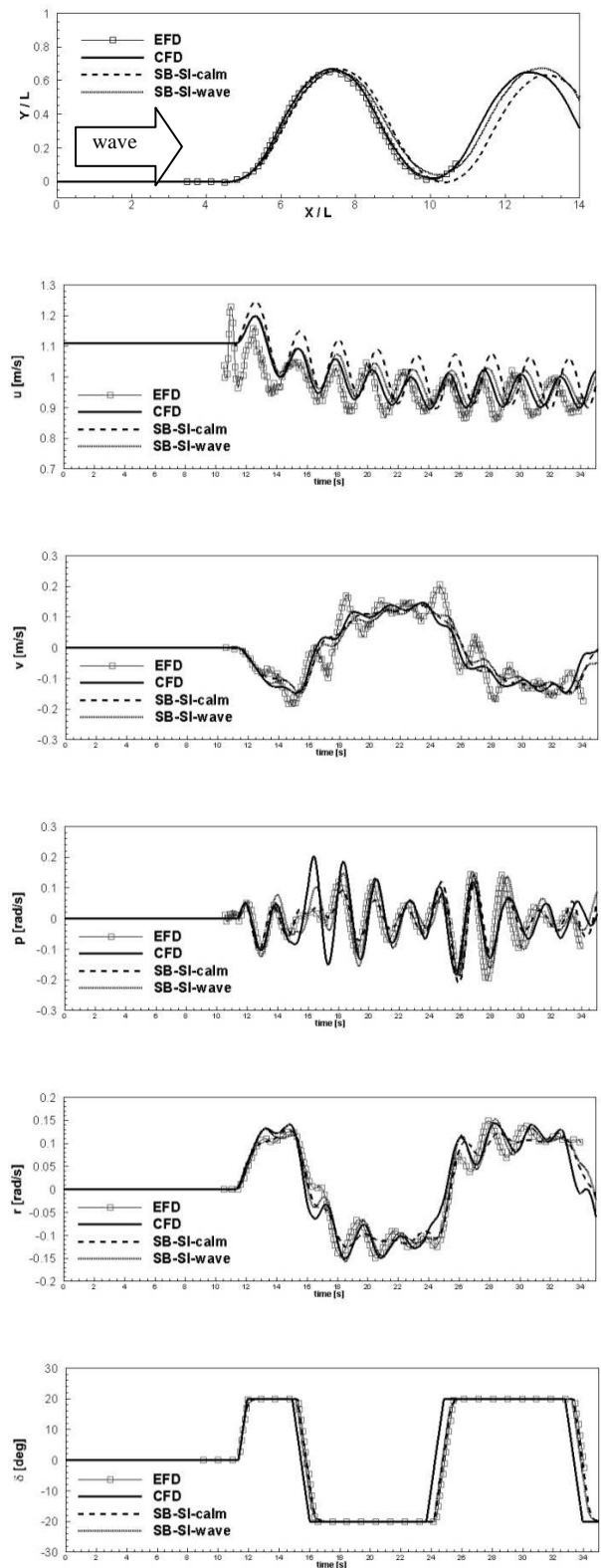


Figure 10: 20/20 zigzag in quartering waves with nominal $Fr=0.20$, wave steepness $1/50$, and wave length to ship length ratio 1.0.



5. CONCLUSIONS

System identification method using CFD free running data is shown to be an efficient approach for estimating maneuvering, rudder, and wave correction coefficients in the SB model. Araki et al. (2012) shows the reasonable maneuvering and rudder coefficients can be obtained from a few CFD free running data in calm water. However the SB model still shows some error predicting the ship motion in waves. The original SB model includes the Froude-Krylov and diffraction forces as the wave forces and wave particle velocity as the wave effect on the propeller and rudder which clearly fails to predict the oscillation amplitudes and the wave drift effects. Therefore the SB wave model is improved by adding correction parameters for Froude-Krylov, diffraction forces, and wave particle velocity. Moreover effects of wave drift forces and maneuvering coefficient variations due to waves are taken into account and these correction parameters are predicted by CLS using the extracted CFD wave forces/effects data. The extracted CFD wave forces/effects data are generated from the CFD free running data in waves and CFD forced motion data in calm water. The SB simulations using the new wave model and estimated wave correction coefficients show much better agreement with CFD than the SB simulations using the original wave model. The CFD simulations are validated with EFD free running results; CFD mostly shows quantitative agreement with EFD which shows possibility of replacing EFD free running trial with CFD simulations.

In future, EFD repeated tests acquired in IIHR wave basin need to be analysed to evaluate the standard deviation of the data. Also more tests will be conducted in IIHR wave basin to study the effects of ship speed and waves conditions on the ship maneuvering. Some of the test conditions will be also performed in National Research Institute of Fisheries Engineering (Japan) to measure the rudder forces in free running tests in calm water and waves, useful to validate SB and CFD rudder forces. The NRIFE free running

data in calm water will be compared with IIHR data to evaluate the facility biases. Note that NRIFE does not have enough equipment to adjust the initial conditions in waves unlike IIHR wave basin. Thus the data in waves cannot be compared among the facilities.

The CFD simulations will be repeated with closer initial condition with IIHR EFD tests to explore the difference between EFD and CFD results. Also, more CFD simulations will be conducted and validated for different ship speeds and wave conditions, including more severe condition with higher ship speed and tougher wave condition near to broaching conditions.

For SB, Froude-Krylov and diffraction forces need to be tuned not just with the amplitude but also with the phase lag. For rudder force variation in wave, it could be more effective to tune the rudder coefficients such as ε and γ_R than wave particle velocity. Both SB wave forces and rudder forces will be validated against EFD data from NRIFE. To provide the quantitative agreement with EFD in more severe conditions such as capsizing, it is necessary for SB model to include nonlinear wave effects in more detail and not just the wave drift forces. For instance, the SB model should include the memory effect functions to explain the frequency-dependency in the damping terms (Mikami and Kashiwagi, 2009) which should be corrected by the SI. Moreover, in severe condition, the rudder and propeller sometime might expose from the water surface due to large motions. This phenomenon could reduce the quality of the maneuvering of a vessel and could result into capsizing due to broaching (Araki et al., 2010). Therefore the rudder and propeller exposing effects will be taken into account in future. Also, the current 4DOF SB model will be extended for 6DOF simulation including heave and pitch motions.

6. ACKNOWLEDGMENTS

This research was sponsored by the Office of Naval Research Grant 000141-01-00-1-7



and NICOP Grant N00014-09-1-1089 under the administration Dr. Patrick Purtell. The CFD simulations were conducted utilizing DoD HPC. The authors are grateful to Mr K. Tanimoto and Ms K. Takagi of Osaka University and Mr A. Hanaoka of The University of Iowa, IIHR for assistance conducting the experiments.

7. REFERENCES

- Abkowitz M. A., 1980, Measurement of Hydrodynamic Characteristics from Ship Maneuvering Trials by System Identification, Advance Copy of Paper, Annual Meeting of SNAM.
- American Bureau of Shipping, 2006, Guide for Vessel Maneuverability, American Bureau of Shipping.
- Araki, M., Umeda N., Yamamura S., Hashimoto H., Matsuda A., 2010, "Broaching Prediction Using an Improved System-Based and Probabilistic Approaches", Proceeding of the 28th Symposium on Naval Hydrodynamics, (USB disk).
- Araki, M., Sadat-Hosseini, H., Sanada, Y. Tanimoto, K., Umeda, N., and Stern, F., 2012, "Estimating Maneuvering Coefficients Using System identification Methods with Experimental, System-based, and CFD Free-running Trial Data", Journal of Ocean Engineering, (accepted for publication).
- Bishop, R., Belknap, W., Turner, C., Simon, B., Kim, J., 2005, "Parametric Investigation on the Influence of GM, Roll Damping, and Above-Water Form on the Roll Response of Model 5613", Report NSWCCD-50-TR-2005/027.
- Carrica, P. M., Huang, J., Noack, R., Kaushik, D., Smith, B., Stern, F., 2010, "Large-scale DES computations of the forward speed diffraction and pitch and heave problems for a surface combatant", Computer & Fluids, vol. 39, Issue 7, pp. 1095-1111.
- Hashimoto, H., Umeda, N., and Matsuda, A., 2011, "Broaching Prediction of a Wave-piercing Tumblehome Vessel with Twin Screw and Twin Rudder", Journal of Marine Science and Technology, Vol.16(4), pp.448-461.
- Hashimoto, H., Stern, F., and Sadat-Hosseini, H., 2008, An Application of CFD for "Advanced Broaching Prediction (2nd Report)", Conference Proceedings of the Japan Society of Naval Architects and Ocean Engineers, Vol. 6, pp. 237-240.
- Kose, K., Yumuro, A., Yoshimura, Y., 1981, "Concrete of Mathematical Model for Ship Maneuverability", 3rd Symposium on Ship Maneuverability, Society of Naval Architects of Japan, pp.27-80, (in Japanese).
- Lasdon, L. S., Waren, A. D., Jain, A., Ratner, M., 1978, "Design and Testing of a Generalized Reduced Gradient Code for Nonlinear Programming", Journal of ACM Transactions on Mathematical Software, Volume 4 Issue 1.
- Mikami, T., Kashiwagi, M., 2009, "Time-Domain Strip Method with Memory-Effect Function Considering Body Nonlinear Wave-Body Interactions (2nd report)", Journal of Marine Science and Technology, Vol.14, No.2, pp.185-199.
- Norrbin, N. H., 1963, "On the Design and Analysis of Zig-Zag test on Base of Quasi linear Frequency Response", Technical Report B104-3, The Swedish State Shipbuilding Experimental Tank, Gothenburg, Sweden.
- Rhee, K. P., Kim, K., 1999, "A new sea trial method for estimating hydrodynamic derivatives", Ship & Ocean Technology Vol.3, Issue 3, pp. 25-44.
- Sadat-Hosseini, H., Carrica, M. P., Stern, F., Umeda, N., Hashimoto, H., Yamamura, S., Matsuda, A., 2011, "CFD, system-based and EFD study of ship dynamic instability events: surf-riding, periodic motion, and broaching",



Journal of Ocean Engineering, Vol. 38, Issue 1, pp. 88-110.

Sanada, Y., Tanimoto, K., Takagi, K., Sano, M., Yeo, D.J., Toda, Y., Stern, F., 2012, "Trajectories of Local Flow Field Measurement around ONR Tumblehome in Maneuvering Motion", 29th Symposium on Naval Hydrodynamics, Gothenburg, Sweden.

Son K. H., Nomoto K., 1982, "Combined behavior of manoeuvring and roll motion in following wave", Journal of the Society of Naval Architects of Japan, Vol.152, pp.207-218.

Stern, F., Agdrup, K., Kim, S. Y., Hochbaum, A. C., Rhee, K. P., Quadvlieg, F., Perdon, P., Hino, T., Broglia, R., and Gorski, J., 2011, "Experience from 2008 – The First Workshop on Verification and Validation of Ship Maneuvering Simulation Methods", Journal of Ship Research, vol.55, No.2, pp.135-147.

Umeda, N., Matsuda, A., Hashimoto, H., Yamamura, S., and Maki, A., 2008, "Model experiments on extreme motions of a wave-piercing Tumblehome vessel in following and quartering waves", Journal of the Japan Society of Naval Architects and Ocean Engineers, Vol. 8, pp.123-129.

Yasukawa, H., 2006, "Simulation of Ship Maneuvering in Waves (1st report: turning motion)", Journal of the Japan Society of Naval Architects and Ocean Engineers, Vol. 4, pp.127-136, (in Japanese).

8. NOMENCLATURE

$a_{1,2,3,4}$: tuning parameter for wave forces amplitude in surge
 a_H : rudder and hull hydrodynamic interaction coefficient in sway
 B : ship breadth
 $b_{1,2,3,4}$: tuning parameter for wave forces amplitude in sway

$C_{1,2,3,4}$: tuning parameter for wave forces amplitude in roll
 C_X : nondimensionalized drift wave force in surge
 C_Y : nondimensionalized drift wave force in sway
 C_N : nondimensionalized drift wave moment in yaw
 d : ship draft
 $d_{1,2,3,4}$: tuning parameter for wave forces amplitude in yaw
 Fr : Froude number
 g : gravitational acceleration
 GZ : restoring arm in roll
 I_{xx} : moment of inertia in roll
 I_{yy} : moment of inertia in yaw
 I_{xxx} : added moment of inertia in roll
 I_{yyy} : added moment of inertia in yaw
 k : wave number
 K_p : derivative of roll moment with roll rate
 K_r : derivative of roll moment with yaw rate
 K_R : rudder force in roll
 K_S : rotational index in nonlinear first order Nomoto's model
 K_u : derivative of roll moment with sway velocity
 K_w : wave moment in roll
 K_w^{Dif} : diffraction wave moment in roll
 K_w^{FK} : Froude-Krylov wave moment in roll
 K_{yyy} : derivative of roll moment with cubed yaw rate
 K_{yyu} : derivative of roll moment with squared yaw rate and sway velocity
 K_{yuu} : derivative of roll moment with squared sway velocity and yaw rate
 K_{uuu} : derivative of roll moment with cubed sway velocity
 K_ϕ : derivative of roll moment with roll angle
 L : ship length
 l_R : longitudinal position of rudder center from center of ship gravity
 m : ship mass
 m_x : added mass in surge
 m_y : added mass in sway
 N_r : derivative of yaw moment with yaw rate
 N_R : rudder force in yaw
 N_S : nonlinear index in nonlinear first order Nomoto's model



- N_v : derivative of yaw moment with sway velocity
 N_w : wave moment in yaw
 N_w^{Dif} : diffraction wave moment in yaw
 N_w^{FK} : Froude-Krylov wave moment in yaw
 N_{rrr} : derivative of yaw moment with cubed yaw rate
 N_{rrv} : derivative of yaw moment with squared yaw rate and sway velocity
 N_{rvv} : derivative of yaw moment with squared sway velocity and yaw rate
 N_{vvv} : derivative of yaw moment with cubed sway velocity
 N_ϕ : derivative of yaw moment with roll angle
 p : roll rate
 r : yaw rate
 R : ship resistance
 T : propeller thrust in surge
 t_R : rudder and hull hydrodynamic interaction coefficient in surge
 T_s : time constant index in nonlinear first order Nomoto's model
 T_w : wave period
 u : surge velocity
 u_w : wave particle velocity in surge
 v : sway velocity
 v_w : wave particle velocity in sway
 W_{CN} : drift wave moment in yaw
 W_{CX} : drift wave force in surge
 W_{CY} : drift wave force in sway
 x_H : rudder and hull hydrodynamic interaction coefficient in yaw
 X_R : rudder force in surge
 X_{rr} : derivative of surge force with squared yaw rate
 X_{rv} : derivative of surge force with yaw rate and sway velocity
 X_{rv} : derivative of surge force with squared sway velocity
 X_w : wave force in surge
 X_w^{Dif} : diffraction wave force in surge
 X_w^{FK} : Froude-Krylov wave force in surge
 Y_r : derivative of sway force with yaw rate
 Y_R : rudder force in sway
 Y_v : derivative of sway force with sway velocity
 Y_w : wave force in sway
 Y_w^{FK} : Froude-Krylov wave force in sway
 Y_w^{Dif} : diffraction wave force in sway
 Y_{rrr} : derivative of sway force with cubed yaw rate
 Y_{rrv} : derivative of sway force with squared yaw rate and sway velocity
 Y_{rvv} : derivative of sway force with squared sway velocity and yaw rate
 Y_{vvv} : derivative of sway force with cubed sway velocity
 Y_ϕ : derivative of sway force with roll angle
 z_H : height of hydrodynamic sway force application point from center of ship gravity
 z_{HR} : height of rudder force application point in roll
 α_K : tuning parameter for drift wave force in surge
 α_Y : tuning parameter for drift wave force in sway
 α_N : tuning parameter for drift wave moment in yaw
 β_1 : tuning parameter for wave particle velocity in surge
 β_2 : tuning parameter for wave particle velocity in sway
 γ_R : flow straitening coefficient
 δ : rudder angle
 ε : rudder effectiveness coefficient
 $\varepsilon_{a1,2,3,4}$: tuning parameter for wave forces phase lag in surge
 $\varepsilon_{b1,2,3,4}$: tuning parameter for wave forces phase lag in sway
 $\varepsilon_{c1,2,3,4}$: tuning parameter for wave forces phase lag in roll
 $\varepsilon_{d1,2,3,4}$: tuning parameter for wave forces phase lag in yaw
 ζ_w : wave amplitudes
 λ : wave length
 ξ_G : longitudinal position of center of ship gravity from a wave trough
 ρ : water density
 ϕ : roll angle
 ψ : yaw angle
 ψ_0 : tuning parameter for wave drift wave force phase lag in surge
 ω : wave frequency





Roll Motion of a Ship with Low Metacentric Height in Bi-chromatic Beam Waves

Gabriele Bulian, *University of Trieste*, gbulian@units.it

Alberto Francescutto, *University of Trieste*, francesc@units.it

Marco Sinibaldi, *University of Trieste*, marco.sinibaldi@phd.units.it

ABSTRACT

This study investigates the roll motion of a ship with low metacentric height and significantly nonlinear restoring when the excitation is given by bi-chromatic and mono-chromatic beam waves. Experiments and simulations have been performed. Simulations are carried out by means of two different 1-DOF models, where roll restoring is modelled either using an absolute or a relative angle approach, and by means of a 6-DOF blended code. Large amplitude sub-harmonic rolling has been identified in experiments and by some of the numerical models. The capability of the mathematical models of reproducing the experimental behaviour is discussed.

Keywords: *nonlinear roll, beam sea, sub-harmonic resonance, bi-chromatic waves, relative angle roll model, absolute angle roll model, 1-DOF simulations, 6-DOF simulations, blended codes*

1. INTRODUCTION

Nonlinearities of roll restoring, especially when strong, make roll motion particularly interesting from the point of view of nonlinear dynamics. One of the most intriguing aspects associated with nonlinear rolling is the possibility of having large amplitude rolling when the frequency of the excitation is far from the roll resonance frequency. In the most common and known case of 1:1 harmonic resonance, large amplitude rolling motions are obtained when the forcing frequency of regular (mono-chromatic) beam waves is slightly shifted from the roll natural frequency, as a result of the bending of the roll response curve associated with the hardening or softening restoring behaviour. However, sub-harmonic/ultra-harmonic resonances could also be possible in beam waves, with rolling occurring at a frequency which is either lower (sub-harmonic motion) or higher (ultra-harmonic motion) than the forcing frequency.

Examples of studies related to sub-harmonic and/or ultra-harmonic resonances in beam regular or irregular waves are those by, e.g., Cardo et al. (1981), Skomedal (1982), Naciri & Lledo (2001), Fujiwara & Ikeda (2007). Recently, however, some attention was given by Bulian & Francescutto (2011) to the case of bi-chromatic beam waves (see also Pessoa et al. (2011)). In particular, bi-chromatic beam waves were used by Bulian & Francescutto (2011) to analyse differences in outcomes from two 1-DOF roll mathematical models based either on a relative or an absolute angle approach for the restoring. Bulian & Francescutto (2011) showed by simulations that the two alternative 1-DOF models could provide clearly different outcomes when the wave forcing is bi-chromatic with forcing frequencies in particular ratios (the same "dangerous" ratios were identified in the past also by Hooft (1982), although on the basis of a different reasoning).



Following the investigation by Bulian & Francescutto (2011), an experimental campaign was setup, with associated further numerical investigation, on the behaviour of a vessel in bi-chromatic, mono-chromatic and irregular beam waves with forcing frequencies far from the roll natural frequency. Herein, results for bi-chromatic cases, and some mono-chromatic tests, are reported. The original intention of the campaign was to check the indications given by the work of Bulian & Francescutto (2011). However, the outcomes from the experimental campaign and from the additional numerical simulations showed a situation more complex than originally expected. The intention of the paper is therefore to report some of the results from this ongoing investigation.

The paper is structured as follows. Firstly a description of employed mathematical models is provided, followed by a description of the experimental setup. Some comparisons between experiments and simulations are then shown and some concluding comments are reported.

2. DESCRIPTION OF EMPLOYED MATHEMATICAL MODELS

In this work two different simulation approaches have been used. On one side simulations have been carried out by modelling roll dynamics as a 1-DOF system, by using two modelling for the restoring term: an absolute angle approach and a relative angle approach. In addition to the simplified 1-DOF approach, a more complex simulation approach has also been employed, by using a 6-DOF blended code capable of addressing some of the nonlinear effects inherent in the studied phenomenon. These approaches are more thoroughly described in the following.

2.1 1-DOF mathematical models

It is known that roll motion in beam waves can be effectively described, especially in case of monochromatic beam regular waves, by

means of simplified 1-DOF nonlinear mathematical models, provided that the coefficients of the model are appropriately specified (Francescutto et al. (1998), IMO (2006), Bulian & Francescutto (2009)). In general, it is of utmost importance that the employed model is capable of reproducing nonlinear effects with respect to both damping and restoring. Nonlinear damping effects are essential to reproduce the increase of dissipation (with respect to linear damping) at large rolling amplitudes. Nonlinear restoring is instead essential in order to reproduce the vast majority of nonlinear phenomena associated with roll (bending of response curve, sub-harmonic and ultra-harmonic resonances, etc.), especially in case of relatively small \overline{GM} . When considering nonlinear restoring and wave action, two main simplified options are basically available (see Bulian & Francescutto (2011) and references therein), i.e.:

- A relative angle model; or
- An absolute angle model.

In this study both approaches have been considered, by keeping, however, an absolute roll velocity approach for the damping term in both cases. The resulting 1-DOF models can be written as follows:

Nonlinear absolute angle model (AbsN):

$$\ddot{\phi} + d(\dot{\phi}) + \omega_0^2 \cdot \frac{\overline{GZ}(\phi)}{GM} = \omega_0^2 \cdot \alpha_{eff}(t) \quad (1)$$

Nonlinear relative angle model (RelN):

$$\ddot{\phi} + d(\dot{\phi}) + \omega_0^2 \cdot \frac{\overline{GZ}(\phi - \alpha_{eff}(t))}{GM} = 0 \quad (2)$$

The effective wave slope $\alpha_{eff}(t)$ is modelled by using the common concept of "effective wave slope coefficient" (or "wave slope reduction coefficient"). The effective wave slope coefficient, $r(\omega)$, is assumed as frequency dependent and it is calculated, starting from linear hydrodynamic calculations, according to Bulian & Francescutto (2009, 2011). It is important to note that basically the

same idea, although limited to a roll-sway model, was also previously employed by Naciri & Lledo (2001) and connections can also be found with the work of Hutchison (1991). The instantaneous effective wave slope is thus modelled, for a generic multi-frequency excitation given by N harmonics, as:

$$\alpha_{eff}(t) = \sum_{j=1}^N r(\omega_j) \cdot \alpha_{0,j} \cdot \cos(\omega_j \cdot t + \psi_j) \quad (3)$$

$$\psi_j = \psi_{wave,j} + \psi_r(\omega_j)$$

In (3), $\alpha_{0,j}$ is the wave slope of the j -th harmonic component, while the term $\psi_r(\omega_j)$ takes into account the phase difference between the instantaneous wave slope and the roll moment in the decoupled roll equation (Naciri & Lledo (2001), Bulian & Francescutto (2009, 2011)). It is important to underline that the forcing term in (3) is assumed to contain only the first-order harmonics. Higher order terms in the forcing, due to hydrodynamic sum-difference frequency effects (Pessoa et al., 2011) are not taken into account.

The damping term is modelled, in a quite flexible form, using an absolute roll velocity approach as:

$$d(\dot{\phi}) = 2 \cdot \mu \cdot \dot{\phi} + \beta \cdot \dot{\phi} |\dot{\phi}| + \delta \cdot \dot{\phi}^3 \quad (4)$$

As discussed by Bulian & Francescutto (2011), the application of the model (1) and the model (2) to simulate the same situation can lead to qualitatively different results when nonlinearities of restoring are significant. The comparison of the outcomes from the "AbsN" and the "RelN" models with experiments is therefore one of the scopes of the reported investigation. It is also worth underlining here that, when the damping term is assumed to be linear and/or when the damping term is based on a relative roll velocity approach, the "RelN" model can be recast in an "absolute angle" form by introducing the "effective relative angle" $\phi - \alpha_{eff}(t)$. In this case, analytical

approaches could be applied, similar to those employed by Cardo et al. (1981).

2.2 6-DOF nonlinear blended simulation method

Although being often very effective, the simulation of roll motion using a 1-DOF dynamical model is only an approximation of the real situation. The ship has, indeed, six degrees of freedom (DOFs) and, in some cases, significant linear/nonlinear coupling between different DOFs can have important effects on the resulting roll motion (e.g. Neves & Rodríguez (2006), Skomedal (1982)).

To investigate the effect of additional DOFs on the resulting simulated dynamics, a nonlinear 6-DOF blended simulation code has been employed. The code is named "SHIXDOF" ("nonlinear SHIP motion simulation program with siX Degrees Of Freedom") (Bulian & Francescutto, 2008) and it was employed in the SAFEDOR benchmark on parametric roll (Spanos & Papanikolaou, 2009). The blended architecture of the simulation method can be considered to follow the line initiated by de Kat & Paulling (1989). The main characteristics of the simulation method are summarised in the following.

Rigid body motion equations are considered fully nonlinear. Given a specified centre O (not necessarily the centre of gravity G) of the ship fixed reference system $S:Oxyz$, the nonlinear rigid body equations of motion are solved in terms of ship-fixed reference system state variables (as it is common in manoeuvring simulations):

$$\begin{cases} m \cdot [\mathbf{u}'_O + \boldsymbol{\omega} \wedge \mathbf{u}_O + \\ + \boldsymbol{\omega}' \wedge \mathbf{x}_G + \boldsymbol{\omega} \wedge (\boldsymbol{\omega} \wedge \mathbf{x}_G)] = \mathbf{f}_{ext} \\ \mathbf{I}_O \cdot \boldsymbol{\omega}' + \boldsymbol{\omega} \wedge (\mathbf{I}_O \cdot \boldsymbol{\omega}') + m \cdot \mathbf{x}_G \wedge \mathbf{u}'_O + \\ + m \cdot \mathbf{x}_G \wedge (\boldsymbol{\omega} \wedge \mathbf{u}_O) = \mathbf{m}_{ext}(O) \end{cases} \quad (5)$$



where the apex ()' indicates time derivative taken in the ship-fixed reference system, m [kg] is the ship mass, $\mathbf{u}_o = (u, v, w)^T$ [m/s] is the speed of the centre of the reference system, $\boldsymbol{\omega} = (p, q, r)^T$ [rad/s] is the rigid body angular velocity, \mathbf{x}_G [m] is the position vector of the centre of gravity in $Oxyz$, \mathbf{I}_o [kg·m²] is the tensor of inertia with respect to the point O , \mathbf{f}_{ext} [N] is the total force due to external effects and $\mathbf{m}_{ext}(O)$ [N·m] is the total moment with respect to O due to external effects. Of course the system of equations (5) is supplemented by the equations which allow to determine the instantaneous position and orientation, in terms of Euler angles, of the ship-fixed reference system $S:Oxyz$ with respect to an earth-fixed reference system $\Sigma:\Omega\xi\eta\zeta$:

$$\begin{aligned} \frac{d}{dt} \begin{pmatrix} \xi_o \\ \eta_o \\ \zeta_o \end{pmatrix} &= \mathbf{R}_{S \rightarrow \Sigma}(\psi, \vartheta, \phi) \cdot \mathbf{u}_o \\ \frac{d}{dt} \begin{pmatrix} \phi \\ \vartheta \\ \psi \end{pmatrix} &= \mathbf{T}_{\omega_s}^{-1}(\psi, \vartheta, \phi) \cdot \boldsymbol{\omega} \end{aligned} \quad (6)$$

where $\mathbf{R}_{S \rightarrow \Sigma}$ and \mathbf{T}_{ω_s} are appropriate transformation matrices depending on the instantaneous Euler angles ψ (yaw), ϑ (pitch) and ϕ (roll).

External actions on the ship, resulting in the force and moment vectors \mathbf{f}_{ext} and $\mathbf{m}_{ext}(O)$, are modelled in order to provide a simulation code capable, in principle, of simulating nonlinear ship manoeuvring in regular and irregular waves (of course with all the pros, cons and limitations of the employed blended approach). The main relevant actions for the particular problem under analysis in this paper are briefly described in the following.

Froude-Krylov pressure (comprising hydrostatic term) is calculated up to the instantaneous wetted surface of the hull in order to catch the effect of geometrical nonlinearities (in particular nonlinear roll restoring). The hull is described by a 3D triangular mesh. The pressure is obtained by the linear Airy pressure plus hydrostatic term with a stretching (following the idea of Wheeler (1969)) intended to guarantee zero pressure at the free surface (on this problem, see also Matusiak (2010), Du et al. (2009)). Higher order terms (e.g. Pessoa et al. (2011)) are not considered. The pressure term due to squared particle's velocities is not considered. As a result, sum-difference frequency effects in multi-chromatic waves are not introduced in the Froude-Krylov pressure field.

Linear potential wave radiation terms (linear wave damping and added mass) are incorporated through the application of convolution integrals following Cummins (1962) taking into account Bailey et al. (1998) for selecting the variables to be used in the convolutions. Kernel functions are determined starting from frequency dependent damping coefficients obtained from a linear strip-theory pre-calculation (Frank (1967), Salvesen et al., (1970)). The same strip-theory linear pre-calculation is also used to determine frequency dependent (wave length dependent) linear diffraction forces, which are used to provide diffraction forces at each simulation time step, depending on the relative position of the ship with respect to each single incident wave component.

Linear manoeuvring terms due to lift effects are based on derivatives from Clarke et al. (1983) with a reduction at large drift angles β of the type $|\cos(\beta)|$ taking into account Karasuno et al. (2003). This reduction is quite important to avoid unreasonably large lift terms at large drifting angles (e.g. in beam waves and/or at low forward speed). Attention is paid to avoid/reduce overlapping with terms coming from the linear radiation model (see some comments on this topic by Ayaz et al. (2006)).



In particular, it is assumed that added mass terms are sufficiently accounted for by the linear wave radiation model. In order to apply a calm water manoeuvring model in a flow field characterised by the presence of orbital velocities due to waves, the idea of an "equivalent surge-yaw-sway motion" is employed, as an extension of the ideas from Artyszuk (2006).

Nonlinear drag terms, representing also what are usually referred as nonlinear contributions to generalised manoeuvring forces, are based on a simplified modelling. The ship centreplane is panelled and elementary forces based on the square of the relative ship-water velocity (taking into account the effect of waves) are calculated at each panel. A drag coefficient, which can depend on the location of the panel, is used in the calculation. The calculation of these forces allows to determine the total force and moment due to drag. The obtained model is basically a simplified cross-flow drag model taking into account the instantaneous relative velocity between the ship and wave particles. It is important to note that this modelling implicitly introduces a nonlinear roll damping effect. The nonlinear force in surge is based on a standard prediction of ship resistance in calm water, taking into account instantaneous fluid velocity due to waves.

For each DOF, additional semi-empirical linear and nonlinear (with respect to the DOF time derivative) damping terms can be introduced. This is particularly important in case of roll where the addition of linear and nonlinear (quadratic/cubic), in roll velocity, terms is often necessary.

Constraints on DOFs can also be used in different forms. For the particular case under analysis, elastic soft springs limiting lateral/longitudinal drifting have been employed.

3. DESCRIPTION OF THE HULL USED IN THE INVESTIGATION

The selection of the hull used in this investigation was based on some main requirements:

- Low metacentric height;
- Significantly nonlinear restoring;
- Sufficient range of positive stability to reduce the risk of capsizing;
- Monohull.

Considering these requirements, it was natural to select a full hull form, with mainly vertical sides, with sufficient freeboard. In order to select a hull form possibly available also to other researchers interested in the subject, it was decided to use a standard "Series 60" hull form with block coefficient equal to 0.8 (Todd et al., 1957). The same hull was tested in the past in beam regular waves (Tzamtzis, 2004).

A model was used in the experiments with a length between perpendiculars of 1.625m (model scale). The model scale offset of the hull used in this investigation is shown in Figure 1, while the main characteristics of the model are summarised in Table 1. Nominal data are those which were employed in the calculations (calculations were set-up and partially carried out before performing the experiments), whereas actual data are those achieved in the experimental setup. In the table, R_{xx} and R_{yy} are, respectively, the dry roll and pitch radii of gyration with respect to the ship centre of gravity. The dry yaw radius of gyration is assumed to be equal to that for pitch. The trim is zero in the nominal condition, and practically zero in the actual setup. It is important to underline that data from executed roll decays are still under analysis due to a series of difficulties which, at the moment of writing, seem to be associated with non negligible surface tension effects (Ueno, 1950). As a result, the determination of roll damping coefficients and natural frequency from experimental decays is still ongoing. The analyses carried out so far indicate that the roll damping used in the simulations in this paper



could be smaller than the actual model damping.

The \overline{GZ} curves from hydrostatic calculations for the considered hull in the nominal and actual conditions are shown in Figure 2. It can be seen that the calm water free trim righting lever in the nominal and actual conditions are very close each other. It can therefore be assumed that the actual tested condition is very well representative of the nominal condition in terms of hydrostatic properties.

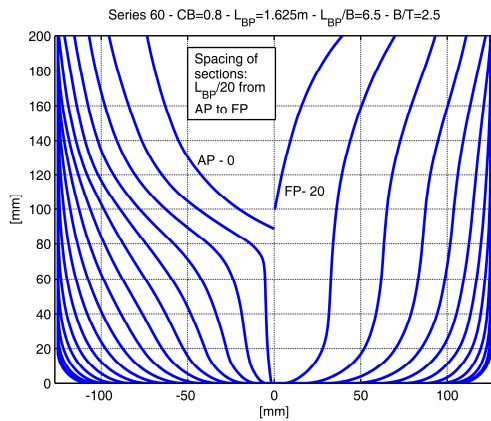


Figure 1: Hull used in the investigation. Model scale.

Table 1: Nominal and actual data of tested model. Data at model scale.

Quantity	Nominal	Actual
Mass [kg]	32.5	32.9
Draught [mm]	100	101
R_{yy}/L_{BP} [nd]	0.250	0.248
R_{xx}/B [nd]	0.362	0.357
\overline{GM} [mm]	4	4
Natural roll period [s]	3.1s	3.3s (still under analysis)
Configuration: bare hull		

4. EXPERIMENTAL RESULTS

A series of experimental tests have been carried out in beam waves. The experimental campaign addressed beam bi-chromatic and

irregular (multi-chromatic) waves. A limited series of checking tests have also been carried out in mono-chromatic (regular) waves. Herein some results are reported only for cases tested in bi-chromatic and mono-chromatic waves.

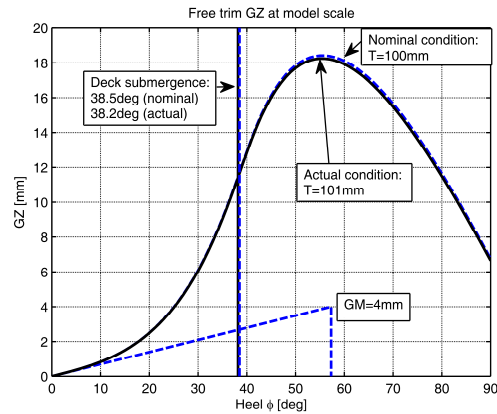


Figure 2: \overline{GZ} curves. Model scale.

Following the numerical 1-DOF investigation by Bulian & Francescutto (2011), the original aim of the tests was to experimentally check the possibility of having a sub-harmonic roll motion with a dominant harmonic close to the roll natural frequency when forcing the ship with high frequency bi-chromatic regular waves having frequencies close to, in particular, two and three times the roll natural frequency. From the experiments carried out, the occurrence of sub-harmonic roll was actually observed. However, in the course of the tests and on the basis of further numerical simulations with different mathematical models, the situation was found to be more complex than originally expected. Indeed, the presence of relatively large amplitude sub-harmonic rolling motions was actually found in the experiments, although the driving source of the observed large amplitude sub-harmonic response has not yet been fully clarified. What is, in particular, not clear is whether the inception of such large amplitude sub-harmonic rolling is governed by the nonlinearities of roll restoring (e.g. Cardo et al. (1981)), or by a possible coupling with heave motion (e.g. Skomedal (1982), Naciri & Lledo (2001), Fujiwara & Ikeda (2007)), or whether both effects, in combination, are necessary to lead to the observed results.

Bi-chromatic experiments have been carried out as follows. Waves have been generated in the towing tank by superimposing two harmonics with frequencies ω_{2k} and ω_{3k} defined as follows:

$$\omega_{2k} = 2 \cdot \omega_{ref} \quad ; \quad \omega_{3k} = 3 \cdot \omega_{ref} \quad ; \quad (7)$$

where $\omega_{ref} = k_{ratio} \cdot \omega_0$

It can be seen that the frequencies of the waves are based on a common reference frequency, ω_{ref} [rad/s], which, in turns, is based on the roll natural frequency ω_0 [rad/s] and a frequency ratio parameter k_{ratio} [nd]. From preliminary analysis of roll decay data, the reference roll natural frequency was chosen as $\omega_0 = 1.913 \text{ rad/s}$ and, considering the hardening restoring of the ship, the frequency ratio parameter k_{ratio} was changed in the range $1.0 \div 2.0$ depending on the observed outcomes. Each bi-chromatic test was associated with a single "steepness parameter" s_w , and each harmonic component was given a wave height corresponding to the steepness parameter s_w . As a result, the maximum instantaneous wave slope theoretically achievable in the framework of linear theory for the tested bi-chromatic waves is $2 \cdot \pi \cdot s_w$. Referring to wave lengths corresponding to each harmonic as λ_{2k} and λ_{3k} , waves have been generated in such a way that, at the rest position of the model along the tank, the nominal wave elevation $\eta(t)$ and wave slope $\alpha(t)$ according to linear theory are, after selecting a suitable reference time instant as $t = 0$:

$$\eta(t) = s_w \cdot \frac{\lambda_{2k}}{2} \cdot \cos(\omega_{2k} \cdot t) + s_w \cdot \frac{\lambda_{3k}}{2} \cdot \cos(\omega_{3k} \cdot t) \quad (8)$$

$$\alpha(t) = s_w \cdot \pi \cdot \sin(\omega_{2k} \cdot t) + s_w \cdot \pi \cdot \sin(\omega_{3k} \cdot t)$$

Wave generation was based on linear considerations. This means that nonlinear effects and experimental uncertainty led to

generated waves close to the nominal ones, although not exactly corresponding to them.

The model was restrained in the tank by two elastic ropes, lying in the fore-aft direction, connected at the bow and at the stern at a height approximately corresponding to the waterplane. Considering the small roll restoring moment of the model in the considered loading condition, particular attention was given, in the connection, to reduce the spurious roll moment of the elastic ropes. This was achieved by using a short intermediate non-elastic connection string, with very limited torsional constant, between each of the two main elastic ropes and the model. Ropes were tensioned in such a way as to have a small dead-band, of the order of some centimetres in terms of sway, before becoming active. The model was positioned in such a way that generated waves came from starboard. Roll motion was measured by using a combination of two instruments: a gyroscope and a static clinometer. The final roll motion is obtained by combining the two signals, with the intention of reducing problems associated with the drifting of the signal of the gyroscope. The two signals are both high-passed through the same digital IIR filter. The high passed component is removed from the clinometer signal, to keep only the low-frequency component. The high-passed roll velocity from the gyro is integrated, and the result from the integration is added to the low frequency part of the clinometer signal. The finally obtained roll signal eventually contains both the low frequency (say average) component, which is difficult to obtain directly from the gyroscope, but it is satisfactorily captured by the static clinometer, and the high frequency (say oscillation) component, which instead is well captured by the gyroscope. This post-processing technique was satisfactorily compared with some sample measurements carried out by using SCraMP (McCue, 2012).

During tests in bi-chromatic waves, large amplitude sub-harmonic roll was clearly identified. In addition to bi-chromatic experiments, a series of experiments using mono-chromatic waves were also carried out.



The intention of the additional mono-chromatic experiments was to check whether the observed sub-harmonic response observed in bi-chromatic waves was also present under mono-chromatic excitation. To this end, monochromatic waves were generated exactly in the same way as done for bi-chromatic waves, but suppressing one of the two harmonic components as necessary (i.e. giving to the relevant harmonic component zero amplitude when generating the wavemaker signal). It is important to underline that the maximum instantaneous wave slope theoretically achievable in the framework of linear theory for the tested mono-chromatic waves is $\pi \cdot s_w$. Checking tests in mono-chromatic waves were carried out only for the largest tested steepness parameter ($s_w = 1/30$).

Results of the experiments are shown in Figure 3, where the roll standard deviation is reported as a function of the frequency ratio parameter k_{ratio} (see (7)) for runs in bi-chromatic and in mono-chromatic waves. The reason for using the roll standard deviation as summarising measure of the rolling motions is that, in principle, the obtained time histories for roll motion could contain multiple harmonics. However, in general, the obtained results are either dominated by a sub-harmonic response, or, in case of most of the mono-chromatic tests, by a harmonic response. As a result, in the very large majority of tested cases, the rolling amplitude can be very well approximate by $\sqrt{2}$ times the reported roll standard deviation. In the other cases, the roll standard deviation can be considered a suitable measure of a roll motion containing multiple harmonics.

By analysing the results in Figure 3, the following major comments can be done:

- In all the tested conditions with bi-chromatic excitation (waves forcing the ship with frequencies $\omega_{2k} = 2 \cdot \omega_{ref}$ and $\omega_{3k} = 3 \cdot \omega_{ref}$), roll motion is dominated by a sub-harmonic response at frequency $\omega = \omega_{1k} = \omega_{ref}$;

- The roll response curve shows a bending towards the high frequency region, which is consistent with the hardening behaviour of the restoring moment (see Figure 2);

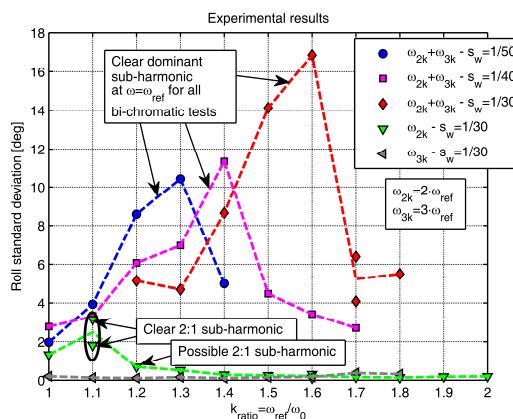


Figure 3: Experimental results from bi-chromatic and mono-chromatic tests.

- The roll response curve show a clear shifting towards the high frequency region as the steepness of the waves increases;
- When forcing the ship with monochromatic waves with frequency $2 \cdot \omega_{ref}$ or frequency $3 \cdot \omega_{ref}$ and steepness $1/30$, in general the roll response is harmonic, at the frequency of the forcing, and with small amplitude. Exceptions are cases with forcing frequency $2 \cdot \omega_{ref}$ with k_{ratio} equal to 1.1 and, to a more limited extend, 1.2, where the roll response is a 2:1 sub-harmonic, although with a small amplitude;
- Sub-harmonic roll motion was not observed in any of the monochromatic tests with frequency $3 \cdot \omega_{ref}$ and steepness $1/30$;
- Large amplitude sub-harmonic roll responses seem to be triggered by the presence of both the harmonics $2 \cdot \omega_{ref}$ and $3 \cdot \omega_{ref}$;
- It shall be underlined that some of the mono-chromatic tests reported at different values of ,frequency ratio parameter k_{ratio} actually correspond to the same wave forcing.

Indeed, $\omega_{2k}(k_{ratio} = 1.5) = \omega_{3k}(k_{ratio} = 1.0)$ and $\omega_{2k}(k_{ratio} = 1.8) = \omega_{3k}(k_{ratio} = 1.2)$. The forcing frequency region for mono-chromatic waves with $\omega_{2k}(k_{ratio} \geq 1.5)$ corresponds to mono-chromatic tests with $\omega_{3k}(k_{ratio} \geq 1.0)$, and results appear as different points only as a consequence of the representation in terms of frequency ratio parameter k_{ratio} , instead of the frequency of the wave;

- Roll motion under bi-chromatic excitation can reach large amplitudes in conditions where linear theory would predict extremely small rolling motions;
- Part of the observed phenomenon could be due to nonlinear sum-difference frequency effects inherent in the wave hydrodynamics, especially in presence of multiple harmonic components (Pessoa et al., 2011).

5. NUMERICAL SIMULATIONS

Numerical simulations have been carried out using nominal parameters (see Table 1), since the analysis of decays is still ongoing and since some of the simulations were carried out before executing experimental tests. Damping coefficients have been taken, in nondimensional form, from a previous series of experiments (Tzamtzis, 2004) carried out, however, with a different metacentric height. The model scale roll natural frequency in the simulations is taken as $\omega_0 = 2.01 \text{ rad/s}$. Nominal damping coefficients in the simulations are taken as follows (see (4)): $\mu/\omega_0 = 1.050 \cdot 10^{-2}$, $\beta = 0.000$, $\delta \cdot \omega_0 = 0.408$. As previously said, however, the analyses of roll decays carried out so far indicate that the roll damping used in the simulations in this paper could be smaller than the actual model damping. Relevant coefficients in the 6-DOF code (damping, drag coefficient, etc.) have been tuned to match the required values. Soft springs have been used in the 6-DOF simulations in order to prevent the model from

drifting in transversal/longitudinal direction and to limit yaw, in a way similar to the setup actually used in the experiments.

5.1 1-DOF mathematical models

Similarly to Bulian & Francescutto (2011), simulations have been carried out using both the absolute angle modelling for the restoring term (see modelling "AbsN" (1)) and the relative angle modelling for the restoring term (see modelling "RelN" (2)). Simulations have been carried out in all cases with an initial ramping time of 1s (model scale). Outcomes from 1-DOF simulations can be summarised as follows:

- Simulations based on the absolute angle modelling (1) ("AbsN") did not show any sub-harmonic roll response, either with bi-chromatic or with mono-chromatic wave excitation. The outcomes from the modelling "AbsN" are basically those given by the linearised version of (1). This is in line with the discussion by Bulian & Francescutto (2011);
- Simulations based on the nonlinear relative angle modelling (2) ("RelN") show the presence of large amplitude sub-harmonic roll responses under bi-chromatic excitation (see Figure 4). However, the large amplitude responses are due to a very large extent to a 3:1 sub-harmonic resonance which occurs even when forcing the system only with mono-chromatic waves (see Figure 5). As a result, using the model "RelN", the presence of two concurrent forcing harmonics is not a necessary condition to trigger the sub-harmonic response.
- The presence of two concurrent harmonics ω_{2k} and ω_{3k} seems to have a visible influence on the roll response curve for $k_{ratio} > 1.5$ in comparison with a mono-chromatic forcing with ω_{2k} (compare Figure 4 with the upper plot of Figure 5). In particular, the presence of the additional forcing term ω_{3k} leads to a shifting of the roll response curve towards the high



frequency region as the forcing steepness parameter increases. It is however important to underline that these high- k_{ratio} resonance peaks of the roll response curve were not observed experimentally (but it shall be noted that high frequency waves have not been tested extensively in the experiments);

- In certain frequency ranges, multiple coexisting solutions have been identified depending on the initial conditions (see Figure 4 and also Figure 5). Large amplitude motions occur only when the initial conditions belong to the appropriate domains of attraction in the plane of initial conditions;
- Numerical simulations did not show any 2:1 sub-harmonic response. This could indicate that the 2:1 sub-harmonic resonance observed in experiments and in 6-DOF simulations (see the next section of this paper) could be due to a coupling with some other DOF, particularly heave (Skomedal (1982) Naciri & Lledo (2001), Fujiwara & Ikeda (2007), IMO (2011));
- It is worth underlining that, for each wave steepness parameter, the two large amplitude branches which are visible in the upper and in the lower plots of Figure 5 are basically the same sub-harmonic resonance curve. Indeed, for a given steepness parameter s_w , forcing with frequency ω_{3k} for $k_{ratio} \geq 1$ is exactly the same as forcing with frequency ω_{2k} with $k_{ratio} \geq 1.5$ (see also the discussion on experimental results). Therefore, the upper and lower graphs in Figure 5 would appear (partially) superimposed if the x-axis were reporting the actual forcing wave frequency.

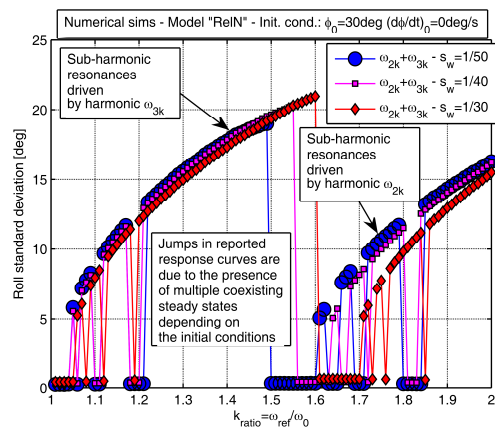


Figure 4: Roll response curves using model "RelN". Bi-chromatic excitation.

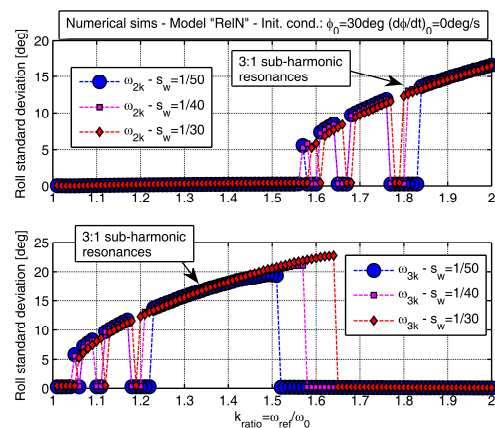


Figure 5: Roll response curves using model "RelN". Mono-chromatic excitation.

5.2 6-DOF mathematical model

Simulations with bi-chromatic waves with steepness 1/50, 1/40 and 1/30 have been carried out. In addition, a series of simulations with monochromatic waves has been carried out only for a wave steepness equal to 1/30. In comparison with 1-DOF simulations, outcomes from the 6-DOF simulations are more in line with the experimental results. The main outcomes from the 6-DOF simulations can be summarised as follows:

- 6-DOF simulations reproduce the inception of large amplitude sub-harmonic motions under bi-chromatic excitation. The bending of the response curve observed in the experiments is correctly reproduced, but the frequency shift of the response curve

observed in the experiment is not so evident in the simulations (see Figure 6 and compare with Figure 3);

- Mono-chromatic waves with steepness 1/30 excite a 2:1 sub-harmonic roll response for simulations with wave frequency $\omega_{2k} = 2.2 \cdot \omega_0$ and $\omega_{2k} = 2.4 \cdot \omega_0$ ($k_{ratio} = \{1.1, 1.2\}$ and $\omega_{wave} = \omega_{2k}$). This result is qualitatively in line with experimental outcomes, although the amplitude of motion is larger than that obtained in the experiments. This 2:1 sub-harmonic resonance, however, is quite sensitive to the linear damping used in the simulations and the large amplitude roll disappears as the additional linear damping in the simulations is increased by 25%-50%;
- Mono-chromatic waves with steepness 1/30 excite a 3:1 sub-harmonic roll response for the simulation with wave frequency $\omega_{3k} = 3.9 \cdot \omega_0$ ($k_{ratio} = 1.3$ and $\omega_{wave} = \omega_{3k}$). In the experiments this 3:1 sub-harmonic was not observed. However, similarly to the case of the 2:1 sub-harmonic discussed above, this 3:1 sub-harmonic resonance is quite sensitive to the linear damping used in the simulations. The large amplitude roll disappears as the additional linear damping in the simulations is increased by 25%-50%;
- Further investigations should concentrate on the analysis of the possible presence of multiple coexisting steady states.

6. FINAL REMARKS

This paper has reported results from an investigation regarding roll motion of a hull with significantly nonlinear restoring and small metacentric height. Experimental tests and numerical simulations with different mathematical models have been carried out in beam bi-chromatic waves. Mono-chromatic waves have also been considered, mainly for comparison/reference purposes, both in experiments and in simulations. The analysis of the obtained data is still ongoing. However a

series of interesting outcomes has been identified.

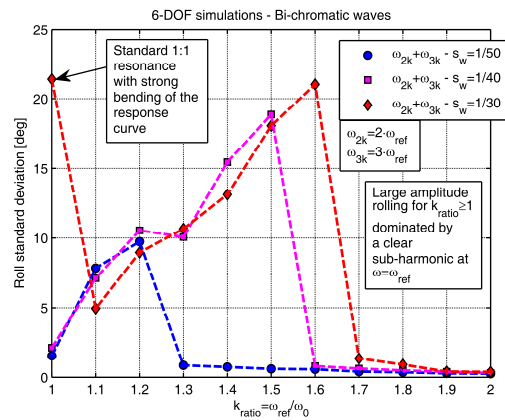


Figure 6: Results from 6-DOF simulations under bi-chromatic excitation.

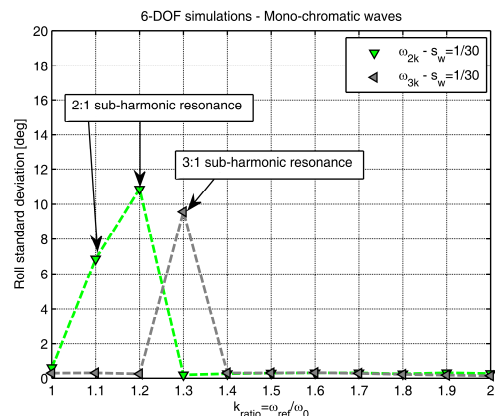


Figure 7: Results from 6-DOF simulations under mono-chromatic excitation.

First of all it was experimentally proved that bi-chromatic high frequency waves having specific frequency ratios among them and with respect to the roll natural frequency can excite large amplitude sub-harmonic rolling motions. In particular, the two considered waves have frequency close to two and three times the roll natural frequency, with proper account for the bending of the roll response curve towards high frequencies due to the hardening restoring of the present hull. However, the driving factor in the observed phenomenon has not been clearly determined. It is indeed not clear, from the experiments, whether the observed phenomenon is governed by a 2:1 or a 3:1 sub-harmonic response, or whether both



frequencies are necessary to trigger the observed large amplitude rolling motions. From the obtained results, however, it seems that both forcing frequencies are necessary.

Qualitative and quantitative comparisons of experimental results with numerical simulations based on different mathematical models have then been carried out. Two 1-DOF models based on either an absolute or a relative angle modelling for the restoring have been employed. In addition, a 6-DOF mathematical model has also been used. The 1-DOF model based on the absolute angle approach for the restoring does not show any evidence of the phenomenon. On the other hand, the 1-DOF model with restoring based on relative angle has shown large amplitude sub-harmonic motions. However, in this latter case, the phenomenon evidenced by the 1-DOF model was clearly governed by a basically 3:1 sub-harmonic response to the wave component having frequency close to three times the roll natural frequency. Therefore, the combination of frequencies was not indicated by the 1-DOF modelling as the governing factor. Finally, the 6-DOF model showed the best qualitative agreement with the experiments, which could highlight the non-negligible influence of coupling of roll with other DOFs (particularly heave). The 6-DOF model showed large amplitude sub-harmonic rolling in the presence of bi-chromatic excitation. On the other hand, tested mono-chromatic waves were not able, in general, to trigger large amplitude sub-harmonic rolling motions in a wide frequency range. Nevertheless, a relatively small range of frequencies was identified with a 2:1 sub-harmonic resonance under mono-chromatic excitation. Similarly, a small frequency range was identified with a 3:1 sub-harmonic resonance under mono-chromatic excitation. However, the outcome, in both conditions, significantly depends on the linear roll damping used in the simulations: an increase in the additional linear damping coefficient by 25%-50% is sufficient to suppress the inception of both the 2:1 and 3:1 sub-harmonic resonance in mono-chromatic waves with steepness 1/30, which indicates the presence of a threshold. It

is worth mentioning that the region of frequencies where this 2:1 sub-harmonic resonance was observed is consistent with the observation of a similar phenomenon also from experiments, although with relatively smaller amplitude in the experiments. The 6-DOF model, finally, indicates that the presence of the two forcing frequencies is necessary to trigger the large amplitude rolling observed in the experiments, and this is consistent with the considerations which can be drawn from the experimental results at the present level of analysis.

7. ACKNOWLEDGEMENTS

The authors wish to thank Prof. M.A.S. Neves (LabOceano, COPPE – Federal University of Rio de Janeiro) for bringing to their attention the work of Hooft (1982). The financial support from "Università degli Studi di Trieste - Finanziamento per Ricercatori di Ateneo (FRA 2011)" is acknowledged.

8. REFERENCES

- Artyszuk, J., 2006, "A Non-Uniform Current in Ship Manoeuvring", Proc. MARSIM2006 - International Conference on Marine Simulation and Ship Manoeuvrability, Terschelling, the Netherlands, June
- Ayaz, Z., Vassalos, D., Spyrou, K.J., 2006, "Manoeuvring behaviour of ships in extreme astern seas", Ocean Engineering, Vol. 33, pp. 2381-2434
- Bailey, P.A., Price, W.G., Temarel, P., 1998, "A Unified Mathematical Model Describing The Manoeuvring of a Ship Travelling in a Seaway", Trans. RINA, Vol. 140, pp. 131-149
- Bulian, G., Francescutto, A., 2008, "SAFEDOR benchmark on parametric roll - Brief description of the simulation methodology employed in the code SHIXDOF under



- development at DINMA", Internal Technical Report, Department DINMA, University of Trieste, Trieste, Italy
- Bulian, G., Francescutto, A., 2009, "Experimental results and numerical simulations on strongly nonlinear rolling of multihulls in moderate beam seas", Proceedings of the Institution of Mechanical Engineers - Part M - Journal of Engineering for the Maritime Environment, Vol. 223, pp. 189-210, doi: 10.1243/14750902JEME126
- Bulian, G., Francescutto, A., 2011, "Effect of roll modelling in beam waves under multi-frequency excitation", Ocean Engineering, Vol. 38, pp. 1448-1463, doi:10.1016/j.oceaneng.2011.07.004
- Cardo, A., Francescutto, A., Nabergoj, R., 1981, "Ultraharmonics and subharmonics in the rolling motion of a ship: steady-state solution", International Shipbuilding Progress, Vol. 28, pp. 234-251
- Clarke, D., Gedling, P., Hine, G., 1983, "The Application of Manoeuvring Criteria in Hull Design Using Linear Theory", Trans. RINA, Vol. 125, pp. 45-68
- Cummins, W.E., 1962, "The Impulse Response Function and Ship Motions", Schiffstechnik, Vol. 47, pp. 101-109
- de Kat, J.O., Paulling, J.R., 1989, "The Simulation of Ship Motions and Capsizing in Severe Seas", Trans. SNAME, Vol. 97, pp. 139-168
- Du, S.X., Hudson, D.A., Price, W.G., Temarel, P., 2009, "Implicit expressions of static and incident wave pressures over the instantaneous wetted surface of ships", Proc. IMechE Part M: J. Engineering for the Maritime Environment, Vol. 223, pp. 239-256, doi: 10.1243/14750902JEME162
- Francescutto, A., Contento, G., Biot, M., Shiffner, L., Caprino, G., 1998, "The Effect of the Excitation Modelling in the Parameter Estimation of Nonlinear Rolling", Proc. 8th International Offshore and Polar Engineering Conference (ISOPE98), Montreal, Vol. 3, pp. 490-498
- Frank, W., 1967, "Oscillation of cylinders in or below the free surface of deep fluids", Report No. 2375, Naval Ship Research and Development Center
- Fujiwara, T, Ikeda, Y., 2007, "Effects of roll damping and heave motion on heavy parametric rolling of a large passenger ship in beam waves", Proc. 9th International Ship Stability Workshop, Hamburg, Germany, CD-ROM
- Hooft, J. P., 1982, "Advanced Dynamics of Marine Structures", USA, John Wiley & Sons, Inc.
- Hutchison, B.L., 1991, "The Transverse Plane Motions of Ships", Marine Technology, Vol. 28, pp. 55-72
- IMO MSC.1/Circ.1200 , 2006, "Interim Guidelines for Alternative Assessment of the Weather Criterion", 24 May, London, UK
- IMO SLF54/INF.12-Annex 3, 2011, "On the Consideration of Lateral Accelerations in Ship Design Rules", Submitted by Germany (SLF54/INF.12 submitted by Japan)
- Karasuno, K., Okano, S., Miyoshi, J., Maekawa, K., 2003, "Predictions of ship's hull hydrodynamic forces and maneuvering motions at slow speed based on a component-type mathematical model", Proc. MARSIM2003, Kanazawa, Japan, 25-28 August, RC-4-(1-11)
- Matusiak, J., 2010, "On the non-linearities of ship's restoring and the Froude-Krylov wave load part", Proc. ITTC Workshop on Seakeeping - V&V for Non-linear



- Seakeeping Analysis, October 19-21, Seoul National University, Seoul, Korea, pp. 151-159
- McCue, L., 2012, "Putting vessel motion research into the hands of operators", Proc. 11th International Conference on Stability of Ships and Ocean Vehicles (STAB2012), Athens, Greece
- Naciri, M., Lledo, N., 2001, "Non-linear low frequency roll excitation of a rectangular barge", Proceedings of 20th International Conference on Offshore Mechanics and Arctic Engineering (OMAE'01), Rio de Janeiro, Brazil, June 3-8, paper number OMAE2001/OFT-1247
- Neves, M.A.S., Rodríguez, C., 2006, "Unstable ship motions resulting from strong nonlinear coupling", Ocean Engineering, Vol. 33, pp. 99-108
- Pessoa, J., Fonseca, N., Guedes Soares, C., 2011, "Experimental and Numerical Study of the Depth Effect on the First Order and Slowly Varying Motions of a Floating Body in Bichromatic Waves", Proc. of the ASME 2010 29th International Conference on Ocean, Offshore and Arctic Engineering (OMAE2010), Shanghai, China, paper OMAE2010-21188
- Salvesen, N., Tuck, E. O., Faltinsen, O., 1970, "Ship Motions and Sea Loads", Trans. SNAME, Vol. 78, pp. 250-287
- Skomedal, N.G., 1982, "Parametric Excitation of Roll Motion and Its Influence on Stability", Proc. Second International Conference on Stability of Ships and Offshore Vehicles (STAB82), Tokyo, October, pp. 113-125
- Spanos, D., Papanikolaou, A., 2009, "SAFEDOR International Benchmark Study on Numerical Simulation Methods for the Prediction of Parametric Rolling of Ships in Waves", Revision 1.0, 30 June, available from <http://www.naval.ntua.gr/sdl/sibs>
- Todd, F. H., Stuntz, G. R., Pien, P. C., 1957, "Series 60 - The Effect upon Resistance and Power of Variation in Ship Proportions", Trans. SNAME, Vol. 65, pp. 445-589
- Tzamtzis, S., 2004, "Development and testing of a procedure for the alternative assessment of Weather Criterion on experimental basis", University of Trieste and National Technical University of Athens.
- Ueno, K., 1950, "Influence of the Surface Tension of the Surrounding Water upon the Free Rolling of Model Ships", Memoirs of the Faculty of Engineering, Kyushu University, 12, pp.21-58
- Wheeler, J.D., 1969, "Method for Calculating Forces Produced by Irregular Waves", Offshore Technology Conference, Dallas, Texas, US, Paper No. 1006



Roll Stabilization by Vertical Thrust-Producing Flapping Wings Using Active Pitch Control

Kostas A. Belibassakis, *School of Naval Architecture and Marine Engineering, National Technical University of Athens, kbel@fluid.mech.ntua.gr*

Gerassimos K. Politis, *School of Naval Architecture and Marine Engineering, National Technical University of Athens, polit@central.ntua.gr*

ABSTRACT

The analysis of vertical oscillating wing located beneath the ship's hull is investigated as an unsteady thrust production mechanism, augmenting the overall propulsion system of the ship. The wing undergoes a combined flapping and pitching oscillatory motion, in a uniform inflow and in the presence of waves. The flapping motion is induced by the motion of the ship in waves, essentially ship rolling and swaying. The pitching motion of the wing about its pivot axis, is properly selected as a function of the ship rolling motion in order to produce thrust, with simultaneous generation of useful antirolling moment for ship stabilization. Ship flow hydrodynamics are modeled using a Rankine source-sink formulation, and ship responses are calculated taking into account the additional forces and moments due to the above biomimetic propulsion system. Extending previous approach by the authors, a 3-D panel method is applied to model the unsteady lifting flow around the system. Free-wake analysis is incorporated to account for the effects of non-linear wing wake dynamics, at high translation velocities and amplitudes of the oscillatory motion.

Keywords: *biomimetic ship propulsion, flapping wings, energy saving devices*

1. INTRODUCTION

Biomimetic propulsors are ideally suited for converting environmental (sea wave) energy to useful thrust. Recent research results concerning flapping foils and wings, supported also by extensive experimental evidence and theoretical analysis, have shown that such systems at proper conditions could achieve high thrust levels; see, e.g., Triantafyllou et al (2000, 2004), Rozhdestvensky & Ryzhov (2003), Taylor et al (2010). In addition, response to the demand of making sea transport more environmentally friendly has been recognized to be an important factor concerning global warming and climatic change. The contribution of cargo ships in world pollution has been recognised as one of the most important factors (e.g. Colville 2001, Flannery 2005), taking also into account the bad fuel quality of seagoing vessels in relation to other modes of transport. Indeed, images and data available from satellites reveal that

large areas around the main sea-ocean shipping lines are almost permanently covered by clouds with large concentrations of pollutants from ships' engines.

In real sea conditions the ship undergoes moderate or high amplitude oscillatory motions due to waves, the most significant being the heaving-pitching and rolling-swaying combinations. A biomimetic propulsor, contrary to a conventional propeller, absorbs the required power by two independent motions. For a fish tail these two motions are heaving and pitching, while for a bird-flight flapping and pitching (or twisting) of bird wings, respectively (see Politis & Tsarsitalidis 2010). The former biomimetic motion has already been considered by the authors, (Politis & Politis 2012, Belibassakis & Politis 2012), in connection with the problem of transforming the ship heaving-pitching energy to useful thrust with simultaneous reduction of the corresponding ship motions. The latter biomimetic motion

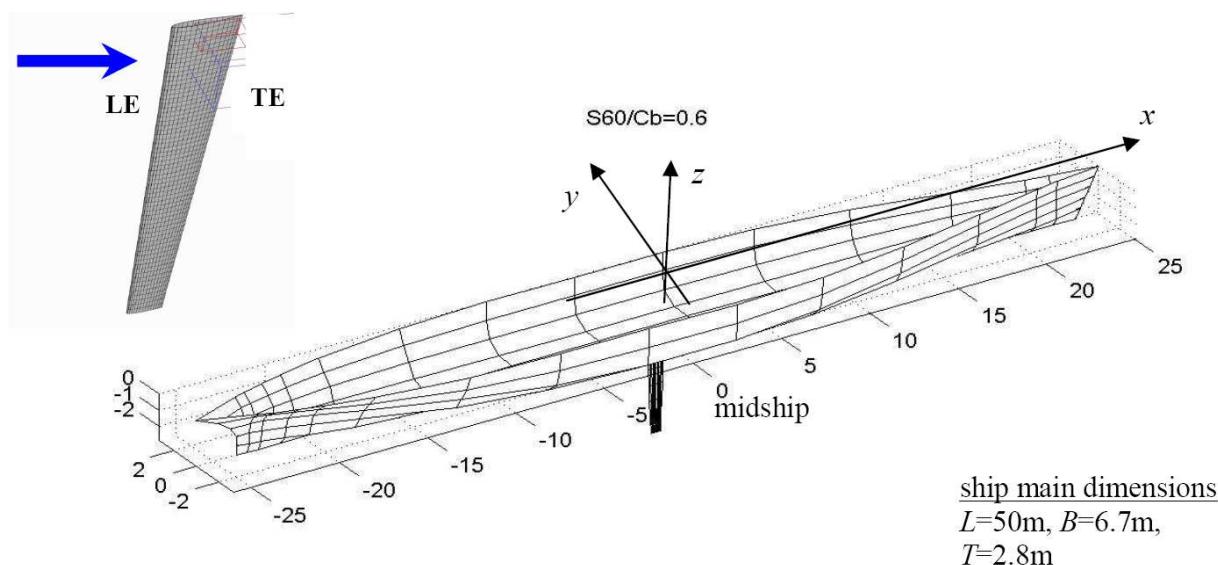


Figure 1: Ship hull equipped with a vertical flapping wing located below the keel, at the midship section. Geometrical details of the flapping wing (with NACA0012 sections) are included in the upper subplot where the main flow direction relative to the flapping wings is indicated by using an arrow.

is the subject of the present investigation. We shall show that such type of wing motion can be used to reduce the ship rolling-swaying motions with simultaneous production of useful propelling thrust. More specifically, in the present work the analysis of a randomly flapping-pitching wing, located beneath the ship's hull, is examined as an unsteady thrust production mechanism, augmenting the overall propulsion system of the ship. The above arrangement increases the draft of the ship, however the wing could be hinged to the hull permitting its folding and storage when not needed or when the ship is docking. The wing undergoes the combined flapping-pitching oscillatory motions, in a uniform inflow (due to ships speed) and in the presence of waves. The flapping motion is induced by the rolling motion of ship in waves. The pitching motion of the wing (about its pivot axis) is actively controlled in terms of the ship rolling-swaying motions (Politis & Politis 2012) in order to (always) produce thrust and generate antirolling moment for ship stabilization. Ship flow hydrodynamics are modelled using a Rankine source-sink formulation and ship motions are calculated taking into account the additional forces and moments due to the above biomimetic wing

propulsion system. For the needs of the linearized theory the wing is modelled using a combination of unsteady lifting line theory with 2D unsteady theory of Theodorsen. For an assessment of this assumption we present comparisons of the simplified model with a 3D panel time-stepping formulation of the unsteady problem (Politis 2009, 2011), which includes the complex unsteady trailing vortex rollup in the modelling of biomimetic wing performance. From this comparison, experience is obtained regarding the required corrections of the simplified model in the case of larger flapping angles of the wing exceeding the range of the linearized theory. It is shown that the above is a good approximation to our problem, due to the relatively small Strouhal number in which such biomimetic wings operate. Numerical results are presented for the developed thrust and the effect on ship motions of a biomimetic system. The present method can serve as a useful tool for assessment and the preliminary design and control of such systems for enhancing the overall ship performance in a wavy environment.

The biomimetic propulsor considered in the present study consists of a single wing, as shown in Fig.1. However the whole performance of the system could be further

enhanced by consideration of multiple wings in various arrangements (see also Belibassakis & Politis 2012).

2. BIOMIMETIC WING THRUSTERS

Kinematics: For the description of the kinematical characteristics of the flapping-pitching wing and of the induced flow dynamics two reference systems are considered such as: the motionless inertial system and the ship-fixed coordinate system, which is steadily translated with velocity U with respect to the former and oscillating with respect to the fundamental degrees of freedom of the floating ship due to waves. This same system is also used to describe the pitching motion of the flapping wing. In the case of simple periodic ship oscillations the relative ship frequency $\omega = 2\pi f$ due to waves is the same as the flapping frequency of the wing. This is due to the fact that the vertical wing is attached to the hull, allowing only pitching motions relative to the ship. Furthermore, the ‘active pitch’ selection algorithm (see next section) enforces pitch motion to follow the flapping motion with the proper phase angle: $\psi = 90^\circ$, which is necessary for the production of thrust. Consequently, pitching motion evolves at the same frequency ω as the ship rolling or wing flapping motions. Expressing the previous discussion quantitatively, the wing pitching axis performs a combined translation (sway) and rotation (roll) given by $h(t) = h_0 \sin(\omega t)$, where h_0 is a spanwise variable amplitude $h_0 = \xi_{20} - z\xi_{40}$ (z denotes the vertical distance of a point of the pitching axis of the wing– it is assumed that the origin of the moving x, y, z system coincides with the centre of flotation of the hull). Simultaneously, the wing undergoes a pitching motion around the pivot axis described by $\theta(t) = -\theta_0 \sin(\omega t + \psi)$.

Dynamics: With the pivot point for the angular motion of the wing located around the 1/3 chord length from the leading edge, a minimization of the required torque for pitching is achieved (Anderson et al 1998, Schouveiler et al 2005, Politis & Politis 2012).

For flapping systems steadily advancing in unbounded fluid the main flow parameter controlling the unsteady lift production mechanism is the Strouhal number $St = 2f h_0 / U$, while, in the absence of flow separation, the Reynolds number has a secondary role affecting viscous drag. For the case of a flapping-pitching wing, the instantaneous angle of attack at the position z is given by:

$$\alpha(z, t) = \mathcal{G}(z, t) - \theta(t) = \tan^{-1}(U^{-1} dh / dt) - \theta(t) \quad (1)$$

where $\theta(t)$ is the instantaneous pitch angle.

For relatively low roll amplitude, purely harmonic motion, and the pitch angle selected according to the discussion of the previous section, relation (1) becomes $\alpha(z, t) = (\mathcal{G}(z) - \theta_0) \cos(\omega t)$, which can be achieved by setting the pitch angle:

$$\theta(t) = \theta_0 \cos(\omega t) = w \mathcal{G}(z) \cos(\omega t), \quad (2)$$

where $\mathcal{G}(z) \approx U^{-1} h_0 \omega$ and w acts as the pitch control parameter (Politis & Politis 2012), usually taking values in $0 < w < 1$, which is amenable to optimization. Decreasing the value of w , the maximum angle of attack is reduced and the wing operates at lighter loads. On the contrary, by increasing the above parameter the wing loading becomes higher and so is the danger of leading edge separation that would lead to significant dynamic stall effects. For a flapping wing the amplitude $\mathcal{G}(z)$ is variable spanwise. Thus determination of pitch requires selection of a reference z -position. We select the midsection of the wing (z_{mid}) in order to control the wing pitch $\theta(t)$. As a result, the instantaneous angle of attack is given by

$$\alpha(z, t) = \tan^{-1}(U^{-1} dh / dt) - w \tan^{-1}(U^{-1} dh_{mid} / dt), \quad (3)$$

where $h_{mid} = \xi_{20} - z_{mid} \xi_{40}$.

Free-surface effects: In the case of the biomimetic system under the calm or wavy



free surface, additional parameters are important, as the Froude number $F = U / (gL)^{1/2}$, where L denotes the characteristic (ship) length and g is gravitational acceleration, as well as various frequency parameter(s) associated with the incoming wave, like $\mu = \omega^2 L / g$ and $\tau = \omega U / g$, the latter being used to distinguish subcritical ($\tau < 1/4$) from supercritical ($\tau > 1/4$) condition.

Geometrical parameters: As far as a standalone flapping wing is concerned, the selection of planform area, in conjunction with horizontal/vertical sweep and twist angles, and generating shapes ranging from simple orthogonal or trapezoidal-like wings to fish-tail like forms, constitutes the set of the most important geometrical parameters (see Politis & Tsarsitalidis 2009). Other significant parameters are the wing aspect ratio, spanwise distribution of chord, thickness and possibly camber of wing sections, as well as the specific wing-sectional form(s). In the case of the wing operating under the hull of the ship, important additional geometrical parameters associated with its arrangement are the longitudinal position, and the clearance(s) with respect to the hull surface.

As an example, which is used in the present work for demonstration purposes, we consider a variant of the series 60 - $C_b=0.60$ ship hull form, shown in Fig.1. The main ship data are listed below:

principal dimensions: $L=50\text{m}$, $B=6.70\text{m}$, $T=2.80\text{m}$

block coefficient: $C_b=0.533$

immersed volume: $\nabla = 500\text{m}^3$, $\Delta=512\text{tn}$ (salt water) wetted/waterplane area: $S_w=380\text{m}^2$, $A_{wL}=225\text{m}^2$

center of flotation: $x_f = -1.15\text{m}$ (LCF aft

midship) vertical center of buoyancy: $KB=1.55\text{m}$ (from BL) longitudinal position: $LCB=-0.266\text{m}$ (from midship) metacentric radius: $BM=1.15\text{m}$.

We also consider the long-center of gravity to coincide with the center of buoyancy, $X_G=-0.266\text{m}$ (aft midship), $Y_G=0$, and $KG=1.80\text{m}$ (from BL), and thus, the metacentric height in the above condition are estimated to be $GM=0.9\text{m}$. Finally, the radii of gyration about the x-axis and y-axis, respectively, are taken $R_{xx}=0.32B$, $R_{yy}=0.23L$. Estimated data concerning wave and total resistance of the above hull, for two representative values of the ship speed in calm water, are given in Table 1.

Table 1: Resistance data of ship hull of Fig.1

U (kn)	$F = U / \sqrt{gL}$	$C_w \times 10^3$	R (kp)	EHP (PS)
10.6	0.25	0.5	1504	110
12.9	0.30	1.8	3465	305

The flapping wing propulsor, shown in Fig.1, is considered to be located at the midship section. The upper end (root) of the wing is assumed at a depth $d=2.8\text{m}$ and the span of the vertical wing is $s=6\text{m}$. The wing planform shape is trapezoidal, the root and tip chords of the wing have lengths $c_r=1\text{m}$, $c_t=0.5\text{m}$, respectively, and the leading edge sweep angle is $A=1.6\text{deg}$ (see Fig.1). On the basis of the above, the wing planform area is $S_w=4.5\text{m}^2$, and thus its aspect ratio is $AR=8$. The wetted area of the wing is the double of its planform area. The wing sections are symmetrical NACA0012, and thus the local max thickness-to-chord ratio is kept constant over the span and equal to 12%. The flapping wing oscillates due to the ship swaying and rolling motions and simultaneously it rotates about a pivot axis passing through 1/3 chordlength distance from the leading edge that coincides with the vertical z-axis when the ship is at the upright position (see Fig.1). The same logic could be also applied to active anti-roll fins to generate propulsion.

3. SHIP AND WING HYDRODYNAMICS

Methods for the calculation of dynamic ship responses in a given sea state have been developed up to a satisfactory level of accuracy; see, e.g., Ohkusu (1996). Various 3D

hydrodynamic models based on BEM, both in the frequency and the time domain, are readily available nowadays, see, e.g., Beck et al (1996), Sclavounos et al (1997). Furthermore, simplified semi-3D theories are also useful in practice (e.g., Arribas 2007). Methods based on numerical simulation of the hydrodynamic analysis of conventional and high-speed ships are valuable tools for use in ship design, and various commercial software packages & tools for the analysis of the dynamic behaviour of ships in waves are available today. In this category belong Rankine panel methods, based on B-spline and NURBS approximations, exhibiting low damping and numerical dispersion; see Sclavounos & Huang (1997), Kring & Sclavounos (1997), Huang & Sclavounos (1998), Kim & Shin (2003). Comprehensive survey of theoretical and computational methods is presented in Beck & Reed (2001).

Moreover, lifting appendages are attached to ship hull in order to improve their calm water performance and reduce responses in waves; see, e.g. Sclavounos & Huang (1997). For example, passive and active systems are frequently used as anti-rolling stabilizers (e.g., Naito & Isshiki 2005). In the context of 3D BEM applications a Rankine panel method developed by Sclavounos & Borgen (2004) has been applied to study the seakeeping performance of a foil-assisted high-speed monohull. In the latter work, the formulation of the seakeeping of ships equipped with lifting appendages is developed, and the mechanisms responsible for the reduction of the vertical motions of high-speed vessels equipped with hydrofoils is studied. The sensitivity of the heave and pitch motions on the longitudinal position of the hydrofoil are studied, finding that the most efficient location for the hydrofoil is at the ship bow. Furthermore, active lifting system and devices used for the motion control of ships and high-speed vessels in a sea state as well as dynamic positioning of offshore vessels have also been extensively studied by Chatzakis & Sclavounos (2006). Developments and applications of control theory for marine vessels are extensively discussed in Fossen (2002). The complexity of

the selected model depends upon the underlying physics, the properties of the controller and the desired performance of the controlled system; see, e.g., Thomas & Sclavounos (2007).

Standard seakeeping analysis in the frequency domain (see, e.g., Sclavounos & Borgen 2004) is used in the present work to obtain the motions and responses of the examined system (ship and flapping wing). The coupled equations of ship's sway $\xi_2 = Re(\xi_{20}e^{i\omega t})$ and roll $\xi_4 = Re(\xi_{40}e^{i\omega t})$ motion (with corresponding complex amplitudes ξ_{20} and ξ_{40}) read as follows:

$$\begin{aligned} &(-\omega^2(m+a_{22})+i\omega b_{22})\xi_{20} + \\ &(-\omega^2(a_{24}+I_{24})+i\omega b_{24})\xi_{40} = F_{20} + X_{20}, \quad (4a) \end{aligned}$$

$$\begin{aligned} &(-\omega^2(a_{42}+I_{42})+i\omega b_{42})\xi_{20} + \\ &(-\omega^2(a_{44}+I_{44})+i\omega b_{44}+c_{44})\xi_{40} = F_{40} + X_{40}, \quad (4b) \end{aligned}$$

where a_{jk} and b_{jk} , $j,k=2,4$, are the (symmetric) added mass and damping coefficients, and m is the total mass of the ship and wing ($m = \Delta$). The involved hydrostatic coefficient is $c_{44} = mgGM$ and the inertia coefficients are $I_{44} = mR_{xx}^2$ and $I_{24} = I_{42} = -mZ_G$ (here $Z_G = T-KG$). The damping terms used in the above system are calculated on the basis of ideal flow hydrodynamics, and are used to provide a first demonstration of the present active anti-rolling thruster. However, this is expected to lead to erroneously large responses around the resonance condition. Enhanced expressions involving viscous damping effects are available and could be used in future extensions for more correct predictions. Moreover, the terms F_{j0} , $j=2,4$ appearing in the right-hand side of Eqs.(4) are the Froude-Krylov and diffraction vertical forces and rolling moment (about the x-axis) amplitudes, respectively. Finally, the terms X_{j0} , $j=2,4$, denote additional force and moment amplitudes due to the operation of flapping wing as an unsteady thruster. The latter are



dependent on the ship's responses, as well as to the incoming wave field. In the present work we employ a simplified lifting-line model to derive analytic expressions of these forces in terms of the oscillatory ship amplitudes and include the effects of flapping wing in the system coefficients. We note here that due to ship hydrodynamics and oscillatory thrust developed by the flapping wing its responses are also coupled with the surge and yaw motions (ξ_1, ξ_6) of the ship. However, taking into account the large mass of ship, in conjunction with installation of energy storage (flywheel-type) systems and the effect of the rudder, at first level of approximation, the above motions are considered to be very small and are neglected.

A low-order panel method, based on simple Rankine source-sink distributions and quadrilateral 4-node elements, is used to obtain the hydrodynamic analysis of the oscillating ship-hull in waves, in the frequency domain, and to treat the steady problem of the ship advancing with forward speed. In both cases, the four-point, upwind finite difference scheme by Dawson (1977) has been used to approximating the horizontal derivatives involved in the (linearized) free surface boundary condition. Details concerning the application of the above method, in the case of the steady problem and in the presence of additional effects from lifting appendages, can be found in Belibassakis (2011). We mention here that a minimum number of 15-20 elements per wavelength is used in discretizing the free surface, in order to eliminate errors due to damping and dispersion associated with the above discrete scheme (see also Sclavounos & Nakos 1988 and Janson 1997). An example concerning the calculated wave field exciting by rolling ship hull motion, for Froude number $F=0.25$ and reduced frequency $\tau = \omega U / g = 0.42$, as predicted by the present model, is shown in Fig. 2. In this case, the half-hull surface is discretized by using a mesh of 22 (in the long direction) by 12 (sectional) panels, and the half symmetric part of the free surface by using a mesh 42 (in the transverse direction) by 118 (in the long

direction) panels. Thus the total number of elements is 5220. Although no special treatment is necessary for enforcing the radiation condition in the supercritical ($\tau > 1/4$) case, an absorbing layer technique is used, based on a matched layer all around the fore and side borders of the computational domain on the free surface; see Nakos & Sclavounos (1988), Nakos *et al* (1994), Sclavounos & Borgen (2004). The thickness of the absorbing layer is of the order of 1-2 characteristic wavelengths and its coefficient is quadratically increasing. The efficiency of this technique to damp the outgoing waves with minimal reflection is dependent on the thickness of the layer. A similar result concerning the steady flow around the same ship hull, also at Froude number $F=0.25$, is shown in Fig. 3. Based on the above analysis the values of the wave resistance coefficient listed in Table 1 have been calculated. The corresponding ones concerning the total calm-water resistance have been obtained from numerical analysis based on RANSE and experimental measurements (see, e.g., Tzabiras 2004).

In the present work, bow-quartering and beam waves ($\beta=150^\circ, 90^\circ$) have been considered as excitation of the hull oscillatory motion. In the examined case the working angle of attack of the flapping wing is given by:

$$a(t) = \frac{1}{U} \left(W \frac{d\xi_2(t)}{dt} + z \frac{d\xi_4(t)}{dt} \right) - \delta(t), \quad (5)$$

where $W = \frac{\partial \varphi_{INC}}{\partial y} n_y + \frac{\partial \varphi_{INC}}{\partial z} n_z$ is the incident wave velocity in the normal direction of the wing pivot axis, $(n_y, n_z) = (\cos(\xi_4), \sin(\xi_4))$, and $\delta(t)$ denotes the flapping wing pitch angle (controlled variable) with respect to the pivot axis.

The above formula is obtained by linearizing for small angles. The first term in parenthesis in the right-hand side is due to the contribution of ship's oscillatory motion and the incoming waves, and this part, considered together, is denoted by:

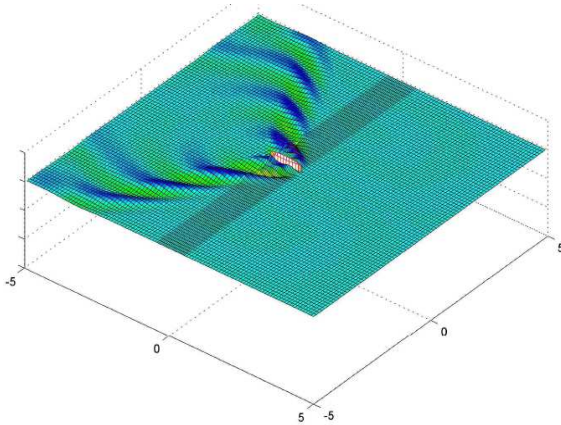


Figure 2: Calculated wave field exciting by ship rolling motion for $F=0.25$ and $\tau=0.42$, as predicted by the present model. Horizontal distances are scaled with respect to ship length.

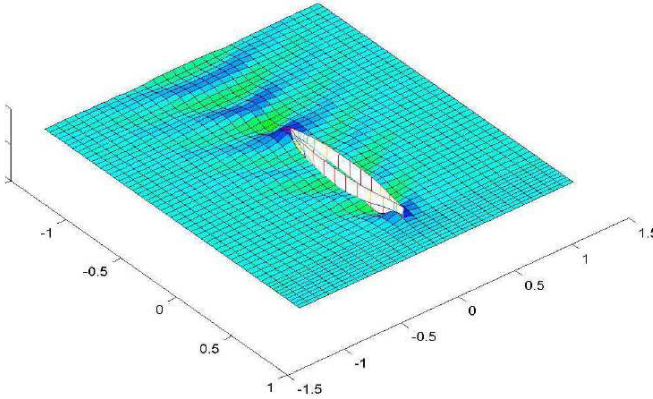


Figure 3: Steady wave pattern for $F=0.25$ as predicted by the present model.

$$\mathcal{G}(z,t) = \frac{1}{U} \left(W - \frac{d\xi_2(t)}{dt} + z \frac{d\xi_4(t)}{dt} \right) \quad (6)$$

In the above formulas φ_{INC} is the incoming wave potential, for unit amplitude (A) of free-surface elevation, which is given by:

$$\varphi_{INC}(\mathbf{x}, z; t) = \text{Re} \left\{ \frac{ig}{\omega_0} \exp(kz) \exp(i(\mathbf{kx} + \omega t)) \right\} \quad (7)$$

where $\mathbf{kx} = kx \cos(\beta) + ky \sin(\beta)$, $k = \omega_0^2 / g$, is the wavenumber of the incident waves and ω_0 is the absolute (angular) frequency.

The corresponding relative frequency (frequency of encounter) is given by

$$\omega = \omega_0 - kU \cos(\beta) = \omega_0 - \omega_0^2 U \cos(\beta) / g \quad (8)$$

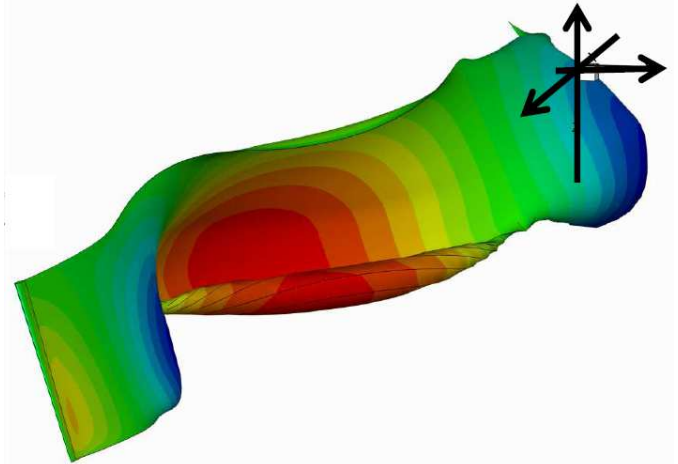


Figure 4: Vortical wake behind the flapping wing in harmonic motion, as calculated by the 3D panel time stepping algorithm. Mean wing speed $U=5.5\text{m/s}$, flapping frequency $\omega=0.628\text{rad/s}$, rolling amplitude $\xi_{40}=20\text{deg}$, wing pitch control parameter $w=0.5$.

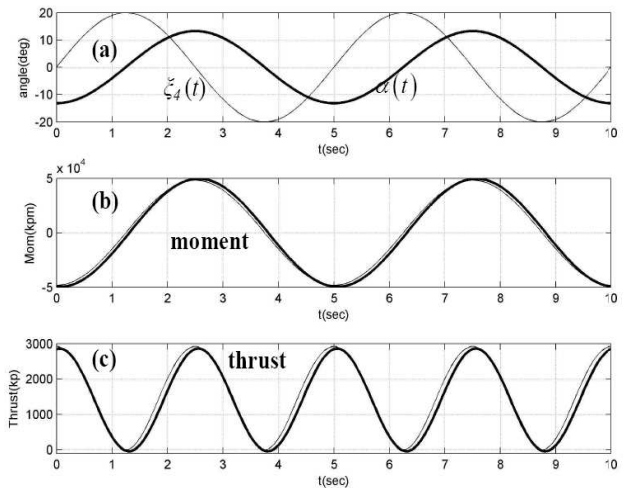


Figure 5: (a) Rolling motion and angle of attack of the flapping wing of Fig. 4. (b) Moment and (c) thrust as calculated by the simple model (thin lines) and the 3D panel time-stepping method (thick lines).

As it was previously discussed in the case of harmonic flapping wing motion, the controlled pitch variable is set $\delta(t) = w \mathcal{G}(z_{mid}, t)$ and the pitch control parameter w ranges from 0 to 1. Thus, the time variation of the angle of attack becomes

$$a(z,t) = \mathcal{G}(z,t) - w \mathcal{G}(z_{mid}, t) \quad (9)$$

with $\mathcal{G}(z,t)$ defined by Eq. (6). Unsteady lifting line models based on the integration of 2D sectional lift along the span, as the ones



developed by Sclavounos (1987) and Guermond & Sellier (1991) can be used to obtain the wing lift and moment (about the pivot axis) coefficients.

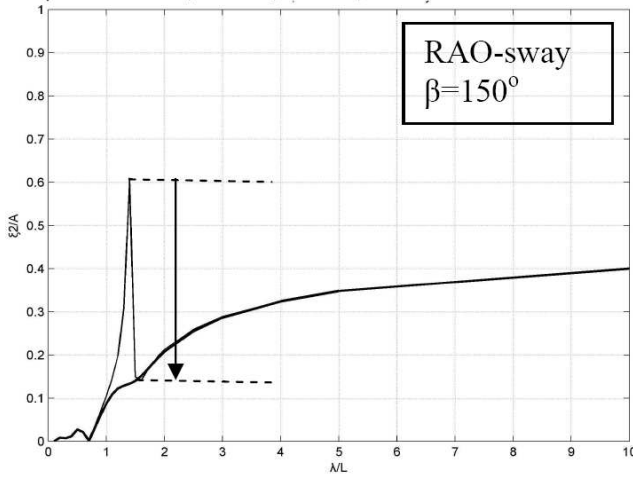


Figure 6: Sway response (ξ_{20}/A) of the ship against non-dimensional wavelength, for $\beta=150^\circ$. The effect of flapping wing propulsor is shown by using a thick solid line, and the reduction of maximum response by an arrow.

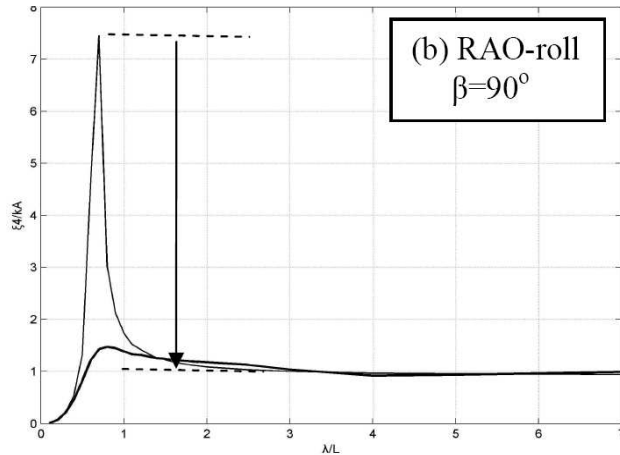


Figure 7: Roll response (ξ_{40}/kA) of the ship against non-dimensional wavelength for (a) $\beta=150^\circ$ and (b) $\beta=90^\circ$. The effect of flapping wing propulsor is shown by using a thick line, and reduction of responses is indicated by an arrow.

In the case of flapping wings operating at relatively low reduced frequencies of oscillation, the previous spanwise integration could be simplified (see also DeLaurier 1993), leading to approximate expressions as follows

$$C_L^{3D} = \frac{AR}{AR+2} \frac{1}{S_w} \int c(z) C_L^{2D}(z) dz \quad (10)$$

where $C_L^{2D}(z)$ denotes the sectional lift coefficient of the wing in the spanwise direction, and $c(z)$ is the chord distribution.

The sectional lift can be estimated by means of unsteady hydrofoil theory (see, e.g., Newman 1977) in terms of the dynamic angle of attack:

$$\alpha(t) = \text{Re} \left[(A_S + A_R + A_W) e^{i\omega t} \right] \quad (11)$$

where $A_S = -(1-w) \frac{i\omega \xi_{20}}{U}$, $A_R = (z - w z_{mid}) \frac{i\omega \xi_{40}}{U}$,

$A_W = (1-w)W/U$, the latter term being associated with incoming wave velocity at the flapping wing. The sectional lift is obtained as a superposition of the solutions corresponding to the oscillating transverse-rotational and sinusoidal gust problems, and in the case of flapping wings of small back-sweep angle (as in the present example) is approximately expressed as follows

$$C_L^{2D} = 2\pi \left(\mathbb{C}(k)(A_S + A_R) \right) + \mathbb{S}(k)A_W + 2\pi k^2 (h_0/c) \quad (12)$$

involving the Theodorsen $\mathbb{C}(k)$ and the Sears functions $\mathbb{S}(k)$. The latter are defined in terms of the Hankel functions of the second kind as follows:

$$\mathbb{C}(k) = H_1^{(2)}(k)/\Pi, \quad \mathbb{S}(k) = 2i/(\pi k \Pi),$$

$$\Pi = H_1^{(2)}(k) + iH_0^{(2)}(k) \quad (13)$$

with $k = \omega c(y)/2U$ the local spanwise value of the reduced frequency of the wing section. The last term in Eq. (12), with $h_0 = \xi_{20} - z\xi_{40}$, is the added mass effect due to roll-induced transverse motion of each wing section (see, e.g. Newman 1977, Sec.5.16), which is considered to be most significant in comparison to the corresponding one due to the rotational wing motion about the pivot axis. For low frequencies of oscillation, and wing reduced frequency k near zero, the functions $\mathbb{C}(k) \approx \mathbb{S}(k) \approx 1.0$, and this result permits us to obtain convenient expressions of the force

and moment due to the operation of vertical flapping wing. Moreover, by considering the contribution of wave velocity very small ($A_w \ll A_s, A_R$), due to the fact that the wing operates submerged at considerable depth below the free surface, the above formulae result in the following approximate expressions for the amplitudes of hydrodynamic transverse force and rolling moment of the flapping wing

$$X_{20} = i\omega(G_S \xi_{20} + G_R \xi_{40}) \quad (14a)$$

$$X_{40} = i\omega(M_S \xi_{20} + M_R \xi_{40}) \quad (14b)$$

Where $G_S = -\gamma(1-w)S_w$,

$$G_R = \gamma \int (z - wz_{mid}) c(z) dz,$$

$$M_S = \gamma(1-w) \int z c(z) dz,$$

$$M_R = -\gamma \int z(z - wz_{mid}) c(z) dz,$$

$\gamma = \chi \pi \rho U \frac{AR}{AR+2}$, and χ is a correlation coefficient taking values near unity that will be explained below.

Using Eqs. (14) in the system (4), we obtain the following modifications of the system (hull and flapping wing) damping coefficients:

$$\delta b_{22} = -G_S, \delta b_{44} = -M_R,$$

$$\delta b_{24} = -G_R, \delta b_{42} = -M_S, \quad (15)$$

Also, the flapping wing added mass produce corresponding modifications in the system coefficients δa_{22} , $j, k = 2, 4$, which however, due to the large dimensions of the ship, are found to be negligible in comparison with the corresponding ones of the oscillating hull. The thrust produced by the flapping wing is approximately calculated as follows

$$\mathcal{T} = (G_S + G_R) \sin(\mathcal{G}(z_{mid}, t)) \quad (16)$$

Enhanced expressions could be obtained by keeping more terms in the expansion of Theodorsen and Sears function about $k=0$, which will result into additional modifications in the hydrodynamic coefficients and excitation forces. More complete unsteady lifting line models, as e.g., the one developed by Guermond and Sellier (1991), could be

employed to overcome such limitations, and this task is left to be examined in future work.

To illustrate the usefulness of the above approximate model, in the simple case of flapping wing in infinite fluid, we present in Figs. 4 and 5 results and comparisons of the calculated lift and thrust by means of the above equations and a 3D panel time stepping algorithm developed by Politis (2009, 2011). In this case the wing undergoes simple harmonic transverse and rotational about its pivot axis motions. In particular, the wake rollup behind the wing as calculated by the 3D panel time-stepping algorithm for the case: $U=5.5\text{m/s}$, $\omega=1.256\text{rad/s}$ and $\xi_{40}=20\text{deg}$, is illustrated in Fig.4. Predictions for the rolling moment and thrust as calculated by the above quasi-steady model and the 3D panel method in the example considered are presented in Fig.5, against the variation of the angle of attack, and are found in relatively good agreement. Moreover, from data shown in Fig.5 and systematic analysis, we can calculate frequency- and amplitude-dependent correction factor χ that could be used to better correlate the results of the above quasi-steady model to the 3D panel time-stepping methodology (cf. Eqs. 14).

The preceding analysis permits us to calculate, at a first order of approximation, the ship responses including the effect of the flapping wing as a thruster, and compare with corresponding seakeeping results without the wing. As an example, the normalized sway response of the ship with respect to the incident wave amplitude (ξ_{20}/A) is plotted in Fig.6, as calculated by the present method, for various values of the non-dimensional wavelength (λ/L), wave incidence $\beta=150^\circ$ and Froude number $F=0.25$. In the same figure the corresponding result obtained with the consideration of the flapping wing is shown by using a thick solid line. We observe a significant reduction of the swaying motion, especially around the resonant condition (indicated by using an arrow), which is due to the damping effect from the operation of the



harmonically oscillating vertical wing. Furthermore, in Fig. 7 the same effect concerning the calculated ship-roll response (ξ_{40}/kA) is presented. In this case head-quartering ($\beta=150^\circ$) and beam ($\beta=90^\circ$) incident waves have been considered. Again we observe that the operation of the flapping wing (results shown by using thick solid lines) leads to significant reduction of roll responses, for all frequencies. This permits safe routing of the ship even in beam seas and rough sea-conditions that would be undesirable and avoided otherwise.

The noticeable reduction of ship responses is evidence of significant wave energy absorption by the present flapping thruster, and also leads to reduction of the added resistance. To provide an indication, for the same as above Froude number $F=0.25$ ($U=10.6\text{kn}$), the added wave resistance without the flapping wing has been estimated by the energy method (see, e.g., Arribas 2008) and for sea state 6 to be of the order of calm-water ship resistance, and is reduced by 25% by the operation of the flapping wing.

4. FLAPPING WINGS AUGMENTING SHIP PROPULSION

Having obtained an estimation of the time history of the ship oscillatory motion from Eqs.(4), including the effects of the oscillating wing operating as a thruster, the instantaneous angle of attack can be determined by Eq. (5) and unsteady 3D non-linear panel methods could be applied to obtain more accurate prediction of the flapping wing characteristics, as well as detailed information concerning local flow velocity and pressure distribution. For this purpose, in the present work we employ the non-linear 3D panel method developed by Politis (2011), which is based on free wake analysis and Morino formulation based on Green's theorem. We note here that the above method includes also viscous drag effects.

The thrust augmentation by means of the operation of the present flapping wing propulsor, as calculated by the present method,

is illustrated in Figs. 8 and 9. In particular, we consider the ship of Fig.1 to travel at constant speed $U=10.6\text{kn}$, in head-quartering waves at sea state 6 (Beaufort scale 7), represented by a sea spectrum corresponding to significant wave height $H_s=5\text{m}$, and peak period $T_p=11\text{s}$, that is shown in Fig.8 by using dotted line (and the Bretschneider model spectrum). The same spectrum in the moving ship frame of reference is also plotted in Fig.8 by using dashed line, as well as the spectrum of the transverse motion response at the wing midspan position, by using a thick solid line. Next, in Fig.9, time series of various quantities including the ship rolling (ξ_4) motion, the angle of attack (α) and the thrust \mathcal{T} (kp) production by the flapping wing, based on setting the control pitch variable $w=0.5$, are shown, as obtained from the corresponding spectra by applying the random phase model (see, e.g., Ochi 1998). In this case, as illustrated in the last subplot of Fig.9, the thrust oscillations are in the interval 0-750kp and have average value of $\mathcal{T}_{av}=150\text{kp}$. Similar analysis for same ship speed $U=12.9\text{kn}$ and beam waves ($\beta=90^\circ$) provides higher value of average thrust $\mathcal{T}_{av}=750\text{kp}$, due to the increase of oscillatory frequency in this case. The last result concerning thrust production, as calculated by the present simplified model, is compared in Fig. 10 against corresponding prediction by the unsteady 3D panel method, showing quite good agreement.

In conclusion, in the example considered and discussed here the flapping wing is shown to produce significant anti-rolling moment fully capable of ship stabilization, while at the same time it provides useful thrust production ranging from 10% to 50% of the corresponding calm-water resistance of the ship at the same speed. Similar devices consisting of heaving horizontal wings, studied by the authors (Belibassakis & Politis 2012), which convert oscillatory motion due to ship heave and pitch motion to thrust, are shown to be well capable to overcome the added resistance due to waves at these ship speeds. Finally, we remark that the torque required for wing pitching according

to the control rule is very small and thus, the present system enhances the overall performance of the ship by producing thrust and providing significant stabilization.

5. CONCLUSIONS

The analysis of a vertical oscillating wing, located beneath the ship's hull, in harmonic and multichromatic motion, is examined as an unsteady thrust production mechanism, augmenting the overall propulsion system of the ship.

The wing undergoes a combined flapping and pitching oscillatory motion, in a uniform inflow and in the presence of waves. The transverse flapping motion is induced by the rolling and swaying motion of ship in waves. The pitching motion of the wing about its pivot axis is properly controlled in terms of the ship rolling-swaying motion in order to result in thrust force production and generate useful antirolling moment for ship stabilization. Ship flow hydrodynamics are modelled using a Rankine source-sink formulation, and ship motions are calculated taking into account the additional forces and moments due to the above flapping propulsion system

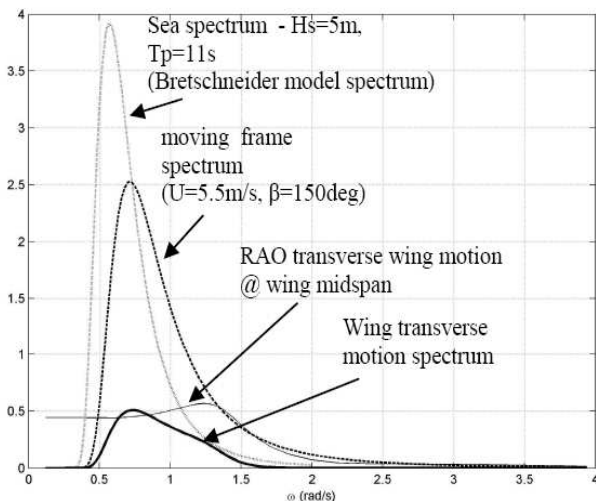


Figure 8: Sea spectrum ($H_s=5\text{m}$, $T_p=11\text{s}$) and transverse motion spectrum at wing midspan, for head-quartering ($\beta=150^\circ$) seas and ship speed $U=10.6\text{kn}$ ($F=0.25$).

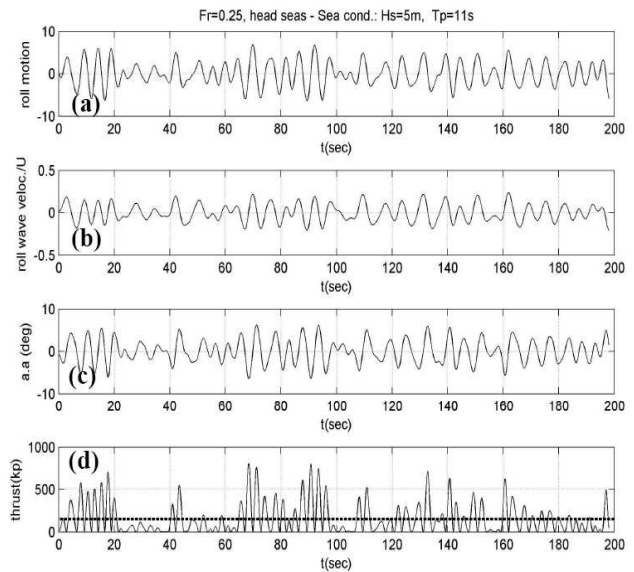


Figure 9: Stochastic responses of ship and flapping wing operating in head-beam ($\beta=150^\circ$) seas at ship speed $U=10.6\text{kn}$ ($F=0.25$). (a) Rolling motion with the flapping wing. (b) Normal velocity at the mid-span position due to ship rolling. (c) Calculated angle of attack at the mid-span position of the flapping wing, using $w=0.5$. (d) Thrust production by the flapping wing (time history). The time average is calculated to be 160kp and is indicated by using dashed line.

Flapping wing hydrodynamics are modelled through simplified lifting model and more accurate unsteady 3D panel method. Our results indicate that significant ship motion stabilization occurs with additional propulsive thrust production. The present method can serve as a useful tool for assessment and the preliminary design and control of such systems for augmenting ship propulsion and stability in rough seas and enhancing overall ship operability.

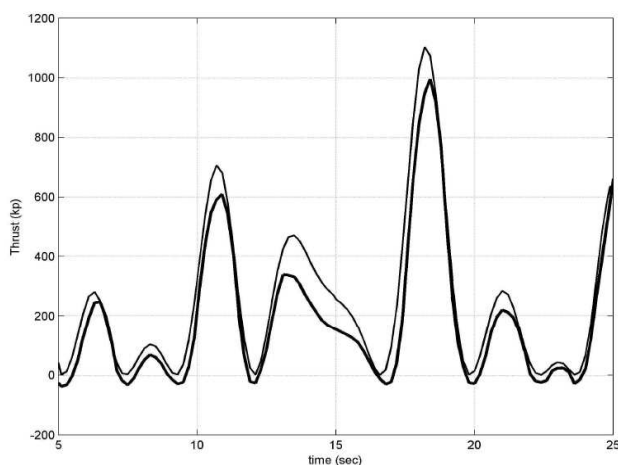


Figure 10: Thrust production by the vertical flapping wing (detail). Results by the simplified model (thin line) in comparison with the unsteady 3D panel method (thick line).

ACKNOWLEDGEMENTS

This work has been supported by the ARISTEIA Programme of National Strategic Reference Framework of Greece (NSRF 2007-2013), project BIO-PROPSHIP entitled: "Augmenting ship propulsion in rough sea by biomimetic-wing system".

6. REFERENCES

- Anderson, J. M., Streitlien, K., Barrett, D.S., Triantafyllou, M.S., 1998, "Oscillating foils of high propulsive efficiency", J. Fluid Mechanics, Vol. 360, 41-72.
- Arribas, P.F., 2007, "Some methods to obtain the added resistance of a ship advancing in waves", Ocean Engineering Vol. 34, 946-955.
- Beck, R.F., Reed, A.M, Rood, E.P., 1996, "Application of modern numerical methods in marine hydrodynamics", Trans.SNAME, Vol.104, 519-537.
- Beck, R.F., Reed, A.M, 2001, "Modern computational methods for ships in a seaway", Trans. SNAME, Vol.109, 1-51.
- Belibassakis, K.A., Politis, G.K., 2012, "Hydro-dynamic analysis of biomimetic wing systems for augmenting ship propulsion", to be presented at the 22nd Intern. Ocean and Polar Engineering Conf. (ISOPE 2012).
- Belibassakis, K., 2011, "A panel method based on vorticity distribution for the calculation of free surface flows around ship hull configurations with lifting bodies". Proc. IMAM 2011, Genoa, Italy.
- Chatzakis I. I., Sclavounos P. D., 2006, "Active motion control of high-speed vessels by state-space methods", J. Ship Res. Vol. 50(1).
- Colvile R.N et al., 2001, "The transport sector as a source of air pollution", Atmospheric Environment Vol. 35, 1537-1565.
- Dawson, C.W., 1977, "A practical computer method for solving ship-wave problems", Proc. 2nd Int. Conf. on Numerical Ship Hydrodynamics, Berkeley, USA.
- DeLaurier, J.D., 1993, "An aerodynamic model for flapping wing flight". The Aeronautical Journal paper no.1853.
- Flannery, T., 2005, "The weather makers", Penguin.
- Fossen T. I., 2002, "Marine Control Systems. Guidance, Navigation and Control of Ships Rigs and Underwater Vehicles". Marine Cybernetics AS, Trondheim, Norway.
- Guermond, J.-L., Sellier, A., 1991, "A unified unsteady lifting line theory", J.Fluid Mechanics Vol. 220, 427-451.
- Huang, Y.F., Sclavounos P.D., 1998, "Nonlinear ship motions", Journ Ship Research Vol. 42(2), 120-130.
- Janson, C.E., 1977, "Potential flow panel methods for the calculation of free-surface flows with lift", Ph.D thesis, Chalmers Univ of Technology, Goeteborg 1997.
- Kim, B., Shin, Y., 2003, "A NURBS panel method for three-dimensional radiation and diffraction problems", J Ship Research, 47(2).
- Kring, D.C., Sclavounos, P.D., 1995, "Numerical stability analysis for time-domain ship motion simulations", Journ Ship Res. 39, 321-327.
- Naito S., Isshiki S., 2005, "Effect of Bow Wings on Ship Propulsion and Motions", Appl. Mech. Rev. Vol. 58(4), 253.



- Nakos D., Sclavounos P. (1990), "On steady and unsteady ship wave patterns", *Journ. Fluid Mech.* Vol. 215, 263–288.
- Nakos D., Kring, D., Sclavounos P., 1994, "Rankine panel methods for transient free surface flows, Proc. 6th Int. Conf. Numerical Ship Hydrodynamics, Iowa City.
- Newman, N., 1977, "Marine Hydrodynamics", MIT Press.
- Ochi, M.K., 1998, "Ocean Waves. The Stochastic Approach", Cambridge University Press.
- Ohkusu, M. (Ed.), 1996, "Advances in Marine Hydrodynamics", Computational Mechanics Publications.
- Politis, G.K., 2009, "A BEM code for the calculation of flow around systems of independently moving bodies including free shear layer dynamics", Proc. Advances in Boundary Element Techniques X. Athens, Greece.
- Politis, G.K., Tsarsitalidis, V.T., 2009, "Simulating Biomimetic (Flapping Foil) Flows for Comprehension, Reverse Engineering and Design", Proc. SMP'09, Trondheim, Norway.
- Politis, G. K. and V. T. Tsarsitalidis (2010). Understanding Birds's Flight, using a 3-D BEM method and a time stepping algorithm. 4th IC-SCCE 2010. Athens, Greece.
- Politis, G.K., 2011, Application of a BEM time stepping algorithm in understanding complex unsteady propulsion hydrodynamic phenomena, Ocean Engineering 38, 699-711.
- Politis, G., Politis, K., 2012, "Biomimetic propulsion under random heaving conditions, using active pitch control", Journal of Fluids & Structures (in press).
- Rozhdestvensky K.V., Ryzhov V.A. (2003), "Aerohydrodynamics of flapping-wing propulsors", Progress Aerospace Sci. Vol. 39 585–633.
- Sclavounos P. (1987), "An unsteady lifting line theory", Journal of Eng. Mathematics Vol. 21, 201.
- Sclavounos P., Nakos, D., 1988, "Stability analysis of panel methods for free surface flows with forward speed", Proc. 17th Symp. Naval Hydrodynamics, The Hague, Netherlands.
- Sclavounos, P., Kring, D., Huang, Y., Mantzaris, D., Kim, S., Kim, Y., 1997, "A computational method as an advanced tool of ship hydrodynamic design", Trans. SNAME Vol. 105, 375-397.
- Sclavounos P.D., Huang, Y.F. 1997, "Rudder winglets on sailing yachts", Marine Technology Vol. 34(3), 211-232.
- Sclavounos P., Borgen H., 2004, "Seakeeping analysis of a high-speed monohull with a motion control bow hydrofoil", J. Ship Research Vol. 48(2), 77-117.
- Schouveiler L., Hover F.S., Triantafyllou M.S. (2005), "Performance of flapping foil propulsion", J. Fluids Struct Vol. 20, 949-959.
- Taylor, G.K, Triantafyllou, M.S, Tropea, C., 2010, "Animal Locomotion", Springer Verlag.
- Thomas B.S., Sclavounos P.D., 2007, "Optimal control theory applied to ship manoeuvring in restricted waters", J. of Engineering Mathematics Vol. 58, 301-315.
- Triantafyllou, M.S., Triantafyllou, G.S., Yue, D., 2000, "Hydro-dynamics of fishlike swimming", An. Rev. Fluid Mech. Vol. 32.
- Triantafyllou, M. S., Techet, A. H., and Hover, F.S., 2004, "Review of experimental work in biomimetic foils", IEEE J. Ocean Eng. Vol. 29, 585–594.
- Tzabiras G.D., 2004, "Resistance and Self-propulsion simulations for a Series-60, Cb=0.6 hull at model and full scale", Ship Technology Research, Vol. 51, 21-34.





Numerical Simulations of Maneuvering and Dynamic Stability of a Containership in Waves

Sungeun (Peter) Kim, ABS, sungeunkim@eagle.org

Young Jae Sung, Hyundai Heavy Industries Co. Ltd, ojae00@hhi.co.kr

ABSTRACT

A nonlinear seakeeping-maneuvering program is developed for numerical study of maneuvering and dynamic stability in regular and irregular waves. The traditional nonlinear time-domain seakeeping panel method NLOAD3D has been extended to the maneuvering problems by considering the resistance, propulsion and maneuvering force models. The maneuvering force model has been successfully calibrated and validated with captive model test data. Numerical simulations for the KCS (KRISO Containership) hull are carried out in calm water and in waves.

Keywords: seakeeping, maneuvering, resistance, propulsion, surf-riding, dynamic stability, panel method NLOAD3D

1. INTRODUCTION

The maneuvering and dynamic stability of ships in severe wave conditions have become important design issues in the maritime and shipbuilding industries. In 2011, the International Maritime Organization's (IMO) Marine Environment Protection Committee (MEPC) adopted the Energy Efficiency Design Index (EEDI) to control CO₂ emissions from international shipping. With regard to the EEDI requirements, the possibility of under-powering can be a safety issue for new ship designs. To ensure the safety of the vessels operating in adverse weather conditions, it is critical for ships to have enough propulsion power to maintain a minimum speed of advance or to have an appropriate course keeping and turning ability without excessive drift. Currently, IMO MEPC is developing guidelines for minimum propulsion power requirements to ensure safe maneuvering in adverse conditions.

Also, IMO is developing the second generation intact stability criteria addressing major dynamic failure modes of ships including surf-riding and broaching conditions in following and stern quartering seas.

These issues are very challenging topics from a hydrodynamic point of view. To consider the maneuvering and dynamic stability in waves, the traditional seakeeping and maneuvering problems need to be solved simultaneously in the time domain. Also, the resistance, propulsion and maneuvering characteristics of the hull, propeller and rudder are to be properly modelled.

In this regard, the traditional nonlinear seakeeping program NLOAD3D has been extended and developed to account for the maneuvering and dynamic stability problems in wind, waves and current. This paper presents the technical background and numerical models implemented in the program NLOAD3D. The resistance and maneuvering force models are numerically calibrated with the model test data in calm water. The wave-induced forces are calculated under the weakly nonlinear formulation considering the nonlinear hydrostatic and Froude-Krylov forces on the hull in waves. Numerical simulations of standard maneuvering tests are presented for KRISO Containership (KCS) hull in calm water and in waves. Also the capability to



simulate the surf-riding of KCS in following seas is successfully demonstrated in the extreme conditions.

2. NUMERICAL APPROACH

2.1 Theoretical Background

Traditional seakeeping analysis solves the wave-body interaction problem to simulate the six-degrees of freedom ship motions in waves. NLOAD3D is the ABS in-house nonlinear seakeeping program, which is a 3D Rankine source panel method that considers the nonlinear hydrostatic and Froude-Krylov forces on the instantaneous wetted hull surface in time domain. Recently NLOAD3D has been used and validated for the parametric roll analysis of containerships in regular and irregular waves (Hong et al., 2009 & 2011, Lee et al., 2011).

Traditional maneuvering analysis considers the 3-DOF large lateral motions of ships in calm water. A set of ordinary differential equations of motions can be represented by resistance, propulsion and maneuvering force models. The standards and criteria for ship manoeuvrability are given in IMO (2002).

For ocean-going ships operating in actual seaways, the characteristics of ship maneuvering performance will be greatly affected by the ship motions and added resistance due to wind, current and waves. To investigate the maneuvering performance in waves, experimental studies have been conducted by many researchers for different ship types including free sailing tests (Hirano et al., 1980, Ueno et al., 2003, Yasukawa, 2006) and captive model tests (Ueno et al., 2000, Yasukawa & Adman, 2006, Lee et al., 2009).

The numerical simulation of maneuvering in waves requires a complete integration and consolidation of traditional seakeeping and maneuvering analysis methods. Recently, the Large Amplitude Motion Program (LAMP)

was extended for ship maneuvering simulation in waves (Yen et al., 2010). In their study, the hull, propeller and rudder forces were considered in addition to the nonlinear wave-body hydrodynamic force acting on the hull.

In this paper, a similar approach has been applied to extend the weakly-nonlinear seakeeping program NLOAD3D for numerical simulation of ship maneuvering in wind, current and waves. Figure 1 shows the typical numerical force models implemented in the NLOAD3D program. Further details of the force models will be described in the following subsections.

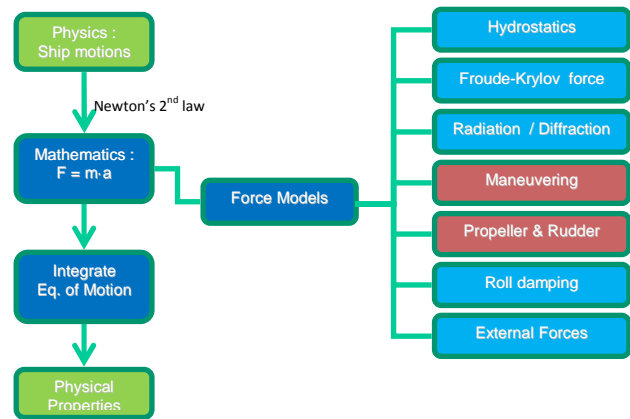


Figure 1: Numerical force model in NLOAD3D.

Equation (1) shows the equations of motion for ship maneuvering simulation, which are typically being used in the component based maneuvering force model. The component based model considers the effects of hull, rudder and propeller in a separate manner.

$$\begin{aligned} m(\dot{u} - vr) &= X_H + X_R + X_P \\ m(\dot{v} + ur) &= Y_H + Y_R \\ I_{ZZ}\dot{r} &= N_H + N_R \end{aligned} \quad (1)$$

where (u, v) is the ship-fixed surge and sway velocity and r is the yaw rate. X_H, X_R, X_P denote the ship-fixed surge force due to hull, rudder and propeller, respectively.

2.2 Maneuvering Force Model

The maneuvering forces and moments on the hull in the horizontal plane must be accurately

modelled for the realistic simulations of ship maneuvering. The potential-flow calculation of the pressure forces on the hull is not complete and must be supplemented by viscous damping coefficients.

The hull forces and moments may come from captive model tests or be estimated from an existing set of hydrodynamic derivatives. Below is a typical set of hydrodynamic derivatives for systems-based methods which are implemented in NLOAD3D.

$$\begin{aligned} X'_H &= X'_{vv}v'^2 + X'_{vr}v'r' + X'_{rr}r'^2 \\ Y'_H &= Y'_v v' + Y'_r r' + Y'_{|v|} v' |v'| + Y'_{|r|} r' |r'| + Y'_{vvr} v'^2 r' + Y'_{vrr} v' r'^2 \\ N'_H &= N'_v v' + N'_r r' + N'_{|v|} v' |v'| + N'_{|r|} r' |r'| \\ &+ N'_{vvr} v'^2 r' + N'_{vrr} v' r'^2 \end{aligned} \quad (2)$$

The standard maneuvering non-dimensional variables are defined by $r' = rLU$, $v' = -\sin(\beta)$, $X' = X/0.5\rho L^2 U^2$, $Y' = Y/0.5\rho L^2 U^2$, and $N' = N/0.5\rho L^3 U^2$, where ρ is the water density, L is the reference ship length and U is the total velocity defined as $\sqrt{u^2 + v^2}$. Also, (X, Y, N) are the dimensional ship-fixed surge, sway forces and yaw moment.

2.3 Rudder Force Model

The rudder force model in NLOAD3D considers the rudder size and location, the deflection limit, and the deflection rate. It is recommended that static rudder tests be conducted with and without the propeller rotating at the self-propulsion rate while varying the rudder angle. The measured lift and drag forces on the rudder may be expressed by the following equations:

$$\begin{aligned} X_R &= C_D * 0.5\rho U_R^2 A_R \\ Y_R &= C_L * 0.5\rho U_R^2 A_R \\ N_R &= -x_R Y_R \end{aligned} \quad (3)$$

where A_R is rudder area and U_R is the rudder inflow velocity defined as $\sqrt{u_R^2 + v_R^2}$ and x_R is

the distance from the ship center of gravity to the center of rudder force. The lift and drag forces on rudder without rotating propeller need to be adjusted by the inflow velocity increment Δu_R so that the rudder forces match the experimental data with propeller rotating at the self-propulsion point. When experimental data are not available, the lift and drag coefficients C_L and C_D may be estimated from the empirical formula (Fujii & Tuda, 1961).

Also the hull and propeller may have a “straightening” effect on the rudder inflow velocity, so when the ship has non-zero sway velocity and yaw rate, the components of relative inflow to the rudder caused by these motions are reduced. This rudder cross flow coefficients may be estimated using an empirical formula based on the block coefficient of the hull (ENDEAVOR 2005):

$$\gamma \approx 1.1633 - 1.9826C_B + 1.3902C_B^2 \quad (4)$$

where γ is the cross-flow coefficient and C_B is the block coefficient.

2.4 Propeller Force Model

The propeller force model can be given by the following equations:

$$X_p = (1-t)\rho n^2 D_p^4 K_T \quad (5)$$

$$K_T = a_0 + a_1 J_p + a_2 J_p^2$$

where K_T is the propeller thrust coefficient and (a_0, a_1, a_2) are determined from the propeller open-water tests or empirical formula. J_p is the propeller advance ratio defined by $J_p = (1 - \omega_p)u / (nD_p)$, where ω_p is the effective wake fraction, u is the ship-fixed surge velocity, n is the propeller rotation rate, and D_p is the propeller diameter.

The propeller operating point can be set at a constant rotation rate. Also the propeller operating point may be set at constant delivered torque or constant delivered power to the



propeller, which will require use of the K_Q curve of the propeller. In that case, since the propeller rotation rate is unknown, the advance coefficient, J , is determined by finding the intersection of the K_Q versus J curve for constant torque.

2.5 Wind and Current Model

A wind force model is considered in NLOAD3D to calculate the forces acting on the ship due to the steady wind blowing over the emerged portion of the hull and the superstructure. Isherwood (1973) proposed a regression model that derives empirical wind forces from several different test establishments on models covering a wide range of merchant ships. A steady, uniform current model is also considered in NLOAD3D in terms of body boundary condition of wave-body interaction problem and also considered in calculating the inflow to the rudder and other appendage force model. However, the wind and current effects are not considered in this study.

3. CAPTIVE MODEL TEST

Typical systems-based maneuvering simulations for calm water solve a set of ordinary differential equations in which maneuvering forces and moments are represented by the hydrodynamic derivatives. These hydrodynamic derivatives can be generated from the captive model tests such as a Planar Motion Mechanism (PMM) test or rotating arm test.

Under a Joint Development Project between ABS and Hyundai Heavy Industries (HHI) in 2011, the PMM tests for a KRISO Containership (KCS) model with 1/40 scale were conducted in calm water and in waves. The maneuvering characteristics of the KCS hull have been studied in SIMMAN 2008. The principal dimensions of KCS are listed in Table 1.

Table 1: Principal dimensions of KCS

	Units	Full Scale	Model Scale
L_{pp}	[m]	230	5.75
B	[m]	32.2	0.805
T	[m]	10.8	0.27
Disp	[m ³]	52030	0.8130
VCG	[m]	14.34	0.36
GM	[m]	0.6	0.015
Speed	knots	24	3.79
Dp	[m]	7.9	0.198
$\dot{\delta}_{Rudder}$	[°/s]	2.32	14.7

Further details on the model setup and test conditions are presented by Sung et. al (2012). The measured maneuvering forces and moments will be used for the numerical tuning of NLOAD3D maneuvering force model, as described in the following section.

4. NUMERICAL TUNINGS

It is important to note that hydrodynamic derivatives from captive model tests or typical system-based methods cannot be used directly in NLOAD3D because the native potential flow calculation contributes some maneuvering forces and moments as well. These hydrodynamic forces and moments must be subtracted out to avoid double counting.

Appendage models, such as rudder and propeller, are also important for the numerical tuning process. Many captive model tests include the appendages and have propellers operating at the model-scale or full-scale self-propulsion point. If the maneuvering forces come from the model tests where rudders and rotating propellers are included, the appropriate appendage models are to be included in the numerical model as well. A numerical tuning procedure for the resistance and maneuvering force models are described in the following subsections.

4.1 Hull Resistance Tuning

First of all, the calm water resistance of NLOAD3D is to be calibrated with experimental data, as follows:

1. Estimate the resistance curve of bare hull from the resistance model tests or CFD calculations.
2. Calculate the resistance curve from a series of unpropelled, bare-hull, constant speed simulations in calm water over a range of ship speeds. In these simulations, the ship is free to heave and pitch so that the steady sinkage and trim is included. Also the hull skin friction and form drag is to be accounted for in the total resistance calculation.
3. Calibrate the calculated resistance curve with experimental data using least-square regression and introducing supplemental damping terms.

Figure 2 shows the resistance curves of the KCS hull in model scale. As seen in the figure, the original calculation before the calibration (blue line) is over-predicting the resistance compared to experimental data. After the calibration, however, the calculated resistance curve (red line) matches the experimental data very well. The calibrated resistance curve will be used to propeller speed tuning and maneuvering simulations. This resistance tuning procedure is fully automated in the program NLOAD3D.

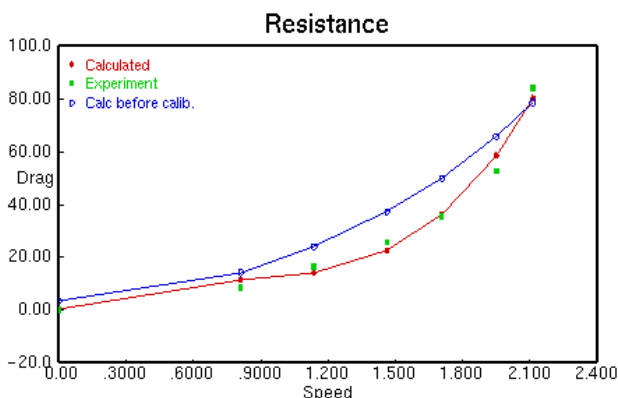


Figure 2: Total resistance curves of KCS

4.2 Maneuvering Force Tuning

Next, the maneuvering force model of NLOAD3D is to be calibrated with the experimental data, as follows.

1. Estimate the maneuvering forces on the hull from the captive model tests or CFD calculations. The maneuvering forces are given by surge force, sway force, and yaw moments as functions of sway velocity and yaw rate.
2. Calculate the maneuvering forces on the hull by running a series of simulations where the hull is forced to move at various combinations of yaw rates and drift angles at a constant total velocity.
3. Calibrate the hydrodynamic derivatives using least-square regression so that the resulting maneuvering forces match experimental data

Figures 3-5 show the calibrated maneuvering forces on the KCS hull compared with the measured data from captive model tests. The non-dimensional surge force X' , sway force Y' , and yaw moment N' are plotted against the drift angle β from and yaw rate r' , as defined in Section 2.

The numerical tuning of hydrodynamic derivatives was carried out for 125 captive model test cases defined by drift angles from -24° to 24° for yaw rate $r'=0$ or and drift angle from -14° to 14° for yaw rates $r' = -0.6$ to 0.6 . This maneuvering force tuning procedure is fully automated in NLOAD3D.

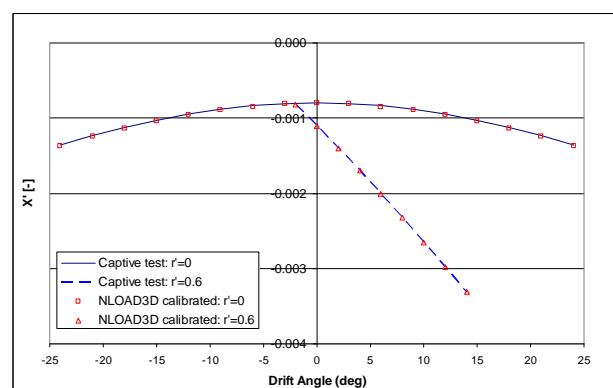


Figure 3: Calibration of surge force on KCS

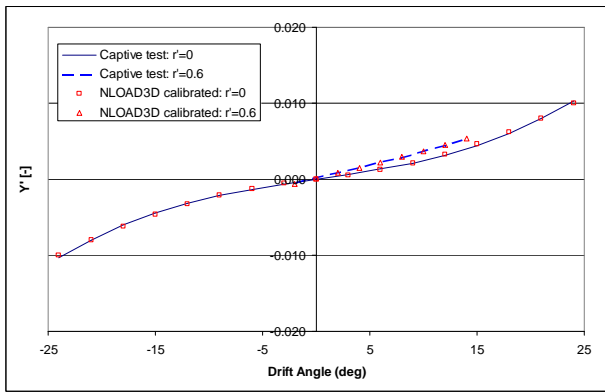


Figure 4: Calibration of sway force on KCS.

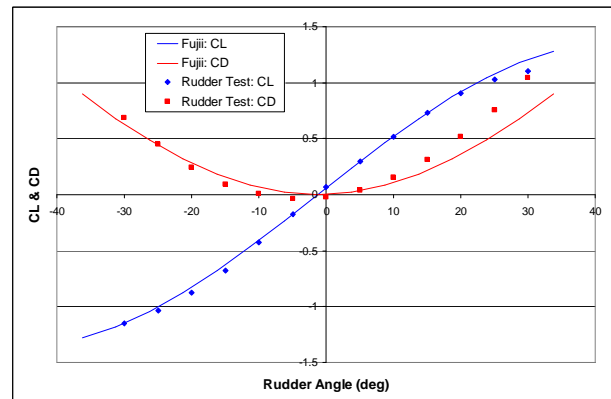


Figure 6: C_L and C_D of the rudder

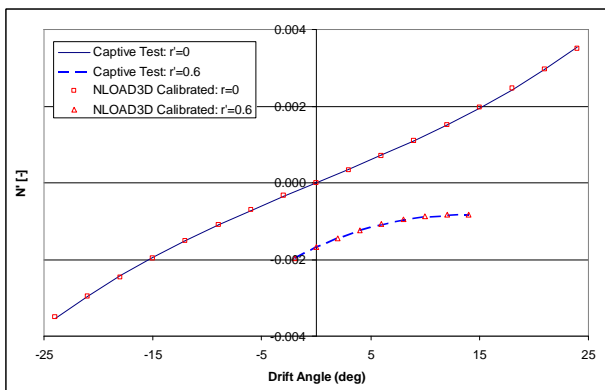


Figure 5: Calibration of yaw moment on KCS.

5. NUMERICAL SIMULATIONS

In this study, all the simulations are carried out for KCS at the model scale of 40.

5.1 Propeller and Rudder Force Models

For the propeller force model, the open water characteristics of an existing propeller are used as follows:

$$K_T = 0.5251 - 0.4816 J_p - 0.0213 J_p^2 \quad (6)$$

$$K_Q = 0.7311 - 0.5850 J_p - 0.0456 J_p^2$$

For the rudder force model, the lift and drag coefficients C_L and C_D are estimated from the Fujii's empirical formula (Fujii & Tuda, 1961). The actual lift and drag forces on the rudder were measured from the captive model tests of the KCS and compared with the Fujii's formula in Figure 6.

5.2 Propeller Speeds in Calm Water

The propeller speed can be determined from the self-propulsion simulation in calm water. A PID (proportional-integral-derivative) control with propeller gains is used in NLOAD3D to find the self-propulsion point. As a result, the propeller speed of 12.69 rps was found at the design speed of 1.952m/s ($F_n=0.26$).

5.3 Speed Reduction in Waves

With a constant engine power or propeller speed, a ship experiences an involuntary speed reduction in waves due to the added resistance. The added resistance can be considered by including the quadratic terms in Bernoulli's equation and the second-order waterline integral at the waterline (Zhang and et. al., 2009).

Figure 7 shows the time histories of ship speed in regular waves at the constant propeller speed of 12.69 rps in head sea condition. The wave length of $\lambda/L_{pp}=1$ and wave heights of $H/\lambda = 0.017, 0.035$ were considered. In the figure, the speed reduction in waves is clearly shown, in proportion to the square of wave heights, as expected. Figure 8 shows the time histories of ship speed in irregular waves at the constant propeller speed of 12.69 rps in head sea condition. The long-crested waves of $H_s=0.2, 0.3m$ and $T_z=3.3s$ with Bretschneider wave spectrum were considered.

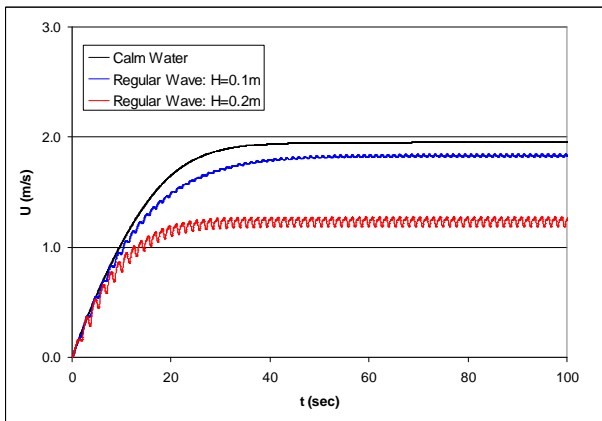


Figure 7: Time history of ship speed in regular head waves at the constant propeller speed of 12.69 rps.

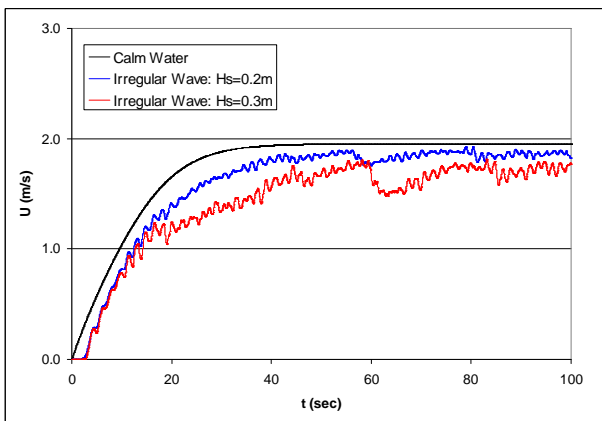


Figure 8: Time history of ship speeds in irregular head waves at the constant propeller speed of 12.69 rps.

5.4 Maneuvering Simulations in Waves

For a fair comparison of maneuvering simulations in calm water and in waves, the approach speed may be maintained at the same design speed by tuning the propeller speed. The required propeller speed can be determined from the self-propulsion point to maintain the design speed in waves. Figure 9 shows the time histories of ship speeds in the regular head waves of $H=0.1\text{m}$ & 0.2m and $\omega=3.26\text{ rad/s}$ (model scale) at the adjusted propeller speeds of 13.72 rps and 16.3 rps, respectively.

Maneuvering simulations of standard turning were carried out in calm water and in waves. Figure 10 shows the turning trajectories of the

KCS with 35 deg rudder deflection in calm water (blue line) and in regular head waves of $H=0.1\text{m}$ (red line) and 0.2m (green line). It can be seen that the turning circle increases and drifts backwards as the wave height increases in a head sea condition, as expected. The drifting behaviour in waves seems to be highly nonlinear depending on the wave amplitudes.

Figure 11 shows the time histories of ship speeds in the irregular head waves of $H_s=0.2\text{m}$ & $T_z=1.37\text{s}$ and $H_s=0.3\text{m}$ & $T_z=1.37\text{s}$ at the adjusted propeller speeds of 13.75 rps and 14.79 rps, respectively. Figure 12 shows the turning trajectories of the KCS with 35 deg rudder deflection in calm water (blue) and in irregular head waves of $H_s=0.2\text{m}$ (red) and 0.3m (green). It is interesting to note that the ship is turning to starboard side and the turning circles are drifting to port side.

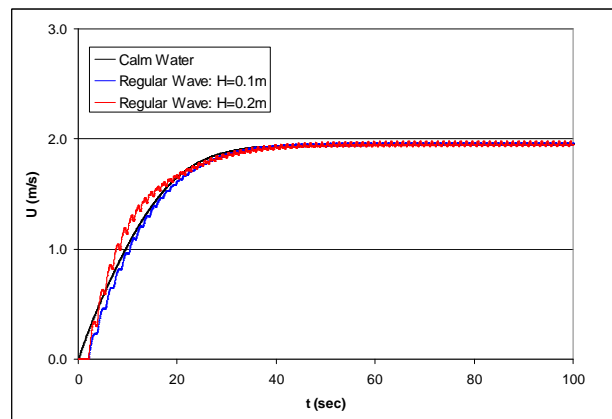


Figure 9: Time history of ship speeds in regular head waves with adjusted propeller speeds.

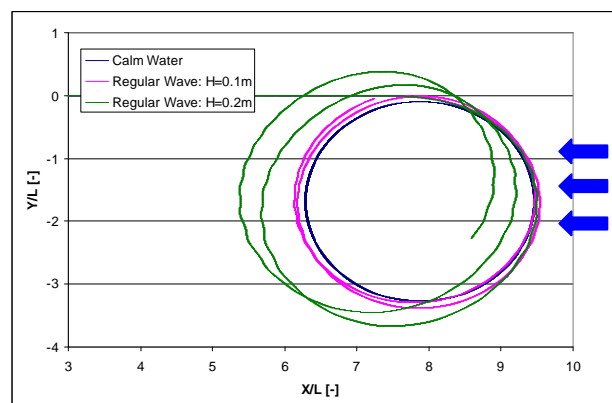


Figure 10: Turning trajectories of KCS at 35deg rudder deflection in regular head waves.

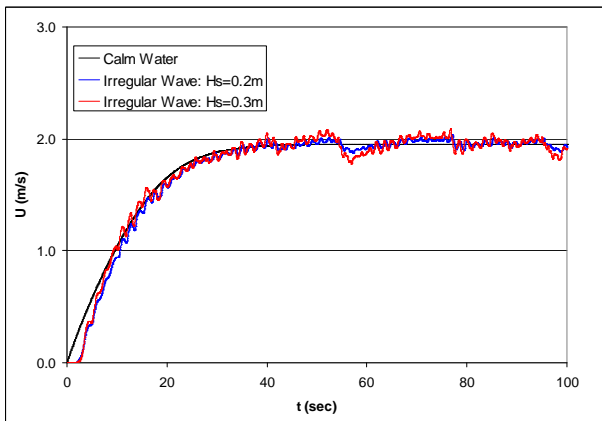


Figure 11: Time history of ship speeds in irregular head waves with adjusted constant propeller speeds.

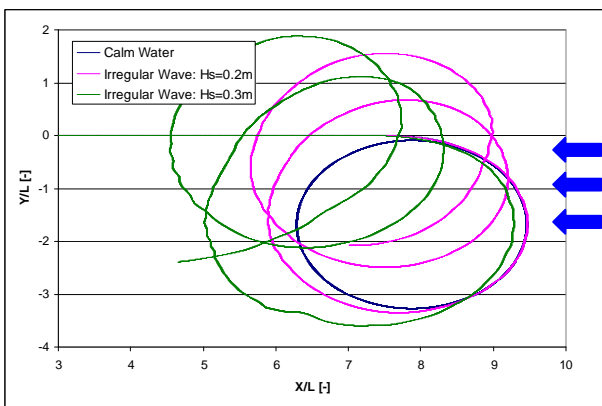


Figure 12: Turning trajectories of the KCS at 35 deg rudder deflection in irregular head waves.

5.5 Surf-Riding in Following Seas

The simulations of surf-riding in following seas were carried out based on the propulsion and maneuvering model of the KCS described in the previous sections.

According to the draft Level 1 criteria of surf-riding (IMO SLF 53/3/8), the critical Froude number of 0.3 is proposed as a threshold for surf-riding of ships in following seas. Table 2 shows the regular wave conditions considered in this study. The ship speeds of $F_n=0.26$ (design speed), $F_n=0.31$ and 0.34 and the wave lengths of $\lambda/L_{pp}=1.0$ and 0.8 in following seas were considered.

Table 2: Regular wave conditions for simulation of surf-riding (model scale)

	RW1	RW2	RW3	RW4	RW5	RW6
U(m/s)	1.95	2.32	2.58	1.95	2.32	2.58
Fn	0.26	0.31	0.34	0.26	0.31	0.34
Heading	0.00	0.00	0.00	0.00	0.00	0.00
λ/L_{pp}	1.00	1.00	1.00	0.80	0.80	0.80
H (m)	0.2	0.2	0.2	0.2	0.2	0.2
H/ λ	0.03	0.03	0.03	0.04	0.04	0.04
Vp(m/s)	3.0	3.0	3.0	2.68	2.68	2.68
U/Vp	0.65	0.77	0.86	0.73	0.86	0.96

The program NLOAD3D was used for the simulation of surf-riding, considering the surge, heave and pitch motions only. The constant propeller speeds of 12.5, 16.67, and 20.05 rps were used, which were determined from the self-propulsion points in calm water at the ship speeds of $F_n=0.26$, 0.31 , and 0.34 , respectively.

Figure 13 shows the time histories of ship speed in following seas with a wavelength of $\lambda/L_{pp}=1.0$. For the case of $F_n=0.34$ (green line), the ship is being accelerated from the self-propulsion speed of 2.58 m/s to wave phase velocity of 3.0 m/s, which is a typical phenomena of “surf-riding” of the ship in following seas.

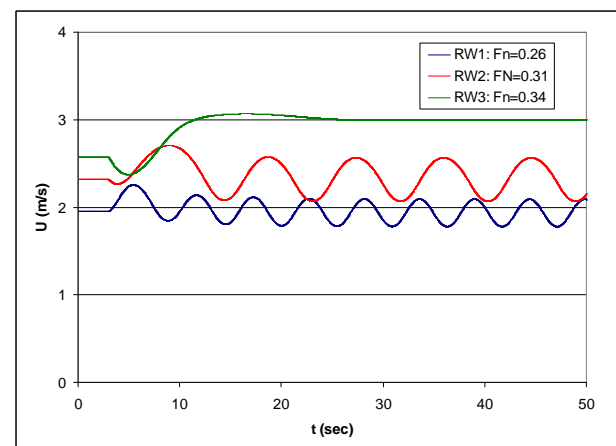


Figure 13: Time histories of ship speed of the KCS in following seas with wavelength of $\lambda/L_{pp}=1.0$.

Figure 14 shows the time histories of nonlinear hydrostatic and Froud-Krylov forces on the hull. It is interesting to note that, for the ship

speed of $F_n=0.34$, the nonlinear hydrostatic and Froud-Krylov force on the hull becomes steady in a positive direction, which seems to be a main driving force of the surf-riding. Figure 15 shows the animation snapshot of the KCS surf-riding in following seas at $F_n=0.34$. The ship and the waves are in the steady surf-riding equilibrium condition with the wave crest located near the stern area.

Figure 16 shows the time histories of ship speed in following seas with a wavelength of $\lambda/L_{pp}=0.8$. The figure shows that, for the regular waves with a wavelength less than ship length, the surf-riding is still occurring at the ship speed of $F_n=0.34$ (green line).

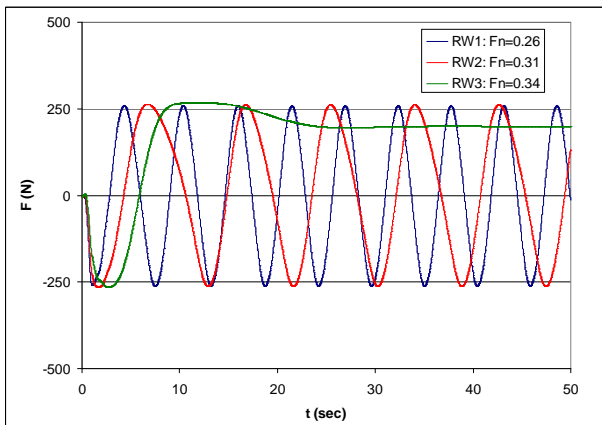


Figure 14: Time histories of nonlinear hydrostatic and Froud-Krylov force on KCS in following seas with wavelength of $\lambda/L_{pp}=1.0$.

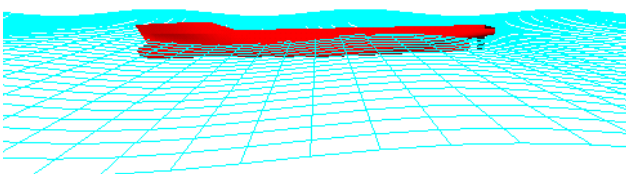


Figure 15: Snapshot of KCS surf-riding in following seas with a wavelength of $\lambda/L_{pp}=1.0$ at $F_n=0.34$.

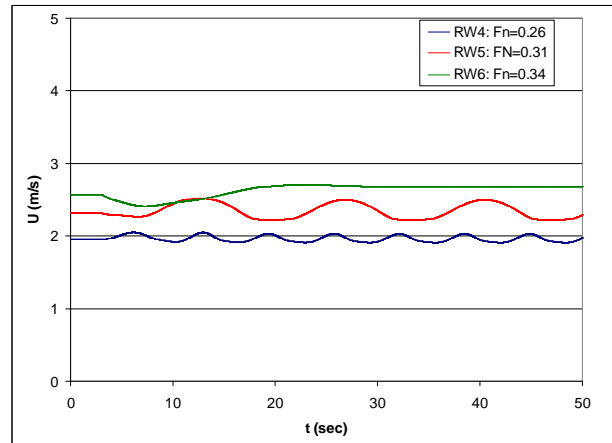


Figure 16: Time histories of ship speed of KCS in following seas with a wavelength of $\lambda/L_{pp}=0.8$.

6. CONCLUSIONS

In this study, the nonlinear seakeeping-maneuvering program NLOAD3D is developed for numerical study of maneuvering and dynamic stability in waves. The numerical models for resistance, propulsion and maneuvering forces were presented and successfully calibrated with the captive model test data. The numerical simulations for the KCS hull were carried out as follows:

- 1) For a head sea condition, the speed reductions of the KCS hull were calculated in regular and irregular waves
- 2) For a head sea condition, the turning simulation of the KCS hull were carried out in regular waves and irregular waves
- 3) For a following sea condition, the surf-riding simulation of the KCS hull were carried out in regular waves

From the current study, the NLOAD3D capabilities for the numerical simulation of maneuvering and dynamic stability in waves were successfully demonstrated. As future work, the wind and current effects on the maneuvering and dynamic stability will be considered for more realistic analysis. Also further validation and numerical study will be



carried out to investigate the nonlinear behaviour of surf-riding and broaching of the ships in following and stern-quartering seas.

7. ACKNOWLEDGMENTS

This work was carried out under the joint development project between ABS and HHI. The authors wish to acknowledge the full support from both companies.

8. REFERENCES

- ENDEAVOR, 2005, "Maneuvering Code Documentation", Department of Ocean and Resources Engineering, University of Hawaii at Manoa.
- Fujii, H. and Tuda, T., 1961, "Experimental Research on Rudder Performance (2)" (in Japanese), Journal of the Society of Naval Architects of Japan, No.110, pp.31-42.
- Hirano, M., Takashina, J., Takaishi Y. and Saruta, T., 1980, "Ship Turning Trajectory in Regular Waves", Transactions of the West-Japan Society of Naval Architects, No.40, pp.17-31
- Hong, S.Y., Yu, H.C., Kim, S. and Sung, H.G., 2009, "Investigation of Parametric Roll of a Containership in Irregular Waves by Numerical Simulation", 10th International Conference on Stability of Ships and Ocean Vehicles.
- Hong, S.Y., Nam, B.W., Yu, H.C., and Kim, S., 2011, "Investigation of Susceptibility of Parametric Roll in Regular and Irregular Waves", Proceedings of 12th International Ship Stability Workshop, Washington D.C.
- ITTC, 2008, "Manoeuvring and Course Keeping in Waves", Proceedings of 25th ITTC, Vol. I, pp. 171-175
- IMO MSC 76/23, 2002, "Standards for Ship Manoeuvrability", Report of the maritime Safety Committee on Its Seventy-Sixth Sessions-Annex 6
- IMO MSC 267(85), 2008, "Adoption of the International Code on Intact Stability", 2008 IS Code
- Lee, S.K., Hwang, S.H., Yun S.W., Rhee, K.P. and Sung, W.J., 2009 "An Experimental Study of a Ship Manoeuvrability in Regular Waves", Proceedings of MARSIM 2009, Panama City, Panama.
- Lee, H.H., Choi, J.H., Yang, J.H. and Kim, S., 2011, "Model Tests and Numerical Analyses for Parametric Roll Assessment of a Large Container Carrier", Proceedings of the 21st International Offshore and Polar Engineering Conference, ISOPE, Maui, Hawaii.
- Stern, F. and Agdrup, K. (editors), 2009, "Proceedings of the Workshop on Verification and Validation of Ship Manoeuvring Simulation Methods, SIMMAN 2008", FORCE Technology, September 2009, Lyngby, Denmark
- Sung, Y-J., Lee H., Lee, T., and Kim, S., 2012, "Captive Model Test and Numerical Simulation on the Manoeuvring Forces in Waves", Proceedings of the 11th International Conference on the Stability of Ships and Ocean Vehicles, Athens, Greece.
- Ueno, M., Nimura, T., Miyazaki, H., and Nonaka, K., 2000, "Steady Wave Forces and Moment Acting on Ships in Manoeuvring Motion in Short Waves" (in Japanese), Journal of the Society of Naval Architects of Japan, No.188, pp.163~172.
- Ueno, M., Nimura, T. and Miyazaki, H., 2003, "Experimental Study on Manoeuvring Motion of a Ship in Waves", Proceedings of MARSIM 2003, Kanazawa, Japan
- Yasukawa, H., 2006, "Simulations of Ship



Maneuvering in Waves (1st report: turning motion)” (in Japanese), Journal of the Society of Naval Architects and Ocean Engineers, Vol.4, pp.127-136.

Yasukawa, H. and Adnan, F.A., 2006, “Experimental Study on Wave-Induced Motions and Steady Drift Forces of an Oblique Moving Ship” (in Japanese), Journal of the Society of Naval Architects and Ocean Engineers of Japan, Vol.3, pp.133-138.

Yen, T-G., Zhang S., Weems, K., and Lin, W-M., 2010, “Development and Validation of Numerical Simulations for Ship Maneuvering in Calm Water and in Waves”, Proceedings of the 28th Symposium on Naval Hydrodynamics, Pasadena, California.

Zhang, S., Weems, K., and Lin, W-M., 2009, “Investigation of the Horizontal Drifting Effects on Ships with Forward Speed”, Proceedings of the ASME 28th International Conference on Ocean Offshore and Arctic Engineering, Honolulu, Hawaii





Model Characteristics and Validation Approach for a Simulation Tool Supporting Direct Stability Assessment

William F. Belknap, *David Taylor Model Basin (NSWCCD)*, william.belknap@navy.mil

Arthur M. Reed, *David Taylor Model Basin (NSWCCD)*, arthur.reed@navy.mil

Michael J. Hughes, *David Taylor Model Basin (NSWCCD)*, michael.j.hughes@navy.mil

ABSTRACT

The present paper asserts which aspects of the physical problem are essential to achieving accurate simulations in extreme wave conditions and therefore must be modeled well in a computationally efficient manner. Chief among these aspects are body-exact hydrostatic, Froude-Krylov, radiation and diffraction forces, nonlinear physics-based hull lift and cross-flow drag, bilge keel, propeller, and rudder forces. Options for numerical models are then presented that are anticipated as providing the best chance of meeting the competing requirements of accuracy and computational efficiency.

Also addressed in this paper is a recommended approach for validation and accreditation of direct stability assessment simulation tools. These components consist of definition of Specific Intended Uses and associated acceptance criteria, qualitative and quantitative validation activities, and characterization of uncertainty.

Keywords:

Direct assessment, simulation, large amplitude motions, nonlinear dynamics, body-exact hydrodynamics, bilge-keel forces, maneuvering in waves, validation

1. INTRODUCTION

The modernization of intact ship stability criteria includes the notion of “direct assessment,” which is the use of simulation tools to quantitatively investigate the probabilities associated with a given vulnerability. The direct assessment approach is only brought to bear when a vulnerability is expected, which means the intent of the assessment is to provide a significantly higher level of insight to the dynamic stability risk than is available through empirical and heuristic means.

Peters, et al. (2012) provide a comprehensive look at how direct assessment applies simulation tools to the problem, including a summary of methods for modeling ship motions. This includes not only 6-Degree-of-Freedom (6-DoF) models intended to

simulate the fully coupled ship motions problem, but also reduced-DoF models that target specific dynamic stability failures. Additionally, the requirement for validation of the simulation tools is discussed.

But while the drive toward stability criteria based on direct assessment is built upon the notion that simulation tools will be validated and accredited for this purpose, the development of the simulation tools that are able to provide sufficiently accurate results in a timely manner is still an area of research. Similarly, the means of validating a given model is also an area of research and development, given the significant challenges involved with the nonlinearity of the dynamics and rarity of the extreme motions.



Perhaps the most difficult subset of the direct assessment simulation options is the full 6-DoF maneuvering-in-waves simulation. This is the simulation approach that is required when the precise failure mechanism is not known a priori, or when a reduced order model has not been validated for particular vulnerability. But while the task of simulating 6-DoF maneuvering-in-waves ship motions can be considered difficult, it is the requirement to do so in a computationally efficient manner that presently leaves these simulation tools in the realm of research and development. The requirement for computational efficiency arises from the need to directly assess ship motions for a wide variety of environmental conditions and for several ship speeds and relative wave headings. Depending on the number of conditions to be simulated and the quantity of simulated data required for each condition (extrapolation methods are needed to ultimately provide failure probabilities – see Peters, et al. (2012) and Belenky & Campbell (2012) for further discussion), “computational efficiency” may mean faster than real time to on the order of 10 to 100 times slower than real time. Such a requirement rules out the use of 3D unsteady

RANS and nonlinear potential flow approaches.

The present paper focuses on the problem of developing 6-DoF maneuvering-in-waves simulation tools that are suitable for use within the direct assessment criteria approach. Following a description of the physical problem to be modeled, arguments are made for qualities of numerical models that capture the important physics in a computationally efficient manner. Also discussed are requirements of and solutions to the problem of validating these simulation tools.

2. PHYSICAL PROBLEM TO BE MODELED

The creation and validation of a simulation tool that supports direct assessment of stability criteria must start from a full accounting of the physical phenomena to be modeled by the tool. The resulting decomposition of this 6-DoF maneuvering-in-waves problem is illustrated in Figure 1 and discussed in the following sub-sections.

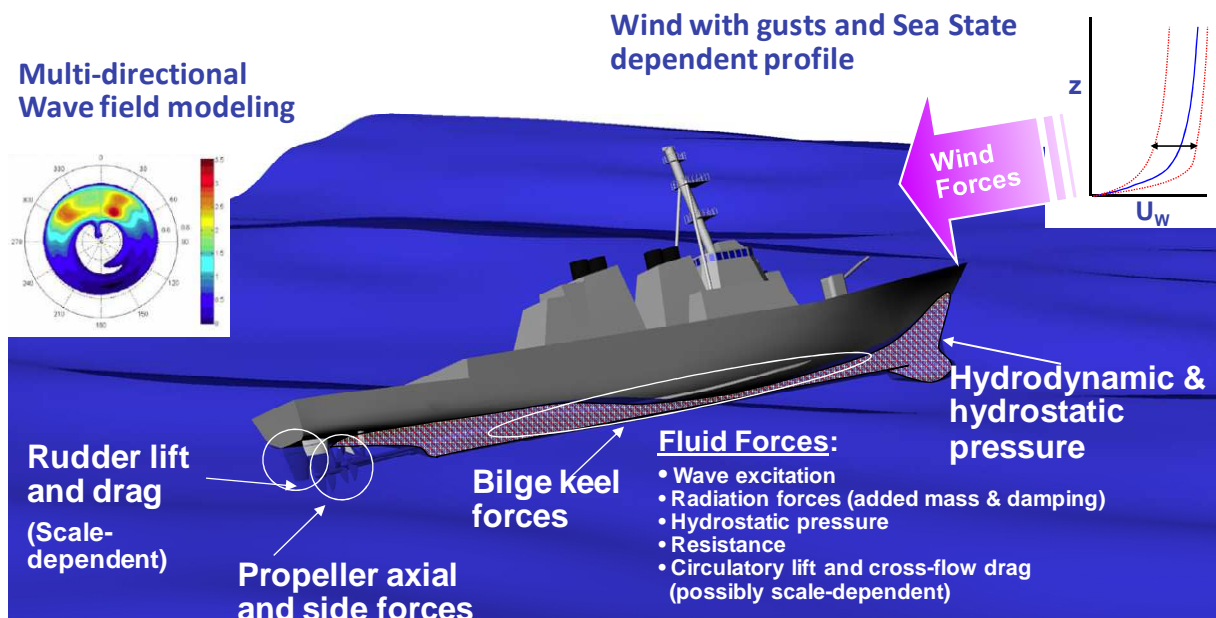


Figure 1: Illustration of the physical problem to be simulated.

2.1 Ship Control Condition

Computational tools that support direct assessment stability criteria are simulating a ship motion problem that is different from a traditional seakeeping problem. The traditional seakeeping problem is to obtain the 6-DoF motions about a mean speed and heading of interest. In that sense, the mean speed and heading are considered known. In contrast to this, dynamic stability simulation tools are solving the “maneuvering-in-waves” problem. This means that the ship is allowed to take whatever course and speed the forces acting upon the vessel dictate. To make this a meaningful problem then, the ship control condition is self-propelled and self-steered in the same manner as the real ship. This requires that the simulation tool model the physics of the propeller and rudder (or waterjet, if applicable) based on the propeller RPM and rudder deflection. The propeller RPM and rudder deflection are computed as part of the simulation and controlled in the same manner as the ship which often means constant RPM, torque, or power for the propeller and an autopilot set to a target heading for the rudder.

2.2 Environment

The ambient environment providing the excitation consists of a multi-directional irregular wave system and coupled wind field. The ocean wave environment can have wind-driven waves that primarily follow the direction of the wind and swell waves that are related to past or distant disturbances, often at a different heading. Furthermore, there will be spreading of energy about the primary direction of each system.

Coupling of the waves with the wind system occurs through the energy transfer of wind to waves and the local effects of the waves on the wind boundary layer profile. While the wave systems are generally considered stationary for the purpose of dynamic stability risk assessments (e.g., wind energy transfer to waves considered as only enough to replace energy lost due to wave breaking), the effect of steep waves on the local

wind field can affect the forcing on the vessel. Chang, et al. (1971) showed experimentally that separation can occur behind the crests of steep waves, leading to a shadowing effect (see Figure 2). Fullerton, et al. (2012) provides a more comprehensive review of the effects of steep waves on local wind profiles.

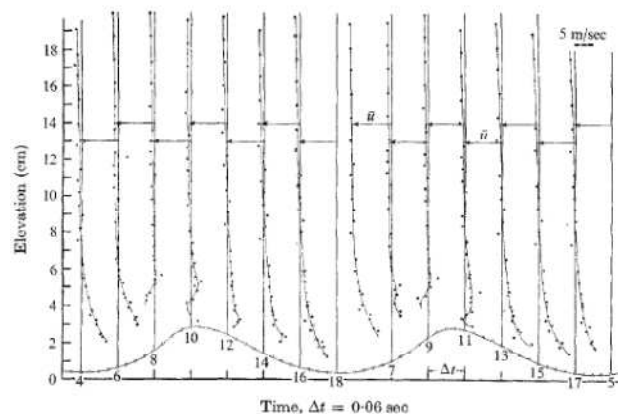


Figure 2: Wind velocity profiles in a steep wave field (wind blowing right to left) [Chang, et al. (1971)]

Other qualities of the ocean environment that need to be considered are the rates of occurrence of large waves and the nonlinearity of the wave pressures and kinematics. Non-steep wave spectra (decaying seas, which have longer modal periods relative to the significant wave height) generally behave linearly and have wave elevations that are normally distributed. However, for the large steep waves in which dynamic stability vulnerabilities are more likely to occur, the statistics of extrema can be non-Gaussian and the wave kinematics and pressures can significantly deviate from linear theory (see Gudmestad, 1993, and Stansberg, et al., 2008).

2.3 Forces

The decomposition of the forces within the physical problem is most easily described from the typical seakeeping and maneuvering points of view. In fact, the aspects of the physical problem that need to be modeled are the same as those required of the seakeeping problem and the maneuvering problem, but with a range



of coupling. However, one aspect that is unique to the physics of the dynamic stability simulation problem is the degree to which nonlinearity is prevalent throughout the constituent forces. Large amplitude motions and steep, large amplitude waves lead to significant changes in the portions of the hull that are wet. For non-wall-sided ships or ships with shallow sections or very low freeboard, the hydrostatic and hydrodynamic forces can deviate significantly from the linear predictions based on the mean wetted hull.

As listed in Figure 1, the forces that must be considered in the dynamic stability simulation problem are:

- Hydrostatic pressure
- Wave excitation forces
 - Diffraction
 - Froude-Krylov
- Radiation force
- Resistance
- Circulatory lift and cross-flow drag on the hull
- Appendage forces
 - Bilge keel
 - Propeller
 - Rudder
- Wind force

The hydrostatic and Froude-Krylov pressures have long been recognized to provide a strong nonlinear influence (see de Kat & Paulling (1989), for example), particularly from the perspective of geometric nonlinearity. Large body motion and large, steep waves lead to significant changes in the waterplane area and center of buoyancy. This has the effect of changing the stiffness in heave, roll, and pitch.

Beyond the hydrostatic and Froude Krylov forces, the remainder of the ideal flow forces is the hydrodynamic disturbance force. This is composed of the diffraction force (excitation due to wave scattering) and radiation force (added mass and wave-making damping). In the conditions relevant to the dynamic stability problem (large motions and steep, large

waves), these forces also exhibit significant nonlinearity to the changes in the wetted portion of the hull. To demonstrate this point, a numerical study was performed for forced motion conditions for a ship in calm water and in waves using numerical models employing varying levels of nonlinearity. Because the prescribed conditions ranged from small-to-large amplitude motions or small-to-large amplitude waves, it was possible to determine the influence of nonlinearity on the various force components. This numerical study is described in full by Telste and Belknap (2008) and summarized by Belknap & Telste (2008) and Reed (2009).

Among the key results, the numerical experiment showed for the pure radiation problem (forced oscillation in calm water) that those simulation approaches that included the geometric nonlinearity in the disturbance force (in addition to the hydrostatic and Froude Krylov force) produced total forces with nonlinear characteristics in the opposite direction as those that included geometric nonlinearity only in the hydrostatic and Froude Krylov force (i.e., “blended method” codes). This is shown in Figure 3, where the completely body-nonlinear approaches are codes NF, L4, and NS. The blended method codes are A2, FD, and L3 (A1 and L1 are completely body-linear codes).

Another part of the numerical experiment showed the importance of the nonlinearity of the hydrodynamic disturbance force in the context of the more realistic problem of large amplitude motion in waves. The test case examined prescribed heave and roll in a steep, large beam sea regular wave ($H/\lambda = 1/10$, $\lambda/L = 1.0$). The motion was prescribed such that relative motion between the body and the free surface was minimized, with the ship essentially contouring the wave. This condition is depicted in

Figure 4. The total ship-fixed vertical force for this condition is shown in Figure 5 and its component forces in Figure 6.

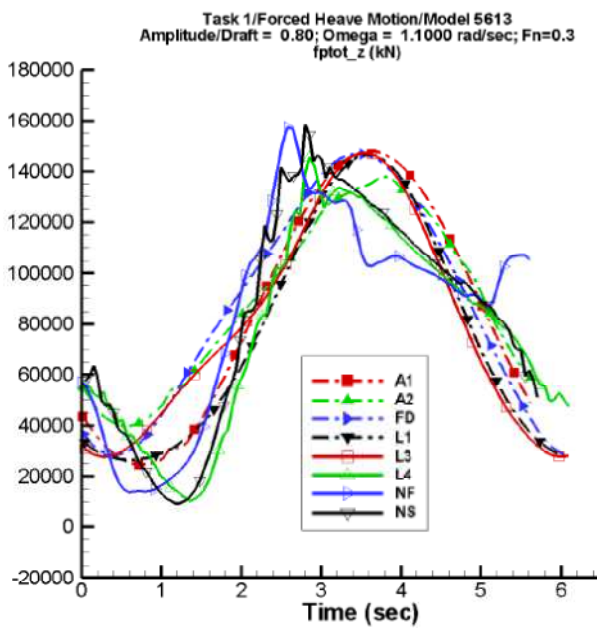


Figure 3: Time-history of total ship-fixed vertical force for ONRTH hull undergoing forced heave in calm water at $F_N = 0.3$ and $\omega = 1.1$ rad/sec, with heave amplitude/draft of 0.8. (Belknap & Telste, 2008).

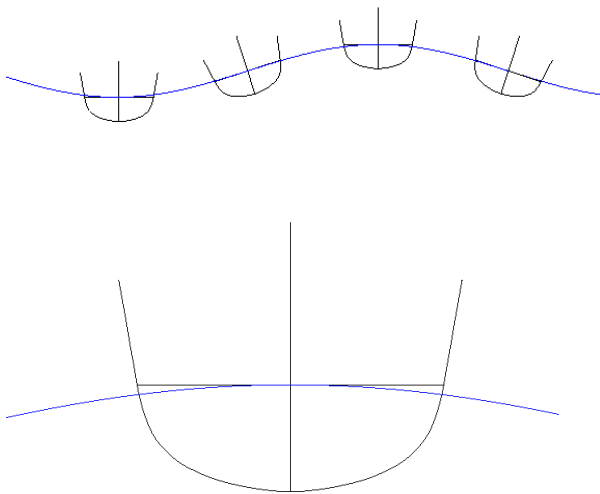


Figure 4: Illustration of beam sea contouring case for m5514: (top) visualization of body position at different phases of wave and (bottom) close-up of wave-body intersection at wave crest (Belknap & Telste, 2008).

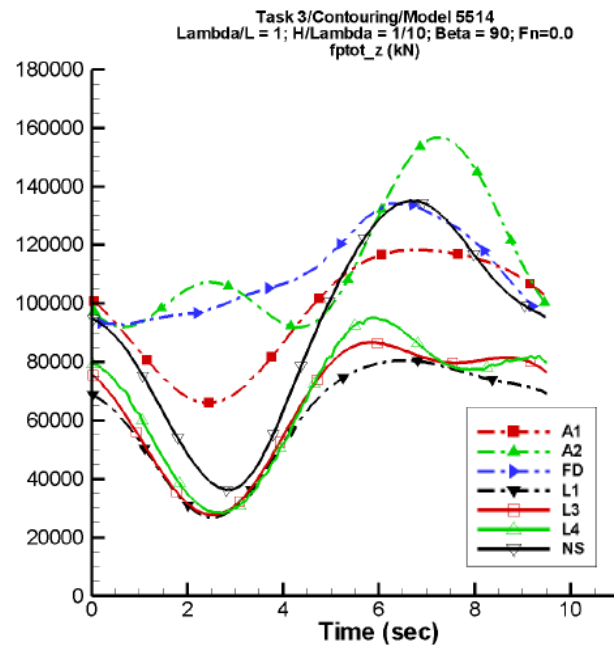


Figure 5: Time history of beam sea contouring case total ship-fixed vertical force time histories for the m5514 hull at $F_n=0.0$ (Belknap & Telste, 2008).

Because the wave is large relative to the size of the ship, the entire ship can be considered close to the free surface in a relative sense. Near the free surface, the dynamic pressure of the incident wave (Froude Krylov force) is essentially equal to the hydrostatic pressure force, but 180 degrees out of phase. The net result is that the Froude Krylov force largely cancels the hydrostatic force, and the remaining force is on the same order as the hydrodynamic disturbance force. This can be seen by the fact that the total force time histories shown in Figure 5 retain the differences seen in the hydrodynamic force time histories in Figure 6a. Thus, it is concluded that an accurate calculation of the radiation and diffraction forces is important.

The delayed wetting of the deck in a rapid sub-mergence (deck-in-water) or shipping of water on deck with rapid emergence (water-on-deck) can be considered a separate part of the hydro-dynamic problem, though it can also be considered a nonlinearity to the hydrostatic, Froude Krylov, and hydrodynamic disturbance forces.

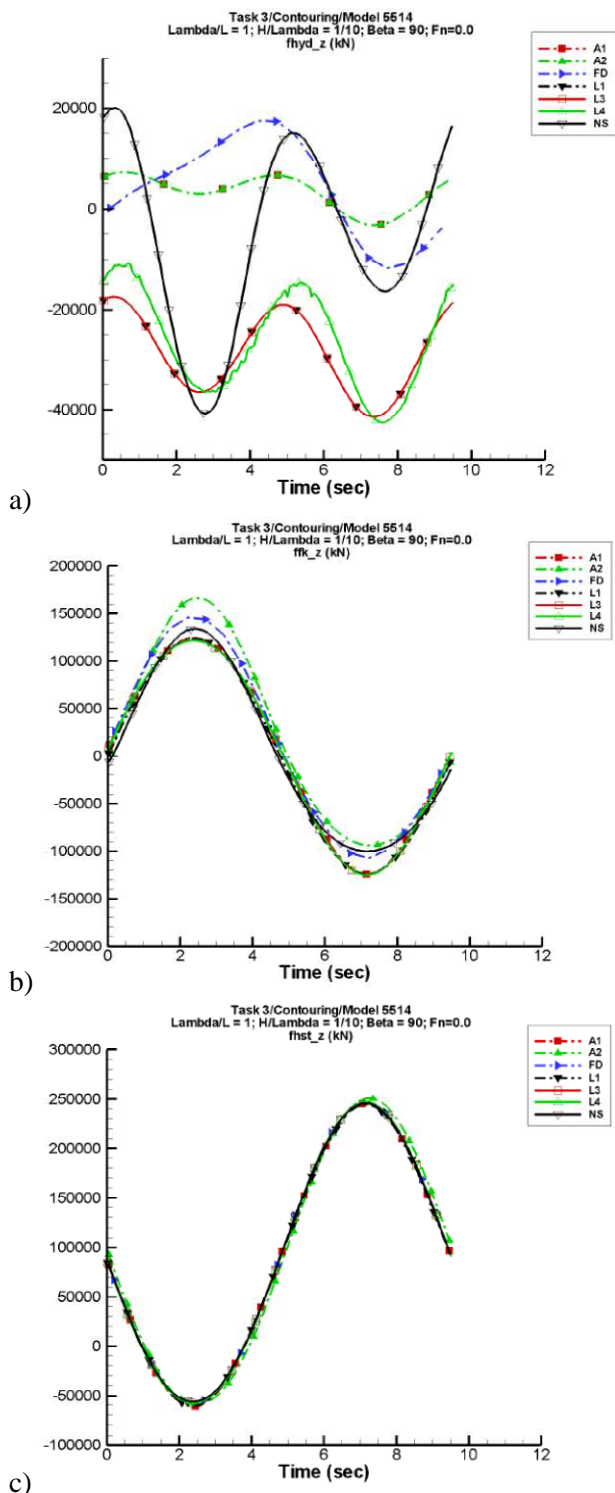


Figure 6: Beam sea contouring case component ship-fixed vertical force time histories for the m5514 hull at $F_n=0.0$: a) hydrodynamic, b) Froude-Krylov, c) hydrostatic (Belknap & Telste, 2008)

The remainder of the physical problem to be modeled covers the portions that include the influence of viscosity, either through shear stress, circulatory lift, or eddy-making damping. In general, these forces can be considered scale-dependent due to Reynolds number effects, though the strength of the scale effects on simulating the dynamic stability problem is not well understood.

The resistance of the ship includes both ideal flow contributions in the form of wave-making resistance as well as viscosity-influenced contributions from skin friction and form drag. For a given ship speed, the resistance force will change as a function of wetted hull area and the changing form of the hull. Furthermore, large amplitude ambient waves provide a change in relative flow velocity, which directly changes the resistance force. This phenomenon has a strong role in determining the incidence of surf-riding.

As stated earlier, the simulation of dynamic stability events is a maneuvering-in-waves problem where the balance of forces determines the speed and heading of the ship. The ship control condition is defined by a known propulsor control (as well as rudder control) that leads to a propulsor force. This propulsor force is the primary “pushing” mechanism for keeping the ship at speed, given that all other forces tend to provide a mean drag force. But like most other forces that need to be modeled for the dynamic stability problem, the behavior of propulsors behind a body that is undergoing large amplitude motion in large waves is very complex. With non-axial inflow, traditional propellers will develop a side-force. Fuhs and Dai (2007) showed via predictions that a 20-deg inflow angle can produce a side force on the order of 50% of the thrust, while Atsavapranee, et al. (2010) showed with a rotating arm model experiment that the sided force can be up to 1/3 the thrust magnitude for typical calm water turning conditions. Large apparent drift angles can arise at the propeller in high yaw rate conditions or in the presence of steep, large beam waves. Given the large longitudinal

moment arm of the propeller, a side force that is on the order of 50% of the propeller thrust can create a large yaw moment, affecting the overall lateral force balance and therefore needs to be modeled. However, determining the inflow to a given propeller is not straightforward. Beyond the complexities of a straight-ahead calm water wake at the propeller disk, the presence of the hull can have a straightening affect on the ambient flow when the ship is inclined relative to the flow. This influence is not as pronounced for a propeller that is more exposed to the free stream flow such as in the case of the outboard propeller on a ship in a turn.

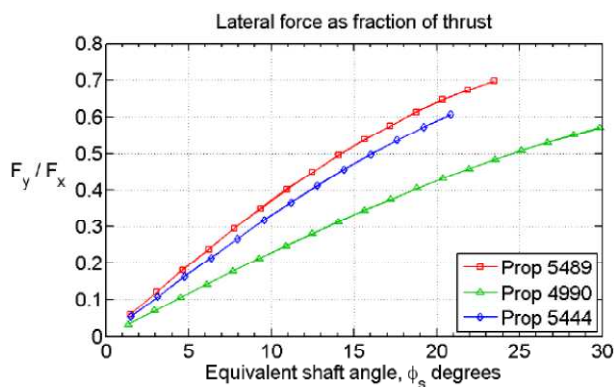


Figure 7: Ratio of propeller side force to axial force as a function of shaft angle relative to inflow (Fuhs & Dai, 2007).

Similar to the affect of the propeller on the problem, the rudder plays a significant role in defining the ship's control condition. Likewise, the effects of large amplitude motions and waves have a strong influence on the rudder forces. The inflow to the rudders includes not only all of the effects relevant to the propeller, but also the accelerated flow from the propeller. The resultant force can generally be determined once the inflow is known, but complications arise in the case of a ventilated rudder. This condition can occur as a large, steep waves passes through the stern sections of the vessel.

From a calm water maneuvering perspective, the propeller and rudder side forces combine with the side forces and yaw

moments provided by the hull lift that arises when the ship is in a turning and/or steady drift condition. This hull lift force behaves as a low aspect ratio lifting surface, shedding vortices along the length of the keel. The presence of bilge keels generally enforces a flow separation point, simplifying the problem from one which the separation point is not known. As follows from low aspect ratio lifting theory, the maximum draft drives the magnitude of the lift force generated. This means that large amplitude motions and waves that create an effective draft increase will have a strong influence on the hull lift force.

As the angle of attack increases, such as in very low speed conditions, hull lift is lost and the dominant viscous force that remains is the cross-flow drag due to eddy-making. Large changes in the wetted hull shape will change the character of the cross-flow drag for a given cross-flow velocity.

The forces on the bilge keels, which are significant contributors to roll damping, are also driven by low aspect ratio lift when the ship has moderate to high forward speed and cross-flow drag when at zero to low forward speed and/or high roll rate. In the case of large amplitude motions and waves, the bilge keels may pierce the free surface, creating large changes in the roll damping behavior. In the presence of long waves (relative to the beam), the orbital velocity must also be considered in the determining the effective inflow velocity.

The final component remaining to be included is the wind force. While this force is clearly a function of the relative wind heading, it is also subject to the wind boundary layer velocity profile changes in steep waves. A ship that finds itself in the trough of a steep wave with a height on the same order of the free-board may have a significantly smaller wind force than it does on the crest of the wave.

3. COMPUTATIONAL MODEL

Once the physical problem has been decomposed and the characteristics relevant to



simulating dynamic stability events have been identified, a computational tool can be selected (or developed, if none found appropriate) that includes the required elements.

Modeling the ship motion hydrodynamic problem can be accomplished in many ways (see Beck & Reed, 2001). Direct assessment of dynamic stability performance requires being able to provide meaningful (statistically speaking) data for many conditions, which means that only computationally efficient approaches can be used. Vassalos, et al. (1998) provide an overview of approaches that specifically have been used for simulating dynamic stability conditions. In general, the only tractable solution is to use potential flow methods to solve the ideal fluid problem and treat appendage and hull lift and cross-flow drag forces as additive forces, with proper accounting for any overlap.

3.1 Ship Control Condition

Because the problem being simulated is a maneuvering-in-waves problem, the numerical model must mimic the controls of the ship being directly assessed. This means that the simulation tool must predict the total motions based on inputs of ordered power or RPM and ordered autopilot heading.

3.2 Environment

To simulate a realistic ocean environment, the simulation tool must be able to model multi-directional/spread seas. Beyond that requirement, much work remains to determine the level of fidelity that must be included in the wave environment model. Linear Airy wave theory appears to be sufficient for non-steep to moderately steep waves in predicting wave kinematics and pressure, at least when Wheeler stretching (Wheeler, 1970) is used to enforce zero-pressure at the free surface. Second-order expansions of the linear solution can provide a correction to the shape of the waves (shallower troughs, taller peaks) and the pressure, though in very steep cases, the second-order expansion may lead to a large non-zero total pressure at the free surface. This is illustrated in Figure 8

for a two-component wave at the x-location under the wave crest.

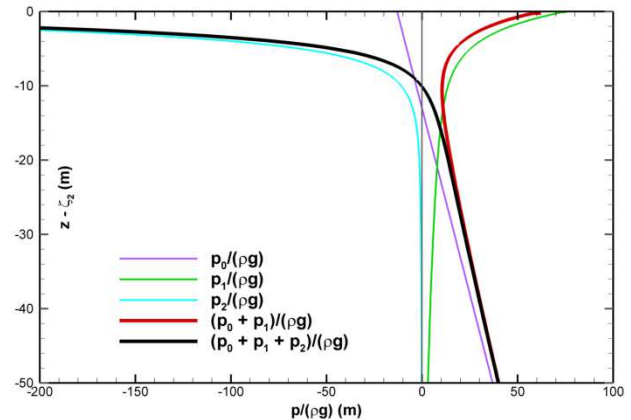


Figure 8: Pressure under a wave crest through second order, $(p_0 + p_1 + p_2)/\rho g$, for the sum of two waves versus the distance below the crest, $z - (\zeta_1 + \zeta_2)$, for two frequencies: $\lambda_1/\lambda_2 = 10$, $H/\lambda = 1/10$, $(\theta_1, \theta_2) = (0, 0)$. (Courtesy of J. Telste).

In the case of the steepest wave fields, linear and second-order expansions may not be sufficient. The evolution of the wave field in a developing sea is subject to energy transfer between high and low frequencies, as well as the continual transfer of energy from wind to waves and loss of energy due to wave breaking. The result is a non-stationary wave field with considerably different behavior than a linear (non-evolutionary) wave system. Research on the statistics of extrema for these highly nonlinear wave fields continues, but early results presented by Kent, et al. (2012) using a pseudo spectral method indicate that the occurrence of extreme peaks can occur significantly more often than those predicted by linear/Gaussian methods. These predictions did not include a wave-breaking model or energy pumping scheme, so these results can only be considered as early indications. The implication if the results are confirmed is that linear wave systems would provide a non-conservative estimate of the rate of occurrence of extreme waves. This is likely to provide a

non-conservative estimate of dynamic stability risk of a ship in those steep, large seaways.

The wind environment can be modeled as a power law boundary layer velocity profile. This profile shape can be adjusted as a function of surface roughness (sea state) and to apply separation adjustments if steepness criteria have been met.

3.3 Forces

Blended methods (nonlinear hydrostatic force and linear hydrodynamic disturbance force) were some of the first employed for simulation of dynamic stability (see de Kat and Paulling, 1989) and remain often employed, because it's relatively straight forward to address nonlinear hydrostatic and Froude Krylov forces. Integration of the ambient fluid pressure on a 3D paneled representation of the ship hull provides a sufficiently high fidelity prediction of the hydrostatic and Froude Krylov forces (see Figure 9 for an example).

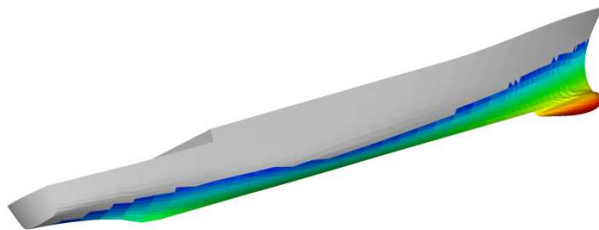


Figure 9: Sample ambient wave pressure on a 3D meshed hull

But while blended method approaches have been popular, they fail to accurately capture the hydrodynamic disturbance force in the cases of large amplitude motion. This might be sufficient for some applications of simulation tools in a direct assessment criterion evaluation, but will not lead to the level of accuracy that is required for others. In the end, the trade space of accuracy versus computational efficiency must be explored to find a suitable approach.

Table 1 shows the matrix of approximate computational efficiency for linear, blended, and completely body-nonlinear approaches that are based on 2D, slender ship, and 3D computations of the hydrodynamic disturbance force. The cells are colored light gray if they are considered acceptable for use as a direct assessment simulation tool, dark gray if it is not, and a gradation of light to dark gray for somewhere in between. Given the number of conditions that need to be simulated and the amount of simulated time required at each condition, it is presumed that a computational tool on the order of “real-time” (i.e. 1 computational second per simulated second) is required.

Table 1: Computational efficiency (computational seconds / simulated seconds)

	Linear	Blended	Nonlinear
2D	$O(10^{-3})$	$O(10^{-1})$	$O(10^0)$
Slender ship			<i>est. $O(10^1)$</i>
3D*	$O(10^0)$	$O(10^1)$	$O(10^3)$

* Time-domain solution of hydrodynamic disturbance for Linear and Blended methods

The competing priority of accuracy is shown for the same design space in Table 2, where level of accuracy is graded as light gray if it contains the required elements of the hydrodynamic problem and dark gray if it lacks the required level of accuracy.

A heuristic composite ranking of computational speed and accuracy is shown in Table 3. More weight is given to computational accuracy than speed, because an incorrect answer does not provide any benefit. The resulting optimal design point is then identified as nonlinear 2D or nonlinear Slender ship. The slenderness of typical ships allows for these design points to be suitable accuracy-wise (assumes that the surge problem is included in the formulation), yet the problem is computationally tractable.



Table 2: Accuracy – capturing physics & nonlinearity

	Linear	Blended	Nonlinear
2D			
Slender ship			
3D			

Table 3: Estimated composite ranking of computational efficiency and ability to capture the relevant physics

	Linear	Blended	Nonlinear
2D			
Slender ship			
3D			

Body-exact strip theories, such as that presented by Bandyk (2009) (see Figure 10), are seen as optimal solutions within this design space. In such an approach, though the time-varying wetted boundary is captured, a linear free surface boundary condition is maintained:

$$\frac{\partial \zeta}{\partial t} = \frac{\partial \phi}{\partial z}, \quad z = 0 \quad (1)$$

$$\frac{\partial \phi}{\partial t} = -g\zeta, \quad z = 0 \quad (2)$$

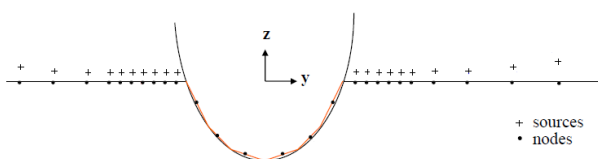


Figure 10: Numerical solution of the time-domain boundary value problem for an example section (from Bandyk, 2009).

This reduced complexity model captures the important body-nonlinearity while neglecting the free-surface nonlinearity in favor of numerical stability. Still, there remain challenges in the numerical implementation,

particularly with respect to handling sections coming out of the water and re-entering, smooth calculation of $d\phi/dt$, and obtaining $\partial\phi/\partial x$. One possible approach for avoiding these numerical difficulties is to use momentum methods as opposed to pressure integration in determining the force. Sclavounos and Lee (2012) show that, using a momentum approach, the force can be determined via a time-derivative of the integrated potentials, rather than an integral of the individual time-derivatives of the potentials.

One final aspect of the overall modeling approach will have a strong influence on the resultant ideal fluid forces and that is the selection of reference frames. At the highest level, a code can choose whether to maintain two sets of equations of motion (solving a maneuvering problem and seakeeping problem for a ship on the mean path as defined by the maneuvering problem) or choosing to solve a single set of equations of motion for the combined maneuvering-in-waves problem.

Having established the basis ideal fluid model as a 2D or slender ship body-nonlinear approach, the viscosity-influence forces (resistance, appendage, and hull lift and cross-flow drag) can be addressed.

The resistance force must separate any wave-making resistance that is captured by the hydrodynamic disturbance force from the remainder of the total resistance. This remainder resistance force may account for changing wetted area, but it is difficult to estimate in a computationally efficient model how the form drag would change in a wave field.

Propeller forces should be modeled in a computationally efficient manner that includes side forces due to oblique inflow. Fuhs & Dai (2007) provide an empirical model for estimating the side forces given an inclination angle and axial force prediction. The axial force can be predicted via an open water J-KT curve. The difficulty in predicting these forces arises in establishing the inflow velocity, which



can vary between port and starboard propellers. For a computationally efficient model, the only tractable solution is to provide the inflow velocity via an empirical model that accounts for the local drift angle and possibly heel angle. The added velocity due to rigid body motions and wave orbital velocities should also be included.

Rudder force models can be computationally efficient and of sufficient fidelity by treating the rudder as a lifting surface and applying the appropriate inflow. Because a full range of inflow conditions is possible, a stall model must be included to capture loss of lift. The inflow can be determined in the same manner as the propeller inflow, but an adjustment needs to be made for the acceleration of the flow from the propeller. The thrust provided by the propeller can be used to determine the increase in velocity.

Given that the hull lift force behaves like a low aspect ratio lifting surface, it is reasonable to use a low aspect ratio lifting surface model for estimating the hull lift force. Work such as that presented by Hooft & Nienhuis (1994), Hughes, et al. (2011), and Greeley & Willemann (2012) are examples of these models. Because these models are often coefficient based, there is a need to obtain the lift coefficients from an empirical model, physical model experiment, or viscous flow numerical tool, such as RANS. If an empirical model is chosen, it is important to avoid those that are not consistent with the features of the ship in question (like a sonar dome or large skeg). Another word of caution is to consider the source of the hull lift coefficients in concert with the hydrodynamic disturbance force. Depending on the formulation and the hydrodynamic reference frame used, transverse wave drag or other lateral plane steady forces may be captured by the potential flow model when the ship is in a turning condition and/or has a drift angle. Therefore, the overlapping physics must be addressed through a corrective force or calibration procedure. Finally, once suitable hull lift coefficients are obtained, there must be a means of adjusting them for

changing draft of the ship, because this is the driving feature of low aspect ratio lifting theory.

Cross-flow drag models are generally tied to the hull lift model in that the coefficients are often attenuated (see Hooft & Nienhuis, 1994) to be consistent with the hull lift force at drift angles less than 90 degrees. And like the hull lift model, the cross-flow drag coefficients can be obtained empirically or directly from physical model experiments or 2D RANS calculations. The model needs to adjust these coefficients or modify the force to account for changing draft. This can be done on a section-by-section basis. While quasi-steady assumptions are the norm, higher fidelity models would incorporate Keulegan-Carpenter (KC) number dependency (see Keulegan & Carpenter, 1958) in the cross-flow drag coefficients.

A force model to capture the forces on the bilge keels follows similarly to the hull lift and cross-flow drag forces. However, because of the simple geometry of bilge keels, the problem is simplified to the low aspect ratio lifting theory for flat plates and cross-flow drag for flat plates. KC number dependency can easily be incorporated in this case. More complex models can use lifting surface techniques to solve the potential flow boundary value problem (see Greeley & Petersen, 2010), but it is not clear that this level of fidelity is required. Input velocities to any bilge keel model need to consider not just body motion, but also wave orbital velocity, particularly the contribution from longer wave lengths.

The final force model required is the wind force model. A coefficient-based model is suitable, such as that provided by Blendermann (1994). One modeling decision that remains though is the most appropriate wind velocity to use when using a complex wind environment model. It is not obvious that the coefficient-based models, which are based on a presumed boundary layer profile, are valid when the environment model includes separated flow conditions.



4. VALIDATION

The final critical step in the direct assessment procedure is to validate the selected simulation tool for the problem of interest. This is far from a trivial task, given the complexities of the physics and the nonlinear dynamical system. Belknap, et al. (2011, 2012) discuss the challenges involved in detail along with a proposed approach for performing validation on dynamic simulation tools. A summary of the issues involved and a recommended process is provided here.

Within the framework of direct assessment of stability risk, the most important step in ensuring that the validation activities are appropriate and properly defined in scope is defining the “Specific Intended Use(s)” (SIUs) of the simulation tool. The SIUs state exactly what problem is being directly assessed and what quantities of interest are being predicted. Therefore, the SIUs will govern what physics need to be modeled, though in general limitations in ship speed are the only clearly beneficial limitations from the perspective of eliminating physics. This is because modeling all 6 degrees of freedom is required to properly include coupling effects (forces and phase). Key aspects that should be clarified in the SIUs are:

- Type of vessel (and appendages)
- Environmental conditions
- Operating conditions (ordered ship speeds and relative wave headings)
- Loading conditions
- Motions and stability failure events of interest
- Statistical quantities of interest
- How the simulation motion data and statistics will be used

Having defined the SIUs, the succeeding question is one of acceptance criteria. These are the conditions that must be met for the simulation tool to be considered acceptable for use in performing a direct assessment of

stability risk. Smith (2012) describes how the acceptance criteria are derived from the Specific Intended Uses, but that ultimately it is up to the certification bodies to determine how accurate is accurate enough.

In order to support the certification bodies in making such a determination, the validation task must produce the evidence that not only can the quantities of interest be predicted to within a given level of quantifiable “error” (the “Quantitative Validation” task), but also that it has done so in a manner that is consistent with the physical problem. This latter point is required so that the certifying authority can have confidence that validation extends beyond the set of direct comparison points submitted for validation. It is accomplished through validation at the physical element level, which does not have quantifiable accuracy requirements. Therefore, this is considered “Qualitative Validation.”

4.1 Qualitative Validation

Grochowalski and Jankowski (2009) noted the importance of validation at the component or “elemental” level as a means of ensuring that the mechanisms that lead to the events of interest are well modeled. The elements can be considered as the individual force model components and/or the elements of the dynamic stability problem domain. As described in an earlier section of this paper, this problem is a large amplitude motion maneuvering-in-waves problem. Various elements to be considered (some of which may be stricken if not relevant to the particular direct assessment) are:

- Wind and wave environment modeling
- Roll damping
- Calm water maneuvering
- Seakeeping
- Nonlinear stiffness
- Appendage forces (including propellers and rudders)
- Maneuvering in small to moderate waves

- Drift forces (including added resistance)
- Surf-riding incidence

Qualitative validation is then achieved upon demonstration that these isolated aspects of the problem are predicted to within a reasonable level of accuracy as determined by a Subject Matter Expert (SME).

Examples of qualitative validation tests and their metrics are provided in Table 4. Another example of qualitative validation is the ability to reproduce specific phenomena in appropriate conditions.

Table 4: Example elemental tests and their qualitative metrics.

Test	Element(s)	Metric(s)
Roll Decay	Roll damping, nonlinear stiffness	Decrement coefficients and periods
Calm water turning circle	“maneuvering” forces, appendage forces	Diameters, steady heel, steady drift
Calm water zig-zag	“maneuvering” forces, radiation, appendage forces	Overshoots, max roll
Regular wave (non-steep) seakeeping	Radiation, diffraction, roll damping	Motion transfer functions: amp. and phase
Regular wave (steep) dyn. stability	(several)	Motion time histories, integrity values, max. value scatter
Forced motion	(several, but isolated)	Force time histories: amp. and phase

An example of this is the incidence of surf-riding in conditions of following regular waves as speed increases across a threshold. This phenomenon is shown by Spyrou (1996) and is depicted in Figure 11.

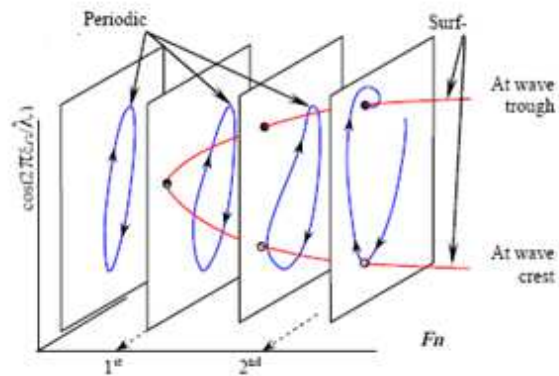


Figure 11: Change from surging to surf-riding behavior with increasing speed (Spyrou, 1996)

4.2 Quantitative Validation

Quantitative validation is a demonstration of the ability to “accurately” predict the quantities of interest, where “accurate” is determined by the acceptance criteria that were developed from the SIUs. This requires having comparison data in real world conditions (i.e. irregular seas in the ship control condition of interest). Preferably, data exists for a wide range of environmental conditions in order to expand the domain of validation. Because while qualitative validation supports the validation of conditions between direct validation points (essentially, indirect or interpolative validation), it is not sufficient for extrapolative validation.

Given the nature of the problem containing stochastic excitation and nonlinear response, it is essential to quantify the uncertainty of both the comparison data and the prediction in order to make a meaningful assessment of simulation accuracy. Determination of stochastic process uncertainty is discussed by Smith (2011, 2012), and it is noted that this is a nontrivial task for the continuous data sets (i.e. time histories) that are of interest.

Another potentially large source of uncertainty is the uncertainty in the definition of the condition being tested. Often, the condition definition is provided as a statement of fact, when in reality there is a level of uncertainty on the defining parameters (e.g.,



wave spectrum, model load condition, relative wave heading). These parameters are the “input” to the simulation, and for different inputs, there is generally a different predicted response. Therefore, it is essential to quantify not only the uncertainty on the inputs, but the uncertainty of the resultant motions based on imprecise knowledge of the inputs. This is referred to as “input uncertainty.”

The topic of addressing error propagation when validating engineering models was investigated by Hills and Trucano (1999). One approach they provide for determining the effect of propagation of input error is the use of Monte Carlo simulation with varying parameters. To test the potential impact on dynamic stability simulation tool validation, a sample study was performed that parametrically varied input parameters over a range of values representative of the level of error that might be seen in a model test. The sample study examined a stern-quartering relative wave condition in a severe sea state, so the results can not be generalized for all conditions. However, they demonstrate the point that input uncertainty must be considered.

The sample study varied the following input parameters:

- Relative wave heading
- Significant wave height
- Modal period
- GM

The size of the errors that determined the parameter range are hypothetical, but not unrealistic for a 95% confidence interval given typical model test set-ups. With the “best estimate” input values set as the basis, the Monte Carlo study varied the four sources of error to include only the upper and lower bounds. This led to a 3x3x3x3 condition matrix (many simulations were performed at each condition), which represents a test with 80 additional conditions compared to running only the “best estimate” condition. This matrix is shown in Table 5.

Table 5: Input value uncertainties for Monte Carlo error propagation simulation matrix.

	Lower Bound	Best Estimate	Upper Bound
Heading	35 deg	45 deg	55 deg
H_{1/3}	11.0m	11.5m	12.0m
T_m	13.0s	14.0s	15.0s
GM	GM ₀ - .05m	GM ₀	GM ₀ + .05m

The resulting rare motions metric (mean crossing rate) for roll is shown for all conditions of the study in Figure 12. The results using the “best estimate” of input values are shown as the blue line and the parametrically varied conditions provide results that are shown at select crossing levels with the red scatter points. At least for this study, the figure shows a significant error propagation in the results which supports the argument that input uncertainty must be considered as part of quantitative validation.

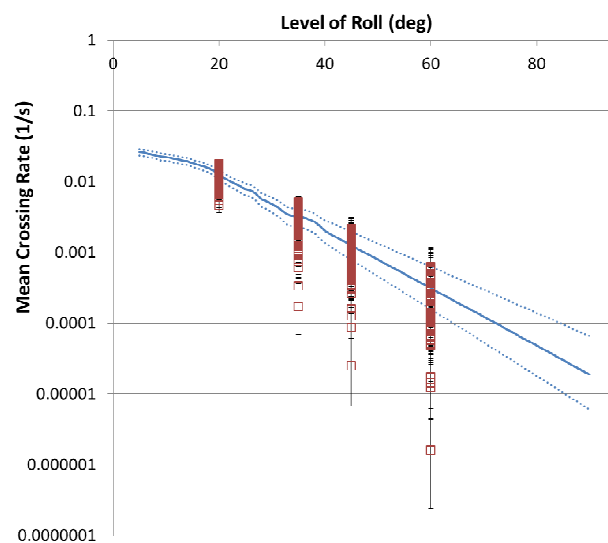


Figure 12: Simulation results for the mean crossing rates for roll using the best estimate of input parameters (solid blue line with dashed blue lines for 95% confidence intervals) and the parametrically varied input parameters (red scatter points with 95% confidence intervals) – presented on a log scale.



5. CONCLUSIONS

The direct assessment approach to demonstrating an acceptable level of dynamic stability risk relies on the presence of simulation tools that are validated for the problems of interest. It is argued that a computationally efficient 6-Degree-of-Freedom model is required in order to capture the fully coupled physics and to provide the sufficient quantity of motion statistics required to determine the risk of a rare event occurring.

After characterizing the elements of the physical problem to be modeled, computationally efficient approaches were described that are deemed to have the best chances for meeting the competing design space needs of computational efficiency and accuracy. It is recognized that there remain continued areas of research, such as the possible need for higher order wave models that can better capture the properties (kinematics, pressures, evolution, and statistics of extremes) of severe sea states most relevant to the dynamic stability problem.

Finally, an approach for validating a direct assessment simulation tool is presented. The approach divides the activity between “Qualitative Validation” and “Quantitative Validation.” Qualitative validation provides confidence that the physics are well modeled, whereas quantitative validation directly tests the simulation tool’s ability to predict the quantities of interest. Quantitative validation must have a rigorous and complete treatment of uncertainty, which must include both stochastic process uncertainty and input uncertainty. In particular, the effect of input uncertainty on simulation results can be stronger than the stochastic process uncertainty. Understanding how consistent this conclusion is throughout the operational domain should be an area of continued study.

6. ACKNOWLEDGEMENTS

The authors would like to acknowledge the technical contributions of Drs. Vadim Belenky

and Chris Kent and Messrs. Brad Campbell and John Telste. This work was supported by Dr. Pat Purtell of ONR and Mr. Jim Webster of NAVSEA.

7. REFERENCES

- Atsavapranee, P., R. Miller, C. Dai, J. Klamo & D. Fry, 2010, “Steady-Turning Experiments and RANS Simulations on a Surface Combatant Hull Form (Model #5617),” Proc. 28th Symp. Naval Hydro., Pasadena, CA.
- Bandyk, P., 2009, “A Body-Exact Strip Theory Approach to Ship-Motion Computations,” Ph.D. Thesis, Univ. Michigan, Dept. Naval Architecture and Marine Engineering.
- Beck, R. F. & A. M. Reed, 2001, “Modern Computational Methods for Ships in a Seaway,” Trans. SNAME, 109:1–51.
- Belenky V. & B. Campbell, 2012, “Statistical Extrapolation for Direct Stability Assessment,” Proc. 11th Int’l Conf. Stability of Ships & Ocean Vehicles, Athens, Greece.
- Belknap W. & J. Telste, 2008, “Identification of Leading Order Nonlinearities from Numerical Forced Motion Experiment Results,” Proc. 27th Symp. Naval Hydro., Seoul, Korea, 18 p.
- Blendermann, W., 1994, “Parameter Identification of Wind Loads on Ships”, J. Wind Engineering and Industrial Aerodynamics, 51:339–351.
- Chang, P. C., E. J. Plate & G. M. Hidy, 1971, “Turbulent air flow over the dominant component of wind-generated water waves.” J. Fluid Mechanics, 47:183–208.
- Fuhs, D. & C. Dai, 2007, “Effect of Cross Flow on Propeller Forces,” Carderock Division, Naval Surface Warfare Center Report NSWCCD-50-TR 2007/046.
- Fullerton, A. M., K. Beale, E. Terrill & D. Dommermuth, 2012, “An Extended Wind Boundary Layer Profile,” Proc. 29th Symp. Naval Hydro., Gothenburg, Sweden.



- Greeley, D. S. & B. J. Petersen, 2010, "Efficient Time-Domain Computation of Bilge Keel Forces," Proc. 28th Symp. Naval Hydro., Pasadena, CA, 17 p.
- Greeley, D. S. & S. Willemann, 2012, "Surface Ship Maneuvering Forces in Calm Water and Waves," Proc. 29th Symp. Naval Hydro., Gothenburg, Sweden.
- Grochowalski, S. & J. Jankowski, 2009, "Validation Methodology for Simulation Software of Ship Behaviour in Extreme Seas," Proc. 10th Int'l Conference on Stability of Ships and Ocean Vehicles, pp. 409-420, St. Petersburg, Russia.
- Gudmestad, O. T., 1993, "Measured and Predicted Deep Water Wave Kinematics in Regular and Irregular Seas," Marine Structures, 6:1-73.
- Hills, R. G. & T. G. Trucano, 1999, "Statistical Validation of Engineering and Scientific Models: Background," SAND99-1256, Sandia National Lab., Albuquerque, NM.
- Hooft, J. P. & U. Nienhuis, 1994, "The Prediction of the Ship's Maneuverability in the Design Stage," Trans. SNAME, 102:419-445.
- Hughes, M. J., P. J. Kopp & R. W. Miller, 2011, "Modeling of hull lift and cross flow drag forces in large waves in a computationally efficient dynamic stability prediction tool," Proc. 12th Int. Ship Stability Workshop, Washington, DC.
- Kat, J. O. de & J. R. Paulling, 1989, "The simulation of ship motions and capsizing in severe seas," Trans. SNAME, 97:139-68.
- Keulegan, G. & L. Carpenter, 1958, "Forces on Cylinders and Plates in an Oscillating Fluid," J. Research of the National Bureau of Standards, 60(5)423-440.
- Kent, C., J. O'Dea, C. Bassler, L. Minnick, 2012, "Statistical Analysis of Simulated Ocean Waves with Varied Non-linearity," Proc. 29th Symp. Naval Hydro., Gothenburg, Sweden.
- Peters, W. S., V. Belenky & A. M. Reed, 2012, "On Regulatory Framework of Direct Stability Assessment," Proc. of 11th Int'l Conf. Stability of Ships & Ocean Vehicles, Athens, Greece.
- Reed, A. M., 2009, "A Naval Perspective on Ship Stability," Proc. 10th Intl. Conf. Stability of Ships and Ocean Vehicles, St. Petersburg, Russia.
- Sclavounos, P. D. & S. Lee, 2012, "A Fluid Impulse Nonlinear Theory of Ship Motions And Sea Loads," Proc. 29th Symp. Naval Hydro., Gothenburg, Sweden.
- Smith, T. C., 2011, "Statistical Data Set Comparison for Continuous, Dependent Data," Proc. 12th International Ship Stability Workshop, 7 p, Washington, DC.
- Smith, T. C., 2012, "Approaches to Ship Motion Simulation Acceptance Criteria," Proc. 11th Int'l Conf. Stability of Ships & Ocean Vehicles, Athens, Greece.
- Spyrou, K. J., 1996, "Dynamic instability in quartering seas: The Behavior of a Ship During Broaching," J. Ship Research, 40(1):46-59.
- Stansberg, C. T., O. T. Gudmestad & S. K. Haver, 2008, "Kinematics under Extreme Waves," J. Offshore Mechanics and Arctic Engineering, 130(2) 020201.1-021013.8.
- Telste, J. G. & W. F. Belknap, 2008, "Potential Flow Forces and Moments from Selected Ship Flow Codes in a Set of Numerical Experiments," Carderock Division, Naval Surface Warfare Center Report NSWCCD-50-TR-2008/040, 15,240 p.
- Vassalos, D., M. Hamamoto, J. O. de Kat, D. Molyneux & A. Papanikolaou, 1998, "The State of the Art in Modelling Ship Stability in Waves," Proc. 25th ATTC, Iowa City, Iowa, 8 p.
- Wheeler, J. D., 1970, "Method for calculating forces produced by irregular waves," J. Petroleum Technol., 249:359-367.



Statistical Extrapolation for Direct Stability Assessment

Vadim Belenky, *David Taylor Model Basin (NSWCCD)*, vadim.belenky@navy.mil

Bradley Campbell, *David Taylor Model Basin (NSWCCD)*, bradley.campbell@navy.mil

ABSTRACT

This paper reviews basic research carried out at David Taylor Model Basin in support of the development of a family of statistical extrapolation methods, including the Peaks Over Threshold (POT) and Envelope Peaks Over Threshold (EPOT) methods. This family of methods is aimed at solving the problem of rarity, which occurs when the mean time before or between the stability failures is large in comparison with the time scale of the ship motion being studied (i.e. roll period or encounter period). The paper considers several general problems, making sure that the correct interpretation of the existing theory is used for development extrapolation methods. In particular the paper addresses: the relationship between probability and time, the application of extreme value theory, the application of envelope theory, and the properties of peaks and both-sides crossings.

Keywords: Extrapolation, upcrossing, extreme values, envelope, peaks-over-threshold.

1. INTRODUCTION

The development of extrapolation methods for the probabilistic assessment of dynamic stability is necessary because, in general, the stability failures are too rare to rely on direct statistical observations of these events using physical model experiments or time-domain numerical simulations. On the other hand, the level of complexity (nonlinearity, in particular) of a dynamical system describing large-amplitude ship motions with sufficient fidelity leaves no choice for a method of assessment, but a model test and/or time-domain numerical simulation.

One of the obvious choices for an extrapolation method was the Peak-over-Threshold method (Pickands, 1975, Smith 1985), since there is a solid mathematical background for this method (Leadbetter, 1991). Application of this method for dynamic stability assessment was considered in Campbell & Belenky (2010). One of the specific issues studied was the relationship between the position of threshold and roll-specific nonlinearity. Another issue studied was that a partial stability failure (large roll event) may occur on both sides (port and starboard). The latter issue motivated use of an

envelope. The result was the Envelope Peak-over-Threshold (EPOT) method. Its place and relationship with other extrapolation methods being developed for probabilistic stability assessment is considered in Belenky, *et al.* (2012).

The development of the EPOT method is described in detail in NSWCCD report (Belenky & Campbell 2011) that is approved for public release. One of the most important aspects of this development is to ensure that the interpretations of the background mathematical concepts (such as the upcrossing, the extreme value, the envelope and so on) are correct and applicable to the problem of ship stability in waves. That is why this basic analysis has such a prominent place in the above reference. The objective of this paper is to highlight the outcome of this analysis.

2. ON THE RELATIONSHIP OF PROBABILITY WITH TIME

The relationship of the probability of a failure and the time of exposure is a common place in the theory of reliability (e.g. Meeker & Escobar, 1998). The understanding that



probabilistic assessment of dynamic stability is a reliability problem and therefore related with time came to Naval Architecture almost half-century ago (Sevastianov, 1963, available in English 1994). Since a stability failure is associated with a Poisson flow event, then the probability of k events occurring during time of exposure T is expressed as:

$$P_T(k) = \frac{(\lambda T)^k}{k!} \cdot \exp(-\lambda T), \quad (1)$$

where λ is the rate of events, which is the mean number of the events per unit of time. It is the inverse of the mean time between events.

The application of Poisson flow requires the events to be independent (other conditions associated with Poisson flow are satisfied automatically). The measure of stability safety in irregular waves is expressed as the probability of no failures occur during the time of exposure ($k=0$), as in equation (2)

$$P_T(k=0) = \exp(-\lambda T). \quad (2)$$

The measure of danger of dynamic stability failure is expressed as the probability of the complimentary event that at least one failure will occur during the specified time of exposure

$$P_T(k \neq 0) = 1 - \exp(-\lambda T). \quad (3)$$

Equation (3) can also be considered as a cumulative distribution function (CDF) of time between or before the stability failure; it is the exponential distribution and its probability density is expressed as:

$$f(T) = \lambda \exp(-\lambda T). \quad (4)$$

The problem of probabilistic assessment of dynamic stability would be completely solved if the rate of events is known. A partial stability failure is related with exceeding a certain level

of roll motion, i.e. a partial stability failure (considering one side only) is an upcrossing of the given level. The rate of upcrossings is available from the general theory of stochastic processes (Kramer & Leadbetter, 1967)

$$\lambda = \int_0^{\infty} \dot{\phi} f(\phi = a, \dot{\phi}) d\dot{\phi}. \quad (5)$$

Here a is the value associated with partial stability failure and $f(\phi = a, \dot{\phi})$ is the joint distribution of roll angles and roll rate evaluated as a roll angle of a .

Thus if the joint distribution of roll and roll rate is known, the problem is solved. However, it is never known exactly because of the nonlinearity of large amplitude ship motions. Moreover, the large value of a is located on the tail of the distribution, which is especially difficult to approximate. However for the linear case, the distributions of roll and roll rate are normal, they are independent (because they are uncorrelated) and the integral in the equation (5) can be evaluated symbolically:

$$\lambda = \frac{1}{2\pi} \sqrt{\frac{V_{\dot{\phi}}}{V_{\phi}}} \exp\left(-\frac{a^2}{2V_{\phi}}\right), \quad (6)$$

where V_{ϕ} is the variance of roll angles and $V_{\dot{\phi}}$ is the variance of roll rates.

The importance of the formula (6) is that it is exact for a normal process. It provides an important validation tool for a solution of a relatively simple problem: given a sufficient number of stability failures observed during a model test or numerical simulation, how is the rate of events estimated? Theoretically there are three ways to estimate this value:

- Count the events and estimate the average number of events per unit of time
- Estimate the mean value of time between the events
- Estimate the mean value of time elapsed before the first event occurs

Theoretically, all these methods are equivalent. Are they practically equivalent too? To find out, consider a data set of wave elevations at a point. The wave elevations have normal distribution, so formula (6) is fully applicable. The sample data set consists of 200 independent records of wave elevations corresponding to Sea State 8 (Significant wave height $H_S=11.5\text{m}$ and modal period $T_m=16.4\text{s}$); the duration of each record is 30 minutes, totalling 100 hours of data. The wave elevations were simulated using Bretschneider spectrum with Fourier series discretized with 180 frequency components.

As all estimates are random numbers, for a comparison to be meaningful, a confidence interval on the estimate is needed. The normal distribution can be assumed for the estimates of the mean values of the time before and between the events. Since the events are assumed to be independent, a normal, Poisson or binomial distribution can be used for the confidence interval of the rate of events.

Figure 1 shows a comparison of the theoretical rate of upcrossing for a level of 5 m (based on equation (6)) with estimates carried out with several methods. The data set consists of 5407 events based on the previously described numerical example. As it can be seen from this figure, all of the estimates contain the theoretical value in their confidence intervals, therefore all the methods were able to yield correct result in this case. It is also clear from the Figure 1 that the methods based on counting of events and time between events provide better estimates than the method based on the time to the first upcrossing, as the latter one utilizes a smaller sample.

Figure 2 compares theoretical rate of upcrossing for a level of 9 m with estimates carried out using these same methods. The data set consists of 153 upcrossings in total and 111 first upcrossings. The estimates obtained with time between or before the crossing(s) do not include the theoretical value in their confidence intervals, while the method based on counting events still yields a correct estimate.

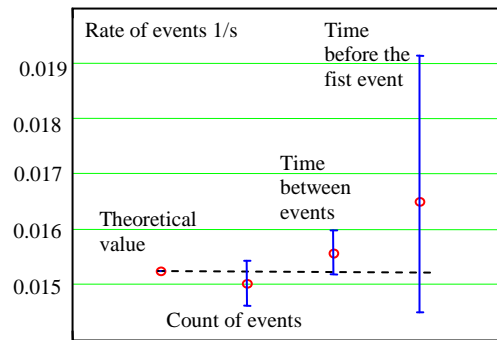


Figure 1: Comparison of Different Methods to Estimate Rate of Events for the Level of 5 m

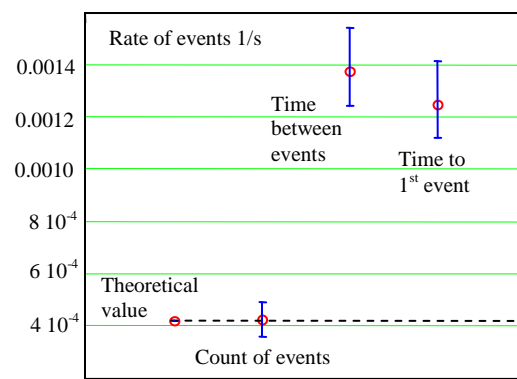


Figure 2: Comparison of Different Methods to Estimate Rate of Events for a Level 9 m

The reason why time-based estimates are biased is that the sample is limited in time. It cannot include any data beyond the duration of a record. Therefore, the mean time before the crossing is biased towards smaller values; thus, rate of events overestimates the true value. While the standard way of correcting such a bias is the procedure of censoring that can be applied to the time before the event (see, for example Meeker & Escobar, 1998), the counting of events provides the least statistical uncertainty and seems to utilize the available data the most efficiently.

Several other time-related issues are considered in the NSWCCD report. One of them is testing if the observed event follows the requirements of Poisson flow. Two methods are proposed to deal with this matter. One is an evaluation of statistical CDF of time between crossings and subsequently using the Kolmogorov-Smirnov (K-S) test against the



equation (3). The rate of events is based on counting. The second method is to use a histogram of the number of events during the given time window and to then compare it with equation (1) using the Pearson chi-square goodness-of-fit test.

Also the distribution of time before and between the events was studied. It was found that despite the bias previously discussed, the distribution of time between events retains the exponential character while the events remain independent. The exponential character was tested using the Pearson chi-square goodness-of-fit test against the PDF equation (4), while the rate of events was taken as an estimate of mean time between the events. Also the estimate of mean value was found to be numerically equal to the estimate of standard deviation (in statistical sense). This is one of the “symptoms” of the exponential distribution.

Once the level was lowered such as the upcrossings become too frequent, the PDF of time between events was no longer exponential. In contrast, the distribution of time before the first event retained the exponential character for any level; this result can be expected since there is only one data point from each record and the records are independent. That means that the non-rejection of the exponential distribution for time between events can be used as an additional indicator of the independence of the events, while the time before the first event cannot be used for this purpose.

3. ON APPLICATION OF EXTREME VALUE DISTRIBUTION

Gumbel (1958) formulated Extreme Value Theory (EVT) in its modern form. One of the immediate applications of EVT was the prediction of extreme flooding based on multi-year observations. There is a series of measurements of the water level in a river observed during a year. Taking the largest measurement for each year, a series of extreme values is created. The basic question posed

was then, “What would be the level for a one-hundred-year flood?” The theory is based on the limit distribution of the first-order statistics of the independent identically distributed (IID) random numbers.

The extension of the extreme value theory for stochastic processes was formalized by Leadbetter, *et al* (1983). The essence of the extreme value theory is that the distribution of the largest value of a process observed during the sufficiently large time window does not depend on the distribution of the instantaneous value of the process, but tends to a limit described by the extreme value distribution. The latter can be one of three types known as type I, II and III or as Gumbel, Freshet and Weibull distribution respectively.

The very formulation of the extreme value theory makes it very attractive for application in probabilistic assessment of dynamic stability (MacTaggart, 2000, MacTaggart & deKat 2000). The two issues that need to be addressed are assessment of statistical uncertainty and relation with time.

Fitting an extreme value distribution is a statistical procedure. While the extreme value theorem provides a formula for the extreme value distribution, the parameters of the distribution still need to be found. There are several techniques available. The most evident is to fit the distribution based on estimates of mean value and a variance (the Method of Moments). Consider Weibull distribution, its PDF is expressed as:

$$f_{EV}(x) = \frac{k}{\alpha} \left(\frac{x-\theta}{\alpha} \right)^{k-1} \exp \left(- \left(\frac{x-\theta}{\alpha} \right)^k \right) \quad (7)$$

$$x \geq \theta,$$

where, k , α and θ are parameters of Weibull distribution. The mean value m_x and the variance V_x of a random variable x distributed with Weibull are known to be:

$$m_x = \alpha \Gamma \left(1 + \frac{1}{k} \right) - \theta, \quad (8)$$

$$V_x = \alpha^2 \Gamma \left(1 + \frac{1}{k} \right) - m_x^2. \quad (9)$$

Consider a sample of extreme values compiled from the largest value from each record of the same length.

$$x_i = \max(\phi_{i,j}); i = 1,..N_r; j = 1,..N_t, \quad (10)$$

where N_r is the number of records and N_t is the number of data points in each record sampled with the constant time step Δt . The shift parameter θ is simply

$$\theta = \min(x_i); i = 1,..N_r. \quad (11)$$

Then, the equations (8) and (9) can be solved as a system of nonlinear algebraic equations, yielding two remaining parameters of Weibull distribution. Alternatively, the method of maximum likelihood can be used (Cohen, 1965).

Estimation of the mean value and variance of the random variable x does not pose any difficulties. Evaluation of their confidence intervals is also trivial, having in mind that kurtosis of Weibull distribution is known. The shift parameter θ is also a random number bearing statistical uncertainty. It can be treated as an order statistic; then appropriate distribution can be used to evaluate the confidence interval, see details in Belenky & Campbell (2011).

To complete the evaluation of the lower and upper boundaries of the confidence interval for the Weibull distribution, a variable can be scaled to correspond to the upper and lower boundaries of the estimate of the variance and shifted to accommodate variability in the mean value estimate and the shift parameter. Then the parameters of the distribution are re-evaluated for the lower and upper boundaries. The result for the wave elevation data set (both PDF and CDF) is shown in Figure 3.

The relationship between the extreme value distribution and time seems to be straight forward. Since the extreme value is relevant to a particular time window ($T_w = N_t \Delta t$) then using the definition of CDF and equation (2), the rate of events is expressed as:

$$\lambda = -\frac{\ln(F_{EV}(a))}{T_w}, \quad (12)$$

where F_{EV} is the CDF of the extreme value distribution. The boundaries of the confidence interval can be calculated applying formula (12) to the upper and lower boundary of the extreme value CDF.

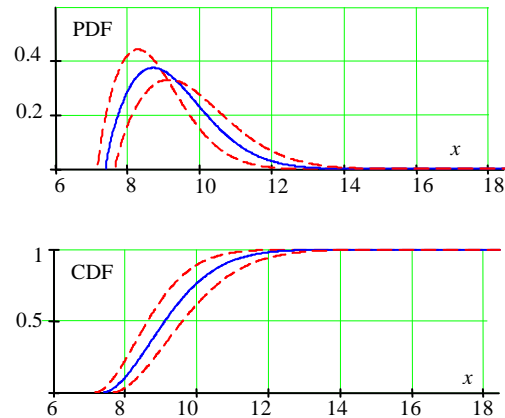


Figure 3: CDF and PDF for Weibull Distribution with Boundaries of Confidence Interval

The rate of events estimated with the extreme value distribution is shown in Figure 4 and compared with the results of other methods. As it can be seen, the estimate from the extreme value distribution has wider confidence interval than the direct counting, but does not suffer from bias, like time-based estimates.

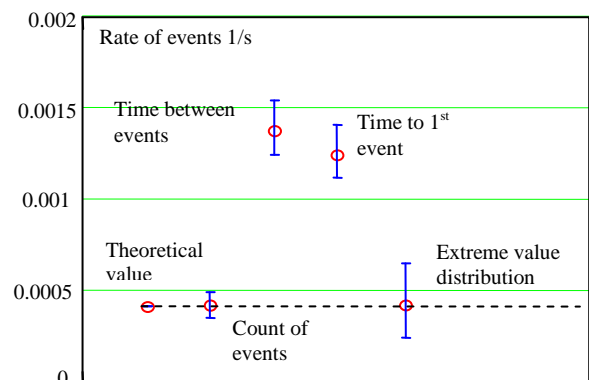


Figure 4: Comparison of Different Methods to Estimate Rate of Events with Results from the Extreme Value Distribution (Level 9 m)



4. PROPERTIES OF PEAKS

A peak of a stochastic process can be defined either as local peak (by the zero-value of the derivative) or a zero-crossing peak (as the largest value between two consecutive zero-crossings). Peaks and extreme values are different from each other. An extreme value is defined as the largest value during a given (fixed) time window. An extreme value is likely to be a peak, but not every peak qualifies as an extreme value.

The distribution of peak values is available for a normal process. In the general case peak values follow the Rice distribution. The Rice distribution tends to a normal distribution with an increase in the spectral bandwidth of the underlying process and is actually normal for white noise (if the autocorrelation is a delta function, there is no memory and a peak does not differ from any other value of the process). For the very narrow-banded process, the peak distribution tends to the Rayleigh distribution:

$$f(a) = \frac{a}{V_x} \exp\left(-\frac{a^2}{2V_x}\right), \quad (13)$$

where a is the value of a peak and V_x is a variance of the normal process $x(t)$.

Figure 5 shows the distribution of local peaks for the wave elevation data set used in the previous section. The dashed line shows a Rayleigh distribution. The most outstanding feature of the histogram is the negative values. They corresponding to secondary peaks resulted from the medium bandwidth.

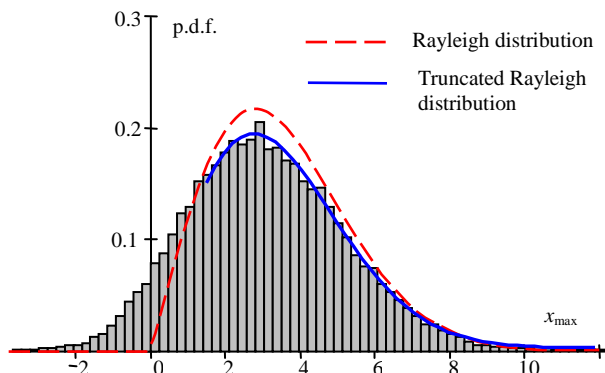


Figure 5: Distribution of Peaks of Wave Elevations

Despite the negative values evident in the histogram, the Rayleigh distribution can be used for relatively large peaks, though it needs to be truncated and re-normalized. It is shown as a solid line in Figure 5, the goodness of fit analysis, (Belenky & Campbell, 2011), did not reject applicability of the truncated Rayleigh distribution.

The distribution of large peaks, nevertheless, does not provide a relationship with time. Strictly speaking, the cumulative distribution function of peaks is the fraction of peaks below the given value. The fraction of peaks above a given value is one minus the CDF at the value (sometimes referred to as the survivor function). When one needs to relate the distribution of peaks with elapsed time, the average period is used. If the time is large enough the CDF may yield reasonable information on how many peaks could exceed a given value.

Taking this idea a little further, it is possible to relate an event of upcrossing of a certain level with a peak exceeding that level. Naturally, if an upcrossing of a level has occurred, the process will peak at the value exceeding this level. Thus a peak exceeding a certain value is a random event following the Poisson distribution, if a level is high enough (so the sequential peaks can be considered as independent events).

The rate of events of peaks exceeding a given level can be estimated by direct counting as:

$$\lambda_p^* = \frac{N_p}{\Delta t \cdot N_t}, \quad (14)$$

where N_p is a number of peaks exceeding a given level observed during N_t time instances, each of the duration Δt .

The statistical uncertainty of this estimate can be done analogously to the estimate of upcrossing rate using either normal or binomial distribution. Figure 6 shows comparison between the rate of peaks exceeding the level

and theoretical upcrossing rate of this level. The first (upper) insert shows also a comparison of statistical estimates of upcrossing and peak-exceedance for 9 m level (as one can see the degree of statistical uncertainty of these estimates is pretty close). The second (lower) insert shows a histogram of number of peaks exceeding the level 9 m during 30 min time window. The line on this insert is the theoretical probability mass function of Poisson distribution. The goodness-of-fit-test did not reject Poisson distribution, see more details in Belenky & Campbell (2011).

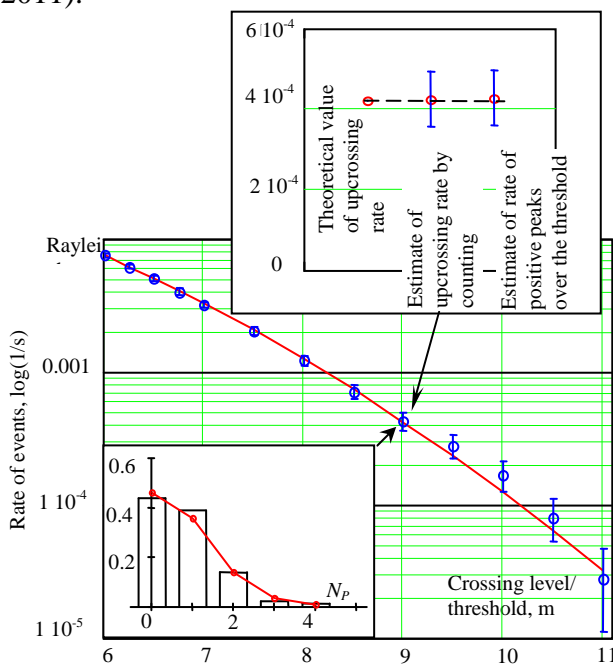


Figure 6: Theoretical Upcrossing Rate (Solid Line) vs. Rate of Events of Peaks Exceeding the Given Level; both Inserts Correspond to the Level of 9 m

5. FORMULATION FOR PEAK-OVER-THRESHOLD (POT) METHOD

Consideration of the probabilistic properties of peaks is important because it clarifies the distinction between them and extreme values, especially in terms of relation with time of exposure. This distinction leads to two formulations for the peak-over-threshold extrapolation method. One is based on the distribution of all the peaks (or only zero-crossing ones) and another on the extreme

value distribution. The commonality between these two approaches actually is more apparent than the difference. Both approaches express the estimate of the rate events with the same formula:

$$\lambda_2^* = \lambda^*(a_1)P(a_2), \quad (15)$$

where a_1 is the intermediate threshold where the rate of upcrossing can be estimated with the direct counting method, $P(a_2)$ is the probability that the level a_2 will be exceeded under the condition that the threshold a_1 is already crossed, see Figure 7.

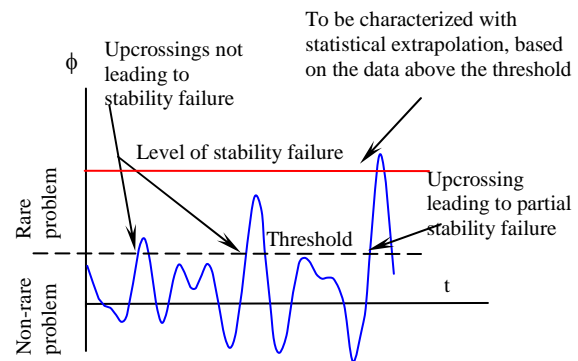


Figure 7: General Scheme of Application of POT Method for Probabilistic Assessment of Stability Failures

The calculation of the probability $P(a_2)$ has two options. The first option is to use the distribution of peaks above the threshold a_1 . Then the calculation is straight forward

$$P(a_2) = 1 - F_{pk}(a_2 | a_1), \quad (16)$$

where F_{pk} is the CDF of the peak values exceeding level a_1 . The second option is to use the extreme value distribution fitted to the data above the threshold a_1 .

$$P(a_2) = -\frac{1}{\lambda_1 T_W} \ln(\exp(-\lambda_1 T_W) + (1 - \exp(-\lambda_1 T_W)) F_{EV}(a_2 | a_1)) \quad (17)$$

where F_{EV} is the CDF of the extreme value distribution fitted above the threshold a_1 , T_W is



the duration of the time window used for collection of the extreme value data.

The POT method may be seen as an implementation of the principle of separation (Belenky, *et al.* 2011). The complex problem is separated into two less complex problems. The non-rare problem is the estimation of the rate of upcrossing over the intermediate threshold that can be done with the direct counting. The rare problem is the extrapolation using either the distribution of peaks or the extreme value distribution based only on the data above the threshold.

This use of the data above the threshold is the essence of the method. Fitting extreme value distribution or distribution of peaks is a statistical procedure. If all the data are used for extrapolation, the result is dominated by the small-amplitude data as the most frequently encountered. If only the data above the threshold (i.e. large-amplitude data) are used for extrapolation, nonlinearity of roll motions is reflected better in the fitted distribution.

6. ON APPLICATION OF THEORY OF ENVELOPE

A partial stability failure occurs when the roll angle exceeds a certain limit on either side of a ship. Thus the probability of exceedance has to be done for both sides. Because of inertia, a large positive roll angle is likely to follow by a large negative roll angle and *vice versa*. These events are too close to each other for the roll autocorrelation function to decay; as a result these two large roll angles cannot be considered as independent events, rendering Poisson flow inapplicable.

Consideration of the envelope instead of the actual roll time history helps to resolve this problem. Two or three large roll angles in a row will result in one envelope exceedance, which is sufficient to manifest the partial stability failure. Envelope theory was originally developed for stationary normal processes

(Rice, 1944, 1945); the principles it is based upon may, however, be extendible to non-Gaussian processes as well. Formally the envelope is defined as:

$$a(t) = \sqrt{x^2 + (H(x))^2}, \quad (18)$$

where x is a stochastic process and $H(x)$ is its Hilbert transform. If the process x can be presented with Fourier series discretized with the frequency set ω_i

$$x(t) = \sum_{i=1}^{N_{\omega}} r_i \cos(\omega_i t + \varphi_i), \quad (19)$$

where r_i and φ_i being amplitude and phases of the of these frequency components, the Hilbert transform is:

$$H(x(t)) = \sum_{i=1}^{N_{\omega}} r_i \sin(\omega_i t + \varphi_i). \quad (20)$$

The definition of the envelope is illustrated in Figure 8, where a fragment of time history of the process x is shown with its Hilbert transform and the resulting envelope. It can be seen from Figure 8 that the envelope is a location of all the peaks of the process $x(t)$ and its Hilbert transform.

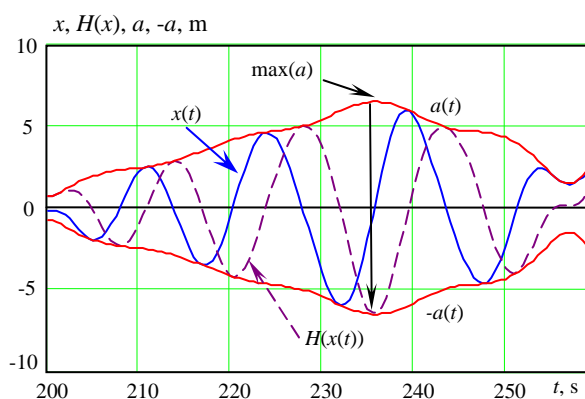


Figure 8: Definition of the Envelope, the Process and its Hilbert Transform

The Hilbert transform can be considered also as a phase shift for 90 degrees for the process $x(t)$. In principle transform with the other phase shifts can be considered too. Figure 9 shows the results of the phase shift with

different angles γ ($\pi/4$, $3\pi/4$, π , $5\pi/4$, $3\pi/2$). This reveals the geometric interpretation of the envelope as a location of peaks of all possible processes obtainable from the original one with the phase shift.

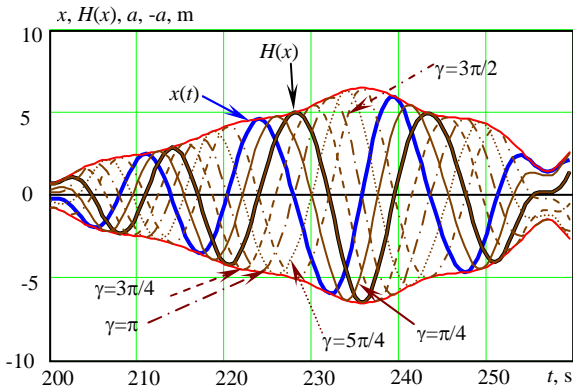


Figure 9: The Envelope and Phase-shifted Processes

This geometric interpretation of the envelope definition (18) also suggests that the local maximum of the envelope may correspond to a peak of the phase-shifted process. For example, the maximum value of the envelope shown in Figure 8 corresponds to the negative peak of the Hilbert transform of the process x (shift $\pi/2$) and not to any value of the process $x(t)$ observed during the considered time interval. Thus using the definition (16) may be not appropriate for the statistical procedure as it may bring so-called “false peaks” that could occur if the phase is shifted. Instead, an approximate peak-based envelope is considered, which is represented by a broken line connecting the absolute values of peaks of the process, see Figure 10.

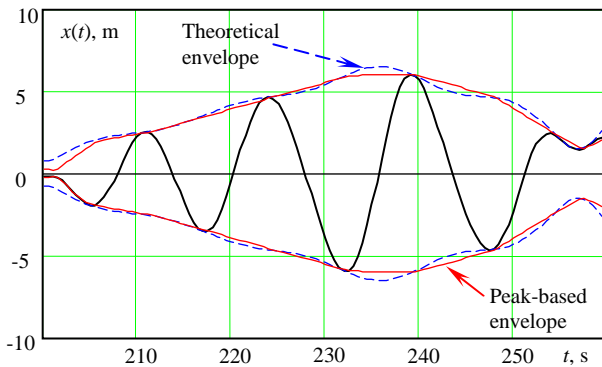


Figure 10: Peak-based and Theoretical Envelopes

It can be shown that a peak-based envelope is a reasonable approximation for the theoretical envelope for the cases of narrow band spectrum (Belenky & Campbell, 2011). For the moderate bandwidth process such as wave elevations, the peak-based envelope behaves differently.

The power of the envelope theory is in the closed-form results available if the original process is normal. These results include (but are not limited to): the distribution of the envelope (Rayleigh), the distribution of the derivative of the envelope (normal), the joint distribution of the instantaneous value and its derivative, and the autocorrelation function of the value of envelope. Figure 11 shows the comparison between the marginal distribution of the values and the derivatives for the theoretical and peak-based envelopes.

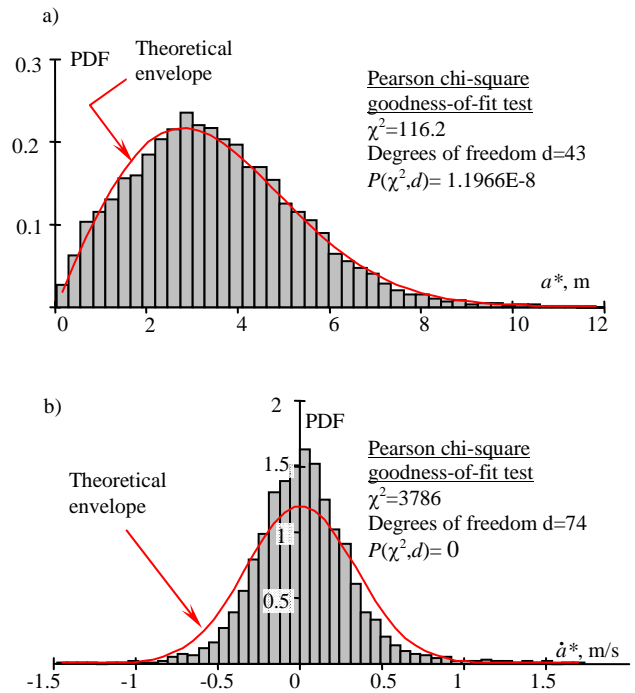


Figure 11: Distributions of the Value (a) and the Derivative (b) of the Theoretical (Solid Line) and Peak-Based Envelope (Histogram)

As it can be expected, the theoretical distributions are rejected for the peak-based envelope. Despite the fact that the distribution of the instantaneous values of the peak-based envelope visually looks Rayleigh-like, the Pearson chi-square goodness of-fit test rejects



this hypothesis. The distribution of the derivatives of the peak-based envelope is also not supported by theory of the envelope. At the same time, if use of the peak-based envelope is limited to registering the exceedances, the inapplicability of the envelope distributions is not relevant, especially, since the initial process is not expected to be normal.

7. BOTH-SIDES CROSSING AND ABSOLUTE VALUE OF PEAKS

As its was already stated in this paper, the motivation for the development of EPOT method was the ability to assess partial stability failure for the both sides, accounting for possible dependence between the positive and negative exceedances. It then makes sense to introduce a both-sides crossing, a random event of upcrossing a given positive value or downcrossing also given negative value. In a general case of a stationary differentiable process, the rate of this random event is expressed as

$$\lambda_{ab} = \int_0^{\infty} f(a, \dot{\phi}) \dot{\phi} d\dot{\phi} - \int_{-\infty}^0 f(b, \dot{\phi}) \dot{\phi} d\dot{\phi}, \quad (21)$$

where a is a given positive threshold and b is given negative threshold. If the process is normal and $a=|b|$, the rate λ_{ab} becomes:

$$\lambda_{ab} = \frac{1}{\pi} \sqrt{\frac{V_{\dot{\phi}}}{V_{\phi}}} \exp\left(-\frac{a^2}{2V_{\phi}}\right). \quad (22)$$

Similar to the case of upcrossings, there is analogy between the random events of both-sides crossing and the exceedance of the positive level by the absolute value of peaks. Probabilistic properties of the absolute values of peaks appear to be similar to those of peaks. Figure 12 shows distribution of the absolute value of the local peaks of wave elevations. Its main difference of the positive peak histogram shown in Figure 5 is “thick” initial part. Trivial enough, the secondary peaks are “folded” onto positive domain. The Pearson chi-square goodness of fit test shows that the truncated Rayleigh distribution is applicable starting with about 1.8 m with the probability of 8.8%.

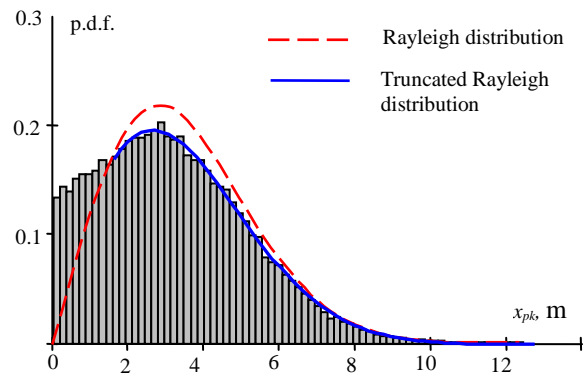


Figure 12: Distribution of Absolute Values of Peaks of Wave Elevations

Statistical estimates of the event rate of the both-sides crossings and the exceedance of the positive level by the absolute value of peaks can be carried out in very similar manner as it was done for upcrossings and peak exceedances. The same can be said on the statistical uncertainty of these estimates. Comparison of these estimates with the theoretical value (20) for the wave elevations has yielded the trivial results shown in Figure 13. Nevertheless, this triviality confirms that the theories involved have been interpreted correctly.

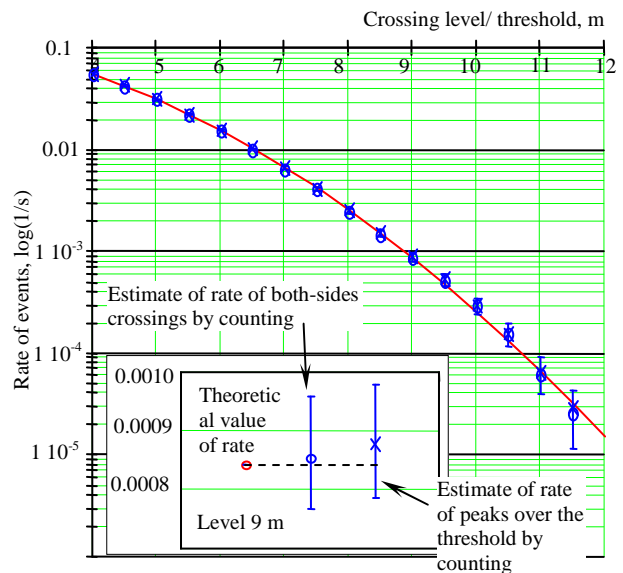


Figure 13: Comparison of Statistical Estimates of Rate of Events of Both-sides Crossings and Exceedances of Absolute Values of Peaks with Theoretical Values

8. ENVELOPE PEAK OVER THRESHOLD (EPOT)

The formulation of the EPOT method is analogous to the POT method examined in Section 5. The differences are as follows:

- the peak-based envelope is used for the non-rare problem
- the absolute values of peaks exceeding the threshold are used to fit the distribution for rare problem (if peak distribution option is used)
- the absolute values of the process above the threshold are used for fitting the extreme value distribution (is the extreme value distribution option is used)

Other than that, the same formulae (15-17) are applicable.

The difficulty associated with this formulation of EPOT is the absence of the theoretical solution. This is a result of application of the peak-based envelope. Nevertheless three approximate solutions can be used for initial validation of EPOT.

For a relatively high level of upcrossing, the difference between the probability of upcrossing of the theoretical envelope and the peak-based envelope may not be that significant, as a large peak of the process belongs to both the theoretical and peak-based envelopes. Therefore the first candidate for the theoretical solution is the rate of upcrossing of the theoretical envelope

$$\lambda_e = a \sqrt{\frac{(\omega_2^2 - \omega_1^2)}{2\pi V_x}} \exp\left(-\frac{a^2}{2V_x}\right), \quad (23)$$

where ω_1 is the mean frequency, ω_2^2 is the second moment of the spectral area, normalized by the variance of the process V_x ; a is the level of crossing. The derivation of this formula is trivial as the distribution of the envelope is Rayleigh and its derivative is normal.

For the very same reason, the Rayleigh distribution can be assumed for the rare solution. The upcrossing rate in the non-rare solution can be approximated as:

$$\xi = \exp(c_0 + c_1 a_1 + c_2 a_1^2), \quad (24)$$

For the purpose of numerical example the coefficients c_0 , c_1 , and c_2 are evaluated from statistics with a least-squares method, see Figure 14.

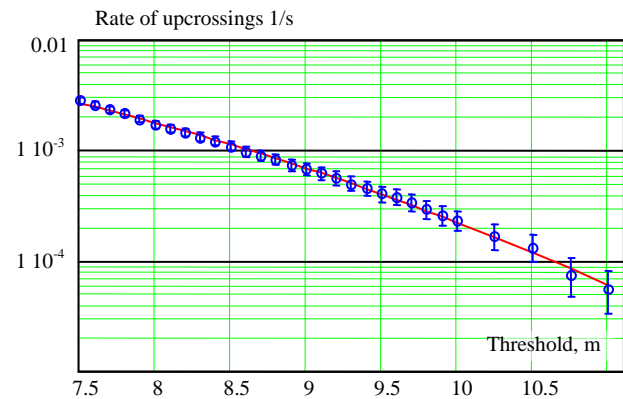


Figure 14: Rate of Upcrossing of the Peak-Based Envelope.

For the very large level of crossings, it may also be possible to use formula (22); it may be so rare that crossing occurs only on one side, so upcrossings of the peak-based envelope and the process itself are identical events.

The comparison is shown in Figure 15 confirms the ability of the EPOT method to yield reasonable predictions with statistical extrapolation. This example, of course, cannot be considered as the complete validation. It should be considered as the most basic step – the ability to reproduce known (however approximate) solution. The problem of validation of EPOT method, as well as a general problem of validation of an extrapolation method for probabilistic ship dynamic assessment is well beyond the scope of this paper.

As there is some scatter with choice of threshold, the extrapolation is performed using several thresholds and the results are averaged. This averaging step is an attempt to balance bias (which may be present for low thresholds) versus scatter (which may be present for high thresholds).

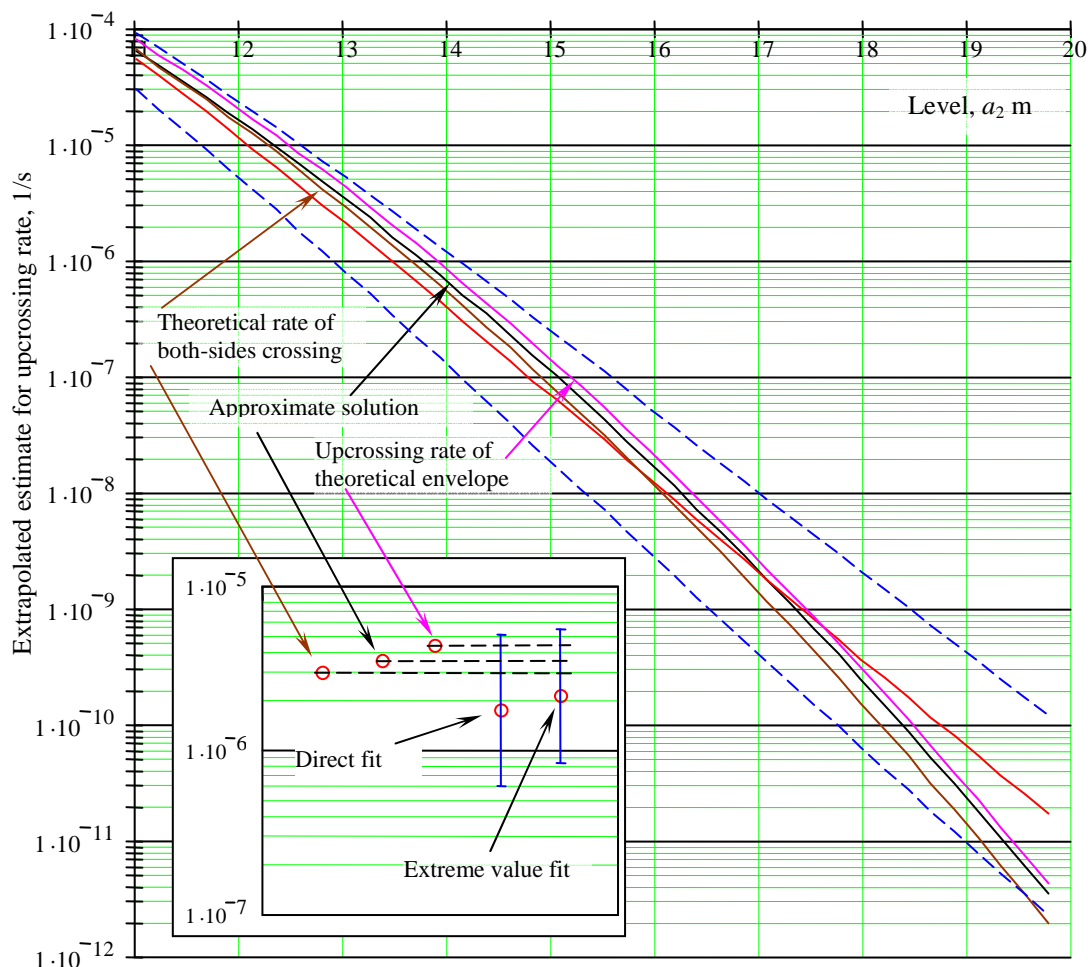


Figure 15: Extrapolated Rate of Upcrossing of the Peak-based Envelope Using Extreme Value distribution. Insert Shows the Extrapolation for the Level of 13 m using both Peak and Extreme Value Distribution. (Campbell & Belenky, 2010)

9. SUMMARY

The objective of this paper was to review basic studies carried out in support of development of the EPOT extrapolation method for the probabilistic assessment of dynamic stability.

The central issue is the relationship between the probability of stability failure and the time of exposure. If the sequential events can be considered as independent, upcrossing theory allows us to relate the probability of failure and the exposure time through the Poisson distribution. The event rate is the only number that needs to be estimated from the sample

data. It was shown that the best way of estimating the event rate is through averaging the number of events per unit of time (this is the direct counting method).

The extreme value distribution can also be used to relate probability with time, as it is associated with a fixed time window. The event rate can be derived from the extreme value distribution; the estimate is statistically identical to that obtained from upcrossing theory.

Probabilistic properties of peaks are also related with time. Events of upcrossing a level and encountering a peak exceeding this level are equivalent if the level is large enough.



Partial stability failure may occur through rolling to both sides of a ship. The peak-based envelope can be used instead of the process itself to avoid dependence between the subsequent port and starboard events. The paper considers some differences between theoretical and the peak-based envelope.

Finally the paper reviews formulation for POT and EPOT and compares EPOT result for wave elevation with approximate theoretical solution

10. ASKNOWLEGEMENTS

The authors wish to thank J. Brown for his support and patience in bring this work to fruition. The work is based on the results of research funded by ONR under Dr. Patrick Purtell. The authors are grateful to Dr. Arthur Reed and Prof. Pol Spanos for their support and guidance in this work.

11. REFERENCES

- Belenky, V., and B. Campbell (2011). Evaluation of the Exceedance Rate of a Stationary Stochastic Process by Statistical Extrapolation Using the Envelope Peaks over Threshold (EPOT) Method. Naval Surface Warfare Center Carderock Division Report NSWCCD-50-TR-2011/032, 216 p.
- Belenky, V., Weems, K.M., Bassler, C.C., Dipper, M.J., Campbell, B., Spyrou K., (2012) "Approaches to Rare Events in Stochastic Dynamics of Ships", Probabilistic Engineering Mechanics 28 (2012) 30–38.
- Beck, R. F. & A. M. Reed, (2001). "Modern computational methods for ships in seaway". Trans. SNAME, Vol. 109, pp. 1–48.
- Campbell, B. and V. Belenky (2010) "Assessment of Short-Term Risk with Monte-Carlo Method" Proc. 11th Int. Ship

Stability Workshop, Wageningen, the Netherlands

- Cohen, C. A. (1965) Maximum Likelihood Estimation in the Weibull Distribution Based on Complete and On Censored Samples. Technometrics, 7(4):579–588.
- Gumbel, E. J. (1958) Statistics of Extremes. Columbia University Press, New York.
- Kramer, H. and Leadbetter, M.R. (1967). Stationary and Related Stochastic Processes, John Wiley, New York
- Leadbetter, M.R., Lindgren G. & H. Rootzen (1983) Extremes and Related Properties of Random Sequences and Processes, Springer-Verlag, N.Y.
- Leadbetter, M.R. (1991) "On a Basis on Peak-over-threshold Modeling" Statistics & Probability and Letters Vol. 12, pp.357-362
- McTaggart, K. A. (2000) "Ongoing Work Examining Capsize Risk of Intact Frigates Using Time Domain Simulation". In Contemporary Ideas of Ship Stability, D. Vassalos, M. Hamamoto, A. Papanikolaou & D. Moulyneux (eds), Elsevier Science, pp. 587–595.
- McTaggart, K. A. & J. O. de Kat (2000) "Capsize Risk of Intact Frigates in Irregular Seas". Trans. SNAME, Vol. 108, pp 147–177.
- Meeker, W. O. & L. A. Escobar (1998) Statistical Methods for Reliability Data. Wiley, New York, 680 p.
- Pickands, J (1975) "Statistical Inference Using Extreme Order Statistics". The Annals of Statistics 3(1):119-131.
- Rice, S.O. (1944) "Mathematical Analysis of Random Noise". Bell System Techn J. Vol 23, No 3, pp. 282–332.
- Rice, S.O. (1945) "Mathematical Analysis of Random Noise". Bell System Techn J. Vol. 24 No 1, pp. 46–156.



Sevastianov, N. B. (1963) “On Probabilistic Approach to Stability Standards”. Trans. Kaliningrad Institute of Technology, Vol. 18, pp. 3–12. (in Russian)

Sevastianov, N. B. (1994) “An Algorithm of Probabilistic Stability Assessment and Standards”. Proc. 5th International

Conference on Stability of Ships and Ocean Vehicles, Melbourne, Florida, USA, Vol. 5.

Smith, R.L. (1985) “Threshold Methods for Sample Extremes”, in:., Statistical Extremes and Applications, J. Tiago de Oliveira, ed. NATO ASI Series (Reidel, Dordrecht) pp. 623-638.



Parameter Estimation of a Mathematical Model Used for Ship Motions in Following Seas Based on the Data Assimilation

Daisuke Terada, *Fisheries Research Agency*, dterada@affrc.go.jp

Hirota Hashimoto, *Osaka University*, h_hashi@naoe.eng.osaka-u.ac.jp

Akihiko Matsuda, *Fisheries Research Agency*, amatsuda@affrc.go.jp

Naoya Umeda, *Osaka University*, umeda@naoe.eng.osaka-u.ac.jp

Tomohiro Furukawa, *Osaka University*, tomohiro_furukawa@naoe.eng.osaka-u.ac.jp

ABSTRACT

A new procedure for parameter estimation of a mathematical model used for ship motions in following seas, based on the data assimilation that is a new statistical technique, is proposed. In this paper, surge motion in astern seas is focused on. In order to examine the effectiveness of the procedure, numerical experiments and model experiments are carried out. In numerical experiments, the ONR tumblehome topside vessel as the sample ship is used. In model experiments, the ONR flare topside vessel as the sample ship is used from the viewpoint of the accuracy of measured data. Obtained findings are reported.

Keywords: Successive data simulation, Monte Carlo filter, General state-space model, surfriding.

1. INTRODUCTION

In this study as to a mathematical model of ship motions in following seas, a new methodology for parameter estimation that is called successive data assimilation is applied. In this methodology, the parameter estimation can be achieved as a framework of a general state-space modeling procedure. That is, the mathematical model used for ship motions in following seas is dealt with as the system model in the general state-space model. Moreover, results of numerical calculation by the mathematical model are improved by using observation data sequence obtained from some methods. In this case, the goodness of estimated results can be evaluated by a log likelihood that is one of the statistical criteria,

and this is most significant point of this methodology. A little past, one of the authors succeeded to identify the maneuverability indices in Nomoto's linear maneuvering model called *KT* model based on successive data assimilation (Terada and Kitagawa, 2009).

On the other hand, as to the mathematical model for broaching prediction in following and stern quartering seas, it has been shown that the 4 degrees of freedom (4 DOF) model developed by Hashimoto et al. (2011) can be done good estimation calculation with respect to the broaching phenomenon comparison with other models. Therefore, we use the model of Hashimoto et al. (2011) as the mathematical model for ship motions. Here, for simplicity, we only focus on ship motions in following



seas, attempt to estimate parameters of the 1 degrees of freedom (1 DOF) model with respect to surge motion only.

The verification of the proposed procedure is carried out based on numerical experiments and model experiments. In numerical experiments, in order to reproduce time series data sequence, as mentioned before the model of Hashimoto et al. is used. In this case, we used the ONR tumblehome topside vessel as the sample ship as well as the study of Hashimoto et al. (2011). Condition in numerical experiments is nominal Froude number (F_n) = 0.2, 0.3 and 0.4, and we chose propeller revolution number and wave exciting surge force as unknown parameters. Note that factors for propeller thrust and resistance have been obtained from model experiments beforehand are required. In model experiments, we used the data that is carried out by Furukawa et al. (2011). In this case, the sample ship is the ONR flare topside vessel. The reason about the difference of the sample ship is that the accuracy of measurement of position of the ship in the basin is improved by introduced new measurement device. Therefore, the relative velocity of the ship can be calculated by using this measured position of the ship, and we can use it as the observation data in the general state-space modeling procedure as well as numerical experiments. Condition in model experiments is nominal F_n = 0.3 and 0.4, and we chose wave exciting surge force as unknown parameters.

From results of numerical experiments, it is confirmed that estimated values of unknown parameters are good agreement with true values of them. And from results of model experiments, it makes clear that the parameter estimation based on the 1 DOF mathematical model for surge motion has some problems. Here, we report the detail of obtained findings and future task.

2. MATHEMATICAL MODEL

In the 4 DOF model proposed by Hashimoto et al. (2011), when we only consider ship motions in the following seas that is the encounter angle with the ship and waves = 0, the model is simplified the following 1 DOF model for surge motion:

$$\frac{d(\xi_G/\lambda)}{dt} = (u - c)/\lambda \quad (1)$$

$$\frac{du}{dt} = \frac{T(u; n) - R(u) + X_a \sin k(\xi_G + \varepsilon_x)}{m + m_x} \quad (2)$$

Here,

$$c = \sqrt{\frac{g\lambda}{2\pi} \left\{ 1 + \left(\frac{2\pi\zeta_a}{\lambda} \right)^2 \right\}} \quad (3)$$

$$X_a = -\rho g \zeta_a k \sqrt{F_c^2 + F_s^2} \quad (4)$$

$$\varepsilon_x = \tan^{-1}(F_s/F_c) \quad (5)$$

$$F_c = \int_{AE}^{FE} \left\{ S(x) e^{-kd(x)/2} \cos kx \right\} dx \quad (6)$$

$$F_s = \int_{AE}^{FE} \left\{ S(x) e^{-kd(x)/2} \sin kx \right\} dx \quad (7)$$

where, c is wave celerity, u is surge velocity, $T(*)$ is propeller thrust, n_p is propeller revolution number, $R(*)$ is ship resistance, X_a is amplitude of wave exciting surge force given as Equation (4), ε_x is phase difference of wave exciting surge force given as Equation (5), ζ_G is longitudinal position of centre of gravity from wave trough, λ is wave length, m is ship mass, m_x is added mass in surge, ζ_a is wave amplitude, $S(x)$ is breadth of each section and

$d(x)$ is draught of each section, respectively. Here, propeller thrust is given as follows:

$$T = (1 - t_p) \rho n_p^2 D_p^4 K_T(J) \quad (8)$$

$$J = \frac{(1 - w_p) u - u_p^W}{n_p D_p} \quad (9)$$

$$u_p^W = -\zeta_a \omega \exp(-kz_p) \times \cos(2\pi \xi_G/\lambda + kx_p) \quad (10)$$

where, t_p is thrust deduction factor, ρ is water density, D_p is propeller diameter, K_T is thrust coefficient of propeller, J is advance coefficient, w_p is effective propeller wake fraction, $k (=2\pi/\lambda)$ is wave number, $\omega (= \sqrt{k/g})$ is wave frequency, x_p is propeller position in x direction and z_p is propeller position in z direction, respectively. Here, the $K_T - J$ curve obtained from propeller open test is shown in Figure 1. Note that we assume $t_p = 0$ and $w_p = 0$ by considering the astern shape of sample ships. And, ship resistance coincide with full scale is calculated by using results obtained from the model test with respect to resistance. The relationship between ship speeds and ship resistance is shown in Figure 2.

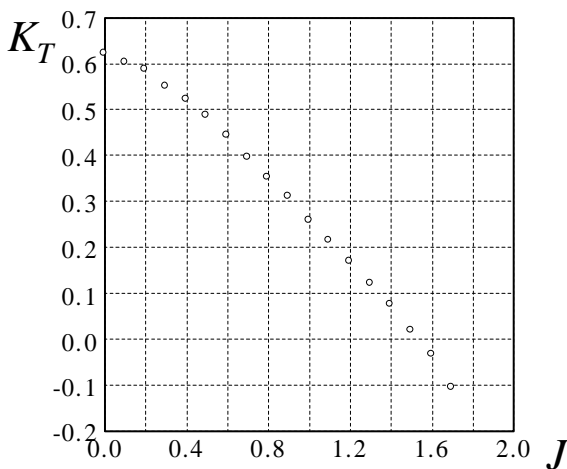


Figure 1: $K_T - J$ curve to estimate propeller thrust in numerical experiments and model experiments.

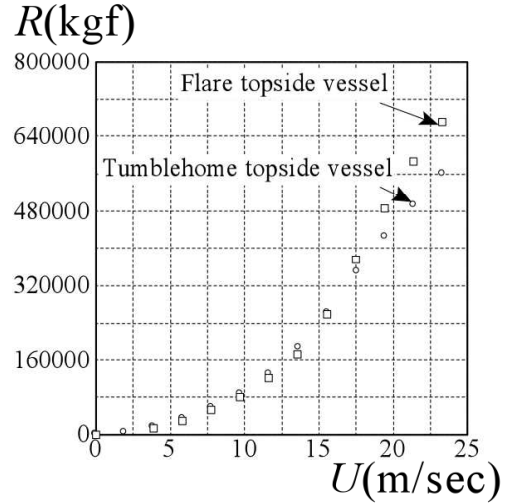


Figure 2: The relationship between ship speeds and ship resistance in full-scale ships

In this study, Equation (1) and (2) are discretized based on the 4-th order Runge-Kutta rule, and ξ_G/λ and u are calculated at intervals of 1/1000 of observation interval. Note that these discretized models are used as the system model in the General State-Space (GSS) modeling procedure. Then, the state vector in numerical experiments and in model experiments is defined as follows:

$$\mathbf{x}(n) = \left[\frac{\xi_G}{\lambda}, u_n, F_s, F_c \right]^T \quad (11)$$

where, notation T means transpose of vector.

3. GENERAL STATE-SPACE MODEL

The successive data assimilation combined with the time series analysis in field of statistical science and computational science is new methodology for data analysis (Nakamura et al., 2005). In this methodology, the mathematical model for the prediction of the phenomenon is treated as the system model of the GSS model in the time series analysis, and the improvement of prediction and the parameter estimation are simultaneously achieved as results of state estimation concerning the GSS model.



As mentioned before, although the system model in the GSS model is the discretized Equation (1) and (2), for simplicity this expresses the following vector form.

$$\mathbf{x}(n) = f(\mathbf{x}(n-1), \mathbf{v}(n)) \quad (12)$$

where, $\mathbf{v}(n)$ is the 4 dimensional white noise sequence with mean 0 and variance co-variance matrix as $diag(\tau^2, \tau^2, 0, 0)$ which is introduced to treat simulation model statistically.

If we can observe the relative velocity with waves, the corresponding to Equation (12) observation model in the GSS model is as follows.

$$y(n) = [0, 1, 0, 0] \mathbf{x}(n) + w(n) \quad (13)$$

where, $y(n)$ is the observation data of the surge velocity and $w(n)$ is the Gaussian white noise sequence with mean 0 and variance σ^2 .

The GSS model in this study contains Equation (12) and (13), and we replace them as follows:

$$\begin{cases} \mathbf{x}(n) = f(\mathbf{x}(n-1), \mathbf{v}(n)) \\ y(n) = [0, 1, 0, 0] \mathbf{x}(n) + w(n) \end{cases} \quad (14)$$

4. MONTE CARLO FILTER

To implement the state estimation of Equation (14), we apply the Monte Carlo filter was proposed by Kitagawa (1996) that is effective to the nonlinear non-Gaussian state-space modeling. It should be noted that in this section, the symbol (n) that is a meaning of variable for the time used in Equation (14) is expressed by subscript symbol, for simple expression of equations. In this method, each probability density function that is the predictor $p(\mathbf{x}_n | \mathbf{Y}_{n-1})$ and the filter $p(\mathbf{x}_n | \mathbf{Y}_n)$; where \mathbf{Y}_n is

the set of observations $\{y_1, \dots, y_n\}$, is approximated by j particles, which can be regarded as independent realizations from that distribution. According to Kitagawa (1996), can be shown that these particles can be recursively given by the following Monte Carlo Filter algorithm:

[Step 1] Generate the 4 dimensional random number $f_0^{(i)} \sim p_0(x)$ for $i = 1 \sim j$.

[Step 2] Repeat the following steps for $n = 1 \sim N$.

(a) Generate the 4 dimensional random number $v_n^{(i)} \sim q(v)$ for $i = 1 \sim j$.

(b) Compute the following equation:

$$p_n^{(i)} = f(f_{n-1}^{(i)}, v_n^{(i)}) \quad (15)$$

(c) Compute the likelihood function as follows:

$$\alpha_n^{(i)} = \frac{1}{\sqrt{2\pi\sigma^2}} \exp\left\{-\frac{(y_n - \mathbf{H}p_n^{(i)})^2}{2\sigma^2}\right\} \quad (16)$$

(d) Generate $f_n^{(i)}$ according the following probability for $i = 1 \sim j$ by the resampling of $p_n^{(1)} \sim p_n^{(j)}$.

$$\Pr(f_n^{(i)} = p_n^{(i)}) = \frac{\alpha_n^{(i)}}{\alpha_n^{(1)} + \dots + \alpha_n^{(j)}} \quad (16)$$

(e) Return to (a).

5. EXPERIMENTS AND DISCUSSION

5.1 Numerical experiments

In order to examine the effectiveness of proposed method for the parameter estimation, numerical experiments that are complete blind test are firstly carried out. In numerical

experiments, unknown parameters are the propeller revolution and the components of wave exciting force. Sample ship is the ONR tumblehome topside vessel. Principal perpendiculars are shown Table 1. As mentioned before, true values of surge motion in numerical experiments are reproduced based on Equation (1) and (2). The characteristics of thrust and resistance shown in Figure 1 and 2 are used. Experimental condition for ship speed is $F_n = 0.2, 0.3$ and 0.4 , respectively. As to wave conditions the wavelength to ship length ratio λ/L is 1.25 and the wave steepness H/λ are $1/20$. True values of unknown parameters are summarized in Table 2. The reproduced time series data is shown in Figure 3. In this figure, (a) shows results of ξ_G/λ , (b) shows results of u , respectively. In these figures, the straight line indicates results of $F_n = 0.2$, the broken line indicates results of $F_n = 0.3$ and the dot line shows results of $F_n = 0.4$, respectively. We emphasize that this numerical experiments are complete blind test. These time series data and information shown in Table 3 were provided by Hashimoto. Terada and Matsuda did the parameter estimation based on the calculation program originally developed.

Table 1. Principal perpendiculars of the ONR tumblehome topside vessel.

	Ship
Length over all: L	154.0 m
Breadth: B	18.8 m
Depth: D	14.5 m
Mean draught: d	5.5 m
Initial trim: τ_0	0.0 rad
Displacement: W	8507 ton
Block coefficient: C_b	0.535

Table 2. True values of unknown parameters.

	Propeller revolution number [rps]	Wave exciting force [kgf]
$F_n = 0.2$	1.33	648806.0
$F_n = 0.3$	2.02	
$F_n = 0.4$	2.78	

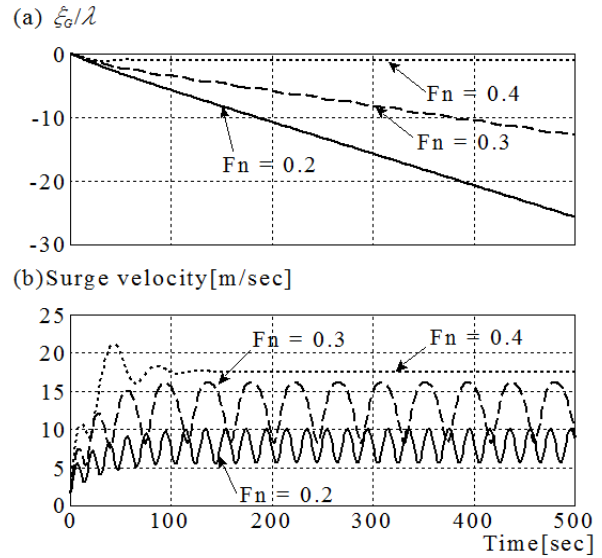


Figure 3: Reproduced time series data.

Table 3. Given data for calculations.

L [m]	g [m/s ²]	m [kgf s ² /m]	m_x [kgf s ² /m]
154.0	9.81	868071.4	86807.1
D_p [m]	x_p [m]	z_p [m]	ρ [kgf s ² /m ⁴]
5.22	65.0	6.51	102.5

Propeller revolution number in estimation calculation was changed in increments of 0.01. The good fit to the data of the model and parameters can be measured by the log likelihood obtained from Equation (16), and the case of maximum log likelihood is chosen as the best one. The log likelihood in each estimation calculation is summarized as in Table 4. From this table, we can see that as to the propeller revolution number in $F_n = 0.2$ and 0.3 , 1.33 [rps] and 2.02 [rps] are chosen as the best one from the view point of the log likelihood. This is completely agreement with true values. On the other hands, we can see that

Table 4. The log likelihood in each propeller revolution number.

$F_n = 0.2$		$F_n = 0.3$		$F_n = 0.4$	
Propeller revolution number [rps]	Log likelihood	Propeller revolution number [rps]	Log likelihood	Propeller revolution number [rps]	Log likelihood
1.20	8720.188	1.90	8710.671	2.70	8695.350
1.30	8726.710	2.00	8719.271	2.71	8696.180
1.31	8726.960	2.01	8719.414	2.72	8696.923
1.32	8727.142	2.02	8719.447	2.73	8697.532
1.33	8727.200	2.03	8719.277	2.74	8698.168
1.34	8727.158	2.04	8718.995	2.75	8698.691
1.35	8727.066	2.05	8718.543	2.76	8699.174
1.36	8726.860	2.06	8717.909	2.77	8699.609
1.37	8726.456	2.07	8717.104	2.78	8699.931
1.38	8726.063	2.08	8716.072	2.79	8700.128
1.39	8725.552	2.09	8714.916	2.80	8700.277
1.40	8724.856	2.10	8713.530	2.90	8697.629



as to the propeller revolution number in $F_n = 0.4, 2.83$ [rps] is chosen as the best one from the view point of the log likelihood. Although the difference of the estimated propeller revolution number and the true one is about 2.2%, we can consider that the good estimation calculation was realized.

Form Figure 4 to 6 shows estimated results of state variables shown in Equation (13). Figure 4 is results of $F_n = 0.2$, Figure 5 is results of $F_n = 0.3$ and Figure 6 is results of $F_n = 0.4$. In these figures, (a) shows results of $\dot{\xi}_G/\lambda$, (b) shows results of u , (c) shows results of sine component of wave exciting force F_s and (d) shows results of cosine component of wave exciting force F_c , respectively. In (a) and (b), the symbol \circ is true values and the straight line is estimated one, respectively. In this case, estimated values indicate the expectation of the filter distribution. From these figures, we can see that estimated results of variables, which is calculated by using the estimated wave exciting force shown in (c) and (d), is almost agreement with true values. The estimated wave exciting force calculated based on Equation (4) from estimated results of (c) and (d) is summarized in Table 5 with the true value and the estimation error. In this case, the estimated wave exciting force indicates the time average. We can see that the estimated wave exciting force is good agreement with the true value within 5% in all F_n .

Table 5. Comparison with true values and estimated one with respect to the wave exciting force.

	True values of wave exciting force [kgf]	Estimated values of wave exciting force [kgf]	Error
$F_n = 0.2$	648806.0	670183.36	3.29%
$F_n = 0.3$		681047.86	4.97%
$F_n = 0.4$		660627.25	1.82%

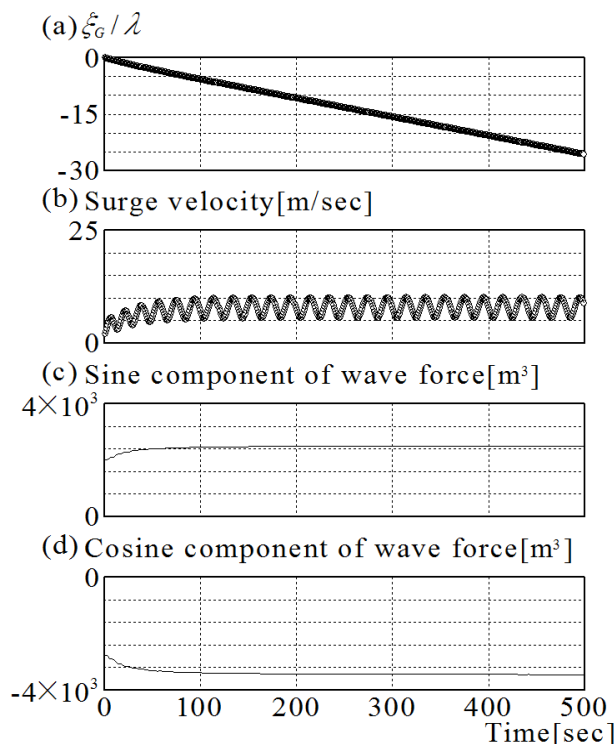


Figure 4: Estimated results of state variables shown in Equation (11) in $F_n = 0.2$.

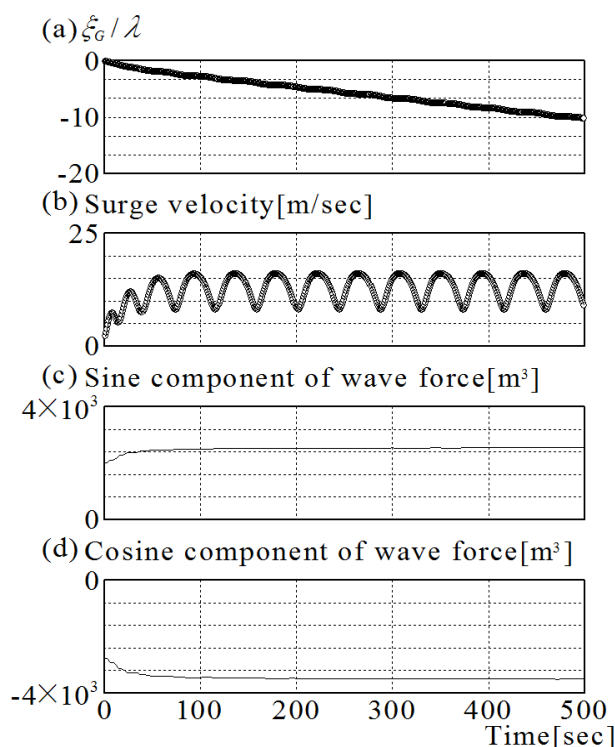


Figure 5: Estimated results of state variables shown in Equation (11) in $F_n = 0.3$.

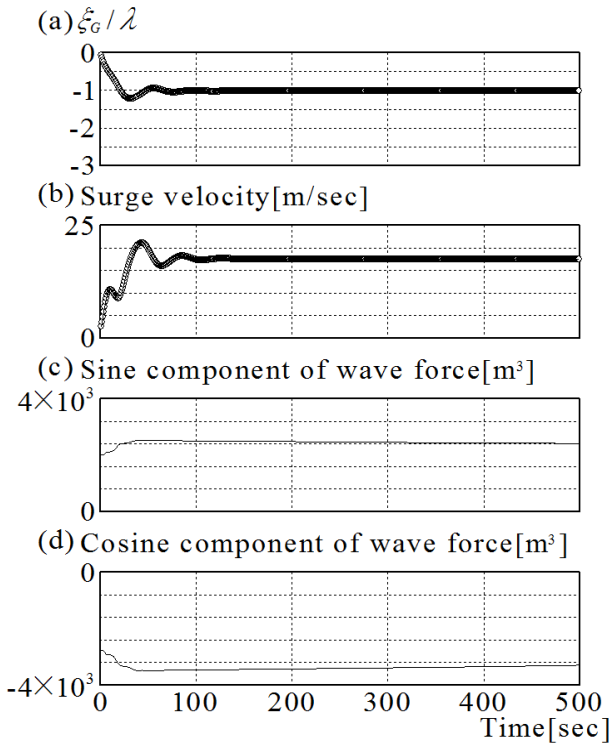


Figure 6: Estimated results of state variables shown in Equation (11) in $Fn = 0.4$.

5.2 Model experiments

Model experiments are next carried out. In model experiments, unknown parameters are only the wave exciting force. Sample ship is the ONR flare topside vessel. Principal perpendiculars are same with Table 1. The characteristics of thrust and resistance shown in Figure 1 and 2 are used. Experimental condition for ship speed is respectively $Fn = 0.3$ and 0.4 and for the desired heading angle for Auto Pilot is 5 degrees. Thus, note that the encounter angle for waves is not the following seas. As to wave conditions the wavelength to ship length ratio λ/L is 1.00 and the wave steepness H/λ are $1/20$. Measured time series data in $Fn = 0.3$ and 0.4 is shown in Figure 7 and 8, respectively. Note that we calculated results of model experiments as one of the full-scale ship. In these figures, (a) indicates the trajectory of the ship, (b) indicates the surge velocity, (c) indicates the roll angle, (d) indicates the pitch angle, (e) indicates the heading angle and (f) indicates the rudder angle, respectively. We can see that the ship

motion is the harmonic in $Fn = 0.3$ and is the surfing after about 80 seconds in $Fn = 0.4$.

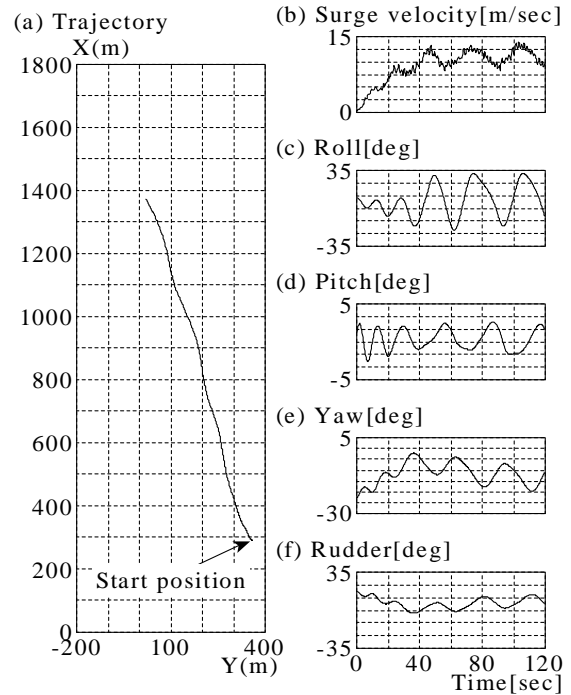


Figure 7: Measured time series data in $Fn = 0.3$.

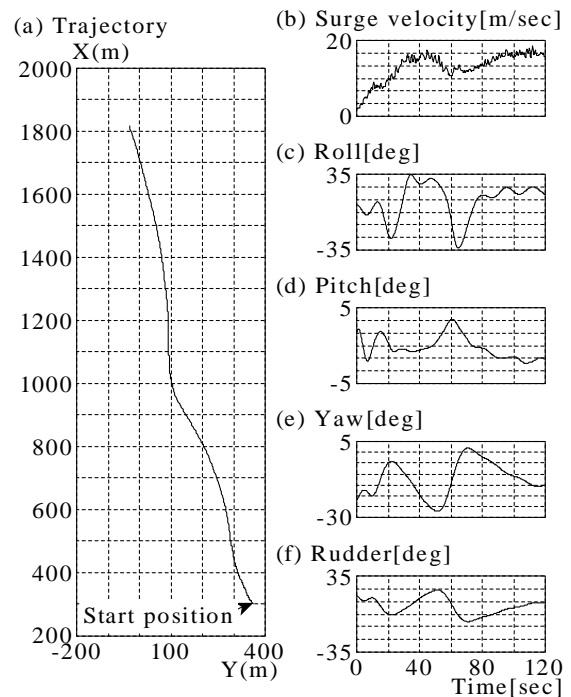


Figure 8: Measured time series data in $Fn = 0.4$.



Figure 9 and 10 show results of the state estimation. In these figures, (a) shows results of ξ_G/λ , (b) shows results of u , (c) shows results of sine component of wave exciting force F_s and (d) shows results of cosine component of wave exciting force F_c , respectively. In (a) and (b), the symbol \circ is measured values and the straight line is estimated one, respectively. In this case, estimated values indicate the expectation of the filter distribution. We can see that when the heading angle is close to 0 degrees, the parameter estimation begin to perform effectively with each case. That is, the case of $Fn = 0.3$ is after about 60 seconds and the case of $Fn = 0.4$ is after about 80 seconds. However, the tendency of phase relation is different between each Fn . It means that the results are not correct. Naturally, the cause is that we used the 1 DOF model. However, when it is expressed in terms of the amplitude of wave exciting force X_a , these values are 2.30×10^5 [kgf] in $Fn = 0.3$ and 1.94×10^5 [kgf] in $Fn = 0.4$, respectively. It is considered that these values are almost same. Therefore, in order to improve the estimation accuracy for

the phase relation, it is necessary to use the 4 DOF model considered the coupling influence between other mode of motions.

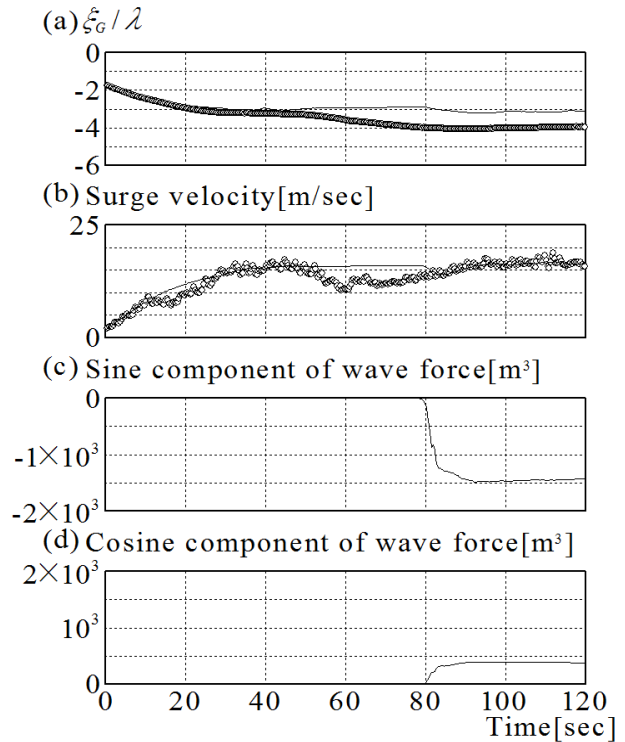


Figure 10: Estimated results of state variable shown in Equation (11) in $Fn = 0.4$.

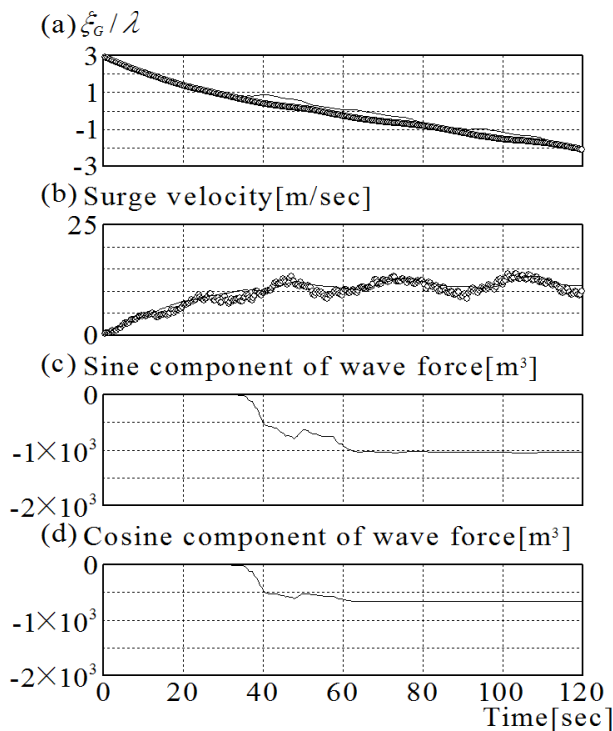


Figure 9: Estimated results of state variable shown in Equation (11) in $Fn = 0.3$.

6. CONCLUSIONS

A new procedure for parameter estimation of a mathematical model used for ship motions in following seas, based on the data assimilation that is a new statistical technique, is proposed. From results of numerical experiments, it makes clear that the proposed procedure is the powerful tool for parameter estimation. From results of model experiments, it makes clear that it is necessary to use the 4 degrees of freedom mathematical model in order to improve the estimation accuracy. This is future task.

7. ACKNOWLEDGMENTS

This work was supported by the US Office of Naval Research contract No.



N000140911089 under the administration of Dr. Patrick Purtell. Computations in the present study were carried out on a High Performance Computing on Vector System at the Agriculture, Forestry and Fisheries Research Information Technology Center for Agriculture, Forestry and Fisheries Research, MAFF, Japan. The authors express this sincere gratitude to the above organizations.

8. REFERENCES

- Furukawa, T., Umeda, N., Matsuda, A., Terada, D. and Hashimoto, H., 2011, "Experimental Study on Above-Water Hull Form Effect on Ship Extreme Motions in Stern Quartering Waves", Proceedings of the Japan Society of Naval Architects and Ocean Engineers, vol. 13 (CD-ROM).
- Kitagawa, G., 1996, "Monte Carlo Filter and Smoother for non-Gaussian nonlinear state space model", Journal of Computational and Graphical Statistics, Vol.5, No.1, pp.1-25.
- Nakamura, K., Ueno, G. and Higuchi, T., 2005, "Data assimilation: Concept and Algorithm", Proceedings of the Institute of Statistical Mathematics, Vol. 53, No. 2, pp.211-229.
- Hashimoto, H., Umeda, N. and Matsuda, A., 2011, "Broaching prediction of a wave-piercing tumblehome vessel with twin screws and twin rudders", Journal of Marine Science and Technology, vol. 16, No. 4, pp.448-461.
- Terada, D. and Kitagawa, G., 2009, "Estimation of the Maneuverability under External Disturbance", Proceedings of 13th International Association of Institutes of Navigation (IAIN) world congress ([http://www.nornav.org/13th - iain - world - congress-and-exhibition-stockholm-october -27th-30th-2009.4518699-27958.html](http://www.nornav.org/13th-ian- world-congress-and-exhibition-stockholm-october-27th-30th-2009.4518699-27958.html)).





Catastrophe Theory: a Modern Approach for the Interpretation of Ship Dynamics in Irregular Waves

Yury Nechaev, *St.Petersburg State Marine Technical University, Russia*, int@csa.ru

ABSTRACT

The establishment of a modern version of catastrophe theory on the basis of integration of classical mathematics, intelligence technologies and high-performance computing is discussed. Basic attention is given on using methods of catastrophe theory in intelligence systems design, whose use is to keep the level of safety of navigation. Examples of practical realization of the developed theory are presented on the operational control of ship dynamics in waves.

Keywords: *catastrophe theory, intelligent system, ship dynamics, irregular waves*

1. INTRODUCTION

Design of new generation intelligent systems (IS) is carried out on the basis of achievements of the catastrophe theory that connect modern mathematical apparatus with high-performance computing. Catastrophe theory serves as a powerful weapon for the processing and formalization of information. It does not replace former methods. Instead, it supplements them with new approaches and models, integrating new knowledge about the dynamics of complex physical systems. A chain of information transformation is thus realized, connecting topological analysis with a systems' synthesis, on the basis of a combination of formal models from the theory of dynamical systems and intelligence technologies.

Catastrophe theory is a mathematical tool that can find application within the limits of XXI century's intelligence technologies. This theory opens ways for seeking not only qualitative, but also quantitative interpretations for processes and phenomena of the real world, not always presuming the facility of experimental check. Indeed, research for sharp, spasmodic changes occurring in the behavior of complex dynamical systems is not always successful on

the basis of physical modeling, while performing suitable natural experiments can be dangerous and often impossible.

Catastrophe theory has arisen as a joint venture of topology with mathematical analysis. Its sources lie in the theory of features of smooth displays of H. Whitney, and also the theory of stability and bifurcation of dynamical systems by A. Poincare, A. Lyapunov and A. Andronov. Merging of these two directions into the uniform harmonious theory with the bright name "Catastrophe Theory" is obliged to efforts of the French mathematician R.Thom (1974) who formulated and proved the core positions of this theory that derives from A. Poincare's idea to study conditions of balance of dynamical systems on the basis of potential functions.

The general approach characterizing methods of the catastrophe theory (Arnold, 1990, Gilmor, 1984, Poston & Steward, 1980, Thom, 1974) can be formulated as follows. Let the mathematical description of behavior of a nonlinear dynamic object be presented in the form of a smooth (differentiable) function (Mathematical Modelling, 1979):

$$\Phi(\theta, \psi, \dots, \zeta) \quad (1)$$



This function determines interrelations of variables (q, y, \dots, z) and let it contain k parameters (C_1, \dots, C_k) . It is possible to determine a set of catastrophes K in the form

$$C = (C_1, \dots, C_k) \quad (2)$$

for which the function $\Phi(\bullet)$ presents some critical points. For the set K , all the partial derivatives

$$\partial\Phi/\partial\theta, \partial\Phi/\partial\psi, \dots, \partial\Phi/\partial\zeta, \quad (3)$$

and also a determinant made of the second derivatives

$$\begin{vmatrix} \frac{\partial^2\Phi}{\partial\theta\partial\psi} & \dots & \frac{\partial^2\Phi}{\partial\theta\partial\zeta} \\ \dots & \dots & \dots \\ \frac{\partial^2\Phi}{\partial\zeta\partial\theta} & \dots & \frac{\partial^2\Phi}{\partial\zeta\partial\zeta} \end{vmatrix} \quad (4)$$

become simultaneously zero at some values (q, y, \dots, z) .

The analysis of this data allows to work out the equation for the set K , containing the parameters C_1, \dots, C_k .

From the moment of inception of catastrophe theory more than 40 years have already passed. Under its influence, new directions of research in the area of topology of complex dynamical systems in various fields of knowledge have been actively developed. In these directions, catastrophe theory does not come as some replacement of more traditional methods, but as a new scientific lead that supports the analysis of qualitative laws and the acquisition of quantitative results for a wide class of fields in the sciences, the arts and the technologies (Arnold, 1990, Gilmor, 1984, Poston & Steward, 1980). At the same time, the classical theory of catastrophes of R.Thom (1974) needs essential expansion and completion. Not only in order to reflect modern lines in research of complex dynamical systems, but also in the formulations and substantiations of various aspects of behavior

of such systems, especially in the conditions of continuous changes in the dynamics of an object and its environment. In essence, it is a quest for a new interpretation of the behavior of nonlinear, non-stationary self-organized systems.

Several years ago I was running a course on «catastrophe theory» so that I could prepare post-graduate students and doctors for this difficult area of mathematics. Valuable input in the training of my pupils in the Moscow State University was offered by the academician V.I.Arnold (1990), who had developed fundamental theoretical results in the field of catastrophe theory as well as in the creation of the theory of features. His advanced mathematical theory offered also possibilities for reducing the required volume of aprioristic information. However, the idea of working out the modern theory of catastrophes belongs to my English and American colleagues. During the International Congress on Applied Mathematics in Edinburgh in 1999, and knowing about my old hobby for topology, some of these colleagues proposed to me, since I was considered as an expert who for several years was dealing with problems of dynamics of nonlinear systems and deterministic chaos, to consider the possibility to formulate the approach and prove the concept of the modern theory of catastrophes (based on essentially new points of view concerning the geometrical and analytical interpretation of the information) in complex dynamic environments characterized by non-stationarity and strong nonlinearity (Nechaev, 2011).

2. PROBLEM STATEMENT

Research on the behavior of complex dynamical systems within the limits of the catastrophe theory is carried out by means of standard procedures that include calculations of critical points for certain parameterized families of functions. It allows to formulate the following research problem of behavior of a

nonlinear non-stationary object functioning in difficult dynamic environment.

Consider an r -parametrical family of functions as follows (Gilmor, 1984, Poston & Steward, 1980) :

$$R^n \rightarrow R, f_{u1}, \dots, f_{ur}(x_1, \dots, x_n) \quad (5)$$

This is equivalent to:

$$f: R^n \times R^r \rightarrow R \quad (6)$$

where: R^n - behavior space; R^r - management space. Our purpose is to classify the properties of these families to within suitable replacements (transformations) of the coordinates which do not change the picture of the critical points. On the basis of such information the analysis of behavior of a nonlinear non-stationary object will be performed, in the course of its evolution in a fuzzy environment (Nechaev, 2011).

From a perspective of system analysis we will consider the principles of construction and synthesis of a conceptual model for the control of ship dynamics on waves on the basis of catastrophe theory. The conceptual model of the considered problem (defining the stream of information during IS functioning), provides the basic system relations that can sustain the functional ability of the whole. It gives the chance to use components comprised of rules of operation (represented below by alphabetical symbols), in accordance to a principle of system decomposition (Mesarovich & Takachara, 1978). Observance of this principle is provided by performing the following rules of system decomposition:

$$R(T) = R(S) \bigcup_i \left(\bigcup_{k=1}^K F(k)(o, a)_i \right); \quad (7)$$

$$R(D) = \bigcup_i \left((o, a)_i \times R(k)(o, a)_i \right); \quad (8)$$

$$\forall \langle o, a \rangle_j \in F(k)(o, a)_i, (F(k)(o, a)_i = 0) \quad (9)$$

where $R(T)$ and $R(D)$ are the elements in the sets representing the decision of a problem of construction of the conceptual scheme for the

investigated problem area: more specifically, $R(T)$ is the set of the allocated pairs $(o, a)_i$ (o - object; a - attribute) at the problem decision on a k - m decomposition step; $R(S)$ is the general number of problems belonging to the considered set; $R(D)$ defines the relation «to depend from» $R(D) \hat{=} R(T) \hat{'} R(T)$; $i=1, \dots, K$; K is the general number of steps towards the decision of a problem $(o, a)_i$, and the condition (9) defines the sequence of decomposition till its end. Lastly, the set $F(k)(o, a)_i$ is such, that

$$\langle o, a \rangle_i \times R(k)(o, a)_i \subseteq R(D) \quad (10)$$

Condition (10) establishes a set of pair names for the objects and attributes from which the value of attribute directed by a problem on an i - m step depends.

In regard to problems of extreme complexity, expansion of fundamental results of the catastrophe theory (Arnold, 1990, Gilmor, 1984, Poston & Steward, 1980) is formulated. This involves a conceptual reorganization of the typical model of catastrophe theory – classical catastrophe of assemblage. By means of such formalization the new theoretical decisions based on models and algorithms of the author (used in practice for working out on-board IS (Nechaev, 2003 & Onboard Intelligence Systems, 2006) have produced some interesting lessons.

3. GENERAL CHARACTERISTIC OF NONLINEAR NON-STATIONARY SYSTEM

As research object, a nonlinear non-stationary system has been chosen, in one of the most complex situations: dynamics of a ship in an emergency condition in waves. This is characterized by complex nonlinear interactions and a continuous change of dynamics (of the object and of its environment) under conditions of uncertainty and incompleteness of the available information. From the point of view of the appendix (body?) of the modern catastrophe theory, it represents a convincing enough example of graphical and



analytical interpretation of behavior of complex dynamical system.

For the construction of the formal control system realizing the concept of dynamics of nonlinear non-stationary object, theoretical models of interaction relating to the dynamics of a ship in an emergency condition in waves (Nechaev, 2011) have been used. As follows from results of research of behavior of a nonlinear non-stationary object in condition of emergency, its dynamics is characterized by the presence of sharp spasmodic changes, depending on the level of external indignations and on other features of the system. For the investigated dynamic object it is possible to consider that the system is “self-organizing” and that its evolution is carried out on the condition of continuous change of dynamics for the object as well as for its environment. Sea waves are represented by the corresponding «climatic spectrum» and by a righting component in the form of the nonlinear spatial function $M(\theta, \varphi, t)$ (Nechaev, 2009). Mathematical models describing dynamics of interaction of ship in emergency with its environment can be derived from the classical model of interaction originally proposed by N.N.Moiseev and further developed in works on ship theories (Onboard Intelligence Systems, 2006). Also, Duffing and Mathieu -type equations can be used for modeling righting components $M(\theta, \varphi, t)$. Classical models of nonlinear dynamics, added by other methods and models, can also be useful and they already find application in current efforts about new generation IS criteria (Nechaev, 2011):

- Methods of a phase plane and statistical tests (Monte-Carlo);
- The theory of chaotic systems and synergetic paradigm.
- Nejro-Fuzzy systems and evolutionary modeling.

The discussed models are characterized by a difficult structure of their dynamics. The

possibility of interpretation of results of hydroaerodynamic interaction of a ship and its environment can be enhanced by the use of certain measurements of dynamics combined with the application of formal mathematical methods. This offers basic advantages like massive? parallelism and nonlinear transformation of the information.

4. FORMAL CATASTROPHE MODEL OF NONLINEAR NON-STATIONARY SYSTEM

By working out the model of catastrophes the problems listed in fig. 1 can be solved. The greatest theoretical interest is represented by the following problems (Nechaev, 2011):

1. Mathematical models, algorithms and program realization of the theory of stability of nonlinear non stationary dynamical systems. Updating of Mathieu’s differential equation (linear model): introduction of nonlinear spatial function of $M(\theta, \varphi, t)$ in the periodic component considering the actually operating righting and revolting components; Updating the Ince-Strut diagram of stability of Mathieu equation (linear model): introduction of nonlinear effects; Estimation of stability of nonlinear non-stationary system on the basis of a functional actions method.

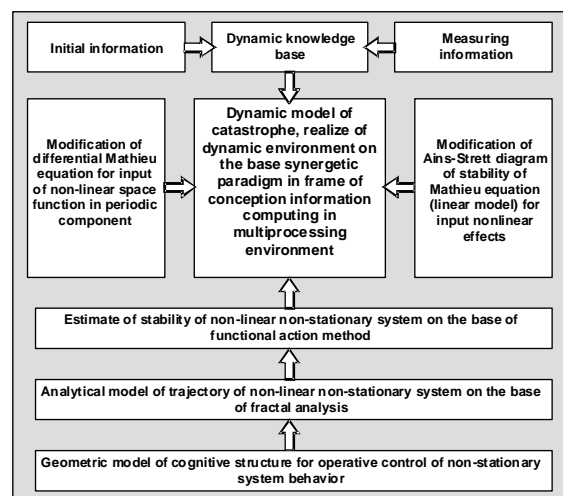


Figure 1: Structure of the dynamic catastrophe model.



A feature of the developed mathematical model (nonlinear Mathieu equation) is that at the right-hand-side of Mathieu's equation no revolting components are present. However, introduction of the function $M(q,y,t)$, obtained on the basis of data processing of physical modeling, automatically includes all components of formal model (Nechaev, 2009): not only the components defined within the limits of a hypothesis of A.N. Krylov, but also diffraction *дифракционную* and interference *интерференционную* whose calculation is practically impossible in the absence of a nonlinear hydrodynamic model of interaction of wave systems during interference of ship and running waves. A feature of the function $M(\theta,\varphi,t)$ as a part of a modified Mathieu equation is that it automatically includes the revolting influence leading to change of parameter as a harmonic function. Thus, the new model allows to overcome the following important problems of interpretation of the dynamic catastrophe model (Nechaev, 2011):

To construct the set displaying the dynamic environment, integrating the influence of external indignations and features of ship dynamics;

To present the dynamic model of catastrophes providing interpretation of current situations in non-stationary dynamic environment.

The developed model, based on a modified Ince-Strutt diagram of stability (linear model), integrates the influence of the nonlinear effects connected with the influence of the function $M(\theta,\varphi,t)$ and the nonlinear *демпфирования* $M_R(\theta',t)$. These components reflect information of ship state evolution (Nechaev, 2011). Function $M_R(\theta',t)$ considers the real interaction of a vessel with an environment for deviations from position of balance, up to full loss of stability (capsizing).

Offered for a stability estimation in development of dynamics of system the method of functional actions is based on development of the theoretical model produced

in research works like (Morce, 1931, Nechaev, 2009). The modified model has received the name of extreme actions (Morce, 1931) for maintenance of an estimation of dynamics of nonlinear non-stationary system in development of a current situation. Formal transformation of the information on the basis of this model is realized in a mode of real time and allows to define probability of capsizing depending on intensity of operating indignations.

2. Construction of model of Ince-Strutt modified diagramme of stability of equation Mathieu (linear model Gilmor, 1984) at the expense of introduction of the nonlinear effects connected with influence of function of $M(\theta,\varphi,t)$ and nonlinear damper $M_R(\theta',t)$, reflecting real transformation of the information at vessel evolution in development of a current situation. And function $M_R(\theta',t)$, considers real of the ship interaction with an environment at the big deviations from position of balance up to full loss of stability (capsizing).

3. Working out of a method of an estimation of stability in development of dynamics of system. This method is based on development of the theoretical model based on a method of functional action. The modified model of functional actions provides an estimation of dynamics of nonlinear non-stationary system in development of a current situation. Formal transformation of the information on the basis of this model is realized in a real time regime and allows to define probability of capsizing depending on intensity of operating indignations.

4. Representation of evolution of dynamics of difficult system on base of synergetic paradigms. The developed model allows to realize dynamics of interaction at interpretation of difficultly formalizable situations within the limits of hypotheses and simplifying assumptions. At the heart of such formalization the geometrical model of behaviour of difficult system in frameworks of the fractal structure



displaying deformation of area, displaying the dynamic environment integrating influence of external indignations and features of dynamics of object is accepted. Possibility of the analysis and the forecast of the current situations connected with blow of collapsing and extreme waves (killer-waves), and also with features of dynamics of loose cargoes as a result opens.

5. Creation of the formal device for construction of cognitive structures at the operative control of a current situation in a real time regime. The basic problem solved in the course of such interpretation, consists in representation of a current situation in idea of a simple and easily perceived image. Unambiguity of identification of model of catastrophe is reached at the expense of use of achievements in area of cognitive modeling and the theory of human-machine systems.

As a result on the basis of achievements of classical mathematics and intelligence technologies the model of the modern theory of catastrophes which is interpreted in on-board intelligence system is created.

The analysis of topology of classical models of catastrophe (Gilmore, 1984, Poston & Steward, 1980, Thom, 1974) has shown, that the fullest description of investigated situations can be reached by means of assemblage catastrophe (Figure 2).

The elements defining this catastrophe, are: $M(t)$ - variety of catastrophe; $F(t)$ - a curve of folds; $\chi(t)$ - catastrophe's display; $B(t)$ - bifurcation set; $C(t)$ - a plane ($a(t)$, $b(t)$); $P(t)$ - an assemblage point; ($x(t)$, $a(t)$, $b(t)$) - set of the points displaying space of catastrophe. The image of $M(t)$ is set by equality ($x(t)$, $-3x^2(t)$, $2x^3(t)$), and bifurcation set $B(t)$ is an image in $C(t)$, set by set of points ($-3x^2(t)$, $2x^3(t)$) = ($a(t)$, $b(t)$). All elements of catastrophe of non-stationary system depend on time t and in the course of evolution continuously change the position. In it, basic difference of the modified model of catastrophe of assemblage from the classical model assumed as a basis for which

all elements are fixed consists and are defined on the basis of standard computing procedures. Thus, the essential lines connected with display of catastrophe, can be presented sequence of spaces:

$$R^2(t) \supseteq R^1(t) \supseteq R^0(t), \quad (11)$$

and bifurcation set $B(t)$ displays this structure and corresponding additional lines that is universality of catastrophes of assemblage. Catastrophe display represents restriction on M of a natural projection:

$$\pi(t): R^n(t) \times R^r(t) \rightarrow R^2 \quad (12)$$

$$\pi(t)[x(t), C(t)] = C(t) \quad (13)$$

where $R^n(t)$ - behaviour space; $R^r(t)$ - management space.

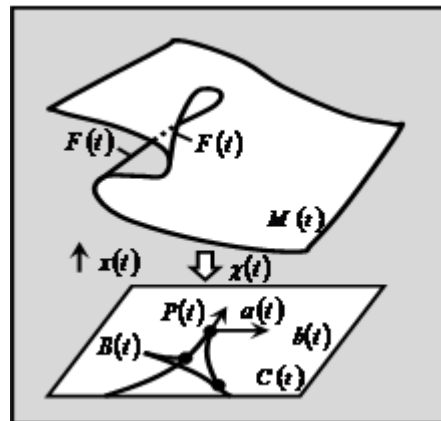


Figure 2: The modified model of assemblage catastrophe of nonlinear non-stationary system.

Bifurcation set $B(t)$ represents an image of special set

$$\chi(t)[S(t)] \subseteq C(t), \quad (14)$$

where $S(t)$ - the variety defining set of points

$$[x(t), C(t)] \in M(t) \quad (15)$$

The set of catastrophe $M(t)$ is represented in the form of subsets the equation

$$DV_e(x,t) = 0, \quad (16)$$



where $V_e(x, t) = V[C(t), x(t)]$ - set of all critical points of potentials $V_e(t)$ from family V .

The important role in a problem of interpretation of considered physical system is played by operating variables (Hayashi, 1964) which are entered for points from (managing directors) and for points from (behavioral) variables. Number r name external dimension (dimension of management). Applying a lemma about splitting for representation of function near to a point where it has co-rank in a kind

$$f(y_1, \dots, y_n) \pm y_{n+1}^2 \pm \dots \pm y_n^2 \quad (17)$$

Allocate essential variables (Hayashi, 1964) y_1, \dots, y_n , and $y_{n+1}^2 \pm \dots \pm y_n^2$ consider as insignificant. On occasion useful there is an introduction of active and passive variables.

So, the entered designations for family of functions

$$f(t): R^n(t) \times R^r(t) \rightarrow R(t) \quad (18)$$

Define spaces internal $R^n(t)$ and external $R^r(t)$ variables which cope by means of the function representing some smooth function $f(t)$. The point $u \in R^n$ for smooth function is called as a critical point, if

$$Df(t)|_u = 0 \quad (19)$$

or in co-ordinates

$$f(t)/x_1|_u = \dots = f/x_n|_u = 0 \quad (20)$$

Value $f(u)$ in a critical point u is called as critical. In a case $n=2$ critical points are classified as local (a minimum, a maximum, an excess point). For $n=2$ $[f(t): R^2(t) \rightarrow R(t)]$ the maximum, a minimum, saddles are most extended.

Changing $a(t)$ at fixed $x(t)$, we receive a straight line in R^3 , the projection которой on a plane $[a(t), b(t)]$ is set by the $b(t) = [-a(t) x(t) - x^3(t)]$. Change $x(t)$ gives the family of straight lines replacing линейчатую a surface, defining

variety of catastrophe $M(t)$. The projection of this family to a plane $[a(t), b(t)]$ gives the family of the straight lines, bending around which characterizes bifurcation set $B(t)$. Hence, the modified model of assemblage displays typical pictures of behavior of difficult physical system and gives bright representation how the variety of catastrophes of $M(t)$ settles down over bifurcation set $B(t)$.

5. DYNAMIC MODEL OF CATASTROPHE

The dynamic model of catastrophe displaying behavior of difficult object, can be presented in the form of a train (Nechaev, 2003):

$$DM(\text{Cat}) = \langle H(\text{Cat}), A(\text{Cat}) \rangle \quad (21)$$

where $H(\text{Cat})$ - a component, interpreting the dynamic environment on the basis of geometrical model of catastrophes; $A(\text{Cat})$ - a component, interpreting the dynamic environment on the basis of analytical model of catastrophes.

Geometrical interpretation of a physical picture of interaction on a basis components $H(\text{Cat})$ looks like:

$$H(\text{Cat}) = \langle B(\theta, t), GZ((\theta, t), C(\theta, t)) \rangle \quad (22)$$

where $B(\theta, t)$ - the bifurcation set representing an image of special set in space of operating parameters; $GZ((\theta, t))$ - the set displaying the dynamic environment, integrating influence of external indignations and features of dynamics of object; $C(\theta, t)$ - the set displaying structural changes in the form of an underwater part of the hull ship, the configurations of an operating waterline caused by continuous change.

Analytical interpretation of a physical picture of interaction on a basis components $A(\text{Cat})$ looks like:

$$A(\text{Cat}) = \langle A(\text{CR}), A(\text{PH}), A(\text{NF}) \rangle \quad (23)$$

where $A(\text{CR})$ - the mathematical model displaying an estimation of the dynamic



environment of interaction on a basis of criteria parities, developed within the limits of standard algorithms of investigated problem area; A(PH) - the mathematical model displaying an estimation of the dynamic environment on a phase plane by means of the theory of stochastic systems, theories of the determined chaos and синергетической paradigms; A(NF) - the mathematical model displaying an estimation of the dynamic environment on the basis of neuro-fuzzy system.

Geometrical and analytical interpretation of complex dynamic system for the modified model of assemblage by methods of the catastrophe theory, is presented on figure 3.

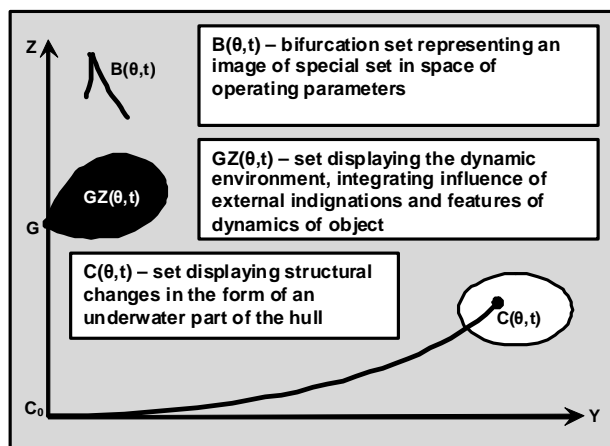


Figure 3: Dynamic model of assemblage catastrophe: geometrical interpretation.

From this drawing it is visible, that the developed model contains three characteristic sets defining dynamics of complex system in the course of its evolution in the non-stationary environment. Sets $B(\theta,t)$, $GZ(\theta,t)$, $C(\theta,t)$ are the integrated characteristics displaying dynamics of process of interaction of a vessel with an environment at various level of external indignations and continuous change of elements of system. At construction of these sets real dynamics of object taking into account influence of the hydro-aerodynamic factors defining model of interaction in the investigated situation is considered. Transition from this general model to concrete realization allows to present dynamics of difficult system

in the form of the modified catastrophe of assemblage.

On Figure 4, integration analytical components at the expense of use of the models based on display of the dynamic environment on a basis of criteria equations A(CR), theories of stochastic systems and the determined chaos, synergetic paradigms A(PH) and theories of neuro-fuzzy systems A(NF) is illustrated.

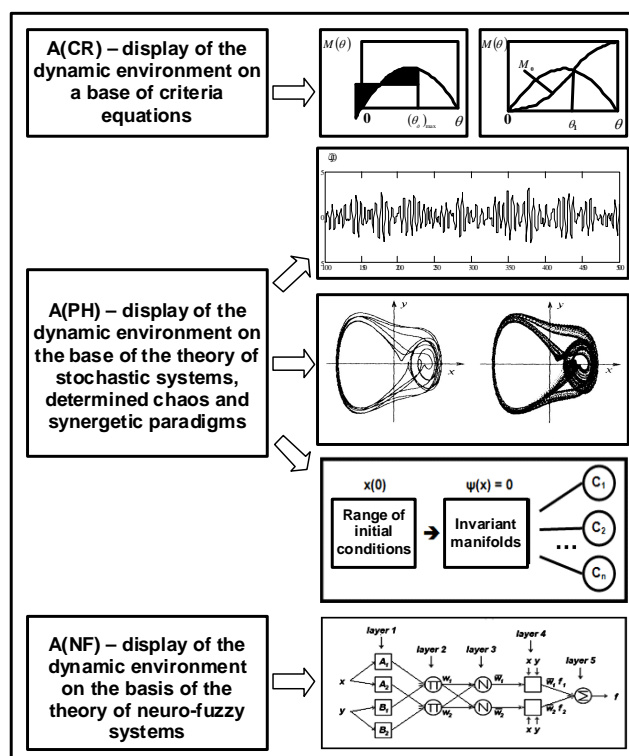


Figure 4: Dynamic model of assemblage catastrophe: analytical interpretation.

The information on conditions of investigated sets at geometrical interpretation in the ship of system evolution is represented in the form of information files of numerical data about functional dependences $B(\theta,t)$, $GZ(\theta,t)$, $C(\theta,t)$, characterizing these sets.

Let's note some general laws in geometrical interpretation of bifurcation sets $B(\theta,t)$, at research of dynamics of a vessel on excitement:

- the point of assemblage P is defined by features of curve $C(\theta,t)$ which is always convex and has a minimum in an initial condition of a ship at $\theta = 0$;

- at small values of a angle θ radiuses of curvature of curve $C(\theta, t)$ in points θ_i ($i=10^\circ, 20^\circ, \dots$) at first increase, and then - start to decrease at increase θ ;
- for courts with a low surface board the set $B(\theta, t)$ usually has no a point of assemblage P and the curve $B(\theta, t)$ gradually moves in a direction of a point of a contact of the curve defining border of area GZ (θ, t) and corresponding to its maximum value.

Difficulties of construction and use of data at the decision of applied problems of the catastrophe theory, including mathematical modeling and forecasting, are connected with definition of functional laws of investigated process by «compression» of the big data files by analytical expressions with the set number of parameters (a direct problem), and also at renewal of values of functional dependences on dark measurements sites of quasi-stationary (a return problem).

Geometrical interpretation of a physical picture of interaction for the nonlinear non-stationary system, realized on the basis of the initial information and the modified model of assemblage by methods of the catastrophe theory, is presented on figure 5.

Here the picture of the modified catastrophe of assemblage with reference to investigated physical system is represented, characteristic points, curves and areas of change of investigated characteristics in plane YZ for the extreme situation characterizing dynamics of an emergency vessel on excitement are shown: m_0 - a metacenter starting position; $m(\theta)$ – metacentric evolute (variety of catastrophe); G_1 - position of the centre of gravity (CG) systems; θ_1 - a corner defining position of balance. Area $GZ(\theta)$ characterizes change of restoring moment $M(\theta)$ for the set corners of a list θ which diagramme is resulted in the right top corner of the screen. Point C_0 is the size centre (CS) a ship at list coal $\theta=0$. The curve $C(\theta)$ describes movings CS depending on q . Radius of curvature of a curve $C(\theta)$ -

метацентрический radius $r(\theta)$ which size at $\theta=0$ defines initial position of the metacenter m_0 . The curve of the metacenters forms metacentric evolute – bifurcation set $B(t)$ the modified model of catastrophe. Owing to symmetry the curve $C(\theta)$ will always have at $\theta=0$ either a local minimum, or a local maximum, and a curve of the metacenters - feature, in this case feature of standard or dual assemblage.

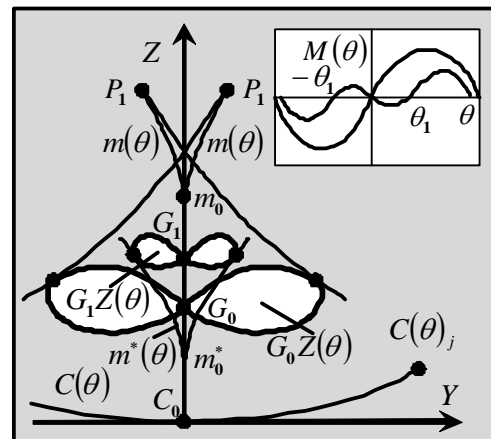


Figure 5: The modified model of the assemblage catastrophe, defining dynamics of an emergency ship on excitement as nonlinear non-stationary system.

Situation interpretation on Figure 5 yields following results. At the moment of occurrence of a hole the system jump moves to a new condition. Occurrence of jump (catastrophe) is caused by sharp change of position of the centre of gravity and deterioration initial metacentric heights owing to formation of the big area of a free surface of a liquid of symmetrically flooded compartment. CG systems practically instantly moves from point G_0 to point G_1 . Thus area $GZ(\theta)$, defining righting moment $M(\theta)$, continuously changing on an irregularity waves considerably decreases, and the ship appears in a critical condition as intensive external indignations can lead to ship overturning. After carrying out of actions for stabilization of a situation the system comes back in area with CG in point G_2 . Non-stationary investigated dynamic processes in a considered situation it is shown



in continuous change of a population mean and a dispersion in the ship of system evolution.

The topological picture on Figure 5 can be added by other points, allowing to consider various conditions of a ship and defining equivalent positions of CG for the capsizing moment, the corners of a list corresponding initial (during the appendix of the heeling moment) and to a final (dynamic) inclination of a ship, and also equivalent positions CG of firm and liquid cargo during loading (unloading) of a ship.

At an estimation of ship stability in critical situations the method of functional actions (Morce, 1931) is used. Realization of this algorithm is based on the stochastic vector equation of indignant of ship dynamics. The operative estimation of stability and probability of capsizing depends on a condition of a ship and current characteristics of wind-wave indignations. The initial information is formed on the basis of the data received from sensors of measuring system. On-board IS uses a topological picture of catastrophe and continuously updates an estimation of probability of capsizing in real time in process of data acquisition about ship rolling. We will notice, that the offered device the asymptotic analysis is new to the management theory dynamic systems, therefore by interface working out «Operator – IS» is provided use of the elementary likelihood schemes for an explanation of the general problematics of the analysis and the forecast of development of an extreme situation. At formalization of the dynamic knowledge base the considered model of catastrophe of assemblage in the ship course of ship evolution is realized within the limits of a quasi-stationary hypothesis. It allows to display on the basis of formal models of fuzzy logic system of functioning IC in a current situation.

6. GEOMETRY OF CATASTROPHE OF NONLINEAR NON-STATIONARY SYSTEM

Let's consider the geometrical images connected with occurrence of catastrophe of nonlinear non-stationary system. Construction of these images is conducted in the fixed points of evolution of investigated dynamic system. These points are established as a result of calculation of a system trajectory of system on the basis of hypotheses and simplifying assumptions (Nechaev, 2011). The hypothesis of quasi-stationary allows to keep theoretical basis of geometrical interpretation of a current situation with use of achievements of the classical theory of catastrophe. Therefore interpretation of behavior of system we will spend within the limits of a quasi-stationary hypothesis for the modified catastrophe of assemblage (Nechaev, 2011). Standard deformation in this catastrophe is set by the formula (Gilmor, 1984, Poston & Steward, 1980). Standard deformation in this catastrophe is set by the formula (Gilmor, 1984, Poston & Steward, 1980):

$$V_a(x,t) = 1/3x^3(t) + a(t)x(t) \quad (24)$$

following from a condition defining an extremum of function

$$\begin{aligned} 0 &= d/dx(1/4x^4(t) + 1/2x^2(t) + b(t)x(t) = \\ &= x^3(t) + a(t)x(t) + b(t) \end{aligned} \quad (25)$$

In which selection of fractions is carried out for reception of the equations of the elementary twisted, and co-ordinates $(x(t), a(t), b(t))$ define parameters of a topological picture for set of catastrophe. The general point of this set has co-ordinates

$$[(x(t),a(t),b(t))] + [x(t), a(t), -a(t)x(t) - x^3(t)](26)$$

That allows to present investigated space of conditions of system $R^2(t)$ in a kind



$$\begin{aligned} R^2(t) &\rightarrow M(t), & [(x(t),a(t)] &\rightarrow [x(t), a(t), -a(t) \\ x(t) - x^3(t) & & & (27) \end{aligned}$$

According to work (Synergetic paradigm, 2000) parametrization of a line of a fold looks like

$$(x(t), -3x^2(t), 2x^3(t)) \quad (28)$$

and bifurcation set is an image of this curve in C

$$(-3x^2(t), 2x^3(t)) = [a(t), b(t)] \quad (29)$$

As it has been shown above, geometrical interpretation of the modified catastrophe of assemblage (figure 1) represents M structure (t) as image of a plane on which there is a straight line of points of a fold, and on this straight line there is point P(t), giving a point of assemblage of variety of catastrophes.

Thus, essential lines of set of catastrophes of M(t) are set by sequence подпространств in the form of structure $R^2(t) \supseteq R^1(t) \supseteq R^0(t)$, which reflects bifurcation set B(t).

In the conditions of waves the investigated model of catastrophe should be considered as initial base for its development on the basis of the account of features of an investigated situation. As theoretical base the results of basic researches formulated in the form of theorems and axioms with reference to investigated dynamic system, and also a cycle of the problems defining formation of methodological base of the appendix of the theory of catastrophes for geometrical and analytical interpretation of the information on dynamics of difficult physical systems, functioning in the conditions of uncertainty are used.

7. MODELS OF CATASTROPHE AND FRACTAL GEOMETRY FOR THE INTERPRETATION OF SHIP EVOLUTION ON WAVES

Let's consider geometrical interpretation of ship dynamics on waves by methods of the catastrophe theory. We will present of ship evolution in the difficult dynamic environment on a basis of fractal geometry. The chaos and an order, their competition and coexistence in frameworks of fractal geometry are characterized by beauty of areas of transition of modeled system in target of attractor. It opens new possibilities of search of law about which existence at studying of processes of ship interaction with an environment earlier did not suspect. At the same time, the processes generating such structures, and fractal updating according to structural dynamics well-known and within long years are studied at interpretation of results of physical experiment (Mesarovich & Takachara, 1978, Nechaev, 2003 & 2009).

Unlike classical models of geometry of fractals, in a considered problem the most complicated nonlinear transformation realized according to features of nonlinear spatial function of $M(\theta, \varphi, t)$, defining of a ship dynamic vessel in a current situation is used (Nechaev, 2003 & 2009). Such transformation displays a real picture of interaction in continuous to the changing environment. The basic properties of a fractal - uniformity and self-similarity thus remain. However it at all those fractals which are described at interpretation of classical models of sets Zhulia and Mandelbrot (Mandelbrot, 1977 & Paigen & Richter, 1993). The idea used Mandelbrot, consisted in that instead of real numbers to consider complex and to observe process $x_0 \rightarrow x_1 \rightarrow x_2 \rightarrow \dots$ not on a straight line, and on a plane. If to set initial value $C=0$ at each iteration the exact square of number is calculated $x_0 \rightarrow x_0^2 \rightarrow x_0^4 \rightarrow x_0^8$. (Mandelbrot, 1977). On Figure 6 comparative data are presented of fractal geometry. Agree, that from the point of view of realization in on-board IS the offered structure differs



compactness and simplicity of display. The carried out analysis has allowed to formulate the modern catastrophe theory on the basis of integration of methods of classical mathematics, intelligence technologies and high-performance means of computing. As a result of such integration the conceptual model of catastrophe of nonlinear non-stationary system has been defined. Thus, we come to a behavior problem of self-organizing systems. For the decision of this problem the theoretical base of the theory of catastrophes, opening new ways and approaches to the decision of this challenge is created. Process of self-organizing demands the deep analysis from positions of the theory of dynamical systems, and interpretation of chaotic behavior in the conditions of continuous change of dynamics of object and an environment is realized on a basis синергетической a synergetic paradigm and the modern computing technologies which are based on methods of artificial intelligence. Integration of these approaches requires to formulate a conceptual basis for constructing the modern theory of catastrophes of complex dynamical systems, in conditions of uncertainty and incompleteness of the initial information.

Other illustration of fractal structures of catastrophe geometry is presented on Figure 7. Here the dynamic picture characterizing difficult transformation of the information at interpretation of loss of stability of oscillatory movement of a ship on waves (capsizing) is shown. Here Figures 1 - 5 note positions of a ship and corresponding of stability diagrammes in development of an extreme situation. Non-stationary it is defined by compression-expansion of fractals in the course of system evolution. Set $GZ(\theta,t)$, displays the dynamic environment of influence of external indignations and features of dynamics of object.

In our case it is necessary to use difficult enough operator of transformation of the information in the non-stationary dynamic environment $X(\theta,\varphi,t) \rightarrow Y(\theta,\varphi,t)$. However the geometrical structure of a fractal at such

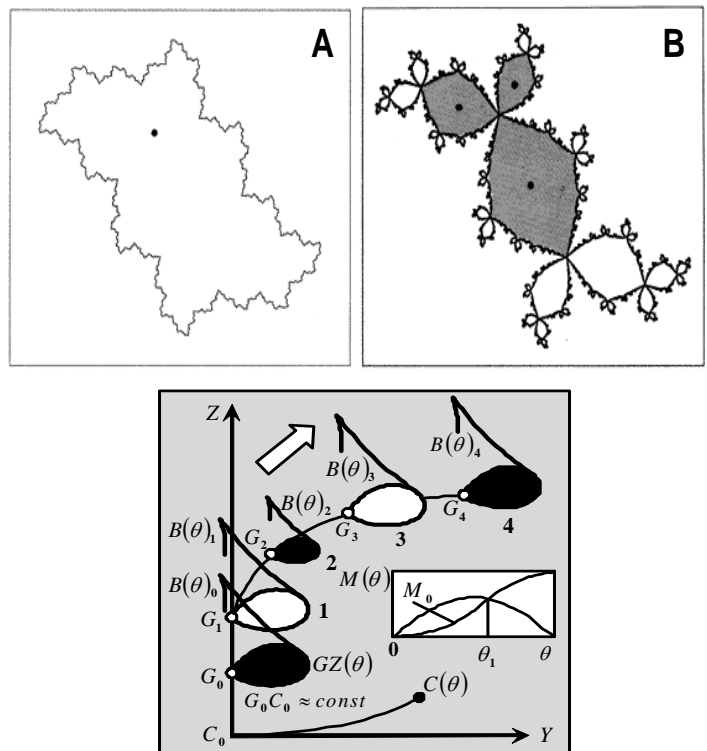


Figure 6: Fractal structures: A – pool of a drawing motionless point; B – pool of a drawing cycle of the period 3; C – fractal movement to target attractor (fractal compression in a point 2 corresponds of ship movement to «potential hole»).

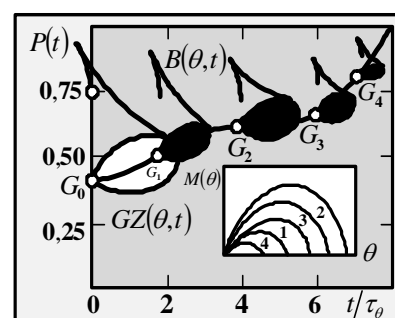


Figure 7: Development of an extreme situation in the non-stationary dynamic environment at interpretation of probability of capsizing.

Reflecting over received set $GZ(\theta,t)$, it is possible to establish unity of the hierarchical organization of such structures and to enter into formal model of catastrophe concept of a fractal and fractal geometry. Algorithms for



reproduction of fractals contain the repeating procedures providing realization of one of the important properties of a fractal - self-similarity. Physical pictures of interaction in non-standard, especially in supernumerary and extreme situations, shows us not easier higher degree, and absolutely other level of complexity. Procedure of construction of a fractal name automodeling if parametres at two adjacent levels are connected with each other by similarity transformation. Asymptotic shows, that investigated fractals possess property incomplete automodeling.

8. CONCLUSIONS

The carried out analysis has allowed to formulate the modern catastrophe theory on the basis of integration of methods of classical mathematics, intelligence technologies and high-performance means of computing. As a result of such integration the conceptual model of catastrophe of nonlinear non-stationary system has been defined. Thus, we come to a behavior problem of self-organizing systems. For the decision of this problem the theoretical base of the theory of catastrophes, opening new ways and approaches to the decision of this challenge is created. Process of self-organizing demands the deep analysis from positions of the theory of dynamical systems, and interpretation of chaotic behavior in the conditions of continuous change of dynamics of object and an environment is realized on a basis синергетической a synergetic paradigm and the modern computing technologies which are based on methods of artificial intelligence. Integration of these approaches requires to formulate a conceptual basis for constructing the modern theory of catastrophes of complex dynamical systems, in conditions of uncertainty and incompleteness of the initial information.

9. REFERENCES

Arnold V.I., 1990, Catastrophe theory – Moskow: Science.

Feder E. Fractals, 1991, Moskow: World.

Gilmor R., 1984, Applied of catastrophe theory. In two books. – Moskow: World.

Hayashi C., 1964, Nonlinear oscillations in physical systems. – McGRAW-Hill COMPANY New York, San Francisco, Toronto, London.

Kronover R.M, 2000, Fractals and chaos in dynamic systems.– Moskow: Postmarket.

Mandelbrot B.B. Fractals, 1977, Form, chance and dimension.- W.N.Freeman. San Francisco, CA.

Mathematical modeling – Moskow: World, 1979.

Mesarovich M., Takachara, 1978, General theory of system: mathematical base. – Moskow: World.

Morce M., 1931, The critical points of a function of n variable, Transaction Amer. Math. Soc. 33, p.p.72 – 91.

Nechaev Yu. I., 2003, Mathematical modeling in on-board real time intelligence systems, Proceedings of the 5th All-Russia scientific and technical conference «Neuroinformatics - 2003», M.: MIFI. Lectures on neuroinformatics. P. 2, p.p.119-179.

Nechaev Yu.I., 2007, Nonlinear dynamic and paradigms computing for analysis of extreme situations, Proceedings of the international conference «Leonard Euler and modern science», Russian Academy Scienses. Санкт-Петербург, , p.p.385 – 390.

Nechaev Yu.I., 2009, Reconstruction of mathematical model of righting component for estimate ship dynamic on the waves, Information-measuring and control systems, No.2. Vol.7, p.p.23 – 33.

Nechaev Yu.I., 2011, Catastrophe theory: modern approach at decision-making. – St.-Petersburg, Art-Express.

Necharv Yu.I., and Dubovik S.A., 2009, Estimation of probability of the big evasion of the indignant dynamic system, Marine



intelligence technologies, No.3 (5), p.p.21 - 27.

Onboard intelligence systems. P.2. Ships systems. – Moskow: Radiotechnic, 2006.

Paigen H.O., and Richter P.H., 1993 Beauty of fractals. - M: World.

Poston T., and Steward I., 1980, Catastrophe theory. – Moskow: World.

Synergetic paradigm. – Moskow. Progress-Tradition, 2000.

Thom R., 1974, Catastrophe theory: Its present state and future perspectives. - Dynamical systems. Warwick. – Berlin–Heidelberg–New York Springer Verlag. 1-75. p.p.366–372. Lecture Notes Math. V. 468.

Zeeman E.C., 1973, Catastrophe theory in brain modeling, Int. J.Neurosci, 6. 1973, p.p.39 – 41.



A Study on Characteristics of Rolling in Head Waves of a Vessel with Strong Nonlinear GZ -curve

Toru Katayama, *Graduate School of Engineering, Osaka Prefecture University,*

katayama@marine.osakafu-u.ac.jp

Shugo Miyamoto, *Graduate School of Engineering, Osaka Prefecture University,*

ss103029@edu.osakafu-u.ac.jp

Hirotsuda Hashimoto, *Graduate School of Engineering, Osaka University,*

h_hashi@naoe.eng.osaka-u.ac.jp

Yoshifumi Tai, *Imabari Shipbuilding Co., LTD, tai.yoshifumi@imazo.com*

ABSTRACT

In this study, the characteristics of rolling in head waves for a vessel with strong nonlinear GZ -curve, which includes parametric rolling, are investigated. Rolling is measured for systematically changed wave length and height under the same forward speed, which is service speed in heavy weather. As the results, the range of T_e/T_ϕ (T_e and T_ϕ are encounter wave period and the roll natural period of the model), when periodic rolling occurs, is wider than that of previous results by Taguchi et al, (2006), and the range spreads out wide area of $T_e/T_\phi > 0.5$. Especially, in the range of $T_e/T_\phi > 0.5$, periodic rolling is caused by large wave height and roll amplitude becomes larger than that at $T_e/T_\phi = 0.5$. It is supposed that the result is caused by change of roll natural period caused by nonlinear GZ -curve. In order to confirm it, numerical simulations are carried out for several variations of GZ -curve. Additionally, roll measurements in irregular waves with Pierson-Moskowitz spectrum are also carried out.

Keywords: *Parametric Rolling, Wide-breadth and Shallow-draft, Strongly Nonlinear-GZ-curve*

1. INTRODUCTION

Ballast water for vessels is significant to prevent their stability and propulsion performance losses, which are caused by their light-draught. However, the International Maritime Organization (IMO) adopted International Convention for the Control and Management of Ships' Ballast Water and Sediments in 2004, because of avoiding its environmental impact.

Then, in order to solve this problem, new hull forms are being designed, which use a

small amount of ballast water or don't need ballast water. For example, one of new designed hull has shallow draft and wide breadth. Such a type of hull may show different roll characteristics from the conventional vessels.

In the previous study (Tai et al, 2011), for a shallow draft and wide breadth vessel, its roll characteristics in beam waves have been investigated experimentally. The results show that its roll natural period is changed by its roll amplitude and its roll resonance occurs in



different wave period depending on different wave height.

In this study, the roll characteristics of the same model (Tai et al, 2011) in head waves (including parametric rolling) are investigated. Roll measurements in regular head waves are carried out. From the results, it is found that large amplitude rolling occurs at wider range of encounter frequency than that of a conventional vessel and it is supposed that it is caused by strong nonlinearity of its *GZ*-curves. Then, in order to be clear the reasons of the results, numerical simulations are carried out. Additionally, the roll characteristics in irregular waves with Pierson-Moskowitz spectrum are also investigated.

2. MODEL AND MEASUREMENT

Fig.1 & Table 1 show a body plan and principal particulars of a model. Fig.2 shows the calculated *GZ*-curve of the model in real scale. In the same figure, the linear *GZ*-value of the model is also shown. The calculated *GZ*-curve shows strong nonlinear characteristics in the range of small roll angles. This is because bilge of the model is exposed above the water surface from the range of small roll angles.

Fig.3 shows measured roll natural period of the model by a free decay test. This figure shows that the roll natural period becomes longer according to increase in roll amplitude. And this is caused by the strong nonlinearity of the *GZ*-curve shown in Fig.2.

In order to investigate the occurrence of periodic rolling, towing tests in regular head waves are carried out at the towing tank of Osaka Prefecture University (length 70m, breadth 3m, depth 1.5m). Fig.4 shows a schematic view of the experiment. A model is attached to the towing carriage with two elastic ropes (Hashimoto et al., 2007). The model is towed at constant forward speed in head waves, and a small disturbance is given. Roll motion is measured by a gyroscope (CROSSBOW

NAV440) and wave elevation is also measured by a servo type wave height meter attached to the towing carriage.

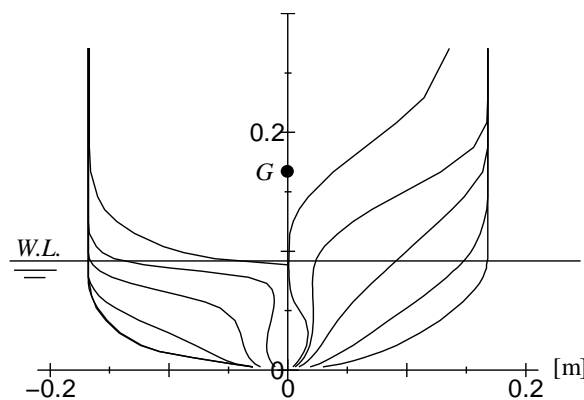


Figure 1: Body plan of the model.

Table 1: Principal particulars of the model.

	ship	model
L_{pp} [m]	192	2.0
B [m]	32.26	0.336
draft: d [m]	9.0	0.0938
KG [m]	17.0	0.177
GM [m]	1.81	0.0189
roll natural period: T_{ϕ} [sec]	18.42	1.88
breadth of bilge-keels	0.7	0.0073
position of bilge-keels	s.s. 3.34-s.s. 5.59	

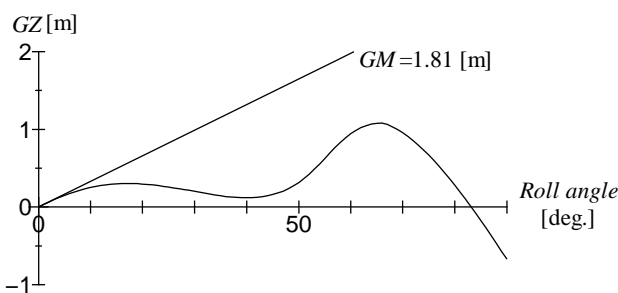


Figure 2: Calculated *GZ*-curve of the model in real scale.

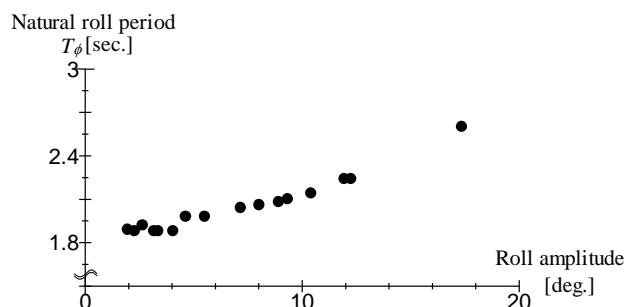


Figure 3: Measured roll natural period of the model.

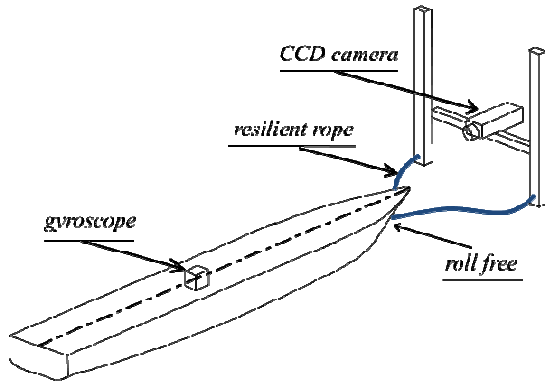


Figure 4: Schematic view of the experiment.

3. ROLL MEASUREMENT IN REGULAR HEAD WAVES

Table 2 shows the experimental conditions. When the model is towed at $F_n=0.083$ in head wave of $T_w=1.05$ sec, the encounter wave period is half of the roll natural period ($T_\phi=1.88$ sec) for small amplitude. This F_n is 7kt in the real scale.

Table 2: Experimental condition.

F_n	0.083
wave period: T_w [sec]	0.99 ~ 1.55
T_e/T_ϕ	0.42 ~ 0.71
wave height: H_w [m]	0.01 ~ 0.05

T_e : encounter wave period [sec]

T_ϕ : roll natural period [sec]

Fig.5 shows examples of typical time histories of measured rolling in regular head waves. The upper figure shows the result that periodic rolling does not occur. The middle figure shows the result that periodic rolling occurs. The bottom figure shows the result that periodic rolling occurs after a small excited disturbance.

Fig.6 shows measured roll amplitudes in regular head waves. In this figure, its horizontal axis is the ratio of encounter wave period to the roll natural period for small amplitude. At $T_e/T_\phi=0.5$, periodic rolling occurs for any wave heights. And, for small wave height, periodic rolling does not occur except at $T_e/T_\phi=0.5$.

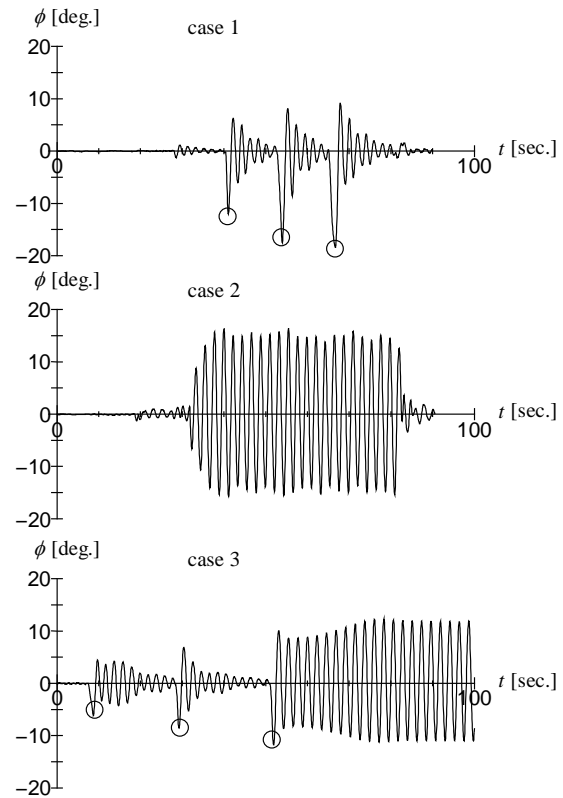


Figure 5: Time histories of measured roll motions in regular head waves. (○:disturbance).

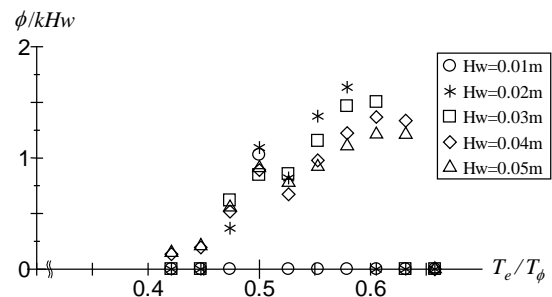


Figure 6: Measured roll amplitude in regular head waves at $F_n=0.083$. (Case 3: $T_e/T_\phi=0.53$, 0.55 , 0.58 at $H_w=0.02$ m, $T_e/T_\phi=0.61$ at $H_w=0.03$ m, $T_e/T_\phi=0.63$ at $H_w=0.04$ m).

Fig.7 shows the measured roll amplitude of a conventional post-panamax container vessel by Taguchi et al. (2006) in order to compare with Fig.6. From the comparisons, it is noted that the range of T_e/T_ϕ where periodic rolling occurs in Fig.6 is wider than that of Fig.7, and the range of Fig.6 spreads wider area of $T_e/T_\phi > 0.5$. Especially, at the range over $T_e/T_\phi = 0.5$, periodic rolling is caused by large



wave height, and its amplitude becomes larger than that at $T_e/T_\phi=0.5$. It is supposed that the spread of occurrence of large amplitude rolling to wider area of $T_e/T_\phi>0.5$ is caused by the strong nonlinearity of GZ-curves.

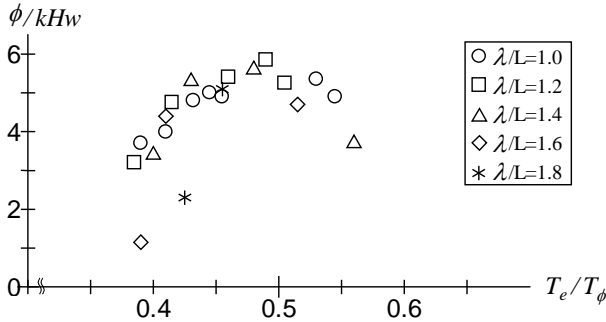


Figure 7: Measured roll amplitude in regular head waves at $H_w=0.11\text{m}$. (citation from Fig.6 in (Taguchi et al, 2006)).

Table 3 shows the experimental condition for the roll measurement in regular head waves with constant wave length ($\lambda/L_{pp} = 1$). When model is towed at $F_n = 0.077$, its encounter wave period is half of the roll natural period for small amplitude ($T_\phi=1.88\text{sec}$). And according to decrease in forward speed, its encounter period becomes long.

$$B_{44}(\phi_a) = \frac{W\Delta GM}{2\omega_e} \quad (1)$$

The measured results are also shown in the same figure. Both results show the same tendency for change of forward speed.

From these results, it is understood that decrease in forward speed causes decrease in roll damping, and roll amplitude becomes larger. On the other hand, roll natural period becomes long according to increase in roll amplitude as shown in Fig.3. Then rolling resonates with increased wave encounter period by decrease in forward speed, and parametric rolling occurs.

Table 3: Experimental conditions.

λ/L_{pp}	1.0		
F_n	0.000	0.032	0.077
T_e/T_ϕ	0.60	0.55	0.5

Fig.8 shows the measured roll amplitude. In this figure, roll amplitude increases according to decrease in forward speed, even if T_e/T_ϕ becomes larger than 0.5.

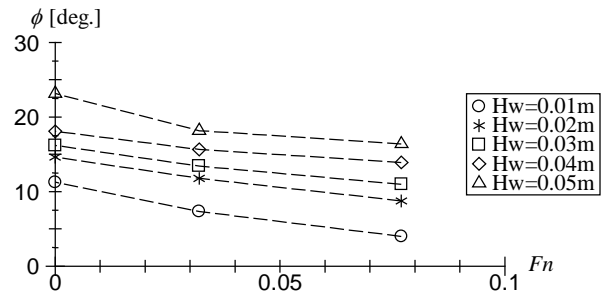


Figure 8: Measured roll amplitude.

In order to make its reason clear, the characteristics of roll damping is investigated by using Ikeda's method, and roll amplitude is estimated by using a simplified estimation for amplitude of parametric rolling (Katayama et al, 2009).

Fig.9 shows the estimated roll damping. The roll damping decreases according to decrease in forward speed. It is caused by decrease in the lift component of roll damping which is caused by forward speed.

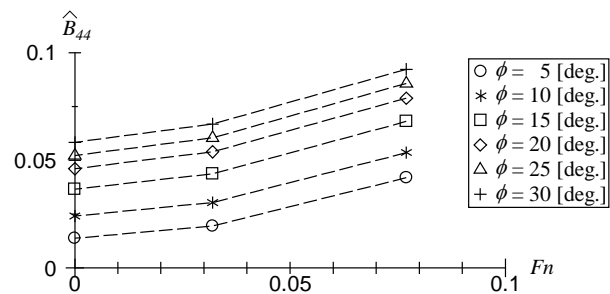


Figure 9: Estimated roll damping coefficient by Ikeda's method.

Fig.10 shows the estimated roll amplitude by Eq.(1) (Katayama et al, 2009).

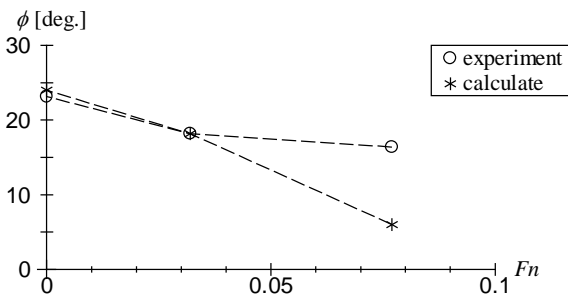


Figure 10: Estimated roll amplitude by Eq.(1). ($H_w=0.05m$)

4. ROLL MEASURING IN IRREGULAR HEAD WAVES

Eq.(2) is one of Pierson-Moskowitz spectrum.

$$S(\omega) = \frac{8.1 \times 10^{-3} \times g^2}{\omega^2} \exp\left(-\frac{3.11/H_w^2}{\omega^4}\right) \quad (2)$$

To make irregular waves, the spectrum is divided into 1000 equally in $\omega=1\sim 15$ rad/sec and a sine wave of each frequency component is superposed. In addition, the phase difference of each frequency component is given as random numbers. The number of measurements is decided by the convergence of variance of rolling (Appendix 1).

In this study, roll measurements are carried out for three significant wave heights, and Fig.11 shows the power spectrums obtained from the measured wave elevations.

Fig.12 shows the probability distributions of the measured roll amplitudes. In this measurement, roll amplitude is not over 10deg at significant wave height=0.04m. The results show that the roll amplitude increases with increase in significant wave height.

Fig.13 shows time histories of measured wave height and rolling at $H_w=0.06m$. In this figure, the ratios of mean encounter wave period to the roll natural period for small amplitude (\bar{T}_e/T_ϕ) at t_1 and t_2 are also shown.

The mean wave heights at t_1 and t_2 are almost same. From this figure, it is found that periodic rolling does not occur at t_1 ($\bar{T}_e/T_\phi < 0.5$), and periodic rolling occurs at t_2 ($\bar{T}_e/T_\phi > 0.5$).

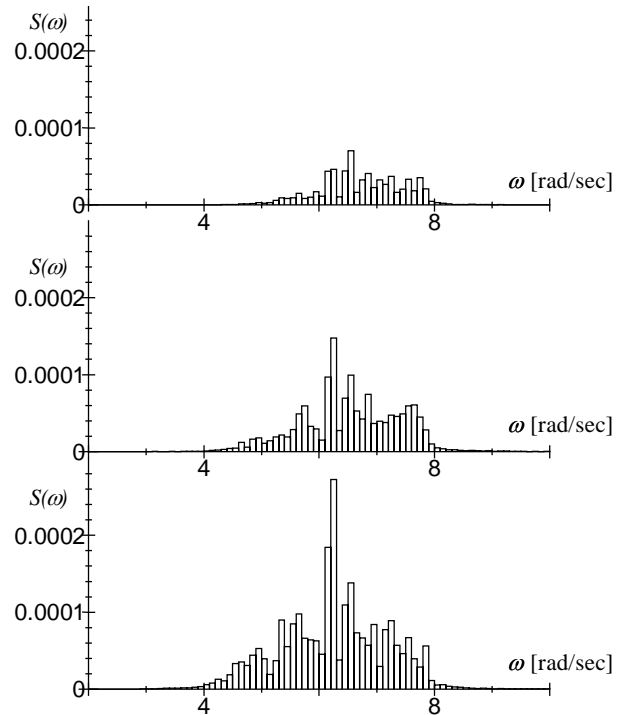


Figure 11: Measured power spectrum of wave height. (1/3 significant wave height = 0.04, 0.05, 0.06m)

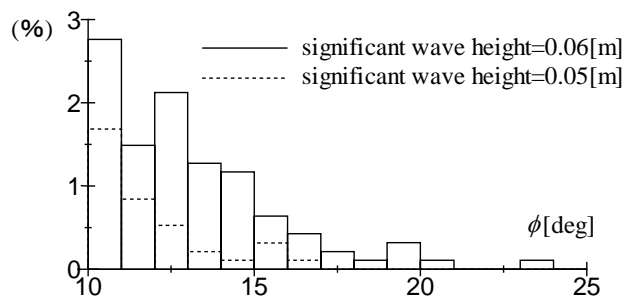


Figure 12: Probability distribution of roll amplitude. (significant wave height = 0.05, 0.06m)

In the Pierson-Moskowitz spectrum expressed by Eq.(2), increase in significant wave height causes increase in mean wave period, therefore the occurrence probability of a wave group containing frequency component of $T_e/T_\phi > 0.5$ mainly also becomes higher. On the other hand, the roll natural period becomes



long according to increase in roll amplitude. Therefore rolling may resonate the wave group containing frequency component of $T_e/T_\phi > 0.5$ mainly.

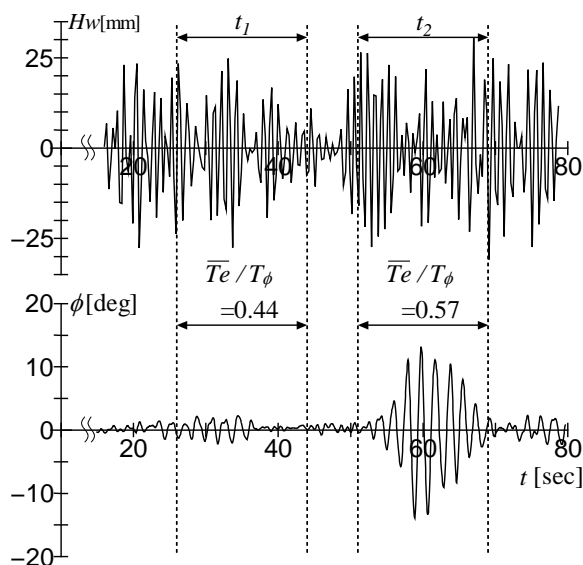


Figure 13: Time histories of measured wave height and roll motion in irregular head waves at $H_w=0.06\text{m}$.

5. ROLL MEASURING IN HEAD WAVES OF TWO DIFFERENT WAVE PERIOD

In the roll measurement in irregular head waves, when mean wave period of group waves is $T_e/T_\phi > 0.5$, periodic rolling occurs. In order to investigate its reasons, the roll measurements are carried out in the waves which are generated by the superposition of two sine waves having different periods. One of two different periods is half ($T_e/T_\phi = 0.5$) of the roll natural period for small amplitude. Moreover, the wave heights of two sine waves are different. (In the following, the component with higher wave height is called Main-wave.) Experimental conditions are shown in Table 4 with the results.

In Table 4, measured roll amplitude is shown. The results show that periodic rolling occurs when period of Main-wave is $T_e/T_\phi = 0.50 \sim 0.61$. As the results, it is confirmed

that rolling can resonate with a wave with $T_e/T_\phi = 0.50 \sim 0.61$ and it is supposed that periodic rolling may occur in a frame of wide line.

Table 4: Measured results.

		$T_e/T_\phi (H_w = 0.01 \text{ m})$						
		0.39	0.45	0.50	0.55	0.61	0.66	0.71
$T_e/T_\phi (H_w = 0.04 \text{ m})$	0.39			×				
	0.45		×	×				
	0.50	10.4	14.1		18.4	15.4	18.3	16.8
	0.55			8.3				
	0.61			16.0				
	0.66			×			×	
	0.71			×				×

ϕ [deg]: periodic rolling occurs

×: periodic rolling does not occur

Colored: periodic rolling occurs in regular waves

6. NUMERICAL SIMULATION

By utilizing the numerical simulation model (Hashimoto and Umeda, 2010), the effects of nonlinearity of GZ -curve on the occurrence of parametric rolling are investigated.

In order to control the nonlinearity of GZ -curve, the breadth-draft ratio (B/d) of original model is changed under the constant displacement. Fig.14 & Fig.15 show modified body plans and GZ -curves. GM for each modified model is adjusted to the same GM as the original model. Moreover, in order to make sure the characteristics of ΔGM of the original and modified models, the estimated ΔGM by the simplified method (Hashimoto et al) are shown in Fig.16.

Fig.17 shows the numerical results for the original model. The calculated results show large amplitude parametric rolling occurs in the wide range over $T_e/T_\phi = 0.5$ and the numerical result shows a good agreement with the measured results.

Figs.18-20 shows the calculated results for the modified models. These results show the roll amplitudes in the range over $T_e/T_\phi = 0.5$ become larger according to the increase in nonlinearity of GZ -curve.

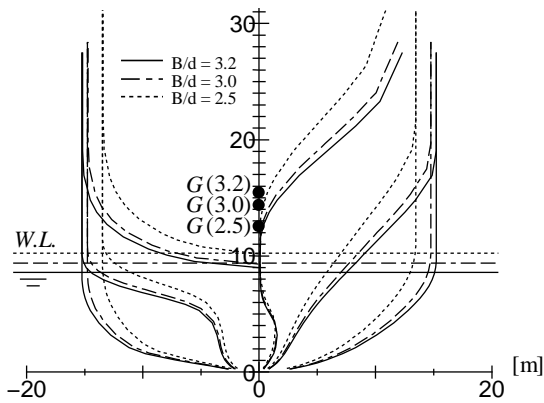


Figure 14: Body plan in real scale. ($B/d=3.2, 3.0, 2.5$)

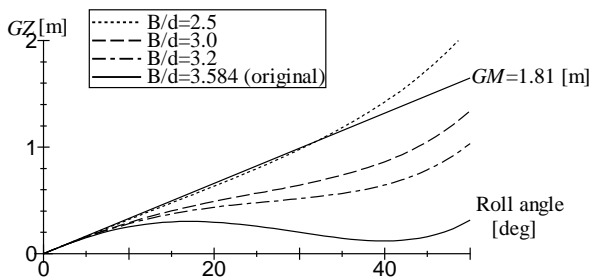


Figure 15: GZ -curve of the model in real scale. ($B/d= 3.584, 3.2, 3.0, 2.5$)

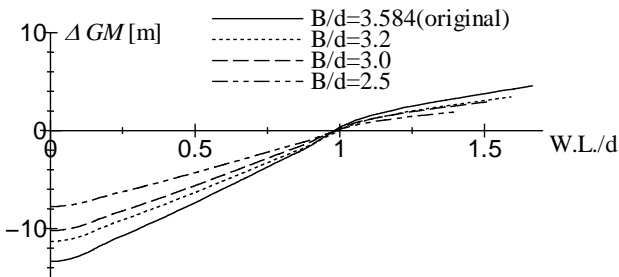


Figure 16: Variation of GM caused by change of water surface of the models in real scale. ($B/d= 3.584, 3.2, 3.0, 2.5$)

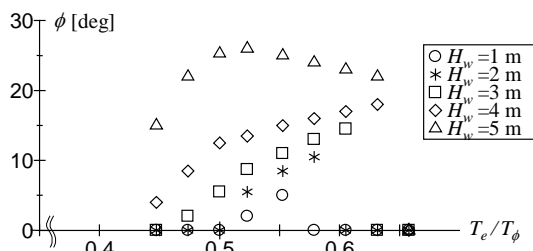


Figure 17: Calculated roll amplitude in regular head waves at $Fn= 0.083$. ($B/d=3.584$)

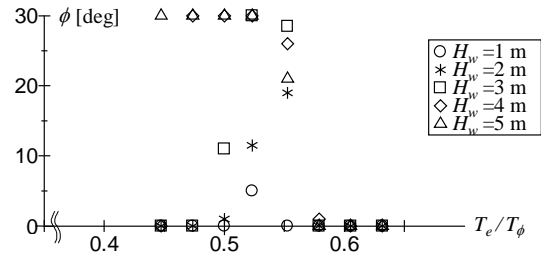


Figure 18: Calculated roll amplitude in regular head waves at $Fn=0.083$. ($B/d=3.2$)

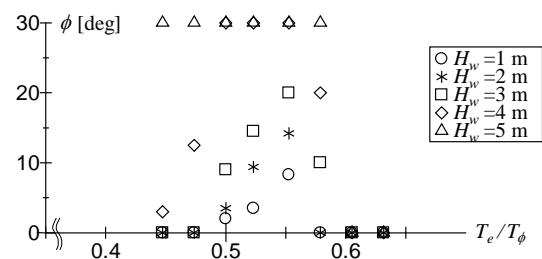


Figure 19: Calculated roll amplitude in regular head waves at $Fn=0.083$. ($B/d=3.0$)

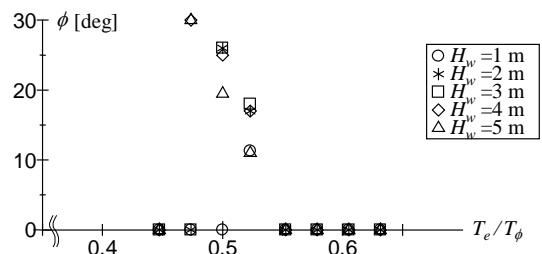


Figure 20: Calculated roll amplitude in regular head waves at $Fn=0.083$. ($B/d=2.5$)

7. CONCLUSIONS

In this study, the roll characteristics of a wide breadth and shallow draft vessel in head waves are investigated. And the following conclusions are obtained.

- In regular head waves, a periodic rolling occurs at wider range of encounter frequency than that of a conventional vessel. Especially, in the range of $T_e/T_\phi > 0.5$, a periodic rolling is caused by large wave height and roll amplitude becomes large.
- Numerical simulations demonstrate that



the large amplitude parametric rolling occurs in the wide range over $T_e/T_\phi=0.5$ because of the strong nonlinearity of GZ-curves.

- There is the possibility that slowdown increases roll amplitude, when parametric rolling occurs at $\lambda/L_{pp}=1.0$.
- It is confirmed by simplified estimation that this phenomenon is caused the following scenario. Slowdown decreases roll damping, and roll amplitude becomes large. On the other hand, roll natural period becomes longer with increase in roll amplitude. Therefore rolling resonates with increased wave encounter period by slowdown.
- In irregular head waves with a Pierson-Moskowitz spectrum, a periodic rolling is caused by resonating with the group waves which contain the frequency component of $T_e/T_\phi > 0.5$ mainly.

8. REFERENCES

- Harukuni Taguchi, Shigesuke Ishida, Hiroshi Sawada and Makiko Minami, 2006, "Model Experiment on Parametric Rolling of a Post-Panamax Containership in Head Waves", Proceedings of the Ninth International Conference on Stability of Ships and Ocean Vehicles.
- Hashimoto, H. and Umeda, N., 2010, "A Study on Quantitative Prediction of Parametric Roll in Regular Waves", Proceedings of the 11th International Ship Stability Workshop, Stability Workshop pp.295-301
- Yoshifumi Tai, Takehiro Ohashi, Toru Katayama and Yoshiho Ikeda, 2011, "An Experimental Study on Stability of a Shallow Draft Vessel in Beam Seas", JASNAOE Journal of the Japan Society of Naval Architects and Ocean Engineers, Vol. 14.
- Hashimoto, H., Sueyoshi, M. and Minegaki S., 2007, "An Estimation of the Anti-Rolling

Tank Performance for Parametric Rolling Prevention", JASNAOE Journal of the Japan Society of Naval Architects and Ocean Engineers, Vol. 6, pp. 305-311.

Yoshiho Ikeda, 2004, "Prediction Methods of Roll Damping of Ships and Their Application to Determine Optimum Stabilization Devices", Marine Technology, Vol. 41, pp. 89-93.

Toru Katayama, Tomoki Taniguchi and Naoya Umeda, 2009, "An Experimental Study on Parametric Rolling of a High Speed Trimaran in Head Seas", JASNAOE Journal of the Japan Society of Naval Architects and Ocean Engineers, Japan, Vol. 10, pp. 57-63.

Hirotsada Hashimoto, Naoya Umeda, Akihiko Matsuda, "Estimation of Parametric Roll in Random Seaways", Parametric Resonance in Dynamical Systems, pp. 45-52.

9. APPENDIX

A.1 The number of times of test in irregular head waves.

From wave height, pitch motion and roll motion, each variance and ensemble mean by Eq(A1), Eq(A2). Fig.A1 shows calculated result. In these figure, a vertical axis is a ratio ensemble mean to standard deviation. Upper and middle figure uses 20 samples and bottom figure uses 30 samples. (1sample = 40 sec) From upper & middle figure, it is found that wave height and pitch motion convergence with 5 samples. On the other hand, roll motion does not convergence until 15 samples. So, this study uses 20 samples.

$$\sigma^2(t) = \sum_{j=1}^{n_s} \frac{(X_j(t_j) - \overline{X}(t))^2}{n-1} \quad (A1)$$

$$\sigma_{erg}^2 = \frac{\sum_{i=1}^N \sum_{j=1}^n \frac{(X_i(t_j) - \overline{X}_i)^2}{n-1}}{N} \quad (A2)$$

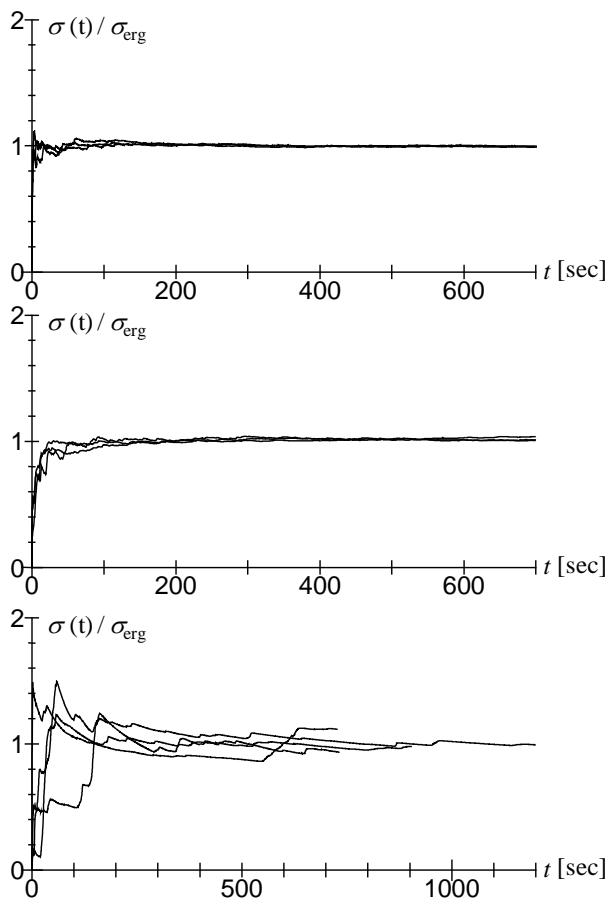


Fig.A1 Standard deviation of wave elevation, pitching and rolling. (1/3 significant wave height = 0.04, 0.05, 0.06 [m])





Ship Roll Motion in Irregular Waves During a Turning Circle Maneuver

Jerzy Matusiak, *Aalto University, Department of Applied Mechanics*, jerzy.matusiak@aalto.fi

Claus Stigler, *Aalto University, Department of Applied Mechanics*, claus.stigler@aalto.fi

ABSTRACT

Motion of a ship in stern quartering seas is investigated in model tests and using the so-called *Laidyn* computational model. Experiments and simulations are conducted as a turning circle maneuver in irregular long-crested waves. The operating condition is selected so that a critical focusing of the irregular waves occurs yielding a resonance of roll motion.

Main elements of the unified model combining ship manoeuvring model and ship motion in waves are described.

Keywords: *ship manoeuvring, seakeeping, quartering waves*

1. INTRODUCTION

Stern quartering seas are known to be often a cause of seakeeping problems. There are several modes of stability loss in stern quartering seas such as broaching, parametric roll resonance or bow diving. Moreover, in certain conditions, there is a danger of roll resonance. The phenomena involved in the latter were much investigated, in particular in Japan (Takaishi 1996, Panjaitan 1998 and the others). A resonant condition for roll occurs as a result of the frequency shift of wave action. In certain quartering or following sea conditions the encounter wave spectrum changes so that the bandwidth of it gets narrower and moves towards low frequencies. This change in frequencies of encounter can be named a focusing effect as nearly all waves, disregarding their length, act on a ship with nearly the same frequency. Moreover, if the action of waves on a ship concentrates at the frequency close to the natural frequency of roll, this yields a resonant condition. This phenomenon is qualitatively taken into account in the IMO's Guidance to the Master (IMO 2007), which identifies dangerous combinations of ship speed, heading and wave period.

Roll resonance due to a focusing effect of quartering sea waves was investigated by model tests and numerical simulations. Experiments and simulations were conducted as a turning circle manoeuvre in irregular long-crested waves. Model tests were carried out in the multifunctional model basin of Aalto University. The primary goal of the investigation was to validate the theoretical model's capability to simulate manoeuvring in irregular waves. The *Laidyn* method is meant for the evaluation of ship motions in waves. The ship is regarded as a rigid intact body. The mathematical model behind the method comprises the elements of manoeuvring and makes allowance for the non-linear large amplitude motions in regular or irregular waves. General description of the method was given in (Matusiak, 2010) and some details of the method were presented in Matusiak (2007). The present paper gives a description of the way the radiation forces and the forces associated with the manoeuvring are combined into a single model. The equations of ship motion are presented as well. These equations do not make a distinction between manoeuvring and the seakeeping motions. A comparison of measured and numerically simulated ship motions in



irregular long-crested waves during a turning circle manoeuvre is presented as well.

2. UNIFIED TREATMENT OF MANEUVERING AND SHIP MOTION IN WAVES

2.1 Hull forces

The main problem of forming a unified model of ship dynamics that is capable to simulate ship maneuvering in waves is a difficulty to present the forces acting on a hull in yaw and sway motion that comprise the maneuvering part and the part associated with the wave action (seakeeping). For this reason sometimes, using a feature of different time scales, the problem of manoeuvring is solved separately from the faster motions in waves. Total response is obtained by a simple superposition of both types of motion.

It is customary to express the hydrodynamic sway force Y_{man} and yaw moment N_{man} acting on a manoeuvring ship with the aid of the so-called stability derivatives as follows

$$\begin{aligned} Y_{man} &= Y_v \dot{v} + Y_v v + Y_r \dot{r} + Y_r r \\ N_{man} &= N_v \dot{v} + N_v v + N_r \dot{r} + N_r r, \end{aligned} \quad (1)$$

where v and r are the velocities of sway and yaw motion components. Equation 1 assumes a linearity dependence of forces and the corresponding motion velocities and accelerations. In the seakeeping theory the corresponding so-called radiation forces acting on an oscillating hull are usually given as

$$\begin{aligned} Y_{rad} &= -a_{22} \dot{v} + b_{22} v - a_{26} \dot{r} + a_{26} r \\ N_{rad} &= -a_{62} \dot{v} + b_{62} v - a_{66} \dot{r} + b_{66} r, \end{aligned} \quad (2)$$

where a and b are denoted as added masses and damping coefficients that are dependent upon the frequency of motion. There is an evident similarity of both sets of above equations (1&2). Terms related to the accelerations can be named added masses, while terms related to

velocities may be denoted as damping. The biggest difference is in the time scale of the considered motions. Manoeuvring motion is relatively slow when compared to ship motion in waves. Added masses and damping related to seakeeping are dependent upon the frequency ω of the oscillatory motion. Bailey et al (1998) have investigated experimentally and using the potential seakeeping theory the frequency dependence of added masses and damping. They have pointed out the relations between the coefficients of both formulations. The coefficients of equations 1 can be understood as a slow manoeuvring force model associated with the motion frequency being zero.

In the time domain simulations of ship motions in waves the history of the previous motion has to be taken into account when evaluating the radiation forces. Time domain approach requires the so-called convolution integral representation of the radiation forces (Cummins, 1962). In this time approach the radiation vector

$$\mathbf{X}_{rad} = \{X_{rad}, Y_{rad}, Z_{rad}, K_{rad}, M_{rad}, N_{rad}\}$$

is represented by the expression

$$\mathbf{X}_{rad}(t) = -\mathbf{a}_{\infty} \ddot{\mathbf{x}}(t) - \int_{-\infty}^t \mathbf{k}(t-\tau) \dot{\mathbf{x}}(\tau) d\tau, \quad (3)$$

where \mathbf{a}_{∞} is the matrix comprising of the added mass coefficients for an infinite frequency and \mathbf{x} is the response vector. Matrix function \mathbf{k} is the so-called retardation function, which takes into account the memory effect of the radiation forces. This function can be evaluated as

$$\mathbf{k}(t) = \frac{2}{\pi} \int_0^{\infty} \mathbf{b}(\omega) \cos(\omega t) d\omega \quad (4)$$

where $\mathbf{b}(\omega)$ is the frequency dependent added damping matrix.

The retardation functions $\mathbf{k}(t)$ can be evaluated before the simulation. The Fast Fourier Transform algorithm can be used when evaluating them (Matusiak, 2001).

2.2 Equations of Motion

The equations of motion solved in time domain and resulting in a simulation of ship motion in waves are given below.

$$\begin{aligned}
 (m+a_{11})\dot{u} + a_{15}\dot{q} &= -mg \sin \theta + X_{\text{resistance}} + \\
 &X_{\text{prop}} + X_{\text{rudder}} + X_{\text{wave}} + X_{\text{man}} \\
 &-k_{15} + (m+a_{22})(rv - qw) \\
 (m+a_{22})\dot{v} + a_{24}\dot{p} + a_{26}\dot{r} &= mg \cos \theta \sin \phi \\
 &+ (m+a_{11})(pw - ru) + Y_{\text{man}} \\
 &+ Y_{\text{rudder}} + Y_{\text{wave}} - k_{22} - k_{24} - k_{26} \\
 (m+a_{33})\dot{w} + a_{35}\dot{q} &= mg \cos \theta \cos \phi \\
 &+ m(uq - vp) + Z_{\text{wave}} - k_{33} - k_{35} \\
 a_{42}\dot{v} + (I_x + a_{44})\dot{p} + a_{46}\dot{r} &= (I_y - I_z)qr \\
 &- Y_{\text{rudder}}z_{\text{rudder}} + K_{\text{wave}} + K_{\text{man}} - k_{44} - k_{42} \\
 &- k_{46} + 2\zeta p\omega_\phi \\
 a_{15}\dot{u} + a_{53}\dot{w} + (I_y + a_{55})\dot{q} &= (I_y - I_x)pr \\
 &+ X_{\text{rudder}}x_{\text{rudder}} + M_{\text{wave}} - k_{55} - k_{53} - k_{15} \\
 a_{62}\dot{v} + a_{64}\dot{p} + (I_z + a_{66})\dot{r} &= (I_x - I_y)pq \\
 &+ Y_{\text{rudder}}x_{\text{rudder}} + N_{\text{man}} + N_{\text{wave}} \\
 &- k_{66} - k_{62} - k_{64}
 \end{aligned} \tag{5}$$

In the above equations m is ship's mass, I_{ij} are mass moments of inertia, terms a_{ij} and k_{ij} are the added mass coefficients corresponding to the infinite frequency and the elements of the memory function respectively. That is a linear potential time-domain seakeeping model is used to describe flow inertia effects. Additional components of the state vector are u , w , p and q , that are velocities of surge, heave, roll and pitch motion components in the body-fixed co-ordinate system. The angular position of the ship is represented by the Euler angles ϕ and θ being roll and pitch angles. The terms depicted by subscript 'man' are the manoeuvring forces and moments represented by hull forces related to yaw and sway velocities, that is $Y_{\text{man}} = Y_v v + Y_r r$ and $N_{\text{man}} = N_v v + N_r r$. Heeling moment K_{man} takes into account the fact that the manoeuvring sway force is located at a certain

distance from the Centre-Of-Gravity. Subscript 'rudder' refers to rudder forces and to the location of the rudder in the body-fixed coordinate system. Forces and moments depicted with subscript 'wave' are the ones incorporating the restoring forces and moments and the wave loads. Thus X_{wave} represents added resistance in waves associated mainly with the variations of wetted surface and the Froude-Krylov pressures. An allowance for a viscous damping of roll is incorporated in the 4th equation. In the 3rd line of this equation ζ stands for a critical damping ratio and ω_ϕ stands for the natural roll angular frequency. Still water resistance $X_{\text{resistance}}$ and propeller thrust X_{prop} are evaluated from a known resistance coefficient and propeller open water characteristics.

On the left-hand-side of equations 5 several terms related to motion accelerations occur in each of the equations. This means that equations are coupled and cannot be solved as such. Before the solution can be calculated, equations 5 have to be de-coupled. This is done numerically at each time step.

Numerical integration of equations 5 in de-coupled form yields the state vector comprised of ship velocity components in the body-fixed coordinate system. Ship position in Earth-fixed coordinate system is obtained using the transformation relation between both frames and by numerically integrating the state vector. Details of the procedure can be found, for instance, in Matusiak (2007).

3. MODEL TESTS

In order to validate the Laidyn method by statistically evaluated random test, Stigler (2012) investigated ship manoeuvring in irregular waves by conducting model tests using a RoPax model. Tens of tests were conducted either as turning circle tests or running the model on a straight course in stern quartering waves.



3.1 Investigated ship

The model was built in a scale of $\lambda = 39.022$. The main dimensions of the RoPax are given in table 1 and the frames are shown in figure 1.

Table 1: Main dimensions and weight data of the RoPax.

Quantity	Symbol	Unit	Value
Length between perpendiculars	L_{oa}	[m]	171.4
	L_{pp}	[m]	158.0
Breadth max. at waterline	B_{wl}	[m]	25.0
Draught	T	[m]	6.1
Displacement	∇	[m ³]	13
			766
Block coefficient	C_B	–	0.571
Centre of gravity:			
From AP	x_{CG}	[m]	74.9
From CL	y_{CG}	[m]	0.0
From BL	z_{CG}	[m]	10.9
Radius of gyration in pitch	k_{yy}/L_{pp}	–	0.25
Transverse metacentric height	GM_{T0}	[m]	1.76

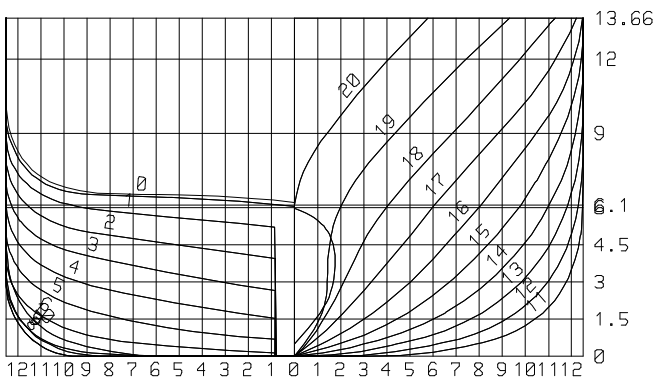


Figure 1: Frames of the RoPax.

3.2 Tests

The turning circle tests were run with self-propelled and radio-controlled model in irregular waves given by the Jonswap-type wave spectrum with the significant wave height $H_S=4.8$ m and

the average period $T_1=5.9$ s. The speed of the model was controlled manually by adjusting the revolutions of propellers. The target value of it was $V_S=16.5$ knots in full-scale. The height of Center-Of-Gravity was adjusted so that the natural roll period in model scale was 3 s, that is it corresponded to the full-scale value $T_\phi=19$ s. This creates a dangerous situation of roll resonance in stern quartering seas leading to the condition presented in figure 2.

For the statistical comparison, three different representations of the wave spectrum and changing release instants for the vessel were chosen in order not to meet the same wave train twice at the same time.

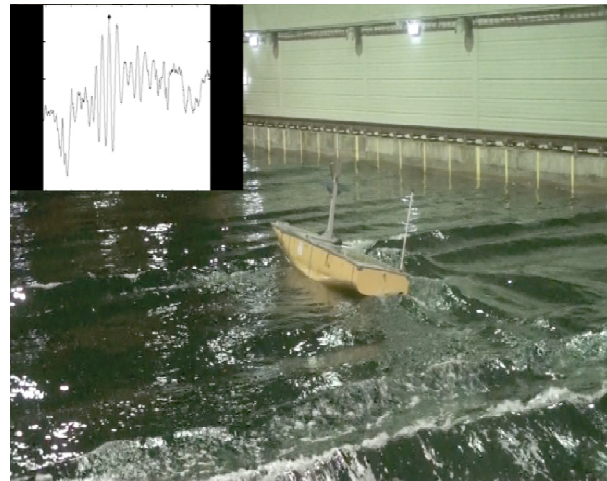


Figure 2: Model of a RoPax vessel in the multifunctional model basin of Aalto University. Instantaneous heel angle of 13 degrees.

The results of an exemplary model test run are shown in figure 3 and 4. The model is released in beam sea condition from the lower part of figure 4. Large angle roll motions are marked with dots. The different conditions of the vessel are also visible in the time history of the roll angle (figure 3).

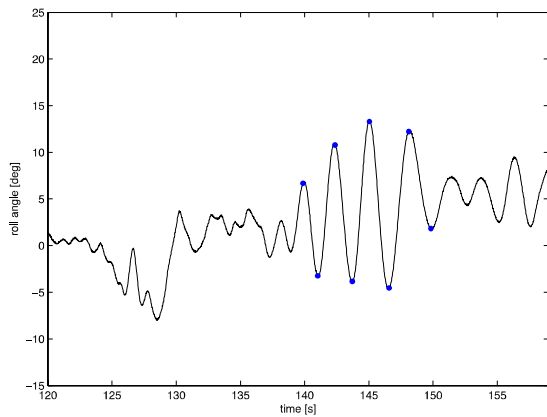


Figure 3: Time-history of roll motion (first stern quartering sea condition) during a turning circle test in irregular waves of significant height $H_S= 4.8$ [m] full-scale. Time is given in model scale. Marked situations represent peak-to-peak roll angles exceeding 8° .

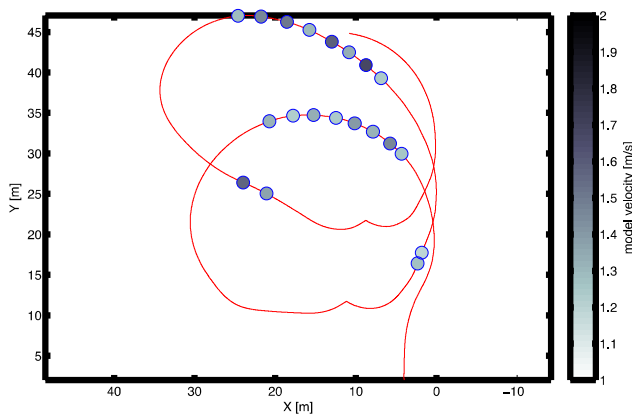


Figure 4: Path of the model during a turning circle evaluated from model speed and heading. Test in irregular waves of significant height $H_S= 4.8$ [m] full-scale. Marked situations represent peak-to-peak roll angles exceeding 8° .

After the calm interval of waiting and the first roll responses in beam seas, caused by waves and rudder actions, the first stern quartering roll resonance appears. This is followed by the second set of large roll angles when entering the sector of stern quartering waves within the second turning circle.

The severe change of the model's course in head waves is a result of voltage peaks coming from the heading measurement unit when changing the sign of the analogue output.

However, as the voltage returns to zero with a small drift only and as the following sea condition is the investigated one, these peaks can be neglected.

The form of roll response data presentation used when analyzing time histories of roll is a heading diagram showing the vessel's heading between the beam sea conditions of -90° (left half of the diagram) and $+90^\circ$ with the 0° heading (following sea) pointing towards the top of the diagram. Every dot represents the maximum peak-to-peak roll angle of one turning circle test divided by two (representing the roll angle to one side) and is coloured by the mean velocity occurring between the two large roll angles. The mean velocity of those situations as well as their standard deviation is given in the diagram's headline. The continuous lines are the calculated mean value of the vessel's heading of the respective resonance group; their standard deviation is depicted with the dashed lines. The blue half circles are isolines of a certain roll angle to one side. (Stigler 2012).

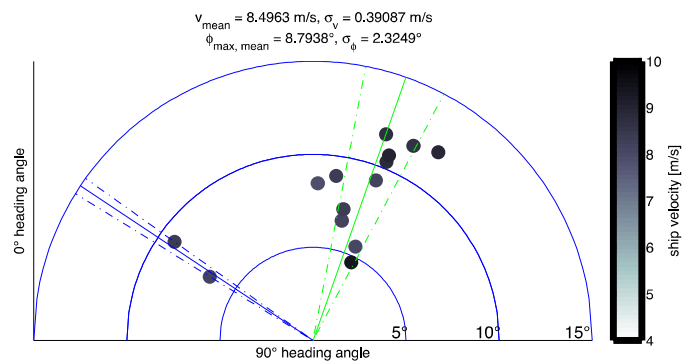


Figure 5: Measured heading regions of large roll angles for an irregular wave with the significant wave height of $H_S= 4.8$ [m] and an average period of $T_1= 5.9$ [s].

4. SIMULATION RESULTS

Simulated ship motion, corresponding to the conditions of model test, is presented in figure 6, while the heading diagram of the



simulation corresponding to the model tests is shown in figure 7.

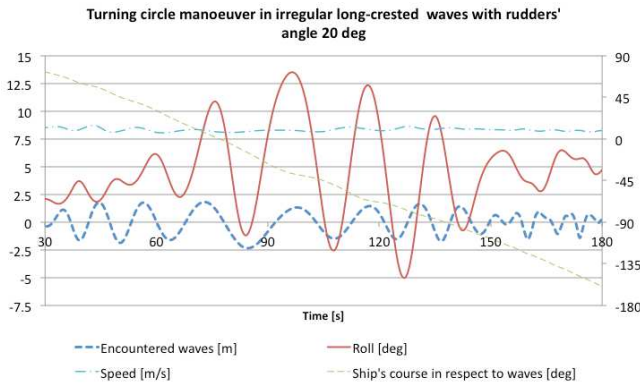


Figure 6: Simulated turning circle test in irregular waves of a significant wave height $H_S=4.8$ [m].

The main features of the model behaviour observed in tests are visible in the simulated results. For the stern quartering seas a focusing effect of irregular waves is observed. Wave group acting on a vessel with a critical frequency yields a resonant roll motion.

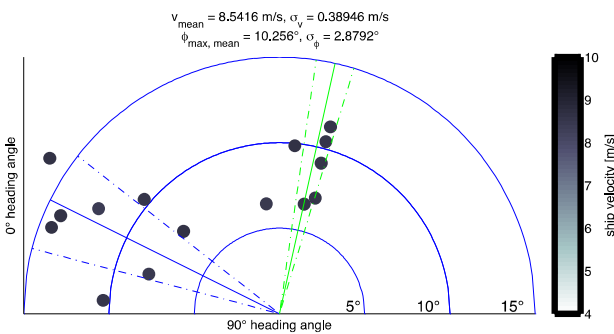


Figure 7: Computed heading regions of large roll angles for an irregular wave with the significant wave height of $H_S=4.8$ [m] and the average period of $T_1=5.9$ [s].

5. COMPARISON

The simulations depict the model tests quite accurately. Although the averaged heading angles with the highest roll angle responses differ a bit in both cases (the first (starboard sea) and the second quarter (port sea) of the turning circle)

the compared angles are always within the range of the standard deviation. Table 2 compares the heading differences and thus the differences between the roll resonance heading angles from the model tests and the simulations with their standard deviation.

Table 2 Comparison of the maximum roll heading angle differences and their standard deviations

Sign of heading	Heading difference [°]	Standard deviation [°]
+ (0° ... +90°)	6.9	8.5
- (-90° ... 0°)	6.5	12.2

A difference between the simulations and the model tests is that the relative number of points contributing to the second quarter (negative heading) is larger in the simulations, whereas it is lower in the model tests. It needs to be stated here that the simulation results are the more reasonable ones in this case, as it is a shortcoming of the model tests that the circular course of the vessel cannot be kept accurately enough throughout the whole run. It is clear that more maximum peak-to-peak events occur in the second quarter, when the vessel is already subject to higher roll angles coming from the first quarter, which are not damped to zero when entering the second resonance zone. In the simulation this results then mostly in higher roll angle responses for the negative heading angles. In the model tests, there are two major factors suppressing the occurrence of larger angles in the second quarter:

In order to save the vessel from colliding with the beach or the carriage in front, the rudder angle was often increased before reaching the part of the turning circle with the largest distance to the wave maker. Thus, the model had less time to develop larger angles in the second quarter and left the resonance area earlier.

Moreover, wave reflections close to the beach change the wave spectrum and may lead to non-resonance situations.



6. CONCLUSIONS

A qualitative agreement of simulation with the model tests results is noted for the investigated turning circle manoeuvre. In conclusion it can be said that time-domain simulation of ship manoeuvring motion in irregular waves is possible.

It is worth of noting that added mass corresponding to infinite frequency and the memory effect taken into account using the retardation function seem to suffice to simulate the considered manoeuvring motion.

There are many interesting matters that are worth of further research. These concern both a development of the mathematical model and improvement of experimental investigations. A quantitative validation would require amongst the others model tracking system and automatic (auto-pilot) control of model. Other types of manoeuvres in waves should be conducted and validated. Certainly there is a room for a further development of a combined model of hydrodynamic forces acting on a manoeuvring ship in waves, better modelling of control forces and propulsion in waves.

7. REFERENCES

- Cummins, W.E. (1962). The impulse response function and ship motions. *Schiffstechnik* pp. 101–109.
- Bailey, P.A. et al (1998). Theoretical and Experimental Techniques for Predicting Seakeeping and Manoeuvring Characteristics. Proceedings of the International Conference on Ship Motions & Manoeuvrability, 18&19 February 1998, London.
- Matusiak, J. (2001) Importance of memory effect for capsizing prediction. 5th International workshop University of Trieste 12. - 13. September 2001. Università di Trieste 2001, 6.3.1 (6 pages).
- Matusiak J. (2007). On certain types of ship response disclosed by the two-stage approach to ship dynamics. ACME, Archives of Civil and Mechanical Engineering, Vol. VII, nro 4, pages 151-166. 2007.
- Matusiak J. (2010). On the modelling of irregular waves in the non-linear ship dynamics method *Laidyn*. 18th International Conference on Hydrodynamics in Ship Design, Safety and Operation; Gdansk 12-14 May 2010.
- Panjaitan J P. (1998). A Study on Ship Motions and Capsizing in Severe Astern Seas. Doctoral Dissertation. Department of Naval Architecture and Ocean Engineering, Faculty of Engineering, Osaka University.
- Revised Guidance To The Master For Avoiding Dangerous Situations In Adverse Weather And Sea Conditions. (2007). IMO, MSC.1/Circ.1228 11 January 2007
- Stigler, C. (2012) Investigation of the behaviour of a RoPax vessel in stern quartering irregular long-crested waves, Student research project. Aalto University & Hamburg University of Technology.
- Takaishi Y. (1996). Probability of encounter high run of waves in the dangerous zone shown on the operational guidance/IMO for following/quartering sea. 2nd Workshop on Stability and Operational Safety of Ships, Osaka University, preprint draft papers, page numbers 43-52. November 1996.





Design Requirements for Stability and Minimal Motions in a Storm

Vasily N. Khramushin, *Sakhalin State University, Yuzhno-Sakhalinsk, Russia,*
V.Khram@GMail.com

ABSTRACT

The hydrodynamics of a ship in a storm is not limited to the hull below the calm-water waterline. In a storm, the operating waterline varies between the bilge and the deck, causing unpredictable waves forces on the hull as well as the possibility of slamming on flat surfaces and the flared side of the vessel.

The present work reveals the early stage of a design process for a hull form taking into account the range of changing of waterline, that insures stability under severe heave. With this approach it is possible to reduce the metacentric height, which minimizes roll resonance. The concept is a consistent ship design; conventional naval architectural approaches will still be needed for successful solutions for reducing the pitching and yawing of the vessel, and also as a necessary condition for using active side stabilizers and other seaworthiness improvements.

Keywords: *design for seaworthiness, stability, rolling, pitching, efficiency of operation*

1. INTRODUCTION

From a design standpoint there is a contradiction in dynamical properties of a ship; improving one leads to the deterioration of another.

So, an attempt to increase the initial static stability results in increased rolling of the ship in severe seas leading to, potentially catastrophic problems with the strength of the hull structure. It is a paradox — attempting to improve static stability may lead to an increased likelihood of capsizing as a result of strong resonant rolling or broaching.

Significant difficulties in the operation of a vessel may occur when the freeboard and reserve buoyancy are too large for the vessel, particularly with the implementation of other requirements without consideration of green water on deck, or by installation of unwieldy life-saving equipment, that can pose a danger for mariners.

Let us consider some elements of hull shape optimization and general ship geometry

from the standpoint of achieving the best seaworthiness of the vessel.

2. MARINE DESIGN EXPERIENCE

A ship design for seaworthiness, considers a hull form with a sharp cruiser stern and no increased freeboard in the bow section. Such a vessel has no flare and no bulbous bow, as too much volume forward makes a ship pitch. Such hull form is capable of maintaining operability in all-weather conditions.

Such a design has almost constant waterplane area as a function of draft and low damping in heave. As a result this vessel's stability in waves is essentially constant; thus the minimum stability occurs at the design condition. To remedy this situation the static stability with varying draft must be changed.

Modern vessels with a wide transom stern and with flare and increased freeboard at the bow, experiencing intensive pitching in longitudinal waves. In this mode of sailing, the hydrodynamic effect of excessive volumes in the



extremities is essential when the hull of a vessel moving thru the wave crest and over the wave through. However, the hydrostatic approach to this problem is not contrary to the implementation of the proposed scheme of the hull design. The objective of this work is finding a compromise between the proposed design scheme and modern hull forms.

2.1 Hydrostatic peculiarities of a highly seaworthy vessel

The hydromechanics of a ship in extreme seas includes some design paradoxes, which significantly affect the seaworthiness of non-optimized vessels, and, in fact, determines the possibility of the all-weather or the special modes of vessel operation in accordance with the vessel's design purpose.

Some elements in the hull forms design are well established in the maritime history, and now their use is somewhat weakened in favor of efficiency of cargo handling, increased volumetric capacity, or sometimes just for aesthetic reasons.

Identification of and optimal resolution of the hydrometrical paradoxes is defined by accounting for the adverse effects of weather through specifically designed lines. Let us consider some specific elements of the hull form:

The metacentric radius r (BM) has cubic dependence on the breadth B .

$$r = J_X/V = \frac{1}{V} \frac{2}{3} \int_{x_K}^{x_H} y^3 dx \Big|_{WL} \quad (1)$$

where V is the displacement; J_X is the transverse moment of inertia of the existing waterplane area relative to the longitudinal x axis; and y is the ordinate of the waterplane, the width of the body at a particular point of x axis at the level of the current waterline WL .

In a storm conditions external forces and moments are created by the curved sea surface and this affects the stability of a ship

$$m_g = \gamma \cdot r \cdot V \cdot \sin(\vartheta) = \gamma \cdot J_X \cdot \sin(\vartheta) \quad (2)$$

where m_g is the exciting moment; $\gamma = 1025 \text{ kg/m}^3$ is the density of water; and ϑ is the angle of wave slope.

Note that this moment is not balanced by the weight of the vessel; this moment reaches its maximum value for vessels with a wide transom sterns. This moment may be dangerous for multihull vessels, because it is directly dependent on the area of waterplane, since the metacentric radius (BM) changes as the cube of the offsets.

The formula for the metacentric radius is consistent with the subsequent results of hydrostatic calculations at large roll angles. To be able to assess the stability of the vessel as a rigid body in a storm, fix the center of gravity at the z -coordinate of the metacenter at a given draft.

To achieve smoothness of roll in a storm, a captain always tries to reduce the metacentric height by raising the KG of the vessel towards the KM -value (fig. 1). This decreases roll motions because of the suppression of external forces by the inertia of the ship. This process is described by the "captain's" formula for initial stability:

$$T_g = C \cdot B / \sqrt{h} = C \cdot B / \sqrt{r + z_C - z_g} \quad (3)$$

where: $C \approx 0,8 \text{ [cm/m}^{1/2}]$ is a dimensional empirical coefficient with a characteristic value for the conventional monohull cargo vessels; z_C is the z -coordinate of the center of buoyancy (KB); and z_g is the z -coordinate of the center of gravity (KG).

If the center of gravity is significantly above the waterline, the ship becomes vulnerable to impact by a single wave from the side.

The contours of the stations in the midship section of the optimized vessel (fig. 2) are close to a circle, and it has a beam-to-draft ratio (B/T) of about two. Accordingly, the z -coordinate of the metacenter will be at about the level of the current waterline. Then, the

effect of a single wave relative to the center of gravity that is located near the metacenter. Such an effect produces a relatively small moment and does not lead to significant roll motions.

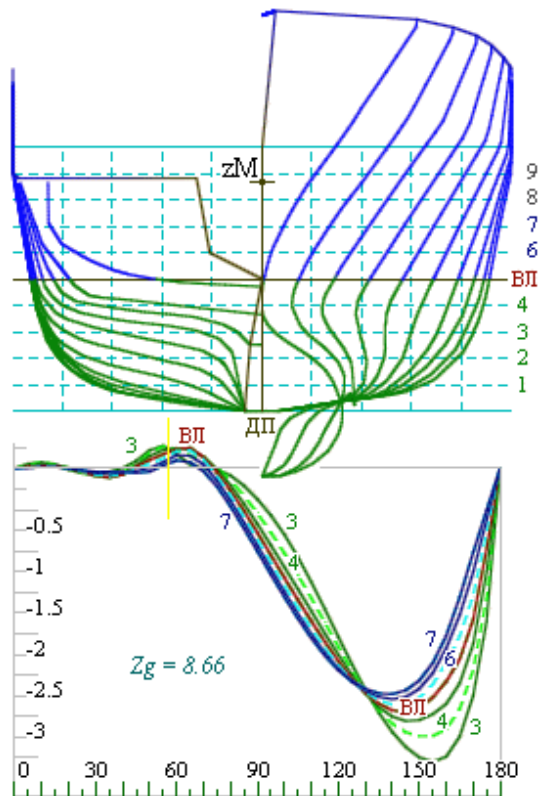


Figure 1: Top: Body plan for conventional hull form; Bottom: the static stability diagrams of the ship for five waterlines, the z -coordinate of the center of gravity is fixed at the position of the metacenter at the design draft. The natural stable position of the ship hull is “keel up”.

The hydrostatic and Froude-Krylov moment in pitch of a long vessel cannot be reduced by increasing the KG , because the longitudinal metacenter is too high. Thus the lines can only be optimized to decrease of external forcing, so the ship will simply contour the waves.

Once the hydrostatic and Froude-Krylov forces are minimized, then a further decrease of pitch and roll motions can be achieved by considering the hydrodynamics of the hull in trochoidal waves. This is a separate problem considered in (Khrushin, 2009)

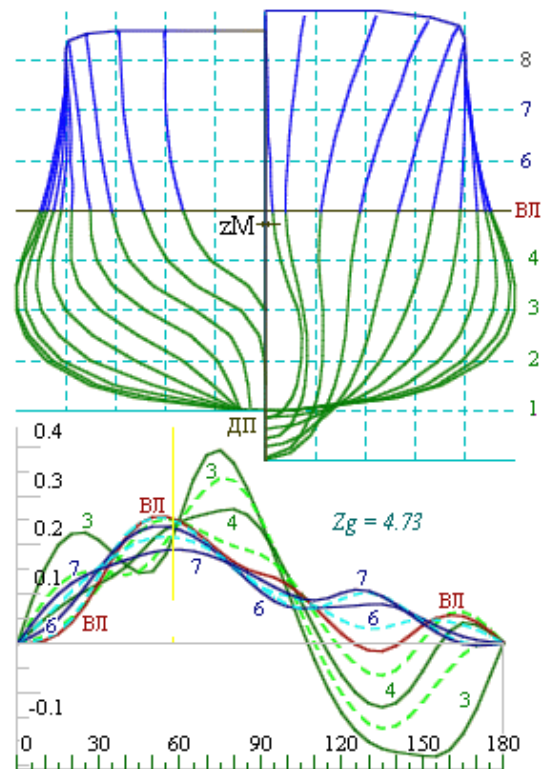


Figure 2: Top: Body plan for optimized hull form; Bottom: the static stability diagrams of the ship for five waterlines, the z -coordinate of the center of gravity is fixed at the position of the metacenter at the design draft. The meta-centric height of the optimized ship can be safely brought to zero at the design draft. GM will be positive for any other draft and there is a large reserve of stability.

Here we focus on a simple optimization of lines by consideration of Froude-Krylov and hydrostatic forces. The main approach is the method so-called non-contradictory design.

3. SHIP STABILITY WHILE OPERATING IN A STORM

The expected technical result is a displacement ship with a relatively deep draft and pointed extremities (cruise stern and “reclined stem” [stem inclined back]). The reserve buoyancy is concentrated in the in the midship section. The GM is minimal at the design draft. Thus, the GM increases with any variation of the draft. This is achieved by special design of the lines (Khrushin, 2011). The



next subsection is focused on analysis of the hydrostatics of the midship section only.

3.1 Analysis of Metacentric Height at Design Draft

The stability of a wall sided ship is characterized by the value of metacentric height h (GM). The variation of GM during heave motions is caused by changes of the vertical position of the center of buoyancy z_c (KB) and volumetric displacement. The GM increases with an increase of KB and decreases with an increase of the displaced volume. We also fix the center of gravity. The transverse moment of inertia of the waterplane J_x is constant since wall-sidedness is assumed,

$$h = z_M - z_g = r + z_C - z_g = J_x/V + z_C - z_g \quad (4)$$

where h is the metacentric height; z_M is the vertical position of the metacenter (KM); z_g is the

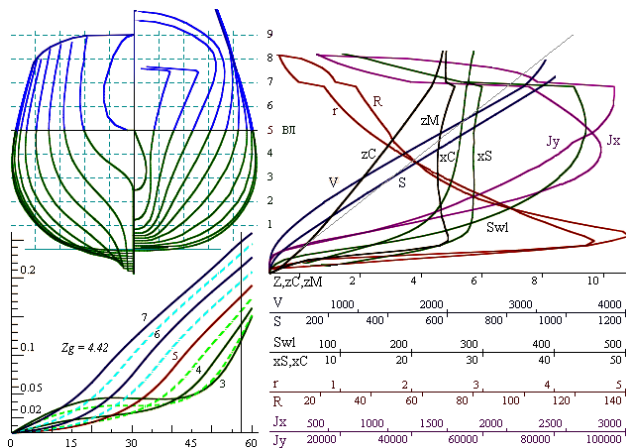


Figure 3: Top left: Body plan for a tug/rescue ship, capable of active maneuvering in severe seas at low speeds; Bottom left: the static stability diagrams of the ship for five waterlines; Right: hydrostatic curves (of particular importance is the location of the metacenter as a function of draft (z_M)).

fixed vertical position of the center of gravity; and r is the transverse metacentric radius (KM). All of the quantities in equation (4), except z_g , are computed as integrals of ship offsets and are functionally related to the draft.

They can be seen in the hydrostatic curves (right-hand side of figs. 3 & 4).

In the case of a wall-sided midship section, the minimum of the vertical position of the metacenter z_M (KM) occurs for $B/T=3$.

Accordingly, for a ship with $B/T > 3$, the minimum z_M (KM) is achieved for a flared configuration due to the rapid increase in $J_x(z)$ on the hydrostatic curves (right-hand side of figs. 3 & 4). The behavior of such ship in a storm includes significant pitch and roll, however, she is capable of contouring waves.

A vessel with good seaworthiness should have $B/T \leq 2$. Thus a minimum KM can be achieved at the design draft. Such a ship must have a tumblehome shape at the waterline.

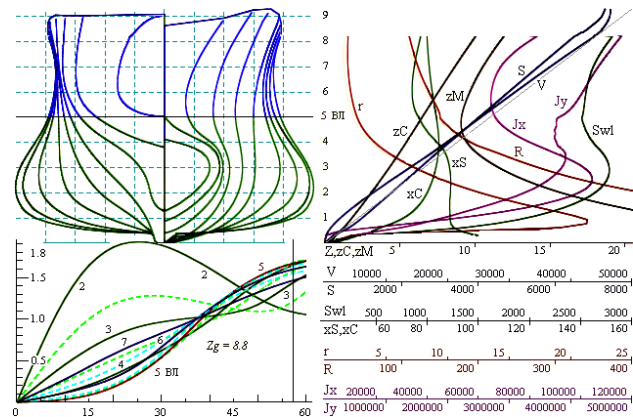


Figure 4: Top left: Body plan for a universal cargo ship, capable of operation in a storm with minimum motions at zero GM values; Bottom left: the static stability diagrams of the ship for five waterlines; Right: hydrostatic curves (of particular importance is the location of the metacenter as a function of draft (z_M)).

Ship lines with a round midship section does not have a clear minimum of KM (z_M in fig. 3). Therefore it becomes important to maintain positive metacentric height, because the reserve stability is small and roll motions may reach large amplitudes. An increase in stability leads to an increase of motions.

The minimum of the KM is shown most clearly for the configuration in fig. 4. The stations have concave shape at the design water-



line — the KM as a function of draft has a minimum around the DWL.

4. BRIEF DESCRIPTION OF THE DRAWINGS

Stability in storm conditions should be provided by shape of the hull as the draft varies. This effect can be easily achieved for a ship design with concave stations at the waterline (fig. 4) and — with the most difficulty for a ship with round stations (fig. 3).

Hydrostatic curves provide a quantitative description of the forms (right-hand side of figs. 3 & 4). The stability is associated with the condition of mutual compensation of the changes of moment $z_C V$ relative to base plane, through the moment of inertia of the waterplane J_X . Geometrically, it is the choice between wall-sided, flared or tumblehome configuration of the midship section at the waterline. In fact, this is the optimization of the angle of side slope at the design draft. The algorithm was implemented in a computer program — “Hull” with Russia state registration number 2010615849.

The GZ curve (figs. 3 & 4, bottom left) is computed for a variety of drafts at a fixed value of KG , the curve with zero metacentric height (labeled “5”) corresponds to the design draft, and other curves (3, 4, 6 & 7) — show positive initial stability as the draft varies.

All calculations were performed for a fixed position of the center of gravity z_g (KG), placed exactly that the metacenter at the design draft, where the initial stability is equal to zero ($h_{WL} = 0$).

The graphs on the right show the hydrostatic curves computed for the vessel depicted on the left.

5. CONCLUSIONS

The paper presents the ways to optimize the initial elements of a ship’s lines based on hydrostatic calculations. This provides a reliable quantitative estimate of the performance of the

vessel in a storm. This hydrostatic assessment of seaworthiness is applicable to all classes of ships and vessels.

All these design solutions and seaworthiness estimations must be explained by operational guidance onboard of ship’s bridge and on shore services. This knowledge can enhance operability of the ship in complex storm and ice conditions. These hydrostatic assessments make-up the foundation for further deeper design optimization based on the fluid mechanics interaction between the hydro- and aero-mechanics of the ship in storm sea and hurricane winds.

6. ACKNOWLEDGMENT

The author is grateful to Dr. Art Reed for his detailed editing that has greatly improved clarity and readability of the text.

7. REFERENCES

- Khramushin V., (2009) “Key Design Solutions and Specifics of Operation in Heavy Weather (Fluid Mechanics Approach to Stabilization of Ship in Heavy Seas)” Proceedings. 10th International Conference on Stability of Ships and Ocean Vehicles. STAB-2009, S-Petersburg, Russia. pp. 473–482.
(<http://www.shipdesign.ru/News/2009/STAB-eng.html>)
- Khramushin V. The ship, the stability in a stormy operation. Patent application ⁽¹⁹⁾RU ⁽¹¹⁾ 2011129192 from 12.07.2011. Sakhalin State University.
(<http://www.shipdesign.ru/Invent/06.html>, *in Russian*).





Stability of Ships in Parametric Roll Resonance Under Time-Varying Heading and Speed

Dominik A. Breu, *Centre for Ships and Ocean Structures, Norwegian University of Science and Technology, Norway*, breu@itk.ntnu.no

Christian Holden, *Department of Engineering Cybernetics, Norwegian University of Science and Technology, Norway*, c.holden@ieee.org

Thor I. Fossen, *Department of Engineering Cybernetics, Norwegian University of Science and Technology, Norway*, fossen@ieee.org

ABSTRACT

In this work, we derive an analytical 1-DOF roll model which is able to describe the dynamics of a ship in parametric resonance. We extend previous results to allow for slowly time-varying heading angle and speed. The hydrostatic and hydrodynamic model coefficients are identified based on simulations of an accurate 6-DOF ship model which accounts for first-order generalized pressure forces and moments by numerical integration of the instantaneous pressure field of the surrounding ocean over the instantaneous submerged hull. We determine functional expressions for the hydrodynamic coefficients which are dependent on the heading angle, resulting in an analytical 1-DOF roll model that is suitable for mathematical analysis and control purposes. We verify the model against the 6-DOF ship model in simulations.

Keywords: *Roll stability, Parametric roll, Nonlinear system, Time-varying system, Automatic control*

1. INTRODUCTION

Parametric roll resonance is a dangerous resonance phenomenon that has the ability to cause extreme roll angles for a wide range of ship types. Parametric roll resonance occurs in head or stern seas, with long-crested waves. The waves cause large changes in the ship's water plane area, resulting in a time-varying restoring term in roll. This effectively renders roll unstable as long as the encounter frequency is within a certain (ship-specific) range. Roll angles of over 40° have been observed on real ships. (Carmel, 2006; France et al., 2001; Galeazzi, 2009; Holden, 2011)

The effect of static encounter frequencies has been extensively investigated (ABS, 2004). Significantly less research has been done on the

effects of time-varying encounter frequencies (Holden, 2011). The encounter frequency (the frequency of the waves as seen from the ship) can be changed via the Doppler effect. In practice, this can be done by changing the velocity of the ship relative to the waves. For most ships, this would be done by changing the surge speed and/or the course angle.

In Breu et al. (2012); Holden et al. (2012), a 6-degree-of-freedom (DOF) and a simplified 1-DOF model for ships in parametric roll with time-varying forward speed was presented and analyzed. The simplified model was also used to stabilize the roll angle by means of changing the forward speed, but not the course.

Changing the course can have adverse effects on the ship. When sailing in head seas, the ship



would not greatly suffer directly induced roll (but could be susceptible to parametric roll) (Holden, 2011). However, changing the course too much would potentially make the ship vulnerable to directly induced roll motion. If the course is changed too little, the ship will still be susceptible to parametric roll resonance. Great care must therefore be used when changing course during parametric roll resonance. These issues have not been extensively addressed by the research community (Holden, 2011).

In this work, we analyze the 6-DOF and 1-DOF models under both time-varying forward speed and yaw angle. The 1-DOF model is extended to incorporate non-constant yaw angles and the model parameters are identified by curve fitting. Stability regions are investigated in simulations.

The remainder of this paper is organized as follows: Section 2 summarizes the 6-DOF ship model as used in Breu et al. (2012). Section 3 presents the extended 1-DOF roll model which is able to handle both time-varying speed and time-varying heading angles. In Section 4, the hydrostatic and the hydrodynamic coefficients of the 1-DOF roll model are identified and the model is verified in Section 5. Section 6 contains the conclusion.

2. 6-DOF SHIP MODEL

In Breu et al. (2012), we derived a highly accurate 6-DOF ship model of a container ship which accounts for the first-order external forces and moments on the ship due to the hydrostatic and hydrodynamic pressure field of the ocean. The ship model is numerical, and the instantaneous ocean pressure is integrated over the instantaneous submerged hull at each time step. This gives the generalized external forces and generalized restoring forces (except gravity) on the ship.

The 6-DOF ship model is given by (Breu et al., 2012; Fossen, 2011)

$$\dot{\boldsymbol{\eta}} = \mathbf{J}(\boldsymbol{\Theta})\mathbf{v} \quad (1)$$

$$\mathbf{M}\dot{\mathbf{v}} + \mathbf{D}(\mathbf{v})\mathbf{v} + \mathbf{C}(\mathbf{v})\mathbf{v} + \mathbf{k}(\boldsymbol{\eta}, t) = \boldsymbol{\tau}_c + \boldsymbol{\tau}_e \quad (2)$$

where the ship's generalized position vector $\boldsymbol{\eta} = [\mathbf{p}^{n\top}, \boldsymbol{\Theta}^\top]^\top \in \mathbb{R}^6$ consists of its position in the inertial frame $\mathbf{p}^n = [x^n, y^n, z^n]^\top \in \mathbb{R}^3$ and the vector of Euler angles $\boldsymbol{\Theta} = [\phi, \theta, \psi]^\top \in \mathbb{R}^3$ which represents its rotation relative to the inertial reference frame. The ship's generalized velocity vector is denoted by $\mathbf{v} = [\mathbf{v}^{b\top}, \boldsymbol{\omega}^{b\top}]^\top \in \mathbb{R}^6$ where $\mathbf{v}^b = [u, v, w]^\top \in \mathbb{R}^3$ is the ship's linear and $\boldsymbol{\omega}^b = [p, q, r]^\top \in \mathbb{R}^3$ the angular velocity vector, both expressed in a body-fixed reference frame. The transformation matrix $\mathbf{J} \in \mathbb{R}^{6 \times 6}$ transforms the body-fixed velocities into inertial reference frame velocities and is as defined in Fossen (2011).

The sum of the rigid-body inertia and added mass is denoted by $\mathbf{M} \in \mathbb{R}^{6 \times 6}$ in (2), whereas $\mathbf{D} \in \mathbb{R}^{6 \times 6}$ and $\mathbf{C} \in \mathbb{R}^{6 \times 6}$ are the damping and the Coriolis/centripetal matrices, respectively. The generalized control forces are $\boldsymbol{\tau}_c \in \mathbb{R}^6$ and the generalized forces due to environmental disturbances other than waves are $\boldsymbol{\tau}_e \in \mathbb{R}^6$ (wave effects are included in \mathbf{k}). The model is equipped with a simple PID controller to maintain course and surge speed.

$\mathbf{k} = \mathbf{k}_p + \mathbf{k}_g \in \mathbb{R}^6$ is the sum of the generalized pressure and the gravity forces where the latter are given by Fossen (2011)

$$\mathbf{k}_g(\boldsymbol{\eta}) = -mg \begin{bmatrix} \mathbf{R}^\top(\boldsymbol{\Theta})\mathbf{e}_z \\ (\mathbf{R}^\top(\boldsymbol{\Theta})\mathbf{e}_z) \times \mathbf{r}_g^b \end{bmatrix}. \quad (3)$$

Here, $\mathbf{r}_g^b \in \mathbb{R}^3$ is the ship's center of gravity in the body-fixed reference frame, $\mathbf{e}_z = [0, 0, 1]^\top$, m the ship's mass, and g the acceleration of

gravity. The rotation matrix $\mathbf{R} \in \mathbb{R}^{3 \times 3}$ is as defined in Fossen (2011).

\mathbf{k}_p is computed by integrating the instantaneous pressure over the instantaneous submerged hull, under the assumption that the ocean pressure field is unchanged by the passage of the ship (the waves are effectively traveling “through” the vessel). We assume that the ship's hull consists of sections, and that each section can be parameterized with parameters a and b . We let the position of a point on the surface of the panel i in the body-fixed reference frame be $\mathbf{r}_i^b(a, b) \in \mathbb{R}^3$. The local pressure field at any given point $\mathbf{r}^n \in \mathbb{R}^3$ in the ocean is, under the same assumptions as in Breu et al. (2012), $\Psi \approx \Psi(\mathbf{r}^n, t) \in \mathbb{R}$ (Faltinsen, 1998; Perez, 2005). By defining

$$\Psi_i(a, b) \triangleq \Psi(\mathbf{R}\mathbf{r}_i^b(a, b) + \mathbf{x}^n, t), \quad (4)$$

the generalized pressure forces of the surrounding ocean on the ship are (Perez, 2005; White, 2002)

$$\mathbf{k}_p(\boldsymbol{\eta}, t) = \sum_i \begin{bmatrix} f_i \\ g_i \end{bmatrix} \quad (5)$$

where

$$\begin{aligned} f_i &= \int_{S_{w,i}} \Psi_i(a, b) \frac{\partial \mathbf{r}_i^b}{\partial a}(a, b) \times \frac{\partial \mathbf{r}_i^b}{\partial b}(a, b) da db \\ g_i &= \int_{S_{w,i}} \Psi_i(a, b) \mathbf{r}_i^b(a, b) \\ &\quad \times \left(\frac{\partial \mathbf{r}_i^b}{\partial a}(a, b) \times \frac{\partial \mathbf{r}_i^b}{\partial b}(a, b) \right) da db \end{aligned}$$

are the forces and moments on panel i due to the pressure of the surrounding ocean. The wetted part of panel i is $S_{w,i}$ and the ship is parameterized so that the normal vector $(\partial \mathbf{r}_i^b / \partial a) \times (\partial \mathbf{r}_i^b / \partial b)$ points out of the hull. The generalized force \mathbf{k}_p accounts for all the

effects of current and waves (Faltinsen, 1998; Perez, 2005).

Note that the pressure forces are not the same as the Froude-Krylov force, although made under somewhat similar assumptions, as the force used in the 6-DOF model – unlike the Froude-Krylov force – is computed based on numerical integration of the instantaneous submerged hull.

Refer to Breu et al. (2012) for further details of the calculation of the generalized pressure forces.

3. 1-DOF ROLL MODEL

The complex 6-DOF ship model (1) and (2) of Section 2 is a numerical model which relies on the integration of the hydrodynamic and hydrostatic pressure field over the instantaneous submerged part of the hull. Though the 6-DOF model is highly suitable for simulation studies, its usability for control purposes and mathematical analysis is limited.

In Breu et al. (2012), we considered the three most important degrees of freedom for a ship in parametric roll resonance, that is, the heave, roll and pitch motions. By using a quasi-steady approach we derived an analytical 1-DOF roll model – a model with an explicit functional (rather than a numerical) relationship between time and wave force – which accurately captured the parametric roll motion of a ship. However, the 1-DOF model in Breu et al. (2012) assumed that only the ship's surge speed could change, while the heading angle was assumed constant.

In this section, we will derive an analytical 1-DOF roll model where the ship's speed and heading angle are allowed to be time-varying, if only slowly. For a large ship, like many ships susceptible to parametric roll (Holden, 2011), this is a reasonable assumption.



Motivated by the model introduced in Breu et al. (2012) and following the same derivation, we tentatively choose the 1-DOF roll model as

$$m_{44}\ddot{\phi} + d_{44}\dot{\phi} + \kappa_2 \cos\left(\int_{t_0}^t \omega_e(\tau) d\tau + \kappa_3\right)\phi + \kappa_1\phi + \kappa_4\phi^3 = \kappa_5 \sin\left(\int_{t_0}^t \omega_e(\tau) d\tau + \kappa_6\right) \quad (6)$$

where m_{44} is the sum of the rigid-body moment of inertia and the added moment of inertia in roll and d_{44} is the linear damping coefficient in roll. The linear and the cubic restoring coefficients in roll are κ_1 and κ_4 , respectively. Those are hydrostatic coefficients and thus assumed constant. The coefficients $\kappa_i = \kappa_i(u, \psi)$, $i \in \{2, 3, 5, 6\}$, may be dependent on the ship's surge speed and heading angle or both (e.g., $\kappa_5 \approx 0$ for head seas).

For simplicity, we assume that the waves are traveling along the inertial x -axis, and are sinusoidal.

The encounter frequency ω_e is the frequency of the waves perceived by an observer moving with the ship. Essentially, the encounter frequency is the Doppler-shifted wave frequency due to the non-zero speed of the ship, and it can be expressed as (Breu et al., 2012)

$$\omega_e = \frac{d}{dt} \left(\omega_0 t - k_w \int_{t_0}^t u^n(\tau) d\tau \right) \approx \omega_0 - k_w \cos(\psi) u \quad (7)$$

where ω_0 is the modal wave frequency, k_w the wave number as seen in the inertial frame and u^n is the ship's speed along the inertial x -axis. It is evident from (7) that the encounter frequency is dependent on both the ship's surge speed and the heading angle.

The model introduced in Breu et al. (2012) and the 1-DOF roll model (6) differ in three major

aspects. Whereas the model in Breu et al. (2012) assumes constant coefficients, most of the model coefficients in (6) are explicitly allowed to be dependent on the ship's surge speed and heading angle. Furthermore, the model (6) incorporates directly excited roll motion by considering the external forcing term on the right hand side of (6) (the Froude-Krylov force (Perez, 2005)) which was neglected in Breu et al. (2012) due to the ship sailing in head sea conditions. Finally, in Breu et al. (2012), $\dot{\psi} \equiv 0$ and $\dot{u} \neq 0$. Here, $\dot{\psi} \neq 0$ and $\dot{u} \neq 0$.

4. MODEL COEFFICIENT IDENTIFICATION

In this section, the coefficients κ_i , $i \in \{1, \dots, 6\}$ of the 1-DOF roll model (6) will be identified from simulations of the 6-DOF model (1) and (2).

The hydrostatic coefficients κ_1 and κ_4 are constants, and they can be determined from simulations without waves. κ_2 and κ_3 are the coefficients of the change in the amplitude of the linear restoring moment in roll and its phase due to the passage of the waves, and account for the coupling of roll to the heave and pitch motions. The external wave forcing is considered by the right hand side of (6) with its hydrodynamic coefficients κ_5 and κ_6 .

4.1 Hydrostatic Coefficients

The constant coefficients κ_1 and κ_4 are found by a free decay test. Define the spring torque for the 1-DOF roll model (6) without wave influence as

$$k_{\bar{\phi}}(t; \bar{\kappa}) = \kappa_1 \phi(t) + \kappa_4 \phi^3(t). \quad (8)$$

The hydrostatic coefficient vector $\bar{\kappa} = [\kappa_1, \kappa_4]$ is identified by a nonlinear least-square curve

fitting of (8) to the pressure-induced generalized forces in roll of the 6-DOF model (1) and (2) simulated in a calm water scenario. Thus, by denoting the fourth element of \mathbf{k} in (2) as $k^{(4)}$, $\bar{\kappa}$ is given by

$$\bar{\kappa} = \arg \min_{\bar{\kappa}} \sum_t \left| k^{(4)}(\boldsymbol{\eta}(t), t) - k_{\bar{\kappa}}(t; \bar{\kappa}) \right|^2 \quad (9)$$

4.2 Hydrodynamic Coefficients

The identification of the hydrodynamic coefficients $\tilde{\kappa} = [\kappa_2, \kappa_3, \kappa_5, \kappa_6]$ is done in the following way:

The complex 6-DOF model is simulated for a wide range of constant u, ψ doubles, and the pressure-induced moment in roll (the fourth element of \mathbf{k} , that is $k^{(4)}$) is saved. We define the sum of the restoring and external moments in roll as

$$k_{\phi}(t; \kappa) = \left[\kappa_1 + \kappa_2 \cos \left(\int_{t_0}^t \omega_e(\tau) d\tau + \kappa_3 \right) \right] \phi(t) + \kappa_4 \phi^3(t) - \kappa_5 \sin \left(\int_{t_0}^t \omega_e(\tau) d\tau + \kappa_6 \right) \quad (10)$$

The coefficients $\tilde{\kappa}$ for these conditions are then found as

$$\tilde{\kappa} = \arg \min_{\tilde{\kappa}} \sum_t \left| k^{(4)}(\boldsymbol{\eta}(t), t) - k_{\phi}(t; \tilde{\kappa}) \right|^2 \quad (11)$$

where we use the values of the hydrostatic coefficients κ_1 and κ_4 found from the free decay tests in Section 4.1. This procedure results in one set of $\tilde{\kappa}$ s per u, ψ double. The parameters for the simulations of the 6-DOF ship model are equivalent to the ones presented in Breu et al. (2012).

Figures 1–4 show the results of this procedure for surge speeds u ranging from 0m/s to 10m/s and for heading angles ψ from 0° to 90°. Note that heading angles of 0° and 90°

correspond to the ship sailing in head sea and beam sea conditions.

The hydrodynamic coefficient κ_6 represents the phase angle of the external sinusoidal wave force. Note that, in head sea conditions ($\psi = 0^\circ$) the amplitude of the external forcing term is zero which can be observed in Figure 3. As a consequence κ_6 cannot be estimated in those conditions.

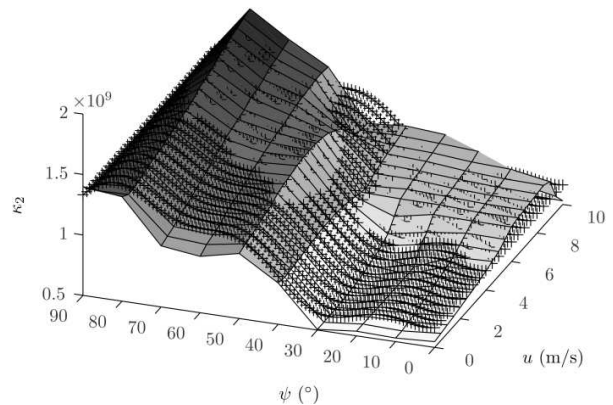


Figure 1: Hydrodynamic coefficient κ_2 and its functional approximation (denoted by +)

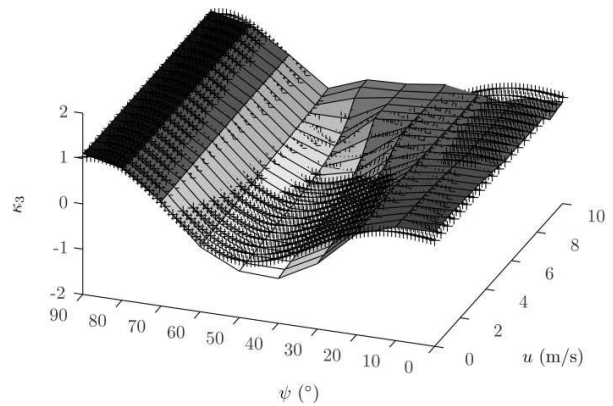


Figure 2: Hydrodynamic coefficient κ_3 and its functional approximation (denoted by +)

4.3 Identification of $\tilde{\kappa}$

We desire a functional expression for the coefficients $\tilde{\kappa}$ for a wide range of surge speeds and heading angles. This allows the analytical analysis of the roll, giving both easier analysis and better simulation than a numerical model.

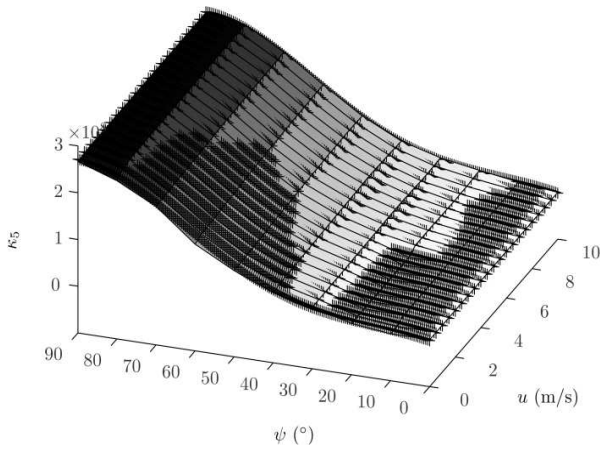


Figure 3: Hydrodynamic coefficient κ_5 and its functional approximation (denoted by +)

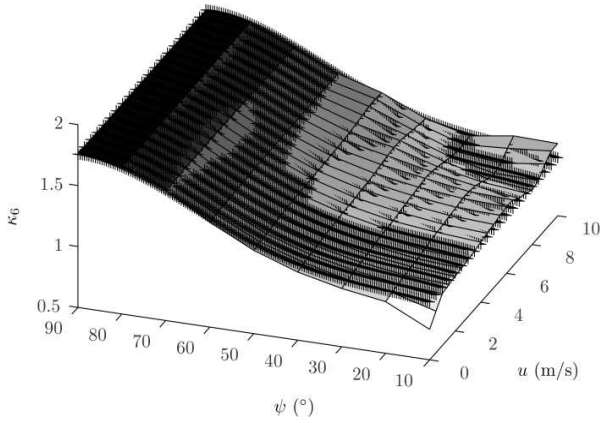


Figure 4: Hydrodynamic coefficient κ_6 and its functional approximation (denoted by +)

We use the values of $\tilde{\kappa}$ obtained in Section 4.2 to derive a functional relationship between ψ and u and $\tilde{\kappa}$. From Figures 1–4, it appears that $\tilde{\kappa}$ predominantly varies with the heading angle ψ , not the surge speed u . Furthermore, the relationship appears to be sinusoidal in nature. We therefore use the following functions for $\tilde{\kappa}$:

$$\begin{aligned} \kappa_2 = \kappa_2(\psi) = & \varkappa_{2,1} \sin(\varkappa_{2,2}\psi + \varkappa_{2,3}) \\ & + \varkappa_{2,4} \sin(\varkappa_{2,5}\psi + \varkappa_{2,6}) \\ & + \varkappa_{2,7} \sin(\varkappa_{2,8}\psi + \varkappa_{2,9}) \end{aligned} \quad (12)$$

$$\begin{aligned} \kappa_3 = \kappa_3(\psi) = & \varkappa_{3,1} \sin(\varkappa_{3,2}\psi + \varkappa_{3,3}) \\ & + \varkappa_{3,4} \sin(\varkappa_{3,5}\psi + \varkappa_{3,6}) \end{aligned} \quad (13)$$

$$\begin{aligned} \kappa_5 = \kappa_5(\psi) = & \varkappa_{5,1} \sin(\varkappa_{5,2}\psi + \varkappa_{5,3}) \\ & + \varkappa_{5,4} \sin(\varkappa_{5,5}\psi + \varkappa_{5,6}) \end{aligned} \quad (14)$$

$$\begin{aligned} \kappa_6 = \kappa_6(\psi) = & \varkappa_{6,1} \sin(\varkappa_{6,2}\psi + \varkappa_{6,3}) \\ & + \varkappa_{6,4} \sin(\varkappa_{6,5}\psi + \varkappa_{6,6}). \end{aligned} \quad (15)$$

To determine the parameter values for $\tilde{\kappa}$, we curve fit the above functions to the data gathered for $\tilde{\kappa}$ in the first step in Section 4.2. The results of the curve fitting of the functions (12)–(15) are shown in Figures 1–4 (denoted by + in the plots).

The coefficients κ_5 and κ_6 , corresponding to the external wave forcing, are very well approximated by the functional expressions (14) and (15). On the other hand, the approximations of κ_2 and κ_3 which account for the coupling of roll to the heave and pitch motion, are less accurately described by (12) and (13). Mainly for large surge speeds and small heading angles, there is a discrepancy between the hydrodynamic coefficients and its functional approximations. In Section 5 it will become evident that this corresponds to when the ship is experiencing parametric roll resonance. However, we will show that the functional expressions for κ_2 and κ_3 are appropriate to describe the roll dynamics to a satisfactory extent.

5. MODEL VERIFICATION

In this section, we verify the 1-DOF roll model of Section 3 with the hydrodynamic coefficients given by the functional expressions presented in Section 4.3. To that matter, we simulate the 1-DOF roll model and compare it to simulations of the complex 6-DOF model of Section 2. The simulations are performed using the same model parameters as in Breu et al. (2012).

5.1 Maximum Roll Angle

We simulate the 6-DOF ship model (1) and (2) for a wide range of surge speeds and heading angles. For each simulation, the surge speed and the heading angle are kept constant (except

for small variations due to the limited bandwidth of the speed and heading controllers). Then, we simulate the 1-DOF roll model (6) where the surge speed and heading angle of the previous simulations of the 6-DOF model enter via the encounter frequency (7). The maximum steady-state roll angles of the various simulation scenarios for the different models are depicted in Figures 5–7.

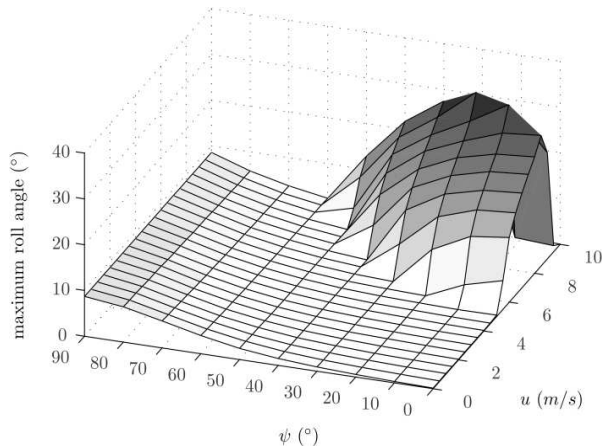


Figure 5: Maximum roll angle, 6-DOF model

From the simulations of the 6-DOF ship model depicted in Figure 5, it is evident that the ship is experiencing parametric roll resonance of up to 30° for large surge speeds and small heading angles. This corresponds to an encounter frequency which is close to twice the natural roll frequency, a well-known criteria for parametric resonance (Nayfeh and Mook, 1995).¹

Furthermore, it is noticeable from Figure 5 that the ship is suffering directly excited roll motions at high heading angles, independent of the surge speed. Those maximum roll angles are considerably lower than the maximum roll angles caused by parametric resonance and peak in beam sea condition.

Figure 6 depicts the simulation results from the 1-DOF roll model where the hydrodynamic coefficients are determined numerically from the simulations of the 6-DOF model for each

simulation scenario. In Figure 7 the maximum roll angles are shown for the 1-DOF model with the hydrodynamic coefficients approximated by the functional expressions of Section 4.3.

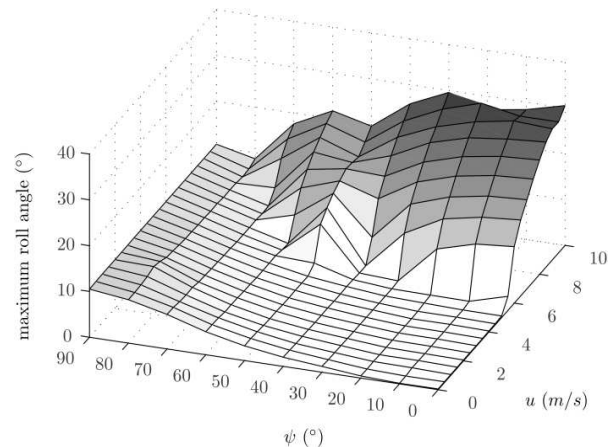


Figure 6: Maximum roll angle, 1-DOF model

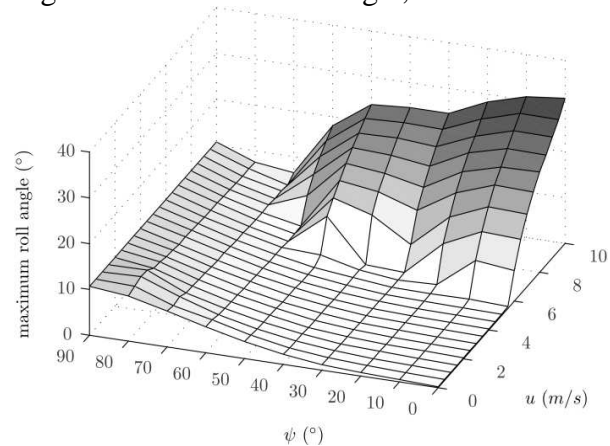


Figure 7: Maximum roll angle, 1-DOF model, functional expressions

The plots of the maximum roll angles in Figures 6 and 7 are very similar. That indicates that the functional approximation of the hydrodynamic model coefficients of Section 4.3 is appropriate.

Comparing the simulations of the 1-DOF roll models in Figures 6 and 7 to the simulations of the 6-DOF model depicted in Figure 5, the 1-DOF roll models are qualitatively quite close to the 6-DOF model for most of the simulation scenarios. The maximum roll angle is slightly overestimated by the 1-DOF models; however that may be explained by the simplifications in the derivation of the 1-DOF models and lack of higher-order restoring coefficients.

¹ The apparent higher roll angle for low, non-zero heading angles might be due to low speed resolution in the border between parametric roll and not parametric roll.



However, for the 1-DOF roll models, the region of parametric roll resonance at large surge speeds extends to higher heading angles than for the 6-DOF model. This is slightly less pronounced for the 1-DOF model with the functional expressions for the coefficients.

This effect is probably caused by two effects: The assumption of speed independence of κ_2 and κ_3 breaks down when the speed range is very large (see Figs 1 and 2); and the behavior at the borders of the area of parametric resonance – especially the non-smooth borders – is difficult to model accurately.

5.2 Time-Varying Heading and Speed

Since the 1-DOF roll model (6) with functional expressions for the hydrodynamic coefficients was derived to allow time-varying heading angle and surge speed, we simulate it for non-constant heading and speed. The results are compared to simulations of the full 6-DOF ship model (1) and (2).

The initial conditions of the simulation scenario are chosen such that the ship is in parametric roll resonance condition, specifically $\psi(0) = 0$, $u(0) = 7\text{ m/s}$. At 200s the surge speed is increased gradually to about 8m/s with a constant acceleration of 0.005 m/s^2 while the heading angle is increased by $0.1^\circ/\text{s}$ to approximately 20° . The surge speed and the heading angle are depicted in Figures 9 and 10, respectively. The oscillations in surge and yaw are due to the limited bandwidth of the PID controllers.

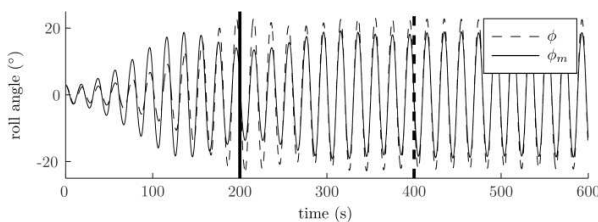


Figure 8: Roll angle

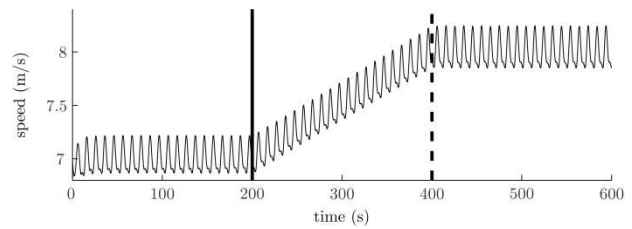


Figure 9: Speed

Figure 8 shows the roll angle of the 6-DOF model ϕ and of the 1-DOF model ϕ_m . The ship is experiencing large roll amplitudes up to about 20° due to parametric roll resonance. The roll angle of the 1-DOF model is qualitatively very close to that of the 6-DOF model, being only slightly underestimated. The sum of the restoring and external moments in roll are depicted in Figure 11, and they show a good match between the 6-DOF model and the 1-DOF model.

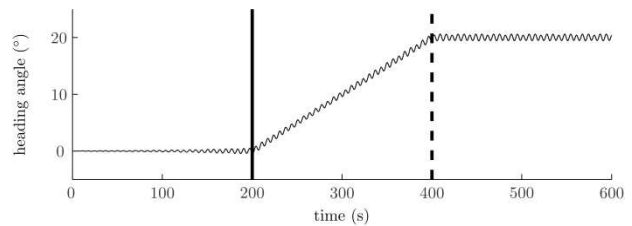


Figure 10: Heading angle

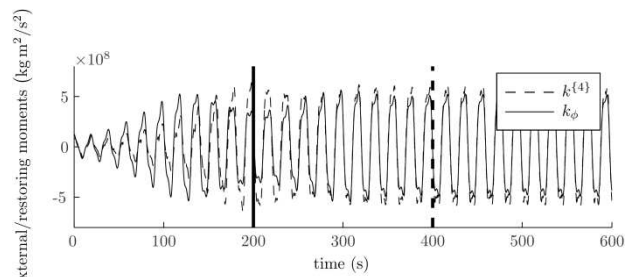


Figure 11: Restoring/ external moments in roll

The simulation scenario with time-varying speed and heading angle indicates that the 1-DOF model with the hydrodynamic coefficients given by heading dependent functions is appropriate to describe the ship's dynamics during parametric roll resonance.



6. CONCLUSIONS

In this work, we have derived a 1-DOF roll model for ships in parametric roll resonance. We have extended the model of previous works to incorporate both slowly time-varying heading angle and surge speed. The proposed 1-DOF roll model is based on the explicit time-solutions of the heave and pitch motions by a quasi-steady approach.

The hydrodynamic coefficients of the 1-DOF roll model are identified from a complex and accurate 6-DOF model of a container ship for certain fixed surge speeds and heading angles. The 6-DOF model, which accounts for first-order generalized pressure forces by integrating the instantaneous pressure field of the ocean numerically over the instantaneous submerged part of the ship hull.

Based on these parameters, we have found functional expressions for the hydrodynamic model coefficients dependent only on the heading angle. The parameters of those functions were found by curve fitting the hydrodynamic coefficients to the coefficients obtained by the 6-DOF ship model for a wide range of ship speeds and heading angles.

We have shown in simulations that the proposed 1-DOF roll model qualitatively describes the results of the 6-DOF model well for various speeds and heading angles and also captures the roll dynamics closely when the speed and the heading angle are time-varying.

ACKNOWLEDGMENTS

This work was funded by the Centre for Ships and Ocean Structures and the Norwegian Research Council.

REFERENCES

ABS, 2004. "Assessment of Parametric Roll Resonance in the Design of Container Carriers." Tech. rep., American Bureau of

Shipping.

Breu, D. A., Holden, C., and Fossen, T. I., 2012. "Ship Model for Parametric Roll Incorporating the Effects of Time-Varying Speed." Fossen, T. I. and Nijmeijer, H. (eds.), Parametric Resonance in Dynamical Systems, Springer, chap. 9. pp. 167–189.

Carmel, S. M., 2006. "Study of Parametric Rolling Event on a Panamax Container Vessel." Journal of the Transportation Research Board, vol. 1963, pp. 56–63.

Faltinsen, O. M., 1998. Sea Loads on Ships and Offshore Structures. Cambridge University Press.

Fossen, T. I., 2011. Handbook of Marine Craft Hydrodynamics and Motion Control. Wiley.

France, W. N., Levadou, M., Treacle, T. W., Paulling, J. R., Michel, R. K., and Moore, C., 2001. "An investigation of head-sea parametric rolling and its influence on container lashing systems." SNAME Annual Meeting.

Galeazzi, R., 2009. Autonomous Supervision and Control of Parametric Roll Resonance. Ph.D. thesis, Technical University of Denmark.

Holden, C., 2011. Modeling and Control of Parametric Roll Resonance. Ph.D. thesis, Norwegian University of Science and Technology.

Holden, C., Breu, D. A., and Fossen, T. I., 2012. "Frequency Detuning Control by Doppler Shift." Fossen, T. I. and Nijmeijer, H. (eds.), Parametric Resonance in Dynamical Systems, Springer, chap. 10. pp. 193–212.

Nayfeh, A. H. and Mook, D. T., 1995. Nonlinear Oscillations. Wiley.

Perez, T., 2005. Ship Motion Control. Advances in Industrial Control. Springer-Verlag, London.

White, F. M., 2002. Fluid Mechanics. McGraw Hill Text.





The Unstable Boundary of Large Amplitude Rolling of a Ship in Waves

Ju Fan, *Shanghai Jiaotong University*, fanju@sjtu.edu.cn

Renchuan Zhu, *Shanghai Jiaotong University*, renchuan@sjtu.edu.cn

Guoping Miao, *Shanghai Jiaotong University*, gpmiao@sjtu.edu.cn

Xianglu Huang, *Shanghai Jiaotong University*, hxl@sjtu.edu.cn

ABSTRACT

The paper deals with the unstable boundary of large amplitude rolling of a ship in waves. It is known that a ship may capsize when the rolling amplitude goes beyond the angles of vanishing stability in case the wave is large enough. But some investigations show that in some cases, the capsize may happen while the rolling angle is below the stability vanishing angle, in the region inside the hetero-clinic orbit, which means the amplitude of rolling is less than the stability vanishing angle, in some condition, the rolling still has the possibility to be unstable and lead ship to capsize. In this paper unstable boundary is investigated both for external excitation and parametric excitation by using the Melnikov method. Some results were obtained, which may be used in the study of ship capsizing in random beam sea.

Keywords: *unstable boundary, hetero-clinic orbit, large amplitude rolling, stability vanishing angle, melnikov method*

1. INTRODUCTION

The stability of the ship is essential for the design of a ship. The possibility of ship capsize in given high waves, is an important problem in the safety consideration for ship design and operation. Due to the strong nonlinear behavior of the problem, it seems that the time domain method is an appropriate way to be used in handling such nonlinear and stochastic problem. At present a lot of researchers have investigated stochastic nonlinear rolling of ship in waves (Kan & Taguchi, 1990, Shen & Huang, 2000, Liu & Tang, 2009). At the same time, the method of first passage also should be involved, which requires the information of boundary beyond which the ship capsize will happen. (Maki & Umeda, 2010). The ordinary way to determine such boundary is using the hetero-clinic orbit in the phase plane together with the consideration of Melnikov function (Troesch &

Falzarano, 1993, Jiang et al, 1996, Spyrou et al, 2002, Wan & Leigh, 2008). But in the time domain analysis the period of the orbit must be taken into consideration. The period or in other words the time required around the hetero—clinic orbit is infinite. So, it seems this is not available because the time of analysis is limited. Together with the period problem, the position of the orbit is also suspicious. Although the hetero-clinic orbit under some conditions will be the stability boundary, it cannot guarantee that the instability will not happen inside the sub-harmonic orbit. It would be very helpful to investigate the behavior of the system when the external excitation acting on sub-harmonic orbits. For this purpose we try to apply some development about the stability of sub-harmonic orbits in non-linear oscillation theory in recent two decades (Guckenheimer & Holmes, 1983, Greenspan & Holmes, 1984, Liu, 1994) on such large amplitude rolling



problem, and to explain what will happen on the sub - harmonic orbits.

In the paper, the outline of the theory applied is described, some numerical results are given and the conclusions of the investigation are reported.

2. THEORY

2.1 Ship Rolling Equation and Periodic Orbits

The motion of a ship rolling in waves can be expressed by the following equation:

$$(I_{44} + J_{44})\ddot{\theta}(t) + \lambda_{44}^{(1)}\dot{\theta}(t) + \lambda_{44}^{(2)}\dot{\theta}(t)|\dot{\theta}(t)| + D(C_1\theta(t) + C_3\theta^3(t)) = F(t) \quad (1)$$

Where $\theta = \theta(t)$ is roll angle; I_{44} , J_{44} are moment of inertia and added moment of inertia respectively; $\lambda_{44}^{(1)}$ is linear damping, $\lambda_{44}^{(2)}$ is nonlinear damping; D is displacement; C_1 is linear restoring coefficient; C_3 is third-order restoring coefficient. Due to $C_3 < 0$, the equation belongs to a softening spring system. By omitting nonlinear damping term, the equation can be changed into the following Duffing's form:

$$\ddot{x} + x - x^3 = -\varepsilon\delta\dot{x} + \varepsilon f \cos \omega t \quad (2)$$

Where $0 < \varepsilon \ll 1$; $\delta, f > 0$ are parameters; ω is the frequency of extra force. The system can be expressed by the equivalent form:

$$\dot{x} = y, \dot{y} = -x + x^3 - \varepsilon\delta y + \varepsilon f \cos \omega t \quad (3)$$

When ε is zero, the above equation is a Hamiltonian system. The Hamiltonian is:

$$H(x, y) = \frac{1}{2}y^2 + \frac{1}{2}x^2 - \frac{1}{4}x^4 = h \quad (4)$$

In the phase plane, there are a hetero-clinic loop ($h=0.25$), which consists of a pair of hetero-clinic orbits, and a family of periodic

orbits with H as a parameter ($0 < h < 0.25$) in the loop. The period of the periodic orbits increases from 2π to ∞ with H increasing monotonously.

The equation of the two hetero-clinic orbits is:

$$x_{\pm}^0(t) = \pm th\left(\frac{t}{\sqrt{2}}\right), y_{\pm}^0(t) = \pm \frac{\sqrt{2}}{2} \sec h^2\left(\frac{t}{\sqrt{2}}\right) \quad (5)$$

To the period orbits with $h = h(k)$, the equation can be expressed by:

$$x_k = \frac{\sqrt{2}k}{\sqrt{1+k^2}} \operatorname{sn}\left(\frac{t}{\sqrt{1+k^2}}, k\right), y_k = \frac{\sqrt{2}k}{1+k^2} \operatorname{cn}\left(\frac{t}{\sqrt{1+k^2}}, k\right) \cdot \operatorname{dn}\left(\frac{t}{\sqrt{1+k^2}}, k\right) \quad (6)$$

Where sn , cn , dn are Jacobi elliptic function; k is the modulus of Elliptic function. The period of orbit is $T_k = 4\sqrt{1+k^2}K(k)$, $K(k)$ is the first complete elliptic integral. The following figure is the family of periodic orbits.

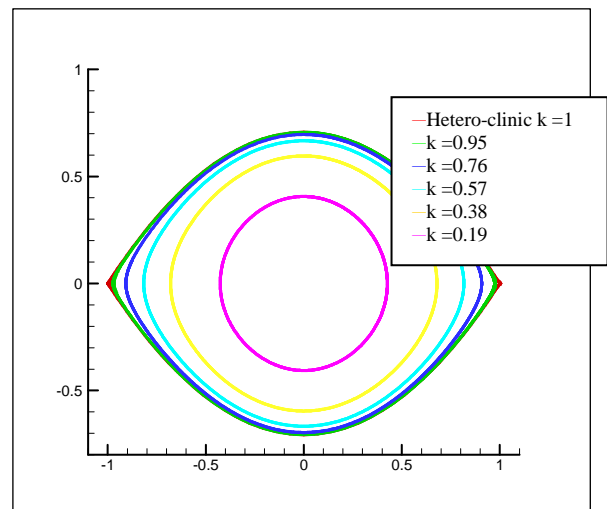


Figure1: Periodic orbits

2.2 Melnikov Function of Periodic Orbits

Based on Poincare map theory, to the Melnikov function for the hetero-clinic orbits, there is threshold value leading to chaos. And to those for the corresponding sub-harmonic orbits, there are threshold values to stable oscillation.



The Melnikov functions of the pair of hetero-clinic orbits are:

$$M_{\pm}(t_0, \delta, f) = \int_{-\infty}^{\infty} [-\delta y_{\pm}^0(t) + f \cos \omega(t+t_0)] y_{\pm}^0(t) dt$$

$$= -\delta \frac{2\sqrt{2}}{3} \pm f \sqrt{2} \pi \omega \operatorname{csch} \left(\frac{\sqrt{2}}{2} \pi \omega \right) \cos \omega t_0 \quad (7)$$

Threshold value for chaos:

$$R^{(1)}_{\infty} = \frac{2}{3\pi\omega} \operatorname{sh} \left(\frac{\sqrt{2}}{2} \pi \omega \right) \quad (8)$$

The Melnikov function for sub-harmonics whose period is $T_k = \frac{2\pi m}{\omega}$, (m and n are a pair of relatively prime integers) is

$$M^{m/n}(t_0, \delta, f) = \int_0^{mT} [-\delta y_k(t) + f \cos \omega(t+t_0)] y_k(t) dt$$

$$= -\delta \frac{8n}{3(1+k^2)^{3/2}} [(k^2-1)K(k) + (1+k^2)E(k)] + f \frac{2\sqrt{2}\pi\omega \operatorname{csch} \left(\frac{\pi m K(k)}{2K(k)} \right) \cos \alpha_0}{3(1+k^2)^{3/2}} \quad (9)$$

where $n=1$ and m is odd

The threshold value to sub-harmonics:

$$R_m^{(1)}(\omega) = \frac{2\sqrt{2}[(1+k^2)E(k) - (1-k^2)K(k)]}{3\pi\omega(1+k^2)^{3/2}} \operatorname{sh} \frac{\pi m K(k)}{2K(k)} \quad (10)$$

$K'(k) = K(k') = K(\sqrt{1-k^2})$, $E(k)$ is the second complete elliptic integral.

For parametric excitation, the equation is similar to the following:

$$\ddot{x} + (1 + \varepsilon f \cos \omega t)x - x^3 = -\varepsilon \delta \dot{x} \quad (11)$$

The Melnikov function of hetero-clinic orbit is obtained as

$$M_{\pm}(t_0, \delta, f) = \int_{-\infty}^{\infty} [-\delta y_{\pm}^0(t) f \cos \omega(t+t_0) x_{\pm}^0(t)] y_{\pm}^0(t) dt$$

$$= -\delta \frac{2\sqrt{2}}{3} - f \pi \omega^2 \operatorname{csch} \left(\frac{\sqrt{2}}{2} \pi \omega \right) \sin \omega t_0 \quad (12)$$

The threshold value for chaos is

$$R^{(2)}_{\infty}(\omega) = \frac{2\sqrt{2}}{3\pi\omega^2} \operatorname{sh} \left(\frac{\sqrt{2}}{2} \pi \omega \right) \quad (13)$$

For the sub-harmonic periodic orbit, the Melnikov function is:

$$M^{m/n}(t_0, \delta, f) = \int_0^{mT} [-\delta y_k(t) - f \cos \alpha(t+t_0) x_k(t)] y_k(t) dt =$$

$$= -\delta \frac{8n}{3(1+k^2)^{3/2}} [(k^2-1)K(k) + (1+k^2)E(k)] -$$

$$- f \frac{\pi^3 m^2}{2(1+k^2)K^2(k)} \operatorname{csch} \frac{\pi n' K(k')}{2K(k)} \sin \alpha_0 \quad (14)$$

where $n=1$ and m is even.

The threshold value for sub-harmonics is

$$R_m^{(2)}(\omega) = \frac{16[(1+k^2)E(k) - (1-k^2)K(k)]}{3\pi^3 m^2 (1+k^2)^{1/2}} \operatorname{sh} \frac{\pi n' K(k')}{2K(k)} \quad (15)$$

2.3 Stability of Sub-harmonic Oscillation

In order to investigate the stability of sub-harmonic oscillation, the disturbance motion on the orbit with period $T_k = \frac{2\pi m}{\omega}$ ($m = 1, 3, 5, \dots$) is examined. Using Taylor series expansion, the perturbed equation can be got. By carrying out averaging transformation, the averaging equation can be obtained. Based on average theorem, the hyperbolic and elliptic fixed points of averaging equation are corresponding to the m order sub-harmonic solutions to equation (3). When ε is small, the stability of fixed point of averaging equation can determine the stability of sub-harmonic solution of equation (3). The trace of the linearized matrix of the averaging equation:

$$\operatorname{tr} A = \frac{\sqrt{\varepsilon \delta \omega}}{2m} \left\{ \frac{8\alpha(1+k^2)}{3k^2(1-k^2)} \operatorname{ctth} \left(\frac{\pi m K(k)}{2K(k)} \right) \left[(1+k^2)E(k) - (1-k^2)K(k) \right] \left[2k^2 K'(k) - (1+k^2)E(k) \right] + \right.$$

$$\left. \frac{4(1+k^2)^{1/2}}{3k^2(1-k^2)K(k)} \left[(1+k^2)E(k) - (1-k^2)K(k) \right]^2 - (1+k^2)^{1/2} E(k) \right\} \quad (16)$$

When $\operatorname{tr} A > 0 (< 0)$ the sub-harmonic solution of equation (3) belongs to saddle or source (sink).



3. DISCUSSION ABOUT THRESHOLD VALUES FOR CHAOS AND STABILITY OF SUB-HARMONICS

3.1 Threshold Values for Chaos and Sub-harmonic Bifurcations

In order to discuss the way to chaos for various values of ω , the magnitudes of $R_m^{(i)}$ compared with that of $R_\infty^{(i)}$ are shown ($i=1,2$; m represents the integers allowed). Through calculation, the graphs of $R_m^{(1)} - R_\infty^{(1)}$ versus ω are presented in Fig. 2.

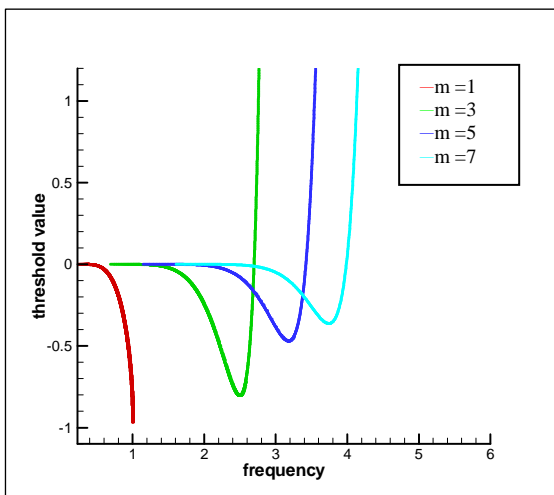


Figure 2: $R_m^{(1)} - R_\infty^{(1)}$

In Fig. 2, the curve of $R_m^{(1)} - R_\infty^{(1)}$ stops at $\omega=1$, $R_m^{(1)}$ tends to ∞ , if $\omega \rightarrow m$ ($m=3,5,\dots$), $R_\infty^{(1)}$ is finite. Using $\omega_3, \omega_5, \dots$ to denote the various frequencies of intersection points of $R_3^{(1)}, R_5^{(1)} \dots$ and $R_\infty^{(1)}$, $\omega_{3,5}$ is the frequency of intersection point of $R_3^{(1)}$ and $R_5^{(1)}$; $\omega_{3,7}$ is the frequency of intersection point of $R_3^{(1)}$ and $R_7^{(1)}$ and so on. When f/δ increases gradually, the way to chaos for system is as follows: (∞ represents chaos)

$$\begin{aligned}
 &0 < \omega < 1 \quad 1 \rightarrow 3 \rightarrow 5 \rightarrow \dots \rightarrow \infty \\
 &1 < \omega < \omega_{3,5} (\approx 2.682) \quad 3 \rightarrow 5 \rightarrow 7 \rightarrow \dots \rightarrow \infty \\
 &\omega_{3,5} < \omega < \omega_{3,7} \quad 5 \rightarrow 3 \rightarrow 7 \rightarrow \dots \rightarrow \infty \\
 &\dots \dots \dots \\
 &\omega_3 (\approx 2.698) < \omega < \omega_{5,7} \quad 5 \rightarrow 7 \rightarrow 9 \rightarrow 11 \rightarrow \dots \rightarrow \infty
 \end{aligned}$$

The variation of $R_m^{(2)} - R_\infty^{(2)}$ with ω is shown in the following figure.

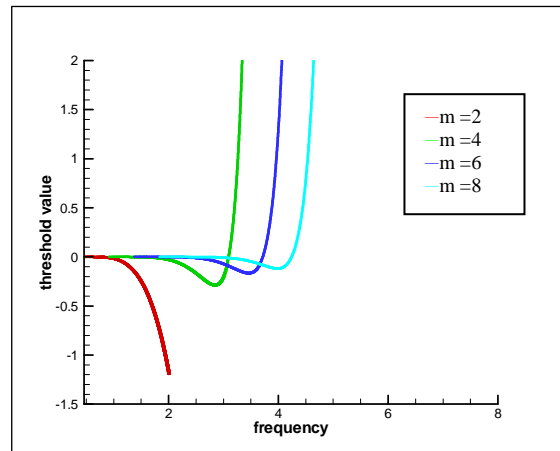


Figure 3: $R_m^{(2)} - R_\infty^{(2)}$

In the above figure, using $\omega_4, \omega_6, \dots$ to denote the various frequencies of intersection points of $R_4^{(2)}, R_6^{(2)} \dots$ and $R_\infty^{(2)}$, $\omega_{4,6}$ is the frequency of intersection point of $R_4^{(2)}$ and $R_6^{(2)}$; $\omega_{4,8}$ is the frequency of intersection point of $R_4^{(2)}$ and $R_8^{(2)}$ and so on. When f/δ increases gradually, the way to chaos for system is as follows:

$$\begin{aligned}
 &0 < \omega < 2 \quad 2 \rightarrow 4 \rightarrow 6 \rightarrow \dots \rightarrow \infty \\
 &2 < \omega < \omega_{4,6} \quad 4 \rightarrow 6 \rightarrow 8 \rightarrow \dots \rightarrow \infty \\
 &\omega_{4,6} < \omega < \omega_{4,8} \quad 6 \rightarrow 4 \rightarrow 8 \rightarrow \dots \rightarrow \infty \\
 &\dots \dots \dots \\
 &\omega_4 < \omega < \omega_{6,8} \quad 6 \rightarrow 8 \rightarrow 10 \rightarrow \dots \rightarrow \infty \text{ and so on.}
 \end{aligned}$$

From the above results, for any fixed ω , when k is sufficiently close to 1, m is sufficiently large. When the amplitude ratio f/δ increases gradually for any fixed ω , the system enters into a chaotic state passing a number of sub-harmonic bifurcations in both external and parametric excitation cases.

For the case with weak damping and periodic external force, when the parameter ratio f/δ increases gradually, the system may pass to chaos through a number of odd-order sub-harmonics bifurcations; For the case of

small damping and periodic parametric excitation, the way to chaos may be a sequence of even-ratio order sub-harmonic bifurcations with the parameter ratio f/δ increasing gradually.

As to both external and parametric excitation cases with the excitation amplitude f and frequency ω on the sub-harmonic orbit, when amplitude increases gradually, the system will lead to chaos through a number of sub-harmonics with k tending to 1.

3.2 Stability on Sub-harmonic Orbit

By using the formula (16), the trace of the linearized matrix of the averaging equation which considers the disturbance on the sub-harmonic orbit was calculated. The traces were expressed as a function of the external frequency or of the modulus. In the region where the system is stable, the trace should be less than zero. Otherwise the system will be unstable. The following figure shows the trace versus frequency.

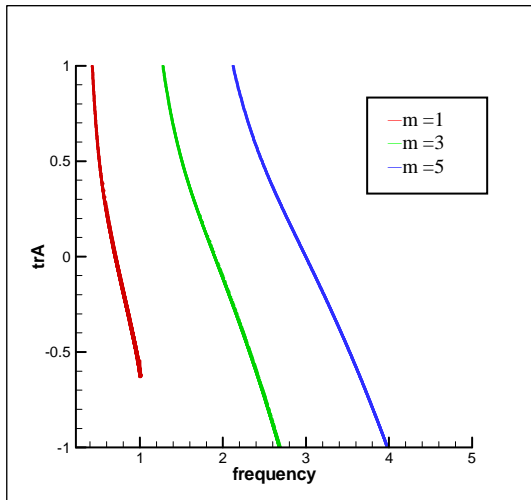


Figure 4: Trace variation with frequency

It is shown clearly in Fig. 4 that the unstable region is in the lower end of frequency. The physical meaning of the results is that instability of oscillation on the sub-harmonic orbits can happen when the excitation frequency is small and the amplitude is large.

From Fig. 4, when the frequency is below 0.7, the $trA > 0$ and the sub-harmonics ($m=1,3,5..$) are unstable.

The relation of modulus k with frequency when m is different is given by the following figure.

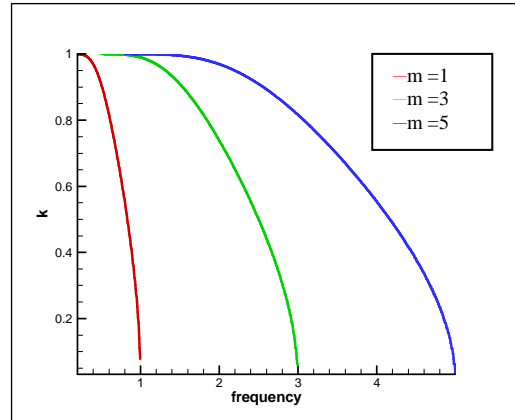


Figure 5: Modulus vs. frequency

From the above figure, the high frequency oscillation is corresponding to higher m as to the same k , which means that they are on the same orbit. The following figure is the trace variation as a function of modulus:

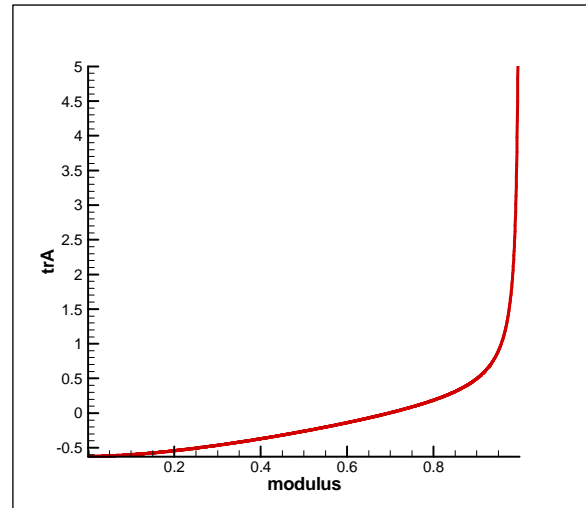


Figure 6: Trace variation with modulus

The result shows that to harmonic excitation, the unstable oscillation of the system will happen when the modulus is larger than 0.7 for the periodic orbit. The oscillation amplitude to the different modulus is as follows:

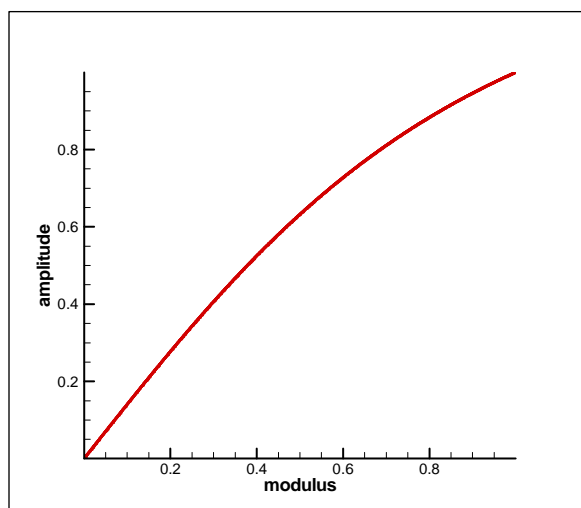


Figure 7: Amplitude vs. modulus

From Fig. 7, the amplitude increases with modulus increasing monotonously. In the above sub-harmonic orbit, amplitude is 0.81 when modulus is 0.7. the trace is reported versus the amplitude in Fig. 8.

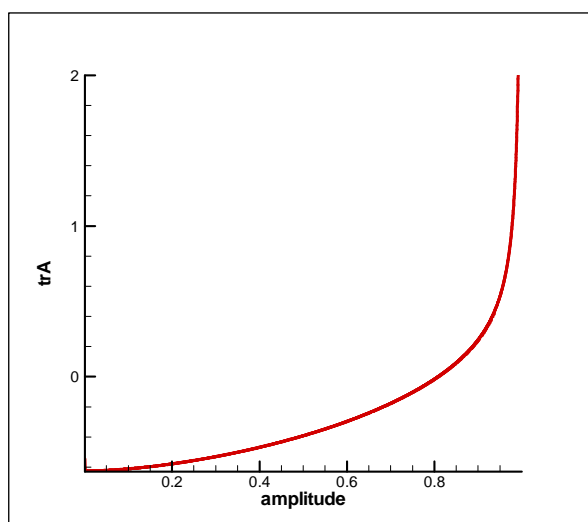


Figure 8: Trace variation with amplitude

If the amplitude is larger than 0.81, the $trA > 0$ and the orbit is unstable. To large amplitude rolling of a ship, the amplitude can be transformed to the corresponding rolling angle. When rolling angle is larger than the corresponding one, the system becomes unstable.

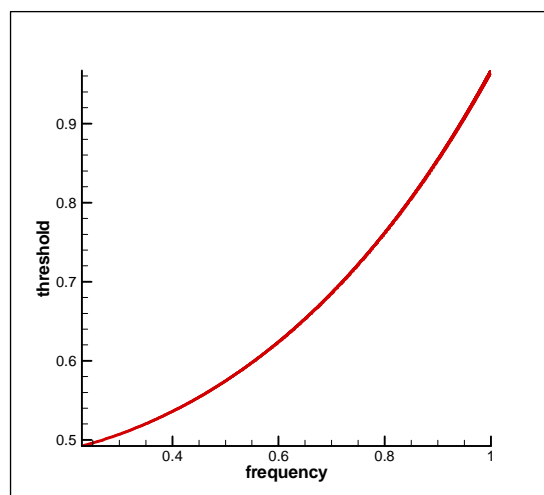


Figure 9: Threshold value vs. frequency

From the above figure, the threshold of chaos increases with frequency increasing gradually on the hetero-clinic orbit. The threshold of chaos is 0.686 for the frequency equal to 0.7. When the parameter ratio f/δ is larger than 0.686, the sub-harmonic oscillation is unstable and enters into chaos if oscillation amplitude is larger than 0.81. To investigate large amplitude rolling of a ship, ship capsizes occurs in this case.

4. CONCLUDING REMARKS

Through the above discussion, the unstable boundary of rolling is investigated by the Melnikov method. Some results were obtained:

As to both external and parametric excitation cases with the excitation amplitude f and frequency ω on the sub-harmonic orbit, when amplitude increases gradually, the system will lead to chaos through a number of sub-harmonics from k tending to 1.

When frequency is below 0.7, the $trA > 0$, the sub-harmonics ($m=1,3,5..$) are unstable. The threshold of chaos is 0.686 with the same frequency on the hetero-clinic orbits. When the parameter ratio f/δ is larger than 0.686, the sub-harmonic orbit is unstable and enters into hetero-clinic orbits if oscillation amplitude is



larger than 0.81 and chaos happen. To investigate large amplitude rolling of a ship, ship capsizes occurs in this case.

To the study of the happening of ship capsizes in random beam waves, it seems that it is rational to use the sub-harmonic orbit inside the hetero-clinic orbit suggested above instead of the hetero-clinic orbit itself.

The above investigation has shown some results about the Melnikov function and threshold value leading to chaos of the hetero-clinic orbit and stability of sub-harmonic orbits for the case including third-order restoring term. To container ship and some other ships, the stability curve includes three terms: linear term, third-order term and fifth-order term. The theoretical method in this paper is available to extend to investigating the case including fifth-order restoring term.

5. REFERENCES

- Greenspan, B., Holmes, P., 1984, "Repeated Resonance and Homo-clinic Bifurcation in a Periodically Forced Family of Oscillators", J. Math. Anal., Vol.15, No.1, pp. 69-97.
- Guckenheimer, J., Holmes, P., 1983, "Nonlinear Oscillations, Dynamical Systems, and Bifurcations of Vector Fields", Applied Mathematical Sciences Vol.42, Springer Press.
- Jiang, C., Troesch, A.W., and Shaw, S.W., 1996, "Highly Nonlinear Rolling Motion of Biased Ships in Random Beam Seas", Journal of Ship Research, Vol.40, No.2, pp. 125-135.
- Kan, M., Taguchi, H., 1990, "Capsizing of a Ship in Quartering Seas (part 2 Chaos and Fractals in Capsizing Phenomenon)", J Soc Nav Arch Jpn, Vol.169, pp. 213-222.
- Liu, L.Q., Tang, Y.G., 2009, "Stochastic Nonlinear Rolling of Ship in Beam Waves", International Shipbuilding Progress, Vol.56, No.1-2, pp. 15-27.
- Liu, Z.R., 1994, "Perturbation Criteria for Chaos", Shanghai Science and Technology education publishing press.
- Maki, A., Umeda, N., 2010, "Melnikov Integral Formula for Beam Sea Roll Motion utilizing a Non-Hamiltonian Exact Hetero-clinic Orbit", J Mar Sci Technol, Vol.15, pp. 102-106.
- Roberts, J.B., 1982, "A Stochastic Theory for Nonlinear Ship Rolling in Irregular Seas", Journal of Ship Research, Vol.26, No.4, pp.229-245.
- Shen, D., Huang X.L., 2000, "The Study of Lasting Time before Capsize of a Ship under Irregular Wave Excitation", Proceedings of 7th International Conference on Stability of Ship and Ocean Vehicles, Lancelton, Australia.
- Spyrou, K.J., Cotton, B., and Gurd, B., 2002, "Analytical Expressions of Capsize Boundary for a Ship with Roll Bias in Beam Waves", Journal of Ship Research, Vol.46, No.3, pp.167-174.
- Troesch, A.W., Falzarano, J.M., 1993, "Modern Nonlinear Dynamical Analysis of Vertical Plane Motion of Planning Hulls", Journal of Ship Research, Vol.37, No.3, pp. 189-199.
- Wan, W., Leigh, M., 2008, "Application of the Extended Melnikov's Method for Single Degree of Freedom Vessel Roll Motion", Ocean Engineering, Vol.35, pp. 1739-1746.





Conditions for Surf-riding in an Irregular Seaway

K. J. Spyrou, *National Technical University of Athens*, spyrou@deslab.ntyua.gr

V. Belenky, *David Taylor Model Basin, Carderock, Washington D.C.*

N. Themelis, *National Technical University of Athens*, nthemelis@naval.ntua.gr

K. Weems, *Science Applications International Corporation*

ABSTRACT

The current study is motivated by a desire to evaluate the probability of surf-riding in irregular seas by posing surf-riding as a threshold-exceedance problem. For steep regular following waves, it is known that celerity is the speed at which, if exceeded by a ship, capture into surf-riding is necessarily incurred. Can this simple phenomenological rule be extended to a stochastic wave environment? To answer this, a suitable definition of wave celerity for an irregular seaway needs to be put forward. In the current work we define celerity as the velocity of propagation of a suitable property of the profile. This leads to the concept of instantaneous celerity which opens a window towards the literature of instantaneous frequency in signal processing. In general, instantaneous celerity cannot be consistently defined as a smooth and constrained curve. Other definitions of local (but not instantaneous) celerity are also possible. In the paper we test these for a number of different selections, obtaining time-dependent celerity curves for various types of waves and we assess the effect of spectrum's band-width, relaxing the requirement of "narrow-bandness". Subsequently we implement simultaneous treatment of the "wave" and "ship" processes and we investigate the potential of applying a local celerity condition for surf-riding prediction. Various patterns of behaviour before and into surf-riding are observed and discussed.

Keywords: *Surf-riding, Wave Celerity, Irregular Waves*

1. INTRODUCTION

In developing a probabilistic evaluation of a ship's tendency for surf-riding, a significant challenge lies in the definition of wave celerity for an irregular sea environment. Specifically, it is not known if some notion of wave velocity pertaining to a multi-frequency wave profile could be used as an unambiguous threshold speed for the prediction of surf-riding, in the same fashion that celerity is used for a regular sea. One sort of statistical celerity would be the so-called "drift velocity," a deterministic quantity based on the ratio of the average wave length to the average wave period. Under the assumption of a Gaussian distribution of wave elevation, Longuet-Higgins (1957) derived approximate closed-form expressions of the velocity distribution for the maxima and minima that appear on a plane (vertical) section

of the profile of a short-crested sea. Given a spectrum, the velocity distributions of the so-called "specular points" of the profile, where the gradients in the two directions of wave propagation match desired constant values, can also be obtained. More recent elaborations on the velocity distributions of various points of random wave surfaces are described in Baxevani et al. (2003), in Aberg and Rychlik (2006, 2007), and elsewhere. In a study that aimed to calculate the probability of encounter of waves that could cause broaching-to, Aberg and Rychlik (2007) selected the "wave centre" (the point of downward zero-crossing) for defining wave velocity in a Gaussian sea. Its distribution was derived for both fixed and moving (with constant speed) observers by using Rice's formula. They also discussed a celerity distribution based on the half wave



length for an approximate, deterministic, dispersion relationship.

Unfortunately, a statistical model of celerity is of limited use for deriving the probability of surf-riding. The process of the difference between celerity and ship speed becomes strongly nonlinear for the parameters' range of interest. Hence, the exact role of celerity for surf-riding in an irregular sea needs to be clarified. Extra details about the context of the discussed problem are found in a companion paper by Belenky et al. (2012).

2. EQUATION OF SHIP MOTION

Consider a wave profile in time and unidirectional space, as follows:

$$\begin{aligned} \zeta(x; t) &= \int_0^\infty \sin(kx - \omega t + \varepsilon^{(r)}(\omega)) \sqrt{2S(\omega)} d\omega = \\ &= \sum_{i=1}^n A_i \sin[k_i(x - c_i t) + \varepsilon_i^{(r)}] \end{aligned} \quad (1)$$

where ζ is the elevation above still water, x is the distance of the considered point of the profile from an earth-fixed origin and t is the corresponding time instant; ω, k are the wave frequency and wave number, respectively; $\varepsilon^{(r)}$ is the random phase; A_i, k_i, c_i and $\varepsilon_i^{(r)}$ are the wave amplitude, number, celerity, and phase, respectively, of the discrete wave component with frequency ω_i ; and $S(\omega)$ is the wave spectrum. The well-known dispersion relation $\omega = \sqrt{gk}$ for each harmonic wave component propagating in deep water is applied. The superscript (r) indicates a random number, uniformly distributed in $[0, 2\pi]$ which specifies the phase of each harmonic component at $t = x = 0$. Note that the "neat" integral representation of the elevation in eq. (1) is not a Riemann-type integral (Pierson 1955; see also discussion in Kinsman 1984).

For a shore-based observer, a basic model of the ship surge motion in this wave could be written as follows (Spyrou 2006):

$$\underbrace{(m - X_{\dot{u}})\ddot{\xi}}_{\text{inertia } M(\ddot{\xi})} - \underbrace{(\tau_2 \dot{\xi}^2 + \tau_1 n \dot{\xi} + \tau_0 n^2)}_{\text{thrust } T(\dot{\xi}; n)} + \underbrace{(r_1 \dot{\xi} + r_2 \dot{\xi}^2 + r_3 \dot{\xi}^3)}_{\text{resistance } R(\dot{\xi})} = 0$$

$$\underbrace{\int_0^\infty \cos\left[\frac{\omega^2}{g}\xi - \omega t + \varepsilon^{(r)}(\omega) + \varepsilon_f(\omega)\right] X_w(\omega) \sqrt{2S(\omega)} d\omega}_{\text{wave force } F(\xi; t)} = 0 \quad (2)$$

where ξ is the instantaneous longitudinal position of the origin of the ship axes; m , and $X_{\dot{u}}$ are the ship's mass and added mass, respectively; n is propeller's rotation rate; and $X_w(\omega)$ and $\varepsilon_f(\omega)$ are the RAO and phase of linear wave surging force corresponding to the ω harmonic wave. After approximating the wave force by a large, but finite, sum of discrete harmonic components, this equation can be expressed, with some rearrangement, as:

$$\begin{aligned} (m - X_{\dot{u}})\ddot{\xi} + r_3 \dot{\xi}^3 + (r_2 - \tau_2)\dot{\xi}^2 + (r_1 - \tau_1 n)\dot{\xi} + \\ + \sum_{i=1}^n f_i \cos[k_i \xi - \omega_i t + \varepsilon_i^{(r)} + \varepsilon_{f_i}] = \tau_0 n^2 \end{aligned} \quad (3)$$

This equation depends explicitly on time t , as for parametrically excited systems. The t dependency can be removed for a regular (monochromatic) sea through a coordinate transformation. But this does not seem to be possible for an irregular sea.

3. INSTANTANEOUS CELERITY FOR GAUSSIAN FORMULATION

When the wave profile is irregular, the frequency and wave number change continually. At first consideration, one might think of an expression of celerity by extending the deterministic relation of the frequency over the wave number. However, this requires meaningful definitions of the localized wave frequency in space and in time. One could extract such quantities by applying a short-time Fourier or by processing the wave profile simultaneously in the time and "frequency" domains by a continuous wavelet transform. However, due to the renowned problem of resolution when the time duration of the considered signal's segment is very short [there can be either temporal or spectral localization, but not both (Gabor limit); see Gabor (1946)] these approaches are ineffective. In signal processing, the idea of "instantaneous frequency" was introduced many years ago, but



has yet to gain universal acceptance – for a review see Boashash (1992). The matter acquires greater importance for non-stationary signals. The Fourier transform is incongruent with the notion of “instantaneous” frequency. The latter is considered by some as a quantity with a different nature, and questions have been raised as to which of the two is actually measured during experiments. Mandel (1974) claimed that the only similarity between the two versions of frequency is that the average frequency of a spectrum derived by the Fourier transform is equal to the time average of the instantaneous frequency. While these ideas determine a possible way to attack the problem, a more direct approach is preferred here.

The mapping of wave phase to the local gradient of the profile is not as apparent as in the periodic case. A quite generic notion could be that celerity is the rate at which some derivative of the wave function is propagated. Since the selection of the propagated property (as well as its quantitative value) may result in different values of celerity, even for a short segment of an irregular profile, in principle such a selection can be tailored to the specific problem of interest. Longuet-Higgins (1957) presented definitions of “velocities of zeros” based on a fixed value of the elevation ζ or of the gradient $\frac{\partial \zeta}{\partial x}$ as follows: consider a function h determined from the wave profile that obtains the value h_0 at $(x_0; t_0)$. On the locus of $h = h_0$ the differential dh is naught by definition, leading to an expression of velocity:

$$dh = h_0 - h_0 = 0 = \frac{\partial h}{\partial x} dx + \frac{\partial h}{\partial t} dt \quad \rightarrow$$

$$c_{h_0} = -\frac{\partial h / \partial t}{\partial h / \partial x} \quad (4)$$

For a deep water wave elevation process represented by a large (theoretically infinite) sum of harmonics waves as described by equation (1), consider a point on the wave profile corresponding to a frozen time instant t_0 and located at a longitudinal distance x_0 from the origin. The instantaneous local wave slope is:

$$\left. \frac{\partial \zeta(x; t_0)}{\partial x} \right|_{x_0} \equiv a(x_0; t_0) = \sum_{i=1}^n \sqrt{2S(\omega_i) \delta \omega} k_i \cos [k_i(x_0 - c_i t_0) + \varepsilon_i^{(r)}] \quad (5)$$

It is possible to trace the locus $x_a(t)$ by marching in time, solving equation (5) numerically for a series of time steps following t_0 . In the first time step, for instance, equation (6) below would be solved to get δx , given a δt (the reverse is in fact computationally more efficient – such cases are encountered later):

$$\sum_{i=1}^n A_i k_i \cos [k_i [x_0 + \delta x - c_i(t_0 + \delta t) + \varepsilon_i^{(r)}]] = \alpha(x_0; t_0) \quad (6)$$

For subsequent steps, the solution $x_0 + \delta x$ will replace x_0 while $t_0 + \delta t$ will replace t_0 and the next nearby solution will be identified. Eventually a series solution is traced:

$$x_a(t) = f(t; a) |_{x_0, t_0} \quad (7)$$

where the subscript on the right-hand side indicates the starting point of the iterative solution process. The time derivative of $x_a(t)$ should produce a “local” celerity function uniquely associated with each pair (x_a, t) :

$$c_a(t) = \dot{x}_a(x; t) = \frac{df(t; a)}{dt} \quad (8)$$

For irregular waves, this local velocity is time-varying. Furthermore, a different celerity value should, in principle, be expected for each point of a profile within an apparent length (e.g. between successive up-crossings).

Following Longuet-Higgins more closely, it is also possible to base celerity on a fixed value of the spatial gradient $h = \frac{\partial \zeta(x; t)}{\partial x}$:

$$c(x, t) = \frac{\frac{\partial^2 \zeta}{\partial x \partial t}}{\frac{\partial^2 \zeta}{\partial x^2}} \quad (9)$$

Note that this expression is not tied to a specific slope value (hence no subscript a),



thus producing a celerity value from an instantaneous position and time.

Approximate calculations of celerity in an irregular seaway might also be contemplated. For example, consider a pair (x, t) that defines a point of the irregular profile in space and time. Fix t and measure the distance between the crests (local maxima) that are found just before and just after x , calling this distance $\tilde{\lambda}$. Subsequently, fix x and measure the corresponding distance of crests in the time domain (just before and just after the considered instant t), noting it as \tilde{T} . This alternative definition of celerity leads to the expression:

$$\tilde{c} = \frac{\tilde{\lambda}}{\tilde{T}} \quad (10)$$

One should recall here that counting distances between crossings (e.g. up-crossings) could lead to a substantially different result for a wave spectrum that is not very narrow-banded. A feature of irregular waves is that individual crests (or troughs) can emerge or vanish. Naval architects have known for many years that they need to cope with such phenomena, e.g. see Vossers 1962; yet the issue is rarely touched, since in most cases the assumption of a narrow band wave spectrum underlies the calculation process. For ‘‘Gaussian’’ elevations, the ratio of the number of zero crossings N_0 to the number of crest and troughs N_1 is defined as follows:

$$\frac{N_0}{N_1} = \sqrt{1 - \varepsilon^2} \quad (11)$$

In this case, ε is the spectrum’s width, with no relation with the phase symbol ε . The generation of troughs with positive elevation as well as of troughs with negative elevation, are phenomena that are expected to make celerity behave in a strongly nonlinear fashion from time to time. The implementation of this definition of celerity is evaluated next for three different characteristic cases.

Example 1

For the first example, consider a wave comprised of three frequencies at ‘‘some distance’’ from each other, as defined in Table 1. The waves are selected to be reasonably steep, yet linear. Figure 1 plots the wave profile in space–time. Merging and separation of waves is observed. Such qualitative changes in the wave profile should be reflected in a sharp change of the value of celerity. At some times, more than one crest may be found between an up-crossing and the successive down-crossing (e.g. two crests with a trough of positive elevation between them). This is the reason for the ratio of equation (11) to become less than 1.

Table 1: Selected linear wave components

k [m ⁻¹]	0.1	0.05	0.14
$\omega = \sqrt{gk}$ [s ⁻¹]	0.99	0.70	1.17
A [m]	1.0	1.4	0.6
Ak	0.1	0.07	0.084
$\varphi = kx - \omega t + \varepsilon$	0.1	0.8	0.5

Figure 2 shows several loci of solutions $x_a(t)$ as defined in equation (7). Curves of similar nature are presented in Sjo (2000), drawn for zero crossing points (these points do not maintain the slope). Recalling that the celerity that corresponds to any one point of these curves is given by the gradient dx_a/dt at that point of the curve, x_a is traced versus t in order to find the locus of points for four different local wave slope values: 0 (i.e. a crest or a trough), 0.0125, 0.025 and 0.05. The solutions are presented in Figure 2 as bunches of four contour lines, with one line per value of slope. Note that, at any time instant, each value of slope can be realised several times, so there are several families of solutions.

In contrast to a periodic wave case, these constant slope lines are neither straight nor parallel to one another. While the gradient, and thus celerity, is mostly not changing much,

there are “strange” regions that basically correspond to the merging of crests. Note in particular the backward turn of some lines – corresponding to the more extreme value of local wave slope 0.05 – that leads to their unification with the corresponding curve of the previous group. It reflects the fact that in the considered wave cycle this value of wave slope was not realized – i.e. the wave was not steep enough. The annihilation (or creation) of such points of constant slope is referred to as “twinkle” (Kratz and Leon 2005).

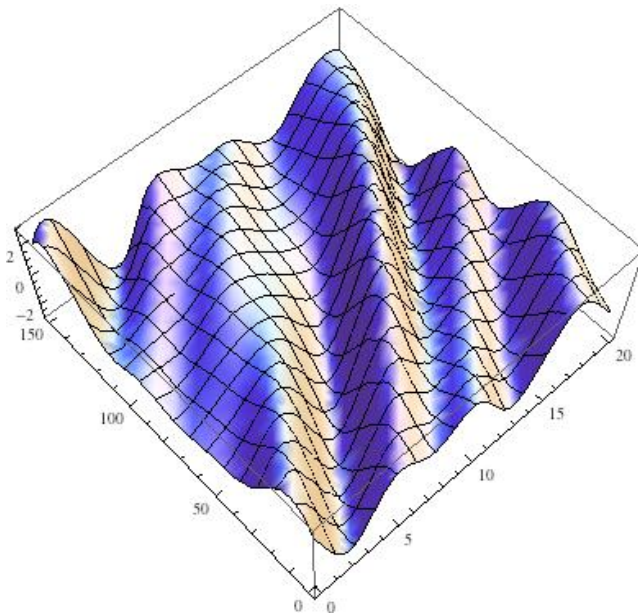


Figure 1: Example 1 wave in space-time.

Example 2

Now consider a wave elevation process defined by the JONSWAP spectrum (Figure 3). This spectrum was discretised using 15 frequencies distributed equidistantly between 0.63 and 1.43 of the peak value. For the prescribed range, the bandwidth parameter ε receives the rather moderate value of 0.315. Sample realisations are plotted in Figure 4. Figure 5 shows contours of slope 0.0 (crests and troughs) as well as slope 0.01 as traced using the solution of $x_{a=0}(t) = f(t; 0)|_{x_0,0}$.

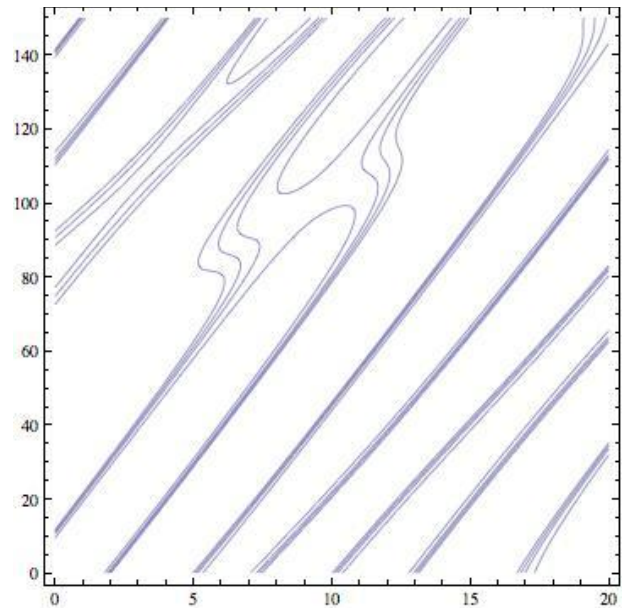


Figure 2: Constant slope contours from the solution of eq. (7), for the three-frequency wave considered as Example 1. The slopes are 0, 0.0125, 0.025 and 0.05. Above the main diagonal, wave slope increases downwards; below it, the increase is upwards.

The celerity curve produced by propagating the first crest that lies right in front of the axes origin is shown in Figure 6. Similar celerity curves referring to the third crest are shown in Figure 7. Table 2 specifies the initial ($t = 0$) ordinates of these points. The variability of celerity is prevalent and spikes are noted. These indicate singular behaviour where and when a relatively steep slope disappears and, as a result, velocity jumps to infinity. This phenomenon has, of course, also been observed before (see for example Baxevani et al. 2003). While the curve could be smoothed or clipped, evaluation of its importance is required.

Finally, the calculated local celerity value is compared to one obtained by applying the approximate expression $\tilde{c} = \tilde{\lambda}/\tilde{T}$. The length and period used for this calculation are explained in Figure 8. The “exact” and approximate values of celerity are compared for two different slope values in Figures 9 and 10. A second alternative celerity calculation was also tested, based on the ratio of apparent half-length to apparent half-period. These



quantities are measured between successive peaks in time and in space, observed before and after a given point (x, t) . This second alternative (also plotted in Figures 9 and 10) seems to be a consistently superior predictor. Such a conclusion is deduced if one compares the position of unfilled squares against the continuous line; and similarly, that of the unfilled circles against the dashed line. It is noted that a similar comparison for the filled symbols (that are based on whole lengths and periods) revealed much larger discrepancies. The examination of other points of the profile gave similar results.

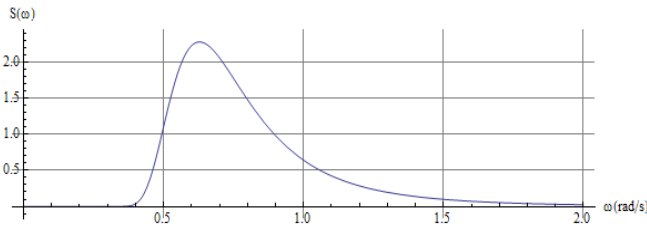


Figure 3: JONSWAP spectrum for $H_S = 4$ m, $T_P = 10$ s (generalized Philip's constant $a_w = 0.00809$ and peakedness parameter $\gamma = 1$).

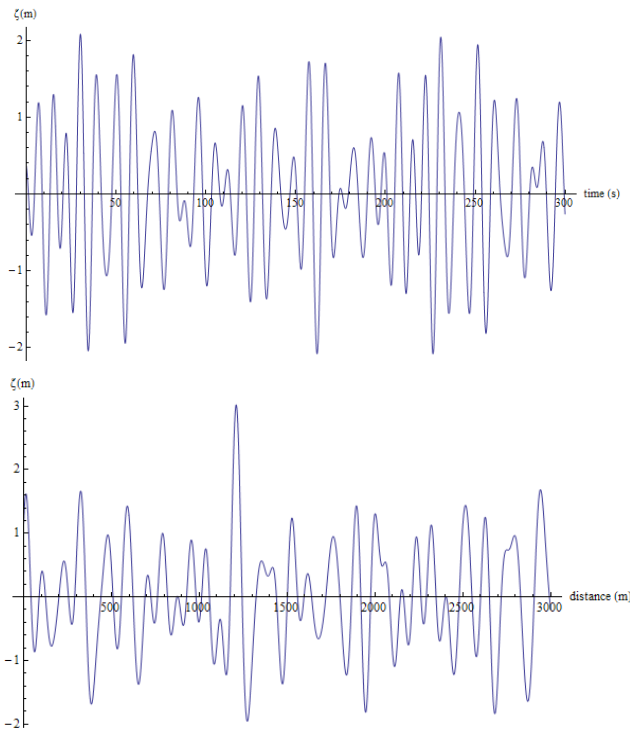


Figure 4: Wave elevations at $x = 100$ m (top) and for $t = 0$ s (bottom).

Table 2: Location of propagated wave profile points at $t = 0$ s.

Slope	x_0 (m)	
	Around Crest 1	Around Crest 3
0	13.23	229.53
1/100	11.47	224.12
1/75	10.87	222.07
-1/100	15.01	234.51
-1/75	15.61	236.18

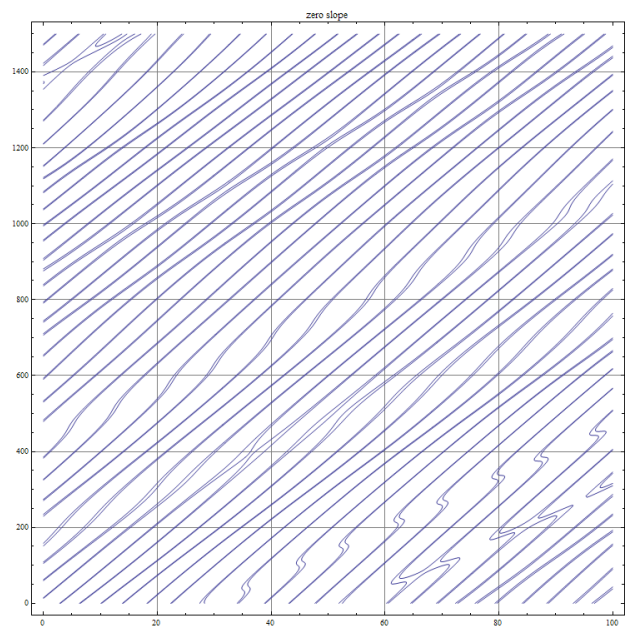


Figure 5: Contour plots for slopes $a = 0, 0.01$.

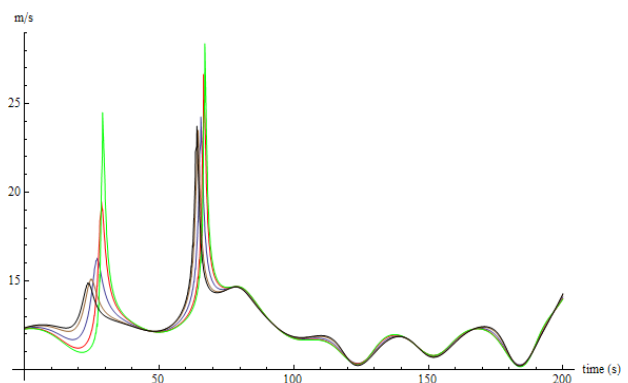


Figure 6: Celerity curves corresponding to wave slopes 1/75, 1/100, 0, -1/100, -1/75 (initially in vicinity of first crest).

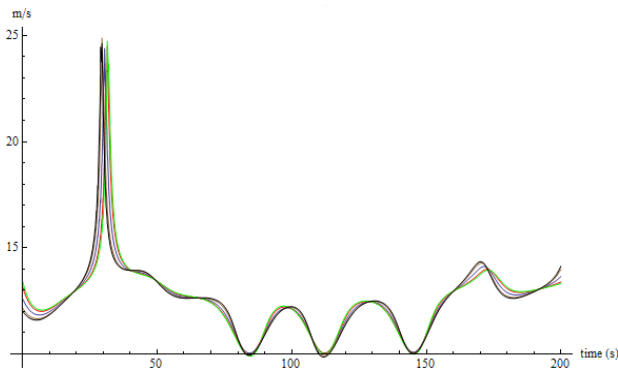


Figure 7: Wave velocity curves for the third crest.

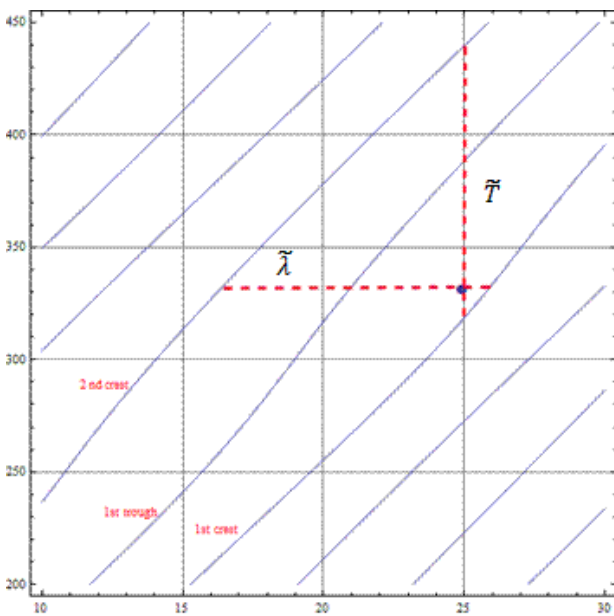


Figure 8: Wave length and wave period used for the approximate calculation of celerity. The dashed lines are measured between crests and the dotted lines between a crest and a trough.

Example 3

For the third example, the same JONSWAP spectrum was assumed. However, only a few frequencies around the peak were used this time. The considered spectral area was enlarged in successive runs in order to have bandwidth as the free parameter (Figure 11).

The celerity curve corresponding to the first crest after the origin is derived for three realisations of each bandwidth and plotted in Figure 12. The three realisations differ only in the (random) phases. As expected, the

variability of celerity in time is intensified as the bandwidth goes up. This trend is consistent for all considered samples.

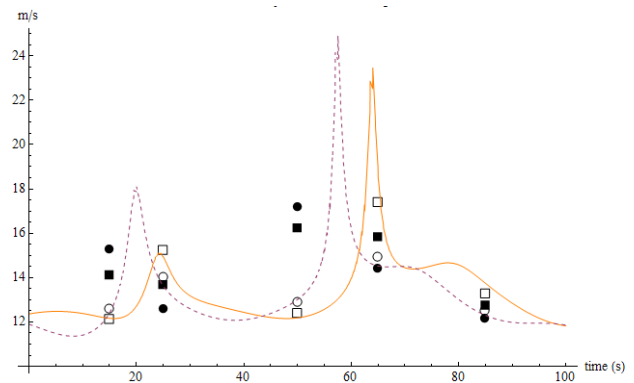


Figure 9: Comparison of the velocities obtained by propagating the first pair of points with slope $a = -1/100$ (see Table 2). The dashed line shows the celerity of the first point on the down-slope with slope a (nearer to crest). The continuous line is for the second point (nearer to trough). Each unfilled symbol refers to distance between successive peaks at the specified instant of time (position is implied). Filled symbols refer to distance between successive crests. Circles refer to the higher point (after the crest) and rectangles to the lower (before the trough).

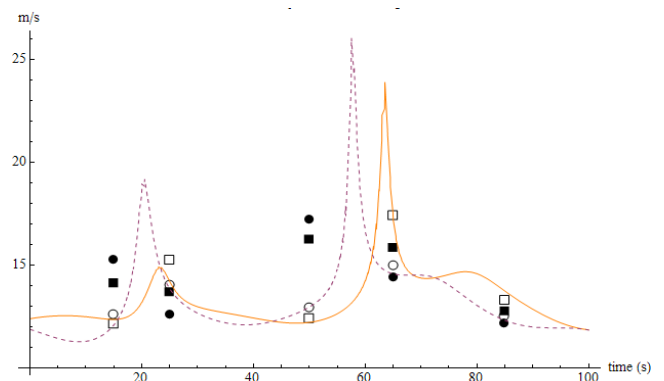


Figure 10: Comparison of velocities similar to Figure 9, but for $a = -1/75$.

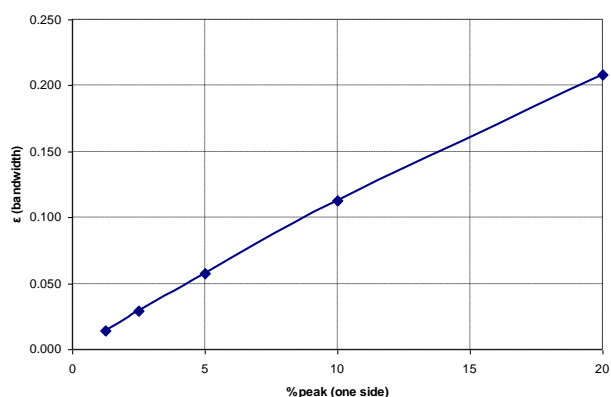


Figure 11: Example 3 spectrum bandwidths.

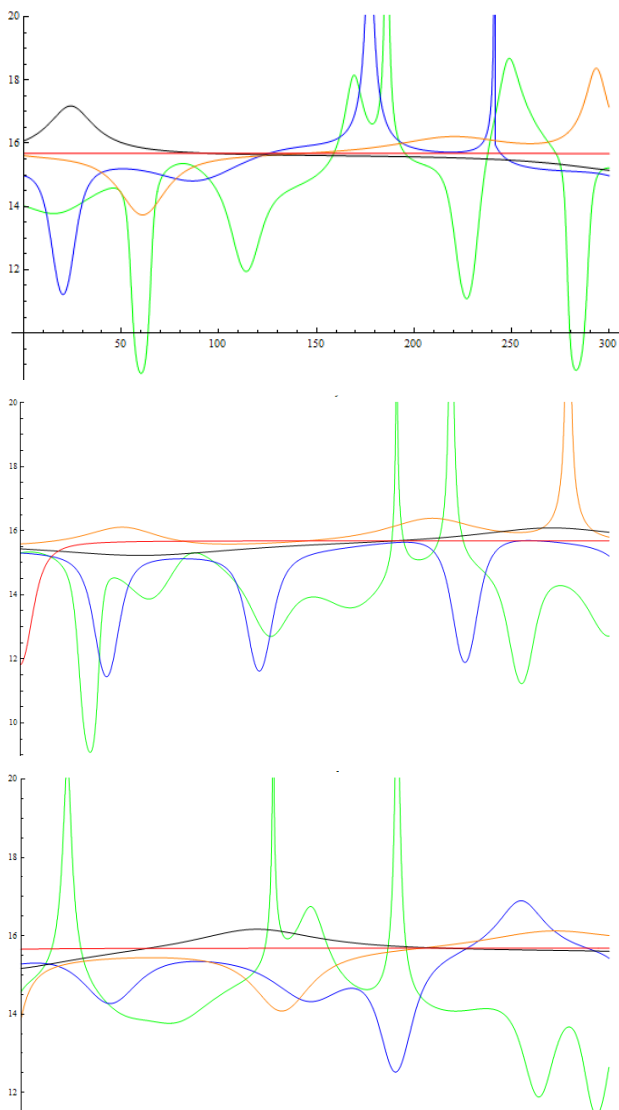


Figure 12: Celerity curves obtained by propagating the first crest for five different bandwidths. The three diagrams differ only in the random phases of the component waves. Red curves correspond to 1.25% of peak period on each side, black 2.5%, orange 5%, blue 10% and green 20%.

4. CELERITY DEFINITION FOR SURF-RIDING ASSESSMENT

The definition of instantaneous celerity suffers from a number of drawbacks. First, no matter what slope value is selected, there will be apparent wave cycles where any given value will not be realized. However, these waves will not be particularly steep and thus are unlikely to create surf-riding. The spikes, which are points where celerity jumps to infinity because of the annihilation of the points with the considered slope value, seem to present a more critical problem.

Another definition of a local (but not instantaneous) celerity that could be tried is based on the steepest point on the down slope of the wave profile that is nearest to the ship. Such a choice has an advantage because it is likely to be closely related to the maximum of the Froude-Krylov surge force acting on the ship, which is well known to have a critical connection with the occurrence of surf-riding. Often, maximum wave force and maximum slope are realized with a small phase difference. Computational burden is not substantially different between the point of maximum wave slope or maximum wave force. However, the first is a local wave characteristic that is in a physical context observable.

At least one point of maximum slope can be found on the down slope of every apparent cycle, yet it can degenerate to zero slope if its vicinity (e.g. its distance from the neighbouring crest) shrinks to a zero length. However, it is believed that such encounters represent relatively mild conditions for the ship and such singular points should therefore be unimportant for the surf-riding probability calculation. For a relatively narrow band sea, such events should be rare. It should be noted that there can be more than one point of locally maximum slope on a down slope.

As a ship advances with respect to a wave profile or the wave profile overtakes the ship, the targeted nearest point of maximum slope will change in a discrete stepped manner at

least once every apparent encounter period. The obtained celerity curve will therefore present points of discontinuity with step-wise change.

In order to calculate the celerity based on the propagation of the point of max slope in the vicinity of the ship, let $\xi(t)$ be the ship's position at some arbitrary time instant t , and search for points of max wave slope that lie near to $\xi(t)$ and are on the down slope. The following equation is solved for $x_{a_{max}} = f(t; a_{max})$, using Newton iterations started from the current position of the ship $\xi(t)$:

$$\frac{\partial^2 \zeta(x_{a_{max}}, t)}{\partial x^2} = 0 \quad (12)$$

Simultaneously, the following inequality should be satisfied to ensure that the point is on the down slope:

$$\frac{\partial^3 \zeta(x_{a_{max}}, t)}{\partial x^3} < 0 \quad (13)$$

For a 4th order finite difference approximation of the derivative, k more points are determined, separated by a time interval δt :

$$\frac{\partial^2 \zeta(x_{a_{max}}, t + \delta t)}{\partial x^2} = 0 \rightarrow x_{a_{max}}^{(k)} = f(t + k \cdot \delta t; a_{max}) \quad (14)$$

Since the time step δt is selected to be very small, the same initial guess $\xi(t)$ should practically suffice unless the initial point is very near to one of the special points mentioned earlier, where a stepped change takes place. Thereafter the celerity can be approximated by the formula:

$$c^{(4)} = \frac{-x_{a_{max}}^{(2)} + 8x_{a_{max}}^{(1)} - 8x_{a_{max}}^{(-1)} + x_{a_{max}}^{(-2)}}{12 \delta t} \quad (15)$$

In order to ensure that the located points truly lie near the ship, the following inequality condition can also be imposed on the solution

$$x_{a_{max}}^{(k)} : \left| x_{a_{max}}^{(k)} - \xi(t) \right| < d \quad (16)$$

where d can be a suitable fraction of the instantaneous wave length.

In the analysis of ship motion data, the celerity is calculated for each time step of the simulation time history by tracking the point of maximum wave slope nearest this ship at that time. The examples below demonstrate the tracking scheme for simulations of the tumble-home ship from the ONR Topside series ($L=154$ m) in regular, bichromatic and irregular waves. In these examples, the simulation time step $\Delta t = 1$ while the tracking time interval $\delta t = 10^{-3}$.

Example 4

Here the scheme is applied for a simulation in regular waves in order to verify that the known regular wave celerity is captured (Figure 13).

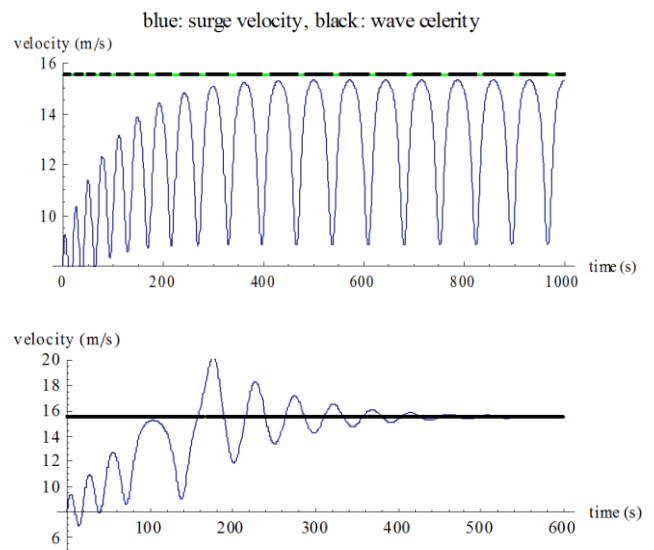


Figure 13: Surging versus celerity for:
 $\zeta_1 = 3.8$ m, $\lambda = 154$ m, $Fn = 0.295$ (upper),
 $\zeta_1 = 3.8$ m, $\lambda = 154$ m, $Fn = 0.324$ (lower).

The calculated celerity curve appears in Figure 13 as a dashed line. In this initial implementation, the procedure is to find a maximum slope point by iterating to solve Equation (12) with the inequality condition of Equation (13).



Example 5

The next example examined bichromatic waves consisting of two wave components. The first scenario has one component with a length equal to the ship length and another component that is longer. A threshold case was identified for a nominal (calm water) speed just below the occurrence of surf-riding (see Figure 14). In a bichromatic sea, the celerities of the two component waves, which are indicated by the red and green lines in Figure 14, define a celerity range that is obeyed only in the smoother regions of the curve of local celerity. Surge velocity came very close, yet did not cross the calculated celerity curve.

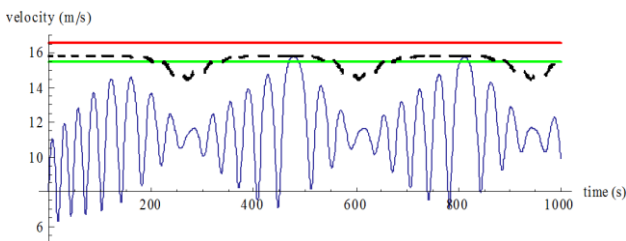


Figure 14: Surging in a bichromatic sea: $\zeta_1 = 2.5$ m, $\lambda = 175$ m and $\zeta_2 = 3.4$ m, $\lambda = 152$ m, ($Fn = 0.28$).

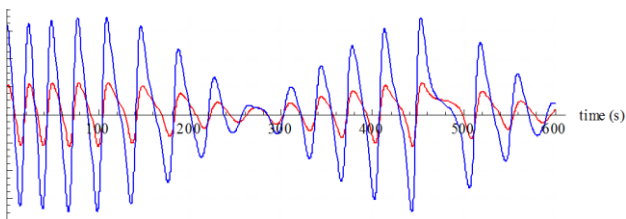


Figure 15: Phasing of wave slope (red) versus Froude-Krylov force (blue).

Figure 15 plots the time histories of Froude-Krylov surge force and the wave slope measured at the ship's instantaneous position. Figure 16 shows contours of the maxima of these quantities on a space-time plot. Both figures suggest that the maximum wave slope is, as expected, a good indicator of the maximum of the wave surging force.

The bichromatic wave simulation was then repeated using the same wave but with a slightly higher self-propulsion speed (Figure 17). This speed plot shows a crossing of the celerity curve, followed by ship motion with mean speed considerably higher than the self-propulsion speed and about the celerity value. This is realization of surf-riding. It is very noteworthy, however, that the observed motion has a persistently strongly oscillatory character.

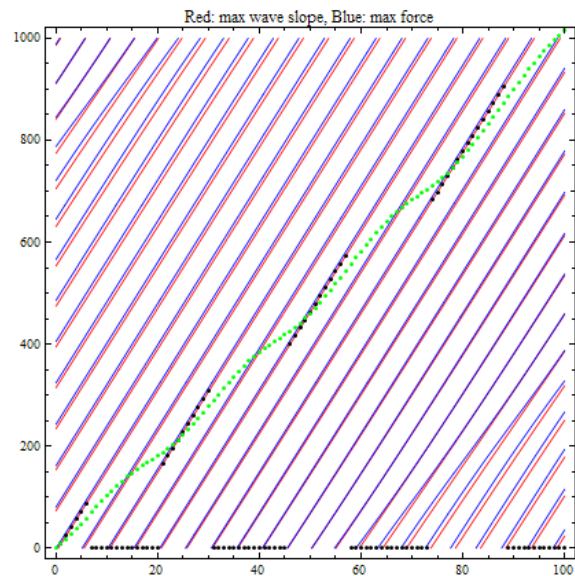


Figure 16: Space-time contour plot for maximum wave slope (red) and maximum force (blue). Green dots indicate the ship's instantaneous position. Blue dots show the identified nearest point of max slope for each ship position.

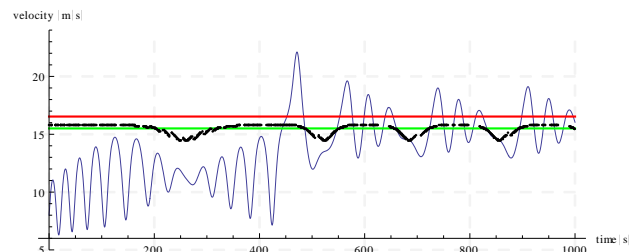


Figure 17: Threshold crossing at $Fn = 0.283$.

An additional bichromatic wave comprised of two long waves of moderate steepness produced a similar pattern. In Figure 18 the nominal speed is just below the surf-riding

threshold, while in Figure 19 the nominal speed is just above the surf-riding threshold.

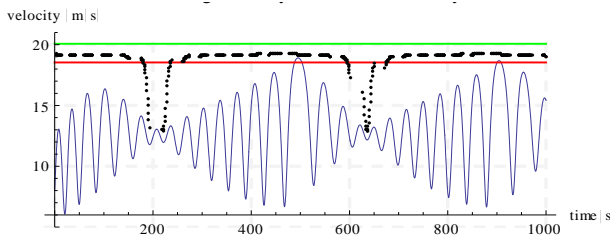


Figure 18: $\zeta_1 = 3.8$ m, $\lambda = 258$ m and $\zeta_2 = 3$ m, $\lambda = 220$ m and $Fn = 0.315$.

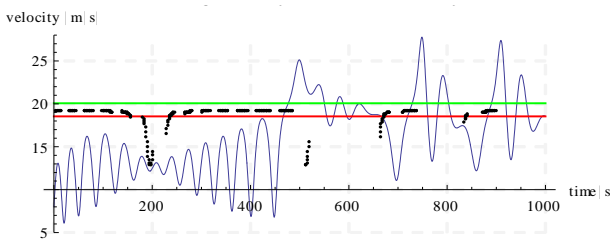


Figure 19: $\zeta_1 = 3.8$ m, $\lambda = 258$ m and $\zeta_2 = 3$ m, $\lambda = 220$ m and $Fn = 0.319$.

The Figure 19 scenario is also plotted in space-time for three different initial conditions, shown in Figure 20. Two of the resulting motion histories soon fall completely on each other, while the third does not. Despite this, the pattern of surf-riding behaviour exhibited in these results is identical. In the first two cases the ship is "caught" by the same wave while in the third case it is not caught by that wave but continues with ordinary surging until it is caught by a later wave.

Another noteworthy feature is seen from the trace of the curves on the time-space plane (Figure 21). While the lines of the two runs that show apparent surf-riding behaviour from the beginning are almost straight and indistinguishable, the third one has lower initial slope, which is indicative of the lower velocity of motion. However, it then "bends" and becomes parallel to the other two once the celerity threshold is exceeded and the ship is captured into surf-riding.

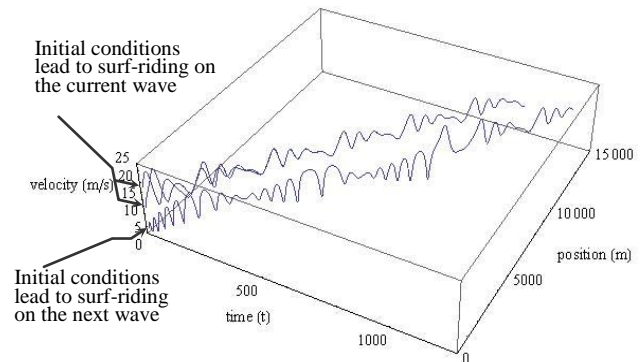


Figure 20: Realisations of surf-riding for different initial conditions (bichromatic wave).

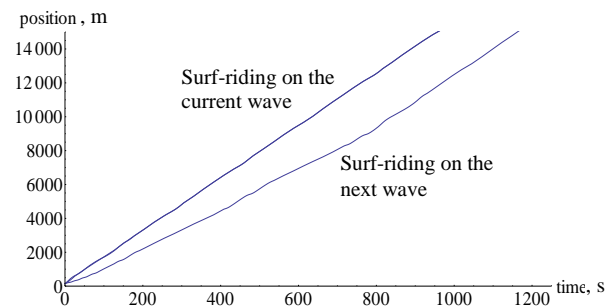


Figure 21: Traces of ship position curves on the time-space plane.

Example 6

The final example of the celerity calculation is an irregular sea case again based on the JONSWAP spectrum ($H_s = 3.5$ m, $T_p = 10$ s). The region of the spectrum at 5% around the peak frequency has been used, corresponding to wave lengths that are very close to the ship length (between 148 and 164 m). Wave realisations were based on six frequencies, with random phases. Ship behaviour for nominal speeds just below and well into the surf-riding regime are shown in Figures 22 and 23, respectively. For reference, the green line indicates the wave celerity corresponding to the mean wave frequency.

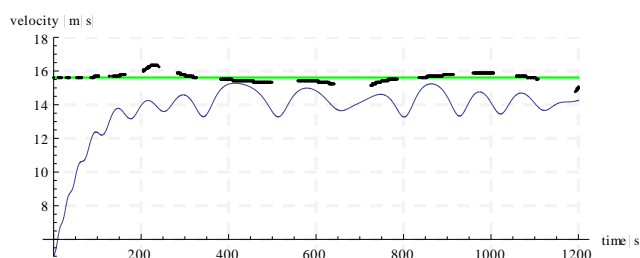


Figure 22: JONSWAP spectrum ($F_n = 0.283$).

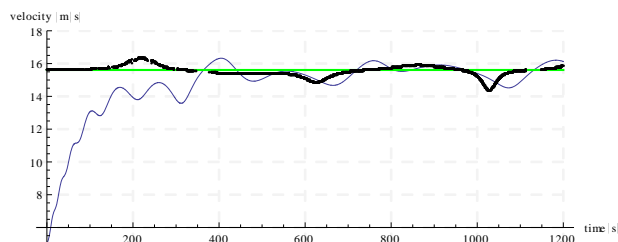


Figure 23: JONSWAP spectrum ($F_n = 0.37$) considering all max slopes (down and up).

As described above, the initial implementation of the celerity calculation only produced a result when the zero-slope point found near the ship was on the down slope. This results in the broken celerity curve in Figure 23. In Figure 24, the celerity calculation considers points on both the up and down slopes to produce a complete, though not necessarily continuous, curve.

5. LAMP IMPLEMENTATION

Following its initial verification using the 1-DOF model of surging, the irregular wave celerity calculation is being implemented in the Large Amplitude Motions Program (LAMP) where it will be used as part of a probabilistic model of surf-riding (Belenky et al. 2012). LAMP is a nonlinear time-domain computer simulation code for ship wave motions and loads that is built around a body-nonlinear 3-D potential flow solution of the wave-body hydrodynamic interaction problem and incorporates models for viscous, lift and propulsor effects. Previous studies have demonstrated that LAMP can simulate the principal phenomena of surf-riding and broaching-to (Spyrou et al. 2009).

The LAMP implementation of the wave celerity calculation generally follows the scheme described above, but has been adapted for LAMP's more general irregular wave models including oblique, short-crested (multi-direction) and nonlinear incident waves. The wave point that is tracked is the maximum wave slope in the direction of ship travel; it is tracked only in that direction, and the resulting wave celerity is calculated in this direction. In this manner, the tracked point is related to the force in the surging direction and the "celerity" characterizes the speed that the ship must reach, at its current heading, to stay at this point of maximum surging force. Note that this "directional" definition of celerity can be quite different from a "physical" wave celerity obtained by observing the motion of a wave feature from a global view point. In fact, for a ship travelling at an angle to long-crested seas, LAMP's "directional" celerity will be larger than the wave "physical" celerity, going to infinity in beam seas. However, this is correct for the consideration of surf-riding, as a ship would need to go infinitely fast to maintain its relative position to the crest or other feature of a beam wave.

Another difference in the LAMP implementation of the wave celerity calculation is that it always searches for the nearest maximum slope point on the down slope even if an up slope maximum is closer. This is done by pre-computing the elevation and its derivatives on a regular spatial interval δx_s in the travel direction and identifying intervals where a down-slope maximum can be found. A careful selection of the interval size can also significantly reduce the number of wave evaluations required to find and track the maximum slope points, which can be very important for wave models that include many components and/or nonlinear terms.

Figure 24 shows a snapshot of a LAMP simulation for the tumblehome hull form from the ONR Topsides series running in long-crested irregular waves. The plot shows the wave profile at that time instance along the

ship's travel direction with marks for the points of maximum down slope and elevation (crest). The wave in this case is derived from a Bretschneider spectrum with $H_s=7\text{m}$ and $T_m12.0\text{s}$.

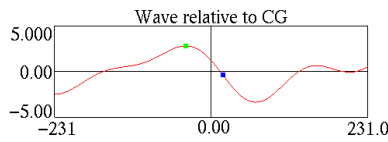


Figure 24: LAMP simulation of ONR Topsides tumblehome hull in irregular following seas.

Figures 25 and 26 show the time histories of the ship speed and the wave celerity for two different propeller rates.

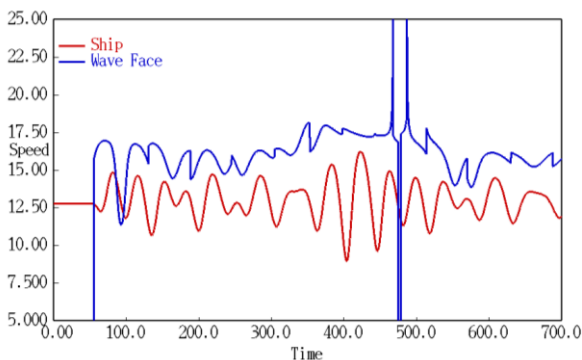


Figure 25: Ship speed and wave celerity for propeller speed of 2.2 rps.

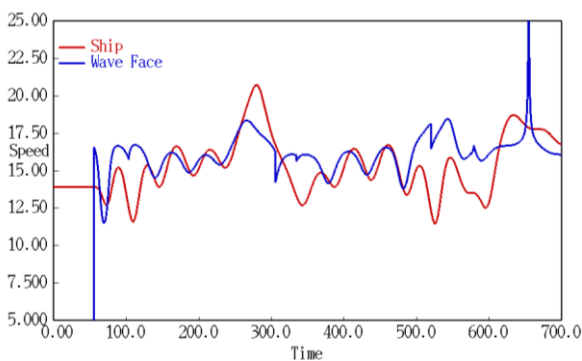


Figure 26: Ship speed and wave celerity for propeller speed of 2.4 rps.

At the lower propeller speed shown in Figure 25, the ship speed oscillates near its calm water speed and below the wave celerity, and no surf-riding is observed. At the higher propeller speed, there are three episodes where the ship's speed upcrosses the wave celerity and is captured into surf-riding for a period of time, matching the wave speed while surf-riding. While the initial wave celerity jump at 60 seconds is a plotting artifact, the other "spikes" in wave speed are cases where the phasing of the wave component produces a very rapid local translation of the point of maximum slope. At ~480s of the first record (Figure 25), an overtaking of one wave by a following one actual causes the maximum point to briefly slide back up the wave face and results in a negative celerity. The identification and handling of such situations is one objective of the current development. Despite these problem points, the present scheme seems to provide a practical calculation of wave celerity that is suitable for characterizing surf-riding in irregular waves.

6. CONCLUSIONS

In the development of a probabilistic model of surf-riding in irregular seas based on the time histories of wave elevation and ship motion, it has been proposed that the phenomena of surf-riding can be characterized by an up-crossing of the wave celerity by the ship speed. In order to implement such a scheme, it is necessary to calculate a relevant instantaneous wave celerity corresponding to the ship's position in the irregular wave at any given time. A scheme has been developed that calculates such a value by finding the point of maximum wave slope on the down slope of the wave nearest the ship and tracking its motion over a series of short time increments. The point of maximum slope has been selected because of its close relationship to the point of maximum wave surging force, which is a closely tied to surf-riding. The tracking scheme has been implemented and demonstrated in both a 1-DOF model of surging and in the LAMP 6-DOF time domain seakeeping code. Initial results indicate this scheme can reliably produce wave celerity



values that can indeed be used to identify surf-riding in irregular waves.

7. ACKNOWLEDGMENTS

The research reported in this paper is funded by the Office of Naval Research (ONR) under Dr. Patrick Purtell and by ONR Global under Dr. Richard Vogelsong. This support is gratefully acknowledged by the authors.

8. REFERENCES

- Aberg, S., and Rychlik, I., 2006, "Role of wave velocity for encountered wave statistics," Proceedings of the Sixteenth (2006) International Offshore and Polar Engineering Conference, San Francisco, California, May 28 - June 2.
- Aberg, S., and Rychlik, I., 2007, "Doppler shift approximations of encountered wave statistics," Ocean Engineering, Vol. 34, 2300-2310.
- Baxevani, A., Podgórski, K., and Rychlik, I., 2003, "Velocities for moving random surfaces", Probabilistic Engineering Mechanics, Vol. 18, 251-271.
- Belenky, V.M., Spyrou, K.J., and Weems, K.M., 2012, "Evaluation of the Probability of Surf-Riding in Irregular Waves with the Time-Split Method," Proceedings of the 11th International Conference on the Stability of Ships and Ocean Vehicles (STAB 2012), Athens, Greece (to appear).
- Boashash, B., 1992, "Estimating and Interpreting The Instantaneous Frequency of a Signal – Part 1: Fundamentals," Proceedings of the IEEE, Vol. 80, 520-538.
- Gabor, D., 1946, "Theory of Communication," Journal of the IEE, Vol. 93, 429-457.
- Kinsman, B., 1984, Wind Waves: Their Generation and Propagation on the Ocean Surface. Dover Publications Inc., New York, ISBN 0-486-64652-1.
- Kratz, M.F., and León, J.R., 2005, "Curve crossings and specular points, d'apres Longuet-Higgins," www.mendeley.com/research/curve-crossings-specular-points-dapres-longuethiggins/#page-1.
- Longuet-Higgins, M.S., 1957, "The Statistical Analysis of a Random, Moving Surface," Philosophical Transactions of the Royal Society of London. Series A, Mathematical and Physical Sciences, Vol. 249, 966, 321-387.
- Mandel, L., 1974, "Interpretation of instantaneous frequency," American Journal of Physics, Vol. 42, 840-846.
- Pierson, W.J., Jr., 1955, "Wind-generated gravity waves", in Advances in Geophysics, Vol. 2, Academic Press Inc. (New York), 93-178.
- Spyrou, K.J., 2006, "Asymmetric surging of ships in following seas and its repercussions for safety", Nonlinear Dynamics (ed. A.H. Nayfeh), Kluwer, Vol. 43, 149-272.
- Spyrou, K.J, Weems, K.M., and Belenky, V., 2009, "Patterns of Surf-Riding and Broaching-to Captured by Advanced Hydrodynamic Modelling," Proceedings of the 10th International Conference on Stability of Ships and Ocean Vehicles (STAB2009), St. Petersburg, Russia.
- Vossers, G., 1962, "Behaviour of Ships in Waves," Volume IIC of Ships and Marine Engines, The Technical Publishing Company H. Stam N.V., Harlem, Netherlands.



Continuation Analysis of Surf-riding and Periodic Responses of a Ship in Steep Quartering Seas

Ioannis Tigkas, *Thenamaris Ships Management Inc.(ex-NTUA)*, i.tigkas@thenamaris.com

Kostas J. Spyrou, *National Technical University of Athens*, k.spyrou@central.ntua.gr

ABSTRACT

Steady-state ship dynamics in steep quartering seas are investigated. Further progress achieved on the implementation of bifurcation analysis for ship motions in regular seas by means of a numerical continuation method is reported. Stationary as well as periodic states are traced and complete bifurcation diagrams, including coexisting ship responses of different type, are presented, considering Froude-Krylov wave excitation. A strong feature of the approach is the inclusion of memory effects within a potential flow framework. The main novelty of the paper lies in the extension of the continuation analysis to 6-D.O.F., for a quartering sea environment. A number of stability diagrams that are produced in an automated and time-efficient manner could be a useful guidance for a Master for avoiding the occurrence of surf-riding and broaching-to.

Keywords: *manoeuvring, surf-riding, broaching-to, bifurcation, homoclinic, continuation, nonlinear dynamics*

1. INTRODUCTION

Instability phenomena in severe astern seas are feared by seafarers from the times when wind was the prime mover (Spyrou, 2010). But it is only since the '40s that they started receiving deeper scientific attention (Davidson, 1948, Rydill, 1959). Shortly it was realised that, some key phenomena responsible for the occurrence of instability in following/quartering seas have a strongly nonlinear nature (e.g. Weinblum and St. Denis, 1950, Grim 1951 & 1963, Wahab & Swaan, 1964). Simulation, i.e. direct numerical integration of the equations of motion, is a very straightforward technique for predicting ship responses from some assumed initial conditions. As a matter of fact, it is used nowadays in almost all investigations having practical orientation (Matora *et al.*, 1981; Fuwa *et al.*, 1981, Renilson, 1982, Hamamoto *et al.*, 1988 and 1989, De Kat & Paulling, 1989; Hamamoto *et al.*, 1994). However, ordinary simulation alone is generally ineffective for understanding, in a deeper sense, a dynamical system's behaviour

and for identifying its stability limitations. Novel techniques that can target more globally and more directly a system's potential for exhibiting rich and unconventional dynamic behaviour need to be implemented. One technique that can help to unravel behavioural changes as some system parameters are varied is numerical "continuation" (e.g. Krauskopf *et al.*, 2007).

In earlier studies this technique was applied for studying surf-riding and broaching-to on the basis of a 4-D.O.F. model (Spyrou, 1995, 1996a and 1996b). In a more recent paper the authors have performed continuation analysis of periodic motions in exact following seas (surging, heaving and pitching), including potential flow memory effects, for a ship that is on the verge of capture to surf-riding (Spyrou & Tigkas, 2011). This work is further expanded here by performing continuation of stationary and periodic responses for all 6-D.O.F. It is demonstrated that, by using the so-called *codimension-2* continuation method, stability diagrams of the system are directly produced.



2. MATHEMATICAL MODEL

2.1 Equations of Motions

Long harmonic waves are considered to propagate from following/ quartering direction relatively to the ship, which is moving with forward speed while performing also parasitic motions in all 6 degrees of freedom, due to waves' effect. A non-inertial system rotating like the moving ship (body-fixed system) is used for monitoring ship velocities and accelerations (SNAME, 1952). Furthermore, two inertial systems are used in secondary role: one fixed at a wave trough, and thus moving with the wave celerity; and also an earth-fixed system (see Fig1). Assuming that the ship behaves as a rigid-body, the equations of motions can be expressed with respect to the body-fixed system as follows*:

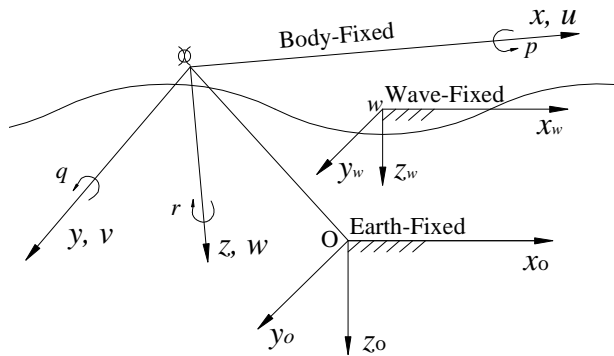


Figure 1: Body-fixed, wave-fixed and earth-fixed coordinate systems.

Surge:

$$m[\dot{u} + qw - rv - x_G(q^2 + r^2) + z_G(pr + \dot{q})] = X - mg \sin \theta$$

Sway:

$$m[\dot{v} + ru - pw + z_G(qr - \dot{p}) + x_G(qp + \dot{r})] = Y + mg \sin \varphi \cos \theta$$

Heave:

$$m[\dot{w} + pv - qu - z_G(p^2 + q^2) + x_G(rp - \dot{q})] = Z + mg \cos \varphi \cos \theta$$

Roll:

$$I_x \dot{p} - mz_G(\dot{v} + ru - pw) - mx_G z_G(\dot{r} + pq) = K$$

Pitch:

$$I_y \dot{q} + (I_x - I_z)rp + mz_G(\dot{u} + qw - rv) - mx_G(\dot{w} + pv - qu) + mx_G z_G(p^2 - r^2) = M - mgx_G \cos \varphi \cos \theta$$

Yaw:

$$I_z \dot{r} + (I_y - I_x)pq + mx_G(\dot{v} + ru - pw) + mz_G x_G(rq - \dot{p}) = N \quad (1)$$

2.2 Hull Forces and Moments

The external forces and moments acting on the ship are expressed in a modular form as a summation of hull reaction, rudder, propeller and wave excitations. For low frequencies of encounter, added mass and damping coefficients are calculated by the "strip theory" method of Clarke (1972). Whilst "old fashioned", this method is easily integrated in a nonlinear dynamical system continuation analysis. Firstly are computed the potential sway added mass coefficients for a number of (time-varying) hull sections up to the wave surface by multi-parameter conformal mapping. Then by integrating along the length of the hull the forces and moments can be found and expressed as accelerations and velocity derivatives by partial differentiation (Tigkas, 2009). Using pre-processing we obtain the added-mass coefficient of a section as a polynomial function of the instantaneous sectional draught. In this method it is assumed that only the wave profile corresponding to the ship's specific longitudinal position on the wave and the ship's heave and pitch responses, influence the draught of each section and consequently the zero-frequency added mass properties. An example of the obtained results

* All symbols are explained in the Nomenclature at the end of the paper.



is shown in Fig. 2. A universal problem is the lack of accurate calculation of the viscous part of the hydrodynamic derivatives that is usually considerable at the sections near the stern. For this reason, in some occasions we applied an empirical hybrid approach, extracting the viscous part from the semi-empirical zero-frequency derivatives and adding it to the “potential” coefficients obtained by Clarke’s method.

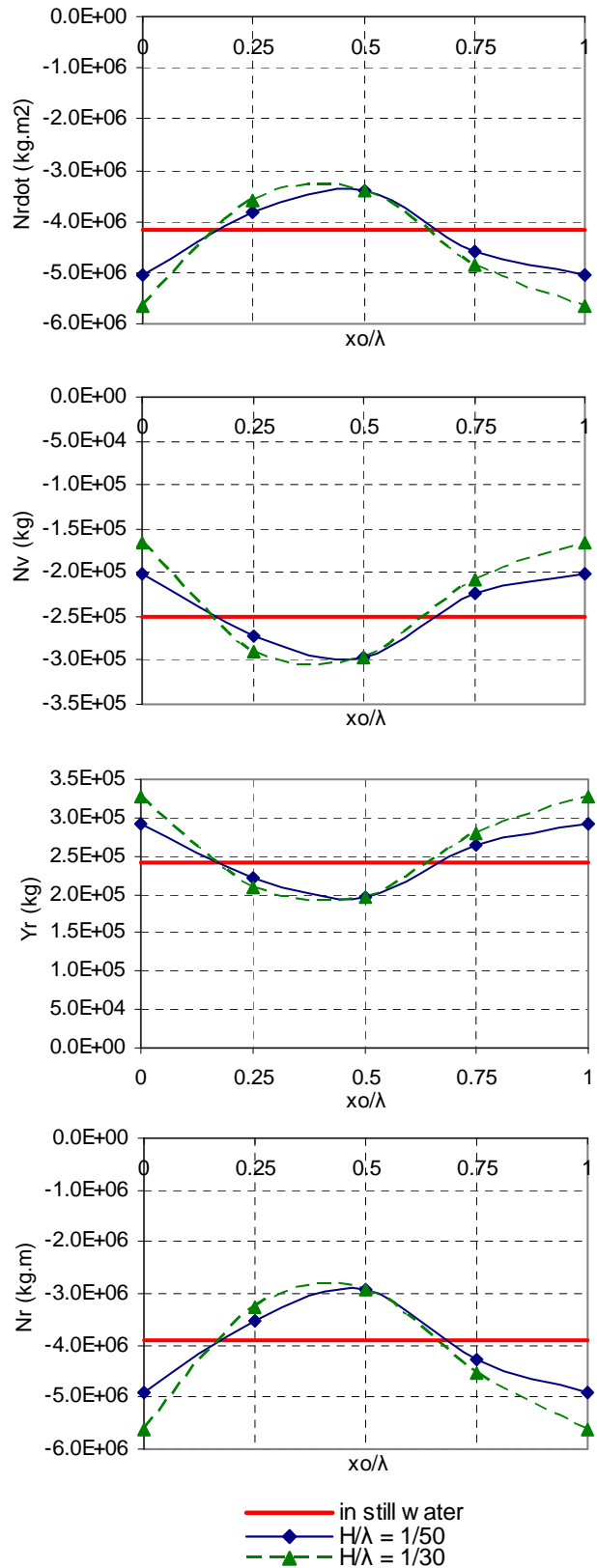
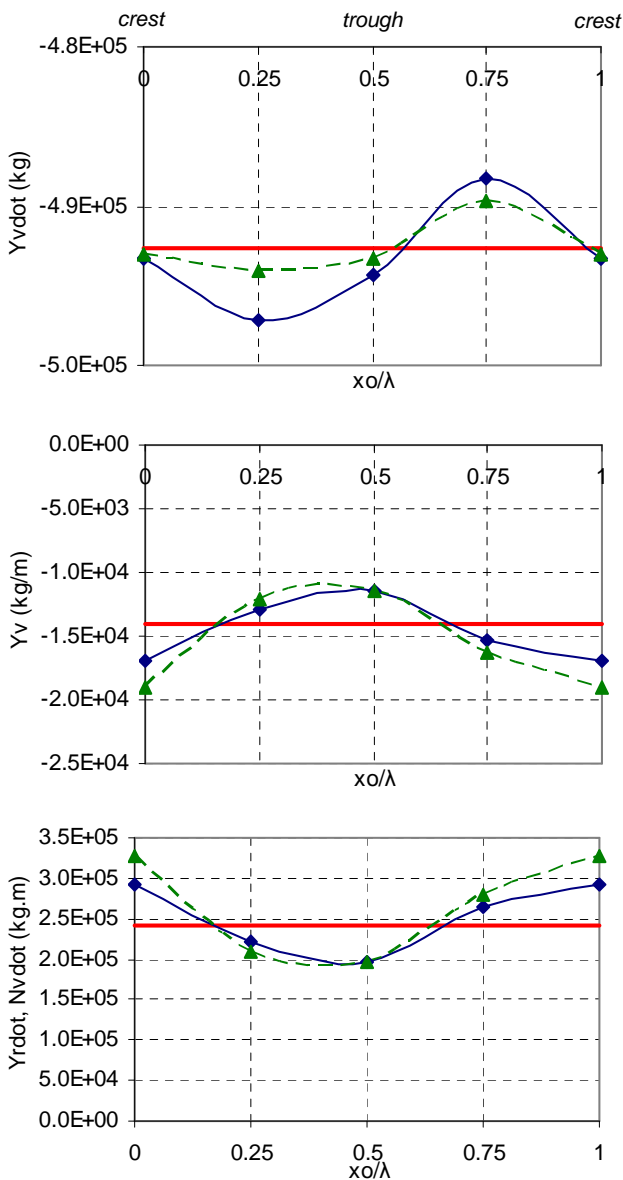


Figure 2: Linear hydrodynamic derivatives for the fishing vessel investigated in Section 4, at different longitudinal positions on a wave starting from a wave crest ($\lambda/L = 2$).



2.3 Memory Effects

To investigate ship motions not only for the stationary condition of surf-riding (zero-frequency of encounter) but for a rather wide range of wave encounter frequencies, “memory effects” should be considered, accounting for fluid’s hydrodynamic radiation loads that are caused in mode i due to ship motion in mode j . According to Cummins (1962) it can be expressed as:

$$F_{Mij}(t) = -A_{ij}(\infty)\dot{v}_j(t) - \underbrace{\int_0^{\infty} K_{ij}(\tau)v_j(t-\tau)d\tau}_{s_{ij}(t)} \quad (2)$$

The impulse response (or retardation) function K_{ij} in the above equation can be written as follows (Ogilvie, 1964; see however also detailed presentation in Taghipour, 2008):

$$K_{ij}(\tau) = \frac{2}{\pi} \int_0^{\infty} [B_{ij}(\omega_e) - B_{ij}(\infty)] \cos(\omega_e \tau) d\omega_e \quad (3)$$

The integro-differential equations (2) can be approximated by a system of ordinary differential equations (O.D.E.s) by means of a standard state-space approximation technique (Tick, 1959, Schmiechen, 1975, Jefferys, 1984). As shown by Schmiechen (1975), the following finite set of recursive first-order linear O.D.E.s can replace eq. (2):

$$\begin{aligned} \dot{s}_{ij}(t) &= s_{ij(1)}(t) - a_{ij(k)}s_{ij(k)}(t) - b_{ij(k)}v_j(t) \\ \dot{s}_{ij(1)}(t) &= s_{ij(2)}(t) - a_{ij(k-1)}s_{ij}(t) - b_{ij(k-1)}v_j(t) \\ \dot{s}_{ij(2)}(t) &= s_{ij(3)}(t) - a_{ij(k-2)}s_{ij}(t) - b_{ij(k-2)}v_j(t) \\ &\dots \quad \dots \quad \dots \quad \dots \\ &\dots \quad \dots \quad \dots \quad \dots \\ \dot{s}_{ij(k)}(t) &= -a_{ij(0)}s_{ij}(t) - b_{ij(0)}v_j(t) \end{aligned} \quad (4)$$

The coefficients $a_{ij(m)}$ and $b_{ij(m)}$ are calculated from curve fitting in frequency domain, on the basis of the values of the added mass and damping terms. However, some attention is required in this identification

scheme, for ensuring that the recursive system of eq. (4) is stable (Tigkas, 2009).

It should be noted however that the developed procedure calculates the hydrodynamic memory accounting also zero frequency effect that has already been calculated by the applied strip - theory method. In order to sort out this overlap issue, from each associated linear hydrodynamic derivative we subtract the corresponding potential part at zero-frequency that was calculated by the potential seakeeping code, that has been used in order to extract the added mass and damping coefficients.

2.4 Wave and Hydrostatic Loads

The wave excitation loads of a rigid body in regular harmonic waves, assuming inviscid and irrotational flow, can be linked with the effects of the incident and the diffracted wave potentials. The Froude-Krylov excitation loads (including hydrostatic) are determined by the integration of the fluid pressure of the submerged portion of the hull, up to the free surface of the incident wave. However, the contribution of the diffracted wave excitation loads are not taken into account in this study. Their calculation in a very low to medium encounter frequency range and the efficient integration of such a scheme with continuation analysis is a demanding task on its own that will be resolved in a future research study. Nevertheless, the inclusion of diffraction loads is only expected to alter quantitatively but not qualitatively the results.

2.5 Rudder and Propeller

Kose’s (1982) model is the basis for calculating rudder forces. As for propulsor’s force, a polynomial fit of available propeller performance data is used for approximating the thrust coefficient K_T as function of propeller’s rate of rotation. Wave effects on the rudder and on the propeller are produced by the variation

of draught at those locations and by the change in the inflow velocity. Rudder's area and aspect ratio "seen" by the water are obtained from its instantaneous draught. Sometimes the propeller might ventilate or even emerge out of the water with significant efficiency loss (Koushan, 2006, Paik *et al.*, 2008). However such losses can vary considerably depending on stern's layout, propeller characteristics and other design characteristics. A simple model calculating the loss of thrust could not be deduced.

When the rudder angle is not taken as fixed, a standard proportional - differential (PD) controller is used, whose equation is expressed in an O.D.E. form as follows:

$$\dot{\delta} = t_r [-\delta - a_\psi (\psi - \psi_r) - a_{\dot{\psi}} b_r r] \quad (5)$$

3. ADAPTING MATHEMATICAL MODEL TO ENABLE CONTINUATION

To conduct continuation analysis a number of transformations were obliged on the described mathematical model:

(a) The investigated dynamical system needed to come into the generic O.D.E. form $\dot{\mathbf{x}} = \mathbf{F}(\mathbf{x}, \mathbf{a}; t)$ where \mathbf{x} is the vector of state variables and \mathbf{a} is the vector of system's parameters. Furthermore, all state variables of the system should be bounded as time progresses. As a matter of fact, continuation analysis could not be attempted before transforming the equations of the system in such a way, so that all state variables take values within bounded limits and, a steady state recognised by the algorithm as such, irrespectively of whether this is stationary or periodic, can be reached.

(b) The last criterion states that the O.D.E.s that constitute the state-space representation should have no explicit dependence upon the time variable. This may include special transformations on the system's form of equations, if the investigated dynamical system

is excited by a time-varying force, as for example the wave load.

The first problem is realised when a state variable of the system increases monotonically to infinity as time progresses. The variable that renders impossible for the system to reach a recurring state and is hence imposing non-conformity to the first requirement, is the distance travelled by the ship in the longitudinal direction. In our mathematical model, this is a state variable used for defining the relative position of the ship on the wave and it appears in the module where the Froude-Krylov forces and moments are calculated. To demonstrate the transformations involved, let's consider the surge wave force. By using the relationship $x = x_0 - ct$, the position-dependent part of this force can be written as:

$$X_{FK} = -\rho g A k \cos \psi \int_{-L/2}^{L/2} S(x_s, T_s) e^{-kT_s(x_s, x_0, t, z, \theta)/2} \sin k(x_s \cos \psi + x) dx_s \quad (6)$$

After trigonometric expansion it is written as follows:

$$X_{FK} = -\rho g A k \cos \psi \int_{-L/2}^{L/2} S(x_s, T_s) e^{-kT_s(x_s, x_0, t, z, \theta)/2} [(\cos kx \cdot \sin kx_s \cos \psi) + (\sin kx \cdot \cos kx_s \cos \psi)] dx_s \quad (7)$$

Two dummy variables $a = \sin kx$ and $b = \cos kx$ are introduced, replacing the cyclic functions of x in eq. (7). The periodic nature of a and b means that these variables are inherently bounded, unlike x which is monotonically increasing. For consistency an extra pair of O.D.E.s needs however to be added (see also Doedel *et al.*, 1997):

$$\begin{aligned} \dot{a} &= a - \omega_e b - a(a^2 + b^2) \\ \dot{b} &= \omega_e a + b - b(a^2 + b^2) \end{aligned} \quad (8)$$

The introduced pair stands basically for a harmonic oscillator that, despite of increasing by two the number of variables of the system,

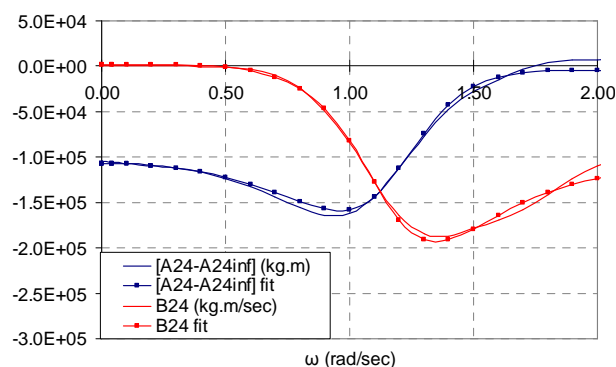
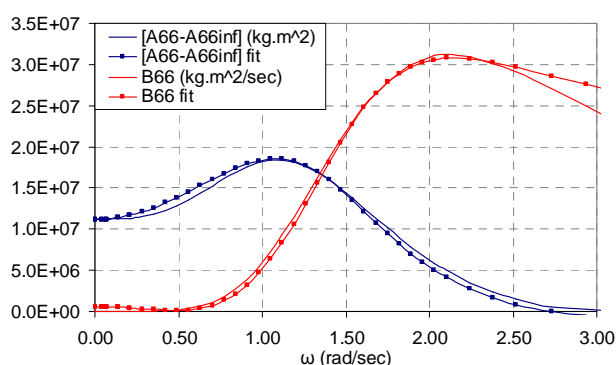
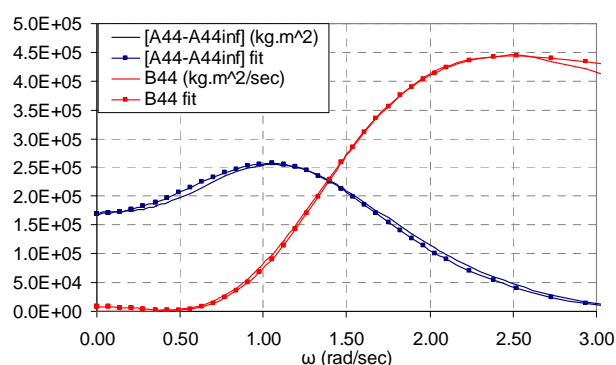
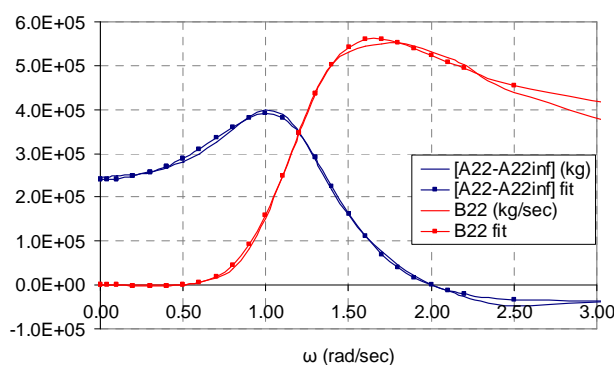


at steady-state it bears no effect on the behaviour relatively to the original system (Spyrou & Tigkas, 2011). This method is applied for all position-dependent forces and moments in all directions of ship motion.

With the above transformations the model can be interfaced with the continuation algorithm where in our case such is MATCONT (Dhooge *et al.*, 2003). The mathematical principles and the main capabilities of this algorithm for investigating nonlinear dynamical systems have been discussed in our earlier works and need not to be repeated (see for example, Spyrou *et al.*, 2007, Spyrou & Tigkas, 2007 and 2011).

4. INVESTIGATION RESULTS

The ship investigated is the well known 34.5m long Japanese fishing vessel ('purse-seiner') that has also been examined several times in the past in free running and captive model tests, numerical analysis of dynamics, and benchmarking evaluations (see for example Umeda *et al.*, 1995, ITTC, 2005). Her added mass and potential damping coefficients at each encounter frequency were identified by the commercial code Trident Waveload (2006). Integrations concerning hull geometry were carried out on the basis of 20 transverse stations along the hull length. For the memory fits discussed earlier, the number of the required linear first-order O.D.E.s of the filter has been investigated and a few values of the order k (see section 2.3) were tested, in each case evaluating the quality of the fit produced (Fig3). The order $k = 3$ seems to be a popular choice in relevant work, e.g. see Holappa & Falzarano (1999). Here it was judged that it provides satisfactory accuracy (see also Spyrou & Tigkas (2011) for more detailed explanation).



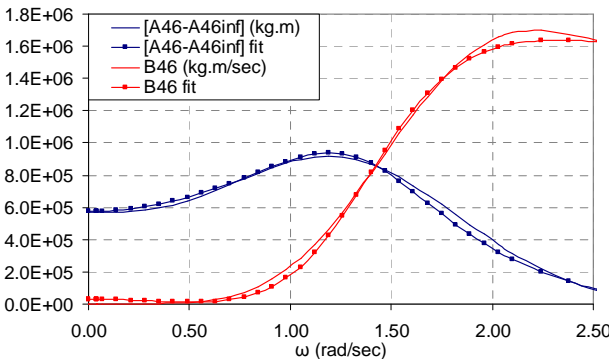
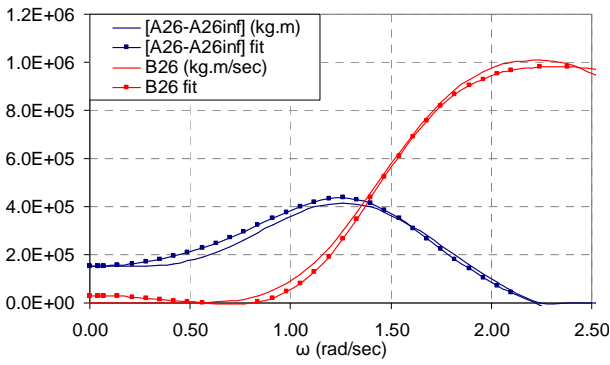


Figure 3: Examples of fits for added mass and damping coefficients for the purse seiner. (Fits for heave, pitch and cross terms of pitch with surge can be found in Spyrou & Tigkas, 2011)

The standard state-space form of the mathematical model after implementing the above described actions is consisted of 77 O.D.E.s. This is considered as a very high number of equations for a continuation study.

4.1 Stationary Responses

In Figure 4 below are shown the obtained “equilibrium headings” for the entire range of rudder angles and for several nominal Froude numbers. These equilibrium headings are unstable unless rudder control exists, in which case the parts of the curve nearer to the trough are stabilised. But for the basic case of a ship without active control, *saddle-type* instabilities are formed between LP1 and LP1’ and between LP2 and LP2’. Equilibrium diagrams for the other modes of motion are also shown in Figure 5.

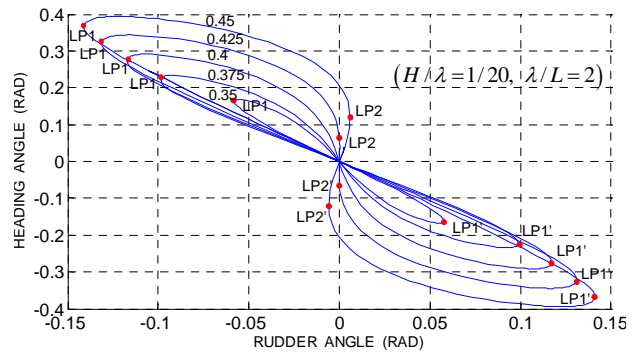


Figure 4: Equilibrium headings in correspondence to rudder angles, based on the 6-D.O.F. model.

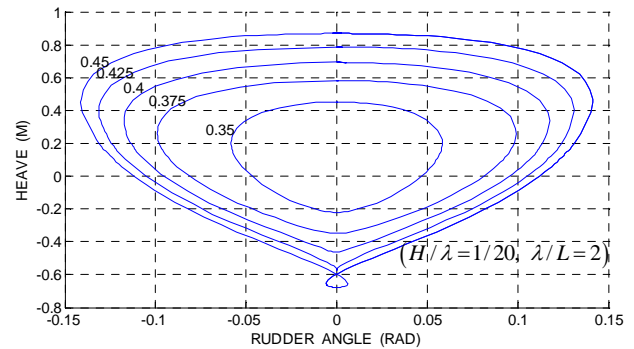
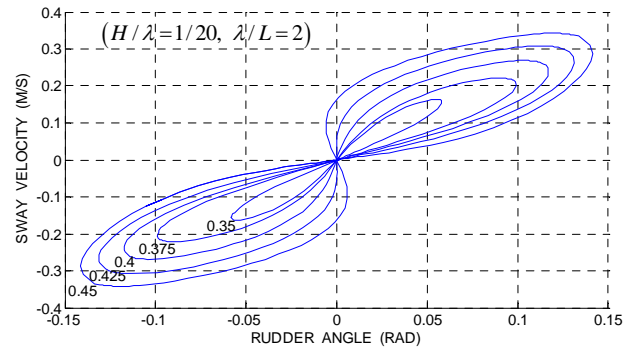


Figure 5: Equilibrium sway velocity (upper) and heave displacement (lower) corresponding to rudder angles for a range of nominal Froude numbers.

Since LP1 points determine the range of potentially stabilisation by rudder control state laws, their locus defines in fact the domain where surf-riding can be experienced in practice. Such a curve can be obtained by *codimension-2* continuation of the *fold* LP1, varying simultaneously Fn and δ . The result is



shown in Figure 6. The branch of LP2 has also been included in this diagram. Even though these latter points do not receive an immediate practical interpretation, their “behaviour” is interesting: at the zero rudder angle and for $Fn = 0.42$, a *cusp* point is formed by the tangential contact of the *saddle - node* branches corresponding to LP2’s evolution.

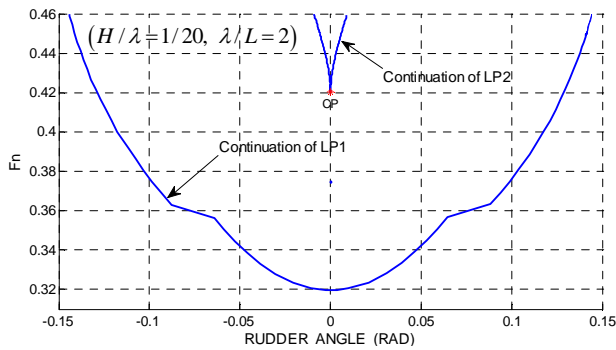


Figure 6: Stability diagram in following/quarterming seas, showing the range of rudder angles where surf-riding is sustainable.

A diagram such as the one of Figure 6 could make a ship Master aware of the range of “equilibrium rudder angles” which could support surf-riding in following/ quarterming seas. Of course the accuracy of the input that can become available to him is critical, especially regarding wave height and period.

The influence of proportional gain on the realized heading in the condition of surf-riding in quarterming seas is illustrated in Figure 7. Accordingly, the upper parts of the curves in Figure 7 from 0 to LP are always stable, where the lower parts are occupied by saddles. Again, LP points indicate the transition of stability and are occurring this time at the maximum possible commanded heading angles for each selected proportional gain. As one expects, larger commanded angles of heading will not correspond to a reduced heading error (commanded heading minus actual heading), but rather practically mean the ship to start turning. It is also evident that at low values of proportional gain, the heading error especially in relatively large commanded heading angles is also large and thus the controller’s function

is problematic. The locus of limit points (LP) is finally obtained by *codimension-2* continuation when varying simultaneously the commanded heading and the proportional gain.

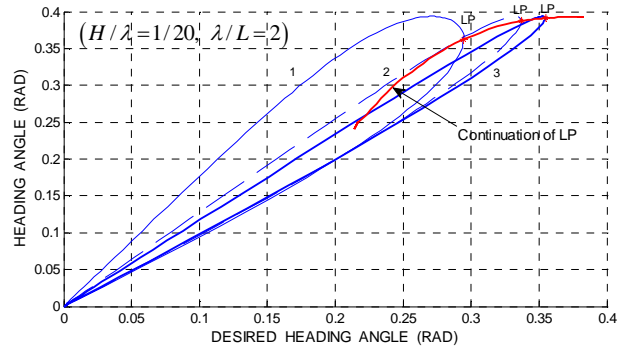


Figure 7: Difference between commanded and actual headings for three different proportional gains (1, 2 and 3), $Fn = 0.45$ and differential gain equal to 1.

Another useful investigation is to determine the locus of lowest nominal Froude numbers for which surf-riding can be realised in quarterming waves. This can also be obtained by *codimension-2* continuation, varying Fn and ψ_r . In the scenario of Figure 8, the control settings were: $t_r = 3$, $a_\psi = 3$, and $b_r = 1$. Several diagrams of this kind for different heights and lengths can also assist on-board decision-making.

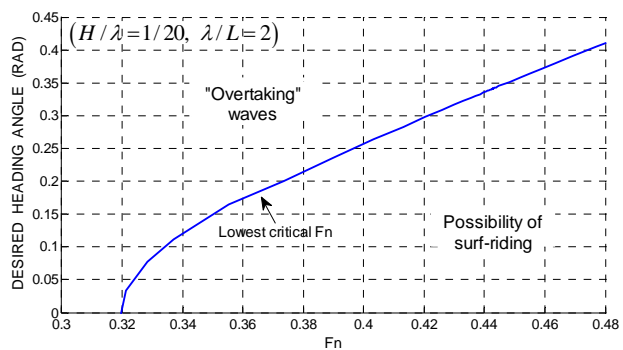


Figure 8: *Codimension-2* bifurcation diagram produced by continuation and showing the lowest nominal Froude number values for which surf-riding can be realised, for a wide range of commanded heading angles.

4.2 Periodic Responses with Active Steering Control

The key element of the current effort targets the periodic responses in quartering waves and furthermore, the conditions that are eligible for broaching-to behaviour not only as a natural consequence of surf-riding but also by a more direct escape mechanism (Spyrou, 1996b and 1997). However controller's settings influence the amplitude of yaw oscillation as well as the maximum commanded heading angle up to which the ship remains controllable.

To run effectively the continuation of these periodic orbits for the complete model in 6-D.O.F. we needed to reduce the system of equations to 42 O.D.E.s by neglecting several memory terms that have a lesser effect on the outcome. Thus, the most influential memory loads kept in this simplified system comprise; s_{22} , s_{26} , s_{33} , s_{35} , s_{44} , s_{55} , s_{53} , s_{66} and s_{62} . Below only two characteristic examples of the several obtained results will be discussed.

Consider firstly the evolution of periodic motions for a fixed commanded heading angle of 15° . For low nominal Froude numbers, ship motion is basically linear but as the speed is increased, it becomes increasingly asymmetrical. As well known, at some stage the periodic behaviour abruptly stops due a *homoclinic connection*. In Figure 9 is shown the contact between the stationary (surf-riding) and the periodic motions that is responsible for this phenomenon. Continuation produces a unique picture of this spectacular encounter between different ship states.

The sequence of phenomena is qualitatively similar to what happens in an exactly following sea environment (see for comparison Spyrou & Tigkas, 2011). However, the critical Froude numbers are moved to slightly higher values since the experienced surge wave force in quartering waves is reduced. Control settings were selected like in section 4.1, sufficient for

keeping the ship on a mean heading very close to the commanded one.

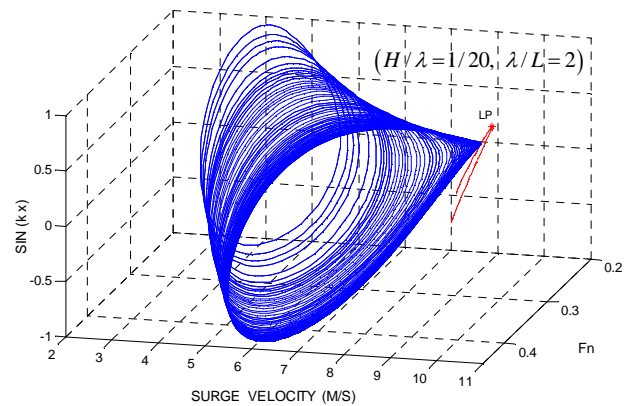


Figure 9: 3-D view of the evolution of limit cycles collapsing onto the branch of saddles, for a fixed 15° desired heading angle.

In the second scenario presented the interest is on the evolution of the periodic motion amplitudes for a fixed nominal Froude number, as the commanded heading angle is increased to values beyond the surf-riding range. As observed in Figures 10 and 11, the amplitudes of both yaw and surge oscillations increase when the commanded heading angle is also increased. Whilst this behaviour continues for the lower range of commanded heading angles, at a critical value of the commanded heading angle a *limit point of cycles (fold of cycles)* is encountered and the stable limit cycles are turned unstable. Thus a sufficient condition for a discontinuous jump to a distant state is established. The created unstable limit cycles continue their evolution “backwards” with increasing amplitude. This phenomenon indicates a different broaching-to scenario at *LPC*, which occurs not due to surf-riding, but directly from periodic oscillations by an over-increased heading angle.

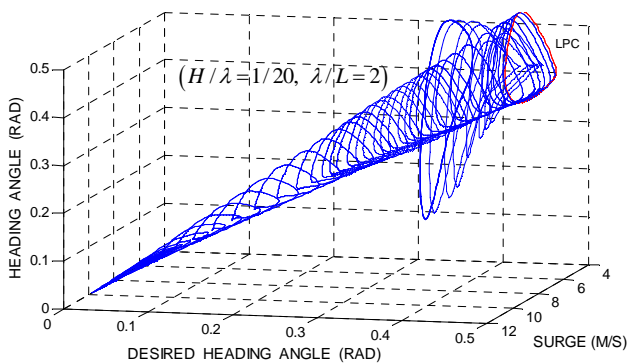


Figure 10: 3-D view of the evolution of limit cycles by increasing the desired heading angle at nominal $F_n = 0.4$

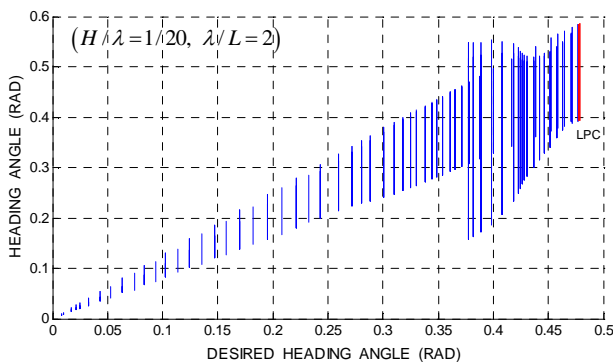


Figure 11: Bifurcation diagram showing the increase of yaw amplitude as the commanded heading angle is increased, at nominal $F_n = 0.4$

5. CONCLUSIONS

A mathematical model in 6-D.O.F. that contains modules for the effect of waves, hull reaction including hydrodynamic memory, propeller and rudder has been developed. The mathematical model is the offspring of an earlier manoeuvring-type model with 4 D.O.F. and it has been brought into such a form that it can be utilised for bifurcation analysis. A continuation analysis algorithm was interfaced with the mathematical model in order to fully capture the stationary and periodic ship motions, with emphasis given at their interactions. Loci in parameters' space of system's bifurcation points have also been traced. The latter can be particularly useful as some of the system's stability boundaries can be automatically produced in this manner.

Design diagrams related with controller tuning and ultimately a complete booklet offering operational guidance for averting broaching-to phenomena in steep quartering seas can also be produced.

In parallel to the achieved progress, several areas requiring further work have emerged. For example, the nonlinear mathematical model developed can be further improved; especially the part related to the calculation of the manoeuvring derivatives and the diffraction wave loads within a user-friendly framework for applying continuation analysis and other nonlinear dynamics techniques. The combined effects of wind and waves can also be studied. Despite that this appears to be straightforward given the current development and previous work studies by the authors (e.g. Spyrou *et al.*, 2007), the wealth of dynamical phenomena that may arise from a combination of excitations, merits in our view a dedicated study. Another, more ambitious, direction of research is the extension of the presented methods of analysis for a probabilistic environment.

6. ACKNOWLEDGMENTS

Ioannis Tigkas would like to thank "Alexander S. Onassis" Public Benefit Foundation for his PhD scholarship at the time of his research studies at NTUA.

7. REFERENCES

- Clarke, D., 1972, "A Two-Dimensional Strip Method for Surface Ship Hull Derivatives: Comparison of Theory with Experiments on a Segmented Tanker Model", *Journal of Mechanical Engineering Science*, Vol. 14, No. 7, pp. 53-61.
- Cummins, W.E., 1962, "The Impulse-Response Function and Ship Motions", *Schiffstechnik*, Vol. 9, No. 47, pp. 101-109.
- Davidson, K.S.M., 1948, "A Note on the Steering Of Ships in Following Seas",



Proceedings of the 7th International Congress of Applied Mechanics, London.

- De Kat J.O. and Paulling J.R., 1989, "The Simulation of Ship Motions and Capsizing in Severe Seas", SNAME Annual Meeting, Presentation, No. 5.
- Dhooge A., Govaerts W., Kuznetsov Yu.A., Mestrom W., Riet A.M. and Sautois B., 2003, "MATCONT and CL_MATCONT: Continuation Toolboxes for MATLAB". Report of Gent and Utrecht Universities.
- Doedel E.J., Champneys A.R., Fairgrieve T.F., Kuznetsov Yu.A., Sandstede B. and Wang X.J., 1997, "AUTO97-00: Continuation and Bifurcation Software for Ordinary Differential Equations (with HomCont)", User's Guide, Concordia University, Montreal, Canada.
- Fuwa T., Sugai K., Yoshino T. and Yamamoto T., 1981, "An Experimental Study on broaching of Small High Speed Boat", Journal of the SNA of Japan, Vol. 150.
- Grim O., 1951, "Das Schiff in von Achtern Auflaufender See", Jahrbuch S.T.G., Bd. 45.
- Grim O., 1963, "Surging Motion and Broaching Tendencies in a Severe Irregular Sea", Deutsche Hydrographische Zeitschrift, Bd. 16.
- Hamamoto M., 1988, "Study on Ship Motions and Capsizing in Following Seas: 1st Report - Equations of Motion for Numerical Simulation", Journal of the SNA of Japan, Vol. 163, pp. 173-180.
- Hamamoto M., 1989, "Study on Ship Motions and Capsizing in Following Seas: 2nd Report - Simulation of Capsizing", Journal of the SNA of Japan, Vol. 163, pp. 123-130.
- Hamamoto M., Fujino M. and Kim Y.S., 1994, "Dynamic Stability of a Ship in Quartering Seas", Proceedings of STAB 94, Melbourne, Florida.
- Holappa K.W. and Falzarano, J.M., 1999, "Application of Extended State-space to Non-linear Ship Rolling", Journal of Ocean Engineering, Vol. 26, p. 227-240.
- ITTC, 2005, "Report of Specialist Committee on Ship Stability in Waves", Proceedings of the ITTC Conference, Edinburgh.
- Jefferys, E.R., 1984, "Simulation of Wave Power Devices", Journal of Applied Ocean Research, No. 6, Vol. 1, pp. 31-39.
- Kose K., 1982, "On a New Mathematical Model of Manoeuvring Motions of A Ship and its Applications", Journal of International Shipbuilding Progress, Vol. 29, No. 336.
- Koushan, K., 2006, "Dynamics of Ventilated Propeller Blade Loading on Thrusters due to Forced Sinusoidal Heave Motion", Proceedings of the 26th Symposium on Naval Hydrodynamics, Rome, Italy.
- Krauskopf B., Osinga H. G. and Galan-Vioque J. (editors), 2007, "Numerical Continuation Methods for Dynamical Systems", Springer Publications.
- Motora S., Fujino M., Koyanagi M., Ishida S., Shimada K. and Maki T., 1981, "A Consideration on the Mechanism of Occurrence of Broaching-to Phenomena", Journal of the SNA of Japan, Vol. 150, pp. 84-97.
- Ogilvie T.F., 1964, "Recent Progress towards the Understanding and Prediction of Ship Motions", Proceedings of the 5th Symposium on Naval Hydrodynamics, Bergen, Norway, pp. 3-79.
- Paik B.G., Lee J.Y. and Lee S.J., 2008, "Effect of Propeller Immersion Depth on the Flow around a Marine Propeller", Journal of Ship Research, Vol. 52, No. 2, pp. 102-113.



- Renilson M., 1982, "An Investigation Into the Factors Affecting the Likelihood of Broaching-to in Following Seas", Proceedings of the STAB 82, Tokyo, pp. 17-28.
- Rydill L.J., 1959, "A Linear Theory for the Steered Motion of Ships in Waves", Transactions of RINA, pp. 81-112.
- Schmiechen M., 1975, "Equations for Non-Quasi-Steady Ship Motions", Seakeeping Committee Report, Proceedings of the 14th ITTC Conference, Ottawa, Canada.
- SNAME, 1952, "Nomenclature for Treating the Motion of a Submerged Body Through Fluid", Technical and Research Bulletin, No. 1-5.
- Spyrou K.J., 1995, "Surf-Riding Yaw Instability and Large Heeling of Ships in Following/ Quartering Waves", Journal of Ship Technology Research, Vol. 42, pp. 103-112.
- Spyrou K.J., 1996a, "Dynamic Instability in Quartering Seas: The Behaviour of a Ship During Broaching", Journal of Ship Research, Vol. 40, No. 1, pp. 46-59.
- Spyrou K.J., 1996b, "Homoclinic Connections and Period Doublings of a Ship Advancing in Quartering Waves", Journal of Chaos, Vol. 6, pp. 209-218.
- Spyrou K.J., 1997, "Dynamic Instability in Quartering Seas – Part III: Nonlinear Effects on Periodic Motions", Journal of Ship Research, Vol. 41, No. 3, pp. 210-223.
- Spyrou, K.J., 2010, "Historical Trails of Ship Broaching-to", Transactions of RINA, Vol. 152, Part A4, pp. 163-173.
- Spyrou K.J., Tigkas I. and Chatzis A., 2007, "Dynamics of a Ship Steering in Wind Revisited", Journal of Ship Research, Vol. 51, No. 2.
- Spyrou K. and Tigkas I.G., 2007, "Principles and Application of Continuation Methods for Ship Design and Operability Analysis", Proceedings of 10th PRADS Symposium, Houston, Texas, USA.
- Spyrou K.J. and Tigkas I.G., 2011, "Nonlinear Surge Dynamics of a Ship in Astern Seas: "Continuation Analysis" of Periodic States with Hydrodynamic Memory", Journal of Ship Research, Vol. 55, No. 1, pp. 19-28.
- Taghipour R., Perez T. and Moan T., 2008, "Hybrid Frequency–Time Domain Models for Dynamic Response Analysis of Marine Structures", Journal of Ocean Engineering, 35, pp. 685-705.
- Tick L.J., 1959, "Differential Equations with Frequency-Dependent Coefficients", Journal of Ship Research, Vol. 3, No. 2, pp. 45-46.
- Tigkas I.G., 2009, "Nonlinear Dynamics Analysis of the Directional Instabilities of Ships in Wind and Waves", PhD Thesis, National Technical University of Athens, Greece.
- Trident F-D Waveload, 2006, "User's Guide and Theory Manual", Martec Ltd, Halifax, Nova Scotia, Canada.
- Umeda N., Hamamoto M., Takaishi Y., Chiba Y., Matsuda A., Sera W., Suzuki S., Spyrou K.J. and Watanabe K., 1995, "Model Experiments of Ship Capsize in Astern Seas", Journal of the SNA of Japan, Vol. 177, pp. 207-218.
- Wahab R. and Swaan W.A., 1964, "Course-keeping and Broaching of Ships in Following Seas", Journal of International Shipbuilding Progress, Vol. 7, No. 4, pp. 293-301.
- Weinblum G. and St. Denis M., 1950, "On the Motions of Ships at Sea", Transactions of SNAME, Vol. 58, pp. 184-248.



NOMENCLATURE

A : wave amplitude	L : ship length	x_o : longitudinal distance travelled by the ship in an earth-fixed system
$A_{ij}(\omega)$: added mass coefficient	m : ship mass	
A_R : rudder area	q, p, r : pitch, roll and yaw angular velocity in a body-fixed system, respectively	x_s : longitudinal distance of a vertical ship section S in the body-fixed system
a_ψ, a_r : proportional, differential gain		
$B_{ij}(\omega)$: damping coefficient	$S(x_s, T_s)$: vertical hull sectional area below instantaneous waterline	x_G, z_G : longitudinal distance from amidships and vertical distance from keel of ship's centre of gravity, respectively.
c : wave celerity	t : time	
F_N : rudder normal force	t_p : thrust deduction coefficient	
F_n : Froude number	t_r : rudder's time constant	Greek letters
H : wave height	$T_s(x_s, x_o, t, z, \theta)$: draught of ship at vertical section S	δ : rudder angle
H/λ : wave steepness	u, v, w : surge, sway and heave velocity in a body-fixed system, respectively	A : rudder aspect ratio
I_x, I_y, I_z : roll, pitch and yaw ship mass moment of inertia	U_R : inflow velocity at rudder	θ : pitch angle
K, M, N : moments in roll, pitch and yaw respectively	X, Y, Z : forces in surge, sway and heave respectively	ρ : water density
$K_{ij}(\tau)$: impulse response function		φ : roll angle
K_T : propeller thrust coefficient		ψ : heading angle
k : wave number ($k = 2\pi/\lambda$)	x : longitudinal distance travelled by the ship, with respect to a system fixed at a wave trough.	ψ_r : desired heading angle
λ : wave length		ω_e : encounter frequency
		ω : wave frequency





Bifurcation from Fluttering to Autorotation of a Hinged Vertical Flat Plate Submitted to a Uniform Current

Antonio Carlos Fernandes, *LOC/COPPE/UFRJ (Federal University of Rio de Janeiro)*,

acfernandes@peno.coppe.ufrj.br

Sina Mirzaei Sefat, *LOC/COPPE/UFRJ (Federal University of Rio de Janeiro)*,

smsefat@peno.coppe.ufrj.br

ABSTRACT

The free falling of objects is a phenomenon that has been observed in the nature. For instance, the leaves of trees may fall in different ways. The objects may fall without a full rotation (fluttering) or with full rotation (tumbling). This has been a matter of research for several authors and difficult to understand due to the complexity of this six degree of freedom problem. The first motivation to study on the flow induced rotation phenomenon was an offshore industry application called the Pendulous Installation Method (PIM) of heavy devices, which is a free falling that occurs in the installation of heavy offshore devices on sea bed. The present work describes the investigations on fluttering and autorotation motions of the interaction of uniform current and freely rotating plate about a fixed vertical axis. According to the dimensional analysis the motion in flow induced rotation is governed essentially by dimensionless moment of inertia, Reynolds number and initial conditions. Certain combinations define the stability boundaries between fluttering and autorotation. Hence, a bifurcation diagram prepared by the experiments to classify different states observed the small fluttering, fluttering and autorotation based on different Reynolds number and dimensionless moment of inertia.

A quasi-steady model is suggested to model the trajectories of flow induced rotation phenomenon and a stability analysis performed to gain insight into the nature of the bifurcation from fluttering to autorotation. At first, the fixed points for different models of motion is obtained and each point analyzed by using the linearized equation. Secondly, the phase diagrams as a function of angular velocity and angle of rotation have been presented for different dynamic models.

Keywords: *Autorotation, Fluttering, Quasi-Steady, Stability Analysis*



1. INTRODUCTION

In this study, the authors are under the impression of fluttering and tumbling phenomenon which happen in the falling objects problems in air or water. In fluttering, the body oscillates either periodically or chaotically from side to side as it descends alternating gliding at low angle of attack and fast rotational motion and tumbling motion is characterized by the end-over-end rotational motion of body (see Andersen, Pesavento & Wang, 2005). In the present case, controlling the oscillatory behavior of manifolds during the pendulous installation method of a manifold (see Fernandes & Mirzaei Sefat, 2011, Fernandes, Mirzaei Sefat, Coelho & Albuquerque, 2011, Fernandes, Mirzaei Sefat, Coelho & Ribeiro, 2010a, Fernandes, Mirzaei Sefat, Coelho & Ribeiro, 2010b) was the first motivation to study the flow induced rotation phenomenon. Therefore, the authors chose to study the behaviour of a hinged flat plate allowed to rotate about its vertical axis, under the influence of uniform current (see Fig. 1). Though, the study on flow induced rotation of a vertical hinged flat plate under the influence of uniform current is a 1-DOF problem, but it aims at the understanding of the fluttering and autorotation problems of falling objects in air or water. The results could be generalized for some other phenomena which are 3-DOF, like PIM method, falling objects, windborne debris, etc.

The fluttering and autorotation are two different phenomena which may occur in flow induced rotation of a plate about a fixed axis, which is free to rotate in the current. In the autorotation, the plate rotates continuously around a vertical axis and it never damps out. On the other hand, the fluttering motion is another unexpected periodic oscillation of the plate around a stable position which the plate is normal to the flow.

Maxwell (1854) was the first who tried to explain tumbling motion of a flat plate. Later,

several experimental researches under both free fall and fixed-axis conditions were made in order to classify and quantify the types of these rotational motions. The theoretical and experimental results before 1979, such as Dupleich (1941), etc, have been evaluated and summarized by Iversen (1979).

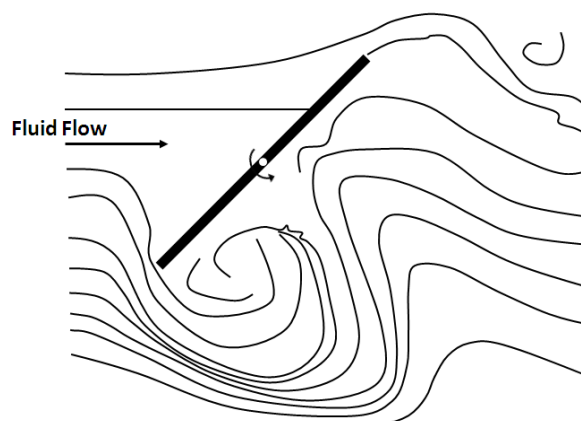


Figure 1: Schematic of flow induced rotation of a flat plate hinged at the center. It is free to rotate in uniform current.

According to the Iversen (1979), the motion of a freely falling and also fixed axis rectangular plate is governed by the Reynolds number, the aspect ratio (ratio of width to span of plate), thickness ratio (ratio of width to thickness of plate) and dimensionless moment of inertia of the flat plate. Actually the motion in free fall and in particular, the transition from fluttering to tumbling, should be completely governed by these parameters. Lugt (1983) argued that, for a viscous fluid, at least qualitatively, a fifth-order polynomial for the damping terms in the pendulum equation is necessary to simulate the self-excited oscillation (fluttering) and autorotation for bodies with axis fixed in a parallel flow.

Field, Klaus, Moore & Nori (1997) prepared a bifurcation diagram based on the experimental data, which shows the dynamical behaviour of falling disks as a function of the two parameters: dimensionless moment of inertia and Reynolds number. According to this bifurcation diagram, depending on the dimensionless moment of inertia, the motion



could be fluttering for smaller dimensionless moment of inertia, or tumbling for larger dimensionless moment of inertia. Based on these measurements, the transition from fluttering to tumbling is nearly independent of Reynolds number and it appears at $I^* \cong 0.04$, where I^* is the dimensionless moment of inertia.

Tachikawa (1983) firstly, presented a two-dimensional equation of motion to explain the trajectories of free falling of square and rectangular plates in a uniform flow. Secondly, he obtained by experiments, the aerodynamic coefficients of autorotation in different square and rectangular flat plates, which are required for solving the equations of motion. The results show that the trajectories of a flat plate released into a flow from rest is closely related to the initial mode of motion and is distributed over a wide range.

Tanabe & Kaneko (1994) gave a phenomenological model for free fall of a paper, assuming zero thickness and incompressible ideal fluid. They discovered five different patterns of: periodic rotation, chaotic rotation, chaotic fluttering, periodic fluttering and simple perpendicular fall. Mittal, Seshadri & Udaykumar (1994) show a computational study on flow induced motion of a hinged plate pinned at its center. Their focus is on the effect of Reynolds number and plate thickness ratio and non-dimensional moment of inertia on vortex induced rotation of plates. Based on their numerical results, they suggest that the flutter and tumble frequencies of large aspect-ratio plates are governed by the Von-Kármán vortex shedding process. Anderen, Pesavento & Wang (2005) investigated the dynamics of freely falling plates experimentally, numerically and by quasi-steady modelling, at Reynolds number of 10^3 , which describes the motion of freely falling rigid plates based on detailed measurement of the plate trajectories and from this to assess the instantaneous fluid forces.

It should be mentioned that most of the previous researches on flow induced rotation, conducted experimentally and rarely numerically. In the present study, at first the flow induced rotation of a fixed axis flat plate is studied experimentally and a bifurcation diagram prepared to classify different states observed the small fluttering, fluttering and autorotation based on different Reynolds number and dimensionless moment of inertia. Then, a quasi-steady model is suggested to model the fluttering and autorotation motions via analytical modelling. Finally, a stability analysis is performed on flow induced rotation phenomenon to gain insight into the nature of transition from fluttering to autorotation.

2. HYDRODYNAMIC FORCES AND MOMENTS OF FLAT PLATE

A flat plate has a simple shape and actually is the simplest airfoil which having no thickness or shape. For small incidence angles of attack, several results were recovered for inviscid and irrotational flow such as the classical results of vortex sheet approach to calculate loads acting in flat plate. But for large incidence angles because of presence of wake behind the flat plate, it is not possible to assume that the flow is inviscid and viscous term plays an important role on the loads and moments acting on the flat plate. One of the methods used to attack the problem was Free-Streamline theory.

The main objective of this theory is to find the free streamlines to define the wake, the location of these free streamlines are initially unknown and must be found as a part of solution, outside the wake the flow is potential and to compute the resulting pressure drag.

According to the experiments, the pressure on the free streamline does tend to remain constant for some distance downstream of the separation point. The shear layers do not continue far downstream as assumed and roll up to form vortices, alternately on each side.



This vortex formation occurs behind all bluff bodies, at a frequency which is a characteristic of each body shape. The flow past a bluff body is considered in two parts (see Fig. 2). Near the body it may be described by the free-streamline theory. As mentioned before, the experiments show that, the pressure in a certain distance downstream of the separation points is approximately constant; this part of the wake will be called the near-wake and the pressure in this region is constant. Downstream regime of wake after the near-wake region, the vortices mix and diffuse rapidly and are eventually dissipated in the wake, this part of the wake will be called the far-wake, or the mixing range. Along the far-wake the mean pressure increases gradually from the wake under-pressure and finally recovers the main stream pressure far downstream.

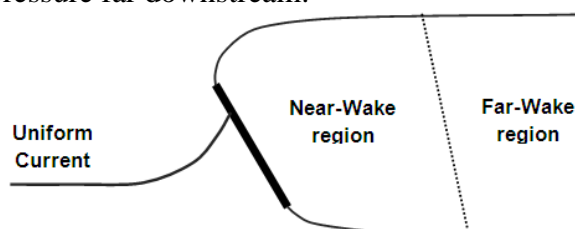


Figure 2: Schematic of free streamline theory, for flow past a flat plate.

The subject of free streamline methods has an interesting history; Kirchhoff was the first who proposed the idea of a wake bounded by free streamlines as a model for the flow behind a bluff body. He used the mathematical methods of Helmholtz to find the irrotational solution for a flat plate set normal to an oncoming stream. According to his assumption, the velocity on the free streamline at separation is equal to the free-stream velocity U . In this case, the pressure at the separation points and behind the separation points is equal to the free-stream pressure, which it is considerable loss of reality. Because this is not in agreement with experience, which shows that the pressure is actually always lower than the free-stream value. In this paper we will focus on the results of a modern view of free streamline theory by Wu & Yao-TSU (1962) to calculate the loads and moment acting on a flat plate. Wu assumed that the pressure in the near-wake region (p_c), is

uniform and constant, which leads to a dimensionless equivalent parameter of p_c , usually called the wake under-pressure coefficient (σ). This parameter characterizes the pressure of wake flow, based on free stream pressure. In fact, the different flow regimes of the fully and partially developed flows can also be indicated by different ranges of σ :

$$\sigma = \frac{P - p_c}{0.5\rho U^2} \quad (1)$$

where P denotes the pressure of the undisturbed free stream, U is its relative velocity, ρ is the fluid density. The wake flow will be called fully developed, if the region of the constant-pressure near-wake extends beyond the trailing edge of the plate and will be called partially developed, if the near-wake region terminates in front of the trailing edge. Figure 3 shows the flow in the physical space (z -plan, where $z = x + iy$).

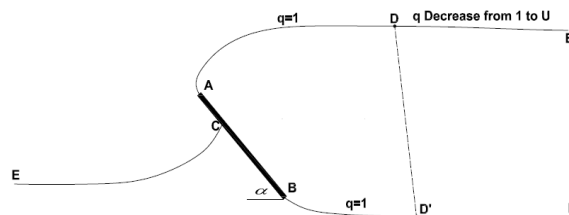


Figure 3: The flow in the physical space.

Hereby, the velocity at separation is normalized to $q=1$ and remains at this value along the free streamlines until the latter reach points D and D' . Downstream of these two points, the free streamlines keep parallel to the free stream on DE and $D'E'$ along which q decreases from unity back to the free stream value U . In order that under-pressure coefficient of the flow be σ with $q=1$ on AD and BD' , U takes the value $(1+\sigma)^{1/2}$. According to the Kirchhoff's classical result, by considering that $\alpha = \pi/2 - \theta$, the normal coefficient of flow past a flat plate ($\sigma=0$) is rewritten as below:

$$C_N = \frac{2\pi \cos \theta}{4 + \pi \cos \theta} \quad (2)$$

In the fully wake flow past a flat plate, the local pressure is everywhere normal to the plate, and there is no singular force at leading edge, therefore C_L and C_D should satisfy the condition

$$C_D/C_L = \tan \theta \quad (3)$$

In the special cases of (i) $\sigma=0$ or (ii) θ close to zero and $\sigma > 0$, the Eq. (3) condition is obviously satisfied. Each angle of attack must be assumed a different bluff body, which has a different pressure on the downstream of separation points. But in the general case, because of the complicated manner in which the dependence on θ and σ appears, the results of streamline theory show that for small angles of θ , less than 45° , the values of C_L and C_D approach respectively the asymptotes (see Wu, Yao-TSU & Wang, 1964) :

$$C_L(\sigma, \theta) = (1 + \sigma) \cdot C_L(0, \theta) \quad (4)$$

$$C_D(\sigma, \theta) = (1 + \sigma) \cdot C_D(0, \theta) \quad (5)$$

$$C_N(\sigma, \theta) = (1 + \sigma) \frac{2\pi \cos \theta}{4 + \pi \cos \theta} \quad (6)$$

This argument is supported by experimental and numerical evidences. The loads and moment coefficients were measured for a fixed flat plate, as a function of different angles of attack by experiments in a flume (22m x 1.4m x 0.5m) at the LOC-COPPE-UFRJ (Laboratory of Waves and Current of COPPE, Federal University of Rio de Janeiro). Similar measurements were carried out by the present authors with a CFD simulation using the ANSYS CFX code (Fernandes & Mirzaei Sefat, 2011, Fernandes, Mirzaei Sefat, Coelho & Ribeiro, 2010a, Fernandes, Mirzaei Sefat,

Coelho & Ribeiro, 2010b). Figure 4 shows the comparison of normal coefficient of streamline theory with $\sigma=1.25$ and experimental results of Hoerner (1965) and also Fernandes, Mirzaei Sefat, Coelho & Ribeiro (2010) numerical results.

Based on Figure 4, the streamline theory results agree very well with numerical and experimental results, especially when θ is less than 55° . This is about the range of interest for modelling the fluttering motion.

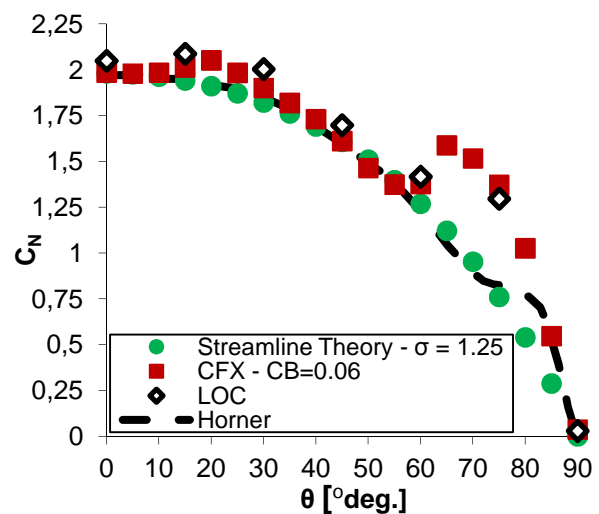


Figure 4: Comparison of normal coefficient of streamline theory with $\sigma=1.25$, and experimental results at LOC and Hoerner (1965) and also Fernandes, Mirzaei Sefat, Coelho & Ribeiro (2010) numerical results.

As we expected, because of constant pressure distribution on the downstream side of separated side of the plate, the location of centre of pressure is independent of all practical range of σ . The constant pressure in downstream side of plate cause to the center of pressure of this side of plate always is in center of plate. Hence the overall center of pressure of plate is only depending on pressure distribution of upstream side of plate. The Kirchhoff's classical formulation for the centre of pressure in term of the width is (Lamb, 1932):

$$c = \frac{3}{4} \cdot \frac{\cos \alpha}{4 + \pi \sin \alpha} b \quad (7)$$



Based on above discussion, the Kirchhoff's classical formulation for the centre of pressure (Eq. (7)) shows a good agreement with numerical results of Fernandes, Mirzaei Sefat, Colho & Ribeiro (2010) and two experimental results of Flachsbart (1932) and Tachikawa (1983) when θ is less than 55° (see Fig. 5):

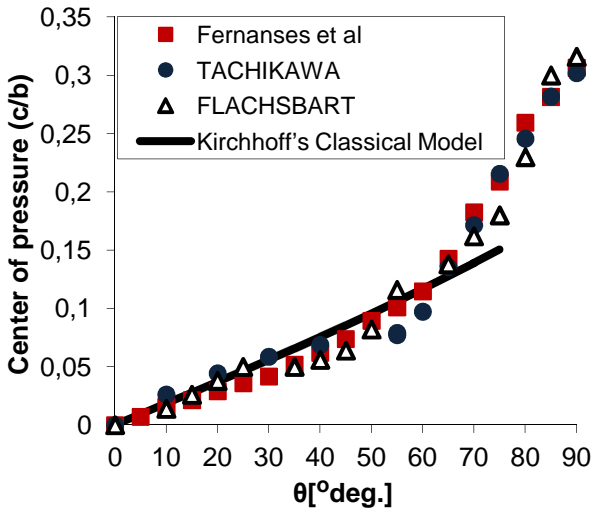


Figure 5: Comparison of position of the centre of pressure with streamline theory (Eq. (7)) and Fernandes, Mirzaei Sefat, Colho & Ribeiro (2010) and two experimental results of Flachsbart (1932) and Tachikawa (1983).

The moment coefficient could be obtained by considering of Eq. (7) for centre of pressure and Eq. (6) for normal coefficient. Hence, the moment coefficient formulation is:

$$C_M = -\frac{3}{4} \frac{\pi \sin 2\theta}{(4 + \pi \cos \theta)^2} \cdot (1 + \sigma) \quad (8)$$

As noted before, the centre of pressure position is independent of σ , and also the normal coefficient formulation of streamline theory has a good accuracy with numerical and experimental results with $\sigma=1.25$. Figure 6 shows the comparison of moment coefficient of streamline theory (Eq. (8)) with $\sigma=1.0$ and also $\sigma=1.25$ and experimental results from LOC and numerical results of Fernandes, Mirzaei Sefat, Colho & Ribeiro (2010). According to the Figure 6 the linear piecewise of streamline theory are in a good agreement with numerical and experimental results, for angles of attack smaller than 55° . This means that the

streamline theory works very well in this range; perhaps more important point of Figure 6 is that the linear behaviour that was observed by experiments in moment coefficient curve has a technical support in this large range. This surprising linear behaviour for moment coefficient which shows up for angles of attack up to 75° is called "hydrodynamic torsional spring" by Fernandes & Mirzaei Sefat (2011).

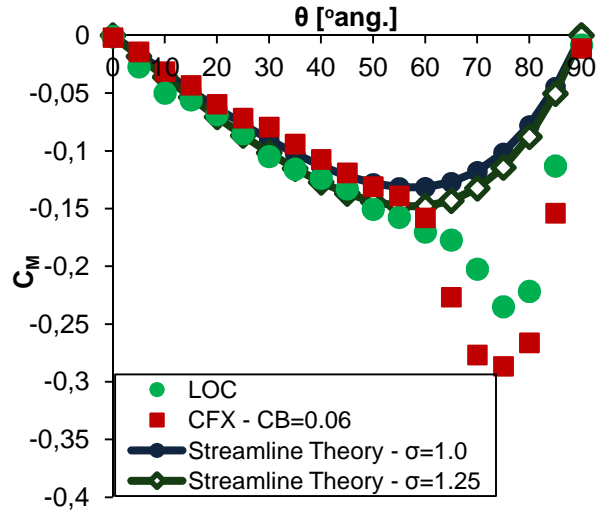


Figure 6: Comparison of moment coefficient of streamline theory (Eq. (8)) with $\sigma=1.0$ and also $\sigma=1.25$ and numerical results of Fernandes, Mirzaei Sefat, Colho & Ribeiro (2010) and experiments at LOC.

Based on the D'Alembert's paradox, the net force on a body which is subjected on an inviscid flow is zero, but not necessarily a zero moment and any shape other than a sphere generates a moment. This moment may be called Munk moment in the elongated body context. The Munk moment arises from the asymmetric location of the stagnation points, where the pressure is highest. In the front of the body there is a decelerating flow and on the back there is an accelerating flow. Letting α represent the angle of attack, the Munk moment is given by (9):

$$M_m = -\frac{1}{2} (m_{yy} - m_{xx}) U^2 \sin 2\alpha \quad (9)$$

where m_{xx} is the added mass along the body x-axis (longitudinal), and m_{yy} is along the body lateral y-axis (transversal). This moment may

be approximated for small angles of incidence. According above statements, the Munk moment coefficient for a flat plate can be express as:

$$C_M = -\left(\frac{\pi}{4}\right) \cdot \sin 2\theta \quad (10)$$

The comparison of the moment coefficient calculated by numerical modelling (Fernandes, Mirzaei Sefat, Colho & Ribeiro, 2010) and experiments at LOC and also the Munk moment coefficient given by (10) are presented in Figure 7. This comparison shows that the range of validity of Eq. (10) is just for $75^\circ \leq \theta \leq 90^\circ$, again as expected, since this is an asymptotic result.

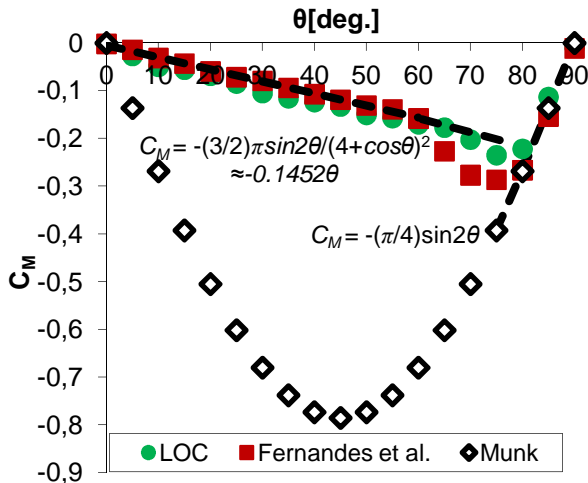


Figure 7: Moment coefficient obtained by experiments at LOC, numerical modeling (Fernandes, Mirzaei Sefat, Colho & Ribeiro, 2010) and also the Munk moment coefficient given by (10), and moment coefficient segments, proposed in Table 1.

Table 1: List of moment coefficient segments

Moment Coefficient	Angle
$C_M = -\frac{3}{2} \cdot \frac{\pi \cdot \sin 2\theta}{(4 + \pi \cos^2 \theta)}$	$0 \leq \theta \leq 75^\circ$
$C_M = -(\pi/4) \sin 2\theta$	$75^\circ < \theta \leq 90^\circ$

3. FLOW INDUCED ROTATION

With the understanding of the static behaviour in one hand, the work went on releasing the flat plate to rotate. Three different

behaviours could be devised experimentally: small fluttering state, fluttering and autorotation, several tests performed at the LOC to investigate these motions of plates with different dimensionless moment of inertia and different ranges of velocity.

In practice it was observed that when the plate was released at an angle less than stall angle (approximately $15^\circ \leq \alpha \leq 15^\circ$) and if the dimensionless moment of inertia is large enough, then the motion is affected by the large lift force and the autorotation will occur. On the other hand, if the plate releases from rest at an angular position in which the flow was stalled (approximately $75^\circ \leq \alpha \leq 75^\circ$), the plate starts to fluttering around a stable position normal to the current. Therefore, the requirements for autorotation are therefore to have a large enough moment of inertia to store sufficient angular moment and also a proper initial condition (angular position or velocity).

Based on the tests on the wind channels by pervious researchers (Field, Klaus, Moore & Nori, 1997, Flachsbart, 1932) and also the experiments in LOC, it is proved that the autorotation occurs at large dimensionless moment of inertia. But in water flume case, because of large density of water in comparison of the air one, reaching to a certain dimensionless moment of inertia the occurrence the autorotation is difficult. For this purpose, as shown in Figure 8, in order to increase the moment of inertia of plate, a bar with length of 1 meter installed on the top of plate. Also, two masses with 1 Kg weight added to system which it could be placed in different level of the bar to provide different moment of inertia.

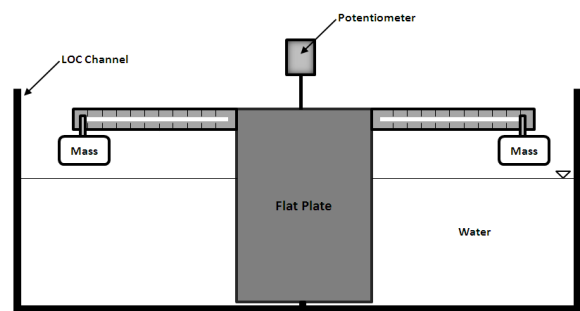


Figure 8: The experimental setup for the fluttering and/or autorotation motion.



3.1. Dimensional Analysis

In order to improve the understanding of flow induced rotation of flat plate, a dimensional analysis is performed. The flow induced rotation motion of a flat plate may be characterized by eight dimensional parameters: b the width of the plate, t the thickness of the plate, ρ_s the density of the plate, ρ_f the density of the fluid, I moment of inertia of plate, A_{66} moment of inertia of added mass, ν the kinematic viscosity of the fluid and U the uniform flow velocity, as summarized in (11):

$$\theta_R = f(b, t, \rho_s, \rho_f, I, A_{66}, \nu, U) \quad (11)$$

Applying Buckingham theorem, the dimensional analysis leads to (12):

$$\theta_R = f\{\beta, \rho^*, A_{66}^*, Re\} \quad (12)$$

where $\beta = t/b$ is the thickness ratio, $\rho^* = \rho_s / \rho_f$ the specific density of the plate, $A_{66}^* = A_{66} / I$ the dimensionless added moment of inertia, and $Re = Ub/\nu$ is Reynolds number. For comparison purpose, instead of A_{66}^* , the work will use $I^* = (128/\pi) \cdot A_{66}^*$ as used by Iversen (1979) and Field, Klaus, Moore & Nori (1997). Therefore, the flow induced rotation motion of a flat plate is governed by the Reynolds number, thickness ratio, dimensionless density and dimensionless added moment of inertia of the flat plate. It should be noted that the dimensionless moment of inertia can be rewritten as a function of dimensionless density and thickness ratio. Hence, the motion in flow induced rotation should be completely governed by dimensionless moment of inertia and Reynolds number.

3.2. Bifurcation Diagram

Based on the experiments at LOC, the bifurcation diagram of Figure 9 is presented as function of different Reynolds numbers and dimensionless moment of inertia to classify the small fluttering state, fluttering and

autorotation motions. It should be mentioned here that the small fluttering state is characterized by small oscillations in the range of $-10^\circ \leq \theta \leq 10^\circ$. Actually, it means that the small fluttering state is fluttering motion with equivalent harmonic angle less than 10° .

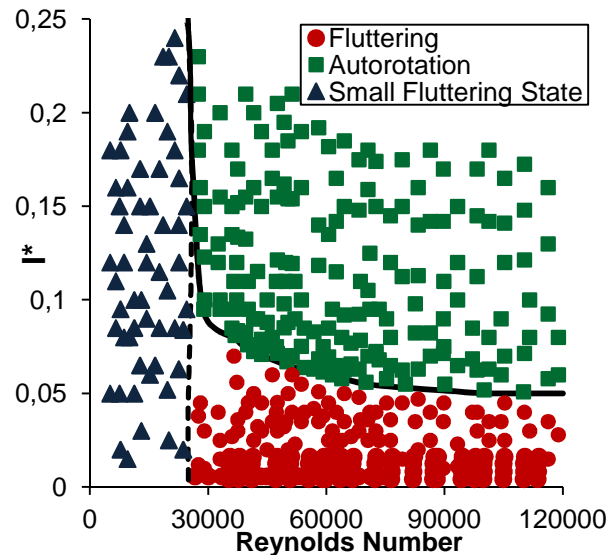


Figure 9: Bifurcation diagram to classify different motions of flow induced rotation based on Reynolds number and dimensionless moment of inertia, obtained by experiments at LOC. Each point means a different test; preliminary phase diagrams will be discussed later.

As shown in Figure 9, at low Reynolds numbers (approximately less than 2500), the plate stays almost at the same initial orientation (small fluttering state). At higher Reynolds numbers, depending on the dimensionless moment of inertia, the motion could be fluttering for smaller dimensionless moment of inertia, or autorotation (tumbling) for large dimensionless moment of inertia. Note that the transition from fluttering to autorotation is nearly independent of Reynolds number and it appears at $I^* = 0.05$ to 0.06 , which is close to the falling disc case reported by Field, Klaus, Moore & Nori (1997), ($I^* \cong 0.04$).

4. QUASI-STEADY MODELING OF AUTOROTATION

A simple linear model for the flow induced rotation of a flat plate in a uniform current which has only one degree of freedom is suggested by applying the angular momentum theorem:

$$(1 + A_{66})\ddot{\theta} = \frac{1}{2}\rho_f C_M S b U^2 \quad (13)$$

By incorporating dimensionless variables $\hat{I} = I/A_{66}$ and $t^* = t \cdot (U/b)$, the equation of motion become:

$$(1 + \hat{I}) \frac{d^2\theta}{dt^{*2}} = \left(\frac{64}{\pi}\right) \cdot C_M \quad (14)$$

This equation can be solved numerically using Runge-Kutta fourth order method. The normal force coefficient and centre of pressure positions obtained for static plates at various angles of attack can be used to obtain moment coefficients in the above equation (Table 2). The numerical calculations were made to compare with the experimental trajectories for autorotation motion recorded at LOC. With the moment coefficient proposed from the experimental results of LOC, the obtained equations of motion are shown at Table 2:

Table 2: Equations of motion based on moment coefficient proposed by experimental results of LOC.

Equation of Motion	Angle
$(1 + \hat{I}) \frac{d^2\theta}{dt^{*2}} + \left(\frac{64}{\pi}\right) \cdot \left(\frac{3}{2}\right) \cdot \frac{\pi \cdot \sin 2\theta}{(4 + \pi \cos \theta)^2} = 0$	$0 \leq \theta \leq 75^\circ$
$(1 + \hat{I}) \frac{d^2\theta}{dt^{*2}} + \left(\frac{64}{\pi}\right) \cdot \left(\frac{\pi}{4}\right) \sin 2\theta = 0$	$75^\circ < \theta \leq 90^\circ$

Figures 10 and 11 show the comparison of the autorotation trajectories recorded by experiments at LOC and the numerical simulation based on the equations of motion of Table 2. The Reynolds Number was kept around 9.95×10^4 . The initial angular position in all Figures is $\theta_0 = 90^\circ$ ($= \alpha_0 = 0^\circ$).

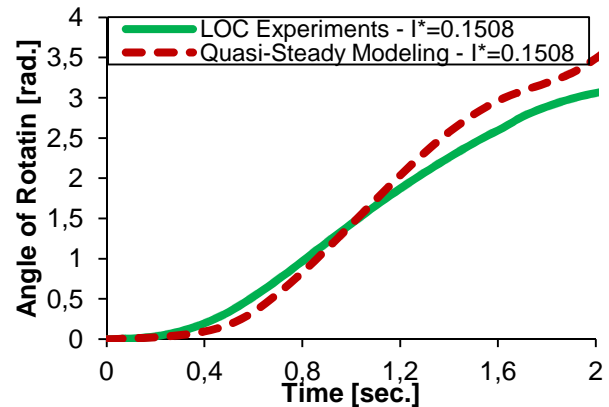


Figure 10: The autorotation motion of plate with $I^* = 0.1508$ and $Re = 9.95 \times 10^4$.

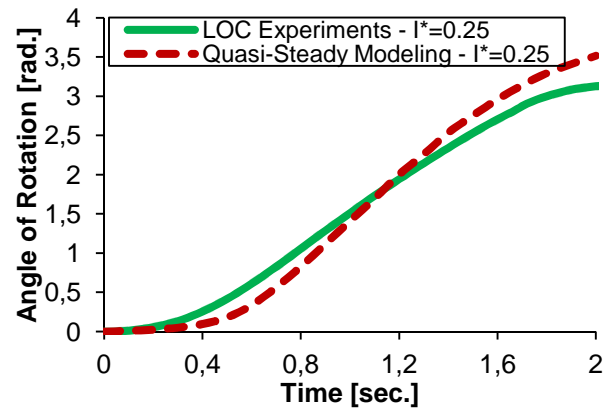


Figure 11: The autorotation motion of plate with $I^* = 0.25$ and $Re = 9.95 \times 10^4$.

As we expected, the numerical modeling simulation of autorotation motion based on LOC moment coefficient model has a good agreement with experiments.

5. STABILITY ANALYSIS OF FLOW INDUCED ROTATION

To gain future insight into the nature of transition between fluttering and autorotation, we considered a phenomenological model of the flow induced rotation of a flat plate hinged at center. The aim of this section is to do a simple stability analysis on the dynamic model of flow induced rotation phenomenon. The fixed points for differential equation models of motion are $(\theta, \dot{\theta}) = (n\pi/2, 0)$, $n = 0, \pm 1, \pm 2, \dots, \pm\infty$. For linearization of equations of motion of Table 2, to obtain a system of ODEs, we set $\theta = y_1$, $\dot{\theta} = y_2$ and also considering the Maclaurin series. Based on



stability analysis on the linearized equations in the neighborhood of the fixed points, we can express that, when $n = 0, \pm 2, \pm 4, \dots$ the critical points are all *Centers*, and on the other hand the critical points with odd value of n are all *Saddle* points. The conservative energy system for differential equation model of flow induced rotation motion is presented in Table 3.

Figure 12 shows trajectories for various values of E and based on equations of motion of table 3. These graphs continue periodically with period π to the left and right. We can see some of the trajectories are ellipse-like and closed (fluttering motion) and some other are wavy (autorotation motion). By considering of Table 3, at point: $y_2 = 0$, we get (15):

$$-\frac{\pi \cdot M^*}{8(1 + A_{66}^*)} \cos 2\theta = c \quad (15)$$

If $\theta = y_1 = \pi/2$, then $E = C$, where $E = -(1/8) \cdot (M^*/(1 + A_{66}^*))$. Hence, if $-C < E < C$, then plates reverse its direction for a $|y_1| = |\theta| < \pi/2$, and these values of E with $|E| < C$ the plate oscillates. This corresponds to the closed trajectories in the figure (fluttering). However, if $E > C$ then $y_2 = 0$ is impossible and the plate makes a whirly motion that appears as wavy trajectories in the phase diagram (autorotation). Finally, the value $E = C$ corresponds to the two “separating trajectories” in Figure 12 connecting the saddle points.

Table 3: The conservative energy system for differential equation model.

The Conservative Energy System
$(1 + A_{66}^*) \ddot{\theta} \cdot \dot{\theta} + (\pi/4) \cdot M^* \sin 2\theta \cdot \dot{\theta} = 0 \Rightarrow$
$\frac{d}{dt} \left[\frac{1}{2} \dot{\theta}^2 - \frac{\pi \cdot M^*}{8(1 + A_{66}^*)} \cos 2\theta \right] = 0$
$\frac{1}{2} \dot{\theta}^2 - \frac{\pi \cdot M^*}{8(1 + A_{66}^*)} \cos 2\theta = E$

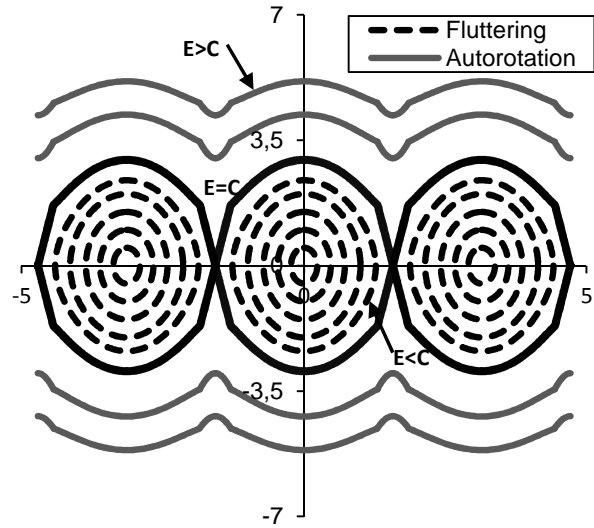


Figure 12: The phase diagram for various values of E and based on equations of motion of table 1.

According to the Figure 12, the value of the separation energy level from fluttering to autorotation is $C \cong 2.95$.

CONCLUSIONS

The free streamline theory is applied to approximate the fully developed wake far downstream. The normal and moment coefficient formulations have been suggested by considering streamline theory for different angles of attack, which these formulations have a good accuracy with experimental and numerical results.

The dimensional analysis proves that the motion in flow induced rotation and in particular, the transition from fluttering to autorotation, should be completely governed by dimensionless moment of inertia (I^*) and Reynolds number (Re). The steady state motion occurs at Reynolds numbers less than 25000, which the plate stays at the same initial orientation. For larger Reynolds numbers, the transition from fluttering to autorotation is nearly independent to Reynolds number and it appears at $I^* = 0.05$ to 0.06 .

The stability analysis was performed on flow induced rotation phenomenon to gain more insight into the nature of transition



between fluttering and autorotation. The system looks conservative. The amount of energy treasure that separates the fluttering from autorotation is identified.

ACKNOWLEDGMENTS

The authors express their thanks to CNPq (Brazilian National Research Council), ANP (Brazilian National Petroleum Agency) and LOC/COPPE/UFRJ (Laboratory of Waves and Current of COPPE, Federal University of Rio de Janeiro).

REFERENCES

- Andersen, V., Pesavento, U., and Wang, Z. J., 2005, "Analysis of transitions between fluttering, tumbling and steady descent of falling cards", Journal of Fluid Mechanics, Vol. 541, pp. 91–104.
- Dupleich, P., 1941, "Rotation in Free Fall of Rectangular Wings of Elongated Shape", NACA Technical Memo, pp. 1201, 1-99.
- Fernandes, A. C. and Mirzaei Sefat, S., 2011, "Fluttering and Autorotation of a vertical Flat Plate about a Fixed Axis Submitted to a Uniform Horizontal Flow" Proceedings of the IUTAM Symposium on Bluff Body Flows, December 12-16, 2011, IIT Kanpur, India.
- Fernandes, A. C. and Mirzaei Sefat, S., 2011, "The Hydrodynamic Torsional Spring in the Flow Induced Fluttering of a Hinged Vertical Flat Plate", Submitted for the Journal of Ocean Engineering.
- Fernandes, A. C., Mirzaei Sefat, S., Coelho, F. M., and Albuquerque, A. S., 2011, "Experimental Investigation of Flow Induced Rotation of Hinged Plates with Different Bluffness in Uniform Flow", Proceedings of the 30th International Conference on Ocean, Offshore and Arctic Engineering - OMAE 2011, June 19-24, 2011, Rotterdam, Netherland.
- Fernandes, A. C., Mirzaei Sefat, S., Coelho, F. M., and Ribeiro, M., 2010, "Investigation of the Flow Induced Small Amplitude Rotation Triggering Flat Plate Fluttering", Proceedings of the 6th IUTAM Symposium on Bluff Body Wakes and Vortex-Induced Vibrations, Capri Island, Italy.
- Fernandes, A. C., Mirzaei Sefat, S., Coelho, F. M., and Ribeiro, M., 2010, "Towards the understanding of Manifold Fluttering during Pendulous Installation: Induced Rotation of Flat Plates in Uniform Flow", Proceedings of the 29th International Conference on Ocean, Offshore and Arctic Engineering, OMAE2010, Shanghai, China.
- Fernandes, A. C., Sales JR, J.S., and Neves, C. R., 2007, "Development of the Pendulous Installation Method for Deploying Heavy Devices in Deep Water by Using Model Testing Concomitantly with Numeric Code", Submitted for publication in the Journal of Offshore Mechanic and Arctic Engineering.
- Fernandes, A. C., Sales JR, J.S., and Neves, C. R., 2007, "The Concomitant Model Testing Approach for the Development of the Pendulous Installation Method of Heavy Devices in Deep Water", Proceedings of the 26th International Conference on Ocean, Offshore and Arctic Engineering - OMAE 2007, San Diego, USA.
- Field, S. B., Klaus, M., Moore, M. G., and Nori, F., 1997, "Chaotic dynamics of falling disks", Nature, Vol. 388, pp. 252-254.
- Flachsbart, O., 1932, "Messungen an ebenen und gewolbten Platten", Ergebnisse der AVA, IV.
- Hoerner, S. F., 1965, "Fluid-Dynamic Drag", Published by Author, New York, US.



- Holmes, JD, Letchford, CW, and Ning Lin., 2006, "Investigations of plate-type windborne debris—Part II: Computed trajectories", Journal of Wind Engineering and Industrial Aerodynamics, Vol. 94, pp. 21–39, 2006.
- Iversen, J. D., 1979, "Autorotating flat-plate wings: the effect of the moment of inertia, geometry and Reynolds number", Journal of Fluid Mechanics, Vol. 92, pp. 327-48.
- Lamb, S. H., 1932, "Hydrodynamics", Cambridge University Press, 6th ed, USA.
- Lugt, H. J., 1983, "Autorotation", Annual Review of Fluid Mechanics, Vol. 15, pp. 123-147.
- Maxwell, J. C., 1854, "On a particular case of the descent of a heavy body in a resisting medium", Journal of Cambridge and Dublin Math, Vol. 9, pp. 145-148.
- Mirzaei Sefat. S. and Fernandes, A. C., 2011, "Flow Induced Rotation of a Flat Plate Subjected in Uniform Current Based on the Streamline Theory", Proceedings of the 30th International Conference on Ocean, Offshore and Arctic Engineering - OMAE 2011, June 19-24, 2011, Rotterdam, Netherland.
- Mittal, R., Seshadri, V., and Udaykumar, H. S., 2004, "Flutter, Tumble and Vortex Induced Autorotation", Journal of Theoretical and Computational Fluid Dynamics, Vol. 17(3), pp. 165-170.
- Tachikawa, M., 1981, "Trajectories and velocities of typhoon-generated missiles, Part I, Aerodynamic characteristics of flat plates and equations of motion", Journal of Architectural Institute of Japan, Vol. 314, pp. 1–10.
- Tachikawa, M., 1983, "Trajectories of flat plates in uniform flow with application to wind-generated missiles", Journal of Wind Engineering and Industrial Aerodynamics, Vol. 14(1-3), pp. 443-453.
- Tanabe, Y. and Kaneko, K., 1994, "Behavior of a falling paper", Journal of Physical Review Letters, Vol. 73(10), pp. 1372-1375.
- Roshko, A., 1953, "On the development of turbulent wakes from vortex streets" NACA, Technical Note: 2913, USA.
- Roshko, A., 1954, "Hodograph for Free-Streamline Theory", NACA, Technical Note: 3168, USA.
- Roshko, A., 1954, "On the drag and shedding frequency of two-dimensional bluff bodies", NACA, Technical Note: 3169, USA.
- Wu, T., 1956, "A free streamline theory for two-dimensional fully cavitated hydrofoils", Journal of Mathematical Physics, Vol. 35, pp. 236-265.
- Wu, T. and Yao-TSU., 1962, "A Wake Model for Free-Streamline Flow Theory Part I. Fully and Partially Developed Wake Flows and Cavity Flows past an Oblique Flat Plate", Journal of Fluid Mechanics, Vol. 13(2), pp. 161-181.
- Wu, T., Yao-TSU., and Wang, D. P., 1964, "A wake model for free-streamline flow theory. Part 2. Cavity flows past obstacles of arbitrary profile", Journal of Fluid Mechanics, Vol. 18(1), pp. 65-93.



Effectiveness of Chaotic System Measures for the Validation of Ship Dynamics Simulations

Michele D Cooper, *Virginia Tech*, mdcarter@vt.edu

Leigh S McCue, *Virginia Tech*, mccue@vt.edu

ABSTRACT

The subject of verification and validation of ship motion models has become a particularly heavily studied topic in recent years, even warranting a dedicated workshop on verification and validation of seakeeping tools (Kim, 2010). The Virginia Tech ship dynamics group has focused largely on the use of quantitative chaotic system metrics for the validation of simulations of chaotic systems, including ship capsize simulations (McCue *et al.*, 2008, 2009; Story, 2009; Story *et al.*, 2010); this philosophy was also commented on by Reed (2009). The purpose of the current study is to provide further examination of the usefulness of several such metrics for both canonical systems as well as for the ship dynamics model derived by Soliman and Thompson (1991). The results presented show good agreement between bifurcation analysis and changes in the system behavior, suggesting that such metrics are effective validation metrics.

Keywords: *chaotic time series, validation, bifurcation analysis*

1 INTRODUCTION

Over the past few decades, the use of simulations has grown to the point where it has been referred to as the “third pillar” of science along with theory and experiments (Oberkampf and Roy 2010); this is particularly true in the ship dynamics community since experiments are difficult and costly to perform. Simulations provide a more manageable outlet to explore different scenarios which a ship might encounter. With these simulations comes the necessity of ensuring that such simulation is performed accurately, which is done through the processes of verification and validation. The main focus for the current study is on validation. For purposes of this work, the authors adopt the definition provided in the current version of the DoD Modeling and

Simulation (M&S) Instruction (2009), which states:

“[Validation is] the process of determining the degree to which a model or simulation and its associated data are an accurate representation of the real world from the perspective of the intended uses of the model.”

Validation has become well defined in field based simulations like Computational Fluid Dynamics (AIAA, 1998) and computational solid mechanics (ASME, 2006). For further readings see texts by Oberkampf and Roy (2010) and Roache (1998) as well as the DoD (2009) and DoN (1999) instructions. To say that one has validated a field based simulation has specific meaning due to well-defined methodologies in the above referenced manuscripts. In general, this is not the case



with chaotic dynamic systems. Historically, visual inspection and later, statistical metrics were the primary means of validating simulation tools. These methods, while useful, leave room for improvement, especially when considering the nature of chaotic time series and their sensitivity to initial conditions. Yee *et al.* (1994, 1996, 1997a, 1997b) applied nonlinear dynamics theories to computational fluid mechanics, and in a philosophically similar manner, Wu *et al.* (2011) applied computational fluid mechanics research to code verification for chaotic systems. This paper seeks to continue these past efforts towards improved validation tools drawing off expertise provided in the time series analysis and computational fluid dynamics research spheres.

The principle behind the use of chaotic systems measures is that they provide a quantitative metric that gives an indication into the underlying governing physics of the system. For example, while comparing capsizes versus non-capsizes for a given simulation/experiment pair may yield a false sense of security/insecurity as it is a binary metric; if the simulation and experiment have similar Lyapunov exponents or entropy or correlation dimension, one might be able to conclude both systems capture the same fundamental physics.

In recent years, several groups have started to utilize metrics that have physical significance as validation tools (Bulian, 2005; McCue *et al.* 2006; McCue *et al.* 2008; Reed, 2009). The work thus far is a positive step forward but there is a need to more fully characterize the capabilities of these physically based metrics, since previous works have primarily focused on using these metrics rather than understanding their role as a validation metric. In comparison to the usual approaches, these physically based metrics could serve to give more insight to the behavior of the system as well as potentially providing insight to why results may not match.

The current work will suggest several such metrics and provide a basic support for their use as a validation tool. Each metric is applied to two different well-known systems in order to aid in understanding the metric behavior. In addition, the metric results are evaluated using bifurcation analysis, which provides a coarse measure of the efficacy of the metrics. These steps provide an initial platform from which to continue the study of these metrics as a validation tool.

2 METHODS

2.1 Dynamical Systems

Two different dynamical systems were used to test the metrics described in the next section. The first system, the Lorenz attractor, is a generic chaotic system, while the second system is a classic ship capsizes model developed by Soliman and Thompson (Soliman and Thompson 1991). Both systems provide an excellent environment to test the following metrics due to their well characterized and understood behavior. The corresponding equations for each system can be seen in Table 1 along with the parameter values that were swept for each parameter. For both systems, 20 randomly generated initial conditions were used; the selection of the initial conditions was bounded roughly according to the size of the attractor for Lorenz, and just large enough to include variations but small enough to still generate stable trajectories for the Soliman and Thompson model (Soliman and Thompson 1991). The Lorenz system simulations included a general sweep of parameters centered around the commonly referenced parameter values for the system (Lorenz – $\sigma=10$, $\beta=8/3$, $r=28$). For the Lorenz attractor, thirty evenly spaced parameter values within this range were run for each randomly generated initial condition. The Soliman and Thompson model was run with forty points within the range to increase resolution of the results.

The use of Lyapunov exponents for validation has been well covered in existing literature (McCue *et al*, 2006, 2008; Story, 2009) and as such will not be included here in the interest of brevity.

2.2 Metrics

Correlation Dimension. The Correlation dimension is commonly referred to as a type of fractal dimension and serves as a measure of the dimensionality of the space occupied by a set of points (Grassberger and Procaccia, 1983). The correlation dimension of a system can be calculated by:

$$C(\varepsilon) = \lim_{N \rightarrow \infty} \frac{g}{N^2} \sim \varepsilon^v \quad (1)$$

where $C(\varepsilon)$ is the correlation integral, g is the total number of pairs of points with a distance less than ε , N is the total number of points, and v is the correlation dimension.

Sample Entropy. Entropy is the measure of disorder or unpredictability of a given system. Note in this case entropy refers to information entropy rather than thermodynamic entropy. Sample entropy is a specific type of information entropy that is used for this work, the particular method of calculation used is defined by Lake *et al* (2002), who provided the code used in this study

(<http://physionet.incor.usp.br/physiotools/sampen/>). Sample entropy can be calculated by finding sets of n points that are within some distance r of each other, with sample entropy being defined as the negative logarithm of the probability that the $n+1$ point is within the set distance r , so that:

$$S(\varepsilon, N) = -\log\left(p\left(x_N \in \varepsilon \mid x_{1, \dots, N-1} \in \varepsilon\right)\right) \quad (2)$$

Proper Orthogonal Decomposition (POD). Partial orthogonal decomposition, also known as principal components analysis or the Karhunen-Loeve transform, transforms a set of correlated variables into a set of linearly independent variables so that the original data can be represented as:

$$\vec{x}_i = \sum_{k=1}^N \lambda_{ik} \vec{v}_k \quad (3)$$

where x represents the vector data points, v represents linearly independent modes, and λ represents projection coefficients weighting each mode to obtain a given data point. POD is unique in that the vectors v are chosen in such a way so that each successive mode accounts for the largest possible variance (Pearson, 1901). Thus, POD gives a simplified view of the data set which contains as much of the energy as possible. This is demonstrated graphically in Figure 1.

Table 1: Systems studied.

System	Equations	Parameters
Lorenz Attractor	$\frac{dx}{dt} = \sigma(y - x)$ $\frac{dy}{dt} = x(r - z) - y$ $\frac{dz}{dt} = xy - \beta z$	$\sigma(0-20)$ $r(14-42)$ $\beta\left(0-\frac{16}{3}\right)$
Soliman & Thompson Ship Capsize Model	$\ddot{\theta} + b_1 \dot{\theta} + b_2 \dot{\theta} \dot{\theta} + c_1 \theta + c_2 \theta \theta + c_3 \theta^3$ $\dots + c_4 \theta \theta^3 + c_5 \theta^5 = \frac{M(t)}{I} + \frac{W_M}{I}$	$\omega = 0.7, H(0.15-0.5)$ $\omega = 0.75, H(0.15-0.5)$ $\omega = 0.8, H(0.15-0.5)$



For the purposes of this paper, trajectories were compared by taking the dot product of their most energetic modes, as calculated by POD. Trajectories on identical attractors should have identical first modes, and hence would have a validation score of 1, with more distant trajectories having lower scores.

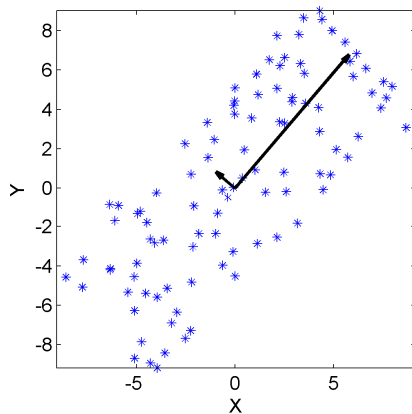


Figure 1: Example of proper orthogonal decomposition. The blue points represent scattered data, while the black arrows represent the first and second modes (with the longer arrow corresponding to the first mode). Note how the first mode is aligned with the largest “spread” of the data.

It should be noted that many of these approaches have already been discussed with application to experimental data in the literature; see, for example, McCue *et al* (2008) which uses recurrence plots, correlation integral, correlation dimension, Poincare sampling, and attractor reconstruction as qualitative and quantitative metrics for comparing numerical simulations to experimental data. The purpose of the present

paper is more fundamental and in line with the bifurcation study for Lyapunov exponents presented in Story *et al* (2009, 2010). Specifically, the authors seek to demonstrate that the quantitative metrics used in this paper correlate to results of bifurcation analysis to determine if the metrics indeed capture changes in fundamental physical behavior. These metrics were tested by introducing known errors to the system in order to determine each metric’s sensitivity to different types of modeling errors for the purpose of simulating experimental data. Viewing these results in light of comparison to similar perturbation studies, along the lines of Story (2009), allow determination as to if the metric, computationally far more efficient and feasible for a limited data set than bifurcation analysis, is an effective quantifiable validation measure.

3 RESULTS & DISCUSSION

As previously mentioned, the metrics laid out in the prior section were tested on two different systems, the Lorenz attractor and the Soliman and Thompson capsizing model.

3.1 Lorenz Attractor

Each parameter was varied in this system according to the methods describe in Section 2.1. The results of each parameter variation (σ , r , β) are presented in a single figure for each metric tested. In each figure there are the results with error bars of \pm one standard deviation at each data point, as well as vertical lines that represents a given bifurcation point. The bifurcation values were obtained from Story (2009).

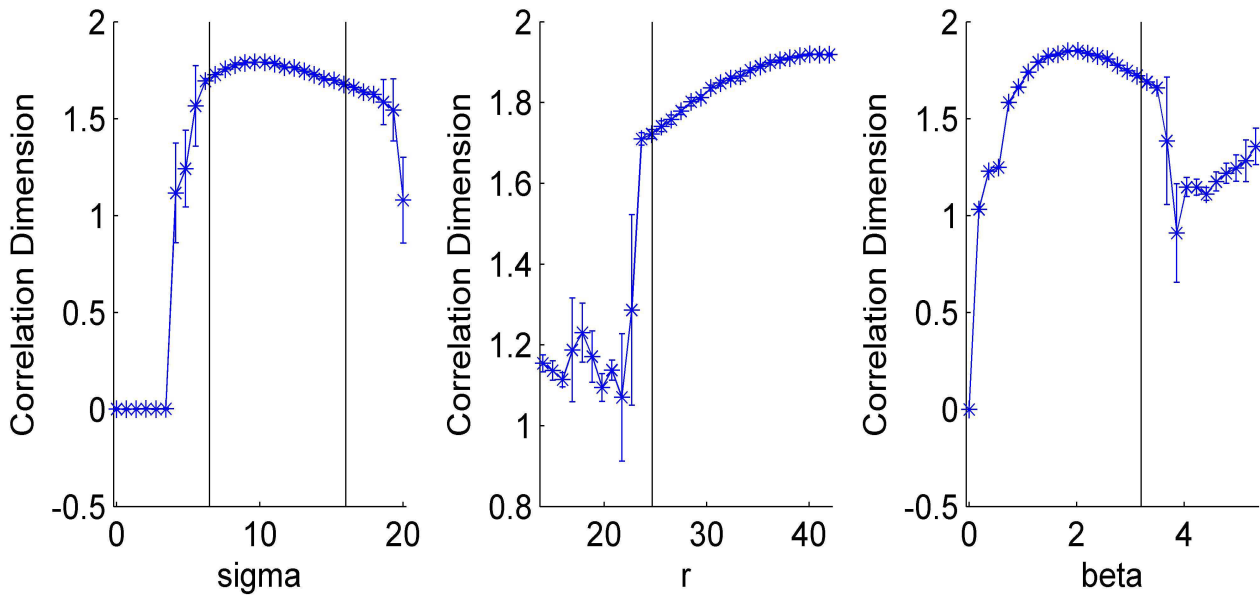


Figure 2: Parameter sweep for correlation dimension (Lorenz).

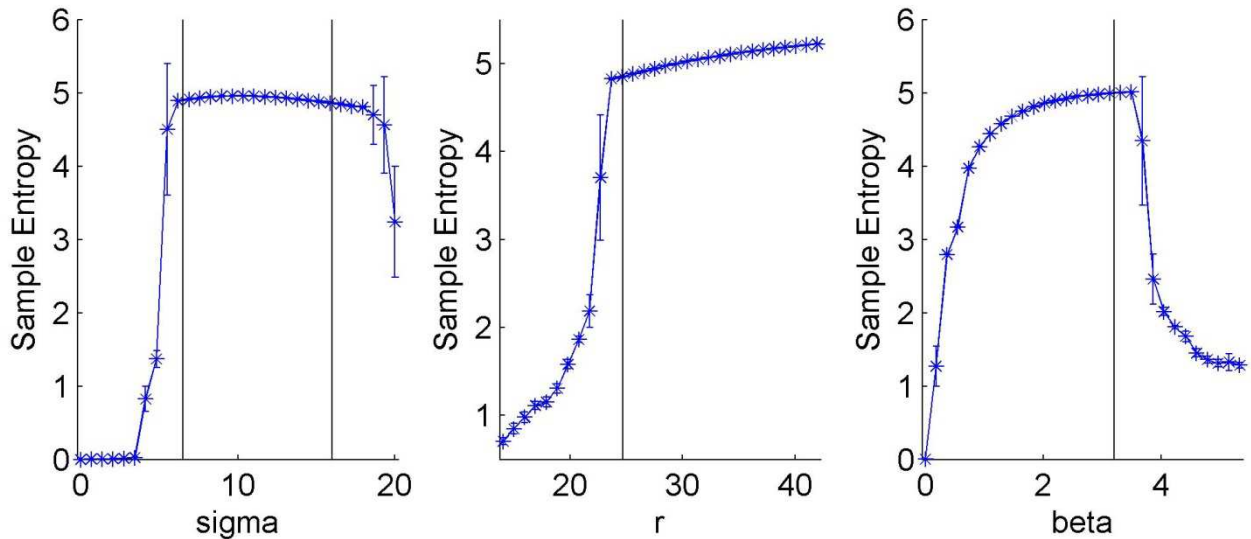


Figure 3: Parameter sweep for sample entropy (Lorenz).

Correlation Dimension. The results for correlation dimension can be seen in Figure 2. For each of the parameter variations there appears to be a relatively close correlation between trend changes in the correlation dimension value and the bifurcations. Another point of interest is that this metric is fairly robust, with respect to initial conditions, as indicated by the small error bars seen in all three parameter variations particularly when distant from a bifurcation. In Figure 2, for small values of σ , correlation dimension

values are also very small, which is due to the fact that the trajectories quickly tend towards the fixed point, which represents a 0-D geometry. As the attractor shape becomes more defined, with increasing σ values, the correlation dimension increases as well. Similar behavior can be seen in the r value changes as well, but the difference is that for small values of r , the correlation dimension is larger than the values for σ because the trajectories do not move as quickly to the fixed point. In addition, the β variations develop similarly to the r variations except

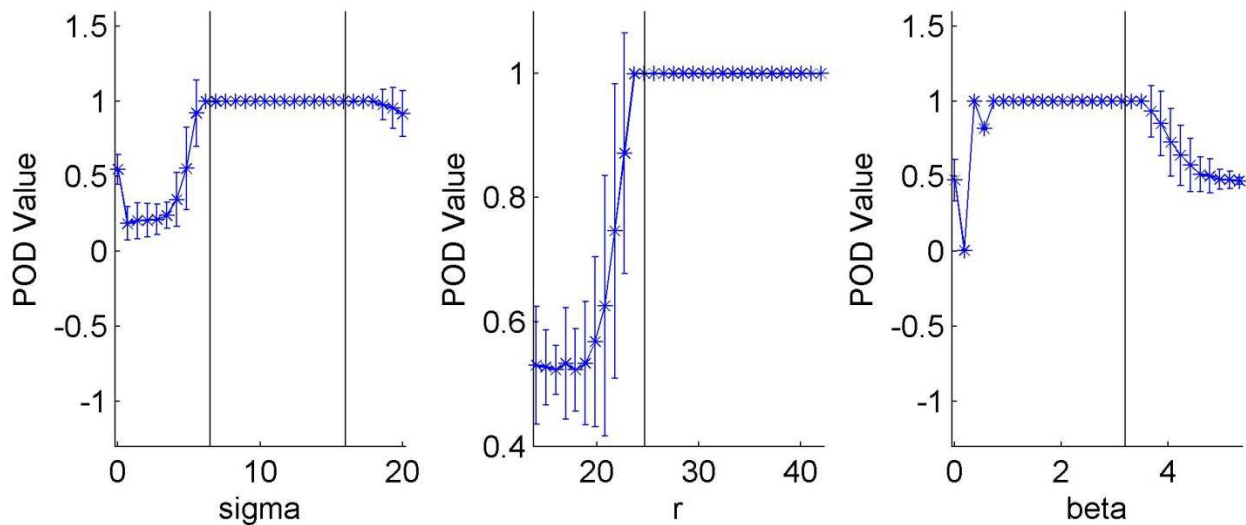


Figure 4: Parameter sweep for POD (Lorenz).

that the attractor becomes fully developed more quickly, as seen by the quickly rising correlation dimension values.

Sample Entropy. The sample entropy results for the Lorenz attractor are shown in Figure 3. These results are quite similar to the correlation dimension results shown in Figure 2. As with the correlation dimensions results, the sample entropy results show trend changes in relatively close proximity to the bifurcations, indicating that this method does correlate to changes in shape/behavior of the attractor. In addition, the error bars are very small for all three parameter variations, indicating this method is robust to initial conditions. Also, small sample entropy values can be seen for small values of σ , which is a similar behavior to that observed with correlation dimension. The same trends can be seen in the r and β variations for sample entropy as well.

POD. The results for the POD metric can be seen in Figure 4. The authors note the error bars are larger with this metric than with the other metrics. For the σ and r variations, the

error bars appear before the bifurcation, which means that there is a larger standard deviation in the results before the attractor is fully developed. This is opposite the behavior observed with β variations; in this case the attractor develops quickly and starts to degrade after the bifurcation, which is where the larger error bars appear. In general the results tend to change near the bifurcation, slightly trending up or down in the cases of σ and β and more sharply with the r variation.

3.2 Soliman & Thompson Model

For the Soliman and Thompson model, the parameter ω , which is the ratio of the forcing frequency to the linear natural frequency, was given three different values, 0.7, 0.75, and 0.8 while the wave height parameter, H , was varied from 0.15 to 0.5. Corresponding figures are presented in the same manner as described in Section 3.1 for the Lorenz attractor. The model was run with the *Gaul* parameter values and the bifurcation values were taken from Table 1 in Soliman and Thompson (1991).

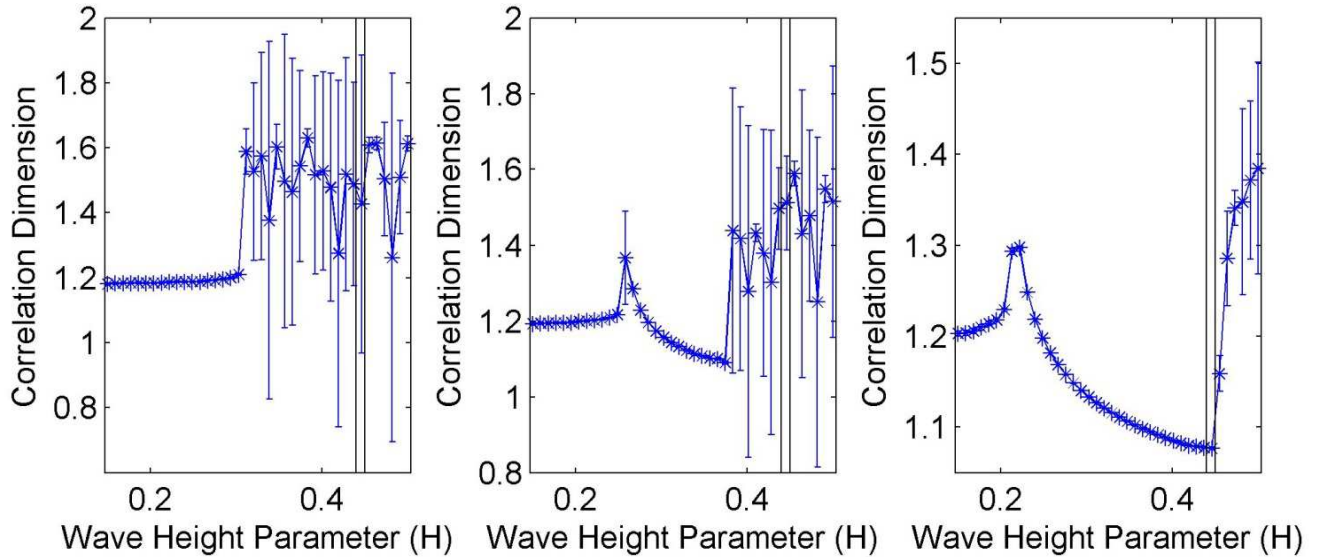


Figure 5: Parameter sweep on H for $\omega=0.7$ (left), 0.75 (middle), and 0.8 (right) for correlation dimension (S&T Model).

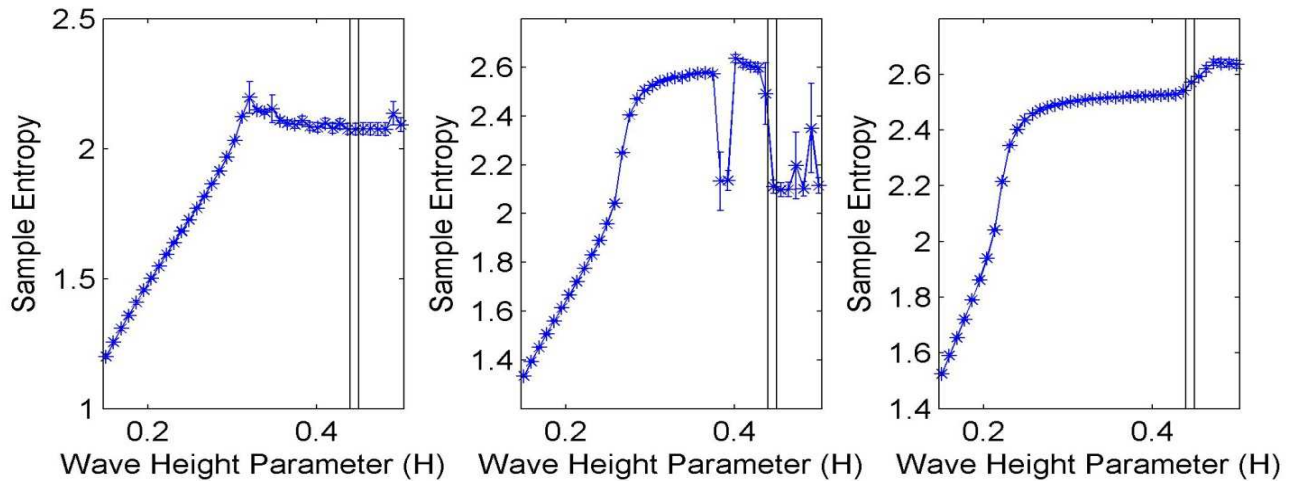


Figure 6: Parameter sweep on H for $\omega=0.7$ (left), 0.75 (middle), and 0.8 (right) for sample entropy (S&T Model).

Correlation Dimension. The results for correlation dimension are shown in Figure 5. It is immediately apparent that there are definite and clear changes in behavior near the bifurcations for all values of ω . Other changes of note are the slight to a sometimes large jump in correlation dimension value and that after the bifurcation the error bars become quite large. The large error bars occur due to the nature of this model, prior to the bifurcation the trajectories are stable, rotating around a fixed point, whereas after the bifurcation the trajectories branch off toward infinity, physically representing capsizing. The correlation dimension is very sensitive to the amount of time spent populating the defined

phase space prior to diverging to infinity and therefore results in a larger spread of data (i.e. higher standard deviation and larger error bars). For the first case, $\omega=0.7$, until the wave height parameter, H, gets to approximately 0.3, the correlation dimension is relatively stable at a value of 1.2, but after the bifurcation the values change drastically due to this phase space sensitivity. The same trend is seen in the second case, $\omega=0.75$, with the exception that there is a small peak in the data around $H=0.26$, which occurs due to a slight growth in the size of the attractor, which then decreases in size slightly as it approaches the bifurcation. The third case, $\omega=0.8$, is very much the same as with the second case, with a slight peak occurring around $H=0.22$.

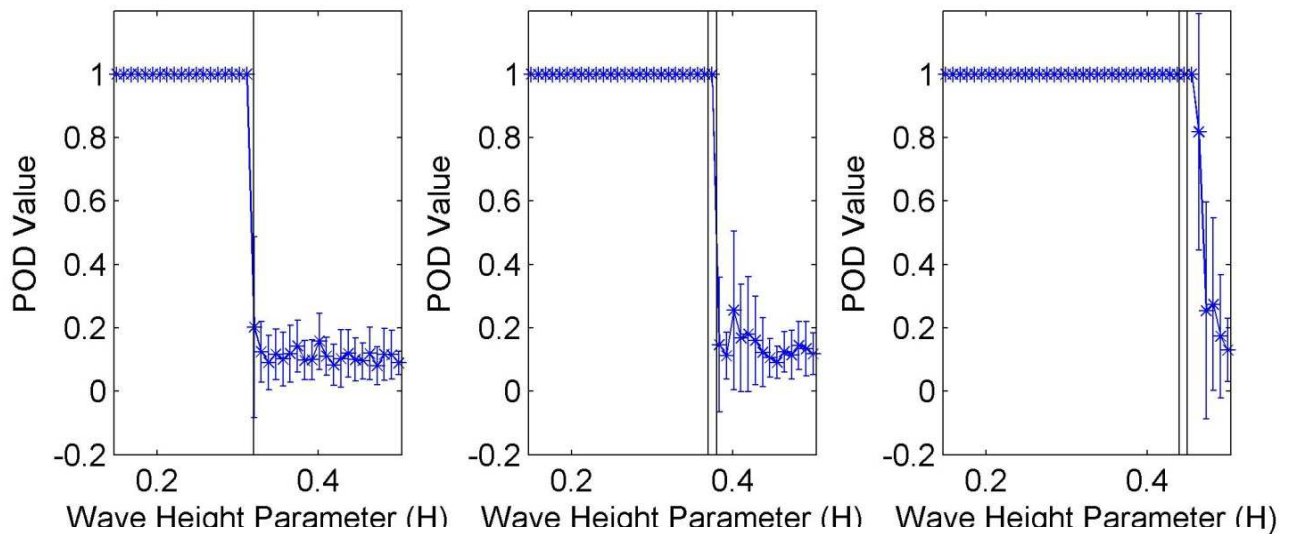


Figure 7: Parameter sweep on H for $\omega=0.7$ (left), 0.75 (middle), and 0.8 (right) for POD (S&T Model).

Sample Entropy. Figure 6 shows the results for Sample Entropy; the primary similarity between the three ω values is that the error bars are very small after the bifurcation and very small prior to bifurcation. For the first case ($\omega=0.7$), there is a gradual upward trend towards the bifurcation, where the results plateau. The second case ($\omega=0.75$) is different because there is a slight drop in the sample entropy value around the bifurcations, but this value increases almost immediately after the bifurcation then decreases again to a plateau. These changes track very well with the changes in the space that the attractor occupies, which corresponds well to what entropy physically represents: a measure of disorder of a system. For the last case ($\omega=0.8$), there is a gradual upward trend in value overall but no clear change in behavior around the bifurcations.

POD. The POD results in Figure 7 show strong changes near the bifurcation for all three values of ω . This occurs because the limit cycle dominates the first mode for all parameter values before the bifurcation. After the bifurcation, however, the escape trajectory dominates the first mode. This accounts both for the changes in the first mode as well as the large increase in variability observed after the bifurcation, as the trajectories escape towards infinity in a variety of directions.

4 CONCLUSIONS

In this work, physically based measures of the properties of chaotic systems have been shown to be effective in detecting changes in system behavior. This suggests that these tools would be quite useful for validation of chaotic time series simulations. There are two branches of future work which can arise from the current study. First, it should be recognized that the methods tested in the current study represent only a small sampling of the metrics available for characterizing chaotic time series. Future works should investigate the usefulness of other measurements, in the hope of finding a suite of effective metrics.

In addition, future studies should examine the ability of different metrics to detect different kinds of introduced errors in systems. It is hypothesized that different metrics will exhibit different sensitivities to different types of modeling errors furthering the notion of a suite approach to chaotic simulation validation, wherein a multitude of different qualitative and quantitative measures, including many currently in practice, are used to compare experimental models to simulation.



5 ACKNOWLEDGEMENTS

The authors are tremendously grateful to the sponsors who supported this work, specifically, Dr. Pat Purtell at the Office of Naval Research under grant numbers ONR N00014-08-1-0695 and N00014-10-1-0398 and Dr. Eduardo Misawa at the National Science Foundation under grant CMMI 0747973.

6 REFERENCES

- AIAA, 1998 (January), "Guide for the Verification and Validation of Computational Fluid Dynamics Simulations", American Institute of Aeronautics and Astronautics, Reston, VA. G-077-1998.
- ASME Performance Test Code Committee 60. 2006, "Guide for verification and validation in computational solid mechanics", American Society of Mechanical Engineers, New York, NY. ASME V&V 10-2006.
- Bulian, G., 2005, "Nonlinear parametric rolling in regular waves—a general procedure for the analytical approximation of the GZ curve and its use in time domain simulations", Ocean Engineering, Vol. 32, Is. 3–4, pp. 309-330.
- Department of Defense. 2009 (December), "DoD Modeling and Simulation (M & S) Verification, Validation, and Accreditation (VV & A)", Department of Defense Instruction 5000.61.
- Department of the Navy. 1999 (April), "Verification, Validation, and Accreditation (VV&A) of Models and Simulations", SECNAV Instruction 5200.40.
- Grassberger P. and I. Procaccia., 1983, "Characterization of Strange Attractors", Physical Review Letters, Vol. 50, Is. 5, pp. 346–349.
- Kim, Y. editor, 2010, Proceedings of the ITTC Workshop on Seakeeping -V&V for Non-linear Seakeeping Analysis, Seoul, Korea, October.
- Lake, D. E., J. S. Richman, M.P. Griffin, and J.R. Moorman, 2002, "Sample entropy analysis of neonatal heart rate variability", American Journal of Physiology - Regulatory, Integrative and Comparative Physiology, Vol. 283, Is. 3, pp. R789-R797.
- McCue, L.S., Belknap, W., and Campbell, B., (2006), "Reconciling experimental and numerical data: techniques of nonlinear seakeeping code validation," invited submission to Marine Systems and Ocean Technology, Vol. 2, Is. 1-2, pp. 55-62. Originally presented at the 8th International Ship Stability Workshop, Istanbul, Turkey, October, 2005.
- McCue, L., W. R. Story, and A. Reed, 2008, "Nonlinear dynamics applied to the validation of computational methods", Proceedings of 27th Symposium on Naval Hydrodynamics, Seoul, Korea, October.
- McCue, L.S., Wu, W., Story, W.R., and Xing, Z., 2009, "Modeling, verification, and validation of chaotic systems with application to ship motions and the Lorenz oscillator", Proceedings of 2009 NSF Engineering Research and Innovation Conference, Honolulu, HI, June.
- Oberkampf, W.L. and C.J. Roy, 2010, Verification and Validation in Scientific Computing. New York, Cambridge University Press.
- Pearson, K., 1901, "On Lines and Planes of Closest Fit to Systems of Points in Space", Philosophical Magazine Vol. 2, Is. 6, pp. 559-572.



- Reed, A., 2009, "A Naval Perspective on Ship Stability", Proceedings of the 10th International Conference on Stability of Ships and Ocean Vehicles, Russia.
- Roache, P. J., 1998, Verification and Validation in Computational Science and Engineering, Albuquerque, NM, Hermosa publishers.
- Soliman, M. S. and J. M. T. Thompson, 1991, "Transient and steady state analysis of capsizing phenomena", Applied Ocean Research, Vol. 13, Is. 2, pp. 82-92.
- Story, W. R., 2009, "Application of Lyapunov Exponents to Strange Attractors and Intact & Damaged Ship Stability", MS Thesis, Blacksburg, Virginia Polytechnic Institute & State University.
- Story, W.R., Xing, Z., Wu, W., and McCue, L.S., 2010, "Validation: a historical look and two suggested techniques", Proceedings of ITTC Workshop on Seakeeping – V&V for Non-linear Seakeeping Analysis, Seoul, Korea, October.
- Wu, W., McCue, L.S., and Roy, C., 2011, "The Method of Manufactured Solutions Applied to Chaotic Systems", Nonlinear Dynamics, Vol. 63, Is. 4, pp. 667-679.
- Yee, H.C., Sweby, P.K., 1994, "Global asymptotic behavior of iterative implicit schemes", Int. J. Bifurc. Chaos, Vol. 4, Is. 6, pp. 1579-1611.
- Yee, H.C., Sweby, P.K., 1996, "Nonlinear dynamics and numerical uncertainties in CFD", Technical Report. NASA Technical Memorandum 110398, NASA, April.
- Yee, H.C., Sweby, P.K., 1997a, "Dynamics of numerics and spurious behaviors in CFD computations", Technical Report RIACS 97.06, Research Institute for Advanced Computer Science NASA Ames Research Center, June.
- Yee, H.C., Torczynski, J.R., Morton, S.A., Visbal, M.R., Sweby, P.K., 1997b, "On spurious behavior of CFD simulations", Proceedings of 13th AIAA Computational Fluid Dynamics Conference, Snowmass, CO.



Damaged Ro-Pax Vessel Time to Capsize

Heng Ran, *SSPA Sweden AB*, heng.ran@sspa.se

Ingvar Rask, *SSPA Sweden AB*, ingvar.rask@sspa.se

Carl-Erik Janson, *Chalmers University of Technology*, carl-erik.janson@chalmers.se

ABSTRACT

The time for a RoPax vessel (M.S. Estonia) to capsize after a hull breach event is investigated with both physical model experiments and computer based time domain simulations. A two compartment side damage is modelled and a series of tests at stationary head wind/wave is performed. A parabolic inflow velocity model is developed to simulate water ingress through the damaged opening. A two dimensional multi-model sloshing model, composed by a non-linear pendulum model near resonance and an acceleration ratio model at non-resonance, is used for calculating ingressed water transverse center of gravity in the damaged compartment and on car deck.

Keywords: *damaged, time to capsize, ingress, sloshing*

1. INTRODUCTION

Damaged ship stability and manoeuvrability are important for life and cargo safety on board a ship. Model tests and computer based simulations have been carried out at SSPA for a RoPax vessel, M.S. Estonia, to study the time and probability to capsize in different sea states.

The study started with testing a 1:40 RoPax vessel model in SSPA's manoeuvring and seakeeping basin. Meanwhile, a simulation programme is being constructed on SSPA's indoor manoeuvring and seakeeping software SEAMAN II. In this software, water ingress, progressive flooding and sloshing are integrated with ship motions in time domain simulation.

Model test is always a good way for damaged ship stability research. However, there are some limitations. For example, the size of the basin limits the towing distance. There is a requirement in damaged ship manoeuvring and seakeeping simulation

software. Damaged ship stability related topics, such as water ingress, progressive flooding, sloshing in tank and sloshing on deck are focused during this research project.

According to the latest ITTC proceeding from the Specialist Committee of Stability in Waves, higher accuracy CFD methods are currently difficult to integrate with ship motion simulations for large deck area, multi-tank configurations. There is appearance of particle methods, showing the ability to model sloshing behaviour. However, the computational cost is expensive, which makes it not practical for full integration with ship motion simulations.

Godderidge, et al. (2012) constructed a rapid sloshing model by simulate internal fluid system as a pendulum. This model is adapted for sloshing simulation at resonance.

The ship motions, time to capsize, tow line force are measured and recorded during the model test. These results are used to validate the simulation software.



2. EXPERIMENT OBJECT AND SCHEME

2.1 Ship model main data

The experiments are carried out with a model of a RoPax vessel. The model is manufactured in scale 1:40. The main data of full scale ship at the intact loading condition are given in Table 1.

The model was equipped with two fixed rudders, propellers and bilge keels. The length of the forward bilge keel is 35.2m and the aft bilge keel is 13.6m. The height of the bilge keels is 0.6m.

Table 1: Main data of the intact ship.

Parameter	Unit	Value
Length, L_{pp}	[m]	137.4
Breadth, moulded	[m]	24.2
Draft, aft	[m]	5.61
Draft, forward	[m]	5.17
Displacement	[m ³]	12 046
Block coefficient	[-]	0.683

2.2 The hull damage

The side damage is caused to the model according to SOLAS damage opening standard (2004) by means of a V-cut in the hull from bottom to top. A two-compartment damage was modelled. There is water ingress to both car deck and compartment under car deck. The depth of the cut is $B/5 = 4.84\text{m}$ and the length is $0.03L+3\text{m} = 7.12\text{m}$. The position of the centre of the damage is 37.8m forward of aft perpendicular, see Figure 1.

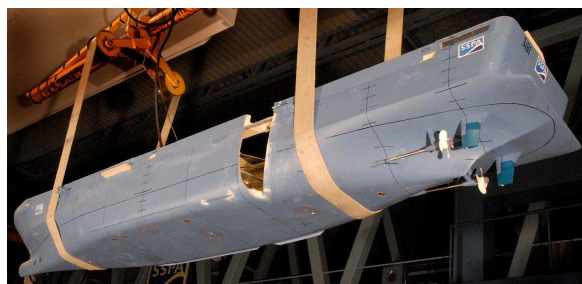


Figure 1: V-cut damage.

The trim angle of the damaged ship is 0.45 degrees relative to the intact ship and the heel angle is 4.0 degrees towards the port side. During model tests, damaged compartments below car deck are flooded with water. There is no obstruction longitudinally along the car deck. Water ingress and progressive flooding on car deck are the main cause of ship sinking in high wave situation.

2.3 The towage system

The length of the towing wire is 800m and the weight in air is 10kg/m corresponding to 8.6kg/m in water for a steel wire. Due to space limitation in the model basin, a truncated towing system has to be designed. The configuration of the system is shown in Figure 2. The system is calibrated and compared with the corresponding full scale catenary characteristics. Stationary ship with no propulsion is modelled during the test. In the working range of the wire, the truncated towing system agrees well with the full scale system.

2.4 The test scheme

A test starts with the model secured to the carriage by means of stretched cords at a position 20m from the wave generators. The air propeller is started and the model is released. The position of the towing point is adjusted in such a way that the model will be kept in a position with the measuring range of the device for measuring the six degrees of freedom.

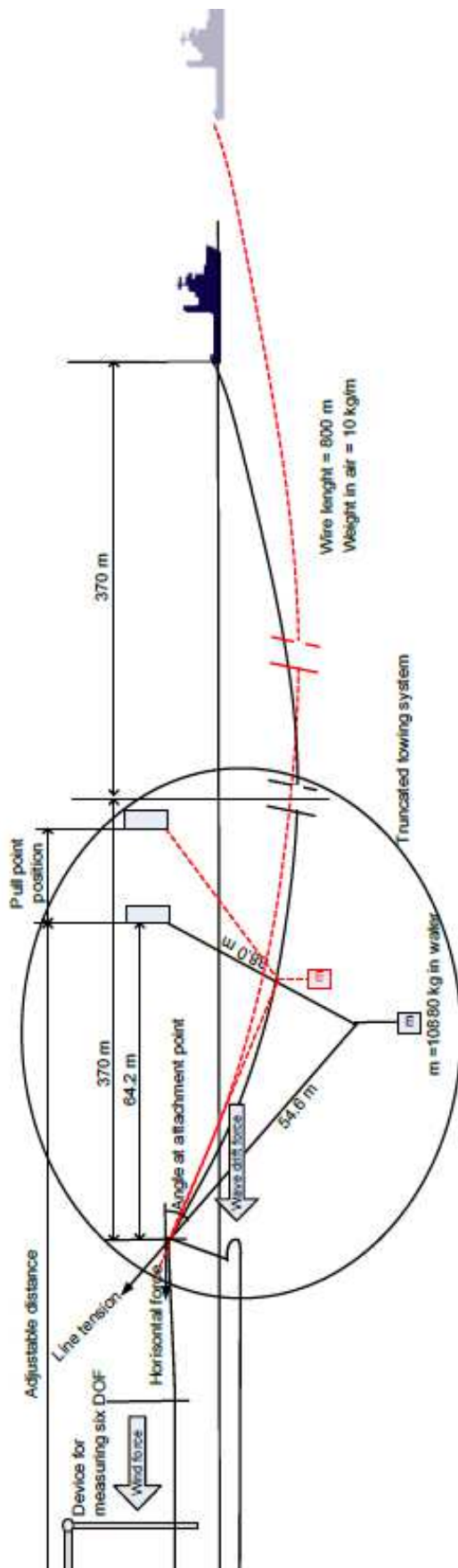


Figure 2: Model test set up.

motion of the model. When the model is in a stable position the wave generators are started

The different wave components are successively sent away towards the model; with the shortest waves first. In such a way that the wave spectrum will be fully developed when all wave components reach the position of the model. Shortly before this the data logging system are started.

A test is interrupted when the average heel angle exceeds 20 degrees or when the duration of the test exceeds 30 minutes full scale time.

The model is then secured to the carriage and drained from the water. In order to be sure that there is no water left in the model before the next test, the trim and heel are checked in a static measurement.

2.5 The Tested Cases

A series of tests are carried out for static ship at sea with significant wave height of 3.5m, 3.75m, 4m, 4.25m and 4.5m. For each wave height, a wind force in the same direction as the wave is calibrated according to the relation between wind speed and wave height recommended by ITTC. The series of tests comprised repetitions in order to create sufficiently consistent relative frequency distribution of the time to capsize.

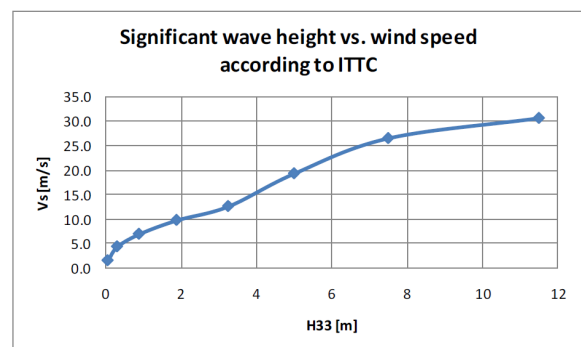


Figure 3: ITTC wind-wave diagram.



3. MATH MODEL FOR SIMULATION

The simulations are carried out with SSPA manoeuvring and seakeeping simulation program SEAMAN II, under different wind, wave conditions. SEAMAN II is a PC based time domain non-linear simulation tool for predicting ship motions both in calm water and in different weather situations. It covers the ship dynamics in all six degrees of freedom, including both first and second order wave forces.

3.1 Wave Model

The wave model is primarily adopted from conventional strip theory based on Lewis in SEAMAN II program. The sectional data is given in the form of section areas, beams, and draughts, and in the form of section off-set points. The section off-set points are used for pressure integration.

The first order wave force comprise linear damping, restoring forces, wave exciting forces and forces due to pressure integration. The second order wave force is calculated with the equation given by O. M. Faltinsen and A. E. Løken (1987).

3.2 Wind Model

SEAMAN II program allows simulation to be carried out at arbitrary wind conditions, comprising constant wind, as well as wind velocity varying around a pre-set mean value according to a certain wind spectra.

The wind spectra used for wind gusts is a Davenport spectrum consisting of five sinusoidal components, each representing a specific frequency and amplitude.

3.3 Constant Velocity Water Ingression Model

When calculating inflow rate through the damage opening, two types of inflow velocity models are constructed for result comparison.

The constant velocity water ingression model assumes that water enters the damage opening with same velocity.

$$q_{in} = v_{in} \cdot opening_area$$

Where,

v_{in} – inflow velocity, m/s

$$v_{in} = v_{wave} - v_{ship} + \frac{2}{3} \sqrt{2 \cdot g \cdot hw}$$

V_{wave} is the decomposed horizontal wave particle velocity in ship beam direction. This variable is very much related to the ship instantaneous yaw angle. V_{ship} is the reversed ship transverse speed at damage centre. It comprises ship transverse speed at ship centre of gravity and transverse velocity due to yaw motion. hw is the water head height at the damage opening.

3.4 Parabolic Velocity Water Ingression Model

When calculating inflow rate through the damage opening, the parabolic water ingression model assumes that the flooding velocity varies along ingression water line with a step size of 0.5m. The ingressed volume through the opening area per second is derived by summation along the h-axis in Figure 3. The thickened curve represents the flow velocity profile.

$$q_{in} = \sum_{istep=1}^{nstep} v_{in} \cdot opening_area_{istep}$$

Where,

$$v_{in} = v_{wave} - v_{ship} + \sqrt{2 \cdot g \cdot (hw - h)}$$

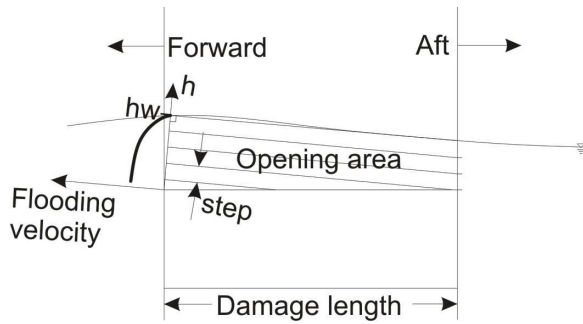


Figure 4: Flooding velocity parabolic profile.

3.5 Sloshing at Non-resonance

Acceleration ratio method is adopted to calculate cases at non-resonance situation, where the free surface of ingressed water changes moderately.

Certain assumptions are made when applying the method. In the programme, the car deck of the RoPax vessel is divided into twenty sections. During each time step, the sloshing phenomenon is simulated for each section in transverse two-dimensional plane. The free surface is assumed to be straight in the transverse plane. The slope of the free surface is calculated with the instantaneous accelerations.

The fundamental principle of acceleration ratio method is fluid static pressure. In ship transverse plane shown in Figure 5, the pressure at certain location below internal water free surface is a function of the location.

$$P(y, z) = \int \frac{\partial P(y, z)}{\partial y} \cdot dy + \int \frac{\partial P(y, z)}{\partial z} \cdot dz \quad (1)$$

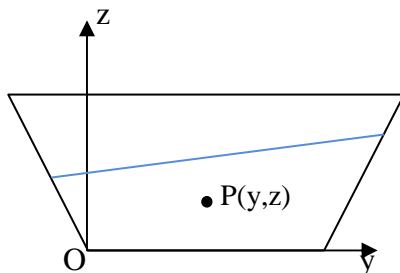


Figure 5: The coordinate system of car deck cross section.

The total force acting on a fluid particle of volume is due to pressure and gravity. According to Robert W. Fox (1985, p 75), in rectangular coordinates the component equations are:

$$-\frac{\partial P(y, z)}{\partial y} + \rho \cdot g_y = \rho \cdot a_y \quad (2)$$

$$-\frac{\partial P(y, z)}{\partial z} + \rho \cdot g_z = \rho \cdot a_z \quad (3)$$

Substituting the partial derivative components in the first equation derives:

$$P(y, z) = -\rho \cdot a_y \cdot dy + \rho \cdot (g_z - a_z) \cdot dz \quad (4)$$

On the internal water free surface:

$$P(y, z) = 0 \quad (5)$$

Gravity acceleration points downwards, i.e. opposite to z-axis in the transverse coordinate system.

$$g_z = -g \quad (6)$$

Therefore, on free surface equation 4 becomes:

$$\frac{-a_y}{g + a_z} = \frac{dz}{dy} = \text{Free surface slope} \quad (7)$$

Internal free surface intersects car deck walls at two inter section points. The coordinates of these intersections points are calculated based on the cross section geometry, volume of water ingression, and free surface slope. The centre of gravity of ingressed water is derived using the coordinates of intersection points and tank corner points.

3.6 Sloshing at Resonance

Pendulum model is adopted from Godderidge, B. et. al. (2012) to calculate sloshing cases near resonance, where the free surface of ingressed water is assumed to deform greatly due to resonance effect. The natural frequency of the water in a rectangular compartment is calculated with equation 8.



Given by linear theory, the natural frequency is related to the filling level of the compartment and compartment dimension along beam direction. Since water level changes during the simulation, the natural frequency is calculated at each time step. $\pm 20\%$ of natural frequency is selected as the prerequisite to initiate pendulum model.

$$\omega_n = \sqrt{\frac{g\pi}{L} \cdot \tanh\left(\frac{h}{L}\pi\right)} \quad (8)$$

A pendulum models the sloshing fluid as a single moving mass. This mass point carries out simple pendulum movement under the excitation of ship side motion.

Based on Newton's second law, the angular acceleration of the pendulum swinging around virtue attachment point is presented with three terms, namely damping force, restoring force and body force.

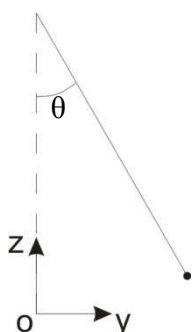


Figure 6: Pendulum model

$$\ddot{\theta} = -\beta_3 \dot{\theta}^3 - \beta \dot{\theta} - \frac{g}{l} \sin(\alpha\theta) + (A_T - A_E - A_C) \quad (9)$$

Where,

β – damping coefficient;

g – gravity;

l – pendulum length;

α – coefficient in displacement function, 1.0225;

A_T – Excitation force induced term;

A_E – Euler force induced term;

A_C – Centrifugal and Coriolis force induced term;

4. EXPERIMENT AND SIMULATION RESULTS

Experiment results focus on probability, and simulation results focus on motion of the ship.

4.1 Probability of Capsize

A series of model basin experiment in head-on waves are performed for the stationary ship model. The test programme is shown in Table 2. Since the ship survived in all the cases at 4.0m wave height, model tests for 3.5m and 3.75m wave height were performed for once each.

Table 2: Model test programme.

$H_{1/3}$ [m]	T_p [s]	Number of tests
3.50	7.48	1
3.75	7.75	1
4.00	8.00	10
4.25	8.25	10

The probability of capsizing within half an hour as function of significant wave height is shown in Figure 7.

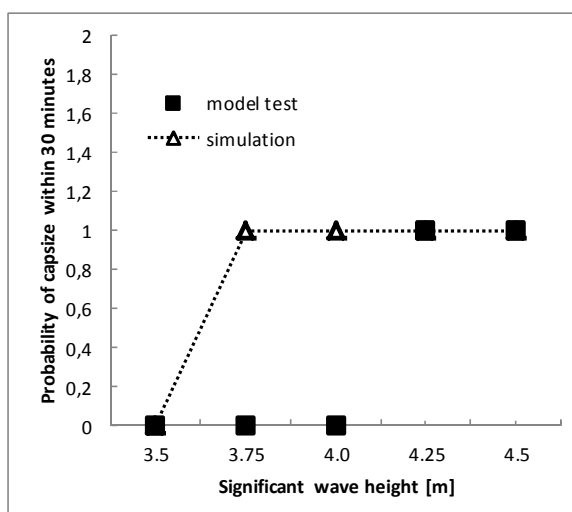


Figure 7: Probability of capsizing.

The simulation results indicate that capsizing for the RoPax vessel happens at 3.75m significant wave height. This result is 0.5m lower than the experiment result.

4.2 Inflow Velocity Profile Influence

In the simulations, the water ingress velocity is modelled with the inflow velocity profile as described in section 3.1. This influences the time to capsize greatly, as compared to a constant inflow velocity model. Figure 8 demonstrates the time to capsize using two different water ingress math models and during model test.

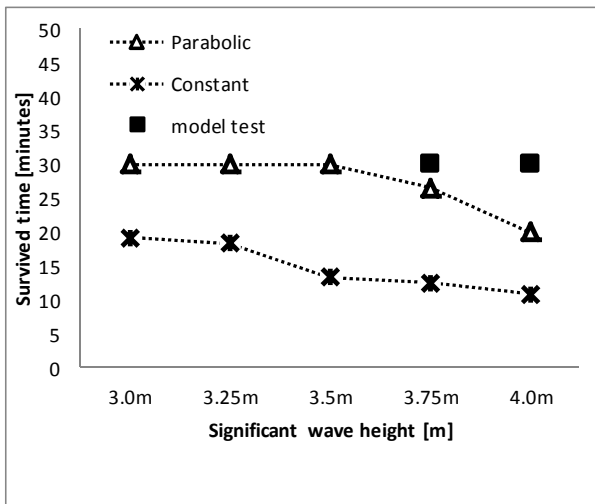


Figure 8: Survived time.

With constant inflow velocity math model, the simulated ship capsized in less than 30 minutes for all cases. The graph illustrates that parabolic inflow velocity profile method improves the accuracy of the simulation programme.

5. CONCLUSION

Model basin experiments result shows that the tested RoPax vessel with side damage opening, could survive in 4.0m wave for over 30 minutes.

Computer based time domain simulations resulted 0.5m lower in surviving wave height for the same ship and damage. The water ingress parabolic velocity profile model improves the simulation accuracy.

6. REFERENCES

- ITTC. The Specialist Committee on Stability, 2008, "Proceeding of the 25th ITTC", Final Report and Recommendations, Vol. II.
- SOLAS. Consolidated Edition, 2004, "International Convention for the Safety of Life at Sea", Chapter II-1, Regulation 8.
- Godderidge, et al., 2012, "A rapid method for the simulation of sloshing using a mathematical model based on the pendulum equation", *Computers and Fluids*, Volume 57, p. 163-171
- Robert W. Fox, Alan T. 2004, "Introduction to Fluid Mechanics", Third edition, New York, Wiley.
- Ottosson, et al, 2008, "Research Study on the Sinking Sequence of MV Estonia.", research report, SSPA.
- Odd M. Faltinsen, et al. 2009, "Sloshing", Cambridge University Press.





Study on the Evaluation for Performance of the Cross-Flooding Arrangements by means of the Computational Fluid Dynamics

Kunihide Ohashi, *Computational Fluid Dynamics Research Group, National Maritime Research Institute, Japan*, k-ohashi@nmri.go.jp

Yoshitaka Ogawa, *Head of Ship Structural Standards Research Group, National Maritime Research Institute, Japan*, ogawa@nmri.go.jp

Koichiro Shiraishi, *Structural Standards Research Group, National Maritime Research Institute, Japan*, shiraishi@nmri.go.jp

ABSTRACT

The performance of cross-flooding arrangements is evaluated by the Computational Fluid Dynamics (CFD). At first, the computation for the simple arrangement is conducted including the scale effect. The model experiments are carried out for the validation of the computational results. Recently, several papers report that the factors which are evaluated by the IMO simplified regression formulae are different from the experimental and computational results. The present results are also compared with the results of the simplified formulae. Finally, the computation for the complex arrangement is carried out and the present result is compared with the existing results.

KEYWORDS: *Damage Stability, Cross-flooding arrangements, Computational Fluid Dynamics*

1. INTRODUCTION

For the further ensuring the safety in terms of damage stability, it is important to evaluate a safety level of damaged ships more quantitatively (e.g., Jalonen, *et al.*, 2010). Furthermore, it is considered that further validation of the evaluation method and tools is significant.

Based on this background, authors investigated the performance of cross-flooding arrangements. Firstly, a factor in terms of the pressure losses in the simple cross-flooding arrangements is evaluated by means of the Computational Fluid Dynamics (CFD). Then,

the model experiments for the validation of the computation are conducted. Also, the present results of the computation and model experiments are compared with the current International Maritime Organization (IMO) requirement including the scale effect by using CFD. The simplified regression formulae is found in the IMO Recommendation (resolution MSC.245(83) (IMO, 2007)) and the estimated values by the formulae have the difference to the recent results (Ruponen, 2012; IMO, 2011; Ogawa, 2011).

Finally, the computation with the complex geometries (Ruponen, 2012) is carried out. The arrangement is including the web frames, the



girders and the stiffeners. The present computational discharge coefficient is compared with the references.

2. CROSS-FLOODING ARRANGEMENTS

2.1 Arrangement 1

The performance of the simple cross-flooding arrangement with manholes is evaluated at first. The pressure loss coefficients through the six units of structural ducts, which are divided by the girders with one or two manholes, and discharge coefficient are computed. The computed structures of cross-flooding ducts are shown in Figure 1. The sketch of girder in the structural ducts with one and two manholes is shown in Figure 2.

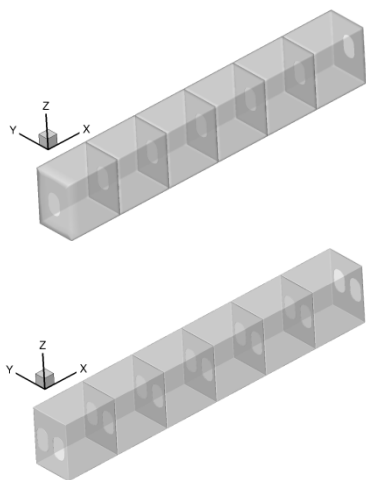


Figure 1: Series of structural ducts with one and two manholes.

2.2 Arrangement 2

The performance of the cross-flooding arrangement with the complex geometries is evaluated. The arrangement in Stening (2011) has the web frame, stiffeners and girders. The computation for the complex arrangement has been carried out by Ruponen, *et al.* (2012) and shows good agreement with the experimental

results. The computation for the arrangement with present method is also carried out and the results are compared with the references.

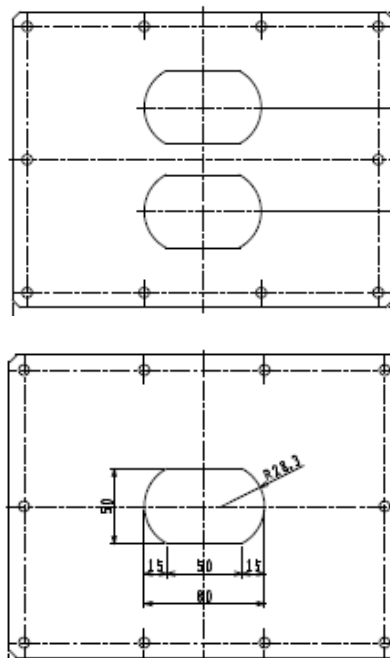


Figure 2: Sketch of girder in the structural ducts.

3. COMPUTATIONAL METHOD

The flow solver used in this study is called SURF (“Solution algorithm for Unstructured RaNS with FVM”) which is under development at National Maritime Research Institute (Hino, 1998, 1999). The governing equations are the unsteady 3D Reynolds averaged Navier-Stokes equations for incompressible flows. Coupling pressure with a velocity field is made by artificial compressibility approach. The final form can be written as follows:

$$\frac{\partial \mathbf{q}}{\partial t} + \frac{\partial \mathbf{q}}{\partial \tau} + \frac{\partial(\mathbf{e} - \mathbf{e}^v)}{\partial x} + \frac{\partial(\mathbf{f} - \mathbf{f}^v)}{\partial y} + \frac{\partial(\mathbf{g} - \mathbf{g}^v)}{\partial z} = 0$$

and

(1)

$$\mathbf{q} = [p \ u \ v \ w]^T$$



In the above, all variables are non-dimensionalized using the reference density ρ_0 , velocity U_0 and length L_0 . The velocity components in the (x, y, z) direction is expressed as (u, v, w) . The inviscid fluxes \mathbf{e} , \mathbf{f} and \mathbf{g} and the viscous fluxes \mathbf{e}^v , \mathbf{f}^v and \mathbf{g}^v are defined as:

$$\mathbf{e} = \begin{bmatrix} \beta u \\ u^2 + p \\ uv \\ uw \end{bmatrix}, \mathbf{f} = \begin{bmatrix} \beta v \\ vu \\ v^2 + p \\ vw \end{bmatrix}, \mathbf{g} = \begin{bmatrix} \beta w \\ wu \\ wv \\ w^2 + p \end{bmatrix}, \quad (2)$$

$$\mathbf{e}^v = \begin{bmatrix} 0 \\ \tau_{xx} \\ \tau_{xy} \\ \tau_{zx} \end{bmatrix}, \mathbf{f}^v = \begin{bmatrix} 0 \\ \tau_{xy} \\ \tau_{yy} \\ \tau_{yz} \end{bmatrix}, \mathbf{g}^v = \begin{bmatrix} 0 \\ \tau_{zx} \\ \tau_{yz} \\ \tau_{zz} \end{bmatrix}$$

where β is a parameter for artificial compressibility and

$$\tau_{ij} = \frac{1}{R} \left(\frac{\partial u_i}{\partial x_j} + \frac{\partial u_j}{\partial x_i} \right) - \overline{u'_i u'_j} \quad (3)$$

where R is the Reynolds number defined as $U_0 L_0 / \nu$ where ν is the kinematic viscosity. $-\overline{u'_i u'_j}$ is Reynolds stress component and the $k-\omega$ SST model (Menter, 1994) is applied.

Since a basic numerical procedure for the Navier-Stokes equations are described by Hino (1998,1999), only the brief outline is given here.

Spatial discretization is based on a cell-centered finite-volume method. A computational domain is divided into unstructured polyhedral cells and flow variables (pressure, velocity and eddy viscosity) are stored in the center of each cell. Cells whose shape are hexahedra, tetrahedra, prisms or pyramids can be used and the combinations of these cells give greater flexibility for handling complex geometry.

For the inviscid fluxes (convection terms and pressure gradient terms), the second order upwind scheme based on the flux-differencing splitting of Roe with the MUSCL approach is employed. The viscous fluxes are evaluated by the second order central scheme. Thus, the overall accuracy in space is the second order.

A dual time stepping approach is used in order to recover incompressibility at each time step. It consists of the second order two-step backward scheme for the physical time stepping and the first order backward Euler scheme is used for the pseudo time. Local time stepping method is used in pseudo time, in which time increment is determined for each cell in such a way that the CFL number is globally constant. A Multigrid method is employed for the fast convergence.

The linear equations derived from the time linearization of the fluxes are solved by the Gauss-Seidel iteration.

4. MODEL EXPERIMENTS

For the validation of computation, model tests for the arrangement 1 are carried out with several variations of a cross-flooding duct design with one and two manholes. A setup of the six cross-duct modules is shown in Figure.3. The scale ratio to the subject model is 1:10. The flow was generated by means of the pump, which is also shown in Figure 3. A mass of inflow was kept constant in the experiments.

A photo of the six cross-duct modules is shown in Figure 4. Experiments are carried out in various conditions of flow in the ducts by adjusting the valve on the ducts. Pressure loss coefficient is calculated based on the measured pressure and the measured stream velocity in the ducts. A pressure, P , is measured by the strain gauge. Stream velocity, U , is measured by the ultrasonic current meter. Total pressure, P_{TOTAL} is evaluated by the combination of static and dynamic pressure, which is evaluated by means of the pressure and stream velocity.



The pressure loss coefficient at i -th unit, K_i , is evaluated by the variation of the total pressure at each duct.

$$P_{TOTAL} = P + 0.5 \rho U^2 \quad (4)$$

$$K_i = \frac{2(P_{TOTAL,i} - P_{TOTAL,i+1})}{\rho U_0^2} \quad (5)$$

Here, ρ and U_0 describe the density of fluid and the stream velocity at the inflow respectively.

Finally, discharge coefficient is obtained by the equation:

$$C_d = \frac{1}{\sqrt{1 + \sum_{i=1}^N K_i}} \quad (6)$$

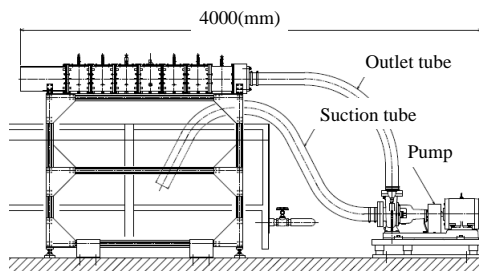


Figure 3: Setup of the six cross-duct modules. (The 1:10 scale model).



Figure 4: Photo of the six cross-duct modules. (The 1:10 scale model).

5. COMPARISON OF COMPUTATION WITH EXPERIMENTS FOR ARRANGEMENT 1

5.1 Computational Results

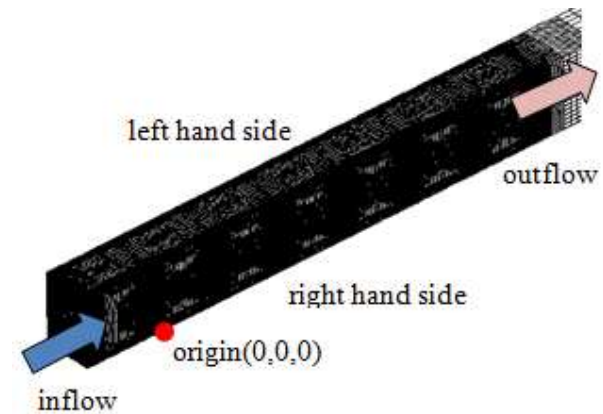


Figure 5: Coordinate system in computation.

The coordinate system in the computation is shown in Figure 5. The computational conditions are set as same as the model experiments. The velocity fields are non-dimensionalized by the inflow velocity at the entrance of the model setting. The length is non-dimensionalized by the duct height. The wall boundary is treated as low-Reynolds number model which means the minimum spacing on the wall is set as y^+ nearly 1.0. The computational grid which is generated by HEXPRESSTM consist from about 3 million hexahedra cells for one manhole case and about 3.8 million hexahedra cells for two manhole case. Reynolds number is set as 4.0×10^5 and the non-dimensionalized physical time step size is 0.1.

Figure 6 shows the computed axial velocity distribution and velocity vectors through the cross-flooding ducts. Velocities in Figure 6 are time-averaged in 1000 computational steps, which is equal to 14 sec. having dimension, from the fully developed flow field.

It is found that water just passed through the manholes is accelerated. It is also found

that water passed through one manhole is more accelerated than that through two manholes.

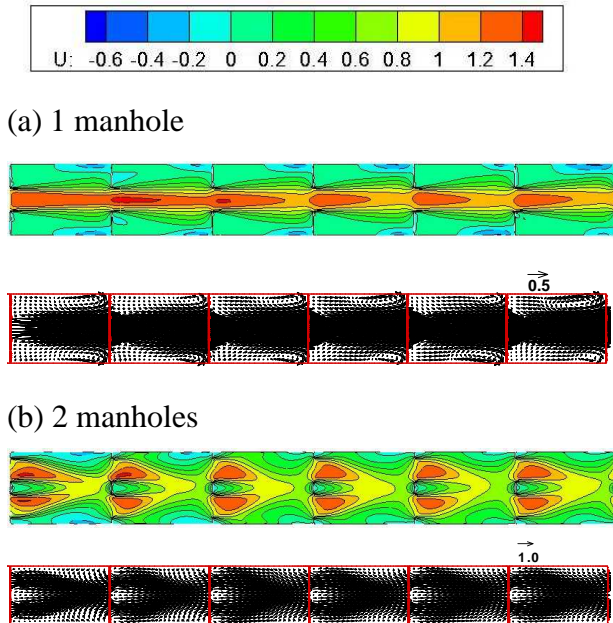


Figure 6: Computed axial velocity distributions through the cross-flooding ducts.

5.2 Comparison with Experiments and the Current IMO Requirement

The computed pressure is compared in Figure 7. The computational results shows similar tendency with the experiments. The pressure of two manholes is higher than the pressure of the one manhole.

The computed pressure loss coefficients and discharge coefficient are compared with experiments. Results of pressure loss coefficients at each structural duct with one manhole and two manholes are shown in Figures 8 and 9. It is found that present computation well explains the experiments. It is clarified that pressure loss coefficients become larger due to the difference of acceleration at manhole.

Furthermore, the computed pressure loss coefficients are compared with the IMO requirements. The Maritime Safety Committee

of the IMO, at its eighty-third session (MSC83), adopted the Recommendation on a standard method for evaluating cross-flooding arrangements (resolution MSC.245(83)). This recommendation, MSC.245(83), provides the method for assessing cross-flooding time through ducts and equalization arrangements, which presents various pressure loss coefficients for water flow through pipes and valves. In addition, appendix 2 in this recommendation contains simplified regression formulae for pressure losses in cross-flooding ducts as a function of the distance between the girders.

On the other hand, in section 4 of the Recommendation, a direct calculation using computational fluid dynamics (CFD), time-domain simulations or model testing is allowed to be used as an alternative to the provisions in sections 2 and 3 of the recommendation. However, the comprehensive verification of applicability of a direct calculation has not necessarily been conducted. For the realization of a reliable direct calculation, it is important to verify the accuracy of the direct computations.

The pressure loss coefficients computed by resolution MSC.245(83) are shown in Figures 8 and 9. It is also found that there are certain discrepancies between computation and the current recommendation, which implies that the recommendation requires different time from commencement of cross-flooding to the final equilibrium by means of the CFD computation and the experiments.

Although the regression formulae have been developed based on CFD computation (IMO, 2007), it is found that the difference of pressure loss coefficients between the Recommendation and the CFD computation seems to be significant.

Finally, the discharge coefficients are compared in Table 1. The difference between the computation and the experiment is from 3% to 7% and smaller than the difference between



the results of IMO Res.245 and the experiments.

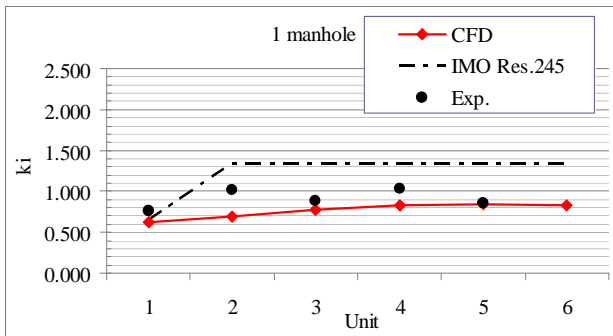


Figure 7: Comparisons of pressure

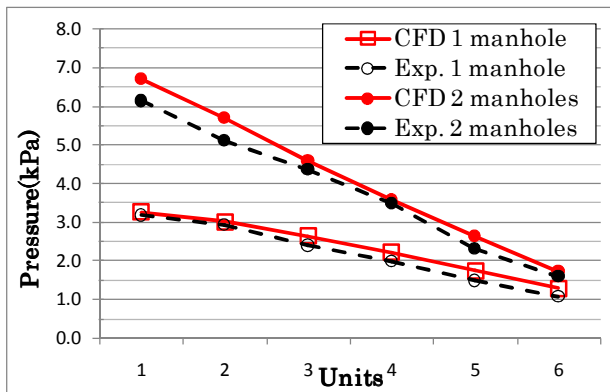


Figure 8: Pressure loss coefficient at each structural duct with 1 manhole.

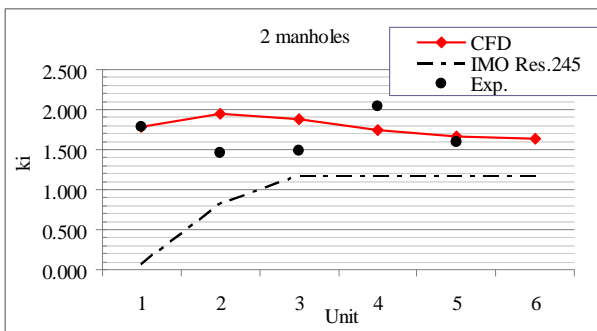


Figure 9: Pressure loss coefficient at each structural duct with 2 manholes.

5.3 Clarification of the Scale Effect

The computation in full scale is conducted to examine the scale effect for the pressure losses. Reynolds number is set as 4.0×10^6 and other conditions are similar to the model scale.

Figure 10 shows computed axial velocity distributions and velocity vectors of the model and full scale. Axial flows near the entrance of the cross flooding duct in the full scale are more accelerated than the flows of the model scale. The pressure gradient becomes larger in the case of high Reynolds number and the flows are also accelerated.

Table 1: Comparisons of discharge coefficient.

Manhole	Case	C_d
1 manhole	Experiment	0.424
	Computation	0.458
	IMO Res.245	0.378
2 manholes	Experiment	0.327
	Computation	0.316
	IMO Res.245	0.392

Figure 11 shows the comparisons of the pressure loss coefficient and Table 2 shows the comparisons of the discharge coefficient. The pressure loss coefficient of the full scale becomes about 15% larger than the coefficient of the model scale, although the influence for the discharge coefficient is small and the difference is about 5% and almost the same order (Ruponen *et al.*, 2012).

Table 2: Comparisons of discharge coefficient.

Manhole	Case	C_d
1 manhole	Computation(Model)	0.458
	Computation(Full)	0.436

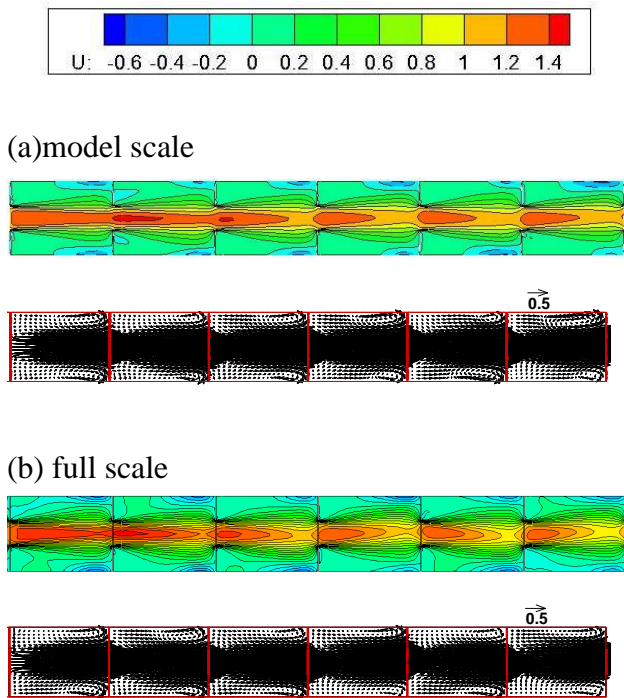


Figure 10: Effect of Reynolds number on the axial velocity distributions through the cross-flooding ducts.

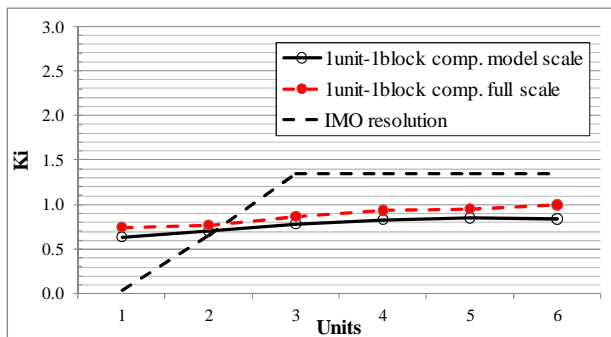


Figure 11: Effect of scale on the pressure loss coefficient at each structural duct with 1 manhole.

6. COMPUTATIONAL RESULTS FOR ARRANGEMENT 2

The arrangement and the boundary conditions are shown in Figure 12. The computational conditions are close to the conditions (Ruponen, 2012) except the inlet and outlet boundary conditions. The inlet and outlet conditions are given by the prescribed pressure in reference

(Ruponen, 2012). Instead of the prescribed pressure conditions, the inflow and outflow conditions are imposed in the present computation. The uniform velocity which are supposed in the reference (Ruponen, 2012) is given at the inlet. The additional box is set at the outlet and the outflow where is the zero pressure condition is set at the exit. The wall boundary is treated as low-Reynolds number model which means the minimum spacing on the wall is set as y^+ nearly 1.0 and the computational grid which is generated by HEXPRESSTM consist from about. 11 million hexahedra cells. Figure 13 shows the computational grids of the one of cross-flooding ducts. The web frames, side girders and stiffeners are included in the arrangement 2. The physical time step size is set as 0.0065 sec. in the computation.

Figure 14 shows that the computed axial velocity distribution which is time-averaged in 2000 computational steps, means being equal to about 13 sec. from the fully developed flow field. The velocity is accelerated after the manholes which is similar to the arrangement 1.

Table 3 shows the comparison of discharge coefficient. The present result is higher than the results (Ruponen, 2012). Present inflow condition gives the better entering of the flows than the prescribed pressure conditions and yields to the high discharge coefficient, which is equals to the low pressure losses.

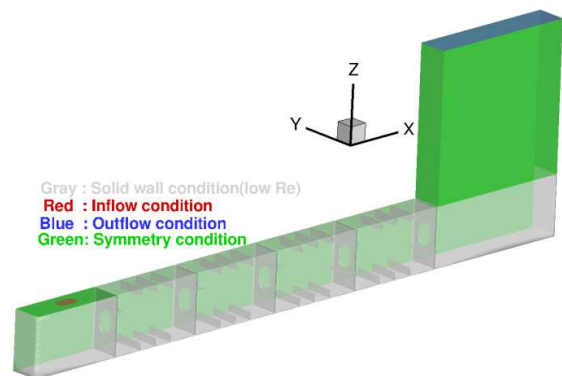


Figure 12: Arrangement 2 and boundary conditions.



Table 3: Comparisons of discharge coefficient.

Case	C_d
Computation(Present)	0.383
Computation(Ruponen,2012)	0.333
Experiment(Stening,2011)	0.339

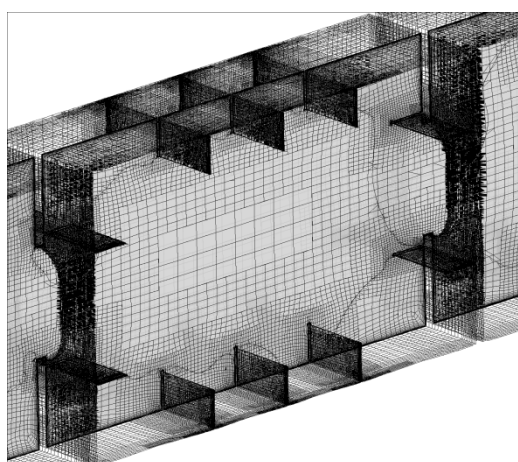


Figure 13: Computational grids.

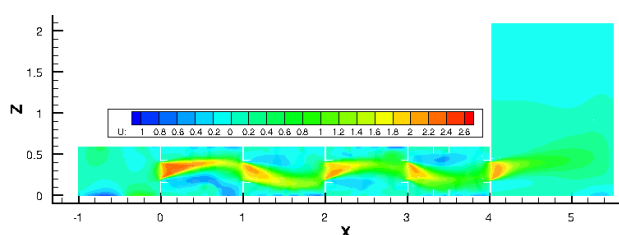


Figure 14: Computed axial velocity distributions.

7. CONCLUSIONS

Direct simulations and the experiments for two cross-flooding arrangements are carried out.

The present computation explains the experiments well for the simple cross-flooding arrangement. The pressure loss coefficients of the present computation and experiment are different from those derived by means of resolution MSC.245(83). Scale effects for the pressure loss coefficient and discharge coefficient are examined. The full-scale pressure loss coefficient is about 15% larger than that of the model, although the influence of the discharge coefficient is about 5% and the result is close to that of the reference.

The computations for the complex arrangement which includes web frames, side girders and stiffeners succeeded, although the discharge coefficient is larger than the reference. The difference in the inlet and outlet conditions is considered to be the cause of the difference, and the results are considered reasonable.

8. ACKNOWLEDGMENTS

The present study was carried out as a part of the research project of Japan Ship Technology and Research Association for ship stability, which is supported by the Nippon Foundation.

9. REFERENCES

- Hino, T., 1998, "Navier-Stokes Computations of Ship Flows on Unstructured Grids," Proc. of the 22nd Symp. Naval Hydro.
- Hino, T., 1999, "An Interface Capturing Method for Free Surface Flow Computations on Unstructured Grids," J. Soc. Naval Archit. Japan, Vol.186, pp.173-183
- IMO MSC.245(83) ,2007, "Recommendation on a Standard Method for Evaluating Cross-Flooding Arrangements," London, UK.
- IMO, 2011, "An analysis of the recommendation on a standard method for evaluation of cross-flooding arrangements



as presented in resolution MSC.245(83).”,
SLF54/INF.4, Submitted by Finland, 14
October 2011.

Jalonen, R., Jasionowski, A., Ruponen, P.,
Mery, N., Papanikolaou, A., Routi, A-L.,
2010, “FLOODSTAND Integrated Flooding
Control and Standard for Stability and
Crises Management”, Proceedings of the
11th International Ship Stability Workshop,
Wageningen, The Netherlands

Menter, F.R., 1994, “Two-Equation Eddy-
Viscosity Turbulence Models for
Engineering Applications”, AIAA J., 32(8),
pp. 1598-1605

Ogawa, Y., Ohashi, K., 2011, “Studies on an
Assessment of Safety with regard to the
Damage Stability of Passenger Ships”, Proc.
12th International Ship Stability Workshop

Ruponen, P., Queutey, P., Kraskowski, M.,
Jalonen, R., Guilmineau, E., 2012, “On the
calculation of cross-flooding time”, Ocean
Engineering, Vol. 40, pp. 27-39

Stening, M., Järvelä, J., Ruponen, P., Jalonen,
R., 2011, “Determination of discharge
coefficients for a cross-flooding duct”,
Ocean Engineering, Vol. 38, pp. 570-578





Flooding Prediction Onboard a Damaged Ship

Pekka Ruponen, *Napa Ltd*, pekka.ruponen@napa.fi

Markku Larmela, *Napa Ltd*, marku.larmela@napa.fi

Petri Pennanen, *Onboard-Napa Ltd*, petri.pennanen@napa.fi

ABSTRACT

Progressive flooding inside a damaged ship can seriously endanger the safety. Level sensors can be used to detect the flooding, and based on this data the breach can be estimated. For decision support the prediction of flooding extent and the intermediate phases is necessary. For this purpose a new simplified, but still reasonable accurate, flooding prediction method has been developed. Details of this algorithm and some test cases, including comparisons to experimental data and time-accurate flooding simulation results, are presented. The application of the developed prediction method as a decision support tool is also discussed.

Keywords: *Progressive flooding, damage stability, decision support, time-to-capsize*

1. INTRODUCTION

When the hull of a ship is breached due to collision or grounding, the floodwater enters the damaged compartments. Open doors and various pipes may result in progressive flooding to undamaged compartments, thus making the situation even more critical. Also before the final floating position the ship may pass through intermediate positions that are more dangerous than the final one. Thus for decision support it is necessary to check the whole process of progressive flooding.

Previously *Ölcer and Majunder (2006)* have presented a system that is based on a database of pre-calculated damage cases. Also *Nilsson and Rutgersson (2006)* have described decision support systems that are based on real-time monitoring and static stability calculations. More recently, *Jasionowski (2011)* has presented a system that estimates the survival probability, and especially, the effect of open watertight doors. However, the method is based on the final condition after flooding. Yet it demonstrates very efficiently the importance of keeping all watertight doors closed while at sea.

A new approach, using the online data from water level sensors, ship motions and door statuses, combined with a 3D model of the ship and time-domain flooding simulation tool provides a better and more realistic estimation of both the damage and its consequences. Direct time-domain flooding simulation was found out to be too slow for practical purposes. On the other hand, onboard the damaged ship there are always several uncertainties involved, and thus minimization of the numerical error in the solution of the governing equations is not a key issue. Thus a completely new approach for calculation of progressive flooding has been developed. This method accounts the intermediate phases of the flooding process and also provides a rough estimation on the time-to-flood. Leaking and collapsing of non-watertight structures (such as closed fire doors) are also taken into account.

The developed new flooding prediction method is tested against both full-scale measurement data and time-accurate simulations with a short time step. In the latter case also leaking and collapsing fire doors are included.



2. BREACH DETECTION

2.1 Use of Level Sensor Data

For reliable flooding prediction the breach size and location need to be known. This is possible only if the ship is equipped with level sensors. The flooding rates can be calculated based on the measurements, compartment geometry and floating position. And further the breach can be estimated based on the flow rates.

IMO has established some basic requirements for flooding detection systems on passenger ships, *IMO (2008)*. A more comprehensive and detailed recommendation has been developed within the FLOODSTAND project, *Penttilä (2012)*.

The idea of using inverse method for prediction of the breach size and location on the basis of level sensor data and short simulations was described in *Penttilä and Ruponen (2010)*. The results were promising but the method was a little too time-consuming, especially when considering that the available input data is rather rough. Therefore, a simplified but faster method was needed.

2.2 Simplified Method

In the simplified approach, flooding predictions are done by modelling each measured flooding as a separate breach to the sea. Thus it is assumed that all floodwater is detected and measured. Consequently, for each flooding detector (or for each compartment with measurement data), there is a corresponding breach definition.

Each individual breach is modelled to extend from deck to deck. This simplified modelling avoids the problems related to the vertical location of the breach. For rooms that are not connected to the hull surface, a simple point opening in the middle of the room

(lowest point) is used. These are illustrated in Fig. 1. Thus the following assumptions are done:

- All floodwater is detected and measured
- The vertical location of the breach has no (significant) effect on progressive flooding
- a room, which is not connected to hull may still be flooding (through a breach)

The breach sizes are calculated separately, based on the measured flooding rate, by using Bernoulli's equation. This means that if the flooding rates of all breaches are added together, the sum is the same as the total measured flooding rate. In this sense the simplification is valid. However this method does not take into account the possibility of undetected flooding.

Separate analysis of breach penetration is not needed since breach detection is based on measured flooding rates.

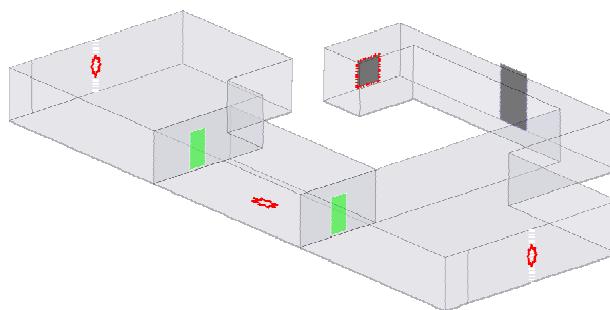


Figure 1: Modelling of small breaches.

3. PREDICTION OF PROGRESSIVE FLOODING

3.1 Governing Equations

During the past decades several calculation methods (see e.g. *ITTC, 2008*) have been developed for prediction of progressive flooding inside a damaged ship. Usually these are based on Bernoulli's equation. The background for the developed method is described in the following.

Conservation of Momentum

Similarly to time-accurate flooding simulation, e.g. *Ruoponen (2007)*, the calculation of flow velocities in the openings is based on the application of Bernoulli's equation. For a streamline from point A that is in the middle of a flooded room to point B in the opening, Bernoulli's equation is:

$$\int_A^B \frac{dp}{\rho} + \frac{1}{2}(u_B^2 - u_A^2) + g(h_B - h_A) = 0 \quad (1)$$

where p is air pressure ρ is density, u is flow velocity, g is acceleration due to gravity and h is height from the reference level.

The equation applies for inviscid and irrotational flow. For water flow the density is constant and thus equation (1) reduces to:

$$p_B - p_A + \frac{1}{2}\rho(u_B^2 - u_A^2) + \rho g(h_B - h_A) = 0 \quad (2)$$

It is assumed that the flow velocity is negligible in the center of the room ($u_A = 0$). The pressure losses in the openings are taken into account by applying semi-empirical discharge coefficients (C_d).

Furthermore, air pressure is assumed to be constant. Consequently, the volumetric flow rate through a small opening is:

$$Q = \text{sign}(H_{\text{eff}}) \cdot C_d \cdot A_{\text{eff}} \sqrt{2g|H_{\text{eff}}|} \quad (3)$$

where C_d is the discharge coefficient (usually assumed to be 0.6), A_{eff} is the effective area of the opening and H_{eff} is the effective pressure head ($h_B - h_A$).

For large openings, integration over the submerged area of the opening is needed. Since this new method for assessing progressive flooding for decision support is intended to be approximate, also the integration can be simplified. In principle, this is done simply by

calculating the submerged area of the opening. Consequently, the resulting water flows are somewhat too large but this is a conservative approach, and thus well justified.

Conservation of Mass

At each time step the conservation of mass must be satisfied in each flooded room. The equation of continuity is:

$$\int_{\Omega} \frac{\partial \rho}{\partial t} d\Omega + \int_S \rho \mathbf{v} \cdot d\mathbf{S} = 0 \quad (4)$$

where ρ is density, \mathbf{v} is the velocity vector and \mathbf{S} is the surface that bounds the control volume Ω . For water flow the density is constant, resulting in:

$$\rho \int_S \mathbf{v} \cdot d\mathbf{S} = 0 \quad (5)$$

In practice this means that for each flooded room:

$$\frac{dV_w}{dt} = \sum_{i=1}^n Q_i \quad (6)$$

where V_w is the volume of water in the room and Q_i is the volumetric flow through an opening i that is connected to the flooded room.

Ship Motions

The ship motions are considered to be quasi-static. In principle this means that at each time step a static floating position of the ship is calculated based on the distribution of floodwater in the compartments. It is also possible to calculate the full stability curve at each time step¹. The stability curve can also be calculated after the flooding prediction for any moment in time, e.g. for the time when the heeling angle reaches the maximum value. For these calculations the floodwater is treated as

¹ E.g. for calculation of the s-factor



added weight and only the possible open-to-sea compartments are treated as lost buoyancy.

In addition it is assumed that the sea is calm. This simplification allows purely deterministic approach, based on the real flooding scenario. On the other hand the increased flooding due to waves is disregarded. However, based on the HARDER statistics over 90% of the collision damages occur in a sea state, where significant wave height is less than 2.0 m, *Tagg and Tuzcu (2003)*. For certain operational areas, such as the Mediterranean, the probability of damage in practically calm sea is even more likely, *Spanos and Papanikolaou (2011)*. Thus for a large passenger ship with dense internal subdivision², the effect of waves on the flooding process can be considered as minimal.

3.2 Principles of the Method

Progressive flooding forms chain(s) of flooded compartments. The principle idea is to keep track on these chains or routes. These are illustrated in Fig. 2. The starting point for each chain is the sea or a damaged compartment that is considered to be open-to-sea (lost buoyancy).

The mass balance in the flooded compartments is solved compartment by compartment, but in a reverse order. Thus the calculation is started from the compartment that was flooded last in the chain. This procedure is continued and finally the damaged compartments are solved. Thus the calculation is “sucking water from the sea” instead of the traditional approach, where floodwater is “pushed” from the sea to the compartments. This reverse order has been found out to significantly stabilize the solution of the governing equations, thus allowing explicit time integration with a long time step.

Water levels in the flooded compartments must remain descending along the chain of

flooded compartments, starting from the sea level. This is a valid limitation since the ship motions are assumed to be slow. This approach stabilizes the calculation in many cases, especially when there are large openings and the effective pressure heads are small. However, it should be noted that the flooding chains may be “broken” if a flooding opening becomes non-immersed due to changes in the floating position of the ship.

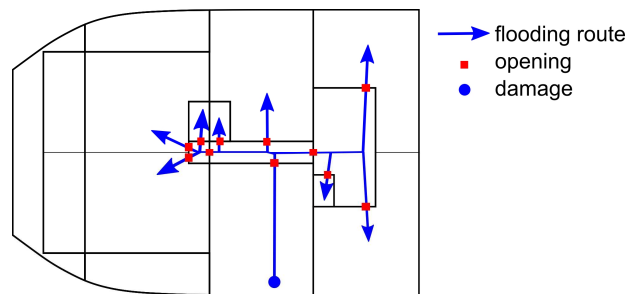


Figure 2: Chains of flooded compartments.

3.3 Calculation of Flooding Progression

Let us first consider the flow through a single opening between two flooded compartments. The situation is illustrated in Fig. 3. For simplicity, it is assumed that $h_1 > h_2$. Based on Bernoulli's equation (3), the volumetric flow rate through the opening is:

$$Q = C_d A \sqrt{2g(h_1 - h_2)} \quad (7)$$

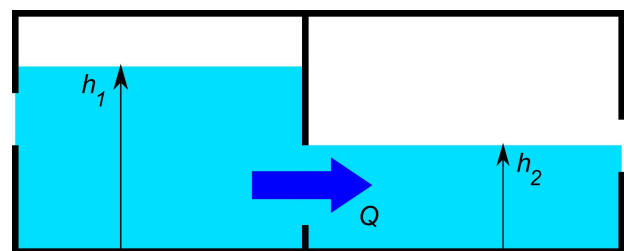


Figure 3: Water flow through an opening.

On the other hand, the flow rate can also be calculated as the time derivatives of the water volumes (when only a single opening is considered):

² No large open spaces like a vehicle deck

$$Q = -\frac{\partial V_1}{\partial t} = -\frac{\partial V_1}{\partial h_1} \frac{\partial h_1}{\partial t} = -S_1 \dot{h}_1 \quad (8)$$

or:

$$Q = \frac{\partial V_2}{\partial t} = \frac{\partial V_2}{\partial h_2} \frac{\partial h_2}{\partial t} = S_2 \dot{h}_2 \quad (9)$$

where S is the free surface area in the flooded compartment (assumed to be constant within time step).

The following notation is used in order to simplify the equations:

$$C_F = C_d A \sqrt{2g} \quad (10)$$

Also the effects of leakage and partially submerged opening can be taken into account by modifying this (dimensional) coefficient.

By combining the equations (8) and (9) and taking into account Bernoulli's equation (7), the time derivative of the pressure head ($h_1 - h_2$) is:

$$\begin{aligned} \dot{h}_1 - \dot{h}_2 &= -Q \left(\frac{1}{S_1} - \frac{1}{S_2} \right) \\ &= -C_F \sqrt{h_1(t) - h_2(t)} \left(\frac{1}{S_1} - \frac{1}{S_2} \right) \end{aligned} \quad (11)$$

Thus the following differential equation is obtained:

$$\frac{\dot{h}_1 - \dot{h}_2}{\sqrt{h_1(t) - h_2(t)}} = -C_F \left(\frac{1}{S_1} - \frac{1}{S_2} \right) \quad (12)$$

Integration of this results in:

$$\begin{aligned} \sqrt{h_1(t) - h_2(t)} &= \\ -\frac{1}{2} C_F \left(\frac{1}{S_1} - \frac{1}{S_2} \right) t + \sqrt{h_1(0) - h_2(0)} \end{aligned} \quad (13)$$

It should be noted that based on the notation (10), the equation (7) for the volumetric flow through the opening is:

$$Q = C_F \sqrt{h_1(t) - h_2(t)} \quad (14)$$

Consequently, the volume of water that flows through the opening during a time step Δt is obtained by integration:

$$\begin{aligned} \Delta V &= \int_0^{\Delta t} C_F \sqrt{h_1(t) - h_2(t)} dt \\ &= C_F \left[\sqrt{h_1 - h_2} \Delta t - \frac{1}{4} C_F \left(\frac{1}{S_1} - \frac{1}{S_2} \right) \Delta t^2 \right] \end{aligned} \quad (15)$$

Furthermore, the effective pressure head $h_1(t) - h_2(t)$ cannot be negative since the flow direction cannot change during the time step. Consequently, the time step Δt has to be limited to:

$$\Delta t = \min \left[\Delta t_0, \frac{2\sqrt{h_1 - h_2}}{C_F \left(\frac{1}{S_1} - \frac{1}{S_2} \right)} \right] \quad (16)$$

where Δt_0 is the initial time step. This situation is illustrated in Fig. 4.

The limitation is necessary for numerical stability but usually it is needed mainly in the beginning of the flooding process, or sometimes when a closed door collapses, since in these cases the flow rates can be large.

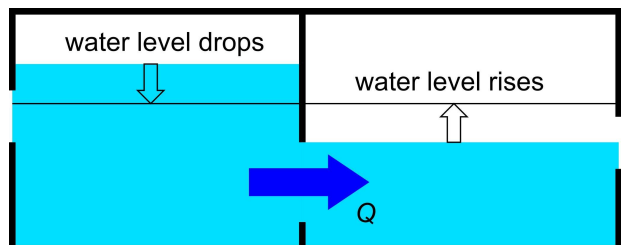


Figure 4: Limitation of time step due to fast flooding.



4. TEST CASES

4.1 Full-Scale Measurements

The first test case is slow progressive flooding through a small opening. The measurement data from the full-scale test with a decommissioned fast attack craft of the Finnish Navy was used. Details of the test case and corresponding time-domain simulations are described in *Ruponen et al. (2010)*.

The damage case is illustrated in Fig. 5. The damage hole is located in an empty side tank and the diameter of the hole is 0.25 m. Water progresses to equipment room and pump room, and finally the heeling is equalized when the side tank on the intact side is also flooded.

The comparison of measured and calculated heel angle is presented in Fig. 6. The simplified method for progressive flooding predicts well the maximum heeling angle and the qualitative development of the flooding process. Also the final equilibrium floating position is the same as measured and obtained with the detailed simulation, whereas the time-to-flood is slightly shorter.

The computation times are listed in Table 1. The calculations were done on a typical laptop and without a user interface for decision support. Thus the presented times do not include the update of the result tables and graphical representation of the situation.



Figure 5: Damage scenario for the full-scale flooding case.

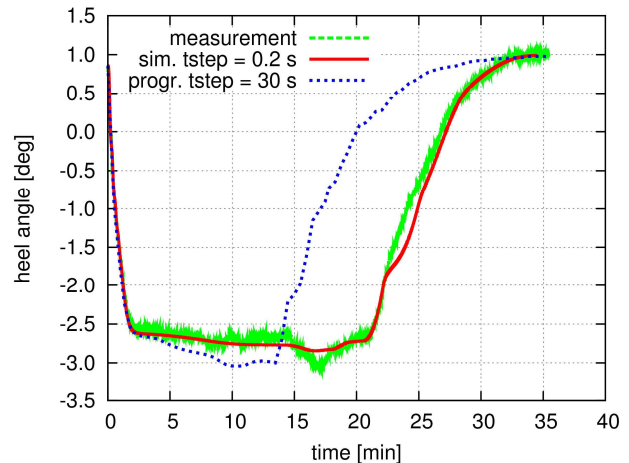


Figure 6: Comparison of heel angle for the full-scale damage case.

Table 1: Comparison of computation times.

Calculation method	Time (s)	%
Experiment (real time)	2100	100.0
Flooding simulation ($\Delta t = 0.2$ s)	245	11.7
Progressive flooding ($\Delta t = 30$ s)	9	0.5

4.2 Extensive Progressive Flooding

The second case study is two-compartment damage in a large passenger ship. The breach is in the lower decks and flooding progresses through staircases and lift trunks to the upper decks. The fire doors are closed and they start to leak, and some of them eventually collapse, under the pressure of the floodwater. The guideline values from the FLOODSTAND project are used for modelling the leaking and collapsing, *SLF 54/INF.8/Rev.1 (2011)*. The flooding scenario is illustrated in Fig. 7.

Results for heel angle and total mass of floodwater with different calculation methods are shown in Fig. 8 and Fig. 9, respectively. The computation times are listed in Table 2. The peak of the heeling angle is predicted rather well, even through the method is fully quasi-stationary. The time-to-flood is a little longer than in time-accurate simulation. However, this mainly concerns the phase of very slow flooding of the cabin areas on the deck 04 through the leaking closed fire doors.

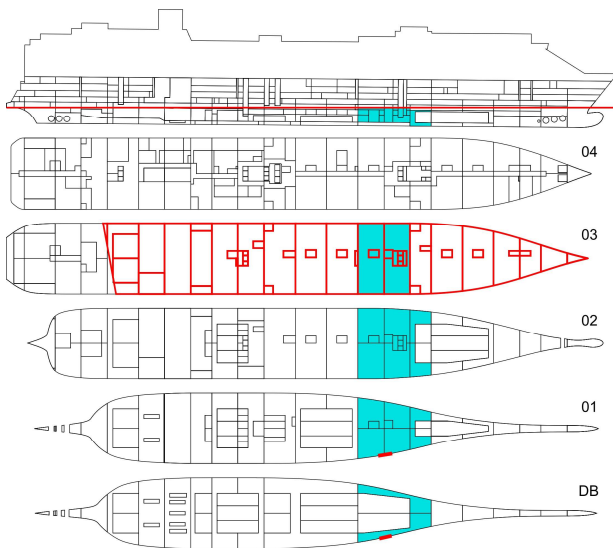


Figure 7: Damage scenario for progressive flooding through leaking and collapsing doors.

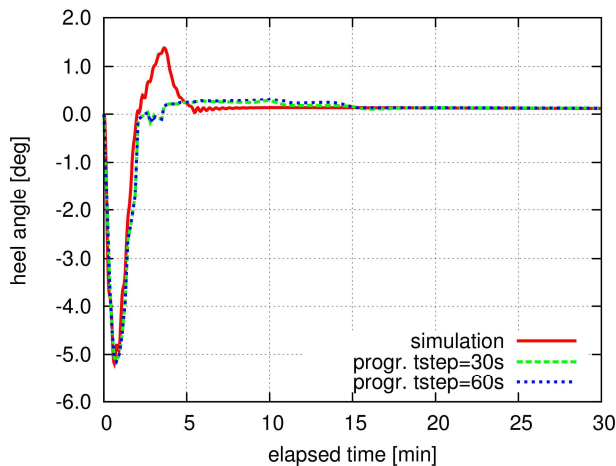


Figure 8: Comparisons of heel angle with different calculation methods.

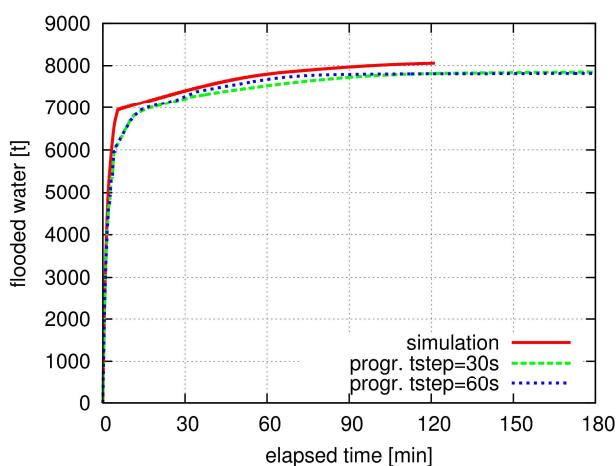


Figure 9: Comparisons of total floodwater mass with different calculation methods.

Table 2: Comparison of computation times.

Calculation method	Time (s)	%
Time-to-flood (from simulation)	7280	100.00
Flooding simulation ($\Delta t = 0.2$ s)	2915	40.04
Progressive flooding ($\Delta t = 30$ s)	16	0.22
Progressive flooding ($\Delta t = 60$ s)	14	0.19

The applied time step in the prediction method has only a small effect on the results, and moreover, the computation times are almost identical. This results from the fact that the longer time step of 60 s is more frequently automatically shortened, as defined in equation (16).

The prediction method does not find the equilibrium condition. The likely reason for this is circulating or oscillating flow between the flooded compartments.

4.3 Effect of Collapsing Doors

The flooding prediction method is intended to be used with a rather long time step in order to get the results as fast as possible. The downturn of this is the notable error in the time when the critical pressure head for the collapsing of a closed door is reached. The situation is illustrated in Fig. 10. This can also be clearly seen as a lower flooding rate during the early phases of the presented test case, Fig. 9.

On the other hand, the delayed collapsing of closed doors often results in larger heeling due to the increased asymmetry of the flooding, especially if there are longitudinal A-class bulkheads in the flooded compartments.

In the presented case study this effect seems to correspond very well with the transient dynamic heeling.

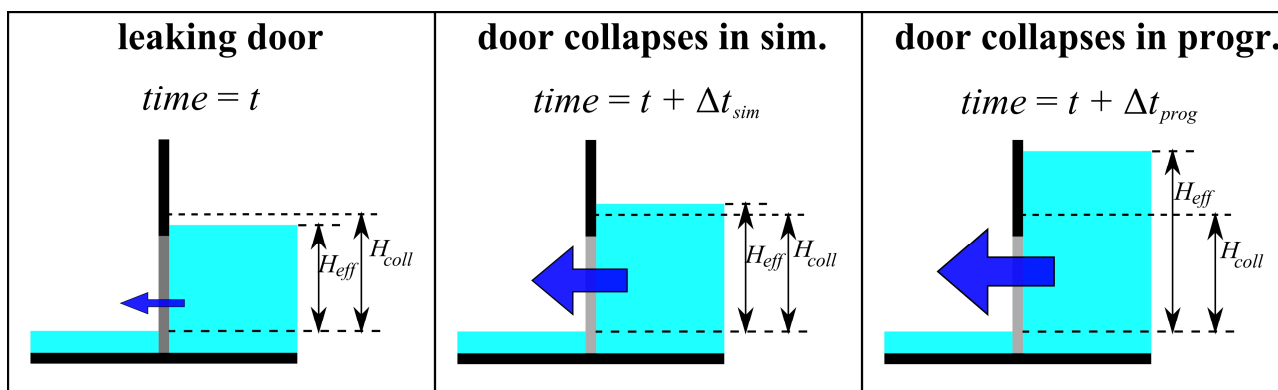


Figure 10: Applied time step Δt affects the time when a closed door collapses, i.e. when the effective pressure head H_{eff} exceeds the collapsing pressure head H_{coll} .

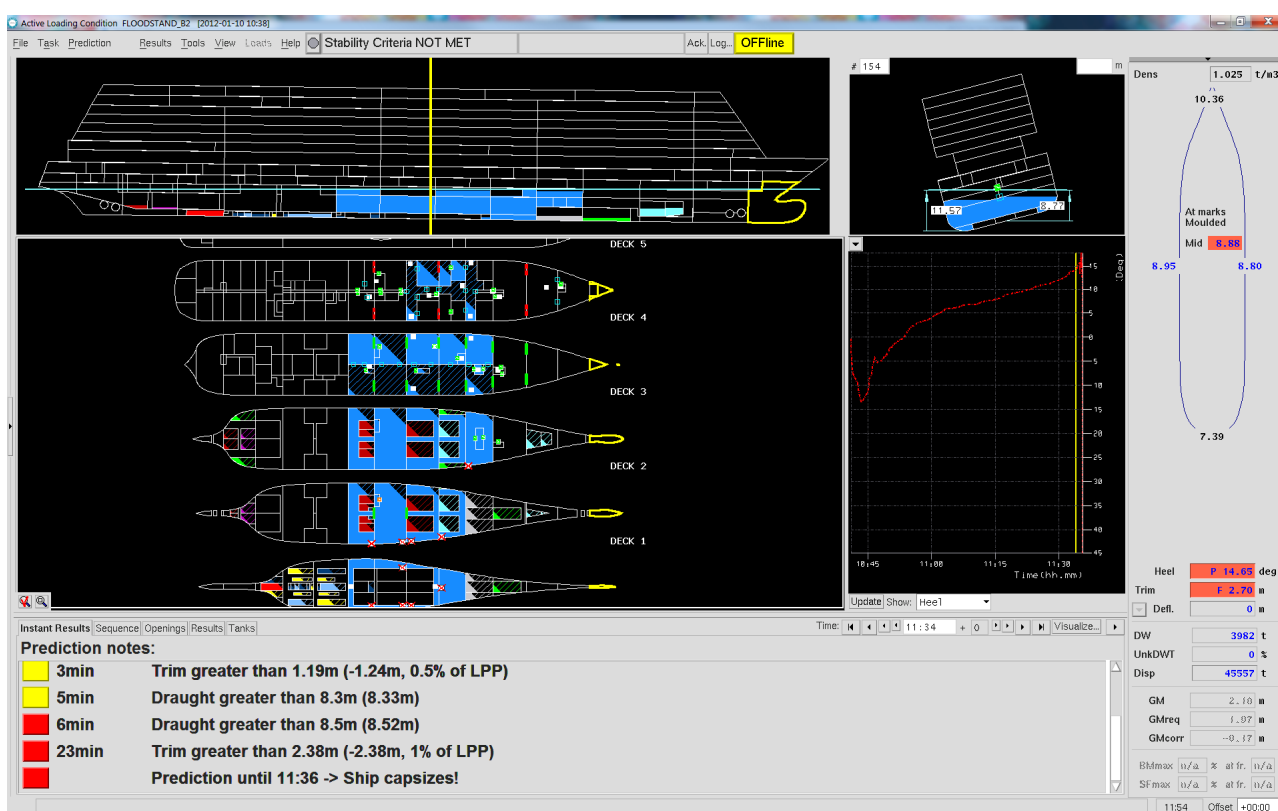


Figure 11: Graphical user interface for the flooding prediction tool, showing results of a damage scenario that ends in rapid capsizing.

5. FLOODING PREDICTION IN DECISION SUPPORT

The developed calculation method for fast prediction of progressive flooding has been implemented into a loading computer for demonstration of the use as a decision support tool. The user interface is shown in Fig. 11.

Onboard a damaged ship, the breach size and location are automatically estimated on the basis of the online level sensor measurement data when flooding is detected. However, the tool can also be used for training purposes, and thus the breach can also be defined manually.

During the computation process some relevant information, such as large heel angle,



is displayed immediately, Fig. 11. After the prediction, the results can be visualized either as an animation or for any time step. This kind of detailed analysis is considered to be very useful when the flooding prediction is used for training purposes.

6. CONCLUSIONS

A completely new approach for prediction of progressive flooding has been developed. It has been tested with two case studies. Firstly for flooding of a small fast attack craft, where full-scale measurement data is available, and then for two-compartment flooding case with a modern large passenger ship design. In both cases the main characteristics of the flooding progression are captured very accurately. This includes the maximum heeling angle and the eventual equilibrium floating position. The results are not time-accurate but the prediction of time-to-flood seems to be somewhat conservative (faster than reality).

The developed method is relatively fast. With the current graphical user interface a one hour prediction is typically completed in less than a minute. Moreover, this may still be improved as the actual computation time for calculation of progressive flooding is much shorter.

The obtained prediction for progressive flooding and the intermediate phases are considered to be very valuable information for decision support in a crisis situation onboard a flooded ship.

7. ACKNOWLEDGMENTS

The research leading to these results has received funding from the European Union's Seventh Framework Program (FP7/2007-2013) under grant agreement no. SCP7-GA-2009-218532 (FLOODSTAND project). The financial support is gratefully acknowledged.

8. REFERENCES

- IMO 2008, Guidelines for Flooding Detection Systems on Passenger Ships, MSC.1/Circ.1291, 8 December 2008.
- ITTC 2008, The Specialist Committee on Stability in Waves, Final Report and Recommendations, Proceedings of the 25th ITTC, Vol. II, pp. 605-639.
- Jasionowski, A. 2011, Decision support for ship flooding crisis management, Ocean Engineering, Vol. 38, pp. 1568-1581.
- Nilsson, R., Rutgersson, O., 2006, Damage Stability and Decision Support – How can we be better prepared and what questions do the teaching face?, Proceedings of the 9th International Conference on Stability of Ships and Ocean Vehicles STAB2006, Rio de Janeiro, Brazil.
- Ölcer, A. I., Majunder, J., 2006, A Case-based Decision Support System for Flooding Crises Onboard Ships, Quality and Reliability Engineering International; 22:59-78.
- Penttilä, P., Ruponen, P., 2010, Use of Level Sensors in Breach Estimation for Damaged Ship, Proceedings of the 5th International Conference on Collision and Grounding of Ships ICCGS 2010, Espoo, Finland 14-16.6.2010, pp. 80-87.
- Penttilä, P., 2012, Design Guidelines for Placement and Technical Requirements of Flooding Sensors in Passenger Ships, FLOODSTAND Deliverable D3.3, http://floodstand.aalto.fi/Info/public_download.html
- Ruponen, P., 2007, Progressive Flooding of a Damaged Passenger Ship, TKK Dissertations 94.
- Ruponen, P., Kurvinen, P., Saisto, I., Harras, J., 2010, Experimental and Numerical Study



on Progressive Flooding in Full-Scale, Transactions of Royal Institute of Naval Architects, Vol. 152, Part A4, International Journal of Maritime Engineering, pp. A-197-207.

SLF 54/INF.8/Rev.1, 2011, Modelling of Leaking and Collapsing of Closed Non-Watertight Doors, submitted by Finland, 28 October 2011.

Spanos, D., Papanikolaou, A., 2011, Considerations on the Survivability Assessment of Damaged Ships, Proceedings of the 12th International Ship Stability Workshop, Washington D.C., U.S.A., pp. 45-52.

Tagg, R., Tuzcu, C., 2003, A Performance-Based Assessment of the Survival of Damaged Ships: Final Outcome of the EU Research Project HARDER, Marine Technology, Vol. 40, No. 4, pp.288-295.



Time Dependent Survivability against Flooding of Passenger Ships in Collision Damages

Dimitris Spanos, *National Technical University of Athens-NTUA*, spanos@deslab.ntua.gr

Apostolos Papanikolaou, *National Technical University of Athens-NTUA*, papa@deslab.ntua.gr

ABSTRACT

The time dependency of the survivability of passenger ships in flooding accidents is shown to be confined within short times after flooding initiation. Both RoRo ferry and cruise type ships demonstrate such behaviour though as vessel types substantially differ with respect to the subdivision and the ship flooding process. The presented research is based on simulations for the probability to capsize and the flooding of ships in collision damages. The systematic fast character of capsize events is shown to be a consequence of large hull breaches. The IMO regulatory concept for *orderly abandonment* for damaged passenger ships, in addition to the *safe return to port* regulatory provisions, are discussed in view of the present results. The timely onboard damage identification and the enhancement of survivability requirements are suggested as rational measures for improved survivability and safety of people onboard passenger ships.

KEYWORDS: *Survivability; flooding; damage stability; time to capsize; passenger ships; orderly abandonment;*

1. TIME FOR ORDERLY ABANDONMENT

The IMO regulatory concept of *safe return to port* for flooding casualties became mandatory for passenger ships (of length 120 m and over) with the resolution *MSC.216(82)*, (2007), through the SOLAS Regulation II-1/8-1: *A passenger ship shall be designed so that specified systems remain operational when the ship is subject to flooding of any single watertight compartment.*

This regulation implements the first part of the guiding approach of IMO to passenger ship's survivability after flooding, according to which ships should be designed for *improved survivability* based on the concept that "*a ship is her own best lifeboat*". Depending on the casualty extent, passengers and crew should be able to either *stay safely on board* while the ship would always be able to proceed back to port at a minimum safe speed or, to *orderly*

evacuate and abandon the ship, if this is deemed necessary. The two folds of the above regulatory approach are:

- a. Safe return to port
- b. Orderly evacuation and abandonment

The goal to enhance the safety of passenger ships was adopted in response to the concerns (of late '90ties) regarding the timely evacuation of the *large passenger ships* in emergency situations and in view of their growing size and the number of people on board, particularly for post panamax cruise ships, which have reached capacities of more than 8,500 people.

Crucial parameters of these developments are the assumed *casualty threshold* namely the damage extent, and the *time frame* namely the time the ship remains viable and operative after damage. As long as the damage extent does not exceed the specified threshold (of one watertight compartment according to the safe



return to port provisions) then the passenger ships should survive infinitely and be able to proceed to a port, whereas when the threshold is exceeded (i.e. breach of two or more compartments) and abandonment becomes a possible event then *sufficient time* should be available to allow a safely and orderly evacuation and abandonment.

So far the *3 hours* survivability has been assumed as a *minimum* time criterion for the orderly abandonment, which includes the start time of the initiating event until all persons have abandoned the ship, *MSC 78/26*, (2004). This time duration is also assumed for the safe return to port provisions, *MSC.216(82)*, (2007). Meanwhile the general time requirement for the mustering, evacuation and abandonment is shorter and is set to *60 min* for passenger ships, or *80 min* for non-RoRo ships with more than three main vertical zones, *MSC.1/Circ.1238*, (2007).

So the time (either as *time to sink* or *to flood* or *to capsize*, or *survive time* and regardless of the particular differences) has become a crucial variable for the safety of damaged passenger ships and forms a major ship *design objective*, especially for larger passenger ships; namely the compliance of the ship design with the orderly abandonment by ensuring sufficiently slow sinking conditions in case of extended ship flooding.

While the *safe return to port* provisions (*MSC.1/Circ.1369*, 2010) are currently under the development of guidelines for implementation (*SLF 54/17*, 2012), the *orderly abandonment* is still an open challenge for passenger ships and is viewed as a long term objective, requiring further progress in the knowledge about the time-dependent survivability and particularly the relationship of the time with the design characteristics of ships, including the life saving appliances.

Nevertheless from the early days of these developments there were concerns about the usefulness of time to flood analyses (*SLF*

48/6/2, 2005). While in *Spanos and Papanikolaou* (2007, 2012) it was pointed out that orderly abandonment of RoRo/passenger ships was not a workable objective either. Extending this research it is illustrated here that cruise ships demonstrate similar characteristics for the time-dependent survivability in flooding. Thereby the identification of some modified objective proves necessary for properly addressing the safety of passengers in flooding casualties.

2. PROBABILISTIC ANALYSIS

2.1 Probability Simulation

Historical data of ship accidents demonstrate that the time a ship takes to sink may be notably scattered. Though the time scatter is not yet well attributed, this variation mostly depends on the particulars of the incident and the extent of hull breach through which flooding occurs.

For specific accident the expected time variation can be quite limited as then most of the determining parameters are specific too. But when considering the survivability of a ship throughout her life, at the stage of ship design, then a generic random hazard environment that accounts for the *wide* range of probable hull damages should be assumed. This results to a much wider variance for the capsize time (compared to a specific accident). This variance is a characteristic of each damaged ship and is evaluated in this research for two vessels, one RoRo ferry and one cruise ship.

The *time to capsize* for given ship is assumed as a random variable depending on the random environmental conditions during a flooding casualty, the random shape and location of the hull breach, and the ship's loading and local details of the flooded spaces. Its statistical probability distribution (when capsize is a possible event) can be approached with a basic *Monte Carlo* MC simulation. The



time to capsize is here sampled from a deterministic time domain simulation for the ship flooding and for a sufficiently large number of damage cases to meet statistical convergence of the results.

With this approach the domain of the possible damage cases is mapped to the sample space of the random variable of the time to capsize. Then the probability distribution can be statistically estimated over the sample space. The two-steps function f for the probability simulation is

$$f : D \xrightarrow{q} \Omega \xrightarrow{p} \mathfrak{R}$$

where D Domain of damage cases
 Ω Sample space of Time to Capsize
 q Mapping of domain
 p Probability measure

2.2 Deterministic Flooding Simulation

For specific damage cases the time to capsize is deterministically estimated with a widely established first-principles numerical simulation approach for ship's flooding in the time domain. The ship flooding problem might be formulated at different level of detail, including even high analysis with CFD techniques for the local flow through openings. However such an approach would not be practical for the probabilistic framework here addressed. Alternatively, an efficient formulation for the flooding rates of the flooded compartments can be based on the modified *Bernoulli* equation, an approach which is widely adopted by researchers, by *Spanos and Papanikolaou* (2001) too. Nevertheless this simulation approach is still computationally demanding and results to marginal applicability for the probabilistic analysis, but for the present research purposes the computational efficiency remains of low significance.

In the deterministic simulation the governing process for the ship flooding and any possible progressive flooding of the connected

spaces is the water flow through the assumed damage openings. The complex arrangement of the watertight compartments is modelled together with the interconnecting openings. Additional openings on the hull shell are assumed, namely the damage openings, through which the ship flooding occurs.

The floodwater mass inside each compartment is time variable and results from the sum of water flux through all the connected openings. The water flux across each opening is assumed to be described by the *Bernoulli* equation and modified with some linear discharge coefficient c_d which accounts for all deviations from the ideal flow. The elementary flux dq is

$$dq(t) = c_d \text{sign}(\Delta H) \sqrt{2g|\Delta H|} dA \quad (1)$$

where ΔH is the difference of water heads in both sides of the assumed opening and dA the elementary area. Here, plane quadrilateral openings were considered and constant ($=0.65$) discharge coefficients.

The ship may also change her position due to the weight of the accumulated floodwater inside the rooms. The nonlinear motion of the ship under the action of the floodwater, and the flooding of the compartments were calculated in coupled way over the time domain. For each run, a capsize event was conventionally detected when heel angle exceeded 45 degrees.

3. STUDY CASE PASSENGER SHIPS

Two passenger ships are discussed in the present investigation, one *RoRo ferry* (which corresponds to *MV Estonia*, sunk on 1994) and one medium size *Cruise* ship (a design concept introduced in the FLOODSTAND 2009-12 research project). The *RoRo* complies with former stability requirements (SOLAS'74) and is characterized by a single, undivided car deck of maximum exploitable area. The *cruise* is developed in compliance with the latest



regulations (SOLAS'09). The main dimensions of the ships are given in Table 1.

Table 1: Main dimensions of the study case passenger ships.

Dimension	RoRo ferry	Cruise
L _{pp} (m)	137.4	216.8
B (m)	24.2	32.2
T (m)	5.4	7.2
D _{DECK} (m)	9.1	9.8
Displ. (tn)	12300	35000

As demonstrated in Figure 1 and Figure 2 both vessels have longitudinal subdivision arrangement comprising of fifteen watertight compartments abaft the collision bulkhead. The bulkhead deck is that of the vehicle deck for *RoRo ferry* and that of No 3 (blue line) for the cruise ship.

For the *RoRo ferry* the modelling of superstructures extended up to one deck over the car deck. The car deck space is assumed watertight and the lower compartments are connected to the upper spaces through the central casings located on the car deck. For the modelling of the cruise ship all decks up to No 7 (three decks above the bulkhead deck) were taken into account. Thereby, with the present modelling (of decks) each watertight compartment (as defined with the transverse bulkheads) is further subdivided vertically into rooms which are interconnected with openings that correspond to doors, stairways and lift wells, whereas all the watertight doors on the transverse watertight bulkheads were assumed always closed as appropriate.

The rooms were treated as unrestricted spaces with homogeneous permeability. Inner boundaries (like A-class) were not modelled, though such boundaries might slow down the flooding in function of the strength (in deformation and collapse) of the non-watertight doors and openings on these boundaries, with evident effect in lower depths of floodwater. Since the collision damages are assumed to extend along the full draught the particular

impact of inner boundaries on the time to flood should be limited to the later stages of flooding.

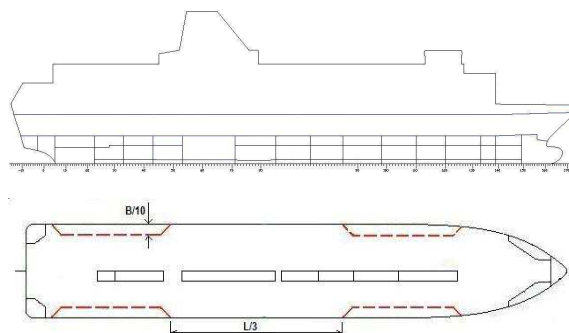


Figure 1: Subdivision layout of RoRo ferry.

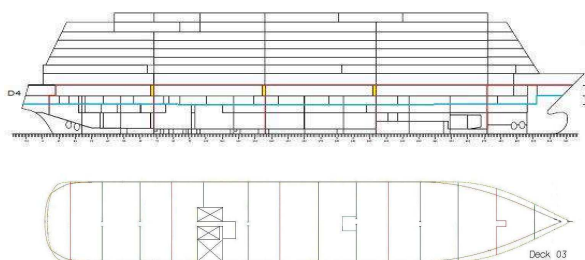


Figure 2: Subdivision of the cruise vessel.

Some basic modifications of the original subdivision layouts were also considered, which were applied above the bulkhead deck and may affect the later stages of the ship flooding too. In this way, four watertight side casings were developed on the car deck of the *RoRo ferry* (dashed lines in Figure 1). For the cruise ship, three transverse bulkheads on deck No 5 could extend upwards the main vertical zones by two decks above the original bulkhead deck (double line on deck No 4 of Figure 2).

4. DOMAIN OF COLLISION DAMAGE CASES

Damage cases that result to ship flooding are determined by the assumed damage openings on the hull shell, the ship's loading condition and the sea waves prevailing during ship flooding incidents. All these parameters were assumed as random variables. The assigned probability models for the opening

dimensions and the significant wave height correspond to collision damages as updated by the HARDER (2000-2003) research project and which form the background of current SOLAS'09 damage stability regulations.

According to the assumed probability model for the significant wave height in collision damages and for *any* ship type, the significant wave height is distributed up to 4.0 m, while a notable percentage of 40% of collision accidents regards collisions in *calm water*. If consider also the small wave conditions (i.e. < 1.0 m) the percentage remarkably raises up to 70%.

The probability for the damage length was that of Figure 3, a piecewise linear function, with some probability (8%) for lengths between 0.15-0.30 of the ship length. Distribution regards the *dimensionless* damage length and the *average* damage equals 6.6% of the ship length. SOLAS'09 assumes this distribution too, however truncated for larger lengths above 60 m, which affects ships of length over 200 m. The here considered cruise ship of length 216 m is marginally affected from such truncation.

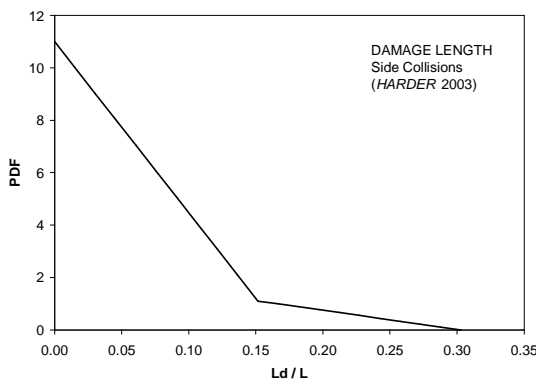


Figure 3: The assumed probability of *damage lengths*.

The probability of ship's displacement (loading conditions) was distributed between three discrete conditions and in line with the SOLAS 2009 regulation, namely 40% for each of the full and the partial draughts and 20% for the light draught condition. The initial stability (metacentric height) for the intact ships was

empirically distributed as shown with Figure 4. The range of *GM* may represent some wider operational conditions, besides minimizes the probability of testing for particular conditions.

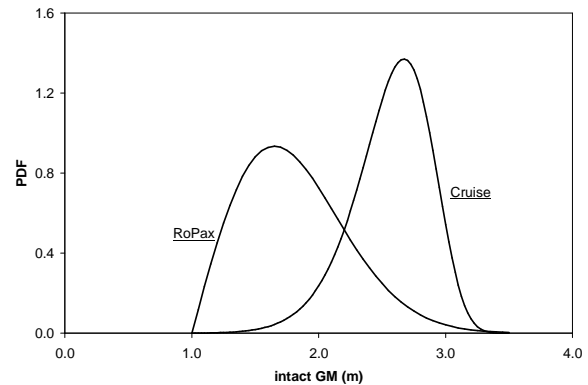


Figure 4: The assumed probabilities for *GM* of the intact ships.

5. PROBABILITY OF TIME TO CAPSIZE

The probability distribution of the time to capsize for the two tested ships and the subdivision modifications was estimated with the probability simulation method and are shown in Figure 5 and Figure 6.

These distributions correspond to ship capsize conditions, whereas for the survive conditions the time is infinite. The probability to capsize within 3 *hours* from the collision incident converges to $4.9 \pm 0.5\%$ and $2.4 \pm 0.3\%$ for *RoRo* ferry and cruise vessel respectively (were the 10% uncertainty is associated with Monte Carlo simulation).

According to these results, the capsize events for both ships were limited within 15 *min* from the assumed damage incident. Such time is rather short and is notably shorter than the set threshold of 3 *hours*, which is the assumed objective for the orderly abandonment of the passenger ships in case of flooding, and still less than 1 *hour* which is the evacuation requirement.

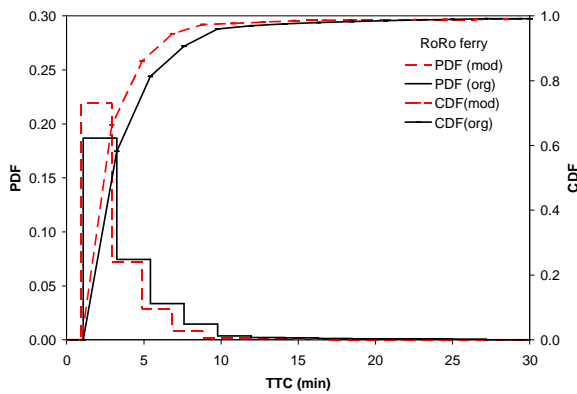


Figure 5: Probability of the *Time to Capsize* for the damaged *RoRo ferry* capsizing in calm water.

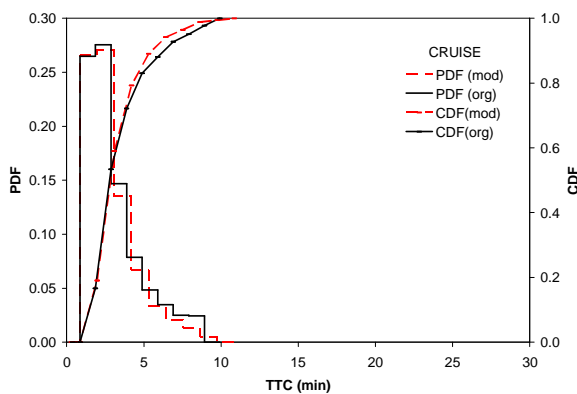


Figure 6: Probability of *Time to Capsize* for the damaged *Cruise ship* capsizing in calm water.

Insignificant effect from the assumed subdivision modifications was recorded too (red dashed lines of Figure 5 and Figure 6). The particular design modifications are mainly effective in later stages of ship flooding, and since here the capsizing events occurred in short times this effect was eventually limited.

Capsizing events for the *RoRo ferry* occur strictly only when the car deck gets damaged. When the hull breach is limited to below this deck, thus the car deck space remains intact, then this large intact volume contributes with large buoyancy and restoring that the ship capsizing is not feasible any more. Note that up-flooding might happen here only through the central casings (Figure 1).

The time to capsizing is distributed within ranges of the same width for both ships, though

the cruise ship is three times larger than the *RoRo*. This is related to the size of the damage opening, which is proportional to the ship length and then to the flooding rates. For the *RoRo ferry* the actual damage sizes are 36% lower than the damages assumed for the cruise ship. Nevertheless, because the capsizing times result short enough, even if equal damage sizes would be assumed for both ships, e.g. those of *RoRo*, then the range of the time to capsizing for the cruise ship would result wider however still short and lower than 20 min.

The corresponding distribution of the damage length for the capsizing events is plotted in Figure 7 and Figure 8, which may well explain the short capsizing times as recorded for both ships. There the capsizing cases are obviously related to large damage openings only. The average damage length converges to 0.19L and 0.18L for each vessel (while the incident damage length averages to 0.066L, whereas 8% exceeds 0.15L as commented in Figure 3). Such large lengths correspond to multiple damaged watertight compartments, namely three or more. Thereby, ships capsize for the large openings only, and then flooding is trivially fast (large damage areas) and the recorded times are short accordingly.

In earlier investigation, *Spanos and Papanikolaou* (2007, 2012), the fast capsizing was shown to be the characteristic behaviour of the damaged *RoRo ferries* in waves too. These ships are vulnerable to the flooding of the car deck which can take place only in the presence of waves exceeding some critical wave height. As long as this critical wave height is exceeded, then the time to capsizing rapidly shortens. And then the time-dependent survivability in waves is limited in short times similarly to the present results.

Cruise ships, differently to *RoRo ferries*, usually do not have large undivided spaces near the sea surface, like the car deck of *RoRo*, and the significance of waves for the distribution of the time to capsizing is expected to be limited. The flooding process for well subdivided ships

follows a sequential flooding of rooms in a cascade mode. The sea waves may not alter the qualitative characteristics of the distribution of Figure 6. This argument is further supported by the low probability of collision in larger waves, as discussed in the previous section for the passenger ships.

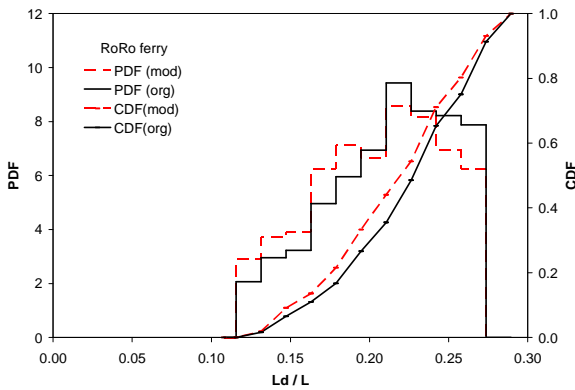


Figure 7: Estimated probability of the *damage length* for *RoRo ferry* capsizing in calm water.

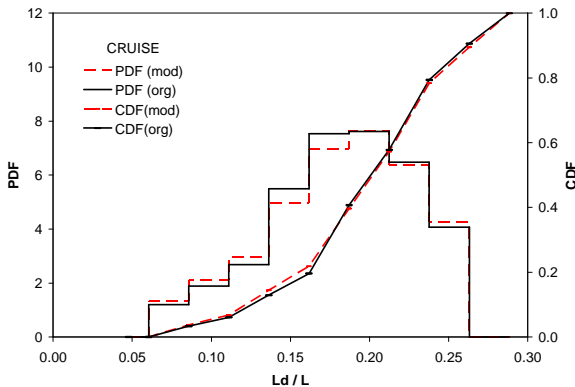


Figure 8: Estimated probability of the *damage length* for *Cruise ship* capsizing in calm water

Capsize in calm water was trivially correlated with zero or very low residual stability, as detailed with Figure 9 and Figure 10. Approximately 80% of cases were fully unstable (zero stability) while for the rest cases the GZ_{max} was low and below 0.10 m. This limit is straightly comparable to the current limit of 0.05 m used by SOLAS 2009 (Ch. II-1, Part A, Reg. 7.2) to define the fully survive capabilities for intermediate stages of flooding. The present results indicate that the current regulation may fail by 10% (i.e. to the probability to exceed 0.05 m). Thus some

refinement of the current s-factor would make sense.

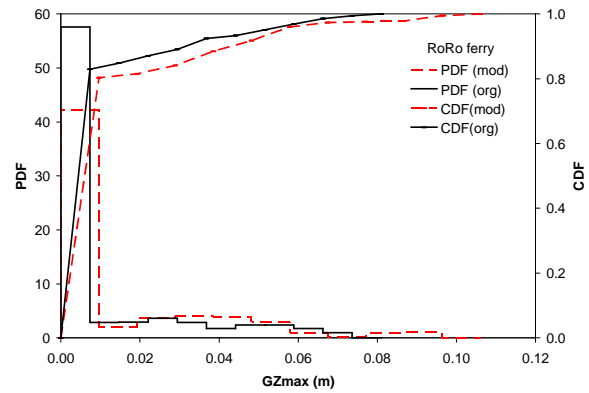


Figure 9: Probability of GZ_{max} for *RoRo ferry* capsizing in calm water.

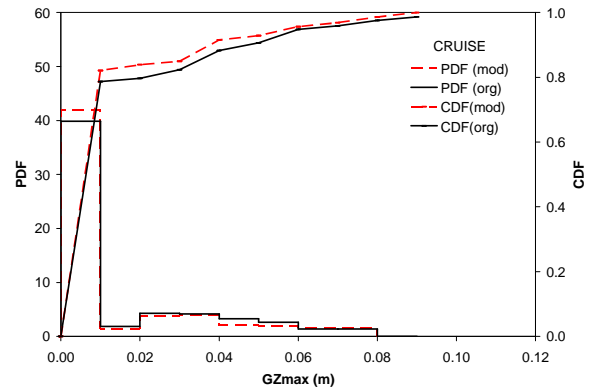


Figure 10: Probability of GZ_{max} for *Cruise ship* capsizing in calm water.

6. DISCUSSION AND FUTURE RESEARCH

The collected results (Figure 5, Figure 6) suggest that when capsizing is a likely event for a passenger ship, then the ship should be abandoned as faster as possible. Capsizing occurs in remarkably shorter times than it would be needed for an orderly abandonment. The 3 hours objective or even the 1 hour requirement for evacuation (*MSC.1/Circ.1238*, 2007) which is closer to the actual evacuation times, are both much longer times than actually required in case of accident. Thus unconditionally, the *orderly abandonment* appears infeasible, while optimistically, it might be only partially accomplished.



The objective for orderly abandonment concerns damages which exceed the current threshold of *one* compartment for the *safe return to port*. The present research points out that loss of passenger ships is fast event and it is connected to three or more compartments damages. While for two compartment damages ships do not capsize and then abandonment is unnecessary in principle.

Therefore, the *timely identification* of the damage case, namely whether it encompasses two or three compartments, proves to be crucial for the onboard safety assessment. The timely identification of survive conditions would allow to keep people on board as much and as long it is assumed safe, instead of ordering the abandonment of the ships and sending people unnecessarily to the sea.

However when considering actual damage incidents then any onboard assessment remains today a challenge, as the onboard and timely identification of actual damage and survivability still suffer by remarkable uncertainty. To the extent this uncertainty can be minimized then the estimated ship's survive time converges to either too long (survive conditions) or short time (capsize conditions). Independently of the identification and assessment capabilities the situation appears practically binary.

The difficulties of the identification are even more stressed if one takes into account that the survivability of the damaged ships is assumed within a probabilistic framework, like the current SOLAS regulations, where deterministic casualty thresholds are not applied (namely full survivability for two or three watertight compartments). And if such deterministic thresholds would be applied then the probabilistic principles and all related advantages would be practically abandoned.

The design of ships with time-dependent survivability and capsize times longer than the present time requirements appears an ineffectual objective. Instead, the *improvement*

of survivability might be always reasonably achieved via shifting present safe boundaries to higher levels, namely by enhancing the typical survivability of the damaged ship through increased survivability requirements.

It is noted that the presented research regards side collision damages, and similar analysis should be extended to different damages, like groundings, for completeness and further strengthening of the findings. Nonetheless because of the fact that ships' capsize occurs trivially for large damages, which are connected with large flooding rates, it could be early inferred that capsize due to grounding damages will be accordingly of short time.

7. CONCLUSIONS

The presented investigation explored the general probability distribution of the time to capsize for two passenger ships of different type in collision damages and was concerned with the detection of possible conditions related to slow ship capsize.

The results demonstrated, however, that sinking and capsize of passenger ships occur systematically in *short times* after the damage incident, as a consequence that ship's loss is trivially connected with large sizes of damage. The estimated times are far less than the current regulatory objective for orderly evacuation and abandonment, and make this objective appearing not workable (at least for the subdivision arrangements tested).

The survivability of damaged ships results practically to be time-independent, while measures for improved survivability seem not sufficient to control the capsize time. Thereby the timely *onboard identification* of the actual damages and survivability proves the most important function, and measure, towards an improved safety of people on passenger ships.



Taking into account the current difficulties for reliable onboard damage identification, an alternative and reasonable objective is always to seek for *higher survivability* requirements (subdivision required index) as counter-measure to the risk of fast capsizing.

Closing this article it is recalled that the present analysis concerns the collision hazard as it is defined through the damage statistics assumed from the current stability regulations (SOLAS'09). Other hazards, like groundings, should be also investigated to complete the research for the *time* characteristics of the sinking passenger ships due to flooding.

ACKNOWLEDGEMENTS

The financial support of this research from the European Commission research project FLOODSTAND (Integrated Flooding Control and Standard for Stability and Crises Management), FP7-RTD-218532 is acknowledged. The European Commission and the authors shall not in any way be liable or responsible for the use of any knowledge, information or data presented, or of the consequences thereof.

REFERENCES

- FLOODSTAND (2009-2012), "Integrated Flooding Control and Standard for Stability and Crises Management", EU research project, FP7-RTD-218532, 2009-2012.
- HARDER (2000-2003), "Harmonization of Rules and Design Rational, European Commission Research Project", FP5, DG XII-BRITE.
- IMO, MSC 78/26, (2004), Report of the MSC on its 78th session, by Secretariat-General, May 28.
- IMO, MSC 82-24-Add.1 (2007), Resolution MSC.216 (82), "Adoption of Amendments to the International Convention for the Safety of Life at Sea", 1974, as amended, Annex2, by the Secretariat, January 12.
- IMO, MSC.1/Circ.1238, (2007), "Guidelines For Evacuation Analysis For New And Existing Passenger Ships", October 30.
- IMO, MSC.1/Circ.1369, (2010), "Interim Explanatory Notes for the Assessment of Passenger Ship Systems' Capabilities after a Fire or Flooding Casualty", 22 June 2010.
- IMO, SLF 48/6/2 (2005), "Passenger Ship Safety", Report of the SDS Correspondence Group, by Sweden and the United States, June 24.
- IMO, SLF 54/17 (2012) Report To The Maritime Safety Committee, by Secretariat, February 3.
- Spanos, D. and Papanikolaou, A., (2001), "On the Stability of Fishing Vessels with Trapped Water on Deck", Journal Ship Technology Research-Schiffstechnik, Vol. 48, Sep.
- Spanos, D. and Papanikolaou, A., (2007), "On The Time to Capsize of a Damaged RoRo/Passenger Ship in Waves", Proc. of the 9th International Ship Stability Workshop, Hamburg, Germany, August 30-31.
- Spanos, D. and Papanikolaou, A., (2012), "On the Time dependent Survivability of ROPAX Ships", Journal of Marine Science and Technology, Vol.17, No.1, pp.40-46, March, DOI 10.1007/s00773-011-0143-0.





An Explicit Progressive Flooding Simulation Method

Hendrik Dankowski, Institute of Ship Design and Ship Safety,
Hamburg University of Technology, dankowski@tu-harburg.de

ABSTRACT

Several severe ship accidents in the past were caused by the flooding of the internal compartmentation of these ships. In most cases the occurred flooding scenario is very complicated and it is not directly obvious, how a certain damage case caused the actual loss of the whole ship. To figure out the most likely scenario, it is necessary to analyze many different possible flooding paths.

For more detailed accident investigations and to prevent such accidents in the future, a new numerical progressive flooding simulation method is developed. A direct approach is chosen, which computes the flux between the compartments based on the Bernoulli equation and the current pressure heads at each intermediate step. The flooding paths are modeled by using graph theory. This quasi-static approach fills the gap between dynamic seakeeping simulations and purely hydrostatic damage calculations.

The developed method is validated by investigating the accident of the S.S. Heraklion occurred in 1966. In addition, the results of the simulation method are compared with model tests of a barge performed by Ruponen at the Helsinki University of Technology in 2006.

Key Words: *Progressive Flooding; Sinking; Ship Design; S.S. Heraklion; Accident Investigation; Ship Safety*

1. INTRODUCTION

Several progressive flooding simulation methods for damaged ships have been developed in recent years (Vassalos et al., 1998; Papanikolaou et al., 2003; Palazzi and de Kat, 2004; Schreuder, 2005; Ruponen, 2007, to mention but a few). These simulations allow to better understand the floating behaviour of ships after damage. The method presented here focuses on the main physical effects and represents a fast, direct approach of solving the underlying mathematical model allowing to investigate several design options in a short period of time.

The simulation method is implemented in the ship design environment E4, a first-principal ship design software used and developed at our institute together with partners from the german shipbuilding industry. In doing so, direct

access to the whole ship data model and already implemented computational algorithms like hydrostatic evaluations is granted.

2. PHYSICAL MODEL

The flooding process is mainly driven by pressure differences leading to relatively slow internal water flows. The surfaces of the water levels are expected to remain mostly horizontal. These kind of flows are quite accurate described by the Bernoulli equation.

2.1 Basic Equations

The flooding of a floating object is driven by certain pressure differences at openings leading to the in- or egress of flood water. These fluxes



can be idealized by the incompressible, stationary, non-viscous and rotational-free Bernoulli equation given in Equation 1 formulated for a streamline connecting point a and point b:

$$\frac{p_a - p_b}{\rho g} + \frac{u_a^2 - u_b^2}{2g} + z_a - z_b - \frac{\varphi_{ab}}{g} = dz. \quad (1)$$

Any dissipative effects are modeled by a semi-empirical discharge coefficient proportional to the flux velocity. If the outflow is free (left side of Figure 1), the pressure height difference is

$$dz = \frac{p_a - p_b}{\rho g} + \frac{u_a^2}{2g} + z_a - z_0. \quad (2)$$

The flux through a deeply submerged opening (right side of Figure 1) is independent of the location z_0 of the opening and given by

$$dz = \frac{p_a - p_b}{\rho g} + \frac{u_a^2 - u_b^2}{2g} + z_a - z_b. \quad (3)$$

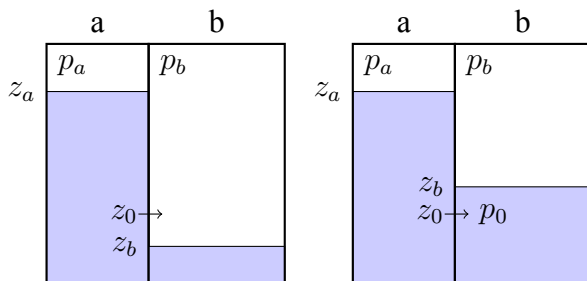


Figure 1 Small openings

This pressure height difference dz yields a fluid velocity

$$u = \sqrt{2g \cdot dz}. \quad (4)$$

The integration of the velocity over the area of the opening under the assumption of a perpendicular flow direction leads to the total flux

$$\begin{aligned} \frac{\partial V}{\partial t} = Q &= \int_A \mathbf{u} \cdot d\mathbf{A} = \int_A \mathbf{u} \cdot \mathbf{n} dA, \\ Q &= \int_A u dA. \end{aligned} \quad (5)$$

2.2 Large Openings

More challenging is the determination of the flux over large openings, since the cross section area and the fluid velocity may vary over the opening. In general, the flux is given by the integral

$$Q = \int_A u dA = \int_t u(z(s)) \cdot y(s) ds, \quad (6)$$

where the velocity u is best described as a function of the earth fixed vertical direction z . The width y of the opening varies in the plane of the cross section. To model any shape of opening, it is described as a plane polygon oriented arbitrary in space. For the flux integration it is discretized in several z -stripes (see Figure 2).

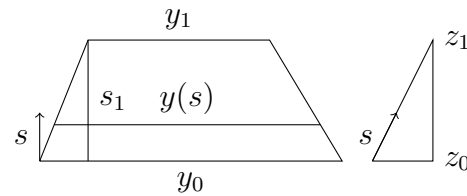


Figure 2 Stripe in z -direction

In this case the relation between the two directions z and s is linear:

$$z(s) = z_0 + s \cdot \frac{z_1 - z_0}{s_1}. \quad (7)$$

The free outflow flux of each stripe can be determined analytically by the definite integral

$$\begin{aligned} Q &= -\frac{2}{3 s_z} \cdot \sqrt{2g} \cdot [y_1 \cdot h_1^{\frac{3}{2}} - y_0 \cdot h_0^{\frac{3}{2}} \\ &+ \frac{2(y_1 - y_0)}{5(z_1 - z_0)} \cdot (h_1^{\frac{5}{2}} - h_0^{\frac{5}{2}})], \end{aligned} \quad (8)$$

with

$$\begin{aligned} \alpha &= \frac{p_a}{\rho g} - \frac{p_b}{\rho g} + \frac{u_a^2}{2g}, \quad s_z = \frac{z_1 - z_0}{s_1}, \\ h_1 &= z_a - z_1 + \alpha, \quad h_0 = z_a - z_0 + \alpha. \end{aligned}$$

Among others Schröder and Zanke (2003) showed that the flux through a rectangular weir is given to be:

$$Q = \frac{2}{3} B \sqrt{2g} h^{\frac{3}{2}}. \quad (9)$$

This is a special of Equation 8 with a constant width $B = y_0 = y_1$ of an upright cross section ($s = 1$), no pressure difference $\alpha = 0$ and height $h = z_a - z_0$ together with $h_1 = 0$.

This kind of flux integration can be performed in the same way for further basic opening shapes like circular holes or manholes.

2.3 Flooding System

The connections between the compartments of a ship by openings are nicely modeled by directed graphs. A simple example is shown in Figure 3 describing the validation case B from Ruponen (2007), which will later be investigated in more details. This graph is de-

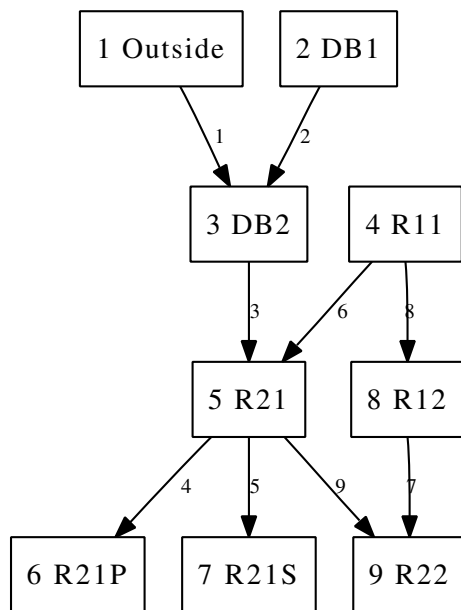


Figure 3 Simple subdivision graph

defined by the edges representing the openings and the neighboring nodes representing the compartments. Each node is defined by an ID number and a name. The direction of the edge defines the sign of the flux through the opening. Using this kind of definition for the flooding system is a very convenient and direct way. All methods and algorithms developed in graph theory can simply be applied to flooding systems of ships. This way questions like “Which neighbors belong to a certain compartment in question?” can easily be answered.

2.4 Mass Balance

Using a flooding graph, the total flux of one compartment is given by the sum over all openings belonging to this compartment. For example, the flux for compartment R21 (No. 5) shown in Figure 3 is given by

$$Q_5 = Q_{o3} - Q_{o4} - Q_{o5} + Q_{o6} - Q_{o9}.$$

Integrating the flux to one compartment in the time domain gives the amount of water transported in a certain time step from one compartment to its neighbor(s):

$$V = \int_t Q(t) dt. \quad (10)$$

This transported water volume leads to new filling levels in the compartments, since the fluid volume in each compartment changes. The determination of this new filling has to be done iterative, since the compartment geometry is usually arbitrary and the filling level depending on the current waterline and fluid volume is not given analytically, especially if the ship is heeled and/or trimmed.

2.5 Flux Integration

The system of ordinary differential equations to be solved is of first order and nonlinear. The volume flux \dot{V} to each compartment must be equal to the flux Q_o through all corresponding openings, where the opening fluxes depend nonlinear on the water heights respectively the water volumes in each compartment.

$$\dot{V}(t) = Q_o(t) \quad (11)$$

$$Q_o(t) \rightarrow f(V(t)) \quad (12)$$

By using a simple Euler forward scheme assuming a constant flux during one time step, the compartments are decoupled, since the new flux depends only on the water heights of the last time step.

$$dV = V^{(t_1)} - V^{(t_0)} = dt \cdot Q_o^{(t_0)} \quad (13)$$

To better account for the nonlinearity and the coupling of the compartments, a kind of



weighted predictor-corrector scheme for the fluxes through the openings is applied

$$dV = dt \cdot (\omega Q_o^{(t_m)} + (1 - \omega) Q_o^{(t_0)}), \quad (14)$$

while the intermediate value $Q_o(t_m)$ is the flux after the prediction step and ω is the relaxation factor. This inner iteration can be sketched as follows:

- Predict opening fluxes
- Propagate predicted volumes assuming a constant flux
- Calculate new filling levels
- Recompute opening fluxes based on these new fillings
- Correct volume fluxes acc. to Equation 14
- Reset volumes and propagate again, recompute filling levels based on the corrected flux and proceed

This strategy avoids efficiently the flux direction change during one time step caused by the explicit characteristic of the method. In practice, only two inner iterations (one predictor-corrector step) are sufficient to reduce the fluctuations and to significantly stabilize the whole simulation.

A direction change in the flux happens, if the filling levels of two neighboring compartments are very close and the propagated volume assumed by a constant flux leads to a change of the sign of the flux. How often this overflowing happens depends on the time step and the size of the opening. Even for a very small time step, the flux only becomes zero if the extrapolated volume change leads to exactly equal filling levels of neighboring compartments in the next time step. In contrast, the weighted predictor-corrector scheme smoothes the flux by using also the flux opening values from the last time step. However, the influence of the filling level fluctuations on the integrated values like the ship motion is usually small.

2.6 Propagation of Full Compartments

If one or more neighboring compartments are completely filled with water, the corresponding compartments are coupled. The following holds in that situation:

- The total flux of a full compartment must be zero
- The water flux from partly filled compartments must be propagated through these full compartments
- The only free variable remaining is the pressure

These conditions lead to a nonlinear system of equations, which must be solved to find the unknown pressure values. The system can be composed by finding a sub-graph of all connected and fully flooded compartments.

As an example, consider again the flooding system illustrated in Figure 3 and the situation when the DB2 compartment is completely filled with water. In that case, the water coming from outside must be propagated through DB2 to the other compartments, while the total flux to DB2 must be zero leading to the following equation:

$$0 = A_1 \cdot \sqrt{\rho g \cdot (z_1 - z_3) + p_1 - p_3} - A_2 \cdot \sqrt{\rho g \cdot (z_2 - z_3) + p_2 - p_3} - A_3 \cdot \sqrt{\rho g \cdot (z_3 - z_5) + p_3 - p_5}. \quad (15)$$

This nonlinear equation has to be solved for the only unknown value p_3 . An analytical solution may only be found for less than three openings connected to a completely filled compartment, but the resulting nonlinear system is usually not very large and can easily be solved with standard iterative algorithms like Powell's method described in Moré et al. (1980).

2.7 Conditions of Openings

To allow the modeling of, for example, breaking doors or windows during flooding, a

pressure head criterion is used for the openings. If the water column height above the opening becomes larger than this defined value, the opening breaks and stays open. This technique may also be used to introduce conditional flooding. A time dependent closure (or opening) of, for example, watertight doors are modeled by a time-dependent discharge coefficient. In the same way the leakage of doors as described in Ruponen and Routi (2011) might be considered.

2.8 Air Compression

In some cases, it might also be necessary to take into account trapped air, although in most cases the assumption of fully ventilated tanks is valid. But the occurrence of air pockets might especially be important for the later phases of a sinking sequence. This effect is taken into account by assuming an ideal gas and the compression to be isotherm according to Boyle's law. The air pressure of the corresponding compartment with the trapped air is increased by the reduction of air volume:

$$p_0 \cdot V_0 = p_1 \cdot V_1. \quad (16)$$

An extension of this simple approach is to model the effect that at a certain pressure, parts of the air solutes in water. The concentration of air in water is proportional to the pressure according to Henry's Law (Henry, 1803):

$$c = \frac{m_{lw}}{V_w} = k \cdot p. \quad (17)$$

The concentration c is linear proportional to the pressure p by a certain constant k . The so-called Henry constant k depends on the mixture of the gas and the temperature. This results in a nonlinear relation for the pressure increase caused by the air compression. Here the pressure increase is lower compared to the case when neglecting the solubility of air in water.

The solute air slowly diffuses in the whole floodwater and may result into the occurrence of bubble flows, if the pressure decreases again in other regions.

2.9 Simulation Overview

To summarize one time step of the flooding simulation, the different parts are listed in the following:

1. Check the opening pressure conditions
2. Perform pressure iteration for full tanks
3. Flux determination of remaining openings
4. Inner iteration for higher-order integration of fluxes
5. Propagation of water volumes
6. Update of filling levels and determination of full tanks
7. Optional air compression
8. Iteration of new floating equilibrium
9. Check of convergence

This is repeated for each time step until either the requested simulation time is reached or a convergence criteria is fulfilled.

3. VALIDATION BY MODEL TESTS

3.1 Introduction

As a first validation of the developed method a comparison with model tests of a box-shaped barge performed at the Ship Laboratory of the Helsinki University of Technology by Ruponen (2006) is made. These model tests were later also used as a validation for Ruponen's simulation method presented in Ruponen (2007). It is also part of the ITTC benchmark test presented in van Walree and Papanikolaou (2007) and used by several other authors to validate their flooding simulation methods (Santos et al., 2009; Strasser et al., 2009; Corrigan and Arias, 2010).



The comparison with one of the test cases is presented in the following, even though the two other test cases were successfully reproduced as well. The naming of the test cases is the same as in Ruponen (2007). The simulated results from the new method are marked with the prefix “calc D.”, the measured values with “meas R.” and the computed values by Ruponen with “calc R.”.

3.2 Computational Setup

The geometry of the barge and the openings together with the loading conditions and all other relevant model data is given in Ruponen (2006), the main dimensions are summarized in Table 1. With these data, a detailed computational model of the same scale as used in the model tests has been defined including the relative large wall thicknesses of the model. The discharge coefficients for the openings are taken from Ruponen (2007).

Table 1 Main dimensions of the barge

Length (oa)	L_{OA}	4.0	m
Height	H	0.8	m
Moulded Breadth	B	0.8	m
Draft design	T	0.5	m

For the simulation a time step of 0.2 seconds is used (compared to 0.05 seconds used by Ruponen), if not mentioned otherwise. The overall simulation of 8 minutes real-time for test case B takes on an ordinary computer approximately 10 seconds for this simple model setup.

3.3 Test Case B

This test case is a very challenging one, since it does not only includes air compression effects, but also complex down-flooding events. The setup is shown in Figure 4.

The simulated trim and heave motion given in Figure 5 and 6 show a very good agreement, even though both simulated results are too small at the end compared to the measured ones. But this can be well explained by the escape of air

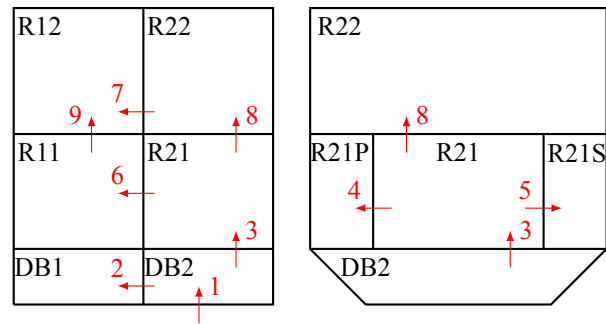


Figure 4 Openings for test case B

leading to a higher total amount of floodwater. In addition, the effect of the selected time step is studied for the trim motion and also shown in Figure 5. The results for larger time steps (5 and 2 seconds) deviate significantly from the measured results. If the time step is reduced below 0.5 seconds, the results clearly converge to the final results. This short convergence study show, that a time step of 0.2 seconds is an appropriate choice for this test case in model scale.

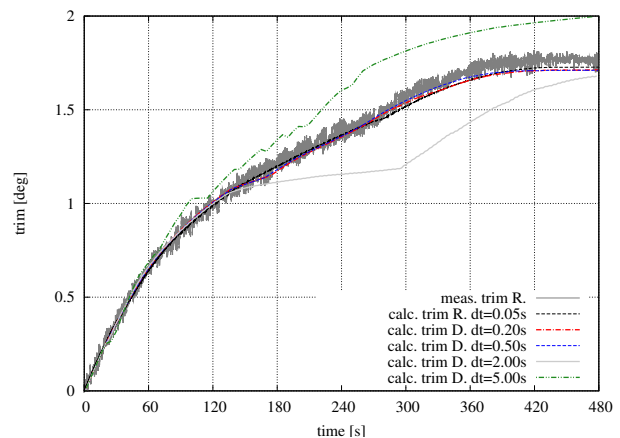


Figure 5 Trim Motion

Looking at the lower double bottom compartments, the compressed air pocket in DB1 plays an important role. The water levels are shown in Figure 7 and the overpressure (difference to ambient pressure) is given in Figure 8, together with the results for a smaller time step of 0.05 seconds. Again, the simulated results are both very similar.

As already mentioned in Ruponen (2007), an air bubble flow occurred, which allowed some air to escape, resulting in a lower overpressure in that compartment and allowing more water

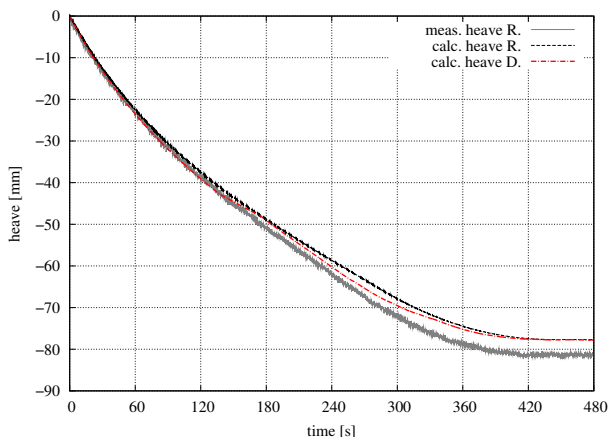


Figure 6 Heave Motion

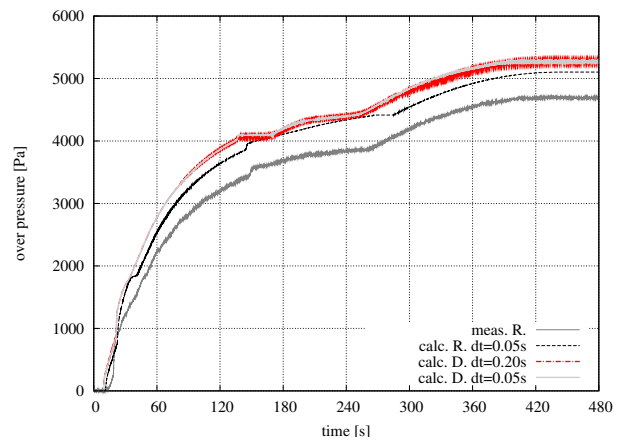


Figure 8 Overpressure in DB1

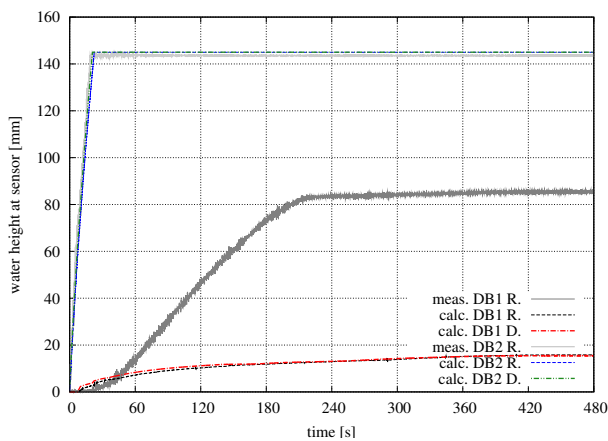


Figure 7 Water Heights in DB1 and DB2

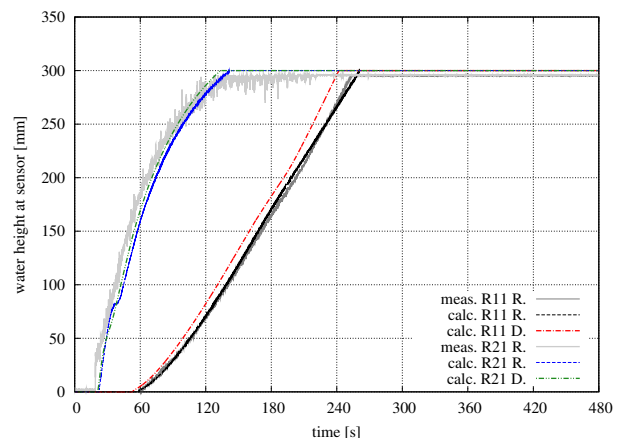


Figure 9 Water Heights in R11 and R21

to enter. Before these bubbles can actually be formed the air probably solutes in the water. This effect may be modelled by taken into account Henry's law, as already mentioned in subsection 2.8. Since the overall effect is quite small, this has not yet been implemented in the current simulation model, but further investigations are planed for the future. The higher oscillations in the overpressure are caused by the larger time step, but these are not reflected by the water height in that compartment. These oscillations are significantly reduced at the smaller time step of 0.05 seconds, as shown in the additional graph in Figure 8.

The water levels in the part between double bottom and upper deck are shown in Figure 9 and 10. It can be observed, that the new simulation predicts a slightly faster rise of water, but this might simply be caused by small differences in the geometry modelling.

The sensitivity of the whole system may best be observed from the water levels of the upper deck compartments shown in Figure 11. Especially in the first phase of flooding, larger differences may be observed. At the end, both simulations reach the same level and the measured values are slightly higher. The reason for that was already explained by the air compression effect. What makes this flooding case quite complicated is the fact, that especially the aft compartment R12 is flooded by an up-flooding opening from R11 but also from the front compartment R22.

3.4 Summary of the Model Test Validation

The new developed method has been successfully validated by the prescribed model tests. All relevant effects have been modelled,

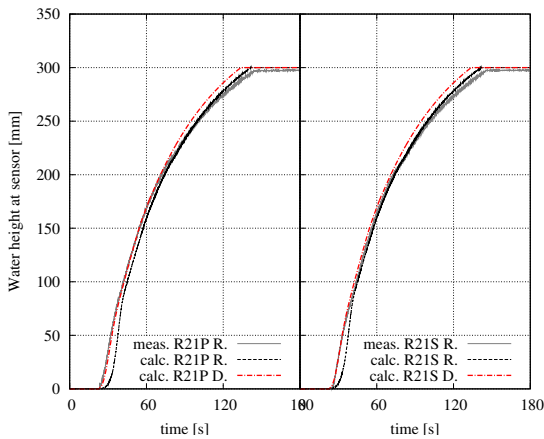


Figure 10 Water Heights in R21P and R21S

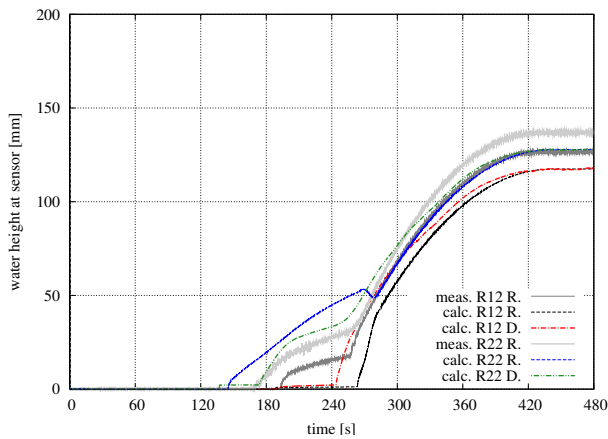


Figure 11 Water Heights in R12 and R22

even though the air compression treatment may require some improvement, but the overall influence is not very large. The new developed method and the one from Ruponen give very similar results. Both methods are based on the same physical assumptions, while the solution of the equations are different. The here presented method chooses a more direct, explicit approach, together with a simple higher-order approach for the flux integration. The solution of a small nonlinear system of equations is only required for fully flooded compartments.

Additionally, in this new approach the compartments are only indirectly coupled in the time domain and not in between one time step, as it is the case in Ruponen, where a pressure-correction equation based system is solved in each time step.

It should also be mentioned, that the simulation of model tests serves very well as a first validation case, but in reality a lot more uncertainties like the correct estimation of the discharge coefficients exist. For this reason, a real accident from the past will be examined in more detail in the following section.

4. THE HERAKLION ACCIDENT

The accident of the S.S. Heraklion will be reinvestigated with the described simulation method to validate the developed method and to better understand the flooding events leading to the loss of the ship.

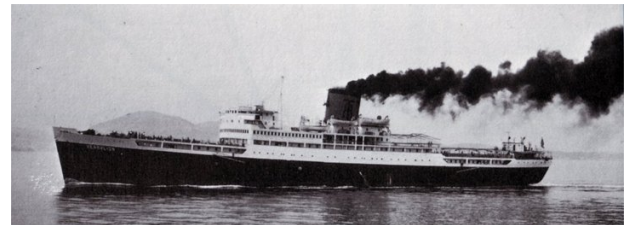


Figure 12 Photo of the S.S. Heraklion

4.1 Introduction

The S.S. Heraklion capsized and sank in heavy weather on the 8th of December 1966 in the Aegean Sea on its voyage from Crete to Piraeus causing the loss of over 200 people's life. The main cause of the accident has been appointed by the former investigations to be a large reefer truck on the vehicle deck, which started to move in rough sea conditions leading to the damaging of a large side door. The resulting water ingress finally resulted in the capsizing and sinking of the vessel.

The main focus of this investigation is to describe the general flooding events after the side door was lost. Even though the accident occurred in heavy weather leading to large ship motions, the general rough flooding events may be described by the here presented quasi-hydrostatic flooding simulation in the time domain neglecting the dynamic components of motion.



The spreading of the ingressed floodwater through the internal subdivision of the ship leads to additional heel and trim moments. As the fluid shifting moments of each compartment are directly taken into account by the prescribed method, a correction of the vertical center of gravity due to free surface effects is in this case not required.

4.2 General Description of the Vessel

The ship was originally built as the S.S. Leicestershire by Fairfield Shipbuilding and Engineering Company in Glasgow in 1949. It was later converted to a passenger ferry sailing on routes in the Aegean Sea. The main particulars are given in Table 2.

Table 2 Main dimensions of the Heraklion

Length (oa)	L_{OA}	146.456	m
Length (bp)	L_{BP}	143.256	m
Moulded Breadth	B	18.288	m
Draft design	T	4.528	m

4.3 Previous Investigations

The available documents from previous investigations are listed in the following:

- Official Accident Report (Frangoulis, 1968)
- Official Report of the Accident Investigation Board (AEENA, 1968)
- Additional Accident Report (Georgiadis, 1968)
- Accident Report (Wendel, 1970)
- Technical Drawings by the Greek naval architect A. Theodoridis

Based on these available documents, the ship data model and the accident situation is reconstructed.

4.4 Final Voyage Condition

The loading condition during the final voyage is thoroughly reconstructed based on the information provided in the accident reports and the capacity plan. In addition, the heeling moment due to wind and the cargo shift as described in Wendel (1970) leads to a heeling angle of approximately 11.5 degrees. These additional heeling moments are modeled as a transversal shift of the center of gravity leading to a cosine shape of the heeling lever. This is assumed to be a well approximation of the wind lever. The condition of the vessel prior to flooding is summarized in Table 3.

Table 3 Assumed condition prior to flooding

Total Mass	Δ	7547	t
Draft at A.P.	T_a	6.02	m
Draft at F.P.	T_f	2.85	m
Heel (pos. stbd)	φ	11.5	deg
Metacentric Height	\overline{GM}	1.14	m

For the flooding simulation it is required to model the whole buoyancy body of the ship including all superstructures, even though these parts are not weathertight or even watertight according to the regulations. In addition, all internal and external openings, like windows and doors on the upper deck, are defined including pressure head conditions for the collapsing of some of the openings. A total number of 81 openings are defined connecting 70 compartments including the ones on the upper decks.

An illustration of the computational model including all openings is shown in Figure 13. Certain special openings are marked with a red dot. These are the large side door of the vehicle deck leading to the first initial water ingress and two doors on the upper decks relevant for the later phase of flooding.

4.5 Most Likely Scenario of the Accident

With the prescribed condition of the ship, a first flooding simulation is started. The interest-

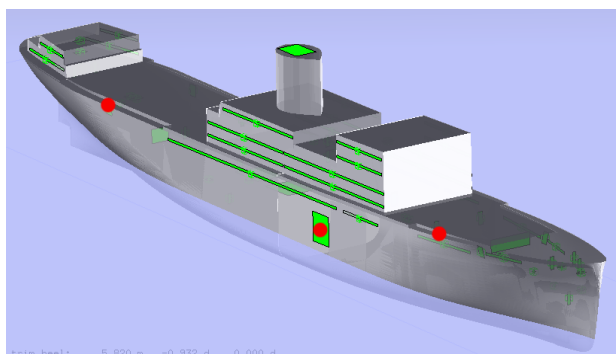


Figure 13 Data model with openings

ing first outcome is, that the flooding stops only after a few moments. This is simply caused by the fact that the water levels of the vehicle deck and the outside sea become equal. This situation is certainly not a very stable one, since one must still keep in mind that this is only a quasi-static simulation. To overcome this pseudo stable point, only a small additional heeling moment is added, represented by an increase of 11 cm of the vertical center of gravity. This critical point will be discussed in more detail in subsection 4.6 by a sensitivity analysis driven by the vertical center of gravity.

The results of the flooding simulation for some significant values are shown in Figure 14 together with a selection of frames of some interesting time steps given in Figure 16. The spreading of the floodwater can be depicted from the volume fillings in percent shown in Figure 15 for some selected compartments.

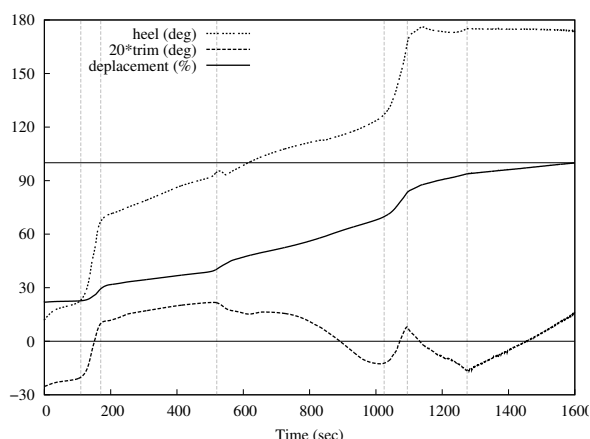


Figure 14 Values over time

After 110 seconds the heeling dramatically increases for around one minute, before the upper decks are immersed providing additional buoyancy for some time. At the same time the Dining Room and the Tourist Saloon, which are located on the upper deck above the Car Deck, start to fill up with water mainly through left open side doors. Due to the forward trim, the flooding of the Tourist Saloon located in the aft of the ship is a little delayed.

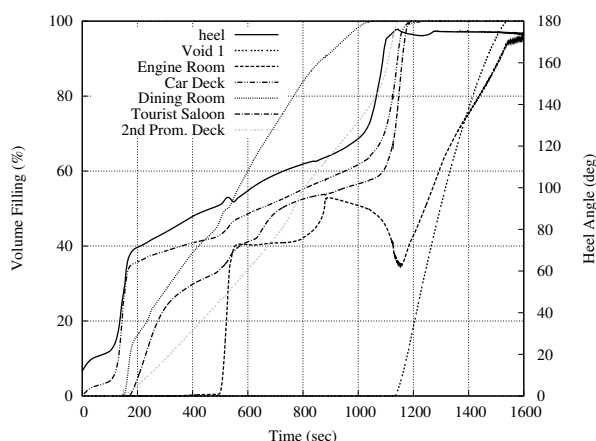


Figure 15 Fillings of selected Compartments

Then the heeling constantly increases until 1000 seconds with a small bump at around 500 seconds, which is caused by the immersion of the funnel leading to a significant down-flooding to the Engine Room also shown in Figure 15. The additional water in the lower parts of the ship stabilizes the ship shortly at that point.

After this long constant and relatively slow increase in heel, the ship moves from around 120 degrees up to 170 degrees in just one minute. This is explained by the immersion of the superstructures from the other side. After around 1300 seconds a stationary state is started when only the displacement and the trim increase almost linear, while the heel stays constant. During this time the void spaces below the vehicle deck, represented by Void 1 in Figure 15, are flooded from inspection manholes located on the portside. At around 1600 seconds (or 27 minutes) the ship vanishes from the sea surface.

4.6 Sensitivity Analysis of Vehicle Deck Immersion

As already mentioned in the last section, the first phase of the vehicle deck flooding through the damage side door may result in a pseudo-stable situation when both water levels become equal. In Figure 17 the heeling angles over time for different vertical centers of gravity (short: \overline{KG}) are plotted. First, the flooding stops only after 1-2 minutes. After a critical value of 11 cm increase in the \overline{KG} is exceeded, the heeling ascends again very fast. The instabil-

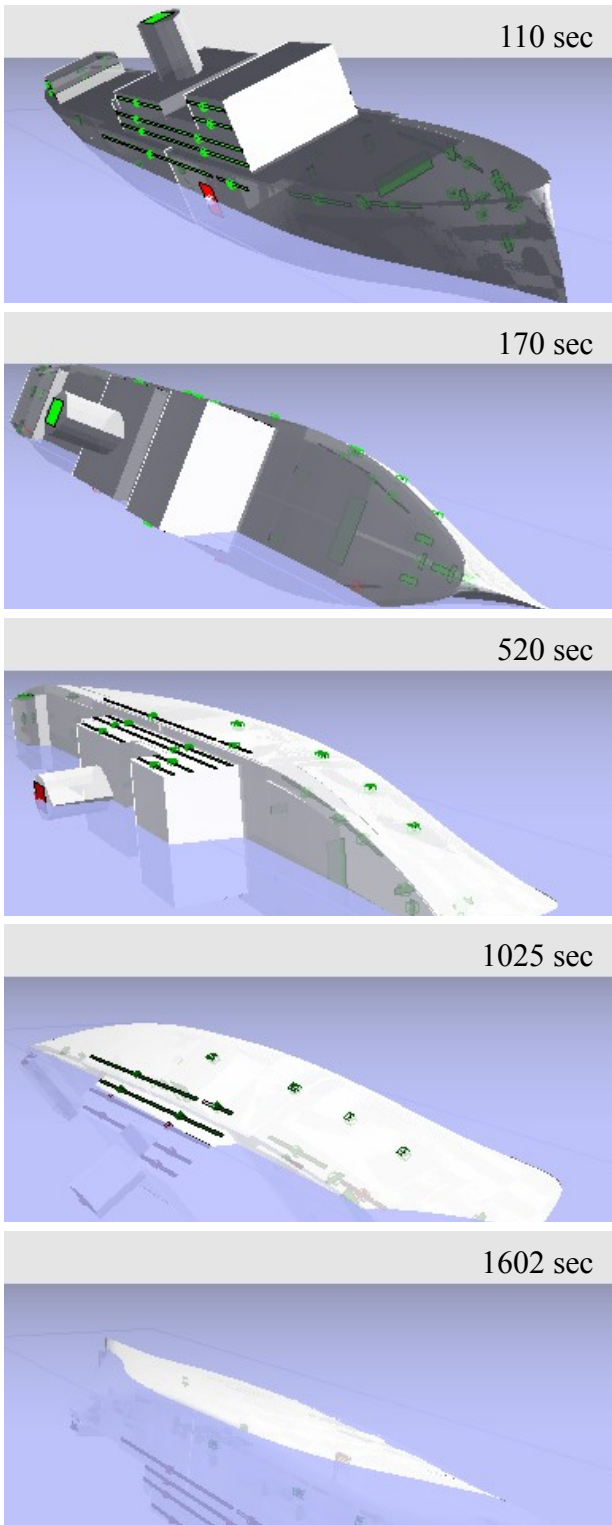


Figure 16 Frames of flooding simulation

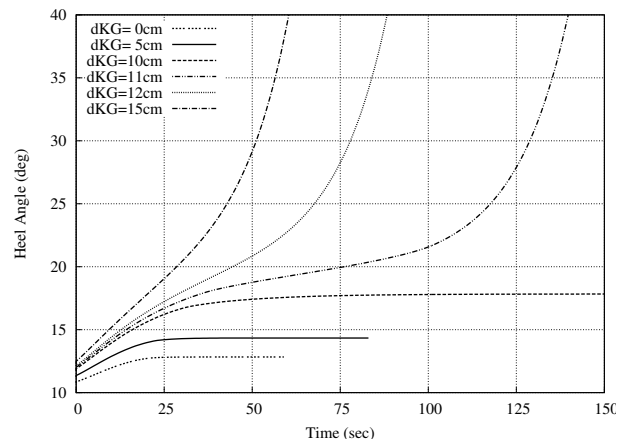


Figure 17 Heel angles of \overline{KG} -Variation

ity of this situation becomes more obvious when leverarm curves are compared for the initial \overline{KG} value. In Figure 18 three different curves are shown. The red and green curves are the lever-

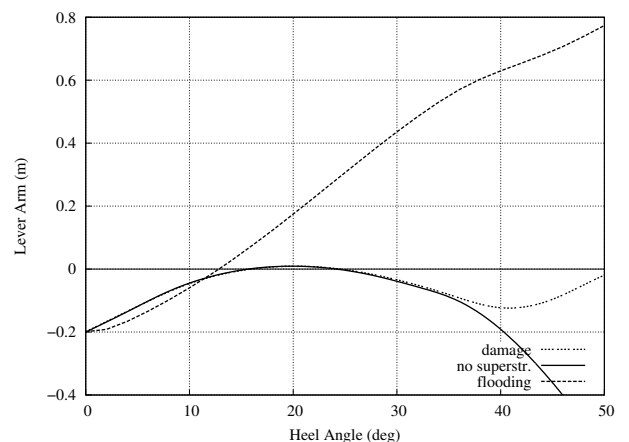


Figure 18 Leverarm curves

arm curves of the case, when the vehicle deck is assumed as a damaged compartment with the



lost buoyancy method. For the red curve, the upper superstructure is also included in the buoyancy body, but its influence is only important for angles greater than 40 degrees. The blue leverarm curve is computed after the flooding simulation with a fixed water mass on the vehicle deck.

At this point the question arises what a leverarm curve should represent. It actually illustrates the capability of a ship to withstand additional heeling moments. This means that if flooding simulations are performed, the leverarm curve becomes also time dependent. If an additional heeling moment is taken into account in the situation of a flooded compartment connected to the outside with equal water levels, the additional heel will again lead to a floodwater ingress. But this makes it quite complicated to compute a complete leverarm curve.

One proposal is to successively increase a heeling lever and to perform a flooding simulation for a specified duration until a new heeling angle is reached. This gives again a series of heeling angles together with leverarms. The interesting parameter in that case would be the time duration of one heeling lever step. The blue leverarm curve shown in Figure 18 actually represents the case when this duration is set to zero. The classical damage case leverarm calculation (represented by the other two curves) is equivalent to the case, when for each heeling angle the flooding simulation is performed until convergence, but only if the initial flooding case is already converged as well.

4.7 Summary of the Accident Investigation

In general, the simulated heeling behaviour after the water ingress matches quite well with the statements of the witnesses mentioned in the previous investigations. The whole behaviour of the ship is reasonable. More advanced seakeeping simulations may provide more accurate results, but the average flooding process is well reproduced by the here presented methods. A very interesting aspect is actually the shown sensibility depending on small changes in the $\bar{K}\bar{G}$ rep-

resenting additional heeling moments. A time dependent calculation of leverarm curves will be an interesting challenge for further investigations.

5. CONCLUSIONS AND OUTLOOK

The new developed flooding simulation method has been successfully validated by standard benchmark model tests and the reinvestigation of the Heraklion accident. This method represents a fast and robust tool for the simulation of floodwater ingress in the time domain and gives very reasonable results for the behaviour of damaged ships in still water conditions. The fast run-time of around 30 seconds for the flooding simulation of the Heraklion accident allows to study several different scenarios in a very short time.

For the aspect of air compression, the solubility of air in water might be an interesting aspect to be implemented in the future. Another aspect would be to model the leakage of doors and other structures, which is probably especially important for accident investigations involving passenger ships. In addition, further investigations relating to leverarm curves in flooding simulations should be carried out. This aspect may also be interesting for the assessment of intermediate stages of damage cases for standard damage calculations according to the current SOLAS regulations.

More practical accident investigations with other ship types like e.g. passenger vessels have to be carried out to further improve and validate the developed method. It may also be possible to couple the developed method with ship motion seakeeping simulation codes.



6. REFERENCES

- AEENA. Official Report of the Accident Investigation Board Heraklion. Technical report, AEENA, 1968.
- Philippe Corrigan and Ana Arias. Flooding simulations of ITTC and SAFEDOR benchmarks test cases using CRS SHIPSURV software. In 11th International Ship Stability Workshop, 2010.
- V. Frangoulis. Official Accident Report Heraklion. Technical report, National Technical University of Athens, 1968.
- S. Georgiadis. Additional Accident Report Heraklion. Technical report, unknown, 1968.
- William Henry. Experiments on the Quantity of Gases Absorbed by Water, at Different Temperatures, and under Different Pressures. Philosophical Transactions of the Royal Society of London, 93:29–274, 1803. doi: 10.1098/rstl.1803.0004. URL <http://rstl.royalsocietypublishing.org/content/93/29.short>.
- Jorge J. Moré, Burton S. Garbow, and Kenneth E. Hillstrom. User Guide for MINPACK-1. Technical Report ANL-80-74, Argonne National Laboratory, Argonne, IL, USA, August 1980.
- Lionel Palazzi and Jan de Kat. Model Experiments and Simulations of a Damaged Ship With Air Flow Taken Into Account. Marine Technology, 41:38–44, 2004.
- A. Papanikolaou, D. Spanos, E. Boulougouris, E. Eliopoulou, and A. Alissafaki. Investigation into the Sinking of the Ro-Ro Passenger Ferry EXPRESS SAMINA. In STAB Conference, number 8 in International Conference on the Stability of Ships and Ocean Vehicles, 2003.
- Pekka Ruponen. Model Tests for the Progressive Flooding of a Boxshaped Barge. 2006.
- Pekka Ruponen. Progressive Flooding of a Damaged Passenger Ship. PhD thesis, Helsinki University of Technology, 2007. URL <http://lib.tkk.fi/Diss/2007/isbn9789512290130/isbn9789512290130.pdf>.
- Pekka Ruponen and Anna-Lea Routi. Guidelines and criteria on leakage occurrence modelling. In FLOODSTAND Project. Napa Ltd and STX Finland, 2011. URL <http://floodstand.aalto.fi>.
- T. A. Santos, P. Dupla, and C. Guedes Soares. Numerical Simulation of the Progressive Flooding of a Box-Shaped Barge. In 10th International Conference on Stability of Ships and Ocean Vehicles, 2009.
- Martin Schreuder. Time Simulation of the Behaviour of Damaged Ships in Waves. Master thesis, Chalmers University of Technology, Göteborg, 2005.
- Ralph Schröder and Ulrich C. E. Zanke. Technische Hydraulik: Kompendium für den Wasserbau. Springer, Berlin, 2. a. edition, May 2003. ISBN 3540000607.
- Clemens Strasser, Andrzej Jasionowski, and Dracos Vassalos. Calculation of Time-to-Flood of a Box-Shaped Barge by Using CFD. In 10th International Conference on Stability of Ships and Ocean Vehicles, 2009.
- F. van Walree and A. Papanikolaou. Benchmark study of numerical codes for the prediction of time to flood of ships: Phase I. In 9th International Ship Stability Workshop, pages 45–52, 2007.
- D. Vassalos, L. Letizia, M. Shaw, and C. MacPherson. An Investigation On The Flooding of Damaged RO-RO Ships. In RINA Transactions. 1998. doi: 10.3940/rina.sbt.1998.d4.
- Kurt Wendel. Gutachten "Heraklion". Technical report, Institut für Schiffbau, 1970.





CFD and EFD Study of Damaged Ship Stability in Calm Water and Regular Waves

Hamid Sadat-Hosseini¹, Dong Hwan Kim², Sung Kyun Lee², Shin Hyung Rhee², Pablo Carrica¹,
Frederick Stern¹, Key-Pyo Rhee²

¹*IIHR – Hydrosience & Engineering, The University of Iowa, Iowa City, USA*

frederick-stern@uiowa.edu

²*Department of Naval Architecture and Ocean Engineering, Seoul National University, Seoul, South Korea*
shr@snu.ac.kr

ABSTRACT

CFD is initially conducted for the flooding process of a damaged compartment with no motions and then extended to flooding process of damaged SSRC cruiser in calm water with 6DOF motions. CFD simulations are also conducted for roll decay in calm water and motions in regular beam waves for 6DOF SSRC under both intact and damaged conditions. The CFD results are validated against EFD data for all simulations. The verification study is conducted for intact ship in waves confirming that the results are not very sensitive to the numerical uncertainty. The CFD flooding process of the compartment with no motion shows good agreement with EFD data for the loads on the compartment. The CFD result for SSRC flooding process in calm water shows that CFD predicts the flooding rate and water heights inside the compartment very well while the induced motion is over predicted. CFD intact and damaged roll decay simulations for SSRC predict the roll amplitude and damping coefficients very well. It is found the damping coefficient is larger and roll frequency is smaller for the roll decay under damaged condition. CFD also showed remarkable agreement with the EFD data for the water heights oscillations inside the compartment. The CFD simulation of intact and damaged SSRC in beam waves for various wave length conditions show good agreement for most of the motions and the water heights inside the compartment while pitch motion is often under predicted. The results for intact and damaged ship show same trend for motions against wave length. For intact condition, EFD and CFD show parametric rolling for shortest wave length condition where the wave frequency is near twice of the roll natural frequency. The current results are promising for CFD to be employed to investigate the flooding process and damaged ship stability.

Keywords: CFD, EFD, Damage Stability, Flooding Procedure

1. INTRODUCTION

The study of dynamic behavior of damaged vessel in waves is the essential aspect of ship design. Based on 26th ITTC Specialist Committee Report on Stability in Waves, the behavior of a damaged ship is affected by three main mechanisms: ship motion in waves, flooding process and interaction between floodwater and ship motion. The potential flow

method is the common approach to the study the damaged ship stability. The 6DOF damaged ship motions in waves were solved by various strip theory or panel method based potential codes in which the accuracy of the predictions was associated with the level of nonlinearity implemented in the code. The flooding process and the flow through opening were calculated from Bernoulli based equations including orifice, sluice gate and weir equations. The interaction between floodwater



and ship motion was treated either as an added weight in equations of motion with a moving center of gravity or as external forces calculated by integrating pressure at the compartment wall. For some potential flow studies, the dynamic effect of flood water were predicted from more complicated methods such as CFD and then coupled with the potential flow solvers for ship motion prediction (Strasser et al., 2009). These studies showed that CFD can improve the modeling of flood water dynamics. The complete CFD simulation of all three main mechanisms of the damaged ship is performed for very limited cases. Gao and Vassalos (2011) demonstrated the capability of CFD prediction for motions of damaged ship free to roll and sway. Gao et al. (2011) validated the CFD simulation for the fixed and free damaged barge in calm water. For free barge, only the heave, pitch and roll motions were considered. The results showed very good agreement with EFD data for ship motions and water height in the damaged compartment.

The objective of the present paper is to demonstrate the capability of CFD and validate the CFD results for 6DOF damaged ship motions in waves and the flooding process. The research is a collaborative project between IIHR and SNU. CFD computations are performed using the CFDSHIP-IOWA V4.5 (Carrica et al., 2010). The test cases include the flooding process of the damaged compartment with no motions in calm water, flooding process of 6DOF damaged SSRC cruiser in calm water, 6DOF motions of SSRC cruiser under intact and damaged condition for roll decay in calm water and lastly 6DOF motions of SSRC cruiser under intact and damaged condition in beam waves. For flooding of the damaged compartment, the results were compared with EFD data from Cho et al. (2006). The flooding procedure, free roll decay in calm water and ship responses in regular beam waves of intact and damaged SSRC were compared against EFD data provided by SNU.

2. EXPERIMENTAL METHOD

2.1 Flooding Procedure for Damaged Compartment with No Motions

The flooding of a damaged compartment with no motion is investigated prior to the 6DOF damaged ship cases to study the loads on the compartment induced by the flooding water. The experiment data was taken from Cho et al. (2006). The experiment was focused on the flooding of damage compartment of PRR02 ship.

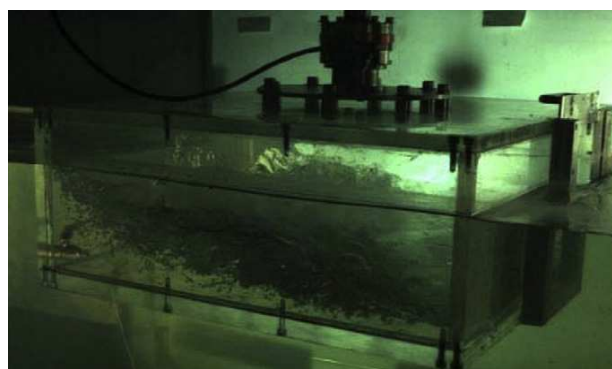


Figure 1: Experiment performed by Cho et al. (2006).

Table 1: The main particulars of the compartment

Description	Symbol	Compartment
Length between perpendiculars [m]	L	0.55
Beam	B/L	0.936
Depth	D/L	0.338
Draft	T/L	0.240
Damage length	l/L	0.309
DOF		motion fixed

The experiment was conducted for a model with the scale ratio of 48.57. Main dimensions for the model test is shown in Table 1. The damaged door opening was located on the starboard. The door was initially closed while the compartment was fixed to the measuring system inside a tank at the desired draft. The damaged inlet was opened during the test and the forces and moments were measured during the flooding.

The experiments were conducted for six different shapes of damage opening for both a

simple compartment with no internal rooms and a compartment with all internal rooms and engine blocks. The provided EFD data were used widely as a benchmark to validate the CFD codes ability to predict the flooding procedure.

In this study, the simple compartment with simple inlet shape was used for the flooding procedure validation of current CFD method. The damaged inlet is in rectangular shape with non-dimensional length of 0.309 and same height as the compartment depth (0.338).

2.2 Flooding Procedure and Roll Decay in Calm water and Motions in Regular Beam Waves for SSRC Cruiser

The SSRC cruiser was designed by Ship Stability Research Center (SSRC) in the UK and used initially for ITTC benchmark test ‘Time-to-Flood, phase 2’. This geometry was also used at benchmark study of numerical codes and model tests performed at Korea Ocean Research and Development Institute (KORDI). The geometry had two compartments; one at the midship section and one near the bow with complex layout including the double bottom, side shells and upper story.

Herein, the experiments for SSRC are conducted with one compartment at midship. The compartment has no double bottom or topper story, as shown in Figure 2. The compartment is divided by a side wall into two rooms. The experiments are conducted in Seoul National University 110m×8m×3.5m Towing Tank (SNUTT) for 1/82.75 scaled model, as shown in Figure 3. Main dimensions for the model ship are provided in Table 2. The tank is equipped with plunger type wave maker that provides regular waves. LCG, VCG and pitching moment of inertia were adjusted by using gyro swing. VCG was double-checked and radius of gyration along x-axis was adjusted by performing another free roll decay test in water.

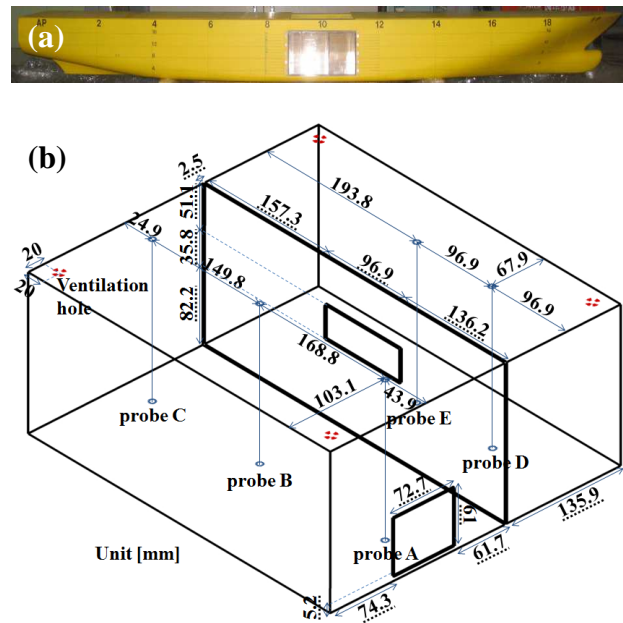


Figure 2: The damaged SSRC model: (a) SSRC cruiser; (b) compartment geometry.

Table 2: The main particulars of SSRC cruiser

Description	Symbol	Particulars
Model scale	-	
Length between perpendiculars [m]	L	3
Beam	B/L	0.143
Depth	D/L	
Draft	T/L	0.034
Damage length	-	0.150
Longitudinal center of gravity	LCG/L	0.520
Vertical center of gravity	VCG/L	0.032
Radius of gyration along x-axis	K_{xx}/L	0.053
Radius of gyration along y-axis	K_{yy}/L	0.250
Radius of gyration along z-axis	K_{zz}/L	0.250

The EFD test matrix and the details of wave conditions for SSRC cruiser are provided in Table 3 and Table 4. The tests include flooding procedure for damaged ship, roll decay for intact and damaged SSRC, and motions in regular waves for intact and damaged SSRC. The tests were performed for zero Fr and all motions were free (6DOF). The wave period for wave cases was chosen to be distributed around the natural period of the roll motion of the intact SSRC cruiser which is 2.055 second. The wave heading is 270 deg (beam waves) i.e. it approaches the ship from the damaged side. For damaged cases, the cases in waves were conducted with both rooms for the compartment while the second



room was excluded for most of the cases in calm water, as shown in Table 3. During the test, the motions, the free surface elevation and water height inside the compartment were measured. Herein, all calm water cases and wave cases with wave conditions 1, 3, 5, 7, 9 are selected for CFD simulations, as shown in Tables 3 and 4.

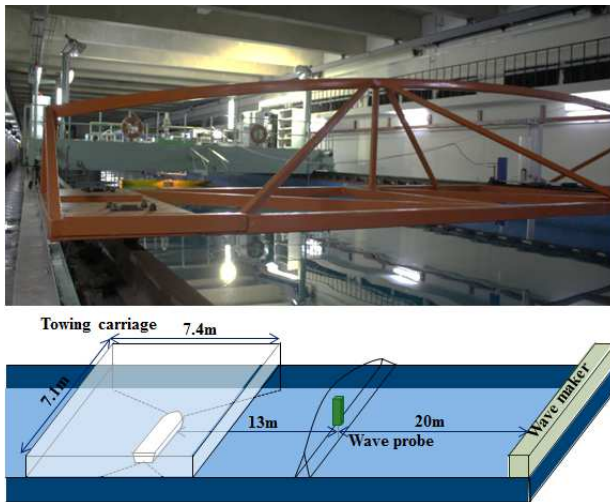


Figure 3: The Seoul National University Towing Tank and details of experiment facilities for regular wave test.

During the test, the motions were measured by integrating the accelerations recorded by accelerometers at 7 points on the model. The measured motions were transferred to the center of gravity of the ship by using the strap-down method. The free surface wave height in the regular waves and water height inside the compartment was measured using a wave probe. For the regular wave cases, all the 6DOF accelerations were recorded while for the flooding procedure and roll decay cases only roll acceleration was recorded as the other ones were so small and difficult to measure. The accelerations were first filtered using band-pass filtering in Matlab and then numerically integrated to get velocities. The velocity data were filtered again and numerically integrated to produce displacement. Thus the EFD data reduction technique might have influence on the accuracy of the data.

Table 3: The EFD test matrix for SSRC cruiser

Cases	Description	State	Initial condition	Comp. Room	Sea condition	Data measured
C1*	Flooding procedure	damaged	-	-	Calm water	ϕ , water height
C2*		intact	$\phi_0=13.7$ 20.5°	-		
C4*			$\phi_0=26.7$	1		
C5*	Roll decay		-25.5°	1	Calm water	ϕ , water height (damaged)
C6*		damaged	15.9°	1		
C7*			-15.6°	1		
C8*			-28.6°	1&2		
RI1*, RI2, RI3*, RI4, RI5*, RI6, RI7*, RI8, RI9*, RI10	Motion in regular	intact	-	-	Regular wave (Table 4)	motions, wave elevation, water height (damaged)
RD1*, RD2, RD3*, RD4, RD5*, RD6, RD7*, RD8, RD9*, RD10	beam wave	damaged	-	1&2		

* selected for CFD simulations.

Table 4: The wave conditions for test cases

Conditions	T [sec]	A [m]	H/ λ
1*	1	0.013010917	1/60
2	1	0.007806549	1/100
3*	1.5	0.029274562	1/60
4	1.5	0.017564734	1/100
5*	1.955	0.049728049	1/60
6	1.955	0.029836829	1/100
7*	2.055	0.054945426	1/60
8	2.055	0.032967256	1/100
9*	2.155	0.060423022	1/60
10	2.155	0.036253813	1/100

* selected for CFD simulations.

For the regular wave cases, a soft spring method was used to compensate the drift motion of the ship for the experiment. One of each ends of four springs were attached to the stationary carriage and the other end of the springs were attached to the aft and fore of the model. Vertical points of all spring were initially touching the water surface such that the springs would not affect the roll motion as much as possible. Spring constant, which mainly affects the spring frequency, was chosen 10N/m to avoid the natural frequency for all 6 motions. To check if the spring force is exactly acting according to its length, a simple measurement was performed. Its length was increased by adding weight at the end of the spring and the force exerted by the spring

was measured. The measurement was only performed statically ignoring the spring behaviour under dynamically changing force. The result of the measurement is shown in Figure 4.

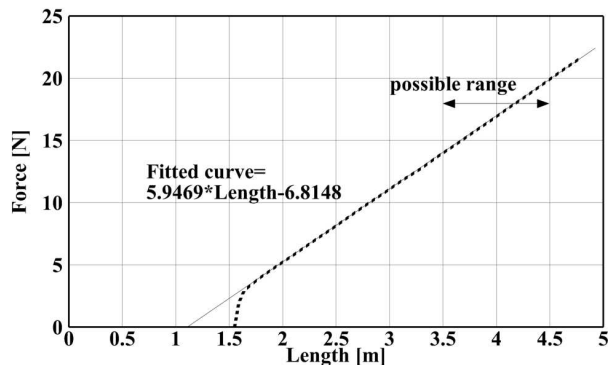


Figure 4: EFD study of linearity of soft spring force.

The measurement showed that the spring force has linear behaviour within the range of possible spring length during the experiment (about 3.7~4.4m). Also, the effective spring stiffness is 5.946 N/m and the forces are off by 6.8148 N from the one estimated by $F=kx$.

Additional mechanism was needed for damaged ship in calm water and regular waves to unlock the damage opening. The damage opening was unlocked using air cylinder which performs fast and it is confirmed its effect to roll motion while it is being opened is negligible. In calm water, the damage opening was opened after the ship was in static equilibrium state. In waves, the damage opening was opened while the ship was on the wave downslope. Figure 5 shows the damaged compartment opening mechanism.

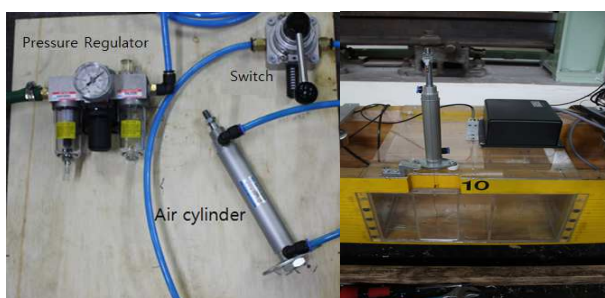


Figure 5: The damaged compartment opening mechanism

3. CFD METHOD

The code CFDShip-Iowa v4.5 (Carrica et al., 2010) is used for the CFD computations. The CFDShip-Iowa is an overset, block structured CFD solver designed for ship applications using either absolute or relative inertial non-orthogonal curvilinear coordinate system for arbitrary moving but non-deforming control volumes. Turbulence models include blended $k-\varepsilon/k-\omega$ based isotropic and anisotropic RANS, and DES approaches with near-wall or wall functions. A single-phase level-set method is used for free-surface capturing. Captive, semi-captive, and full 6DOF capabilities for multi-objects with parent/child hierarchy are available. Numerical methods include advanced iterative solvers, higher order finite differences with conservative formulation, PISO or projection methods for pressure-velocity coupling, and parallelization with MPI-based domain decomposition. Dynamic overset grids use SUGGAR to compute the domain connectivity.

For the current simulations, absolute inertial earth-fixed coordinates are employed with $k-\varepsilon/k-\omega$ turbulence model using no wall function. The location of the free-surface is given by the 'zero' value of the level-set function, positive in water and negative in air. The 6DOF rigid body equations of motion are solved including spring forces/moments. The governing equations are discretized using finite difference schemes on body-fitted curvilinear grids. The time derivatives in the turbulence and momentum equations are discretized using 2nd order finite Euler backward difference. Convection terms in the turbulence and momentum equations are discretized with higher order upwind formula. The viscous term in momentum and turbulent equations are computed with similar considerations using a second order difference scheme. Projection method, a two-stage fractional step scheme, is employed to couple pressure field and velocity effectively using the PETSc toolkit. In order to solve the system of discretized governing equations, between three and five inner



iterations are used in each time step and solutions are considered to be converged once the error for velocities, pressure, and level set reach to less than 10^{-5} , 10^{-8} , and 10^{-5} respectively.

The spring forces for all 6DOF are first calculated in earth fixed coordinate system and then transformed to ship-fixed to be included in the forces on the right hand side of the equations of motion. The moments induced by spring force were calculated by cross production of moments arm with spring forces described in ship-fixed coordinate and then included in the moments on the right hand side of the equations of motion.

Calculation of spring location attached to ship in inertial coordinate was performed using equation (1):

$${}^O\vec{r}_E^P = {}^O\vec{r}_E^G + {}^G\vec{r}_E^P = {}^O\vec{r}_E^G + \mathbf{R}_S^{E,G} \cdot {}^G\vec{r}_S^P \quad (1)$$

Here, r is the displacement vector and R is the rotational matrix. The subscript for the vectors represent coordinate where the unit vector is described, the right superscript for the vector represents the end point of vector and the left superscript for the vector represents starting point of the vector. For the rotational matrix R , the subscript represents current coordinate system and right superscript represents coordinate system to be transformed. E and S subscripts refer to earth-fixed coordinate system and ship-fixed coordinate system. O , G , P and C superscripts reflect the origin of the earth-fixed coordinate system, center of gravity of ship, spring location attached to the ship and spring location attached to the towing carriage, respectively.

The spring force was calculated as follows:

$${}^P\vec{F}_{iE}^C = \frac{{}^O\vec{r}_E^{C_i} - {}^O\vec{r}_E^P}{\left| {}^O\vec{r}_E^{C_i} - {}^O\vec{r}_E^P \right|} \cdot f\left(\left| {}^O\vec{r}_E^{C_i} - {}^O\vec{r}_E^P \right| \right) \quad (2)$$

where F_i is the force vector for spring i and f is the spring force function which is a function of the length of spring. In this case,

the formula from experiment (Figure 4) was used.

The total spring induced forces were sum of the forces induced by each spring as shown in Eq. (3). Then the total forces were transformed into ship coordinate system (Eq. (4)).

$${}^P\vec{F}_E^C = \sum_{i=1}^4 {}^P\vec{F}_{iE}^C \quad (3)$$

$${}^P\vec{F}_S^C = \mathbf{R}_E^S \cdot {}^P\vec{F}_E^C \quad (4)$$

For the moment calculation induced by spring force, each spring forces were transformed to ship coordinate system first.

$${}^P\vec{F}_{iS}^C = \mathbf{R}_E^S \cdot {}^P\vec{F}_{iE}^C \quad (5)$$

Then, the moment induced by each spring was calculated by doing cross product for each moment arm with forces. Total moment was sum of each moment.

$${}^P\mathbf{M}_{iS} = \left({}^E\vec{r}_S^{C_i} - {}^E\vec{r}_S^P \right) \times {}^P\vec{F}_{iS}^C \quad (6)$$

$${}^P\mathbf{M}_S = \sum_{i=1}^4 {}^P\mathbf{M}_{iS} \quad (7)$$

After calculating the total spring moments in ship-fixed coordinates, they were added to the forces on the right hand side of the equations of motion. The forces on the right hand side of the equations are the fluid forces integrated at each time step not only on the ship hull but also inside the flooded compartment. This means that the change of the ship mass and/or center of gravity due to the flooding are already included in the integrated forces and thus, unlike in traditional methods, there's no need to modify the equations of motion. In the traditional methods for damaged ships the forces inside the compartment are not included in the total forces acting on the ship and thus the flooded compartments are treated as an additional weight to the ship. The added weight then changes the center of gravity and moments of inertia of the ship and consequently the

equations of motion have to be solved for the ship with the new center of gravity and moments of inertia.

3.1 Computational Domain, Boundary Conditions and Grids

The computational domain extends from $-5 < x < 5$, $-4.5 < y < 5.5$, $-1.25 < z < 0.1$ for the compartment with no motions, $-1.5 < x < 1.5$, $-1.2 < y < 1.2$, $-1 < z < 0.25$ for roll decay and flooding procedure test of intact/damaged SSRC cruiser and $-1.5 < x < 1.5$, $-2 < y < 1$, $-1 < z < 0.25$ for regular wave test of intact/damaged SSRC cruiser in dimensionless coordinates based on ship length. The ship axis is aligned with x with the bow at $x=0$ and the stern at $x=1$. The y axis is positive to starboard with z pointing upward. The free surface at rest lies at $z=0$. Boundary conditions are applied as described in Carrica et al. (2010). Non slip boundary condition is imposed on all of the damaged compartment walls to take into account the friction forces as well.

The computational grids are overset, with independent grids assembled together to generate the total grid. The grid used for the fixed compartment simulation includes the compartment and background. For SSRC, the grid includes the ship hull boundary layer, compartment, refinements, and background. The boundary layer grids are generated with a hyperbolic grid generator by using 'Gridgen V15.11'. Because CFD ship hull is symmetric respect to center-plane, only the grid for one side of the ship was generated and then mirrored respect to center-plane (Double-O grid topology). Two Cartesian grids are used for the inside of the rooms 1 and 2 of the compartment. Also Cartesian grids are used for refinements and background. For fixed compartment, the grid size is 3.2M allocated on 25 cores. For SSRC, the grid size ranges from 6.3M to 28.5M depending on the damage/intact conditions and calm water/wave conditions of the simulations as shown in Table 5. The details of grid system for SSRC with damaged ship with the compartment with two rooms are

shown in Figure 6. As it is shown, the grid on the hull is designed to be very fine for the region near the damage opening.

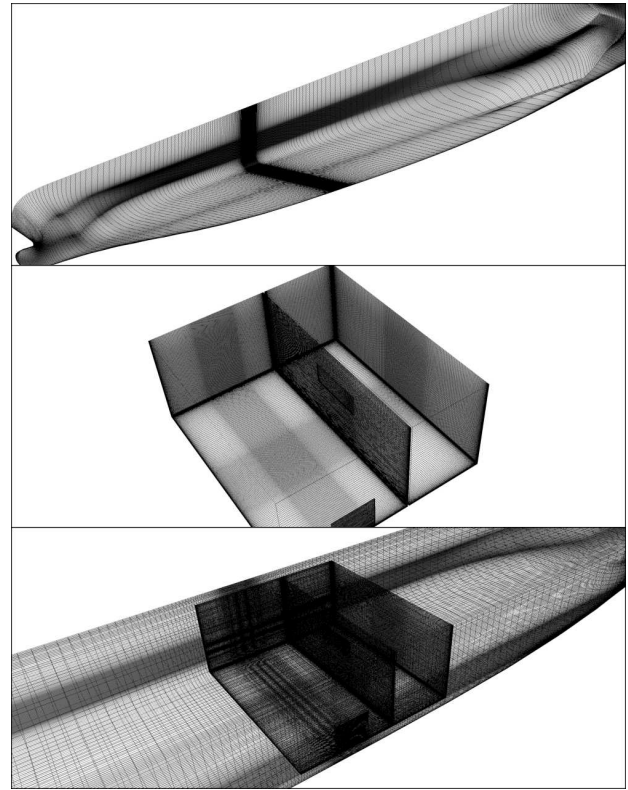


Figure 6: Grid topology for damaged SSRC cruiser and the compartment.

4. RESULTS

4.1 Verification Study

The iterative, grid and time step uncertainties are investigated for the intact ship in regular waves with $\lambda = 2.4L$ and $Ak = 0.052$ (case RI9). The grid verification study is conducted using grid triplets G3, G2 and G1, shown in Table 5. The coarse grid G3 and fine grid G1 are generated from medium grid G2 used for intact ship for case RI9 with total grids of 7.1M, using coarsen/refinement ratio of $\sqrt{2}$. The G1 and G3 have 19.9M and 2.4M grid points, respectively. The time step verification study is performed for G2 with $r_T = \sqrt{2}$, $\Delta t = 0.005, 0.0071$ and 0.01 sec.

The iterative uncertainty listed in Table 6 shows very small uncertainty for all of



amplitudes and phases with maximum uncertainties for heave and surge motion. U_I of the motions are fairly large for some motions compared to U_G , U_T , ε_{I2_G} and ε_{I2_T} . The average uncertainty is about $U_I = 0.75\% S_I$ for amplitudes and $1.22\% S_I$ for phases, showing the results are fairly insensitive to the iterative errors.

The results for grid uncertainty show oscillatory convergence for yaw amplitudes with $R_G = -0.56$ and oscillatory divergence for roll amplitude with $R_G = -3.77$. All other amplitudes show monotonically convergence with the order of accuracy P_G about 1.5 for most of the amplitudes. The U_G ranges from 0.06 to $2.09\% S_I$ in which the minimum is for heave motion and maximum is for pitch motion. The phase show oscillatory convergence for surge and roll while others show monotonically convergence. The average grid uncertainty for phases is about 10% while the amplitudes show only $1.28\% S_I$ grid uncertainty. The overall grid uncertainty is about $6\% S_I$ suggesting that the results are not

very sensitive to the current grid sizes as shown in Figure 7.

The time step uncertainty results show oscillatory convergence for amplitudes of angular motions with average $R_G = -0.15$ and monotonically convergence for surge and heave motions with $R_G = 0.18$ and 0.64 , respectively. The average uncertainty of amplitudes is $0.18\% S_I$, about 10% of the grid uncertainty for amplitudes. The time step verification study for phases shows oscillatory convergence for heave and pitch, monotonically convergence for surge, roll and yaw phases and oscillatory divergence for sway phase. The time step uncertainty for phases is $3.49\% S_I$ in average, one third of the grid uncertainty for phases. The total time step uncertainty is about $2.17\% S_I$, showing that the results are insensitive to the time step size as shown in Figure 8. The simulation uncertainty is computed based on the iterative, grid and time step uncertainties. The results show $USN = 1.05\% S_I$ for amplitudes and $USN = 8.3\% S_I$ for phase, resulting in the total simulation uncertainty of $7.02\% S_I$.

Table 5: Summary of grid sizes for all CFD simulations

Grid (simulation)	BL P&S	Ref. 1	Ref. 2	Ref. 3	Back-ground	Comp. Room 1	Comp. Room 2	Air Pipe	Connec-tion 1	Connec-tion 2	TOT
G1 (R19, V&V-fine)	226×72×173	134×93×145	134×93×145	240×127×189	155×197×159	-	-	-	-	-	19.9M
G2 (R15, R17, R19, V&V-medium)	160×51×123	95×66×103	95×66×103	170×90×134	110×140×113	-	-	-	-	-	7.09M
G3 (R19, V&V-coarse)	113×36×86	67×46×72	67×46×72	120×63×94	77×98×79	-	-	-	-	-	2.45M
G4 (Fixed Comp)	59×40×108	100×100×90	-	-	150×150×72	80×61×50	-	-	10×6×50	-	3.2M
G5 (C2, C3)	160×51×123	95×66×103	95×66×103	170×80×108	150×120×88	-	-	-	-	-	6.3M
G6 (R11, R13)	160×51×123	95×66×103	95×66×103	170×80×188	120×360×148	-	-	-	-	-	12.2M
G7 (C1, C4, C5, C6, C7)	331×41×227	95×65×126	95×65×126	170×110×173	150×120×143	193×159×203	-	3×60×3	80×18×80	-	19.8M
G8 (C8)	331×41×227	95×65×126	95×65×126	170×110×173	150×120×143	193×221×226	104×221×226	3×60×3	80×18×80	22×70×49	28.5M
G9 (RD1, RD3)	331×41×227	95×65×126	95×65×126	170×108×198	120×360×148	193×159×203	-	3×60×3	80×18×80	-	24.1M
G10 (RD5, RD7, RD9)	331×41×227	95×65×126	95×65×126	170×110×173	110×140×113	193×221×226	120×221×171	3×60×3	80×18×80	22×70×49	27.1M

4.2 Flooding Procedure for Damaged Compartment with No Motions

The EFD and CFD comparison for the time history of x and y moments acting on the compartment with no motions during the flooding procedure are presented in Figure 9.

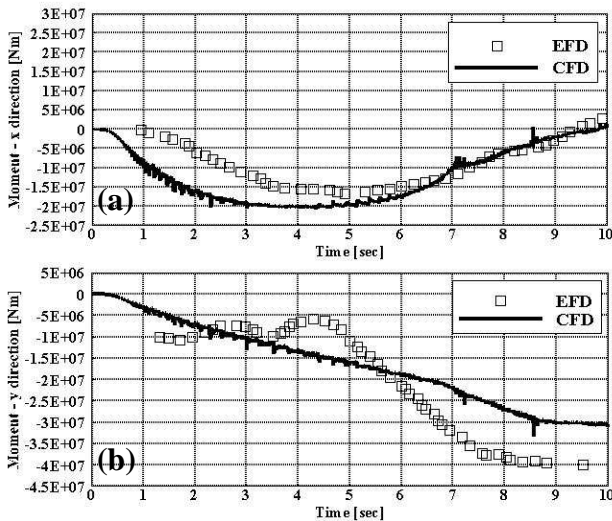


Figure 7: EFD and CFD comparison of forces on the compartment: (a) moment for x direction; (b) moment for y direction.

The results show CFD can predict the trend of both moments fairly well. The x moment increases during the flooding and reaches its maximum when the water inside the compartment flows from starboard to portside and hits the wall on the portside. Note that the damaged opening is at starboard. The CFD x-moment shows the peak at the earlier time suggesting fairly higher rate of flooding compared with EFD data. This is due to the fact that in CFD the air compression trapped in the chamber is neglected while the opening door is below the water free surface and the air is trapped and compressed in EFD. Also some differences between EFD and CFD could be due to the CFD grid size as it was not very fine to resolve the hydrodynamic forces inside the compartment induced by flooding. The y-moment shows zero at $t=0$ increasing about linearly during the flooding. The y-moment is due the generated circulation inside the compartment. After finishing the flooding procedure the y-moment reaches to zero as shown in Cho et al (2006).

Table 6: Verification study for the intact ship in regular waves with $\lambda=2.4L$ and $Ak=0.052$ (case RI9)

type		x_0 [m]	y_0 [m]	z_0 [m]	ϕ_0 [deg]	θ_0 [deg]	ψ_0 [deg]	x_{e1} [deg]	y_{e1} [deg]	z_{e1} [deg]	ϕ_{e1} [deg]	θ_{e1} [deg]	ψ_{e1} [deg]	Ave. A.	Ave. ϵ	Total
Uncertainty of grid spacing refinement ratio= $\sqrt{2}$ $G3=3M, G2=7M, G1=21M$	R_G	0.36	0.62	0.30	-3.77	0.33	-0.56	-0.08	2.15	1.55	-0.85	0.01	0.29			
	type	MC	MC	MC	OD	MC	OC	OC	MC	MC	OC	MC	MC			
	P_G	1.47	0.69	1.75	-	1.58	-	-	1.11	0.63	-	6.77	1.79			
	$\epsilon_{12,G}\%S_1$	2.59%	0.39%	4.73%	1.55%	3.74%	-3.32%	0.41%	0.24%	4.37%	-2.69%	0.01%	-0.83%			
	$U_G\%S_1$	1.76%	1.21%	0.06%	-	2.09%	-	-	1.54%	36.73%	-	0.00%	0.31%	1.28%	9.64%	6.24%
Uncertainty of time step refinement ratio= $\sqrt{2}$ $\Delta t_3=0.01, \Delta t_2=0.0071, \Delta t_1=0.005$	R_T	0.18	-2.08	0.64	-0.04	-0.11	-0.30	0.47	-4.21	-0.76	0.07	-0.09	0.34			
	type	MC	OD	MC	OC	OC	OC	MC	OD	OC	MC	OC	MC			
	P_T	2.47	-	0.65	-	-	-	1.08	-	-	3.90	-	1.55			
	$\epsilon_{12,T}\%S_1$	-0.51%	0.19%	-0.10%	-0.13%	0.38%	-1.30%	5.59%	-0.06%	0.26%	-0.47%	0.09%	-4.62%			
	$U_T\%S_1$	0.04%	-	0.33%	-	-	-	7.73%	-	-	0.03%	-	2.71%	0.18%	3.49%	2.17%
Uncertainty of iteration	$U_I\%S_1$	1.45%	0.33%	1.29%	0.35%	0.63%	0.45%	1.95%	0.28%	4.59%	0.00%	0.52%	0.00%	0.75%	1.22%	1.98%
	$U_I/\epsilon_{12,G}$	0.56	0.84	0.27	0.22	0.17	-0.14	4.75	1.16	1.05	0.00	65.57	0.00			
	$U_I/\epsilon_{12,T}$	-2.84	1.73	-12.97	-2.76	1.66	-0.35	0.35	-4.73	17.67	0.00	5.85	0.00			
	U_I/U_G	0.83	0.27	23.01	-	0.30	-	-	0.18	0.12	-	-	0.00			
	U_I/U_T	37.03	-	3.92	-	-	-	0.25	-	-	0.00	-	0.00			
	$U_{SN}\%S_1$	2.28%	1.26%	1.33%	0.35%	0.63%	0.45%	7.97%	1.56%	37.01%	0.03%	0.52%	2.73%	1.05%	8.30%	7.02%

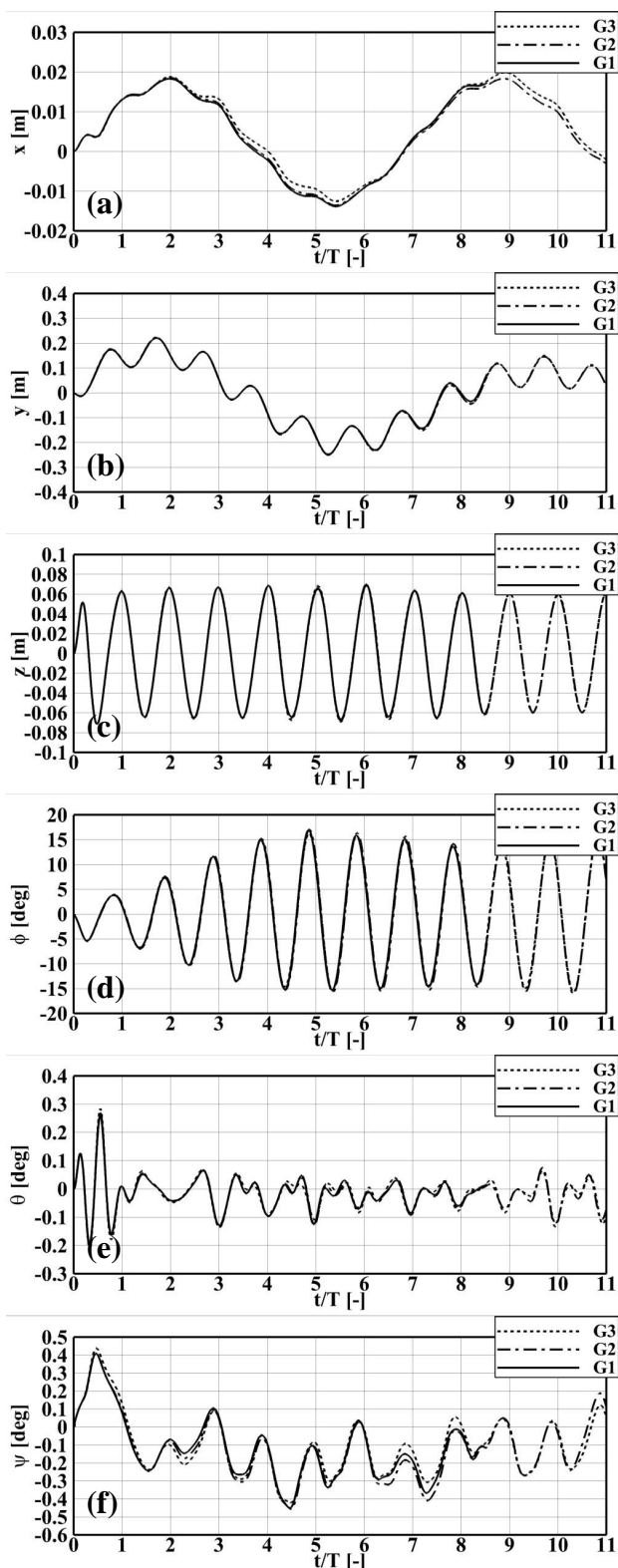


Figure 8: The grid verification study for the intact ship in regular waves with $\lambda=2.4L$ and $A_k=0.052$ (case RI9).

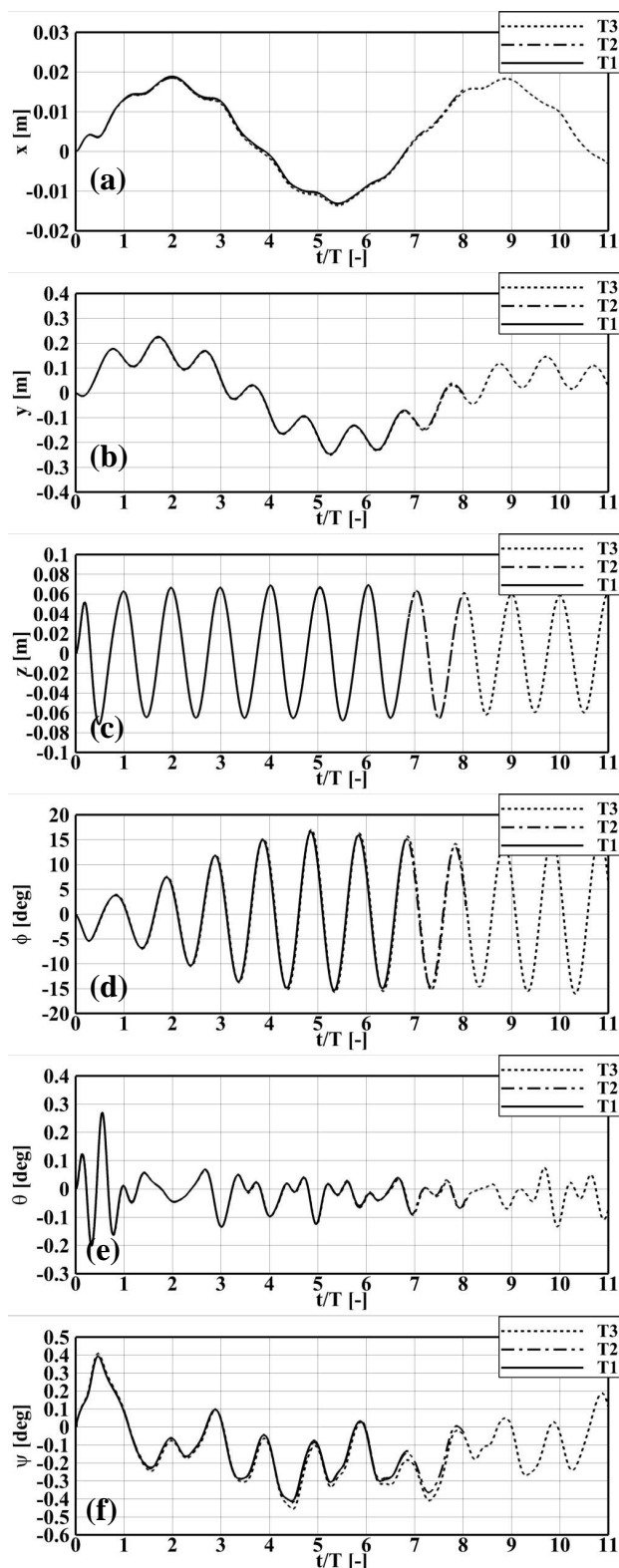


Figure 9: The time step verification study for the intact ship in regular waves with $\lambda=2.4L$ and $A_k=0.052$ (case RI9).

4.3 Flooding Procedure of Damaged SSRC Cruiser

The flooding process of SSRC in calm water is simulated to validate the prediction of the flooding rate and water height inside the compartment while the ship is free to 6DOF motions. Figure 10 shows EFD and CFD roll motion time history along with the water heights at points A, B and C inside the compartment. EFD data shows that the roll motion is zero before flooding reaching to mean value of -3 deg after the flooding i.e. the ship is tilted to the damaged side (starboard). The roll motion oscillates at period of about 2.25 sec which is the natural period of the damaged SSRC. This is about 10% larger than the natural period of intact SSRC (2.055 sec) as mentioned earlier. The EFD water height at point A shows the water height increase quickly to about 0.04 m and then stays at this level up to $t=2$ sec. At this moment the water reflected by the wall at the other side of the compartment reaches to point A and thus the water height increases to the average of 0.08 m at point A. The water heights at point B and C also show same trend but they stay at 0.04m for shorter time as points B and C are closer to the end of the compartment and see the reflected water sooner. After the transient region, the water heights at points A and C oscillate with roll motion. The water heights at point A and C show 180 deg phase lag as point A is located on starboard and point C is located on portside. The average of water height at point C is smaller because the ship is tilted toward the starboard. The water height at point B oscillates with very small amplitude as point B is located on the roll axis. CFD over predicts the roll motion but the water heights are predicted fairly well. The source of the differences could be investigated if the other motions were available for EFD and could be compared with CFD results. For transient region (when the compartment is getting flooded), CFD shows very good agreement with water heights at point A and C but not for water height at point B. CFD shows fairly constant water height at point B up to $t=1.5$ sec and then the water height increases as the reflected water from end of compartment reaches point B (see Figure 11). After the compartment is fully flooded, the CFD water

heights show oscillations at roll natural period, similar to EFD.

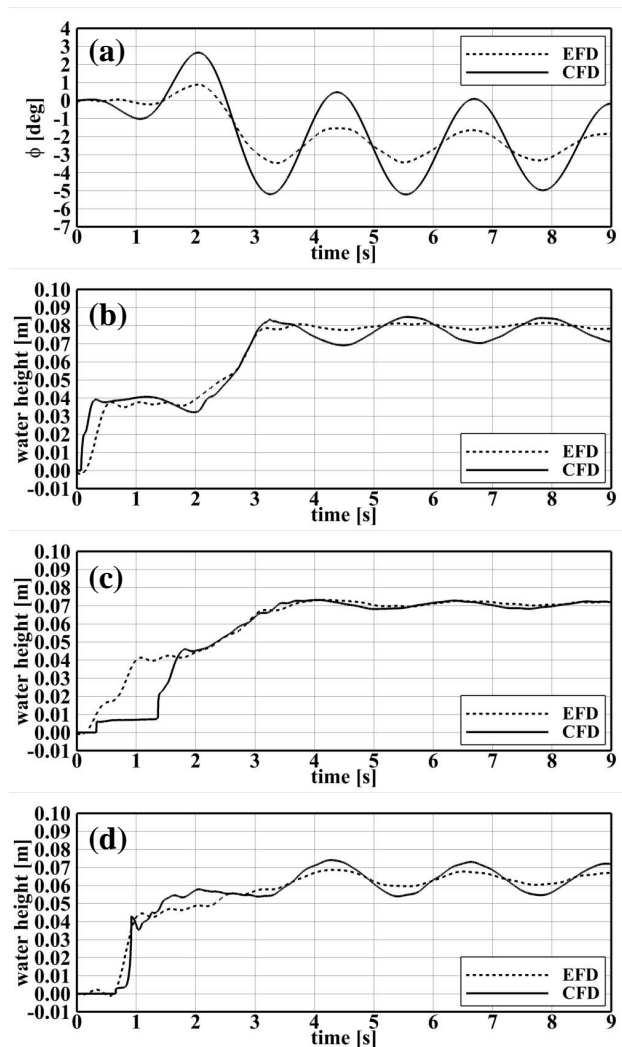


Figure 10: CFD and EFD comparison of the flooding procedure for damaged SSRC cruiser in calm water: (a) roll history; (b) probe A; (c) probe B; (d) probe C.

4.4 Roll Decay of Intact SSRC Cruiser

Roll decay simulation for intact SSRC cruiser was validated prior to the damaged cases.

All motions were free (6DOF) similar to EFD. Two initial roll angle 13.696° and 20.502° were simulated. The initial roll is imposed while the ship was free to other modes of motion with no external force. This is different with EFD where the most far point in beam direction from longitudinal center of



gravity was pushed with external force until the roll angle reached its designed value. In Fact, EFD external force could induce initial heave and pitch motions which are not considered in CFD.

The EFD and CFD roll time history comparison is shown in Figure 12. EFD time history shows the model reaches to about 30% of the initial roll angle after six cycles. The mean value of roll angle is about zero and the period of the roll decay is fairly constant for both initial roll angle cases. For CFD simulation, EFD K_{xx} values were adjusted by comparing EFD and CFD predicted period as EFD usually has difficulties to fix K_{xx} of the model to the desired value. The adjusted K_{xx} is $0.0501 \cdot L$ compared to the EFD reported value of $0.053 \cdot L$. The CFD results show very good agreement with EFD data for first three cycles. However there are some discrepancy in roll amplitude between CFD and EFD as roll angle decays which could be partially due to EFD roll displacement measured from acceleration data through filtering process and numerical integration and/or errors in CFD simulation.

Figure 13 compares CFD and EFD damped natural roll frequency vs. mean roll angle. The damped roll frequency is evaluated from the time difference for the two subsequent peaks in each roll cycle. EFD damped natural frequency is close to $f_{\phi d} = 0.5$ Hz at large ϕ_m and then decreases to average of 0.49 HZ for decreasing ϕ_m . Thus the damped roll frequency changes only about 2%, confirming that the restoring moment of the ship is fairly linear. The damped roll frequency at small roll angle is close to hydrostatic natural roll frequency $f_{\phi h} = \sqrt{gGM/k_{xx}} = 0.487$ HZ, as expected. The CFD predicts the decreasing trend of roll frequency vs. mean roll angle and shows fairly good agreement with EFD.

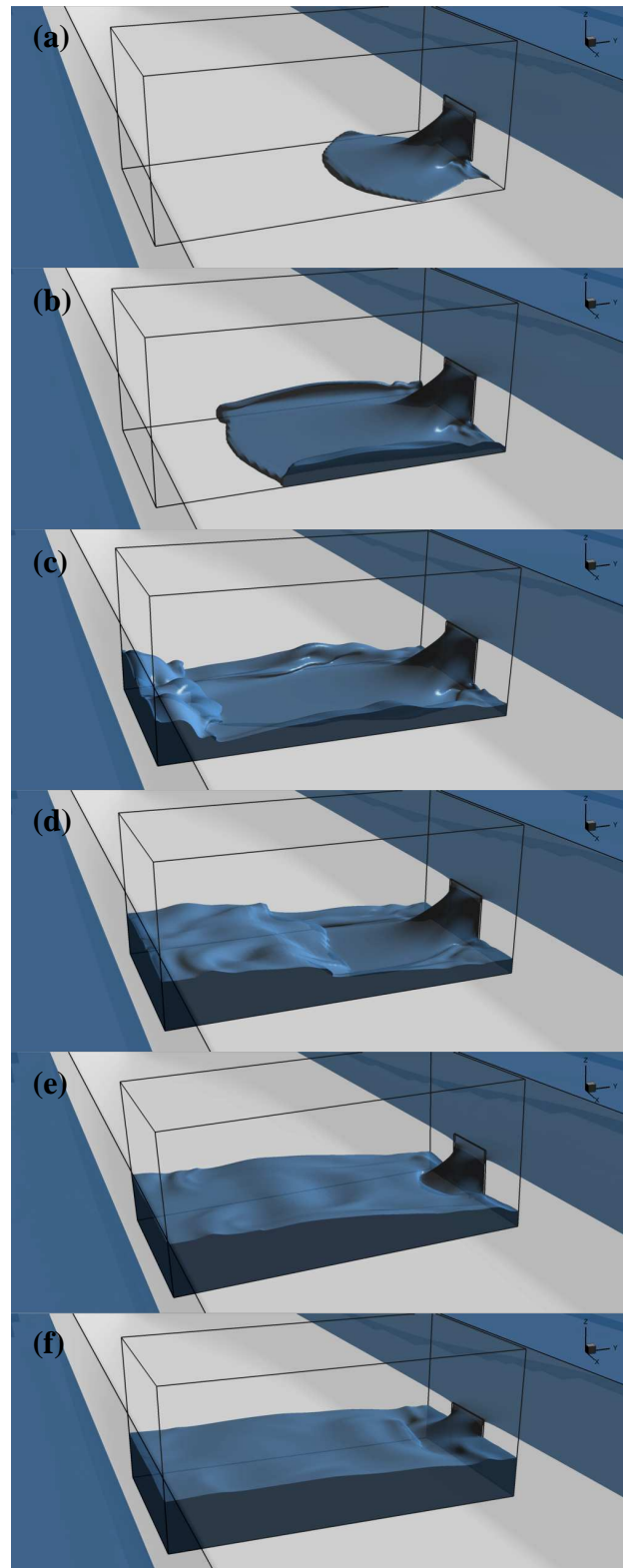


Figure 11: CFD prediction of flooding procedure for damaged SSRC cruiser: (a) $t=0.25s$; (b) $t=0.5s$; (c) $t=1.0s$; (d) $t=1.5s$; (e) $t=2.0s$; (f) $t=2.5s$.

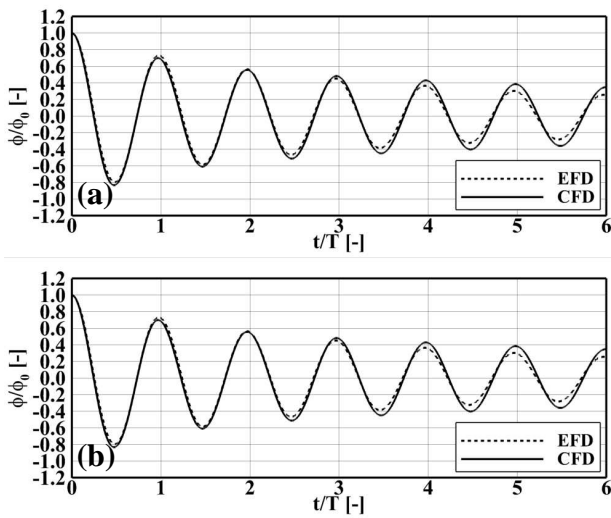


Figure 12: EFD and CFD roll decay time history for intact SSRC cruiser: (a) $\phi_0=13.696^\circ$; (b) $\phi_0=20.502^\circ$.

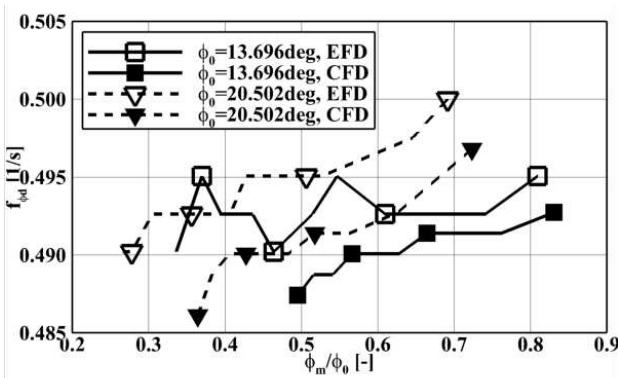


Figure 13: EFD and CFD damped natural roll frequency vs. mean roll angle of intact SSRC cruiser in roll decay.

Figure 14 compares EFD and CFD linear and cubic damping coefficients (α, γ) estimated based on Himeno method (1981). For linear damping coefficient, EFD shows the damping coefficient increases with increasing the initial roll angle. For cubical damping coefficient, EFD shows zero value suggesting that the roll motion decays linearly. For linear damping, CFD shows very good agreement for roll decay with initial roll of 20.1° while the damping coefficient is under predicted for roll decay with initial roll angle of 13.696° . The initial heave and pitch motion in EFD induced by external force might have non negligible effect on roll damping for smaller initial roll angle which provides large comparison error with

CFD. For cubical damping coefficient, CFD shows zero value, similar to EFD.

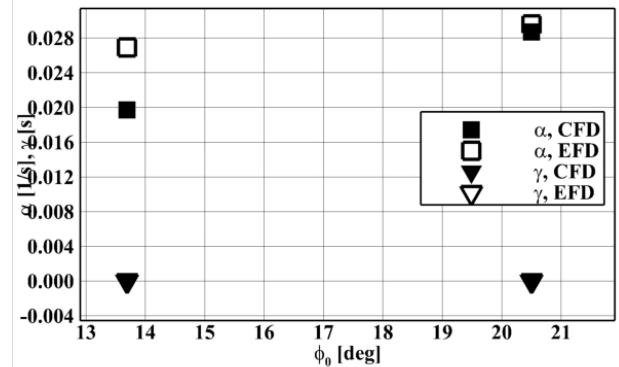


Figure 14: EFD and CFD damping coefficients in roll decay for intact SSRC cruiser.

4.5 Roll Decay of Damaged SSRC Cruiser

The damaged cases were conducted for SSRC with one- and two-room compartment, as shown in Table 3. Four cases with initial roll angle of about $\pm 16^\circ$ and $\pm 26^\circ$ ($+15.9^\circ$ and -15.6° ; $+26.7^\circ$ and -25.5°) are conducted for SSRC with one-room compartment and one case with initial roll angle of -28.6° is conducted with including the second room in the test. The negative initial roll angle shows roll to starboard where the damage opening is located and positive initial roll angle shows roll opposite to the damage side. The initial water height inside the compartment is at the same level as outside as the damage opening connects the inside and outside water and small vent located on top of the compartment provides atmosphere pressure inside the compartment. All motions during the simulation were free (6DOF) similar to EFD.

The EFD and CFD roll time history comparison is shown in Figure 15. For all EFD cases, it is shown that the roll amplitude reaches to large value when the ship rolls to the damaged side (dimensional roll angle is negative). This is due to the fact that the restoring moment decreases when the ship rolls from the intact side toward the damaged side. This also provides a negative mean value for all the damaged cases meaning that the ship is tilted toward the damaged side. The mean



value is about -3 deg for one room compartment cases and -6 deg for two room compartment case, as shown in Table 7. Comparing the EFD roll angle for $\phi_0 = -15.6^\circ$ with the data for intact condition with $\phi_0 = 13.696^\circ$ shows that the roll amplitude for $\phi_0 = -15.6^\circ$ when ship rolls to the intact side is smaller than the roll for the intact condition as the water inside the compartment acts as anti-roll tank. The CFD results show remarkable agreement with EFD roll amplitude and period for cases with one room compartment. However, the mean value predictions show mainly large errors for the cases with initial roll to the damaged side, as shown in Table 7. This could be due to the difference between EFD and CFD setup as mentioned earlier. In CFD, the initial roll is imposed while the ship was free to other modes of motion with no external force. This is different with EFD where the most far point in beam direction from longitudinal center of gravity was pushed with external force until the roll angle reached its designed value. In Fact, EFD external force could induce initial heave and pitch motions which are not considered in CFD. For $\phi_0 = -28.6^\circ$, which was performed with two-room compartment, CFD predicts the amplitude very well but the period is over predicted. In fact due to more reduction of the restoring moment for damaged ship with two rooms compartment, the GM value is smaller and thus the period is longer compared to that for one room compartment case. Thus, CFD results are reasonable and probably the difference between CFD and EFD originates from the change of center of gravity of EFD model when the model with two-room compartment was being prepared.

Figure 16 and 17 show the EFD and CFD comparison of the water height inside the compartment for $\phi_0 = -25.5^\circ$ and $\phi_0 = -28.6^\circ$, respectively. The water height is measured at points A, B and C inside the first room of compartment and points D and E inside the second room of the compartment as shown in Figure 2. Point A is close to the opening, point B is in the middle of the room and point C is

close to the wall on the other side of the first room. Point D and E are at the same transversal locations as points A and B but located in the second room (see Figure 2). Figure 16 shows that the free surface oscillates at roll period at points A and C with amplitude decreasing by time as the roll motion reduces. There is a 180 deg phase lag between water heights at points A and C as one is located on the starboard and the other once is located on the portside. The EFD free surface elevation at point B has fairly constant value as point B is at the middle, located on the roll axis. The average of water height for all the three points is about 0.06 m, the same as the water depth inside the compartment. CFD predicts very well the mean, amplitude and phase of the water heights in all three locations. CFD shows some nonlinearity in the wave heights at high frequencies probably due to the sloshing event in the compartment.

Figure 17 shows the water height at both rooms for $\phi_0 = -28.6^\circ$. The EFD water height at point A, B and C are pretty close to what was observed for $\phi_0 = -25.5^\circ$ with one room compartment. The water height at point E shows constant value similar to that of point B. However, the water height is larger meaning that the water height inside the second room is higher probably due to the bow down position of the ship during roll decay which delivers water from the first room to the second room. The water height at point D shows smaller amplitude compared to that for point A in first room. This difference could be due to the fact that point A is close to the opening in first room. CFD shows very good agreement for the amplitude of water heights at all locations. However, there are some discrepancies for the phases. This is due to the phase difference observed in CFD and EFD roll motion comparison as shown in Figure 15.

Figure 18 compares CFD and EFD damped natural roll frequency vs. mean roll angle for cases with one-room compartment. EFD and CFD damped frequency is fairly close to $f_{\phi_d} = 0.44$ Hz for all ϕ_m . The results compared with

the intact ones show 10% smaller frequency for the roll decay under damaged condition. This is due to the reduction of restoring moment or GM of the ship hull in damaged condition.

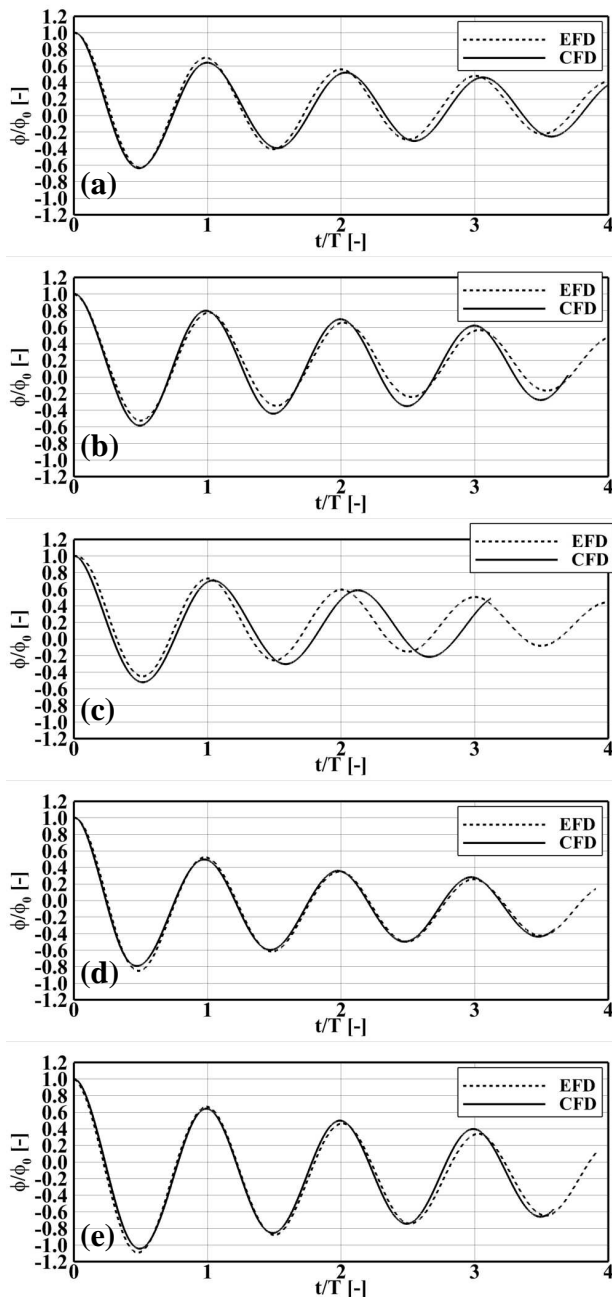


Figure 15: EFD and CFD roll decay time history for damaged SSRC cruiser: (a) $\phi_0=-25.5^\circ$; (b) $\phi_0=-15.6^\circ$; (c) $\phi_0=-28.6^\circ$; (d) $\phi_0=26.7^\circ$; (e) $\phi_0=15.9^\circ$.

Table 7 Mean value for damage roll decay

case	EFD	CFD	%E
C4	-2.22	-2.21	0.68
C5	-3.01	-2.48	17.65
C6	-2.63	-2.30	12.74
C7	-2.78	-2.51	9.79
C8	-5.74	-4.94	13.97

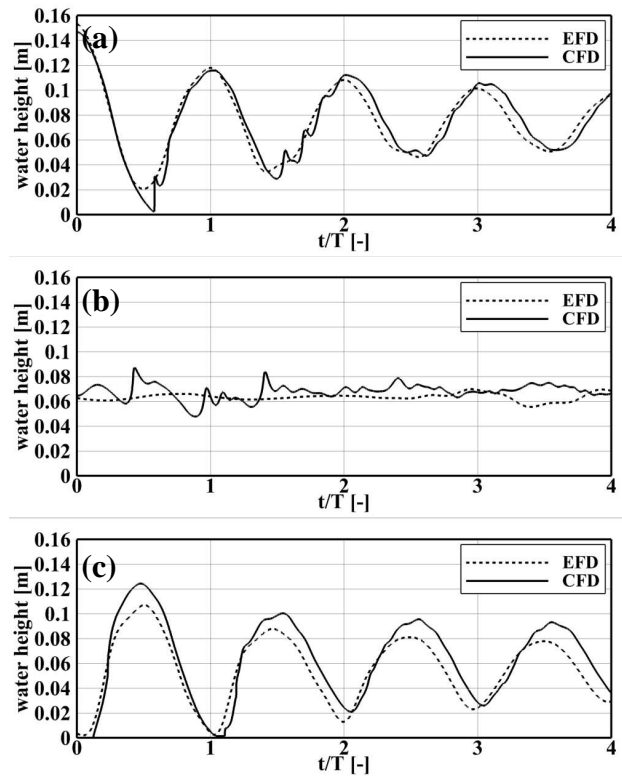


Figure 16: EFD and CFD water height time history for damaged SSRC cruiser in roll decay with initial roll angle of $\phi_0=-25.5^\circ$.

Figure 19 compares EFD and CFD linear and nonlinear damping coefficients estimated based on Himeno method (1981). The EFD linear damping coefficients are larger than those for intact cases. The cubical damping coefficient is zero for large initial roll angle. CFD predicts the linear damping coefficients very well for all cases. The linear damping increases with initial roll angle similar to EFD. The CFD nonlinear damping coefficients are zero for all cases unlike EFD which showed zero value only for the case with large angle. The large errors for small initial roll angle could be due to the EFD data reduction technique which might have influence on the accuracy of the data as mentioned earlier.

Figure 20 and 21 show the water free surface deformation inside and outside the compartment during roll decay with initial roll of about -25.5° and $\phi_0=-28.6^\circ$, respectively. When the ship rolls to portside the water inside compartment flows opposite to the damage side



and hits the compartment wall causing sloshing. The sloshing event generates waves moving toward the damaged side on the starboard and assists the draining in first room when the opening door comes out of the water. As shown, the draining makes very complex free surface deformation around the opening due to the ship motion and the sloshing wave.

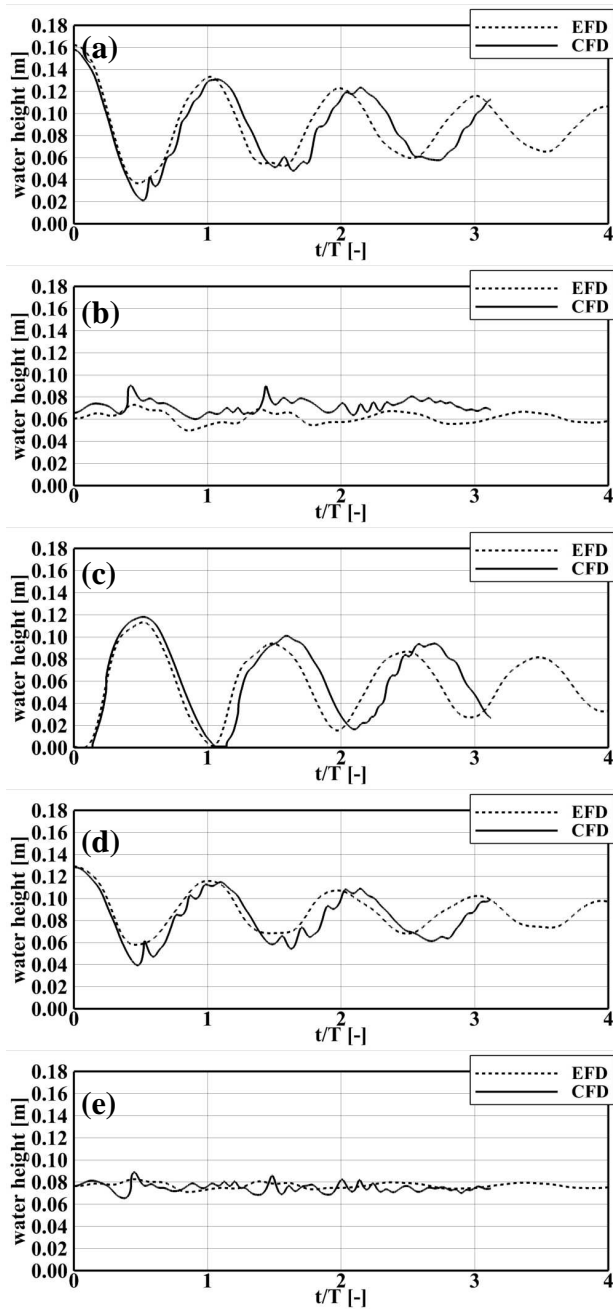


Figure 17: EFD and CFD water height time history for damaged SSRC cruiser in roll decay with initial roll angle of $\phi_0 = -28.6^\circ$.

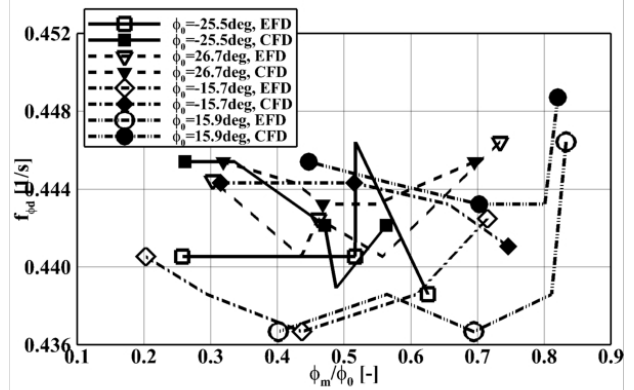


Figure 18 EFD and CFD damped natural roll frequency vs. mean roll angle for damaged SSRC cruiser in roll decay.

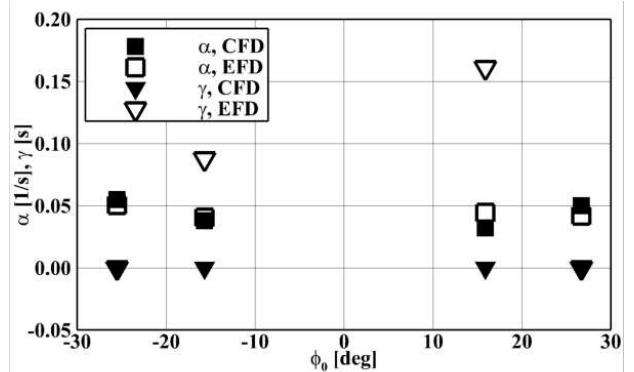


Figure 19: EFD and CFD damping coefficients in roll decay for damaged SSRC cruiser.

4.6 Motions in Regular Beam Waves of Intact SSRC cruiser

The regular wave cases for intact SSRC cruiser were validated prior to the damaged cases. The simulations of intact SSRC in waves are conducted for wave conditions R1, R3, R5, R7 and R9 with $H/\lambda = 1/60$ as listed in Table 4.

Figure 22 shows time history of intact ship motions for case RI9, listed in Table 3. The wave length is about $2.4L$ and the wave slope is 0.052 . The spring frequency is filtered in EFD and CFD time histories using band-pass filtering in Matlab to investigate the wave induced motions. EFD results show sinusoidal behaviour for most of the motions, oscillating at wave frequency. The induced surge motion is very small while the amplitude of sway and heave motions are close to the wave amplitude A . The induced roll motion is about 15 deg, 5

times larger than the wave slope. This shows that the roll is excited by wave with frequency close to the roll natural frequency as the roll amplitude in long beam waves should be close to A_k . The pitch and yaw motions are fairly small. The CFD and EFD surge motions show some differences since EFD surge is very small

and not converged such that the EFD surge motion does not show harmonic oscillation with steady amplitude. CFD predicts sway, heave and roll motions with remarkable agreement. However, the pitch amplitude is under predicted significantly and yaw is slightly over predicted.

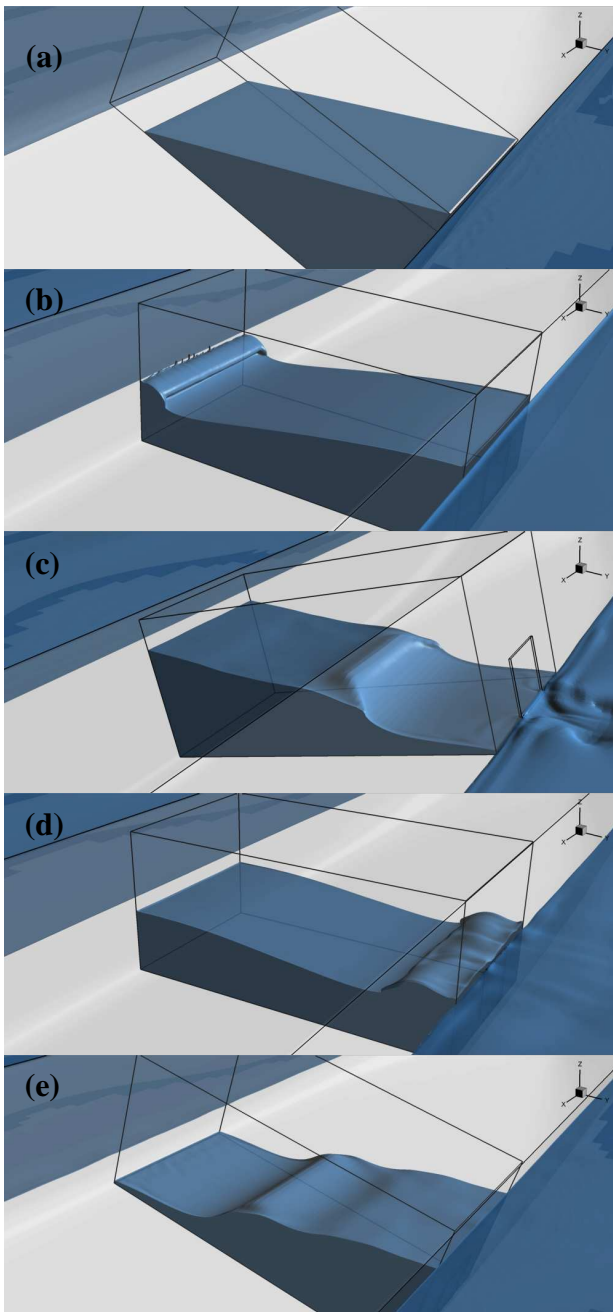


Figure 20: Free surface deformation for damaged roll decay with initial roll of -25.5° : (a) $t=0$; (b) $t=T/4$; (c) $t=T/2$; (d) $t=3T/4$; (e) $t=T$.

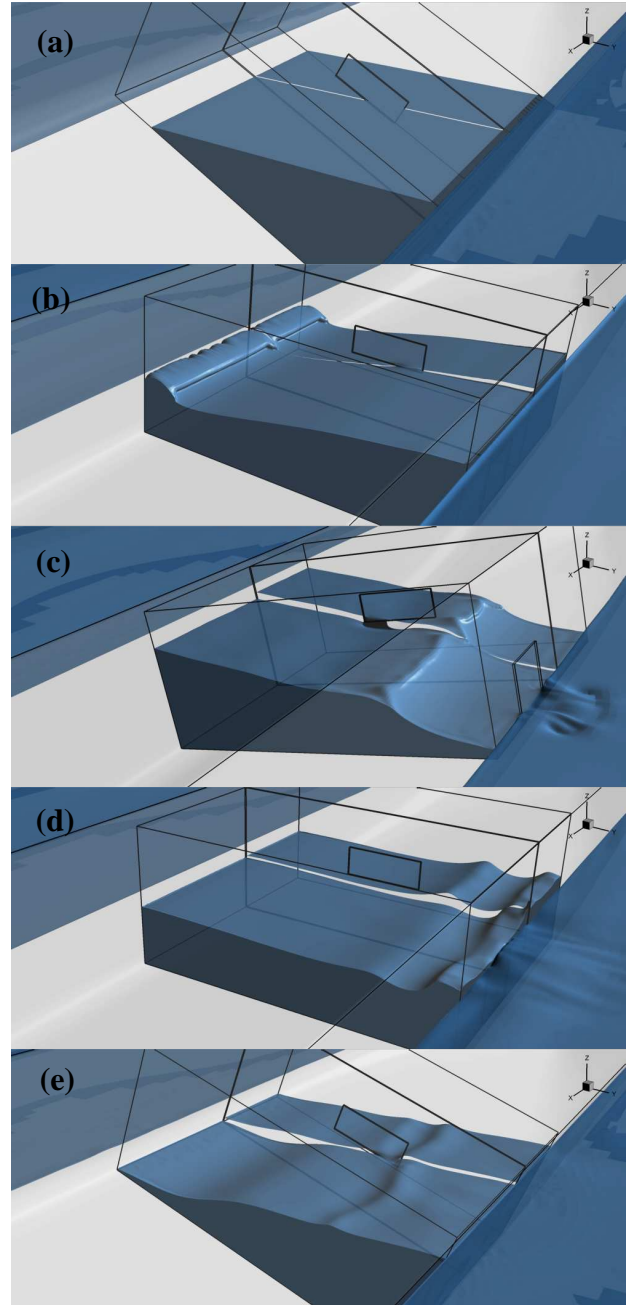


Figure 21: Free surface deformation for damaged roll decay with initial roll of -28.6° : (a) $t=0$; (b) $t=T/4$; (c) $t=T/2$; (d) $t=3T/4$; (e) $t=T$.

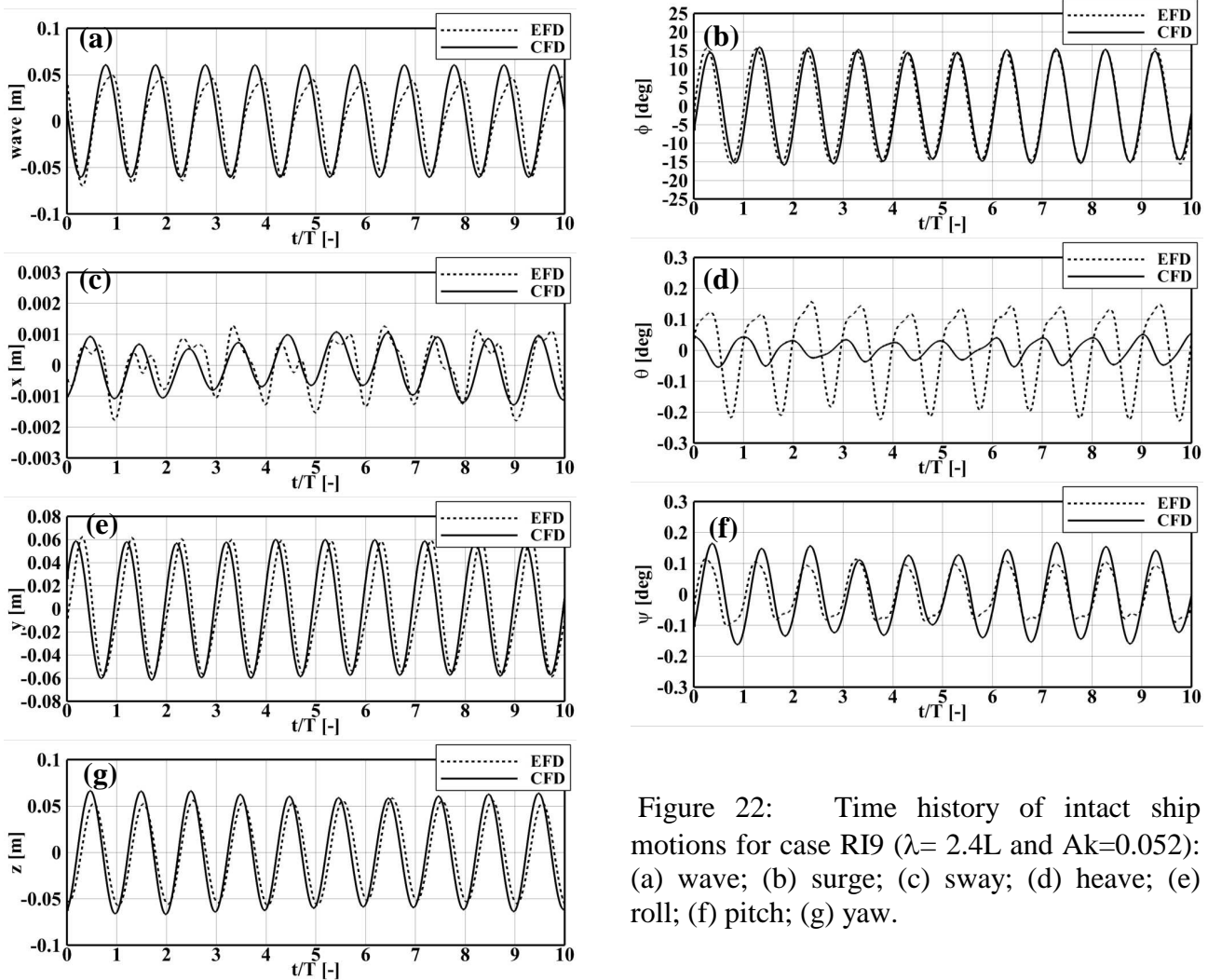


Figure 22: Time history of intact ship motions for case RI9 ($\lambda = 2.4L$ and $Ak=0.052$): (a) wave; (b) surge; (c) sway; (d) heave; (e) roll; (f) pitch; (g) yaw.

Figure 23 shows the EFD and CFD comparison for case RI7, with same wave slope but with smaller wave period/wave length compared to previous case. The wave length for case RI7 is about $2.2L$ corresponding to wave period of $T=2.055$ sec, same as SSRC roll natural frequency. The EFD results show sinusoidal behaviour for all motions except surge as before. Here, CFD also shows good agreement with EFD data for most of the motions. However, the pitch motion is under predicted as before. Also, the sway motion is out of phase compared with EFD data. The results show larger roll amplitude compared to that for case RI9 while other motions are fairly similar. This is due to the fact that the wave length is very large compared to ship beam for case RI7 and RI9 such that heave and pitch would be far from the resonant conditions and only show the behaviour which is expected in

long waves. Note that wave frequency is 0.49HZ while SSRC heave and pitch frequencies are about 1.2 HZ and 1.3HZ , estimated from below equations:

$$f_z = \sqrt{gC_{WP} / (8\pi^2 C_B T)} \quad (8)$$

$$f_\theta = \sqrt{gB^3 C_{IT} / (96\pi^2 \hat{I}_y L^4)} \quad (9)$$

where C_{WP} is water plane area coefficient, C_B is block coefficient, T is draft, $C_{IT} = 12I_T / B^3 L$ is the coefficient of inertia of the water plane area about the y axis, and $\hat{I}_y = I_y / (\rho L^5)$ is a non-dimensional mass moment of inertia about the y axis. The empirical formula for both heave and pitch frequencies are derived under the assumption

that the added mass/inertia of heave/pitch is the same as the ship mass/moment of inertia.

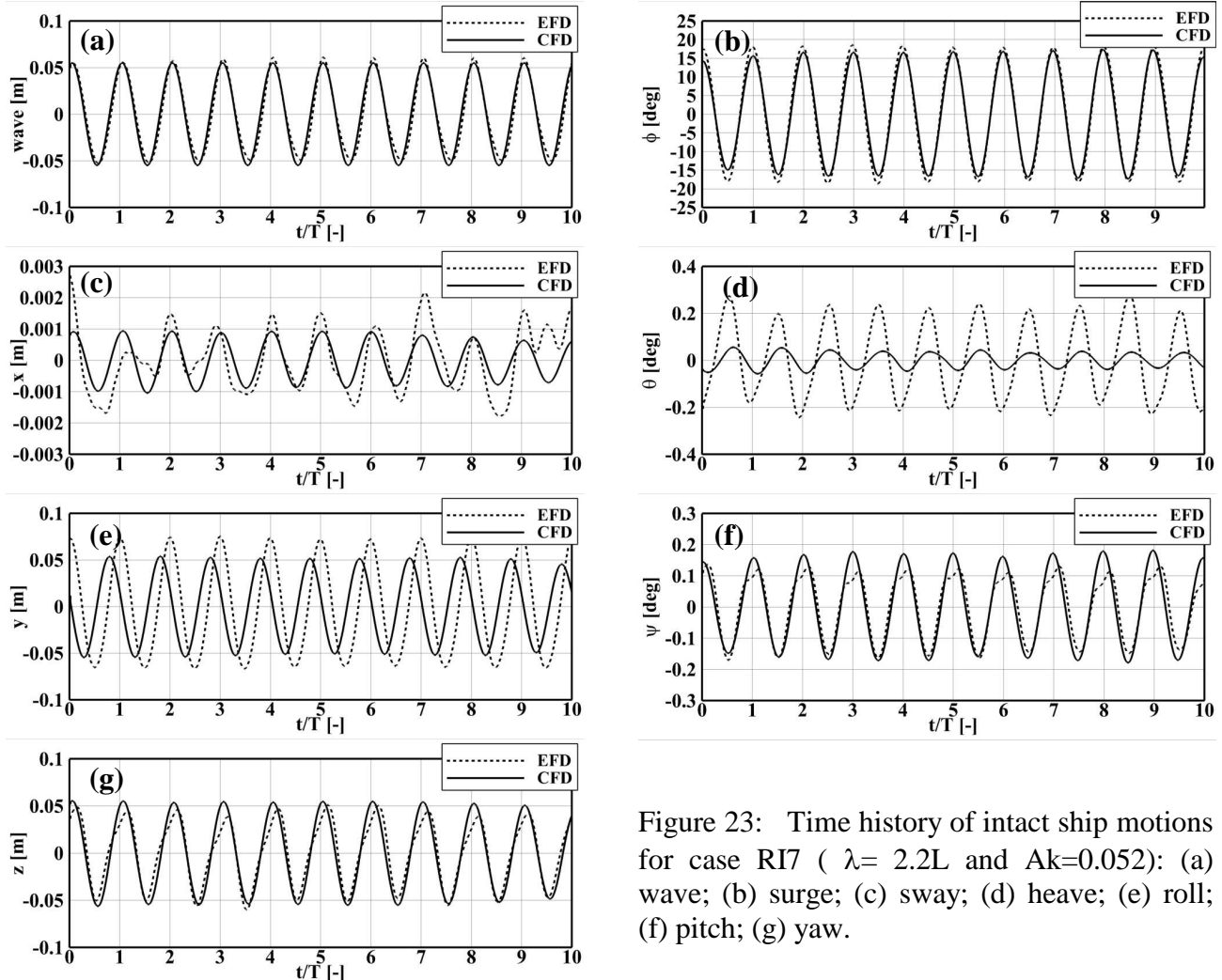


Figure 23: Time history of intact ship motions for case RI7 ($\lambda = 2.2L$ and $Ak=0.052$): (a) wave; (b) surge; (c) sway; (d) heave; (e) roll; (f) pitch; (g) yaw.

For intact ship case RI5 and RI3, the EFD and CFD time histories are not shown here as the results are very close to those shown for cases RI9 and RI7 since all cases are in long wave length conditions. However, the roll amplitude decreases for case RI5 and RI3 compared to case RI9 and RI7 as the wave frequency is far from the natural roll frequency. Anyhow, the EFD and CFD motions for cases RI5 and RI3 will be reported in RAO figures.

Figure 24 shows EFD and CFD results for case RI1. Since wave frequency is about twice of the roll natural frequency, parametric rolling is observed for this case. Thus, EFD data shows that roll oscillates at half of wave frequency with roll amplitude gradually increased to about 18 deg. The EFD sway, pitch and yaw motions also oscillate at the roll

natural frequency. The sway and yaw oscillations are due to first order coupling with roll as discussed in Sadat-Hosseini et al. (2010). However, the pitch motion has higher order coupling with roll and it is not expected to oscillate at roll natural frequency. Thus, there is a possibility of errors in the measurement of EFD pitch motion. The EFD surge and heave show oscillations mostly at wave frequency as the coupling between roll and surge/heave is second order. CFD results show good agreement for surge and heave motions. The amplitude and phase of roll and yaw motions are also well predicted after the roll amplitude reaches to large values. However, CFD under predicts the sway and pitch motions.

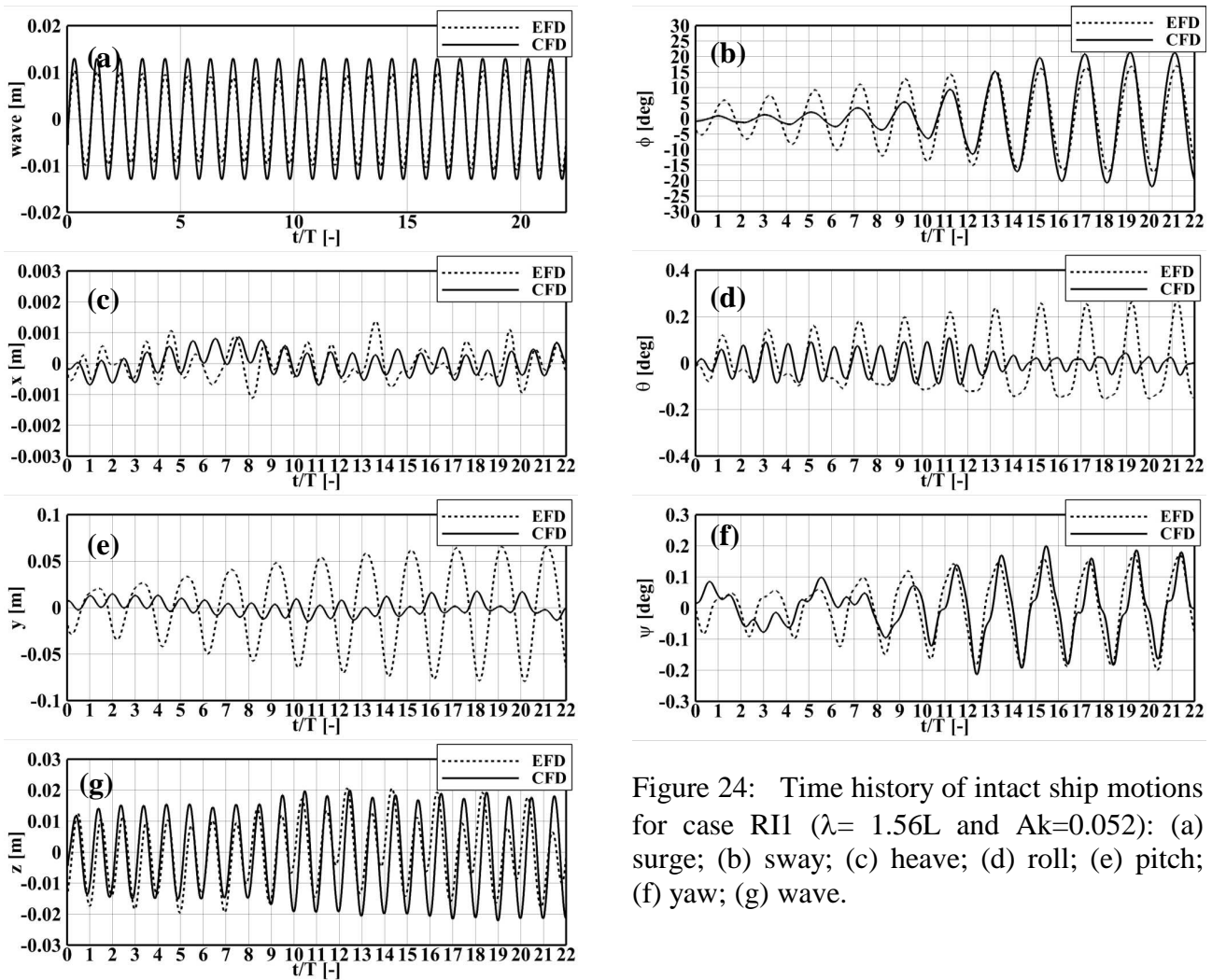


Figure 24: Time history of intact ship motions for case RI1 ($\lambda=1.56L$ and $Ak=0.052$): (a) surge; (b) sway; (c) heave; (d) roll; (e) pitch; (f) yaw; (g) wave.

The ship first harmonics for all wave length conditions at $Ak=0.052$ are shown in Figure 25. The EFD surge motion amplitude increases with decreasing wave length while the sway motion decreases by decreasing the wave length. EFD roll, pitch and yaw motions show fairly similar trend. All are large at long wave where the wave frequency is close to natural roll frequency and then decrease to small value for shorter waves. Note that herein only first harmonic amplitudes are plotted such that case RI1 ($\lambda/L=0.52$) shows fairly zero amplitudes here while the second harmonic amplitudes induced by parametric roll for case RI1 are large. CFD predicts the trend for most of the motions very well. However, the pitch motion is under predicted around the resonance condition. The overall average of prediction error is 23%D excluding the pitch motion errors.

4.7 Motions in Regular Beam Waves of Damaged SSRC Cruiser

The damaged cases are conducted at the same wave condition for the intact cases as shown in Table 3 and 4. The motions and water heights for case RD9 are shown in Figure 26. The damage door was closed initially and then released during the test at $t/T=2.4$, as marked in the plots. The EFD results show that the flooding increases the amplitude of sway, roll, pitch and yaw. However, the amplitude of heave amplitude decreases after opening the damage door. The water height inside the compartment shows that the water height rises in the compartment with high rate after opening the damage door such that after two cycles of motions, the water height at point B reaches to average value of 0.06m, same level as outside water. Also after opening the



damage door, there is a time lag between water height increase at points A and B as point B is not close to the opening and sees the water after point A. However, the measured water height at point C located very far from the opening shows that this point sees the water sooner than point B which is impossible. This suggests errors in the data which might be due to measuring system or the data reduction techniques. After the compartment is fully flooded ($t/T=5$), the water height mean value at points A and C are about 0.06 m but the amplitudes of water height are still growing due to the increase of roll motion after flooding. It seems that the roll motion and consequently the water height amplitude reach to stable amplitude after $t/T=9$. During the test, the second room is not flooded at all such that the water heights at point D and E are zero. The CFD results show that CFD could predict very well most of the motions while CFD under predicts the pitch motion and predicts the sway motion with a phase lag as before. The opening door was closed initially and then released during the test, mimicking EFD. However, the CFD water heights show that the door is opened a bit later than the experiment. This causes some differences in the transient region for water heights inside the compartment. However, the agreement with EFD is remarkable after the compartment is fully flooded. Note that CFD also shows no water in the second room during the simulation.

The motions and water heights for case RD7 are shown in Figure 27. Most of EFD motions and water heights for this case are similar to those for case RD9. However, the roll motion is smaller as wave length for case RD9 is close to resonance condition for roll motion. Note that the natural roll period for damaged ship is about 2.25 sec (10% higher than the roll period for intact condition), as shown in Figure 18. This means that the roll for damaged ship would be excited by a wave length of $2.47L$, close to the wave condition for case RD9. The CFD simulation for motions show same trend as previous cases i.e. under predicting pitch motion predicting sway motion

with a phase lag. For water heights, the CFD prediction is much better for this case as the door is opened exactly when the EFD door was opened. This results in remarkable agreement with EFD for water heights even during the transit region when the compartment is getting flooded.

The ship responses for case RD3 and case RD5 are close to those for case RD7 and RD9 as all of them are at long waves. Thus, herein the time history of motions and water heights are not shown for cases RD3 and RD5. The EFD and CFD comparison for case RD1 is shown in Figure 28. Parametric roll is not observed for case 1 unlike the intact condition. Since the natural roll period for damaged ship is 10% higher than the roll period for intact condition (see Figure 18), the roll period would be about 2.3 times of the wave period for case RD1, fairly far from the critical condition for parametric rolling. The wave length is fairly short ($0.52L$) for this case and thus most of the motions are very small compared to the other cases. The CFD simulation shows good agreement for surge, heave and yaw motions. The sway motion and pitch are not predicted well again. The CFD roll motion also shows discrepancy with EFD data which results in differences between EFD and CFD water heights inside the compartment.

The free surface elevation inside the compartment and around the ship is illustrated for case RD7 and RD9, as shown in Figure 29 and Figure 30. For Figure 29 shows the free surface in transient region during the flooding for case RD7. Figure 30 shows the free surface for four wave phases when ship is fully flooded for case RD9. Similar to the damaged roll decay cases, the sloshing occurs in the compartment. The sloshing also provides complex free surface deformation around the opening after draining the water. Figure 30 also shows that the second room is not flooded during the simulation, similar to EFD.

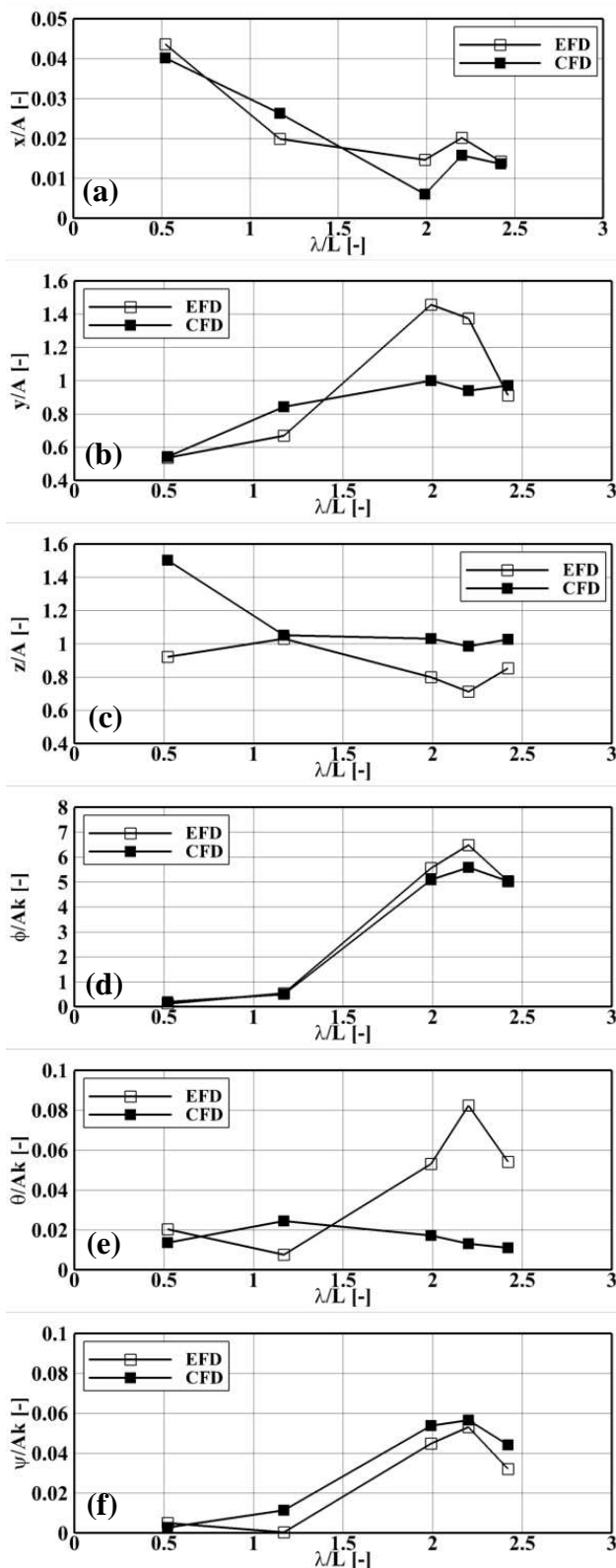


Figure 25: RAO of intact ship motions in beam waves with $Ak=0.052$: (a) surge; (b) sway; (c) heave; (d) roll; (e) pitch; (f) yaw.

The first harmonic amplitudes of damaged ship responses are plotted in Figure 31. The EFD results show that the surge motion increases with decreasing wave length. The sway, roll and yaw motions increase from short to long waves. The roll motion increases to large values at long waves as the ship is excited by a frequency close to roll natural frequency. Overall the trends of ship responses are very similar to those for intact ship. CFD could predict the motions fairly well. The average of CFD prediction errors is 26%D excluding the errors for pitch motion.

5. CONCLUSION AND FUTURE WORK

CFD is validated for the flooding process of a damaged compartment with no motions and flooding process of damaged SSRC cruiser in calm water with 6DOF motions. CFD simulations are also conducted for roll decay in calm water and motions in regular beam waves for 6DOF SSRC under both intact and damaged conditions. The verification study is conducted for intact ship in waves to evaluate the simulation uncertainty.

The iterative, grid and time step uncertainty were estimated for intact ship motions in beam waves with $\lambda=2.4L$ and $Ak=0.052$. The average of the grid, time step and iterative uncertainty is about $U_G=6.24\% S_I$, $U_T=2.17\% S_I$ and $U_I=1.98\% S_I$. The total simulation uncertainty is determined $U_{SN}=7.02\% S_I$ for current simulations suggesting that the results are not very sensitive to the numerical uncertainty.

The CFD simulation for the flooding process for SSRC under 6DOF motions in calm water shows some differences with roll motion but the water heights are predicted very well. CFD shows the roll and consequently the water heights oscillate at natural roll period of the damaged ship. CFD results could capture the complex free surface shape inside the compartment generated by the flooded water and the reflected water by the walls inside the compartment.

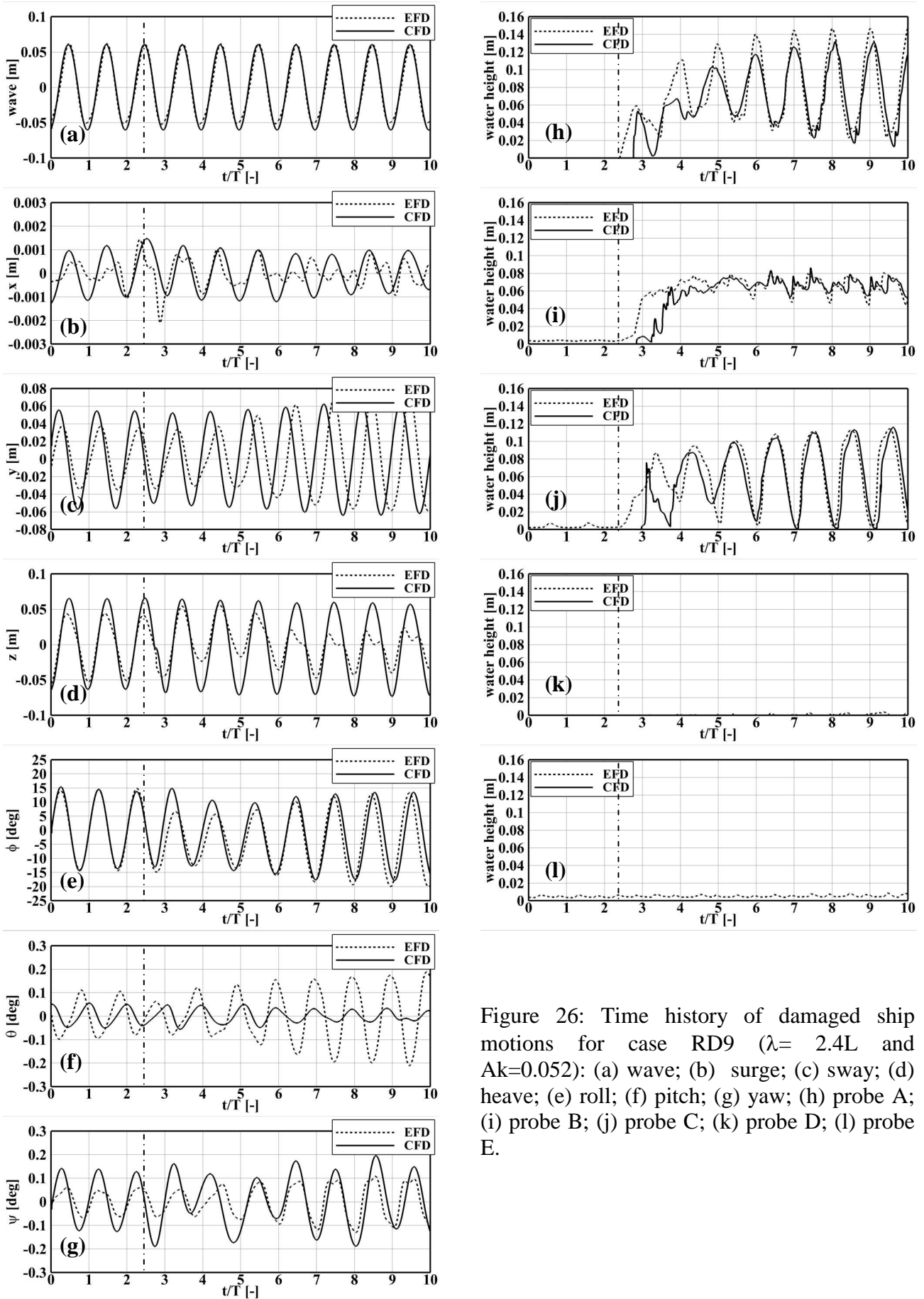


Figure 26: Time history of damaged ship motions for case RD9 ($\lambda = 2.4L$ and $Ak = 0.052$): (a) wave; (b) surge; (c) sway; (d) heave; (e) roll; (f) pitch; (g) yaw; (h) probe A; (i) probe B; (j) probe C; (k) probe D; (l) probe E.

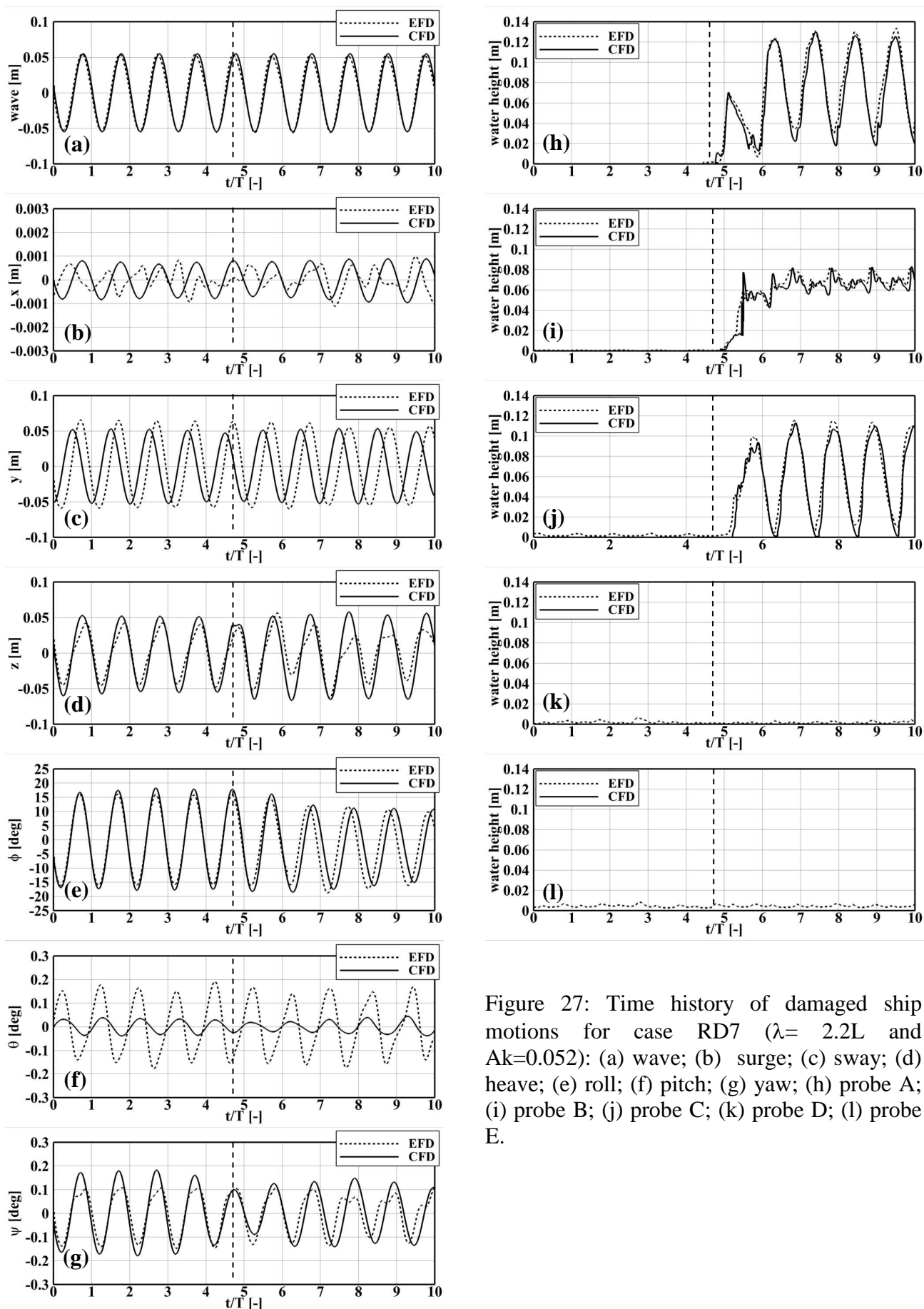
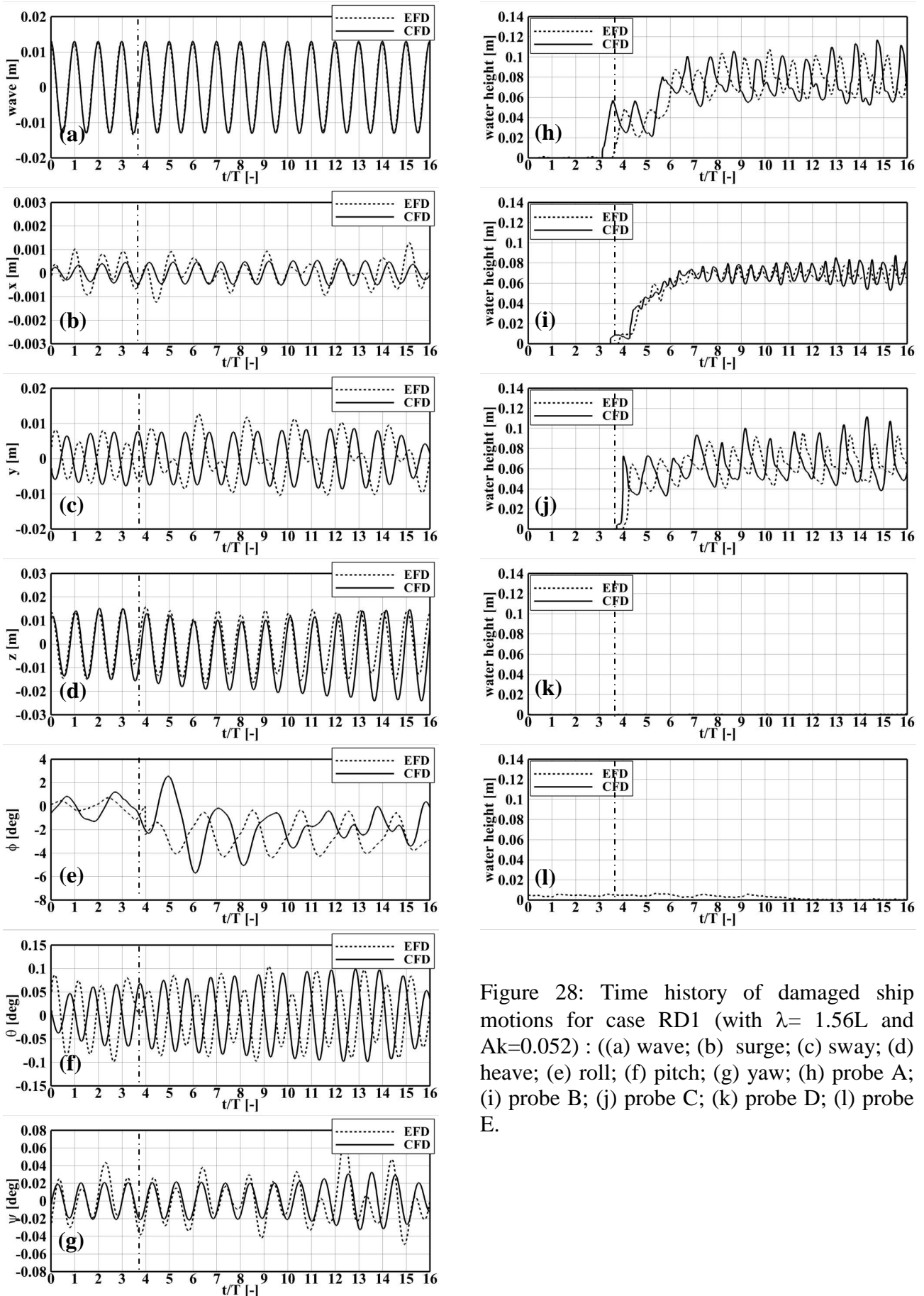


Figure 27: Time history of damaged ship motions for case RD7 ($\lambda= 2.2L$ and $Ak=0.052$): (a) wave; (b) surge; (c) sway; (d) heave; (e) roll; (f) pitch; (g) yaw; (h) probe A; (i) probe B; (j) probe C; (k) probe D; (l) probe E.



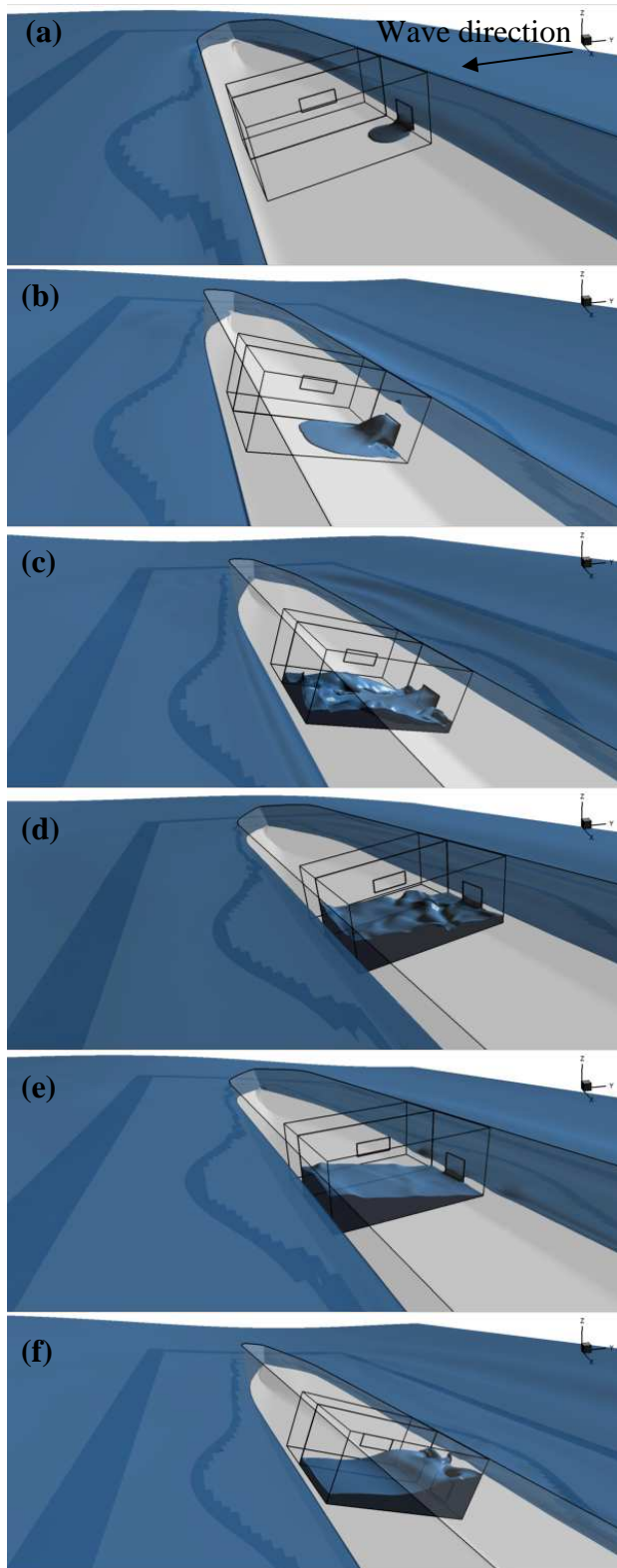


Figure 29 Free-surface elevation inside the compartment and near the ship during the flooding for case RD7: (a) $t=0.27s$; (b) $t=0.82s$; (c) $t=1.38s$; (d) $t=1.93s$; (e) $t=2.48s$; (f) $t=3.04s$.

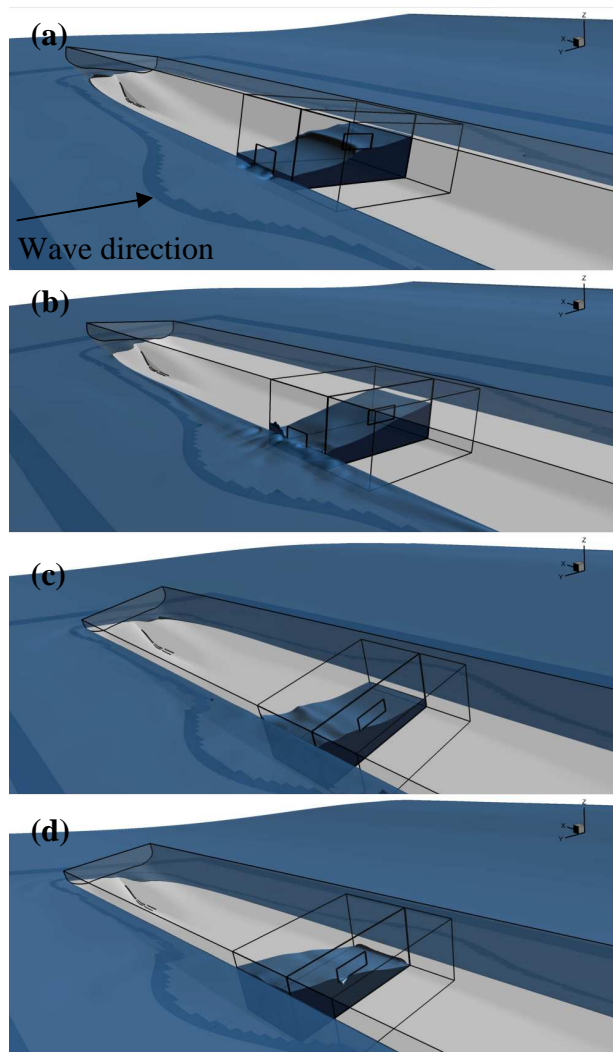


Figure 30: Free-surface elevation inside the compartment and near the ship after the compartment is fully flooded for case RD9 ($\lambda=2.4L$ and $Ak=0.052$): (a) $\varepsilon=0^\circ$; (b) $\varepsilon=90^\circ$; (c) $\varepsilon=180^\circ$; (d) $\varepsilon=270^\circ$.

CFD intact and damaged roll decay simulations predict the roll amplitude and damping coefficients very well. It is found the damping coefficient is larger and roll frequency is smaller for the roll decay under damaged condition. CFD also predicts the water heights inside the compartment for the damaged ship with remarkable agreement with EFD data. CFD also shows some nonlinearity in the wave heights at high frequencies probably due to the sloshing event in the compartment.

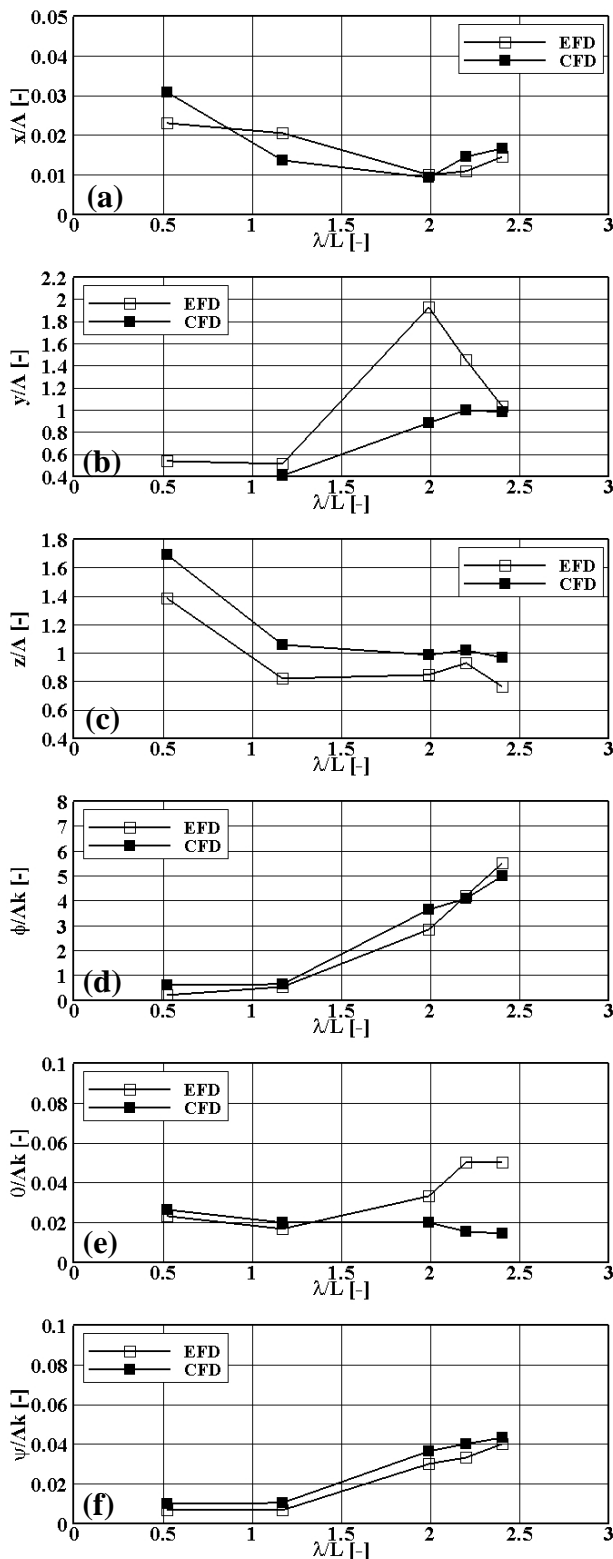


Figure 31: RAO of damaged ship motions in beam waves with $Ak=0.052$: (a) surge; (b) sway; (c) heave; (d) roll; (e) pitch; (f) yaw.

The CFD simulations of intact and damaged SSRC in beam waves show very good agreement for most of the motions and water heights inside the compartment for the damaged ship. However, the pitch motion is mostly under predicted and the predicted sway motion shows often a phase lag with the data. For intact condition, CFD could predict the trend of motions against wave length. The roll motion showed a very large value at long waves due to the resonance condition. Similar to EFD, CFD show parametric rolling for shortest wave length condition as the wave frequency was about twice the natural roll frequency. The average prediction error for intact cases is 23%D excluding the large errors for pitch motion. For damaged ship, the opening door was closed initially and then released during the test, mimicking EFD. CFD could predict the flooding rate very well. CFD show flooding only for first room of the compartment, similar to EFD. The CFD results show sloshing waves generated in the compartment due to the ship motions. The roll motion shows that the flooded ship is tilted toward the damage side. The average of CFD prediction errors for damaged ship is 26%D excluding the errors for pitch motion.

For future, the flooding and ship motions of damaged ship in waves will be studied for more wave heading conditions. Furthermore, damaged stability in following or head waves with forward speed will also be investigated.

6. ACKNOWLEDGEMENTS

This research was sponsored by the Office of Naval Research Grant N000141-21-05-6-8 and NICOP Grant N000140-91-10-9-1 under the administration Dr. Patrick Purtell.

7. REFERENCES

Carrica, P. M., Huang, J., Noack, R., Kaushik, D., Smith, B., Stern, F., (2010), Large-scale DES computations of the forward speed diffraction and pitch and heave problems



for a surface combatant, Computer & Fluids,
vol. 39, Issue 7, pp. 1095-1111.

Cho, S., Hong, S., Kim, Y., (2006),
Investigation of dynamic characteristics of
the flooding water of the damaged
compartment of an ITTC RoRo-Passenger,
J. of the Soc. of Naval Architects of Korea,
Vol. 43, Issue 4, pp.451-459

Gao, Q. and Vassalos, D., (2011), Numerical
Study of the Roll Decay of Intact and
Damaged Ships, Proceeding of 11th
International Ship Stability Workshop.

Gao, Z., Gao, Q., Vassalos, D., (2011),
Numerical simulation of flooding of a
damaged ship, Journal of Ocean
Engineering (In Press).

Himeno, Y. (1981). Prediction of Ship Roll
Damping – State of the Art, University of
Michigan, Report No. 239.

Sadat-Hosseini, H., Stern, F., Olivieri, A.,
Campana, E., Hashimoto, H., Umeda, N.,
Bulian, G., and Francescutto, A., (2010),
“Head-waves parametric rolling of surface
combatant”, Journal of Ocean Engineering,
Vol. 37, Issue 10, Pages 859-878.

Strasser, C., Jasionowski, A. and Vassalos, D.,
(2009), Calculation of the Time-to-Flood of
a Box-Shaped Barge using CFD, Proc. 10th
Int’l Conf. Stability of Ships & Ocean
Vehicles, St. Petersburg, Russia, pp. 733–
740.



A Study for the Harmonized Probabilistic Approach for Damage Stability Taking Account of the Difference Between Collision and Grounding

Koichiro Shiraishi, *National Maritime Research Institute, Japan*, shiraishi@nmri.go.jp

Yoshitaka Ogawa, *National Maritime Research Institute, Japan*, ogawa@nmri.go.jp

ABSTRACT

In the case of grounding, there is a certain possibility of rescue after beaching. Authors conducted research on such safe beaching, and found that the probability of safe beaching after grounding accidents is about 80%. This is a significant number, which cannot be neglected. Therefore, it is important to consider the survivability after beaching in developing probabilistic stability requirements to bottom damage. Based on this understanding, the authors developed a new methodology of probabilistic bottom damage stability requirements.

Keywords: *Grounding, Beaching Factor, Probabilistic Bottom Damage Stability Requirement and Goal Based Approach.*

1. INTRODUCTION

There are two types of cause of flooding accident, which are correlated closely with damage stability. One is the collision between two ships at sea. In the case of collision, the struck ship could have a breach in its side-wall and then water ingress could occur. Depending on the extent of the damage, the struck ship could lose its buoyancy and will be in danger of sinking. The other incident is grounding. In the case of grounding, the hull bottom of the ship contacts with seabed and could be damaged. If the extent of the damage is not so small, the risk of sinking and/or capsizing could increase.

It is noteworthy here, however, that a grounding accident occurs only when the ship draught is comparable to water depth. This means that the ship is more likely to be beached. Consequently, ship survivability can be ensured and the risk of sink and/or capsizing can be limited.

Therefore, the difference between collision and grounding should be taken into account for

quantifying the risk in damage stability. However, in the framework of the current regulation for damage stability, the current probabilistic requirement was composed by assuming the collision. On the other hand, the current requirement related to the grounding is deterministic requirement although there is a certain possibility of rescue after beaching.

Based on the background, studies for the risk based damage stability have been carrying out (Papanikolaou et al., 2011, Vanem & Skjong, 2004). The present study is in the same line with those studies. In the present study, the probability of survival after the loss of buoyancy and/or stability due to grounding is quantified. A methodology for the probability of survival in the case grounding with index indicated as Z factor is proposed. The Z factor is evaluated based on the analysis in the worldwide sea area. It is clarified that derived probability Z is significant and important when we assess the risk after grounding.



2. RISK ANALYSIS IN TERMS OF GROUNDING

To investigate the probability of safe beaching, the authors conducted the event tree analysis of grounding accidents, which is extracted from Marine Accidents Inquiry in Japan (Ogawa & Shiraishi, 2011a). Figure 1 shows the event tree for grounding accident based on the real casualty data. In the present analysis from 1989 to 2010, 106 cargo ships and 46 oil carriers were investigated.

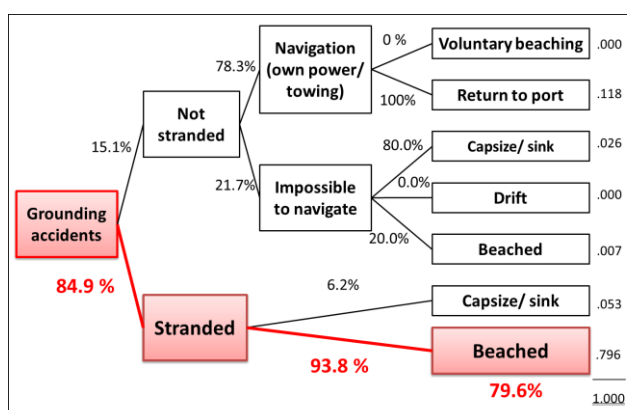


Figure 1: The event tree for grounding accident based on the real casualty data.

As a result, following features of the grounding accidents are found.

A ship was stranded with a probability of more than 84.9%

After a ship was stranded, the ship ended with safe beaching with a probability of more than 90%

In total, the probability that a ship was safely beached after a ship's bottom was damaged comprised 79.6% of the times.

In this event tree, the probability of 80% is too high to be neglected when considering probabilistic requirements. Thus, it is reasonable and essential to consider the survivability after beaching.

Based on the background, studies for the risk based damage stability are carrying out (Papanikolaou et al., 2011, Vanem & Skjong, 2004). The authors presented a new formula for quantifying the probability of survival in the

case grounding with index indicated as Z. Here the probability of survival after the loss of buoyancy and/or stability due to grounding is taken into account. In this paper, a methodology for the probability of survival, Z factor, is proposed. Z factor in the 16 worldwide sea area is computed. It is clarified that derived probability Z is significant and important when we assess the risk after grounding.

3. SURVIVABILITY IN THE CASE OF GROUNDING

Firstly, the probability of survival in the current framework of regulation is shown as eq. (1). Only a collision accident is assumed in this probabilistic formula.

$$A^c = \sum (p_i^c \times s_i^c) \quad (1)$$

where: A_i^c represents the probability of survival in the case of collision; i represents each compartment or group of compartments under consideration; p_i^c accounts for the probability that only the compartment or group of compartments under consideration may be flooded in the case of collision; s_i^c accounts for the probability of survival after flooding the compartment or group of compartments under consideration in the case of collision.

The current regulation for damage stability does not take into account of safe beaching. Therefore, the current criteria for collision are not applicable to grounding.

Based on the risk analysis in the previous chapter, it is reasonable and essential to consider the survivability after beaching. Therefore, the current probabilistic formula is not applicable in the case of grounding,

Based on the background, a new formula for quantifying the probability of survival in the case of grounding is developed as follows:

$$A^g = \sum [(p_i^g \times s_i^g) + Z \times \{p_i^g \times (1 - s_i^g)\}] \quad (2)$$

where: A_i^s represents the probability of survival in the case of grounding; i represents each compartment or group of compartments under consideration; p_i^s accounts for the probability that only the compartment or group of compartments under consideration may be flooded in the case grounding; s_i^s accounts for the probability of survival after flooding in the case grounding the compartment or group of compartments under consideration; and Z represents the probability of safe beaching after the ship's bottom is damaged through grounding accidents.

The first term of eq. (2) describes the probability of survival when the ship has sufficient buoyancy and/or stability. The second term of eq. (2) describes the probability of survival as a result of safe beaching when the ship loses sufficient buoyancy and/or stability. The value of Z depends on not only the ship itself but also geometry of the relevant sea bed. The unsolved problem is a way to determine the value of Z .

Therefore, we derive the value of Z by the following three processes. Firstly, boundary points of the possibility for the grounding accident are evaluated. Secondly, the probability of beaching is evaluated based on the relation between draft of ship and geometry of the relevant sea bed. Finally, the probability of survival is evaluated taking account of the final heel angle of the ship.

3.1 Specification of the area where grounding accident can occur

Firstly, the area where a ship can contact with sea bed is specified. It is known that a grounding accident occurs only when the ship draught is comparable to water depth. Therefore, sea area can be divided into two areas. One is that a grounding accident can occur and the other is that a grounding accident can't occur. It is specified based on the relation between the ship as a subject and the geometry of the relevant sea bed. Here, two areas are determined by means of the following relation.

$$d \leq w \rightarrow \text{No possibility of grounding accident} \quad (3)$$

$$d > w \rightarrow \text{Possibility of grounding accident} \quad (4)$$

Here, d is the draft of the ship as a subject and w is the depth of the sea. The geometric relation is shown in Figure 2.

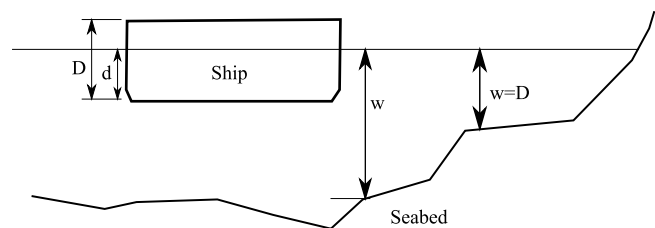


Figure 2: Geometric relation between ship and sea bed.

The boundary points between two specified areas tend to be the starting point of the occurrence of the grounding accident. Assuming that the boundary points are the points where the draft of the ship as a subject is same as the depth of the sea as a subject, the points are extracted by means of edge detection in the image processing algorithm (Ziou & Tabbone, 1998).

As an example, the boundary points of Tokyo bay are specified. Figure 3 shows the bathymetry of Tokyo Bay. Figure 4 shows the boundary points of Tokyo bay at $w = 12[m]$. It is found that boundary points of Tokyo bay are consistent with the bathymetry.

3.2 Probability of beaching

The stranded ship does not necessarily stay at the grounding spot, and could drift due to wind and current. Based on the analysis of casualty data of Japan, it was found that maximum drifting distance after grounding accident was about 2 miles. So, in our



investigation, the drifting distance is defined 4,000 meters.

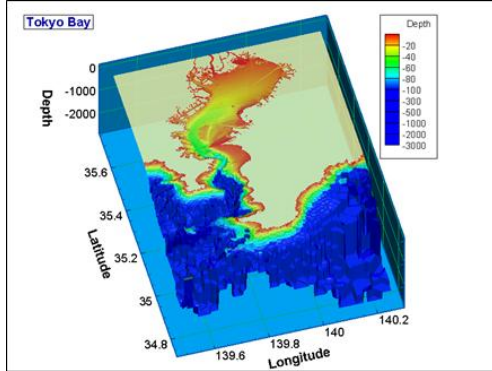


Figure 3: Bathymetric feature of Tokyo Bay.

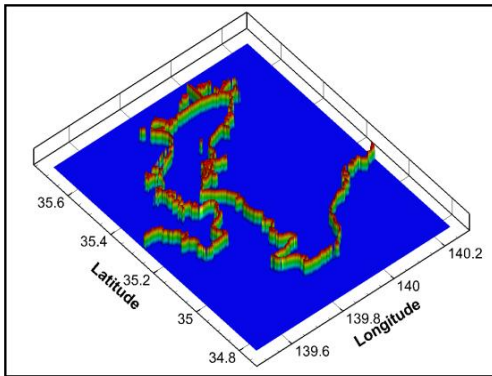


Figure 4: Boundary points of Tokyo bay at $w = 12[m]$.

Here, a circle from boundary points with a radius r is considered as the drifting distance. The probability of the beaching of ship is evaluated in this circle. It is assumed that the ship can be beached in the case that its draft is larger than the depth of the point.

The relation to the grounding line and the ship drifting range is shown in Figure 5. It is found that both land and sea area is included in the circle as a subject. Therefore, the probability of beaching $p_b(i)$ is considered by excluding the land area. It is described by the following formula.

$$p_b(i) = \frac{n_s(i)}{n_r(i) - n_l(i)} \quad (5)$$

Here, the number of the grid points contained within the assumed area is $n_r(i)$. The number of the points of the land within the assumed area is $n_l(i)$. The number of safety beaching points contained within the moving range is $n_s(i)$. The index of a point on the boundary points is i .

3.3 Probability of survival

The probability of non-capsizing $p_c(i)$ is evaluated based on the following two criteria. One is criterion of the sinking, and the other is criterion of the capsizing. Figure 6 shows the flow chart of the detection of the safe beaching points.

First, check whether or not to sink by the relations between draft of ship and water depth. Next, check whether or not to capsize by the heel angle of ship. If the points meet the above two criteria, they are the safe beaching points. The detail of the two criteria is described in the following section

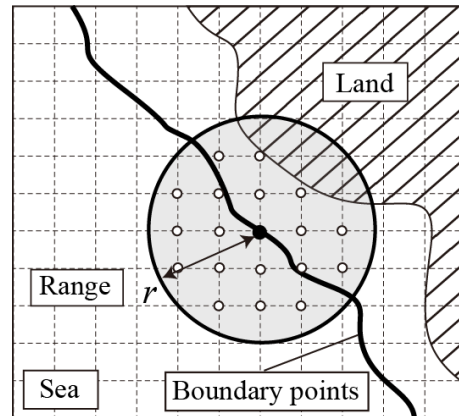


Figure 5: Definition of the relation between the grounding line and the ship drifting range.

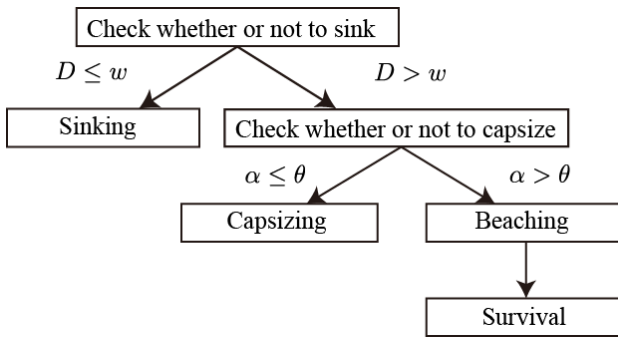


Figure 6: Flow chart of the evaluation of the probability of survival.

(1) Judgment of the sinking

It is found that there are some points where the depth of the sea is larger than the one of the subject ship within the shore side from boundary points. Therefore, the possibility of sinking is evaluated by the following relation:

$$D \leq w \rightarrow \text{Sinking} \quad (6)$$

$$D > w \rightarrow \text{Safety} \quad (7)$$

(2) Judgment condition of the capsizing.

If there is a vertical interval on the beaching point, the ship could beach having heel angle. The heel angle θ is expressed by the following equation:

$$\theta = \arcsin\left(\frac{h}{B/2}\right) \quad (8)$$

Here, B is the vessel's breadth, and h is the vertical interval. Figure 7 shows the definition of the heel angle.

If the heel angle is larger than maximum heel angle α , the vessel could capsize. In such cases, the ship is judged to be capsized. The geometric condition of the point is denoted by the following relation:

$$\theta \leq \alpha \rightarrow \text{Safety} \quad (9)$$

$$\theta > \alpha \rightarrow \text{Capsizing} \quad (10)$$

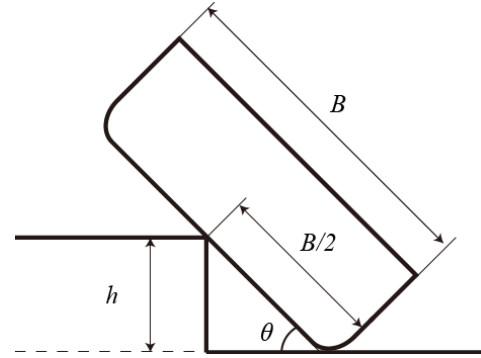


Figure 7: Definition of the heel angle of the vessel.

The maximum heel angle α was set to severest 7 degrees.

The points to meet the above two conditions are the safe beaching points. Figure 6 shows the flow chart of the detection of the safe beaching points. The probability of survival is described by the following formula.

$$p_c(i) = \frac{n_c(i)}{n_s(i)} \quad (11)$$

Here, the number of the grid points, which meet the above two conditions, are $n_c(i)$. The index of a point on the boundary points is i .

Finally, the probability of survival Z can be evaluated by the average of the probability at each boundary points, which is computed by multiplying the probability of beaching and the probability of non-capsizing. The probability is described by the following equation using Equation (5) and (11),

$$Z = \frac{1}{M} \sum_{i=1}^M p_b(i) \cdot p_c(i) \quad (12)$$

where, M is the number of the points on the boundary points.



3.4 Seabed conditions

There are various seabed conditions in the worldwide sea area. The situation of bottom damage may change with seabed conditions. Therefore, the Z factor is evaluated by taking account of seabed conditions.

Investigation for seabed condition is conducted using the nautical chart of the world. As a result, the rock was about 27.1% of the whole. Therefore, the safe beaching area was about 72.9% of the whole. Figure 8 shows the distribution of the seabed conditions.

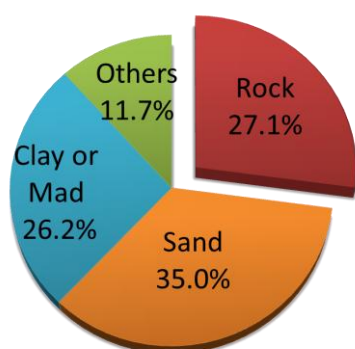


Figure 8: The distribution of seabed conditions.

4. ANALYSIS OF Z FACTOR

4.1 Computational Settings

In analysis of Z factor, 16 sea areas in the world, where grounding accidents occur most frequently is considered. In order to identify those sea areas, the statistics of grounding accidents is used. The statistics was derived from IHS Fairplay database in terms of all type of ships. Figure 9 shows the selected the 16 sea areas.

The bathymetry data was extracted by means of the electronic nautical chart (ENC) for a voyage. The used ENC data was C-Map of Jeppese. ENC data was used for Chart Rescue of software NSS. Chart Rescue can be displayed in the form of an electronic chart and a paper chart. Chart Rescue is customized so that it can extract the bathymetry data of the

arbitrary range from ENC data. The mesh size used in the extraction of the bathymetry data is 100m×100m . Parameter for computation is shown in Table 1.

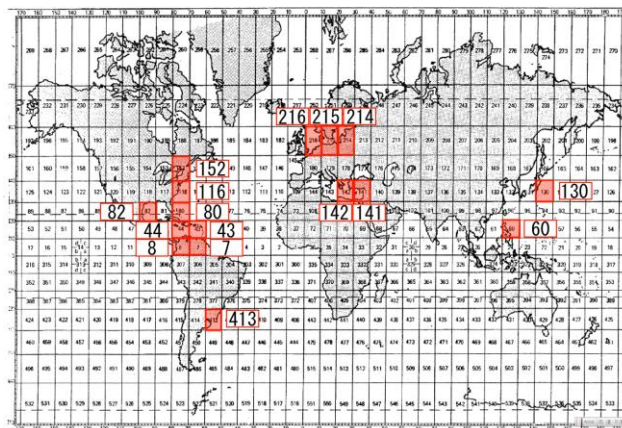


Figure 9: The identified sea areas in the computation.

Table 1: The computational conditions.

Draft [m]	3, 6, 9 12, 15, 18, 21 24, 27, 30, 33, 36, 39, 42, 45, 48
Depth [m]	10, 20, 30, 40, 50
Breadth [m]	20, 30, 40, 50
Range [m]	4,000
Max. heel angle [deg.]	7

4.2 Computed Results

The computational results of Z factor are shown in Figure 10. The x-axis indicates freeboard of ships. The y-axis indicates the value of Z factor. These plots in this figure indicate the average value of Z factor for each freeboard. In this figure, the value of Z factor tends to monotone increasing against the freeboard. And, the Z factor depends on the relation between the ship and the geometry of seabed.

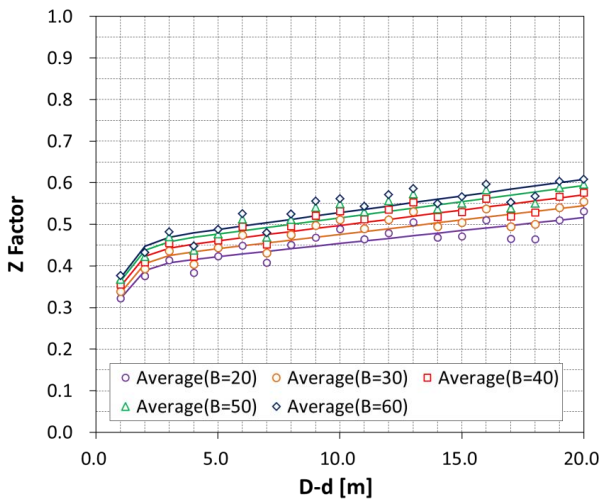


Figure 10: Results of the probability of survival: Z factor in 16 sea areas.

4.3 Comparison to the Real Casualty Data

Next, the computational results of Z factor are checked through the comparison with the real casualty data, which is shown in Figure 1 as the event tree. It is found that both the event tree and the computation indicate the significant value for the probability of safe beaching. It is clarified that this probability is essential to consider the survivability after grounding. On the other hand, there are quantitative differences between two probabilities. In this computation, it is assumed that the bottom damage can be occurred when a ship bottom just touches the relevant seabed. This means that the beaching factor by the presented computation is evaluated strictly.

5. APPLICATION TO THE RULE CALCULATION

5.1 Approximation Formula of Z Factor

For calculation of Z factor, the authors propose an approximated formula of Z factor based on the computation. The computational results of Z factor has following features. First, Z factor is function of the freeboard ($D-d$)

and the breadth (B). Next, Z factor is exponentially-increased until 4 m in freeboard. And, Z factor is linearly-increasing over 4 m in freeboard. Considering these features, Z factor can be expressed easily using the following formula.

$$Z = \gamma \times \left[a(D-d) + b \{1 - \exp(-c(D-d))\} \right] \quad (13)$$

The coefficients a, b and c are a function of breadth of ship. These coefficients are linearly-increasing against the ship breadth. Figure 11 shows the coefficients of the approximated formula. The coefficient γ is a parameter of seabed conditions. In this paper, γ is set to 0.729 taking account of the investigation of the seabed conditions.

By means of eq. (13), it is possible to calculate the attained index for grounding, which can be described as eq. (2). In eq. (2), the beaching factor Z can be computed by means of eq. (13). With regard to the component of eq. (2) other than Z factor, the probability to survive: s_i^g can be calculated by means of same methodology in the current regulation. The probability for bottom damage p_i^g can be also calculated by means of the formulae developed by the GOALDS project (Papanikolaou et al 2011). It is clarified that the probability of survival after grounding including the case of losing buoyancy can be calculated by means of the present formulae. It is pragmatic to evaluate the risk due to grounding rationally.

6. CONCLUSION

It is found that the probability of safe beaching in the case grounding accidents is significant through the event tree analysis. Based on these findings, the authors proposed a new methodology for quantifying the probability of survival in the case grounding, and proposed a new concept for the probability of safe beaching "Z".

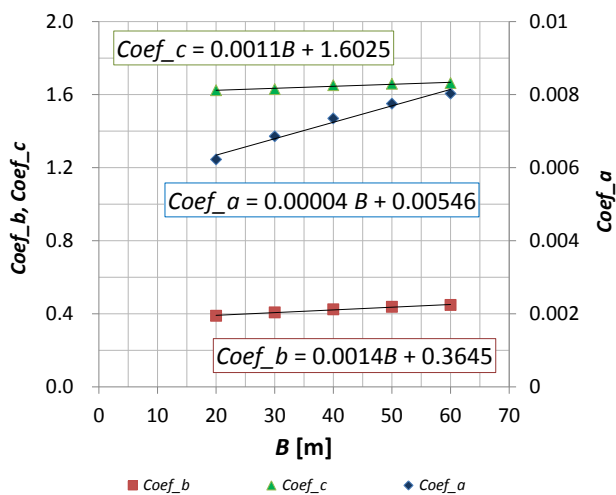


Figure 11: The coefficients of the approximated formula.

For verification, the computation of beaching factor was conducted in the world wide sea area where grounding accidents occur more frequently based on the casualty data. As a result, the computational results of beaching factor well explained the statistics derived from the real casualty data. It was clarified that derived probability is significant and important when the risk after grounding is accessed.

The beaching factor can be approximated as a function of a ship breadth. Therefore, this factor can be easily calculated practically. It was confirmed that the present methodology can evaluate the risk due to grounding rationally.

7. ACKNOWLEDGEMENT

The present study was carried out as part of the research project of Japan Ship Technology and Research Association for ship stability, which is supported by the Nippon Foundation.

The present research and development has been carried out as part of Joint Research Project supported by ClassNK. The authors would like to thank ClassNK for their support of this project.

8. REFERENCES

- Shiraishi, K., Ogawa, Y. and Nakamura, K., 2011a, "Harmonized Probabilistic Approach for Damage Stability - Difference between Collision and Grounding -", *Conference Proceedings of the Japan Society of Naval Architects and Ocean Engineers*, Vol. 13, pp.275-276.
- Ogawa, Y., Shiraishi, K., Nakamura, K. and Umeda, N., 2011b, "A Study for a Risk Based Approach for Damage Stability in the Case of Grounding", *Conference Proceedings of the Japan Society of Naval Architects and Ocean Engineers*, Vol. 13, pp.277-280.
- Papanikolaou, A., Bulian and G., Mains, C., 2011, "GOALDS - Goal Based Damaged Stability: Collision and Grounding Damages", *Proceedings of the 12th International Ship Stability Workshop*, pp.37-44.
- Vanem, E. and Skjong, R., 2004, "Collision and Grounding of Passenger Ships - Risk Assessment and Emergency Evacuations", *Proceedings from International Congress on Collision and Grounding of Ships, ICCGS 2004*, pp.195-202.
- Ziou, D. and Tabbone, S. 1998, Edge Detection Techniques An Overview, *International Journal of Pattern Recognition and Image Analysis*, 8(4), pp.537-559.



Developing the p -factor for grounding

Maciej Pawłowski, *School of Ocean Engineering and Ship Technology,*
TU Gdansk, 80–233, Poland, mpawlow45@gmail.com

Dagmara Głowacka, *School of Ocean Engineering and Ship Technology,*
TU Gdansk, 80–233, Poland, dagolomea@googlemail.com

ABSTRACT

The paper provides alternative formulations for the probability of flooding a compartment due to grounding (the p factor) embedded in the GOALDS database on grounding damage (Papanikolaou, 2011 and 2012). The original GOALDS formulations are provided in reference (Bulian, 2011), employing rational functions for damage distributions, whereas the alternative ones are based on exponential or triangular distributions. This made it possible to arrive at a closed form for the p factor.

Keywords: *factor p , grounding damage statistics, rulemaking*

1. INTRODUCTION

Formulations for the probability of flooding a bottom compartment due to grounding (the p factor) have to be embedded in damage statistics. The p -factor is proportional to the first integral curve of the cumulative distribution function (CDF) of damage size. Such a curve is insensitive to the quality of approximation of the probability distribution function (pdf) for damage size, which opens room for assumed distributions, provided they have the same end values of the CDF and the same *average* value as statistical distributions. Other features of damage distributions are meaningless as far as the p -factor is concerned. Knowing that the assumed distributions can be described by functions easy for integration, leads to analytical expressions for the p -factor.

2. DAMAGE STATISTICS

Grounding damage is a five-dimensional random variable, described by five quantities. These are: the longitudinal damage location x , measured from the aft terminal of the ship to the *centre* of damage, transverse damage location y , measured from the starboard to the centre of the damage, damage length l , damage width w ,

and damage penetration z (in the vertical direction). For reasons of consistency with the IMO practice, the centre of the damage describes its location on the ship.

2.1 Longitudinal Damage Location

A marginal distribution of the nondimensional damage location $\xi = x/L_{pp}$, in the form of histogram, is shown in Figure 1, based on statistical data comprising 341 damage cases of grounding. According to these data the mean value $\bar{\xi} = 0.613$. As can be seen from Figure 1, the statistical distribution can be well approximated by a trapezoidal distribution, keeping the same average, varying linearly from a value 0.324 at the aft to 1.676 at the forward end of the pdf.

A marginal distribution of the nondimensional damage location $\xi_F = x_F/L_{pp}$, according to the GOALDS data for all ships is shown in Figure 2, where x_F is the distance of the forward end of the damage from the aft perpendicular, based on 262 damage cases of grounding. According to these data the mean value of ξ_F equals $E(\xi_F) = 0.737$. The statistical distribution can be very well approximated by a quadratic distribution. If ships with length $L_{pp} < 80$ m are excluded from the statistics the mean $E(\xi_F) = 0.715$ is somewhat smaller than for the whole sample.

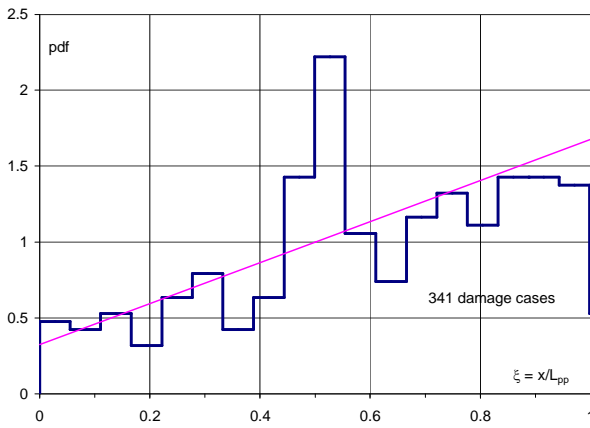


Figure 1: Marginal distribution of nondimensional damage location along the ship length.

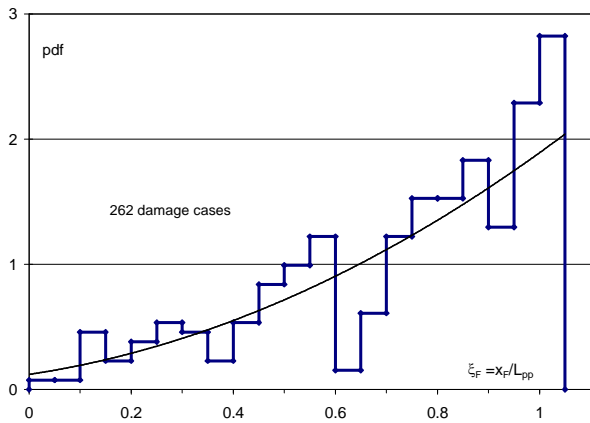


Figure 2: Marginal distribution of nondimensional damage forward end location.

Here arises a question, whether the two sets of data are statistically different? The mean value of ξ can be easily estimated, using the data for the forward location of the damage ξ_F and the simple relationship between the two quantities: $\xi = \xi_F - \frac{1}{2}\lambda$. Assuming that the random variables ξ_F and λ are independent of each other, the following is obtained:

$$E(\xi) = E(\xi_F) - \frac{1}{2}E(\lambda),$$

where E stands for the mean value. Since the mean length for grounding damage $E(\lambda) \approx 0.2$, and $E(\xi_F) = 0.737$, therefore $E(\xi) = 0.637$, which is not very different from the previous mean $E(\xi) = 0.613$. For ships with $L_{pp} > 80$ m, $E(\xi) = 0.615$, i.e. almost the same, as the previous mean. This proves that the distribution of ξ can be well approximated by a trapezoidal distribution, whose pdf is:

$$f(\xi) = 1 + m(\xi - 0.5), \quad (1)$$

where m is the rate of change (the inclination of the straight line). For a trapezoidal distribution there is a simple link between the mean value and the inclination of the linear pdf. Since $\bar{\xi} = \frac{1}{2} + \frac{1}{12}m$, therefore:

$$m = 12(\bar{\xi} - 0.5). \quad (2)$$

To avoid negative values of $f(\xi)$, $m < 2$, which takes place, if $\bar{\xi} < \frac{2}{3}$. The end values of the pdf equals $1 \pm \frac{1}{2}m$, with minus for the aft, and plus for the forward end. For $\bar{\xi} = 0.615$, the above yields $m = 1.38$, with the end values equal to 0.31 and 1.69.

2.2 Damage Length

A marginal distribution of the nondimensional damage length $\lambda = l/L_{pp}$ in the form of histogram is shown in Figure 3, based on statistical data comprising 225 damage cases of grounding for various ships. According to these data the mean value of λ equals $\bar{\lambda} = 0.199$.

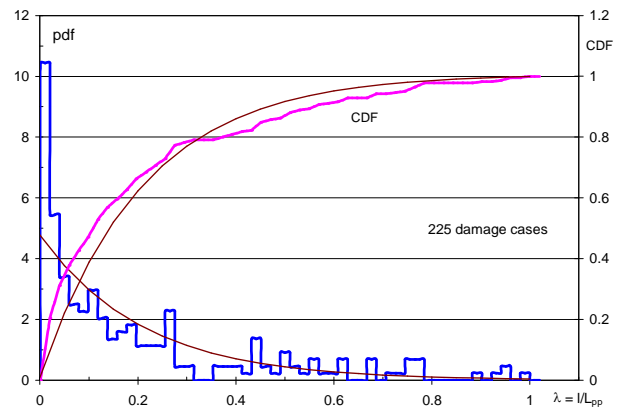


Figure 3: Marginal distribution of nondimensional damage length $\lambda = l/L_{pp}$.

As can be seen from Figure 3, histogram of λ can be well approximated by an exponential distribution, of the general form:

$$f = \alpha e^{-\alpha v}, \quad (3)$$

truncated at $v = 1$, whose CDF is given by

$$F = F_0 + 1 - e^{-\alpha v}, \quad (4)$$

where α is a constant, termed in physics as the logarithmic decrement of suppression, and v ($= \lambda$ or ω) is any random variable, related to the nondimensional damage size. The term $F_0 = e^{-\alpha}$ is the initial value of CDF at $v = 0$. For $v = 1$, equation (4) yields exactly $F = 1$, which means that there are no *measured* damages extending over the entire ship length or breath. The constant α is chosen such to yield the same average as from the statistics. The mean value for the above distribution is *solely* defined by the decrement of suppression, as follows:

$$\bar{v} = [1 - (1 + \alpha)e^{-\alpha}]/\alpha. \quad (5)$$

The mean is a non-monotonic function of α , reaching a maximum value 0.298 at $\alpha = 1.793$. Of practical meaning is the range of $\alpha > \alpha_{max} = 1.793$. In other words, the CDF given by equation 4 is valid for distributions with mean values less than $0.298 \approx 0.3$, which perfectly corresponds to distributions of nondimensional damage size due to grounding.

2.3 Damage Width

A marginal distribution of the nondimensional damage width $\omega = w/B$ in the form of histogram is shown in Figure 5, based on statistical data comprising 204 damage cases of grounding for various ships. According to these data the mean value of ω equals $E(\omega) = 0.134$.

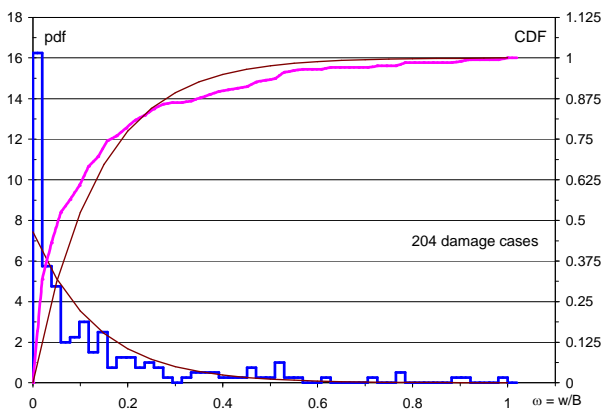


Figure 4: Marginal distribution of nondimensional damage width $\omega = w/L_{pp}$.

As can be seen, the statistical distribution is well approximated by the exponential one with the

decrement of suppression $\alpha = 7.44$, yielding the initial value $F_0 = 0.0006$. The probability density at the end of distribution (at $\omega = 1$) equals $f_1 = \alpha F_0 = 0.0044$. The damage width that is exceeded by 3% of damage cases (a 3% quantile) equals $\omega_{3\%} \approx 0.47$, and $\omega_{1\%} \approx 0.61$.

2.4 Damage Penetration

A marginal distribution of the nondimensional damage penetration $\zeta = z/z_{max}$ in the form of histogram is shown in Figure 6, based on statistical data comprising 124 grounding damages for various ships. According to these data the mean value $E(\zeta) = 0.189$.

As can be seen, looking particularly at the CDF the statistical distribution is also well approximated by an exponential one with the decrement of suppression $\alpha = 5.1$, yielding the initial value $F_0 = 0.0061$. The probability density at the end of distribution (at $\zeta = 1$) equals $f_1 = \alpha F_0 = 0.0311$. The damage penetration with a 3% protection equals $\zeta_{3\%} \approx 0.65$, and $\zeta_{1\%} \approx 0.81$.

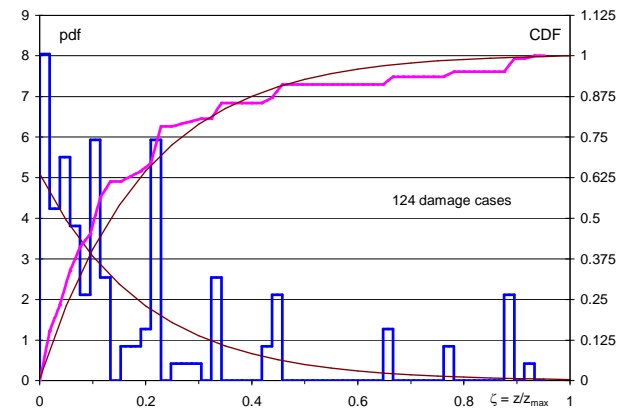


Figure 5: Marginal distribution of nondimensional damage penetration $\zeta = z/z_{max}$.

The maximum penetration is assumed to be constant and equal to $z_{max} = 4.5$ m, irrespective of the ship size. Even if this quantity value varies with the ship size, the distribution of the normalised damage penetration ζ would be independent of z_{max} , that is to say – of the ship size. Statistics indicate that z_{max} is constant for ships with L_{pp} greater than about 150 m. For smaller ships the z_{max} value could be decreased proportionally to L_{pp} , but not less than 2 m.



3. DISTRIBUTIONS OF THE POTENTIAL DAMAGE SIZE

The centre of the damage describes position of the damage across the ship breadth and length. Therefore, the domain of such damages is an isosceles triangle.

3.1 Damage Length

For calculating the p factor in the case of transverse subdivision only, the knowledge of the joint probability density function (pdf) for the nondimensional damage location and damage length $f(\xi, \lambda_x)$ is of basic importance. Assuming that $\lambda_x = l/L$ is independent of $\xi = x/L$ the joint pdf for the two-dimensional damage (ξ, λ_x) can be presented as follows:

$$f(\xi, \lambda_x) = f(\xi)f_c(\lambda_x),$$

where $f_c(\lambda_x) = f(\lambda_x|\xi) \equiv f(\lambda_{xp})$ is a conditional distribution density of λ_x without including damages terminated by either end of the ship, that is, for damages lying inside the ship. Those damages are termed in Goals as potential damages. Their distribution is virtually impossible to obtain from statistics. To yield a value of 1, the above pdf has to be distributed over the entire square in Figure 7, instead of the triangle. The shaded area comprises damages terminated by the ends of the ship.

To find the conditional distribution density for (the potential nondimensional damage length) λ_x , we have to resort to the relationships that hold between the marginal and joint distributions, discussed thoroughly by Pawłowski (2004, 2005). A simple algebraic equation for the conditional CDF of $\lambda_x \equiv \lambda$ (suffix x is dropped for abbreviation) is then obtained:

$$1 - F(\lambda) = [1 - F_c(\lambda)]F(\xi)^{1-\frac{1}{2}\lambda}, \quad (6)$$

provided that the two marginal distributions $F(\xi)$ and $F(\lambda)$ are known from statistics. The above equation defines the probability of exceeding a specified value of λ by the nondimensional damage length, which equals obviously $1 - F(\lambda)$. On the other hand, this probability equals the integral

of $f(\xi, \lambda)$ over square $A'ABB'$ (see Figure 7), whose sides equal to $1 - \lambda$. Hence

$$\begin{aligned} \int_G f dG &= \int_{\lambda}^1 \int_A^B f_c(\lambda)f(\xi)d\lambda d\xi \\ &= \int_{\lambda}^1 f_c(\lambda)d\lambda \int_A^B f(\xi)d\xi, \end{aligned}$$

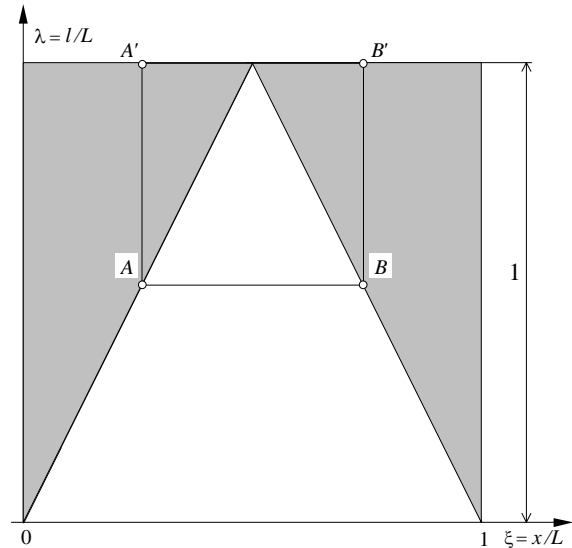


Figure 6: Domain of integration for the probability $1 - F(\lambda_x)$ in equation (6).

which is the same as equation (6), where G is the domain defined by square $A'ABB'$. A double integral could be replaced by iterated integrals, as the functions $f(\xi)$ and $f_c(\lambda)$ are independent of each other. The following results then for the conditional CDF from equation (6):

$$1 - F_c(\lambda) = \frac{1 - F(\lambda)}{F(\xi = 1 - \frac{1}{2}\lambda) - F(\xi = \frac{1}{2}\lambda)},$$

where $F(\lambda)$ and $F(\xi)$ are the marginal CDF of λ and ξ . For a trapezoidal distribution the nominator $F(\xi = 1 - \frac{1}{2}\lambda) - F(\xi = \frac{1}{2}\lambda)$ equals $1 - \lambda$, irrespective of m . Hence,

$$F_c(\lambda) = 1 - \frac{1 - F}{1 - \lambda}, \quad \text{for } \lambda < 1. \quad (7)$$

It is interesting that the conditional distribution of (potential) λ is unaffected by the distribution of damage location, if ξ is distributed linearly. It follows from equation (7) that for $\lambda = 0$ both distributions have the same initial value $F_c(0) =$

F_0 , whereas for $\lambda = 1$ it is indefinite, as both the denominator and nominator vanish at that point. Using the L'Hôspital rule, we get that

$$F_c(\lambda=1^-) = 1 - f_1, \quad (8)$$

where $f_1 = \alpha F_0$. Hence, at the end of distribution (at $\lambda = 1$) the conditional CDF of λ (for potential damage λ_{xp}) has a jump f_1 , equal to pdf at the end of distribution, solely dependent on the decrement of suppression α . In other words, contrary to measured damages the potential grounding damage with a zero length and a length extending over the entire ship length have finite mass probabilities, which is reasonable.

The conditional CDF obtained from equation (7) for the parameter $\alpha = 4.78$ is shown in Figure 7. The initial value of CDF equals $F_0 = e^{-\alpha} = 0.0084$. A jump at $\lambda = 1$ equals to $f_1 = \alpha F_0 = 0.0401$ is clearly observed, which denotes a finite probability for *potential* damages extending for the whole ship. This function is indispensable for deriving the p factor.

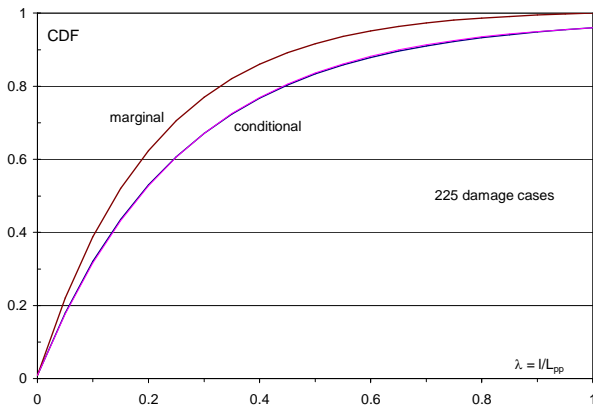


Figure 7: Marginal and conditional CDF for nondimensional damage length $\lambda = l/L_{pp}$.

The conditional CDF in Figure 7 can be perfectly approximated by the equation:

$$F_c = F_0 + c(1 - e^{-\alpha_1 v}), \quad (9)$$

solely dependent on the suppression parameter α_1 , where the constant $c = (F_1 - F_0)/(1 - e^{-\alpha_1})$, with $v = \lambda$. The constant c is chosen such that a graph of the above equation passes through F_0 and F_1 at the ends of distribution, irrespective

of the decrement of suppression α_1 . For $\alpha_1 = 3.81$, found by the least squares method, the said graph coincides with the conditional CDF, therefore it is almost invisible in Figure 7.

The mean potential damage length, resulting from equation (9), is given by the equation:

$$\bar{\lambda}_p = (1 - F_0 - c) + (F_1 - F_0)/\alpha_1. \quad (10)$$

The conditional CDF of the nondimensional damage length λ , corresponds to damages located at the midships, that is, for $\xi = 0.5$. For other damage locations the above distribution is truncated at the boundary of the domain at $\lambda = \lambda_\xi$, where the CDF has a jump to a value of 1. A maximum extent of damage length λ_ξ at given damage location equals $\lambda_\xi = \min(2\xi, 2 - 2\xi)$.

Area above the CDF up to a horizontal line at a value 1 equals the mean value. It is therefore obvious from Figure 7 that the mean length for the conditional distribution (for damages lying inside the ship and unaffected by the ships ends) is larger than that for the marginal distribution of measured damage lengths. For the marginal one the mean value of $\bar{\lambda} = 0.199$, whereas for the conditional distribution (of potential damage length) $\bar{\lambda}_p = 0.268$, obtained from equation (10). Such a big increase of the average length is mainly attributed to the jump at the end of distribution equal to $f_1 = 0.04$.

3.2 Damage Width

Things look similar for the damage width. As the centre of the damage describes the position of the damage across the ship breadth, the domain of such damages is also an isosceles triangle. For calculating the p_i factor, the knowledge of the joint probability density function (pdf) for the nondimensional damage location and damage width $f(\eta, \omega)$ is needed.

Assuming that the nondimensional damage width $\omega = w/B$ is independent of $\eta = y/B$ the joint pdf for the two-dimensional damage (η, ω) can be presented as follows:

$$f(\eta, \omega) = f(\eta)f_c(\omega),$$



where $f_c(\omega) = f(\omega|\eta) \equiv f(\omega_p)$ is a conditional distribution density of ω without including damages terminated by the sides of the ship, that is, for damages lying inside the ship, termed as potential damages. Their distribution is virtually impossible to obtain from statistics. To yield a value of 1, the above pdf has to be distributed over the entire square in Figure 8, instead of the triangle. The shaded area comprises damages terminated by the sides of the ship.

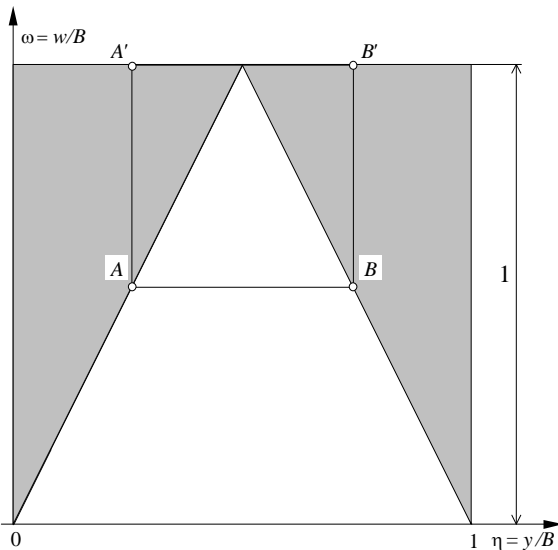


Figure 8: Domain of integration for the probability $1 - F(\omega)$ in equation (11).

To find the conditional distribution density for potential ω , we have to resort as before to the relationships that hold between the marginal and joint distributions. The following is obtained:

$$1 - F(\omega) = [1 - F_c(\omega)] F(\eta)_{\omega/2}^{1-\omega/2}, \quad (11)$$

provided that the two marginal distributions $F(\eta)$ and $F(\omega)$ are known from statistics. Due to lack of data, it is assumed that the distribution of damages across the ship breadth is uniform. Apart from that equation (11) is virtually the same as equation (6).

For a uniform distribution of η , probability density $f(\eta) = 1$, and the last term in equation (11) equals $1 - \omega$, as in the case of trapezoidal distribution. Hence, the conditional CDF of ω is given by equation (7), with λ replaced by ω .

The conditional CDF for the potential damage width obtained from equation (7) is shown in Figure 9. As before, it is perfectly approximated by equation (9), with $v = \omega$. For $\alpha_1 = 6.35$, found by the least squares method, a graph according to equation (9) coincides with the conditional CDF, therefore it is almost invisible in Figure 9. The mean potential damage width, resulting from equation (10) equals $\bar{\omega}_p = 0.159$, while the mean for measured damages $\bar{\omega} = 0.134$.

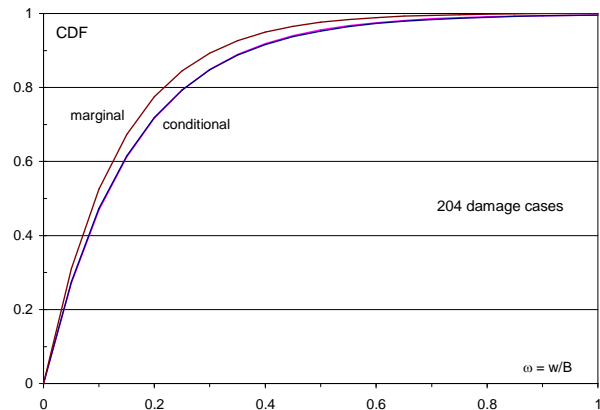


Figure 9: Marginal and conditional CDF for nondimensional damage width $\omega = w/B$.

3.3 Damage Penetration

Finally, we can go to the determination of the distribution of the damage penetration. In this case the fitting is straightforward. Since the damage penetration is not affected by geometrical boundaries, the potential damage penetration is the *same* as the measured damage penetration.

4. PROBABILITY OF FLOODING A SINGLE BOTTOM COMPARTMENT

It is sufficient to derive formulations for the probability p of flooding a single bottom compartment. The probability p_i of flooding a group of adjacent compartments can be expressed in terms of the probabilities of flooding single compartments, which make up that group, exactly as in the case of collision damage, making use of linearity of the p -factor.

In general, the probability of flooding a *single* compartment is given by the equation:

$$p = \int_G f dG, \quad (12)$$

in which the joint probability density function $f = f(\xi, \eta, \lambda_p, \omega_p, \zeta)$ is integrated over the domain G , comprising damages opening the space under consideration.

If we assume that all the random variables characterising the damage are independent, then the joint probability density function appearing in equation (12) can be written as a product of the marginal probability density functions:

$$f(\xi, \eta, \lambda_p, \omega_p, \zeta) = f(\xi)f(\eta)f(\lambda_p)f(\omega_p)f(\zeta),$$

where $f(\eta) = 1$. Accordingly, equation (12) can be expressed as a product of three factors:

$$p = p_L p_T p_V, \quad (13)$$

where p_L takes into account only subdivision of the ship in the longitudinal direction (i.e. the presence of transverse bulkheads), p_T takes into account only subdivision of the ship in the transverse direction (i.e. the presence of longitudinal bulkheads), and p_V takes into account only subdivision of the ship in the vertical direction (i.e. the presence of horizontal subdivision). The three factors are as follows:

$$\begin{aligned} p_L &= \int_{G_L} f(\xi)f(\lambda_p) dG_L, \\ p_T &= \int_{G_T} f(\eta)f(\omega_p) dG_T = \int_{G_T} f(\omega_p) dG_T, \\ p_V &= \int_{G_V} f(\zeta) dG_V, \end{aligned} \quad (14)$$

where G_L is an appropriate sub-triangle (sub-domain) in Figure 6, defined by the transverse bulkheads, G_T is an appropriate sub-triangle in Figure 8, defined by the longitudinal bulkheads (see Figure 10), and G_V is an appropriate sub-interval along the axis ζ , defined by the horizontal subdivision.

Performing first integration along the appropriate axis of the damage from $v = 0$ to v' at the boundary of the sub-domain, the following is obtained:

$$\begin{aligned} p_L &= \int_c f(\xi)F_c(\lambda'_p) d\xi, \\ p_T &= \int_c F_c(\omega'_p) d\eta, \\ p_V &= \int_{\zeta_1}^{\zeta_2} f(\zeta) d\zeta = F(\zeta) \Big|_{\zeta_1}^{\zeta_2}, \end{aligned} \quad (15)$$

where F stands for the CDF, and integration takes place respectively between the aft and forward transverse bulkheads, the starboard and portside longitudinal bulkheads, and between the lower and upper horizontal subdivision. The quantity $\lambda'_p = 2(\xi - \xi_1)$, and $\omega'_p = 2(\eta - \eta_1)$, if at the left half of the domain c , or $\lambda'_p = 2(\xi_2 - \xi)$, $\omega'_p = 2(\eta_2 - \eta)$, if at the right half of the domain c , is a value of damage size at the boundary of the domain (sides a and b in Figure 10). Further down, suffix p (for the potential damage) is dropped, for abbreviation.

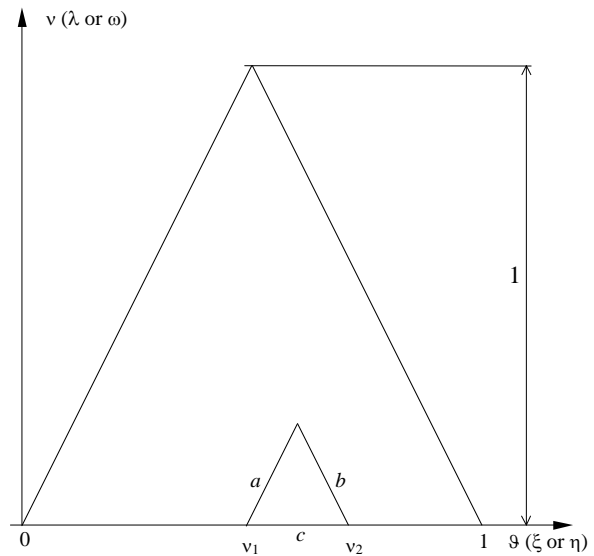


Figure 10: Domain of integration for probability p_L and p_T .

For a compartment extending over the entire ship length (or breadth), we get immediately from the above equations that the factor $p = 1$.

Further integration is performed substituting for ϑ (ξ or η) the appropriate equation of sides a or b – the boundaries of the triangle G_i (see Figure 10) that are as follows:

$$\vartheta = \vartheta_{12} \pm \frac{1}{2}(J - v'), \quad (16)$$



with + for side b and – for side a of the triangle, where $\vartheta_{12} = \frac{1}{2}(\vartheta_1 + \vartheta_2)$ is the nondimensional position of the centre of the compartment, and $J = \vartheta_2 - \vartheta_1$ is the nondimensional size of the compartment. After substitution, the sign ' at v' can be eventually dropped. As equations of the sides are different and values of $F_c(v')$ at these sides may also be different, it is convenient to split equations (13) into two integrals: over the left and right half of the triangle, divided at the axis of symmetry at $\vartheta = \vartheta_{12}$. Hence: p_L (or p_r) = $p_l + p_r$, where

$$p_l = \int_{\vartheta_1}^{\vartheta_{12}} f(\vartheta)F_c(v')d\vartheta = \frac{1}{2} \int_0^J f(\vartheta')F_c(v)dv \quad (17)$$

$$p_r = \int_{\vartheta_{12}}^{\vartheta_2} f(\vartheta)F_c(v')d\vartheta = \frac{1}{2} \int_0^J f(\vartheta')F_c(v)dv ,$$

and $f(\vartheta')$ are functions of v obtained after substitution for ϑ the equations of respective sides. For a linear distribution of ϑ , the pdf of ϑ can be expressed in two forms:

$$f(\vartheta) = a + m(\vartheta - \vartheta_{12}), \text{ or} \quad (18)$$

$$f(\vartheta') = a \pm \frac{1}{2}m(J - v'),$$

where a is the density of ϑ at the mid-length of the compartment ϑ_{12} , and $m = 1.38$ is a slope of the density function $f(\xi)$. The other expression is obtained, making use of equation (16). For a uniform distribution $m = 0$, and $a = 1$.

The results of integration for the value p depend on the location of the compartment, whether inside or an end compartment. For a compartment adjacent to either boundary of the ship $v' = 1$, $F_c(1) = 1$, the following is obtained from equations (17):

$$p_l = \int_{\vartheta_1}^{\vartheta_{12}} f(\vartheta)d\vartheta = F \Big|_0^{\frac{1}{2}J} ,$$

$$p_r = \int_{\vartheta_{12}}^{\vartheta_2} f(\vartheta)d\vartheta = F \Big|_{1-\frac{1}{2}J}^1 .$$

In other words, p_l or p_r equals the increase of the CDF of ϑ (ξ or η) over the half of the base J adjacent to the boundary. For a trapezoidal distribution (1),

$$p_l = \frac{1}{2}aJ - \frac{1}{8}mJ^2, \quad (19)$$

$$p_r = \frac{1}{2}aJ + \frac{1}{8}mJ^2,$$

For a uniform distribution $m = 0$, $a = 1$, the above yields $p_l = p_r = \frac{1}{2}J$.

For the other cases, the two characteristic values p_l and p_r can be obtained from equations (17). For a linear distribution of ϑ , expressing $f(\vartheta')$ with the help of equation (18), the following is obtained:

$$p_l = \frac{1}{2}aI_1 - \frac{1}{4}mI_2, \quad (20)$$

$$p_r = \frac{1}{2}aI_1 + \frac{1}{4}mI_2,$$

where I_1 and I_2 are the first and second integral curves of the conditional (potential) CDF $F_c(v)$, taken for $v = J$:

$$I_1 = \int_0^J F_c(v)dv , \quad (21)$$

$$I_2 = \int_0^J (J - v)F_c(v)dv = \int_0^J I_1(v)dv ,$$

where $J = \vartheta_2 - \vartheta_1$ is the nondimensional size of the compartment l/L_{pp} or w/B . The quantity I_1 represents area under $F_c(v)$ over the range from zero to J , whereas I_2 is the static moment of area under $F_c(v)$ for $v \leq J$, calculated with respect to $v = J$. It can be shown that $I_1 < J$, and $I_2 < \frac{1}{2}J^2$. As can be seen, equations (20) have a similar format to equations (19), in which J is replaced by I_1 , and J^2 by $\frac{1}{2}I_2$. For a uniform distribution $m = 0$, $a = 1$, therefore $p_l = p_r = \frac{1}{2}I_1$.

Expressing $F_c(v)$ by equation (9), the following is obtained for I_1 and I_2 :

$$I_1 = (F_0 + c)J - (c/\alpha_1)(1 - e^{-\alpha_1 J}), \quad (22)$$

$$I_2 = \frac{1}{2}(F_0 + c)J^2 - (c/\alpha_1)J + (c/\alpha_1^2)(1 - e^{-\alpha_1 J}),$$

where $F_0 = 0.0084$, $c = 0.9730$, and $\alpha_1 = 3.81$, as derived earlier for the nondimensional potential damage length, and $F_0 = 0.0006$, $c = 0.9968$, and $\alpha_1 = 6.35$ for the nondimensional potential damage width. Graphs of the above integrals are shown in Figure 11. For $J = 1$, the end values in the case of damage length equal $I_1 = 0.732$, and $I_2 = 0.301$, whereas in the case of damage width $I_1 = 0.841$, while the second integral curve does not apply.

It can be shown, using relations provided earlier, that a tangent to I_1 at $J = 1$ cuts the abscissa axis at a point J_0 , given by:

$$(1 - \bar{v})/F_1 = 1 - J_0, \quad (23)$$

where \bar{v} is the mean nondimensional damage size, and F_1 is the end value of the CDF of the potential damage size before the jump at $v = 1$. For the nondimensional potential damage length $J_0 = 0.238$, and for the nondimensional potential damage width $J_0 = 0.156$ (see Figure 11). J_0 is the same as the mean value of the nondimensional potential damage size for $v < 1$, i.e. excluding damages with $v = 1$. Therefore, $J_0 < \bar{v}$. The inclination of the tangent equals F_1 . In general, the end value of I_1 equals $I_1(1) = 1 - \bar{v}$.

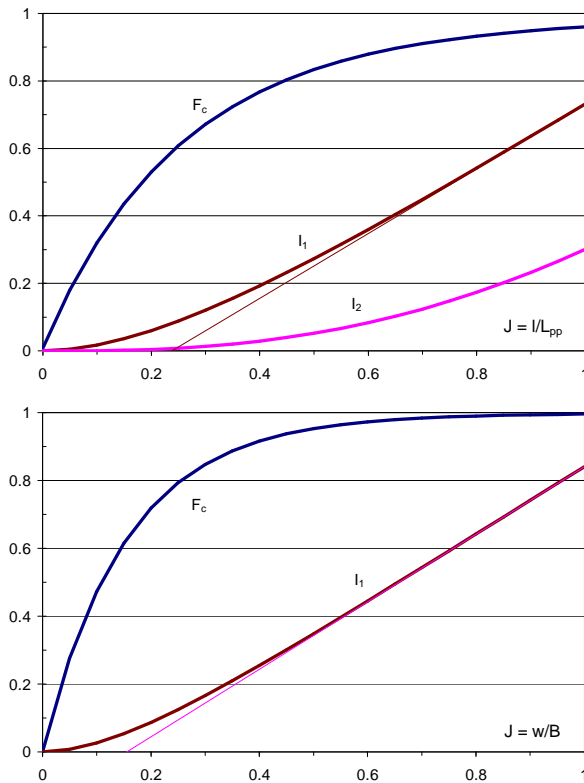


Figure 11: Conditional CDF for nondimensional damage size v and its integral curves.

For compartments located inside the ship, the probability $p = p_l + p_r$. It follows immediately from equation (20) that

$$p = aI_1. \quad (24)$$

Hence, the probability of flooding for these compartments is such as if the density function

$f(v)$ was constant over the compartment, with the mean value at the centre of the compartment. Since for $J \rightarrow 1$, $a = 1$, therefore $p_L = I_1(1) = 0.732$, which means that in 26.8% of grounding cases the damage is terminated by either extremity of the ship length or both.

In the case of a uniform distribution of the damage, as in the case of the transverse damage, the probability of flooding an inside compartment equals $p = I_1$. The factor p in such a case is independent of the location of the compartment. For $J \rightarrow 1$, $p_r = I_1(1) = 0.841$, which means that in 15.9% of grounding cases the damage is terminated by either side of the ship or both.

For end compartments the probability $p = p_l + p_r$. Making use of equations (19) and (20), the following result for the factor p :

$$p = \frac{1}{2}a(J + I_1) - \frac{1}{8}m(J^2 - 2I_2),$$

for an aft compartment, and (25)

$$p = \frac{1}{2}a(J + I_1) + \frac{1}{8}m(J^2 - 2I_2),$$

for a forward compartment.

For an aft compartment with $J \rightarrow 1$, the probability of flooding equals $p = 0.797$. As $I_1(1) = 0.732$, this means that in 6.5% of grounding cases the damage is terminated by the aft extremity of the ship. Whereas for a forward compartment with $J \rightarrow 1$, the value of $p = 0.935$, which means that in 20.3% of grounding cases the damage is terminated by the forward extremity of the ship. There are then 6.5% + 20.3% = 26.8% of damages terminated by either end of the ship. As $1 - I_1(1)$ equals the same percent 26.8%, this means that there are no *measured* damages extending over the entire ship length.

For a uniform distribution $m = 0$, $a = 1$, as in the case of the transverse damage, the above yields immediately:

$$p = \frac{1}{2}(J + I_1), \quad (26)$$

For a side compartment with $J \rightarrow 1$, the probability of flooding a compartment equals $p = 0.92$. As $I_1(1) = 0.841$, this means that in 7.9% of all grounding cases the damage is terminated by a side of the ship. As there are two sides, there



are together 15.9% of damages terminated by either side of the ship. As $1 - I_1(1)$ equals the same percent 15.9%, there are no *measured* damages extending over the entire ship breadth.

Equally good results can be obtained by triangular distributions, whose density varies linearly from a value $f=f_0$ at $v=0$, to $f=0$, at $v=v_{max} < 1$. Outside this range, $f \equiv 0$. At $v=0$ and 1 the probability distribution takes on finite values p_0 and p_1 . The two integral curves are given then by the equations:

$$\begin{aligned} I_1 &= -A_1 + F_1 v + A_1(1 - v/v_{max})^3 \\ I_2 &= A_2 - A_1 v + \frac{1}{2} F_1 v^2 - A_2(1 - v/v_{max})^4, \end{aligned} \quad (27)$$

where $A_0 = 1 - p_0 - p_1$, $A_1 = \frac{1}{3} A_0 v_{max}$, and $A_2 = \frac{1}{4} A_1 v_{max}$. For $v > v_{max}$, the last term vanishes. The mean value equals $\bar{v} = A_1 + p_1$.

If the same mean values are adopted for the exponential and triangular distributions, the differences between the integral curves, shown in Figure 11, are hardly visible.

5. CONCLUSIONS

The paper demonstrates that it is possible to derive strict but simple mathematical formulations for the factor p , based on grounding damage statistics. Using strict formulations is essential to avoid negative probabilities for groups of compartments, calculated by a linear combination of the probabilities for single compartments, related to the group of compartments under consideration. Such a p factor is sensitive to numerical inaccuracies.

Formulations for the p -factor are insensitive for the quality of approximation of statistical distributions as long as the mean value is maintained. Contrary to histograms (pdf functions), the mean is statistically well conditioned.

The formulations for the p factor can be easily modified, if that proves necessary in the future, if new damage statistics for grounding is avail-

able. The most important of all statistical characteristics is the mean size of damage, which is, however, very unlikely to change with new data.

REFERENCES

- Bulian G., Francescutto A., 2011, "Probability of flooding due to grounding damage using a p-factor formulation, Integrated damage stability standard", http://147.102.98.1/outcome/pub/index.php?dir=&file=DINMA_p_factors_for_RINA_20110113.pdf.
- Papanikolaou A., Bulian G. and Mains C., 2011, GOALDS – Goal Based Damaged Stability: Collision and Grounding Damages, Proceedings of the 12th Int. Ship Stability Workshop, 8 pp., Washington DC, USA, 12–15 June.
- Papanikolaou A., 2012, GOALDS – Goal Based Damaged Stability Objectives & Overview of Results, IMO SLF 54, London, 17th January 2012, <http://147.102.98.1/outcome/pub/index.php?dir=&file=GOALDS-%20JAN%202012-IMO-SLF54-OVERALL-APAP.pdf>
- Pawłowski M., 2004, Subdivision and damage stability of ships, Euro-MTEC book series, Foundation for the Promotion of Maritime Industry, Gdansk, ISBN 83-919488-6-2, 311 pp.
- Pawłowski M., 2005, "Probability of flooding a compartment (the p_i factor) – a critique and a proposal", Proceedings of the Institution of Mechanical Engineers, Part M: J. Engineering for the Maritime Environment, 2005, Vol. 219, pp. 185–201.



The Numerical Study of Hydrodynamic Coefficients by RANS

Qiuxin Gao, *University of Strathclyde, Gao.q.x@strath.ac.uk*
Dracos Vassalos, *University of Strathclyde, D.Vassalos@strath.ac.uk*

ABSTRACT

In the paper, a CFD solver is applied to study the roll coefficients of a appended ship model with forward speed. Two approaches based on RANS and VOF modelling are adopted, namely, roll decay and forced roll motion. The results of roll coefficients from two approaches are compared and validated against model test data. The effects of viscosity on the hydrodynamic coefficients are studied by solving Euler equation. Additionally, the numerical simulation of forced roll motion at full scale is performed. The present results show that the influences of viscosity and scale on hydrodynamic coefficients except ship resistance are not large.

KEYWORDS: *RANS, Hydrodynamic coefficients, Roll decay, Forced roll motion*

1. INTRODUCTION

Roll motion is one of the most important ship motions among others, causing the discomfort to both passengers and crew on board, generating a risk of cargo shifting, affecting the operation of equipments, and being susceptible to the encounter frequency resulting in sharp amplification and subsequently loss of stability/capsizing. The prediction of roll motion needs the knowledge of roll moments acting on the ship. Among them, roll damping moment is subject to significant viscous and nonlinear effects and is most essential in estimating ship response in calm water and in waves.

There are several theoretical and experimental work to model the roll damping. Hishida proposed a theoretical model of roll damping in oscillatory wave [Hishida, 1952]. Tanaka studied the effect of bilge keel on roll damping [Tanaka 1957]. Yamaguchi investigated forward speed effects on roll damping [Yamanouchi 1961]. Ikeda introduced the empirical methods to estimate various roll damping components [Ikeda 1978]. Himeno reviewed the state of the art of

roll damping modelling [Himeno, 1981]. Lin studied roll damping based on potential theory and nonlinear ship motion model [Lin 2008]. With the rapid advance of high performance computing (HPC) technology and numerical methodology of Computational Fluid Dynamics (CFD), There are increasing interest to study ship roll motion by using RANS approaches. Wilson [2002] and Gao [2010] et al studied the roll decay of DTMB 5415 with forward speed. However, up to now, there is no systematic comparison of roll motions with and without viscous effects, in model scale and full scale.

In the paper, the numerical simulations of roll decay of DTMB 5415 are carried out firstly by RANS method. The computed result are compared with the model tests. Next, the simulations of forced roll motion near natural roll frequency are conducted and results of roll damping and added inertial moments are compared with those from roll decay. Then, the numerical simulation of forced roll motion by Euler method is made and viscous effects are studied. Finally RANS simulation at full scale is performed to check the scale effects.



2. MATHEMATICAL MODELLING

The Reynolds averaged Navier-Stokes (RANS) equations with VOF modeling of free surface and SST K- ω turbulence closure were solved. The governing equations can be written as below.

$$\nabla \cdot \mathbf{u} = 0 \quad (1)$$

$$\frac{\partial \mathbf{u}}{\partial t} + \mathbf{u} \cdot \nabla \mathbf{u} = -\frac{1}{\rho} \nabla p - \mathbf{g} + \nu \nabla^2 \mathbf{u} \quad (2)$$

$$\frac{\partial}{\partial t}(\rho K) + \nabla \cdot (\rho \mathbf{u} K) = \nabla \cdot (\Gamma_K \nabla K) + S_K \quad (3)$$

$$\frac{\partial}{\partial t}(\rho \omega) + \nabla \cdot (\rho \mathbf{u} \omega) = \nabla \cdot (\Gamma_\omega \nabla \omega) + S_\omega \quad (4)$$

$$\frac{\partial}{\partial t}(\mathbf{r}_w) + \nabla \cdot (\mathbf{r}_w \mathbf{u}) = 0. \quad (5)$$

2.1 Computational domain

The computational domain is a numerical rolling tank with 4 ship lengths long, 2 ship lengths wide and 2 ship length deep. The strategy of moving mesh and grid interface is used to cope with free roll motions.

2.2 Boundary condition

Open channel boundary conditions were implemented at outlet.

Velocity components and turbulence quantities are given at velocity inlet.

Slip wall is imposed on tank wall and wall function is used on hull boundary.

2.3 Numerical detail

Second order upwinding interpolation for convection was used. SIMPLE algorithm was applied to solve pressure. Geometric

reconstruction of volume fraction is used to capture free surface. The hydrodynamic and hydrostatic forces were computed and used to analyze the roll coefficients by least square fitting.

The detail of theory and usage can be found in FLUENT manual.

2.4 Parallel computing

The calculations were run on a High Performance Computer (HPC) with 8*130 (nodes) processors provided by Esteem Systems Ltd in partnership with SUN Microsystems (now Oracle).

The machine has a theoretical peak performance of 13 TeraFlops—thirteen thousand billion operations per second.

For a typical roll calculation of 2M cells, it takes roughly 20 hours of clock time for computational time 20 seconds using 16 cores.

3. ROLL DECAY

The test case was used in Gothenburg CFD workshop 2010. The main features of the roll decay test case of DTMB5415 are given below and geometry in Figure 1:

1. Bare hull with bilge keels
2. Towing condition in calm water
3. Sinkage: $s = 2.93 \times 10^{-4}$
4. Trim: $t = -3.47 \times 10^{-2}^\circ$
5. The model speed is 1.53m/s
6. The Froude number is 0.138
7. Reynolds number 2.56×10^6
8. The initial roll angle is 10 degrees



Figure 1: DTMB 5415

The hybrid meshes were generated with special care of resolution in the boundary layer and near free surface. In total, 3.1M grids were used. The computed roll decay time record was compared with measurement in Figure 1.

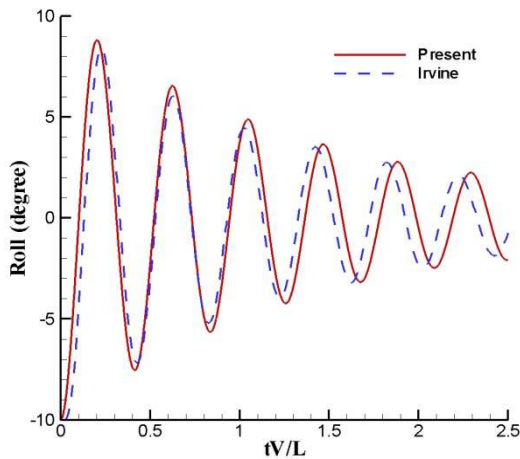


Figure 2: DTMB5415 Roll decay history

The comparison shows that the agreements between calculation and model test are acceptable with slightly larger period and smaller damping from calculation.

The computed and measured longitudinal velocity contours at start of second cycle are shown in Figures 2 and 3. It can be seen that the velocity distributions between calculation and measurement are consistent with boundary layer generally thin on the windside and thick on the leeside of bilge keel.

The numerical validation of DTMB5415 roll decay with sonar dome, transom and bilge keel indicates the numerical accuracy is satisfactory and numerical simulation can be used to study roll damping.

From the time series of roll decay, natural roll frequency and hydrodynamic coefficients are obtained. The natural roll frequency is 0.595. Non-dimensional added inertial moment and damping coefficients are 0.039(A44) and 0.0087(B44) respectively.

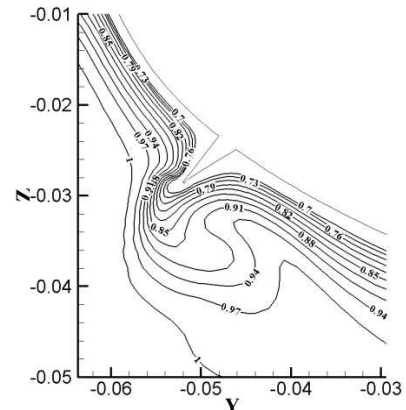


Figure 3: Computed u contour

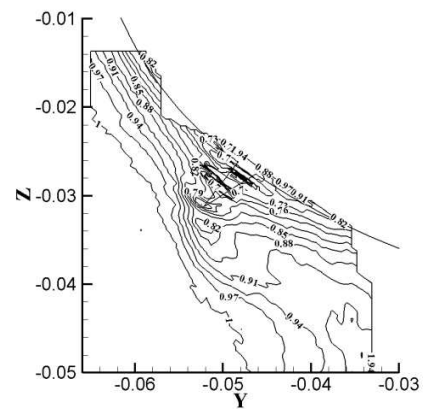


Figure 4: Measured u contour

4. FORCED ROLL MOTION

There are two methods to obtain roll damping coefficients. One is roll decay as detailed in the last paragraph. The other is the forced roll motion. In this study, the numerical simulations of forced roll motions of DTMB5415 model with same forward speed and amplitude were made. The frequencies are 0.4, 0.595 and 0.8 respectively at and near natural roll frequency. The computed pressure and the friction forces (moments) were exported for analysis. The total forces and moments acting on the hull are the summation of those due to pressure and friction as shown in Figure 5. It can be seen that total roll moments increase with the increase of frequency. The total roll moment approaches to hydrostatic one at low



frequency. The computed roll moments are then separated into hydrostatic and hydrodynamic as shown in Figure 6.

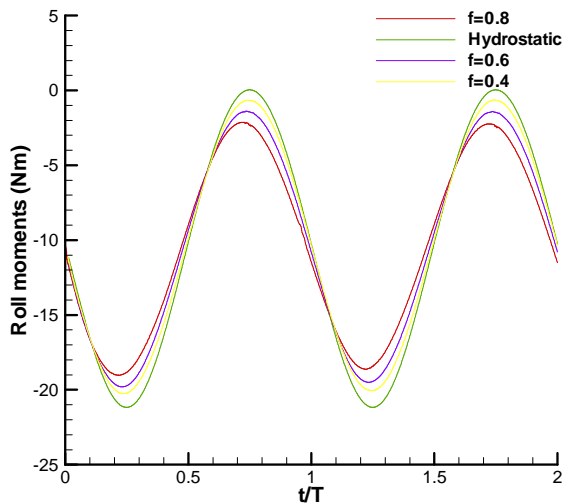


Figure 5: Comparison of roll moments.

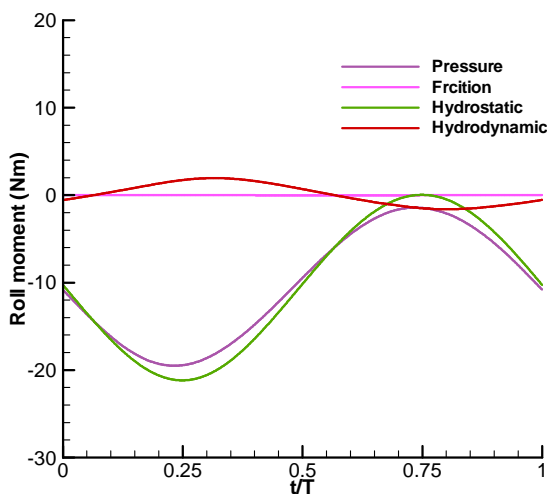


Figure 6: Components of roll moments at frequency 0.595

The hydrodynamic roll moments are separated into two orthogonal components. One is related to roll velocity and the other to roll acceleration. The roll damping is derived by equivalent linear method. The hydrodynamic coefficients are non-dimensional as below:

$$A_{44} = \frac{a_{\phi}}{\rho \cdot \nabla \cdot B^2}$$

$$B_{44} = \frac{b_{\phi}}{\rho \cdot \nabla \cdot B^2 \sqrt{\frac{2 \cdot g}{B}}}$$

The results of roll damping are compared in the Table 1

Table 1: Hydrodynamic coefficients

Method	Frequency	A ₄₄	B ₄₄	Roll (°)
Forced roll	0.4	0.058	0.0047	10
Forced roll	0.595	0.045	0.0086	10
Forced roll	0.8	0.042	0.0142	10
Roll decay	0.595	0.039	0.0087	10

It can be seen from table 1 that added inertial coefficient decreases with the increase of frequency. The added inertial coefficient from roll decay is lower than those from forced roll motion due to the effects of roll amplitude. The damping coefficients increase with the increase of roll frequency. Normally, damping coefficient will reach maximum near natural roll frequency. In this study, damping coefficient increases from frequency 0.4-0.8. It is seen that the damping coefficients from roll decay and forced roll motion at same frequency are close.

5. THE EFFECT OF VISCOSITY

To study the effects of viscosity on hydrodynamic coefficients, the simulation of forced roll motion was made by Euler method. In Euler equation, there is no viscosity, thus no roll moment due to friction and vorticity.

Only inviscid roll moments due to wave, bilge keel and lift are computed. The frequency is 0.595. The comparison of hydrodynamic roll moments is shown in Figure 7. It can be seen there are only small effects of viscosity on hydrodynamic roll moments. The amplitude of computed roll moment by Euler equation is smaller and there is a phase difference due to neglect of viscosity. The added inertial and damping coefficients are 0.044 and 0.0072 respectively.

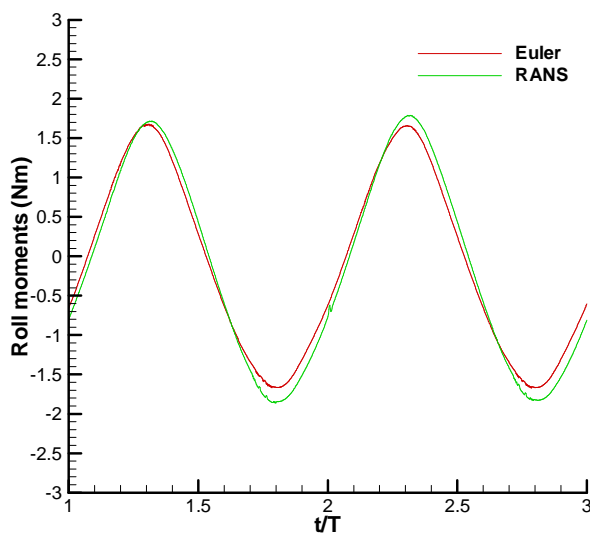


Figure 7: Natural roll frequency

6. SCALE EFFECTS

The simulation of forced roll motion at full scale was carried out by RANS method. The comparison of hydrodynamic roll moments are shown in Figure 8. It can be seen that there is little scale effect on hydrodynamic loads. The hydrodynamic coefficients from model scale can be used to predict ship roll motion in full scale.

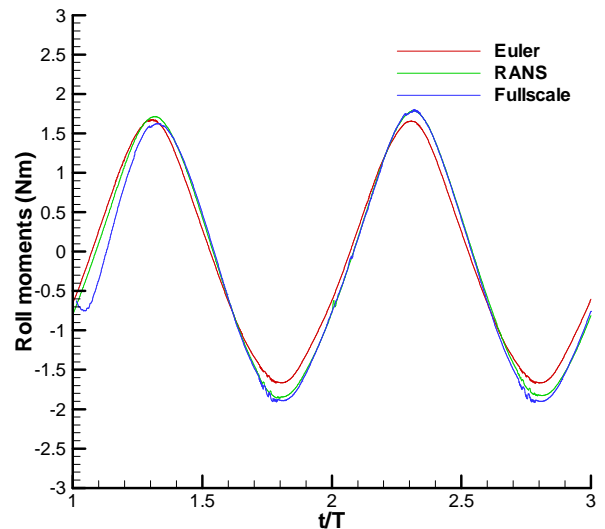


Figure 8: Case study of A44

7. CONCLUSIONS

The numerical simulations of roll decay and forced roll motions were carried out by RANS and Euler methods. Based on the results, the following conclusions are drawn:

- The validations of test case DTMB5415 in roll decay show that numerical results of roll decay history and velocity contour agree reasonably well with experiment data. RANS method can be applied to predict roll decay of practical hull form with bulbous bow, transom and bilge keel.
- The hydrodynamic coefficients from forced roll motion are dependent on roll frequency. The added inertial coefficients decrease but damping coefficients increase with the increase of frequency.
- The damping coefficients from roll decay and forced roll motion at same frequency are close. However, added inertial coefficient is higher from forced roll motion.
- The effects of viscosity on hydrodynamic coefficients are small from simulation of forced roll motion by Euler method. However, the effects may become larger at low speed.



- The scale effects on hydrodynamic coefficients are small. The results of damping coefficient at model scale can be used to predict ship motion in waves.

8. ACKNOWLEDGMENTS

The authors appreciate Faculty of Engineering for the use of HPC.

REFERENCES

- Hishida T, "Study on the wave making resistance for rolling of ships", parts 1-6, JSNA Japan, 45-61, 1952.
- Tanaka N, "A study on the bilge keel", part 1, JSNA Japan 101:99-101, 1957
- Yamanouchi Y, "Analysis of ship response in waves, part 1 JSNA 109: 169-183, 1961
- Ikeda Y., Himeno Y., and Tanaka, N., "A prediction methods for ship roll damping", Report No. 00405 of Department of Naval Architecture, University of Osaka prefecture, 1978.
- Himeno Y, "Prediction of ship roll damping – state of the art", Department of Naval Architecture and Marine Engineering, report No. 239 University of Michigan, 1981.
- Ray Qing Lin, Weijia Kuang, "Modelling nonlinear roll damping with a self-consistent, strongly nonlinear ship motion model", J Mar Sci Technol 13:127-137, 2008.
- Wilson R. and Stern F., (2002), "Unsteady RANS Simulation of a Surface Combatant with Roll Motion", 24th Symposium on Naval Hydrodynamics, Fukuoka, Japan.
- Gao Q, Jin W. and Vassalos D. (2010), "Simulation of roll decay by RANS approach", Gothenburg CFD workshop, Sweden



Numerical Simulation Method for Coupling of Tank Fluid and Ship Roll Motions

Hirotsada Hashimoto, *Osaka University*, h_hashi@naoe.eng.osaka-u.ac.jp

Yuto Ito, *Osaka University*, yuto_ito@naoe.eng.osaka-u.ac.jp

Nagisa Kawakami, *Osaka University*, nagisa_kawakami@naoe.eng.osaka-u.ac.jp

Makoto Sueyoshi, *Kyushu University*, sueyoshi@riam.kyushu-u.ac.jp

ABSTRACT

A numerical simulation method for coupling of tank fluid and ship motions is developed by combining the moving particle semi-implicit method (MPS method) used as the flow solver in a tank and ordinary ship motion prediction solving differential equations. Firstly a forced roll test is conducted to examine the applicability of the MPS method for violent flows in a tank. Then the developed hybrid simulation method is validated by comparing numerical results with the experimental ones. As a result, it is demonstrated that the proposed method can well predict the dynamic coupling of tank fluid and ship roll motions.

Keywords: *MPS method, Tank, Ship, Coupling, Hybrid Simulation Method*

1. INTRODUCTION

It is an important issue to predict dynamic coupling of tank fluid and ship motions, e.g. sloshing analysis of LNG carriers and FPSOs, and designing of anti-rolling tanks to prevent severe rolling. In order to provide reliable solutions for such fully coupled problems, an advanced numerical simulation method is required, which can take account of the hydrodynamic coupling effect between a ship and tank fluid. For the estimation of hydrodynamic forces of tank fluid, there are some reports applying particle methods for their analyses. [Iglesias et al., 2003] [Delorme et al., 2006] For realising coupling simulations of tank fluid and ship motions, a hybrid numerical simulation method is developed by combining the MPS method used as the flow solver in a tank and an ordinary time-domain simulation method solving ship motion equations. Delorme et al. (2006) reported a similar attempt applying the smoothed particle hydrodynamics (SPH) to a sloshing problem.

In our method, the coupling force from the tank fluid to the ship is estimated by the MPS method, and the ship motion coupled with the tank fluid is predicted by solving the differential equation of ship motions with taking the estimated coupling force into account.

In this research, roll motions of a ship equipped with a water tank is examined for the validation of the developed simulation method. Firstly a series of forced roll test is carried out to evaluate the capability of the MPS method for the estimation of the hydrodynamic coupling force from the tank fluid to the ship. Comparisons between the forced roll tests and the computational results demonstrate that the MPS method well reproduces the violent deformations of the free surface in the tank, and also the hydrodynamic coupling force. Secondly model experiments are conducted to measure roll motions of a pure car and truck carrier (PCTC) equipped with a water tank to validate the proposed hybrid simulation



method. In the experiment, the roll decaying in calm water and the large amplitude rolling in head seas are measured with and without the tank water. Comparisons of the ship motions coupled with the tank water demonstrate that the developed numerical simulation method can predict the dynamic coupling, depending on the tank shapes, of the tank water and the ship roll motions.

2. NUMERICAL SIMULATION METHOD

2.1 MPS Method

The moving particle semi-implicit method (MPS method) was developed by Koshizuka and Oka (1996) for solving incompressible fluids. The MPS method is one of the meshfree particle methods, which can deal with violent deformations of free surface. The governing equations of the MPS method, dealing with incompressible fluid, are expressed as Eqs. (1)-(2). The first- and the second-order differential operators in Eq.(2) are calculated with the discrete models called particle interaction models using a weight function. The weight function is shown in Eq. (3). Since the MPS method is fully lagrangian scheme, considering particles as discrete points, the advection term does not appear in the momentum equation. In the MPS method, the gravity and the viscous terms are solved explicitly and the Poisson equation for the pressure is solved implicitly.

There were a several researches applying the MPS method to violent flow problems. [Sueyoshi et al., 2008] [Shibata et al., 2009] [Hashimoto et al., 2011]. It has been well validated that the MPS method has good capability and high numerical stability for highly nonlinear surface flows. The details of the MPS method used in this study can be found in the literature. [Sueyoshi et al., 2008]

$$\frac{D\rho}{Dt} = 0 \quad (1)$$

$$\frac{D\mathbf{u}}{Dt} = -\frac{1}{\rho}\nabla p + \nu\nabla^2\mathbf{u} + \mathbf{g} \quad (2)$$

$$w(r) = \begin{cases} \frac{r_e}{r} - 1 & 0 \leq r < r_e \\ 0 & r_e \leq r \end{cases} \quad (3)$$

2.2 Hybrid Simulation Method

The authors have developed the hybrid numerical simulation method for dynamic coupling of tank fluid and ship motions by combining the MPS method used as the flow solver in a tank and ordinary ship motion prediction solving equations of ship motions. Since the MPS method is one of the meshfree particle methods, nonlinear surface flows, e.g. fluid separation and coalescence, are easily treated. The hydrodynamic coupling force from the tank fluid to the ship is estimated from the pressure distribution in the tank obtained by the MPS method in each time step. The hydrodynamic forces acting on the ship are calculated by a strip theory, in which the sectional hydrodynamic forces based on a potential flow theory are integrated along the ship. The flow chart of the developed hybrid simulation method is shown in Fig.1.

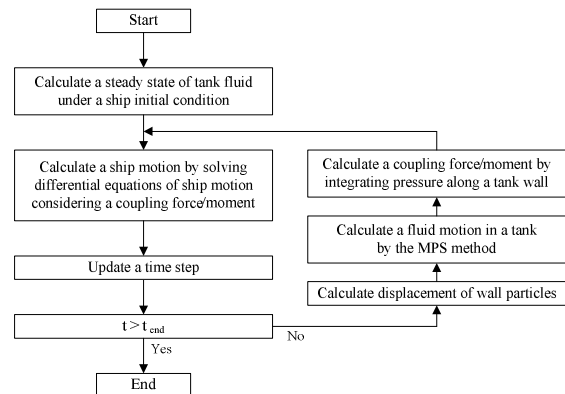


Figure 1: Flow chart of the hybrid simulation

Since the tank motion follows the ship motion, the coupled ship motion can be predicted if the hydrodynamic forces acting on the ship and the tank are estimated. In the proposed method, the tank fluid is solved by the MPS method, and the pressure distribution

in the tank is obtained in each time step. Therefore the hydrodynamic coupling force can be calculated by integrating the local pressures at each boundary particle along the tank inner wall. The ship motions coupled with the tank fluid are solved by the numerical integration of the ship motion equations with taking account of the estimated coupling force as an external force. The displacement and the velocity of the wall particles, consisting of the tank, induced by the ship motions is calculated by the coordinate conversion around the centre of ship gravity, and are given to the MPS computation as the boundary condition in a next step. By solving the ship and fluid motions simultaneously, the coupled motions can be simulated in time domain as the dynamic solution. In this study, a single degree of roll motion with a water tank is considered as a first step. Here it is assumed that the tank has 2-dimensional shapes for neglecting complicated 3-dimensional effects.

3. VALIDATION OF MPS METHOD

It is important to examine the validity of the MPS method itself as the flow solver in a tank in advance of the validation of the hybrid simulation method. Therefore the MPS simulations are executed and compared them with model experiments of forced roll test to investigate the accuracy and the applicability of the MPS method.

3.1 MPS Simulation

The MPS method solves the flow in the tank, and then the pressure distribution is obtained. In each time step, the hydrodynamic coupling force which acts on the ship as a rotational moment ($K_{coupling}$) is calculated by integrating the local pressures along with the tank inner wall as shown in Eq.(4). The numerical conditions used for the MPS simulations are shown in Table 1.

$$K_{coupling} = l_k \sum_i p_i \mathbf{n}_i \Delta S_i \times (\mathbf{r}_i - \mathbf{r}_g) \quad (4)$$

Table 1: Numerical conditions

item	value
time step (s)	0.0002
distance of adjacent particles (m)	0.001
total number of particles (rectangle, U-tube)	13152, 13530
relaxation factor α	0.25
incompressibility condition	PND

3.2 Tank Shape

In this research, two different shapes of tank are tested. One is a simple rectangle tank and another is a U-tube tank like anti-rolling tanks. The principal dimensions and their definitions are shown in Tables 2-3 and Figs.2-3, respectively.

Table 2: Principal dimensions of the rectangle tank

B_T	0.42m	L_T	0.12m
H_T	0.13m	H_W	0.025m

Table 3: Principal dimensions of the U-tube tank

B_T	0.42m	B_D	0.2
L_T	0.12m	H_D	0.01m
H_T	0.13m	H_W	0.04m



Figure 2: Definition of parameters of the rectangle tank.

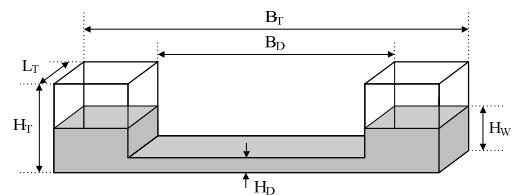


Figure 3: Definition of parameters of the U-tube tank.



3.3 Forced Roll Test

Forced roll tests of a 1/64 scaled PCTC model equipped with the rectangle or the U-tube tank are conducted to examine the capability of the MPS method for violent flows in the tanks and the coupling effects. The principal particulars of the subject PCTC are shown in Table 4, and the experimental setup for the forced roll tests is shown in Fig.4. The roll moments around the centre of rotation are measured by a dynamometer. In the experiments, the height of centre of rotation is set to coincide with that of the centre of ship gravity. The hydrodynamic coupling roll moment from the tank to the ship can be determined by subtracting the measured data with the water from that without the water. The free surface deformations under the forced roll condition are recorded by a digital video camera. The coordinate system of the measurements is shown in Fig.5.

The coupling roll moments calculated by the MPS method are compared with the experimental results. Fig.5 shows the comparison of the coupling roll moment for the rectangle tank. Here the roll amplitude, ϕ_a , is 30 degrees and the roll periods, T_ϕ are 3.25 and 1.75 seconds. Comparisons of the water deformation are also shown in Fig.6. In case of the rectangle tank, the coupling moment is predicted almost quantitatively by the MPS method both in the amplitude and the phase even for the shorter period. From the comparisons of the free surface deformation, the nonlinear flows in the tank i.e. running up along the side wall, overturning, and breaking, is well reproduced by the MPS method. Figs.7-8 show comparisons of the coupling roll moment for the U-tube tank. There is the discrepancy because the movement of the water is slightly underestimated in the MPS simulation as shown in Fig.8. This underestimation might be because of the limitation in the prediction of the large vortexes generated from the water duct edges. Although the numerical result is different to some extent, the prediction accuracy of the coupling moment is acceptable from a practical view

point. These comparisons for the two tanks indicate that the MPS method has good potential to solve the violent surface flows, and to estimate the coupling force from the tank to the ship. The similar comparisons of the forced roll test with an irregular roll signal can be found in the appendix.

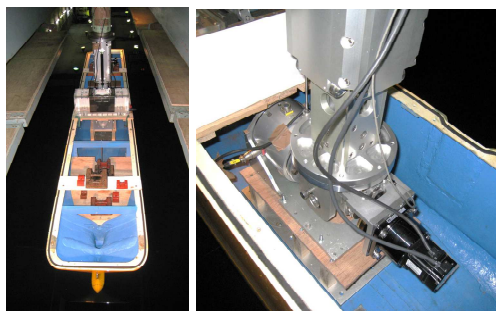


Figure 4: Experimental setup for forced roll tests.

Table 4: Principal particulars of the PCTC

	ship
length: L_{pp}	192.0 m
breadth:	32.26 m
depth: D	37.0 m
mean draught: T	8.18 m
block coefficient: C_b	0.54
longitudinal position of centre of gravity: x_{CG}	4.67 m aft
metacentric height: GM	1.25 m
natural roll period: T_ϕ	22.0 s

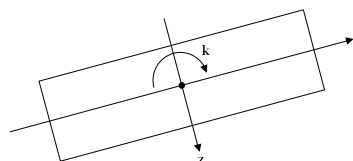


Figure 5: Coordinate system of the forced roll tests.

4. VALIDATION OF HYBRID SIMULATION METHOD

Since the applicability of the MPS method to the violent surface flows of the tank fluid is confirmed through the comparisons with the model experiments of forced roll test, the

validation of the proposed hybrid simulation method for the ship-tank coupling motions is attempted.

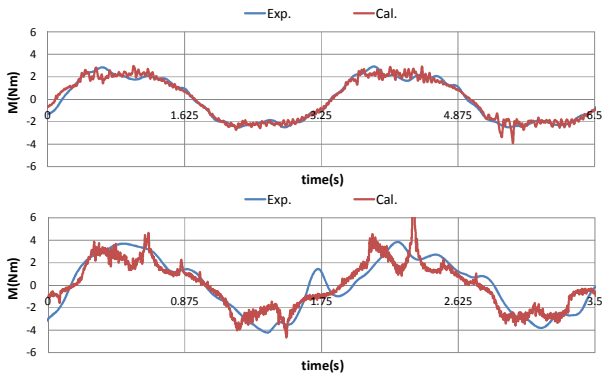


Figure 6: Comparisons of the coupling moment between the experiment and the MPS simulation with $\phi_a=30\text{deg.}$ for the rectangle tank (above: $T_\phi=3.25\text{sec.}$, below: $T_\phi=1.75\text{sec.}$)



Figure 7: Comparisons of the water deformation between the experiment and the MPS simulation with $\phi_a=30\text{deg.}$ for the rectangle tank (above: $T_\phi=3.25\text{sec.}$, below: $T_\phi=1.75\text{sec.}$)

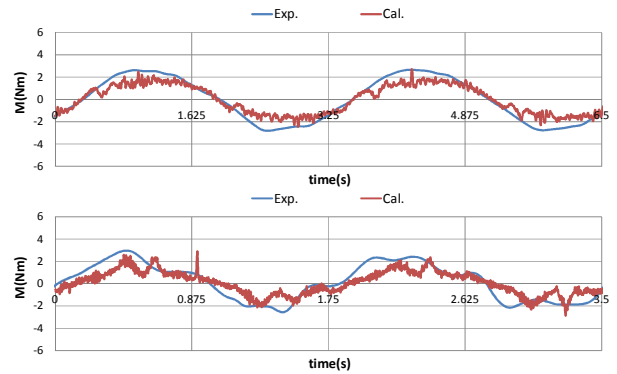


Figure 8: Comparisons of the coupling moment between the experiment and the MPS simulation with $\phi_a=30\text{deg.}$ for the U-tube tank (above: $T_\phi=3.25\text{sec.}$, below: $T_\phi=1.75\text{sec.}$)

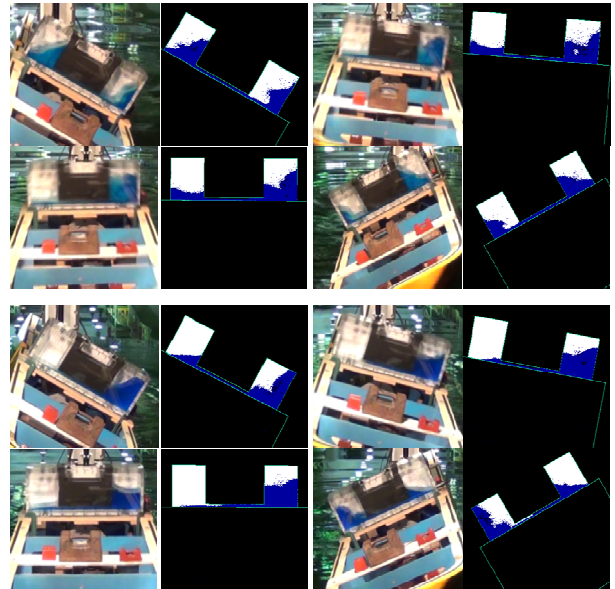


Figure 9: Comparisons of the water deformation between the experiment and the MPS simulation with $\phi_a=30\text{deg.}$ for the U-tube tank (above: $T_\phi=3.25\text{sec.}$, below: $T_\phi=1.75\text{sec.}$)

4.1 Model Experiment

Model experiments are conducted to measure roll motions of the PCTC model equipped with the rectangle or U-tube tank. The roll decaying motion (free roll) in calm water and the wave-excited roll motion in head seas are measured. In the head sea condition, the specific wave condition ($\omega_\phi \approx 1/2\omega_c$) is used



to observe the large amplitude roll motion, so called parametric roll. In the experiment, the wave length to ship length ratio, λ/L , of 1.25 and the wave steepness, H/λ , of 0.03 are selected for the parametric roll observation. The ship motions are measured by an onboard gyro scope and the water flows in the tank is done by a digital video camera. These measurements are conducted with and without the tank water to examine the effect of the tank water on the ship roll motion. In the experiment, the water level (H_W) for the rectangle tank is 0.03125m and that for the U-tube tank is 0.05m. Other dimensions of the tanks are the same as those of the forced roll test shown in Tables 2-3.

4.2 Mathematical Model

The mathematical models used for the prediction of the roll decay and the parametric roll in head seas are shown in Eqs.(5)-(6). The moment of inertia in roll, including the added moment of inertia, is estimated from the measured natural roll period and the metacentric height. The linear and the quadratic roll damping coefficients of the ship are estimated from the roll extinction curve without the tank water. The coefficients relating to the roll restoring variation, i.e. GM_{mean} and GM_{amp} , are calculated by the coupled heave-roll-pitch mathematical model based on a nonlinear strip method developed for the prediction of large amplitude parametric roll [Hashimoto & Umeda, 2010].

$$(I_{xx} + J_{xx})\ddot{\phi} + K_{\dot{\phi}}\dot{\phi} + K_{\phi_2}\dot{\phi}|\dot{\phi}| + W \cdot GZ = K_{coupling} \quad (5)$$

$$(I_{xx} + J_{xx})\ddot{\phi} + K_{\dot{\phi}}\dot{\phi} + K_{\phi_2}\dot{\phi}|\dot{\phi}| + W \cdot GZ + W(GM_{mean} + GM_{amp} \cos \omega_e t)\phi = K_{coupling} \quad (6)$$

4.3 Roll Decay

Comparisons of the time series of the roll decay with/without the tank water are shown in Fig.10. Here the differential equation of Eq.(5)

is solved by the Euler method and the time interval for the numerical integration is 0.0002 seconds. In the case with the tank water, the roll period becomes longer than that without the water due to the free water effect. In addition, the damping rate becomes larger depending on the tank shape. The numerical result well reproduces the experimentally confirmed trends for both the tanks. The calculated time variations of the roll components, which are the ship damping moment, the ship restoring moment, and the coupling moment, are shown in Fig.11. In both the cases, the coupling moment varies with the opposite phase to the restoring moment and it results in reducing the apparent restoring moment. The numerical result well explains the free water effect confirmed in the model experiment.

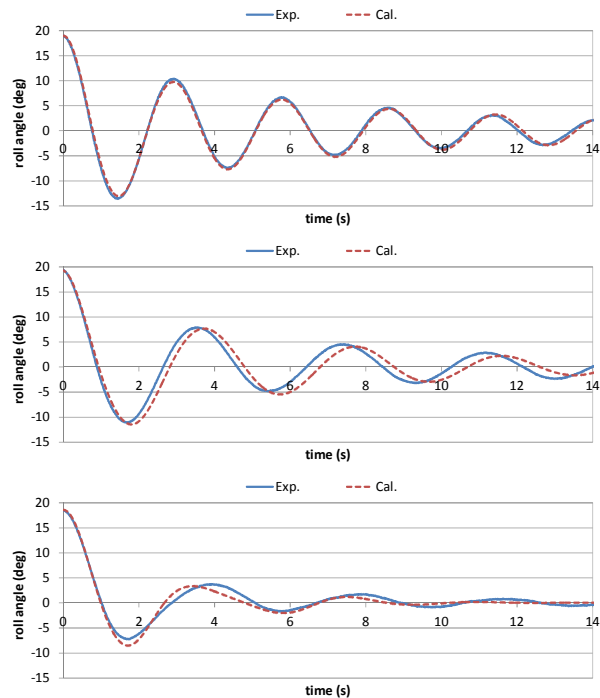


Figure 10: Comparisons of the roll decaying curve between the experiment and the coupling simulation (top: no water, middle: rectangle, bottom: U-tube).

4.4 Parametric Roll

Firstly numerical simulations of the head-sea parametric roll are executed for the case

without the tank water. Comparisons of the time series of the parametric roll are shown in Fig.12. In this case, Eq(6) is used for the prediction of the coupled roll motion. Here the mean and the amplitude of the metacentric height variation are calculated for the constant heel angle of 15 degrees. Even for the large amplitude of parametric roll over 30 degrees, the numerical simulation agrees well with the experimental result. This means the differential equation of Eq.(6) is appropriate enough for the prediction of parametric roll when there is no tank water. Secondly numerical simulations with the rectangle and the U-tube tanks are executed and comparisons with the model experiment are shown also in Fig.12. In the experimental results, the roll amplitude of parametric roll increases for the rectangle tank and decreases for the U-tube tank as compared to the result with no tank water. The calculated results predict the change of roll amplitude almost quantitatively. This indicates the tank water behaviour and the hydrodynamic coupling force are accurately simulated.

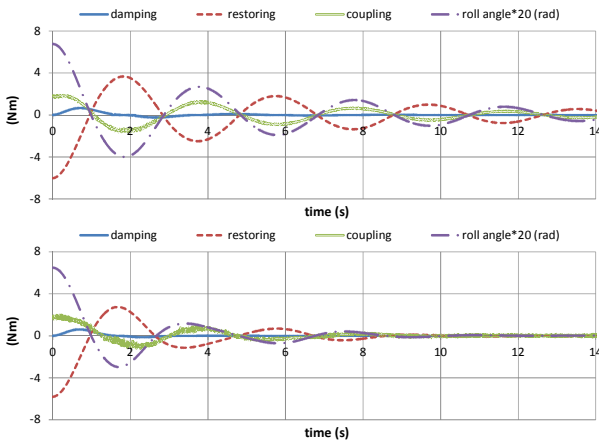


Figure 11: Comparisons of the calculated roll components during roll decaying (above: rectangle, below: U-tube).

Fig.13 shows the comparison of the free surface deformations during the parametric roll. It is demonstrated that the nonlinear deformations of the free surface due to the large rolling motion are well captured by the proposed method. Fig.14 shows time variations of the roll components and Fig.15 shows a comparison of the coupling force between the two tanks. For the rectangle tank, the coupling

moment decreases the roll damping after passing the upright condition while it does not for the U-tube tank. Therefore the roll amplitude of parametric roll increases for the rectangle tank and decreases for the U-tube tank because of the phase difference of the coupling force.

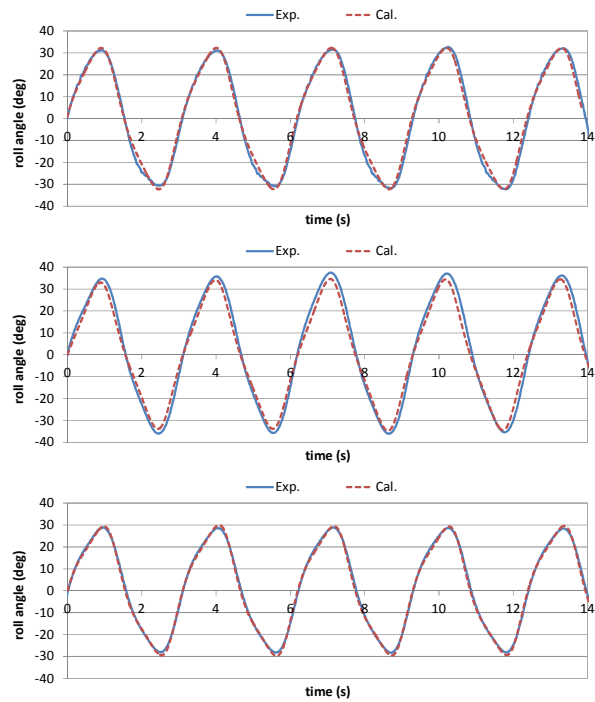


Figure 12: Comparisons of the parametric roll between the experiment and the coupling simulation with $H/\lambda=0.03$ and $\lambda/L=1.25$ (top: no water, middle: rectangle, bottom: U-tube)

These comparisons demonstrate that the developed numerical simulation method provides the accurate solution of the dynamic coupling of the tank fluid and the ship roll motions. Further improvement of the simulation model, e.g. expansion of the mathematical model to a multi-freedom model, is requested for the next step.

5. CONCLUSIONS

A numerical simulation method for coupling of tank fluid and ship motions is developed, which solves differential equations of ship motions with taking account of hydrodynamic



coupling forces calculated by the MPS method. In order to examine the capability of the MPS method for the violent flow in the tank, and for the coupling force to the ship, forced roll tests are conducted for a rectangle and a U-tube tank.

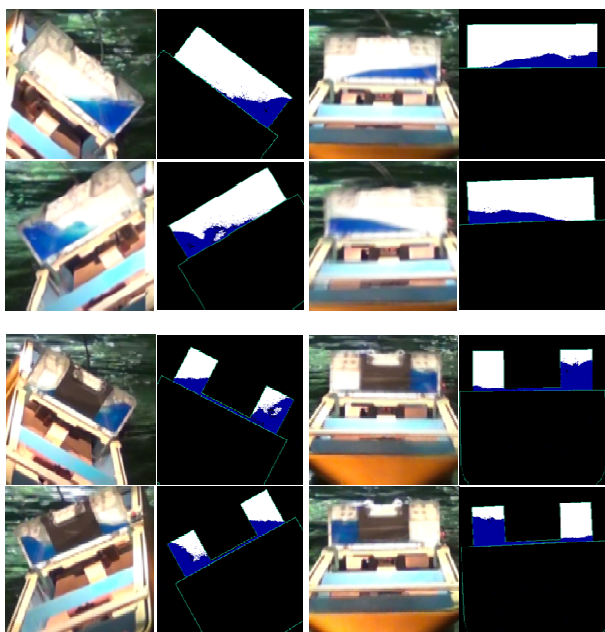


Figure 13: Comparisons of the water deformation between the experiment and the coupling simulation with $H/\lambda=0.03$ and $\lambda/L=1.25$ (top: no water, middle: rectangle, bottom: U-tube)

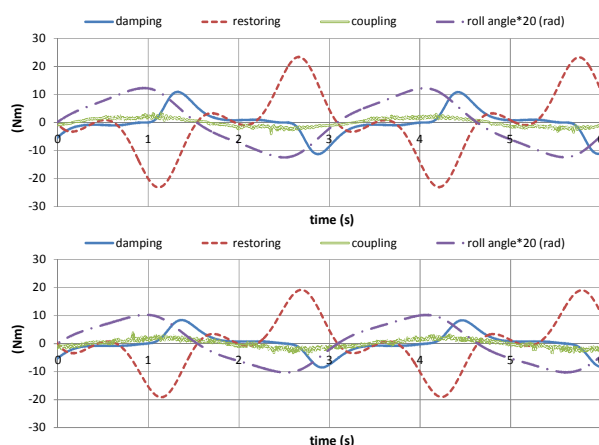


Figure 14: Comparisons of the calculated roll components during parametric roll (above: rectangle, below: u-tube).

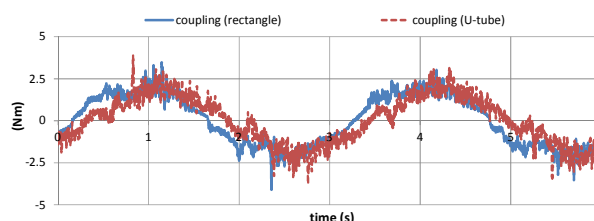


Figure 15: Comparison of the coupling force between the two tanks during parametric roll

From the comparisons with the model experiments, it is confirmed that the MPS method has good potential to solve the violent flows in the tank, and to estimate the hydrodynamic coupling force. In order to validate the proposed hybrid simulation method, the numerical results are compared with the model experiments of the roll decay and the parametric roll using a PCTC model equipped with the rectangle/U-tube tank. As the result, it is demonstrated that the proposed method can predict the coupled motions of the tank fluid and the ship roll almost quantitatively even with the violent deformations of the tank water. This simulation method could be one of the solutions for ship-tank coupling problems where the nonlinear interaction cannot be neglected.

6. ACKNOWLEDGMENTS

This work was supported by a Grant-in Aid for Scientific Research of the Japan Society for Promotion of Science (No.22686081).

7. REFERENCES

- Delorme, L., Bulian, G., Mc Cue, L. and Souto Iglesias, A., 2006b, Coupling between sloshing and ship roll motion: Comparison between nonlinear potential theory and SPH, Proceedings of the 26th Symposium on Naval Hydrodynamics, Rome, Vol.II, pp.259-270.
- Delorme, L., Casasus, L, Perez Rojas, L. and Souto Iglesias, A., 2006a, "Calculation of Liquid Loads Response to Forced Roll with Smoothed Particle Hydrodynamics",

Proceedings of the 9th International Conference on the Stability of Ships and Ocean Vehicles, Rio de Janeiro, Vol.2, pp.761-770.

Hashimoto, H., Sugimoto, T., Ito, Y. and Sueyoshi, M., 2011, "Two-Dimensional Simulations of a Damaged Ship Using the MPS Method", Proceedings of the 21st International Offshore and Polar Engineering Conference, Maui, pp.618-625.

Hashimoto, H. and Umeda, N., 2010, "A Study on Quantitative Prediction of Parametric Roll in Regular Waves," Proceedings of the 11th International Ship Stability Workshop, Wageningen, pp.295-301.

Hashimoto, H., Umeda, N. and Sogawa, Y., 2011, "Prediction of Parametric Rolling in Irregular Head Waves", Proceedings of the 12th International Ship Stability Workshop, Washington D.C., pp.213-218.

Koshizuka, S. and Oka, 1996, "Moving Particle Semi-implicit Method for Fragmentation of Incompressible Fluid," Nuclear Science and Engineering, Vol 123, pp 421-434.

Shibata, K., Koshizuka, S., and Tanizawa, K., 2009, "Three-dimensional numerical analysis of shipping water onto a moving ship using a particle method", Journal of Marine Science and Technology, Vol.14, pp.214-227.

Souto Iglesias, A., Perez Rojas, L and Delorme, L, 2003, "Investigation of Anti-Roll Tanks Using a Particle Method", Proceedings of the 8th International Conference on the Stability of Ships and Ocean Vehicles, Madrid, pp.617-631.

Sueyoshi, M., Kashiwagi, M., and Naito, S., 2008, "Numerical simulation of wave-induced nonlinear motions of a two-dimensional floating body by the moving particle semi-implicit method", Journal of Marine Science and Technology, Vol.13,

pp.85-94.

8. APPENDIX

We have also conducted the forced roll tests with the irregular roll signal. Here the input roll data is made from a time series of parametric roll in irregular head waves calculated by the numerical simulation program called OU-PR [Hashimoto et al., 2011]. The irregular roll signal is given to the MPS computation as the time-varying boundary condition. Comparisons of the coupling roll moment between the model experiments and the MPS method are shown in Figs.16. The MPS method can estimate the coupling moment with the irregular roll signal as well as the sinusoidal roll signal without any changes of the algorithm. Therefore the developed hybrid simulation method can be easily applied to irregular rolling problems.

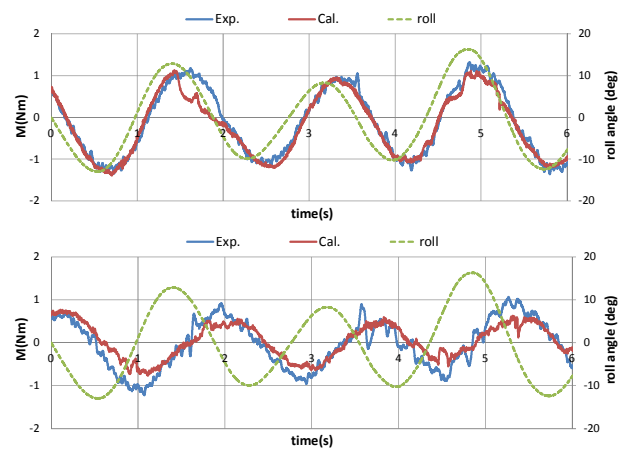


Figure 16: Comparisons of the coupling moment between the experiment and the MPS simulation with the irregular roll signal (above: rectangle, below: U-tube)





3D GPU SPH Analysis of Coupled Sloshing and Roll Motion

Luis Pérez-Rojas, *CEHINAV, ETSIN, UPM, Madrid, Spain*, luis.perezrojas@upm.es

José L. Cercós-Pita, *CEHINAV, ETSIN, UPM, Madrid, Spain*, jl.cercos@upm.es

ABSTRACT

The coupled roll motion response of a single degree of freedom system to which a passive anti-roll tank has been attached is considered and its performance studied numerically with a 3D GPU SPH code, aimed at simulating the sloshing flows occurring inside the tank. Results are compared with experiments from [Bulian et al, *JHR*, 48, 2010] in which 2D simulations were also presented. Progress achieved thereafter is documented, mainly consisting in the implementation of a parallelized solver that runs on a GPU card, which allows the simulation of low resolution 3D and high resolution 2D computations.

Keywords: *SPH, antiroll tanks, single degree of freedom systems, SDOF, GPU, sloshing*

1. INTRODUCTION

Ship motions are affected by sloshing flows occurring inside her liquid cargo tanks, as has already been documented both numerically and experimentally in the literature. Nam et al. (2009) for instance, use a finite difference method to model the flow inside the tanks and a linear sea-keeping code for the vessel motions simulation. A multimodal approach to sloshing presents large problems in resonance condition due to the lack of an intrinsic dissipation mechanism. Mesh based simulation techniques often struggle with sloshing flows due to the tremendous fragmentation that takes place at the free surface in resonance conditions. Due to this, meshless methods like SPH become an attractive option to simulate these flows, albeit to tackle 6 degrees of freedom, a full 3D SPH solver is necessary.

The onset of sloshing flows inside tanks has been used in order to dampen the roll motion. The antiroll tank concept is equivalent to the tuned sloshing damper or tuned liquid damper (TLD) concept in Civil Engineering. In the

existing literature, two approaches can be found to characterise the behaviour of a TLD exposed to external excitations. The first one consists in imposing a periodic motion on the TLD by using a shaking table or a forced roll motion device and measuring the response in terms of lateral force or moment (Tait et al., 2005; Souto-Iglesias et al. 2006). The other approach, more complex, and the one the present paper deals with, is to consider the motion response of the coupled system and tank-structure, subjected to external excitation in terms of force, moment or even induced motion to the tank interfaced with an elastic structure. With this second approach the damping characteristics, inertia and restoring terms are also relevant in the dynamic analysis. Realistic motions of the structure that are the outcome of this process can be compared with design limit states (Bulian et al, 2010; Attari and Rofooei, 2008).

In this paper, the SDOF system of (Bulian et al, 2010), to which a partially filled tank has been attached is considered. The roll motion is modelled by means of an "exact" (from the



dynamics point of view) 1-DOF approach. The moment created by the fluid with respect to the rolling axis is simulated and results for different roll angles are compared. It is important to underline that the present experimental/numerical approach removes the difficulties usually encountered in a correct modelling of the actual ship roll motion. Indeed, when numerical simulations are compared with experimental tests carried out on ship models excited by waves, it is almost never completely clear where the real source of discrepancy between experimental results and numerical prediction comes from, i.e. whether the reason is to be sought in the modelling of sea-ship interaction or in the modelling of sea-tank interaction. In the present tests, being the dynamics of the mechanical system practically known "exactly" (at least at a reasonable level of accuracy, with some question mark on damping at small rolling angles), any significant discrepancy is likely to be sought in the simulation method.

The numerical simulations have been performed using the SPH particle method. SPH has been successfully applied to shallow depth sloshing problems with periodic oscillation in sway (Landrini et al. 2003) and roll (Souto et al., 2006) motions. It had also been applied to a coupled motion problem (Bulian et al, 2010), showing promising results. Nevertheless, in (Bulian et al, 2010), the computations were carried out in 2D whilst 3D computations are presented herein. A significant progress in this regard has been recently achieved through the use of graphical cards (GPUs) that can perform massive parallel SPH computations (Herauld et al, 2010, Rey-Villaverde et al., 2011). These cards are extremely cheap and incorporate of the order of 500 processors each, substantially speeding up SPH computations. It would be extremely interesting to obtain an accurate description of the effect of the flow inside the tank to the system using a GPU based SPH solver, since SPH is, in principle, able to deal with highly distorted free surface flows. Checking whether

this is feasible is the main objective of the present work.

The paper is organized as follows. Firstly, the experiments are briefly described. Secondly, the GPU based SPH implementation is described. Thirdly, the simulation results are presented and compared with the experimental ones. Finally, some conclusions are drawn and future work threads hinted.

2. EXPERIMENTS AND MECHANICAL MODEL

2.1 Experiments

The experiments were conducted with the tank testing device of the CEHINAV group (see Souto-Iglesias et al 2011 for a detailed description). The standard forced motion configuration of the device, used regularly in the design of anti-roll tanks, was modified by disconnecting the driving electrical engine from the tank holding structure, in order to allow a free motion of the tank.

The tank is rectangular, 900x508x62mm. A horizontal linear guide consisting of a controllable electrical engine that laterally moves a weight with a specified motion has been attached. This weight is intended to generate a heeling moment in order to reproduce the wave action on the roll motion.

The water depth (H) whose first sloshing frequency matches the first own frequency of the structural system ω_0 (3.26 rad/s) has been chosen for the experiments and the same frequency has been chosen for the weight movement. This resonance condition is the hardest to tackle since in this condition the system accumulates energy in every cycle which then has to be dissipated by the fluid through internal dissipation and breaking in order to reach a steady state condition.

The amplitude of the weight motion has been chosen as $A=100$ mm. This combination

of frequency and amplitude were the ones analyzed in greater detail in (Bulian et al, 2010). Three different liquids have been used, namely: water, sunflower oil and glycerin, covering 3 different orders of Reynolds numbers. In the case of water, the dissipation comes from breaking and internal dissipation while the larger viscosity of oil and glycerine does not allow such breaking to take place thus inducing much smaller dampening effects than water. The experiments have been considered relevant by the SPHERIC ERCOFTAC Interest group on SPH as a benchmark for validation and further information about the experimental data can be found in the SPHERIC site and in (Bulian et al, 2010).

2.2 Analytical Model of the System

An analytical model of the SDOF structural system used in the experiments is needed in order to incorporate it into the structural part of the SPH code. This model was obtained by deducing the coefficients after carefully analyzing a set of tests with the empty tank and deriving a data-consistent damping term model. The analytical model used to describe the behaviour of the system is, in general, as follows:

$$\left[I_o + m \xi_m^2(t) \right] \cdot \ddot{\phi} + 2m \xi_m(t) \dot{\xi}_m(t) \cdot \dot{\phi} - g \cdot S_G \cdot \sin(\phi) + m \cdot g \cdot \xi_m(t) \cdot \cos(\phi) = Q_{damp}(t) + Q_{fluid}(t) \quad (1)$$

$$Q_{damp}(t) = -K_{df} \cdot \text{sign}(\dot{\phi}) - B_\phi \cdot \dot{\phi} \quad (2)$$

where:

- ϕ [rad] is the roll angle.
- g [m/s^2] is the gravitational acceleration.
- I_o [$kg \cdot m^2$] is the polar moment of inertia of the rigid system.
- m [kg] is the mass of the moving weight.
- $\xi_m(t)$ [m] is the instantaneous (imposed) position of the excitation weight along the linear guide (tank-fixed reference system).
- $\dot{\xi}_m(t)$ [m/s] time derivative of $\xi_m(t)$ [m].
- $S_G = M_R \cdot \eta_G$ [$kg \cdot m$] is the static moment of the rigid system with respect to the rotation axis.

- M_R [kg] is the total mass of the rigid system.
- η_G [m] is the (signed) distance of the centre of gravity of the rigid system with respect to the rotation axis (tank-fixed reference system).
- $Q_{damp}(t) = -K_{df} \cdot \text{sign}(\dot{\phi}) - B_\phi \cdot \dot{\phi}$ [$N \cdot m$] is the assumed form of roll damping moment with a:
 - A dry friction term $-K_{df} \cdot \text{sign}(\dot{\phi})$ with K_{df} [$N \cdot m$] being the dry friction coefficient.
 - A linear damping term $-B_\phi \cdot \dot{\phi}$ with
 - B_ϕ [$N \cdot m / (rad/s)$] being the linear damping coefficient.
- $Q_{fluid}(t)$ [$N \cdot m$] is the fluid moment.

By using a set of inclining as well as decay tests, the unknown parameters have been experimentally determined, including the natural frequency of the rigid system ω_0 . The values of these parameters can be found in table 1.

Table 1: Mechanical parameters of the rigid system

Quantity	Units	Value
S_G	$kg \cdot m$	-29.2
I_o	$kg \cdot m^2$	26.9
K_{df}	$N \cdot m$	0.540
B_ϕ	$N \cdot m / (rad / s)$	0.326
ω_0	rad / s	3.26

2.3 Dissipation Indicator

The rotating mechanical system stores energy in kinetic and potential forms. There is a transfer between these forms of energy during each rotation cycle. This accumulation is significantly reduced with the fluid action, which dissipates part of that energy in every cycle. Since the potential energy is proportional to the square of the rotation angle amplitude, a reasonable indicator of the TLD dampening performance is defined as the ratio of the empty tank motion amplitude and the partially filled tank motion amplitude, as in (Bulian et al., 2010).



3. GPU-SPH FORMULATION

3.1 General

The recent implantation of graphic process units (GPUs) in scientific computation has drastically increased the processing speed of several applications. Not many years ago, parallel computing was restricted to super-computing centers or large and expensive clusters. Nowadays, thanks to the arrival of GPU multicore processors originally designed for graphic processing, massively parallel processing is becoming increasingly more accessible and cheaper for the developer.

Increasing the efficiency of the algorithms involved not only depends on the specific hardware improvements, but also on the new approaches aimed at maximizing available resources and minimizing costs. In the case of GPU processors, it is necessary to note that the computational power lies in its specialization. The GPU multicore architecture is designed for highly efficient graphic processing. To explore the degree of adaptability of the GPU technology to certain algorithms which simulate large particle systems, first we analyze which steps of the SPH (Smoothed Particle Hydrodynamics) code are more suitable to be parallelized, as well as different strategies for the parallelization of the main subroutines. This requires the evaluation of any problematic aspect and the consequent speedup and scalability obtained.

Since the SPH methodology generally uses an explicit resolution scheme, their algorithms are easily parallelized to its minimum unit (particles, cells). However, there are certain subroutines whose GPU parallelization is not immediate; in those cases, different strategies will be implemented focusing on obtaining the maximum increase of the CPU versatility. Although it is always possible to use the CPU in those subroutines whose parallelization is problematic, this should be avoided due to the relatively high latencies associated with data transfers between CPU and GPU and the

consequent reductions in computational performance.

3.2 GP-GPU: OPEN CL Implementation

Traditionally, the GP-GPU has been developed using special languages (shaders) as GLSL, CG, or HLSL and incorporated as extensions of the OpenGL and Direct3D APIs. Learning GP-GPU programming not only required graphic programming as a prerequisite, but also required a considerable expertise in APIs and graphic languages. Currently, developing GP-GPU applications is done with the help of programming environments specifically designed to develop this type of codes such as the CUDA or OpenCL platforms.

Regarding the GPU architecture, a scheme of the processors distribution in the graphic cards used, is shown in figure 1. Basically, the GPU is distributed in a set of multiprocessors. Each multiprocessor typically hosts 8 scalar processors with NVIDIA architectures. From the viewpoint of parallel codes, the first important concept to consider is related to the kernel functions (analogous to the shaders in the graphic computing context). When a kernel is called, it launches a vector of N threads where each thread is executed in a different processor. In turn, every thread executes the instructions found in the kernel function sequentially. Once the kernel function is called, the N threads perform the instructions in parallel. Threads are grouped into blocks of threads. The threads associated in a specific block are executed in a common multiprocessor (8 single processors) where they can share variables and make use of the shared memory space associated to each multiprocessor.

When a kernel is called, blocks of threads are listed and distributed in the available multiprocessors. The threads of a block are executed simultaneously on a single multiprocessor, while multiple blocks could be executed concurrently in one multiprocessor.

Once all the threads of a block have been processed, new blocks are launched in the vacant multiprocessors. One multiprocessor can concurrently execute hundreds of threads. To efficiently manage the large number of threads, it uses a special architecture called SIMT (Single Instruction, Multiple Thread). The total amount of threads is divided into 32 unit packs called warps. In the SIMT architecture, the threads of a warp execute the same kernel instruction at the same time. In order to make a parallel implementation, achieve maximum transfer rates and avoid bottlenecks, it is crucial to understand the GPU memory hierarchy in order to manage different memory spaces .

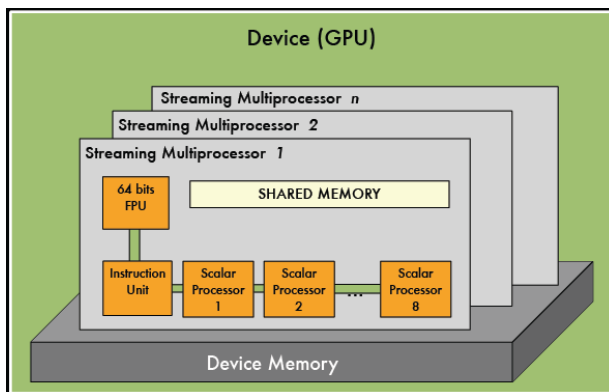


Figure 1: Basic architecture of a GPU card.

3.3 SPH parallel code.

Smoothed Particle Hydrodynamics (SPH) is a Lagrangian method, with no computational mesh that has been widely employed to study free-surface flows (Monaghan, 1994). A recent comprehensive review can be found in (Monaghan, 2005).

Due to the large number of interactions for each particle at each time step, when SPH codes are computed on a single CPU they usually require a large computational time. When millions of particles are required to accurately compute a physical process, only a parallel computing setup can guarantee efficient computational times. Due to the inexorable development of the market of video

games and multimedia, the GPU power and streaming multi-processor technology has increased much faster than CPUs. Thus, GPUs now appear as an accessible alternative to accelerate SPH models using a powerful parallel programming model where the graphics cards are used as the execution device. Their performance can be compared with large cluster machines. A huge advantage is the price and the easy maintenance GPUs require in comparison with large multi-core systems. The capability of GPUs to handle SPH was shown by the pioneer work of Harada et al. (2007).

A weakly compressible SPH implementation has been chosen for the simulations, using a Wendland kernel, a second order Leap-Frog time integration scheme and Monaghan, Cleary and Gingold's (Monaghan et al., 1983) viscosity formula (MCG formula from now on). The no-slip boundary condition is simulated using several rows of fixed fluid particles attached to the solid boundary (Macià et al., 2011). Although we kindly refer the reader to (Souto-Iglesias et al., 2006, Rey-Villaverde et al., 2011) for further details on the GPU-SPH implementation used in the present work, let's point out some details about its dissipation mechanisms.

In (Colagrossi et al., 2011) it was demonstrated that in the continuum, MCG viscosity formula provides the correct viscous dissipation for free surface flows. This viscosity formulation was originally devised as an artificial viscosity but was later shown to be a consistent Newtonian viscous term for incompressible flows (Hu and Adams, 2006). When comparing the kinematic viscosity with the artificial viscosity, the following relation is obtained in 2D and an equivalent one with a denominator of 15 in 3D:

$$\nu = \frac{1}{8} \alpha h c_s \quad (3)$$

The α factor should be no less than 0.01 if time integration is expected to remain stable (Monaghan 1994), with c_s being 10 times the



maximum expected velocity and h the smoothing length. This link sets the minimum value of the kinematic viscosity for a certain resolution (keep in mind that in practical terms the typical particle distance Δx is proportional to h). Since the computational effort was limited to 2 days per case (around $3e5$ particles), it was not feasible to perform a full resolution 3D computation for the water and oil cases.

4. RESULTS

4.1 General

In order to limit the computational effort, the simulations have been run up to 30 seconds (~15 oscillation cycles). Results are presented in terms of the angle across the time history and comparing experimental with simulation results for each fluid. Free surface shape results are also presented.

4.2 Glycerin

For the glycerin case, the fluid adheres to the walls of the tank due to its large dynamic viscosity (0.934 Pa/s, around 1000 times larger than water). Therefore, the effect of the front and aft walls may have an effect in the simulations when comparing the 3D with the 2D case. The stability criterion of equation 1 is fulfilled for the 3D simulation with 300,000 particles. The maximum experimental angle after 30 seconds is 17 degrees, while the 2D simulation angle only reaches 7 degrees (figure 2). This is a consequence of the dissipation being much larger in the 2D simulation compared to the experiments due to the absence of the front and aft wall boundary layers. Therefore in this case the 2D hypothesis is not acceptable.

The 3D simulation result is much closer to the experimental one (13 degrees compared to 17 in the experiments) although identifying the origin of the discrepancies requires further

research work. In both the 2D and 3D simulations there is a slight lag compared to the experimental result.

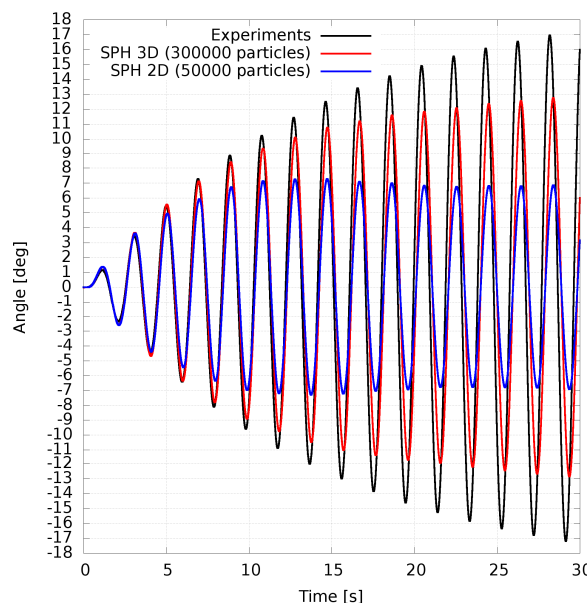


Figure 2: Glycerin case roll angle.

4.3 Oil

The 2D case can be run at full resolution in regards to correctly modelling the dynamic viscosity of the fluid (0.045 Pa/s) by using 200,000 particles. Around 5 million particles would be necessary to run a 3D case and this was not possible at this stage due to the time necessary to obtain a reasonable estimation of the damping effect (30 seconds).

The maximum experimental angle was 12 degrees, while the maximum angle in the 2D simulation was 10 degrees. The accuracy is therefore reasonable. The time history of the experiments and simulations can be appreciated in figure 3. In the simulation there is a slight lag compared to the experimental result.

4.4 Water

The effective viscosity that can be reached for this case with 100,000 particles in 2D was 0.068114 Pa/s, more than one order of magnitude larger than real water viscosity and

quite similar to oil. It was therefore not possible to run a 3D simulation. In the water case, the influence of both the front and back walls is negligible and the 2D approximation should therefore provide reasonable results.

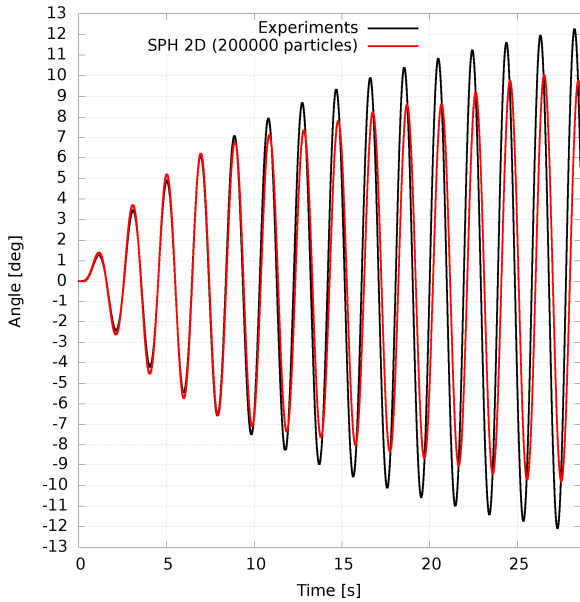


Figure 3: Oil case roll angle.

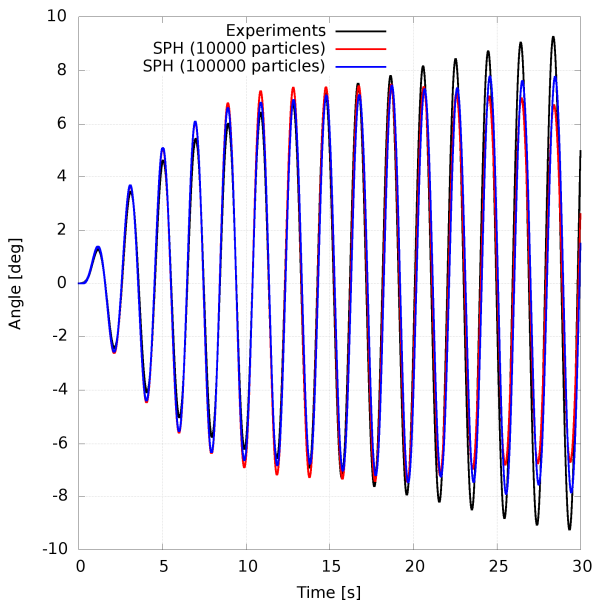


Figure 4: Water results.

The maximum experimental angle was 9.5 degrees, while the maximum angle in the 2D simulation was 7.9 degrees. The accuracy is therefore reasonable. The time history of the experiments and simulations can be appreciated in figure 4 where two resolutions results are

presented. In the simulation, no lag is present compared to the experimental result.

4.5 Free surface shape

Together with the roll angle time history it is relevant to analyze the free surface evolution for each case. In figure 5, the free surface is presented for the 2D simulations of the three liquids when $t=9.43s$ ($t/T_0=4.9$, T_0 being the first sloshing period). In this instant the tank is in its horizontal position for the water case while there is a slight deviation from this position for the oil and a more significant one for the glycerin case. The free surface pattern is quite different for the glycerin as compared to the water and oil cases, for which, as already discussed, the effective numerical viscosity was finally similar for this resolution. The glycerine shape is single valued while a breaking wave is observed in the oil case and the building up of a breaking wave can be appreciated for the water case.

As the simulation evolves to a point of extreme roll angle ($t=10s$, $t/T_0=5.2$, figure 6), a strong wave run-up with overturning waves and breaking takes place for the oil and the water simulations while a mild run-up occurs for the glycerin. The matching of these cases with the experiments can be observed by comparing figure 6 with figures 7 and 9.

The objective of the present paper is to assess the capabilities of SPH to deal with full 3D flows coupling problems in resonance conditions, where attenuating the vessel motion by dissipating energy through sloshing is the main target. 3D Results of the computations with glycerin are presented in figures 8 and 9. As discussed in section 4.2, the 2D simulation presents a much larger dissipation than the experimental one due to the absence of the effect of the back and front walls of the container. If the free surface shape of the glycerin in 2D for $t=9.43s$ in figure 5 is compared with the 3D one in figure 8, the matching with the experiments is much better for the 3D case, which is coherent with the roll angle found for both cases, as presented in figure 2. This tendency is confirmed by looking



at the $t=10s$ frames. In the 2D simulation shown in figure 6, a mild but significant wave run-up is apparent. This is not the case in 3D as can be seen in both the experiments and 3D simulations (figure 9).

Another interesting feature that can be observed in figures 8 and 9, is how the fluid sticks to the wall in both the simulations and experiments, thus confirming the importance of the front and back walls of the container in flow dynamics.

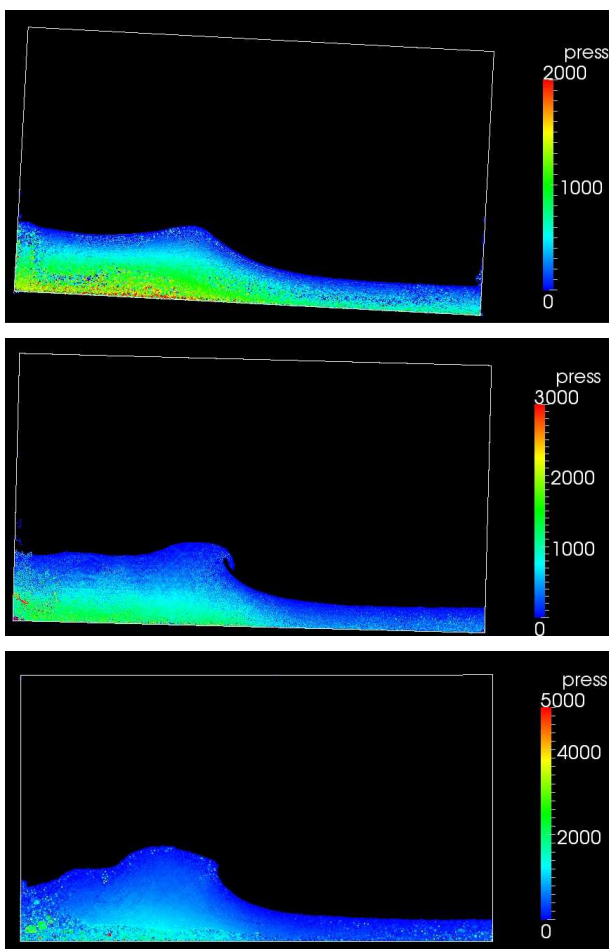


Figure 5: Glycerin (top), oil (mid), water (bottom), $t=9.43s$.

5. CONCLUSIONS

The roll motion response of a single degree of freedom (SDOF) structural system for which an “exact” analytic mechanical model is available and to which a rigid rectangular partially filled liquid tank was attached has

been considered. The coupled sloshing and SDOF system motion in resonance conditions has been numerically studied with a 3D GUP based SPH model and compared with the experimental results.

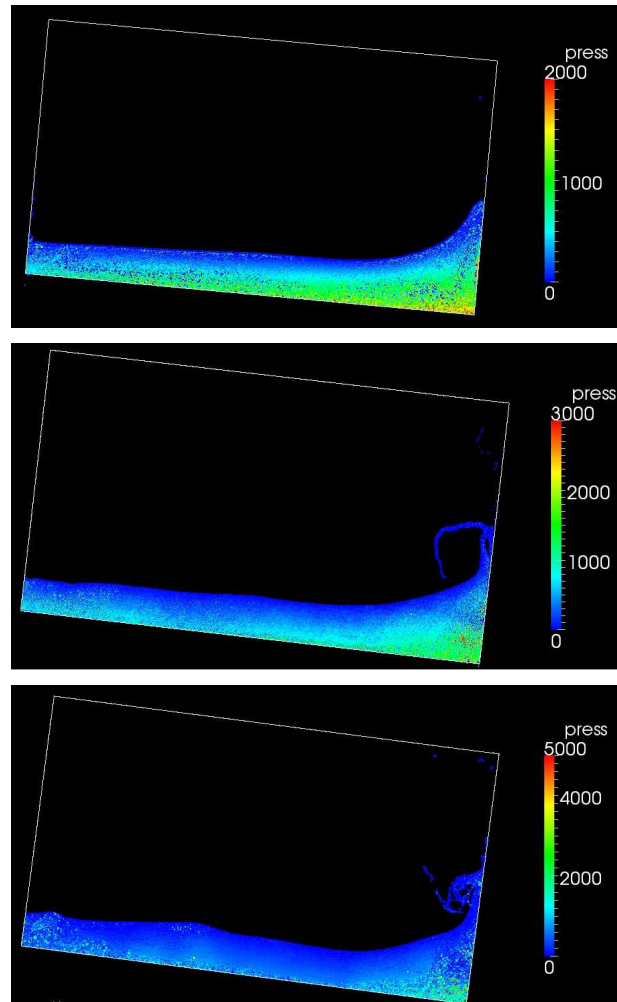


Figure 6: Glycerin (top), oil (mid), water (bottom), $t=10s$.

In order to characterise the type flow dynamics effects on the response curves, simulations have been performed with liquids of different viscosity, concluding that increasing the viscosity prevents the onset of breaking waves. The capabilities of SPH to treat this coupling problem have been assessed. From the comparisons with the experiments, it seems that SPH is able to capture part of the dissipation effects due to wave breaking which is reflected in reasonably accurate damping reduction ratios.

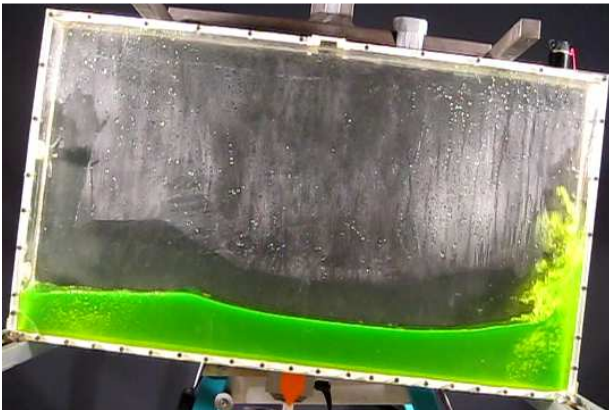
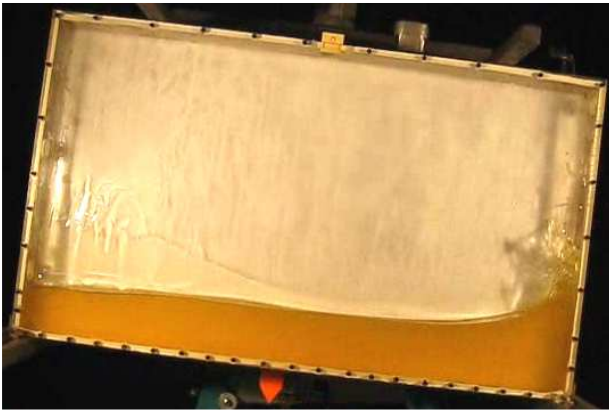


Figure 7: Experiments, oil (top), water (mid), $t=10s$.

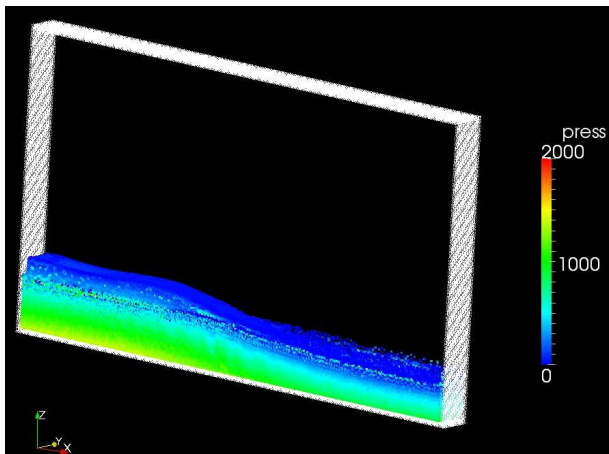
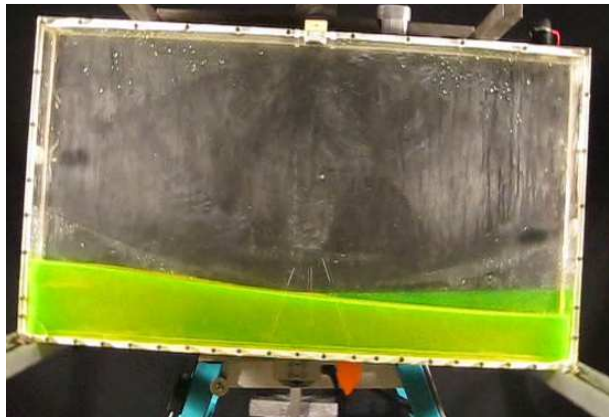


Figure 8: Glycerin, $t=9.43s$, experiment (top) 3D simulation (bottom).

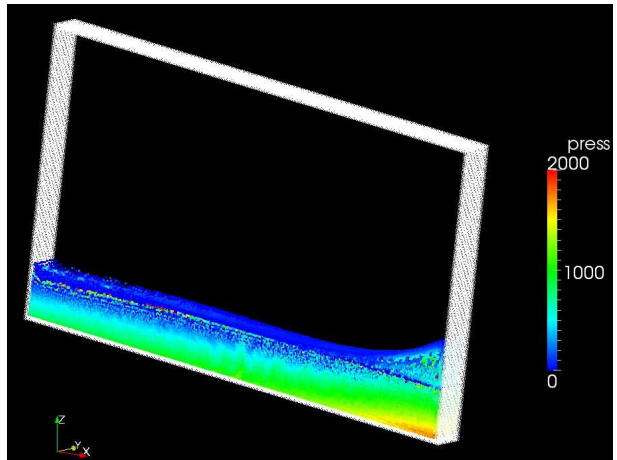
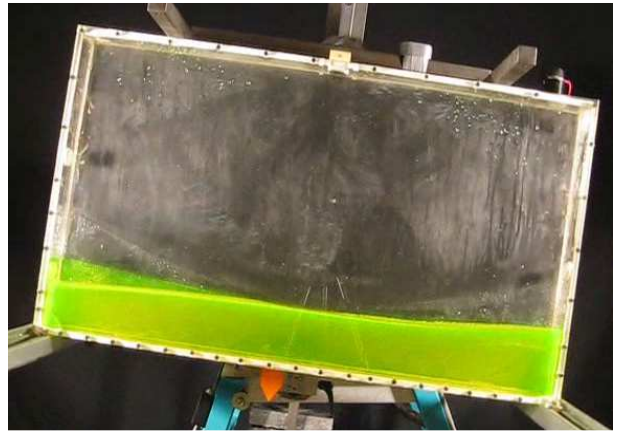


Figure 9: Glycerin, $t=10s$, experiment (top) 3D simulation (bottom).

Nevertheless, there are intrinsic limitations in the stability of the method that limit the effective Reynolds number which can be reached for a certain resolution. Further work has to be done in this regard.

The next step along this path is to incorporate the SPH model of the tanks internal flow into a 6DOF ship motions model.

6. ACKNOWLEDGEMENTS

The research leading to these results has received funding from the Spanish Ministry for Science and Innovation under grant TRA2010-16988, "Caracterización Numérica y Experimental de las Cargas Fluido-Dinámicas en el transporte de Gas Licuado".



7. REFERENCES

- Attari, N.K.A., Rofooei, F.R., 2008, "On lateral response of structures containing a cylindrical liquid tank under the effect of fluid/structure resonances", Journal of Sound and Vibration, 318, 4-5, 1154-1179
- Bulian, G., Souto-Iglesias, A., Delorme, L., Botia-Vera, E., 2010. "SPH simulation of a tuned liquid damper with angular motion", Journal of Hydraulic Research, Vol. 48 (Extra Issue), pp. 28-39.
- Colagrossi, A., Antuono, M., Souto-Iglesias, A., Le Touzé, D., 2011, "Theoretical analysis and numerical verification of the consistency of viscous smoothed-particle-hydrodynamics formulations in simulating free-surface flows". Physical Review E, Vol. 84, pp.26705+.
- Harada, T., Koshizuka, S., Kawaguchi, Y., 2007. Smoothed particle hydrodynamics on GPUs. Proc. of the Computer Graphics International Conference. pp. 63-70.
- Herault, A., Bilotta, G., Dalrymple, R. A., 2010. "SPH on GPU with CUDA". Journal of Hydraulic Research, Vol. 48 (Extra Issue), pp. 74-79.
- Hu, X. Y., Adams, N. A., 2006. "Angular-momentum conservative Smoothed Particle Hydrodynamics for incompressible viscous flows", Physics of Fluids, Vol. 18, pp. 702-706.
- Landrini, M., Colagrossi, A., Faltinsen, O. M., 2003. Sloshing in 2-D flows by the SPH method. Proceedings of the 8th International Conference on Numerical Ship Hydrodynamics.
- Maciá, F., Antuono, M., González, L. M., Colagrossi, A., 2011, Theoretical analysis of the no-slip boundary condition enforcement in SPH methods, Progress of Theoretical Physics, Vol., 125, pp. 1091-121.
- Monaghan, J. J., 2005. "Smoothed particle hydrodynamics". Reports on Progress in Physics, Vol. 68, pp. 1703-1759.
- Monaghan, J. J., Gingold, R. A., 1983. "Shock simulation by the particle method SPH". Journal of Computational Physics, Vol. 52, pp. 374-389.
- Nam, B.-W., Kim, Y., Kim, D.-W., Kim, Y.-S., 2009. "Experimental and numerical studies on ship motion responses coupled with sloshing in waves", Journal of Ship Research, Vol. 53, pp 68-82.
- Rey-Villaverde, A., Cercos-Pita, J. L., Souto-Iglesias, A., González, L. M., 2011. Particle methods parallel implementations by GP-GPU strategies. Proceedings of the II International Conference on Particle-based Methods - Fundamentals and Applications, PARTICLES 2011.
- Souto-Iglesias, A., Botia-Vera, E., Martín, A., Pérez-Arribas, F., Nov. 2011. A set of canonical problems in sloshing. part 0: Experimental setup and data processing. Ocean Engineering, Vol. 38, pp. 1823-1830.
- Souto-Iglesias, A., Delorme, L., Rojas, P.L., & Abril, S., 2006, "Liquid moment amplitude assessment in sloshing type problems with SPH". Ocean Engineering, 33 , 11-12.
- Tait, M.J., A.A. El Damatty And N. Isyumov, 2005, "An Investigation of Tuned Liquid Dampers Equipped With Damping Screens under 2D Excitation". Earthquake Engineering & Structural Dynamics 34 (7): 719-735.



Use of Granular Material Dynamics Simulation for the Study of Cargo Shift of Ships

Christos C. Spandonidis & Kostas J. Spyrou, *School of Naval Architecture and Marine Engineering*
National Technical University of Athens, spandonx@mymail.ntua.gr, k.spyrou@central.ntua.gr

ABSTRACT

In the current paper a modelling approach of granular material dynamics that can be interfaced with a ship motion model is described. Firstly, the existing simulation methods are critically assessed. Then, the adopted “discrete-particle” approach is described which is based on the so called “Molecular Dynamics” method. Some preliminary, yet characteristic, simulation results are produced, for a rectangular container vibrated in sway, in heave and in roll. The movement of cargo’s centre of mass is monitored. Critical parameter values (frequency, angle of tilt) for cargo shift and some preliminary comparison with the requirements of the international grain transport regulations are included.

Keywords: *granular material, molecular dynamics, liquefaction*

1. INTRODUCTION

Whilst the physical appearance of materials found in nature is quite varied, they can be classified under the four well-known states of matter: plasma, gas, liquid and solid. Yet experience suggests that some material cannot be put strictly under one category, because they bear the physical properties of two or more states of matter. Granular materials are ubiquitous in nature and yet they present high interest for the industry, being the second most manipulated material (Richard, 2005). Simply stated, by granular material is meant a conglomeration of discrete solid, macroscopic particles characterized by a loss of energy whenever these particles interact (Brown & Richards 1970). Despite their seeming simplicity, under different circumstances granular materials can exhibit substantial macroscopic differences in their behaviour. Subsequently, their handling often needs special attention. According to estimates, 40% of the capacity of many industrial plants are wasted because of problems related to the transport of these materials (Ennis et al., 1994). On the other hand, improvements in

computational methods and resources in recent years have enabled significant progress internationally in the modelling of these materials that has led to better understanding of the behaviour of granular materials under a variety of excitations.

For naval architecture, the study of the behaviour of granular materials should be a topic of great interest, since cargo shift represents a major hazard for ship safety and probably the most common cause of capsizing of large ships. However, the application of direct scientific modelling approaches for this important topic is basically non-existent. The current regulatory regime is governed by IMO’s Solid Bulk Cargoes Code [IMSB Code 268(85)] which however is prescriptive and largely empirical.

Recently there has been a spate of bulk carrier casualties with considerable loss of life, ostensibly initiated by the phenomenon known as “liquefaction”. As a matter of fact, liquefaction is a particularly dangerous issue since it turns what appears to be an apparently safe cargo like iron, nickel ore and core or sand slurry, into an easily movable cargo with a very detrimental effect on a vessel’s stability. The



oscillatory movement leads to compaction of the intra-particle spaces in the cargo. If combined with the presence of moisture exceeding the limits that are prescribed in the IMSB Code (more specifically, the Transportable Moisture Limit and the Flow Moisture Limit), conditions sometimes are created for the cargo to behave like a liquid.

In the current paper however, our focus is on the basic modeling of cargo shift phenomena, irrespectively of moisture. After a brief presentation of the existing simulation methods together with their limitations, in the following we describe a modelling approach that should lead, after interfacing with a ship motions model, to an integrated environment of ship – granular – material – dynamics investigation. A rectangular container is vibrated in roll, sway and heave and a preliminary identification of critical values for cargo shift is performed, taking into account international regulations' requirements. It is believed that the simulation model can be a useful investigation tool before applying experimental methods.

2. RESEARCH PROGRESS

Notable names such as Coulomb, whose law of friction was originally stated for granular materials, Faraday, who discovered the convective instability in a vibrated container filled with powder, Reynolds, Hertz and others contributed to the body of research performed in this area. Brigadier Ralph Alger Bagnold was an early pioneer of the physics of granular matter and his book "The Physics of Blown Sand and Desert Dunes" remains an important reference to this day. Furthermore, various experimental works have been performed (an activity intensified in recent years) sometimes using quite sophisticated equipment. Wong et al (2005) used Positron Emission Particle Tracking to examine the quality of solids behaviour in vertically vibrated beds with heap formation, surface waves and arching. Sellerio et al (2011) studied experimentally the mechanical behaviours of granular materials submitted to forced

vibrations, by the use of mechanical spectroscopy. Kawaguchi (2010) applied Magnetic Resonance Imaging to some dense granular flows or fluid-particle flows, such as the rotating drum, vibrated granular bed, hopper flow and spouted bed. His results confirm all the other observations.

In addition to experimental techniques, several theories have been applied for the handling of describing granular matter. In contrast to smooth particle dynamics method, where the continuum system itself is approximated by a discrete set of fluid particles, in the case of granular materials, continuum fields need to be constructed from discrete particle data. Specifically, these approaches are interested in deriving macroscopic fields, such as density, velocity and stress tensor from averages of microscopic variables such as the positions, velocities of, and forces on, each particle. In all these methods the important issue is to compute the continuum fields in the most appropriate way; that is to satisfy conservation laws. Among other approaches the coarse-graining approach (Goldhirsch, 2010) and the method of planes (Todd et al, 1995) are very popular. A general drawback for all these methods is that they are not universal (for every kind of grain) and sometimes they are leading to contradictory results because of the problems that they have near boundaries (Weinhart et al, 2012).

Despite, though, the great interest an overall coherent framework of granular materials investigation has not been fully set up yet. Scientific analysis refers mostly to a few prominent (primarily soil mechanics) problems. Performing similar research with relevance to ships is quite complex due to the dynamic nature of ship and cargo responses to random environmental excitations, the variety of transported materials substantially differing in properties and sizes, the presence of humidity etc. Nevertheless, with the vast computer power that is available today it seems that modelling work on this topic is possible.



3. EXISTING SIMULATION METHODS

Experiments with engineering devices are frequently expensive and sometimes even dangerous. Combined with the fact that there is no comprehensive theory on granular materials, numerical simulations can be used to reliably predict the behaviour of such materials for specific scenarios of container size, fullness, material type and size etc. Numerical simulations of interacting discrete media drive in the last twenty years an ever - growing interest in the granular microstructure and its link with macroscopic behaviour. Even by personal computers, sophisticated 2D or 3D systems of 20,000 particles can be simulated over a real time of a few seconds to a few minutes, offering the possibility to explore the effect of many parameters that would be hardly accessible by direct experimentation. Below is given a brief description of the most important simulation methods that are currently applied internationally:

3.1 Event-driven Molecular Dynamics

Molecular dynamics algorithms can be divided into two broad classes: those for soft and for hard bodies. The hard sphere modelling (event- driven molecular dynamics) is based on the absence of interpenetration or deformation during impact. It implies that velocities change according to the collision rule but the positions of the particles are the same before and after such an event. During the time intervals between collisions, the particles move along known ballistic trajectories. Therefore, the positions of the particles at the time of the next collision can be computed in one step. The calculation is purely algebraic because collisions are taken to be perfectly elastic: during a collision no energy is transferred either to deform or to change its internal state. The loss of linear momentum is characterized solely by means of the coefficient of elastic restitution, at least when rotations are neglected. In spite of its algebraic determinism, the algorithm produces phase-space trajectories that are chaotic, chaotic not only because of collisions, but also because of a delicate

coupling among the algorithm, software and hardware. That's why the simulation of granular gases is the main application of event-driven method. However the application of event-driven simulations is justified. Muller & Poschel (2012) showed that depending on the material and system parameters, the assumption of instantaneous events may fail.

3.2 Soft sphere Molecular Dynamics

The soft sphere approximation is based on an entirely different principle. Soft sphere Molecular Dynamics (called Molecular Dynamics from now on) plays the most important role among the simulation methods for granular systems. It is the time-dependent numerical solution of Newton's equation of motion for all particles of which the granular material consists. This method allows us, in principle, to simulate systems of complicatedly shaped particles in dynamic and static situations, and also in the case of multi-particle contacts. Here friction and elastic restitution come into play when spheres penetrate into each other, and the magnitude of the interaction depends on the penetration depth. Such simulations have been proven to be very useful and predictive in many applications, in particular when the dynamical behavior of the grains dominates the system properties. Molecular Dynamics requires only one precondition: one needs to know the forces and torques acting between contacting particles as functions of the particles' positions, their velocities, their angular orientation, and their angular velocities.

Although Molecular Dynamics provides an exact description of granular systems as the trajectory of each grain is computed, its application is restricted to rather small system size due to the time-intensive numerical solution of Newton's equation of motion. Since Molecular Dynamics is the method used in this project for the simulation of granular dynamics an extended description of this method is given in the next part. Pioneering work in the field of Molecular Dynamics of granular materials has been done by Cundall (1979).



3.3 Direct Simulation Monte Carlo

The method of Direct Simulation Monte Carlo is intended to solve the Boltzmann or Boltzmann–Enskog equation, i.e., it determines the velocity distribution as a function of the spatial position r and time t . This integration is performed by subjecting imaginary probability units $\Delta f(r, t)$ to the action of the collision operator. Since the velocity distribution function represents the probability to find a particle in a certain phase space interval, in a sense, these probability units can be understood as quasi-particles.

Direct Simulation Monte Carlo, is more efficient than the event-driven method, although, further simplifying assumptions are required. The necessary precondition of uncorrelated motion of particles (molecular chaos assumption) is approximately valid for dilute granular systems, also called granular gases. As granular gases have been studied intensively by means of kinetic theory, Direct Simulation Monte Carlo is suited for direct comparison with the results of kinetic theory.

In addition, although the physical and mathematical basis of Monte Carlo may be less transparent to a novice that for molecular dynamics, Monte Carlo is usually easier than molecular dynamics to code in a high-level language such as C++. Monte Carlo is also easier than Molecular Dynamics to implement for systems in which it is difficult to extract the intermolecular force law from the potential function. Systems having this difficulty include those composed of molecules that interact through discontinuous forces; examples are the hard-sphere and hard convex-body models. Similar difficulties arise in systems for which the potential function is a complicated multidimensional surface, such as might be generated by ab initio calculations.

For determination of simple equilibrium properties such as the pressure in atomic fluids, Monte Carlo and Molecular Dynamics are equally effective: both require about the same amount of computer time to attain similar levels of statistical precision. However, Molecular Dynamics more efficiently evaluates

such properties as the heat capacity, compressibility, and interfacial properties. Besides configurational properties, Molecular Dynamics also provides access to dynamic quantities such as transport coefficients and time correlation functions. Such dynamic quantities cannot generally be obtained by Monte Carlo, although certain kinds of dynamic behavior may be deduced from Monte Carlo simulations (Baumann, 1993). Molecular dynamics also offers certain computational advantages because of the deterministic way in which it generates trajectories. The presence of an explicit time variable allows us to estimate the length need for a run: the duration must be at least several multiples of the relaxation time for the slowest phenomenon being studied. No such convenient guide is available for estimating the length required for a Monte Carlo calculation. Finally many kinds of small errors in a molecular dynamics program tend to accumulate with time and so become apparent as violations of conservation principles; in contrast, subtle errors in a Monte Carlo program may not blatantly advertise their presence. As a result DSMC should be used with some care as inappropriate application may easily lead to non-physical results.

3.4 Rigid Body Dynamics

The idea of Rigid-Body Dynamics is complementary to the idea of Molecular Dynamics. While Molecular Dynamics simulations are always based on the evaluation of interaction forces, *Rigid-Body Dynamics* (sometimes also called *Contact Dynamics*) is based on the opposite idea: The interaction forces are determined from consistency requirements on the behavior of the particles. With much higher numerical effort Rigid-Body Dynamics allows for highly realistic simulation of systems comprising very stiff particles of complicated shape, which exhibit slow dynamics. However, as a direct consequence of disregarding material properties we have to sacrifice the uniqueness of the contact forces. Thus, the algorithm does not necessarily compute the physically-correct sets of contact

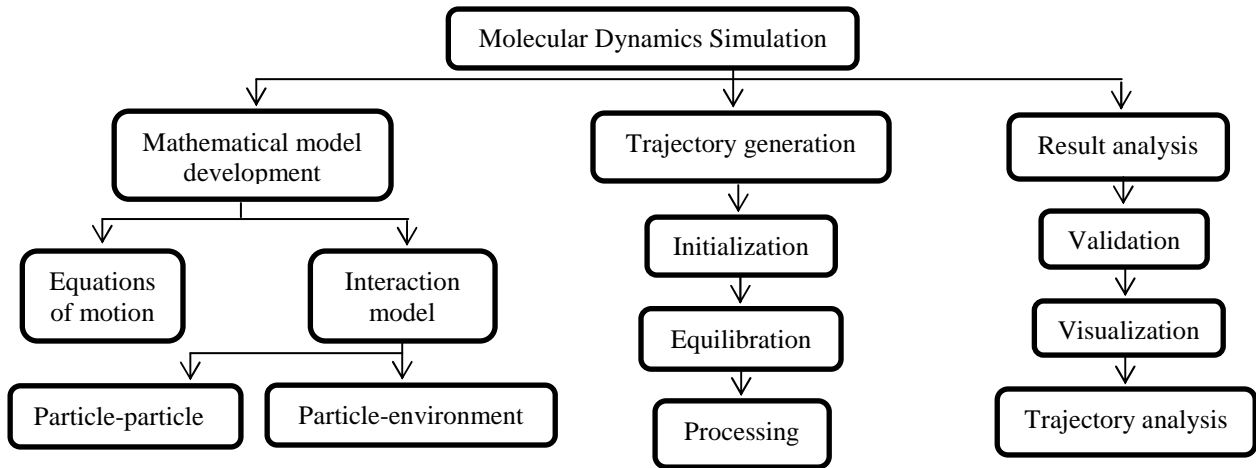


Figure 1: Elements of molecular dynamics simulation.

forces of a many-particle system, but one out of many (in general out of an infinite set of contact forces). Therefore, it cannot be assured that the system behaves in a physically-realistic way. Rigid-Body Dynamics has also been applied to granular systems, where frictionless smooth spheres have been simulated. A practical description of the application of Rigid-Body Dynamics to systems of spheres is presented by Unger et al (2002).

3.5 Other Methods

Besides the above mentioned there exists a number of further methods and algorithms for the simulation of granular systems. Some of these methods turn out to be significantly more efficient than the above mentioned ones, although they are restricted to certain types of problems. The most important further methods are Cellular Automata and bottom-to-top reconstruction which treat the system as a sequence of single particle problems (The algorithm may yield satisfactory results when treating systems where the boundary conditions change only very slowly. In such cases Molecular Dynamics is frequently inefficient).

4. OUR SIMULATION APPROACH

Our discrete-particle fluid model is based on the soft sphere Molecular Dynamics method. Granules are considered at this stage as smooth spherical particles with slightly different diameters (3 mm diameter with

standard deviation 5%) that can translate or rotate in any direction. Furthermore, for the needs of this work we assume dry granular materials (granular solid and aggregate). The analysis is based on the C++ algorithm, described by Poeschel & Schwager (2005). We have chosen C++, instead of Fortran or some ready to use molecular dynamics simulator such as LAMMPS (also written in C++) and NAMD since the Standard Template Library (STL) provides structures (e.g. vectors and sets) that allow for the implementation of complex algorithms at relatively low programming effort. As illustrated in Figure 1, Molecular Dynamics Simulation is associated with three tasks: developing a mathematical model, using the model in a simulation and analyzing the simulation results.

Model development, includes choosing a form for the potential (intermolecular and molecular – environment) and then deriving appropriate equations of motion in order to model individual particles. For our study, we consider nonlinear frictional forces that act normally and transverse to the line of contact during collisions as shown in Figure 2. For the normal force we adopt the dissipative Hertz-type force for viscoelastic materials presented by Brilliantov et al (1996):

$$F_n = -\tilde{k}_n \xi^{3/2} - \gamma_n \xi^{1/2} \dot{\xi} \quad (1)$$



where γ_n is a damping constant connected to the radii of the spheres and the coefficients of bulk viscosity. k_n is a non-linear stiffness of a spring whose elongation is ζ ($\zeta = \max(0, R_1 + R_2 - |r_2 - r_1|)$), the deformation of the grain, connected to the elastic properties (Young Modulus, Poisson ratio) and to the radii of the spheres. For the transverse force we adopt the model proposed by Haff & Werner (1986):

$$F_t = -\min(|\gamma_s u_s|, |\mu F_n|) \cdot \text{sign}(u_s) \quad (2)$$

Here γ_s is a shear damping constant without physical interpretation, u_s is the shear velocity component and μ stands for the dynamic friction coefficient. Since we consider only isolated systems, the equations of motion are simply obtained from Newton's second law. Thus the problem is reduced to the integration of Newton's equations of motion for the translational and rotational degrees of freedom.

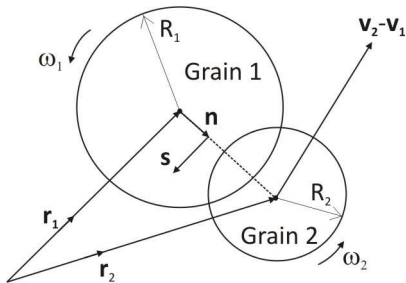


Figure 2: Grain penetration.

In our case (2D system) the angular orientation of a particle is described by a single angle φ_i and the moment of inertia reduces to a scalar value J_i :

$$m_i \frac{d^2 r_i}{dt^2} = F_i(r_j, u_j, \varphi_j, \omega_j)$$

$$I_i \frac{d^2 \varphi_i}{dt^2} = \frac{1}{J_i} M_i(r_j, u_j, \varphi_j, \omega_j), \quad (3)$$

The force F_i , the torque M_i , which act on particle i of mass m_i and the moment of inertia J_i , are functions of the particle positions r_j and their angular orientations.

Trajectory generation refers to movements' simulation of a large number of the model particles and divides into three major parts: initialization, equilibration and production. Of the large number of finite-difference methods that can be devised we use an efficient predictor-corrector method introduced by Gear (1971) which has proven to be powerful for Molecular Dynamics, because of its numerical stability. In specific Gear algorithm predicts molecular positions at time $t+\Delta t$ using a fifth order Taylor series based on positions and their derivatives at time t , evaluates the force on each grain at time $t+\Delta t$ using the predicted positions and Newton's 2nd law and finally correct the predicted positions and their derivatives using the discrepancy between the predicted acceleration and that given by evaluated force. To gain computational time efficiency a Neighbour List algorithm (Verlet, 1967) is introduced. For each grain i , the method maintains a list of neighboring grains that lie within a predefined distance of i . As a result the list identifies those grains that contribute to the force on grain i .

To gain result analysis; that is reliability analysis of computed trajectories, analysis of simulation data for the required collective phenomenon and visualization of trajectories, we use the software package Paraview 3.12 (Sawley et al, 2007). ParaView is an open-source, multi-platform application for the visualization and analysis of scientific datasets, primarily those that are defined natively in a two- or three-dimensional space including those that extend into the temporal dimension. The front end graphical user interface (GUI) has an open, flexible and intuitive user interface that still gives you fine grained and open ended control of the data manipulation and display processing needed to explore and present complex data as you see fit.

5. SIMULATION RESULTS

For the purpose of our work we consider a mobile, rectangular, smooth and rigid tank, filled partly by dry granular material. The origin of the coordinate system is placed at the left side of tank's bottom (Figure 3). Tank is free to move in any possible direction. Following Schafer et al (1996), our tank walls are built of particles to model surface roughness. Motion of the walls is prescribed and it can be periodic or random. In this specific application the model consists of 2.200 particles of which approximately 1800 can move relatively to the tank (the rest are wall particles). Tank length and height are denoted by l , h and for our case their values are 19.2 and 6.4cm, respectively. In order to facilitate the validation of our code by comparing some of the results directly with experimental data given by Drake (1991) and Forester (1994), we use a specific granular material, namely the cellulose acetate spheres of mass 1.48×10^{-4} kg. In Table 1 are presented the exact numerical values for the particle coefficients.

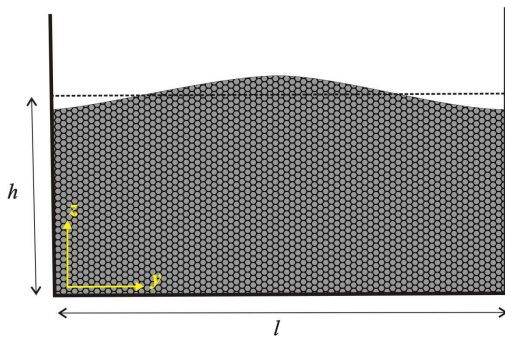


Figure 3: The origin of the coordinate system is placed at the left side of tank's bottom.

5.1 Sway

We monitored the movement of the mass centre of the granules inside the tank, under sway oscillation. Furthermore, in order to have direct visual observation of the behaviour, we animated the whole movement of the system (this is the most time consuming step and the reason that we restrict our investigation only to the first seconds of the movement).

Table 1: Numerical values for particle coefficients.

Parameter	value
Diameter (mm)	$3 \pm 5\%$
Mass (kg)	1.48×10^{-4}
Poisson ratio	0.28
Young modulus (N/m ²)	3.2×10^9
Coulomb friction (μ)	0.25 ± 0.02
Shear damping (γ_s)	20 Nsec/m

* Cellulose acetate particles

Even though our model could be used to simulate any realistic external oscillation (e.g. sea waves), we assume prescriptive periodic external excitation of the form $n_1 \cdot \sin(2\pi f_1 \cdot t)$, where n_1 and f_1 are horizontal excitation's amplitude and frequency, respectively. By giving to n_1 a constant value (10cm) we are able to test system's behaviour under various excitation frequencies. Figure 4 presents a tank snapshot when $f_1 = 2\text{Hz}$ (Figures 4 to 9 are presented at the end of the paper). One second after the excitation begun, the free surface started to behave like a liquid surface. Figure 5 presents the horizontal (left) and vertical (right) movement of the mass centre when the system oscillates under five different excitation frequencies. As it is shown, for $f_1 = 0.2\text{Hz}$ the mass centre is practically insensitive, in both the y and z directions. This implies that the particles follow the movement of the tank. As the frequency increases the mass centre starts to oscillate both along the y and z axes with a period close to that of the external excitations period. As expected, under a high frequency external excitation the free surface moves almost like a fluid and patterns of high amplitude waves are produced. An interesting point of observation is that the mass centre does not remain at the middle of the tank, as was expected, but it is shifted by about 2cm along the y and z axes. This is due to the distribution inhomogeneity of particle diameter and the gaps that exist between them.



5.2 Heave

Thinking in the same way as for the sway oscillation and assuming periodic external excitation of the form $n_3 \cdot \sin(2\pi f_3 \cdot t)$, where n_3 and f_3 are vertical excitation's amplitude and frequency, respectively, behaviour was tested under various excitation frequencies (as was the case for n_1 , n_3 has a constant value of 10 cm). In Figure 6 is shown a snapshot of system's behaviour for $f_3 = 2\text{Hz}$. In a short while the free surface started moving in the horizontal direction. As it is shown in Figure 7, where the horizontal (left) and vertical (right) movement of the mass centre under various excitation frequencies is presented, the mass centre of the system for small excitation frequencies follows the movement of the tank. However a small oscillation of the mass centre along the z axis exists, in contrast to what is happening in the y axis where the mass centre appears as practically fixed. Nevertheless, for an excitation frequency $f_3 = 2\text{Hz}$ the mass centre starts to oscillate both along the y and z axes. This means that, there is a critical value of frequency, after which a wavy free surface occurs. Once again, due to the distribution inhomogeneity of particle diameter and of gaps between them, the mass centre is not at the middle of the tank, as one would have expected, but it is shifted by about 2 cm along the y and z axes.

5.3 Roll

According to IMO's Solid Bulk Cargoes Code [IMSB Code 268(85)], solid bulk cargoes should be classified, where appropriate, in accordance with the UN Manual of Tests and Criteria, part III. The various properties of a solid bulk cargo need to be determined, as required by this Code. Among other cargo information required, one should determine the *angle of repose*; that is the maximum slope angle of non-cohesive (i.e. free-flowing) granular material. It is measured as the angle between a horizontal plane and the cone slope of such material. The angle of repose is a characteristic of non-cohesive bulk cargoes. It

is indicative of cargo stability and it establishes which provisions of the Code apply. The recommended test method is the tilting box method which is suitable for non-cohesive granular materials with a grain size not greater than 10 mm. A box (600mm long, 400mm wide and 200mm high) is filled with the material to be tested and the tilting system (rate of tilting should be approximately $0.3^\circ/\text{s}$) is then activated and stopped when the material just begins to slide in bulk.

We tested the response of the free surface under different rates of tilting. It was found that the model seems to predict the group of angles of repose in which the material can be classified ($<20^\circ$, between 20° and 30° or $>30^\circ$ etc.). For the considered material (cellulose acetate) the angle of repose is close to 15° . Hence, it belongs to the "below 20° " group of materials and it has to be handled diligently. However, for the prediction of the exact angle of repose one needs to handle effectively the shape of the initial surface which is currently receiving our detailed consideration. In Figure 8 are presented three time instants of the tilting tank, with rate of tilt $1.2^\circ/\text{s}$. As shown, the free surface is practically not moving till the angle takes a critical value. From this point the grains begin to flow. In Figure 9 the movement of the mass centre for two different tilting rates is presented. The left diagram corresponds to a rate of $17.2^\circ/\text{sec}$ and the right diagram to a rate of $1.2^\circ/\text{sec}$. The interesting result is that both rates produce almost the same angle of repose. An explanation for this is that, both the tank and the angle of cellulose acetate with diameter 3 mm are quite small. However for smaller rate the results are more distinct; that is the exact point of the angle of repose is represented by a big step in the curve. It is expected that, for different material and tank sizes the two rates may produce angles with a larger difference.

6. CONCLUDING REMARKS

In the first part of this paper the existing methods of simulation of granular material behaviour, together with their limitations, were

discussed. In particular, the so called molecular dynamics (soft sphere) method, which is the basis of our investigation, was presented in detail. Starting from the properties of the elementary granules that make up the material of interest (in this case cellulose acetate; however other materials more relevant to transported ship cargo in bulk are also currently considered) and by incorporating their mutual interactions, we have built a simulation model. Attention was paid the model to be general enough so that to be capable to predict the behaviour of a real granular cargo in a variety of situations. The simulation model is currently

considered for interfacing with a ship motions model. In the current report we restricted our scope in the case of prescribed harmonic external excitation.

Some first simulation results for a rectangular container vibrated in roll, sway and heave, were presented. Experimental reproduction of the results is currently underway and it will provide more confidence on the practical applicability of the method. Of course after experimental validation of results, the method will be used for materials relevant to ship cargo.

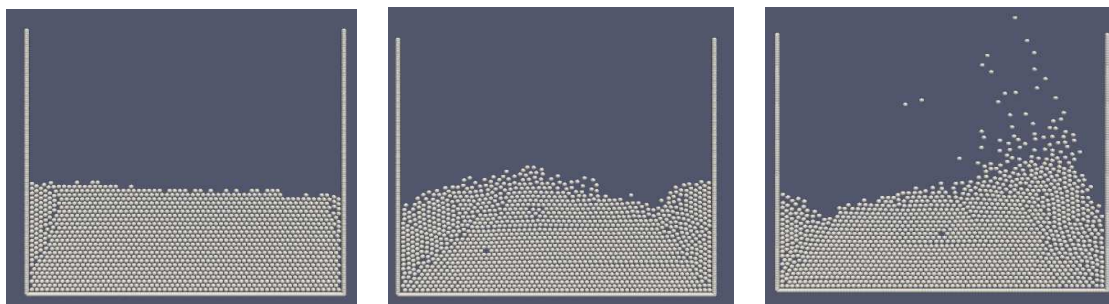


Figure 4: Different time moments (0, 1.6 and 3 s, left to right) for sway vibration at 2Hz.

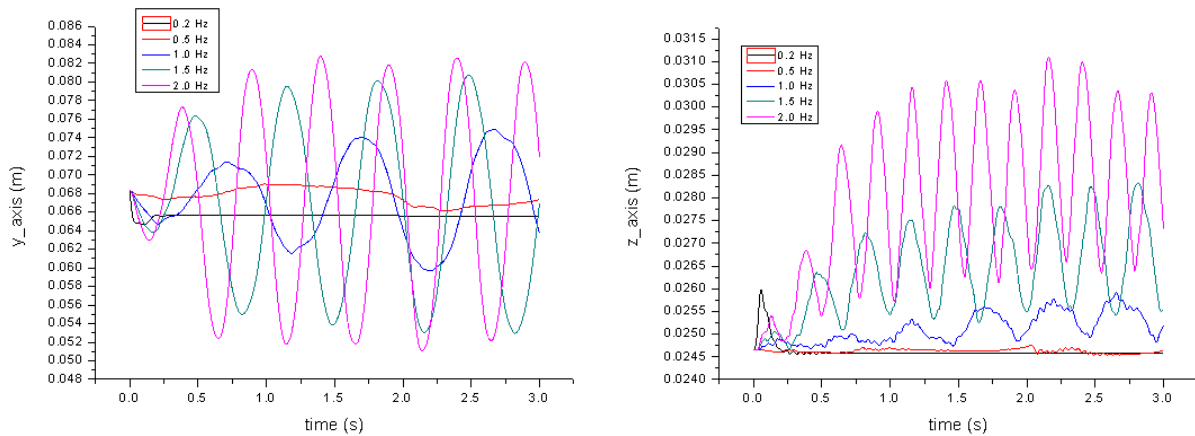


Figure 5: Horizontal (left) and vertical (right) movement of the mass center under sway vibration.

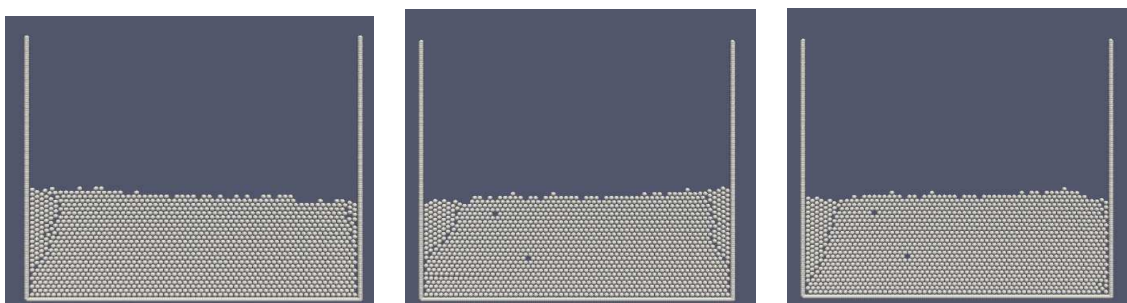


Figure 6: Different time moments (0, 1.6 and 3 s, left to right) for heave vibration at 2Hz.

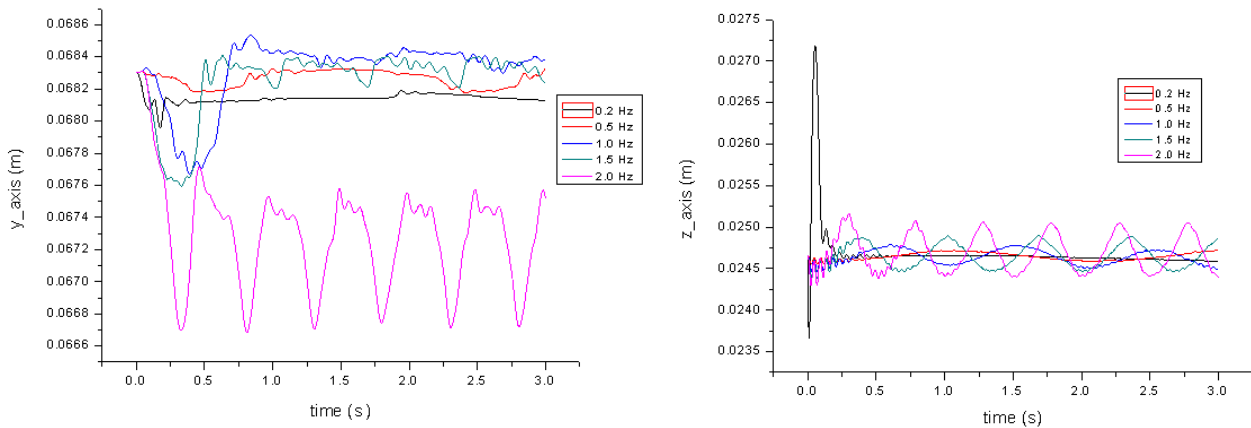


Figure 7: Horizontal (left) and vertical (right) movement of the mass center under heave vibration.

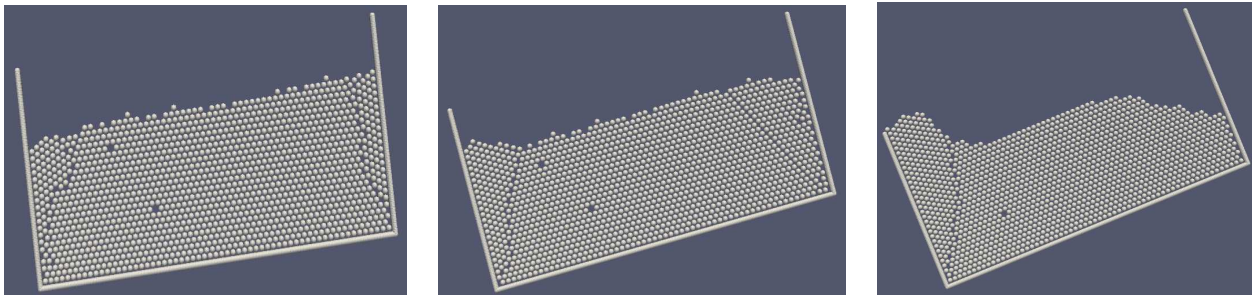


Figure 8: Different time moments (12, 14.3 and 17 s, left to right) for roll excitation.

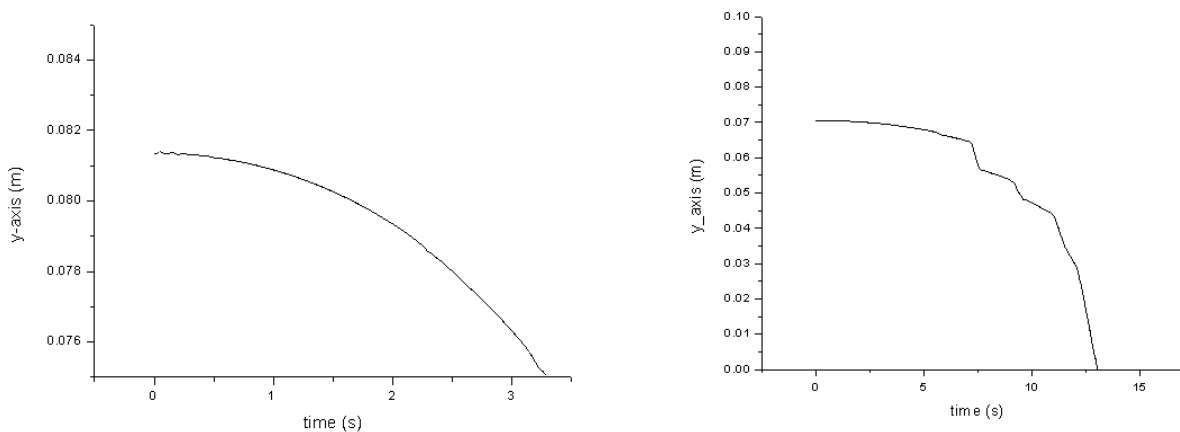


Figure 9: Horizontal movement of the mass center under roll excitation for 17.2⁰/s (left) and 1.2⁰/s (right) tilting rate.

7. REFERENCES

Baumann G, Jobs E, Wolf D.E, 1993, “Granular cocktail rotated and shaken”, Fractals, 1:767.

Brilliantov N. V, Spahn F., Hertzsch J.-M, Poschel T. , 1996, “A model for collisions in granular gases”, Phys. Rev. E, 53:5382.

Brown, R., and Richards J. C., 1970, “Principles of Powder Mechanics”,



- Pergamon, Oxford, UK. 21485-4.
- Cundall P. A., Strack O.D.L, 1979, "A discrete numerical model for granular assemblies", Geotechnique, 29:47.
- Drake TG., 1991, "Granular flow: Physical experiments and their implications for microstructural theories," J. Fluid Mech, 225: 12.
- Ennis, B. J., Green J., Davies R, 1994, "The Legacy Of Neglect In The United-States." Chemical Engineering Progress 90(4): 32-43.
- Foerster S. F, Louge M.Y, Chang H, Allia K., 1994, "Measurements of the collision properties of small spheres", Phys. Fluids 6: 1108.
- Gear C. W., 1971, "Numerical Initial Value Problems in Ordinary Differential Equations.", Prentice-Hall, Englewood Cliffs.
- Goldhirsch I., 2010, "Stress, stress asymmetry and couple stress: from discrete particles to continuous fields". Gran Mat 12(3):239-252.
- Haff P. K., Werner B. T., 1986, "Computer simulation of the mechanical sorting of grains" Powder Techn., 48:239.
- Kawaguchi T., 2010, "MRI measurement of granular flows and fluid-particle flows", Advanced Powder Technology, 21 (3), pp. 235-241.
- Muller P., Poschel T., 2012, "Oblique impact of frictionless spheres: on the limitations of hard sphere models for granular dynamics". Gran Mat (published online first 22 February 2012).
- Poschel T., Schwager T. 2005, "Computational Granular Dynamics", New York: Springer – Berlin, Heidelberg. ISBN: 978-3-540-21485-4.
- Richard, P., 2005, "Slow relaxation and compaction of granular systems", Nature Materials 4: 121–128.
- Sawley M, Biddiscombe J., Favre J., 2007, "Advanced visualization of large datasets for discrete element method simulations", DEM 07 proceedings.
- Schafer J., S. Dippel, and D. E. Wolf. Force schemes in simulations of granular materials. J. Physique I, 6:5, 1996.
- Todd BD., Evans DJ., Divis PJ., 1995, "Pressure tensor for inhomogeneous fluids". Phys Rev E 52(2): 1627-1638.
- Unger T., Brendel L., Wolf D. E., Kertesz J., 2002, "Elastic behavior in contact dynamics of rigid particles", Phys. Rev. E, 65:061305.
- Verlet, L., 1967, "Computer 'experiments' on classical fluids. I. Thermodynamical properties of Lennard-Jones molecules". Phys. Rev. 159: 98–103.
- Weinhart T., Thornton A., Luding S., Bokhove O., 2012, "From discrete particles to continuum fields near a boundary". Gran Mat (published online first 14 February 2012).
- Wong, Yee Sun; Gan, Chee Hong; Wang, Chi-Hwa, 2005, "Study on Granular Dynamics in Vertically Vibrated Beds using Tracking Technique", DSpace@MIT, Singapore-MIT Alliance, MEBS.





Investigation on Parametrically Excited Motions of Spar Platforms in Waves

Claudio A. Rodríguez, *LabOceano – COPPE/UFRJ, Rio de Janeiro, Brazil,*

claudiorc@peno.coppe.ufrj.br

Marcelo A. S. Neves, *LabOceano – COPPE/UFRJ, Rio de Janeiro, Brazil,*

masn@peno.coppe.ufrj.br

ABSTRACT

As offshore oil exploration goes into deeper waters, spar platforms appear as a good alternative for oil field developments due to their inherent hydrodynamic behaviour regarding its vertical motions response in waves. Spar's long natural periods in heave and pitch guarantee the good linear responses of the associated motions; however, nonlinear unstable motions can be triggered. Many numerical and experimental investigations have put forward the reasoning that this kind of floating structure is prone to parametrically induced motions due to changes in their pure hydrostatic restoring. Based on an analytical model, the present paper demonstrates that the main contribution to parametric excitation comes from variations in the pressure field associated to the incident wave and not from purely nonlinear hydrostatic actions. A nonlinear mathematical model based on Taylor series expansions, Neves and Rodríguez (2006), is employed to explain the underlying mechanism that leads to the phenomenon of Mathieu instability in vertical deep drafted cylinders. Analytical expressions are derived for the nonlinear hydrostatic and Froude-Krilov actions. A set of coupled time-dependent equations is obtained. Based on that, general conditions for the appearance of principal resonances are derived. These analytical results are verified by means of numerical simulations. Numerical analyses are carried out for regular wave conditions and a domain of parametric amplifications is obtained.

Keywords: *spar platforms, stability, parametric roll, nonlinear dynamics*

1. INTRODUCTION

As offshore oil exploration goes into deeper waters, spar platforms appear as a good alternative for oil field developments due to their inherent hydrodynamic behavior regarding its vertical motion responses in waves. Generally speaking, spar's long natural periods in heave and pitch guarantee good linear responses of these motions. However, nonlinear unstable motions can be triggered when heave resonance produces large heave motions even with relatively small wave excitation. Under these circumstances and due to nonlinear restoring coupling among the vertical modes, roll motions can also be amplified. This phenomenon

in spar platforms has been studied in earlier works (Haslum & Faltinsen, 1999, Rho et al., 2002, Koo et al., 2004, Hong et al., 2005) as Mathieu type instabilities associated with time dependent characteristic of roll/pitch hydrostatic restoring.

In the pertinent literature a common assumption is that Froude-Krilov forces and moments are not relevant for the stability problem of spar platforms, Bin-Bin et al. (2011), Koo et al. (2004). One of the aims of the present paper is to examine the validity of such simplifying hypothesis. One of the consequences of disregarding wave passage effect is that roll and pitch restoring actions become the same and



some confusion may then be established between pitch (directly excited) and the internally excited roll motion.

In a more general perspective, a literature review reveals that there are many different mathematical models for spar dynamic analysis. Liao & Yeung (2001), Koo et al. (2004), Liaw et al. (1993), Liaw (1994) models consider the roll (pitch) affected by heave but heave not affected by roll (pitch). In this context the authors of the present paper felt it would be appropriate to revisit the problem of parametric resonance of spar platforms employing a purely analytical mathematical model previously developed for parametric rolling of ships and recently expanded to a proper modelling of deep drafted bodies, Rodríguez (2010), Rodríguez & Neves (2012). Hopefully, as an analytical model, it may contribute to a better understanding of the problem, to be achieved in a rational way.

Employing a panel method Neves et al. (2008) advocated the need for heave-roll-pitch complete coupling and the consideration of nonlinear Froude-Krilov in all modes for a robust modelling of parametric roll excitation of spar platforms. The relevance of non-linear Froude-Krilov actions in inducing unstable roll motions had already been introduced by Neves & Rodríguez (2006) in the context of parametric rolling of ships. Kleiman & Gotlieb (2008) applied the same reasoning for ships with vertical walls. Yumin Liu et al. (2010) numerically investigated heave/pitch nonlinear coupling including nonlinear wave passage effects in both regular and irregular waves.

Two-fold objectives for the paper have been defined: a) consolidate an analytically derived coupled model for parametric resonance of deep drafted spar platforms in waves and b) demonstrate that the analytical model is capable of revealing complex nonlinearities under resonant conditions.

Haslum & Faltinsen (1999) reported on some few test results with a very small 1:300 model scale of a spar, in which large angles have been reached somewhat away from the

Mathieu tuning corresponding to the first region of instability. The paper gave an indication that parametric excitation may take place at large drafted vertical circular cylinders, but their experimental results were scarce, not providing a consistent set of data for comparisons. In the present study, a simplified form of a spar platform tested by Hong et al. (2005) is used for the numerical investigations, but only qualitative reference is made to these results.

The present analytical description of the restoring actions takes into account nonlinear coupling terms in the heave, pitch and roll modes, wave elevation profile and wave pressure field variation along the hull, Rodríguez & Neves (2012). With this new modelling for restoring actions, spar motions are numerically investigated. Results are presented for typical unstable conditions reported in other authors' previous experimental works. Parametric amplification domain (PAD), a plot of instability regions with response amplitudes due to parametric resonance for different excitation frequencies and wave amplitudes, is computed for the platform. Some interesting dynamical characteristics are revealed and discussed, in particular the quantitative contribution of pure hydrostatics and Froude-Krilov to the inception of unstable motions.

2. EQUATIONS OF MOTION

The floater's behaviour in waves can be described by a set of equations based on the second Newton's law. As main interest is on vertical motions (heave, roll and pitch) and the resonant phenomena associated to them in longitudinal waves, only 3-DOF need be considered and the restoring actions (including wave effects) should be described nonlinearly. Forces/moments of other nature such as hydrodynamic reactions (added mass and potential damping), or diffraction forces/moments can be described using the linear approach. Viscous effects in the damping force and moments are considered in an approximated way, based on empirical evidence.

Body and wave motions are described by making use of coordinate axes positioned at the mean water-surface. The equations of motion for the spar platform become:

$$(m + Z_z)\ddot{z} + Z_{\dot{z}}\dot{z} + Z_z\dot{z} + Z_{\dot{\theta}}\dot{\theta} + Z(z, \phi, \theta) = Z_{w0} \cos(\omega t + \alpha_z) \quad (1)$$

$$(J_x + K_{\dot{\phi}})\ddot{\phi} + K_{\dot{\phi}}\dot{\phi} + K(z, \phi, \theta) = 0 \quad (2)$$

$$(J_y + M_{\dot{\theta}})\ddot{\theta} + M_{\dot{z}}\dot{z} + M_z\dot{z} + M_{\dot{\theta}}\dot{\theta} + M(z, \phi, \theta) = M_{w0} \cos(\omega t + \alpha_{\theta}) \quad (3)$$

where the double dot terms denote accelerations, single dot terms denote velocities and coefficients with subscripts associated to these terms are added mass and damping coefficients, respectively. Hull mass is m and J_x and J_y are mass moments of inertia in roll and pitch, respectively. For damping terms, instead of adopting a quadratic damping to represent viscous effects, it was considered an equivalent linear damping approach in percentage of the critical damping (2.0% for heave, and 1.9% for roll and pitch). The adopted damping levels are similar to those obtained by Hong et al. (2005). Z_{w0} and M_{w0} represent the amplitudes of the linear wave exciting force and moment in heave and pitch, respectively, while α_z and α_{θ} denote the phase angles of the heave and pitch wave exciting actions with respect to the wave elevation.

3. RESTORING ACTIONS

Restoring actions in the case of a SPAR platform have been derived in Rodríguez and Neves (2012). These may be expressed as:

$$\begin{aligned} Z(z, \phi, \theta) &= Z_H + Z_W \\ &= Z_{CW}(z) + \frac{1}{2}Z_{\phi\phi}z^2 + \frac{1}{2}Z_{\theta\theta}\theta^2 \\ &+ Z_{\zeta z}(t)z + Z_{\zeta\theta}(t)\theta + Z_{\zeta\phi\phi}(t)\phi^2 \end{aligned} \quad (4)$$

$$\begin{aligned} K(z, \phi, \theta) &= K_H + K_W \\ &= M_{CW}(\phi) + \frac{1}{2}[K_{zz}z^2 + K_{\theta\theta}\theta^2]\phi \\ &+ [K_{\zeta\phi}(t) + K_{\zeta z\phi}(t)z + K_{\zeta\phi\theta}(t)\theta + K_{\zeta\zeta\phi}(t)]\phi \end{aligned} \quad (5)$$

$$\begin{aligned} M(z, \phi, \theta) &= M_H + M_W \\ &= M_{CW}(\theta) + \frac{1}{2}M_{zz\theta}z^2\theta + \frac{1}{2}M_{\phi\phi\theta}\phi^2\theta \\ &+ M_{\zeta z}(t)z + M_{\zeta\theta}(t)\theta + M_{\zeta\phi\phi}(t)\phi^2 \end{aligned} \quad (6)$$

Where $Z_{CW}(z) = \rho g A_0 z$ is the linear restoring coefficient in heave, $K_{CW}(\phi)$ and $M_{CW}(\theta)$ are the pure calm water restoring moments (here adjusted up to third order) in roll and pitch, respectively. Clearly, its linear term is $\rho g \nabla_0 \overline{GM}_0$, where ρ is water density, g is gravity acceleration, A_0 is the waterline area, ∇_0 is the displaced volume and \overline{GM}_0 is the initial metacentric height. In the above equations subscripts H and W indicate restoring actions due to hydrostatic and wave pressure fields, respectively. Wave term coefficients are denoted by their first subscript ζ , which corresponds to:

$$\zeta = A_w \cos(kX - \omega t) \quad (7)$$

where A_w and ω are wave amplitude and frequency, respectively, and k is wave number. Eq. (7) is a sinusoidal long-crested wave train system described in a $CXYZ$ inertial reference frame; the well known corresponding incident velocity potential (assuming deepwater) is given by:

$$\Phi_I = A_w \left(\frac{g}{k} \right)^{1/2} e^{kz} \sin(kX - \omega t) \quad (8)$$

Analytical expressions (valid for general hull forms) of the non-zero nonlinear Froude-Krilov coefficients appearing in equations (4-6) are given in Tables 1-3 for the heave, roll and pitch modes, respectively, see also Rodríguez & Neves (2012).



Table 1: Heave F-K restoring coefficients

$Z_{\zeta z}(t) = 2\rho g \int_L \left(\frac{\partial \bar{y}}{\partial \bar{z}} - \bar{y} k e^{k \bar{z}_b} \right) \zeta dx$
$Z_{\zeta 0}(t) = -2\rho g \int_L \left(\frac{\partial \bar{y}}{\partial \bar{z}} - \bar{y} k e^{k \bar{z}_b} \right) \bar{x} \zeta dx$
$Z_{\zeta \zeta z}(t) = -2\rho g \int_L \left(\frac{\partial \bar{y}}{\partial \bar{z}} \right) k e^{k \bar{z}_b} \zeta^2 dx$
$Z_{\zeta \zeta z z}(t) = \rho g \int_L \left(\frac{\partial \bar{y}}{\partial \bar{z}} \right) k e^{k \bar{z}_b} \zeta dx$
$Z_{\zeta \zeta 0}(t) = -2\rho g \int_L \left(\frac{\partial \bar{y}}{\partial \bar{z}} \right) k e^{k \bar{z}_b} \bar{x} \zeta dx$
$Z_{\zeta \phi \phi}(t) = -\rho g \int_L \left[2\bar{y} \left(\frac{\partial \bar{y}}{\partial \bar{z}} \right)^2 + \bar{y} - \bar{y}^2 \left(\frac{\partial \bar{y}}{\partial \bar{z}} \right) k e^{k \bar{z}_b} \right] \zeta dx$
$Z_{\zeta \zeta 0}(t) = 2\rho g \int_L \left(\frac{\partial \bar{y}}{\partial \bar{z}} \right) k e^{k \bar{z}_b} \bar{x} \zeta^2 dx$
$Z_{\zeta \phi 0}(t) = \rho g \int_L \left(\frac{\partial \bar{y}}{\partial \bar{z}} \right) k e^{k \bar{z}_b} \bar{x}^2 \zeta dx$

Table 2: Roll F-K restoring coefficients

$K_{\zeta \phi}(t) = 2\rho g \int_L \left[\bar{y}^2 \frac{\partial \bar{y}}{\partial \bar{z}} - \frac{1}{3} \bar{y}^3 k e^{k \bar{z}_b} - S_b \bar{z}_b k e^{k \bar{z}_b} \right] \zeta dx$
$K_{\zeta \zeta \phi}(t) = \rho g \int_L \left[2\bar{y} \left(\frac{\partial \bar{y}}{\partial \bar{z}} \right)^2 + \bar{y} - 2\bar{y}^2 \left(\frac{\partial \bar{y}}{\partial \bar{z}} \right) k e^{k \bar{z}_b} \right] \zeta^2 dx$
$K_{\zeta \phi \phi}(t) = -\rho g \int_L \left[4\bar{y} \left(\frac{\partial \bar{y}}{\partial \bar{z}} \right)^2 + 2\bar{y} - 2\bar{y}^2 \left(\frac{\partial \bar{y}}{\partial \bar{z}} \right) k e^{k \bar{z}_b} \right] \zeta dx$
$K_{\zeta \phi 0}(t) = \rho g \int_L \left[4\bar{x}\bar{y} \left(\frac{\partial \bar{y}}{\partial \bar{z}} \right)^2 + 2\bar{x}\bar{y} - 2\bar{x}\bar{y}^2 \left(\frac{\partial \bar{y}}{\partial \bar{z}} \right) k e^{k \bar{z}_b} \right] \zeta dx$

Table 3: Pitch F-K restoring coefficients

$M_{\zeta z}(t) = -2\rho g \int_L \left(\frac{\partial \bar{y}}{\partial \bar{z}} - \bar{y} k e^{k \bar{z}_b} \right) \bar{x} \zeta dx$
$M_{\zeta 0}(t) = 2\rho g \int_L \left(\frac{\partial \bar{y}}{\partial \bar{z}} - \bar{y} k e^{k \bar{z}_b} \right) \bar{x}^2 \zeta dx$
$M_{\zeta \zeta z}(t) = 2\rho g \int_L \left(\frac{\partial \bar{y}}{\partial \bar{z}} \right) k e^{k \bar{z}_b} \bar{x} \zeta^2 dx$
$M_{\zeta \zeta z z}(t) = -\rho g \int_L \left(\frac{\partial \bar{y}}{\partial \bar{z}} \right) k e^{k \bar{z}_b} \bar{x} \zeta dx$
$M_{\zeta \zeta 0}(t) = 2\rho g \int_L \left(\frac{\partial \bar{y}}{\partial \bar{z}} \right) k e^{k \bar{z}_b} \bar{x}^2 \zeta dx$
$M_{\zeta \phi \phi}(t) = \rho g \int_L \left[2\bar{y} \left(\frac{\partial \bar{y}}{\partial \bar{z}} \right)^2 + \bar{y} - \bar{y}^2 \left(\frac{\partial \bar{y}}{\partial \bar{z}} \right) k e^{k \bar{z}_b} \right] \bar{x} \zeta dx$
$M_{\zeta \zeta 0}(t) = -2\rho g \int_L \left(\frac{\partial \bar{y}}{\partial \bar{z}} \right) k e^{k \bar{z}_b} \bar{x}^2 \zeta^2 dx$
$M_{\zeta \phi 0}(t) = -\rho g \int_L \left(\frac{\partial \bar{y}}{\partial \bar{z}} \right) k e^{k \bar{z}_b} \bar{x}^3 \zeta dx$

The expressions presented in those tables are functions of the geometric parameters of the transverse sections of the hull, so that \bar{x} , \bar{y} are coordinates of waterline, S_b is the transversal submersed area, and \bar{z}_b is the vertical coordinate of its centroid. It is important to notice that the above coefficients have, for general hull forms, two contributions:

a) one is purely geometrical due to form variations (with longitudinal integrals of flare at mean water-line $\partial \bar{y} / \partial \bar{z}$ and other geometrical characteristics) and,

b) the other one is due to wave elevation and pressure attenuation (so-called Smith effect). The Smith effect terms have been derived following the reasoning of Paulling (1961).

In the case of a spar with vertical walls, the geometrical terms containing $\partial \bar{y} / \partial \bar{z}$ in Tables 1-3 are zero. Therefore, the only non-zero coefficients are those defined in Eqs. 4-6, which are summarized as follows:

$$Z_{\phi \phi z} = Z_{00z} = K_{zz\phi} = M_{zz0} = \rho g A_0 \quad (9)$$

$$K_{00\phi} = M_{\phi\phi 0} = \rho g I_0 \quad (10)$$

$$Z_{\zeta z}(t) = 2Z_{\zeta\phi\phi}(t) = -2\rho g \int_L \left(\bar{y} k e^{k \bar{z}_b} \right) \zeta dx \quad (11)$$

$$Z_{\zeta 0}(t) = M_{\zeta z}(t) = 2\rho g \int_L \left(\bar{y} k e^{k \bar{z}_b} \right) \bar{x} \zeta dx \quad (12)$$

$$K_{\zeta\phi}(t) = -2\rho g \int_L \left(\frac{1}{3} \bar{y}^3 + S_b \bar{z}_b \right) k e^{k \bar{z}_b} \zeta dx \quad (13)$$

$$K_{\zeta z\phi}(t) = -2\rho g \int_L \bar{y} \zeta dx \quad (14)$$

$$K_{\zeta\phi 0}(t) = 2M_{\zeta\phi\phi}(t) = \rho g \int_L 2\bar{x}\bar{y} \zeta dx \quad (15)$$

$$K_{\zeta\zeta\phi}(t) = \rho g \int_L \bar{y} \zeta^2 dx \quad (16)$$

$$M_{\zeta_0}(t) = -2\rho g \int_L (\bar{y} k e^{kz_b}) \bar{x}^2 \zeta dx \quad (17)$$

where I_0 is the second area moment of the waterplane. The coefficients defined in eqs. (9-17) may be separated into three main groups:

a) $Z_{\phi\phi z}, Z_{\theta\theta z}, K_{zz\phi}, K_{\theta\theta\phi}, M_{zz\theta}$ and $M_{\phi\phi\theta}$ are third order hydrostatic coefficients;

b) $K_{\zeta z\phi}, K_{\zeta\phi\theta}, K_{\zeta\zeta\phi}$ and $M_{\zeta\phi\phi}$ are third order moment coefficients associated only to wave elevation ζ ; and,

c) $Z_{\zeta z}, Z_{\zeta\theta}, K_{zz\zeta}, K_{\zeta\phi}, M_{\zeta z}$ and $M_{\zeta\theta}$ are second order coefficients determined by pressure variations due to pressure attenuation (Smith effect).

As discussed in Neves et al. (2008), parametric excitation in conditions close to the exact Mathieu tuning ($T_{n4} = 2T_w$) is governed by second order terms in equations (4-6). Therefore it may be concluded that parametric excitations in spar platforms are strictly governed by the influence of the Smith effect. A complementary tentative conclusion derived from equation (13), to be verified by means of future specific experiments, is that the amplitude of roll parametric excitation shall be larger for spar platforms with larger drafts.

4. NUMERICAL SIMULATIONS

A vertical cylindrical shape is used in the simulations as a simplified spar platform. The main characteristics are described in Table 4. An illustration of the cylinder is given in Figure 1. The cylinder was taken with the same main dimensions and inertial characteristics of the spar investigated in Hong et al. (2005), but without consideration of the moonpool.

The set of differential equations (1-3) with restoring actions as defined in equations (4-17) can be efficiently solved for different combinations of wave periods and wave amplitudes.

Steady-state roll amplitudes are captured and plotted in the form of a numerical mapping in which a colour-scale is introduced to reflect the intensity of roll responses, see Rodríguez & Neves (2011). Figure 2 shows the obtained numerical mapping. Similar plots may in principle be obtained reflecting the heave and pitch tendency to display unstable responses.

Table 4: Spar main characteristics

Parameter	Value
Diameter, D [m]	37.20
Depth, H [m]	213.20
Draught, T [m]	198.10
Displacement, Δ [t]	220691
Metacentric height, \overline{GM}_o [m]	10.08
Roll gyration radius, r_{xx}^* [m]	59.20
Pitch gyration radius, r_{yy}^* [m]	59.20
Heave natural period, T_{n3} [s]	29.91
Roll / pitch natural period, T_{n4}, T_{n5} [s]	49.00

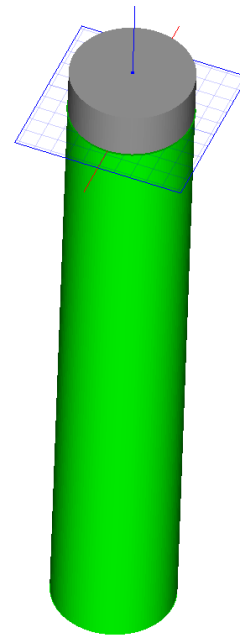


Figure 1: Spar hull sketch.

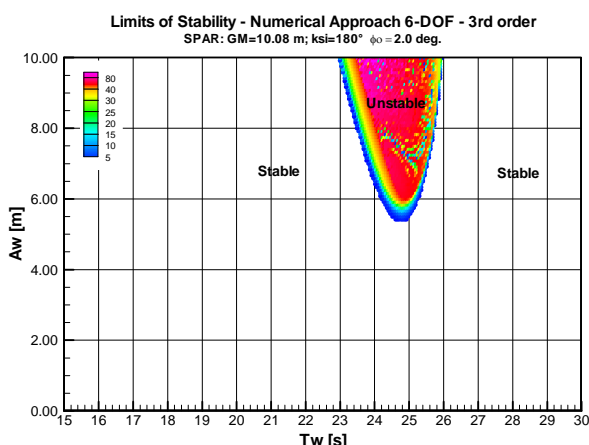


Figure 2: Domain of roll parametric amplification in the region close to $T_{n4} = 2T_w$.

The domain in Figure 2 does not display upper frontiers as is usual with many ship hulls but it has a back-bone clearly inclined to the left. This is compatible with effects associated with nonlinear detuning dependent on wave amplitude, as discussed in Rodríguez & Neves (2011) in the case of a fishing vessel and a container vessel. The present results point-out to a spar with more peculiar results than the previously investigated spar reported in Rodríguez & Neves (2012).

With the aim of getting a deeper insight of the coupling taking place, in the following few figures a closer look will be devoted to the heave, roll and pitch time-series at two selected points of the domain of parametric excitation.

Figure 3 shows the heave, roll and pitch responses for wave period $T_w=24s$, wave amplitude $A_w=7.5$ m. The period in this case is slightly below half the roll natural period and slightly below the heave natural period. All modes have reached steady state responses after a slow growing process. The roll motion response period is clearly double the heave and pitch response periods. Roll amplitudes reach 40 degrees, whereas pitch motions remain limited in the range of 2.2 degrees. The graphs display results for both with Smith effect consideration and without Smith effect. In case Smith effect is not considered, roll mode is not excited at all. Pitch motion is not affected by the consideration of Smith effect. The heave

mode is significantly affected when this effect is considered, mainly due to the coupling with roll motion which exists in this case.

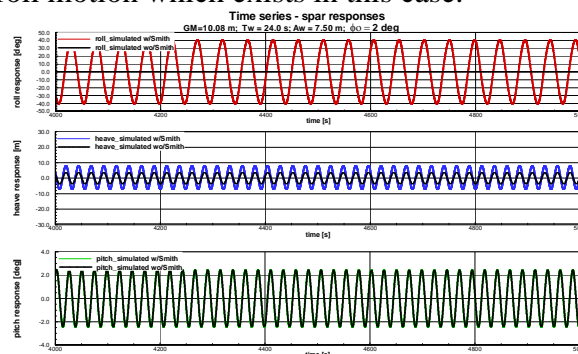


Figure 3: Heave, roll and pitch responses, $T_w=24s$, $A_w=7.5$ m.

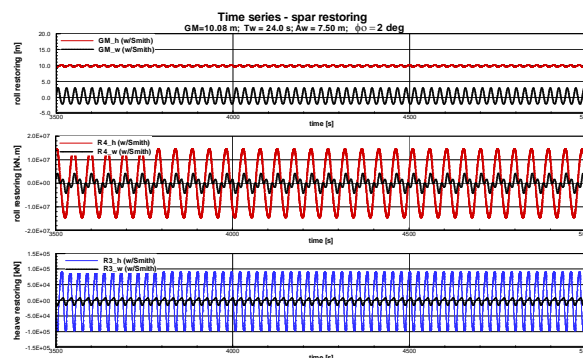


Figure 4: a) Instantaneous GM contributions: due to ship motions and due to wave pressure; b) Roll restoring moment; c) Heave restoring force, $T_w=24s$, $A_w=7.5$ m.

Figure 4 shows time series for a) instantaneous metacentric height (GM) contributions: purely hydrostatic & wave induced, b) restoring moment and c) restoring force in heave, all of them computed for the same conditions of Figure 2. Values obtained when only hydrostatic terms are considered and values when only Froude-Krilov terms are shown separately, in both cases taking into consideration Smith effect. In the upper graph, it is possible to notice that the instantaneous hydrostatic metacentric height has only very small oscillations around the large initial metacentric height, $GM_0 = 10.08$ m. On the other hand, instantaneous metacentric height due to wave field pressures has larger amplitudes. Both functions respond mainly at wave period. It is evident that these oscillatory changes of the

metacentric height due to wave field pressures will act as an internal parametric excitation. The middle graph gives the roll restoring moment, that is, the instantaneous GM multiplied by $\rho g \nabla_0$ times the instantaneous roll angle. The interesting results are that the hydrostatic contribution to the roll restoring moment takes place at a period slightly lower than the roll natural period; and the wave contribution has two periods. Lower graph shows heave restoring force which is realized at wave period.

In order to clarify the dynamical characteristics of the different responses, frequency decomposition of three roll-related signals are given in Figure 5. In the two upper graphs it is observed that both roll motion and hydrostatic restoring moment spectra are centered close to roll natural period (in fact, double the wave period).

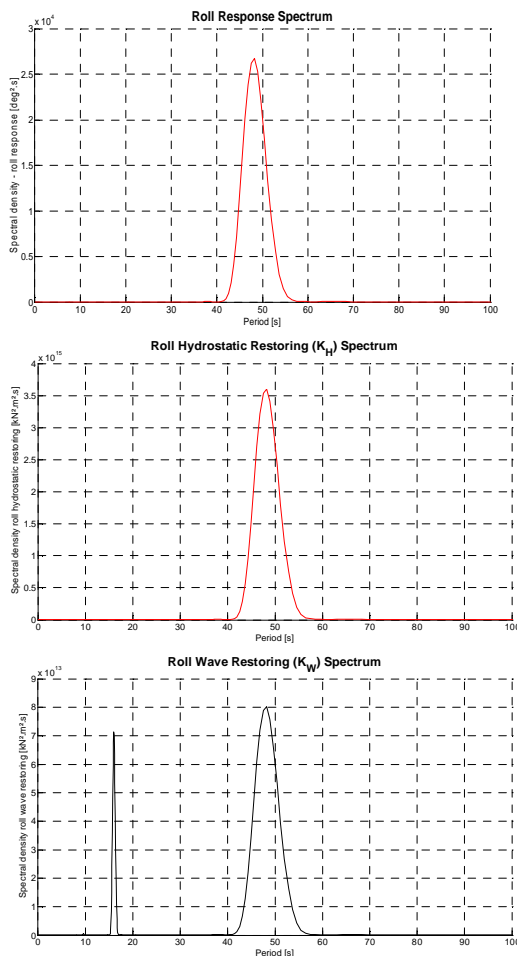


Figure 5: Roll spectra for $T_w=24s$, $A_w=7.5$ m: a) roll response (from Fig. 3); b) hydrostatic restoring moment; c) wave restoring moment.

On the other hand frequency decomposition of roll wave restoring moment shows two contributions, a main one close to double the exciting period and a second one at about $T \approx 16$ s, a super-harmonic contribution at a third of the roll response period.

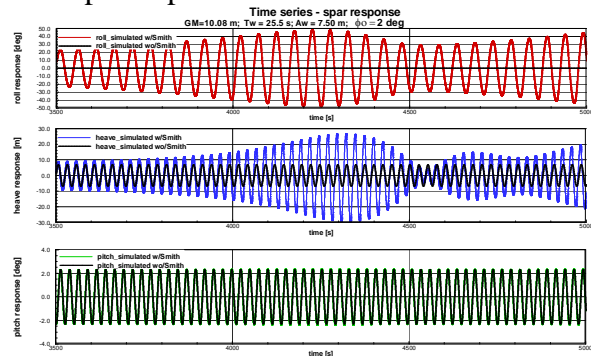


Figure 6: Heave, roll and pitch motions, $T_w=25.5s$, $A_w=7.5$ m.

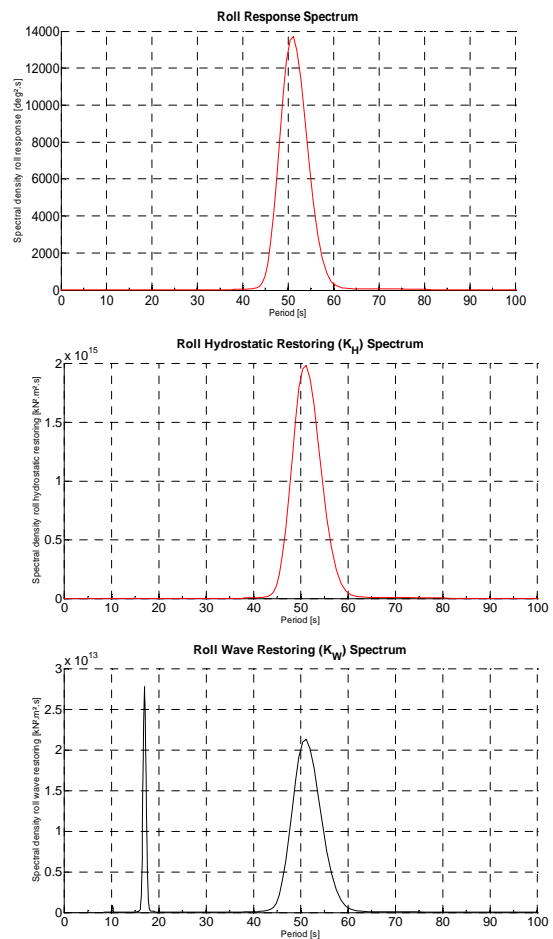


Figure 7: Roll spectra for $T_w=25.5s$, $A_w=7.5$ m: a) response; b) hydrostatic restoring moment; c) wave restoring moment.



Now, let the exciting period be slightly above half the roll natural period, $T_w=25.5$ s, and the wave amplitude be the same as before. The results are given in Figure 6. Now, a much more intense exchange of energy between the heave and roll modes takes place, whereas the pitch motion remains practically unaffected.

The coupling between heave and roll is of such nature that as roll amplification starts to develop (at roll natural period) heave motion increases (at wave period) correspondingly. Subsequently, as the heave motion reaches much larger values it induces a period detuning to the roll motion, which then progressively loses energy, leading, through coupling, to energy losses in heave.

Figure 7 shows the corresponding roll spectra for the conditions of Figure 6, $T_w=25.5$ s, $A_w=7.5$ m. Roll spectrum and roll hydrostatic restoring moment spectrum are centered around a period which is double the wave period. Roll wave restoring moment spectrum has two contributions, a main one close to double the exciting period and a second one at about $T \approx 17$ s, a super-harmonic contribution at a third of the roll response period.

5. CONCLUSIONS

Unstable motions of a deep drafted spar platform have been investigated employing an analytical mathematical model previously developed for typical hull forms. It has been shown that in the case of deep drafted bodies additional terms associated with Smith effect are required in order to model the appearance of parametric roll.

Numerical limits of stability have been obtained; they display a back-bone clearly inclined to the range of lower periods. A dynamical analysis has been performed showing unexpected (at least for this type of vertically walled floater) levels of coupling between heave and pitch motions. Strong and complex interactions

are obtained for periods close to the exact Mathieu tuning, $T_{n4} = 2T_w$.

It has also been shown that at this Mathieu tuning, hydrostatic pressure field does not induce any parametric amplification. Wave pressure field with its characteristic attenuation is the key element in the internal excitation of spar platforms.

It is concluded from the numerical/analytical analysis that a full assessment of spar responses in waves should involve heave, roll and pitch modes in a coupled frame. Finally, it has been found that externally and internally excited pitch motions do not undergo significant unstable responses. The situation is not the same in the case of internally excited roll motion, which may reach undesirable amplifications.

Future research shall contemplate:

- a) a dedicated experimental programme for validating the present research work;
- b) determination of a more precise damping model from roll decrement tests;
- c) check the analytically derived coefficients against their counterparts obtained from a more time consuming panel method algorithm;
- d) extension of the mathematical model to irregular seas, to be accomplished by means of frequency decomposition of wave-terms.

6. ACKNOWLEDGMENTS

The present investigation is supported by CNPq within the STAB project (Nonlinear Stability of Ships). The Authors also acknowledge financial support from CAPES, FAPERJ and LabOceano.



7. REFERENCES

- Bin-Bin Li, Jin-Ping Ou and Bin Teng, 2011. "Numerical Investigation of Damping Effects on Coupled Heave and Pitch Motion of an Innovative Deep Draft Multi-SPAR." Journal of Marine Science and Technology, Vol. 19, No 2, pp-231-244.
- Haslum, H.A., and Faltinsen, O.M., 1999. "Alternative Shape of Spar Platform for Use in Hostile Areas", Proceedings of Offshore Technology Conference, Paper No. OTC10953, Houston.
- Hong Y., Lee, D., Choi, Y., Hong, S. and Kim, S., 2005. "An Experimental Study on the Extreme Motion Responses of a SPAR Platform in the Heave Resonant Waves." In: Proceedings of the 15th International Offshore and Polar Engineering Conference (ISOPE'2005), Seoul, Korea.
- Kleiman, A. and Gotlieb, O., 2008. "Nonlinear Dynamics and Internal Resonances of a Ship with a Rectangular Cross-Section in Head Seas." In: Proceedings of the 27th ASME International Conference on Offshore Mechanics and Arctic Engineering, OMAE 2008, Paper OMAE2008-57691, Lisbon, June, 15-20.
- Koo, B.J., Kim, M.H. and Randall R.E., 2004. "Mathieu Instability of a Spar Platform with Mooring and Risers". Ocean Engineering, (31), pp. 2175-2208.
- Liao, S.-W. and Yeung, R. W., 2001. "Investigation of the Mathieu Instability of Roll Motion by a Time-Domain Viscous-Fluid Method". The 16th International Workshop on Water Waves and Floating Bodies. Hiroshima, Japan, April.
- Liaw, C. Y., Bishop, S. R. and Thompson, J. M. T., 1993, "Heave-Excited Rolling Motion of a Rectangular Vessel in Head Seas". International Journal of Offshore and Polar Engineering, vol. 3, no. 1 (Mar), pp. 26-31.
- Liaw, C. Y., 1994. "Dynamic Instability of a Parametrically Excited Ship Rolling Model", International Journal of Offshore and Polar Engineering, vol. 4, no. 2 (Jun), pp. 106-111.
- Neves, M.A.S. and Rodríguez, C.A., 2006. "On Unstable Ship Motions Resulting from Strong Non-Linear Coupling", Ocean Engineering, Vol. 33, no. 14 (Oct.), pp. 1853-1883.
- Neves, M.A.S., Sphaier S.H., Mattoso, B.M., Rodríguez, C., Santos, A., Vileti, V. and Torres, F.G.S., 2008. "Parametric Resonance of Mono-column Structures". In: Proceedings of the 6th Osaka Colloquium on Seakeeping and Stability of Ships, 26-28th March, Osaka, Japan.
- Paulling, J.R., 1961. "The Transverse Stability of a Ship in a Longitudinal Seaway". Journal of Ship Research, vol. 4, no. 4 (Mar.), pp. 37-49.
- Rodríguez, C.A., 2010. "On the Nonlinear Dynamics of Parametric Rolling". D.Sc. Thesis, COPPE - Universidade Federal do Rio de Janeiro, Brazil. (in Portuguese).
- Rodríguez, C.A. and Neves, M.A.S., 2012. "Nonlinear Instabilities of SPAR Platforms in Waves". Paper OMAE2012-83577, Rio de Janeiro, July.
- Yumin Liu, Hongmei Yan and Tin-Woo Yung, 2010. "Nonlinear Resonant Response of Deep Draft Platforms in Surface Waves", Paper OMAE2010-20823, Shanghai, China.





A Study on Unstable Motions of a Tension Leg Platform in Close Proximity to a Large FPSO

Luis Alberto Rivera, *COPPE/UFRJ*, luisrivera@peno.coppe.ufrj.br

Marcelo A. S. Neves, *LabOceano COPPE/UFRJ*, masn@peno.coppe.ufrj.br

Roberto E. Cruz, *PETROBRAS*, redwacruz@petrobras.com.br

Paulo de Tarso T. Esperança, *LabOceano, COPPE/UFRJ*, ptarso@laboceano.coppe.ufrj.br

ABSTRACT

The present paper elaborates on model experimental results obtained from tests conducted with a TLP connected to a nearby positioned FPSO. The tests revealed, at a given range of wave periods, the onset of unexpected large oscillatory yaw motions of the platform whereas the FPSO remained rather stable when the TLP was directly excited in sway. The paper summarizes the model experiments emphasizing the types of coupled motions taking place. It is observed that as the yaw motion develops increasing amplitudes the sway motion is reduced, pointing out to an interesting exchange of energy between the sway and yaw modes. A mathematical model is proposed to describe the main aspects of the two-body moored system. In principle a 12 DOF model is contemplated. Numerical simulations are compared to the time series obtained from the experiments showing adequate agreement.

Keywords: *Parametric resonance; Non-linear coupling; Tension Leg Wellhead Platform*

1. INTRODUCTION

A significant part of technical literature on TLP designs deals with structural dynamics and fatigue reliability of the tendons, see for example Ximenes (1991), as rigid body motions of such platforms are in general said to be “satisfactory”. The conceptual design of conventional Tension Leg Platforms (TLPs) was developed with the aim of reducing vertical motions to a minimum while at the same time keeping horizontal translational motions circumscribed to a quite limited area; practical experience has confirmed the intrinsically stable characteristics of this type of offshore platform, Brewer (1975), Denise and Heaf (1979). However, the inclusion of additional mooring lines to the unit or the proximity of another body may alter the dynamical behavior of the system; under

these circumstances large unstable motions may develop. Essentially, this is the focus of the present investigation.

Model experimental results obtained from recently conducted tests with a TLP (in fact a Tension Leg Wellhead Platform) connected to a nearby positioned FPSO surprisingly revealed, at a given range of wave exciting periods, the onset of quite large oscillatory yaw motions whereas the FPSO remained rather stable when the TLWP was directly excited in sway. In such wave incidence the TLWP’s yaw mode was not directly excited. The aim of the present paper is to contribute to a better understanding of these large yaw oscillations through numerical and analytical modeling. The line of investigation adopted here is that these large yaw motions are the result of internal excitations of the two-body



system induced by sway motions, thus characterizing the occurrence of parametric resonance.

The paper summarizes the model experiments emphasizing the types of coupled motions taking place. An interesting exchange of energy between the sway and yaw motion is observed: as yaw motion develops increasingly unstable motions at twice the period of the waves, the directly excited sway motion (taking place at wave period) is reduced. This should be recognized as a revealing aspect of strongly non-linear coupled parametric resonant motions. After the description of the experimental results of the two-body moored system (in principle a 12 DOF problem) the proposed mathematical model is introduced. Physical arguments are invoked for numerically solving the problem in 7 DOF. Using this reduced model numerical simulations have been compared to experimental results, see Cruz (2010), Cruz et al. (2012). In general these comparisons show good agreement, indicating that the main nonlinear couplings are well captured by the numerical model.

In the present paper, in order to provide a better understanding of the complex dynamic structure responsible for the observed TLWP's yaw amplifications, an analytical mathematical modeling of the surge, sway and yaw coupling is introduced. The final aim here is to develop an analytical tool that would allow for a rationally exercised dissection of the system, thus having an anatomical description of the system for a critical analysis. For this purpose the restoring actions introduced by the mooring lines, tendons and connecting lines will be decomposed by means of multivariable Taylor series. It is expected that this methodology will help to clarify what are the lines inducing internal excitation to the system, therefore contributing to improved design of the two-body system free from unacceptable unstable motions.

2. THE FPSO AND TLWP

Figure 1 shows the upper view of the layout set up during the tests: on the left the Tension Leg Wellhead Platform (TLWP), the large FPSO on the right. The FPSO model is moored by four oblique horizontal mooring lines displayed at the bow and stern of the hull. The FPSO is connected to the TLWP by two lines. The TLWP has two oblique horizontal mooring lines displayed in the opposite side of its connections to the FPSO. The main mooring system of the TLWP is provided by four vertical tendons. In all cases considered in the present report the two-body system was directly excited by regular waves coming from the left to the right.

Figure 2 illustrates the general aspects of the two hulls. The model scale adopted in the experiments was 1:100. The main dimensions of the FPSO and TLWP are described in Tables A1 and A2, respectively, presented in the Appendix.

The regular waves test program was as defined in Table 1. The test identification refers to wave period T (sec) and wave height H (m). The two-body system is described in principle by 12 degrees of freedom (nomenclature defined in Table 2).

3. THE MOORING SYSTEM

Figure 3 illustrates the FPSO (M1 to M4) horizontal moorings, 4 TLWP tendons (T1 to T4), 2 TLWP mooring lines (M5 and M6) and two lines connecting the two units (M7 and M8).

TLWP tendons length and diameter (real scale) are 975m and 1.1m, respectively. More details on the mooring arrangements may be found in Cruz (2010), Cruz et al. (2012). Considering linear rigidities and main added mass terms the estimated natural periods are given in Table 3.

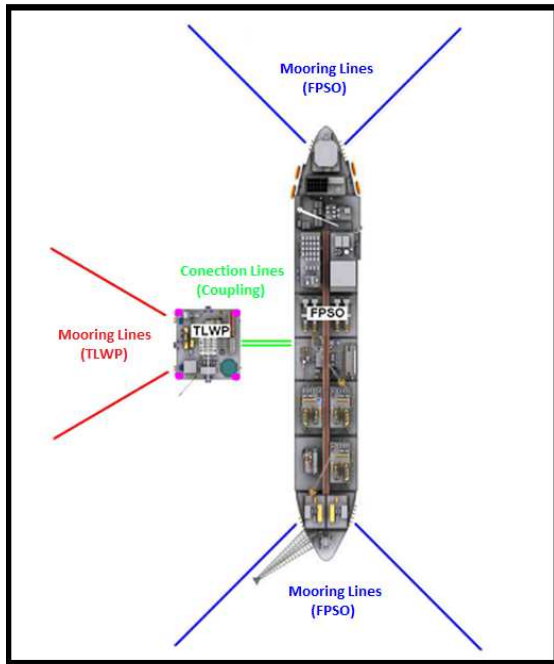


Figure 1: Two-body arrangement showing the mooring set-up during experiments.

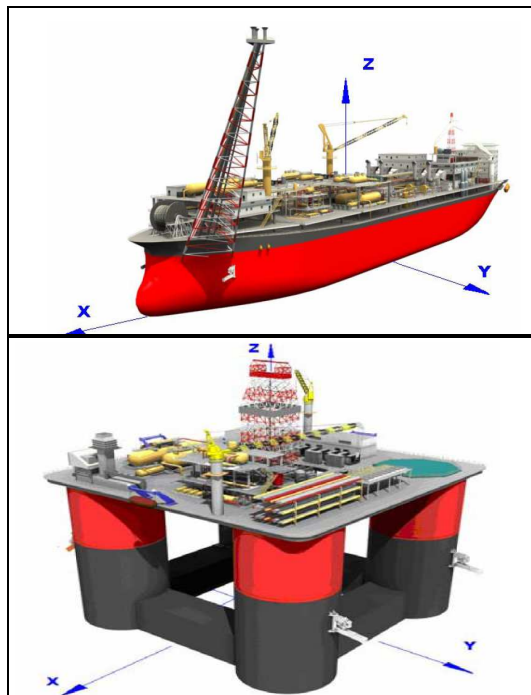


Figure 2: Illustration of a) FPSO b) TLWP.

Table 1: Tested conditions.

T [s]	H [m]	T [s]	H [m]
7.00	1.50	14.00	2.80
9.00	2.00	15.00	3.00
10.00	2.00	17.00	3.40
11.00	2.20	20.00	4.00
12.00	2.40	25.00	5.00
13.00	2.60		

Table 2: Definition of motions.

x_1	Surge FPSO	x	Surge TLWP
y_1	Sway FPSO	y	Sway TLWP
z_1	Heave FPSO	z	Heave TLWP
ϕ_1	Roll FPSO	ϕ	Roll TLWP
θ_1	Pitch FPSO	θ	Pitch TLWP
ψ_1	Yaw FPSO	ψ	Yaw TLWP

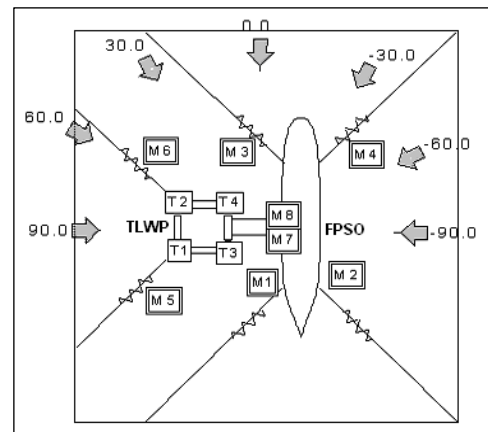


Figure 3: Mooring set up at the tests.

Table 3: Natural periods [sec].

Tnx_1	127.0	Tnx	64.5
Tny_1	23.4	Tny	7.1
Tnz_1	11.7	$Tn\psi$	33.6
$Tn\phi_1$	10.2		

4. ANALYSIS OF TEST RESULTS

Figure 4 summarizes the steady state motion amplitudes (divided by wave amplitude) observed in the whole range of tested periods for the FPSO in surge, sway, heave and roll modes. This indicates that the FPSO has limited responses in the whole



range of periods. The heave and roll amplitudes at resonance are of the order 0.5m/m and 6 degrees/m, respectively. The horizontal motions of the TLWP are given in Figure 5. The surprising characteristic occurred in the tests is observed: the appearance of large yaw motions for the TLWP in the range of periods 12~15sec. These are typically resonant motions, which take place despite the fact that the yaw motion was not directly excited in the series of experiments under discussion. The surge mode is also larger at this range of periods. It is important to notice that the surge mode, as the yaw mode, is not externally excited.

Taking into account these observations it may be relevant to investigate the sway characteristics of the TLWP, which is an externally excited mode. In particular, the peculiar two-peaked pattern of responses in the range of periods from 10 to 17 seconds, well above the natural period ($T_{ny}=7.1sec$). Additionally, it is observed that at the sway natural period there is no large response. Indeed, for $T=11sec$ and $T=15sec$ the sway amplitude is large, whereas in between these periods the responses are much smaller, corresponding exactly to the range of large yaw motions. This indicates some level of strong nonlinear coupling between the sway and yaw modes in which an increase in yaw motions induces a corresponding reduction of the sway motions, possibly an exchange of energy between the two modes. This suggests that nonlinear parametric resonance may be governing the dynamics of the platform.

A better perception of the type of prevailing resonant motion is gained when the experimental time series of sway and yaw motions -obtained from a resonant condition- are plotted together, as shown in Figure 6. In this case the wave period is $T=14sec$. The incident wave is originated at about $t=300sec$.

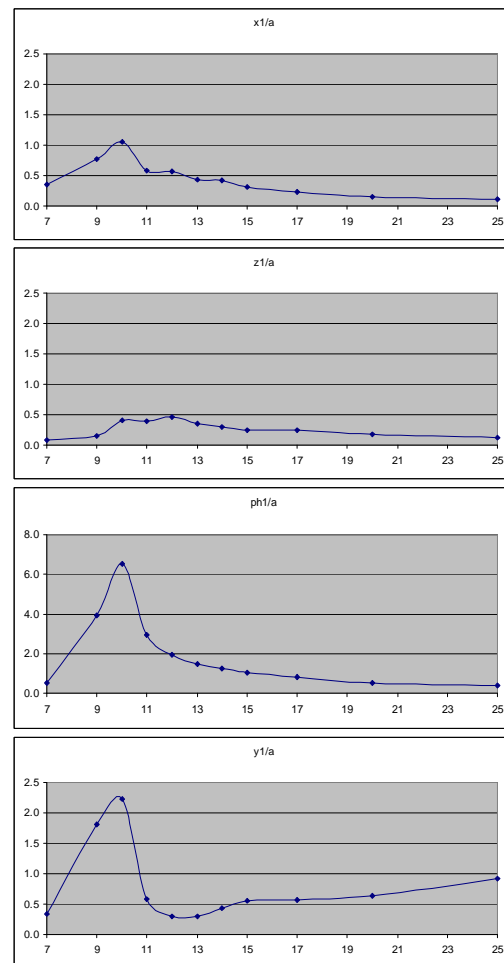


Figure 4: FPSO test responses for different periods: a) surge; b) sway; c) heave; d) roll.

The figure shows that asymmetric sway motion starting at about 450sec develops at this wave period. After some cycles symmetric yaw motions develop increasing amplitudes, reaching some stable steady state motion at around 800sec. It is observed that the yaw motion is responding at a period corresponding to nearly double the wave period, suggesting that parametric resonance in yaw is being developed fed by the directly excited sway motion. Another interesting aspect may be recognized: as the large yaw motions develop, there is a complementary reduction in the sway motion, suggesting an interesting strong nonlinear coupling between the two modes. This is in general the observed picture in the range of wave periods corresponding to yaw amplifications. In order

to contribute to a better understanding of these complicate couplings and instabilities a mathematical model has been developed. It is expected that through analytical and numerical modeling an engineering diagnosis of the observed instabilization process may be reached and consequently modifications in the project may be proposed through rational analysis.

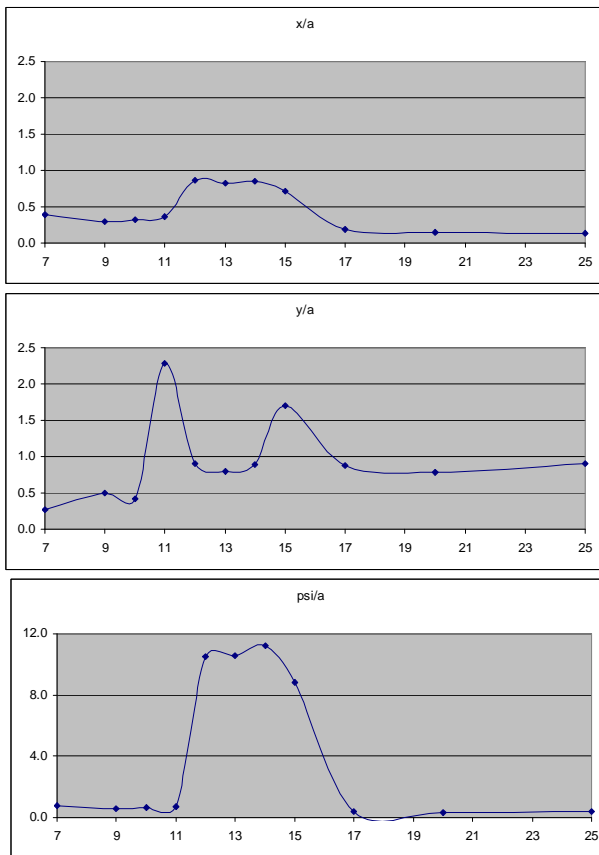


Figure 5: TLWP test responses for different periods: a) surge; b) sway; c) yaw.

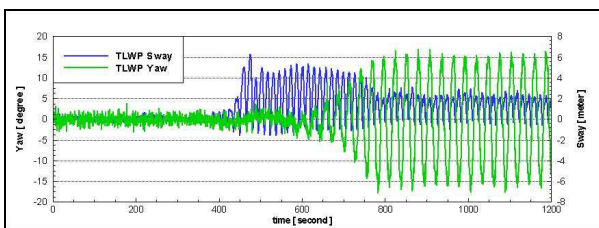


Figure 6: TLWP sway and yaw time series from experiments, wave period $T=14sec$, wave height $H=2.8m$.

5. MATHEMATICAL MODEL

The two-body system is defined by a 12-DOF nonlinear model expressed as:

$$(\mathbf{M}+\mathbf{A})\ddot{\mathbf{s}}+\mathbf{B}_L\dot{\mathbf{s}}+\mathbf{B}_{NL}(\dot{\mathbf{s}})+\mathbf{c}_r(\mathbf{s},\zeta)=\mathbf{c}_{ext}(\zeta,\dot{\zeta},\ddot{\zeta}) \quad (1)$$

where the displacement vector is:

$$\mathbf{s}(t)=[x_1 \ y_1 \ z_1 \ \phi_1 \ \theta_1 \ \psi_1 \ x \ y \ z \ \phi \ \theta \ \psi]^T$$

In Eq. (1) \mathbf{M} is a 12 x 12 matrix which describes hull inertia characteristics. \mathbf{A} is also a 12 x 12 matrix, whose elements represent hydrodynamic generalized added masses. \mathbf{B}_L and $\mathbf{B}_{NL}(\dot{\mathbf{s}})$ describe the hydrodynamic reactions dependent on the FPSO and platform velocities (damping). The latter incorporates non-linear terms due to the great influence of viscosity on tendons, pontoons and columns of the TLWP and roll motion of the FPSO. $\mathbf{c}_r(\mathbf{s},\zeta)$ is a 12 x 1 vector which describes non-linear restoring forces and moments dependent on the relative motions between the platform and the mooring lines. It also considers the influence of the wave passage on the tendons tension. On the right hand side of Eq. (1), the generalized vector $\mathbf{c}_{ext}(\zeta,\dot{\zeta},\ddot{\zeta})$ represents linear wave external excitation, composed of the Froude-Krilov and diffraction wave forcing terms, dependent on wave heading, excitation frequency ω_w , wave amplitude A_w and time t .

Taking into account the prevailing physics and the particular transversal wave excitation considered, without loss of generality the 12-DOF problem will be restricted to the following 7-DOF coupled problem: x_1 (surge), y_1 (sway), z_1 (heave) and ϕ_1 (roll) for the FPSO and x (surge), y (sway) and ψ (yaw) for the TLWP.



6. HYDRODYNAMIC COEFFICIENTS AND NON LINEAR DAMPING

Matrices **A** and **B** are computed by means of WAMIT computer code. The same applies to $\mathbf{c}_{\text{ext}}(\zeta, \dot{\zeta}, \ddot{\zeta})$. In addition to potential damping, additional damping has been considered for the following motions: a) horizontal motions of TLWP; b) horizontal motions of FPSO; roll motion of FPSO. Drag quadratic terms in Morison formula have been used as an approximation for calculation of non-linear damping of the TLWP, being applied to columns, tendons and pontoons. These actions are computed by taking into account the instantaneous velocities of the body, and disregarding the influence of fluid velocities. For some specific wave periods the TLWP responded with large angular displacements in yaw. For this reason a quadratic damping model was considered for this platform motion mode.

6.1 TLWP Columns

Assuming an angular displacement ψ with corresponding yaw velocity $\dot{\psi}$ and linear velocities \dot{x} and \dot{y} , the drag forces and moment for each column are expressed as:

$$X(\dot{x}, \dot{y}, \dot{\psi}) = -\frac{1}{2} \rho S_c C_{dc} [\dot{x} - \dot{\psi} R \sin(\psi + \beta)].$$

$$\left\{ \dot{x}^2 + \dot{y}^2 + \dot{\psi}^2 R^2 - 2 \dot{\psi} R [\dot{y} \cos(\psi + \beta) - \dot{x} \sin(\psi + \beta)] \right\}^{1/2} \quad (2)$$

$$Y(\dot{x}, \dot{y}, \dot{\psi}) = -\frac{1}{2} \rho S_c C_{dc} [\dot{y} + \dot{\psi} R \cos(\psi + \beta)].$$

$$\left\{ \dot{x}^2 + \dot{y}^2 + \dot{\psi}^2 R^2 - 2 \dot{\psi} R [\dot{y} \cos(\psi + \beta) - \dot{x} \sin(\psi + \beta)] \right\}^{1/2} \quad (3)$$

$$N(\dot{x}, \dot{y}, \dot{\psi}) =$$

$$-\frac{1}{2} \rho S_c C_{dc} [\dot{\psi} R^2 + \dot{y} R \cos(\psi + \beta) - \dot{x} R \sin(\psi + \beta)].$$

$$\left\{ \dot{x}^2 + \dot{y}^2 + \dot{\psi}^2 R^2 - 2 \dot{\psi} R [\dot{y} \cos(\psi + \beta) - \dot{x} \sin(\psi + \beta)] \right\}^{1/2} \quad (4)$$

where $\beta = n\pi/4; n=1,3,5,7$. Finally, these are summed up to obtain the total drag forces and moment. In the above expressions ρ is density, S_c and C_{dc} are the representative

area and drag coefficient of column, respectively, R is the distance from the centre of each column to the unit origin and β is the local angle of the element in relation to TLWP reference.

6.2 TLWP Tendons

The procedure for calculating the drag force and moment in a tendon is similar to the preceding one. But in this case we need to integrate the force along the tendon length because the local velocity changes from zero at the ground up to a maximum at the TLWP. As a result of integration the total force on each tendon is one third of the force on the column:

$$X(\dot{x}, \dot{y}, \dot{\psi}) = -\frac{1}{6} \rho S_t C_{dt} [\dot{x} - \dot{\psi} R \sin(\psi + \beta)].$$

$$\left\{ \dot{x}^2 + \dot{y}^2 + \dot{\psi}^2 R^2 - 2 \dot{\psi} R [\dot{y} \cos(\psi + \beta) - \dot{x} \sin(\psi + \beta)] \right\}^{1/2} \quad (5)$$

$$Y(\dot{x}, \dot{y}, \dot{\psi}) = -\frac{1}{6} \rho S_t C_{dt} [\dot{y} + \dot{\psi} R \cos(\psi + \beta)].$$

$$\left\{ \dot{x}^2 + \dot{y}^2 + \dot{\psi}^2 R^2 - 2 \dot{\psi} R [\dot{y} \cos(\psi + \beta) - \dot{x} \sin(\psi + \beta)] \right\}^{1/2} \quad (6)$$

$$N(\dot{x}, \dot{y}, \dot{\psi}) =$$

$$-\frac{1}{6} \rho S_t C_{dt} [\dot{\psi} R^2 + \dot{y} R \cos(\psi + \beta) - \dot{x} R \sin(\psi + \beta)].$$

$$\left\{ \dot{x}^2 + \dot{y}^2 + \dot{\psi}^2 R^2 - 2 \dot{\psi} R [\dot{y} \cos(\psi + \beta) - \dot{x} \sin(\psi + \beta)] \right\}^{1/2} \quad (7)$$

finally, they are summed up to obtain the total drag forces and moment on tendons.

6.3 TLWP pontoons

In order to simplify the calculation the coupled term between angular and linear velocities is not considered. A transformation matrix is used to transport translational velocities and drag forces from the local system to the global system:

$$N(\dot{\psi}) = \frac{-1/2 \rho \cdot S_p \cdot L^3 C_{dp}}{32} \dot{\psi} |\dot{\psi}| \quad (8)$$

$$X(\dot{x})_{local} = -\rho h L C_d \dot{x}_{local} |\dot{x}_{local}| \quad (9)$$

$$Y(\dot{y})_{local} = -\rho h L C_d \dot{y}_{local} |\dot{y}_{local}| \quad (10)$$

$$\begin{bmatrix} \dot{x}_{local} \\ \dot{y}_{local} \end{bmatrix} = \begin{bmatrix} \cos(\psi) & \sin(\psi) \\ -\sin(\psi) & \cos(\psi) \end{bmatrix} \cdot \begin{bmatrix} \dot{x} \\ \dot{y} \end{bmatrix} \quad (11)$$

$$\begin{bmatrix} X(\dot{x}) \\ Y(\dot{y}) \end{bmatrix} = \begin{bmatrix} \cos(\psi) & -\sin(\psi) \\ \sin(\psi) & \cos(\psi) \end{bmatrix} \cdot \begin{bmatrix} X(\dot{x})_{local} \\ Y(\dot{y})_{local} \end{bmatrix} \quad (12)$$

6.4 FPSO Horizontal Motions

For the quadratic damping of the FPSO the drag coefficients (Cd) were experimentally obtained by means of captive tests of the hull under current action. The drag is therefore given as:

$$X_1(\dot{x}_1) = -0.5 \rho S C_d \dot{x}_1 |\dot{x}_1| \quad (13)$$

$$Y_1(\dot{y}_1) = -0.5 \rho S C_d \dot{y}_1 |\dot{y}_1| \quad (14)$$

6.5 FPSO Roll Motion

In the case of the FPSO roll motion, instead of adopting a quadratic damping, it was considered an additional linear damping of 1,5% of the critical damping to represent viscous effects. This damping level was obtained by adjusting the theoretical roll response curve to the experimental response curve of the FPSO under beam regular wave excitation.

7. RESTORING ACTIONS AND NUMERICAL ANALYSIS

These are composed of hydrostatic and individual mooring forces and moments (horizontal for the FPSO and TLWP, vertical for the tendons of TLWP). As TLWP vertical motions were neglected, the unit will not present hydrostatic restoring forces or moment. The platform will only present horizontal restoring forces and moment due to mooring lines, connecting lines and tendons. Hydrostatic restoring forces and moments are considered to be linear. Individual horizontal and vertical mooring actions are considered to be non-linear restoring actions. In the numerical analysis restoring forces and moments due to FPSO and TLWP mooring lines, TLWP tendons and connecting lines between the two bodies have been modeled taking into account their elastic characteristics and modes of displacement. The numerical model has been described in detail in Cruz et al. (2012). In this section of the present paper some results from the numerical model are compared to experimental results.

The interest here is to verify whether the numerical model is capable of capturing the complex coupling between the TLWP sway and yaw modes observed at the range of wave periods in which yaw amplification takes place, as shown in Figure 6. For this purpose Figure 7 shows comparisons of experimental and numerical time series of these motions for $T=14sec$, $H=2.8m$. It is observed that the essential aspects of the coupling are captured by the numerical model: a) sway motions responses are observed at wave period, yaw motions at double the wave period; therefore, the essential nonlinear sway-yaw exchange of energy is captured; b) as the yaw amplitudes start to amplify the sway amplitudes move from an attractor of large amplitudes to another one of markedly lower sway amplitudes; c) final sway and yaw amplitudes are in good agreement with the experimental results; d) there are some differences between



the transient phase of numerical and experimental amplification and decaying processes; these are clearly due to lack of information about the initial conditions prevailing in the experiments. These transient phase discrepancies may be mitigated when different initial conditions are considered in the numerical simulations, as discussed in Rodriguez and Neves (2012).

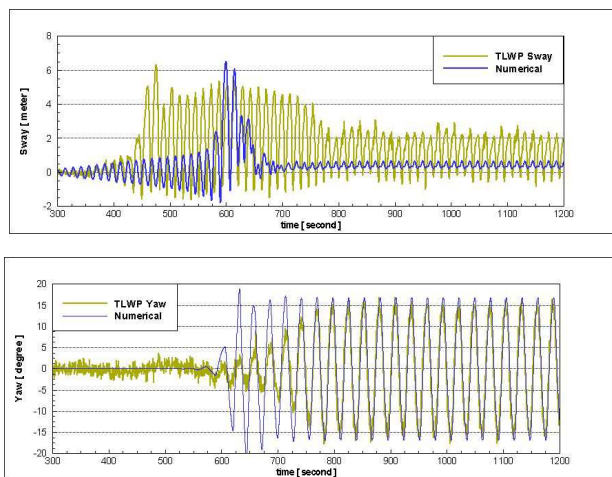


Figure 7: Comparison of numerical and experimental sway and yaw coupled motions, period $T=14sec$, wave height $H=2.8m$.

Figure 8 shows comparisons of the spectra obtained from the experimental and numerical yaw time series for a range of periods. The figure demonstrates that in general good agreement is obtained for these periods and indicates that in all cases the yaw responses take place at the period which corresponds to double the exciting period.

Figure 9 shows a comparison of TLWP's surge motion time series for $T=12sec$, $H=2.4m$. It is observed that there is acceptable agreement both in terms of steady state response amplitude and period. Figure 10 shows the comparisons of the surge spectra obtained from the experimental and numerical surge time series for the range of periods between 12 and 15 seconds.

These motions are slightly over-estimated, with responses taking place at double the exciting period, following the same pattern of the TLWP yaw motions.

TLWP sway motions mainly respond at wave period, whereas the surge and yaw respond at twice the excitation period. TLWP yaw motions are considerably large; numerical results compare very well with those from experiments. It is verified that surge responses takes place at the same period as yaw. It has been pointed out that in the TLWP case neither surge nor yaw are directly excited by the incoming waves. As indicated in Table 3 the yaw natural period is $T_{n\psi} = 33.6sec$ whereas the surge natural period is much larger, $T_{nx} = 64.5sec$. Therefore, for the exciting range of wave periods in which yaw amplifications are observed the first Mathieu tuning is attained, indicating that yaw motion is undergoing parametric resonance. At the same time yaw motion is leading surge motion at the same period of oscillation. This observed tendency may be appreciated in Fig. 11 which shows the surge, sway and yaw motions for $T = 13sec$, $H = 2.6m$: large sway motions induce yaw amplification which forces surge motion to respond at the yaw oscillating period.

8. ANALYTICAL MODEL

In the present problem restoring terms are due to mooring lines, tendons and connecting lines. These expressions may be summed-up and expressed in terms of multivariable Taylor series expansions taken with respect to the mean equilibrium position. Expansions are here defined with terms up to third order of the expansions. As the focus here lies in the surge, sway and yaw motions of the TLWP, it is assumed that the FPSO is fixed at its mean position for the assessment of the connecting actions.

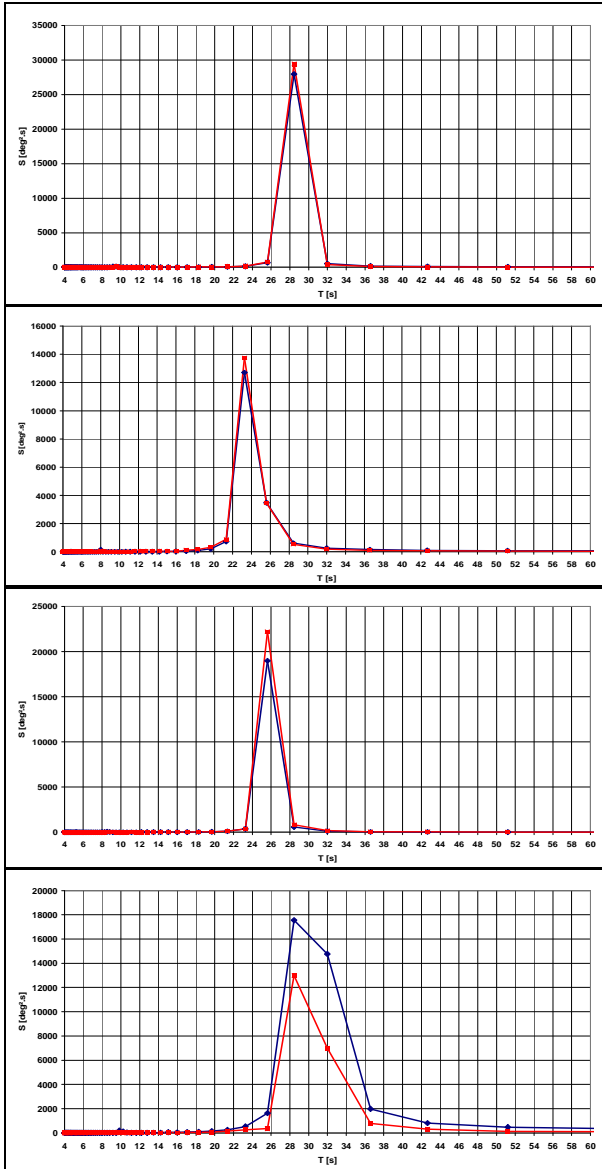


Figure 8 : TLWP yaw motion, a) T=12sec; b) T=13sec; c) T=14sec; d) T=15sec.

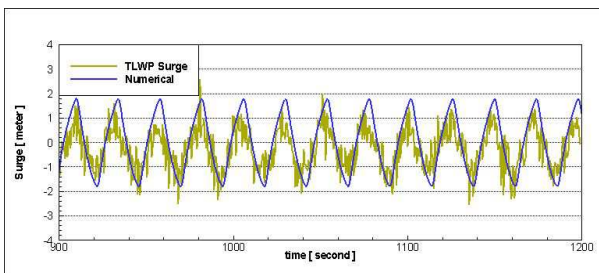


Figure 9: Comparison of numerical and experimental TLWP surge motion, $T=12sec$, $H=2.4m$.

Adopting a nomenclature similar to that of Neves and Rodríguez (2007), non-linear restoring actions may be expressed as:

$$\mathbf{c}_r = \mathbf{c}_{r(s)}^{(1)} + \left(\mathbf{c}_{r(s)}^{(2)} + \mathbf{c}_{r(\zeta)}^{(2)} \right) + \mathbf{c}_{r(s)}^{(3)}$$

$$= \begin{bmatrix} X_{r(s)}^{(1)} \\ Y_{r(s)}^{(1)} \\ N_{r(s)}^{(1)} \end{bmatrix} + \begin{bmatrix} X_{r(s)}^{(2)} + X_{r(\zeta)}^{(2)} \\ Y_{r(s)}^{(2)} + Y_{r(\zeta)}^{(2)} \\ N_{r(s)}^{(2)} + N_{r(\zeta)}^{(2)} \end{bmatrix} + \begin{bmatrix} X_{r(s)}^{(3)} \\ Y_{r(s)}^{(3)} \\ N_{r(s)}^{(3)} \end{bmatrix} \quad (15)$$

where superscripts (1)–(3) refer to first, second and third order restoring terms, respectively:

$$X_{r(s)}^{(1)} = X_x x + X_\psi \psi$$

$$Y_{r(s)}^{(1)} = Y_y y$$

$$N_{r(s)}^{(1)} = N_\psi \psi + N_x x \quad (16)$$

Second order actions are composed of two terms. Subscripts (s) refer to body motions, whereas (ζ) refer to wave passage effects on the tendons described above. According to the derivations, second order restoring actions (motions) may be defined as:

$$X_{r(s)}^{(2)} = X_{xy} xy + X_{y\psi} y\psi$$

$$Y_{r(s)}^{(2)} = \frac{1}{2} \left[Y_{xx} x^2 + 2Y_{x\psi} x\psi + Y_{yy} y^2 + Y_{\psi\psi} \psi^2 \right]$$

$$N_{r(s)}^{(2)} = N_{xy} xy + N_{y\psi} y\psi \quad (17)$$

and third order restoring actions as:

$$X_{r(s)}^{(3)} = \frac{1}{6} \left[X_{xxx} x^3 + 3X_{xx\psi} x^2\psi + 3X_{yyx} y^2x + 3X_{yy\psi} y^2\psi + 3X_{\psi\psi x} \psi^2x + X_{\psi\psi\psi} \psi^3 \right]$$

$$Y_{r(s)}^{(3)} = \frac{1}{6} \left[Y_{yyy} y^3 + 3Y_{xy} x^2y + 3Y_{\psi\psi y} \psi^2y \right]$$

$$N_{r(s)}^{(3)} = \frac{1}{6} \left[N_{xxx} x^3 + 3N_{xx\psi} x^2\psi + 3N_{yyx} y^2x + 3N_{yy\psi} y^2\psi + 3N_{\psi\psi x} \psi^2x + N_{\psi\psi\psi} \psi^3 \right] \quad (18)$$

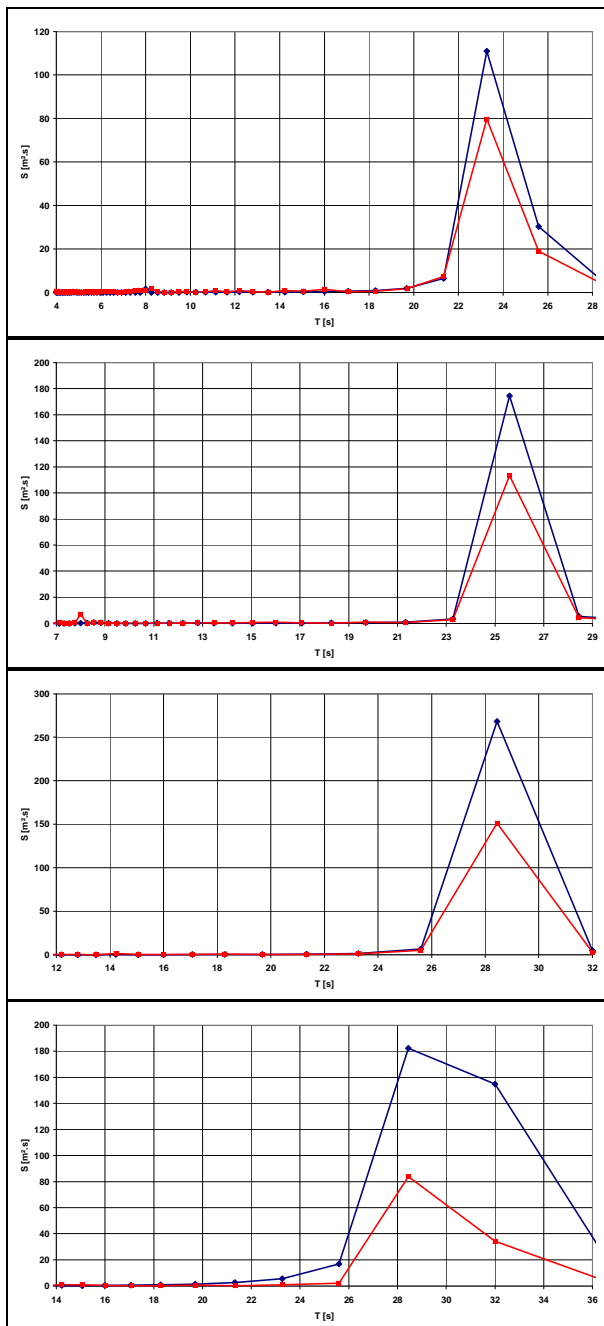


Figure 10 : TLWP surge motion spectra: a) $T=12sec$; b) $T=13sec$; c) $T=14sec$; d) $T=15sec$.

Since platform vertical motions are not considered, the length of the tendons may be assumed to remain constant for small horizontal displacements; however, it does not imply that there is no variation of the tension on the vertical tendons.

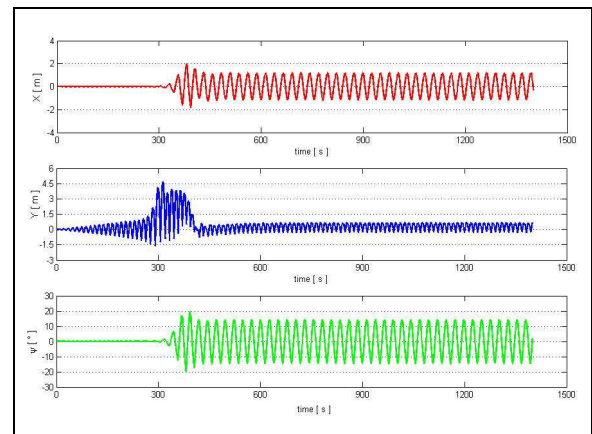


Figure 11: Surge, sway and yaw motions, $T = 13sec$, $H = 2.6m$.

The tension may be varying as a result of the cyclic wave vertical force on the platform. Thus, a restoring force depending on the tension will be varying in time. The expressions for the tendons restoring forces and moment due to a linear variation are given as:

$$X_T = \left[\frac{4T}{L_0} \right] x \quad Y_T = \left[\frac{4T}{L_0} \right] y$$

$$N_T = \left[\frac{4T \cdot R^2}{L_0} \right] \psi \quad (19)$$

where R is the distance of the tendon to the centre of reference at the platform. Considering the wave vertical force on the platform for each tendon:

$$T(t) = T_0 + \frac{Z_w(t)}{4} \quad (20)$$

Each of the above contributions will be composed of a pre-tension T_0 plus a harmonic contribution due to wave action. In regular waves, vertical wave exciting force on the platform may be assumed as a simple harmonic:

$$Z_w(t) = Z_{w0} \cos(\omega_w t + \gamma_{zw}) \quad (21)$$

Following the same nomenclature, the wave passage contributions are represented as:

$$\begin{aligned} X_{r(\zeta)}^{(2)} &= X_{\zeta x}(t)x \\ Y_{r(\zeta)}^{(2)} &= Y_{\zeta y}(t)y \\ N_{r(\zeta)}^{(2)} &= N_{\zeta \psi}(t)\psi \end{aligned} \quad (22)$$

These are second order terms in the sense that they represent first order vertical wave force $Z_w(t)$ multiplied by first order displacements x, y and ψ . The implication here is that, as indicated above, in principle the tendons may induce small time-dependent internal excitations to the surge, sway and yaw modes of the platform.

Each coefficient in equations (16-19) corresponds to constant derivatives, each one being the sum of three contributions: mooring lines, tendons and connecting lines. The derivatives were obtained by means of MAPLE computer code. In general the obtained expressions of these coefficients are too long to be presented here. For this reason, only the corresponding numerical values will be shown here.

Figures 12, 13, show fits of the numerical model against the adopted third order Taylor series expansion representation of the forces and moment employed in the analytical model. The figure shows that the third order model represents quite efficiently the nonlinearities of the physical restoring problem up to quite large yaw angles.

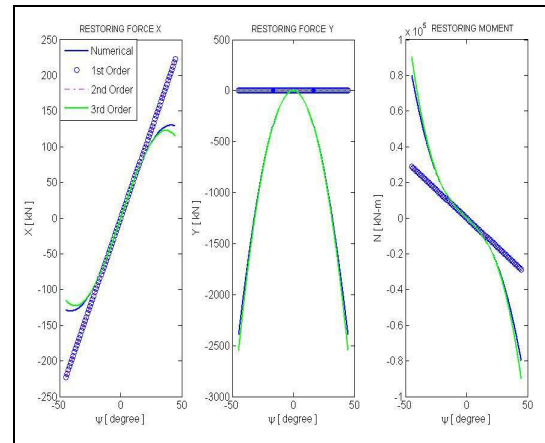


Figure 12: Dependence of forces and moment due to mooring lines on yaw motions.

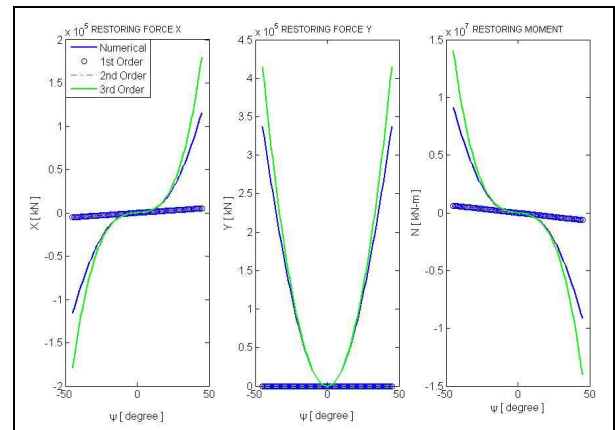


Figure 13: Dependence of forces and moment due to connecting lines on yaw motions.

Therefore, considering the above expressions for equations (16, 17, 18 and 22), complete restoring coupling is provided between surge, sway and yaw modes for the TLWP. Numerical values of all constant restoring coefficients are given in Tables 4-6 (already including the Taylor series multipliers) for the separated influence of tendons, mooring lines and connecting lines, respectively.



Table 4: Restoring coefficients - tendons.

		X	Y	N
1st Order	x	-130.3		
	y		-130.3	
	ψ			-94045.1
3rd Order	$x^2.y$		-7.0E-02	
	$x^2.\psi$			-1.0E+02
	y^3		-7.0E-02	
	$y^2.x$	-7.0E-02		
	$y^2.\psi$			-1.0E+02
	ψ^3			-2.1E+4
	$\psi^2.x$	-1.0E+02		
	$\psi^2.y$		-1.0E+02	
	x.y. ψ			

Table 5: Restoring coefficients - mooring lines.

		X	Y	N
1st Order	x	-51.4		283.4
	y		-226	
	ψ	283.4		-36763
2nd Order	x^2		-8.7E-02	
	xy	-1.7E-01		-8.6
	x ψ		-8.6E+00	
	y^2		-6.3E-02	
	y ψ	-		-8257.7
	ψ^2		-4.1E+03	
3rd Order	x^3	-5.5E-05		-5.0E-03
	$x^2.y$		4.1E-05	
	$x^2.\psi$			-6.2E+00
	y^3		9.9E-05	
	$y^2.x$	4.1E-05		7.0E-03
	$y^2.\psi$	7.0E-03		6.6E-01
	ψ^3	-		-1.3E+05
	$\psi^2.x$	-		-6.7E+02
	$\psi^2.y$		6.6E-01	
x.y.		1.4E-02		

Sub-harmonic resonance may be induced mainly by second order terms, as discussed by Neves and Rodríguez (2007), corresponding to responses at twice the exciting period, the first zone of instability of the Ince-Strutt diagram. Obviously first order terms do not induce parametric resonance and third order

terms induce resonance at the wave period and a complementary period shift, Neves and Rodríguez (2007). It is realized that equations (17 and 22) are therefore the ones with direct interest in the present analysis. They reveal that, at least in principle, all three modes may undergo parametric resonance.

Table 6: Restoring coefficients - connecting lines.

		X	Y	N
1st Order	x	-240		6600
	y		-31626	
	ψ	6600		-796134
2nd Order	x^2		313.86	
	xy	672.3		-17262
	x ψ		-1.7E+04	
	y^2			
	y ψ	-17262		1344428.
	ψ^2		672214.1	
3rd Order	x^3	-6.3E+00		172.6
	$x^2.y$		1.3E+01	
	$x^2.\psi$	517.9		-22760
	y^3			
	$y^2.x$	1.3E+01		-345.3
	$y^2.\psi$	-345.3		9494.3
	ψ^3	360871		-
	$\psi^2.x$	-22760		1062612
	$\psi^2.y$		9494.3	
	x.y. ψ		-6.9E+02	

Tendons alone cannot induce parametric amplification, as all their second order terms are zero, as shown in Table 4. On the other hand, wave passage effects on their tensions tend to be very small when compared with the effect of mooring lines and connecting lines. The main reason is that the vertical wave force on the TLWP is very small in the range of interest here, i.e., periods between 12 to 15 seconds. This is due to a typical platform design configuration usually adopted for minimizing heave responses, as discussed in De Conti et al. (2010).



Tables 4-6 demonstrate that parametric amplifications of the TLWP are largely governed by the mooring lines and connecting lines. In particular, it is observed that coefficient $N_{y\psi}=1344428.25\text{kN}$ for the connecting lines, given in Table 6, is much larger than $N_{y\psi}=-8257.7\text{kN}$ given in Table 5, which is the corresponding value for the mooring lines. This is the main coefficient in the yaw equation responsible for the transfer of externally excited sway motion into internally excited yaw motion. It is then concluded that the connecting lines are the main agent of parametric amplification.

On the other hand it may be concluded that the term $Y_{\psi\psi}\psi^2$ in equation (17) is the one responsible for the reduction in the sway motions that take place as yaw motions amplify. Again, consulting Tables 5 and 6, it is possible to conclude that the connecting lines are mainly responsible for the strong coupling observed in the experiments.

9. CONCLUSIONS

A mathematical model for the analysis of parametric resonance in yaw of a TLWP platform has been described. It has been shown that the encountered amplifications are consistent with instabilities of the Mathieu type. Numerical simulations are well compared to experimental results. A strong coupling between sway and yaw is evident from the experiments. This important coupling is captured in the numerical simulations.

It has been shown that the restoring system provided by the mooring lines, tendons and connecting lines leads to sub-harmonic motions not only in the yaw mode, but also in the surge mode.

It has also been shown that parametric excitation resulting from oscillatory loading of the tendons due to the vertical wave force on the platform is negligible. It is concluded

that the connecting lines are the main agent for yaw parametric amplification of the TLWP.

Hydrodynamic loading, due to the close proximity of the two bodies, is obviously asymmetric. The relevance of these asymmetries is a topic for future research.

10. ACKNOWLEDGEMENTS

The present investigation is supported by CNPq within the STAB project (Non-linear Stability of Ships) coordinated by the second author. Authors also acknowledge financial support from CAPES, FAPERJ, PETROBRAS and LabOceano.

11. REFERENCES

- Brewer, J.H., 1975, "The Tension Leg Platform Concept". *American Petroleum Institute, Annual Meeting Papers, Division of Production, Dallas, Texas.*
- Cruz, R.E., 2010, "Dynamic Simulation of Two Coupled Bodies under Regular Waves Excitation". M.Sc. Dissertation, COPPE/UFRJ (in Portuguese).
- Cruz, R.E., Neves, M.A.S., Rivera, L.A. and Esperança, P.T.T., 2012, "An Investigation on the Excitation of Yaw Parametric Resonance of a Tension Leg Platform", Paper OMAE2012-83574, Rio de Janeiro, June 2012.
- De Conti, M., Andrade, B. and Birk, L., 2009, "Differentiation between the Lower and Upper Parts of Columns of a Semi-Submersible for Heave Response Improvement". *Marine Systems & Ocean Technology*, Vol 4, No 2, pp. 63-72.
- Denise, J-P. F. and Heaf, N.J., 1979, "A Comparison between Linear and Non-Linear Response of a Proposed Tension



Leg Production Platform”. OTC 3555, In: Proceedings of the 11th Offshore Technology Conference, Houston, Texas.

Neves, M.A.S. and Rodríguez, C.A., 2007, ‘Influence of Non-Linearities on the Limits of Stability of Ships Rolling in Head Seas’. Ocean Engineering. Vol. 34, pp 1618-1630.

Paulling, J.R. and Rosenberg, R.M, 1959, “On Unstable Ship Motions Resulting From Non-Linear Coupling”. Journal of Ship Research, Vol. 3, no. 1 (Jun.), pp. 36-46.

Rodríguez, C.A. and Neves, M.A.S., 2012, “Domains of Parametric Roll Amplification for Different Hull Forms”. In: Parametric Resonance in Dynamical Systems, Chapter 6, Ed.: T.I.Fossen and H. Nijmeijer, Springer Science, New York.

Ximenes, M.C.C., 1991, “Fatigue Reliability and Inspection of TLP Tendon System”. Marine Technology, Vol. 28, No. 2, March, pp. 99-110.

Table A2: Main characteristics of TLWP.

Length – L (m)	55.0
Breadth – B (m)	55.0
Depth – H (m)	39.3
Draft – D (m)	25.0
Columns diameter – Dc [m]	17.0
Height of pontoons – Hp [m]	10.0
Width of pontoons – Lp [m]	10.0
Displacement (ton)	20000
Pre-traction (kN)	127000

APPENDIX

Table A1: Main characteristics of FPSO.

Length between perpendiculars – Lpp (m)	297.0
Breadth – B (m)	53.8
Depth – H (m)	27.5
Draft – D (m)	17.9
Displacement (ton)	232000



The Hydrodynamics of Submerged Prolate Spheroidal Bodies in Infinite Water Depth

Ioannis K. Chatjigeorgiou, chatzi@naval.ntua.gr

Spyros A. Mavrakos, mavrakos@naval.ntua.gr

Thomas P. Mazarakos, tmazarakos@naval.ntua.gr

Laboratory of Floating Structures and Mooring Systems, School of Naval Architecture and Marine Engineering, National Technical University of Athens, 9 Heroon Polytechniou Ave, 15773 Zografos Campus, Athens, Greece

ABSTRACT

It is the purpose of this study to provide the analytic solution for the hydrodynamic diffraction problem by stationary, submerged prolate spheroidal bodies subjected to harmonic incident waves in infinite water depth. The feasibility of the derivation of an analytic solution is assisted by the axisymmetry of the concerned geometry which makes possible the separation of variables. The analytical process employs the multipole formulas derived by Thorne (1953) which describe the velocity potential at singular points within a fluid domain with free upper surface and infinite water depth. The multipole expansion is used to analytically formulate the diffraction component of the velocity potential which is initially described by relations involving both spherical and polar coordinates. The goal is to transform the constituent terms of the multipole expansion as well as the incident wave component in prolate spheroidal coordinates. To this end, the appropriate addition theorems are derived which recast Thorne's (1953) formula into infinite series of associated Legendre functions.

Keywords: *prolate spheroids, addition theorems, multipole potentials, Legendre functions*

1. INTRODUCTION

The hydrodynamics of axisymmetric bodies of revolution are being extensively investigated for decades. However, unlike cylindrical bodies for which the reported works are exhaustive, analytical studies on spheroids subjected to potential flows are encountered infrequently and they are exhausted mainly on spheres. Gray (1978) investigated the scattering of surface waves by a submerged sphere formulating the problem as an integral equation and expanding Green's function and the velocity potentials in spherical harmonics. Wang (1986) extended the method of Havelock (1955) on the waves induced by a floating oscillating sphere, to tackle the diffraction and

radiation problems of a fully immersed sphere in deep water. The mathematical formulation was based on Thorne's (1953) multipole potentials associated with infinite depth. Thorne's (1953) formulas for finite depth were employed by Linton (1991), Rahman (2001) and Wu et al. (1994). Linton (1991) investigated the diffraction and radiation problems by a submerged sphere whereas Rahman (2001) focused only on the scattering problem but he also presented results for the free surface elevation above the assumed stationary sphere. Wu et al. (1994) used the same multipole expansion to calculate the drift forces induced on the sphere in finite depth while Wu & Eatock Taylor (1988) and (1990) adopted a rather different line of approach and



expressed the potential by means of a Green function and a distribution of sources over the body surface, written in terms of Legendre functions.

The pioneer in the area of the hydrodynamics of spheroids is unquestionably Sir Thomas Havelock (1931a,b) and (1950) who calculated the wave resistance of a submerged spheroid by replacing it with a distribution of sources and sinks, or of doublets. The research on the hydrodynamics of spheroids was enhanced by Wu & Eatock Taylor (1987) and (1989) who considered a submerged spheroid with its longitudinal axis of symmetry parallel to the free surface and provided solutions for the linear forces. The final goal of the authors was to tackle the problem of a spheroid with forward speed and as a first step they examined the scattering problem using the traditional source distribution method. The analytical aspect of their study relies on the expansion of source strengths into a series of Legendre functions. Finally, although not explicitly connected with hydrodynamics there are also studies reported in the literature that deal with the potential in spheroidal coordinates (Wang, 1988; Wang, 1989, Miloh, 1990).

Thorne's (1953) formulas have been proven very efficient for dealing with the hydrodynamics of submerged spheres without forward speed provided that the multipole expansions will be properly transformed into a spherical coordinate system (e.g. Wang, 1986; Linton, 1991; Rahman, 2001; Wu et al., 1994). For spheroidal bodies other than spheres, such as prolate or oblate spheroids, the employment of these formulas is admittedly a complicated task as they engage both spherical and cylindrical coordinates. Nevertheless the reward of using multipole expansions is that they result in analytical, closed form solutions.

The work that is undertaken in the present tackles the hydrodynamic diffraction problem by a submerged prolate spheroid with vertical

semi-major axis by employing Thorne's (1953) multipole potentials for infinite depth.

The relevant procedure adopts Wang's (1986) formulation. In the present study, the various terms of the potentials are properly transformed into a prolate spheroidal system fixed on the center of the body. This task required extensive and complicated mathematical manipulations which are described succinctly in the main text. In fact, the derived expressions can be considered as the associated addition theorems that transform relations which are initially expressed in spherical and cylindrical coordinates to prolate spheroidal systems. Further, the governing expressions are employed to describe both the incident and the diffraction velocity potentials while the final solution is achieved by applying the zero velocity condition on the wetted surface of the submerged spheroid.

2. COORDINATE SYSTEMS

A prolate spheroid (Fig1) is considered immersed at a distance f below the undisturbed free surface. A Cartesian coordinate system (x,y,z) fixed on the free surface is defined, with its vertical z axis pointing downwards (see Fig2). The associated Cartesian coordinate system fixed on the center of the spheroid is denoted by (x,y,z^*) so that $z=z^*+f$. We begin with the transformation formulas from prolate spheroidal to Cartesian coordinates. These are (Moon and Spencer, 1971)

$$x = c \sinh u \sin \vartheta \cos \psi \quad (1)$$

$$y = c \sinh u \sin \vartheta \sin \psi \quad (2)$$

$$z^* = c \cosh u \cos \vartheta \quad (3)$$

with $0 \leq u < \infty$, $0 \leq \vartheta \leq \pi$ and $0 \leq \psi < 2\pi$.

The radial distance from the center of the spheroid at the (x,y) plane is denoted by R and it is given by

$$R = \sqrt{x^2 + y^2} = c \sinh u \sin \vartheta \quad (4)$$

$$x = r \sin \theta \cos \psi \quad (7)$$

$$y = r \sin \vartheta \sin \psi \quad (8)$$

$$z^* = r \cos \vartheta \quad (9)$$

$$0 \leq r < \infty, 0 \leq \theta \leq \pi \text{ and } 0 \leq \psi < 2\pi.$$

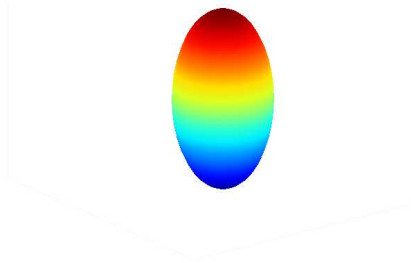


Figure 1: 3D image of a prolate spheroid with vertical major axis of symmetry.

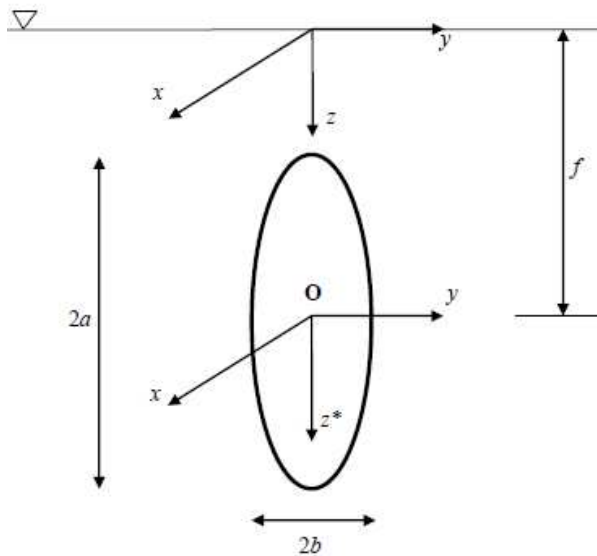


Figure 2: Sketch of the spheroid; coordinate systems and geometrical definitions

Here we employ the notation due originally to Nicholson (1924) according to which

$$R = c \sqrt{(1 - \mu^2)(\xi^2 - 1)} \quad (5)$$

$$z^* = c \mu \xi \quad (6)$$

where $\xi = \cosh u$ and $\mu = \cos \vartheta$. It is noted that (R, z^*) are cylindrical coordinates. Letting $\xi = i\zeta$ and replacing c by $ce^{-1/2i\pi}$, R and z^* remain unchanged and they are expressed in terms of the associated oblate spheroidal coordinates with the same origin. Finally a spherical (r, θ, ψ) system is defined, fixed on the center of the spheroid of Fig2 with

3. VELOCITY POTENTIALS

3.1 The Boundary Value Problem

For an incompressible and inviscid fluid, and for the small amplitude wave theory with irrotational harmonic motion, we can express the fluid motion by introducing a velocity potential which in spheroidal coordinates will be denoted by $\Phi(u, \vartheta, \psi; t)$. Furthermore, the velocity potential can be written as

$$\Phi(u, \vartheta, \psi; t) = \text{Re}(\phi(u, \vartheta, \psi) e^{-i\omega t}) \quad (10)$$

where ω , is the wave frequency and ϕ is the time independent complex potential. The potential ϕ must satisfy the Laplace equation everywhere in the fluid domain

$$\nabla^2 \phi = 0 \quad (11)$$

the free surface boundary condition at $z=0$,

$$\frac{\partial \phi}{\partial z} + K\phi = 0 \quad (12)$$

and the bottom boundary condition for $z \rightarrow \infty$

$$\frac{\partial \phi}{\partial z} = 0 \quad (13)$$

In equation (12) $K = \omega^2/g$ where g is the gravitational acceleration.

The total velocity potential ϕ is further decomposed into the incident and the diffraction components which are denoted by ϕ_I and ϕ_D respectively. The boundary value



problem is completed by introducing the radiation condition which must be satisfied by the diffraction potential

$$\lim_{R \rightarrow \infty} \sqrt{R} \left(\frac{\partial}{\partial R} - ik_0 \right) \phi_D = 0 \quad (14)$$

and the zero velocity condition on the wetted surface of the body

$$\left(\frac{\partial \phi}{\partial u} \right)_{u=u_0} = 0 \quad (15)$$

where u_0 is used to denote the boundary of the body in spheroidal coordinates. In fact u_0 is given by $u_0 = \tanh^{-1}(b/a)$ (see Fig2). Here $a = c \cosh u_0$ and $b = c \sinh u_0$ denote respectively the semi-major and the semi-minor axes of the spheroid. In equation (14) k_0 denotes the wavenumber which for infinite water depth is equal to $K = \omega^2/g$.

3.2 Incident Wave Potential

An incident wave of linear amplitude A can be described by

$$\phi_I(u, \vartheta, \psi) = \omega A \sum_{m=0}^{\infty} \hat{\phi}_I^m(u, \vartheta) \cos m\psi \quad (16)$$

The goal here is to recast properly ϕ_I in order to be expressed in prolate spheroidal coordinates. Nevertheless, it is originally expressed in cylindrical coordinates according to

$$\phi_I^m(R, z) = \frac{1}{K} e^{-Kz} \varepsilon_m i^m J_m(KR) \quad (17)$$

where $\varepsilon_m = 1$ for $m=0$ and $\varepsilon_m = 2$ for $m \geq 1$ and J_m is the m th order Bessel function of the first kind.

3.3 Diffraction Potential

The diffraction potential will be given in terms of a multipole expansion. In

hydrodynamics, multipole expansions describe the velocity potential at singular points within a fluid domain with free upper surface. The singularities at these points are characterized by their giving rise to potentials which are typical singular solutions of Laplace's equation in the neighborhood of the singularity. In addition, multipole potentials satisfy the free surface and bottom boundary conditions and behave like outgoing waves far away from the singular point which in the case of spheres or spheroids will be the center of the body.

For the problem at hand the function representing the diffraction potential is initially written as

$$\phi_D(u, \vartheta, \psi) = \omega A e^{-Kf} \sum_{m=0}^{\infty} \hat{\phi}_D^m(u, \vartheta) \cos m\psi \quad (18)$$

The generalized potential $\hat{\phi}_D^m(u, \vartheta)$ will be given in terms of Thorne's (1953) formulas for infinite water depth. First, Wang's (1986) notation is applied writing the multipole expansion in spherical coordinates as

$$\hat{\phi}_n^m(r, \theta) = \hat{\psi}_n^m(r, \theta) + i \hat{\chi}_n^m(r, \theta) \quad (19)$$

Then according to Thorne (1953), the right hand side components of equation (19) will be given by

$$\hat{\psi}_n^m = \frac{P_n^m(\cos \theta)}{r^{n+1}} + \frac{(-1)^{m+n-1}}{(n-m)!} \quad (20)$$

$$\times PV \int_0^{\infty} \frac{K+k}{K-k} k^n e^{-k(z+f)} J_m(kR) dk$$

and

$$\hat{\chi}_n^m = \frac{(-1)^{m+n}}{(n-m)!} 2\pi K^{n+1} e^{-K(z+f)} J_m(KR) \quad (21)$$

where PV indicates that Cauchy's principal value of the integral is taken and P_n^m denotes



the associated Legendre function of the first kind with order m and degree n . It is noted that equations (20) and (21) combine both spherical (r, θ) and polar (R, z) coordinates. The first term of $\hat{\psi}_n^m$ corresponds to a multipole singularity in an infinite medium and it is adjusted with the second term to satisfy the free surface condition (12). The function $\hat{\chi}_n^m$ represents a standing wave potential, satisfying the same free surface condition. It should be noted that $\hat{\psi}_n^m$ is regular and bounded in the half plane $z \geq 0$.

For $z > -f$ Wang (1986) invoked the identity of Gray et al. (1931)

$$\frac{P_n^m(\cos \theta')}{r'^{n+1}} = \frac{1}{(n-m)!} \int_0^\infty k^n e^{-k(z+f)} J_m(kR) dk \quad (22)$$

to expand $\hat{\phi}_D^m$ in the following form

$$\hat{\phi}_D^m = a^{m+2} F_m^m \hat{\phi}_m^m + \sum_{n=m+1}^\infty a^{n+2} F_n^m \hat{\Omega}_n^m \quad (23)$$

where

$$\hat{\Omega}_n^m = \frac{P_n^m(\cos \theta)}{r^{n+1}} + \frac{K}{n-m} \frac{P_{n-1}^m(\cos \theta)}{r^n} + (-1)^{m+n} \left[\frac{P_n^m(\cos \theta')}{r'^{n+1}} + \frac{K}{n-m} \frac{P_{n-1}^m(\cos \theta')}{r'^n} \right] \quad (24)$$

In equation (23) F_n^m are the unknown expansion coefficients which will be calculated by employing the zero velocity condition on the surface of the prolate spheroid. Also, in equations (22) and (24) (r', θ') are spherical coordinates referred to the image point $(0, 0, -f)$. This completes the effort for writing the

general expression that describes the diffraction potential. Indeed this is given by equation (18) where $\hat{\phi}_D^m$ is composed by the products given in equations (23), (19)-(21) and (24). Clearly, these equations involve both spherical (r, θ) and cylindrical coordinates (R, z) . Thus, in order to apply the multipole expansion and accordingly the diffraction potential to prolate spheroidal bodies, the various terms must be transformed into the associated spheroidal coordinates (u, ϑ, ψ) or equivalently into prolate (ξ, μ, ψ) spheroidal coordinates. The governing relations are given in the following section.

4. TRANSFORMATION OF THE POTENTIALS INTO PROLATE SPHEROIDAL COORDINATES

There are several terms which must be properly manipulated. Nevertheless, these terms fall into three major categories involving the products (i) $P_n^m(\cos \theta)/r^{n+1}$; (ii) $e^{-k(z+f)} J_m(kR)$; (iii) $P_n^m(\cos \theta')/r'^{n+1}$. The second term is also involved into the incident wave potential (see equation (17)).

The procedure for transforming the above mentioned terms into prolate spheroidal coordinates is extensive and extremely complicated. Thus, only the final relations will be given in the present. It is noted that the derivation procedure employs the theory developed by Cooke (1953) and (1956) whereas various forms of Bessel functions ascending series are required (Watson, 1966; Abramowitz & Stegun, 1970). The obtained relations, which are given in the following, can be considered as the governing addition theorems that transform relations originally defined in spherical and polar coordinates into prolate spheroidal coordinates. It is also noted that Cook's (1953) and (1956) relations are given in terms of oblate spheroidal coordinates and that required an additional effort to obtain the associated expressions into prolate



spheroidal coordinates. In particular it can be shown that the following relations are valid

$$\frac{P_n^m(\cos \theta)}{r^{n+1}} = \frac{(2/c)^{n+1}}{(n-m)! \pi^{1/2}} \sum_{s=m}^{\infty} (-1)^s \times \frac{(1/2 + n + 2s - 2m) \Gamma(1/2 + n + s - m)}{\Gamma(s - m + 1)} \times \frac{\Gamma(n + 2s - 3m + 1)}{\Gamma(n + 2s - m + 1)} \quad (25)$$

$$\times P_{n+2s-2m}^m(\mu) Q_{n+2s-2m}^m(\xi)$$

$$J_m(kR)e^{-kz^*} = \sqrt{\frac{\pi}{2kc}} \sum_{s=m}^{\infty} (-1)^{s-m} \times \frac{(2s+1)\Gamma(s-m+1)}{\Gamma(s+m+1)} I_{s+1/2}(kc) \quad (26)$$

$$\times P_s^m(\mu) P_s^m(\xi)$$

$$\phi_I^m(u, \vartheta) = \frac{1}{K} e^{-Kf} \varepsilon_m i^m \sqrt{\frac{\pi}{2Kc}} \times \sum_{s=m}^{\infty} (-1)^{s-m} \frac{(2s+1)\Gamma(s-m+1)}{\Gamma(s+m+1)} \quad (27)$$

$$\times I_{s+1/2}(Kc) P_s^m(\mu) P_s^m(\xi)$$

$$\hat{\chi}_m^m(u, \vartheta) = 2\pi K^{m+1} e^{-2Kf} \sqrt{\frac{\pi}{2Kc}} \times \sum_{s=m}^{\infty} (-1)^{s-m} \frac{(2s+1)\Gamma(s-m+1)}{\Gamma(s+m+1)} \quad (28)$$

$$\times I_{s+1/2}(Kc) P_s^m(\mu) P_s^m(\xi)$$

$$(-1)^{m+n} \left[\frac{P_n^m(\cos \theta')}{r'^{n+1}} + \frac{K}{n-m} \frac{P_{n-1}^m(\cos \theta')}{r'^n} \right] =$$

$$\frac{1}{(n-m)!} \sqrt{\frac{\pi}{2c}} \sum_{s=m}^{\infty} (-1)^{n+s} (2s+1)$$

$$\times \frac{\Gamma(s-m+1)}{\Gamma(s+m+1)} (A_{ns} + KA_{n-1,s}) P_s^m(\mu) P_s^m(\xi) \quad (29)$$

$$\hat{\psi}_m^m = \frac{(2/c)^{m+1}}{\pi^{1/2}} \sum_{s=m}^{\infty} (-1)^s \times \frac{(1/2 + 2s - m) \Gamma(s + 1/2) \Gamma(2s - 2m + 1)}{\Gamma(s - m + 1) \Gamma(2s + 1)} \times P_{2s-m}^m(\mu) Q_{2s-m}^m(\xi) \quad (30)$$

$$+ \sqrt{\frac{\pi}{2c}} \sum_{s=m}^{\infty} (-1)^{s-m} \frac{(2s+1)\Gamma(s-m+1)}{\Gamma(s+m+1)} \times J(Kf; m, s) P_s^m(\mu) P_s^m(\xi)$$

In equations (25)-(30) I_ν denotes the modified Bessel function of the first kind or order ν whereas Q_n^m is the associate Legendre function of the second kind with order m and degree n . In addition it holds that

$$A_{ns} = \sum_{p=0}^{\infty} \left(\frac{c}{2}\right)^{2p+s+1/2} \left(\frac{1}{2f}\right)^{2p+n+s+1} \times \frac{\Gamma(2p+n+s+1)}{p! \Gamma(s+p+3/2)} \quad (31)$$

$$J(Kf; m, s) = \sum_{q=0}^{\infty} \left(\frac{c}{2}\right)^{s+2q+1/2} \times \frac{K^{m+s+2q+1}}{q! \Gamma(s+q+3/2)} I(Kf; m, s, q) \quad (32)$$

$$I(Kf; m, s, q) = PV \int_0^{\infty} w^{m+s+2q} e^{-2Kfw} \times \left(1 + \frac{2}{w-1}\right) dw \quad (33)$$

Cauchy's Principal Value Integral of equation (33) is expressed analytically according to

$$I(Kf; m, s, q) = \frac{(m+s+2q)!}{(2Kf)^{m+s+2q+1}} + 2 \left[\sum_{j=1}^{m+s+2q} \frac{(j-1)!}{(2Kf)^j} - e^{-2Kf} Ei(2Kf) \right] \quad (34)$$

where



$$Ei(x) = \int_{-\infty}^x \frac{e^{-t}}{t} dt \quad (35)$$

is the exponential integral function.

5. EXPANSION COEFFICIENTS AND EXCITING FORCES

Equations (25)-(35) allow expressing the diffraction and the incident wave potentials in terms of prolate spheroidal coordinates and employ the zero velocity kinematical condition on the wetted surface of the spheroid. This is

$$\frac{\partial \hat{\phi}_D^m(u, \vartheta)}{\partial u} = -e^{Kf} \frac{\partial \phi_I^m(u, \vartheta)}{\partial u} \quad (36)$$

at $u=u_0$ and $0 \leq \vartheta \leq \pi$. After making use of the orthogonality relation of Legendre functions (Abramowitz & Stegun, 1970)

$$\int_{-1}^1 P_n^m(\mu) P_s^m(\mu) d\mu = \frac{\delta_{ns} (n+m)!}{(n+1/2)(n-m)!} \quad (37)$$

where δ_{ns} is Kroneker's delta, equation (36) yields the following linear system that provides the unknown expansion coefficients F_n^m

$$F_m^m C_{ms}^m + \sum_{n=m+1}^{\infty} F_n^m C_{ns}^m = B_s^m \quad (38)$$

For making the numerical computations feasible, the above system must be truncated to account for a finite number of modes M . The indices in equation (38) vary like $m=0,1,\dots,M$ and $n, s=m,m+1,\dots,M$. Equation (38) is solved M times for all orders m . For $m=0$, the elements C_{ms}^m and B_s^m compose a $N \times N$ complex matrix and a $N \times 1$ complex vector respectively, where $N=M+1$. For all subsequent orders the dimensions of the matrices are continuously reduced by one, whereas for the last order $M+1$ equation (38) becomes a simple linear algebraic equation. The expressions that

provide the elements C_{ms}^m , C_{ns}^m and B_s^m are rather lengthy and complicated and their details are omitted.

Next, the hydrodynamic pressure is obtained by

$$p = -i\omega\rho(\phi_I + \phi_D) \quad (39)$$

and accordingly, the hydrodynamic forces will be given by

$$F_j = -i\omega\rho \iint_{S_0} (\phi_I + \phi_D) n_j dS \quad (40)$$

where S_0 denotes the wetted surface of the spheroid, ρ is the water density and n_j ($j=x,y,z$) is the normal out of the body surface with

$$n_x = \frac{a \sin \vartheta \cos \psi}{(b^2 \cos^2 \vartheta + a^2 \sin^2 \vartheta)^{1/2}} \quad (41)$$

$$n_y = \frac{a \sin \vartheta \sin \psi}{(b^2 \cos^2 \vartheta + a^2 \sin^2 \vartheta)^{1/2}} \quad (42)$$

$$n_z = \frac{b \cos \vartheta}{(b^2 \cos^2 \vartheta + a^2 \sin^2 \vartheta)^{1/2}} \quad (43)$$

6. NUMERICAL RESULTS AND DISCUSSION

The analytical method outlined thoroughly in the previous sections was accordingly applied to calculate the linear hydrodynamic exciting forces which are exerted on different volume prolate spheroids subjected to monochromatic incident waves. For comparative purposes, the present method results were validated against the computations of an existing numerical code that employs the Panel Method (Mavrakos et al., 1984). To this end a prolate spheroid with $b/a=0.5$ was discretized by 652 elements using 599 points (see Fig3) and was tested numerically for three different immersions, i.e. $f/a=1.5, 2.5$ and 3.5 . The associated results are depicted respectively



in Figs4-6. It should be noted that the exciting forces which are presented throughout this paper have been normalized by $\rho g a^2 A$ and they are given against the nondimensional wave frequency Ka .

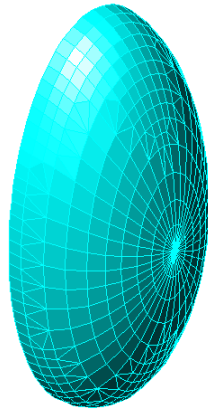


Figure 3: Panel discretization with 652 elements and 599 points of the half volume of a prolate spheroid with $b/a=0.5$

A crucial factor associated with the convergence of the present analytical method is the order of truncation of equation (38). The number of modes M which are needed to achieve convergence is related with the volume of the body and the immersion depth. For relative deep placements such as the cases examined with the aid of Figs4-6, $M=17$ was proven to be sufficient to achieve convergence up to the third decimal point.

Figs 4-6 demonstrate a favorable convergence between the present analytical method and the numerical Panel Method. For the specific spheroid volume and for $f/a=1.5$, the surge forces are obviously larger than the heave forces, whereas for deeper placements the maxima shift towards smaller wave frequencies. Moreover, deeper immersion results in smaller exciting forces, as it was expected.

A different immersion depth, i.e. $f/a=1.25$ is examined with the aid of Figs7-8. Here, surge and heave forces are plotted separately

whereas different spheroid volumes are investigated ($b/a=0.1$ through 0.9). It is evident that both surge and heave forces are increased for increasing volume while the maxima occur at the same vertical axis. Thus, it is deduced that the frequency of the maximum exciting force is governed primarily by the immersion depth.

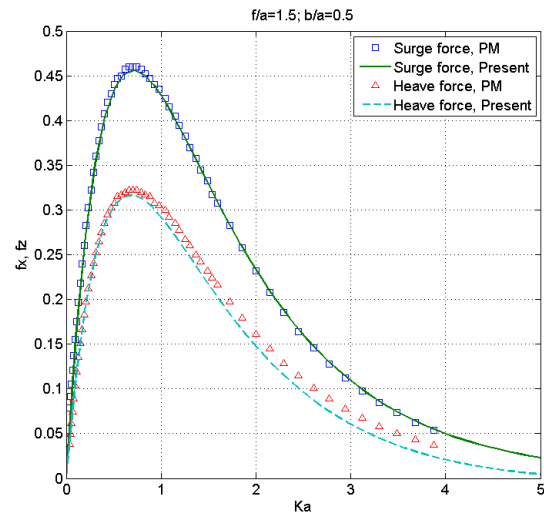


Figure 4: Magnitudes of the hydrodynamic exciting forces on a prolate spheroid with $b/a=0.5$, fixed at immersion $f/a=1.5$

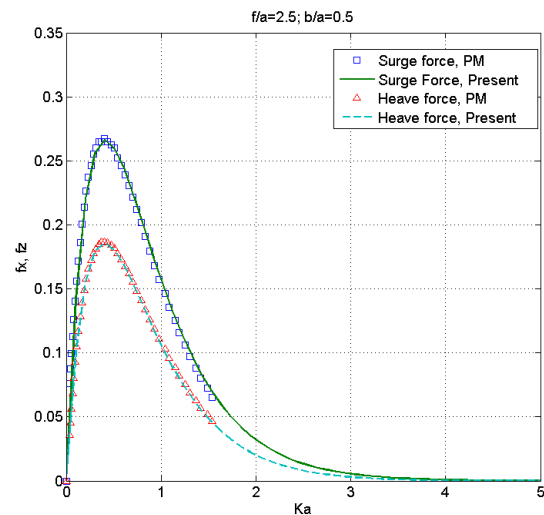


Figure 5: Magnitudes of the hydrodynamic exciting forces on a prolate spheroid with $b/a=0.5$, fixed at immersion $f/a=2.5$

The hydrodynamic loading in both directions show an asymptotic tendency to zero for large wave frequencies, but this remark does not hold for all cases. In particular, the wave exciting force in heave for large volume

spheroids ($b/a=0.7$ to 0.9) shows in a more pronounced way the well-known cancelation frequency.

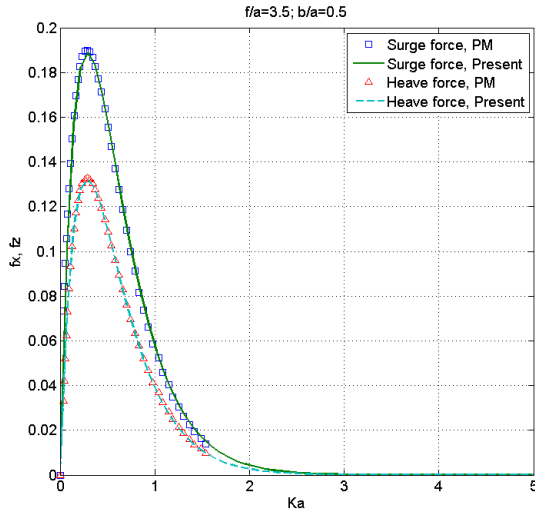


Figure 6: Magnitudes of the hydrodynamic exciting forces on a prolate spheroid with $b/a=0.5$, fixed at immersion $f/a=3.5$

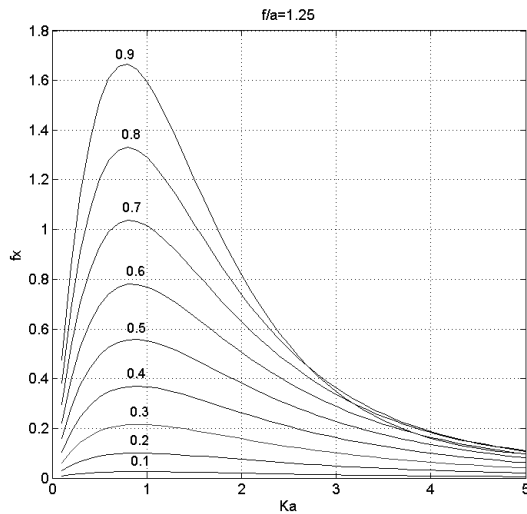


Figure 7: Magnitudes of the surge exciting force on different volume prolate spheroids fixed at immersion $f/a=1.25$

To provide further insight to this interesting finding additional calculations were performed having a large volume spheroid ($b/a=0.9$) to nearly touch the free surface ($f/a=1.01$). The associated results are depicted in Fig9 and apart from the cancelation frequency show a second local maximum, typical for bodies having their displaced volume transposed to larger depths (similar behavior as for

compound floating cylinders or semi-submersibles). It should be also mentioned that $M=17$ modes were proven insufficient to achieve convergence. In order to have accurate predictions additional modes were used and eventually, convergence was observed using $M=25$ modes.

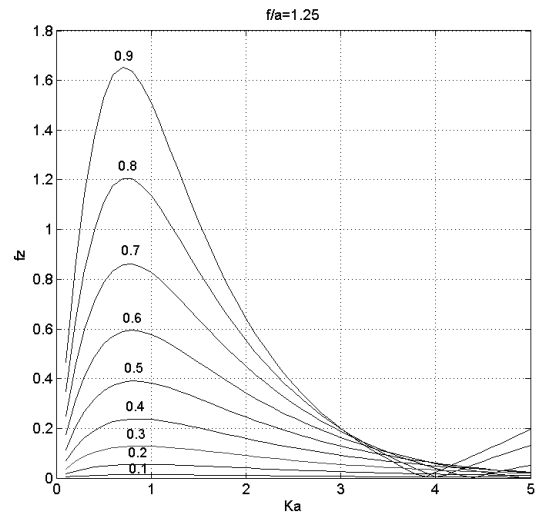


Figure 8: Magnitudes of the heave exciting force on different volume prolate spheroids fixed at immersion $f/a=1.25$

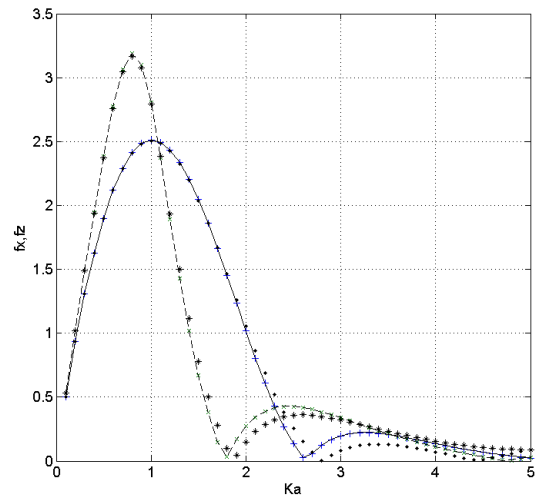


Figure 9: Magnitudes of the exciting forces on a prolate spheroid close to the free surface ($b/a=0.9$; $f/a=1.01$). Horizontal forces \bullet : $M=15$; $+$: $M=25$; $—$: $M=27$. Vertical forces $*$: $M=15$; \times : $M=25$; $- - -$: $M=27$



7. CONCLUDING REMARKS

This study dealt with the hydrodynamic diffraction problem by submerged stationary prolate spheroidal bodies subjected to monochromatic incident waves in infinite water depth. The solution to the problem was sought analytically and effort has been made to achieve a closed-form formulation for the total velocity potential. The analytical process employed Thorne's (1953) multipole potentials which were properly transformed into prolate spheroidal coordinates. This task required the derivation of the governing addition theorems that transform spherical and polar to spheroidal coordinates.

The final analytic formulas were validated against the numerical predictions of a Panel Method and favorable coincidence was observed. The calculations manifested reasonable and expected characteristics as for example smaller hydrodynamic loading for deeper immersions and hydrodynamic loading amplification for larger volume bodies at fixed immersion. Worth mentioning features, such as occurrences of cancellation frequencies in the transfer functions of hydrodynamic loading were observed for negligible immersions i.e. when the body nearly touches the free surface.

REFERENCES

- Abramowitz, M., and Stegun, I.A., 1970, "Handbook of mathematical functions", Dover Publications Inc, New York.
- Cooke, J.C., 1953, "Some properties of Legendre functions", Proc Cambridge Phil Society, Vol. 49, pp. 162-164.
- Cooke, J.C., 1956, "Some relations between Bessel and Legendre functions" Monatshefte für Mathematik, Vol. 60, pp. 322-328.
- Gray, A., Mathews, G.B. and McRobert, T.M., 1931, "A treatise on Bessel functions and their applications for physics" (2nd edition).
- Gray, E.P., 1978, "Scattering of a surface wave by a submerged sphere", J Eng Math, Vol. 12, pp.15-41.
- Havelock, T.H., 1931a, "The wave resistance of a spheroid", Proc Royal Soc London Vol. A131, pp.275-285.
- Havelock, T.H., 1931b, "The wave resistance of an ellipsoid", Proc Royal Soc London, Vol. A132, pp. 480-486.
- Havelock, T.H., 1950, "The forces on a submerged spheroid moving in a circular path", Proc Royal Soc London, Vol. A201, pp. 297-305.
- Havelock, T.H., 1955, "Waves due to floating sphere making periodic heaving oscillations", Proc Royal Soc London, Vol. A231, pp. 1-7.
- Mavrakos, S.A., Bardis, L. (1984), Hydrodynamic Characteristics of Large Offshore Units, Proceedings, 3rd I.M.A.E.M. International Congress on Marine Technology, Athens, Greece, June 1984, 505-513.
- Linton, C.M., 1991, "Radiation and diffraction of water waves by a submerged sphere in finite depth", Ocean Eng, Vol. 18, pp. 61-74.
- Miloh, T., 1990, "A note on the potential of a homogeneous ellipsoid in ellipsoidal coordinates", J Phys. A: Math. Gen, Vol. 23, pp. 581-584.
- Moon, P. and Spencer, D.E., 1971, "Field theory handbook" Springer-Verlag, Berlin.
- Nicholson, J.W., 1924, "Oblate Spheroidal Harmonics and their applications", Phil. Trans. R. Soc. London, Vol. A224, pp. 49-93.



- Rahman, M., 2001, "Simulation of diffraction of ocean waves by a submerged sphere in finite depth", Applied Ocean Research, Vol. 23, pp. 305-317.
- Thorne, R.C., 1953, "Multipole expansions in the theory of surface waves", Proc Camb Phil Soc, Vol. 49, pp.707-716.
- Wang, S., 1986, "Motions of a spherical submarine in waves", Ocean Eng, Vol. 13, pp. 249-271.
- Wang, W.X., 1988, "The potential for a homogeneous spheroid in a spheroidal coordinate system: I. At an exterior point", J Phys. A: Math. Gen, Vol. 21, pp. 4245-4250.
- Wang, W.X., 1989, "The potential for a homogeneous spheroid in spheroidal coordinate system. II. At an interior point", J Phys. A: Math. Gen, Vol. 22, pp. 1459-1462.
- Watson, G.N., 1966, "A treatise theory on the theory of Bessel functions", Cambridge University Press (2nd edition), London.
- Wu, G.X. and Eatock Taylor, R., 1987, "The exciting force on a submerged spheroid in regular waves", J Fluid Mech, Vol. 182, pp. 411-426.
- Wu, G.X. and Eatock Taylor, R., 1988, "Radiation and diffraction of water waves by a submerged sphere at forward speed", Proc Royal Soc London, Vol. A413, pp. 433-461.
- Wu, G.X. and Eatock Taylor, R., 1989, "On radiation and diffraction of surface waves by submerged spheroids", J Ship Res, Vol. 33, pp. 84-92.
- Wu, G.X. and Eatock Taylor, R., 1990, "The hydrodynamic forces on a submerged sphere moving on a circular path", Proc Royal Soc London, Vol. A428, pp. 215-227.
- Wu, G.X., Witz, J.A., Ma, Q. and Brown, D.T., 1994, "Analysis of wave induced drift forces acting on a submerged sphere in finite water depth", Applied Ocean Research, Vol. 16, pp. 353-361.





Dynamic Transverse Stability for High Speed Craft

Carolyn Q. Judge, *United States Naval Academy*, judge@usna.edu

ABSTRACT

Even in calm water, high-speed vessels can display unstable behaviors, such as chine walking, sudden large heel, and porpoising. Large heel results from the loss of transverse stability due to high forward speed. When a planing craft begins to plane, the hydrodynamic lift forces raise the hull out of the water, reducing the underwater submergence. The available righting moment due to the hydrostatic buoyancy is, therefore, reduced. As the righting moment due to hydrostatic buoyancy is reduced, the righting moment due to dynamic effects becomes important. These hydrodynamic righting effects are related to the hydrodynamic lift. This paper explores the relationship between the hydrostatic righting moment, the hydrodynamic righting moment, and the total roll restoring moment of a planing craft operating at planing speeds. A series of tow tests using a prismatic hull with a constant deadrise of 20° measured the righting moment at various angles of heel and at various model velocities. The model was completely constrained in heave, pitch, sway, roll, yaw and surge. The underwater volume is determined from the known hull configuration and the underwater photography of the keel and chine wetted lengths. The results presented include the total righting moment with the hydrostatic and hydrodynamic contributions for various model speeds at two model displacements.

Keywords: *planing craft, transverse stability, roll restoring moment, static lift, dynamic lift*

1. INTRODUCTION

For planing hulls, the forces acting on the hull are dominated by the complex hydrodynamics of planing. The dynamic lift reduces the submergence of the hull, allowing small motions to result in large changes in wetted surface area. Linearity assumptions are then less valid since hydrodynamic forces dominate in the planing regime. The problem of dynamic stability of high speed planing craft has been known for many years. Codega and Lewis (1987) described a class of high-speed planing boats that exhibited dynamic instabilities such as the craft trimming by the bow, rolling to a large angle of heel to port, and broaching violently to starboard. Blount and Codega (1992) presented data on boats that exhibited non-oscillatory dynamic instabilities and suggested quantitative criteria for

development of dynamically stable planing boats.

Recently there has been research into the stability of planing craft in the transverse plane. Ranzenbach and Bowles (2010) performed Dynamic Inclining Tests on three different hull shapes to establish transverse dynamic stability. Each model was ballasted to 5 degrees of static heel and then run down the tank at several different speeds in this asymmetric ballast condition. The hull was defined as dynamically unstable when the heel angle increased significantly and the hull as dynamically stable if the heel angle reduced at planing speed. The RANS CFD (Reynolds Averaged Navier Stokes Computational Fluid Dynamics program) used to analyze the tested models was not able to correctly match the experimental results qualitatively, but did correctly predict the propensity of a particular



hull form to exhibit dynamic instability via the Dynamic Inclining Test. Katayama *et al.* (2007) found that instability is strongly influenced by the running attitude of the hull at high speeds. Katayama *et al.* measured the rise, trim angle and heel angle for two models free in heave, pitch and roll and measured the rise and trim angle for the same models when fixed in zero roll. The underwater surface was recorded and both models were found to experience instability when the wetted surface remained close to the keel (the waterplane became narrow). Katayama *et al.* developed a sectional roll restoring moment equation based on formulas proposed by Smiley (1952) and Payne (1994) that showed the roll restoring force decreased due to the point of action approaching the keel line.

Lewandowski (1996) developed the roll restoring moment for a planing hull as a static restoring moment combined with a dynamic restoring moment. He found that the roll stability of a hard-chine planing craft was generally increased by dynamic effects for vertical center of gravity positions below a critical value. This paper compares the experimental results for roll restoring moment with predictions based on the method given in Lewandowski (1996).

Testing was done in the United States Naval Academy Hydromechanics Laboratory's 380 foot tow tank. A prismatic wooden model with a deadrise of 20° was fixed in pitch, heave, heel, and sway and towed through a range of constant speeds in calm water. The test matrix consisted of a series of static tests with the model fixed in heel. The heave (lift), sway, and roll moment were recorded and underwater photographs taken for each run. This paper compares the roll moment measured during the static heel tests with different predictions for roll moment based on heel angle.

Table 1: Characteristics of Planing Hull Model.

Length on the waterline	1.524 m (5 ft)					
Chine beam	0.448 m (1.47 ft)					
Deadrise	20°					
KG	0.134 m (0.44 ft)					
Displacement	13.5 kg (29.8 lb)			26.5 kg (58.4 lb)		
LCG (fwd transom)	0.305 m (1.0 ft)			0.594 m (1.95 ft)		
Model Speeds, Fr	2.9	3.6	4.3	2.9	3.6	4.3
Trim, τ	3.8°	3.3°	2.9°	4°	3.3°	2.7°
Transom Depth (relative to calm water)	0.09 m (0.30 ft)	0.08 m (0.25 ft)	0.07 m (0.22 ft)	0.06 m (0.19 ft)	0.05 m (0.16 ft)	0.04 m (0.15 ft)
Keel Wetted Length/Beam ($\phi = 0^\circ$)	1.91	1.95	1.88	2.82	2.60	2.64
Chine Wetted Length/Beam ($\phi = 0^\circ$)	0.18	0.0	0.0	1.30	0.98	0.65

2. PREDICTIONS FOR ROLL RESTORING MOMENT

Lewandowski (1996) developed the roll restoring moment from an evaluation of the roll moment due to hydrostatic forces and the moment due to dynamic lift. The static restoring moment is based on the transverse waterplane area moment of inertia, the vertical distance from the assumed center of buoyancy to the center of gravity, and the buoyancy force due to the “underwater” volume while planing. Since these quantities vary with speed, the static restoring moment is speed dependent and generally decreases with increasing speed. The dynamic roll restoring moment is based on the empirically determined dynamic lift from Brown (1971). This dynamic lift is used to compute the contributions of the port and starboard sides using an “effective” deadrise angle. The “effective” deadrise angle is the hull deadrise angle minus the roll angle on the side rolled down and the hull deadrise angle plus the roll angle on the side rolled up. The center of pressure is determined from Smiley (1952).

2.1 Static Roll Restoring Moment

For a planing hull, the static restoring moment is difficult to predict or measure



experimentally. For a displacement hull, the roll restoring moment is due to the hydrostatic pressure acting on the underwater portion of the hull. For a planing hull there is an “underwater” portion that can be defined relative to the undisturbed free surface. However, because of water pile-up (where the free surface encounters the forward portion of the hull) and separation of the water flow at the chines and transom, the wetted surface is different than predicted by the intersection of the hull and the undisturbed free surface. In addition, the pressure acting on the wetted surface cannot be considered simply hydrostatic. Therefore, it is difficult to determine how the forces acting on the wetted surface relate to a traditional roll restoring moment for a displacement hull.

Lewandowski Method for Prediction of Static Restoring Moment

Lewandowski (1996) develops a “static” roll restoring moment by considering the waterplane area created from the planing wetted surface. He assumes the roll restoring moment behaves linearly with roll angle, such that the static contribution to the roll restoring moment is

$$M_{static}^* = (-\rho g I_T + BG \cdot \Delta s) \cdot \varphi. \quad (1)$$

I_T is the transverse waterplane area moment of inertia, BG is the vertical distance from the assumed center of buoyancy of the “underwater” volume to the center of gravity, Δ_s is the “static lift” due to the hydrostatic pressure on the hull, and φ is the heel angle. The hydrostatic pressure is assumed to act on the full wetted surface area of the hull. The transverse waterplane area moment of inertia for a prismatic hull is

$$I_T = \frac{b^3}{48} (L_k + 3L_c) \quad (2)$$

where L_k and L_c are the wetted keel and chine lengths, respectively, and b is the average wetted chine beam. The vertical distance from

the “underwater” volume to the center of gravity is

$$BG = KG - \frac{b}{6} \tan \beta \left(1 + \frac{L_c}{L_k} \right) \quad (3)$$

Lewandowski uses an expression for the “static lift” from Brown (1971) that is based on integrating the hydrostatic pressure acting on the equivalent wetted surface for a stationary hull,

$$\Delta_s \approx 0.25 \rho g b^3 \lambda^2 \sin 2\tau \quad (4)$$

where τ is the trim angle and λ is the mean wetted length to beam ratio

$$\lambda \equiv \frac{L_k + L_c}{2b}. \quad (5)$$

The transom is not wet as the water breaks clear and, therefore, pressure acting on the transom is atmospheric. This is expected to reduce the static pressure forces on the defined underwater hull and Brown (1971) empirically found a factor of 0.624 to be appropriate. Thus, the equation for the static roll restoring moment is

$$M_{static} = 0.624 \cdot M_{static}^* \quad (6)$$

Underwater Volume based on Flat Water Surface Intersection with the Planing Hull (UVFWS)

As mentioned, the actual pressure acting on the wetted surface is not the same as the hydrostatic pressure acting on the hull of a displacement vessel. The expression developed above is an estimate of the equivalent hydrostatic lift determined from treating the wetted surface on the planing hull the same as the wetted surface on a displacement hull and applying an empirically determined reduction to account for the dry transom. For comparison, consider the same trim and heave as the hull at planing speed, but the roll restoring moment is evaluated assuming the hull is stationary. In other words, the underwater is determined from the intersection



of the flat water surface and the planing hull (referred in the figures as UVFWS – Underwater Volume based on Flat Water Surface). The sinkage and trim of the model is held fixed as the values for zero roll, then rolled about an axis through the center of gravity and parallel to the keel. If the hull is not moving, there is no water pile-up and the transom is wet. The displacement of this imaginary stationary hull would not equal the weight of the planing craft, but hydrostatic roll restoring moment at each angle of heel can be determined. This static roll restoring moment can be compared with the estimated “static” roll restoring moment determined from the dynamic wetted lengths as explained above.

2.2 Dynamic Roll Restoring Moment

The dynamic roll restoring moment is due to the dynamic lift forces acting on the planing surface. The magnitude of the lift force differs on the port and starboard because of the roll angle. The dynamic nature of the pressure force complicates the calculation of the location of this force.

Lewandowski Method for Prediction of Dynamic Restoring Moment

Lewandowski (1996) estimates these lift forces using empirical relationships developed by Brown (1971). To determine the difference in lift forces on the starboard and port sides when the hull begins to heel, the “effective” deadrise angle is used (see Figure 1),

$$\beta_{e,starboard} = \beta - \varphi; \beta_{e,port} = \beta + \varphi. \quad (7)$$

The mean wetted length for the port and starboard sides depends on the chine wetted length. When the hull heels the chine wetted length changes, so the mean wetted length becomes different for the port and starboard sides. Savitsky (1964) determined the chine and keel wetted lengths to be related by the chine wetted beam, the deadrise angle and the trim angle.

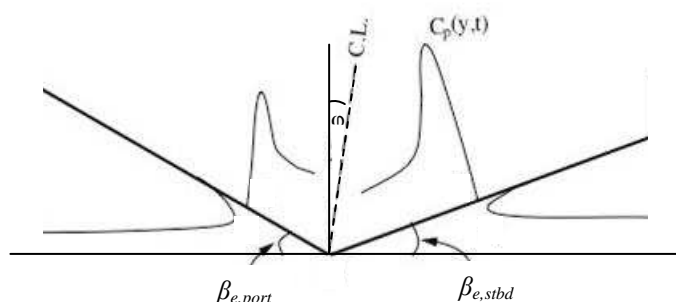


Figure 1: Sketch Showing “Effective” Deadrise of Prismatic Hull Heeled at Angle φ .

Lewandowski give the dynamic lift for the port side as

$$F_{d,port} = \frac{1}{2} \rho U^2 b^2 \cdot \sin 2\tau \cdot \left[\frac{\pi}{4} (1 - \sin \beta_{e,port}) \cos \tau \frac{\lambda_{port}}{1 + \lambda_{port}} + \frac{1.33}{4} \lambda_{port} \cos \tau \sin 2\tau \cos \beta_{e,port} \right] \quad (8)$$

and the starboard side dynamic lift can be found in the same way. To find the dynamic roll restoring moment, the location of the lift force with respect to the center of gravity needs to be determined. Lewandowski uses an expression from Smiley (1952) for the location of dynamic pressure on a prismatic hull. Lewandowski gives the dynamic roll restoring moment about the center of gravity as

$$M_{dynamic} = (F_{d,port} - F_{d,starboard}) \cdot \left(0.8 \cdot \frac{\pi b}{8 \cos \beta} - KG \cdot \sin \beta \right). \quad (9)$$

Wagner Method for Prediction of Dynamic Restoring Moment

Another way to determine the dynamic roll restoring moment is to consider the dynamic lift force predicted using Wagner’s two-dimensional water impact method (Wagner, 1932) combined with a 2.5D ($2D + t$) theory presented in Faltinsen (2005). Wagner’s method results in most of the lift force occurring in the wetted region where the chines are dry. In the aft portion of the hull, where the

chines are wet, the dynamic lift force is small compared with the forward portion of the wetted surface. For this paper, only the lift generated in the “chines-dry” portion of the hull will be included. Wagner’s method provides an equation for the dynamic pressure due to slamming of a two-dimensional wedge impacting the calm water surface as,

$$p - p_a = \rho V \frac{c}{(c^2 - y^2)^{1/2}} \frac{dc}{dt} + \rho \frac{dV}{dt} (c^2 - y^2)^{1/2} \quad (10)$$

where V is the vertical velocity of the wedge impacting the water surface, c is the instantaneous intersection between the free surface and the deadrise surface, and y is the transverse location where the pressure is occurring. Figure 2 shows a physical representation for the variables c and V .

Figure 2: Sketch Showing Variables c and V from Equation (10).

For a symmetric impact with a wedge of deadrise angle, β , falling with constant vertical velocity, V , point c is determined as a function of time as

$$c(t) = \frac{\pi V t}{2 \tan \beta} \quad (11)$$

A two-dimensional wedge impacting a calm surface can be used to solve the dynamic lift on a prismatic planing surface using a method described as 2D + t by Faltinsen (2005). The falling wedge in time represents the sections of the prismatic hull in space. The vertical fall velocity, V , and time for the impacting wedge relates to the forward velocity, U , and longitudinal position for the prismatic hull as

$$Vt = (U\tau) \left(\frac{x}{U} \right) = \tau x \quad (12)$$

where τ is the trim angle of the prismatic hull and x is the longitudinal position along the hull. Following the procedure described by Faltinsen (2005) to determine the steady heel restoring moment due to dynamic forces, the roll

restoring moment about the center of gravity due to the hydrodynamic pressure is given by

$$M_{dynamic} = \rho U^2 b^3 \tau \left[\frac{1}{24} \left(\frac{1}{\cos^2 \beta_{e, stbd}} - \frac{1}{\cos^2 \beta_{e, port}} \right) - \frac{KG}{b} \left(\frac{\pi}{16} \right) \left(\frac{\sin \beta}{\cos \beta_{e, stbd}} - \frac{\sin \beta}{\cos \beta_{e, port}} \right) \right] \quad (13)$$

where $\beta_{e, port}$ and $\beta_{e, stbd}$ are defined as above.

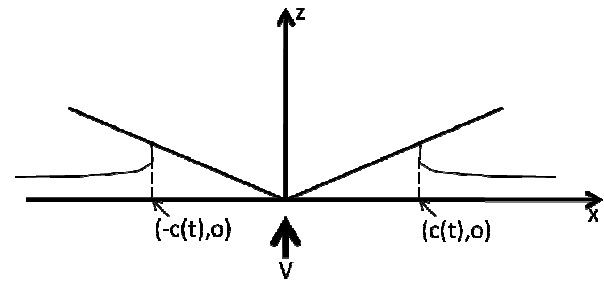


Figure 2: Sketch Showing Variables c and V from Equation (10).

Total Restoring Moment

The total roll restoring moment is a combination of the static and dynamic lift contributions. The total roll restoring moment can also be estimated by combining the dynamic lift predicted by Wagner’s method and the 2D + t theory with the static roll moment predicted using basic hydrostatic analysis with the trim and heave the same as for the planing condition (UVFWS).

3. ANALYTICAL AND EXPERIMENTAL COMPARISONS

Plot (a) in Figures 3 through 8 compares the Lewandowski static restoring moment and the restoring moment for the model in calm water using the planing trim and heave (UVFWS). For the lighter displacement, the Lewandowski static moment, which uses the dynamic wetted lengths, gives very similar results to the UVFWS static prediction based on zero hull speed and calm water. For the heavier displacement the static roll moment predicted by Lewandowski’s method is close to double



the prediction based on a stationary hull in calm water (UVFWS). This implies that the reduction factor of 0.624 for the dry transom reduces the hydrostatic lift less than the increase in hydrostatic lift due to the water pile-up. The total restoring moment measured experimentally is included in all the plots. In Figure 4(a), the static roll restoring moment predicted using Lewandowski's method accounts for almost this entire experimentally measured roll restoring moment.

Plot (b) in Figures 3 through 8 compares the dynamic roll restoring moment predicted from Lewandowski's method with the dynamic roll restoring moment predicted from Wagner's method. Lewandowski's method prediction of the dynamic moment contribution is consistently greater than the total measured moment at all roll angles and for both displacements. The method is particularly inaccurate at higher angles, at the higher model speeds, and for the lighter displacement. In these cases, the Lewandowski method predicts a sharp change in slope around 20° (the model's deadrise angle). The dynamic roll restoring moment from the Wagner method shows a similar trend to the measured moment, although is less than the total moment in all conditions. The two methods (Lewandowski and Wagner) are for constant deadrise hulls and once the chine is lower than the keel (i.e. when the roll angle is greater than 20°), these methods are no longer valid. They are included in the plots simply for reference. However, the Lewandowski method is showing difficulties at roll angles much lower than 20° . This dynamic roll moment prediction becomes a larger percentage of the total roll moment as the model speed increases, as would be expected.

Plot (c) in Figures 3 through 8 shows the experimentally measured roll moment compared with the combination of the static and dynamic restoring moments shown in plots (a) and (b). The total roll restoring moment predicted using Lewandowski's method over-predicts the roll moment, although this is primarily due to the dynamic component. The

dynamic contribution is much larger than the static contribution for all cases. For comparison, the dynamic roll restoring moment calculated from Wagner's method is combined with the roll restoring moment determined for the stationary hull (UVFWS). Compared with the Lewandowski method, this approximation gives reasonable predictions for the total roll restoring moment. The predicted roll moment curve has more curvature with roll angle than the measured roll moment. The approximation tends to slightly under-predict the total roll moment for the heavier displacement. For the lighter displacement, this combination of dynamic and static roll restoring moment tends to under-predict the moment at small angles and over-predict the total moment at the larger angles.

Overall, the predictions based on the equations from Lewandowski significantly over-predict the roll restoring moment while a combination of dynamic roll restoring moment based on Wagner's method and a hydrostatic analysis of roll restoring moment provides a more reasonable prediction.

4. CONCLUSIONS

The prediction method for roll restoring moment developed by Lewandowski (1996) significantly over-predicts the total roll restoring moment. The static moment predicted by Lewandowski's method is similar to the hydrostatic roll moment predicted by the planing hull's trim and heave position (assuming the vessel was not actually moving) for the lighter displacement model. However, for the heavier displacement model the Lewandowski equation predicts a "static" roll restoring moment that is significantly greater than the equivalent restoring moment from hydrostatic analysis. The comparison with the UVFWS static analysis indicates that the effect of the water pile-up is greater than the reduction in pressure due to the dry transom. The Lewandowski static roll restoring moment is based on the transverse waterplane area



moment of inertia, the vertical distance from the assumed center of buoyancy to the center of gravity, and the buoyancy force due to the “underwater” volume while planing. All of these quantities are evaluated assuming a symmetric underwater shape (where the starboard chine wetted length is equal to the port chine wetted length). However, the chine wetted lengths change as the hull heels and the high side wetted length can go to zero while the low side wetted length continues to increase with roll angle. Therefore, it might be possible to improve on this formulation if the actual underwater volume (based on the dynamic wetted lengths) was used.

The Lewandowski method for dynamic roll moment does account for the different chine wetted lengths when determining the dynamic lift on each side of the hull. The method assumes the keel wetted length does not change with roll angle, but measurements of the keel wetted length during the experiment showed this to be a reasonable assumption. Lewandowski’s method assumes the center of pressure does not change with roll angle (the actual deadrise rather than the effective deadrise is used for calculating the lever arm). This is clearly not valid at the larger roll angles. Similarly, the wetted surface is assumed to reach the chine on both sides and this was not the case for the port side (with starboard heel) for the heavier displacement at large heel angles nor was the case at any heel angles for the lighter displacement. There is a large difference in magnitude between the dynamic restoring moment predicted using the Wagner method and the Lewandowski prediction. The Wagner prediction is much more reasonable when compared with the experimental data.

It is interesting to note that the combination of a purely hydrostatic analysis of the hull in the planing heave and trim condition combined with the prediction of dynamic restoring moment derived from Wagner’s method gives reasonable agreement with the experimental results. This indicates the contribution from

hydrostatics is less than expected from the wetted surface area. It is likely the actual static roll moment contribution for the planing hull is even less than the purely hydrostatic analysis predicts since the Wagner dynamic moment prediction is expected to under-predict the roll moment. It is clear the interaction of the hydrostatic and hydrodynamic pressure forces acting on a planing hull is not fully understood. This remains an important area for future research.

5. ACKNOWLEDGEMENTS

The author wishes to acknowledge the work William Beaver and Dan Rhodes, of the Hydromechanics Laboratory at the United States Naval Academy, who put considerable effort and talent into construction of the Forced Roll Mechanism and data collection for this ambitious project. The support of the Office of Naval Research through grant N0001411WX21106 is gratefully acknowledged.

6. REFERENCES

Blount, D. L. and Codega, L. T., “Dynamic Stability of Planing Boats”, Marine Technology, Vol. 29, No. 1, Jan 1992, pp. 40-12.

Brown, P.W. “An Experimental and Theoretical Study of Planing Surfaces with Trim Flaps”, Davidson Laboratory Report SIT-DL-71-1463, Stevens Institute of Technology, Hoboken, N.J., 1971.

Codega, L. and Lewis, J., “A Case Study of Dynamic Instability in a Planing Hull”, Marine Technology, Vol. 24, No. 2, April 1987, pp. 143-163.

Faltinsen, O., (2005) Hydrodynamics of High-Speed Marine Vehicles, New York, N.Y., Cambridge University Press, pp. 1-454.



Ikeda, Y. and Katayama, T., “Stability of High Speed Craft”, Contemporary Ideas on Ship Stability, 2000, p. 401-409.

Katayama, T., Fujimoto, M., and Ikeda, Y., “A Study on Transverse Stability Loss of Planing Craft at Super High Forward Speed”, International Shipbuilding Progress, Vol. 54, 2007, pp. 365-377.

Lewandowski, E.M., “Prediction of the Dynamic Roll Stability of Hard-Chine Planing Craft”, Journal of Ship Research, Vol. 40, No. 2, June 1996, pp. 144-148.

Payne, P.R., “Recent Developments in ‘Added-Mass’ Planing Theory”, Ocean Engineering, Vol. 21, No. 3, 1994, pp. 257-309.

Ranzenbach, R. and Bowles, J., “Hull Forms with Low Cruise Speed Resistance and High Speed Dynamic Stability – Experiments and Computations”, *Proceedings of the 29th American Towing Tank Conference*, Annapolis, MD, August 2010, pp. 251-259.

Savitsky, D., “Hydrodynamic Design of Planing Hulls”, Marine Technology, Vol. 1, No. 1, Oct 1964, pp. 71-95.

Smiley, R.F., “A Theoretical and Experimental Investigation of the Effects of Yaw on Pressures, Forces, and Moments During Seaplane Landing and Planing”, NACA Technical Note 2817, 1952.

Wagner, H., “The Landing of Seaplanes”, NACA TN 622, 1932.

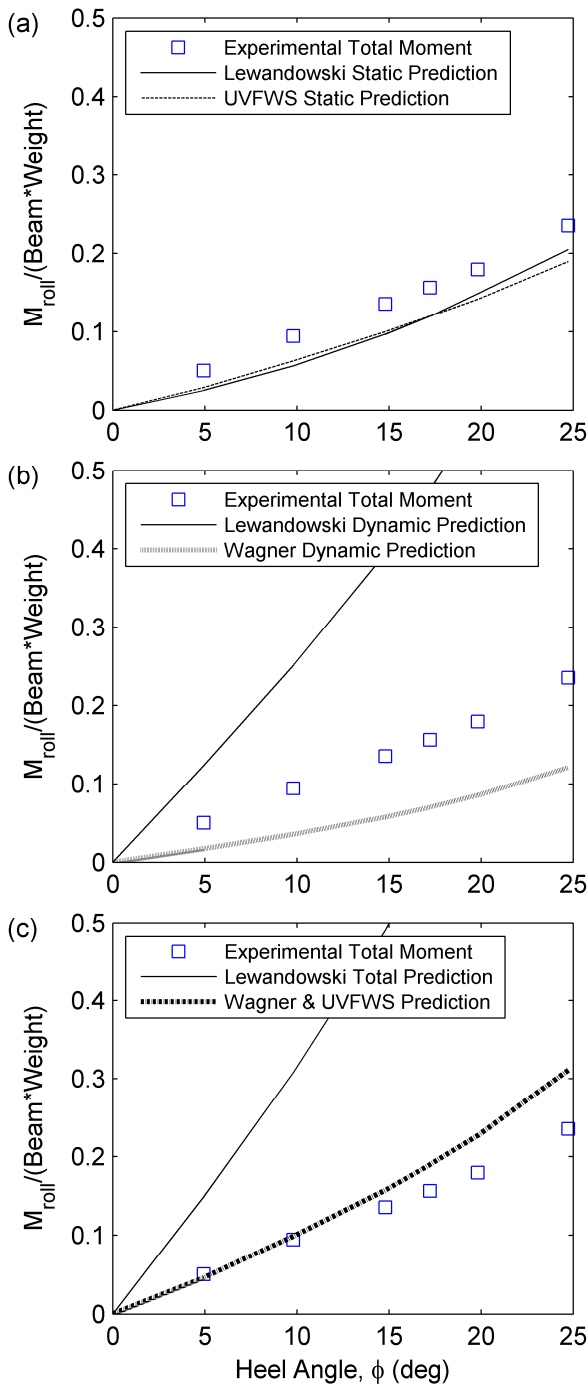


Figure 3: Roll Restoring Moment Predictions and Measurements for the Lighter Displacement at a Beam Froude Number of 2.9

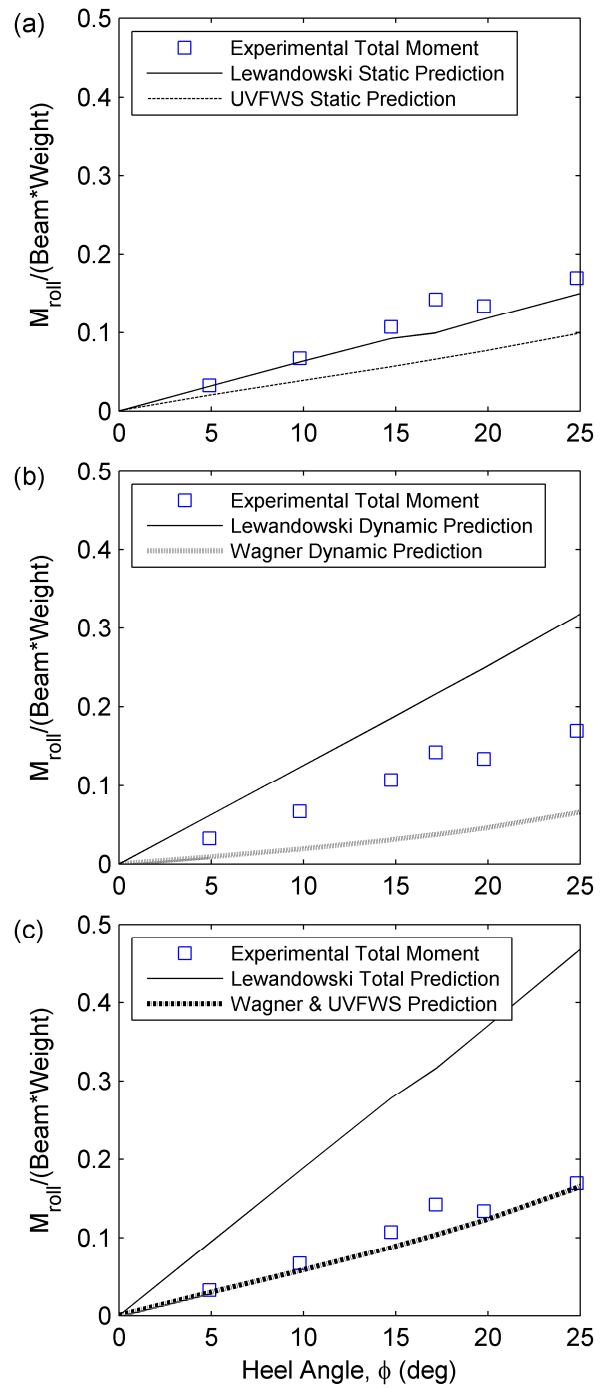


Figure 4: Roll Restoring Moment Predictions and Measurements for the Heavier Displacement at a Beam Froude Number of 2.9

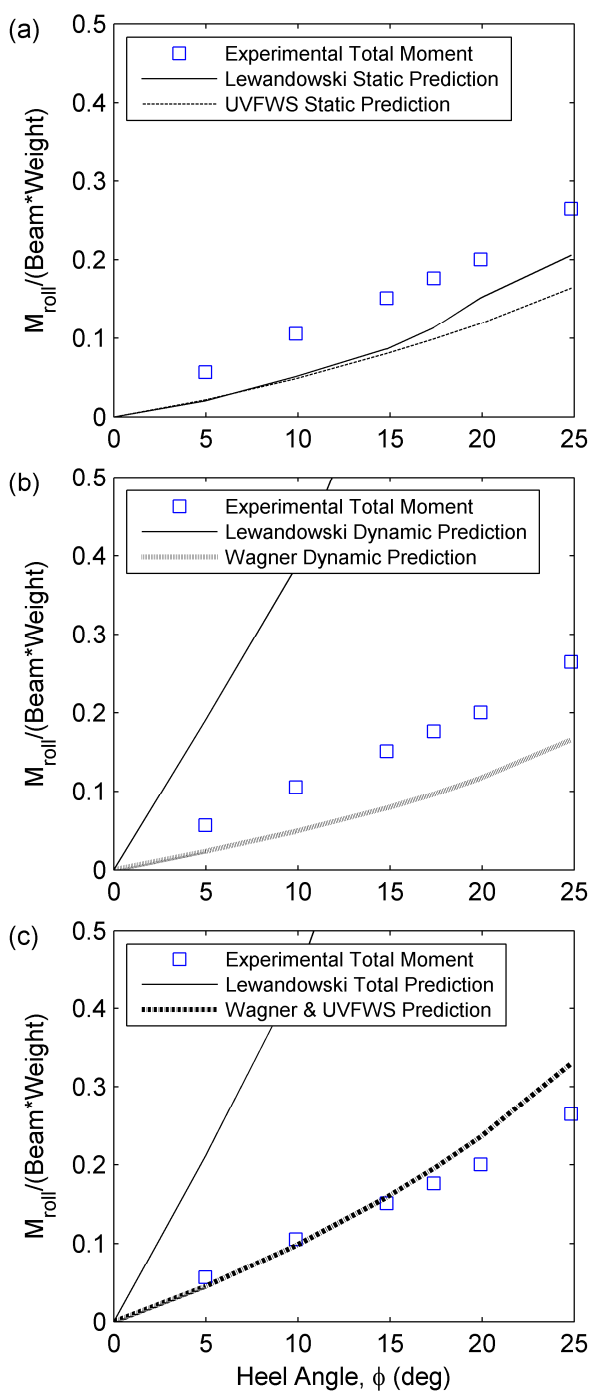


Figure 5: Roll Restoring Moment Predictions and Measurements for the Lighter Displacement at a Beam Froude Number of 3.6

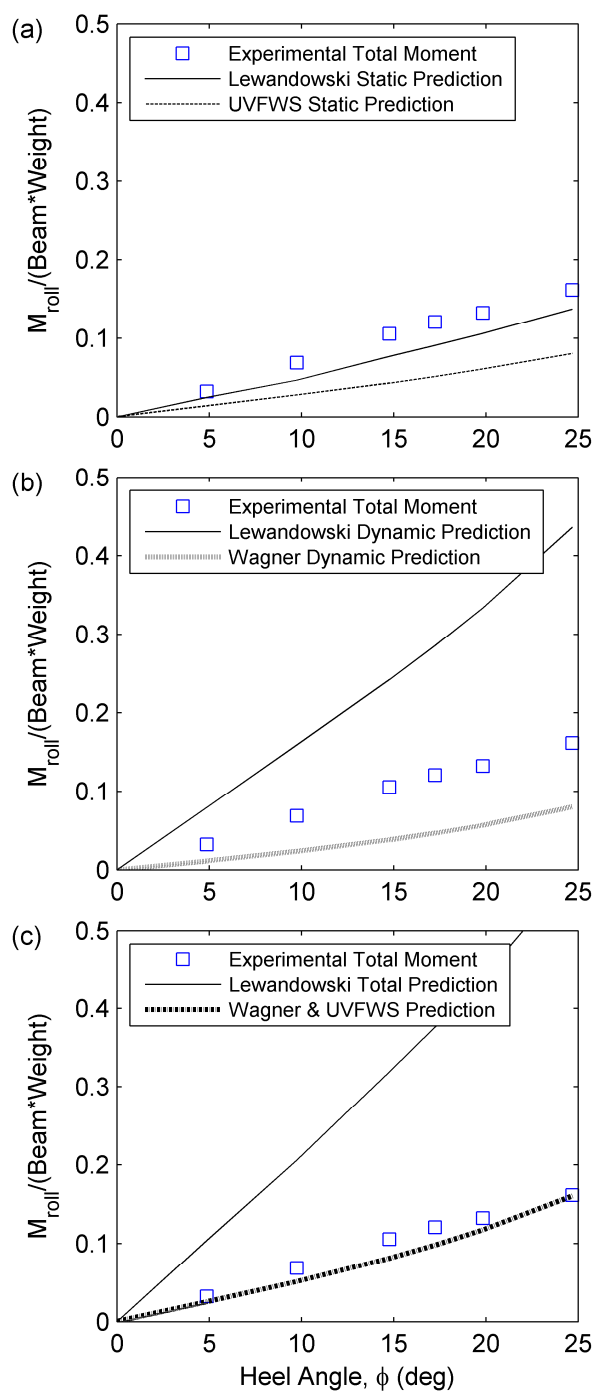


Figure 6: Roll Restoring Moment Predictions and Measurements for the Heavier Displacement at a Beam Froude Number of 3.6

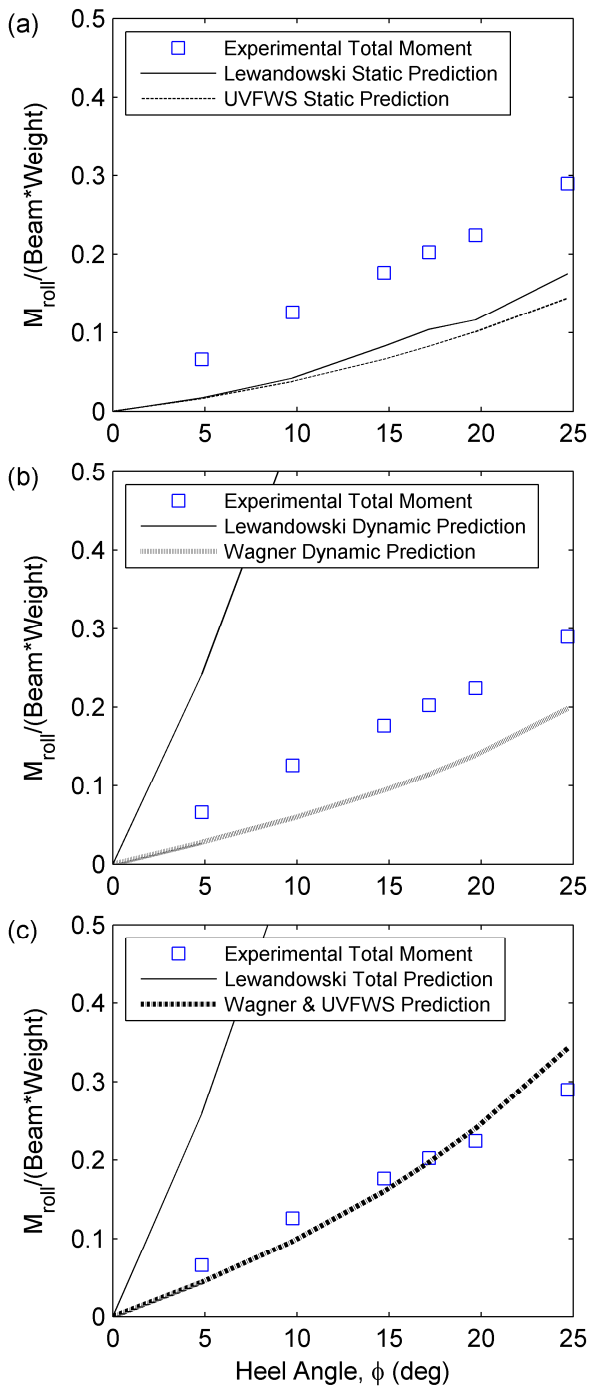


Figure 7: Roll Restoring Moment Predictions and Measurements for the Heavier Displacement at a Beam Froude Number of 4.3

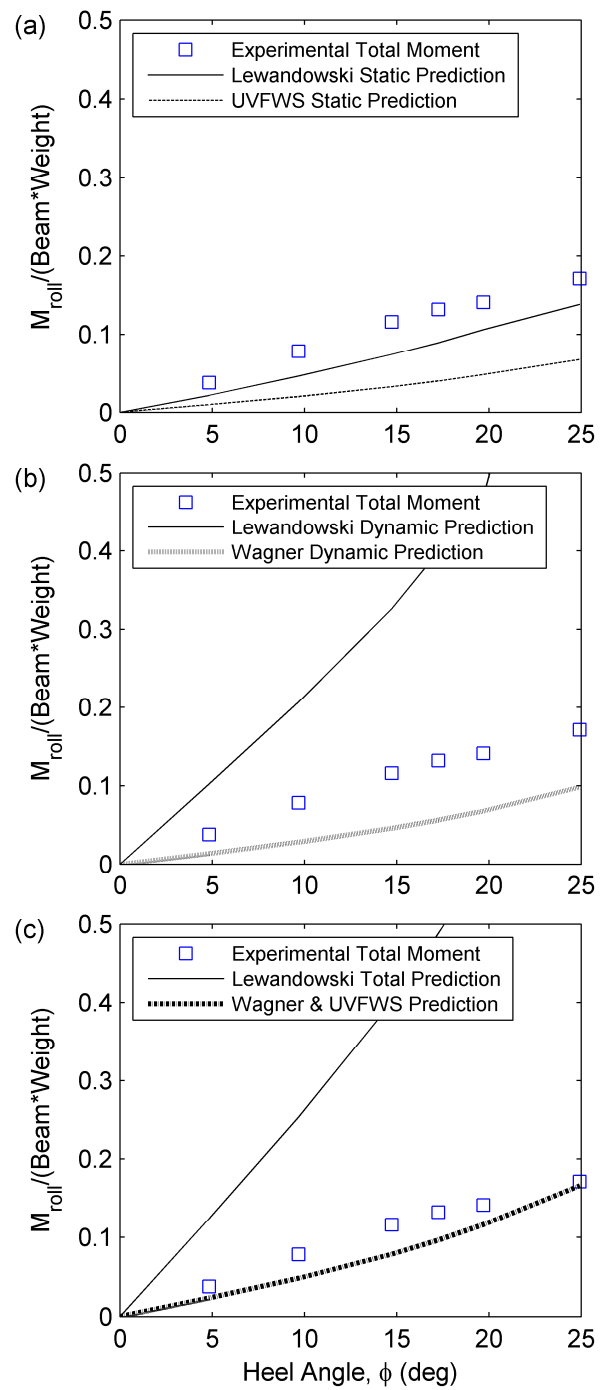


Figure 8: Roll Restoring Moment Predictions and Measurements for the Lighter Displacement at a Beam Froude Number of 4.3





Bow Diving of Semi-Swath Vessel in Following Seas and Fins Stabilizer Effect

Adi Maimun, *Department of Marine Technology, Universiti Teknologi Malaysia*, adi@fkm.utm.my
Rahimuddin, *Department of Marine Technology, Universiti Teknologi Malaysia & Department of Naval Architecture and Marine Engineering, Universita Hasanuddin. Ministry of Science, Technology & Innovation, Malaysia, Ministry of Indonesian Higher Education, and Government of Province Sulawesi Selatan, Indonesia under Human Resource Development Program,*

rahimnav@gmail.com

Muhamad Pauzi Abdul Ghani, *Department of Marine Technology, Universiti Teknologi Malaysia,*
pauziir@gmail.com

Andi Haris Muhammad, *Department of Naval Architecture and Marine Engineering, Universita Hasanuddin,* andi_haris@ft.unhas.ac.id

ABSTRACT

In this research, the performance of a Semi-SWATH (Small Waterplane Area) vessel design was evaluated in following seas condition. In sea condition, a semi-SWATH vessel may have bow-dive when her amidships was just passing the crest and her speed was slightly higher than the wave celerity, and the wavelength slightly longer than her length. The bow-dive was frequently accompanied with surf condition. The critical situation was mainly due to the low water plane area and buoyancy at the bow. A numerical simulation program in 3DOF (surge, heave and pitch) with time varying model equation was developed. Using the simulation program, this study focuses on the bow-dive aspect and the effects of fins stabilizer; fixed and active. The results of the numerical simulations were compared with those of model tests carried out in a 120m long towing tank at Marine Laboratory of Universiti Teknologi Malaysia (UTM). Results from numerical simulations showed that bow-dive of Semi-SWATH vessel could be effectively reduced by active fins stabilizer.

Keywords: *bow-dive, semi-SWATH, fin stabilizer.*

1. INTRODUCTION

In sea waves a ship's dynamics is normally based on periodic - like motions. In following waves, the ship may encounter some conditions, such as; entrapment, surfing and bow or deck diving. Entrapment occurs when the ship attempts to move faster than the dominant waves or swell but she is unable do so. While surf-riding occurs when a ship in high waves, in following or quartering seas, has almost equal speed to the dominant wave's celerity and accelerating rapidly down-wave.

Bow diving occurs when a high speed ship buries its bow in a wave. Although taking water over the bow is common in all ships, bow diving is notable for the fact that it causes all ways to be lost, the ship experiencing a severe bow-down pitch and becoming in undated forward. It is particularly severe for ships such as catamaran with slender cross structure and limited buoyancy forward, occurs especially when the ship is going faster than the dominant waves. These conditions are important for the safety of the ship at sea, (Dand 2005). In high sea, multihull ship such as catamaran tends having surf-riding and may have a bow diving effect sailing in following sea (Dand 2006). For Semi-SWATH, the



tendency of occurring bow diving may increase with hers more slender cross deck and limited fore hull buoyancy than catamaran. Otherwise, restoring force is an important aspect of the occurring of bow-diving, (Katayama, Tamura et al. 2003).

In condition of ship having bow-diving in high waves in following seas, it always proceeded by surf-riding indicated by acceleration of advancing motion in the wave-down (Matsuda, Hasimoto et al. 2004). The motion increases inertial mass of ship surfing to the trough, hitting the wave-up and have a bow-diving. The effect of this condition may be reduced by reducing the revolution of propeller. However, once a ship captured by a wave, reducing the revolution of propeller is not always be a good measure to escape from the surf-riding condition, (Umeda 1990).

An early mathematical model for twin-hull with integration of fin stabilizer was introduced in 1974 by Lee and Martin. The model based on the procedure of selection of most desirable fin size to ensure the stability and adequate damping for heave and pitch, and to maintain the natural periods. The model didn't take into account the effect of activation fin (Lee and Martin 1974). Later, Mc Creight and Stahl develop the model by integrating active fin stabilizer and obtain the fin combination based on semi empirical lift and drag coefficients, (McCreight and Stahl 1983).

In twin-hull ship, a design of semi-SWATH with fin stabilizer at fore and aft end of hulls were used to decrease the effect of porpoising affected by the increasing speed in head seas. However, in following seas, the fin may decrease the effect of having surf-riding and bow-diving effect. The fins act as a wing-foil aim to increase the lift and damping force in the sea.

Over past thirty-five years, research on fin applications mostly to maintain the roll motion. Along with an increase of ship speed, the dynamic of vertical motion increased. SWATH ship indicated has more dynamic motion with

the increase of speed even porpoising phenomenon occurs as a drawback of the ship. However, application of the fin stabilizer can increase the ship damping to restrain the effect of external forces and moment, (Bhattacharya 1978; Djackov 2005).

In this paper, the dynamic motion of semi-SWATH in following seas and the effects of fins stabilizer were studied in domain of simulation. The ship behaviour in relation of bow-dive and the wave parameters were investigated. The initial condition that can lead to an oscillatory motion used was a regular wave with ratios of wave and ship parameters.

2. MATHEMATICAL MODEL

2.1 Ship Motion Model

The mathematical model of ship motion was modelled in 3DOF of surge, heave, and pitch motion. The ship motion can be expressed in the coordinate space with each translational and rotational motion, using the rules of the three axis of right hand. Ship movements generally translated in two coordinates of space systems. One fixed reference coordinate system on earth (OXYZ) and one moving coordinate system is placed on the ship ($Ox_s Y_s Z_s$). The fixed coordinate system located at a calm water surface with Z axis pointing upwards. Moving coordinate system is located at the centre of gravity, moving with speed V_s .

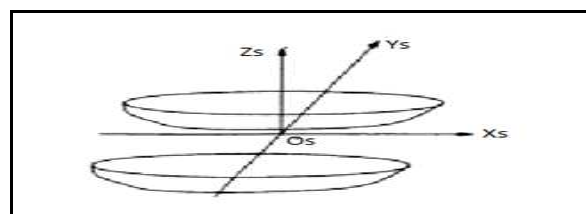


Figure 1: The origin coordinate axis of multihull ship at center of gravity.

The harmonic motions of the ship in longitudinal and vertical motions were considered. Even though the motions have a cross effect on each other, the coupling between them is negligible (Umeda 1990).

However, between the vertical motions of heave and pitch, the coupling effect is significant (Lloyd 1998).

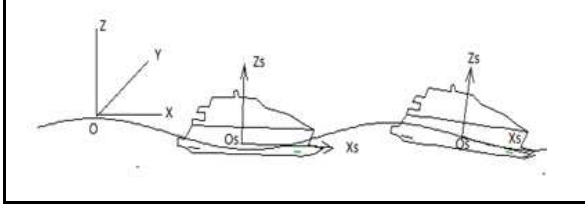


Figure 2: Fixed and moving coordinate axis.

The motions were expressed in a second order of linear differential equations, m is mass, a is added mass, b is damping and c is restoring coefficients. Index $1,3,5$ indicate surge, heave and pitch respectively and F is force or moment of wave as in following form;

$$\begin{aligned} (a_{11} + m)\ddot{x}_1 + [R(u) - T(u, n)] &= F_1^w - mg \sin \theta \\ (a_{33} + m)\ddot{x}_3 + b_{33}\dot{x}_3 + c_{33}x_3 + a_{35}\ddot{x}_5 + b_{35}\dot{x}_5 + c_{33}x_5 \dots & \\ = F_3 + mg \cos \theta & \\ a_{53}\ddot{x}_3 + b_{53}\dot{x}_3 + c_{53}x_3 + (a_{55} + I_{55})\ddot{x}_5 + b_{55}\dot{x}_5 + c_{55}x_5 \dots & \\ = F_5 - x_5 mg \cos \theta & \end{aligned} \quad (1)$$

Surge motion is a longitudinal motion superimposed on the propeller thrust, hull resistance, and harmonic incident wave force of Froude-Krylov, (Umeda 1990; Wu, Spyrou et al. 2010; Spyrou and Tingkas 2011). In this paper, the vertical motion of heave and pitch by the effect of ship weight in wave-down and wave-up in following sea considered affect the harmonic motion and the encounter frequency since there a surge motion change. The model was integrated with fins stabilizer, the resistance and propeller thrust into the equations (1) as follows;

$$\begin{aligned} (a_{11} + m)\ddot{x}_1 + \{[3r_3c^2 + 2(r_2 - \tau_2)c + r_1] - \tau_1 n\}\dot{x}_1 \dots & \\ + [3r_3c + (r_2 - \tau_2)]\dot{x}_1^2 + r_3\dot{x}_1^3 = (\tau_2c^2 + \tau_1cn + \tau_0n^2) \dots & \\ - (r_1c + r_2c^2 + r_3c^3) - f \sin(kx_1) - mg \sin x_5 + F_1^f & \\ (a_{33} + m + a_{33}^f + m_f)\ddot{x}_3 + (b_{33} + b_f)\dot{x}_3 + c_{33}x_3 \dots & \\ + (a_{35} - l(m_f + a_{33}^f))\ddot{x}_5 + (b_{35} - b_f)\dot{x}_5 + (c_{35} + c_{35}^f)x_5 \dots & \\ = F_3^w + F_3^f + mg \cos x_5 & \end{aligned} \quad (2.a)$$

(2.b)

$$\begin{aligned} (a_{53} - l(m_f + a_{33}^f))\ddot{x}_3 + (b_{53} - b_f)\dot{x}_3 + c_{53}x_3 + (a_{55} + I_{55} \dots & \\ + l^2(m_f + a_{33}^f))\ddot{x}_5 + (b_{55} + b_f)\dot{x}_5 + (c_{55} - c_{55}^f)x_5 \dots & \\ = F_5^w + F_5^f - x_{5(G)}mg \cos x_5 & \end{aligned} \quad (2.c)$$

superscript of w, f, p indicate wave, fin and propeller respectively.

$$\begin{aligned} R(u) &= r_1u + r_2u^2 + r_3u^3 \\ T(u, n) &= (1 - t_p)\rho n^2 D_p^4 K_T(u, n) \end{aligned} \quad (3)$$

$$\begin{aligned} K_T(u, n) &= K_0 + K_1 J(u, n) + K_2 J^2(u, n) \\ J(u, n) &= \frac{u(1 - w_p)}{n D_p} \end{aligned} \quad (4)$$

$$\begin{aligned} T(u, n) &= \tau_0 n^2 + \tau_1 u n + \tau_2 u^2 \\ \tau_0 &= \kappa_0 (1 - t_p) \rho D_p^4 \quad \tau_1 = \kappa_1 (1 - t_p) (1 - w_p) \rho D_p^3 \\ \tau_2 &= \kappa_2 (1 - t_p) (1 - w_p)^2 \rho D_p^2 \end{aligned} \quad (5)$$

The ship resistance equation is a polynomial, arranged from the resistance test data as a function of the ship speed u . The thrust propeller obtained using the Wageningen B-series propeller data, (Bernitsas, Ray et al. 1981). The thrust influenced by velocity of water incoming the propeller, number of revolution n , diameter D_p , and advanced coefficients J , (Wu, Spyrou et al. 2010). The surge speed \dot{x}_1 is the relative of ship velocity u and the wave celerity c written as $\dot{x}_1 = u - c$ Moreover, the water velocity at propeller by integrating the water perturbation might be obtained as follows, (Spyrou and Tingkas 2011);

$$\begin{aligned} u &\approx u_0 + u_{(p)} \\ u &\approx u_0 + \frac{1}{D_p} \int_{D_p} k \zeta_a V_w e^{-kz} \cos k(x - V_w t) dz \end{aligned}$$

The model in equation (2) can be simplified in state space form as shown below;

$$\begin{aligned} \mathbf{M}(t) \dot{\mathbf{x}}(t) &= \mathbf{A}(t) \mathbf{x}(t) + \mathbf{B}(t) \mathbf{u}(t) \\ \dot{\mathbf{x}}(t) &= \mathbf{M}^{-1}(t) \mathbf{A}(t) \mathbf{x}(t) + \mathbf{M}^{-1}(t) \mathbf{B}(t) \mathbf{u}(t) \\ \dot{\mathbf{x}}(t) &= \mathbf{A}_t(t) \mathbf{x}(t) + \mathbf{B}_t(t) \mathbf{u}(t) \\ \mathbf{y}(t) &= \mathbf{C}(t) \mathbf{x}(t) \end{aligned} \quad (6)$$



\mathbf{M} is the added mass matrix, \mathbf{A} is a variable state matrix consists of damping and stiff coefficients, \mathbf{B} is a matrix of input coefficients, \mathbf{u} is a vector of input system consists of external force and moment, \mathbf{x} is a vector of state variable, and \mathbf{y} is vector of output variable. Solution of the state space form (6) can be obtained as follows;

$$\mathbf{x}(t) = e^{\mathbf{A}(t-t_0)} \mathbf{x}(t_0) + \int_{t_0}^t e^{\mathbf{A}(t-\tau)} \mathbf{B}_t(\tau) \mathbf{u}(\tau) d\tau \quad (7)$$

The equation above is solved using a discrete integration as follows;

$$\mathbf{x}[(k+1)T] = \phi[(k+1)T, kT] \mathbf{x}(kT) \dots + \int_{kT}^{(k+1)T} \phi[(k+1)T, \tau] \mathbf{B}_t(\tau) \mathbf{u}(\tau) d\tau \quad (8)$$

The integration equation simply calculated using a simple discrete integral, (Rosko 1971) as follow;

$$\mathbf{x}[(k+1)T] = \phi[(k+1)T, kT] \mathbf{x}(kT) + \frac{T}{2} \mathbf{B}_t[(k+1)T] \mathbf{u}[(k+1)T] \dots + \frac{T}{2} \phi[(k+1)T, kT] \mathbf{B}_t(kT) \mathbf{u}[(k+1)T] \quad (9)$$

$$\phi[(k+1)T, kT] = e^{\int_{kT}^{(k+1)T} \mathbf{A}(\beta) d\beta} \quad (10)$$

2.2 Fin Stabilizer Model

The mathematical model of a servo control of fin stabilizer is based on first order equation in Laplace function, (Amerongen 1982; Klught 1987). The model of the steering rudder machine with settling time τ_r , desired fin angle δ_d , and fin angle δ as well, written as follows;

$$\frac{\delta(s)}{\delta_d(s)} = \frac{1}{1 + \tau_r s}$$

or in the form of inverse Laplace form written as follows;

$$\delta(t) = \int_0^{\infty} e^{-\tau t} e^{-st} \delta_d(t) dt \quad (11)$$

The model of fin stabilizer system was compared to the servo control system as shown in Figure 3.

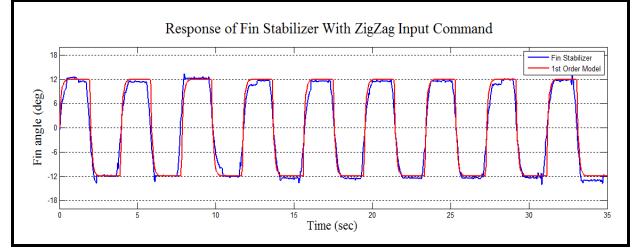


Figure 3: Response of servo control system of motor (exp) and first order of servo model (sim), $\tau_r=0.6$ sec.

2.3 Fin Force and Moment

The force and moment of fin stabilizer calculation using the wing model equation, influenced by the angle of attack and the losses of effective lift of fin (E). The losses of lift of fin consist of; losses by the submergence of fin, interaction of fore and aft fin and hull boundary layer. The losses of lift coefficient is obtained using empirical data of a fin combination that found in research of Lloyd, (Lloyd 1998; Kenevissi, Atlar et al. 2003).

$$E = \frac{\text{Effective lift of fin}}{\text{Nominal lift of fin}}$$

The lift force and moment of fins along the projected fin area A were obtained as follows;

$$F_L = \frac{1}{2} \rho V_s^2 A E C_L(\alpha) \quad (12)$$

$$F_D = \frac{1}{2} \rho V_s^2 A E C_D(\alpha)$$

$$M = F_L l_f$$

$$\alpha = x_5 + \delta + \frac{-\dot{x}_3 - \dot{x}_5 l_f + v}{V_s} \quad (13)$$

$$v = \zeta_a V_w k e^{-kz} \sin k(x - V_w t) \quad (14)$$

Total fin angle α_f to the normal axis of motion consist of pitch angle θ , fin angle δ and attack angle α by incoming flow to axis of fin as shown in Figure 4. The ship speed $V_s = u$ and the vertical water velocity, v .

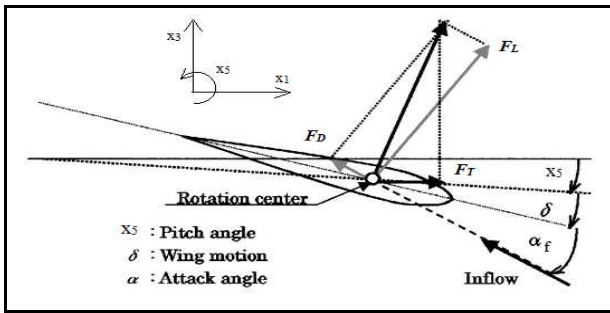


Figure 4: Vector force of fin stabilizer.

The fin stabilizer has a symmetrically streamlined section. At a small angle of attack, the lift coefficient ($dC_L/d\alpha$) increases linearly with the incidence angle. The lift curve slope of rectangular plan forms as a function of an aspect ratio written as follows, (Whicker and Fehlner 1958);

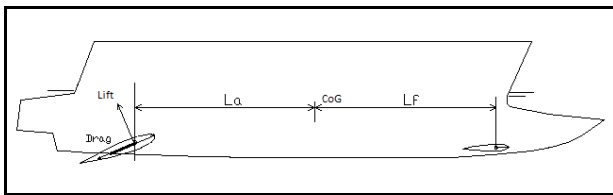


Figure 5: Longitudinal position of fin stabilizer

$$\frac{dC_L}{d\alpha} = \frac{1.8 \pi a_F}{1.8 + \sqrt{a_F^2 + 4}} \quad \text{rad}^{-1} \quad (15)$$

Lift and drag coefficients C_L and C_D were calculated as follows;

$$C_L(\alpha) = \frac{dC_L}{d\alpha} \alpha \quad C_D(\alpha) = C_{D0} + \frac{C_L^2(\alpha)}{0.9 \pi a} \quad (16)$$

C_{D0} is the minimum section drag. In this research the minimum section drag coefficient is $C_{D0}=0.0065$, (Perez 2005).

2.4 Control System

In order to control the ship motion, fin stabilizer used as an actuator to affect the ship motion by the effect of wave disturbance. The control system consists of an inner loop and outer loop controller. The inner loop controller regulates the angle of fins stabilizer using a servo system with control signal from the outer

loop controller. The outer loop controller calculates the control signal proportionally to the pitch angle using fuzzy logic algorithm. The concept of fuzzy logic rules is based on interpretation of human skill regulating the ship motions like on how the inverted pendulum is controlled being at its stable position, arranged in basic method of Fuzzy Mamdani (Amerongen, Lemke et al. 1977).

3. SIMULATION PROGRAM

In order to study the ship behaviour in following sea waves, a time domain simulation program was developed and performed the ship behaviour in following regular waves with fixed and active fins stabilizer. The program simulates the semi-SWATH ship with ship particulars as shown in Table 1.

The heave and pitch coefficients of added mass and damping were calculated at each encounter frequency based on Frank close fit method. The added mass coefficient of surge motion obtained by surge oscillation test in towing tank, (Brien and Kuchenreuther 1957) and damping coefficient derived from the slope of the resistance test. The stations integrated concerning hull geometry were carried out based on 20 stations along the hull length.

Table 1: Model particulars

Length	2.311 m
Breadth	0.8 m
Draft	0.2 m
Deck high	0.36 m
Hull distance	0.64 m
Fin Type	NACA 0015
Fore fins	0.146Ls (from FP), 0.28T(from BL)
Aft fins	0.816Ls (from FP), 0.32T(from BL)

The flow chart of time domain simulation program is shown in Figure 6. The hydrodynamic coefficients were loaded into



computer memory. During running, the coefficient can be retrieved according to the changes of encountering frequencies by the surge motion.

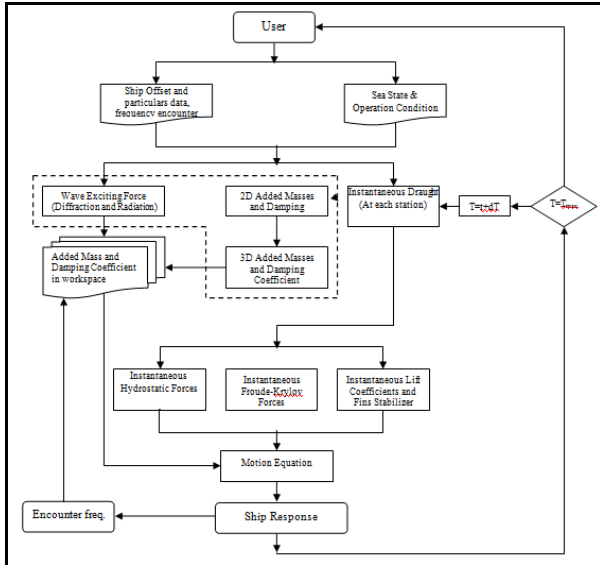


Figure 6: Numerical simulation diagram.

The vertical clearance of deck line and wave profiles ζ_{bow} at l_x distance from the centre of rotation of pitch angle θ is calculated as follows;

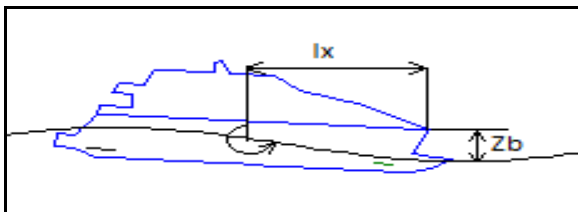


Figure 7: The clearance of the bow deck and wave profile.

$$z_b = h - x_3 + l_x \sin \theta - \zeta_{bow} \quad (17)$$

3.1 Validation

3.1.1 Surge Force

In captive model test, the longitudinal acceleration is restrained as shown in Figure 8. Ratio of the model speed to wave's celerity was set to 1.13, the wave steepness was 0.06 and the wave length to ship length ratio was

1.0. The model attached to air strut of the carriage and running in constant speed. Validation of surge motion is obtained by comparing the simulation results of surge force and the surge force measured when the model is advancing in the waves from crest to trough or vice versa. This is in accordance with Newton's 2nd Law of motion that the relationship between longitudinal acceleration of the ship is linear to the force acting on it.

The decrease of the force measured indicated there is a weight force assisting the model to accelerate (surfing condition) or the increase of force measured indicates there is a weight force that cause the model to decelerate (climbing condition) where the revolution of propeller in simulation is set constant. The seakeeping in following sea and the comparison results of force were shown in Figure 9 and Figure 10 respectively. The results showed a good comparison.

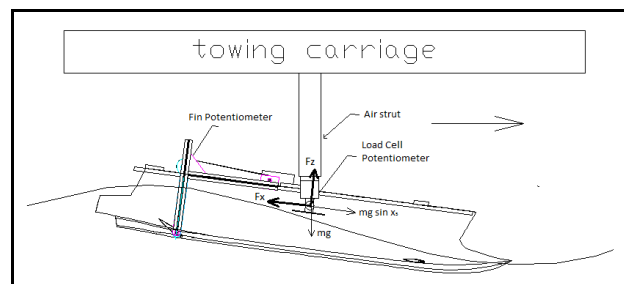


Figure 8: Longitudinal and vertical force at load cell.



Figure 9: Seakeeping test in following sea, conducted in towing tank.

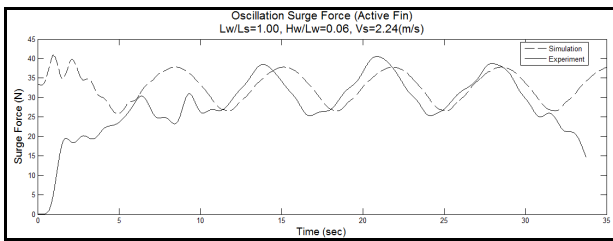


Figure 10: Oscillation force in following seas in harmonic force of surfing and climbing condition.

3.1.2 Heave and Pitch

Validation of vertical heave and pitch motion of simulation was conducted by comparing the heave displacement and pitch angle. The model was in following waves with active fin stabilizer. The results of validation were shown in Figures 8-10 and Figure 13. The solid line represents test results and dashed line represents simulation results. The validation results in heave showed the test has higher than simulation results, whilst the pitch angle and fin angle has a good comparison.

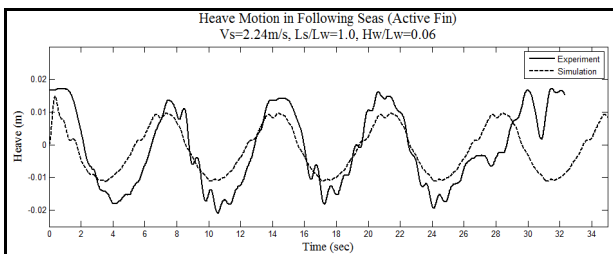


Figure 11: Heave in following seas with active fin stabilizer.

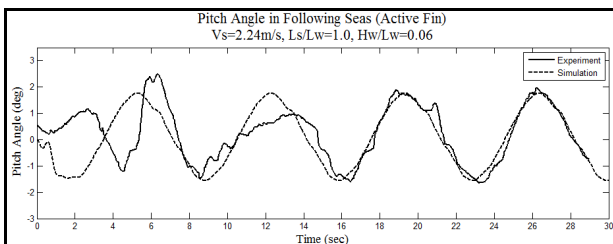


Figure 12: Pitch angle in following seas with active fin stabilizer.

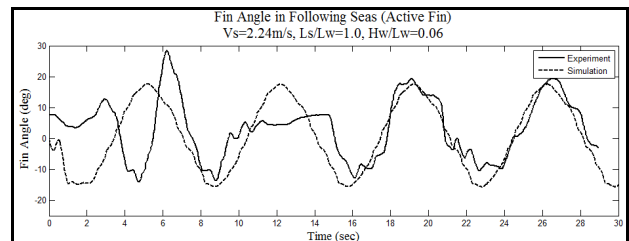


Figure 13: Fin angle with active fin stabilizer.

3.2 Simulation Results

The ratio of wave and ship parameters in following seas was simulated for certain variations. This is to determine the extent of the influence of wave parameters on the ship performance. The parameters of simulations were; the ratio of ship speed and wave celerity (V_s/V_w), the ratio of wavelength and ship length (L_w/L_s), and the ratio of wave high and the wave length (H_w/L_w). In analyzing the bow-dive of the ship response in time domain, the ship motion considered was the ship overtaking the waves in following seas. The parameters of simulations were tabulated as in Table 2.

Figures 14-18 showed the ship response having minimum clearance between wet foredeck and wave surface at the bow. The ship's fins were fixed at fore and aft. In this condition found the extreme bow-dive at $L_w/L_s=1.25$ and $H_w/L_w=0.08$, the bow-dive resulted in the fore-deck to be immersed as shown in Figure 15. While the bow-dive at $L_w/L_s=1.0$ resulted at speed ratio $V_s/V_w \approx 1.18$ and 1.25 , the bow-dive at $L_w/L_s=1.5$ resulted at $V_s/V_w \approx 1.25$ and ≥ 1.30 as shown in Figure 14 and Figure 16. In Figure 17 and Figure 18 the bow-dive in the foredeck was not immersed at ratio $L_w/L_s \geq 1.75$. The bow-dive tends to be decreased. The illustration of bow-dive with the foredeck was immersed was shown in Figure 28.

The clearance between foredeck and wave's surface with fixed fins stabilizer seams has linear trend. The clearance is decrease with increase of ratio H_w/L_w , whilst it has non linear changes with increase of ratio V_s/V_w .

Further, in Figure 19-23, at the bow the ship equipped fixed fin and active fin stabilizer at



the stern. The ship response showed the bow-dive did not result in the foredeck to be immersed in the range of parameters studied. The bow-dive showed the decreased of the wet foredeck clearance with increase of wave steepness and wave length. The active fin stabilizer performed to reduce the pitch angle as shown in Figure 27 compare to Figure 26. The fin stabilizer reduced the pitch angle which it causes the ship weight effect in longitudinal force in the wave-down was reduced.

Table 2: Simulation parameters.

Lw/Ls	Hw/Lw	Vs/Vw
1.0	0.05; 0.06; 0.07; 0.08;	1.10; 1.15; 1.18; 1.20; 1.23; 1.25; 1.27; 1.30; 1.33; 1.35;
1.25		
1.50		
1.75		
2.0		

Furthermore, the active fin stabilizer can restrain the ship having a bow-dive by reducing the ship surge velocity, as shown in Figure 27 compare to Figure 26. The advance of the active fin stabilizer was its capability to reduce the possibility of the ship having a bow-dive, as well as in reducing the effect of ship surfing. It was shown in all conditions of the active fin stabilizer in the range of parameters studied, where the relative change of surge velocity was below of its initial as shown in Figure 27. However, this led the ship having some condition that the ship did not overtake the waves and being entrapped in between the crest of the waves. The ship with active fin overtakes the waves at $V_s/V_w \geq 1.23$ whilst with fixed fin stabilizer the ship overtakes the waves at $V_s/V_w \geq 1.15$. The illustration of the entrapped ship condition was shown in Figure 29.

4. CONCLUSION

In this paper, the semi-SWATH ship was simulated for following sea with variations of ship speed, wave length, wave height, and wave steepness with passive and active fins

stabilizers. From the results, it can be concluded that;

For the condition of fixed fin stabilizer, bow-dive occurs for the condition of wave steepness, $H_w/L_w=0.08$, and wavelength at ratio $L_w/L_s < 1.75$ with certain ratio of ship speed and wave celerity, whilst with the active fin stabilizer, the bow-dive did not occur.

Active fin stabilizer has a significant effect preventing a bow-dive condition happened by decrease the the pitch angle and the surge velocity. However, the ship may have to be in entrapped condition.

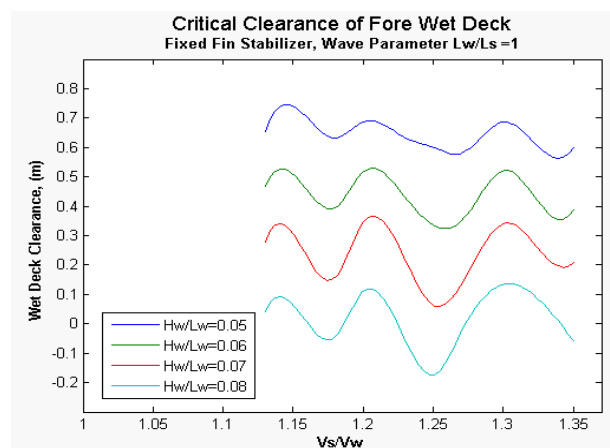


Figure 14: Critical clearance of fore wet deck a with fixed fin stabilizer at fore and aft hull. The wave parameter was $L_w/L_s=1.0$.

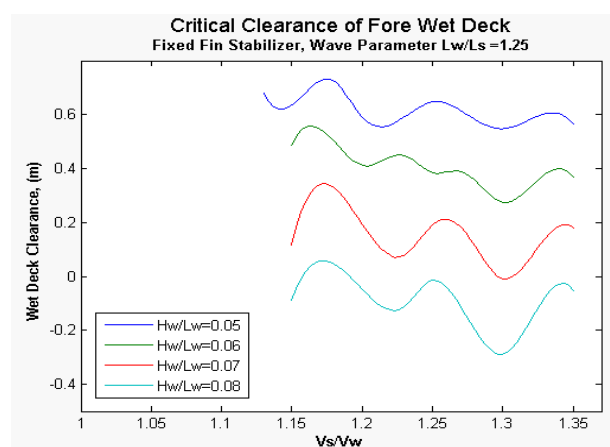


Figure 15: Critical clearance of fore wet deck a with fixed fin stabilizer at fore and aft hull. The wave parameter was $L_w/L_s=1.25$.

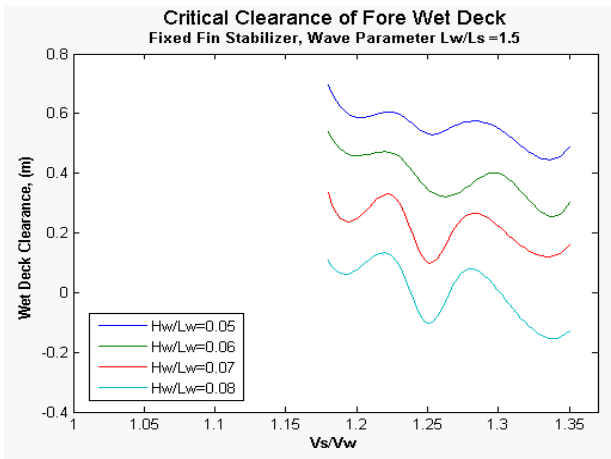


Figure 16: Critical clearance of fore wet deck with fixed fin stabilizer at fore and aft hull. The wave parameter was $L_w/L_s=1.5$.

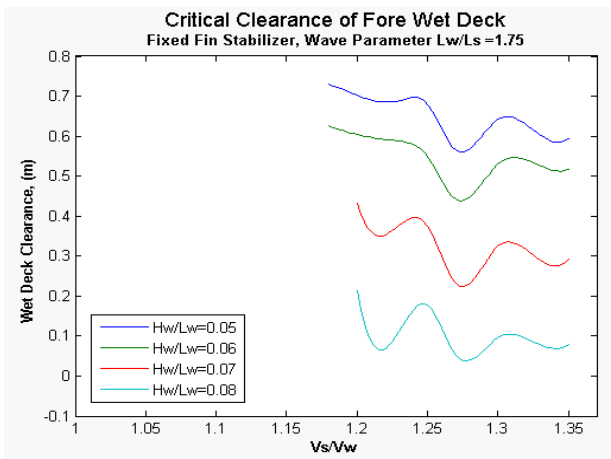


Figure 17: Critical clearance of fore wet deck with fixed fin stabilizer at fore and aft hull. The wave parameter was $L_w/L_s=1.75$.

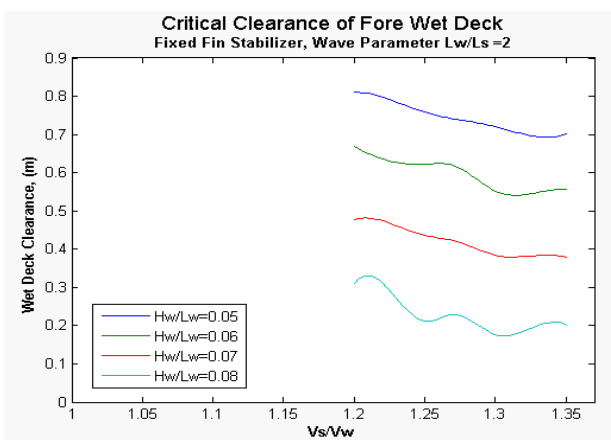


Figure 18: Critical clearance of fore wet deck with fixed fin stabilizer at fore and aft hull. The wave parameter was $L_w/L_s=2.0$.

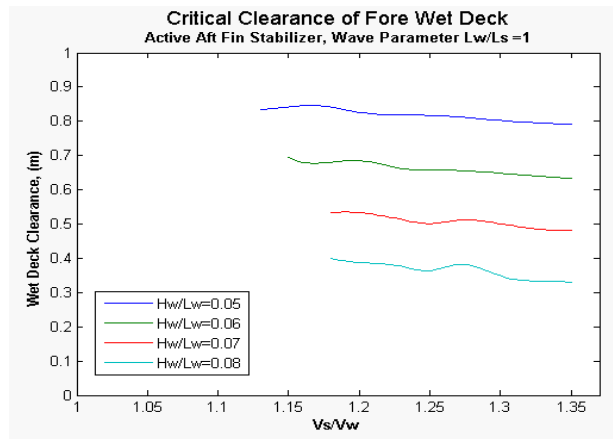


Figure 19: Critical clearance of fore wet deck with fixed fin at fore and active fin at aft hull. The wave parameter was $L_w/L_s=1.0$.

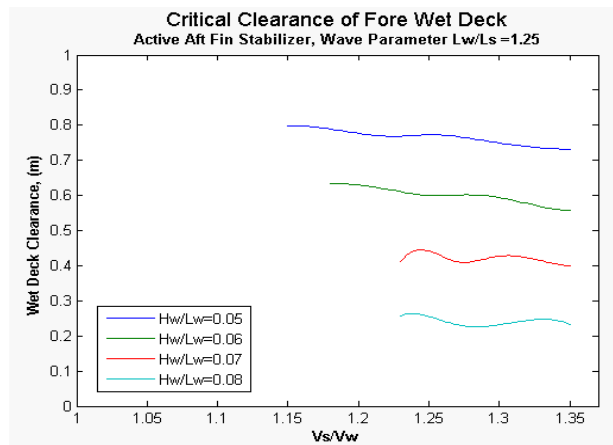


Figure 20: Critical clearance of fore wet deck with fixed fin at fore and active fin at aft hull. The wave parameter was $L_w/L_s=1.25$.

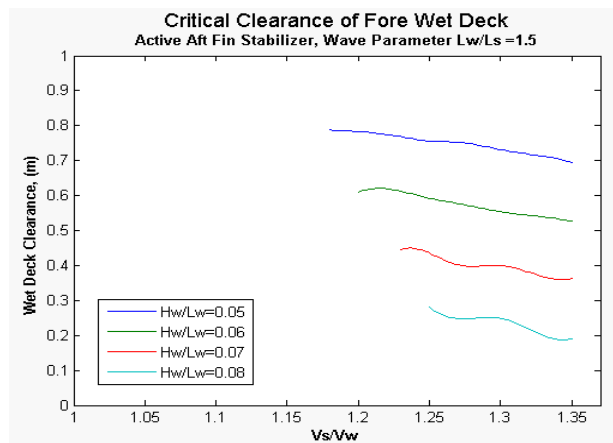


Figure 21: Critical clearance of fore wet deck with fixed fin at fore and active fin at aft hull. The wave parameter was $L_w/L_s=1.50$.

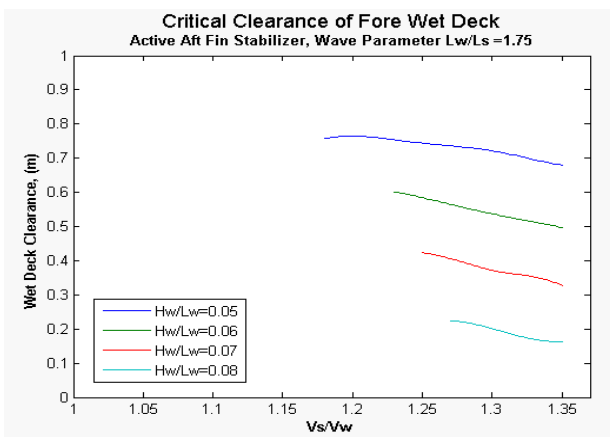


Figure 22: Critical clearance of fore wet deck with fixed fin at fore and active fin at aft hull. The wave parameter was $L_w/L_s=1.75$.

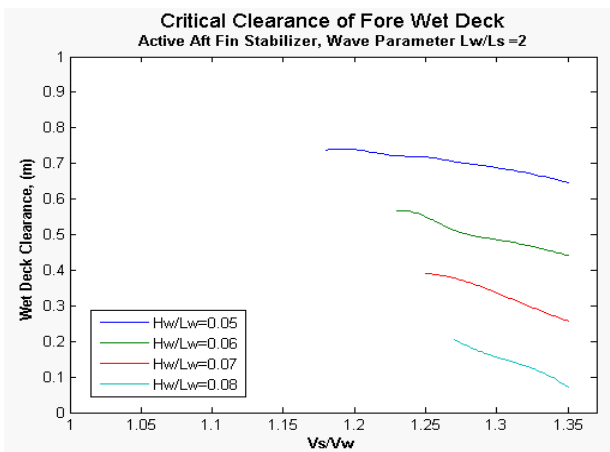


Figure 23: Critical clearance of fore wet deck with fixed fin at fore and active fin at aft hull. The wave parameter was $L_w/L_s=2.0$.

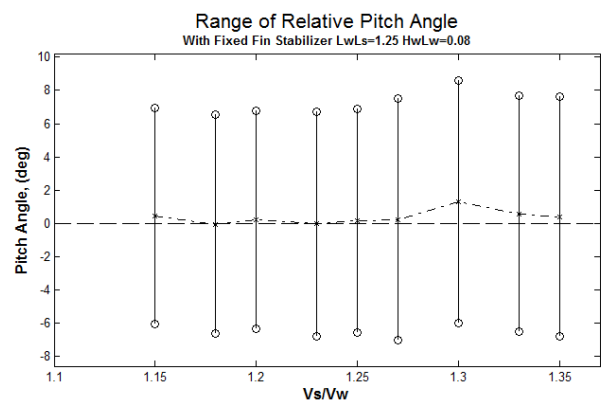


Figure 24: Range of pitch angle with fixed fin at bow and stern. The points indicate maximum, minimum, and half of both points. The ship entrapped below $V_s/V_w=1.15$.

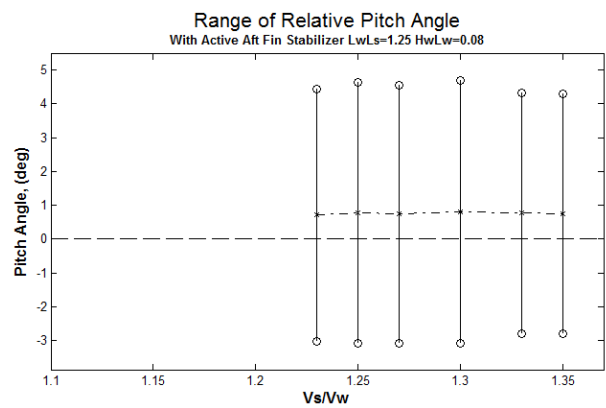


Figure 25: Range of relative surge velocity with fixed fin at bow and active fin at stern. The points indicate maximum, middle, and minimum. The ship entrapped below $V_s/V_w=1.23$.

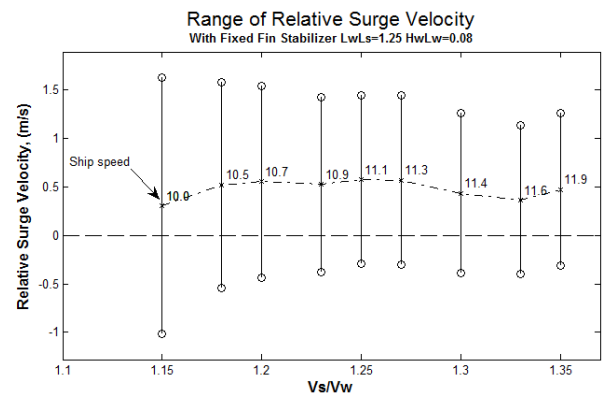


Figure 26: Range of relative surge velocity with fixed fin at bow and stern. The points indicate maximum, middle, and minimum. The ship entrapped below $V_s/V_w=1.15$.

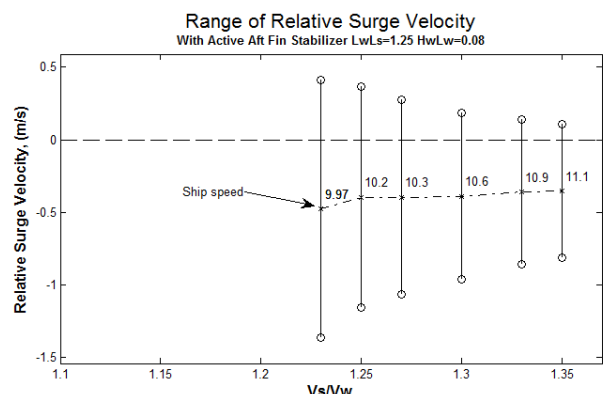


Figure 27: Range of relative surge velocity with fixed fin at bow and active fin at stern. The points indicate maximum, middle, and minimum. The ship entrapped below $V_s/V_w=1.23$.

Illustration of Bow-Dive of Ship Response with Fin Stabilizer in Following Sea

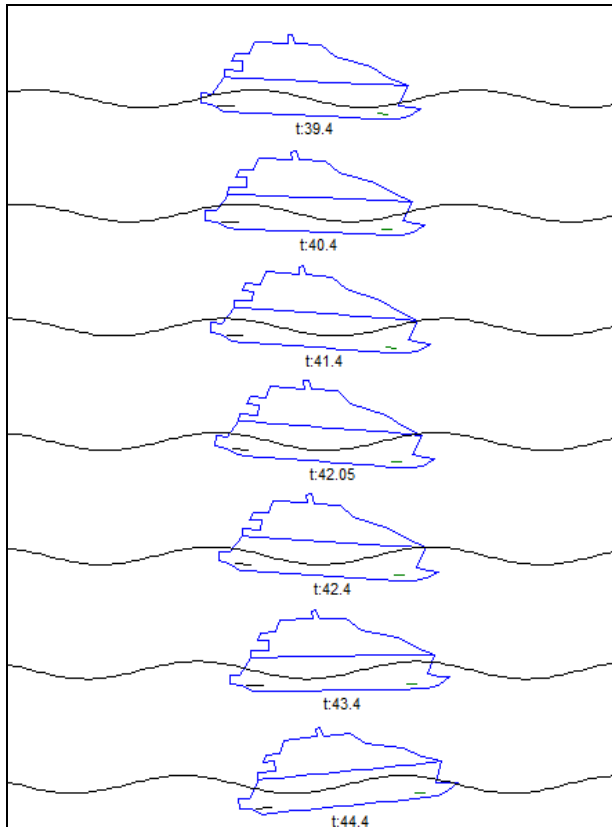


Figure 28: Ship motion in following seas with fixed fins, $L_w/L_s=1.0$, $H_w/L_w=0.08$ and $V_s/V_w=1,25$. The ship experienced foredeck to be immersed at time of 41.4 sec.

Illustration of Bow-Dive of Ship Response with Fin Stabilizer in Following Sea

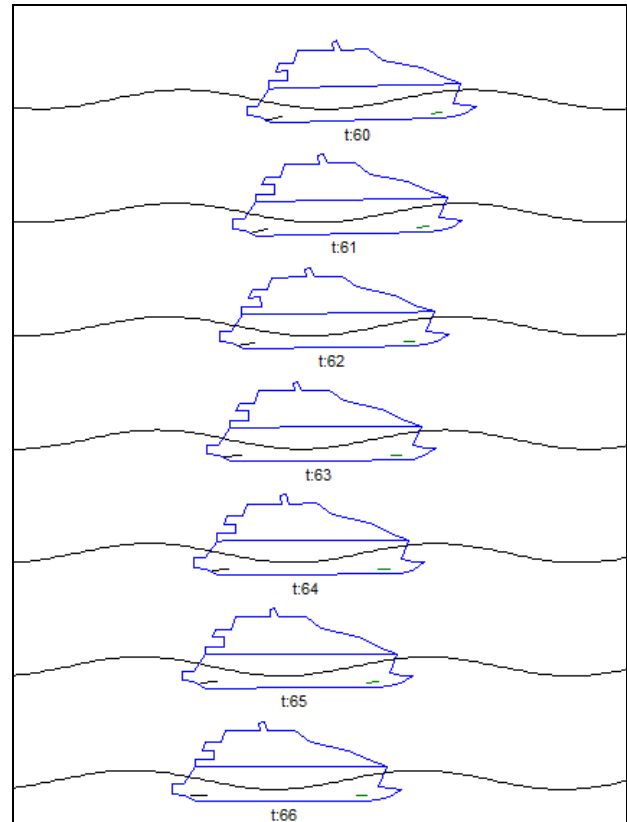


Figure 29: The ship with active fins stabilizer, $L_w/L_s=1.25$, $H_w/L_w=0.07$ and $V_s/V_w=1,13$. The simulation resulted the ship was entrapped between the wave's crest.

5. REFERENCES

Amerongen, J. V. (1982), "Adaptive Steering of Ships - A Model Reference Approach to Improved Maneuvering and Economic Course", PhD Thesis, Delft University.

Amerongen, J. van, H.R. van Nauta Lemke and J.C.T. van der Veen (1977), "An Autopilot for Ships Designed With Fuzzy Sets", Proceedings 5th IFAC/IFIP Conference on Digital Computer Applications to Process Control, The Hague, The Netherlands.

Bernitsas, M. M., Ray, D., & Kinley, P. (1981),

"Kt, Kq and Efficiency Curves for The Wageningen B-Series Propellers", Report No. 237, Dept of Naval Architecture and Marine Engineering, College of Engineering, University of Michigan.

Bhattacharya, R. (1978), "Dynamics of Marine Vehicles", New York, John Wiley & Sons.

Brien, J. T. O. and D. I. Kuchenreuther (1957), "Free Oscillation in Surge and Sway of A Moored Floating Dr Dock", 6th ICCE, Gainesville, Florida.

Dand, I. W. (2005), "High Speed Craft in Following and Astern Quartering Seas", Summary Report MCA Research Study 502 (Unpublished Experimental and Computer



Model). BMT SeaTech Ltd.

Dand, I. W. (2006), "High Speed Craft Bow Diving in Following Seas", Proceedings of International Conference on High Speed Craft, ACV's, WIG's and Hydrofoils, RINA.

Djachkov, V., & Makov, J. (2005), "Seakeeping of A Fast Displacement Catamaran", Transport, 20(1), pp14-22.

Katayama, T., Tamura, K., & Ikeda, Y. (2003). A Study on Bow-Diving for Planing Craft-Criteria of Bow-Diving Occurring, Journal of the Kansai Society of Naval Architects, 239, pp 87-94.

Kenevissi, F., M. Atlar, et al. (2003), "A New Generation Motion Control System for Twin-Hull Vessels Using a Neural Optimal Controller", Marine Technology and SNAME News (Control): 13.

Klugt, P. G. M. V. D. (1987), "Rudder Roll Stabilization", PhD Thesis, Delft University of Technology.

Lee, C. M., & Martin, M. (1974), "Determination of Size of Stabilizing Fins for Small Waterplane Area Twin-Hull Ships", Report No. ADA002427, David Taylor Naval Ship Research and Development Centre.

Lloyd, A. R. J. M. (1998), "Seakeeping: Ship Behavior In Rough Weather", Gosport A.R.J.M. Lloyd.

Matsuda, A., H. Hasimoto, et al. (2004), "Capsizing Due to Bow-Diving in Following Waves", International Shipbuilding, 51: 13.

McCreight, K. K. and R. Stahl (1983), "Vertical Plane Motions of SWATH Ships in Regular Waves", Report No. ADA130516, David Taylor Naval Ship Research and Development Centre.

Perez, T. (2005), "Ship Motion Control" (1st Edition), Norway, Springer.

Rosko, J. S. (1971), "Digital Simulation of Physical Systems", Massachusetts, Addison-Wesley Publishing Company.

Spyrou, K. J. and I. G. Tingkas (2011), "Nonlinear surge dynamics of a ship in astern seas: Continuation analysis of a periodic states with hydrodynamic memory", Journal of Ship Research, 55(1), pp19-28.

Umeda, N. (1990), "Probabilistic Study on Surf-Riding of a Ship in Irregular Following Seas", The 4th International Conference on Stability of Ships and Ocean Vehicles (STAB90), Naples, Italia.

Whicker, L. F. and L. F. Fehlner (1958), "Free-Stream Characteristics of A Family of Low Aspect Ratio All Movable Control Surfaces For Application to Ship Design", Report No. ADA014272, David Taylor Model Basin.

Wu, W., Spyrou, K. J., and McCue, L. S. (2010), "Improved Prediction of the Treshold of Surf-Riding of A Ship in Steep Following Sea". Ocean Engineering, 37, pp.1103-1110.



FLO/FLO Heavy Lift Critical Stability Phases

Paul Handler, *Military Sealift Command, USA* paul.handler@navy.mil

Vincent Jarecki, *NAVSEA, SUPSALV, USA* vincent.jarecki@navy.mil

Hendrik Bruhns, *Herbert-ABS Software Solutions LLC, USA* hbruhns@herbertsoftware.com

ABSTRACT

The US Navy has used FLO/FLO heavy lift transport as an alternative to towing for the transport of damaged vessels as well as transport of smaller vessels not suited for ocean transit. There are critical stability considerations that have to be assessed prior to conducting a heavy lift operation, specifically “Draft at Instability” and “Minimum Stability”.

During de-ballasting of the heavy lift ship with the lifted vessel on the docking blocks, the reaction of the docking blocks on the lifted vessel is effectively the same as removing weight from the vessels keel. This raises the lifted vessels centre of gravity thus reducing the vessels metacentric height until the vessels GM will be zero.

During a critical part of the heavy lift evolution the cargo deck of the heavy lift ship will be completely submerged. During this phase only the water-plane of the hull structure which extends above the cargo deck will provide stability to the heavy lift ship. The heavy lift ship will pass through a phase of “Minimum Stability”, which should not occur at the same time that the lifted vessel assumes its “Draft at Instability”. The lifted vessel and the heavy lift ship may roll out of phase, causing landing problems, or causing the lifted vessel and/or the heavy lift ship to become unstable, assume a large list or capsize.

HECSALV and POSSE are effective tools in modelling critical stability phases for FLO/FLO heavy lift operations. This paper discusses the critical stability phases of a FLO/FLO heavy lift operation, and the methods and practices to plan for and mitigate effects of reduced stability at these phases.

Keywords: Heavy Lift, Stability Phases, Draft at Instability, FLO/FLO, Minimum Stability, Semi-Submersible

1. BACKGROUND

In recent years the US Navy has been relying more and more on heavy lift transport as an alternative to towing for the transport of damaged vessels, as well as transport of smaller vessels not suited for ocean transit. Although there are different types of heavy lift vessels, this paper will focus on FLO/FLO heavy lift transport utilizing semi-submersible ships.

A semi-submersible heavy lift ship is an ocean-going vessel capable of submerging its open deck to below the water's surface in order to allow another vessel to be floated over it and landed on docking blocks (which are pre-set on the deck of the heavy lift ship). When the heavy lift ship is subsequently de-ballasted it lifts the other vessel out of the water in a process very similar to the operation of a floating dry-dock. The lifted vessel can then be



transported to its destination on the deck of the heavy lift ship.

In 2000, the USS Cole was transported from Yemen aboard M/V Blue Marlin, a heavy lift transport vessel owned and operated by the Dutch firm, Dockwise Shipping BV. Similar operations were done to transport Samuel B. Roberts (FFG 58) to the United States following mine damage in 1988, and in 1991/1992 during Operations Desert Shield and Desert Storm. The Roberts was transported to the United States on the Dutch-flag heavy-lift ship, Mighty Servant 2.

Since the US Navy does not own any FLO/FLO heavy lift ships, it relies on MSC (Military Sealift Command) to charter commercial heavy lift vessels to perform heavy lift operations. In the last 10 years MSC contracted heavy-lift transport vessels to move forward-deployed MHCs (coastal mine hunters) and MCMs (mine countermeasure ships) from Ingleside, Texas, to the Persian Gulf and the Far East, as well as to move US Army watercraft to Kuwait.

FLO/FLO heavy lift transport is particularly suitable for transport of mine hunters and mine countermeasure ships. These ships have specially constructed hulls and engines that are not built for the rigors of transoceanic travel. During the transit from Texas to the Persian Gulf or the Far East, the engines and hull would incur such wear and tear as to require dry-docking and repairs upon arrival. Apart from protecting these ships, carrying them aboard a heavy lift ship saves a significant amount of time. Whereas it would take about 60 days for a mine hunter to travel to the Persian Gulf on its own power, it takes about 40 days to travel aboard a heavy lift ship.

Prior to and during a heavy lift operation, there are critical stability considerations that need to be planned for and addressed, specifically "Draft at Instability" and "Minimum Stability".

2. DISCUSSION

2.1 Draft at Instability

During ballasting/de-ballasting of the heavy lift ship with the lifted vessel on the docking blocks, the reaction on the docking blocks is equal to the difference in displacement of the lifted vessel at the floating draft and the displacement at the waterline under consideration in the landed condition. The effect of keel block reaction is a virtual rise in the centre of gravity of the lifted vessel and subsequent reduction in the vessels GM (metacentric height). The keel blocks are assumed to be knife edge supports and offer no resistance to overturning.

As the heavy lift ship is being pumped down, or the vertical lift is being raised, the keel block reaction is being increased. The vertical centre of gravity will eventually rise to a position where the virtual metacentric height (GvM1) at the new waterline (WL1) and the righting arm for small angles of heel will become zero. The ship's draft at this condition of zero GvM1 is called the draft at instability.

If the draft at instability is reached before the ship has landed fore and aft on the keel blocks, then the ship will become unstable. On the other hand, if the draft at instability is not reached until well after the ship has landed fore and aft, then the ship remains stable throughout the landing evolution.

Generally speaking, if the difference between the draft at landing and the draft at instability is 1 foot or greater, then the ship has acceptable stability for landing on the keel blocks. If the difference between the draft at landing and the draft at instability is less than one foot but equal to or greater than 6 inches, then pre-positioned side blocks will be required. If the difference between the draft at landing and the draft at instability is less than 6 inches, then the ship does not have acceptable stability for landing

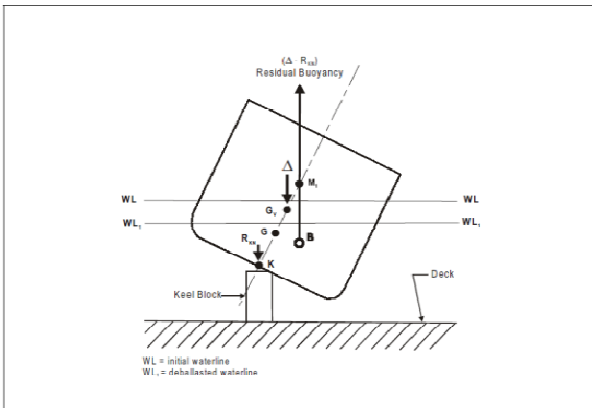


Figure 1: Draft at Instability

If calculations show that the ship will become unstable before landing fore-and-aft, action must be taken to remedy the situation. The first and most obvious remedy would be to remove the trim of a ship to conform to the profile of the docking blocks. A ship in this condition would land fore-and-aft at approximately the same time. If the trim cannot be altered to conform to the profile of the docking blocks, the vertical centre of gravity of the ship must be lowered to improve GM. This may be accomplished by the addition, removal, or relocation of weights, or reduction of free surface on board the ship.

2.2 Minimum Stability

During a FLO/FLO heavy lift evolution, stability of the heavy lift ship/lifted vessel system can be considered in 5 separate phases. These are as follows:

Phase 1 – Heavy lift ship at full submergence with the lifted vessel (asset) afloat,

Phase 2 – The lifted vessel makes contact with the blocks,

Phase 3 – The lifted vessel is hard on the blocks, with the heavy lift ship trimmed to bring the cargo deck out of the water,

Phase 4 – With the forward end of the heavy lift ship cargo deck out of the water, trim is removed to bring the rest of the cargo deck out of the water,

Phase 5 – Heavy lift ship fully de-ballasted

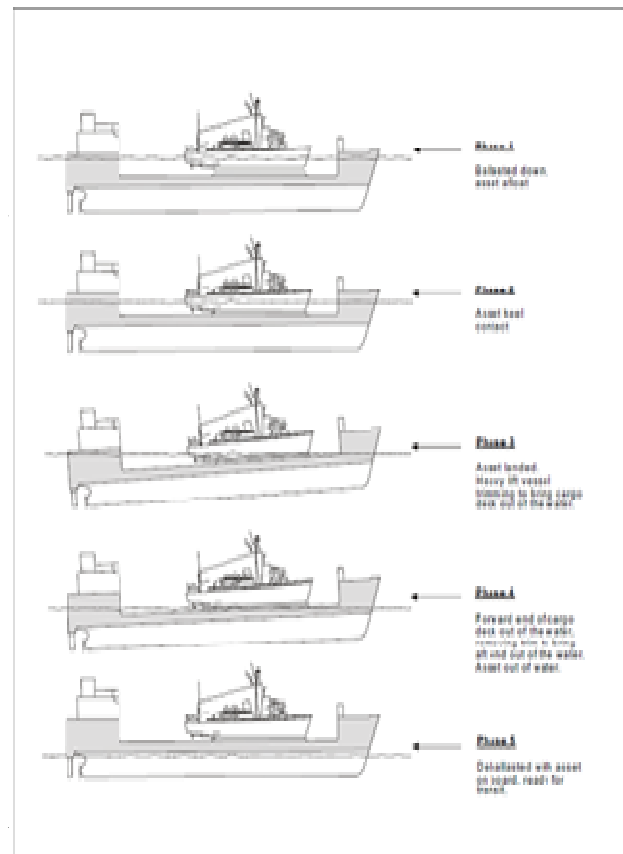


Figure 2: Phases of Stability

As the cargo deck of the heavy lift ship goes into or out of the water, the ship's stability changes rapidly and substantially. When the cargo deck of the heavy lift ship is completely submerged stability is a function of the water-plane cut by the hull structure which extends above the cargo deck. For a vessel design with wing walls, this can be illustrated as follows:

The wing walls cut the water-plane and provide the stabilizing force. As the ship takes on a list, the wing wall on the low side gets deeper in the water and a stabilizing buoyant force develops which tries to right the ship. The wing on the high side is losing buoyancy which also has a



stabilizing effect. However, the lower hull and cargo deck stay below the waterline and do not contribute to the righting effect. During this time the heavy lift ship will pass through a phase of minimum stability (minimum GM).

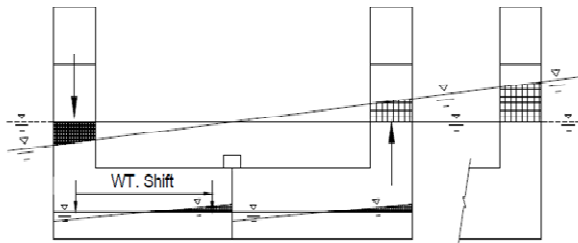


Figure 3: Minimum Stability

Additionally, during this phase, the water levels in the ballast tanks will be changing, resulting in a free surface effect to further reduce stability. As the ship lists, the water will level out. A wedge of water will shift from the high side to the low side. This will shift the centre of gravity towards the low side and will tend to increase the list.

To control the effects of reduced stability at the minimum stability phase, it is usually necessary to apply trim and/or list to the heavy lift ship to increase the water-plane area. This practice relies heavily on the master's experience and sometimes trial and error. If too much trim is applied to the heavy lift ship the lifted vessel can slide off the blocks, not enough and the heavy lift ship can heel over due to insufficient GM.

The point of minimum stability should be compared to the minimum stability conditions for the lifted vessel. The point of minimum stability of the heavy lift ship should not occur at the same time that the lifted vessel assumes its draft at instability. If this happens, the lifted vessel and the heavy lift ship may roll out of phase, causing landing problems, or causing the lifted vessel and/or the heavy lift ship to become unstable, assume a large list or capsize.

The US Navy requires that during operations involving lifting of U.S. Navy assets, the heavy

lift ship must maintain a GM (including free surface correction) of no less than 3.28 feet (1 meter). Trim of the heavy lift ship of up to 3° may be included to meet the minimum GM.

To waive the 1 meter minimum GM, the lifted vessel must be hard on the blocks before the phase of minimum stability, and the minimum GM (not accounting for the list) must be at least 0.5 feet (0.15m) in all phases of the operation, including the free surface effect.

2.3 Modelling with HECSALV or POSSE

The US Navy uses the Program of Ship Salvage Engineering (POSSE), developed by Herbert-ABS Software Solutions LLC. The commercial version is known as HECSALV, and is utilized to model stability, motions, structural loading, and salvage of stranded and/or damaged vessels.

Recently the US Navy, the Royal Navy, and Herbert-ABS cooperated to expand and refine POSSE/HECSALV to model the entire FLO/FLO evolution. This includes stability, structural loading, and motions of the transport vessel and warship, both separately prior to the lift and as a combined system during the lifting and transport operation.

To analyse a heavy lift in POSSE a full model must be developed for both the heavy lift ship and the lifted ship. Each model includes all the data necessary to define and analyse the loading of both vessels and includes the full geometry of the hull and tanks defined using offsets, tankage details, strength limits, etc. Once modelled there are two fundamentally different calculation methods available in HECSALV/POSSE to analyse a heavy lift operation. These approaches include a rigid ship analysis and a flexible ship analysis. For both approaches tools are provided to define the docking block plan either from an existing docking plan, or develop a new docking plan for special situations such as a damaged vessel.

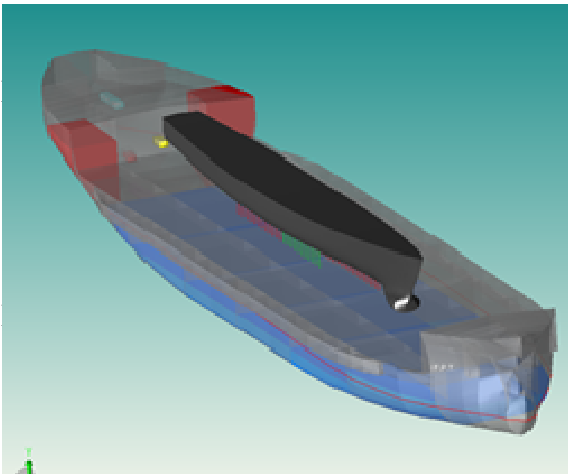


Figure 4: HECSALV 3D Graphic

The rigid ship analysis treats both ships as rigid bodies and seeks a solution in the form of a classic static equilibrium, with the weight of the lifted ship applied to the HL one through the blocks, which are internally represented as miscellaneous weights. The buoyancy of the HL ship is instead applied to the lifted vessel through the blocks, represented internally as pliable grounding pinnacles. Using available time sequence tools the rigid ship approach can be used to evaluate the detailed stability and strength status of the heavy lift ship and the lifted ship at any step in the sequence so that both the “Draft at Instability” of the lifted ship and the “Minimum Stability” of the combined heavy lift ship can be determined. The rigid ship approach adopts an iterative methodology to find the equilibrium solution, where it first analyses the lifted ship assuming a set of dock block locations to get a ground reaction, then applying those loads to the HL ship, adjusting the dock block locations to reflect the new HL ship drafts and heel, computing a new set of reactions, then applying those to the HL ship, and so on. It converges when the reaction doesn't change very much. It handles only pure vertical forces.

The other method available in HECSALV/POSSE to analyse heavy lift operations is the flexible ship analysis. This uses two beam finite element models connected

by a set of rigid links and a set of unidirectional springs.



Figure 5: Heavy-lift Model

The beams are located at the base of the HL ship and the height of the centre of gravity of the lifted ship. This FE model can be viewed for any HL/Lifted ship configuration when the flexible ship analysis is run. This analysis approach can be used for more detailed analysis of block reactions and strength.

3. CONCLUSIONS

Prior to and during a FLO/FLO heavy lift operation, there are stability considerations that need to be planned for and addressed. The critical stability considerations are draft at instability and minimum stability. The Program of Ship Salvage Engineering (POSSE) developed by Herbert-ABS Software Solutions LLC has recently been expanded to include the capability to model an entire FLO/FLO operation. This expansion includes two fundamentally different calculation methods which are effective tools in modelling the critical stability phases for heavy lift operations, a rigid ship analysis and a flexible ship analysis. Further evaluation and experience will better refine these tools.



4. REFERENCES

HEGER Dry Dock, 2005, Inc. – Dock-master
Training Manual.

MIL-STD-1625D – Safety Certification
Program for Dry-docking Facilities and
Shipbuilding Ways for U.S. NAVY Ships.

NSTM Chapter 997 (ACN 6) - Docking
Instruction and Routine Work in Dry Dock.

U.S. NAVY Towing Manual, Revision 3,
Chapter 8 – Heavy Lift Transport.

Operability of French Naval Ships over 50 Years

Brice Beaupuy, Nicolas Stachelhausen, Jean-Yves Billard, *Ecole Navale*

Emmanuel Mogicato, Pierre Vonier, Jean-François Leguen,

DGA Hydrodynamics (ex Bassin d'essais des carènes), jean-francois.le-guen@dga.defense.gouv.fr



ABSTRACT

This paper describes a work performed in intend to correlate results of direct capsizing probability evaluation with classical criteria on the base of four French ships designed in the past 50 years and widely operated in the French navy in the past years. Among those ships two of them have been decommissioned. The method of capsizing probability evaluation used by the French basin is presented and, on the basis of the result obtained, a value of the safe ship operability is proposed. Based on these criteria three of the investigated ships are judged as safe, the fourth which is slightly under the criteria is operated with weather criterion restrictions.

Keywords: *Risk assessment, probability evaluation, stability evolution, criteria correlation*

1. INTRODUCTION

Recent evolutions of stability criteria (Francescutto, 2010) and new methods developed for risk assessment (Ypma 2012, Derbanne 2008, Belenky 2008) have opened new perspectives regarding the future of stability assessment. These recent works are the culmination of many years' efforts (de Kat 1990) on ship dynamics and dynamic stability. On these new bases it is of main interest to apply these new methods both on ships build during the few past decades to check how those ships, reputed as safe, are evaluated making use of the recently developed tools and on new designs recently launched. Moreover, as far as new criteria make use of different level of

stability assessment, it seems interesting to correlate the classical criteria with the direct evaluation of the capsize probability on the base of the aforementioned ships.

For that purpose we have chosen a series of French naval ships that have been deployed from the fifties to the nineties. For each ship, the classical criteria are evaluated and the capsizing risk is computed by use of a large ship motion simulation program. The aim of the paper is to describe the risk assessment method, that allows an evaluation of the long term capsizing probability, and the correlation realized between the classical criteria and the estimated risks.



2. SHIPS RETAINED FOR THE COMPARISON

Four navy ships have been retained for this study. All of them were designed with stability criteria based on Sarchin ang Golberg's paper. Only the load case corresponding to the Full Load Displacement has been investigated. Further studies are required to explore other load cases for those ships. Their main particulars are given in Table 1 (from the older to the youngest).

The first one, Le Corse, S1, is a frigate built in the fifties and decommissioned at the end of the seventies. In spite of her small dimensions this frigate had a good reputation of stability among the sailors that have served on board.

The second one, Jeanne d'Arc, S2, is a larger ship built in the sixties and recently decommissioned. Her reputation was excellent and in spite of very hard meteorological conditions encountered no sailor on board has ever been frightened by the sea conditions even when she reached 50° of heel in the roaming fifties (cover page picture).

The third, a smaller ship, CMT, S3, is known to have a poor stability level (Leguen 2010). In heavy seas special rules of maneuvers are prescribed to low capsizes probability. Modifications are in progress to improve the safety level of those ships that have more than ten years of expected life. Present computations have been made on the unmodified design and present thus a higher level of risk.

The fourth French frigate, S4, has been designed in the eighties. She has a correct stability level and is operated without weather limitation.

Ship	Displacement (FLD) [t]	LWL [m]	B [m]
S1	1700	95	10
S2	13269	172	22
S3	649	47.1	9
S4	3894	115	14

3. NUMERICAL TOOLS

3.1 Fastabi

Stability criteria are evaluated with an in-house stability program name FASTABI developed by DGA Hydrodynamics and used at *Ecole navale* for education of naval cadets. The program uses a panel decomposition of the hull, shown on figure 1, and determines the hydrostatic pressure on each of them. Hydrostatic forces and moments are then determined by integration over the all wetted surface. Plane or sinusoidal free surface can be used for the determination of hydrostatic forces in calm water, sagging or hogging conditions (present study will be completed by a comparison of rules and deterministic loads, on the same outline than the ones presented in this paper for stability). The free surface effect resulting from liquid taking place in tanks is taking into account by meshing the latter and filling them up to the actual level. Each type of tank of the ship can also be automatically meshed by FASTABI, assuming that the walls located in the hull are planar surfaces. Damage stability evaluations are possible with FASTABI but not used yet in this study. For the present study FASTABI performed stability analysis using current naval ships regulation, issued by DGA.

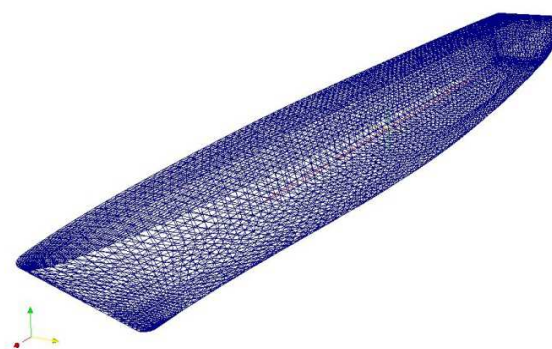


Figure 1: Finite Element Mesh used by FASTABI

For large values of heel angles, taken into account the geometry of waterproof upper bridge and superstructures is of main importance. The difficulty in that matter is that rules and reality may differ. Ordinary this

difference is not accounted for but in our case, as we want to correlate rules calculation with reality, we have to focus on this point.

3.2 Fredyn

FREDYN is a sea keeping numerical tool developed by the Cooperative Research Navies, CRNav (Ypma and Harmesen -2012) and used by Naval Stability Standards Working Group, NSSWG to assess the capsizing probability (intact and damaged) for naval ships, mainly frigates (Harmesen et Marshall, 2012). It is a 6DOF tool for ship large motions evaluation, with a strip theory based pre-processor followed by a temporal solver using non-linear forces (Froude Krylov forces applied on the actual wetted hull surface). In our case we have used version 9.8 of the code, in order to be able to use numerical results of previous studies for one of the four ships. On the same way, the postprocessor tool of FREDYN for the calculation of the risk was not used, but the ones developed some years ago internally (Leguen ISSW 2010).

3.3 Naval Ship Stability Rules

As for many navies, French stability naval rules are based on USN standard, well described in the famous SNAME paper from Sarchin and Goldberg (Sarchin 1962). In France this study can be located in rules of the naval authority (DGA) in design rules of DCNS and in the naval ships standard (BVNR) of the French classification society, Bureau Veritas.

For intact stability French rules are to be investigated through the following analysis:

- Righting arms (GZ curve) of the ship in the different loading condition
- Behaviour of the ship under heeling actions such as :
 - Severe wind and rolling
 - Icing accretion
 - High speed turning
 - Heavy cargo lifting

- Crowding of the personal to one side of the ship
- Contemporary action of wind and the personal crowding

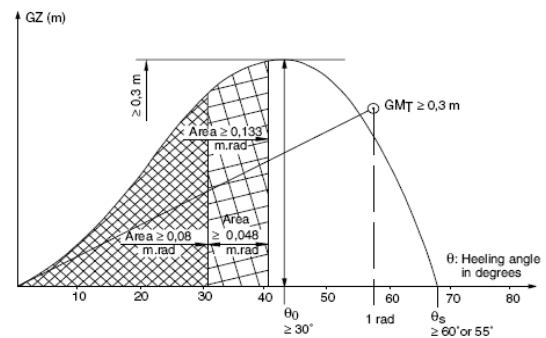


Figure 2: Righting arms curve from BVNR.

At the present time only the first point was analysed for this study (no heeling actions). Criteria used for the study are given in table 2 and illustrated on figure 2.

Value of the initial metacentric height corrected for free surface effect	Not less than 0.3 m
A ₁ , Area under the righting arm curve up to 30°	Not less than 0.080 m.rad
A ₂ , Area under the righting arm curve up to 40°	Not less than 0.133 m.rad
A ₃ , Area under the righting arm curve between 30° and 40°	Not less than 0.048 m.rad
Value of the maximum righting arm curve	Not less than 0.3 m.rad
Heeling angle corresponding to the maximum righting arm curve (\square GZ _{max})	Not less than 30°
Value of the capsizing angle (55° if \square > 5000 t) (\square s)	Higher than 60°

3.4 Application of stability criteria for the four ships

For a given geometry and a given load case the software determines the GZ curve and the different values used to verify the stability criteria. A summary of the values obtained (or estimated) for the different criteria (for the end of lives of ships) is given in table 3.



	S1	S2	S3	S4
GM _t [m]	0.91	1.82	0.54	0.756
A ₁ [m.rad]	0.11	0.295	0.066	0.131
A ₂ [m.rad]	0.186	0.558	0.11	0.246
A ₃ [m.rad]	0.076	0.263	0.045	0.115
GZ _{max} [m]	0.46	1.92	0.34	0.78
□ GZ _{max} [°]	38	44	52	50
□ s [°]	70	96	83	78

It can be seen, from the previous table that, for the loading conditions retained in this work, the CMT is under the required levels for the criteria associated with the GZ curve areas.

Moreover, as far as the meshes used by the two codes are independently defined from the same CAD description, a particular attention has been put to insure that the dynamical code (FREDYN), operated for the risk evaluation, and the static code (FASTABI), used to compute the stability criteria, have an equivalent perception of the ship stability curve. For that purpose a comparison of the hydrostatics curves and GZ curves determined by FASTABI and FREDYN have been systematically performed. Differences may appear due to a different discretization realized in FASTABI and FREDYN. Data has been adjusted (mesh refinement in FASTABI, addition of frames in FREDYN) to have less than 1% of difference between the two sets of results. The GZ curves for the Jeanne d'Arc at DCC are given on figure 3. It can be observed that very little differences remain after this fairing process.

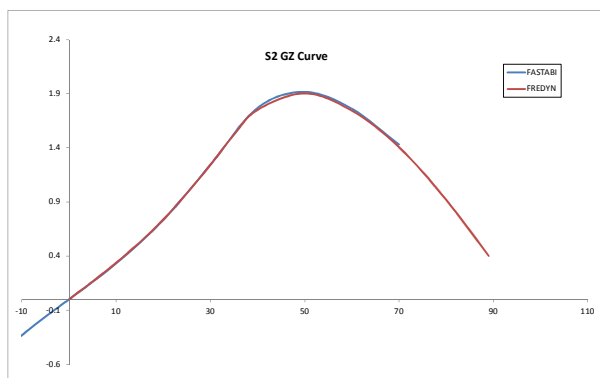


Figure 3: GZ curves obtained both by FASTABI and FREDYN on Jeanne d'Arc.

4. DETERMINATION OF SHIP OPERABILITY

Operability, P_{op} , can be defined as the probability for the ship to be operated safely from her launching to the end of her operative life. If P_{cap} is the probability of capsizing determined for the same period, we can write:

$$P_{op} = 1 - P_{cap} \quad (1)$$

To define the operability the following hypothesis are used:

- The ship is supposed to be operated in the Atlantic Ocean. She has an equal probability to be everywhere in the ocean.
- The sea state is mono directional.
- Her headings are spread from 0° to 360° with an equal probability.
- Her speed is spread between 5 knots and her maximum speed with an equal probability (excepted for S4 where no forward speed was used due to a low maximum speed, 12 kts., comparatively to the others, about 30 kts). For each run the ship speed is evaluated in waves and kept constant in mean by a slight variation of the rotational velocity of the shafts. This long and tedious procedure avoids bias effects that may impact the evaluation and the representation of capsizing probability.
- Each simulation is realized for duration of 3600 s.
- The limit roll angle for capsizing is fixed at 45°.
 - Yaw DDL has been blocked to avoid broaching.
 - Pierson-Moskovitz sea spectrum.

The value of 45° has been chosen by reference to model tests performed on CMT, the fourth naval ships retained in the present study. Even if the defined angle is far from the vanishing stability angle it has been retained because, for this specific value the same probability of capsizing is obtained both in Fredyn computations and in model tests results. In a next future a relationship between the static vanishing stability angle, θ_s , and the limit roll angle for capsizing will be searched for. At the very moment the value of 45° has also been

chosen for safety reasons and applied on the four ships even if a more refined method should include an adapted value of this limiting angle function of each ship geometry.

For each run the successive maximum of roll angles are kept and post treated using a Weibull method proposed by Derbanne et al. (2008) in order to define the capsize probability for particular conditions (H_s , T_p , Ship speed and heading). In this method probabilities are applied to the roll angles and fitted by a Weibull law of probability using a moment method with $R_{1/3}$ and $R_{1/10}$ (mean of one third and one tenth of the extremes roll motions).

On each one hour trip simulation, extrapolation to the defined value of roll angle (45° in our case) allows the evaluation of capsize probability on individual wave (green line). This process, illustrated on figure 4 allows the determination of the short term probability, p_i . These values are reported on polar plots of figure 5 for a sea state characterized by $H_s = 4.5$ m, $T_m = 8$ s. Limits of safety levels were arbitrary chosen for figure 5 as 1% and 50%.

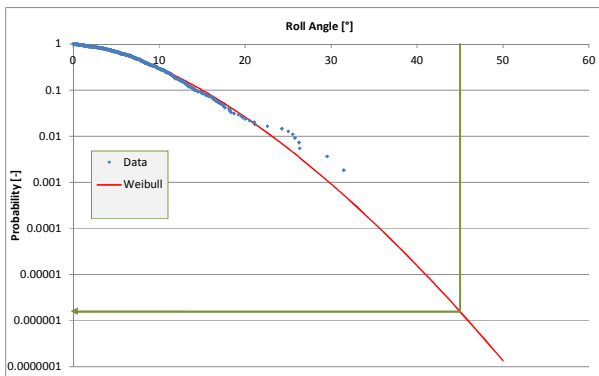


Figure 4: Rough data and Weibull law of probability fitted on the data.

To take into account for various heading and speed a mean value $P_i(X)$ of the probabilities p_i is evaluated on sea state and operation conditions X . For the evaluation of long term probability, an atlas of sea state describing the relation H_s - T_p for North Atlantic has been used (US Coast Guards Table). The long term probability is then evaluated by:

$$P_{\text{cap}}(X, T) = \left(\sum_i \alpha_i P_i(X) \frac{T_{SS}}{T_{Zi}} \right)^{\frac{T}{T_{SS}}} \quad (2)$$

Where α_i is the probability of occurrence of condition i (issued from the atlas), T_{Zi} is period of zero up-crossing of the roll motion on the condition i , T_{SS} is the characteristic duration of one sea state, 4 hours in our case, and T is the total duration of the probability estimation, 30 years in the present study.

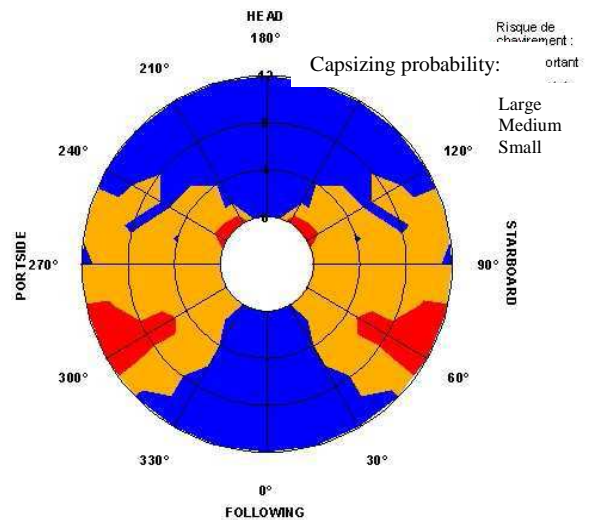


Figure 5: Polar plot of capsize probability.

5. RESULTS

The overall values of operability have been determined using the previously described procedure and reported in table 4 for the four naval ships.

	S1 [%]	S2 [%]	S3 [%]	S4 [%]
Operability	96.25	99.00	95.53	91.00

A tentative correlation between criteria and operability has been attempted. On the following figures 6 and 7 values of the criteria have been reported versus operability for the four ships and a linear regression has been determined. Moreover, the value of the criteria has been reported on the different figures and the value of the operability for which the regression intersects the criteria value has been determined.

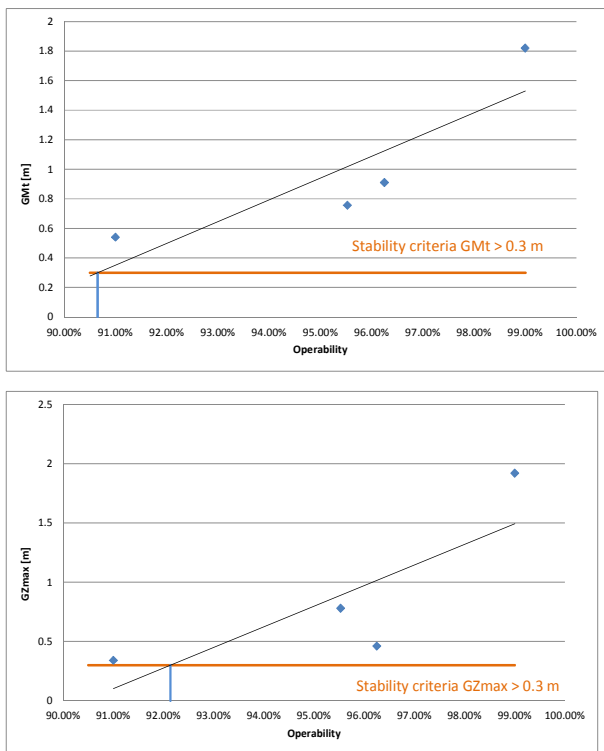


Figure 6: GM_t and GZ_{max} of the four ships versus operability.

In Table 5 the values of operability at intersection between our regression and the related criteria have been reported. It can be noticed that, but for the GM criteria for which the value (90.65%) is a little lower, the value seem constant at a value not far from 92.5%.

Table 5: Values of operability at regression vs stability criteria intersection	
	Operability
GM_t	90.65%
GZ_{max}	92.14%
A_1	92.72%
A_2	92.63%
A_3	92.30%

Thus it seems that a value of the operability of about 93% could be required to secure a reasonable level of safety for those ships.

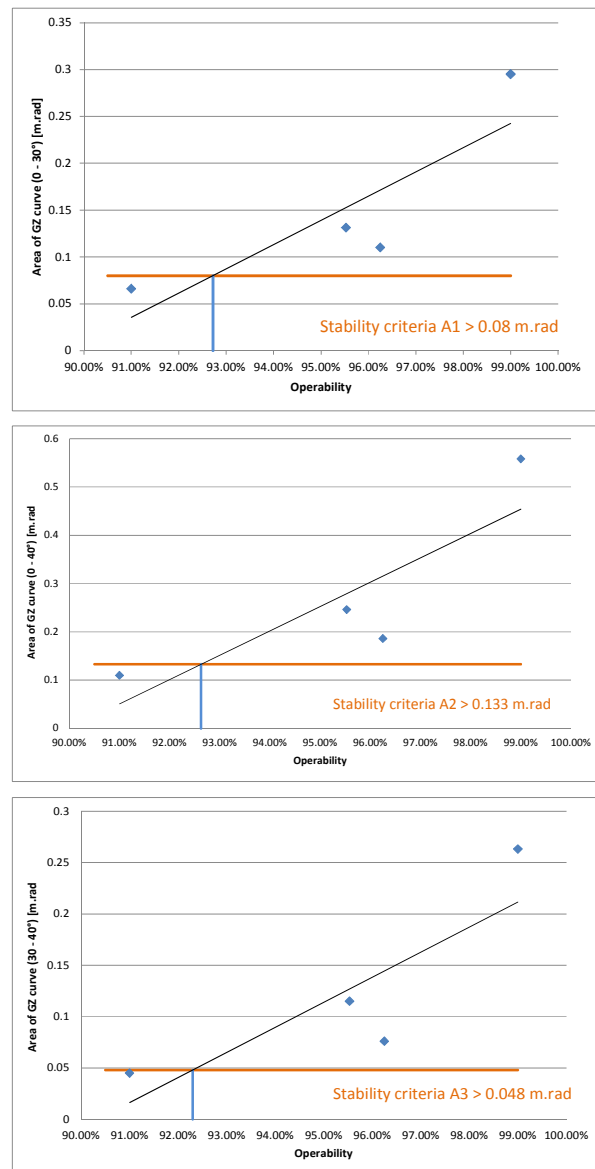


Figure 7: A_1 , A_2 and A_3 of the four ships versus operability.

6. DISCUSSION AND CONCLUSION

In the present paper a global criteria based on the overall operability of the ship is proposed. Based on an operability of 93% determined by the present method the stability of the ship is insured with an equal level of safety as the one provided by the actual stability criteria imposed by the regulation. The effectiveness of the proposed value is based on the experience of the sailors who have reported dangerous situations concerning the CMT (weather limitations of employment were set to



secure this ship), while no particular risk has been reported on the other three vessels.

It is obvious that statistics produced from the calculations on only four ships are not properly evaluated and the conclusions drawn here are only the beginnings of a larger effort in which other vessels and other loading cases will be studied. Nevertheless it can be said that even if rules evolve from the first ship, no clear trend on the effect of age was found because rules doesn't change enough to observe a significant improvement in safety. Less general correlation between safety and launched dates of ships than between safety and size of ships were found.

This work will be integrated in the NSSWG work plan (Harmsen 2012) in order to increase the number of ships detailed in the data base.

7. ACKNOWLEDGMENTS

The authors wish to acknowledge the French Ministry of Defense (DGA / Ecole navale) which has funded the project.

8. REFERENCES

- Belenky V., de Kat J. O., Umeda N., 2008, "Toward Performance-Based Criteria for Intact Stability", Marine Technology, Vol 45, n° 2 p 102 - 120
- Derbanne Q., Leguen J.-F., Dupau T., 2008, "Long-Term Non-Linear Bending Moment Prediction", 27th International Conference on Offshore Mechanics and Arctic Engineering (OMAE 2008), Estoril, Portugal.
- Francescutto A., Umeda N., 2010, "Current Status of New Generation Intact Stability Criteria Development", Proceedings of the 11th International Ship Stability Workshop, Wageningen, The Netherlands, p 1 - 5
- Harmsen H., Marshall S., 2012, "Deriving Intact Stability Criteria from the Capsize Probability of Naval Frigates", Proc. of the 11th Intern. Ship Stability Conference, Athens, Greece, 2012.
- De Kat J. O., "The numerical modeling of ship motions and capsizing in severe seas", 1990, Journal of Ship Research, Vol 34, n° 4, p 289 - 301
- de Kat J. O., Brouwer R, McTaggart K A, Thomas W L, 1994, "Intact Ship Survivability in Extreme Waves: New Criteria from a Research and Navy Perspective", 5th Intl. Conf. on Stability of Ships and Ocean Vehicles-Vol. 1.
- Leguen J.-F., Caquineau C., Morigato E., Dupau T., Régnier E., Vonier P., Dispa H., Lorin F., 2010, "Operator Guidance for French Mine Hunters", Proc. of the 11th Intern. Ship Stability Workshop, Wageningen, Netherlands.
- Sarchin T., Goldberg L., 1962, "Stability and buoyancy criteria for U.S. Naval Surface Ships", SNAME Transactions, Vol 70, p 418-458.
- Ypma E., Harmsen E., 2012, "Development of a new methodology to predict the capsizing risk of ships", Proceedings of the 11th International Conference on the Stability of Ships and Ocean Vehicles, 23-28 September 2012, Athens, Greece.





Development and Validation of a Time Domain Seakeeping Code for a Destroyer Hull Form Operating in Extreme Sea States

Frans van Walree, *Maritime Research Institute Netherlands*, F.v.Walree@marin.nl

ABSTRACT

The paper describes the validation of a time domain method to simulate the behaviour of a destroyer operating in steep, stern-quartering seas. A method is described to reconstruct experimental wave trains in a simulation method and two deterministic validation cases are presented and discussed.

Keywords: model test, simulation, stern-quartering seas, deterministic validation

1. INTRODUCTION

The operability and safety of a ship depends on its behaviour in waves. At higher speed in steep waves from aft ward directions dynamic stability risks may exist. These risks can be investigated by means of model tests. Provided these tests are properly executed, they offer the most reliable information on dynamic stability.

Issues in the use of model testing are the costs, the limited statistical reliability of the tests in irregular waves, the limited flexibility, some limitations in representation of the physics of ship behaviour in waves from the stern quarter and the fact that the test results are not always easy to understand. The limitations in the physical representation relate to viscous effects in the components of the hull resistance with an effect on the propeller loading and thereby on the rudder inflow, in some of the smaller components of the roll damping, in components of the manoeuvring reaction forces and in the (dynamic) stall of the rudders. Also the neglect of wind on the roll damping, the wind heel and on the propeller loading and related steering has an effect. Issues that are modelled implicitly correctly are the natural peak-trough a-symmetry in steep waves, the presence of breaking waves, the wave induced forces on the propeller and rudder, rudder and propeller ventilation and down-stream effects

of vortices from the bilges and bilge keels on the rudder.

In order to understand the physics of dynamic stability, numerical modelling has been pursued for some time. Although the latest CFD techniques have undoubtedly the largest potential, they have not met the expectations yet. This is partly due to the problems of modelling the generation, propagation and absorption of steep waves in a limited computational domain and partly to the local physical character of issues like spilling wave crests on deck, roll damping from bilge keels and rudder stall and ventilation and the role of the propeller herein. In combination with the required domain size, this yields an extreme computational effort.

In between the above two techniques are hybrid models, which combine the efficiency of potential flow theory with empirical modules covering the non-linear aspects of manoeuvring and roll damping. After validation, these models are particularly used in assessing capsizing risk.

The present paper deals with validation of such a simulation method for a destroyer hull form operating in steep stern-quartering seas. A description of the simulation method is given first.



Next, the experimental arrangement is described.

The last section deals with deterministic validation, including the method to reconstruct the experimental wave train in a simulation program.

2. SIMULATION METHOD

Predicting the motion performance of ships operating in steep stern-quartering sea states is more complicated than that for beam or head seas. In steep stern-quartering seas motion amplitudes may be large and both vertical and horizontal plane motions (course keeping) are important. Ideally, prediction methods should be capable of accounting for:

- Six degrees of freedom motions, especially the coupling between sway, yaw and roll,
- Large motion amplitudes,
- Non-linear waves: dynamic stability problems are generally most severe in steep waves for which non-linear effects are of importance,
- Time-varying wetted hull geometry and its effects on restoring forces, wave excitation, wave diffraction and wave radiation forces,
- Deck-edge immersion and dynamics of water on deck,
- Forward speed and the effects of friction and flow separation on hydrodynamic properties: in stern-quartering seas the wave encounter frequency is generally low so that potential flow damping is relatively low,
- Propulsion and steering: the speed variations in the horizontal plane should be predicted adequately, and course keeping is important with respect to broaching,
- The contribution of the wind to the roll damping and the roll excitation.

Prediction methods that are capable of handling the above are in principle capable to simulate phenomena like capsizing due to loss of stability in waves, water on deck and surf riding and broaching. However, fully non-

linear simulation methods are scarce and rather computationally intensive. When a large number of conditions needs to be investigated the required simulation times become impractical. Therefore, there is a need for fast time simulation methods. These are based on partial linearization of the hydrodynamic problem. Such a method is described below.

FREDYN (De Kat *et al.* 2002), is a fast-time, blended, seakeeping-manoeuving simulation method. It has been developed by the Cooperative Research Navies (CRN: US Navy/NSWC Carderock, UK-MoD/Qinetiq, DGA/BEC-France, US Coast Guard, DoD/DSTO-Australia, DND/DRDC Atlantic-Canada and Netherlands Navy/MARIN). FREDYN is based on:

- Added mass and damping from strip theory in the frequency domain applied in the time domain through retardation functions, accounting for the wetted geometry at rest only, neglecting the effects of wave reflection and radiation in the relative wave elevation,
- Froude-Krylov forces through a 3D panel method using the undisturbed wave pressures on the instantaneous submerged body,
- Linear irregular, long and short crested waves,
- Deck-edge immersion and quasi-steady deck wetting on basis of ship motions and the incident and diffracted waves, while the generated wave associated with forward speed is obtained from a steady-flow linear panel method,
- Empirical manoeuvring coefficients (for frigates),
- Cross-flow drag method for additional non-linear damping and wave excitation,
- Calm water resistance curve,
- Propulsion and steering using propeller open water characteristics, semi-empirical lifting surface characteristics and propeller-rudder interaction coefficients,
- Autopilot steering,
- FDS (Blok and Aalbers, 1991) and IHT (Himeno, 1981) roll damping method,

- Unsteady wind loading based on coefficients derived from wind tunnel tests.

The FREDYN software development started in the late 1980's. Originally it was a time domain simulation method for frigate manoeuvring and in subsequent years many modules for prediction of motions in waves have been added. In the late 2000's CRN realised that the FREDYN code required restructuring. This work was completed recently. FREDYN is now linked to an advanced simulation framework (MARIN-XMF) and the software code is completely object oriented. Figure 1 shows the FREDYN visualisation and user interface. The re-structured software allows for an easy link to for instance bridge simulators, see Figure 2 (from Marshall, 2010), and other simulation software.

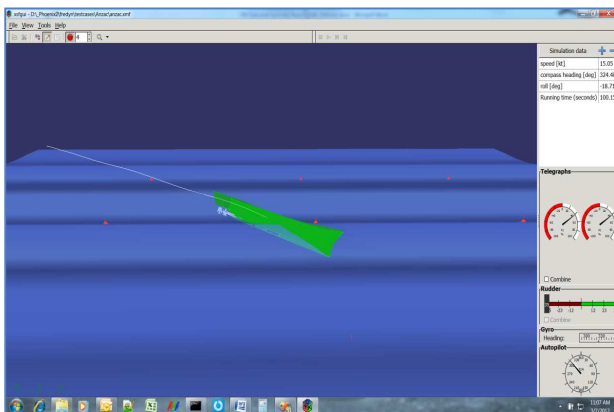


Figure 1: Fredyn visualisation and user interface.



Figure 2: Bridge simulator view

FREDYN is now a versatile tool that is used by CRN for the Naval Ship Stability Working Group (NSSWG) to perform capsize risk assessments, see Ypma and Harmsen (2012). For a single ship and loading condition such a risk assessment requires about 6,500 one hour simulations. For 11 ships comprising 47 ship-loading conditions combinations 300,000 one-hour simulations are required. Although FREDYN is a fast-time tool (about real time) it requires a powerful grid of work stations to keep the duration of such a large amount of simulations within practical limits. FREDYN has been well validated for operational conditions, and to a lesser extent for more severe sea conditions (in regular waves). In order to validate FREDYN for the larger temporal wave steepness occurring in irregular waves, and to validate the recent method to determine deck-edge immersion and water on deck effects in particular, a series of model tests have been performed for CRN at MARIN. These are described in the next Section.

3. MODEL TESTS

Model tests have been performed on a European version (MARIN model m7967) of the well known destroyer hull form DTMB-M5514 (Pre-contract DDG 51) in steep stern-quartering seas. The tests have been performed in MARIN's Seakeeping and Manoeuvring Basin which measures 170x40x5 m in length, width and depth respectively. Table 1 shows the main particulars of the hull form and Figures 3 and 4 show the hull form sections and the model during testing, respectively. The model was equipped with twin propellers, rudders and bilge keels. The model scale was 35.45.

Table 1: Main Particulars

Length between perpendiculars (m)	142.25
Beam on waterline (m)	19.06
Draught forward (m)	6.15
Draught aft (m)	6.15
Displacement (ton)	8643
Metacentric height (m)	1.00
Natural roll period (sec)	16.10



Previous validation of FREDYN for the present hull form indicated that using the undisturbed wave height in combination with the instantaneous position of the ship in the wave field, to obtain deck-edge immersion and the amount of water on deck, leads to rather conservative capsize risk predictions. In order to improve this, FREDYN was extended with a more accurate method to determine deck-edge immersion, see Carette and Van Walree (2010).

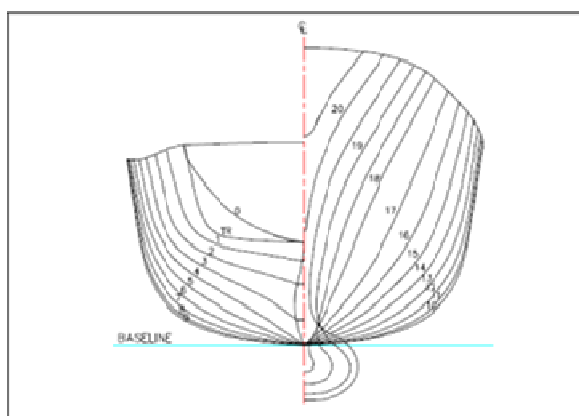


Figure 3: Hull form sections



Figure 4: Model during free running test

Free running, self-propelled and self-steered tests were performed in long crested irregular seas. The model was given a relatively low initial stability ($GM = 1.0$ m) to have large amplitude roll motions, up to capsizing. The conditions for a selection of tests are shown in Table 2. These tests were performed for further validation of the deck-edge immersion method and more in general

for validation of FREDYN for large amplitude motion conditions.

Table 2a: Test conditions

Test No.	Speed (kts)	Heading (deg)	H _s (m)	T _p (sec)
205	24.1	300	10.0	10.5
218	24.3	330	7.50	9.0

Table 2b: Test conditions-continued

Test No.	Test duration (sec)	Number of wave encounters
205	1800	130
218	1800	75

4. DETERMINISTIC VALIDATION OF FREDYN

As shown in Table 2, the number of encountered waves in stern quartering seas is quite low, although the test duration was 1800 sec full scale. For reliable statistics such as standard deviations, significant values and probability of exceedances of motions at least 200 wave encounters are required. For assessments of rare events such as broaches and capsize a much higher number of wave encounters is required.

A way to circumvent the need for lengthy model tests and simulations when validating ship motions in following and stern-quartering seas is to run the simulations in the same wave train as the experiments, i.e. deterministic validation.

The presently adopted procedure for deterministic validation starts with determining the wave spectrum components from the experimental wave train. These are determined by means of spectral analysis of the wave train measured while travelling at very low speed through the basin, without the model present. This yields an “average” wave spectrum valid anywhere in the basin.

During the model tests, the wave height was measured by wave probes attached to the carriage (following the self-propelled and self-steered model) at three locations. The mean position of the wave probes was:

- probe 1: 1.5 ship lengths in front of the model, at the centre line,
- probe 2: 0.25 ship lengths next to the model, at midship windward side,
- probe 3: 1.0 ship lengths next to the model, at midship leeward side.

The phase angles of the spectrum components ε are determined by means of a non-linear minimisation procedure (IMSL routine RNLIN). In this procedure the difference between the measured and reconstructed wave trains, ζ_m and ζ_e respectively, is minimised at each time step by varying the phase angles. The measured wave train ζ_m is that measured during the actual model tests. The object function F at time t , and the reconstructed wave train at wave probe j are defined by:

$$F_j(t) = \zeta_{mj}(t) - \zeta_{ej}(t) \quad (1)$$

$$\zeta_{ej}(t) = \sum_{i=1}^N A_i \cos(k_i \tilde{x}_j - \omega_i t + \varepsilon_i) \quad (2)$$

where $A_i = \sqrt{2\Delta\omega_i S_i}$ is the wave amplitude of spectral component i , $k_i = \omega_i^2 / g$ is the wave number, $\tilde{x}_j(t) = x_j(t)\cos\psi + y_j(t)\sin\psi$ is the position of wave probe j in the wave field, ω is the wave frequency, (x_j, y_j) is the position of the wave probe in the basin reference system and ψ is the wave direction. The number of spectral components used N is 240.

The object function is minimised using the observations (measurements) at the three wave probe positions sequentially at each time step, yielding the phase angles ε . The length of the measurements signals is typically 300 seconds per wave probe, per run. The number of observations used per run is typically 600 per wave probe. The assumption is then that

equation (2) is valid for arbitrary positions (x, y) in the neighbourhood of the ship. Figure 5 shows a comparison between the measured wave train and the reconstructed wave train at wave probe 2 for test 205.

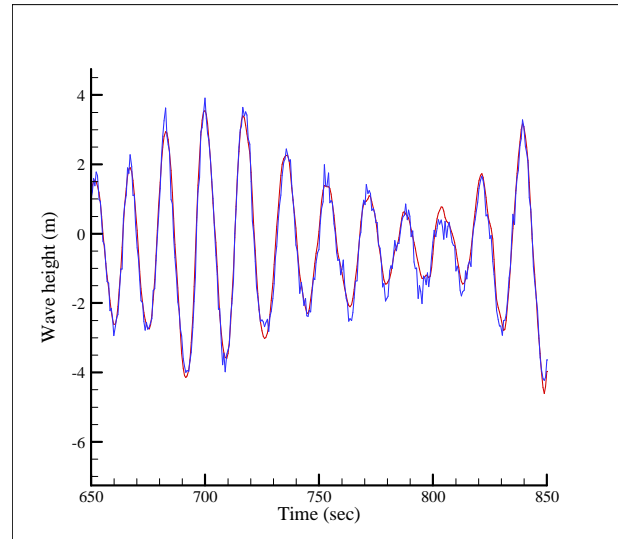


Figure 5: Comparison between measured (blue) and reconstructed (red) wave train encountered by model

In principle one can now perform the deterministic validation study. However, simulation methods can not predict the motions of the ship perfectly and sooner or later the x - y track of the ship will deviate from that in the experiments. A different position in the wave field means that a different wave will be met and the deterministic comparison needs to stop.

This problem can be circumvented by forcing the position and speed in the horizontal plane in the simulation method to be equal to that of the experiments. This would be a viable solution for head waves simulations, but for simulations in oblique seas the vertical plane motions will be affected due to this forcing, which is undesirable. A more elegant and general approach is to use an interpolation table for the model x - y position versus time when determining the wave kinematics in the simulation method. In this way the actual tracks may be different, but still the wave kinematics are evaluated at the position corresponding to that of the experiments.



Simulations in the reconstructed wave field were performed by means of FREDYN. The velocities and positions of the model at the start of the measurements were used as initial conditions. The retardation functions were not initialised, i.e. the memory effect associated with the start-up phase of each run was not taken in to account. The rudder and propeller arrangements, including autopilot gains, in FREDYN were the same as used for the model tests. The propeller RPM in FREDYN was set such that the mean speed during the selected run corresponded to that of the experiments. The roll damping was *not* tuned on basis of the experimental results; at high speed the roll decay is too fast to allow for tuning. Figures 6 through 11 show a comparison between the measured and the simulated ship motions and forward speed, for the first run of Test 218 where relatively low waves were met at a low encounter frequency. The ship operates in conditions where broaching may occur. The red (dashed) signals denote the FREDYN results while the green signals denote the experimental results, including measurement noise.

The figures show that the sway motion is reasonably predicted by FREDYN, however it starts to deviate after about 180 seconds of simulation. The heave motion in FREDYN follows the measured values quite well, the same is true for pitch and yaw. The roll motion and forward speed are also not badly predicted.

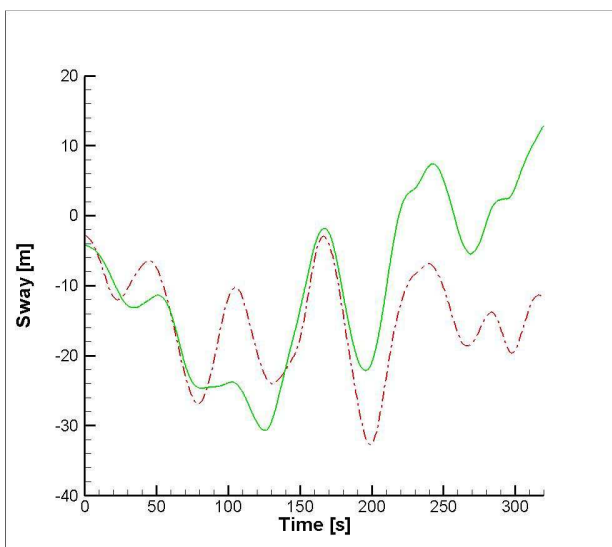


Figure 6: Comparison sway Test 218

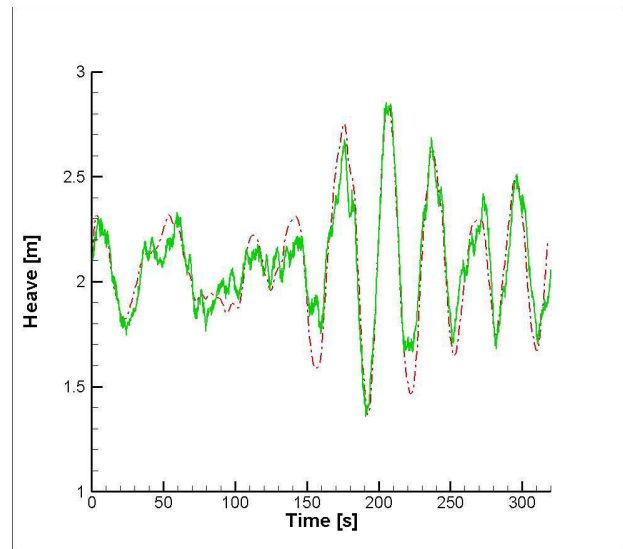


Figure 7: Comparison heave Test 218

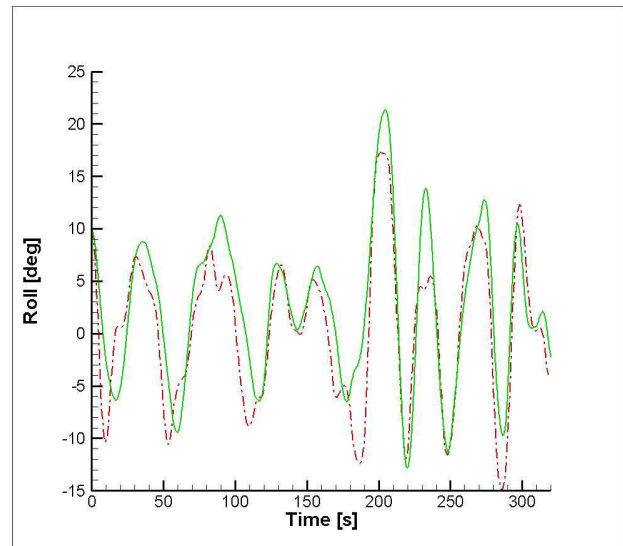


Figure 8: Comparison roll Test 218

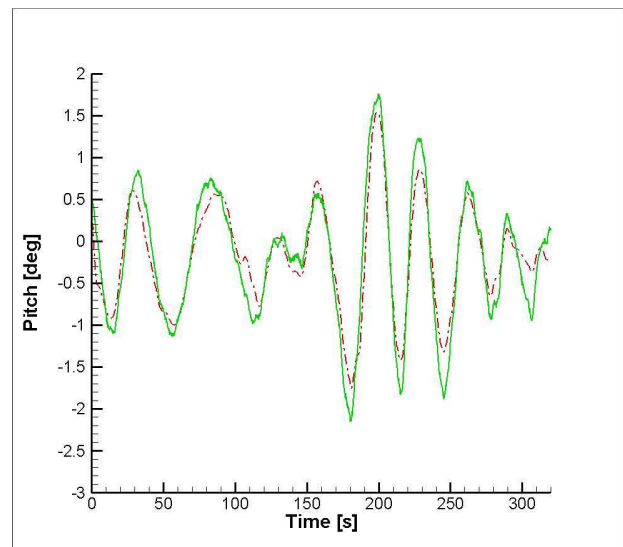


Figure 9: Comparison pitch Test 218

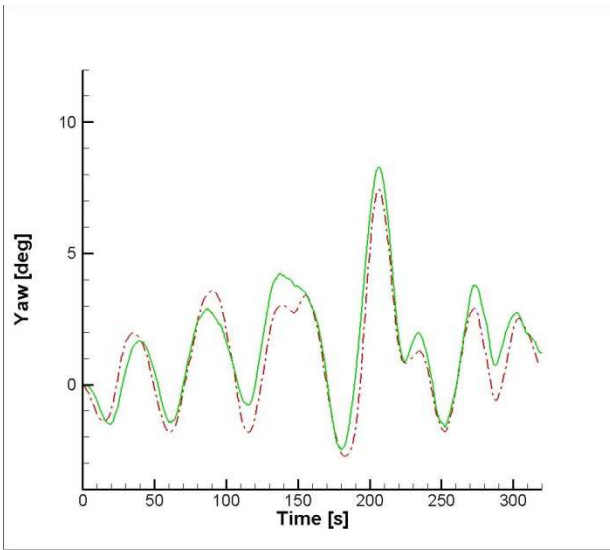


Figure 10: Comparison yaw Test 218

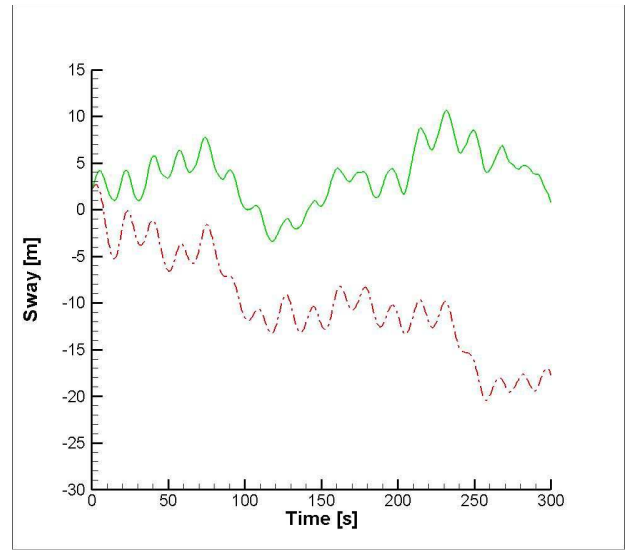


Figure 12: Comparison sway Test 205

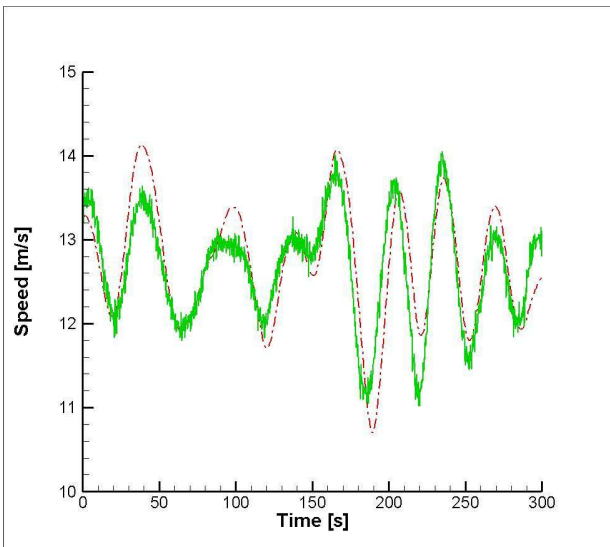


Figure 11: Comparison speed Test 218

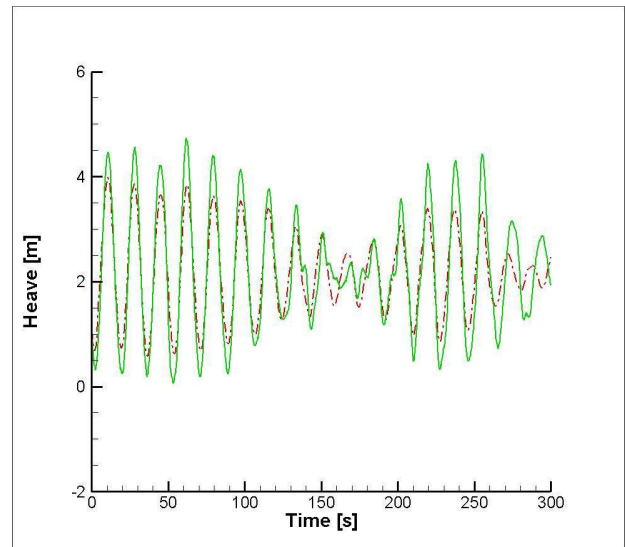


Figure 13: Comparison heave Test 205

Test 205 presents results for a higher waves with a higher encounter frequency. Under these conditions the ship experiences resonant roll. Figures 12 through 17 show the comparisons between FREDYN and experimental time series.

The sway motions in FREDYN show similar first order wave motion variations as the model test data, however the mean sway motion deviates from the start of the run. Heave, pitch and roll tend to be under-predicted by FREDYN although the phasing is quite well in line with the experimental data. The same is true for the yaw motion while the forward speed variations are reasonably well predicted.

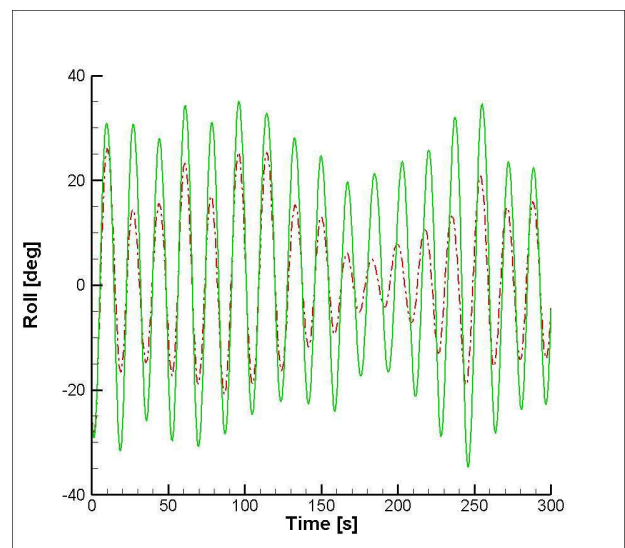


Figure 14: Comparison roll Test 205

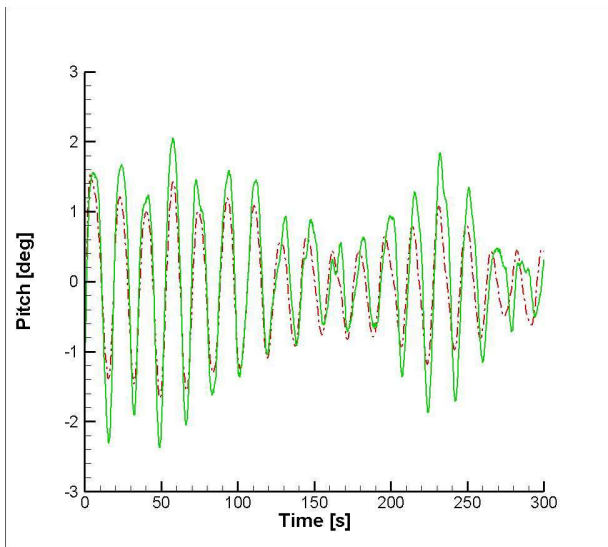


Figure 15: Comparison pitch Test 205

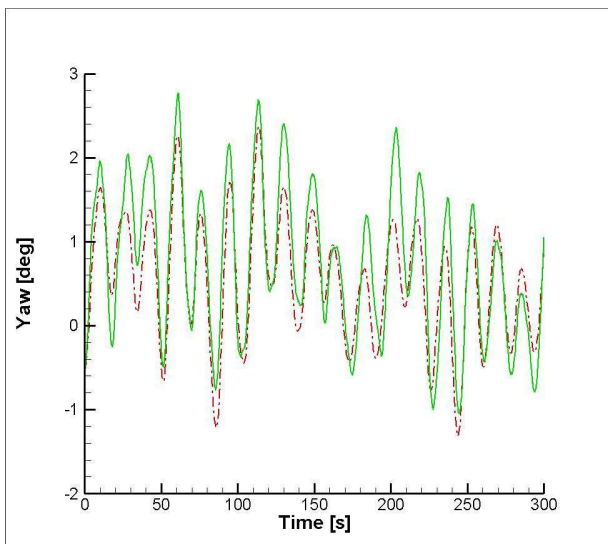


Figure 16: Comparison yaw Test 205

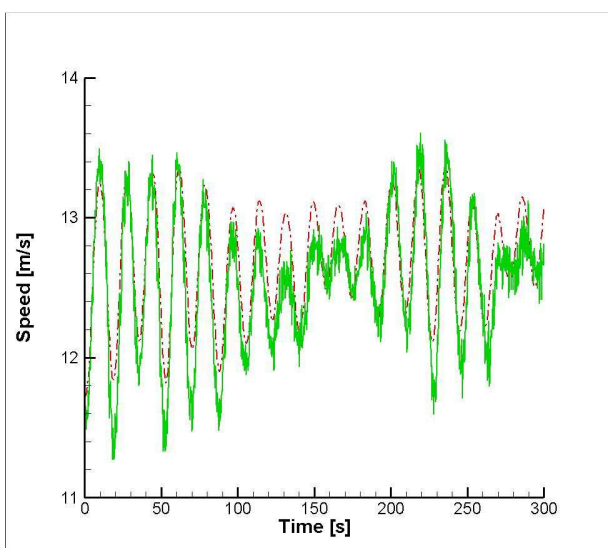


Figure 17: Comparison speed Test 205

5. CONCLUSIONS

A method has been presented to reconstruct experimental wave trains in a simulation program. The method is applied in the FREDYN simulation tool for a destroyer model operating in high stern quartering sea states at relatively high speed. The methodology is seen to produce acceptable results in general and enables one to validate simulation tools for rare events and large amplitude motions without relying on statistics.

A future improvement in the deterministic validation methodology can be obtained by starting the experimental data recording at zero speed and forcing the ship in the simulation method to have the same accelerations during the start-up transient so that the retardation functions will be initialised when the actual measurements start.

6. ACKNOWLEDGMENTS

Permission from the Cooperative Research Navies group to use the model test data is gratefully acknowledged.

7. REFERENCES

- Blok J.J. and Aalbers A.B., 1991, 'Roll damping due to lift effects on high speed mono hulls', 1st International Conference of High Speed Sea Transportation, FAST'91, Trondheim, Norway.
- Carette N. F. A. J. and Walree F. van, 2010, 'Validation of Time Domain Seakeeping Codes for a Destroyer Hull Form Operating in Steep Stern-quartering Seas', ITTC Workshop on Seakeeping, Seoul, Korea.
- Himeno Y., 1981, 'Prediction of Ship Roll Damping - State of the Art', Department of Naval Architecture and Marine



Engineering, University of Michigan,
Report No. 239.

Kat J.O., Pinkster D.J. and McTaggart K.A.,
2002, 'Random waves and capsize
probability based on large amplitude
motion analysis', 21st International
Conference on Offshore Mechanics and
Arctic Engineering, OMAE02, Oslo,
Norway.

Marshall S., 2010, 'Heavy weather Ship Hand-
ling Bridge Simulation', 11th International
Ship Stability Workshop, Wageningen.

Ypma E.L. and Harmsen E., 2012, 'Devel-
opment of a new methodology to predict
the capsize risk of ships', 11th International
Conference on the Stability of Ships and
Ocean Vehicles, Athens, Greece.





An Investigation on Stability under Dead Ship Condition of a Tumblehome Hull

Min Gu, *China Ship Scientific Research Center, Wuxi, China*, gumin666@gmail.com

Jiang Lu, *China Ship Scientific Research Center, Wuxi, China*, lujiang1980@yahoo.com.cn

Tianhua Wang, *China Ship Scientific Research Center, Wuxi, China*, tianhua_wang@126.com

ABSTRACT

Vulnerability criteria of stability under dead ship condition are now under development by the International Maritime Organization (IMO) in the framework of second generation intact stability criteria. A mathematical model for rolling in irregular beam wind and waves is presented and the Monte Carlo method is used in order to estimate the capsizing probability under dead ship condition. This method is applied to an unconventional “tumblehome” hull and the effect on stability of freeboard and metacentric height under dead ship condition of the tumblehome hull are investigated. Finally, model experiment is done. The tumblehome hull could be vulnerable in terms of stability under dead ship condition due to the low freeboard.

Keywords: dynamic stability; stability under dead ship condition; capsizing; tumblehome; vulnerability criteria

1. INTRODUCTION

Vulnerability criteria of stability under dead ship condition are under development at the International Maritime Organization (IMO) for insuring the safety of ships in waves, especially for unconventional ships. In recent years, unconventional ships, such as “tumblehome” ships attract many countries attention because these ships have better performance than conventional hulls, especially in propulsive and seakeeping performance. However, these improvements of the tumblehome hull could make tumblehome ships suffer stability failures in severe waves (Bassler et al., 2007, Belenky et al., 2008). Therefore, it is necessary to investigate the dynamic stability of the tumblehome hull.

Head-sea parametric rolling of the ONR tumblehome has been investigated, e.g. by Olivieri et al. (2010) and by Hashimoto et al. (2009). Pure loss of stability of the ONR tumblehome in following seas has been

investigated, e.g. by Hashimoto (2009). Broaching of the ONR tumblehome was investigated e.g. by Araki et al. (2010) and Hashimoto et al. (2011). The split-time method was presented by Belenky et al. (2008) to deal with capsizing probability of the ONR tumblehome under dead ship condition. One of the authors presented a coupled heave-pitch-surge-roll mathematical model, with added resistance taken into account, for investigating parametric rolling in head seas, (2010, 2011a). He also investigated the effect of parametric rolling on added resistance in regular head seas (2011b). However, investigations of stability under dead ship condition for unconventional ships (like “tumblehome” ships) are still rare. These ships could be vulnerable, under dead ship condition, in terms of their stability. This is one of the major failure modes. To develop vulnerability criteria, it is necessary to investigate the stability under dead ship condition of tumblehome hulls.



2. SUBJECT SHIP

Principal particulars and body plan of the subject ship are shown in Table 1 and in Fig.1. Restoring arm curves in calm water with different freeboards and metacentric heights are shown in figs.2 and 3, respectively.

Table1: Principal particulars of the tumblehome

Items	Ship	Model
Length: L_{pp}	132.0m	3.667m
Breadth: B	14.8m	0.411m
Depth: D	8.6/11.5m	0.239/0.319m
Draft: d	4.3m	0.119m
Displacement: W	4236t	88.6Kg
Longitudinal position of center of buoyancy from midship: LCB	1.700m aft	0.0472m aft
Metacentric height: GM	2.0m	0.0556m
Nature roll period: T_{ϕ}	8.808s	1.468s
Radius of gyration in pitch: K_{yy}	$0.24L_{pp}$	$0.24L_{pp}$
Block coefficient: C_b	0.492	0.492

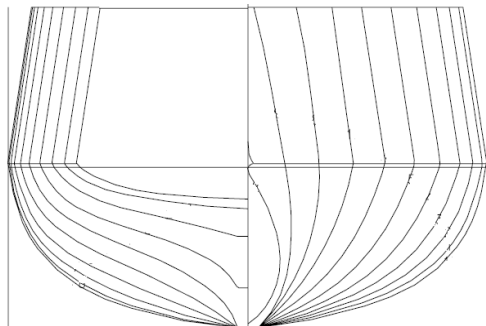


Figure 1: Body plan of the tumblehome

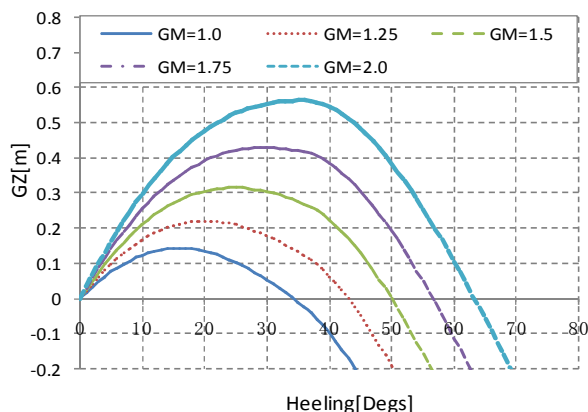


Figure 2: Restoring arm curve in calm water (D=8.6m)

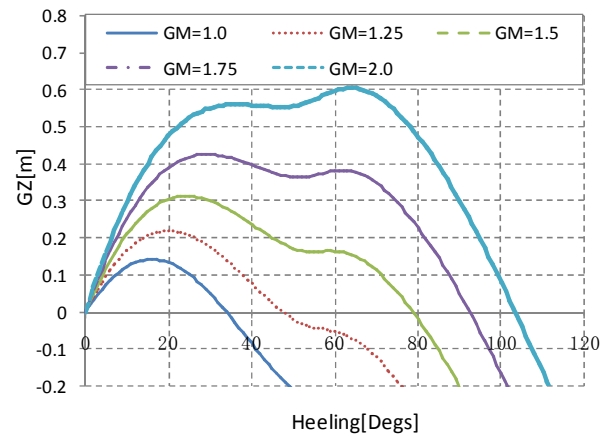


Figure 3: Restoring arm curve in calm water (D=11.5m)

3. MATHEMATICAL MODEL

In order to calculate the probability of stability failure under dead ship condition, the following nonlinear and uncoupled equation, with stochastic wave excitation and wind moment taken into account, is used.

$$\ddot{\phi} + 2\mu\dot{\phi} + \beta|\dot{\phi}|\dot{\phi} + \frac{W}{(I_{xx} + J_{xx})} GZ(\phi) = \frac{M_{wind}(t) + M_{wave}(t)}{(I_{xx} + J_{xx})} \quad (1)$$

where ϕ : roll angle, μ : linear roll damping coefficient, β : quadratic roll damping coefficient, W : ship weight, I_{xx} : moment of inertia in roll, J_{xx} : added moment of inertia in roll, GZ : righting arm, $M_{wind}(t)$: wind induced moment consisting of the steady and fluctuating wind moment. $M_{wave}(t)$ is wave exciting moment of Froude - Krylov component, and this because the roll diffraction moment and roll radiation moment due to sway can cancel out when the wave length is sufficiently longer than the ship breadth (Japan 2010). Dots denote differentiation with time.

The wind induced excitation moment can be calculated by the following equation:

$$W_{wind}(t) = 0.5 \times \rho_{air} C_m U_w^2 A_L H_C + \rho_{air} C_m U_w^2 A_L H_C U(t) \quad (2)$$

where: ρ_{air} : air density, C_m : the aerodynamic drag coefficient, U_w : mean wind velocity, and $U(t)$ is fluctuating wind velocity calculated by the Davenport spectrum (Japan 2010, Umeda 1992). Furthermore,

A_L : lateral windage area and H_C : the height of the center of the wind force from the center of the hydrodynamic reaction force.

The fluctuating wind velocity is calculated by the following equation (the Davenport spectrum is used).

$$U(t) = \sum_{i=1}^{N_w} b_i \sin(\omega_i t + \varepsilon_i)$$

$$b_i = \sqrt{2S_{wind}(\omega_i) \delta \omega}$$

$$S_{wind}(\omega_i) = K \frac{U_w}{\omega_i} \frac{X_D^2}{(1 + X_D^2)^{4/3}} \quad (3)$$

where

$$K = 0.03, X_D = 600 \frac{\omega_i}{\pi U_w} \quad (4)$$

The wave exciting moment of Froude-Krylov component can be calculated by the following equation:

$$W_{wave}(t) = W \cdot GM \cdot \gamma \cdot \Theta(t) \quad (5)$$

where γ is the effective wave slope coefficient calculated by recommended formula in 2008IS code, and $\Theta(t)$ is a wave slope calculated by the ITTC wave spectrum $S_{wave}(\omega)$ as follows.

$$\Theta(t) = \sum_{i=1}^{N_w} \frac{\omega_i^2}{g} a_i \sin(\omega_i t + \varepsilon_i)$$

$$a_i = \sqrt{2S_{wave}(\omega_i) \delta \omega} \quad (6)$$

4. EXPERIMENTS AND SIMULATIONS

Experiments with a 1/36 scaled model of the tumblehome ship were conducted at the Seakeeping Basin of the China Ship Scientific Research Center. The ship model was fixed by four wires with four short springs connected to the bow and the stern respectively in beam seas. Test conditions in the experiment are shown in table 2.

Table 2: Test conditions

		H(m)	T(s)		H(m)	T(s)
		Test1	2.52		18.0	Test8
regular waves	Test2	2.52	16.2	Test9	2.52	8.4
	Test3	2.52	13.2	Test10	2.52	7.8
	Test4	2.52	12.0	Test11	2.52	7.2
	Test5	2.52	10.2	Test12	2.52	6.6
	Test6	2.52	9.6	Test13	2.52	5.4
	Test7	2.52	9.0			
	irregular waves		$H_{1/3}$ (m)	T_p (s)		$H_{1/3}$ (m)
Test14		3.10	9.11	Test16	6.16	12.31
Test15		4.2	10.77	Test17	7.52	13.63

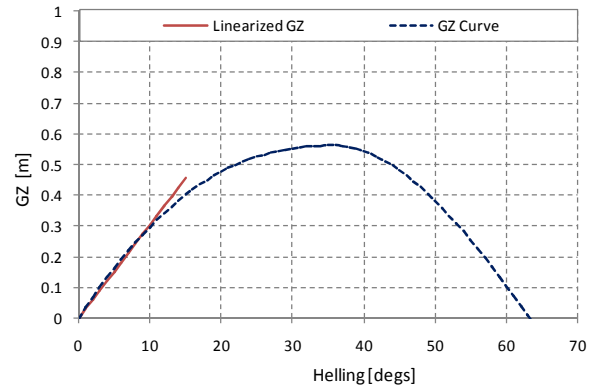


Figure 4: Linearized GZ curve and GZ curve in calm water at GM=2.0m (D=8.6m).

The resonance period in simulation with exact GZ curve is larger than that in experiment as shown in Fig.5. GZ curve is linearized within small roll angle as shown in Fig.4 and the resonance period in simulation with linearized GZ is same with that in experiment as shown in Fig.5. This indicates that the nonlinear relation of GZ with large roll angles could change the resonance period of rolling in beam seas. This means the method of piece-wise linear GZ curve recommended in IMO SLF53 for predicting stability under dead



ship condition could change the actual resonance period of rolling in simulation. The roll amplitudes in simulation are larger than that in the experiment as shown in Fig. 5. This is because the model ship could be overdamped by the four fixed wires with four short springs connected to the bow and the stern respectively.

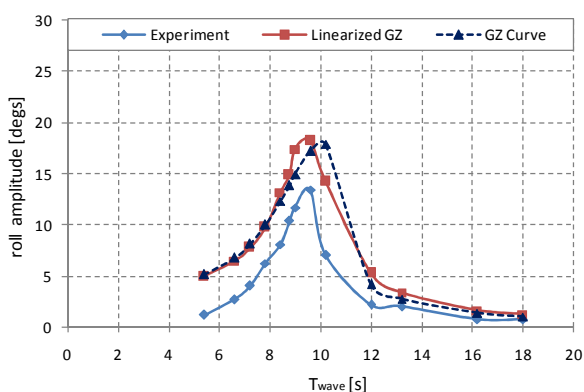


Figure 5: Roll amplitude in simulations and experiments with $H=2.52\text{m}$, $F_n=0.0$, $\chi=90^\circ$, $GM=2.0\text{m}$ and different wave periods.

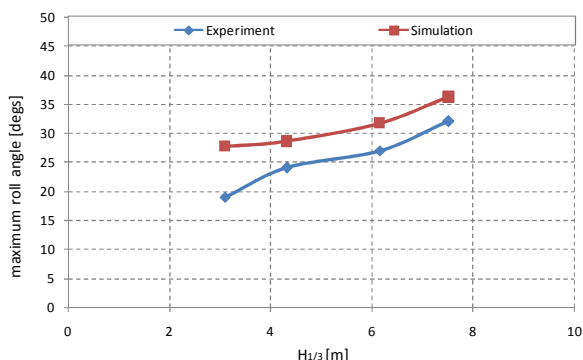


Figure 6: Maximum roll angle in simulations and experiments with $F_n=0.0$, $\chi=90^\circ$, $GM=2.0\text{m}$ with different significant wave height.

The simulated wave profiles do not correspond to those in the Seakeeping Basin. Thus the simulation is executed for ten realizations with different random phases of component waves as shown in Fig.7, and maximum roll angles in irregular beam seas are significantly different with different seed number due to limited simulating time. Although the minimum values of maximum roll angles in ten realizations of simulations are compared with

that in one realization of experiments, the simulations overestimate maximum roll angles as shown in Fig.6, which is also confirmed in regular beam seas. The main reason is that the model ship could be overdamped by the four fixed wires with four short springs; second reason is that free rolling in calm water could underestimate the rolling damping in waves with large rolling; the third reason is that the formula recommended by IMO for calculating wave slope coefficient calculated would be conservative. These three reasons are preferably to be further investigated in future.

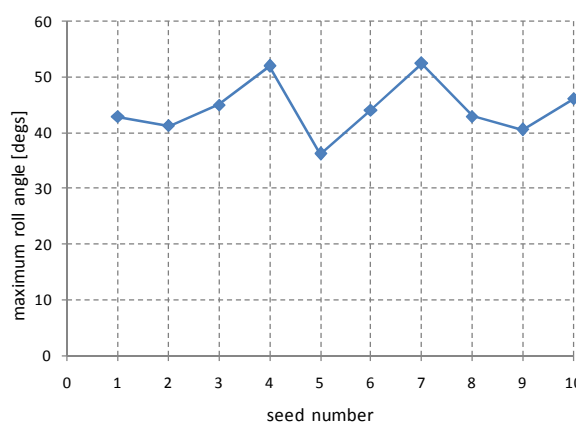


Figure 7: Maximum roll angles in simulations with $H_{1/3}=7.52\text{m}$, $T_p=13.63\text{s}$, $F_n=0.0$, $\chi=90^\circ$, $GM=2.0\text{m}$ and different seed number.

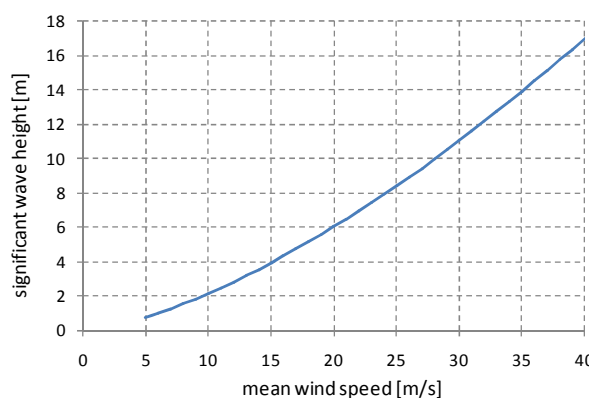


Figure 8: The function of significant wave height with mean wind speed.

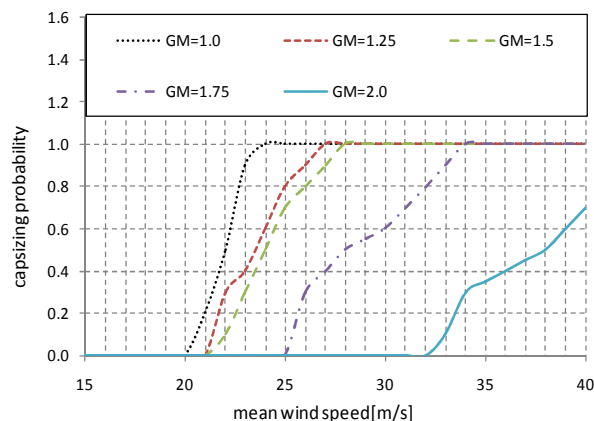


Figure 9: Capsizing probability with different mean wind speed at depth=8.6m.

The function of significant wave height with mean wind speed is shown in Fig.8 which is obtained by the formula recommended by IMO. Vanish angle of stability is set as capsizing roll angle, and Eq.(1) is used to calculate maximum roll angle in irregular beam seas, and then Monte Carlo method is used to estimate the capsizing probability for stability under dead ship condition.

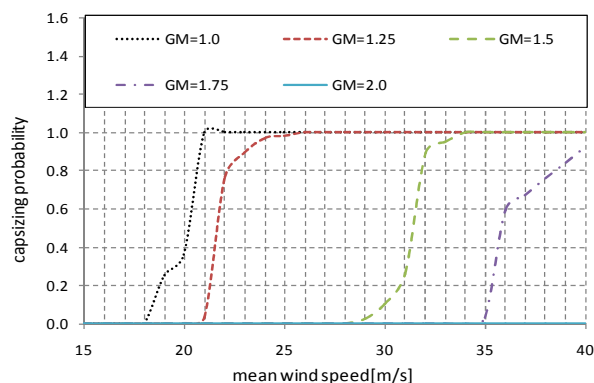


Figure 10: Capsizing probability with different mean wind speed at depth=11.5m.

The capsizing probability is increasing with GM decreases as shown in Figs.9 and 10. The stability in still water becomes better with a more high freeboard except for small GM as show in Figs. 2 and 3, and the capsizing probability is also decreasing as shown in Figs.9 and 10. Especially is that capsizing does not occur when GM is 2.0m. This means the tumblehome ship could be vulnerable of stability under dead ship condition due to a low

freeboard, and could never capsize in theory due to enough GM and appropriate freeboard. The limited wind speed in Weather Criterion could be larger than 35m/s for judging the vulnerable to stability under dead ship condition for a tumblehome ship as shown in Fig.10.

5. CONCLUSIONS

As a result of a systematic study on stability under dead ship condition of a tumblehome hull, the following remarks are noted:

- 1) The tumblehome ship could be vulnerable of stability under dead ship condition with a low freeboard and the limited wind speed in Weather Criterion could be larger than 35m/s.
- 2) A nonlinear and uncoupled roll equation with Monte Carlo method could successfully calculate the probability of stability failure under dead ship condition although it is a simple 1DOF approach.
- 3) The tumblehome ship could never capsize in theory with enough GM and appropriate freeboard.

6. ACKNOWLEDGEMENTS

The authors sincerely thank Prof. N. Umeda from Osaka University (Japan) for providing the authors with his useful advice on predicting stability under dead ship condition.

7. REFERENCES

- Araki M., Umeda N., Hashimoto H. and Matsuda A., 2010, "Broaching Prediction Using an Improved System-Based Approach", 28th Symposium on Naval Hydrodynamics, Pasadena, California.
- Bassler C., Campbell B. and Belknap W., 2007, "Dynamic Stability of Flared and Tumblehome Hull Forms in waves", 9th International Ship Stability Workshop,



Hamburg, German.

Science and Technology, Vol. 16, No.3, pp. 283-293.

Belenky V., Weems K.M., Lin W.M. 2008, "Numerical Procedure for Evaluation of Capsizing Probability with Split Time Method", 27th Symposium on Naval Hydrodynamics, Seoul, Korea.

Olivieri, A., Francescutto A., Campana E. and Stern F., 2010, "Experimental investigation of Parametric Roll in regular head waves for the ONR Tumblehome", 28th Symposium on Naval Hydrodynamics, Pasadena, California.

Hashimoto H., 2009, "Pure Loss of Stability of a Tumblehome Hull in Following Seas", Proceeding of 19th International Offshore and Polar Engineering Conference, Osaka, Japan.

Umeda N, Ikeda Y and Suzuki S., 1992 "Risk Analysis Applied to the Capsizing of High-Speed Craft in Beam Sea" .Proceedings of 5th International Symposium on Practical Design of Ships and Mobile Units, New Castle upon Tyne, Vol.2, pp1131-1145

Hashimoto H., Umeda N., Sogawa Y. and Matsuda A., 2009, "Parametric Roll of a Tumblehome Hull in Head Seas", Proceeding of 19th International Offshore and Polar Engineering Conference, Osaka, Japan.

Hashimoto H., Umeda N. and Matsuda A., 2011, "Broaching Prediction of a Wave-piercing Tumblehome Vessel with Twin Screws and Twin Rudders", Journal of Marine Science and Technology, Vol. 16, No.4, pp. 448-461.

Japan. 2010, "Draft Direct Assessment on Stability under Dead Ship Condition and Its Numerical Validation", SLF53/INF.10, Annex7, IMO.

Lu J., Umeda N. and Kun M., 2010, "Modeling Parametric Rolling in Regular and Irregular Head Seas with Added Resistance Taken into Account", Proceeding of 5th Asia-Pacific Workshop on Marine Hydrodynamics, Osaka, Japan, pp.93-98.

Lu J., Umeda N. and Ma K., 2011a, "Predicting Parametric Rolling in Irregular Head Seas with Added Resistance Taken into Account", Journal of Marine Science and Technology, Vol. 16, No.4, pp. 462-471.

Lu J., Umeda N. and Ma K., 2011b, "Theoretical Study on the Effect of Parametric Rolling on Added Resistance in Regular Head Seas", Journal of Marine



Mathieu Instability of Surfacing Submarine

Sergei Karlinskiy, *Senior Engineer*, Sergei.Karlinsky@yandex.ru

Andrei Efimov, *Senior Specialist*, *Central Design Bureau for Marine Engineering "Rubin"*,

neptun@ckb-rubin.ru

ABSTRACT

It is known that a submarine in near sea surface position as well as during surfacing/submerging in waves may become unstable. The paper presented assumes that there are two reasons of the instability: (1) first and second order wave excitation ("suction" force and moment, for example); (2) Mathieu roll/pitch instability, mainly due to the submarine heaving and pitching.

A time domain simulation of the submarine confused motion is the main technique for the stability study

Keywords: submarine, heaving, rolling, pitching, metacentric height, GM, Mathieu, instability.

1. INTRODUCTION

A submarine during surfacing/submerging as well as in heaving in a surface position in waves may become unstable. This occurs because as the submarine hull heaves up and down, its center of buoyancy also moves up and down, center of gravity also moves up and down (due to processes in the permeable section of the submarine hull near the waterline) and at the same time there is a change in water plane area and, so, metacentric height values changes accordingly (up to negative value). Large roll/pitch angles can appear due to the listed reasons. This phenomenon is known as parametric resonance, or as Mathieu instability.

2. KINDS OF MATHIEU INSTABILITY

There are several kinds of Mathieu instability. The one that bit a submarine crossing the sea surface in waves is the coupling between heave and roll/pitch responses. This occurs because the roll/pitch restoring moments changes as the submarine

heaves up and down. This phenomenon acts like a driving moment for the roll/pitch motions. If the heave natural period is at one-half of the roll/pitch period (or multiple to one-half)

$$T_Z = (n/2) T_{\theta/\psi} \quad (1)$$

where T_Z is the heave natural period,

$T_{\theta/\psi}$ is the roll/pitch natural period

$$n = 1, 2, 3 \dots$$

the roll/pitch resonance occurs and (in a lack of damping) there can be large roll/pitch responses. For very large waves the heave motion does not have to be exactly one-half the roll/pitch period for this to happen.

The another type of the heave - roll/pitch Mathieu instability occurs when a substantial wave period is close to the resonant heave period. The two responses (wave induced and resonant) create a periodic beating type heave motion those frequency is a difference of two mentioned above frequencies. If this difference



frequency happens to be equal the roll/pitch natural frequency another roll/pitch instability may result. A critical wave period T_C for this phenomenon is defined by

$$T_C = [(1/T_Z) + (1/T_{\theta/\psi})]^{-1} \quad (2)$$

where T_Z is the heave natural period (average),

$T_{\theta/\psi}$ is the roll/pitch natural period (also average).

For the typical submarine mentioned below (see Table 1): $T_Z = 9.5$ sec; $T_{\psi} = 10.3$ sec; $T_{\theta} = 10.3$ sec.

So for rolling as well, as for pitching

$$T_C = 5.2 \text{ sec}$$

This wave period is quite frequent in seas, so the heave - roll/pitch Mathieu instability (also named as a parametric resonance), is a rather probable.

There is a third type Mathieu instability we might be concerned with, also due heave motion. That is owing to a tapering in water plane area with heave (e.g. with the permeable section of the submarine hull near the waterline) then the heave restoring force will A simplified method to investigate the submarine motion is to employ linear radiation-diffraction analysis to determine the diffracted wave field and the linearized submarine motion.

3. SUBMARINE MOTION TIME DOMAIN SIMULATION

The submarine floating instability may be investigated by a time domain simulation.

be a function of heave motion. This can result in an instability if the motion is a fraction or multiple of the heave natural period. This is analogous to someone pushing a child on a swing. If the "push" is timed to correspond with the natural pendulum period of the swing the amplitude of the motion can get very high without inputting much energy.

The instability of non Mathieu type can be caused by second order wave forces and moments acting in vertical plane – so named “suction” forces and moments. These vertical forces and moments vary substantially in approaching to sea surface and can provoke suction of the upper submarine deck to the sea surface. This is the main reason why submarines are unable to float near sea surface in extreme seas.

The mean drift force/moment in heave, roll and pitch (suction force and moments) must be calculated by integrating the 2nd order mean wave pressure over the wetted surface of the structure. This usually requires a finer discretization of the geometry. The vertical mean drift force (suction force), is of interest for submarines structures with small water plane area of a fin, but the large plane of a submarine upper deck that provides a large suction force.

Computer time domain simulation of the submarine motion can be done by use of the partially linearized equations of the submarine motion in a vicinity of the sea surface. They are presented simplistically as below:



$$(M+\lambda_{33}) (d^2z/dt^2) + C_{33} (dz/dt) + \rho g S(z) = A_z \cos (\omega t + \delta_z) + F_{SZ} \quad (3)$$

$$(J_x + \lambda_{44}) (d^2\theta/dt^2) + C_{44} (d\theta/dt) + \rho g V h(z) = A_\theta \cos (\omega t + \delta_\theta) + M_{SX} \quad (4)$$

$$(J_y + \lambda_{55}) (d^2\psi/dt^2) + C_{55} (d\psi/dt) + \rho g V H(z) = A_\psi \cos (\omega t + \delta_\psi) + M_{SY} \quad (5)$$

where

M = submarine mass, tonnes;

J_x, J_y = moments of inertia of the submarine hull, tonnes*m²;

z, θ, ψ = vertical (m), roll, pitch (dg) motions;

$\lambda_{33}, \lambda_{44}, \lambda_{55}$ = added masses and moments of inertia coefficients of the submarine hull;

C_{33}, C_{44}, C_{55} = drag coefficients;

ρ = seawater density, tonnes/m³;

$S(z)$ = current waterline area, m²;

V = initial volume of the submarine hull, m³;

h/H = transversal/longitudinal methacentric height, m;

A_z, A_θ, A_ψ = amplitudes of the wave forces and moments;

ω = wave frequency, 1/sec;

$\delta_z, \delta_\theta, \delta_\psi$ = phases of corresponding wave forces.

F_{SZ}, M_{SX}, M_{SY} = wave 2nd order force and moments (suction force and moments)

As it can be seen, all mentioned equations are of a Mathieu type equations and so, the submarine motion can be subjected by several types of Mathieu's instability.

For example, as brief approximation it can be assumed that the restoring moment can be defined as

$$\rho g V h = \rho g V [h_0 + a_z \cos(\omega t)] \quad (6)$$

where

h_0 (or H_0) = initial transversal/longitudinal methacentric height (without taking the submarine oscillations into account);

a_z = heave amplitude, m

For mono-harmonic excitation (6) the values a_z and ω are constant, so the elastic members in equations (4) and (5) are harmonics, and solutions of the Mathieu equation are well known.

Nevertheless, in purpose to evaluate an influence of nonlinearities, the equations (3) to (5) were determined by use of the FEM program "Anchored Structures" (by St.-Petersburg Technical University) which deals with dynamic nonlinear processes and performs frequency calculations as well as a time domain simulation. Main approaches and solutions of this program including solutions on parametric oscillations are in accordance with DNV-RP-C205 "Environmental Conditions and Environmental Loads" [1].

The submarine main particulars are shown in Table 1 (See also snapshots at Figures 1 to 3).

Computer time domain simulation is done for the submarine in three positions for examination of the mentioned above propositions (See Figures 1 to 3).



Table 1: Submarine main particulars

Particular	Symbol	Submarine draught (depth), m		
		4.5	7.75	11
Dimensions, m	LxBxH	63x6.8x6.75		
Mass, tonnes	M	1390	1990	2050
Center of gravity height (COG), m	z_g	3.25	3.46	3.48
Displacement*, m^3	V	1360	1950	2000
Transversal methacentric height (TGM), m	h	0.32	-0.005	0.09
Longitudinal methacentric height (LGM), m	H_m	62.2	1.0	0.09

* Sea water density is assumed as 1.025 tonnes/ m^3

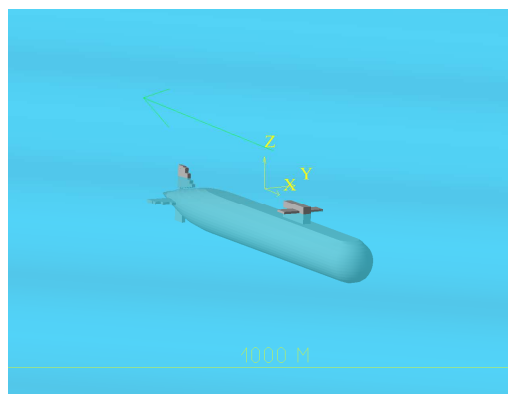


Figure 3: Motion of the submarine in the intermediate semi-submerged position (7.75 m draught)

As wave excitation in the time simulation were used the regular wave of $H_s = 4.5$ m and period of $T_p = 10$ sec.

A preliminary linear analysis has been done using the Response Amplitude Operators (RAO's) for three kinds of motions (heave, roll, pitch) that have been obtained by frequency calculations. The RAO's shown at Figures 4 to 6, were calculated for the submarine intermediate semi-submerged position (7.75 m draught, see Figure 3) which can occur when the submarine is pulled up by a suction force (See Figure 11) as well, as in case of the submarine surfacing/submerging.

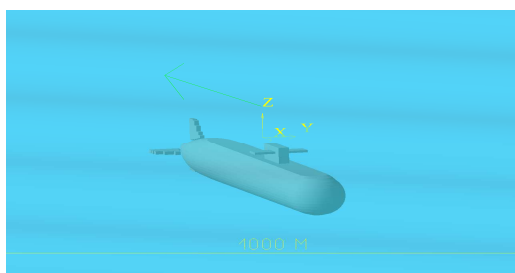


Figure 1: Motion of the submarine in a fully submerged position (11 m draught)

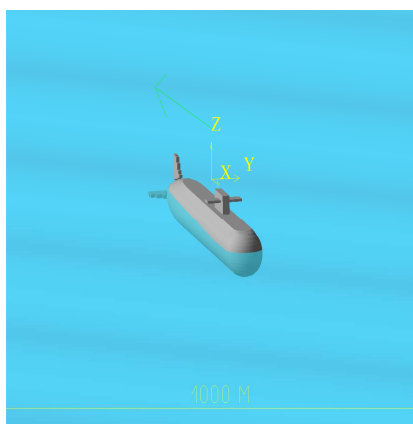


Figure 2: Motion of the submarine in a surfaced position (4.5 m draught)

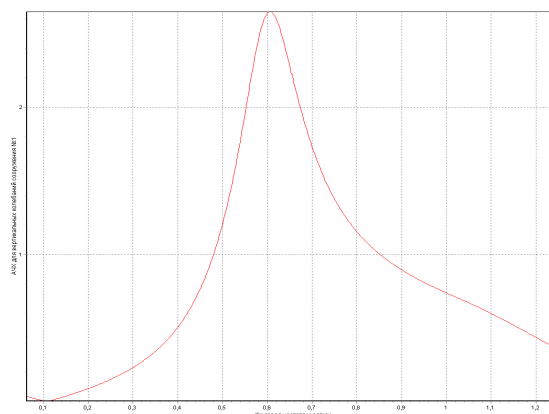


Figure 4: RAO of the submarine heave motion

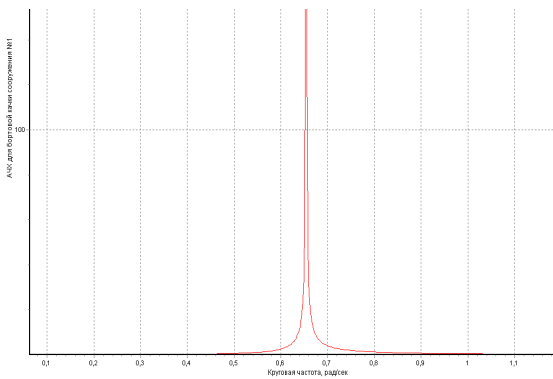


Figure 5: RAO of the submarine roll motion

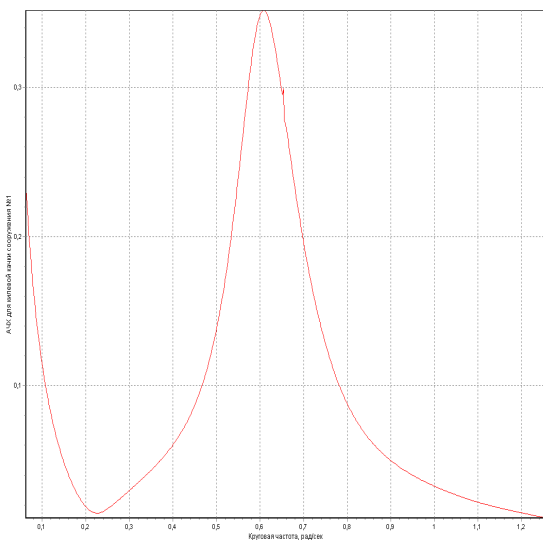


Figure 6: RAO of the submarine pitch motion

As it can be seen from the graphs of the RAO's the natural periods are as follows:

Heave: $T_z = 10.3$ sec

Roll: $T_\theta = 9.5$ sec

Pitch: $T_\psi = 10.3$ sec

Mentioned above natural periods actually can be much more due to sharp decrease of the longitudinal and transversal GM in process of the submarine descending.

As it can be seen from results of the motion time simulation (see Figure 11 and 12), the actual submarine draught in waves can become 6 m or less due to the wave unduced suction force. In the same time, in the process of

heaving the submarine draught varies from 6.5 to 8.5 m. Figures 7 and 8 show that the negative GM (both transversal and longitudinal) appears between 6 to 7.3 m draught.

The negative GM at the plot between 6 to 7.3 m draught can lead to excitation of parametric oscillations of Mathieu type.

In this case, the only nonlinear technique like a time domain simulation leads to the correct result.

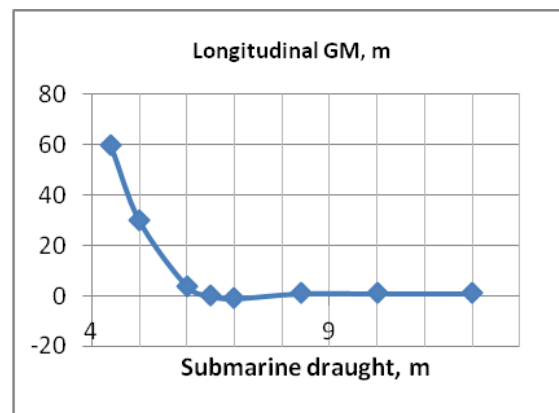


Figure 7: Longitudinal GM v/s the submarine draught.

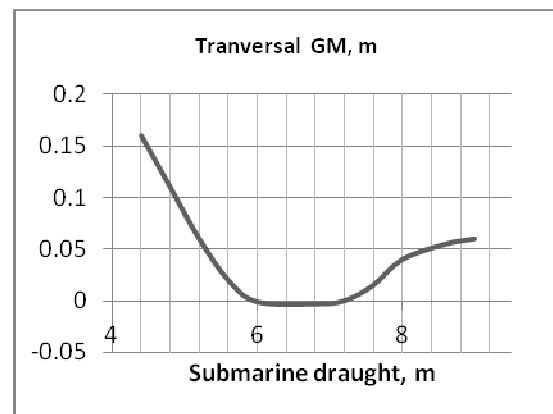


Figure 8: Transversal GM v/s the submarine draught

4 MOTION TIME DOMAIN SIMULATION

The time domain simulation of the submarine motion in a vicinity of a sea surface



have been fulfilled by use of the program “Anchored Structures” as mentioned above. The simulation is done for submarine specified draught 7.75 m which is between submarine upper deck and upper end of the fin (i.e. near planes).

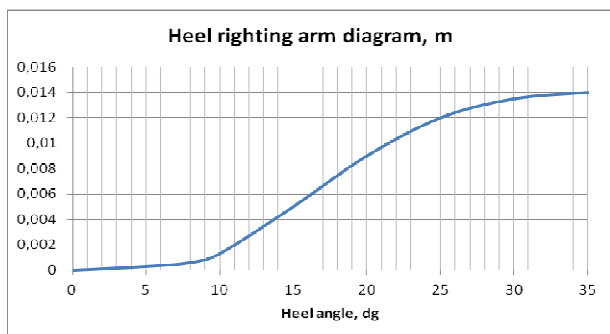


Figure 9: Heel righting arm at the draught of 7.75 m, m

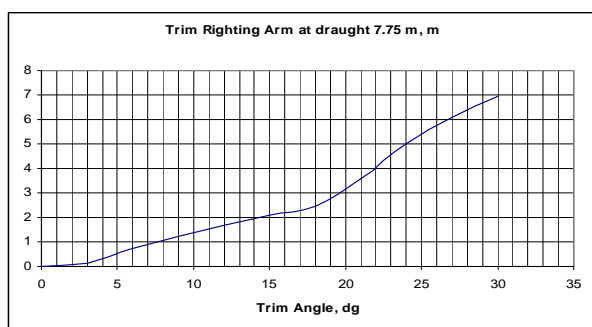


Figure 10: Trim righting arm at the draught of 7.75 m, m

As first the hydrostatic calculations were fulfilled and the stability parameters were obtained. The heel and trim righting arms diagrams are shown at Figures 9 and 10. As can be seen the righting arms are fully positive and GM is also positive. But, as had been mentioned above, the actual submarine draught in waves can become 6 m or less due to the suction force, and so the negative GM and negative heel and trim righting arm will appear.

The time domain simulation was carried out under the excitation of the regular wave of $H_s = 4.5$ m and period of $T_p = 10$ sec.

The submarine heaving excited by waves, provokes such a situation that appears as the Mathieu’s instability. The time domain simulation of the submarine motion has demonstrated the phenomenon of a sharp increase of the submarine oscillations (heave, pitch, roll) as a result of the Mathieu’s instability enhanced by wave excitation. The snap-shot at Figure 11 shows the unstable submarine position in the intermediate draught and trim. This position is caused by the submarine ascending higher than 7.75 m under action of the wave induced suction force.

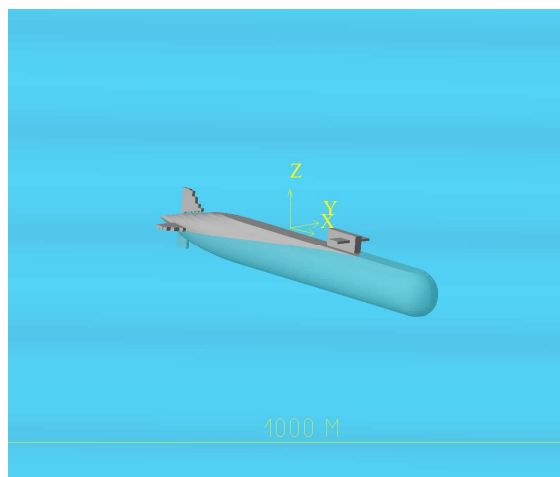


Figure 11: The submarine pulled up by a suction force

The results of the time simulation are shown in the graph of Figure 12. The growing parametric oscillations: heaving, rolling, pitching) of the submarine in the position shown at Figure 11, had appeared due to the common Mathieu instability. The main reason of the instability is the submarine heaving, caused by the wave excitation. As can be seen from Figure 12 the heaving amplitude exceed 2 m, and after it rolling/pitching amplitude grows in 2 or 3 times.

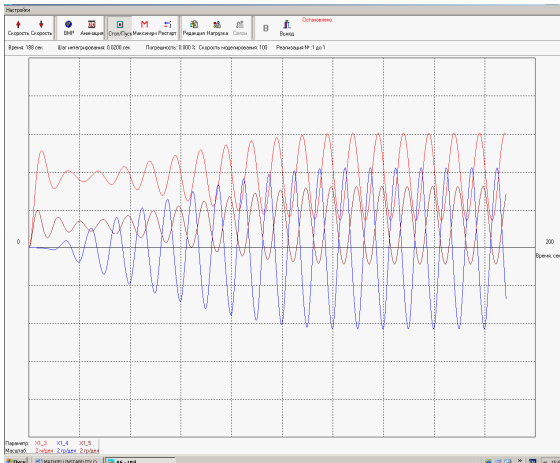


Figure 12: The growing parametric oscillations (heave, roll, pitch) of the submarine in the position shown at Figure 12 (red is heaving, blue - rolling)

5 REFERENCES

Baranov A., Efimov, A. and Mrykin, V.,
2003, "Surfacing Submarine Stability",
Proceedings of the STAB Conference, Madrid

DNV-RP-C205, 2007, "Environmental Conditions
and Environmental Loads".





Naval Landing Craft Stability – Simulation of Extreme Roll Motions and Shipping of Water into the Well Deck

Peter Hayes, *DNPS, Department of Defence, Australia*, peter.hayes5@defence.gov.au

Warren Smith, *University of New South Wales Canberra, Australia*, w.smith@adfa.edu.au

Martin Renilson, *Higher College of Technology, UAE*, martin.renilson@hct.ac.ae

Stuart Cannon, *DSTO, Department of Defence, Australia*, stuart.cannon@dstodefence.gov.au

The views expressed in this paper are those of the authors and not necessarily endorsed by the Department of Defence, Australia.

ABSTRACT

The stability criteria that need to be applied to landing craft are currently being investigated through various research programs sponsored by the Australian Department of Defence. One of these research programs involved extensive semi-captive model tests in beam waves, based on a series of three models having different freeboards and a common, removable bulwark. The various hull/bulwark configurations were tested at three KG values in regular waves.

In a substantial number of cases, there was significant water on deck or water in the well. Ship motion simulation studies have subsequently been performed to compare with the model data. The premise was that if adequate correlation was obtained, simulation could be used to assess survivability in irregular waves.

Keywords: *Landing Craft, Stability, Simulation, Water on Deck*

1. INTRODUCTION

The Royal Australian Navy (RAN) assesses the stability of landing craft using naval stability criteria largely derived from those presented by Sarchin and Goldberg (1962). The stability criteria that need to be applied to landing craft are currently being investigated through various research programs by the Defence Science and Technology Organisation (DSTO), the Directorate of Navy Platform Systems (DNPS), the University of New South Wales Canberra at the Australian Defence Force Academy (UNSW) and the Australian Maritime College (AMC).

One of these research programs involved extensive semi-captive model tests in beam waves. Ship motion simulation studies have subsequently been performed to compare with the model data. This paper focuses on the nu-

merical analysis: modelling the hulls, well and restraint system; tuning the roll damping; and presenting and discussing the results.

2. STABILITY RESEARCH

Existing stability criteria are based on the still water characteristics of the vessel, incorporating factors to account for operation in severe environments. Some, such as the basic International Maritime Organisation (IMO) criteria, require nominated characteristics of the righting arm curve, including minimum areas under the GZ curve and minimum GM values. These were based on earlier work, such as that by Rahola (1939). Because these types of criteria have been derived empirically they are strictly only applicable to the data set and the environments used in their derivation. However



these criteria have been extended to many vessel types and sizes not in the original data set.

More recently, quasi-static criteria that attempt to include the effects of wind and waves have been introduced. In these criteria, wave effects are usually introduced to the still-water righting arm curve by a 'roll-back' angle. Wind effects are introduced by determining the upright wind heeling lever and applying an assumed function defining the variation with heel. The authors are unaware of any standards that allow for the effects on stability of the entry of green seas into wells.

The wind/wave criteria do not address other forms of instability in waves, for example that resulting from a broaching event. There is now considerable research being conducted to include more aspects of dynamic stability. The Cooperative Research Navies (CRN) project, of which Australia is a member, developed the ship motion and dynamic stability simulation software, FREDYN, originally developed for slender monohulls. The CRN continues to develop FREDYN, expanding the range of hull forms. Use of this type of software, in conjunction with the results of model and full scale trials as benchmarking tests, will ultimately allow more comprehensive stability criteria to be derived than those currently available.

3. INTACT STABILITY EXPERIMENTAL PROGRAM

Hayes *et.al* (2010, 2012) presented an intact stability experimental program based on a family of three geometrically similar models with different hull depths, fitted at times with a bulwark making an enclosed well. The design of the models is shown in Figure 1.

These models were intended to be generic rather than representative of existing designs. At a scale of 1:26, the 70 mm depth model approximates a contemporary RAN design. Where full scale or full size are discussed in this paper, a scale of 1:26 applies.

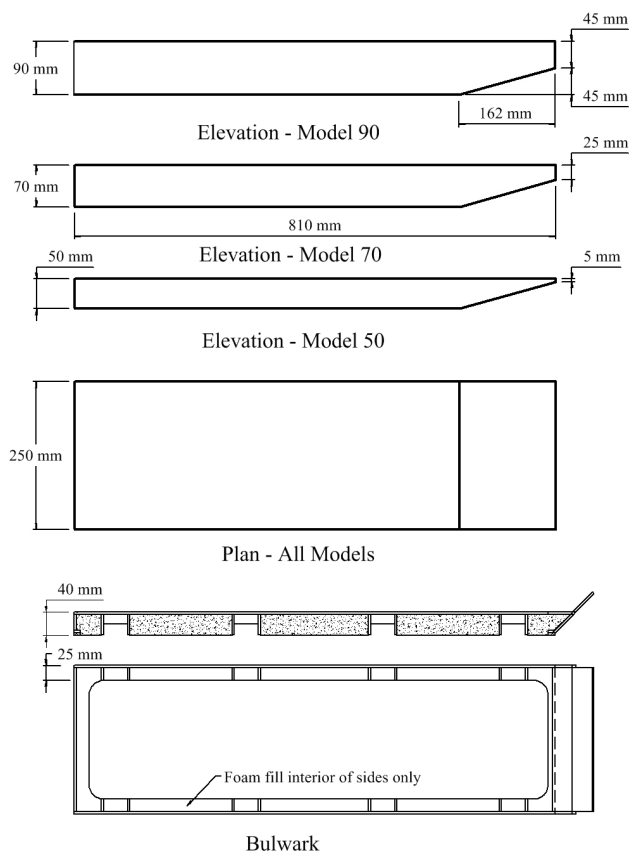


Figure 1: Design of Generic Model Series

The intention was to experimentally determine roll responses to waves at different values of freeboard and KG. The model configuration details and those of the corresponding nominal full size vessels are shown in Table 1. Three values of KG were tested, ranging from 76 mm to 116 mm at model scale.

An experimental research program, designed to assist with the validation of FREDYN, was conducted in the towing tank at AMC, Launceston, in 2009 and 2010. The models were tested in steep regular beam waves at the three KG values.

Significant data has been collected to help validate FREDYN for use with landing craft. The data collected consisted of the roll and heave response of the models in regular waves. Wave heights were large for the model, corresponding to 1.3 m to 3.9 m wave heights for a full scale 21 m vessel. The models were tethered to limit sway, surge and yaw.

Table 1: Test Configuration Details

Parameter	Model	Full Size
Scale Ratio	26	
Length BP	810.00 mm	21.06 m
Beam	250.00 mm	6.50 m
Draught	42.00 mm	1.09 m
Displacement	7.60 kg	133.70 t
KM	158.50 mm	4.12 m
50mm Model		
Freeboard to deck	8.00 mm	0.21 m
Freeboard to Bulwark	48.00 mm	1.25 m
70mm Model		
Freeboard to deck	28.00 mm	0.73 m
Freeboard to Bulwark	68.00 mm	1.77 m
90mm Model		
Freeboard to deck	48.00 mm	1.25 m
Freeboard to Bulwark	88.00 mm	2.29 m
Low KG		
KG	76.00 mm	1.98 m
GM	82.50 mm	2.15 m
Radius Gyration in Roll	100.00 mm	2.60 m
Natural Roll Frequency	1.14 Hz	0.22 Hz
Natural Roll Period	0.88 sec	4.47 sec
Middle KG		
KG	96.00 mm	2.50 m
GM	62.50 mm	1.63 m
Radius Gyration in Roll	100.00 mm	2.60 m
Natural Roll Frequency	0.93 Hz	0.18 Hz
Natural Roll Period	1.08 sec	5.48 sec
High KG		
KG	116.00 mm	3.02 m
GM	42.50 mm	1.11 m
Radius Gyration in Roll	100.00 mm	2.60 m
Natural Roll Frequency	0.68 Hz	0.13 Hz
Natural Roll Period	1.47 sec	7.50 sec

The experimental test set-up is shown in Figure 2. Linear displacement transducers were employed to measure roll and heave. The transducer lines and the mooring system have been highlighted in white. The mooring system con-

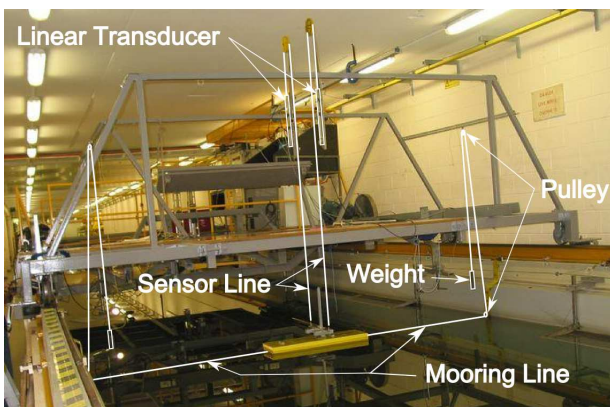


Figure 2: Experimental Set-Up

sisted of lines passed through pulleys to suspended weights, creating approximately constant force mooring lines of variable length.

4. FREDYN MODELLING

The hulls were modelled in 3D CAD software at full scale, from which the FREDYN data was developed. FREDYN cannot directly account for a well that can take on water. In the cases where a bulwark was fitted, the hull was modelled as closed to the top of the bulwark and the well modelled as a series of tanks. The well was subdivided into four equal sections longitudinally and two transversely. Openings to the sea were defined on the top surface of all tanks and each common tank boundary was defined as an opening. Default flow rates were used for all openings. This scheme was adopted to provide for some measure of progressive flow in the FREDYN flooding module.

Figure 3 shows an isometric view of one of the configurations modelled – based on the 70 mm depth model fitted with the bulwark with closed freeing ports.

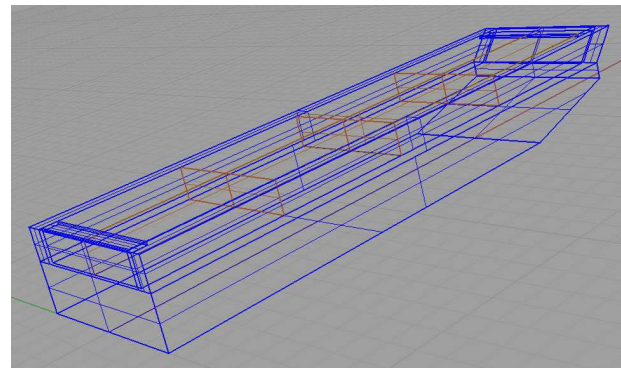


Figure 3: Isometric View of a 3D CAD Model

User defined roll damping coefficients were determined by trial in a multi stage process:

- The KG was set such that the GM calculated by FREDYN matched the scaled model GM. It was found that small adjustments in KG were necessary – most likely experimental error in determining the model KG and possibly the method of calculating the hydrostatics employed by FREDYN.



- The radius of gyration was set such that the frequencies matched. The radius of gyration needed to be adjusted by substantial amounts at the medium and higher KGs: 2.5 m (95% of scaled value); 2.95 m (68%) and 3.27 m (69%) for the low, medium and high KG configurations respectively. This is most likely experimental error – the tilt frame used to measure the radius of gyration was designed for much larger models than tested in this program. A more accurate method of determining the radius of gyration is required.
- Initial angle and the linear and quadratic damping coefficients were adjusted by trial and error to get the best fit between the numerically predicted roll decay curve and the experimentally measured one.

Initially, models with each of the three KGs were tested separately. The resulting coefficients were similar, so further tests were conducted to see if a common set could be determined. The final linear and quadratic damping

values adopted for all numerical runs were:

$$b_{lin} = 220 \text{ kNms/rad}$$

$$b_{quad} = 1400 \text{ kNms}^2/\text{rad}^2.$$

These values gave a very good correlation between the predicted roll decay using FREDYN and the actual roll decay obtained from the roll damping experiments, as shown in Figure 4. There were no forward speed dependent damping values defined.

The tethering arrangement was modelled numerically by two methods:

- Sway and yaw fixed to simulate that the model was largely restrained in these degrees of freedom – labeled ‘FREDYN Surge Yaw’ or ‘FREDYN SY’
- Mooring lines from the model to fixed positions corresponding to the tank sides, with the spring constant of the mooring lines selected by trial to match observed deflection as closely possible – labeled ‘FREDYN Mooring’ or ‘FREDYN M’.

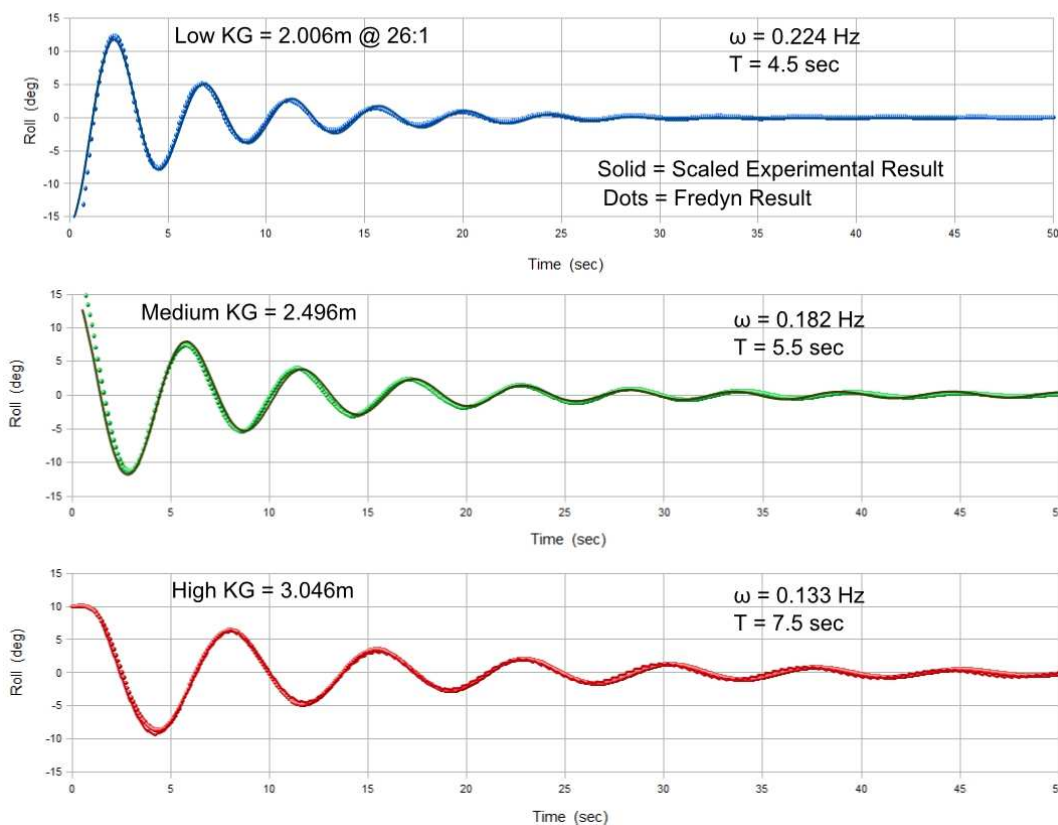


Figure 4: Comparisons of FREDYN Roll Decay Predictions to Experimental Roll Decay

5. NUMERICAL PREDICTIONS

FREDYN was used to predict the vessel motions in regular waves at the scaled wave heights and periods corresponding to the experimental data. Simulations were run for 100 seconds, including the default wave ramp up of 30 seconds. Deep, fresh water was assumed.

Examples of the results in the time domain are given in Figures 5, 6 and 7. In these runs, FREDYN predicted an immediate capsizing (which did not occur in the experimental series), no water entering the well and moderate water entering the well respectively. Note the average list angle that occurs after the water is taken onboard.

The Appendix presents selected results, showing numerical predictions with the corresponding model data. These results have been examined by two methods. The first was a direct comparison of the real time FREDYN predicted roll to experimentally measured roll. The second was by plotting and comparing predicted and measured roll angles for non-dimensional frequency ($=$ wave frequency / vessel natural frequency).

Figure 8 shows the real time roll comparison for run 216 at full scale, based on the 70 mm model with bulwark fitted. This run was a small wave, 1.3 m, at about the natural frequency. There was no water over the bulwark and the model lay beam onto the waves without corkscrewing.

Figure 9 shows the roll comparison for run 210, using the 70 mm model with bulwark fitted. This run was a medium wave, 2.6 m, at a wave frequency higher than the natural frequency. The following observations apply:

- There was some water over the bulwark and the model corkscrewed a little.
- The model displayed an average list.
- The FREDYN predictions using the mooring exhibited the same trends, especially

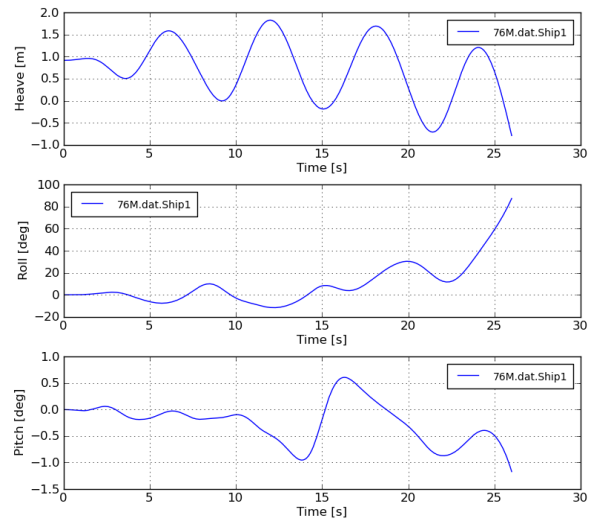


Figure 5: FREDYN Predictions for Run 76 with mooring

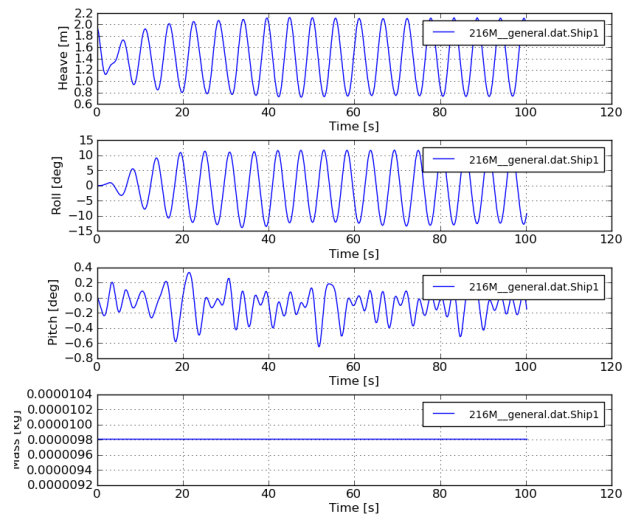


Figure 6: FREDYN Predictions for Run 216 with mooring

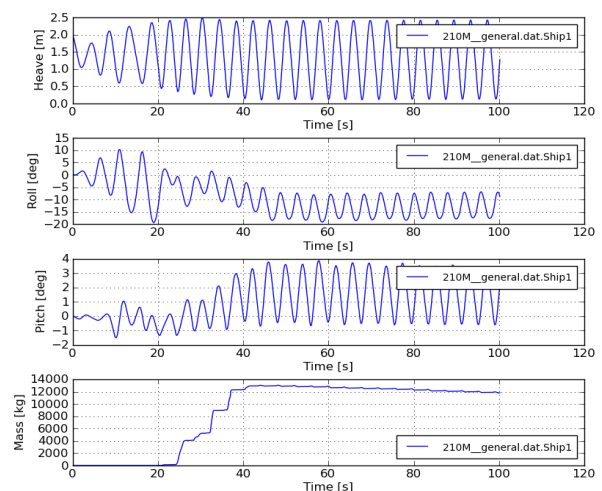


Figure 7: FREDYN Predictions for Run 210 with mooring

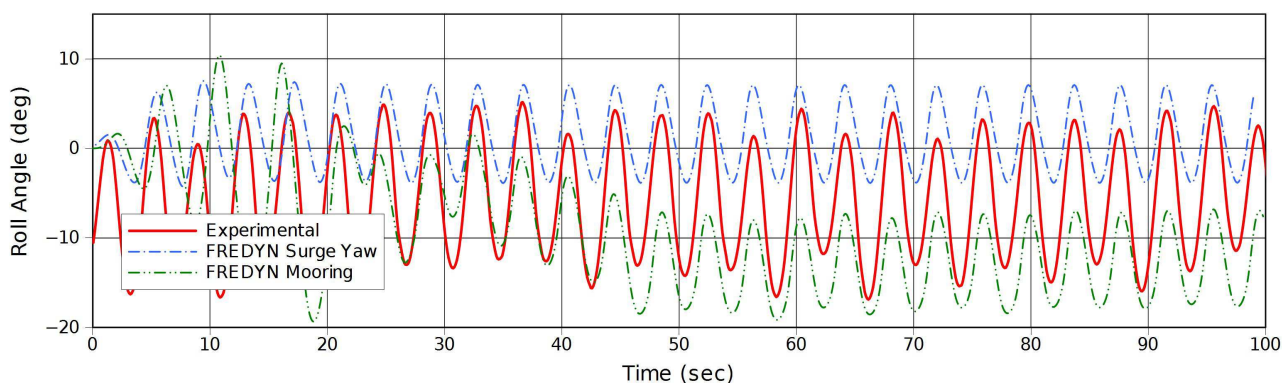


Figure 8: Run 216 FREDYN and Experimental Real Time Roll

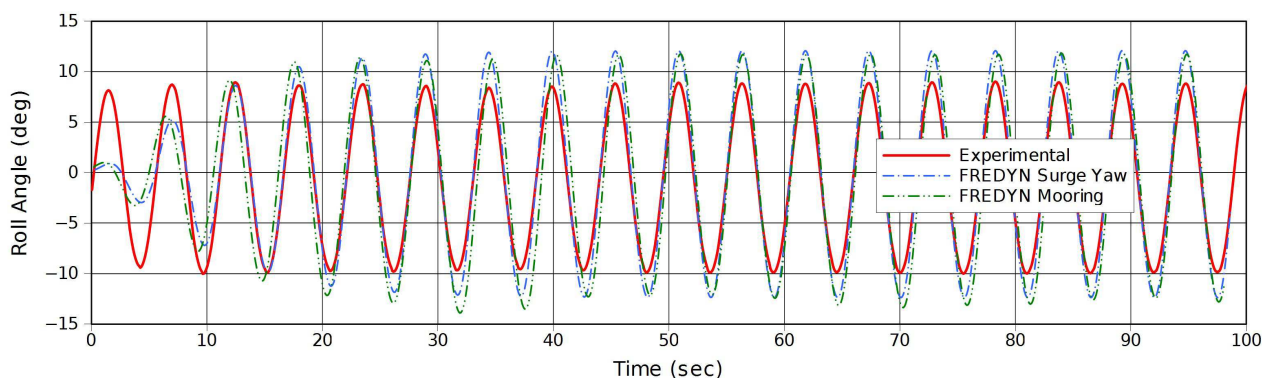


Figure 9: Run 210 FREDYN and Experimental Real Time Roll

- after some water was taken at 30–40 seconds (refer to Figure 7) although list and roll magnitude were not the same.
- The FREDYN predictions using fixed sway and yaw did not take on water.

A number of comparisons of predicted and measured roll angles for non-dimensional frequency are presented in Figures 10, 11, 12 and 13. In these plots, the lines are cubic splines, passing through the data points. The curves do not necessarily show the shape of the underlying function but mainly serve to connect a family of data points. Not all model runs were analysed using FREDYN. Any additional experimental data points have been included.

Figure 10 shows the roll amplitudes for the 90 mm model without bulwark, at the low KG value, in 100 mm waves (2.6 m at full size). The data points correspond to runs 14, 16, 17 and 19. In the model experiments, there was water over the deck for the two higher frequencies. FREDYN predictions tend to give larger

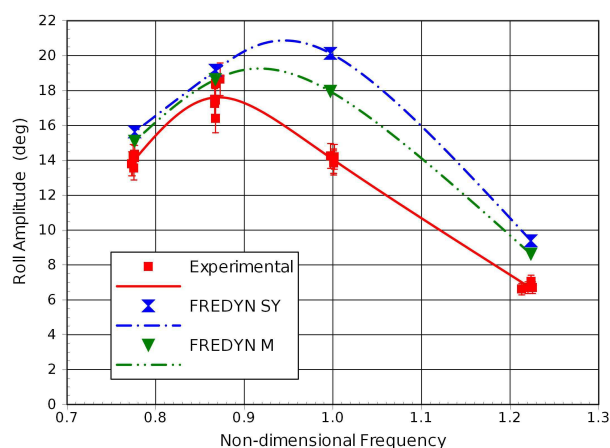


Figure 10: Roll of 90 mm Model without bulwark, low KG, in 100 mm waves

roll angles, especially around the vessel natural roll frequency.

Figure 11 shows the roll amplitudes for the same model, configured to the high KG value in 50 mm waves (1.3 m at full size). Cork-

screwing was very minimal. The data points correspond to runs 194, 195, 196, 197 and 198.

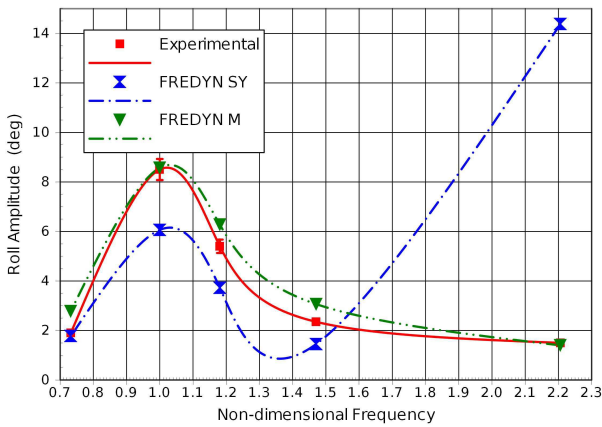


Figure 11: Roll of 90 mm Model without bulwark, high KG, in 50 mm waves

The FREDYN predictions using the mooring closely match the experimental data. Figure 12 shows roll amplitudes for the 70 mm model with bulwark and closed freeing ports, at the medium KG value, in 100 mm waves (2.6 m at full size). The data points correspond to runs 208, 209, 210, 211, 212, 213, and 215. In the model experiments, there was water into the well at the three higher frequencies. FREDYN predicted water into the well for most runs and generally matched the experimental roll data with a few exceptions.

Figure 13 shows the measured and predicted roll amplitudes for the same 70 mm model configuration but in 50 mm waves (1.3 m at full

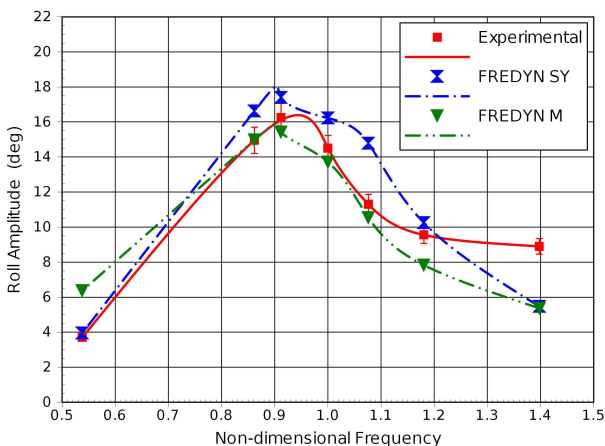


Figure 12: Roll of 70 mm Model with bulwark and closed freeing ports, medium KG, in 100 mm waves

size). The data points correspond to runs 216, 217, 218 and 219. There was no water into the well recorded during the experimental series as was also predicted by FREDYN. The FREDYN predictions tend to show larger roll angles.

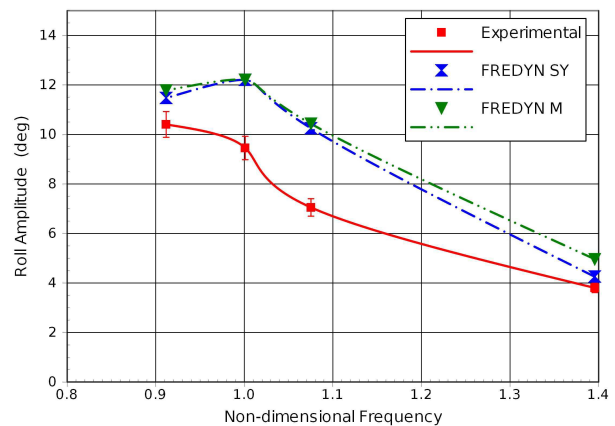


Figure 13: Roll of 70 mm Model with bulwark and closed freeing ports, medium KG, in 50 mm waves

Where there is no water taken onto the deck or into the well, the FREDYN-predicted motion closely matched the observed model motion, provided that the model lay beam onto the waves. At frequencies significantly higher than the natural frequency, the model tended to lie oblique to the waves and corkscrew. This effect was accentuated whenever the model drifted away from the centre of the tank so that the mooring lines were at markedly different angles. As the model drifted away from the centre of the tank, pitch increased and roll decreased. A spring based mooring system would tend to keep lengths similar. This can make it difficult to compare the experimental results to the numerical predictions.

Once water was taken over the deck or into the well, the detail of the FREDYN predictions could, and often did, differ to measured motions, though amplitudes were still similar. The flooding module in FREDYN was used to model water in the well. This module maintains the water surface horizontal and does not include sloshing effects. The observed behaviour



was that the water was splashed out by the incoming water when large green sea events occurred and/or sloshed out depending on fill level and frequency. The well acted like a simple stabilizer tank, at some frequencies countering the roll and at others augmenting the roll. Maximum sloshing appeared to occur when countering the roll. Figure 12 appears to be showing an augmented roll effect in the experimental data at the highest frequency.

6. CONCLUSIONS

This is a work in progress. The results obtained so far are promising. In many cases, especially those involving little or no water on deck, real time roll motions predicted by the numerical tool, FREDYN, are very close to the observed model motions. Generally, provided input parameters such as roll damping had been carefully selected, FREDYN seemed to reasonably predict the roll amplitudes of a landing craft in regular waves but tended to be conservative — larger roll angles and more capsizes were predicted than observed in the experimental program. Fixing sway and yaw as a simple method of modelling the experimental restraint would appear to be incorrect.

Determining suitable roll damping coefficients was a critical factor. When FREDYN, or other similar well benchmarked tools, become available for routine stability investigation, recommended default parameters for a variety of vessel types will need to be provided – it is not always possible to conduct roll decay tests.

7. REFERENCES

FREDYN: A Computer Program for the Simulation of a Steered Ship in Extreme Seas and Wind, Version 10.2, 2010, CRNAV, Maritime Research Institute Netherlands.

Hayes, P., Smith, W., Renilson, M. And Cannon, S. 2010, *Stability Criteria for Landing*

Craft, International Maritime Conference Pacific 2010, Sydney, January.

Hayes, P., Smith, W., Renilson, M. And Cannon, S. 2012, *Naval Landing Craft Stability*, International Maritime Conference Pacific 2012, Sydney, January.

Rahola, J. 1939, *The Judging of the Stability of Ships and the Determination of the Minimum Amount of Stability*, doctoral thesis, The University of Finland, Helsinki, Finland, May.

Sarchin, T.H. & Goldberg, L.L. 1962, 'Stability and Buoyancy Criteria for U.S. Naval Surface Ships', *SNAME Transactions*, vol. 70.

APPENDIX: TABULATED RESULTS

This Appendix presents selected results, showing numerical predictions with the corresponding model data. Some explanation of this data is in order:

- The left side of each table presents wave data at model scale. The right side presents the corresponding data at full scale.
- Water on deck is very subjective. During the experimental program, a scale of none (N), the deck with some running water (slight or S) through moderate (M) to solidly or heavily (H) covered was applied. Where FREDYN predicted amounts of water in the well, a percentage was taken (N = 0%, S < 10%, M < 20%, H ≥ 20%) as being approximately equivalent.
- Roll angles are double angle values.
- The roll predicted by FREDYN was estimated from a plot of the output, ignoring the ramp up and the capsize sequence if any.
- Where no roll angle is presented, capsize occurred almost immediately. Refer to Figure 5 for an example.



Table 2: Results for Configurations without the Bulwark Fitted

		Model					FREDYN - Ship @ 1:26						
Run	KG (mm)	Wave		Roll Response			Wave		Sway/Yaw		Mooring		
		H (mm)	f (Hz)	Roll (deg)	WoD	Cap?	H (m)	T (sec)	Roll (deg)	Cap?	Roll (deg)	Cap?	
Model 09-10, 90mm Depth													
32	76	53.8	1.397	11.9	M	N	1.399	3.650	19	N	19	N	
33	76	55.7	1.140	28.6	N	N	1.448	4.473	30	N	29	N	
14	76	99.4	1.395	14.1	H	N	2.584	3.655	19	N	17	N	
16	76	103.3	1.137	28.5	M	N	2.686	4.485	40	N	36	N	
17	76	102.2	0.989	36.8	N	N	2.657	5.156	38	N	37	N	
19	76	106.3	0.885	28.7	N	N	2.764	5.762	31	N	30	N	
239	96	102.6	1.000	23.0	S	N	2.668	5.099	29	N	27	N	
237	96	106.9	0.931	28.9	S	N	2.779	5.477	37	N	34	N	
238	96	108.1	0.849	32.5	N	N	2.811	6.006	36	N	36	N	
198	116	51.4	1.500	3.0	S	N	1.336	3.399	29	N	3	N	
195	116	51.4	1.000	4.7	N	N	1.336	5.099	3	N	6	N	
196	116	53.7	0.803	10.8	N	N	1.396	6.350	7	N	13	N	
194	116	50.5	0.680	17.0	N	N	1.313	7.499	12	N	17	N	
197	116	52.1	0.498	3.8	N	N	1.355	10.239	4	N	6	N	
201	116	103.0	1.001	10.1	S	N	2.678	5.094	5	N	9	N	
200	116	106.3	0.804	17.0	N	N	2.764	6.342	13	N	17	N	
199	116	106.9	0.680	25.3	N	N	2.779	7.499	20	N	24	N	
Model 09-11, 70mm Depth													
47	76	41	1.99	4	M	N	1.066	2.564	4	N	4	N	
35	76	104.1	1.139	21.6	H	N	2.707	4.477	29	N	22	N	
36	76	103.7	0.987	32.5	S	N	2.696	5.166	39	N	39	N	
37	76	109.6	0.885	26.1	N	N	2.850	5.762	32	N	31	N	
230	96	105.0	1.299	9.0	H	N	2.730	3.925		YES		YES	
229	96	102.3	0.999	15.5	M	N	2.660	5.104	16	N	12	N	
227	96	105.6	0.933	21.9	M	N	2.746	5.465	29	N	18	N	
228	96	106.8	0.851	27.8	S	N	2.777	5.992	35	N	34	N	
169	116	52.6	0.677	16.2	N	N	1.368	7.532	12	N	17	N	
172	116	102.5	1.000	6.8	M	N	2.665	5.099		YES		YES	
171	116	108.0	0.800	14.8	S	N	2.808	6.374	12	N	12	N	
Model 09-12, 50mm Depth													
72	76	99.4	1.39	14.9	H	N	2.584	3.663		YES		YES	
75	76	103.9	0.987	19.6	H	N	2.701	5.166		YES		YES	
76	76	106.8	0.883	15.4	M	N	2.777	5.775		YES		YES	
242	96	51.9	0.998	22.0	M	N	1.349	5.109		YES		YES	
240	96	53.6	0.930	16.0	M	N	1.394	5.483		YES		YES	
241	96	53.9	0.849	13.0	S	N	1.401	6.006	6	N		YES	



Table 3: Results for Configurations without the Bulwark Fitted

Model		FREDYN - Ship @ 1:26													
Run	KG (mm)	Wave		Roll Response			Wave		Sway/Yaw			Mooring			
		H (mm)	f (Hz)	Roll (deg)	WoD	Cap?	H (m)	T (sec)	Roll (deg)	WoD	Cap?	Roll (deg)	WoD	Cap?	
Model 09-11, 70mm Depth, with Bulwark (Closed Freeing Ports)															
50	76	107.8	1.140	28.7	M	N	2.803	4.473	38	S	N	33	M	N	
59	76	105.7	0.988	35.8	S	N	2.748	5.161	40	M	N	36	M	N	
61	76	105.3	0.885	27.2	N	N	2.738	5.762	35	M	N	32	M	N	
219	96	53.3	1.298	7.6	N	N	1.386	3.928	9	N	N	10	N	N	
218	96	50.9	1.000	14.1	N	N	1.323	5.099	20	N	N	21	N	N	
216	96	52.5	0.931	18.9	N	N	1.365	5.477	24	N	N	24	N	N	
217	96	54.1	0.848	20.8	N	N	1.407	6.013	23	N	N	24	N	N	
210	96	103.8	1.300	17.8	H	N	2.699	3.922	11	N	N	11	M	N	
209	96	110.2	1.098	19.1	H	N	2.865	4.644	20	S	N	16	S	N	
211	96	96.6	1.001	22.6	S	N	2.512	5.094	30	S	N	21	S	N	
208	96	106.5	0.930	29.0	N	N	2.769	5.483	32	S	N	27	S	N	
213	96	108.7	0.848	32.5	N	N	2.826	6.013	35	S	N	31	S	N	
212	96	108.6	0.802	29.9	N	N	2.824	6.358	33	S	N	30	S	N	
215	96	108.9	0.500	7.4	N	N	2.831	10.198	8	N	N	13	M	N	
148	116	49.9	1.897	1.1	S	N	1.297	2.688	1	N	N	2	N	N	
147	116	50.6	0.998	4.3	N	N	1.316	5.109	3	N	N	6	N	N	
146	116	51.5	0.678	18.5	N	N	1.339	7.521	13	N	N	17	N	N	
149	116	51.3	0.500	4.6	N	N	1.334	10.198	4	N	N	6	N	N	
156	116	108.6	1.200	14.0	H	N	2.824	4.249		H	YES		H	YES	
154	116	103.4	1.000	9.7	N	N	2.688	5.099	5	N	N	14	M	N	
153	116	102.0	0.996	10.1	S	N	2.652	5.119	5	N	N	13	M	N	
151	116	106.4	0.801	16.7	N	N	2.766	6.366	15	N	N	16	N	N	
150	116	105.3	0.681	26.9	N	N	2.738	7.488	21	S	N	24	N	N	
Model 09-12, 50mm Depth, with Bulwark (Closed Freeing Ports)															
86	76	105.1	1.14	27.9	H	N	2.733	4.465	39	S	N	33	H	N	
87	76	96.7	1.139	20.8	H	N	2.514	4.477	18	S	N	17	H	N	
84	76	104.5	0.987	30.3	M	N	2.717	5.166	41	H	N	40	H	N	
83	76	107.5	0.884	30.2	N	N	2.795	5.768	35	H	N	33	H	N	
247	96	102.9	1.300	19.6	H	N	2.675	3.922		H	YES	8	M	N	
246	96	105.3	0.999	21.6	M	N	2.738	5.104	28	S	N	27	S	N	
245	96	107.0	0.930	27.8	S	N	2.782	5.483	35	S	N	32	S	N	
178	116	109.2	1.200	16.7	H	N	2.839	4.249		H	YES		S	N	
177	116	103.0	1.000	10.4	S	N	2.678	5.099	4	N	N	6	H	N	
176	116	105.4	0.678	28.2	N	N	2.740	7.521	18	S	N	24	N	N	



An Investigation on Parametric Rolling of a Tumblehome Hull

Jiang Lu, *China Ship Scientific Research Center, Wuxi, China*, lujiang1980@yahoo.com.cn

Min Gu, *China Ship Scientific Research Center, Wuxi, China*, gumin666@gmail.com

ABSTRACT

Vulnerability criteria for parametric rolling are now under development by the International Maritime Organization (IMO) in the framework of the 2nd generation intact stability criteria. One coupled heave-pitch-roll mathematical model is presented for predicting parametric rolling in which the nonlinear Froude-Krylov component of roll restoring variation is calculated by integrating wave pressure up to wave surface with heave and pitch motions obtained by a strip theory applied to an upright hull and the hydrodynamic effect is nonlinearly extrapolated with regards to the roll angle. This method is applied to one unconventional “tumblehome” hull, and the vulnerability of the tumblehome ship for parametric rolling is investigated. Furthermore the hydrodynamic effect on parametric rolling is also investigated.

Keywords: parametric rolling; dynamic stability; capsizes; tumblehome; vulnerability criteria

1. INTRODUCTION

The vulnerability criteria on parametric rolling are under development at International Maritime Organization (IMO) in the second intact stability criteria for insuring the safety of ships in waves, especially for unconventional ships. In recent years, unconventional ships, such as “tumblehome” ships attract many country’s attentions because the ships have better performance than conventional hulls, such as propulsion and seakeeping performance. However, these improvements of the tumblehome hull could make tumblehome ships suffer stability failures in severe waves (Bassler et al., 2007, Belenky et al., 2008). Therefore, it is necessary to investigate the dynamic stability of the tumblehome hull.

Head-sea parametric rolling of the ONR tumblehome was investigated by Olivieri et al. (2010) and Hashimoto et al. (2009). Pure loss of stability of the ONR tumblehome in following seas was investigated by Hashimoto (2009). Broaching of the ONR tumblehome

was investigated by Araki et al. (2010) and Hashimoto et al. (2011) respectively. A coupled heave-pitch-surge-roll mathematical model, with added resistance taken into account, was presented by one of the authors for investigating parametric rolling in head seas (Lu et al. 2010, 2011a). Also, the effect of parametric rolling on added resistance in regular head seas was investigated by the same author (Lu et al. 2011b). Investigations, however, of parametric rolling for unconventional “tumblehome” ships are still few. On the other hand, “tumblehome” ships could be vulnerable to parametric rolling which is one of major failure modes. Therefore, it is necessary to investigate parametric rolling of tumblehome hulls for deriving vulnerability criteria. Furthermore, the hydrodynamic effect of radiation and diffraction on parametric rolling need also to be investigated because, based on the linearity assumption, this effect could become too large for high speed of ship in severe waves.



2. SUBJECT SHIP

Principal particulars and body plan of the subject ship of a tumblehome are shown in Table 1 and Fig.1. Restoring arm curves in calm water with different metacentric heights are shown in Fig.2.

Table1: Principal particulars of the tumblehome

Items	Ship
Length: L_{pp}	132.0m
Breadth: B	14.8m
Depth: D	11.5m
Draft: d	4.3m
Displacement: W	4236t
Longitudinal position of center of buoyancy from midship: LCB	aft
Metacentric height: GM	2.0m
Nature roll period: T_{ϕ}	8.808s
Radius of gyration in pitch: K_{yy}	$0.24L_{pp}$
Block coefficient: C_b	0.492

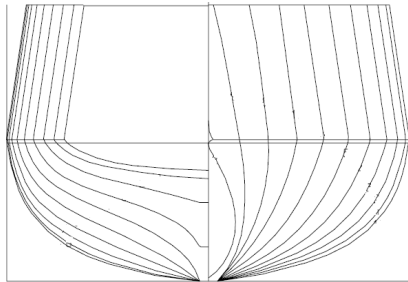


Figure 1: Body plan of the tumblehome.

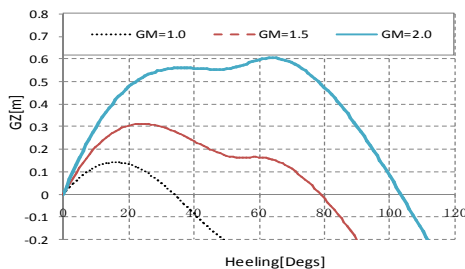


Figure 2: Restoring arm curve in calm water

3. MATHEMATICAL MODEL

The mathematical model for parametric rolling prediction in regular waves is expressed

as Eq.1. In head seas, predicting parametric rolling is not so easy because dynamic coupling with heave and pitch motions are significant. Thus the relative position of ship to waves which is an important factor for calculating restoring variation in waves is significantly affected by heave and pitch motions. Here heave and pitch motions in Eq.2 were obtained by a strip theory applied to an upright hull. Instantaneous heeling angle is used to determine the instantaneous relative position of ship to waves, and then instantaneous area of wet sections are calculated for estimating the restoring variation of Froude-Krylov component as show in Eq.3 In other words, coupling from heave and pitch to roll is taken into account but not vice versa. The restoring variation consists of two components. One is the nonlinear Froude-Krylov component, which is calculated by integrating wave pressure up to wave surface with heave and pitch motions obtained by a strip theory. The other is the hydrodynamic effect which consists of radiation and diffraction components acting on a heeled hull as a linear component with respect to wave height (Umeda et al., 2004, Lu et al., 2010). The hydrodynamic effect which is considered as an additional effect on GZ is nonlinearly extrapolated with regards to the roll angle (Lu et al., 2011a).

$$\ddot{\phi} + 2\mu\dot{\phi} + \gamma\phi^3 + \frac{W}{(I_{xx} + J_{xx})}GZ(t, X_G, \zeta_G, \theta, \phi) = 0 \quad (1)$$

$$\begin{aligned} \zeta_G(X_G, t) &= \zeta_{Ga} \cos(\omega t - kX_G \cos \chi + \delta_H) \\ \theta(X_G, t) &= \theta_a \cos(\omega t - kX_G \cos \chi + \delta_\theta) \end{aligned} \quad (2)$$

where ϕ : roll angle, μ : linear roll damping coefficient, γ : cubic roll damping coefficient, W : ship weight, I_{xx} : moment of inertia in roll, J_{xx} : added moment of inertia in roll, GZ : righting arm, t : time, ζ_G : heave displacement, θ : pitch angle, X_G : instantaneous ship longitudinal position and here constant speed is considered. Furthermore, ζ_{Ga} : amplitude of heaving, δ_H : initial phase of heaving; θ_a : amplitude of pitching, δ_θ : initial phase of pitching; ω : wave

frequency, k : the wave number, χ : the angle of wave incidence. $\chi = \pi$ corresponds to head seas. The dot denotes differentiation with time.

The Froude-Krylov component of restoring variation is calculated by integrating the incident wave pressure around the instantaneous wetted hull surface. As a result, the following formula is used.

$$W \cdot GZ = \rho g \int_L y'(x, X_G, t) \cdot A(x, X_G, t) dx + \rho g \sin \chi \int_L z'(x, X_G, t) \cdot F(x) \cdot A(x, X_G, t) \cdot \sin k(\xi_{G0} + (X_G + x) \cos \chi - c \cdot t) dx$$

$$F(x) = \zeta_a k \frac{\sin(k \frac{B(x)}{2} \sin \chi)}{k \frac{B(x)}{2} \sin \chi} e^{-kd(x)}$$
(3)

where, $A(x, X_G, t)$: the submerged area of local section of the ship; $y'(x, X_G, t)$: the transverse position of buoyancy centre of local section, $z'(x, X_G, t)$: the vertical position of buoyancy centre of local section, $\xi_{G0} = 0$: the initial longitudinal position of a ship centre from a wave trough, x : longitudinal position from the ship gravity centre, $B(x)$: ship breadth at x section, $d(x)$: draught of x section, ρ : water density and g : gravitational acceleration, c : the velocity of wave.

The radiation and diffraction components of the restoring variation are calculated as follows.

$$GZ_{R\&D} = -M_X(X_G, t) / W$$

$$M_X = K - (KG - D)Y = M_{XC} + iM_{XS}$$
(4)

$$M_{Xa} = \sqrt{M_{XC}^2 + M_{XS}^2}$$

$$M_X(X_G, t) = M_{Xa} \cos(\omega t - kX_G \cos \chi + \delta_{MX})$$

$$Y = F_Y - (A_{23} \zeta + B_{23} \zeta + C_{23} \zeta + A_{25} \theta + B_{25} \theta + C_{25} \theta)$$

$$K = M_\phi - (A_{33} \zeta + B_{33} \zeta + C_{33} \zeta + A_{35} \theta + B_{35} \theta + C_{35} \theta)$$
(5)

where, KG : the distance from the keel to the gravity of ship; D : draft; M_{Xa} : amplitude of the radiation and diffraction components of the restoring variation, δ_{MX} : the initial phase of the radiation and diffraction components of the restoring variation.

Formulae of the wave exciting force in sway direction, F_Y , and moment in roll direction, M_ϕ are available in the reference (Fujino and Sakurai, 1982) as well as those for coupling coefficients in reference (Lee and Kim, 1982).

4. SIMULATIONS AND DISCUSSIONS

The experiment with a 1/36 scaled model of the tumblehome ship was conducted at the seakeeping and maneuvering basin of China Ship Scientific Research Center (CSSRC) for investigating its stability under dead ship condition (Gu et al., 2012), and the same damping test is used in this research for getting roll damping coefficient.

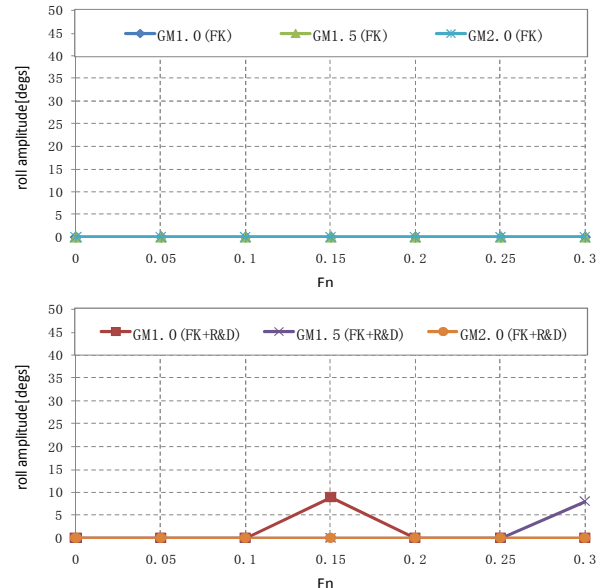


Figure 3: Roll amplitude in simulations with $\lambda/L_{pp}=1.0$, $H/\lambda=0.01$, $\chi=180^\circ$ and different GM and Fn .

The mathematical model of Eq.1 is used for predicting parametric rolling of the tumblehome ship, and the key point of this mathematical model is restoring's variation in waves. Here the restoring variation of the nonlinear Froude-Krylov component only (FK) and the restoring variation of nonlinear Froude-Krylov component and radiation and diffraction components (FK+R&D) are considered respectively. Figs. 3~6 give the results of parametric rolling with different GM, wave height and Froude Number. The



tumblehome ship with small GM is more vulnerable to parametric rolling than that with large GM, and could capsize with small GM due to parametric rolling. The tumblehome ship is not vulnerable to parametric rolling when only nonlinear Froude-Krylov component of restoring variation is considered, while it is vulnerable to parametric rolling when the hydrodynamic effect is taken into account, especially for high speed.

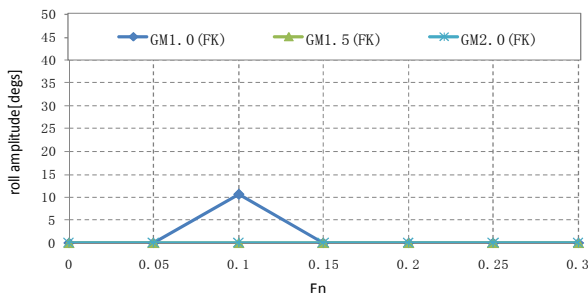


Figure 4: Roll amplitude in simulations with $\lambda/L_{pp}=1.0$, $H/\lambda=0.02$, $\chi=180^\circ$ and different GM and F_n .

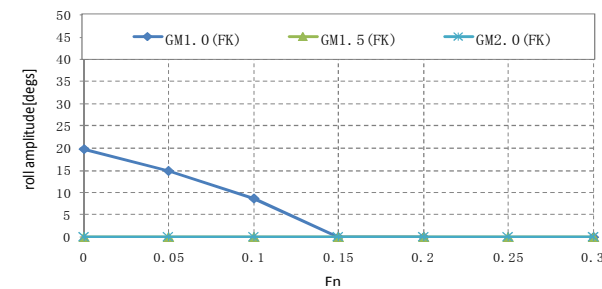


Figure 5: Roll amplitude in simulations with $\lambda/L_{pp}=1.0$, $H/\lambda=0.03$, $\chi=180^\circ$ and different GM and F_n .

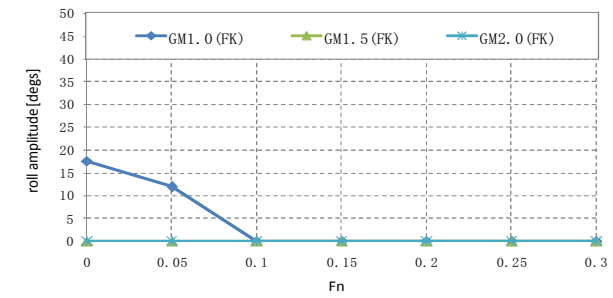
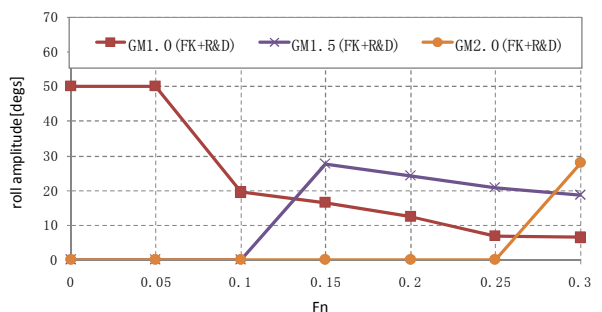


Figure 6: Roll amplitude in simulations with $\lambda/L_{pp}=1.0$, $H/\lambda=0.04$, $\chi=180^\circ$ and different GM and F_n .

This hydrodynamic effect is analyzed in Figs 7 to 14.

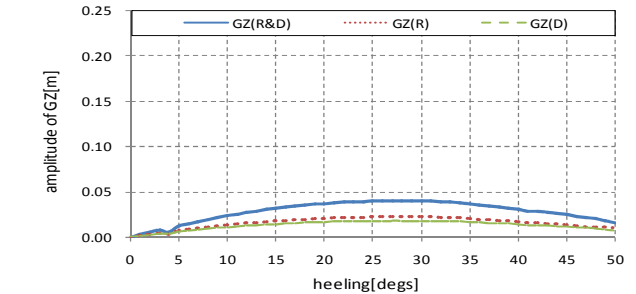


Figure 7: Radiation and diffraction components of GZ with $F_n=0.0$, $\lambda/L_{pp}=1.0$, $H=2m$, $\chi=180^\circ$ and $GM=1.5m$.

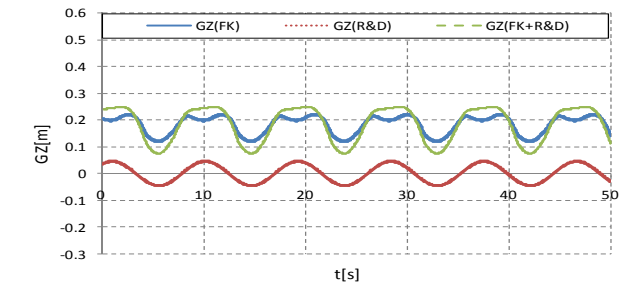


Figure 8: Roll restoring variation with $F_n=0.0$, $\lambda/L_{pp}=1.0$, $H/\lambda=0.03$, $\chi=180^\circ$, $GM=1.5m$ and $\phi_c=10deg$.

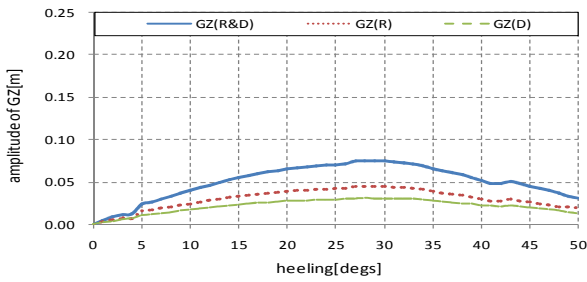


Figure 9: Radiation and diffraction components of GZ with $F_n=0.1, \lambda/L_{pp}=1.0, H=2m, \chi=180^\circ$ and $GM=1.5m$.

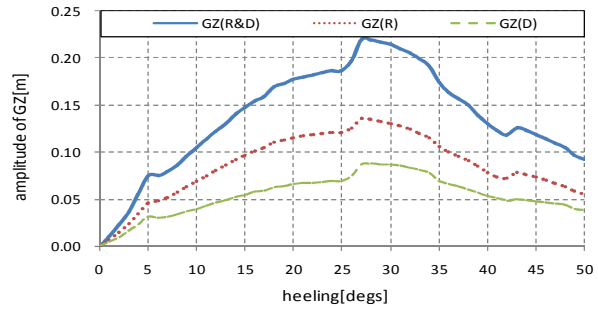


Figure 13: Radiation and diffraction components of GZ with $F_n=0.3, \lambda/L_{pp}=1.0, H=2m, \chi=180^\circ$ and $GM=1.5m$.

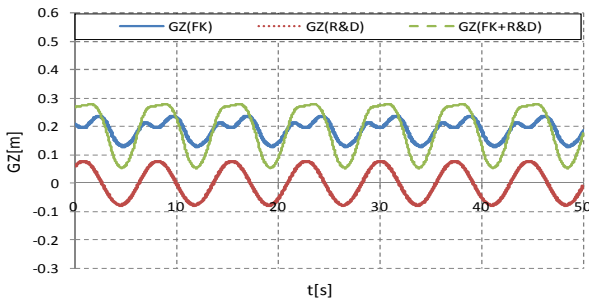


Figure 10: Roll restoring variation with $F_n=0.1, \lambda/L_{pp}=1.0, H/\lambda=0.03, \chi=180^\circ, GM=1.5m$ and $\phi_c=10\text{deg}$.

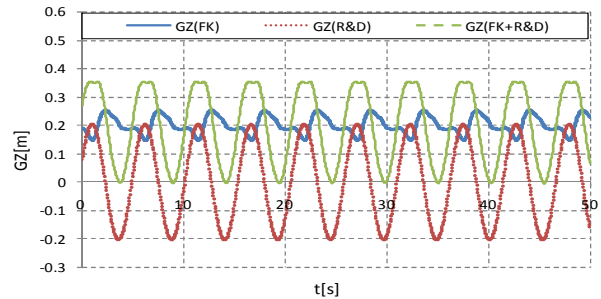


Figure 14: Roll restoring variation with $F_n=0.3, \lambda/L_{pp}=1.0, H/\lambda=0.03, \chi=180^\circ, GM=1.5m$ and $\phi_c=10\text{deg}$.

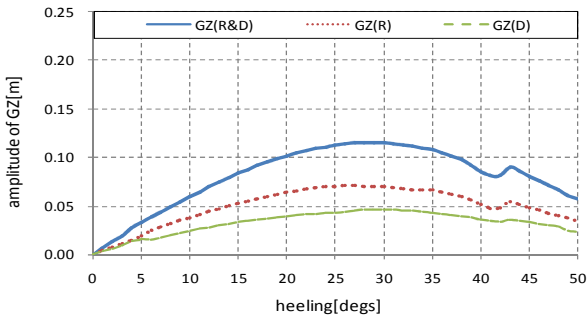


Figure 11: Radiation and diffraction components of GZ with $F_n=0.2, \lambda/L_{pp}=1.0, H=2m, \chi=180^\circ$ and $GM=1.5m$.

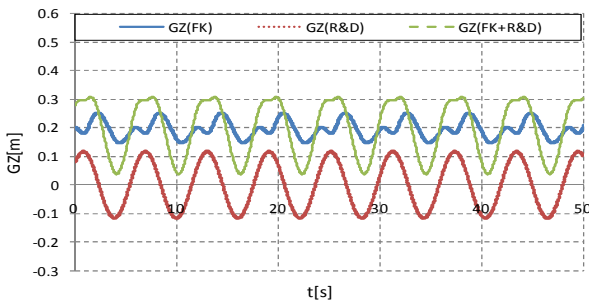


Figure 12: Roll restoring variation with $F_n=0.2, \lambda/L_{pp}=1.0, H/\lambda=0.03, \chi=180^\circ, GM=1.5m$ and $\phi_c=10\text{deg}$.

The relationship between the amplitude of GZ(R&D) and roll angle is shown in Figs.7,9,11 and 13. It indicates the amplitudes of GZ(R&D) have a nonlinear relationship with roll angle, and the amplitude of GZ(R&D) becomes larger as F_n becomes larger. This also supports the conclusion in one published paper (Lu et al., 2011a), therefore hydrodynamic restoring variation component should be nonlinearly modelled. The radiation and diffraction components are also compared, and hydrodynamic effect of radiation component is larger than that of diffraction component as show in Figs 7 to 14.

Because the tumblehome could be vulnerable of parametric rolling with the hydrodynamic effect, especially at large wave height and speed, the hydrodynamic effect is compared with the restoring variation of nonlinear Froude-Krylov component. As shown in Figs.8, 10, 12 and 14, the restoring



variation with the Froude-Krylov, radiation and diffraction components is larger than that with the Froude-Krylov on its own, and when the speed become large, the hydrodynamic effect plays an important role for predicting parametric rolling. Hashimoto et al (2009) also shows that the restoring variation with the Froude-Krylov on its own is smaller than that in experiment for a specific ONR tumblehome ship. For improving the accuracy of predicting parametric rolling, hydrodynamic effect should be taken into account.

The hydrodynamic effect becomes large with high speed, and here the hydrodynamic effect is supposed as a linear component with respect to wave height (Umeda et al., 2004, Lu et al., 2010). If the tumblehome ship encounters large wave height with high speed, the hydrodynamic effect could be very large, and could prevail over the effect of Froude-Krylov force for predicting parametric rolling and could also over predicting parametric rolling. Thus the hydrodynamic effect should be further investigated in future, especially at sever waves with high speed.

5. CONCLUSIONS

As a result of a systematic study on the parametric rolling of a tumblehome hull in head regular seas, the following remarks are noted:

- 1) The tumblehome ship with small GM could be vulnerable to parametric rolling and could capsize due to parametric rolling.
- 2) The tumblehome could be not vulnerable to parametric rolling with appropriate GM except with high speed in severe waves due to the hydrodynamic effect and the effect of radiation component which is more significant than that of the diffraction component.
- 3) The restoring variation with the Froude-Krylov, radiation and diffraction components is larger than that with the Froude-Krylov on its own and the hydrodynamic effect should be taken into account for conservatively predicting parametric rolling in stability criteria for "direct assessment".

The hydrodynamic effect on parametric rolling with high speed in severe waves should be further investigated in the future.

6. ACKNOWLEDGEMENTS

The authors sincerely thank Prof. N. Umeda from Osaka University (Japan) for providing the authors with his useful advice on predicting parametric rolling in waves.

7. REFERENCES

- Araki M., Umeda N., Hashimoto H. and Matsuda A., 2010, "Broaching Prediction Using an Improved System-Based Approach", 28th Symposium on Naval Hydrodynamics, Pasadena, California.
- Bassler C., Campbell B. and Belknap W., 2007, "Dynamic Stability of Flared and Tumblehome Hull Forms in waves", 9th International Ship Stability Workshop, Hamburg, German.
- Belenky V., Weems K.M., Lin W.M. 2008, "Numerical Procedure for Evaluation of Capsizing Probability with Split Time Method", 27th Symposium on Naval Hydrodynamics, Seoul, Korea.
- Fujino M., Sakurai S. 1982, "On the Evaluation of Wave Exciting Roll Moment by strip Method", Journal of the Society of Naval Architects of Japan, 152: 125-137(in Japanese).
- Hashimoto H., 2009, "Pure Loss of Stability of a Tumblehome Hull in Following Seas", Proceeding of 19th International Offshore and Polar Engineering Conference, Osaka, Japan.
- Hashimoto H., Umeda N., Sogawa Y. and Matsuda A., 2009, "Parametric Roll of a Tumblehome Hull in Head Seas", Proceeding of 19th International Offshore



- and Polar Engineering Conference, Osaka, Japan.
- Hashimoto H., Umeda N. and Matsuda A., 2011, “Broaching Prediction of a Wave-piercing Tumblehome Vessel with Twin Screws and Twin Rudders”, Journal of Marine Science and Technology, Vol. 16, No. 4, pp. 448-461.
- Lee M.C. and Kim K.H. 1982, “Prediction of Motion of Ships in Damaged Condition in Waves”, Proceeding of the 2nd International Conference on the Stability of Ships and Ocean Vehicles, the Society of Naval Architects of Japan, pp. 13-26
- Lu J., Umeda N. and Kun M., 2010, “Modeling Parametric Rolling in Regular and Irregular Head Seas with Added Resistance Taken into Account”, Proceeding of 5th Asia-Pacific Workshop on Marine Hydrodynamics, Osaka, Japan, pp. 93-98.
- Lu J., Umeda N. and Ma K., 2011a, “Predicting Parametric Rolling in Irregular Head Seas with Added Resistance Taken into Account”, Journal of Marine Science and Technology, Vol. 16, No. 4, pp. 462-471.
- Lu J., Umeda N. and Ma K., 2011b, “Theoretical Study on the Effect of Parametric Rolling on Added Resistance in Regular Head Seas”, Journal of Marine Science and Technology, Vol. 16, No. 3, pp. 283-293.
- Olivieri, A., Francescutto A., Campana E. and Stern F., 2010, “Experimental investigation of Parametric Roll in regular head waves for the ONR Tumblehome”, 28th Symposium on Naval Hydrodynamics, Pasadena, California.
- Umeda N, Ohkura S., Urano S., Hori M. and Hashimoto H., 2004 “Some Remarks on Theoretical Modelling of Intact Stability” .Proceedings of 7th International Ship Stability Workshop, Shanghai, pp. 85-91.
- Gu M., Lu J. And Wang T. ,2012 “An Investigation on Stability under Dead Ship Condition of a Tumblehome Hull” .Proceedings of 11th International International Conference on the Stability of Ships and Ocean Vehicles, Athens, Greece.





Experimental Parametric Roll Resonance Characterization of a Stern Trawler in Head Seas

Marcos Míguez González, *GII, University of A Coruña, Spain*, mmiguez@udc.es

Vicente Díaz Casás, *GII, University of A Coruña, Spain*, vdiaz@udc.es

Fernando López Peña, *GII, University of A Coruña, Spain*, flop@udc.es

Luis Pérez Rojas, *Model Basin, ETSIN, Technical University of Madrid*, luis.perezrojas@udc.es

ABSTRACT

Parametric roll resonance is a well known phenomenon that, under certain conditions, induces very large amplitude roll motions that could lead to consequences ranging from simple minor issues to even catastrophic ones. The need for a parametric roll real time prediction system has been stated by the industry in the last years. This work describes the results of the scale model experiments of a stern trawler under parametric roll conditions; the objective of these tests is to characterize its dynamical behaviour in these situations, and to test in realistic conditions the roll motion forecasting system developed by the authors. Moreover, the results of these forecasts for some test cases are also presented in this work.

Keywords: *parametric roll, fishing vessels, model tests*

1. INTRODUCTION

Parametric roll resonance is a well known and broadly studied phenomenon for the maritime community. Under a set of given conditions, including a wave encounter frequency of approximately twice the ship's natural roll frequency, a wavelength almost equal to the ship length and a wave amplitude larger than a ship dependent threshold, the roll motion of a ship sailing in head or stern seas and affected by roll resonance could quickly increase, reaching very large roll angles with apparently no transversal excitation that generates those motions.

Parametric rolling is caused by the periodic variations of stability levels due to wave passing along the hull and is more severe in those ships where those variations are larger, such as containerships, Ro-Ro vessels, cruise ships or fishing vessels (due to large bow flares

or hanging sterns). The consequences of such an event could range from simple minor issues, to catastrophic cargo damage, crew or passenger injuries or even ship capsizing.

This fact has empowered the industry and the research community to develop different strategies to prevent parametric roll resonance from appearing (France et al., 2001, Dohlie, 2006, IMO, 2007).

The first step in this direction was the development of guidelines to the masters to avoid those situations in which resonance was more likely to develop. These guidelines are mainly based on the observation of the prevailing sea conditions and ship sailing characteristics, and the use of polar diagrams to determine if the ship is on a risky area (IMO, 2004).



This manual methodology has been followed by the development of specific software (Amarcon Octopus¹, SeaWare enRoute²), that based on the same principles of combined analysis of weather forecast reports and ship sailing parameters, including heading and speed, define resonance risk areas in a medium time horizon (15 to 30 minutes). A detailed review of this topic can be found in (Themelis and Spyrou, 2007).

Finally, in the last five years, a third approach has started being developed. The main characteristic of these systems is the capability to detect the appearance of parametric rolling in the short term, alerting the crew and allowing them to take immediate corrective measures. Some of these alternatives are those of Holden et al. (2007), McCue and Bulian (2007), Galeazzi et al. (2010) or that proposed by the authors of this work (Míguez et al, 2010,2011), based on the application of neural networks.

The main objective of the algorithms described in these last two references, is to be integrated in a parametric roll advance warning and detection system, that will be based on a two step alarm approach. A first warning should be displayed to the crew based on the analysis of the sailing conditions, following the approach of the guidance software mentioned above and that will alert the crew about the possible risk of roll resonance. The second warning should be generated by the short term detection schemes, and will alert from the near development of the phenomenon.

The present work has two main objectives. On one hand, studying the dynamic behaviour of the vessel in parametric rolling conditions; this information will be of paramount importance for determining under which sailing parameters the ship is in risk of resonance, and so for the display of the aforementioned first step alarm.

On the other hand, the short term detection algorithms developed by the authors have been, by now, tested against a mathematical model of three degrees of freedom in head regular waves (Míguez et al., 2010). However, it is also necessary to study their performance under more realistic conditions, such as irregular waves. This analysis has also been carried out in this work.

In order to cover these two main objectives, an extensive towing tank test campaign has been accomplished in the Towing Tank of the ETSIN (Technical University of Madrid).

A scale model of a medium sized trawler with high tendency to developing parametric roll has been used and test runs at different speeds and longitudinal wave types (both regular and irregular), leading to resonant and non resonant behaviours, have been done.

In this work, the results of some of the aforementioned tests are presented, together with the conclusions obtained after their study, aimed at characterizing the phenomenon of parametric rolling for the selected ship.

Furthermore, the roll motion time series obtained with the parametric roll prediction system for some of the test runs will be presented, analyzing the performance of the system in a quite realistic scenario

2. MODEL TESTS

2.1 Stern Trawler Model

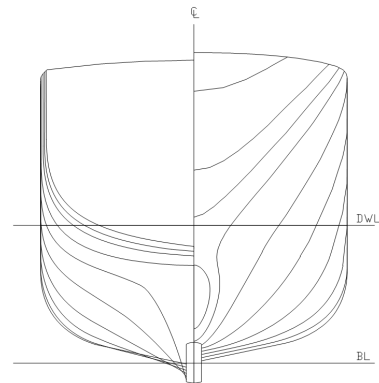
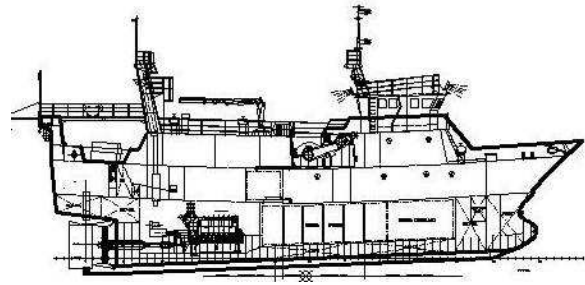
The ship analyzed in this work is a medium sized stern trawler, with an acute tendency towards developing parametric roll resonance in not very heavy seas, in part due to its transom stern hull forms. This ship has also been studied by de Juana Gamero et al. (2005) and its main characteristics are described in Table 1. A 1/18.75th scale model has been used for the towing tank experiments.

¹ www.amarcon.com

² www.amiwx.com

Table 1: Test vessel main characteristics

Overall Length	34.50 m
Breadth	8.00 m
Depth	3.65 m
Displacement	450.0 t
Metacentric Height	0.35 m
Natural Roll Frequency	0.563 rad/s



2.2 Experimental Arrangement

The aforementioned scale model tests have been carried out in the test basin of the Escuela Técnica Superior de Ingenieros Navales of the Technical University of Madrid. This towing tank is 100 meters long, 3.8 meters wide and 2.2 meters deep. It is equipped with a screen type wave generator, directed by an AwaSys³ wave generation software, capable of generating longitudinal regular and irregular waves according to a broad set of parameters and spectra. The basin is also equipped with a towing carriage able to develop a speed of up to 4.5 m/s.

The scale model is a wooden one with adjustable weights. Roll and pitch angles together with roll and pitch accelerations have been measured at a 50 Hz frequency through three onboard mounted accelerometers. Wave elevation has also been measured, using a carriage mounted wave probe.

Figure 1: Selected stern trawler arrangement and hull forms

Taking in account that the surge, sway and yaw influence in the development of parametric roll resonance may be neglected compared to that of heave, roll and pitch (Neves and Rodriguez, 2006), the model restraining devices were fitted to try to limit the first three motions to the minimum possible. These restraining devices consisted in two ropes fixed to an articulation in the bow, while another one was fitted at the same level to the transom.

While carrying out the zero speed experiments, the forward ropes were fastened to the sides of the basin, forming an isosceles triangle, while the stern one was fastened to the towing carriage, situated immediately after the model. In the case of the forward speed experiments, bow ropes were fastened to the carriage, while the stern one was holding from a beam extending after the carriage from its rear part.

³ <http://www.hydrosoft.civil.aau.dk/AwaSys/>

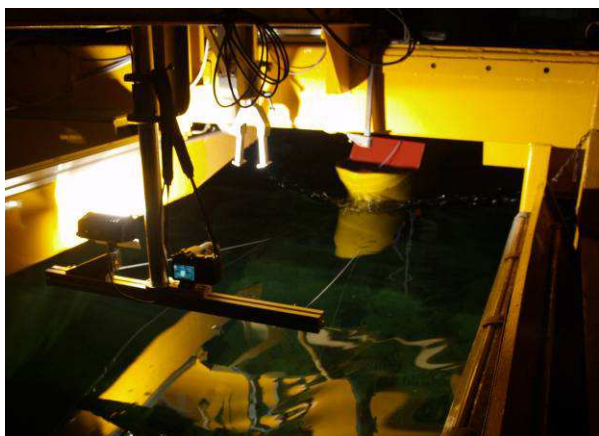


Figure 2 Model arrangement.

2.3 Test Cases

The main objective of the tests was to study the development of the parametric roll resonance phenomenon under different sailing situations, from the simplest to more realistic ones, including the analysis of the influence of forward speed and wave parameters on the intensity of the phenomenon.

The test campaign was divided in two. On one hand, the ship has been tested in longitudinal linear Airy waves, for different values of encounter frequency-natural roll frequency ratio, wave amplitude and forward speed. The main objective of this first part was to determine the influence of frequency ratios, forward speed and wave amplitude on the amplitude of rolling motions.

On the other hand, test in longitudinal irregular waves have also been carried out, for a given wave spectra, with the objective of determining how the spectrum parameters affect the development of parametric roll resonance.

Regular Waves. As has been previously described, the main parameter affecting the appearance or parametric roll resonance is the ratio between encounter frequency and natural roll frequency. The most critical value is around 2, but resonance is also likely for ratios

between 1.9 and 2.2. Once this condition is satisfied, other parameters are also needed to trigger resonance. Wave amplitude should be over a given threshold and regarding wavelength, the more similar to ship length, the larger the developed roll motions will be.

The proposed test matrix includes, at four different forward speeds, test cases for combinations of frequency ratios between 1.7 and 2.3 and wave heights between 0.5 and 3 m; the complete test set is composed of 24 different combinations for the zero speed case, 16 for Froude numbers of 0.1 and 0.2 and 13 for the Froude 0.3 case.

One of the main objectives of this study was to determine the areas in which, as a function of wave height and encounter frequency – natural roll frequency ratio, and for different forward speeds, parametric rolling takes place (limits of stability). From the analysis of these regions, the risk state of the ship at every moment could be determined, making it possible to trigger the first step alarm described above.

Two examples of these limits of stability could be seen in Figures 3 and 4, for Froude numbers of 0 and 0.2 respectively, where resonant and non resonant combinations are shown.

As can be seen from those figures, reduced damping in the zero speed case implies that parametric roll develops at smaller wave heights than in the case with forward speed. Moreover, it can be appreciated that the non stable region tends to extend to the right in the Fn 0.2 case; this fact has been already described by Neves and Rodríguez (2007), and is due to the strong coupling between vertical motions (heave and pitch) and roll.

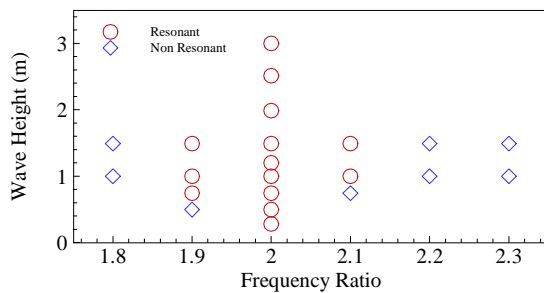


Figure 3: Stability limits. $F_n = 0$.

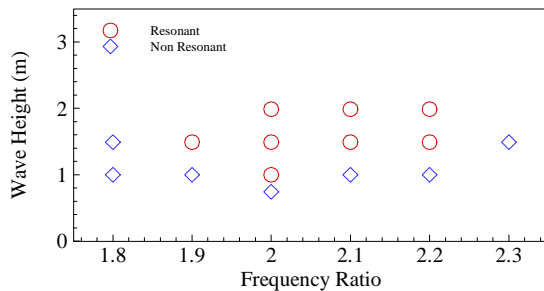


Figure 4: Stability limits. $F_n = 0.2$.

Regarding the influence of forward speed and wave height in the amplitude of the generated roll motions, from the observation of Figure 5, it can be concluded that an increase in wave height implies, in all cases, and increase in the amplitude of the steady state roll motion. Referring to forward speed, at the lowest wave heights, it has been observed that higher speeds imply lower angles, although the difference is not very significant at the smaller Froude numbers. However, at larger wave heights, it has been observed that the increase of speed could lead to an amplification of roll motion, as could be appreciated for the case of $F_n 0.2$ and a wave height of 2 m.

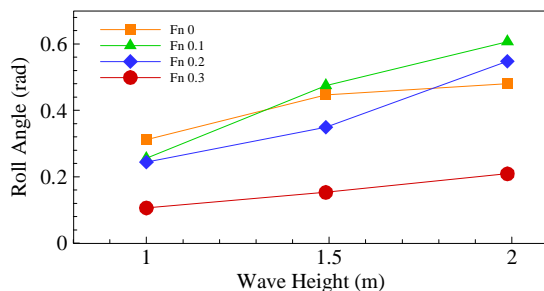


Figure 5: Roll angle as a function of wave height and Froude number. Frequency ratio = 2.

Irregular Waves. In the irregular wave case, experiments at four different forward speeds have also been carried out. TMA spectrum (Bouws et al., 1985) has been selected for wave generation. In order to study the influence of significant wave height, peak frequency and peak enhancement factor (PEF) on resonance development and amplitude, combinations of significant wave heights from 1 to 2.5 meters, encounter peak frequency – natural roll frequency ratios from 1.9 to 2.2 and peak enhancement factors of 3,5 and 7 have been considered.

Regarding the influence of wave height in the roll motion, the values of the average and maximum reached roll angles for tests at zero forward speed, peak frequency – natural roll frequency ratio of 2 and four different significant wave heights, are presented on Figure 6.

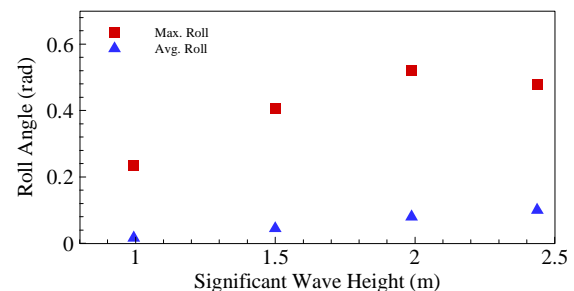


Figure 6: Significant wave height influence on roll motion. $F_n = 0$. Frequency ratio = 2. $PEF = 7$.

From its analysis, it can be concluded that the effects of an increase in significant wave height in the irregular wave case, are the same as those observed in regular waves regarding roll motion, including the reduced amplification at the largest values of wave height for the maximum roll values. Moreover, it can be observed that maximum roll amplitudes are very similar to those of the regular wave case. These is due to the fact that those values are achieved during parametric roll events, caused by the most energetic waves in the vicinity of the peak spectrum and with a height similar to the significant one, which



could be assimilated to a regular wave of that characteristics.

For studying the influence of frequency ratio and peak enhancement factor, the results obtained for the Froude 0.2 tests cases will be presented. These tests consist of a total of 34 runs carried out at encounter peak frequency – natural roll frequency ratios between 1.9 and 2.2, peak enhancement factors of 3.5 and 7 and a significant wave height of 1.5 meters. The results of the average mean and maximum roll angles for all the series with the same parameters combination are presented in Figure 7.

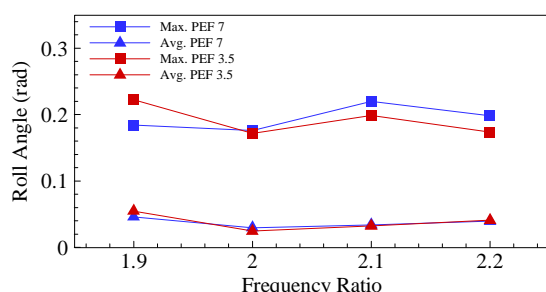


Figure 7: Frequency ratio and PEF influence on roll motion.

From the analysis of the aforementioned graph, and regarding the effects of the peak enhancement factor, it can be observed that higher PEF values imply higher maximum roll amplitudes, which coincide with resonance periods due to waves with frequencies near the spectrum peak. Considering the fact that higher PEF values mean more energetic waves in the near vicinity of the peak, the observed behaviour is clear. Moreover, the maximum roll values are found at the neighbour values to the resonant tuning ratio, i.e. 1.9 and 2.1, while amplitude decreases while moving further to the right (2.2 ratio).

3. PARAMETRIC ROLL FORECASTING

The analysis carried out in the previous section, was aimed at increasing the knowledge about the selected trawler dynamics in resonant conditions, in order to be able to determine its

risk while sailing from the analysis of the present conditions and to trigger a first step alarm.

In order to detect the onset of parametric roll resonance in the short term, the authors have proposed the use of Artificial Neural Networks (ANNs) to forecast the ship roll motions, while the parametric roll detection should be done by analyzing these forecasted data.

ANNs are a type of mathematic algorithm with the property of adequately approximating any function, also nonlinear ones, if a good selection of its architecture is done (Cybenko, 1989) and after a process of training.

These algorithms have been broadly used in many fields; in ship motion analysis, some references of the use of ANNs could be Ebada and Abdel-Maksoud (2006) or Xing and McCue (2009).

Basically, ANNs are composed of an input layer, which receive the data, a series of hidden layers that contain the neurons, which process the data, and an output layer. In each neuron, the inputs are weighed, a bias is added and a summation of all the inputs is carried out. This summation is then processed by an activation function and the result is sent to the next neuron layer.

The training process consists in feeding the network with known data, including inputs and their corresponding outputs, and adjusting the weights and biases to minimize error between target and network result.

The selected architecture has 40 inputs (corresponding to 20 seconds of the roll time series) and 1 output (the 0.5 seconds ahead prediction). The forecasting process is done by feeding the network with those 40 inputs and recursively executing the system in order to obtain the desired forecast length.

In (Míguez González et al., 2010), the authors applied this methodology to forecast ship motions from a three degrees of freedom mathematical model in longitudinal regular waves, obtaining promising results. However, the need for investigating their performance in more realistic conditions was acknowledged.

3.1 Test Cases

In order to test the behavior of the proposed system in such a more realistic scenario, the data obtained from the towing tank tests, for a speed equivalent to a Froude number of 0.2 (7 knots of real ship speed), both in regular and irregular seas, have been used.

In the regular wave case, training and testing time series have been obtained from 16 experiments with different values of wave frequency and amplitude, with an average full scale length of 420 seconds. Encounter frequency – natural roll frequency ratio ranged from 1.8 to 2.3, implying that there were cases where parametric roll was not present. This fact allowed us to evaluate the performance of the system in a condition where only small roll amplitudes appeared due to external transversal excitations (cases that were not present in the mathematical model tests, as no other excitation was present apart from head waves).

The testing of the system has been done by using a time series corresponding to a frequency ratio of 2.0 and a wave amplitude of 0.745 m, in which parametric rolling is fully developed (Test 1).

During the experiments, time series were sampled at a frequency of 50 Hz. For generating the ANN training and test cases, time series were resampled at 2 Hz and divided into 40+1 time steps, being the 40 inputs of the network and their corresponding output. 11169

training cases were obtained this way from the experimental data.

In the irregular wave case, the training and testing of the MPNN system has been done through the experiments corresponding to the TMA spectrum, peak shape parameter of 7 and significant wave height of 1.5 meters. The whole set of training cases has been obtained from 15 time series where roll resonance either takes place or not, with an average real scale length of about 380 seconds.

For testing the system, two time series have been selected, one corresponding to a frequency ratio of 2.1 in which resonance takes place (Test 2) and the other to 2.0 in which it doesn't (Test 3).

Following the same methodology described for the regular waves, 10898 cases were obtained and used in the training process.

Taking into account that realistic data implies the need of a more complex model for obtaining good results, different network structures have been tested in both cases, modifying the number of hidden layers and neurons. The results obtained with the best performing structure for a forecast of 10 seconds ahead, will be presented in the next section.

3.2 Results

Regarding the regular wave case, in Figure 8, the results obtained with the best performing MPNN (three layers and 30 neurons per layer), are included. The obtained error value (MSE) for the presented case is 12.04×10^{-4} .

Referring to the irregular wave case, in Figures 9 and 10, the selected test time series are presented.

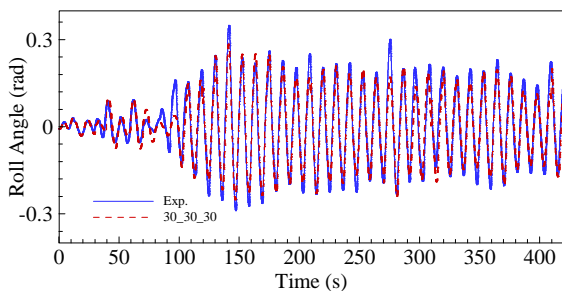


Figure 8: Test 1. Forecast results. 30 neuron, 3 layer MP.

As can be seen, in Test 2 no parametric rolling events develop, being only present small amplitude roll motions due to the natural roll motion of the ship and the effects of the present external disturbances (towing device, wall rebounds, etc.). The maximum roll amplitude reaches approximately 0.13 rad (7.4 degrees) around the second 225, and soon dissipates into the average of 1.2 degrees that could be found along the whole time series.

In test 3, no large roll motions appear until a slightly larger roll to port around second 215 and an adequate wave sequence, excite an episode of parametric rolling, that lasts for 6 rolling cycles (approximately from second 240 to 310) and that dissipates when wave conditions change. The error values (MSE) of these predictions are 5.60×10^{-4} for Test 2 and 6.66×10^{-4} for Test 3.

From the results and figures above, it can be concluded that the forecasts provided by the networks are very accurate in all test cases, precisely tracking the ship roll response.

In Test 1, the prediction precisely estimates steady state roll angle and the transient during resonance development, and also the peaks present around second 50.

Regarding the irregular waves, in Test 2 the system tracks the roll motion without overpredictions that could lead to misdetections.

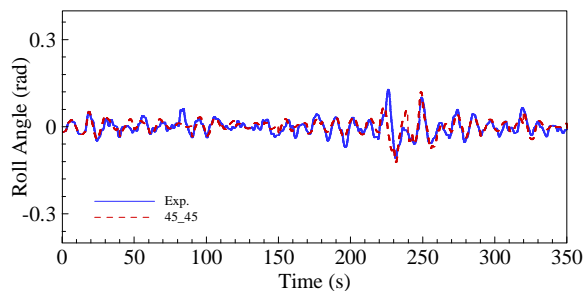


Figure 9: Test 2. Forecast results. 45 neuron, 2 layer MP.

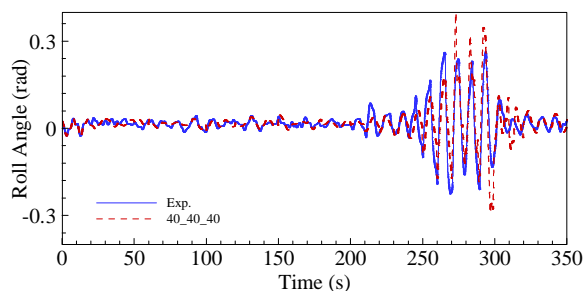


Figure 10 Test 3. Forecast results. 40 neuron, 3 layer MP.

In Test 3, the forecaster performs in the same way until resonance starts to develop around second 240, and tracks the increasing in roll motion until steady state is reached. Once in this point, some overestimation of roll amplitude could be appreciated.

4. CONCLUSIONS

This work presented part of the activities carried out by the authors for developing a parametric roll advance warning/detection system, that could prevent the crews of the vessel about the ship suffering an episode of parametric roll resonance and also alert them in the short term if the phenomenon is developing.

In this occasion, two main objectives were followed: on one hand, the study of ship behaviour in realistic conditions under parametric resonance; on the other, the testing of a neural networks based roll motion forecasting system in such conditions.



This was done by carrying out towing tank tests of a stern trawler with an acute tendency for developing parametric rolling. Many runs were done, both in regular and irregular waves, in order to determine how the different parameters involved, influenced the roll motion of the ship.

Moreover, the proposed forecasting system was tested against realistic conditions, in two different scenarios, taken from the towing tank tests described above; the first consisted in a regular wave case in which roll resonance was fully developed, while the second consisted in an irregular wave case.

Three test cases were considered, using the MPNN for making 10 seconds ahead predictions of roll motion. Although these tests showed very promising results, and support the idea of applying ANN for obtaining a parametric roll detection system, further work is needed to obtain accurate results in a longer time horizon.

5. ACKNOWLEDGEMENTS

The present work was supported by the Spanish Ministry of Education under the FPU program, grant AP2006-03211 and by MICIIN project TRA2009-13805 and Xunta de Galicia project 08DPI011CT with EDF funding.

The last author acknowledges the financial support of MICIIN through the project TRA2008-03184.

6. REFERENCES

Bouws, E., Günther, H., Rosenthal, W., Vincent, C.L., 1985. "Similarity of the Wind Wave Spectrum in Finite Depth Water 1. Spectral Form". Journal of Geophysical Research, Vol. 90.

Cybenko, G., 1989. "Approximation by superposition of a sigmoidal function".

Mathematics of Control, Signals and Systems. Vol. 2, pp. 303-314.

De Juana Gamo, J., Arias Rodrigo, C., Pérez Rojas, L., 2005. "On the Parametric Rolling of Fishing Vessels". 1st International Conference on Marine Research and Transportation.

Dohlie, K., 2006. "Parametric rolling. A problem solved?" DNV Containership Update. N° 1, February 2006.

Ebada, A., Abdel-Maksoud, M. (2006). "Prediction of ship turning manoeuvre using Artificial Neural Networks (ANN)". 5th International Conference on Computer Applications and Information Technology in the Maritime Industries.

France, W.N., Levadou, M., Treacle, T. W. , Paulling, J. R., Michel, R. K. , Moore C. , 2001. "An Investigation of Head-Sea Parametric Rolling and its Influence on Container Lashing Systems". SNAME Annual Meeting.

Galeazzi, R., Blanke, M., Poulsen, N. K., 2010. "Early Detection of Parametric Roll Resonance on Container Ship". Submitted to IEEE Transactions on Control Systems Technology.

Holden, C., Perez, T., Fossen, T. I., 2007. "Frequency-Motivated Observer Design for the Prediction of Parametric Roll Resonance". IFAC Conference on Control Applications in Marine Systems.

International Maritime Organization (IMO), 2007. "Recordings of head sea parametric rolling on a PCTC". SLF 47/6/6. 47th Session Sub-Committee on Stability and Load Lines and on Fishing Vessels Safety.

International Maritime Organization (IMO), 2004. "MSC Circ. 1228. Revised Guidance to the Master for Avoiding Dangerous Situations in Adverse Weather and Sea



Conditions”.

- McCue, L.S., Bulian, G., 2007. “A numerical feasibility study of a parametric roll advance warning system”. Journal of Offshore Mechanics and Arctic Engineering. Vol. 129, Issue 3, pp. 165-175.
- Míguez Gonzalez, M., López Peña, F, Díaz Casás, V., Santos Neves, M.A. , 2010. “An Artificial Neural Network Approach for Parametric Rolling Prediction”. 11th International Symposium on Practical Design of Ships and Other Floating Structures.
- Míguez González, M., López Peña, F., Díaz Casás, V., Galeazzi, R., Blanke, M., 2011. “Prediction of Parametric Roll Resonance by Multilayer Perceptron Neural Network”. Twenty-first International Offshore and Polar Engineering Conference.
- Neves, M. A. S., Rodríguez, C. A., 2007. “Influence of non-linearities on the limits of stability of ships rolling in head seas”. Ocean Engineering. Vol. 34, pp. 1618-1630.
- Neves, M. A. S., Rodríguez, C. A., 2006. “On unstable ship motions resulting from strong non-linear coupling”. Ocean Engineering. Vol. 33, pp. 1853-1883.
- Themelis, N., Spyrou, K. J., 2007. “Probabilistic assessment of ship stability”. Trans. SNAME. Vol. 115, pp. 181-206.
- Xing, Z., McCue, L., 2009. “Parameter Identification For Two Nonlinear Models Of Ship Rolling Using Neural Networks”. 10th International Conference on Stability of Ships and Ocean Vehicles.



The Safest Catch Program – Fishermen Taking Ownership of Safety

Gina McKay, Program Manager, *Fish Safe BC*, gina@fishsafebc.com

John Krgovich, Program Coordinator, *Fish Safe BC*, john@fishsafebc.com

Barb Howe, M. Ed., Education Consultant, *Fish Safe BC*, quinte@shaw.ca

ABSTRACT

Fish Safe BC is marking the third year of its Safest Catch program to improve fishing vessel safety. Traditional efforts to improve safety in the commercial fishing industry in Canada have for the most part been regulatory, and reducing the number of vessel losses, injuries and deaths in the fishing sector remain a top priority. The Safest Catch program approaches vessel safety with the belief and goal that if fishermen take ownership of safety, the number of losses and injuries will decrease. The program employs fishermen, trained as Safety Advisors, to help other fishermen develop their own vessel specific safety programs.

Keywords: *fishing, safety, ownership, safety culture*

1. INTRODUCTION

Commercial fishing safety continues to be a conundrum to regulatory agencies with a mandate to reduce the number of vessel losses, fatalities and accidents in the fish harvesting sector internationally. In 1997 Canada reported that fishing fatalities were 3.5 times the national average. The compelling nature of these numbers has continued into the 21st century. The Transportation Safety Board of Canada (2011) reported that an average of 14 people died in commercial fishing accidents in Canada each year between 1999 and 2008.

Canadian regulations for commercial fishing have remained relatively unchanged over several decades. Transport Canada, the federal regulatory agency responsible for commercial fishing safety is in the process of finishing the 'new' Small Fishing Vessel Regulations enabled with the coming into force of the Canada Shipping Act 2001 (CSA 2001) in 2007. Nonetheless even with regulations in force compliance presents a challenge as a significant portion of the fleet is not captured by any regulatory inspection regime. Poggie & Pollnac (1997) suggest that

although fishermen may carry safety equipment to be compliant, they often do not know how to use or maintain it.

Although commercial fishing is risky business, research findings suggest fishermen tend to trivialize the importance of, or deny the importance of safety equipment. Downplaying risks or denying them altogether can filter out safety information and negate the value of safety initiatives (Wagner, 2000). It could be that the use and maintenance of safety equipment isn't part of the world that many fishermen inhabit. A world where accepting risk may be the norm, and reality is the daily consequences of working on a moving platform. Additionally it is a world with economic pressures, onerous fisheries management programs, and a myriad of other policies that shape their behavior in an environment of uncertain resources, weather and market conditions (Windle, Neis, Bornstein & Navaro)

The complexity of fishing vessel safety continues to underpin disquieting Canadian statistics. The problems refuse to go away, regardless of efforts by regulators and educators. In the last decade an interesting new variable to the conundrum of vessel safety has emerged – the call for a safety



culture in the fishing industry. The regulators and to some extent the educators have passed the ball to the fishermen - with an implication that if fishermen would embrace a safety culture a lot of the safety problems would go away. The term 'safety culture' has origins in the Chernobyl nuclear disaster in 1986 and there are a multitude of descriptions of what that culture looks like. Dr. James Reason (1994) provided the easy to get a handle on definition of a safety culture as "the way we do business around here" which covers both actions and outcomes.

At the International Fishing Industry Safety and Health (IFISH) Conference held in 2000, John Lang, Chief Inspector of Marine Accidents, Marine Accident Investigation Branch of the United Kingdom (MAIB) suggested that fishermen need to change habits of a lifetime and it is fishermen themselves who are best placed to change things (Lang, 2000). Because fishermen are the main actors in catching fish, they logically are also the main actors in re-defining "the way we do business around here on the boat".

This is what Fish Safe BC calls "taking ownership of safety" - truly believing that safety equipment and practices make a difference and should be embedded within everyday fishing operations.

2. FISH SAFE BC

Fish Safe BC is a program developed in 2005 by fishermen, administered by the BC Seafood Alliance (BCSA), and is responsible for promoting safety and health programs identified by the Fish Safe Advisory Committee. That committee actively includes fishermen, marine educators, naval architects, marine insurers, fishing companies and marine regulators – all with a collective mandate that fishermen will own and be responsible for safety on their vessels.

Fish Safe BC is the responsibility of the Program Manager and is funded by commercial fishermen through a partnership arrangement with WorkSafeBC who collect insurance assessments from fishermen

through fish landings. Fishermen agreed to add an additional levy in order to have a portion of the assessments allocated to Fish Safe BC for the development of safety tools and programs. An annual budget of \$250,000 was set aside for Fish Safe in 2005 over seven years. That annual budget is now \$400,000. In addition to this core funding, Fish Safe BC has secured additional funding for educational programs.

In 2005 Transport Canada provided \$125,000 in funding to design a stability program, develop all instructional materials, deliver and fully evaluate the course. To date over 900 fishermen have voluntarily attended the Stability Education program, which has received national as well as international attention.

3. SAFEST CATCH PROGRAM - OVERVIEW

In 2009 Fish Safe BC received \$750,000 over three years from Canadian Search and Rescue New Initiatives Funding (SAR-NIF) to develop and implement the Safest Catch program for fishermen that would:

1. Use fishermen to advise other fishermen about how to make safety an integral part of their commercial fishing business.
2. Enable fishermen to take ownership and responsibility for safety on board.
3. Reduce the number of Search and Rescue responses to fishing vessels.

The key resource for the Safest Catch program is fishermen trained as safety Advisors, equipped and available to help their peers take ownership of safety on board. Safety consultants are employed by many other occupational work sectors to advise on safety and safety management systems, but this has not been done in the commercial fishing industry.

This program is the first of its kind – coordinating existing training and safety resources into a comprehensive fishing safety

program with trained Advisors “reaching the guys on the boats” one on one, helping them write safety procedures, do effective drills and be current with new safety tools and tips. Advisor visits are vessel specific and at no cost. An overview of the elements of an Advisor’s vessel visit is shown in Figure 1.

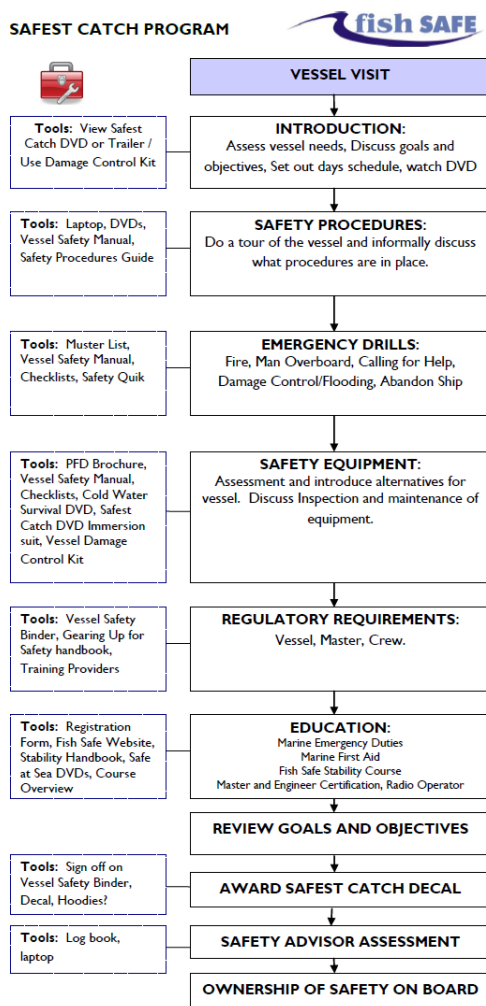


Figure 1

4. SAFEST CATCH QUARTERLY REPORTS

The Safest Catch program will be captured by excerpts from the quarterly reports submitted to SAR-NIF, the funding agency. This format has been chosen because it best reflects the multiple processes involved in implementing a comprehensive safety program for the commercial fishing industry. And also using a Milestone reporting

framework affords a sense of real-time program development and progress.

4.1 Milestone 1 – Gearing Up

The filming and production of the Safest Catch motivational DVD featuring fishermen on the east and west coast talking about their onboard safety practices was completed. A short trailer was also produced that has been used at several industry events including annual general meetings of the BCSA, Underwater Harvesters Association, Area A Crab Association and the Canadian Sablefish Association. It was also used to introduce the program nationally to the Canadian Marine Advisory Council (CMAC) in April 2009. The program has had immediate uptake by both the fishing industry and regulatory agencies.

Work has started on the design of an interactive procedures template CD. Reference information is still being compiled, including video clips that will help fishermen develop vessel specific onboard safety procedures. A Safety Quik emergency drill guide has been developed.

The two week training program for the Advisors is being finalized after consultation with regulatory agencies, the Fish Safe Advisory Committee and an education consultant.

4.2 Milestone 2 – Advisors Hired

Advisors were selected and have completed the two week training program. The Advisor toolkit is still being developed. A resource library has been organized with material provided by TC, WorkSafe BC, Canadian Coast Guard and the TSB. Much of the reference material has been electronically stored on Advisor’s laptops for access during a vessel visit.

Each vessel that participates will receive a vessel binder, the Safest Catch DVD, Safety Quik, and the Safe at Sea procedures CD



template. These tools provide the basis for a vessel specific safety program. Both pictures and text can be entered into the CD template, and it can be updated with new information or later revised. The vessel will also be given a damage control kit and a Safest Catch certificate and decal. The skippers and crew also receive Safest Catch logo hoodies.

The Safety Quik emergency drills guide has received international recognition, a “heads-up” from Transport Canada and we’ve received several inquiries from training schools who want to use it as part of their Marine Emergency Duties training. This type of feedback tells us that the program is filling a gap between regulatory requirements and onboard practices. A fishing orientation workshop is being planned with TC Inspectors to help them better understand the commercial fishing fleet. It will be hosted by a panel of fishermen.

4.3 Milestone 3 – What no agenda?

Advisors are amazed at the level of interest shown by vessel owners, skippers and crew. The safety equipment orientation onboard that skippers and crew give to Advisors has been eye opening when equipment tested showed immediate flaws – for example tangled lines on liferings and expired EPIRB batteries. These deficiencies make a point for regular checks and drills. Advisors spend time explaining the ownership perspective of the program – that it is not an inspection and there is no pass or fail associated with their visit.

Fishermen are still getting their heads around the fact that someone with no agenda or regulatory authority is available to assist them in designing a safety program. Advisors report that many fishermen are just now learning that there even are regulatory requirements to have a muster list and maintain an emergency drills log. There is a large gap to fill in communicating regulatory information. Skippers ask questions about regulatory compliance – and it is explained

that a vessel specific safety program will for the most part, make them compliant.

It’s evident that for many boats one visit isn’t long enough to cover the whole Safest Catch program. Also sometimes the boat is getting ready to go fishing and there isn’t a lot of time available. Advisors now establish visit objectives with the skipper and a time frame for completing the program.

Working with the Pacific Fishermen’s Mutual Marine Insurance group we distributed 1200 Safest Catch brochures to fishermen by mail. A two page ad featuring the entire brochure appeared in BC’s leading trade magazine *Western Mariner*, and *The Fishermen* newspaper featured a full page article on the Safest Catch program. Together these publications have a monthly circulation of 35,000.

4.4 Milestone 4 – Real Fishermen wear PFDs

Advisors now also carry a kit bag with samples of some of the new safety gear now available including different personal floatation devices (PFDs), immersion suits, hard hats and other safety products.

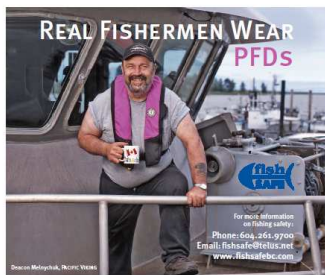
The fishermen in Powell River and Sooke organized themselves into groups and invited Advisors to work with them over a period of two days. They first met all together to watch the Safest Catch DVD and get a general overview of the program. The Advisors visited all the boats over the next day and a half. This generated more requests for vessel visits.

The Advisors have visited 48 vessels to date, 40 have completed the safety orientation and safety drills part of the program, 20 have written instructions and there are 17 program ‘graduates’ who have received a decal for their boat. Approximately 160 fishermen have participated in the Safest Catch, and although a small sampling, a ten question electronic survey was sent to program participants for a barometer reading.



The program has been well received by all fishermen who have had a Safest Catch Advisor visit. Many respondents said the most valuable part of the visit was learning how to do drills and how to develop emergency procedures. Several fishermen ranked the Advisor as the “most valuable” part of the program. From a formative perspective, some indicated they wanted more explanation on how to use Safety Quik drill guide. This was passed on to Advisors.

A “Real Fishermen wear PFDs” campaign featuring posters with well known fishermen on the coast is now underway.



Advisors keep a personal log of each vessel they visit. The log documents what was accomplished as well as significant events, ideas or questions, a “to do” list to help vessels complete the program, and reflections on their performance as an Advisor. Logs are circulated amongst all the Advisors and will help determine content for additional Advisor training workshops. We have started conducting Advisor audits.

4.5 Milestone 5 – Sharpening Tools

All program material was reviewed. We’ve increased the distribution of Safety Quik, giving a copy to every crew member so they can personalize it with their own notes. TC has asked to distribute Safety Quik nation wide, The Safe at Sea procedures CD, the backbone of the Safest Catch program, has been the most time consuming and difficult item in the toolbox. We’re on our second version of the CD template and have added a MAC version.

The Safe at Sea DVD shows real fishermen telling personal stories and has proven to be a good tool for Advisors to get crews talking and telling stories that often include near misses. The poster sized laminated and erasable Muster List for each vessel works well.

Advisors explain to skippers and crew that a good way to start writing procedures is by answering the question “what do I do on deck that could kill me”. This question gets everyone involved and thinking about how they do business on deck.

WorkSafeBC safety officers are distributing Safest Catch program information, and have also said that they are now seeing more fishermen wearing PFDs. They are also considering how to reward participants with an incentive program based on the assessments fishermen pay into WorkSafeBC. There are now 110 vessels engaged in the program and 33 have completed it entirely and received a certificate and decal.

4.6 Milestone 6 – “The Big Gorilla”

The Safest Catch program was featured at the Standing Committee on Fishing Vessel Safety at National CMAC in Ottawa. Safest Catch DVDs in both English and French were distributed at this National forum. The east coast tends to default to a compliance driven safety program – having TC be responsible for their safety rather than taking ownership of safety themselves.

Fish Safe was invited to present at the United States National Transportation Safety Board’s Fishing Vessel Safety Forum in Washington D.C. This forum discussed the difficulty of communicating safety information to fishermen. A “feet on the dock” approach was emphasized, much like the Safest Catch. Another topic was the “Big Gorilla in Safety” – the human factor. Fishermen’s perception of risk, and their ability to increase their awareness of these risks, needs to be tied to a decrease in risk tolerance, and this decrease in risk tolerance



must become an integral part of their fishing operations – “how we do business on this boat”.

4.7 Milestone 7 – Spreading the Word

This quarter 26 vessel visits were conducted in eleven different communities on seven different gear types. Almost 100 fishermen participated in the program over this three month period. Fish Safe shared a booth with Western Mariner Magazine at the Pacific Marine Expo in November. Over 300 fishermen from Canada attended Expo, and it was also a great opportunity for Fish Safe to learn about new safety equipment from Expo exhibitors.

We attended the Native Brotherhood of BC convention, the Underwater Harvesters Association AGM, along with Trawl and Mutual Marine Insurance meetings and vessel visits have been lined up as a result.

Fish Safe met with TC representatives while at National CMAC and discussed the proposed Safety Management System regulations for fishing vessels. We submitted a request to complete a gap analysis on the Safest Catch to determine if the program will meet or exceed regulatory requirements. The gap analysis is now being conducted.

4.8 Milestone 8 – Herring Drills Day

We have increased the request for Advisors by attending industry meetings and now all gear types have been reached. Total vessel visits is 206 to dive, gillnet, longline, seine, trap, trawl, troll and fish packing vessels.

To promote the Safest Catch program and the importance of practicing drills, the BC herring fishery participated in the first ever fleet wide safety drill. We were not sure what the uptake would be, and were overwhelmed when over 100 fishermen registered to participate. When the abandon ship drill was announced over the VHF radio, each vessel completed an abandon ship drill that included a mock mayday call, donning immersion suits

and mustering the crew at the liferaft. The first vessel to complete the drill won a prize, and when boats completed their drill they called in and were entered in a draw for Mustang Rescue Sticks and PFDs as prizes.

Fish Safe met with Nesika Insurance and their underwriter. The underwriter was favourably impressed with the Safest Catch and will offer a 10% discount to fishermen who have participated in the program.

We worked with WorkSafeBC to see if the Safest Catch Program could be considered equivalent to their existing Certificate of Recognition Program. It looks like a self audit component will be required – which will also meet TC’s safety management system requirements.

4.9 Milestone 9 – Reflections

The first year of the Safest Catch program was spent mainly in development and training, and the second year in outreach to contact as many vessels as possible. As we reviewed this quarter’s Advisor logs it is evident how the fishing industry is recognizing the value of the Safest Catch.

The program continues to mature and we are seeing changes throughout the fleet with onboard safety. Perhaps the most exciting event this reporting season came from a return visit to Prince Rupert where for the first time the Safest Catch program has been credited with saving lives. The skipper and crew told the Advisor the chain of events that led to their fishing vessel capsizing. On their first visit the Advisor had showed the crew how to do an abandon ship drill and launch the raft. The skipper this visit said *“It all happened so fast...about 90 seconds and the boat capsized. We were so glad that you helped us do that drill. I told my crew to get the liferaft and they knew exactly how to get it into the water and we were able to step off the overturning boat right into the raft”*.

In another instance a skipper told how a crewman fell overboard while they were trying to free a line from the propeller. The crewman was wearing a PFD and they had



their man overboard equipment ready and were successful in recovering their mate because they had done a retrieval drill during an Advisor visit earlier that year.

Understanding the importance of meeting fishermen where they live, we continued to attend weekly lunch and coffee meetings with fishermen at various haunts around Vancouver.

4.10 Milestone 10 – Thinking Outside the “Vessel Visit Box”

This quarter there were some challenges because fisheries on the coast experienced good runs and good fishing and everyone was out fishing including the Advisors, so it was difficult to coordinate mutually agreeable times for vessel visits. This allowed us to think about other ways to move forward with new fleet events within the Safest Catch program.

Similar to the Herring Drills Day, we conducted a Prince Rupert Drills Day. Over 20 vessels participated representing the majority of the fleet that was in Prince Rupert that day and prizes were awarded.

The first Fraser River gillnet fishery gave us an opportunity to reach another fleet. With two fatalities due to falls overboard from small fishing vessels this year we decided to focus on PFDs. Everyone found wearing a PFD during the fishery would receive an award. Two Advisors stormed the docks letting the fleet know that Fish Safe would be out the next day looking for PFDs. Prize packages were assembled, draw forms printed and an “i fish safe” decal produced that were given to everyone who was wearing a PFD. The grand prize for the draw was a waterproof handheld VHF.

It was a quarter with a lot of outreach and regular meetings. We started work on another training workshop for the Advisors based on what we are learning from the Advisor audits. We also interviewed two potential new Advisors. One is a second generation

Vietnamese crab fishermen 100% fluent in English as well as Vietnamese. He is excited about working with the large Vietnamese crab fleet.

From meetings with Transport Canada we learned that they support the Safest Catch program and see it as a national model for safety management systems in the fishing sector. Eric Holliday, Fish Safety Foundation, New Zealand suggests that as a Safety Management System the Safest Catch will set the benchmark for the Canadian fishing industry, as well as placing Canada and Fish Safe BC at the forefront of fishing safety initiatives internationally (2010).

4.11 Milestone 11 – The Value of Stories

The highlight this quarter was that stories fishermen have been sharing with the Advisors – are being used by the Advisors when they visit other vessels. Stories are authentic and an important way to highlight the importance of having a safety program on board.

More industry events, trade shows meetings and dock walks continued to create awareness of the program, sign ups for vessel visits and reaching portions of the fleet with limited exposure to the Safest Catch program thus far. We have had requests for vessel visits from 243 fishermen and have visited 171 vessels and talked with over 800 fishermen. Decals for completing the whole Safest Catch program have been awarded to 71 boats. Advisors will continue to return to vessels still working on their safety programs.

Audits on the Advisors are complete. The Advisors have different levels of comfort with elements of the Safest Catch program. Some need help with their laptop computers and software, and others need to work on their understanding of regulatory requirements. They all need a refresher in presentation skills including asking open questions to gather



information from the fishermen they visit. Also there are some inconsistencies in how the elements of the Safest Catch program are being presented. The audit process has been very helpful in determining content for another Advisor training session. A one day computer workshop has also been scheduled.

We started filming the Advisors doing vessel visits and delivering the Safest Catch program. Fishermen were captured live on film initially showing tentative interest and gradually becoming enthusiastic participants. The video will be completed in time to present it at the April 2012 National CMAC in Ottawa. Other uses for this DVD documenting the Safest Catch include promotion of the program, helping other fishing organizations implement the program, and training new Advisors.

The two new Advisors are now on board. Both are from the small boat fleet which is the largest fleet on the west coast. TC inspections to not capture this less than 15 gross ton or less than 12 metre demographic.

Safest Catch Advisors attended a Cold Water Immersion Workshop that showed the latest techniques for treating hypothermia including hands on work retrieving and packaging a person who is suffering from hypothermia.

A summative evaluation of the Safest Catch program by Verita Strategy Group is near completion and will form the basis of the final report to SAR-NIF due in April 2012.

5. CONCLUSIONS

We believe the answer to the age old question of how to improve fishing vessel safety is to provide fishermen with the tools they need to come home safely. Too simple you say, and it is, the key lies in the delivery.

In order for any safety program to be effective it must reside on board the vessel and as the Safest Catch program proves all

tools must be delivered on board or be easily transferred to the boat.

Fishermen in BC are changing how they “do business around here on the boat”, and no longer accept death as a part of their job; now believe they can and will come home safely.

6. REFERENCES

Holliday, E., 2010, “Fishing Vessel Safety Management System, a Report to Fish Safe BC”, unpublished report, Fish Safety Foundation – Hooked on Safety, New Zealand.

Lang, J.S., 2000, “Fishing Vessel Safety – A Marine Accident Investigator’s Perspective”, Proceedings of the International Fishing Industry Safety and Health Conference, J. Lincoln et al., National Institute for Occupational Safety and Health, Cincinnati, OH, pp. 67-74.

Poggie, J.J. and Pollnac, R.B., 1997, “Safety Training and Oceanic Fishing”, Marine Fisheries Review, 59(2), pp. 25-28.

Reason, J., 1994, “Human Factor”, Cambridge University Press, p. 173.

Transportation Safety Board, “Safety Issues Investigation Into Fishing Safety in Canada”, Draft Report M09Z0001, 2011.

Wagner, B., 2000, “Safety and Health in the Fishing Industry: An ILO Perspective”, Proceedings of the International Fishing Industry Safety and Health Conference, J. Lincoln et al., National Institute for Occupational Safety and Health, Cincinnati, OH, pp. 13-34.

Windle, M.J.S., Neis, B., Bornstein, S., and Navarro, P., 2006, “Fishing Occupational Health and Safety: A Comparative Analysis of Regulatory Regimes”, SafetyNet, Memorial University of Newfoundland, St. John’s, NL, p.15.



Small Fishing Vessels Study and Modelling for the Improvement of the Behaviour in Extreme Seas

Antoine Pagès, *Sirehna*, antoine.pages@sirehna.com

Jean-Jacques Maisonneuve, *Sirehna*, jean-jacques.maisonneuve@sirehna.com

Clève Wandji, *Bureau Veritas*, cleve.wandji@bureauveritas.com

Philippe Corrigan, *Bureau Veritas*, philippe.corrigan@bureauveritas.com

Benoît Vincent, *Ifremer*, benoit.vincent@ifremer.fr

ABSTRACT

Commercial fishing is one of the most dangerous primary activities. Most of the 24000 yearly accidents identified by IMO are occurring on small vessels. The French SOS-Stabilité research project aims at better knowing and modelling dynamic stability issues occurring on small fishing vessels (12 to 24 m), prior to the development of solutions for improving their behaviour, through the evolution of the ship design and through the design of appropriate embedded systems. This paper presents the first part of the project: sea and model tests, development of a ship behaviour time-domain simulator (including fishing gear modelling capabilities) and first validation of this simulation tool.

Keywords: *SOS-Stabilité, time-domain simulator, small fishing vessel, dynamic stability, non-linear effects*

1. INTRODUCTION

The French SOS-Stabilité research project¹ aims at better knowing and modelling dynamic stability issues occurring on small fishing vessels, prior to the development of solutions for improving their behaviour, through the evolution of the ship design and through the design of appropriate embedded systems. The developments undertaken within the scope of the project are made in connection with existing regulations about small fishing vessels.

During the first part of the project, sea trials and model tests with a 23 m trawler have been carried out and have helped developing and

validating the general models implemented in a ship behaviour time-domain simulator, and more specifically the fishing, sea-keeping and manoeuvrability models.

The sea trials consisted in measuring various loads (rudder, trawler lines, etc.) and the ship behaviour at sea. The basin trials consisted in the study of the ship behaviour in following, quartering and beam seas, with and without speed.

The aim of the time-domain simulator is to model the dynamic behaviour of ships in rough seas, with small calculation time, to enable systematic variations and analyses of small fishing vessels safety with relation to their dynamic stability. The main focus is the phenomena observed in following seas, like broaching-to, involving a strong coupling between the ship's degrees of freedom and strong variations of its roll and yaw stability characteristics. The

¹ SOS-Stabilité, project supported by the French ministry of industry, regions Bretagne, PACA and Pays de la Loire; improvement of small fishing vessels safety; partners: Bureau d'études Mauric, Bureau Veritas, IFREMER, Institut Maritime de Prévention, Société des Etablissement Merré, PRINCIPIA SAS, SIREHNA.



stability in operation at low speed, with the fishing gear active, is also addressed.

2. REGULATION

A review of the relevant regulations of Bureau Veritas (BV) rules, European Union (EU) and international (IMO) rules, for dynamic stability on fishing vessels was conducted. Apart from aspects strictly related to the stability, the regulations on equipment that may impact on the stability of fishing vessels have also been reviewed. Moreover, in addition to existing recommendations and regulations, international developments in progress on these issues were included in this study.

Nowadays, there are no mandatory international regulations concerning the stability of fishing vessels. The Torremolinos protocol provides provisions for vessels of length greater than 24 m, but it has not yet entered into force. However, this protocol has been integrated into EU directive, and it is mandatory for all European states.

French regulations on fishing vessels are very thorough, covering all sizes of vessels, which are divided into three categories: less than 12 m (division 227), from 12 to 24 m (division 226) and over 24 m (division 228, which is the French transcription of the EU directive).

It is worth emphasizing some specific points in the above mentioned regulations.

- The current intact stability criteria are mainly related to quasi-static notions associated with the stem and freeboard heights, with areas of righting lever curve and initial metacentric height. The dynamic stability phenomena should also be integrated in the intact stability code in 2014, through the second generation criteria (but these criteria are not specific prior to fishing vessel).
- Downflooding angles are extremely important. They are related to the definition of enclosed spaces, whose misinter-

pretation led to disaster, especially with the effect of freeing ports in enclosed spaces.

- The influence of free surface effect is treated in a simplified way. On the other hand damage stability is not considered for fishing vessels (there are just a few recommendations in the Torremolinos convention on this subject), although fishing vessels have already been lost due to insufficient stability after damage.
- The influence of underwater obstacles is considered only in the French regulations for vessels under 24 m and in a very simplified way.
- Stability criteria assessments are made under some assumptions (closing openings, automatic limitations of the load in the fishing rope, etc...) which, if they are not fulfilled by the crews, can lead to loss of stability.
- There are no performance criteria for course control systems on swell.

3. THE TARGET SHIP

The ship chosen for the various tests (both sea and model trials) is the 23m trawler ship “Anthinéas”, build in 1991 in France. Its home port is Les Sables d’Olonne. Its main particulars are given in Table 1 and a side view is shown below.

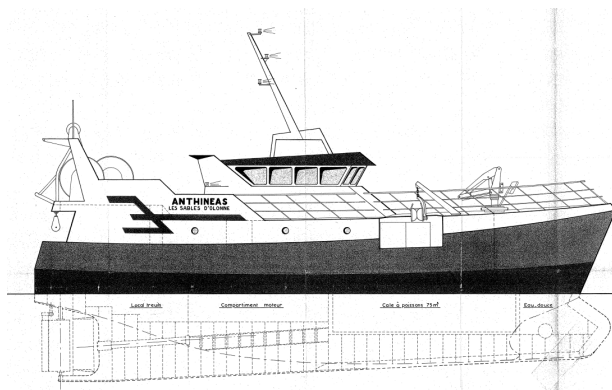


Figure 1: View of the Anthinéas trawler.



The fishing gear is made up of twin trawls towed by three warps. It is used for bottom trawling.

The main reasons that have led to the choice of this trawler are the fact that its dimensions fit in the aimed dimensions of the SOS-Stabilité project (12 to 24 m), the closeness of its home port (making instrumentation installation and onboard engineers turnover easier) and the will of its owners to cooperate on this project.

4. EXPERIMENTS

4.1 Sea Trials

The main objective of the sea trials was to gain some experience about the fishing environment, the behaviour of a standard trawler and the possible measurements onboard. Therefore the sea trials were carried out onboard an operational ship with the will not to interfere with the crew normal activities; in particular this implied some restrictions about the control of the trials conditions, the embedded measurement systems and their ease of use.

Instrumentation. The instrumentation installed onboard can be broken down into four groups.

- “Movements” group: measurement of the ship movements (attitude, speed over ground, accelerations, angular speeds) and ship trajectory (heading, latitude, longitude).
- “Controls” group: measurement of the propeller pitch, engine speed, steering angle, rudder forces.
- “Warps” group: measurement of the forces and orientation of the three warps.
- “Environment” group: measurement of the wind speed and direction, sea-state estimation.

Trials. During the trials, the ship sailed in the Bay of Biscay, close to the shore (about 10

nautical miles), between Saint-Gilles-Croix-de-Vie and Oléron Island during 12 days in September 2009. Except during one day (during which the sea state was 4), the sea state encountered was not greater than 2.

Several kinds of trials were carried out both during fishing (usual manoeuvres) and during voyage (dedicated tests). The displacement during the trials varied from 206 t to 182 t. The main variations were the oil, fresh water and catch weight.

During fishing, the following tests were carried out:

- action of fishing, with or without turning;
- hauling action;
- veering out action.

During voyage, the following tests were carried out:

- turning;
- roll decay tests;
- deceleration;
- speed tests.

4.2 Model Tests

One of the SOS-Stabilité project objectives is the identification and modelling of the most extreme and critical conditions for the ship stability. Therefore, model tests were carried out in order to be able to control the environment, and particularly to generate rough waves, and to measure the corresponding non-linear ship response.

Two main campaigns were carried out:

- the first one with zero-ship-speed in order to study beam seas with varying down-flooding conditions and following seas while fishing; it took place at the wave tank at Ecole Centrale de Nantes (ECN, France), which is 50 m long, 30 m wide and 5 m deep; the wave generator can create regular and irregular waves up to 0.3 m height;
- the second one with forward speed and



following seas; it took place at the Seakeeping and Maneuvering Basin at MARIN (Netherlands), which is 170 m long, 40 m wide and 5 m deep; the wave generator can create regular and irregular waves up to 1 m height.

A complementary outdoor campaign was also carried out without waves in order to set the autopilot, to study the ship behaviour in calm water and to check its performances before the tests in MARIN.

Model description. The model used for the basin trials is a model of the Anthinéas trawler at 1/11 scale. The chosen displacement is 250 t at full scale, corresponding to the departure loading case with the worst initial stability according to the stability characteristics. Another loading case was also used during the MARIN tests, derived from the latter by simply raising the ship centre of gravity, which led to a “damaged” GM.

The main particulars for the chosen displacement at model scale and full scale are shown in Table 1.

The model ship is fitted with an electric engine with a maximum power of 390 W; the maximum shaft rotation obtained is 2000 RPM.

In order to model the full scale ship roll behaviour as well as possible, the model ship is fitted with bilge keels with dimensions corresponding to those of the full scale ship.

Since downflooding is one of the main concerns of the basin trials, the model ship is also fitted with openings on the main deck, consisting of scuppers to evacuate green water and of possible entrance for downflooding.

The study of the behaviour of the ship while fishing is also a great concern. Therefore several fishing gear towing points are available. The fishing gear is modelled by a simple bungee, of which the stiffness and damping are known.

Table 1: Main particulars of Anthinéas trawler at model and full scale.

Scale	Model	Full
Length overall (m)	2.08	22.89
Length between perpendiculars (m)	1.85	20.39
Overall breadth (m)	0.64	7.04
Forward draught (m)	0.27	2.97
Aft draught (m)	0.345	3.8
Light displacement (t)	-	173
Displacement (t)	0.188	250
Possible downflooding volume (L)	50	66550
Nominal GM (m)	0.0657	0.723
Damaged GM (m)	0.046	0.506

Instrumentation. The various measurements and recording systems used during the model tests were:

- a trajectography system allowing to measure the 6 degrees of freedom of the ship;
- an inertial unit measuring the ship attitude;
- dynamometers allowing to measure all the relevant forces (propulsion thrust and torque, rudder screw, fishing gear forces);
- capacitive probes to measure the relative water height at three points of the ship;
- 2 cameras, shooting different places depending on the tests;
- a GPS antenna to measure the ship speed and position (for the outdoor tests only).

Zero-speed tests. Three kinds of tests were carried out at zero-speed:

- beam sea with varying wave period;
- following sea with the ship hold still by cables (bungees) with varying wave period and varying engine speed;
- ship hold still by cables (bungees) without waves and qualitative simulation of the snagging of a fishing gear.

Outdoor tests. Outdoor tests on the Erdre River (near Nantes) were carried out in order to study the ship behaviour in calm water (manoeuvrability, resistance, acceleration, deceleration), check the propulsion capabilities and set the autopilot. The various tests carried out were:



- ship speed obtained for several engine speeds in order to draw the propulsion calibration curve;
- acceleration test to work out the time and distance to sail at maximum speed and the speed variation in time;
- deceleration speed to work out the time and distance for the ship to stop and the speed variation in time; this test can help getting access to the ship resistance;
- turning circles for various ship speeds and rudder angles to help getting access to the manoeuvring coefficients.

Tests with forward speed. Three kinds of tests were carried out with forward speed:

- regular beam sea at 2 forward speeds (voyage and fishing speeds) with wave period corresponding to the ship roll period;
- following sea at varying wave period (slightly overtaking waves, slightly overtaken waves, maximum wave camber and high wave period);
- following quartering sea (30° and 45°) at varying wave period (slightly overtaking waves, slightly overtaken waves and maximum wave camber).

During all the tests, the ship steering was controlled by an autopilot.

5. TIME-DOMAIN SIMULATION

The time-domain simulator developed in the scope of the SOS-Stabilité project is meant to be a simplified simulator allowing to take into account the forces of interest while keeping low calculation time; this must enable to use the simulator in an efficient way for quick design assessment and systematic variations, ... The modelling of the forces implemented in the simulator are detailed below.

5.1 Description, Capabilities, Method

The simulator is made up of a block solving the dynamics equations for a six degree of

freedom solid body and of various modules modelling the external forces (propulsion, resistance, manoeuvrability, fishing, etc.). A specific feature of the simulator is that non-linear effects are taken into account in order to model large ship motions correctly, but with simplified approaches. In particular, the hydrostatic and hydrodynamic Froude-Krylov effects as well as roll damping are modelled in a non-linear way.

Basic models. The external forces implemented in the simulator are listed below.

- Propulsion: propeller thrust depending on the propeller rotation speed and propeller pitch and on the ship speed of advance; the module coefficients are determined based on known, experimental or estimated data.
- Resistance: longitudinal and vertical forces and pitch moment depending on the ship relative speed of advance, based on statistical models (Holtrop, 1982, 1984).
- Manoeuvrability: longitudinal and lateral forces and yaw moment depending on the ship relative speed with respect to water (taking drift and wave orbital velocity into account) and yaw speed; the manoeuvrability model used is a calm water “classical” model close to the one proposed by Lewis (1989).
- Rudder: specific rudder module taking into account the propeller slipstream (Brix, 1993) and the wave orbital velocity at the rudder location.
- Lifting surfaces: general module to take into account the effect of lifting surfaces, like bilge keels, by the mean of lift and drag coefficient.
- Hydrostatic and hydrodynamic (incident wave) model: computation of the water pressure around the ship hull (Froude-Krylov) neglecting diffraction forces; the model ensures that non-linearities due to extreme motions are accounted for; some more details are given further.
- Weight: forces due to gravity.
- Radiation: only the added inertia and radiation damping coefficients are accounted for, obtained by a frequency-do-



main calculation.

- Damping: heave, roll and pitch linear damping and roll quadratic damping coefficients, obtained from experimental or empirical (Himeno, 1981) data; the coefficients can be dependent on the ship speed of advance.
- Wind: longitudinal and lateral forces and yaw moment depending on the ship relative speed with respect to wind and yaw speed.
- Fishing: several options, detailed further, are available to compute fishing forces; the snagging of a fishing gear can also be simulated.
- Flooding: forces due to green water and its propagation within the various ship tanks (engine room, ship room...); the water dynamics within the compartments (sloshing) are not directly accounted for.

Regular and irregular waves can be used within the simulator. Irregular waves are modelled through a superposition of regular waves (Airy model). Therefore a wave system is defined by the spectral characteristics of each of its components: amplitude, period, phase and propagation direction. Cross seas can also be used.

An autopilot block can also be used to control the ship heading. The autopilot can therefore be changed easily. This feature is needed in the scope of the SOS-Stabilité project since one of the goal of this project is the improvement of the ship control, especially in following seas.

Hydrostatic and hydrodynamic model. The water pressure around the ship hull (Froude-Krylov) is computed taking into account the relative position of the ship against the free surface (including incident waves).

The ship is modelled by a simple mesh so that the total pressure forces are obtained by integration of the pressure over all the immersed cells. A mesh example is shown in the figure below.

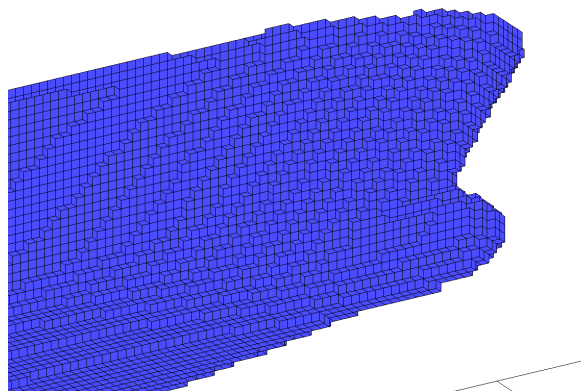


Figure 2: View of the forward part of the Anthinéas mesh.

The pressure used to compute the Froude-Krylov forces integrates the dynamics due to waves; this dynamic part depends on the spatial and temporal position. The free surface is supposed not to be modified by the body, that is the pressure variations due to the presence of the body (diffraction forces) are neglected.

This model ensures that the real immersed part of the ship is taken into account in the computation of hydrostatic and incident wave forces whatever the position and attitude of the ship, and therefore ensures that non-linearities due to extreme motions are accounted for.

Fishing. The fishing forces can be modelled in two different ways, depending on the intended result precision and computational time.

The most complete and precise method is the coupling of the simulator with a dedicated trawl gear simulation software, DynamiT, developed by Ifremer. This tool fully models the trawl gear (bottom or pelagic trawls, single, twin or more trawls, panels...) and simulates the dynamics of the fishing gear. Netting material, made of meshes, is modelled by a cylinders-net. Netting and other elements (floats, ground gear, doors ...) are modelled by damping forces (drag and lift), hydrostatic forces and inertia forces that are calculated along the deformation of the structure in the water by an

implicit time solver. Water motion is supposed not to be affected by the gear motion. Interaction with the seabed is modelled with Newton friction law. Obstruction on the seabed, one of the main event that can strongly affect the trawler, can be simulated by forcing the kinematics of any element of the trawl gear (for instance a part of the ground gear speed becoming null). Thus, for example, it is possible to analyse the damping effect of trawl doors onto the warp tension during the obstruction process. The outputs are all the information about the fishing gear geometry (positions, openings, door to door distance...) and forces (rig tensions, towing force...). The results obtained by coupling the ship simulator and trawl gear simulator are used to develop and improve a simplified fishing model to be implemented directly within the ship simulator.

Within the simplified model, the fishing gear consists in one bar (2 for twin trawls), representing the trawl, linked to the ship by 2 warps (3 for twin trawls), which are modelled by a catenary. A sketch of this modelling is shown below.

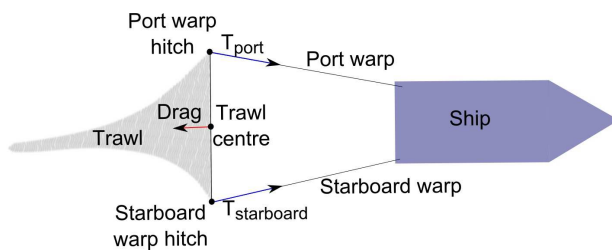


Figure 3: Fishing gear simplified model.

In this way, each fishing gear is defined by a mass-stiffness system with 3 degrees of freedom: longitudinal and transverse translations and rotation about the vertical axis, the trawl depth being considered constant. The loads applied to each fishing gear are then the warps tensions, the trawl hydrodynamic resistance and the friction of the trawl on the seabed. These loads are added to the other external forces for the resolution of the dynamics equations.

5.2 Validation

The validation of a simulator is a very important step to gain confidence in its results. Several qualitative and quantitative validations have been carried out, in particular for non-linear phenomena:

- qualitative validation of parametric roll using previous trials carried out by Sirehna on a 80 m fishing vessel (Maisonneuve, 2007);
- qualitative validation of broaching-to using model trials with a Japanese fishing vessel (Umeda et al., 1999, Umeda, 2000).
- quantitative validation using the trials carried out during SOS-Stabilité project and described above.

Parametric roll. Sea trials have been carried out by Sirehna (Maisonneuve, 2007) on an 80 m fishing vessel prone to parametric roll. The environmental conditions encountered during the trials have been reproduced in the simulator. The trials movements and the simulator results are shown in the figures below. Heave is positive downwards, roll is positive to starboard and pitch is positive bow up. The arrows on the graphs indicate a minimum in heave, which means the ship is on a wave crest.

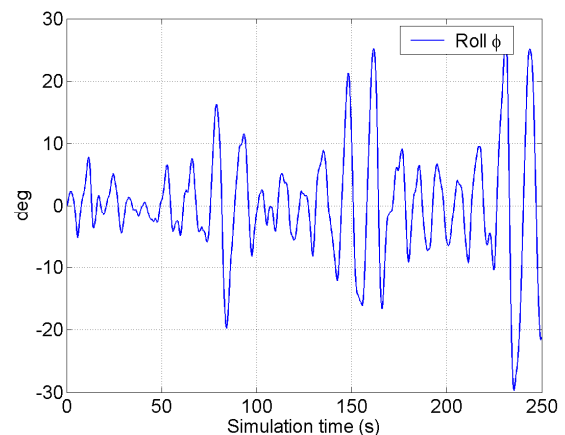


Figure 4: Roll variations (simulator).

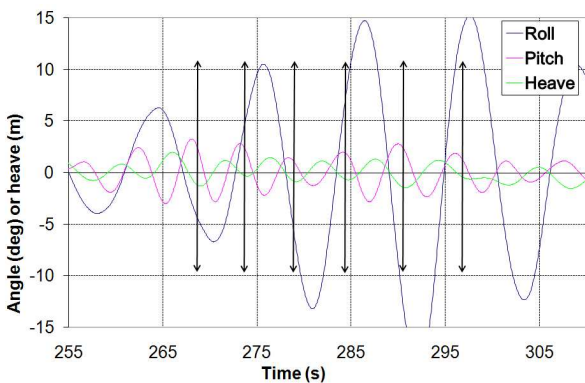


Figure 5: Heave, roll and pitch variations (trials).

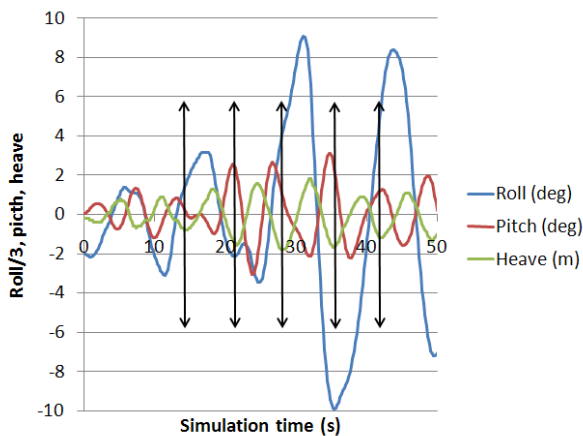


Figure 6: Heave, roll and pitch variations (simulator); note: roll has been divided by 3.

It can be seen that parametric roll is obtained with the simulator (apparition of “bursts” of large roll); this non-linear phenomenon is obtained “naturally”, without triggering it. The phases between heave, roll and pitch are very similar for trials and simulation: the instants when the ship is on a wave crest happen slightly before the instants of roll extremum. The main difference between trials and simulation is the greater amplitude of the movements, particularly roll, for simulation. A reason to that difference can be the use of only linear damping coefficients within the simulator (no quadratic coefficients have been used in order to simplify the data setting).

Broaching-to. Basin trials have been carried out by Umeda (1999, 2000) on a 35 m Japanese fishing vessel (at 1/15 scale) prone to

broaching. The trials were carried out with regular waves.

The test-case has been modelled in the simulator, with three wave conditions (increase in wave height and period from the first one to the third one and variation of wave angle) all three conditions led to capsizing due to broaching-to during Umeda’s trials. The following figures show the Euler angles variations obtained with the simulator for the first and third wave conditions.



Figure 7: Euler angles obtained with the simulator for the first wave conditions.

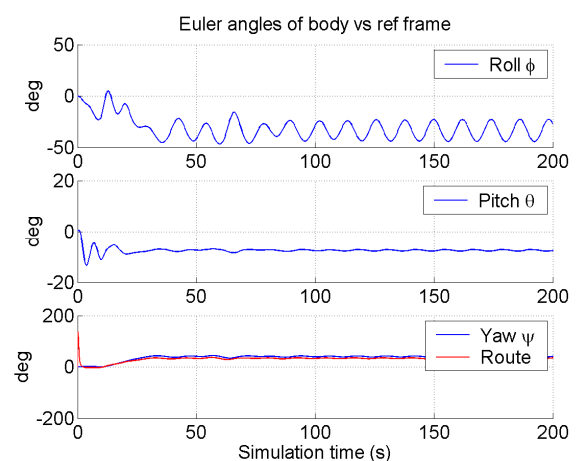


Figure 8: Euler angles obtained with the simulator for the third wave conditions.

The three simulated cases lead to broaching-to (the yaw angle deviates of about 40°

from its initial value and large roll angles are obtained), but only the first two lead to capsizing due to broaching-to. These results show that broaching-to is qualitatively obtained by the models implemented in the simulator; these models need to be improved to obtain good quantitative agreement with experiments.

Validation using sea trials and model outdoor tests. The sea trials and the model outdoor tests can be used to validate the calm water behaviour of Anthinéas (validation of the modules implemented in the simulator and setting of the coefficients for the specific ship chosen for the study). The figures below show a comparison of experimental and computed results for some elementary validations; the experimental values have been converted from model scale to full scale.

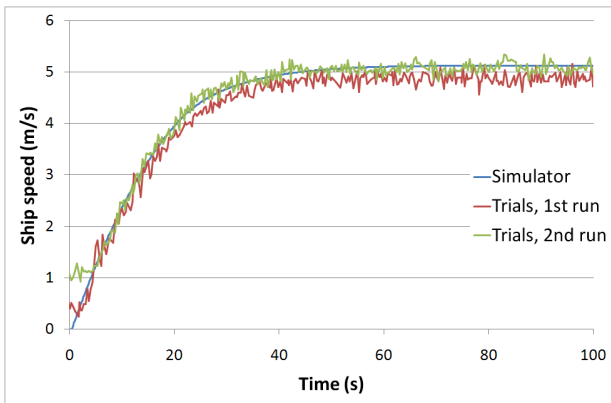


Figure 9: Ship speed variation during acceleration (model tests / simulator).

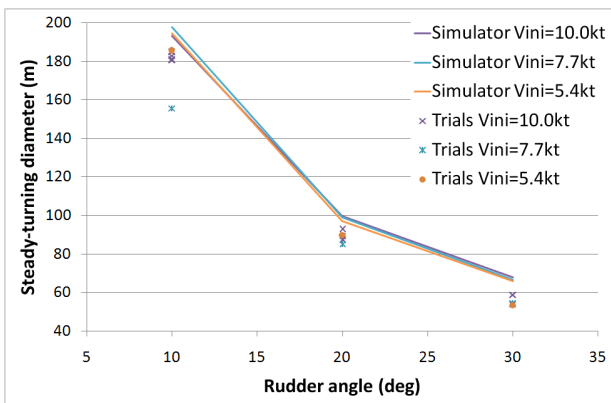


Figure 10: Steady-turning diameter for 3 rudder angles (model tests / simulator).

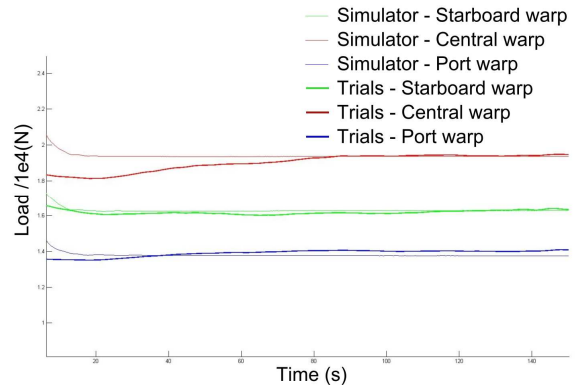


Figure 11: Warp loads (sea trials / simulator); trial signals have been filtered.

The simulation results are close to the experimental ones for the elementary tests shown here as well as for the others: the modelled ship behaviour is meeting the one observed during the trials.

Validation using basin trials. Once the Anthinéas parameters are set, the basin trials can be used to validate the modules involved in the ship behaviour in waves (Froude-Krylov forces, roll quadratic damping, ...). The figures and tables below show a comparison of experimental and computed results for some of the trials carried out in ECN basin; the experimental values have been converted from model scale to full scale.

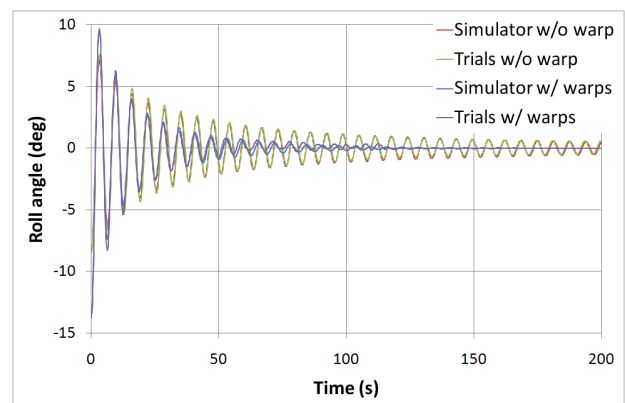


Figure 12: Roll decay tests with and without warps, without forward speed.



Table 2: Roll, pitch and heave amplitudes with various regular beam seas without forward speed

Wave parameters			Trials response amplitudes			Simulator response amplitudes		
Wave period (s)	Wave height (m)	Run type	Roll (deg)	Pitch (deg)	Heave (m)	Roll (deg)	Pitch (deg)	Heave (m)
6.30	1.1	Roll resonance	14.0	0.7	1.2	14.5	2.0	1.5
6.30	2.2	Roll resonance	24.0	2.7	2.5	24.0	3.0	2.5
6.30	3.3	Roll resonance	29.0	3.7	3.7	31.0	2.0	3.3
9.95	5.5	High period	13.3	3.1	4.9	13.5	1.0	5.8
9.95	9.9	High period	18.5	2.2	10.1	20.0	2.0	10.7

The results show that the ship behaviour for beam seas without speed is correctly modelled by the simulator. Further use of ECN trials is still to be done, especially tests implying following seas, warps, green water and flooding.

The following figures now show a comparison of experimental and computed results for some of the trials carried out in MARIN basin; again, the experimental values have been converted from model scale to full scale.

The comparison of trials and simulator results show good qualitative agreement. Some quantitative improvements need to be done:

- for quartering sea, drift speed obtained with the simulator is a bit lower, leading to a phase shift between roll signals;
- movements in following sea tend to be overestimated with the simulator.

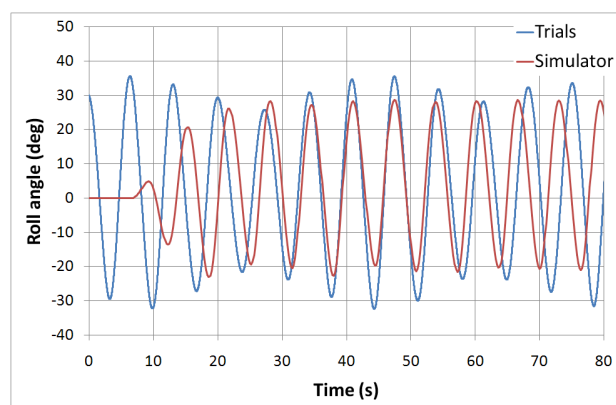


Figure 13: Roll variation for regular beam sea ($H_{\text{wave}}=3.3$ m, period=ship roll period) with forward speed ($V=10$ kt).

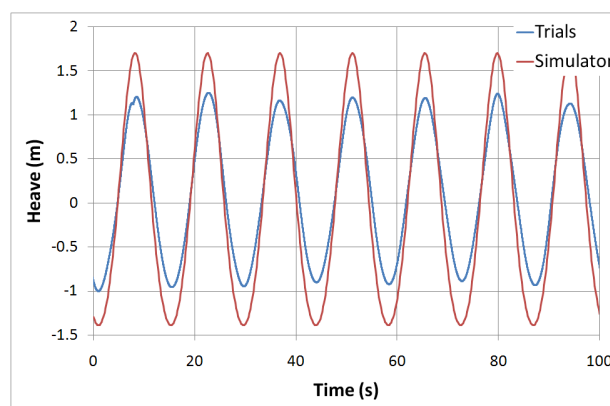


Figure 14: Heave variation for regular following sea ($H_{\text{wave}}=3.3$ m, $T=9$ s) with forward speed ($V=10$ kt).

Further use of the MARIN trials is still to be done, especially tests implying following and quartering seas with low encounter period.

6. NEXT STEPS

The trials, especially those carried out in ECN and MARIN, need to be further analysed and used for the simulator validation.

In addition to this work, sea trials with a 1/3 scale model and developments of solutions to improve the small fishing vessels behaviour are planned before the end of the SOS-Stabilité project.

6.1 Large scale Trials Platform

High sea states are very critical conditions for the seakeeping of small fishing vessels, particularly for quartering and following seas. To observe these conditions and the corresponding ship behaviour, nor basin trials neither sea trials are ideal. Basin trials need very sophisticated equipment to avoid scale effects and recreate realistic environmental conditions. Sea trials on full scale ships are often limited by the possible embedded instrumentation (which must not be inconvenient for the usual operation of the ship), the crew safety and the ability to vary the ship configuration.



Therefore, to avoid the disadvantages of basin and full scale trials, a 1/3 scale model of the Anthinéas has been built and must be used for sea trials. The so-called “large scale trials platform” has been designed to easily vary some of its characteristics (loading, stability, fishing gear towing points, free surface tanks ...) and is unmanned, totally waterproof and unsinkable so that it can meet extreme sea states possibly leading to capsizing.

6.2 Development of Safety Improvement Solutions

The experiments and the simulations presented above and those to be carried out in the future enable to gain knowledge of the small fishing vessels behaviour in extreme seas. From this knowledge, some leads for the improvement of these ships safety can be drawn.

A first lead is the use of suitable passive (detection of dangerous conditions and warning of the crew) and/or active (specific autopilot and control of the fishing gear) embedded systems. Such embedded systems are being developed within the project.

Another lead is the development of innovative ship designs, fishing gear designs and ship-fishing gear interfaces. Such developments are also carried out within the project.

6.3 Exploitation of Project Results

The final step of the project is the dissemination of the gained knowledge. The exploitation of the results will be done by:

- the setting up of specific education / training programs dedicated to the safety of fishing vessels in extreme seas;
- the definition of operational limitations, recommendations and links with regulations for the behaviour of small fishing vessels in extreme seas.

7. REFERENCES

- Brix, J., 1993, “Manoeuvring Technical Manual”, Seehafen Verlag, Hamburg.
- Himeno, Y., 1981, “Prediction of ship roll damping - State of the art”, Research Report, Department of Naval Architecture and Marine Engineering, College of Engineering, The University of Michigan, Ann Arbor, Michigan.
- Holtrop, J. and Mennen, G.G.J., 1982, “An Approximate Powering Prediction Method”, International Shipbuilding Progress, Vol. 29, pp. 166-170.
- Holtrop, J., 1984, “A Statistical Re-analysis of Resistance and Propulsion Data”, International Shipbuilding Progress, Vol. 31, pp. 272-276.
- Lewis, E.V., 1989, “Principles of Naval Architecture, Second Revision, Vol. III, Motions in Waves and Controllability”, SNAME.
- Maisonneuve, J.J., 2007, “Rapport des essais en mer sur le navire P85”, Technical report, Sirehna.
- Umeda, N. et al., 1999, “Stability assessment for intact ships in light of model experiments”, Journal of Marine Science and Technology, Vol. 4, n°2, pp. 45-57.
- Umeda, N., 2000, “Data of Model Experiments for Ship A-2”, 23rd ITTC Specialist Committee on Prediction of Extreme Motions and Capsizing.





Operational Guidance with Respect to Pure Loss of Stability and Parametric Rolling

Erik Ovegård, *Seaware AB & KTH Royal Institute of Technology*, ovegard@kth.se

Anders Rosén, *KTH Royal Institute of Technology*, aro@kth.se

Mikael Palmquist, *Seaware AB*, mikael.palmquist@seaware.se

Mikael Huss, *Wallenius Marine AB*, mikael.huss@walleniusmarine.com

ABSTRACT

This paper reviews two previously presented simplified methods for assessment of pure loss of stability and parametric rolling based on linear signal theory. The methods are evaluated in relation to full-scale incidents and time-domain simulations. Underlying assumptions and tuning of the critical levels in the simplified methods with reference to time-domain simulations is discussed. Given proper tuning the methods are concluded to provide a feasible basis for ship specific on-board operational guidance.

Keywords: *pure loss of stability, parametric roll, full-scale incidents, time-domain simulations, operational guidance*

1 INTRODUCTION

Total intact stability failures as the capsizing of the Ro-Ro ship *Finnbirch* (Hellner & Bexell 2008) and partial failures with container vessels and Pure Car and Truck Carriers (e.g. France et al 2003, Palmquist & Nygren 2004) have made it clear that the prevailing intact stability standards do not provide a satisfactory level of safety for all ship types. The primary mechanism in these incidents has been the restoring force variation due to the ships varying position in heading or following seas, resulting in pure loss of stability or parametric rolling.

Pure loss of stability and parametric rolling are two of the dynamic stability failure modes identified in the 2008 Intact Stability Code (IMO 2008) and targeted in the on-going

development of the second generation intact stability criteria within the IMO (IMO 2012). As described in Francescutto & Umeda (2010), the second generation intact stability criteria are based on a four levelled assessment approach. The two first levels are so called vulnerability criteria. If a ship is confirmed to be vulnerable to a particular failure mode on these levels, direct stability assessment should be used to reduce the vulnerability, either by revision of the design, or by development of ship-specific operational guidance to assist the crew in operating the ship in a safe manner. The development of criteria for levels 1 and 2 is progressing, and draft criteria for these levels are outlined in IMO (2012). The principles and details for the direct stability assessment and the ship-specific operational guidance are still unsettled.



This paper is an attempt to contribute to the discussion on direct assessment and operational guidance in the development of the second generation intact stability criteria. The paper reviews two previously presented simplified methods for assessment of pure loss of stability (Bulian 2010) and parametric rolling (Dunwoody 1989a&b). Being based on linear signal theory both methods are computationally very efficient, which makes them interesting for application in real time on board operational guidance. The methods are here evaluated in relation to full-scale incidents and time-domain simulations in irregular longitudinal waves. Underlying assumptions are discussed, along with tuning of the critical levels in the simplified methods with reference to time-domain simulations. Implementation of the simplified methods in on-board operational guidance systems is also discussed.

2 SIMPLIFIED METHODS

2.1 GM spectra

Both methods are based on the assumption that the roll restoring variation in irregular waves can be considered as a linear stationary Gaussian stochastic process. The restoring variation is represented by the variation in metacentric height

$$x(t) = GM(t) - GM_{cw} \quad (1)$$

where $GM(t)$ is the momentary metacentric height and GM_{cw} is the calm water metacentric height. According to linear signal theory the spectral representation of $x(t)$ is calculated as

$$S_x(\omega) = |f_{GM}(\omega)|^2 S_w(\omega) \quad (2)$$

where $S_w(\omega)$ is the wave energy spectrum and $f_{GM}(\omega)$ is the linear transfer function of the metacentric height fluctuation. In the present study $f_{GM}(\omega)$ is in principle calculated

based on the approach in Palmquist (1994). This implies integration of the undisturbed incident linear wave pressure field over the momentarily submerged hull surface for a wave passage, with the ship in quasi-static equilibrium in heave and pitch in following seas, and dynamically balanced in heave and pitch based on linear strip calculations in head seas. Alternative approaches for the pressure integration could work equally well. Another approach could be to use Grim's effective wave (Grim 1961).

2.2 Parametric Roll

Following Dunwoody (1989b), the analogy between the metacentric height variation in waves and the reduction of the effective roll damping is here used to formulate a Parametric Roll Failure Index (PRFI). According to Dunwoody (1989b) a roll motion is stable if

$$\zeta > E[\zeta^*] \quad (3)$$

where ζ is the linear roll damping expressed as a fraction of the critical damping, and $E[\zeta^*]$ is the expected value of the metacentric height variation related roll damping reduction ζ^* . By assuming that the GM variation $x(t)$ is a broad-banded linear stationary Gaussian process, and by further considering that principal 2:1 parametric rolling is related to GM fluctuations at twice the roll natural frequency, the corresponding expected value of the metacentric height variation related roll damping reduction can be expressed as

$$E[\zeta^*] = \frac{\pi g^2 S_x(2\omega_n)}{4\omega_n \omega_d^2 r^4} \quad (4)$$

where ω_n is the un-damped roll natural frequency; ω_d is the damped roll natural frequency; r is the roll radius of gyration; and g is the gravitational constant. Based on this, a Parametric Roll Failure Index (PRFI) is in the present study formulated as

$$PRFI = E[\zeta^*]/\zeta \quad (5)$$

2.3 Pure Loss of Stability

Following Bulian (2010), a pure loss of stability failure is assumed to occur when the persistence time τ of $GM(t)$ below a critical level GM_{crit} is longer than a critical threshold, τ_{crit} . A Pure Loss Failure Index (PLFI) is formulated as the probability that at least one pure loss of stability failure occurs within a certain exposure time span $[0, T_{exp}]$.

The index is derived as follows. Based on the assumption that $x(t)$ is a stationary Gaussian process, the average down-crossing frequency below a critical level,

$$x_L = GM_{crit} - GM_{cw} \leq 0, \quad (6)$$

can be expressed as

$$\lambda_{x_L} = \frac{1}{2\pi} \omega_z e^{-\frac{x_L^2}{2m_{0,e}}} \quad (7)$$

where

$$\omega_z = \sqrt{m_{2,e}/m_{0,e}} \quad (8)$$

is the average zero-crossing encounter frequency. The spectral moments are determined from the GM variation spectrum according to

$$m_{n,e} = \int_0^\infty |\omega_e|^n S_x(\omega) d\omega \quad (9)$$

If the down-crossing process is assumed to be a Poisson process, the failure process will also be a Poisson process. The intensity of the failure process can hereby be expressed as

$$\lambda_F = P_{exc}(\tau_{crit}) \lambda_{x_L} \quad (10)$$

where

$$P_{exc}(\tau_{crit}) = 1 - cdf_T(\tau_{crit}) \quad (11)$$

is the probability of the persistence time exceeding the critical threshold time. By assuming $x(t)$ to be a narrow banded process, the cumulative distribution for the persistence time can be expressed as

$$cdf_T(\tau) = 1 - e^{-\frac{x_L^2}{2m_{0,e}} \tan^2\left(\frac{\omega_z \tau}{2}\right)} \quad (12)$$

The Pure Loss Failure Index (PLFI) can then finally be expressed as

$$PLFI = 1 - e^{-\lambda_F T_{exp}} \quad (13)$$

3 FULL-SCALE INCIDENTS

Three well documented full-scale incidents with pure loss of stability and parametric rolling are used as reference in the evaluation of the simplified methods. This section describes the ships and the incidents, while results are given in a following section.

3.1 PCTC's

Two incidents with parametric rolling are studied. The incidents occurred with two different individuals of the same PCTC design (Pure Car and Truck Carriers), and are reported in detail as Case I and Case II in Rosén et al (2012). Ship data is given in Table 1 and Table 2.

Table 1: Data for the studied PCTC's where U is the ship speed in m/s and B is the ship beam in metres.

Length between perpendiculars [m]	219
Equivalent linear roll damping at 10° [-]	0.0212+0.003U
Roll radius of inertia [m]	0.45B



Table 2: Loading conditions of the studied cases.

	Case I	Case II
Metacentric height [m]	1.2	2.3
Natural roll period [s]	28	21
Speed [kn]	10	9-14
Relative heading [deg]	0 (following)	140-190 (head)

The roll damping, which is particularly crucial in parametric rolling, has been determined from model tests as reported in Söder et al (2012). In the time domain simulations, speed dependent linear-quadratic roll damping has been used and in the PRFI the speed dependent linearized damping has been used. It can further be commented that the GZ-curves for these vessels are practically linear between 0 and 55 degrees.

In Case I the ship experienced roll angles up to 30 degrees at 10 knots in following seas. According to hindcast data the significant wave height was 4 metres and the peak period 9.2 seconds. In the present study this is represented by a JONSWAP spectrum with a peak enhancement factor of 3.3. In Case II the ship encountered head sea parametric rolling with amplitudes up to 20 degrees a number of times during a period of four hours while travelling with a speed around 11 knots. Here wave data is available from a nearby wave buoy which recorded a significant wave height between 5 and 6 meters and a peak period between 11 and 13.5 seconds. The measured spectrum is used in the calculations in the present study.

3.2 Finnbirch

Also the capsizing of the RoRo ship Finnbirch is studied. According to the accident report the cause of the accident was reduction of stability in quartering seas resulting in roll angles up to around 40 degrees, which in turn resulted in cargo shift (Hellner & Bexell 2008). Main particulars and loading condition at the accident are given in Table 3. It should be

noted that some of the data is approximate. The hull geometry has been digitized from a printed body plan in the accident report. The actual roll damping is unknown and is here approximated as linear and 10% of critical damping. This is further discussed below. As seen in Figure 1 the GZ curve is rather unconventional with a plateau between 20 and 40 degrees and a local minimum at 30 degrees. This is an effect of the ship being equipped with sponsons.

The sea state at the accident is by Hellner & Bexell (2008) characterized by a period of 6.7 s and a significant wave height of 4 metres. In the calculations in the present study this is represented by a JONSWAP spectrum with a mean period of 6.7 s, a peak period of 8.3 s, a significant wave height of 4 metres, and a peak enhancement factor of 3.3.

Table 3: Main particulars and loading and operational conditions for Finnbirch at the time of the accident.

Length between perpendiculars [m]	137
Roll damping (assumed) [%]	10
Roll radius of inertia (assumed) [m]	0.358
Metacentric height, incl. free liquid surfaces [m]	1.355
Natural roll period [s]	15
Speed [kn]	18
Relative heading [deg]	20

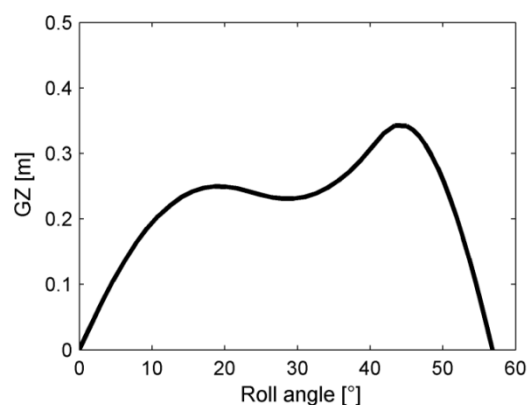


Figure 1: The GZ curve of Finnbirch at the incident.



4 TIME-DOMAIN SIMULATIONS

To enable evaluation of the simplified methods for a broader range of speeds and sea states, the full-scale observations are complemented with time-domain simulations. The simulations are also used as basis for tuning the critical levels in the simplified methods.

The time-domain simulations are performed with a typical “hybrid” method, where radiation and diffraction forces are determined based on linear strip theory complemented with a linear-quadratic roll damping model, while the Froude-Krylov forces and restoring forces are computed by integrating the undisturbed incident wave pressure field over the momentarily submerged hull surface. Details of the simulation method are found in Hua & Palmquist (1995). The method has been thoroughly evaluated and performed well in the SAFEDOR benchmark study on parametric rolling (Spanos & Papanikolaou 2009).

Linear potential irregular waves are in the present study composed by superimposing 200 regular components derived from wave energy spectra with random phases. Considering the so called practical nonergodicity of the parametric roll phenomena (e.g. Umeda et al 2012) the results for a certain speed and sea state combination are determined statistically from simulations in 15 different wave realizations each comprising 500 seconds. Future work should consider increased realization time as well as number of realizations, to ensure statistically converged results.

The simulations are in this study limited to heave, pitch, and roll, in long crested longitudinal waves. To enable development of parametric roll or loss of stability related heel despite the symmetric wave conditions, the ships are in the simulations loaded to a static heel of one degree. The limitations in degrees of freedom and wave direction should be kept

in mind when interpreting the results. Omitting surge should for example be non-conservative for pure loss of stability and conservative for head sea parametric rolling, since surge would increase the time on the crest in following seas (Spyrou 2000) and would have a de-tuning effect on the phase match in head seas (Vidic-Perunovic & Jensen 2009). Considering the linear modelling of the radiation and diffraction forces it should also be remembered that the validity of the simulations is questionable for very large roll angles.

5 RESULTS

The simplified methods and the related failure indices (PRFI & PLFI) consider the *causes* of parametric roll or pure loss of stability in terms of stability limits. The full-scale incidents, on the other hand, are *consequences* of exceeding the stability limits. The focus will here be on qualitative comparison between the failure indices, the roll angles observed in the full-scale incidents, and roll angles from the time-domain simulations. In future work it could be considered to also evaluate the stability limits quantitatively based on time-domain simulations.

5.1 Parametric Roll

Figure 2 gives an example of time series from simulations of the following seas parametric roll incident, PCTC Case I. The simulations are concluded to give a good representation of the full-scale incident where roll angles developed up to 30 degrees.

Additional results for PCTC Case I are given in Figure 3 for a range of speeds and wave heights for the peak period 9.2 seconds at the incident. The star marks the speed and significant wave height at the incident. The grey scales are simulated roll angles in degrees.



The coarse lines are limit curves for the parametric roll failure index, PRFI=1, 2, 4.

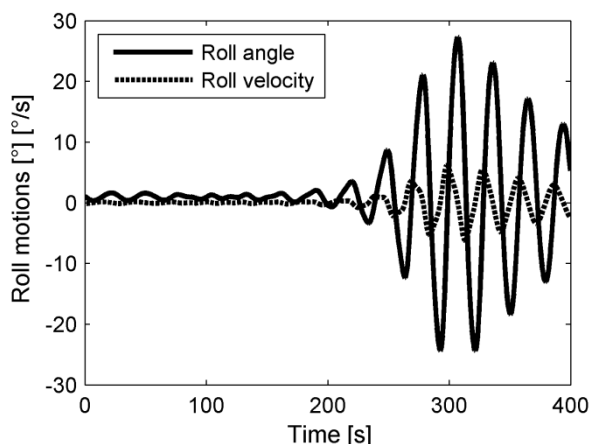


Figure 2: Example of time series from simulations in the conditions at the following sea parametric roll incident PCTC Case I.

As seen the index captures the incident and the speed range were the largest roll angles develops in the simulations. The stability limit is theoretically defined by PRFI=1. This however seems to be very conservative if comparing with the simulations, while PRFI=4 looks more feasible for use in practice in operational guidance.

As seen, rather large roll angles develop in the simulations for speeds in the range 11-13 knots and wave heights in the range 4-6 metres. This is however not captured by the PRFI. Instead all limit curves converge around 11 knots. This is related to the fact that the GM spectrum is very narrow banded for these speeds. It is here obvious that the broad-band assumption for the GM spectrum, used in the derivation of the PRFI, is violated. For practical use in operational guidance this limitation could to some extent be compensated for, when calculating the expected value of the damping reduction, by replacing $S_x(2\omega_n)$ in (4) with

$$\frac{1}{2\Delta\omega} \int_{2\omega_n - \Delta\omega}^{2\omega_n + \Delta\omega} S_x(\omega) d\omega \quad (14)$$

for some small value $\Delta\omega$. The validity of the band width assumptions is discussed further in section 6.2 below.

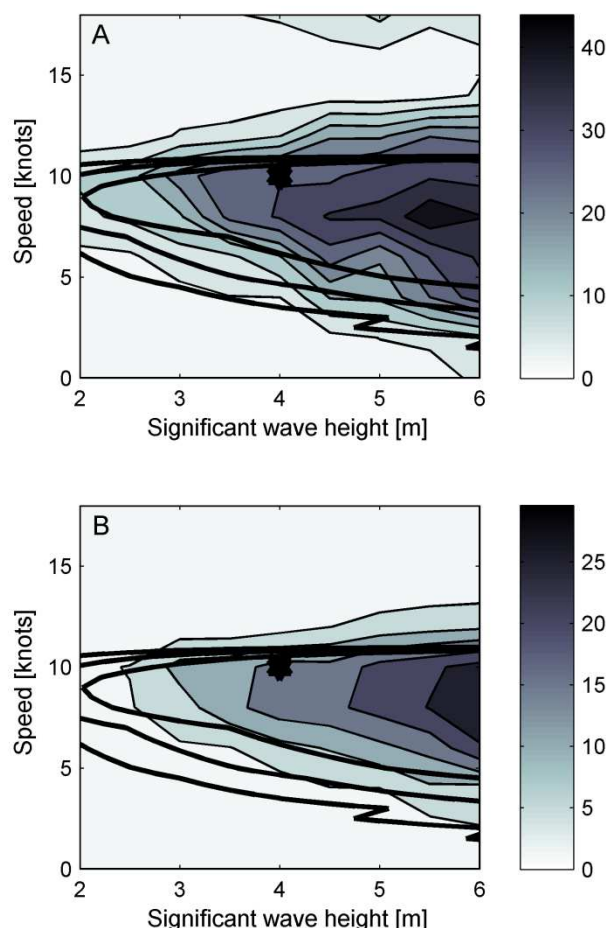


Figure 3: Results related to the PCTC Case I for a wave spectrum peak period of 9.2 s. Star: Speed and wave height at the incident. Coarse lines from outer to inner: PRFI=1, 2 and 4. Grey scales: Simulated roll angles in degrees; (A) overall maximum roll angle, (B) average of the maximum roll angles, from all 15 realizations for each speed - sea state combination.

Also for the head sea parametric roll incident PCTC Case II where roll angles developed up to 20 degrees, the time-domain

simulations are concluded to give a reasonable representation. Figure 4 summarizes results related to PCTC Case II for the measured wave spectrum scaled to different wave heights. As for the previous case, the PRFI captures the incident, but the theoretical stability limit $PRFI=1$ is too conservative if comparing with the simulations. The stability limit $PRFI=4$ found appropriate for PCTC Case I for use in operational guidance, also seems to be appropriate for PCTC Case II.

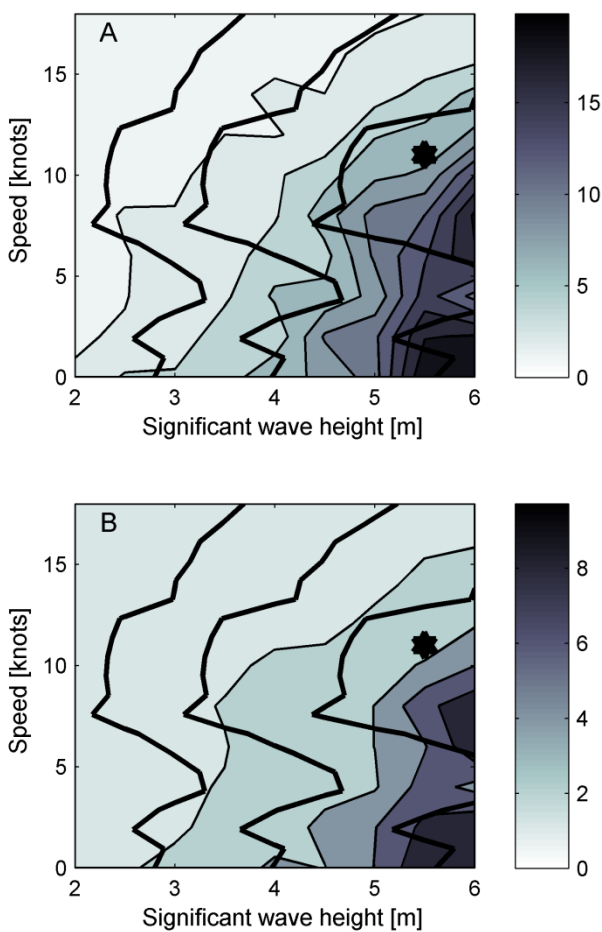


Figure 4: Results related to the PCTC Case II for the measured wave spectrum scaled to different wave heights. Star: Speed and wave height at the incident. Coarse lines from left to right: $PRFI=1, 2$ and 4 . Grey scales: Simulated roll angles in degrees; (A) overall maximum roll angle, (B) average of the maximum roll

angles, from all 15 realizations for each speed - sea state combination.

5.2 Pure loss of stability

Results related to the Finnbirch case are summarized in Figure 5. The star marks the incident where roll angles developed up to around 40 degrees. The coarse lines and the grey scales display respectively $PLFI = 0.1\%$ for $T_{exp}=3600$ seconds and simulated maximum roll angles in degrees, at various speeds and wave heights for the peak period 8.3 seconds at the incident. The $PLFI$ limit 0.1% has here been chosen as an example to represent a low probability. The exposure time of one hour should be representative for the time period during which a sea state can be considered stationary. As seen in the simulation results, large roll angles develop in two different speed regimes. The lower speed regime is identified as parametric rolling and will be discussed further below. The high speed regime is identified as pure loss of stability.

A parametrical study is made to investigate the influence of the critical time and critical GM on the $PLFI$. In Figure 5A the critical GM is varied between -0.45 m and 0.45 m for a critical time of 7.5 seconds. As seen, increasing the critical GM will primarily decrease the critical wave height and to some extent also the critical speed. In Figure 5B the critical time is varied, in a similar way, between 5.5 s and 9.5 s for a critical GM of 0.15 metres. Here the primary influence is on the speed, where the critical speed decreases with critical time. In this way the critical limits may be tuned to appropriate levels based on simulations and known incidents. This tuning may also compensate for simplifications in the $PLFI$ model. Considering the here presented simulations and the Finnbirch incident, appropriate limits could for example be $GM_{crit}=0.15$ metre and $\tau_{crit}=7.5$ seconds. It is noteworthy that these constants and



PLFI=0.1% are chosen somewhat arbitrary and that further work is needed to determine if the PLFI should be seen as an actual probabilistic measure or as another tuning parameter.

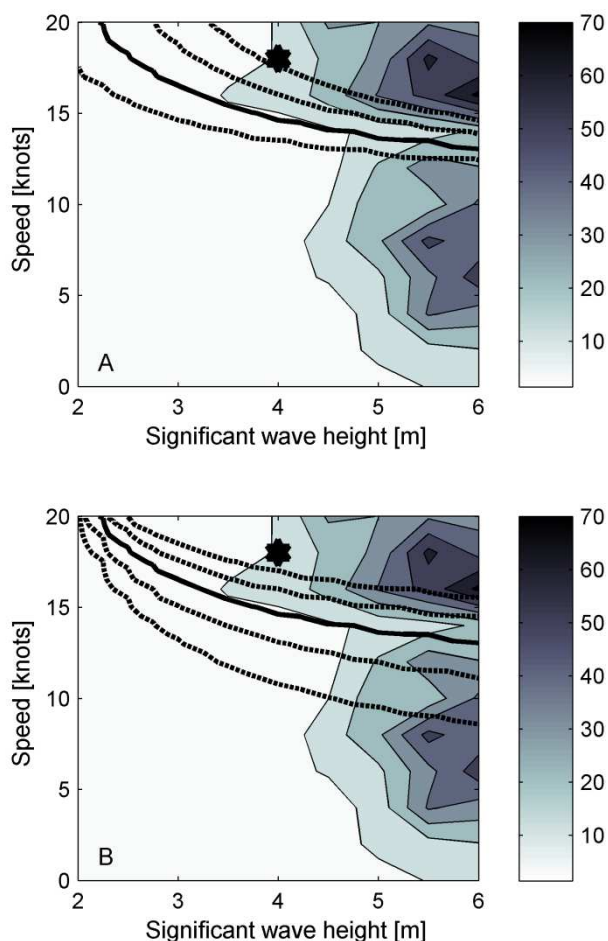


Figure 5: Results related to Finnbirch. The star marks the incident. Wave spectrum peak period 8.3 s. Grey scales: Simulated overall maximum roll angle in degrees in all 15 realizations for each speed-sea state combination. Coarse lines: PLFI=0.1% for $T_{exp}=3600$ s; (A) $\tau_{crit}=7.5$ s and from top to bottom $GM_{crit}=-0.45, -0.15, 0.15, 0.45$ m (solid line $GM_{crit}=0.15$ m); (B) $GM_{crit}=0.15$ m and from bottom to top $\tau_{crit}=5.5, 6.5, 7.5, 8.5, 9.5$ s (solid line $\tau_{crit}=7.5$ s).

A parametrical study is also made to investigate the influence of the metacentric height. Simulations with varying GM are made

at 18 knots and a significant wave height of 4 meter. The maximum roll angles for each realization are given in Figure 6 together with the PLFI in percent for $GM_{crit}=0.15$ metre and $\tau_{crit}=7.5$ seconds. The time domain simulations have a clear GM threshold where the roll motions change from relatively small to large angles and capsize. The PLFI clearly captures this phenomenon. Matching the simulated GM threshold and the corresponding PLFI threshold could provide a systematic approach for tuning GM_{crit} and τ_{crit} .

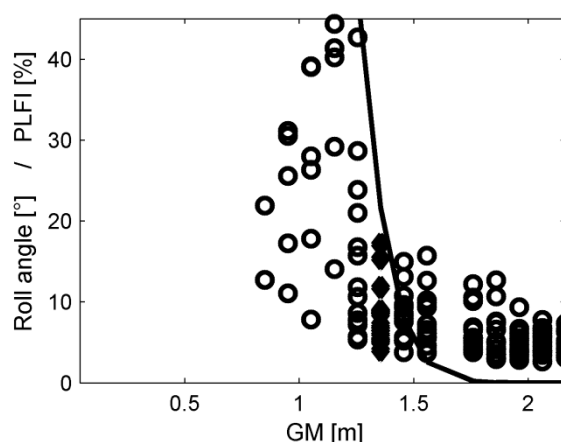


Figure 6: Maximum roll angles at each realization with different GM and the PLFI in percent. For GMs less than 1 meter almost all simulations ended with roll angles larger than 45° and are therefore not visible in the figure. All simulations run at a significant wave height of 4 m, a peak period of 8.3 s and a speed of 18 knots.

In the case of pure loss of stability, damping is generally considered to be of minor importance (Spyrou 2000). This is probably true at transient events where the ship capsizes due to one single wave passage. For ships with high sides, such as the here studied RoRo-ships, loss of stability however more commonly has an oscillating character. This is exemplified in Figure 7 where loss of stability can be seen as periods of more or less constant roll velocity corresponding to zero roll

moment. When running simulations with roll damping varied between 2 and 10% it is therefore not surprising to see a dependency on roll damping. In Figure 8 these simulations are visualized as the maximum roll angle for each realization.

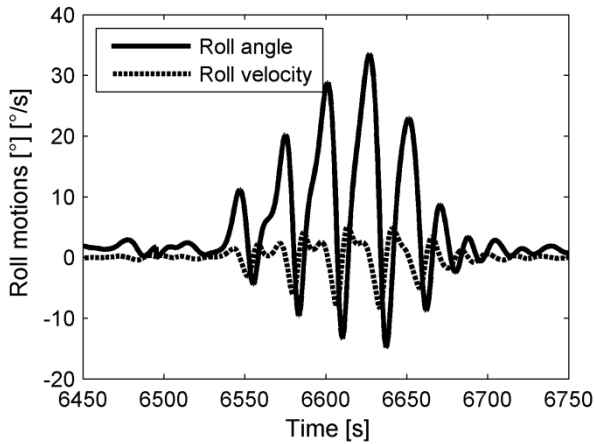


Figure 7: Example of time series with roll angle and roll velocity from the Finnbirch simulations at a significant wave height of 4.5 meters, a peak period of 8.3 s and a speed of 18 knots.

The low speed regime with large roll angles seen in Figure 5 may be identified as parametric rolling by comparing the roll motion and the GM variation in the frequency domain. As seen in Figure 9 there is a 2:1 ratio between the peak frequencies of the GM variation spectrum and the roll spectrum. The same observation of parametric rolling for lower speeds for the Finnbirch case is also observed by Krüger et al. (2008) with the E4-ROLLS simulation code.

In Figure 9 it can further be noticed that the roll frequency is quite far from the calm water natural roll frequency, 0.42 rad/s compared to 0.30 rad/s. This corresponds to a decrease of the average GM to 1.15 meter in waves. In its current form the PRFI does not capture this change and therefore the PRFI is not compared to time-domain simulations related to the Finnbirch case.

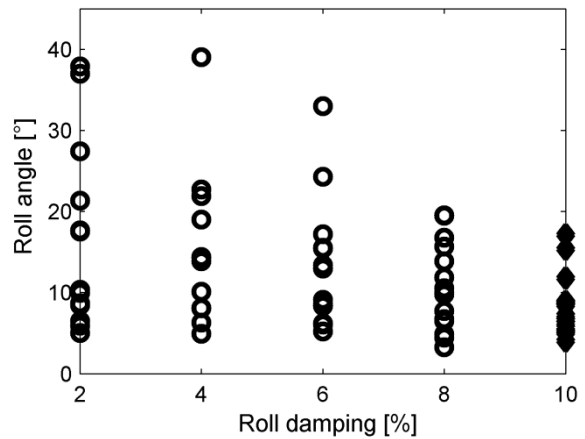


Figure 8: The maximum roll angle for each realization with different damping. All simulations run at a significant wave height of 4 m and a speed of 18 knots.

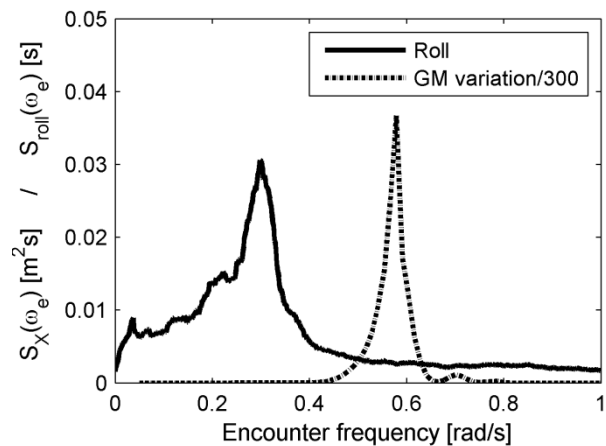


Figure 9: Spectra of simulated roll (all realizations) and calculated GM variation for Finnbirch at 6 knots in 6 meter waves and a peak period of 8.3 s.

6 DISCUSSIONS

6.1 Linearity assumption for the $GM(t)$ process

Both methods are dependent on the assumption that $GM(t)$ is a linear process. In



earlier work, Palmquist (1994) showed that this process is actually a non-linear, and therefore non-Gaussian, process, which may be approximated as the sum of a linear Gaussian process (the first order variation) and a slowly varying non-linear process. Calculations of GM in longitudinal regular waves often shows significant drift of the mean GM, which corresponds to a slowly varying component in irregular waves related to the envelope function of the first order variation. The fact that the simplified methods in this paper neglects these higher order effects is probably the most important limitation and should be subject to further work. Such work should consider ship types showing significant mean GM drift as well as nonlinear GZ curves at moderate roll angles. As seen in the simulations for the Finnbirch case in the low speed regime with parametric rolling, the effects are a shift in natural roll frequency that will influence the resonance. For the pure loss of stability phenomenon the most important effect implies a shift in the actual critical GM reduction threshold.

Regarding the applicability of assuming the first order GM variation to be a linear process, the transfer function f_{GM} in equation 2 was calculated for wave heights between 1 and 6 meters. Figure 10 shows the first order GM variation at wave frequencies where f_{GM} has its maximum, as a function of wave height. As seen, the variation is fairly linear for the cases considered here. For practical purposes, the calculation of f_{GM} may use linearization with respect to a suitable wave height in order to reduce the error in relevant sea states. In this paper a wave height of 3 m has been used to calculate all GM transfer functions.

6.2 Bandwidth assumptions

In this work, the pure loss failure index (PLFI) is based on the narrow band approach in Bulian (2010). The matter of classifying a

process as being narrow or broad banded is very much depending on the specific application. From the results presented here for the Finnbirch case, with ship speeds up to Froude number 0.27, the narrow band approach still seems quite acceptable. Care should however be taken not to extend the method to faster vessels such as fast passenger ferries and naval ships. It should also be noted that this study is limited to just a few wave periods.

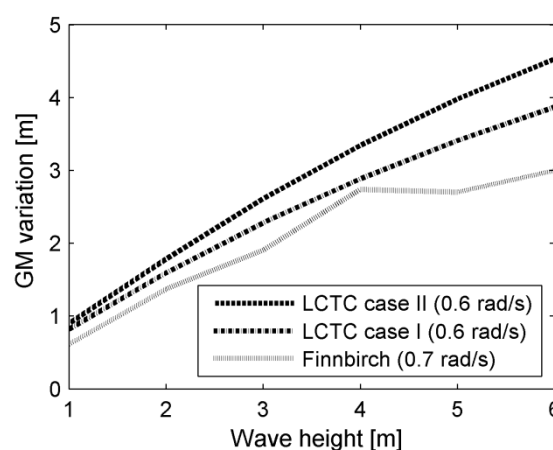


Figure 10: The first order GM variation, at wave frequencies corresponding to $\max(f_{GM})$, as function of wave height for the cases in this study.

Dunwoody (1989b) presents a narrow band and a wide band approach to determining the expected value of the equivalent damping reduction $E[\zeta^*]$. In this paper the wide band approach has been used for parametric rolling. Figure 11 shows the GM variation spectra for the three cases. For following seas, such as in the PCTC Case I, the wide band approach may be questionable. However, the presented results show that this simplified method and the PRFI nevertheless is capable of identifying the risk zone in terms of ship speed and wave height in fair agreement with time domain simulations.

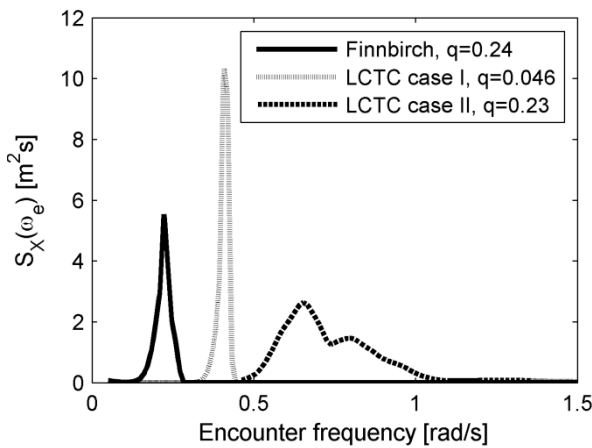


Figure 11: The GM spectrums in the encounter frequency domain for the three cases and the bandwidth parameter, q , calculated according to Bulian (2010).

6.3 Operational guidance

The idea of operational guidance for strongly non-linear phenomena such as pure loss of stability and parametric rolling is indeed a challenge. Not only are we dealing with very complex dynamic systems, but also with a quite complex stochastic excitation. Also, in reality, most important parameters are much less clearly defined than in theoretical or experimental studies. For example: wave spectral shapes are arbitrary, mixed seas is rather a rule than an exception, roll damping is seldom accurately known, and the effect of free surfaces in liquid tanks can be uncertain in a dynamic rolling situation.

For ship specific operational guidance there are basically three different possible approaches:

- Pre-computed polar plots based on extensive time-domain simulations for all sea states, loading conditions, etc. (e.g. Levadou & Gaillard 2003)
- Real-time on board (or possibly shore-side) time-domain simulations based on actual

sea state and loading condition (e.g. Krüger et al. 2008)

- Simplified methods able to identify stability boundaries instead of providing quantitative roll angle predictions.

While the first approach, based on pre-computed information, allows for very detailed and advanced simulation models to be used, it will in practice have difficulties to adapt to actual conditions with complex wave spectra and mixed seas. The matrix of simulated conditions would grow to unrealistic proportions as non-linear phenomena require a very high resolution multi-dimensional grid of simulation conditions. The second approach, based on real-time simulations of actual conditions, is probably the ultimate goal. However, at present this approach would require rather simplified simulation models to be utilized with respect to CPU efficiency. It is also important to keep in mind that the quantitative accuracy of “hybrid” non-linear simulation models still can be debated (see e.g. Spanos & Papanikolaou 2009). Therefore the concept presented here, i.e. using simplified models to identify risk boundaries instead of actually predicting their consequences, appears attractive from a practical perspective since it allows for very fast computations based on actual conditions in terms of loading condition, roll damping and complex wave spectra.

The methods presented in this paper are since 2011 implemented in the Seaware EnRoute Live software and currently being evaluated on all vessels in the Wallenius fleet. As presented in the results section, tuning of these criteria is of vital importance and has been done using full-scale data in combination with time-domain simulations as presented here.

In the current implementation being evaluated, GM variation RAO's are pre-calculated for the ship in question for a range



of speeds, loading conditions (draught and trim matrix) and relative wave directions. Hereby GM spectra can be easily calculated on-board in real-time for arbitrary short-crested irregular waves. For route planning the wave conditions are formulated based on weather forecasts, while for real-time guidance the wave conditions are instead formulated based on in-situ wave measurements.

Figure 12 is an example of how the criteria can be presented on board for operational guidance. On the radial axis is the speed and on the angular axis the course. The contours represent the risk of one, or multiple failure modes for the different courses and speeds. In this case the PLFI for PCTC case I. The current course and speed is marked with a symbol.

7 CONCLUSIONS

In this paper, two previously presented simplified methods for assessment of pure loss of stability (Bulian 2010) and parametric rolling (Dunwoody 1989a&b) have been evaluated as a basis for operational guidance. Both these methods are based on linear signal theory and are aimed at identifying stability boundaries. The common core is the assumption that the metacentric height variation in irregular waves can be considered as a linear stationary Gaussian stochastic process, and thereby be represented by GM variation spectra.

Both methods have been evaluated in relation to full-scale incidents and non-linear time-domain simulations using a 3 degree-of-freedom “hybrid” model. The results show that, provided that parameters such as critical levels are tuned properly, the methods are capable of identifying risk zones in terms of ship speed and wave height in fair agreement with full-scale incidents and time-domain simulations. Hence, the approach is concluded to provide a

feasible basis for real-time on board operational guidance.

The most important limitation of the presented approach is found to be related to effects of higher-order GM variation, manifesting itself as a shift in the average GM. Further work is needed here as well as to verify the tuning for more complex sea states and oblique wave directions.

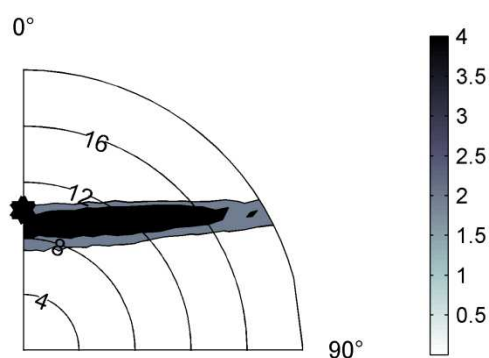


Figure 12: The PRFI for PCTC case I at a significant wave height of 4 meter and peak period of 9.24 s. The course and speed at the incident is marked with a star.

8 ACKNOWLEDGMENTS

This research has been financially supported by the Swedish Mercantile Marine Foundation (Stiftelsen Sveriges Sjömanshus) and the Swedish Maritime Administration (Sjöfartsverket) which are both gratefully acknowledged.

9 REFERENCES

Bulian G., 2010, “Checking Vulnerability to Pure Loss of Stability in Long Crested Following Waves: A Probabilistic Approach”, *Ocean Engineering*, 37, pp. 1007-1026.



- Dunwoody A.B., 1989a, "Roll of a Ship in Astern Seas – Metacentric Height Spectra", Jour. of Ship Research, 33(3), pp. 221-228.
- Dunwoody A.B., 1989b, "Roll of a Ship in Astern Seas – Response to GM Fluctuations", Jour. of Ship Research, 33(4), pp. 284-290.
- France W.N., et al, 2003, "An Investigation of Head-Sea Parametric Rolling and its Influence on Container Lashing Systems", Marine Technology 40(1), pp. 1-19.
- Francescutto A., Umeda N., 2010, "Current Status of New Generation Intact Stability Criteria Development", 11th Intl Ship Stability Workshop (ISSW2010), Wageningen, The Netherlands.
- Grim, O., 1961, "Beitrag zu dem Problem der Sicherheit des Schiffes im Seegang", Schiff und Hafen, No. 6, 1961, pp. 490-497.
- Hellner C., Bexell Y., 2008, "Loss of M/S Finnbirch Between Öland and Gotland 1 November 2006", Swedish Accident Investigation Board, Report RS 2008:03e.
- Hua J., Palmquist M., 1995, "A Description of SMS – A Computer Code for Ship Motion Simulation", Report 9502, KTH Royal Institute of Technology, Sweden.
- IMO, 2008, "International Code on Intact Stability", Resolution MSC.267(85).
- IMO, 2012, "Development of Second Generation Intact Stability Criteria, Report of the Working Group", SLF 54/WP.3.
- Krüger S., Kluwe F., Vorhölter, H., 2008, "Decision Support for Large Amplitude Roll Motions based on Nonlinear Time-Domain Simulations", 7th Intl Conf on Computer Applications and Information Technology in the Maritime Industries (COMPIT), Liege, Belgium.
- Levadou M., Gaillarde G., 2003, "Operational Guidance to Avoid Parametric Rolling", Design and Operation of Containerships, pp. 75-86, RINA, London, UK.
- Palmquist M., 1994, "On the Statistical Properties of the Metacentric Height of Ships in Following Seas", 5th Intl Conf on Stability of Ship and Ocean Vehicles (STAB1994), USA.
- Palmquist M., Nygren C., 2004, "Recordings of Head-Sea Parametric Rolling on a PCTC", Annex in IMO SLF 47/INF.5.
- Rosén A., Huss M., Palmquist M., 2012, "Experience from Parametric Rolling of Ships", chapter in Fossen T.I., Nijmeijer H., Parametric Resonance in Dynamical Systems, Springer.
- Spanos D., Papanikolaou A., 2009, "Benchmark Study on Numerical Simulation Methods for the Prediction of Parametric Roll of Ships in Waves", 10th Intl Conf on Stability of Ships and Ocean Vehicles (STAB2009), Russia.
- Spyrou K.J., 2000, "A Comparison between the Yaw and Roll Dynamics in Astern Seas and the Effect of Nonlinear Surge on Capsize", 7th Intl Conf on Stability of Ships and Ocean Vehicles (STAB2000), Australia.
- Söder C-J, Rosén A., Werner S., Huss M., Kutenkeuler J., 2012, "Assessment of Ship Roll Damping Through Full Scale and Model Scale Experiments and Semi-Empirical Methods", 11th Intl Conf on the Stability of Ships and Ocean Vehicles (STAB 2012), Greece.
- Umeda N., et al, 2012. "Estimation of Parametric Roll in Random Seaways", chapter in Fossen T.I., Nijmeijer H.,



Parametric Resonance in Dynamical Systems, Springer.

Vidic-Perunovic J., Jensen J.J., 2009,
"Parametric Roll due to Hull Instantaneous
Volumetric Changes and Speed Variations",
Ocean Engineering, 36, pp.891–899.



Analysis of Onboard Ship Stability and Loading Instruments from Developer's Perspective

Metin Taylan, *ITU, Naval Architecture and Ocean Engineering Faculty*, taylan@itu.edu.tr

Bulent Sener, *Delta Marine Co.*, bsener@deltamarine.com.tr

Yasar Gul, *MESH Engineering & Software Co.*, y.gul@mesh.com.tr

Dirim Sener, *MESH Engineering & Software Co.*, d.sener@mesh.com.tr

Cemal Sahin, *MESH Engineering & Software Co.*, c.sahin@mesh.com.tr

ABSTRACT

In recent years, ship stability and strength calculations have been performed by onboard ship stability and loading instruments installed in ships. Although it is not mandatory for all ship types for the time being, it is believed to be so in the near future. This paper examines the influence of onboard ship stability instruments in shipping industry and the details of stability and strength calculation schemes and design process of type-3 stability software based on the international regulations. Development of such software requires in depth knowledge in both naval architecture and software engineering. Structural details, stages of planning and calculation and computer architecture methods used in the design process are outlined. Infrastructure of the code was explained and testing procedures were detailed.

Keywords: *stability instrument, ship stability software, loading computer system, computer architecture, ship strength calculations, loading instrument, DeltaLoad.*

1. INTRODUCTION

Recent developments in computer and software technologies inevitably have been widely applied to naval architecture and marine shipping. Stability instruments or loading computers help ship operators, classification societies and flag state authorities to a great deal since they help masters, surveyors and inspectors to fulfill their duties in a very short time than the conventional routines. The masters have the liberty and comfort of monitoring hydrostatics, stability and strength of their ships during loading/unloading sequences on a real time basis. Not only they ease the workload of masters in a way, but also they may reduce the loading/unloading related stability accidents and time spent at port stays. Although these instruments are not meant to replace the traditional stability booklet, they have emerged to

complement them offering almost the same information in a different medium.

International Maritime Organization (IMO) and some other international and/or national societies have taken the matter seriously and issued regulatory rules and measures for such devices. In the revised intact stability code of IMO, namely 2008 IS Code, in Part B, Chapter 4, stability calculations performed by stability instruments classifies types of software and specification and certification of onboard computers and software used on them as the recommended criteria. There are also other criteria and recommendations by IACS specifying details of such instruments. 2008 IS Code, Chapter 4 also mentions the functional requirements such as deadweight data items, loading condition particulars, stability details etc. of such software. The acceptable tolerances of the cal-



culations performed and the approval procedure based on the performance are also specified within the same document.

MSC.1/Circ.1229, sets up guidelines for the approval of stability Instruments. Furthermore, the circular also provides the acceptable tolerances for hull form dependent parameters such as displacement, centers of buoyancy, metacentric heights, compartment dependent parameters along with trim and stability characteristics. IACS UR_L5 document titled Onboard Computers for Stability Calculations, reveals similar guidelines and specifications for stability instruments. For the longitudinal strength calculations, MSC Circ.836 and IACS Rec.48 may be referred to for further details. Some of the classification societies have their own approval and testing procedures primarily in line with IMO and IACS interpretations. At the most recent SLF meeting, it was suggested that the guidelines for the approval of stability instruments (MSC.1/Circ.1229), which already cover the required accuracy for damage stability calculations, should also be acceptable for safe return to port calculations. There are ongoing discussions on mandatory carriage requirements of stability instruments on tankers and inclusion of icing on timber deck cargo ship at MSC lately.

The importance of using computers both in design and operation is inevitable in shipbuilding and marine industry. Development of such software requires in depth knowledge on naval architecture, computer engineering along with general awareness of basic engineering concepts. In this paper, the importance and impact of naval architectural software have been evaluated and development of the loading software (DeltaLoad Plus) has been analyzed. This project is funded by the Scientific and Technological Research Council of Turkey (TUBITAK), and is about to be completed shortly. The constituents of the algorithm, rationale behind the engineering calculations and computer architecture have been outlined in the following sections.

2. SHIP STABILITY AND LOADING INSTRUMENTS

Ship stability instrument is the name attributed to the onboard ship stability computers, including the software running on it, by IMO. They slightly differ from the generic or land-based ship stability programs by their nature. These instruments are designed to be ship specific since they are customized to run on a particular ship, using the intrinsic related data. Unlike general ship stability software which performs standard naval architectural calculations such as hydrostatics, intact and damage stability and strength, they are expected to carry out simulations to optimize various loading/unloading scenarios in order to help the master in routine operations.

In view of these facts, shipboard stability software must possess certain qualities and merits. As a rule of thumb, it must be reliable and user friendly as may be expected from any computer software. Accurate results, a legible and flexible output report, and easily updated database and libraries are then ordinarily expected. From a developers point of view, since different type of ships have different hull and tank geometries, different cargo specifications and need to comply with specific set of criteria, ship specific subroutines must be established for each ship type (Couser, 2002; Couser, 2003; Kavitha, 2010).

3. ARCHITECTURAL STRUCTURE OF THE SOFTWARE

Initial stage of the software development process commences with a detailed plan of the main structure. Breaking down the tasks into work packages will help the developers to estimate overall schedule in advance. The outcome of each work package will produce required input to the succeeding work packages. The work packages consist of the following items;

- Literature review and analysis
- Modeling and design



- Software development
- Laboratory and site testing and improvement

Each work package is explained below in details.

3.1 Literature Review and Analysis

This work package contains a comprehensive literature review of the items lie under the heading of each work package and analysis of the outcomes. Various resources on related subjects such as books, journal and conference articles, reports of scientific research, graduate theses, National and International rules and regulations and internet sources have been examined carefully (Avriel et al, 1998; Maritech Project 2000; Taylan, 2007; Min et al, 2010; Odabasi and Taylan, 2003). An inclusive report was put together on key issues that would be utilized throughout the project. Similar products available in the sector were also investigated. Having completed the literature review, a more clear idea about the related parameters such as user interface, functionality of the software, software requirements, software input and output may be obtained.

3.2 Modeling and Design

Within the framework of upper level design which defines the technical specifications, operational processes and required calculations to be performed by the software, detailed design of the software has been dealt with in this work package, Figure 1 (Gielingh, 2008). The database and database engine design and calculation library design are the most crucial tasks of this package. The user interface design, report engine design, electronic communication interface design and loading/unloading operation module are the tasks to be sought within the same work package.

The role of user interface are; how the engineering calculations will be performed by rele-

vant modules, what type of output will be produced, and how the results will be confirmed by the criteria for safety. The naval architectural calculations are typically comprised of displacement, deadweight, weight, buoyancy and centers, free surface corrections, hydrostatics, intact and damage stability calculations, longitudinal and local strength calculations, draft survey and squat calculations (Lewis, 1988; DDS 079-1, 1975; 2008 IS Code, 2009; Briggs, 2009; Briggs and Dagget, 2009).

3.2.1 Detailed Design of the Software

The structure of the database which will be referenced by the modules and libraries is established by UML diagrams. The database engine on the other hand, is file based and will work in XML format. In regard to the fundamental methods and functions of the database engine, the input and output are going to be depicted by UML diagrams (Campbell et al, 2002, Wong and Sun, 2006).

The calculation engine design may be one of the most important tasks of the project. The design of the calculation engine is planned to be modular and independent in nature. The modules are to be structured as an independent library wherever possible. The calculation algorithms which will be developed during the engine design are object oriented and shown respective UML diagrams. This design methodology enables one to re-use the algorithms as needed. The following modules are planned to be established:

- Weight and centers of gravity module
- Hydrostatic module (intact and damage)
- GZ curve module
- Longitudinal strength module (shearing force, bending moment, torsional moment, ship deflection)
- Local strength module
- Online data transfer module (from tank level measurement system)
- Loading / unloading optimization and simulation module



- Rules and limitations definition module
- Cargo definition module (chemical liquid, oil, bulk, grain, ro-ro, container, etc.)
- Auxiliary modules (draft survey, squat calculations)
- Ship-specific loading modules (container loading, ro-ro loading, grain loading, project cargo loading)

The user interface design should include items under the following main headings; the menu, compartment list, ship sketch, brief results and alarms and warnings. For a modern

and user friendly interface, an available tool in the market will be used.

For the report engine design, the relevant module of the above-mentioned commercial tool is planned to be employed. Some of the reports to be produced are as follows; standard reports, cargo plan reports, grain loading reports, damage stability reports and user defined reports.

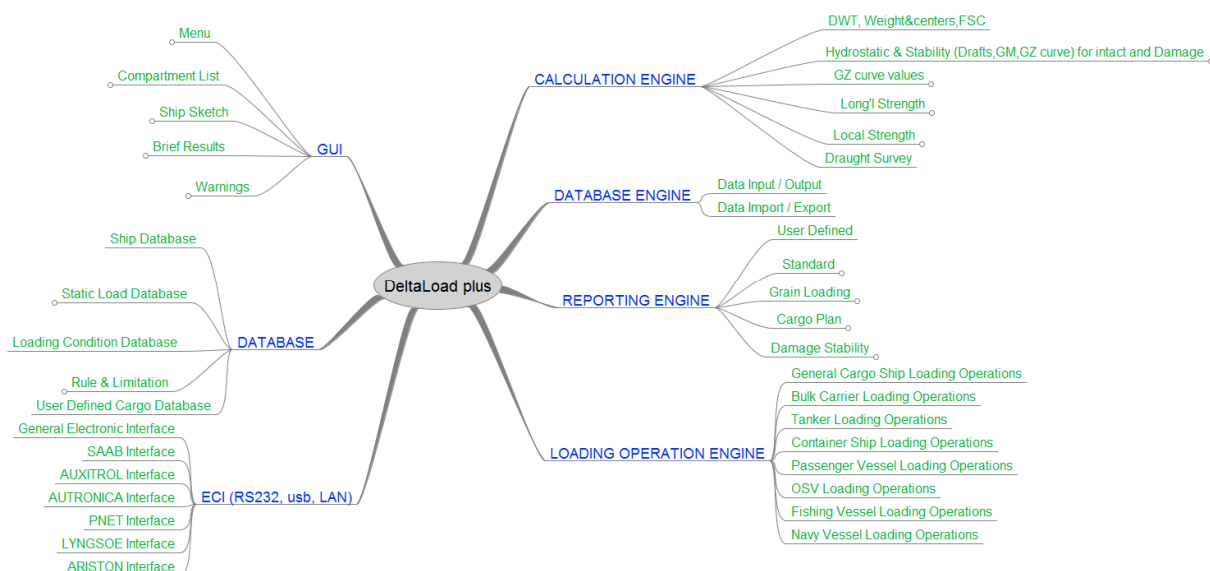


Figure 1: Upper level design scheme of DeltaLoad Plus.

The loading operations module acts like a reference library which controls and manages loading operations for various ship types. The methods and functions within this module check the loading operation whether it is suitable for the ship and in compliance with the pertinent rules. The software was intended to be installed on a range of ship types and thus loading operations module must contain sub-modules for each specific ship type. UML diagram (flowchart and state diagrams if necessary) for each sub-module will be drawn depending on the general and ship dependent limitations and compliance with the rules.

This module communicates with tank level measurement systems and similar electronic devices. The electronic communication interface requirements will be prepared in line with the analyses during modeling and design processes. It has to be parametric in order to be compatible with the innovative systems. The module is able to read the communication parameters of the available systems from the data file in XML format and transfer the loading information (volume, weight, temperature etc.) into the software.

The success criteria for this module are set if all the following are achieved without any failure:

- UML Class diagrams
- UML Sequence diagrams
- UML Use Case diagrams
- UML Activity diagrams
- UML Component diagrams
- UML State diagrams
- UML Package diagrams

3.3 Software Development

For the development of the above-mentioned modules, the designs in UML diagrams arranged earlier will be taken into account. Appropriate Microsoft tools are used as application tools. The waterfall method is used during software development (Cloutier, 2004; Ji and Sedano, 2011). Software development process in the waterfall method is comprised of analysis, design, coding, testing, version and maintenance stages. Like in the case of the waterfall method, in conventional software methods these stages work linearly. Each stage uses the output which is produced by the preceding one. It then evaluates what has taken in that can be utilized by the successive stage.

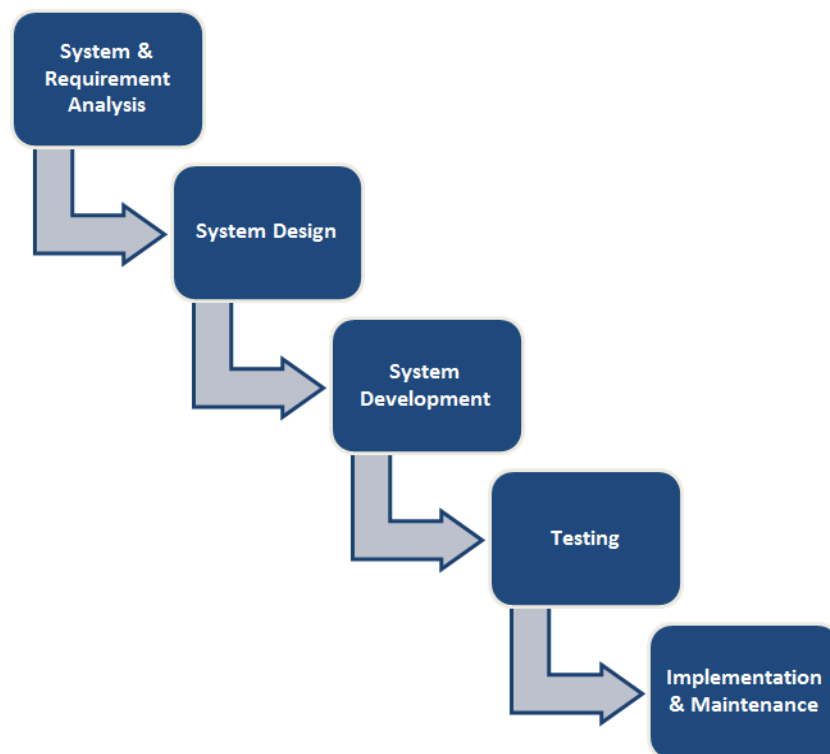


Figure 2: Waterfall methodology.

3.4 Laboratory and On-site Testing and Improvements

The software requires testing during and after the development processes. There are several stages of testing that the software needs to

pass through. Laboratory tests may be looked at as system tests and performance tests. System tests assure that the developed version of the software functions properly on systems having the minimum configuration of the



specified operating system. Performance tests on the other hand, after the system tests, verify the existence of pre-defined functions, computation time and check that the software performs required calculations for each ship type correctly and interfaces work properly.

End-user acceptability tests include the above-mentioned system and performance tests and sufficiency of the software in terms of functionality, performance, calculations, accuracy, reporting etc. During these tests, any changes and additional demands are determined and taken into consideration as appropriate.

The final tests for the software are carried out by the internationally recognized organizations on the entire system. The system, performance, interfaces, speed, calculations and compliance with international rules and regulations are gone through an intensive testing procedure.

Final phase of this work package evaluates the results of all testing schemes. If any flaws and deficiencies are detected or reported as a result of these tests, they are immediately taken into consideration and mitigated. Apart from the possible mistakes and shortcomings, any reasonable demands from the customers are also deliberated and applied wherever possible.

4. PROJECT MANAGEMENT

Like any vast project, this software development project demands a professional project management and possibly a competent tool to handle tremendous amount of different tasks in every work package. A tight schedule necessitates careful planning and control of successive tasks during the entire project. Any delays at some point of the workflow may be quite costly at the final destination. It is very crucial that the team members of the project must be kept updated about the timely progress in a regular basis. Since minor local delays are inevitable, the entire workflow must updated concurrently

to estimate the penalty on the overall schedule or to take necessary precautions and appropriate corrective actions immediately. A powerful project management tool (RITMIQ), which helps to plan and control the project and use all available resources effectively, has been employed in this project.

5. RISK ASSESSMENT AND RISK MANAGEMENT PLAN

A risk management plan was put forward for this project in order to identify possible risks that may shadow the success of the project and take necessary action to eliminate them or lessen their effects wherever needed.

Risk assessment includes the approach for data collection and assessment of the collected data in the project. In this approach, the owner of the risk is determined and then the owner analyzes this risk and determines the measures to be taken to mitigate them. A general list of possible risk scenarios collected from various sources is outlined in the plan. Classification of risks may be listed in main categories as follows:

- Personal risks (human error, personnel problems, lack of knowledge and expertise)
- Technological risks (wrong system architecture or modeling, security, communication problems, data and system losses)
- Organizational risks (insufficient communication between IT and work groups, insufficient planning/budgeting, faulty project management and resource utilization)
- Legal risks (bankruptcies and legal disputes between parties)
- External risks (force majeure, sabotage, terrorist attacks, cyber-attacks, war, fire, flood etc.)

5.1 Risk Calculation Measures

When assessing risk scenarios, it is important to realize that “the worst case” is taken into account instead of “average values” for each scenario. If three different threat and impacts are present for a scenario, the threat with the highest level impact is reflected for the

general impact level for that particular scenario. Similarly, if a service area is composed of various sub-areas and these sub-areas have different severity of impact, the severest threat and impact belong to that sub-area is taken into account for the entire service area.



Figure 3: Project management details.

5.2 Impact Assessment

Each risk group is analyzed to determine the severity of a possible impact it may achieve. This analysis contains all assumptions, limitations and sensitivities for the pertinent risk item. Each item is added to the “reaction to the risk plan” and the probability of risk occurrence and its impact (impact score) are determined. Multiplying these two criteria yields the risk score of that particular item. Prioritization between the risks can then be made based on the impact score. A sample graphical representation of risk for a particular scenario is depicted in Figure 4.

		Sample				
		9	7	5	3	1
Probability	9	Green	Yellow	Red	Red	Red
	7	Green	Yellow	Yellow	Red	Red
	5	Green	Green	Yellow	Yellow	Red
	3	Green	Green	Green	Yellow	Yellow
	1	Green	Green	Green	Green	Green
		1	3	5	7	9
		Impact				

Figure 4: Probability of risk and impact for a risk area.



6. CONCLUSIONS

In this paper, a ship stability instrument was scrutinized from the developer's perspective. Stability and strength calculations have been performed routinely for a long time all over the world. Ship stability instruments are however recognized internationally either by mandates or recommendations of IMO recently. They are believed to be mandatory soon for most ship types since they offer fast and reliable solutions to ship stability and strength calculations. They speed up loading/unloading and other ship operations in a safe manner saving vast amount of port-stay time and, in turn, money.

Developing a ship stability instrument is not a straight-forward task. Like any other software, there are customary expectations from the software such as reliability, speed, cost and user-friendliness along with other special requests depending on the ship type. From naval architectural point of view, many parameters need to be considered for the engineering calculations. Approximations and integration procedures should be monitored carefully to avoid cumulative and/or rounding errors. All related international and national rules and regulations must be gathered and stored in the rules library for different ship types. Limiting tolerances for certain values of ship parameters shall be met to comply with the final approval criteria. Characteristics of special cargo (chemicals, petroleum products, steel coils, grain etc.) are dealt with carefully when establishing loading scenarios and simulations. Damage stability and strength analysis has recently entered in the portfolio of stability instruments. Container loading/unloading sequence and stowage are also optimization problems by their nature and considered seriously in this software.

On the other side of the token, computer architecture and computer engineering skills need to be employed in order to achieve the above-mentioned engineering calculations fast and correctly. Waterfall methodology was preferred for the upper level software development throughout the project. Ship specific, commer-

cially available tools have been employed to perform certain tasks. The user and electronic device communication interfaces are recognized as important parameters and are handled with accordingly. Input, output, graphical and report design have an important influence on the data transport, user-friendliness and operational effectiveness of the software. The project management were facilitated by a robust tool namely RITMIQ under the supervision of competent personnel. A risk management plan has been employed throughout to pinpoint the risks and seek remedial actions for their mitigation or calculate their possible impact on the project.

It is believed that ship stability instruments are essential tools to assist the masters and ship operators. New generation stability instruments are capable of handling even a wider range of intact and damaged stability and strength calculations including icing considerations, squat predictions etc. They also help greatly to port authorities and surveyors in routine tasks.

ACKNOWLEDGMENTS: The authors of this paper are indebted to the Scientific and Technological Research Council of Turkey (TUBITAK) for funding this invaluable project. The authors also wish to express their deepest gratitude to MESH Engineering and Software Corporation and Delta Marine Company for their help and support throughout this study. Kind permissions of both companies to use and analyze DeltaLoad loading software and DeltaLoad Plus loading software under development and RITMIQ project management software are sincerely appreciated.

DEDICATION: This paper is dedicated to the memory of Prof. A.Y. Odabasi who died in 2009 and contributed to naval architecture and ship stability in particular a great deal.

REFERENCES

Avriel, M, Penn, M., Shpirer, N. and Witteboon, S., 1998, "Stowage Planning for



- Container Ships to Reduce the Number of Shifts”, Annals of Operations Research, Vol.76, pp.55- 71.
- Briggs, M.J., 2009, “Ankudinov Ship Squat Predictions - Part I: Theory, Parameters, and FORTRAN Programs”, Coastal and Hydraulics Engineering Technical Note ERDC/CHL CHETN-IX-19, Vicksburg, MS: U.S. Army Engineer Research and Development Center.
- Briggs, M.J. and Daggett, L., 2009, “Ankudinov Ship Squat Predictions - Part II: Laboratory and Field Comparisons and Validations”, Coastal and Hydraulics Engineering Technical Note ERDC/CHL CHETN-IX-20, Vicksburg, MS: U.S. Army Engineer Research and Development Center.
- Campbell, L.A., Cheng, B.H.C., McUmber, W.E. and Stirewalt, R.E.K., 2002, “Automatically Detecting and Visualizing Errors in UML Diagrams”, Requirements Engineering, Vol.7, pp.264-287.
- Cloutier, R.J., 2004, “Migrating from a Waterfall Systems Engineering Approach to an Object Oriented Approach – Lessons Learned”, ICSE and INCOSE 2004 Region II Conference Proceedings, Las Vegas, Nevada, USA.
- Couser, P., 2003, “A Software Developer’s Perspective of Stability Criteria”, STAB 2003, 8th International Conference on the Stability of Ships and Ocean Vehicles, Madrid, Spain.
- Couser, P., 2002, “Use of Computers in the Design of High-Speed Craft”, RINA WA High-Speed Craft Technology and Operation, Fremantle, WA.
- Design Data Sheet – Stability and Buoyancy of U.S. Naval Surface Ships, DSS 079-1, 1975, Department of the Navy, Naval Ship Engineering Center.
- Gielingh, W., 2008, “An Assessment of the Current State of Product Data Technologies”, Computer-Aided Design 40, pp.750–759.
- Ji, F. and Sedano, T., 2011, “Comparing Extreme Programming and Waterfall Project Results”, CSEE&T 2011, pp. 482-486, Waikiki, Honolulu, HI, USA.
- Kavitha, P., Narayanan, K.P. and Sudheer, C.B., 2010, “Software Development for the Analysis and Design of Ship Berthing Structures”, Proceedings of International Conference on Advances in Civil Engineering, Trabzon, Turkey.
- Lewis, E.V. (Editor), 1998, Principles of Naval Architecture, SNAME, Jersey City, NJ, 2nd edition.
- Min, Z., Low, M.Y.H., Jing, H.W., Ying, H.S., Fan, L. and Aye, W.C., 2010, “Improving Ship Stability in Automated Stowage Planning for Large Containerships”, Proceedings of the International Multi-Conference of Engineers and Computer Scientists, Vol. III, IMECS 2010, Hong Kong.
- MSC.1/Circ.1229, 2007, Guidelines for the Approval of Stability Instruments.
- Odabasi, A.Y. and Taylan, M., 2003, “Marpol 25A: Is It Safety or Absurdity?” 8th International Conference on the Stability of Ships and Ocean Vehicles, Spain.
- SOLAS Consolidated Edition. IMO, 1997.
- Specification for Parametric Ship Design Software Development, 2000, Maritech ASE - Project 99-21.
- Taylan, M., 2007, “On the Parametric Resonance of Container Ships”, Ocean Engineering Vol.34, pp.1021-1027.
- Wong, K. and Sun, D., 2006, “On Evaluating the Layout of UML Diagrams for Program Comprehension”, Software Qual J., Vol.14, pp.233–259.
- 2008 IS Code, IMO Publications, 2009 Edition.





Putting Vessel Motion Research into the Hands of Operators

Leigh McCue, *Virginia Tech*, mccue@vt.edu

ABSTRACT

In the summer of 2011, a simple, efficient, and low development cost Small Craft Motion Program (SCraMP) was released for iOS (iPhone 4, iPod Touch 4G, iPad 2, and more recent devices). The purpose of this effort was to empower low budget operators, specifically fishermen, with critical information pertaining to the state of their vessel. Capitalizing upon internal device hardware that would have cost thousands of dollars only a few years ago, the iOS application provides the ability to view and record motion and location data. Additionally, the application provides a safety index, GM, and period metrics reflecting the severity of motions, and a direct tie-in to wave buoy data, all in a simple and interactive graphical user interface. While the initial target was to appeal to financially-constrained fishermen, perhaps surprisingly, opportunities for use were found across a range of operational environments well outside the envisioned scope. This paper describes the motivation, development, and deployment of this low-cost, far-reaching, small craft motion tool with emphasis on general philosophy towards broad technology transition in the 21st century 'wired' environment.

Keywords: *fishing safety, capsizes, iOS*

1. INTRODUCTION

Commercial fishing is consistently one of the most dangerous occupations in the world; in the United States it often ranks as the most dangerous occupation with a popular television show, *The Deadliest Catch*, highlighting the plight of commercial fishermen. The question becomes, then, how to put vessel dynamics research into the hands of fishermen operating on a limited budget in a harsh physical environment. Retrofitting state of the art motion monitoring systems is both costly and impractical in a space constrained boat, with fiscally constrained fishermen, where electronics must be viewed as at least somewhat disposable due to the harsh nature of the work environment. Yet, it is rare these days to find any adult in a first world country go much of anywhere without a cellphone, often a smartphone. Many adults are carrying accelerometers, gyroscopes, and a

microprocessor in their pocket, without even realizing it. This paper describes the implementation of a Small Craft Motion Program (SCraMP) in the iOS environment such that it can be readily deployed, via the iTunes app store, to iPhone 4, iPad 2, and iPod 4G and more recent devices. The following sections of this paper describe the actual app and the safety metric incorporated into the app, user feedback, and planned future revisions.

SCraMP makes use of iOS devices' accelerometer, gyroscope, location capabilities, and microprocessor. Examples of the iPhone 4 hardware are shown in Figure 1, reproduced from Chipworks (2010). In Figure 1(a), the MEMS sensors are shown; the accelerometer, labeled with '33DH' is identified by Chipworks (2010) as the 3mmx3mm STMicroelectronics LIS331DLH. The gyroscope labeled with 'AGD1' is identified by Chipworks (2010) as the 4mm by 4mm



STMicroelectronics L3G4200D 3-axis gyroscope. The Apple A4 Microprocessor used in the iPhone 4 is also visible in this image. In Figure 1(b) the AKM Semiconductor magnetometer AKM8975 is visible above and to the right of the Samsung flash memory. The iPhone 4 also has a Broadcom BCM4750 GPS, whereas the iPod and non-3G iPads do not have a GPS; instead their location data is based on WiFi information, and is therefore less useful when at sea, for example. The Apple Core Motion Framework provides the programmer the ability to output accelerometer or gyroscope data independently or fused data, which accounts for gravity and drift (Apple, 2011). Apple does restrict ranges of applicable hardware, for example, while the accelerometer is rated to as much as $\pm 8g$ and output rates as high as 1kHz (STMicroelectronics, 2012), Apple's CoreMotion framework appears to cap accelerations to $\pm 3g$, and the author's experience shows that the device is typically capable of maximum accelerometer sample rates between 50-100 Hz.



Figure 1(b): iPhone 4 hardware, images reproduced from Chipworks (2010)

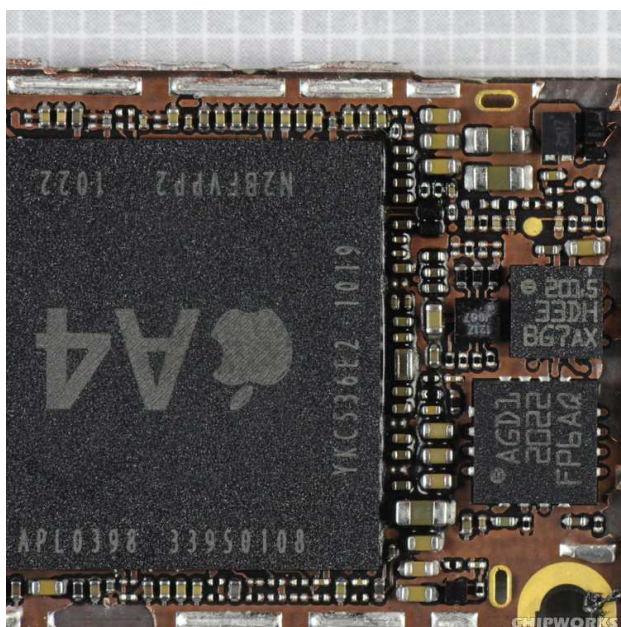


Figure 1(a): iPhone 4 MEMs sensors and processor, images reproduced from Chipworks (2010)

2.0 RELEASE EVOLUTIONS

Version 1.0, August, 2011: The initial release of SCraMP provided a user with rotation and acceleration data in graphical form, a customizable warning index based upon roll displacement, pitch displacement, and heave acceleration data (described subsequently in section 3.0), and an ongoing display of roll motion with statistics of past motions shown, the concept being that if roll motions deviate substantially from past motions, this can provide the basis of a warning for phenomena such as downflooding (McCue, 2008). Sample screen images from this V1.0 are in Figure 2. For the sake of brevity, screen images are only provided for the original and most current, as of this writing, V3.8 versions of SCraMP to illustrate the evolution of the application.



Version 2.0, August, 2011: In V2.0 of SCraMP, the user was provided the ability to select the scale of the axes upon which they display acceleration and rotation data. A fifth tab with location data, specifically latitude, longitude, course and speed, was added to the interface. Additionally, minor edits included adding statistics for pitch motions and a numerical readout of acceleration and rotation data was (in addition to the graphical display).

Version 3.0, September, 2011: Major edits in version 3.0 were to allow the user to select which degrees of freedom (s)he wishes to see displayed and addition of a recording feature. To maintain a five tab graphical user interface (more than five becomes a less-intuitive layout), the statistics tab was removed freeing up space for the recording tab. Anecdotal user feedback indicated that the statistical information was less critical than the other information provided. In this version, recorded data could be sent to the user via e-mail.

Version 3.1, October, 2011: This minor revision added an indicator on all tabs to indicate when data recording is in progress.

Version 3.2, November, 2011: This revision was focused on maintaining functionality through the iOS5 operating system update.

Version 3.3, December, 2011: In version 3.3 the user was provided the ability to save large data files locally and move them via iTunes rather than being restricted to the maximum file size allowed in an e-mail.

Version 3.4, December, 2011: A link to RSS feeds from the National Data Buoy Center is provided to the user such that data for all buoys within 100 miles of the user are readily available.

Version 3.5, January, 2012: Location data (latitude, longitude, course, and speed) were added to the recording feature.

Version 3.6, January, 2012: GM and period estimates were added with the ‘Index’ screen generalized to a ‘Safety Metrics’ screen. The user must enter vessel beam for the GM calculation, and may enter desirable ranges for GM or roll period to tailor those warning indicators.

Version 3.7, March, 2012: This version of the app added heading and compass information, a zeroing option for angular motions, automatic storing of user settings, and the choice of two different coordinate systems. Using the Apple CoreMotion API, rotations are reported in an earth-fixed Euler angle reference frame. Version 3.7 provides the user the option to use a Tait-Bryan transformation instead, which corresponds to the boat-coordinate system more commonly implied when naval architects use the terms “roll” and “pitch.” Rotations in both coordinate systems are recorded when data is collected.

Version 3.8, May 2012: Audible warning alarms and universal iPad support was added in this version. Sample screen capture images from Version 3.8, the most current version as of this writing, are given in Figure 3.

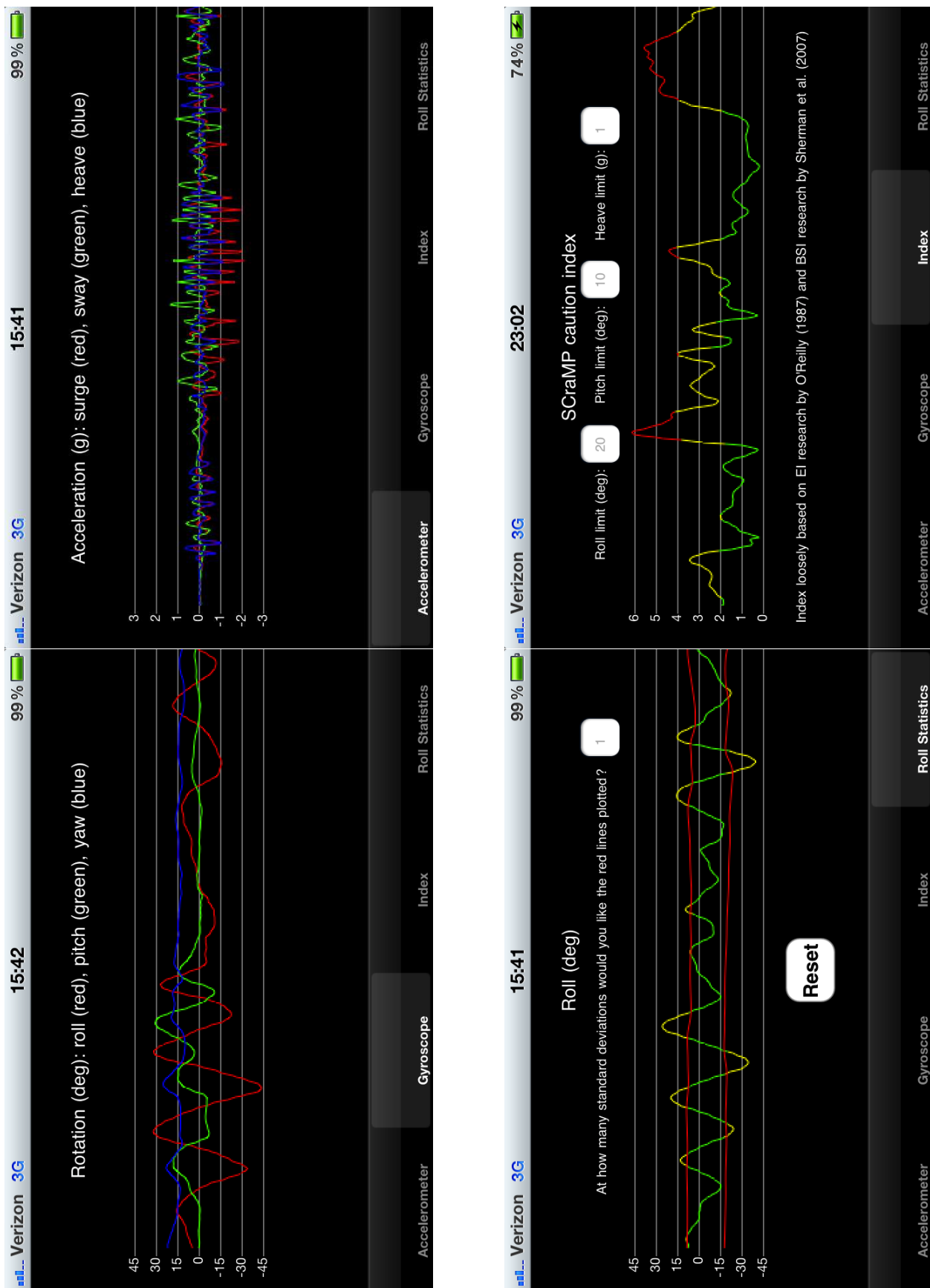
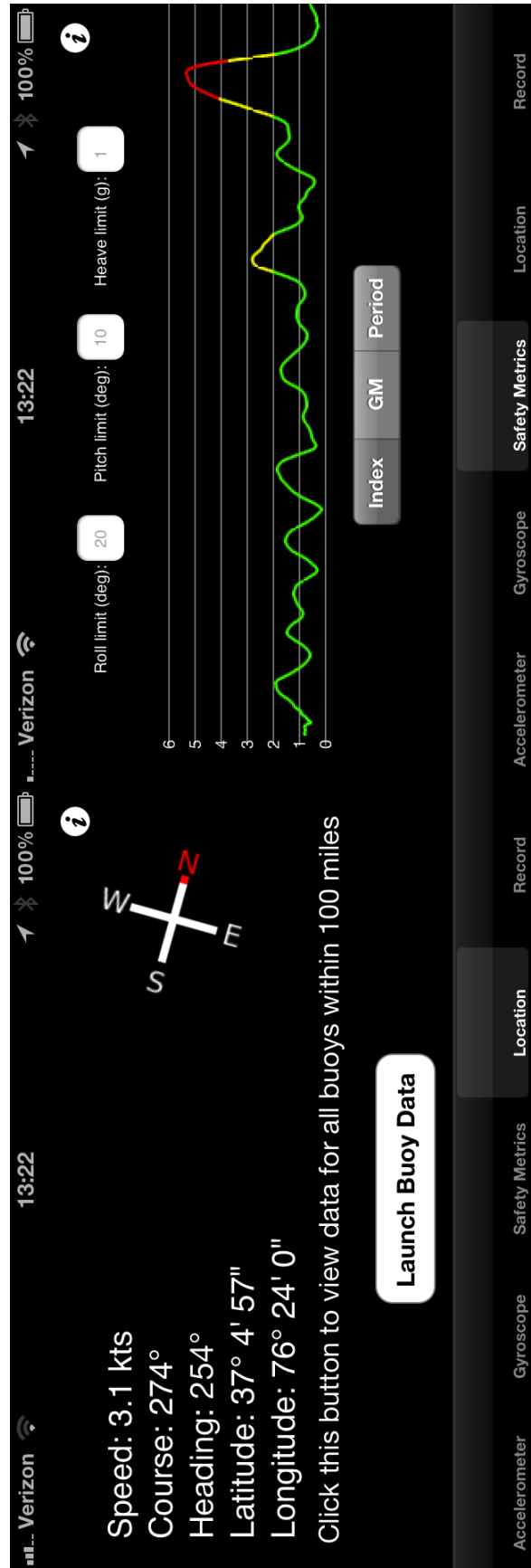
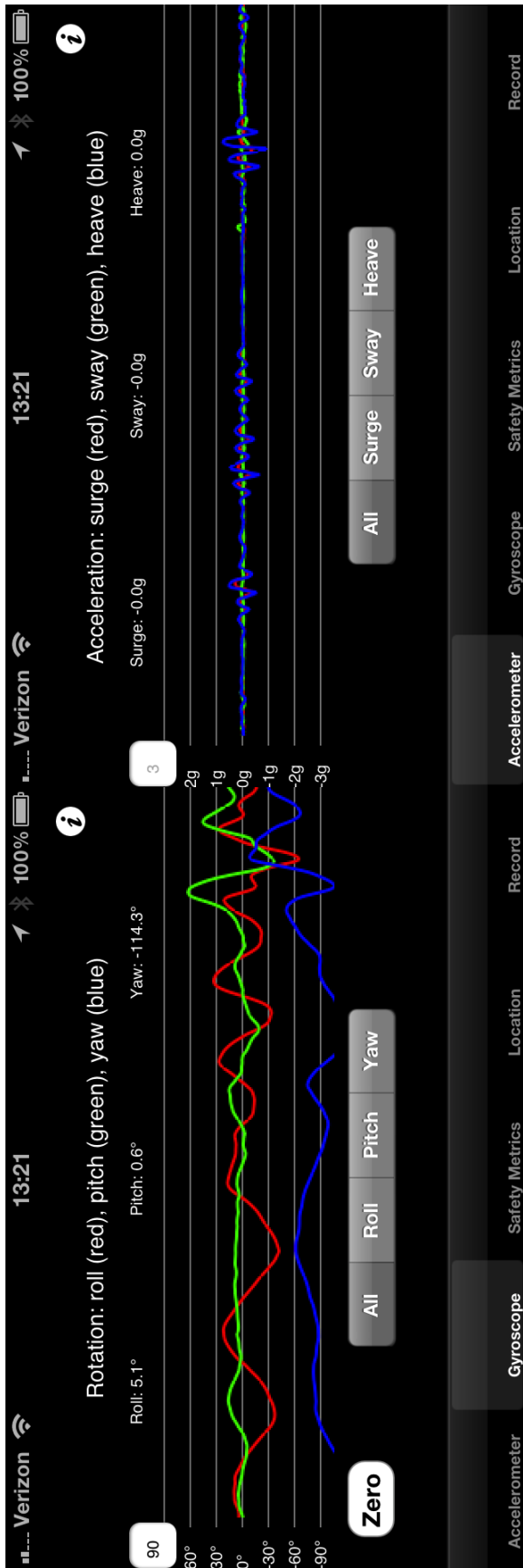


Figure 2: Sample screen images from SCraMP



V1.0



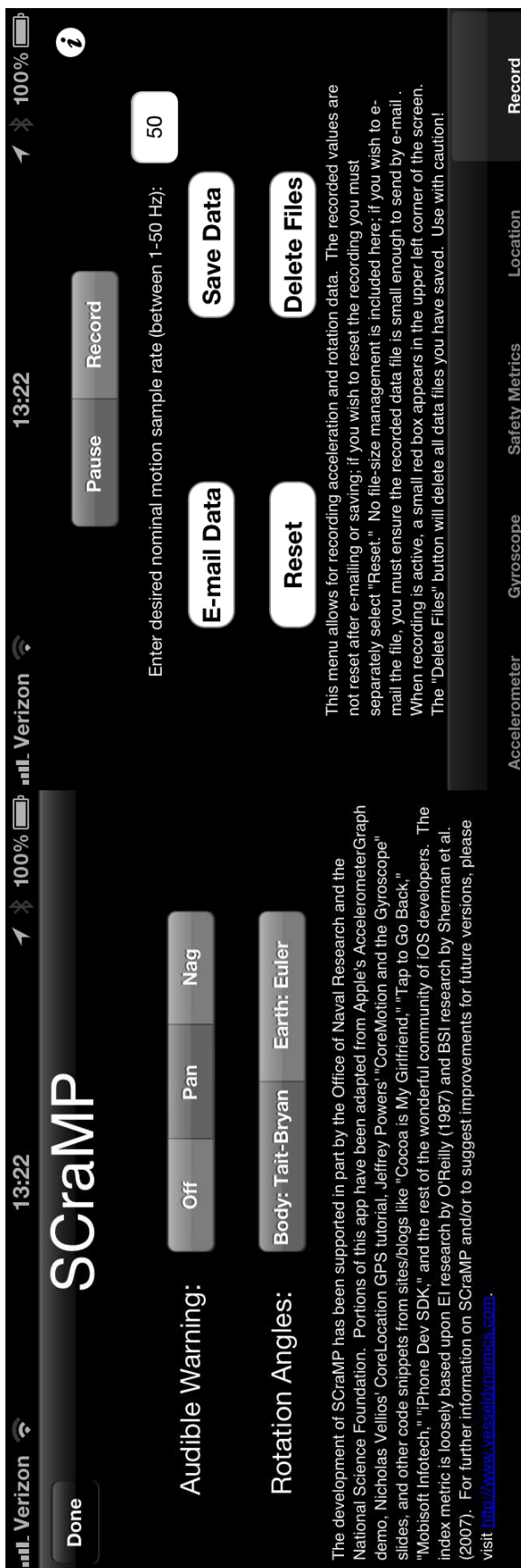


Figure 3: Sample screen images from SCraMP V3.8

3.0 SAFETY METRICS

3.1 Index

The index metric is loosely based upon Energy Index (EI) research by O'Reilly (1987) and BSI research by Sherman *et al.* (2007). O'Reilly (1987) introduced the "Energy Index" concept as part of his "Landing Period Designator" (LPD) as a mechanism to provide an index metric of the severity of ship motions for rotorcraft launch and recovery operations. By providing an index metric, usually displayed in a green/yellow/red display, which captures multi-dimensional behavior, landing safety officers, for purposes of LPD applications, or captains, for more general purposes, are given an easy to read guide toward safe operations.

O'Reilly's (1987) energy index is given in Equation (1), where x, y, and z denote surge, sway, and heave and with an overdot reflecting differentiation with respect to time. To the knowledge of the author, units are mixed in this formulation. Philosophically the concept was for an energy-like metric, but not a true measure of any physical quantity.

$$EI = \sqrt{x^2 + \dot{x}^2 + y^2 + \dot{y}^2 + z^2 + \dot{z}^2} \quad (1)$$

Ferrier has continued O'Reilly's work into the present with a more complex, and shrouded index tool, to which the interested reader is referred to Ferrier *et al* (1998, 2000) amongst other references by Ferrier and his colleagues. In an effort to benchmark the effectiveness of indicial landing period designator systems, Sherman *et al* (2007) defined a simple benchmark index as given in Equation (2).

$$BSI = 2|roll| + 2|pitch| \quad (2)$$

While Ferrier's index clearly outperformed Sherman (2007)'s benchmark index, one perhaps surprising appearance in the Sherman *et al* study was the relative effectiveness of highly simplistic metrics. Based upon this



metric philosophy of reducing motions to a single green/yellow/red warning metric, the index metric contained in SCraMP is given in Equation (3), where ϕ is roll, θ is pitch, and z is heave. Again, overdots denote derivatives with respect to time.

$$Index = 4 \sqrt{\left(\frac{\phi}{\phi_{limit}}\right)^2 + \left(\frac{\theta}{\theta_{limit}}\right)^2 + \left(\frac{\ddot{z}}{\ddot{z}_{limit}}\right)^2} \quad (3)$$

The graphical display of the index is set to be green from 0-2, yellow from 2-4, and red from 4-6. If any one parameter reaches its limit value, red is displayed. Because small craft operators are the target audience, roll and pitch displacements along with heave accelerations were identified as critical parameters for the index metric. Note the operator is able to tailor the metric to their needs and craft by entering their desired roll, pitch, and heave limits. Future versions of SCraMP are likely to include multiple index forms, that is, inclusion of other degrees of freedom for indices to address a range of dynamic phenomena, in addition to the ability to customize individual indices.

3.2 Period and GM

Under this “Safety Metrics” tab, two physical measurements, an estimate of GM and roll period, are also provided. The roll period calculation is based upon time between zero up-crossings. The GM estimate is calculated per Equation 4, which appears in numerous references, such as Goldberg (1988) and the IMO’s Maritime Safety Committee (2010). In Equation 4, B denotes the beam of the craft in feet, T is the roll period in seconds, and C is an empirical constant; taken for purposes of this application to be $0.44 \text{ s}/\sqrt{ft}$ (which corresponds to approximately $0.8 \text{ s}/\sqrt{m}$, typical of that reported in references using metric units).

$$GM = \left(\frac{CB}{T}\right)^2 \quad (4)$$

As noted in Principles of Naval

Architecture, “the external rolling forces due to waves and wind tend to distort the relationship of [Equation 4]. Hence, caution must be exercised in calculating GM values from periods of roll observed at sea, particularly for small craft” (Goldberg, 1988).

The user must enter the craft’s beam for the GM metric. For both the period and GM estimates, the user may provide minimum and maximum values outside of which they wish to be warned of anomalous behaviour; additionally, monitoring trend behaviour can be indicative of emergent issues.

4.0 USER FEEDBACK AND IMPACT

While a formal assessment is still pending, based upon comments and e-mails, the concept of putting a free tool running on a relatively inexpensive platform appears to be a success. True to the form of its deployment, news of the application has spread primarily by word of mouth, electronic press release, and social media (see Figure 4 for example, as a Twitter press release from Virginia Tech finds its way to the American Fisheries Society).

Close communication with those in the field has been essential to successful development and deployment of this application. For example, the initial versions of this application did not use GPS/location information or have recording functionality because I, as the developer, feared users, specifically those in the fishing community, might be leery of any tool that pinpoints their location and records vessel data. However, in immediate feedback from users of V1.0, the two most requested items were GPS and recording capabilities. Similarly, the roll period and GM estimates were added after communication with an epidemiologist who relayed the comment that one fisherman liked the application because he often, when laying in his bunk, would count off roll periods to verify that all was well above decks.



Figure 4: Twitter example of the power of social media in spreading everyman-accessible research.

In academia, the topic of “impact factor” is often near the forefront of any research publication discussion. In that sense, this type of project results in a new perspective on impact factor. The true impact of this form of research dissemination, in which hundreds or thousands of potential users around the globe can be reached with minimal distribution cost via a widely used platform (iOS, Android, etc...) is a game changer when it comes to putting life-saving research and tools into the hands of those who need it most. Figure 5 provides a graphic display of the reach of SCraMP V3.7.

In 2009, fishers and related fishing workers had an occupational fatal injury rate of 203.6 per 100,000 full-time equivalent workers, 58 times the fatal injury rate for all workers in the United States (US Bureau of Labor Statistics, 2011). Therefore, while this application clearly does not represent the cutting edge of research,

it does provide an easy and inexpensive mechanism to rapidly disseminate access to a simplified form of research that can save lives. The researcher investment in developing an alternative of this sort, when viewed in that context, is negligible.

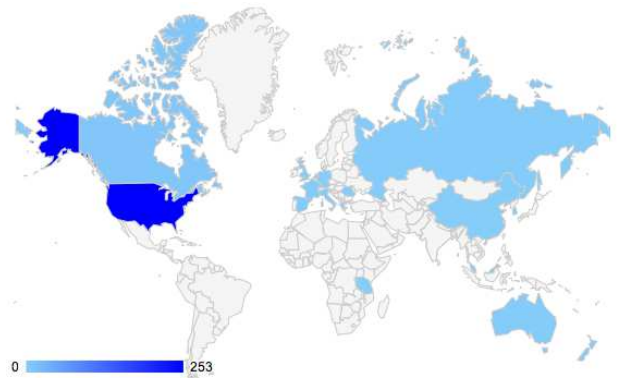


Figure 5: Locations of SCraMP V3.7 users.

5.0 FUTURE WORK

The primary emphasis for future work on this application is to formalize the assessment. Additionally, future versions of the application will feature more forms of the warning index tailored to different applications to broaden applicability between the range of craft sizes, from small craft to large vessels. The author has been working toward quantification of the accuracy of this as a data acquisition tool by comparison to comparable sensor packages. Similarly, the author has been collecting user feedback, most specifically within the US commercial fishing industry. Details of the comparison testing and user feedback are planned for future publication as the results of those efforts are preliminary at this stage.

6.0 ACKNOWLEDGEMENTS

The development of SCraMP has been supported in part by the Office of Naval Research and the National Science Foundation. Portions of this application were developed while the author was on sabbatical at the Naval Surface Warfare Center’s Combatant Craft



Division, funded under the ASEE-ONR Sabbatical Leave Program by Dr. Robert Brizzolara. The author is tremendously grateful for feedback and encouragement on this application from Charlie Weil, Gabriele Bulian, Ryan Faber, Jennifer Lincoln, and other users. Preliminary assessment efforts for this application are being supported by a Virginia Tech Occupational Safety and Health Research Center Granata Seed Grant.

7.0 REFERENCES

- Apple, "Core Motion Framework Reference," http://developer.apple.com/library/ios/#documentation/CoreMotion/Reference/CoreMotion_Reference/_index.html, *iOS Developer Library*, 2011.
- Chipworks, "Teardown of the Apple iPhone 4 Smart Phone," <http://www.chipworks.com/en/technical-competitive-analysis/resources/recent-teardowns/2010/06/silicon-teardown-of-the-apple-iphone-4-smart-phone/>, published June, 2010.
- Ferrier, B. and Manning, T., "Simulation and Testing of the Landing Period Designator (LPD) Helicopter Recovery Aid." *Naval Engineers Journal* **110**(1): 189-205, 1998.
- Ferrier, B., Applebee, T., Manning, A., James, D.. "Landing Period Designator Visual Helicopter Recovery Aide; Theory and Real-Time Application," *Proceedings of the American Helicopter Society*, Washington, 2000.
- Goldberg, L., "Chapter II Intact Stability," *Principles of Naval Architecture, Volume I, Stability and Strength*, E.V. Lewis (ed.), Society of Naval Architects and Marine Engineers, Jersey City, NJ, 1988.
- iTunes Preview, "SCraMP for iPhone 4, iPhone 4S, iPod touch (4th generation), iPad 2 Wi-Fi, and iPad 2 Wi-Fi + 3G on the iTunes App Store" <http://itunes.apple.com/us/app/scramp/id456343416?mt=8>, downloaded January, 2012.
- Maritime Safety Committee, "Report of the Maritime Safety Committee on its eighty-seventh session," MSC 87/26/Add.2, International Maritime Organization, June, 2010.
- McCue, L.S., "Motion prediction envelopes for intact and damaged hulls," Proceedings of the 10th International Ship Stability Workshop, Korea, March, 2008.
- O'Reilly, P. J. F. (1987). "Aircraft/Deck Interface Dynamics for Destroyers." *Marine Technology*, Volume 24, Number 1, pp. 15-25
- Sherman, B., McCue, L.S., Bi, P., and Milgram, J., "Assessing the effectiveness of dynamic deck motion limit systems," Conference Paper No. PRADS2007-20290, 10th International Symposium on Practical Design of Ships and Other Floating Structures, Houston, Texas, October, 2007.
- STMicroelectronics, "LIS 331DLH MEMS digital output motion sensor ultra low-power high performance 3-axes "nano" accelerometer" http://www.st.com/internet/com/TECHNICAL_RESOURCES/TECHNICAL_LITERATURE/DATASHEET/CD00213470.pdf, downloaded January 2012.
- US Bureau of Labor Statistics, "Number and rate of fatal occupational injuries, by occupation group, 2009," <http://www.bls.gov/iif/oshwc/foi/cfch0008.pdf>, 2011.





Spend Less, Save More (Lives)

Barry Deakin, *Wolfson Unit MTIA, University of Southampton*, bd1@soton.ac.uk

ABSTRACT

This paper questions whether we should re-direct our efforts to improve safety at sea, suggesting that most research does little to save lives. It promotes the view that we are missing an opportunity for very simple means of assessment that might benefit a wider range of seafarers. Data from the author's own research, principally for the UK's Maritime and Coastguard Agency, is combined with findings of other significant research projects, such as HARDER, as well as the latest casualty reports and investigations, to demonstrate that we have the knowledge to develop excellent tools for safety assessment and guidance.

Keywords: *Stability, safety, criteria, guidance*

1. INTRODUCTION

It is the author's view that many researchers have a tendency to complicate the subject and their findings, and that there is a strong case for taking a much simpler and more pragmatic approach if we really have a desire to improve safety at sea. Stability assessment and regulation are necessary, but they need not be complicated or expensive. This is particularly important for small vessels, where most fatalities occur.

The most effective path to safety though, is through education and the provision of information on the level of safety of a particular operation. Conventional pass/fail criteria and stability information booklets do nothing to provide this, and we await the development through IMO of the Second Generation Criteria to see if they improve that situation. The method proposed here offers practical safety guidance in relation to the size of the vessel and the prevailing seastate.

2. WHERE DOES THE MONEY GO?

It is inevitable that research efforts are concentrated on subjects that attract funding. Gov-

ernment funding is likely to be driven by defence strategy and politics, so is more likely to be available for naval vessels, for issues that attract widespread publicity such as the safety of passenger vessels, or for parts of the industry able to apply significant commercial pressure; typically major shipping companies.

Inspection of the proceedings of STAB2009 reveals that, of the 70 papers, most addressed large ship stability, almost 70% concerned methods of numerical prediction of ship dynamics, and 14% were specific to parametric rolling. There was only one paper that addressed small craft specifically, describing model simulation of fishing vessel casualties.

If we go back a further 15 years to STAB1994 we find that, again, more than half of the papers were on numerical simulations, but there were some differences in the spread of interest. For example, only two papers concentrated on parametric rolling, while 10% addressed the stability and safety of small vessels, predominantly fishing vessels.

On the basis of this very simplistic view, it appears that the majority of our efforts are concentrated on developing ever more reliable methods of predicting the motions of large ves-



sels, and that these efforts are increasing. Research devoted to small vessel safety appears to be decreasing, or perhaps is not presented at these STAB conferences. This reflects what one might expect in view of the most likely sources of funding.

Despite this extensive investment in stability research during the last two decades, much assessment of stability still relies on criteria derived from Rahola's work, published in 1939. Things are changing now, as the IMO is committed to developing a revised Intact Stability Code, and considerable effort is being directed towards it. Whether the revised Code will provide a more reliable assessment of the level of safety remains to be seen, but it is unlikely to be as simple as the current criteria.

3. WHERE ARE THE FATALITIES?

Between 1994 and 2007, the number of lives lost on cargo ships ranged between 100 and 400 per year. This includes deaths from all causes, not just stability related incidents.

Since the Second World War there have been a number of well publicised, major maritime disasters, and inevitably the highest casualty numbers occur when passenger vessels are involved. Most fatalities have been caused by fire, explosion or grounding, with few major accidents caused by loss of stability or buoyancy. Below is a list of those incidents which have resulted in the loss of at least 500 lives as a result of stability or loading deficiencies, since 1945.

Le Joola; an overloaded Senegalese ferry that capsized in rough seas in 2002, with over 1800 lives lost.

Estonia; a Baltic Sea ferry that capsized in 1994, following failure of the bow door, with the loss of almost 1000 lives.

Bukoba; an overloaded passenger ferry that sank on Lake Victoria in 1996 with the loss of about 800 lives.

Princess of the Stars; a Philippines ferry that sank in a Typhoon in 2008 with the loss of about 700 lives.

Ramdas; an Indian passenger ship that capsized in 1947 with the loss of 625 lives.

Shamia; a Bangladesh ferry that capsized in a storm on the Meghna river in 1986 with the loss of about 600 lives.

Of these 6 casualties over the past 66 years, the worst four occurred during the last 20 years, and suggest that the carriage of passengers at sea is not getting any safer. Two of those were heavily overloaded vessels however, and no amount of stability research will help vessels that are loaded far beyond their safe design limits.

The investigation into the loss of the Princess of the Stars concluded that the captain made an error of judgment in continuing his voyage into known severe weather, and this perhaps is a case where improved safety guidance might have made a difference.

The loss of the Estonia resulted in tremendous research effort, particularly around Europe, as indeed did the capsizing 7 years earlier of the Herald of Free Enterprise, which resulted in the loss of 193 lives. These two incidents demonstrate the influence of public opinion, media coverage and political pressure in encouraging investment in stability research.

In round figures, the statistics suggest an average of around 1000 shipping fatalities per year, which makes it a relatively safe form of transport. This is not the full story though, and we have all seen references to the International Labour Organisation's estimates of a global death toll of 24,000 per year in the fishing industry alone. These don't appear in most shipping statistics. They are predominantly in small



vessels in less industrialised countries, but fishing has one of the highest fatality rates in all countries, regardless of the level of sophistication of the local industry. Fifteen years ago in the USA it was believed to be more than 40 times higher than the national occupational average (Petursdottir et al, 2001), and it remained so in 2008. Current UK figures show it to be 115 times higher than for shore based workers. Not all of these deaths are caused by stability and loading incidents, but capsizing and foundering frequently result in the loss of all crew.

4. DOES STAB REPRESENT OUR BEST EFFORTS?

Because of the pressures on academics to publish, the STAB conferences, like so many other scientific fora and journals, attract predominantly academic papers. Academic studies frequently take the form of 3 year post-graduate projects and attract a high level of mathematics or numerical analysis. Typically they lead to further interesting research but have little direct application to industry.

Applied research conducted for industry is more likely to result in practical solutions, but is less likely to appear because it might be confidential, those involved cannot afford the time to prepare papers or participate, and there is little incentive for them to do so. The state of the art in industry therefore is not often represented in engineering conferences, and an example in the field of stability is the successful effort by the Icelandic Maritime Administration to reduce fishing vessel losses by capsize (Vig-gósson & Bernodsson, 2009). Between 1969 and 2002, 71 vessels capsized with the loss of 129 crew but since 2003 no vessels have capsized. This has been achieved partly by improving the fleet, but also through education and the provision of useful information. The innovative methods they developed could be implemented elsewhere but are not widely known and have not been disseminated at STAB.

5. ARE COLLABORATIVE PROJECTS PRODUCTIVE?

Most of us will have heard the phrase “A camel is a horse designed by committee”. With the contemporary trend for major research funding to be allocated to international collaborative projects, we should be careful to avoid the development of too many camels. Some prominent recent developments have been through many committee stages before the research recommendations are finalised. These recommendations then are discussed, and perhaps adjusted, by national or international regulatory committees, such as IMO.

The reasons for such collaboration are laudable and one can appreciate the hopes of the funding bodies that the best resources will be brought together to find great solutions, but they are not necessarily the most efficient use of research funding.

As consultants who work directly for industry on most of our projects, and occasionally for Governments or other funding bodies on contract research, we have no doubt that we can work most efficiently when we do not need to collaborate or coordinate our work with others. This is not arrogance, or an argument against all collaborative research, because it does have valuable benefits. Rather, it is a belief that we can offer good, practical solutions to problems most efficiently when we are given a clear remit and are left to conduct the technical work with a minimum of administrative effort. We do, of course, discuss specific issues with others when necessary and appropriate.

Two examples of different projects are considered to illustrate this point.

6. THE HARDER PROJECT

A good example of a recent major collaboration was the EU research project HARDER (Harmonisation of Rules and Design Rationale), which involved a consortium of 19 or-



ganisations from industry and academia. The project cost €4.5M and included some complex physical modelling on seven vessels. A number of papers have been published which present selected data and findings, for example Tagg & Tuzcu (2002).

A principal finding of that project was that the stability parameter that correlated most closely with wave height to cause capsize was the range of residual stability after damage. The GZmax values also showed reasonable correlation, although they varied with vessel type, and it was concluded that the most useful measure of survivability is a criterion based on the product of the two. Their recommended formula (1) for a survivability factor, s , was adopted by IMO as a basis for the probabilistic damage stability regulations of SOLAS 2009.

$$s = K \left[\frac{\text{GZmax}}{0.12} \times \frac{\text{Range}}{16} \right]^{\frac{1}{4}} \quad (1)$$

Where K is a constant, depending on ship type, GZmax is in metres, and Range is the range of positive stability in degrees.

It is unclear from Tagg & Tuzcu (2002) whether the HARDER researchers considered the inclusion of displacement or other ship dimensions to relate ship size to wave height, and thereby make their formula truly non-dimensional. The project concentrated on large ships, and their aim was to develop a method of assessment for certain types of ship, not a method that might be applied to vessels of any size. Notwithstanding that, the authors of that paper apparently believed the formula to be non-dimensional as they state "...since all factors in the equation are already non-dimensionalized."

The values 0.12 and 16 in their formula were empirically derived values of GZ and range, and the formula therefore appears non-dimensional. The use of a constant value to replace GZ in this way, however, returns the formula to a dimensional form. In practice, for

a limited range of vessel sizes and types, GZ curve characteristics tend to be similar because of regulatory or practical design constraints. The formula may be effective for a limited range of vessels, therefore, in the same way as conventional criteria that apply constant minima for all vessels, but it is no more non-dimensional than they are. If very small vessels had been considered it is likely that different constants, or perhaps a different formula, might have been required to fit their test results. Indeed, different values have been recommended to replace the constant 0.12 for ships of different types, such as Ro-Pax ships, where the value 0.25 is more appropriate. This aspect is discussed further in Tsakalakis et al (2009).

It is common for regulations to have different approaches or formulae for different sizes or types of ships, but it presents problems if design trends take new vessels outside the range of those used in the rule development. It would be preferable for truly harmonised standards to be non-dimensional and capable of assessing all vessels with a common formula.

Can a formula that requires significantly different empirical constants, depending on some definition of the ship type, really be regarded as harmonised? When designs develop away from the norm, how do they fit the formula?

Following independent trialling of the method by industry, prior to implementation of SOLAS 2009, some problems with its application were encountered. Vassalos & Jasionowski (2009) described these and concluded "...there is new evidence emerging that indicates gross errors in the derivation of survival factors, demanding swift action by the profession to avert 'embarrassment' on a global scale".

7. MCA RESEARCH PROJECT 509

A project that set out with very different aims but resulted in similar findings was the Maritime & Coastguard Agency's Research

Project 509. The remit was to assess the level of safety provided by the criteria for multihulls in the IMO HSC2000, and compare it with that provided by the criteria for monohulls. It was conducted independently by the Wolfson Unit, with a budget of only 3% of that of the HARDER project. It included model tests on six vessels, in a total of 53 intact and damage configurations (Deakin 2005).

On such a small budget the model tests were somewhat simpler than those in the HARDER project. They were no less valuable and informative however, with over 800 test cases, each conducted at a full range of headings to the waves to determine the vulnerability to capsize.

The problem with model tests of criteria, rather than specific ships, is that the model equally could represent a ship of a different size, at a different scale. Indeed it could represent a ship of any size. Only at one scale would the test condition represent a ship that just complies with the minimum criteria. Scaled to represent a smaller ship it would fail the criteria whilst a larger ship would have stability in excess of the minimum criteria because, although regulatory criteria do not vary with ship size, the GZ values are not non-dimensional. The work highlighted the fact that the level of safety provided by the criteria is dependent on the size of the vessel and the seastate in which it operates. Criteria based on the positive range of stability are the exception to this, because range is a non-dimensional parameter, unlike GZ or the area under the GZ curve.

Whilst it was not the objective, the outcome of the work was a recommendation for a new criterion, or method of estimating the minimum level of safety of a vessel, given its size and stability. As in the HARDER project, it was recognised that vulnerability to capsize depended largely on the residual range of stability but the secondary characteristic was found to be the maximum righting moment, rather than GZmax. A strong relationship was found between the critical wave height and the follow-

ing combination of residual stability characteristics:

$$\frac{\text{Range}\sqrt{\text{RMmax}}}{B} \quad (2)$$

Where Range is the range of positive residual stability in degrees, RMmax is the maximum residual righting moment in tonne.metres, and B is the beam of the vessel in metres.

This differs from the parameters used in most conventional stability criteria because it includes displacement in the righting moment term, which is beneficial, and beam, which is not. Although wide beam provides good initial stability, if two vessels of different beams have similar stability characteristics, the one with the wider beam generally will be more vulnerable to capsize.

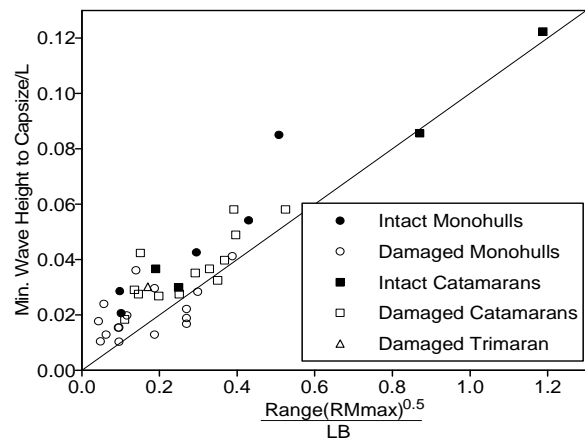


Figure 1: Relationship between stability and the minimum wave height to capsize from Research Project 509.

Figure 1 presents a summary of the model test capsize data, and demonstrates that the critical wave height appears to be independent of hull shape or damage configuration. The data have been made non-dimensional using the overall length to normalise both axes. Any model or ship capsize data can be compared on this graph.

The line on the graph represents the simplest formula that provides an effective fit to



the data. It was proposed as a method of estimating the critical wave height and is defined as:

$$\text{Critical Wave Height} = \frac{\text{Range} \sqrt{\text{RMmax}}}{10B} \quad (3)$$

To address safety in a seastate, it was proposed that the critical significant height be defined as:

$$\text{Critical Sig.Height} = \frac{\text{Range} \sqrt{\text{RMmax}}}{20B} \quad (4)$$

Since these formulae are derived from the non-dimensional relationship, they offer a truly harmonised means of estimating capsizing vulnerability, with no reference to vessel type or variation of constants. They do not pretend to offer a prediction of when a capsizing might occur, merely a limit within which a vessel can expect to be safe from capsizing. When operating beyond that limit a vessel may be vulnerable to capsizing, although the probability of capsizing may not be high.

When the formula was developed, early in 2005, it was based on these limited model test data. Subsequent analysis of other model tests, including those of the HARDER project, and documented ship capsizes has provided additional support for it (Deakin 2010). Figure 2 presents the evidence collected to date, all of which supports this simple formula.

Some casualty data lie on the proposed line, while others are substantially above it. The latter is to be expected in general because the line is an attempt to estimate the minimum wave height to capsizing, for the worst possible heading and wave frequency. Most model tests are not designed to identify this case, and we cannot assume that ship capsizes occur in the worst possible circumstances. Indeed, if the ship is under control, the crew generally make an effort to select a heading that they perceive to be relatively safe.

The latest additions to our casualty database have come from a recent investigation into the loss of the fishing vessel Trident in 1974, and are identified on Figure 2. The investigation concluded that the vessel capsized as a result of wave action and its stability therefore was inadequate for operation in that seastate (Young, 2011). For the casualty, the seastate obviously is an estimate. For the model test, the stability was not exactly the same as that of the ship, so the point lies at a different x-ordinate, but from the actual wave height time history it has been possible to determine the wave height that caused the capsizing (MARIN, 2008). This result represents the lowest seastate in which capsizing occurred in the model tests, but tests were not conducted in lower seastates, so it may not represent the minimum possible wave height to cause capsizing, which the line on the graph aims to represent.

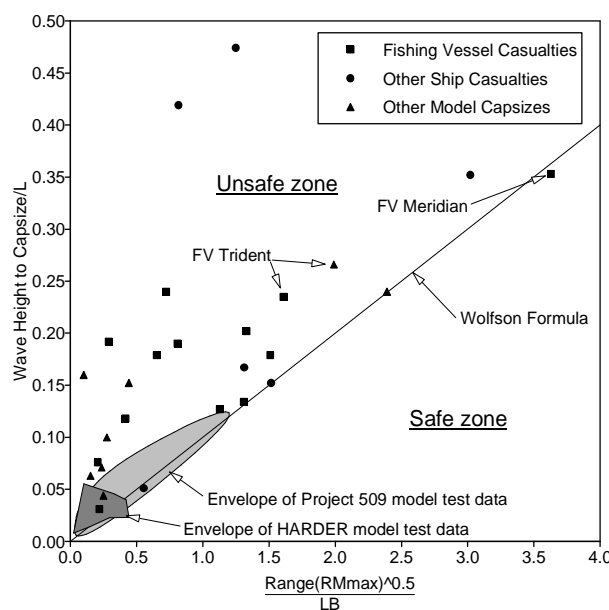


Figure 2: Correlation of casualty and model data with the proposed formula.

8. APPLICATIONS OF THE RESEARCH

The application of the HARDER project remains isolated to damage stability assessment of specific types of large vessels, as prescribed in the SOLAS requirements agreed at IMO. There it should provide a valuable tool to help



prevent loss of life, particularly when applied to passenger ships, and in time we may know whether it is a successful tool. Its adoption perhaps was inevitable, given the financial and political commitment to its development and the prominence of the organisations involved, but it is very sad that it appears to have no application to smaller vessels.

The Wolfson Unit's formula can be applied to any size and type of vessel. In the current climate it may be seen as too simplistic for adoption by IMO but, in the author's view, simplicity can be a strength. Regardless of its regulatory application, it is worthy of consideration as a basis for preliminary design assessment or, more importantly, for operational safety guidance.

An example where regulations proved inadequate but guidance might have been of value was Meridian, identified on Figure 2. This fishing vessel capsized while on guard duty in the North Sea in 2006 with the loss of all four crew. It had stability characteristics well in excess of the IMO minimum criteria, but was in severe weather with waves up to about 8 metres, and was only 22.7m long. With such good stability, its loss came as a surprise to the accident investigators, but safety guidance based on a formula such as this might have warned the crew, as the weather worsened, that they were operating with marginal safety.

The formula was used in the development of simple safety guidance for fishermen, as presented at STAB2006 (Deakin 2006). By considering the anticipated loading and lifting cases, the maximum recommended seastates can be determined to inform operational decisions. This is the most important and valuable development, and worthy of wider application.

The concept was further simplified for application to small boats without any stability information. The method provides approximate safety guidance based on the length and beam of a boat, by relating the residual freeboard to

the seastate. Three safety zones are defined, and are displayed on a single page Stability Notice which can be posted in the wheelhouse:

Green: "Safe" in all but extreme seastates

Amber: "Low level of safety" and should be restricted to low seastates

Red: "Unsafe, and danger of capsize" unless restricted to calm conditions and with extreme caution.

The seastate boundaries are defined by their significant height, H_s , in relation to boat size.

$$\text{Green/amber} \quad H_{s_{\text{amber}}} = \sqrt{1 + 0.4LOA} - 1 \quad (5)$$

$$\text{Amber/red} \quad H_{s_{\text{red}}} = (H_{s_{\text{amber}}})/2 \quad (6)$$

For vessels with no stability data the recommended minimum residual freeboards, F , that correspond to these seastates are:

Decked boats

$$\text{Green/amber} \quad F_{\text{amber}} = \frac{B}{L}(H_{s_{\text{amber}}}) \quad (7)$$

$$\text{Amber/red} \quad F_{\text{red}} = (F_{\text{amber}})/2 \quad (8)$$

Undecked boats

$$\text{Amber/red} \quad F_{\text{red}} = \frac{2.6B}{L}(H_{s_{\text{red}}}) \quad (9)$$

All units are metres. These formulae can be applied in a few minutes by anyone capable of using a tape measure and calculator, and might help to raise the safety awareness of those using small craft. They were derived using data for UK fishing vessels, for which they were harmonised with the IMO criteria, but the author believes that they can be applied much more widely, to many types of craft. This is just one method, and perhaps requires greater validation and development for wider application, but illustrates that practical solutions can be found without great expense.



Figure 3: FV Aleyna, photographed in 2006. She capsized in 2008 while fishing as a beam trawler.

The photograph in Figure 3 was taken in 2006. It shows a vessel of 14 metres which operated with very low freeboard for many years. Superimposed on the photograph is a freeboard guidance mark proposed as a means of relating the safety guidance directly to the vessel, for all to see. The mark spans the freeboards from “green” at the bottom to “red” at the top, as defined by equations (7) and (8). It is clear that, even when rigged as a stern trawler, and when upright, the vessel was operating predominantly in the amber or red safety zones. In 2007 it was rigged with heavier beam trawling gear and the safety margins would have been even smaller, but the heeling moments would have been much greater. The vessel capsized while trawling in 2008.

These marks are not intended to have any regulatory purpose, but to ensure that the owner, crew, their wives and indeed the whole community, become familiar with the level of

safety of a vessel and its limitations. They may help in raising safety awareness generally.

9. OUR RESPONSIBILITIES

In an ideal world, naval architects would take responsibility to make ships as safe as possible. We know how to make ships safer, but safety always comes at a cost. In practice, therefore, naval architects must find a compromise between safety and the cost of the ship, or the economics of its operation. Invariably they design the vessel to the regulatory minima, because that gives the most economical solution with acceptable safety. Traditionally, regulations and stability information booklets have done nothing to provide safety guidance to the master of a ship. They give the operator the confidence to go to sea in the belief that the ship is safe if operated within the specified range of loading conditions. It may



not be safe though, particularly if it is a small vessel in big seas.

We should all take responsibility for the safety of seafarers and passengers by developing and promoting the use of practical methods of assessing the level of safety of a ship in a range of seastates. We should be honest about the limiting seastates in which a ship might remain safe from capsizing.

Regulators have the greatest responsibility, but too often they are intimidated by industrial and political pressure. In the UK, for example, the proposal to provide small fishing vessels with the safety information and freeboard guidance marks as described above was opposed by the MCA, the UK's Government safety agency. Their argument was that it might reduce the market value of vessels with particularly low freeboard and make them difficult to insure.

As researchers, we should be honest about the value of our work in improving safety of lives at sea. Valuable resources are invested in stability research every year, but most of it is of no value to the majority of seafarers. We can strive for accurate capsizing simulation, but capsizing prediction is not a precise science. Can we do more to improve safety statistics? The author believes that we can, and looking beyond the limitations of STAB is important.

10. CONCLUSION

We all hope that funding for stability research will continue to be forthcoming. We should use what we learn to improve safety for all, by developing formulae like (3) or (4). These offer an honest means of safety assessment that takes account of size and seastate, and can be used to provide simple operational guidance.

We should put pressure on Governments to introduce requirements for simple safety guidance information, not complex regulation.

11. REFERENCES

- Deakin, B., 2005, "An Experimental Evaluation of the Stability Criteria of the HSC Code" International Conference on Fast Sea Transportation, FAST'2005.
- Deakin, B., 2006, "Developing Simple Safety Guidance for Fishermen", STAB 2006.
- Deakin, B., 2010, "Collating Evidence for a Universal Method of Stability Assessment or Guidance", Trans RINA, Vol. 152, Part A2, International Journal of Maritime Engineering.
- MARIN, 2008, "Seakeeping Tests for FV Trident", Volumes 1 & 2.
- Petursdottir, G., Hannibalsson, O. & Turner, J., 2001, "Safety at sea as an Integral Part of Fisheries Management", Food & Agriculture Organisation, Fisheries Circular No. 966.
- Tagg, R. & Tuzcu, C., 2002, "A Performance-based Assessment of the Survival of Damaged Ships". Final Outcome of the EU Research Project HARDER, Proceedings of the 6th International Ship Stability Workshop, Webb Institute.
- Tsakalakis, N., Vassalos, D. & Romanas, P., 2009, "Goal-Based Ship Subdivision and Layout", STAB 2009.
- Vassalos, D. & Jasionowski, A., 2007 "SOLAS 2009 – Raising the Alarm", 10th International Ship Stability Workshop, Hamburg.
- Viggósson, G. & Bernodsson, J. 2009, "The Icelandic Information System on Weather and Sea State", Seminar on Fishing Vessels' Crews and Stability, Vigo.
- Young, Sir S.S.T., Normandale, F.G. & Macwhirter N., 2011, Rehearing of the Formal Investigation Into the Loss of the Motor Fishing Vessel 'Trident'".





Nonlinear Observer Design for Parametric Roll Resonance

Dennis J.W. Belleter, *Department of Mechanical Engineering, Eindhoven University of Technology, The Netherlands*, d.j.w.belleter@student.tue.nl

Dominik A. Breu, *Centre for Ships and Ocean Structures, Norwegian University of Science and Technology, Norway*, breu@itk.ntnu.no

Thor I. Fossen, *Department of Engineering Cybernetics, Norwegian University of Science and Technology, Norway*, fossen@ieee.org

Henk Nijmeijer, *Department of Mechanical Engineering, Eindhoven University of Technology, The Netherlands*, h.nijmeijer@tue.nl

ABSTRACT

In this work a nonlinear two degrees-of-freedom (DOF) ship model is considered. For this model a state observer is designed in this paper. The type of state observer that is chosen is an Extended Kalman filter (EKF). First the theory for the design of an EKF is presented. Using this theory an observer in the form of an EKF is then designed to estimate the wave frequency and wave encounter frequency for the ship experiencing parametric roll resonance. The performance of the proposed EKF is verified by a simulation study. In the simulation study the estimates of the observer are compared against fictive measurements generated by a measurement generation model. The model determines the necessary control input to obtain a desired velocity and contains a wave spectrum model to excite the ship model.

Keywords: *Parametric roll, Nonlinear system, Observer design, Extended Kalman filter*

1. INTRODUCTION

Parametric roll resonance is a dangerous nonlinear resonance phenomenon for ships that can cause roll oscillations up to $\pm 40^\circ$ (France et al., 2003). Certain ship types such as fishing vessels and container ships have been shown to be especially prone to parametric roll resonance in moderate to heavy head or stern seas, with long crested waves. Parametric roll is induced by variations in the ship's transverse stability during a wave passage. (Carmel, 2006; France et al., 2003)

A lot of research has been done to model parametric roll and the ship's dynamics during parametric roll, see for instance Fossen and

Nijmeijer (2012) and Neves and Rodríguez (2005) and the references therein. Recent active control approaches are based on changing the ship's forward velocity (Holden et al., 2012), resulting in a Doppler shift of the frequency at which the ship is meeting the waves, the wave encounter frequency. Frequency detuning control can be used to alter the wave frequency out of a (ship specific) frequency range where the ship is susceptible to parametric roll (Holden et al., 2012).

Assuming constant heading, the wave encounter frequency is dependent on the wave frequency and the ship's speed. Frequency detuning control generally assumes the knowledge of both. However, while the ship's



speed is generally known the wave frequency is not and is nontrivial to obtain by measurements in a practical situation at sea. Consequently, a state observer to estimate the wave frequency and wave encounter frequency is crucial for the applicability of the frequency detuning control.

The 2-DOF ship model under investigation is a state-space model with five states. These states are the roll angle φ , the roll rate $\dot{\varphi}$, the velocity in surge direction u , the wave frequency ω_0 and the wave encounter frequency ω_e . This results in the state vector:

$$x = [\varphi, \dot{\varphi}, u, \omega_0, \omega_e]^\top \quad (1)$$

The roll angle, roll rate, and the velocity in surge direction are assumed to be measured. The wave frequency and wave encounter frequency need to be estimated by the state observer.

The paper is organized as follows. In Section 2 the model of the ship under investigation is introduced. The theory for the design of an EKF is introduced in Section 3. Followed by a simulation study in Section 4 where the EKF is used to estimate the wave frequency and wave encounter frequency.

2. THE SHIP MODEL

In this section the ship model under investigation with state vector (1) is introduced.

Table 1. Model parameters

Sym.	Quantity
m_1	mass and added mass in surge
d_1	linear damping in surge
μ	control input in surge
m_2	added mass and inertia in roll
d_2	linear damping in roll
B_i	disturbance amplitude
w_i	velocity disturbance frequency

\overline{GM}_a	amplitude of change in meta-centric height
\overline{GM}_m	mean value of meta-centric height
ρ	density of water
∇	water displacement of the ship
g	gravitational acceleration

The roll dynamics for the ship in Table 1 is given by:

$$m_2 \ddot{\varphi} + d_2 \dot{\varphi} + k(1 + A \cos(\omega_e t)) \varphi = 0 \quad (2)$$

with $A = \overline{GM}_a / \overline{GM}_m$ and $k = \rho g \nabla \overline{GM}_m$. This roll dynamics is a simplified version of the models in Fossen (2011).

The surge dynamics is given by:

$$m_1 \dot{u}(t) + d_1 u(t) = \mu + \sum_i B_i \cos(\omega_i t) \quad (3)$$

where μ is the control input in surge and $\sum_i B_i \cos(\omega_i t)$ is a disturbance due to a sinusoidal wave spectrum. The wave frequency is assumed to be constant and the wave encounter frequency can be obtained by (Fossen, 2011):

$$\omega_e(u(t), \omega_0, \beta_w) = \left| \omega_0 - \frac{\omega_0^2}{g} U(t) \cos(\beta_w) \right| \quad (4)$$

The assumption is made that the velocity in sway is much smaller than the velocity in surge such that the speed of the ship is given by $U(t) = \sqrt{u^2(t) + v^2(t)} \approx u(t)$. Moreover, it is assumed that the ship is sailing in head seas ($\beta_w = 180^\circ$). Hence, (4) is reduced to:

$$\omega_e(u(t), \omega_0) = \left| \omega_0 + \frac{\omega_0^2}{g} u(t) \right| \quad (5)$$

Using (2)–(5) a state-space model for the system can be formulated as:

$$\dot{x} = f(x, \mu, t) = \begin{bmatrix} x_2 \\ \frac{-(d_2 x_2 + k(1 + A \cos(x_5 t))x_1)}{m_2} \\ \frac{\mu}{m_1} - \frac{d_1 x_3}{m_1} + \sum_i B_i \cos(\omega_i t) \\ 0 \\ x_4^2 \left(\frac{\mu}{m_1} - \frac{d_1 x_3}{m_1} + \sum_i B_i \cos(\omega_i t) \right) \\ g \end{bmatrix} \quad (6)$$

$$y = h(x) = [x_1, x_2, x_3]^T$$

3. DESIGN OF THE EKF

In this section an algorithm for a discrete-time EKF obtained from Simon (2006) will be presented. However, to implement the algorithm the model (6) needs to be discretized first. The discretization takes the form:

$$\begin{aligned} x_k &= F_{k-1} x_{k-1} + G_{k-1} \mu_{k-1} + w_{k-1} \\ y_k &= H_k x_k + v_k \end{aligned} \quad (7)$$

where

$$\begin{aligned} F_{k-1} &= \exp\left(\frac{\partial f}{\partial x} \Big|_{\hat{x}_{k-1}^+} T\right) \\ G_{k-1} &= \int_0^T \exp\left(\frac{\partial f}{\partial x} \Big|_{\hat{x}_{k-1}^+} \tau\right) d\tau \frac{\partial f}{\partial \mu} \\ H_k &= \frac{\partial y_k}{\partial x} \Big|_{\hat{x}_k^-} \end{aligned} \quad (8)$$

Here T is the sampling time chosen as 0,1 seconds and w_{k-1} and v_k are Gaussian white noise processes with zero mean and covariance matrices Q and R , respectively. The covariance matrix of the measurement noise R is chosen as a constant diagonal matrix with entries based on the variances of the sensors, that is,

$$R = \text{diag}(\sigma_\varphi^2, \sigma_\phi^2, \sigma_u^2)$$

The estimation of the process noise covariance matrix Q is more complicated. For the measured states it should represent the uncertainty in the model equations. Note that for equations that are modeled exactly, like the first equation of (6), process noise can be omitted or given a small positive value for numerical purposes. For the states to be estimated it should represent the covariance of the noise driving the state estimates. These driving noise terms for the wave frequency and wave encounter frequency should not be chosen too large or the filter might become too aggressive in its adjustments. Moreover the state estimates might converge to the wrong value if Q is too large. Especially the entry for the wave frequency should be chosen very small since estimation of the wave frequency is a parameter estimation problem. Making Q a constant diagonal matrix yields:

$$Q = \text{diag}(Q_\varphi, Q_\phi, Q_u, Q_{\omega_0}, Q_{\omega_c})$$

Now the EKF can be initialized by:

$$\begin{aligned} \hat{x}_0^+ &= E(x_0) \\ P_0^+ &= E[(x_0 - \hat{x}_0^+)(x_0 - \hat{x}_0^+)^T] \end{aligned} \quad (9)$$

Here \hat{x}_0^+ denotes the original estimate for the states and P_0^+ is the initial state error covariance.

Then, at each discrete-time step of the Kalman filter the following has to be calculated. First the time update is done:

$$\begin{aligned} P_k^- &= F_{k-1} P_{k-1}^+ F_{k-1}^T + Q \\ \hat{x}_k^- &= f_{k-1}(\hat{x}_{k-1}^+, \mu_{k-1}, 0) \end{aligned} \quad (10)$$

with P_k^- the error covariance matrix of the error $\hat{x}_{k-1}^+ - \hat{x}_k^-$. In the time update the model is applied to the system to update the state estimate. The state error covariance is updated using the linearized system matrix form (8), the a posteriori state error covariance from the



previous time step and the covariance of the process noise.

The measurement update can then be done as in Simon (2006):

$$\begin{aligned} K_k &= P_k^- H_k^T (H_k P_k^- H_k^T + R)^{-1} \\ \hat{x}_k^+ &= \hat{x}_k^- + K_k (y_k - h_k(\hat{x}_k^-, 0)) \\ P_k^+ &= (I - K_k H_k) P_k^- (I - K_k H_k)^T + K_k R K_k^T \end{aligned} \quad (11)$$

where K_k is the Kalman gain, \hat{x}_k^+ is the a posteriori state estimate after the k -th time step and P_k^+ is the error covariance matrix of the error $\hat{x}_k^+ - \hat{x}_k^-$. The Kalman gain is calculated using the linearized measurements of (8) the a priori state error covariance and the covariance of the measurement noise. The estimate of the states is adapted by multiplying the error in the measured variables with the Kalman gain. Finally the a posteriori state error covariance is calculated using the Kalman gain and the covariance of the measurement noise.

As mentioned in Simon (2006), alternate formulations for K_k and P_k^+ can be chosen. However the formulations chosen here are to guarantee that P_k^+ is symmetric and positive definite as long as P_k^- is positive definite.

4. FREQUENCY ESTIMATION

The EKF of Section 3 will now be applied to the ship model (6) to create an EKF for the ship model. The EKF will be analyzed in a simulation study. However, to perform the measurement update, the Kalman filter needs a measurement of the roll angle, roll rate, and the surge velocity. Hence, a model to generate a fictive measurement is created first. This model includes a second-order wave model and a velocity controller. The wave model is based on the second-order wave model found in Fossen (2011) and takes the form:

$$h(s) = \frac{2\lambda\omega_0\sigma s}{s^2 + 2\lambda\omega_0 s + \omega_0^2} \quad (12)$$

where λ is a damping coefficient and σ is a constant describing the wave intensity. Both of these parameters are determined by a linearization of the wave spectrum as in Fossen (2011). The velocity controller is designed such that it keeps the velocity at a pre-described reference value r . The desired velocity u_d is generated by the second-order reference model:

$$\ddot{u}_d + 2\xi\omega_{lp}\dot{u}_d + \omega_{lp}^2 u_d = \omega_{lp}^2 r \quad (13)$$

with $\omega_{lp} = 0,1 \text{ rad/s}$ and relative damping $\xi = 1$.

Combining this with the surge model of (3) yields:

$$\begin{aligned} \dot{u} &= -\frac{d_1}{m_1} u + \frac{1}{m_1} \mu \\ \mu &= m_1 \left(\dot{u}_d + \frac{d_1}{m_1} u_d \right) \end{aligned} \quad (14)$$

The following acceleration profile is obtained:

$$\dot{u} = \dot{u}_d + \frac{d_1}{m_1} (u - u_d) \quad (15)$$

The wave disturbance and the measurement noise are added to the velocity after numerical integration to create a disturbed velocity profile. In addition to the wave model and the velocity controller the measurement model also has dynamical equations for the roll angle and roll rate. The EKF tracks these profiles.

For the unmeasured variables a confidence interval for the estimates is also given. This confidence interval is calculated using the diagonal elements of the state error covariance matrix resulting in:

$$\hat{x}_{99\%} = \hat{x} \pm 3\sqrt{P_{ii}}$$

A simulation study is now preformed in which the EKF needs to estimate a wave frequency of 0,4684rad / s. In the simulation study the ship accelerates to a constant velocity of 5,66m / s. This velocity is chosen such that the wave encounter frequency is about twice the ship's natural roll frequency given the specified wave frequency. As a consequence, the ship is experiencing parametric rolling which is apparent from the roll angle and roll rate plots in Figure 1. The initial conditions for the simulation study are chosen as:

$$[\varphi \quad \dot{\varphi} \quad u \quad \omega_0 \quad \omega_e]^T = \left[\frac{2\pi}{90} \quad \frac{\pi}{90} \quad 5 \quad \frac{1}{2} \quad 0.62 \right]^T$$

The simulation results for the measured variables can be seen in Figure 1. It can clearly be seen from Figure 1 that the estimation of the measured variables roll angle, roll rate, and surge velocity is trivial and they are estimated nearly perfect. For the velocity the EKF is tuned such that the filter does not follow all the disturbances on the velocity. This improves the estimate of the wave encounter frequency, which strongly depends on the velocity. Note that the maximum roll angle that is achieved in the simulation is approximately 0,5 rad which corresponds to about 29° and that the ship rolls with an angular speed of 0,15 rad/s which corresponds to about 9°/s. This is quite a heavy resonance. The resonance is lost after about 2400 seconds. The effect of this on the estimation of the unknown frequencies will be demonstrated later.

The results of the estimation of the wave frequency can be seen in Figure 2. Figure 2 has a plot of the wave frequency estimate including the confidence interval and a plot with a detail of the mean of the wave frequency estimate.

From Figure 2 it can be seen that the mean is estimated quite well until the resonance is lost; after this the estimate retains a bias. This is due to the fact that the estimation of the wave frequency is a parameter estimation process.

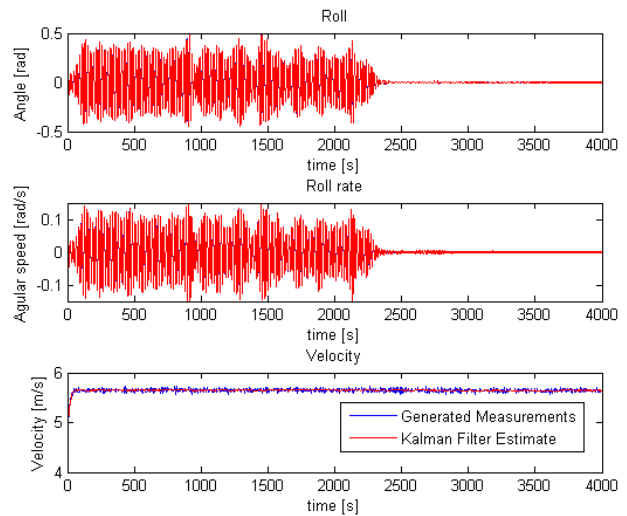


Figure 1: EKF frequency estimation of the measured states for the ship in resonance

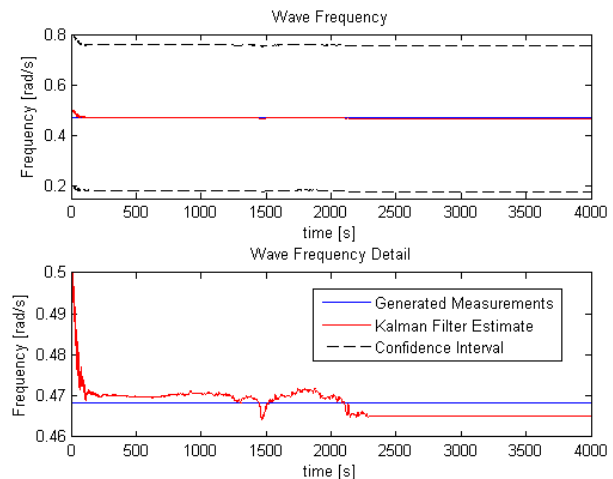


Figure 2: EKF frequency estimation of the wave frequency with detail of the mean estimate

This means that the estimate for the wave frequency is not adjusted in the time update (10) since $\dot{\omega}_0 = 0$. Hence, the state estimate is only adjusted by the measurement update (11). This makes the adjustment of the state estimate dependent on the size of the Kalman gain and the error in the measured variables. When the resonance is lost at about 2400 seconds, the error in the state estimate of the roll angle also reduces significantly and the wave frequency state estimate is hardly adjusted.

From Figure 2 it can also be seen that the confidence interval for the wave frequency estimate only converges very slowly. This can



also be attributed to the fact that the estimation of the wave frequency is a parameter estimation process. The adaptation of the state error covariance of the wave frequency in (10) is governed by the small process noise term driving the estimate of the wave frequency.

Figure 3 shows the results of the estimation of the wave encounter frequency. The top plot in Figure 3 shows the wave encounter frequency estimate and its confidence interval. The bottom plot in Figure 3 shows a detail of the estimate of the wave encounter frequency and its confidence interval.

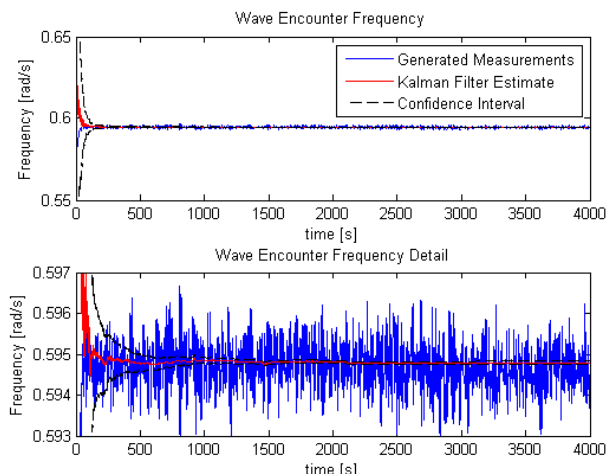


Figure 3: EKF frequency estimation of the wave encounter frequency with a detail of the mean estimate

From Figure 3 it can be seen that the estimate for the wave encounter frequency converges to the correct value quite fast. Moreover the confidence interval also converges to within acceptable bounds quite fast. Note here that just like with the estimation of the velocity the filter is tuned such that the estimate tracks the mean of the wave encounter frequency and does not try to track all the disturbances. This would cause a filter that is too aggressive and is more likely to diverge. A close inspection of the wave encounter frequency estimate shows that when the resonance is lost, the estimate of the wave encounter frequency is adjusted less and the confidence interval increases a little. This is because the noise terms become more dominant for small values of the states. When the noise is larger with respect to the states the

uncertainty in the state estimates becomes larger. Hence, the state error covariance increases.

Good initial performance of the filter is obtained by a suitable choice of the initial state error covariance. For the measured states this is not an issue, however for the unmeasured states it is. If the initial error covariance is chosen too small the filter will be sluggish and it will take longer for the estimate to converge or it might not converge at all. If the initial state error covariance is chosen too large the filter will react very aggressive in the beginning which can cause the state estimate to overshoot the true value and oscillate around it for a while. Both under tuning and over tuning of the initial state error covariance can cause the wave frequency to diverge. Hence, it is important to have a good initial estimate of the wave frequency when initializing the filter. Figure 4 shows the wave frequency and wave encounter frequency for a filter with large initial error covariance to illustrate the mentioned problems.

For convergence the choice of the process noise covariance is also important. Large values for the process noise covariance will allow the filter to track the noisy signals of the velocity in Figure 1 and the wave encounter frequency in Figure 3 more closely. However, large values for the process noise covariance will also cause the filter to be more sensitive to e.g. a loss of the resonance which can cause the state estimate of the wave frequency and wave encounter frequency to diverge and their confidence interval to increase. However the filter will always need some process noise to adjust the estimates.

5. CONCLUSIONS

An EKF used as a state observer has been designed to estimate the wave frequency and wave encounter frequency of a ship experiencing parametric roll. This observer is designed on the basis of a ship model.

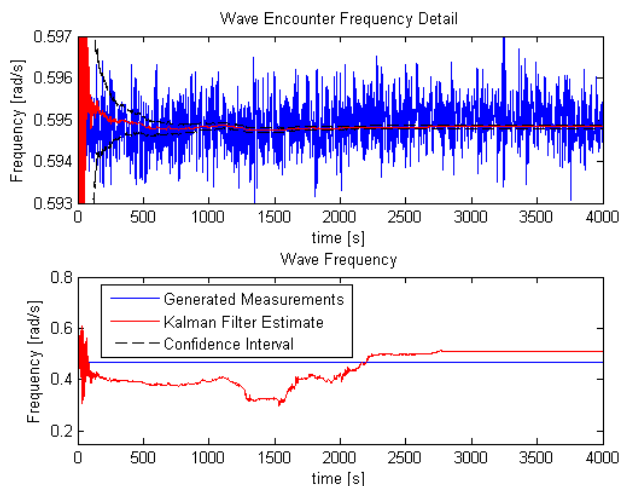


Figure 4: Wave encounter frequency and wave frequency estimate with large initial error covariance

The estimation of the wave frequency proved to be quite difficult due to the fact that the estimation of the wave frequency is a parameter estimation process. It has been shown that this parameter estimation process needs the parametric resonance to readily adjust the state estimate. Moreover the confidence interval only converges very slowly since it is only adapted by the small process noise term driving the filter. The estimate for the mean of the wave encounter frequency is good and converges fast. The confidence interval for the wave encounter frequency also converges to an acceptable value quite fast. It has to be noted though that estimation of the wave encounter frequency also becomes more difficult when the resonance is lost. The filter is sensitive to tuning of the initial state error covariance matrix and to the tuning of the process noise covariance matrix. This can cause a long time for convergence of especially the wave frequency. Hence, for good performance of the filter and convergence it is important to make a suitable choice for the process noise error covariance and the initial state error covariance.

6. REFERENCES

Carmel, S. M., 2006. "Study of parametric rolling event on a panamax container vessel." Journal of the Transportation

Research Board, vol. 1963, pp. 56–63.

Fossen, T. I., 2011. Handbook of Marine Craft Hydrodynamics and Motion Control. Wiley.

Fossen, T. I. and Nijmeijer, H. (eds.), 2012. Parametric Resonance in Dynamical Systems. Springer.

France, W., Levadou, M., Treakle, T. W., Paulling, J. R., Michel, R. K., and Moore, C., 2003. "An investigation of head-sea parametric rolling and its influence on container lashing systems." Marine Technology, vol. 40, No.1, pp. 1–19.

Holden, C., Breu, D. A., and Fossen, T. I., 2012. "Frequency Detuning Control by Doppler Shift." Fossen, T. I. and Nijmeijer, H. (eds.), Parametric Resonance in Dynamical Systems, Springer.

Neves, M. A. S. and Rodríguez, C. A., 2005. "On unstable ship motions resulting from strong non-linear coupling." Ocean Engineering, vol. 33, pp. 1853–1883.

Simon, D., 2006. Optimal state estimation. Wiley.





Monitoring of Dynamic Stability via Ship's Motion Responses

Hossein Enshaei, *Newcastle University*, h.enshaei@ncl.ac.uk
Richard Birmingham, *Newcastle University*, r.w.birmingham@ncl.ac.uk

ABSTRACT

Exploring the links between sea state and a ship's course provides the opportunity to monitor dynamic stability and hence to avoid significant changes of stability. The experimental test on a Ro-Ro model in irregular sea confirmed the ability of heave and pitch motion to mimic the current sea condition. Therefore detection of peak frequencies and associated magnitudes could be utilised to limit a large ship's motion. Motion responses are considered as signals with time-dependent spectral content, and signal processing as a suitable technique for detection, estimation and analysis of recorded time-varying signals. The method is fast enough to be considered as online monitoring of dynamic stability.

Keywords: *dynamic stability, motion response, peak frequency, signal processing*

1. INTRODUCTION

Stability is one of the most important requirements for safe operation of a ship, as insufficient stability can lead to the capsizing of a vessel and the loss of life and property. For safe operation it is essential to maintain adequate stability during all operational and loading conditions. Ships sailing in adverse weather conditions are likely to encounter various kinds of dangerous phenomena.

Of a ship's dynamic responses, synchronous rolling and high roll motions are two potential dangers facing a ship and that can be avoided by taking appropriate action in ample time.

Over the past two decades, significant progress has been made in understanding of ship dynamics and its application to predicting ship motions, in employing model testing techniques, and in advanced computational methods (Belenky *et al.*, 2008). However, several limitations and deficiencies in these techniques still exist, such as uncertainty in

defining the no return heeling threshold or in defining the level of safety and reliability, or in accepting inadequate simplifications, and these have rendered the results not always completely successful (Francescutto, 2004).

However, very little attention has been paid to evaluating the responses of a vessel in calculating the stability parameters using the current International Code on Intact Stability (IS Code), as the data concerning stability that is available to the ship's operator is generally still based on a ship's hydrostatics.

It was emphasised in IMO 2002 that a range of sea conditions should be taken into account when developing an instrument for evaluating the effects of a ship's design parameters on ship safety in a seaway. In line with this, the International Towing Tank Conference (ITTC) 2005 considered specific operational aspects when evaluating the safety level of a ship. The evaluation should consist of a series of specified physical tests for given scenarios and environmental conditions.



According to Francescutto (2004), intact stability criteria fulfil the design purposes by and large however to assure absolute safety, attention should be more focused on operational measures.

A reliable, easily applicable method is essential in order to alleviate the dangers of heavy seas, be it a following, quartering, beam or head sea and such a method should avoid any manual computation. One solution is to address the ship's stability, in particular from the operational point of view. Operational stability is very complex but one important task is to explore the links between the sea state and the ship's course.

It is obvious that in dealing with real time stability issues, the key factor is the current sea state which should be addressed in the assessment of adequate intact stability.

the wave induced motion responses of a ship are an attractive method of assessing and comparing the performance of ships in rough weather. Ship motions and the waves encountered can be recorded simultaneously and analysed using spectral analysis techniques. However, waves are irregular and without an accurate technique for recording them, the results obtained are unreliable estimates of the sea state. This becomes even more complicated when the ship is underway and the frequency of wave encountered changes.

This paper demonstrates that some influential parameters of encountered waves can be detected through the monitoring of heave and pitch motions. Because of a strong

coupling nature, these motions are in tune with irregular wave patterns and therefore their responses can be regarded as applicable tools for the detection and estimation of the influential wave parameters. This information can be used by the master in making operational decisions.

The stability status changes during operations and decisions taken regarding stability should not rely solely on the experience of the master. This proposed method makes it possible to be aware of a developing critical situation that could result in the stability condition deteriorating, thus maximising the time available to take corrective action by means of altering course.

2. AIMS AND OBJECTIVES

The motions behaviour of ships in an environment that is characterized by waves and winds varies according to the different sea types encountered and this adds to the complexity of the dynamic responses when underway.

The aim of this paper is to demonstrate that it is possible to avoid high roll angles and hence excessive reductions of stability over long periods of time which increases the probability of capsizing. Detection of the peak frequency of motion and its corresponding magnitude in time can be a practical solution to monitoring the vulnerability of ships in different seas and operating conditions. Therefore the peak frequency of irregular waves that are encountered can be detected by

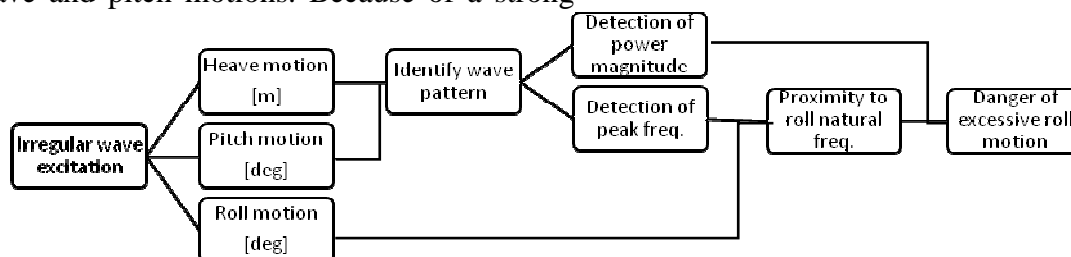


Figure 1: Block diagram of the methodology to predict high roll motion.



the spectral analysis of heave and pitch motions over time. The paper also intends to evaluate the sensitivity of the roll response to ranges of encountered peak frequency that are close to the roll natural frequency using an approach as shown in Figure 1.

Ship's motion is of a time-varying nature and can be measured by the means of sensors as a continuous time signal. Therefore signal processing techniques can be employed as a tool to analyse such a signal for subsequent operational purposes.

The objective of this study has been to select a suitable method and develop a computer program using signal processing techniques in order to detect and indirectly estimate the influential wave parameters through measurements of motion responses. The program could help an operator to take corrective action to prevent a dangerous situation and avoid eventual stability failure. This could be reliable method, which can be a supplement to the current IMO recommendations (IMO, 2007), to avoid dangerous situations from developing in adverse weather and extreme sea conditions.

3. METHODOLOGY

An experimental model-based approach was chosen for the development of practical tools to deal with the problem of dynamic stability in waves. Six degrees of freedom motion response tests of a Ro-Ro model have been carried out in simulated irregular waves under intact conditions. A stationary model was tested in different sea states and ship headings and the investigation was limited to the effects of encountered frequency components and the associated magnitude of energy of the ship's motion responses. The measurements are presented and discussed in terms of peak frequency and peak power in the motion responses of the model.

This study uses Short Time Fourier Transform (STFT) technique to detect and demonstrate the identified influential parameters. Therefore vulnerability of ships in different seas and operating conditions can be monitored to provide early warning of developing critical stability situations. This span can be achieved in a sufficiently short time of about half a minute.

4. SIGNAL PROCESSING

Without a proper technique for recording and analysing the actual waves experienced in real time by a ship the results obtained can only be related to potentially unreliable visual estimates of the sea state.

The first time that it was suggested that the ship itself could be treated as filter with input not of the electrical signals but of the waves, was in 1953 by St Denis and Pierson.

The majority of signals encountered in the real world vary with time. Sea waves and swell could also be considered as signals with time-dependent spectral content which are self generated in nature. Taking a ship's parameters and loading conditions into consideration, the vessel's motion responses could be the best representation of the current sea conditions. The processing of such signals can thus be used to form the basis of more complex motions analysis of ships at sea.

Accuracy, availability or delays in obtaining data for the analysis of a time series are the main constraints to implement appropriate instrumentation and analysis methods for the online monitoring of ship responses. Measurements of local waves while the ship is underway are the leading challenges; however signal processing techniques can be effective in detection of wave's influential parameters through analysis of ship motion responses. Some of the variables of the system can be detected by spectral analysis of heave and pitch responses.



These variables reflect the wave peak frequencies and associated magnitudes which can cause high roll motions when it is in line with natural roll frequency.

In this study Short Time Fourier Transform (STFT) method is used to analyse recorded time series of ship's motion responses for specified short time period.

4.1 Signal Processing Methodology

From a mathematics point of view, a given signal can be represented in an infinite number of ways via different expansions. The Fourier transform, however, has been the most common tool used to study a signal's frequency properties. The two most frequency approaches to describe a signal's behaviour in terms of frequency are the Fourier transform (linear) and the power spectrum (quadratic). However, based on either the Fourier transform or the power spectrum alone, it is hard to tell whether or not a signal's frequency contents evolve in time. Although the phase characteristic of Fourier transform $S(\omega)$ contains the time information, it is difficult to establish a point-to-point relationship between the time signal $s(t)$ and $S(\omega)$ based upon the conventional Fourier analysis. This is because the basis functions used in the classical Fourier analysis do not associate with any particular time instant, and thus the resulting measurements do not explicitly reflect a signal's time-varying nature.

The introduction of time-frequency (TF) signal processing has led to it being possible to represent and characterize time-varying signals using time-frequency distribution (TFD) (Boashash, 2003). TFD are two-dimensional functions which provide time and spectral information simultaneously. The distribution of signal energy over the TF plane uncovers information not available in the time or frequency domains alone. This includes a number of components that are present in the signal such as; time duration,

frequency bands, relative amplitudes, phase information and Instantaneous Frequency in the TF plane (Shafi, 2009).

A typical goal in signal processing is to find a representation in which certain attributes of the signal are made explicit. Therefore, the central issues of signal processing are how to construct a set of the elementary functions $\{\psi_n\}_{n \in \mathbb{Z}}$ and how to compute the corresponding dual functions $\{\hat{\psi}_n\}_{n \in \mathbb{Z}}$. Either of these can be used for the analysis functions to compute the expansion coefficients or the transform. For good results, the set of analysis functions should be simple to use and able to achieve a high level resolution.

5. DESCRIPTION OF EXPERIMENT SET-UP, TEST CONDITIONS AND MEASUREMENTS

A range of significant wave heights and peak frequencies were chosen in order to develop a particular short-term sea state with a Pierson Moskowitz (PM) sea spectrum. The experiments were carried out in the towing tank of the University of Newcastle-upon-Tyne. The experiments involved systematic measurements of the heave, pitch and roll motions of a stationary model in an intact condition for three different headings in irregular seas.

In the experimental programme, waves were generated by a group of wave makers at one end of the tank. The wave heights and periods were monitored and recorded using two wave probes and an associated monitor.



Figure 2: The Ro-Ro model in the towing tank with the Qualisys markers in place.

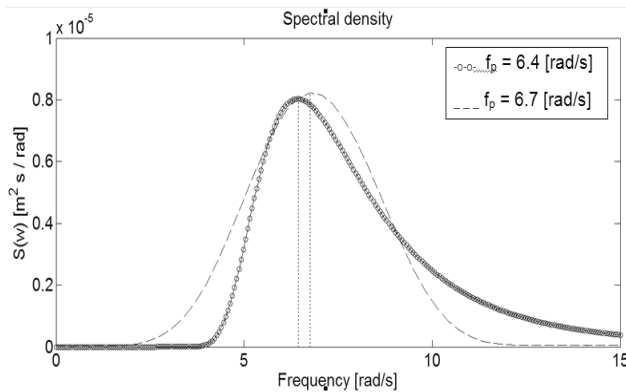


Figure 3: Comparison of Pierson Moskowitz sea spectrums developed by continuous time-varying data and WAFO mathematical modelling.

A Qualisys Track Manager (QTM) with a ProRelex motion capture camera was used to track the motions of the model under the different wave conditions and to process the video data directly and then convert it into coordinates. This system offers a quick way to obtain accurate 6 degrees of freedom (DOF) information compared with more traditional methods using motion sensors attached to a model.

The data output has 6DOF tracking which in every frame locates the current position and orientation of one or more rigid bodies in the measurement space.

A general view of the Ro-Ro model condition with attached Qualisys markers is shown in Figure 2.

5.1 Particulars of the Model

The study was carried out using an available RO-RO ship for which model test data obtained from previous experiments was available together with the main particulars of the model (Emin *et al.*, 2004). Prior to the experiments, the mass of the bare model was measured and then ballasted with weights to obtain an even keel. The model ratio is 1:125 which is suitable for the size of the towing tank facility (Arias, 1998a, 1998b).

5.2 Accuracy of Data

in order to ensure that the data collected from the wave probes matched with the desired output spectrum, test data was evaluated in the Wave Analysis for Fatigue and Oceanography (WAFO) environment (WAFO, 2000).

In Figure 3 the input signal to the wave maker consisted of the significant wave height (H_S) of 0.024 m and a peak frequency of 1.02 Hz (6.4 rad/s). The spectrum output characteristic was compared against a mathematical model with a H_S of 0.027 m and a peak frequency of 1.06 Hz (6.7 rad/s).

Figure 3: Comparison of Pierson Moskowitz sea spectrums developed by continuous time-varying data and WAFO mathematical modelling.

Although there is a slight difference between the two curves shown in Figure 3, the model's motion responses were compared against the characteristics of the generated spectrum, which is depicted as the estimated frequency peak and the power peak in the figures shown in the results given in Section 6, below.

In order to consider the possible influence of the nonlinear interactions between encountered, reflected, and radiated waves, the readings of the two wave probes were compared against each other. Although there was found to be a slight difference in the output histograms, the statistical variance and mean remained exactly the same for every test conditions undertaken.

5.3 Test Conditions

The total number of recorded runs was 27, which comprised of three peak frequencies, with three significant wave heights and three heading angles. The heading angles were 0°, 45° and 90° corresponding to following, quartering and beam seas, respectively.



Table 1 lists the intended spectrum characteristics applied to the wave maker in order to generate irregular waves. Due to the large volume of the results obtained after analysis of each motion response, only a sample of the analysed power spectrum in the model scale conditions is shown in Figure 4, based on the model peak frequency of 0.965Hz and a H_s of 0.072 m.

Table 1: Experimental wave conditions

Peak Frequency (Hz)		Significant wave Height, H_s (m)		Sea state
Model	Ship	Model	Ship	
0.695	0.062	0.024	3	Low
1.022	0.091	0.048	6	Medium
1.579	0.142	0.072	9	High

Each test was run for eight minutes in order to avoid initially unreliable results and once the irregular wave was fully developed then the various motions were recorded. The wave conditions stated above were selected in order to maximise the possible benefits from the test runs over a wide range of frequencies. The model was free from green water effects and the mooring lines did not apply any excessive force to avoid restraining the motions.

6. RESULTS

The continuous time-varying data of both the motion responses and the incoming waves were recorded using LabVIEW software. The recorded data was analysed using power spectral density (PSD) method, which describes how the power of a signal or time series is distributed with frequency. The time domain window selected was the Hanning type and the sampling rate for data acquisition was 100 Hz. The results of free decay tests are given in Table 2.

Table 2: Measured natural frequency of model.

Particulars	Heave	Pitch	Roll
Natural frequency of model (Hz)	1.48	1.71	1.4

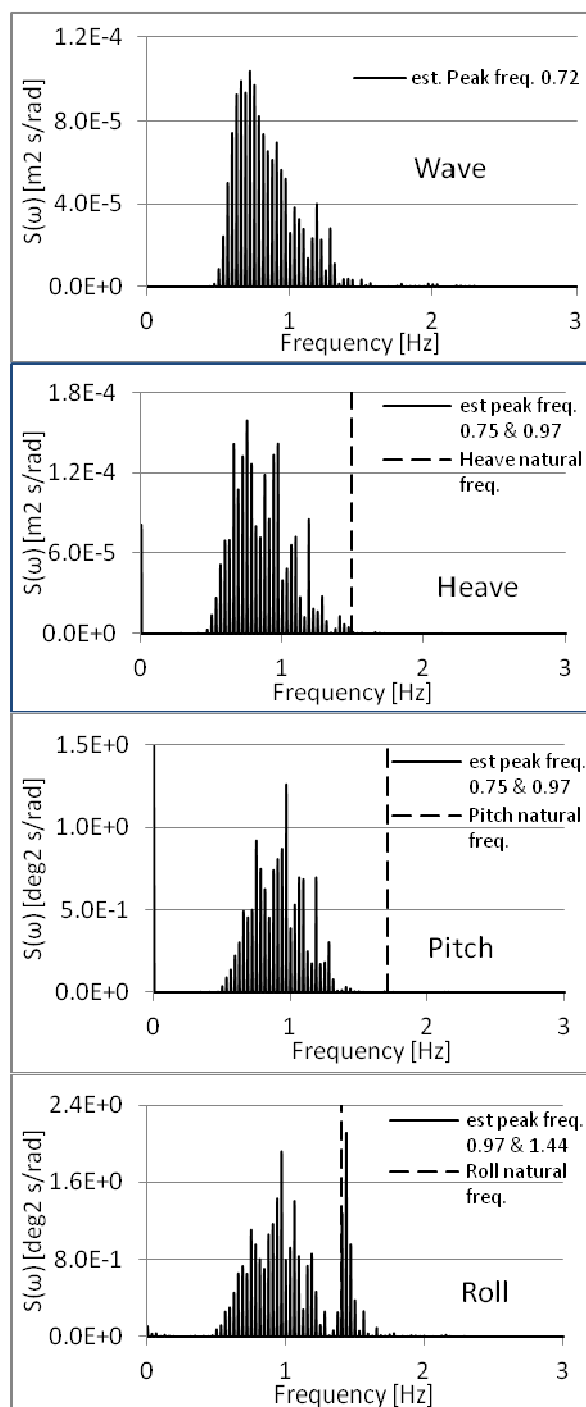


Figure 4: Power spectral analysis of Wave, Heave, Pitch and Roll motions of the model.



The figures presented in this section represent the motion responses of the ship; the x-axis presents the sea conditions (defined as 'low', 'medium' and 'high' for the three different peak frequencies that were utilised in generating the wave spectrum) and the y-axis is either the estimated frequency peak (rad/s) or the estimated power peak (deg² s/rad for pitch and roll, m² s/rad for heave). the respective motions have been scaled for ease of comparison.

In the following discussions, the main emphasis is on the effects of the estimated frequency peak and the power peak on the motion responses and on any other notable trends that are observed in the response curves.

6.1 Motion Responses in a Following Sea

The responses of the pitch and heave motions are seen to be strongly coupled and closely follow the peak frequency of waves in different sea conditions. However, the roll motion maintains a response that is close to its natural frequency.

A similar trend can also be observed where the value of H_S is increased. However, the coupling effect of heave and pitch under low sea conditions is not as strong as in high sea conditions and it appears to be less significant at a medium H_S value. The roll response however remains nearly constant for every sea condition and H_S value tested.

The changes in heave and pitch magnitudes are in line with changes in wave magnitude. However, the roll magnitude does not reflect these changes and follows a steady trend with a slight decrease at high frequencies.

The rate of roll motion response increases in the higher sea state where the range of wave peak frequencies is closer to the

model's natural roll frequency and it reaches its maximum at the large H_S value. The coupling effects of heave and pitch motions are obvious in all sea conditions and at every H_S value tested and their magnitude remains high except when at high frequencies.

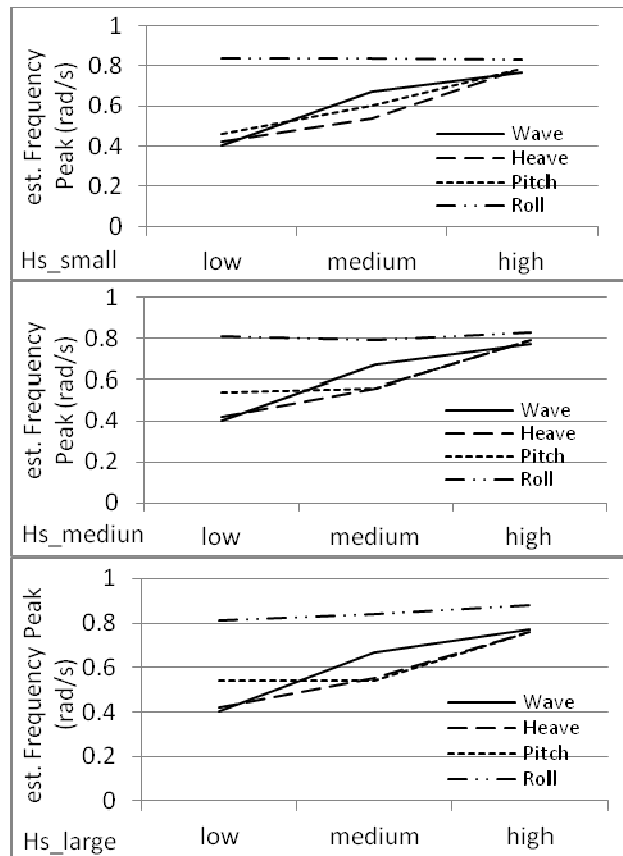


Figure 5: Comparison of peak frequencies for each sea condition tested in a quartering sea. a) small H_S , b) medium H_S , c) large H_S .

6.2 Motion Responses in Quartering Sea

The results in Figure 6 are interesting and comparable with the results obtained from the following sea tests which indicate that a change of sea direction from stern to quarter has less of an effect on peak frequencies. The coupling effects of heave and pitch motions are similarly maintained throughout the change in heading angle.



The trend in changing amplitude as depicted in Figure 6 is complementary and corresponds with roll responses in a following sea. The magnitudes of heave and pitch motions reach their maximums in medium sea conditions.

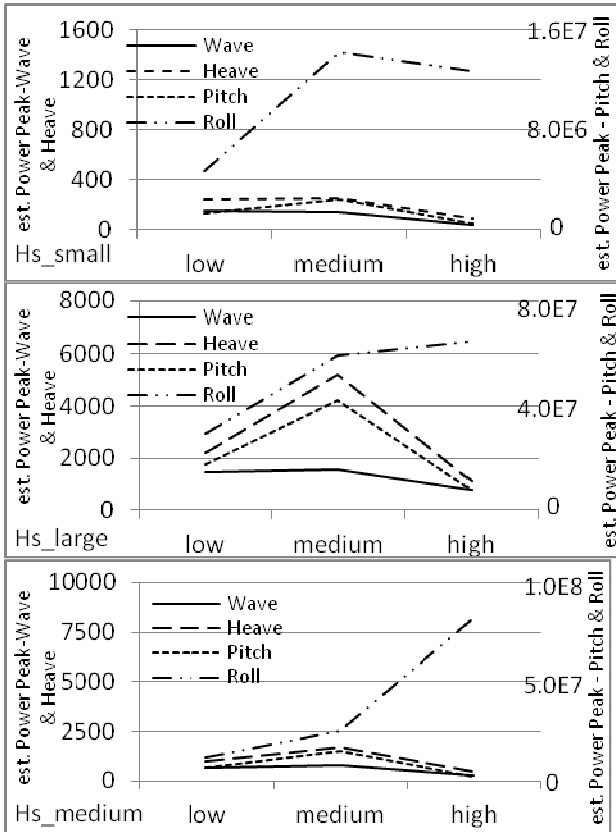


Figure 6: Comparison of energy magnitudes for each wave condition tested in a quartering sea: a) small H_s , b) medium H_s , c) large H_s .

6.3 Motion Responses in a Beam Sea

The consistency in maintaining peak frequency in roll motions is also observed in a beam sea. The strong couplings amongst all motion responses are dominated by roll and heave motions around the roll natural frequency. The pitch motion response tracks the wave peak frequency but being less sensitive in the low sea condition.

The magnitudes of motions are scaled, and the trend that is observed is a good indication of coupling effects being dominated by roll response in beam seas.

It was observed that the roll motion maintains its highest oscillation around the natural frequency in all sea conditions regardless of the heading angle. Roll is magnified when the peak frequency of the wave approaches the natural roll frequency of the model; therefore, keeping these apart avoids the potential for a large amplitude motion response. Alteration of course away from a beam sea would reduce the roll motion.

6.4 Roll Response in all Sea Conditions at Different Headings

Frequency ranges of the generated wave spectrum increased towards the higher sea conditions and it is apparent that the level of wave energy has to decrease at higher frequencies.

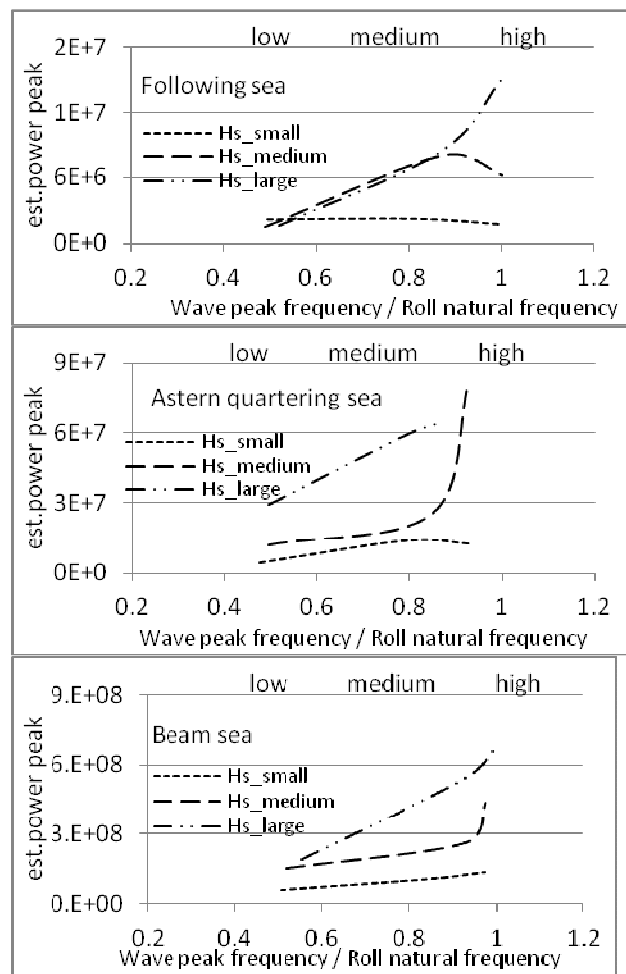


Figure 7: Roll responses under different wave operating conditions.

Figure 8 shows that the roll responses are directly related to the ratio of the wave peak frequency to the roll natural frequency and that the maximum responses occur around unity and which subsequently becomes exponential. The wave energy has less effect on the power magnitude of the roll motions. It also shows that the maximum power peak is obtained during beam seas and is reduced in a following sea.

7. DETECTION OF WAVE INFLUENTIAL PARAMETERS

For the online monitoring of ship's dynamic stability a relatively reliable and fast method is required in order to detect the wave peak frequency and associated magnitude. By referring to Figure 4 it is evident those eight minutes of exposure time duration is rather long and that a ship could have been seriously damaged in a critical situation. However, it is possible to detect these influential parameters in much shorter periods, potentially in as little as fractions of a minute by using signal processing techniques.

The STFT approach was chosen in this study to analyse the recorded data. This data is for incoming waves as well as heave, pitch and roll motions in the form of continuous time varying signals. STFT has a number of attractive features which can detect the signal characteristics that are not obvious either in the time domain or in the frequency domain alone. Detection and estimation of peak frequency and associated amplitude is achieved in a fraction of a minute.

Spectrogram can be employed to visualise the detected signal for monitoring purpose where the changes are imminent and displayed graphically.

A spectrogram of each motion response is shown in the Figure 8 as obtained after computing STFT of the signal. The STFT spectrogram is calculated as the magnitude

square of the elements in STFT. Because the FFT returns symmetric results, the spectrogram shows only the left half of the STFT. In Figure 8 the top left window is an intensity graph used to display the spectrogram. It returns the quadratic time-frequency representation of the signal and each row corresponds to the instantaneous power spectrum at a certain moment in time. The lower window depicts the sampled time signal and the right window the corresponding frequencies of the sampled signal obtained by FFT.

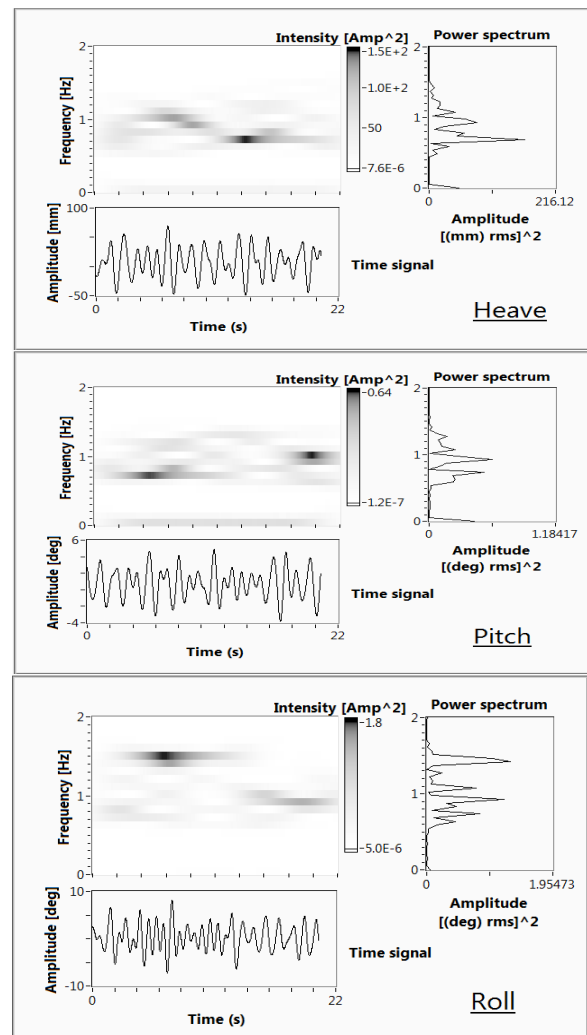


Figure 8: Detected and estimated peak frequency and magnitude of heave, pitch and roll responses for a sample of 20sec duration.



Energy density distribution and peak frequencies are detected and estimated by TFA through a Hanning window. Frequency bins and window length are both set to be 1024Hz.

7.1 Effect of Window and Sampling on the Quality of Detection

An important feature of a spectrogram is readability which is achieved when there is a good concentration of the signal components. The type of window and the sampling size can influence the visual interpretation which is necessary for obtaining a good discrimination between known patterns.

A window function is a mathematical function that is zero-valued outside of some selected interval. The type of window functions chosen has a significant effect on the detection of roll peak frequency response.

The most significant drawback of the STFT as an estimator is in the TF resolution trade-off that results from windowing of the signal. The window length shapes the time resolution and the frequency resolution of the STFT. A narrow window results in fine time but a coarse frequency resolution because of the short time duration and wide frequency bandwidth. However, conversely a wide window results in fine frequency but a coarse time resolution. Therefore the window length should be calibrated for optimum concentration and obviously better resolution.

The other two characteristics of windowing which can affect the quality and the resolution of a detected signal are the sampling size and the frequency bin.

8. SUMMARY AND CONCLUSIONS

This study was carried out in two stages. The first stage was based on the spectral analysis of the motions response test of a

model of a Ro-Ro vessel in irregular waves. Six degrees of freedom motion responses of the stationary model were measured over 27 different combinations of wave peak frequencies and significant wave heights in different heading angles.

In the second stage, the focus was on exploring the signal processing technique in order to detect and estimate the peak frequency and associated magnitude of motion responses.

The following conclusions can be drawn from this study:

- One of the significant findings to emerge from this study is that the peak frequency of both heave and pitch motions tend to follow irregular wave peak frequencies for all headings. The only exception is the heave motion in a beam sea which couples with the roll motion.
- It was observed that roll motion tends to oscillate around the model's natural frequency in all sea conditions and different heading angles. Roll is sensitive to a limited range of encountered peak frequencies associated with the sea state and the distribution of the response energy is concentrated at the natural frequency.
- Taken together, these findings suggest that heave and pitch motions could serve to identify the encountered wave pattern to become a suitable tool for the detection of wave's peak frequency and magnitude.
- The results of this study indicate that the instantaneous frequency and power magnitude of heave, pitch and roll motions could be obtained through a signal processing technique. The STFT is a suitable method for the detection and estimation of a time varying signal of motion responses.
- The significance of this method, if used for monitoring, is that the detection of the



influential parameters can be achieved in a fraction of a minute.

An implication of these findings is that they can be used in enhancing the safe operation of a ship via the development of a tool to monitor ship motions and appropriately advise the navigator to take corrective action.

Such a tool could:

- Evaluate the potential vulnerability of a ship to adverse sea conditions by detecting components of encountered frequency and their corresponding magnitude.
- Detect parameters that can be used as performance indicators to warn of the development of a critical situation and hence a reduction in stability.
- Advise an alteration of course and heading relative to the waves in ample time to avoid large and potentially dangerous roll motions.

If the concept is to be moved forward, a better understanding of the different hull responses needs to be developed. Obviously the effects of length, displacement and speed should be taken into consideration.

9. REFERENCES

- Arias, C., 1998, "Selection of Design Cases and Operation Scenarios, "DEXTREMEL Report", Report No DTR-1.0-AESA-03.98, Rev. 2.
- Belenky, V., Ottodekat, J. et al., 2008, "Toward Performance-Based Criteria for Intact Stability", *Marine Technology*, 45, 2, pp. 101-123.
- Boashash, B., 2003, "Time-Frequency Signal Analysis and Processing", Prentice-Hall, NJ, USA.
- Emin, K., Atlar, M., Incecik, A., 2004, "An Experimental Study of Motion Behaviour with an Intact and Damaged Ro-Ro Ship Model", *Ocean Engineering* 31, 483-512.
- Francescutto, A., 2004, "Intact Ship Stability: The Way Ahead", *Marine Technology*, Vol. 41, No. 1, January 2004, pp. 31-37.
- IMO, 2002, "International Maritime Organization Document SLF 45/6/ 7, Head Sea Parametric Rolling and Its Influence on Container Lashing Systems", Submitted by the United States, Subcommittee on Stability and Load Lines, and on Fishing Vessels Safety, 45th session, July 22-26, London.
- IMO, 2007, "Revised Guidance to the Master for Avoiding Dangerous Situations in Adverse Weather and Sea Conditions", MSC.1/Circ.1228.
- ITTC, 2005, "Basic Frameworks for Stability Assessment - 4.2", Proceedings of the 24th ITTC - Volume II, Edinburgh, UK.
- Shafi, I., Ahmad, J., Ismail Shah, S., Kashif, F.M., 2009, "Techniques to Obtain Good Resolution and Concentrated Time-Frequency Distributions: A Review", *EURASIP Journal on Advances in Signal Processing*, (Article ID 673539), pp. 43.
- St Denis, M. P., W.J., 1953, "On the Motions of Ships in Confused Seas", *TSNAME*.
- WAFO, 2000, "A Matlab Toolbox for Analysis of Random Waves and Loads", Lund Institute of Technology, Centre for Mathematical Science, Version 2.0.02.





Blind Estimation of Wave State from Ship Motions in Navigation

JIANG Lin, *University of Yunnan China, mumgift@gmail.com*

LI Ji-de, *University of Harbin Engineering, College of Ship Engineering, IN 150001, China*

ABSTRACT

In_situ and real time information of ocean wave states is indispensable for safety and reliability of shipping and seakeeping study. To avoid heavy burden of installation and maintaining of wave measuring devices in rough sea, we take ship as a wave sensor, utilize ship motion in navigation to estimate ship transfer function and wave spectral simultaneously based on blind signal processing. This algorithm uses short time series and the ship motion RAO is assumed unknown.

Keywords: *ship motion, blind identification, wave spectra, inverse problem, optimization*

1. INTRODUCTION

Now, in addition to theoretic wave spectral (Wen 1993), we can gain wave states information by wave rider buoy, SAR and X-band Marine Radar, and measured ship motion. WaMoS II (Skey, S., K. 2006) provide acceptable directional ocean wave and sea surface wind information on a global scale.

Buoy records can convert the measured heave, pitch and roll into wave height and slopes, and have highest accuracy, but it is confined to the fixed site.

Based on radar backscatter information rather than the wave elevation itself, wave retrieval from radar images has higher computational complexity (Nieto, J.C. G.R. 2004) and installation height requirement.

Utilizing ship as a wave sensor is another way to obtain wave information, it can provide wave information along seaway with less calculation and no extra installation cost.

Some efforts have already been described (Iseki, T. 2000, Eduardo A.2003, Ulrik Dam Nielsen 2005, Johuson M. C 2005). Those methods can provide directional spectra on board, but they all based on cross spectrum and RAO prepared beforehand. Therefore, it is hard to avoid the uncertainty caused by the fluctuation of sailing conditions.

Another effort (Johuson M. C 2005), formulate the relationship between the ship motion and wave states with a simple statistic estimation, the estimation is based on past, instead now.

2. BLIND IDENTIFICATION

In_situ and real time information of ocean wave states is indispensable for safety and reliability of shipping and seakeeping study.

Our work is to explore the feasibility of applying Blind Signal Processing method in retrieving wave state information and ship



motion transfer function in near real-time simultaneously. This is a kind of blind inverse question, and has wide applications (Joseph Lardies2011, E.Caetano 2006). Civil Engineering structures have peculiar characteristics (large size and relatively low natural frequencies) that make difficult the current application of classical input output modal identification techniques. Therefore, there is presently a clear tendency worldwide to explore and improve the potential of output-only modal identification techniques.

2.1 Generating simulation environments

Knowing the mean square spectral density function $S(\omega)$ of the wave elevation $\zeta(t)$, shortly called wave spectrum, the elevation of an irregular sea can be modeled as a finite sum of sinusoidal components with a random initial phase.

For short-crested seas, the amplitudes of wave components are determined with directional wave spectrum $S(\omega, \alpha)$

$$\zeta_{ij} = \sqrt{2S(\omega_i, \alpha_j)} \Delta_\alpha \Delta_\omega \quad (1)$$

$$\zeta(t) = \sum_{j=1}^N \sum_{i=1}^M \{ \zeta_{ij} \cdot \cos(\omega_i t + \varepsilon_{ij}) \} \quad (2)$$

Then, the ship motion in irregular sea can be written as

$$x(t) = \sum_{i=1}^M [h_{yi} \cdot \zeta_{ai} \cos(\omega_{ei} t + \varepsilon_{yi} + \varepsilon_i)] \quad (3)$$

Where, ε_i is random initial phase of the irregular waves, h_{yi} , ε_{yi} are the amplitude and phase of ship motion transfer function, corresponding to the regular input wave component in unit amplitude at ω_{ei} .

After sampling and combining with additive noise $z(n)$, the observed time series of ship motion is

$$y(n) = x(n) + z(n) \quad (4)$$

Figure 2 shows the simulated pitch motion in heading sea.

2.2 Initial estimation

In order to suppress the noise with symmetric probability density functions and extend the adaptation to non-minimum phase ship motion system, we chose fourth-order cumulants as the input of the blind identification algorithm. The analytic representation of ship motion signal

$$Y(n) = Hilbert\{y(n)\} \quad (5)$$

And the definition of fourth-order cumulants of it is

$$C_{4y} = cum\{Y^*(n), Y^*(n + \tau_1), Y(n + \tau_2), Y(n + \tau_3)\} \quad (6)$$

Under assumption AS1~AS4 (Zhang 2002), the estimations of AR can be obtained based on 1-D slices of the 4th order cumulants

$$\sum_{i=0}^p a(i)C_{4y}(m-i, n) = 0 \quad (7)$$

The transfer function of the AR model is

$$H(z) = \frac{1}{1 + a(1)z^{-1} + a(2)z^{-2} + \dots + a(p)z^{-p}} \quad (8)$$

For $z = e^{j\omega}$, the frequency response function:

$$H(j\omega) = \frac{1}{1 + a(1)e^{-j\omega} + a(2)e^{-j2\omega} + \dots + a(p)e^{-jp\omega}} \\ = \text{Re}[H(j\omega)] + j \text{Im}[H(j\omega)] = H_0(\omega)e^{j\varphi(\omega)} \quad (9)$$

Where, $H_0(\omega)$ is the initial modeling of ship motion, and the start point of iterative optimization.

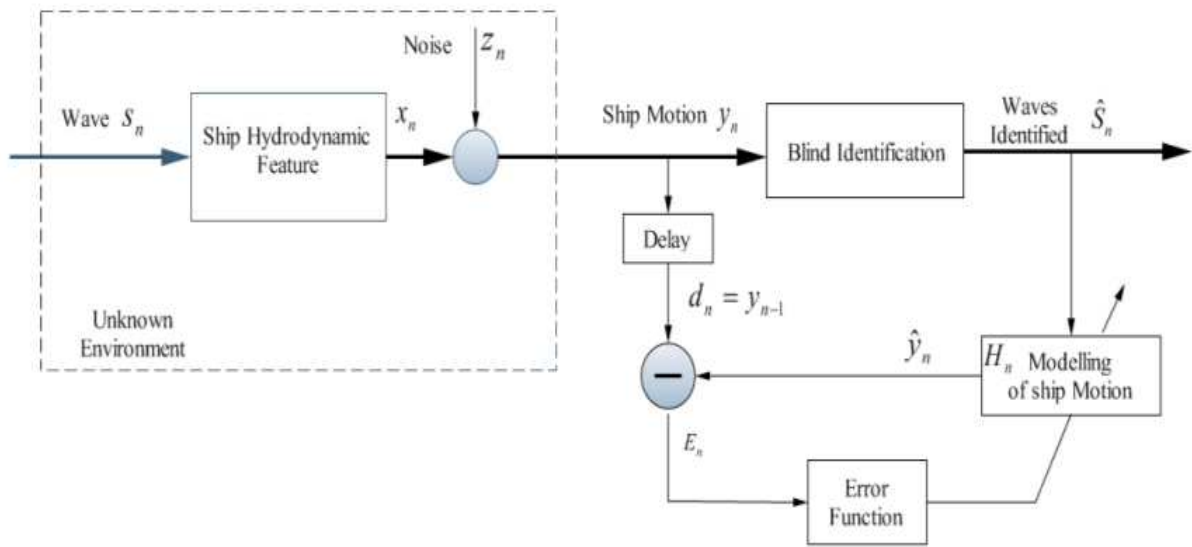


Figure 1: Blind identification.

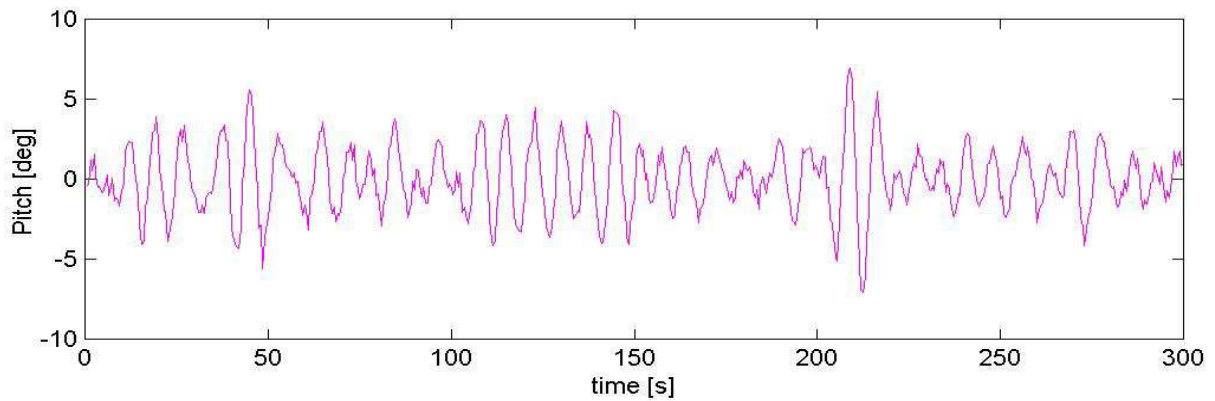


Figure 2: Pitch motion in heading sea (Simulated).

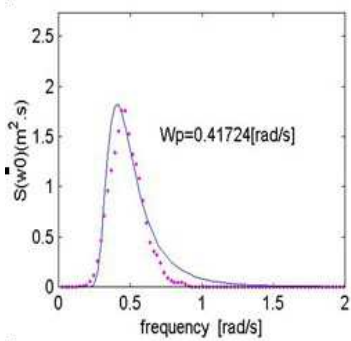


Figure 3: Wave spectrum

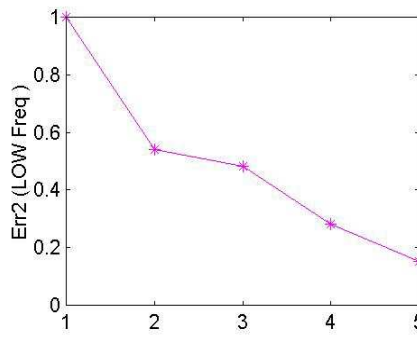


Figure 4: Convergence

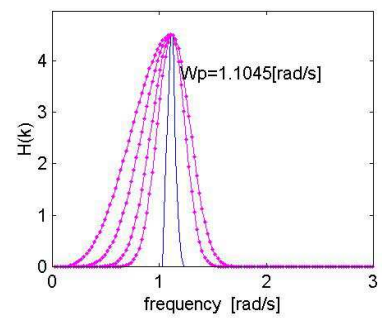


Figure 5: Optimization

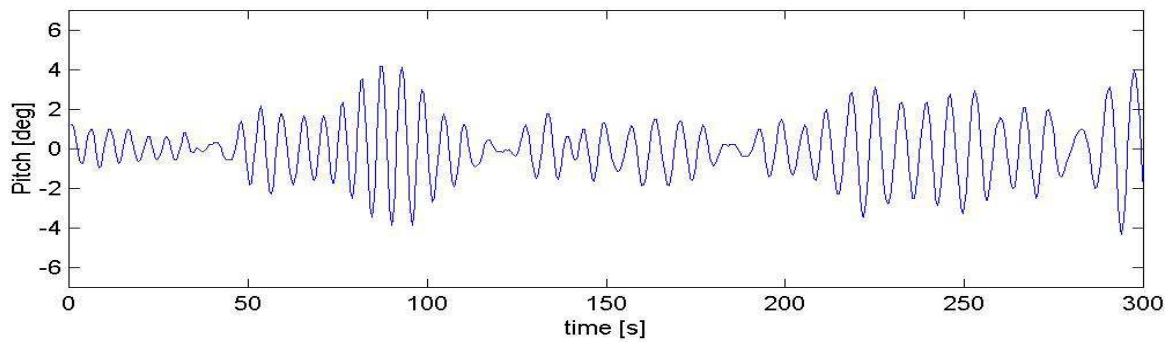


Figure 6: Pitch motion in heading sea (Observed in a sea trial)

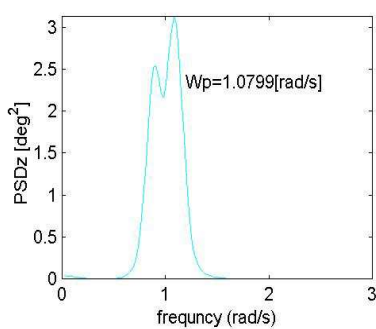


Figure 7: Motion spectrum

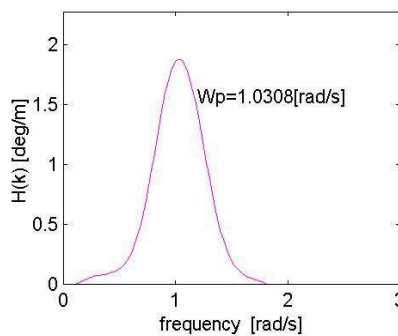


Figure 8: Pitch H(k)

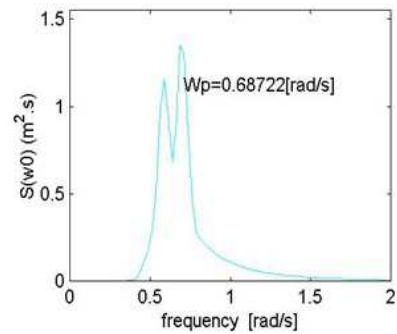


Figure 9: Wave spectrum

Instead using long data sequence as most HOS based methods required, we adopted short data sequence for the blind identification, 256×4 . This help to improve the real-time features of the estimation, but the results are more sensitive to noise, especially at very low SNR. This is one of the reasons to use optimization iteration.

Inverse problems, especially the 1-D blind identification are known to be mathematically ill-posed, solutions being extremely sensitive to small variations in the observed output.

In order to avoid heavy deconvolution noise, three feature of pitch motion, ie narrow band, nonnegative, near normal, were utilized as regularizations in the process of minimizing error function

$$E(k) = \left\| D(k) - \hat{Y}(k) \right\|^2 \quad (10)$$

In a few steps, as shown in figure 4, the

optimization process fulfil two tasks simultaneously. The first, pitch motion transfer function is determined (figure 5); the second, wave spectrum is identified (figure 3).

2.4 The Results

Some sea trial data were used to verify the blind estimation method. As Figure 6 shows, the pitch motion time history in heading sea is the input of the blind identification algorithm, the outputs is pitch motion transfer function (figure 8), and the wave spectrum (figure 9). And, Figure 7 shows the power spectrum of the pitch motion time history in heading sea.

3. CONCLUSION

In assessment of seakeeping performance, it is hard to identify wave states and the ship



motion, and ship motion model at same time exactly.

The proposed algorithm does not require ship motion model, and is able to get in-situ sea states information at real time. Corresponding to the ship motion, the estimated wave spectrum describe the current driving source of the ship motion, this wave states information is fundamental for seakeeping performance study and ship operation safety.

Based on the initial research, a new research project was established, and we are working on it in a more comprehensive way both in time and frequency domain, aim to provide in situ information for seakeeping study and ship opration.

REFERENCES

- Caetano E., and C. Moutinho, (2006), From Input-Output to Output-Only Modal Identification of Civil Engineering Structures, Internal Operational Modal analysis Conference , pp 1-22.
- Dannenberg Jens and Katrin Hessner, 2010, "The On Board Wave and Motion Estimator OWME", *Proceedings of the Twentieth (2010) International Offshore and Polar Engineering Conference Beijing*, China, June ,pp20-25.
- Eduardo A., (2003), Estimating directional wave spectrum based on stationary ship motion measurements. *Journal of Applied Ocean Research* 25, pp243–261.
- Iseki Toshio, (2000). Bayesian estimation of directional wave spectra based on ship motions. pp215-219
- Iseki, T., Ohtsu, K., & Fujino, M. ,(1992), "A study on estimation of directional spectra based on ship motions", *Journal of Japan Institute of Navigation* 86, pp179-188.
- Johuson M. C. and Wilson. P. A., (2005), Sea state estimated from ship motions by a simple statistical approach. *International Journal of Maritime Engineering*, Royal Institution of Naval Architects.pp35-51
- Lardies Joseph and Ta Minh-Ngi, (2011), Modal parameter identification of stay cables from output-only measurements in *Mechanical Systems and Signal Processing*,pp133-150
- Nielsen Ulrik Dam, (2005), "Estimation of Directional Wave Spectra from Measured Ship Responses", DTU Mechanics, Section for Coastal, Maritime and Structural Engineering. Phd thesis.
- Nieto, J.C. G.R. Rodríguez, K.Hessner, and P. I.González, (2004): Inversion of Marine Radar Images for Surface Wave Analysis. *Journal of Atmospheric and Oceanic Technology*, 21, pp1291-1300.
- Skey, S., K. Hessner, K. Reichert, J. Dittmer, I. Tränkman, and D. Resio, (2006): Spectral and Individual Wave Measurements by WaMoS II at Duck, *13 th Ocean Sciences Meeting*.
- Wen, S.-C., Guo, P.-F., and Zhang, D.-C.,(1993), Analytically derived wind-wave directional spectrum. Part1. Derivation of the spectrum. *Journal of oceanography* 49(2), pp131-147.
- Wen, S.-C., Guo, Pei-Fang, Zhang, D.-C., Guan, Chang-Long, and Zhan, H.-G. , (1993). Analytically derived wind-wave directional spectrum, Part 2. Characteristics, comparison and verification of spectrum. *Journal of oceanography* 49(2), pp149-172.
- Zhang Xianda, (2002), *Modern Signal Processing*. Beijing, Qinghua Univ. Press.





System Identification for Wave Measurements Using Ship as a Buoy

Alexander Degtyarev, *Saint-Petersburg State University, Faculty of Applied Mathematics and Control Processes, Russia, deg@csa.ru*

Ilya Busko, *Saint-Petersburg State University, Faculty of Applied Mathematics and Control Processes, Russia, trassae95st@mail.ru*

Yury Nechaev, *St.Petersburg State Marine Technical University, Russia, int@csa.ru*

ABSTRACT

Use ship as a buoy is well known approach now. It takes possibility to understand sea state in seagoing conditions and to predict local wave weather. For correct identification of sea state it is necessary to solve inverse problem of ship motion, when we have to on the basis of known class of models describing ship motion on waves, parameters of ship state and motion and realizations of different kinds of ship motion to determine character of input process (sea waves). In the paper problems of computation procedures for onboard systems are discussed. Linear and nonlinear classes of ship motion models are considered. Use of ship motion models with single and multi degree of freedom are considered too. Results of full scale experiments with different types of ship are shown.

Keywords: *wave parameters, identification algorithm, adaptive model, uncertainty, intelligent system.*

1. INTRODUCTION

In evaluating wave parameters of marine dynamic objects in the operating conditions one of the most difficult problems is to restore the perturbation spectrum. The problem is solved on the basis of indirect dynamic measurements of oscillation motion of the dynamic object (DO) in a seaway. As shown in (Nechaev, 2005), there is a black-box identification problem in adaptive control when DO operate. Both the structure and parameters of perturbation are unknown and there is a need to restore the required characteristics in the real-time mode. The paper deals with the problem of parametric identification based on the adaptive model that can be carried out in the on-board

intelligent system (IS) of the new generation (On-board systems, 2006), (Nechaev,2011).

2. FORMULATION OF THE ADAPTIVE IDENTIFICATION PROBLEM

2.1 Overview

The first researcher to raise the wave parameter identification problem on the basis of object behavior was Y. Nechaev (Nechaev, 1990, 1996). Further this problem was developed in other works that used the same approach. Over the past ten years, this problem has become rather popular and there have appeared different approaches to the wave spectrum evaluation. The works of



(Nielsen, 2006, 2008, 2011), (Simons, 2010), (Pascoal, 2009) and others are of the most significance. The aims of many works were the methods allowed to obtain estimates of the wave spectrum through the ship's response to external effects. Research was made to find out whether these methods were possible and could be applied. Besides, the comparative research of various methods was made. Some works investigated how much the use of a method is determined by various physical parameters and how much the wave spectrum evaluation depends on the method applied (Iseki, 2001), (Nielsen, 2011). The Bayesian approach was one of the most popular evaluation approaches in terms of sea environment (Iseki, 2001), (Nielsen, 2008). The Kalman filter is also used by some researchers to solve the problem (Pascoal, 2009). However, only the evaluation of the integral parameters can be considered as a complete solution. The integral parameters are the parameters of the spectral density of wind waves, represented by any form of approximation, for example, that of Barling (Nielsen, 2011).

2.2 Formulation

Fig. 1 shows a general functional diagram of the wave parameter identification (Eykhoff, 1974) when sea DO with a single input and a single output is in the operation. The roll sensor $X(t)$ sends signals from the measuring system to the DO input and the adaptive model. The output of the system is represented as:

$$y(k,t) = y(k) + s(k), \quad (1)$$

where $y(k)$ is the output signal of the object; $s(k)$ is an additive noise. The identification error is the following:

$$\varepsilon_k = y(k,t) - y^*(k,t), \quad (2)$$

It is the difference between the output signals $y(k, t)$ and model $y^*(k, t)$.

The sent signal is pre-processed in the initial IS information conversion module where it is filtered and converted to digital codes (On-board systems, 2006).

The adaptive model is adjusted to ensure that its output signal is consistent with the output signal of an unknown object according to the best mean-square approximation criterion. According to this criterion the error must tend to the minimum value. Satisfactory approximation of signals is possible when the adaptive model provides an effective coefficient readjustment algorithm.

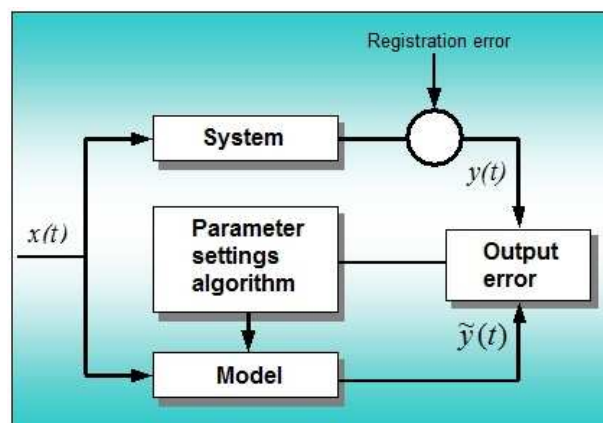


Figure1: The structural diagram of identification.

After adapting the model there can arise situations when both the structure and the parameters of the unknown object are determined but the correlation between the input and output signals is preserved. The reason is that in practical applications the identified object is "is a noise object", i.e. it has an internal random perturbations. The noise component of the output signal is considered as an additive random noise that is not generally correlated with the output signal of a dynamic object. Therefore, when the adaptive algorithm is properly configured, the signal at its output is fully consistent with the input signal except for the noise component. This means that the weighting factors in the adaptation process converge to the optimal



values which are independent of the system noise.

When black-box control objects are identified, a priori knowledge about the behavior of a dynamic object on a sea is used to select the setting parameters of the adaptive model. According to the analysis of the tests (On-board systems, 2006), in practice it is enough to have preliminary information about the transient response setting time t_{set} , because the time to adapt model T_a depends on the time required to establish the correlation $T_a \leq t_{set}$. This dependence is valid for a pronounced oscillatory process.

Thus, the algorithm of the adaptive identification of wave parameters can be executed as a sequence of steps:

Step 1. The time quantization interval is set in the time interval $T_0 \in [t_1, t_k]$.

Step 2. The allowed T_a adaptation time is set based on the analysis of the field data (On-board systems, 2006).

Step 3. The required identification accuracy is set with the allowable value of the relative error of the adaptive algorithm.

Step 4. The condition for convergence of the adaptation process is determined.

Step 5. Adaptive identification requirements in the real-time mode are stated.

The Identification algorithm is implemented in a multiprocessor computing environment based on the dynamic knowledge base of the onboard intelligent system. The wave identification problem is connected with the uncertainty registration and has two important aspects. The first aspect is connected with the a priori uncertainty of the perturbation spectrum, the second deals with the construction of the identification algorithm in harmful interference when the level of disturbance is commensurate with the level of noise.

3. THE CONCEPT OF WAVE IDENTIFICATION

The traditional approach used by many researchers rests on the assumption that a vessel can be represented as a linear system. It is in the assuming of the possibility of representing a vessel by linear system. This is crucially important as this approach makes it possible to apply the correlation between the input and output spectral densities to reconstruct wave parameters. It is known that in this case relation between the input and output spectral densities to restore the wave parameters.

$$S_y(\sigma) = |\Phi_{xy}(\sigma)|^2 S_x(\sigma), \quad (3)$$

where $S_x(\sigma)$ is a spectral density of the input process that can be associated with the disturbance, i.e. sea waves; $S_y(\sigma)$ is a spectral density of the output process, i.e. the registered process of ship vibrations caused by waves; $\Phi_{xy}(\sigma)$ is a transfer function of a linear system.

In this case it is possible to use a standard wave reconstruction scheme (On-board systems, 2006) (Fig. 2). At fig.2 φ , v are a heading angle and vessel speed; MS is a measurement system, $\theta(t)$, $\psi(t)$ are rolling and pitching; $S(\sigma)$ is estimation of spectral density of ship motion.

The following works are focused to the solution to the problem in terms of the classical control theory and neuro fuzzy systems (Nechaev, 2003, 2005, 2011). The analysis of these studies makes it possible for us to state the major issues: to formulate the following main issues:

1. Noise level or other physical interferences can make it difficult to detect. To detect a noise signal or highlight a desired signal to background processes due to other physical causes. As a consequence, only uninformative signals are received.

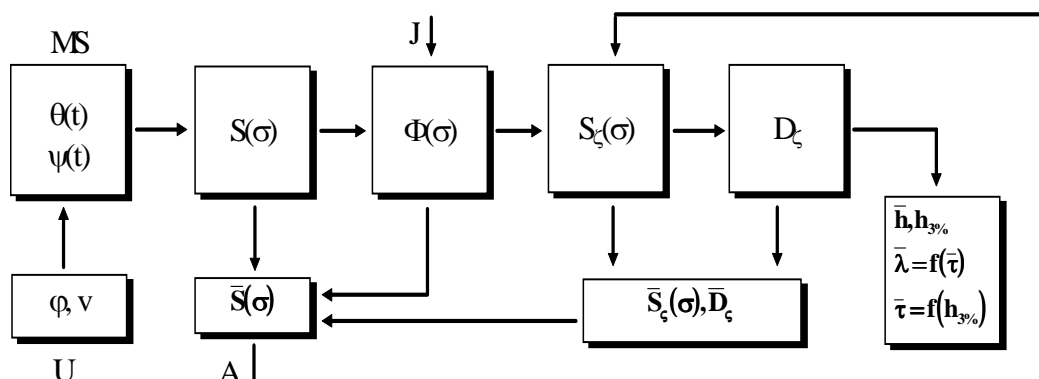


Figure 2: The algorithm for wave identification in case of a linear system.

2. Use of spectral density approximations can facilitate wind-wave reconstruction (see, e.g. (Nielsen, 2011)).
3. To register non-linear oscillation, the assumptions used in case of a linear system cannot be applied. Assumption violation of system linearity for registration of non-linear oscillations. This situation often occurs in case of strong external influences.

To solve these problems it is possible to use additional information to cross-check the results obtained in different ways. To obtain a reliable signal, both oscillation processes – pitch and roll of a dynamic object can be used (see Fig.2). The results to be used for wave reconstruction will be different for each of the processes. At the same time it is possible to select information components and increase the accuracy of wave identification if different data sources are considered during the experiment.

Another problem associated with the use of well-known spectral density approximations can be solved based on the “climate spectrum” concept (Boukhanovsky et al., 2000, Degtyarev, 2011). Proceeding from this concept, if the operation area, season and weather history are known, it is possible to set in the wave reconstruction procedure certain spectral density approximations typical of the current conditions.

The integrated approach can be applied to solve the non-linearity problem. The easiest way is to select the optimal conditions to register dynamic object oscillations. Before the wave reconstruction procedure the nonlinearity degree of the recorded process should be determined. Algorithm (On-board systems, 2006) can be applied for this procedure. This algorithm makes it possible to determine the equilibrium position of a dynamical system depending on the degree of oscillation asymmetry caused by the nonlinear pitching and roll. This approach can be used to select the conditions to record dynamic object oscillations or adjust the results obtained using the statistical linearization methods.

For a given set of external perturbations the problem of implementing the “climate spectrum” concept provides preliminary systematic simulation of the pitch and roll movements of a dynamic object in various operating conditions. These data reflect qualitative changes of the dynamic object response to specified external influences. They are stored in the knowledge base of an on-board intelligent system and used to identify wave parameters on the basis of the previous behavior of a dynamic object. In this case the problem of identification is as follows. The storm development forecast is based on the wave alteration within a specified time interval in the real-time mode.

The data of the dynamic measurements of the pitch and roll make it possible to use an iterative algorithm of wave adaptive identification (Fig.3). The algorithm is a result of developing the approach mentioned in work (Blagodarny, 2011). The algorithm is implemented in the time interval specified according to the situation under control. Moreover, the sensor values of the motion are read in each time interval and the iteration of the algorithm occurs in the following sequence:

1. Spectra typical of the navigation area are selected.
2. Perturbation functions for each spectrum are constructed.
3. According to the selected mathematical model motion equation is calculated.
4. As a result both measurement data and the set of motion equation solutions are obtained. The solution is selected according to the specified criterion.

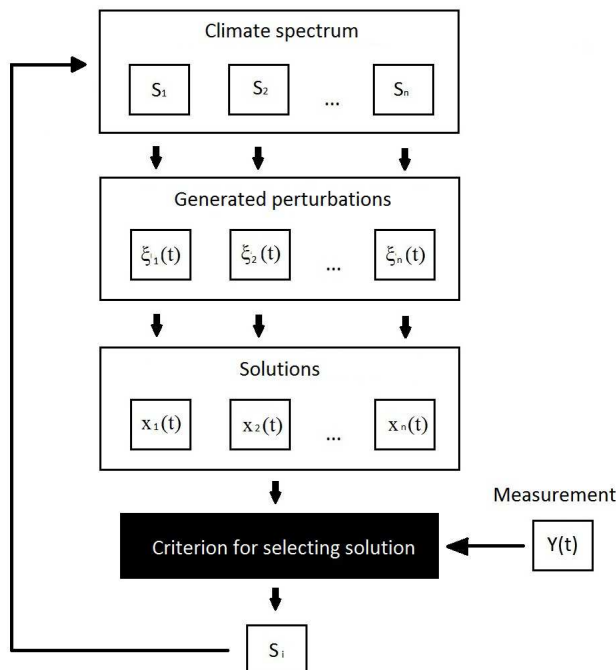


Figure 3: Adaptive identification algorithm of wave parameters.

5. One of the characteristic spectra is selected from the iteration output for last time interval. The output of the iteration is allocated one of the characteristic spectra for last time point.

Then, after a specified time interval the next iteration of the algorithm starts. It gives a possible form at the next time point. It differs from the abovementioned iteration in the following way: if the typical spectra are selected, the spectrum from the previous iteration will be considered. Thus, after some time we will have a picture of the wave spectrum change.

4. PRACTICAL IMPLEMENTATION

The adaptive identification algorithm is difficult to use when the dynamic environment is uncertain. This calls for the comprehensive analysis of non-standard situations and the search for relevant models showing the dynamics of interaction. Difficulties in using of an adaptive identification algorithm in the conditions of uncertain dynamic environment. They led to a comprehensive analysis of non-standard situations and search of relevant models which can show dynamics of interaction. To assess the adequacy of the method the approach based on the parameter identification and the concept of dynamic environment formalization can be used in uncertain environment (Nechaev, 2001). In terms of this concept small, large and full uncertainty is considered. The computer simulation shows that that the developed adaptive algorithm gives satisfactory results in the conditions of small and even considerable uncertainty. However, difficulties arise when it comes to modeling the behavior of sea dynamic object in highly uncertain environment. These difficulties are associated with the formalization of initial information.



The parametric identification algorithm is used as a basic model for the comparative analysis. The algorithm has the following features:

1. The identification process involves calculating deviation between the response of the model built on the dynamic measurement results and the reference response expected from the results of the precedent logical inference (Nechaev, 2005);
2. The model parameters are set so as to achieve the minimum divergence data for the current model and the reference model;
3. Reference response data are represented in a blurred, indistinct way, whereas the model's response is represented as a point estimation based on the defuzzification procedure.

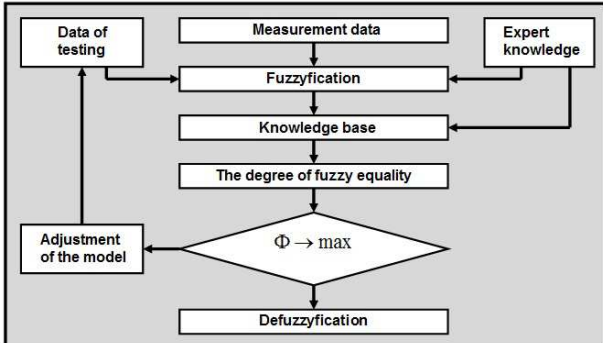


Figure 4: Data used to identify the interaction model in a complex dynamic environment.

The approach is based on representing the construction of the reference model, quantitative estimation of parameters and the appropriate adjustment of the current model. The information flow implementing the information conversion algorithm for the identification problem in complex dynamic environments is presented in Fig.4. Expert knowledge is defined as information including experimental studies developing the dynamic object design, and the dynamic

measurement data obtained when the IS operates under various conditions.

The model validity is evaluated by comparing the current $M[S(Cur)]$ and the reference $M[S(Prec)]$ model. The developed model is adequate for the selected precedent if adequacy criterion satisfies the following form:

$$CR\{M[S(Cur)], M[S(Prec)]\} \in \mu(tr), \quad (4)$$

where $\mu(tr)$ is a membership function that determines the threshold values of fuzzy equality situations $\mu(tr) \in [0.8;1.0]$.

4.1 Fuzzy inference on precedent

The mechanism of fuzzy inference on precedent involves the use of computing technology based on the transformation of a priori data in the information processing paradigm in a multiprocessor computing environment. The general scheme of the transformation using competing technologies is presented in Fig. 4.

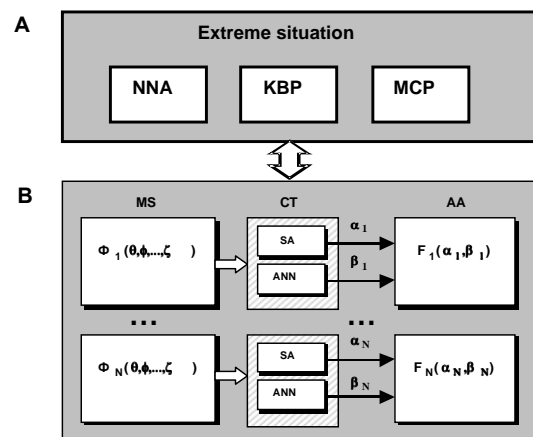


Figure 5: The information flow in the problem of forming a model of fuzzy inference on precedent (A) in a multiprocessor computing environment (B).

NNA is identification algorithms; CWR is a knowledge base of precedents; MCP is a block of modeling and comparative analysis

of precedents; MS is a measuring system, CT is competing technologies; AA is the analysis of alternatives, $\Phi 1(\cdot), \dots, \Phi N(\cdot)$ are initial data submitted for SA and ANN competing algorithms (SA and ANN); $\alpha 1\beta 1, \dots, \alpha N \beta N$ are output data for SA and ANN; $F 1(\cdot), \dots, F N(\cdot)$ are situation models defined as a result of alternative analysis.

The logical on precedent is a cyclic and integrated process of the problem-solving. The task is formalized as follows. Let us assume that the set of precedents $r_i \in R (i=1, \dots, N)$ is located in the N -dimensional space, where each precedent is represented by its vector $a_j = (a_{j1}, \dots, a_{jn})$ ($j=1, \dots, n$), and the whole set is represented by the precedence matrix $W (N, n)$. In this space the precedents form a number of compact domains $R_k (k = 1, \dots, K)$. The analysis aims at identifying the local domains of the precedent classes. This is possible due to the classification of precedents based on the sets of identification algorithm models. The classification algorithm implements the minimization of the functional:

$$G(z_1, \dots, z_M) = \left(\frac{1}{N} \right) \sum_{j=1}^K \sum_{a \in r_j} \|a - z_i^*\|^2 \rightarrow \min, \quad (5)$$

where N_j is a number of precedents in the set r_i ; K is a number of domains; z_i^* is the average value of the set.

4.2 Fuzzy formal system of identification

In extreme situations the formulation of the production rule base that describes the behavior of the simulated dynamic object under the influence of external perturbations is based on the model:

$$\begin{aligned} &\text{IF } U_1 \text{ is } A_{1j} \text{ AND } \dots \text{ AND } U_m \text{ is } A_{km} \\ &\text{THEN } \pi_1 \text{ is } B_{1l} \text{ AND } \dots \text{ AND } \pi_n \text{ is } B_{nl}, \end{aligned} \quad (6)$$

where $U_J (J=1, \dots, m)$ are control actions, $A_{kJ} (J=1, \dots, m, k=1, \dots, p)$ are situations that determines the peculiarity of the external perturbation; $\Pi_i (i=\pi_1, \dots, \pi_n)$ are variables of the process of membership function (MF). $\Pi_i (i=\pi_1, \dots, \pi_n)$ are set for input and output variables of the developed adaptive model. The form of MF should not contradict the reliability requirements of the identification procedure. The requirements are set in the formalization of the adaptive model.

The parameter identification procedure is to perform the following steps:

1. According to the plan developed by computer simulation the initial array of adaptive model parameters of wave recovery is formed.
2. Transfer of the external perturbation values is performed in a fuzzy form (fuzzyfication). The transfer depends on the configuration of climatic wave spectrum where the dynamic object operates and the response of adaptive model. The output response is transformed into fuzzy-term set of output variables with the corresponding MF $\mu(\pi_i^*)$. The current situation is formed and the values MF $\mu(U_J^*)$ for each control actions are retrieved.
3. In the models of precedent knowledge base aggregation procedure of precondition truth degrees is carried out. The truth degrees of preconditions $(\alpha_1, \dots, \alpha_n)$ of each rules are calculated:

$$\alpha_n = \wedge \{ \mu_{A_{11}}(U_1^*), \dots, \mu_{A_{m1}}(U_m^*) \}, \quad (7)$$

where \wedge is the symbol of conjunction.

4. The composition between the calculated values of precondition truth degree of each rule and the corresponding MF of its conclusion $\mu_{Bij}(\pi_i)$ is carried out. New fuzzy sets of terms where MF $\mu_{Bij}^*(\pi_i)$ are formed as the result of the operation



for each variable. The disjunction is performed that determines the situations $s_j^* (j=1, \dots, m)$.

- Two fuzzy situations are formed: s_j^* is defined on basis of priori information and the current s_j^{AM} appearing on the adaptive model. Then the fuzzy equality degree of situations $v(s_1^*, s_1^{AM})$ is computed:

$$v(s_j^*, s_j^{AM}) = \bigwedge_{\pi_i \in \Pi} \left(\bigwedge_{B_{ij} \in B_i} \left(\mu_{B_{ij}}(\pi_i) \leftrightarrow \mu_{B_{ij}}(\pi_i^*) \right) \right), \quad (8)$$

and the statement truth degree of the equivalence MF:

$$\mu_{B_i}(p_i) \leftrightarrow \mu_{B_i}(p_i^*) = \left(\bigwedge \left(\begin{aligned} & \left(\bigvee \left(\left(1 - \mu_{B_{ij}}^*(p_i) \right), \mu_{B_{ij}}(p_i^*) \leftrightarrow \mu_{B_i}(p_i^*) \right) \right), \\ & \left(\bigvee \left(\mu_{B_{ij}}(p_i^*), \left(1 - \mu_{B_{ij}}^*(p_i^*) \right) \right) \right) \right) \right), \quad (9) \end{aligned} \right)$$

where \leftrightarrow is the symbol of equivalence.

The identification procedure will terminate when the maximum degree of fuzzy equality $v(s_1^*, s_1^M) \rightarrow \max$ achieves. Then the transfer for verify the model adequacy is carried out.

4.3 Selection model and adequacy evaluation under the principle competition

The interpretation of decisions various models can be used in the adaptive identification problem based on the principle competition. The simplest model is associated with the construction and the analysis of the selection model. The selection and justification of the best solution based on the principle competition (Nechaev, 2003) the model of selection (Aizerman, 1990) allows to carry out a target restriction of alternatives.

To formalize the problem the standard situations $S(t)(a(t))$ have to be defined. These situations require to make a decision on the basis of dynamic measurements D_1 and priori information D_2 that are contained in the IS

database in form of various information sources. A set of acceptable situations $S(t)(a(t))$, that provides a reliable solution is allocated among the standard situations.

Let us assume that a control action establishing the uniqueness of the solution is determined as $u(t)$. And write:

$$S(t)(a(t), u(t)) \in S(t)^*(a(t), u(t)), \quad (10)$$

where $a(t)$ are parameters of the problem to be solved in time t .

To solve the current problem of operation control under certain parameters and control actions the time interval is denoted as $[t_0, t_k]$. And the required data is determined by the structures:

$$\begin{aligned} D_{1i} &\in \{D_1\}, (i = 1, \dots, m), \\ D_{2j} &\in \{D_2\}, (j = 1, \dots, n), \\ m &\ll |\{D_1\}|, n \ll |\{D_2\}|, \end{aligned} \quad (11)$$

where m, n are number of the measurements, modeling and priori information describing the current situation, the symbol \ll means that data and documents are ordered by importance.

The adaptive identification model is considered adequate for process of interaction the dynamic object and sea if the adequacy criterion is satisfied:

$$v_{CA}(s_1^*, s_1^{AM}) \geq t_R \quad (12)$$

where t_R is the threshold of the fuzzy equality situations $t_R \in [0.6; 1.0]$. Selection of threshold value depends on requirements rigidity for adaptive model accuracy. The problem it is advisable to set the following threshold values $t_R \in [0.6; 0.8]$, since uncertainty it is almost impossible to determine more accurate variable values of the interaction process of all simulated situations. The results of experimental researches show that the

developed approach provides a greater evaluation degree of external perturbation in contrast with those forecast GPS that is derived from land-based meteorological stations.

5. RESULTS OF FULL SCALE TESTS

At the end of the paper let us present some results of full scale tests. To verify the correctness of the algorithm of wave identification (wave measurements using ship as a buoy) applied in the on-board intelligent system full scale tests with a small ship and container ship were carried out. The first experiment was conducted in the Black Sea. The second experiment was conducted in the Mediterranean. Indirect determination of wave intensity on the basis of the above algorithm, as well as instrumental measurements with different sensors were carried out during the experiments. The experimental results are shown in the table.

Sea state	Laser Sensor (m)	Buoy (m)	String wave recorder	Algorithm (m)	Max. divergence (%)
3			1.17	1.23	5.1
4	1.8	1.74	1.76	1.85	6.3
5	3.28	3.17		3.4	7.2
6	5.72	5.61		5.83	3.9

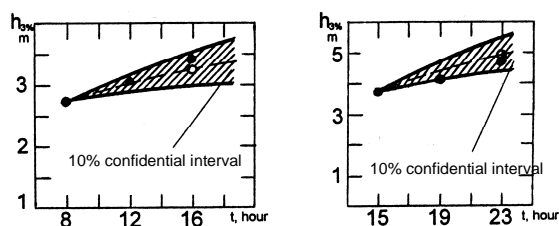


Figure 6: Results of sea state prediction using proposed algorithm for small ship (left) and container ship (right)

Also on the basis of the proposed algorithm and the wave climate model of the considered region prediction of the sea state development was carried out. The results were compared at the right time with wave measurements. The results of prediction are shown in Figure 6.

Here, the white circles marked a predicted wave height, black circles show the values obtained from measurements. The shaded cone represents a 10% confidential interval.

As seen from the results the accuracy of wave identification and prediction is good.

6. CONCLUSIONS

The problem of wave parameter identification under uncertainty is one of the important directions of solving general problem when the IS operates to ensure seaworthiness of offshore dynamic objects. To solve the problem an efficient algorithm of adaptive identification is proposed. The algorithm is based on principles of information processing in multiprocessor computing environment. Under inaccurate and uncertainty of the initial data the solution of control emergency situation problem is carried out by constructing rational calculation schemes of interpretation the current situation based on achievements of modern mathematics and computer intelligence technologies. Constructing the identification procedure in complex dynamic environment the significant effect can be achieved by switching fuzzy logic basis and using logical inference on precedent. Under the influence of new ideas and approaches new possibilities are opened up to investigate the behavior of sea dynamic objects under various conditions that are specific for area when they operate.

7. REFERENCES

- Aizerman M.A., Alexerov F.T. (1990) The choice of options. Fundamentals of the theory. – Nauka, Moscow, 240p. (in Russian)
- Blagodatny N.S., Kobozev V.Yu. (2011) “The method of identification and verification of the adequacy of a simulation model of the process”, Proceedings of International Conference on Soft Computing and



- Measurement SCM-2011, St.Petersburg, Vol. 1, pp. 137-140. (in Russian)
- Boukhanovsky A., Degtyarev A., Lopatoukhin L., Rozhkov V. (2000) "Stable states of wave climate: applications for risk estimation", Proceedings of the International conference STAB'2000, Launceston, Tasmania, Australia, Vol.2, pp. 831-846
- Degtyarev A. (2011) "New Approach to Wave Weather Scenarios Modeling". Contemporary Ideas on Ship Stability and Capsizing in Waves, Fluid Mechanics and Its Applications, M.A.S.Neves et al. (eds.), Springer, v.97, pp.599-617
- Eykhoff P. (1974) System identification. Parameter and State Estimation. – John Wiley and Sons, 555p.
- Iseki T., Terada D. (2001) "Bayesian Estimation of Directional Wave Spectra for Ship Guidance System", Proceedings of the 11th International Offshore and Polar Engineering Conference Stavanger, Norway
- Nechaev Yu.I. (1990) "Operational control of the dynamics of the vessel in rough seas with the help of an expert system", Proceedings of the Conference on experimental hydrodynamics, Kaliningrad, pp.34-37 (in Russian)
- Nechaev Yu.I. (1996) "Investigation of the dynamics of wind and wave fields using marine intelligent real-time systems". Navigation and Hydrography, 3, pp.24-30 (in Russian)
- Nechaev Yu.I. (2003) "Mathematical modelling in on-board real time intelligent systems", Proceedings of 5th National Conference "Neuroinformatics – 2003", Moscow, Lectures in neuroinformatics, Vol.2, pp.119-179 (in Russian)
- Nechaev Yu.I., Tikhonov D.G. (2005) "Neural prediction based on the inference of precedents", Proceedings of 7th National Conference "Neuroinformatics – 2005", Moscow, Vol.2, pp.197-204 (in Russian)
- Nechaev Yu.I. (2011) Catastrophe theory: the modern approach to decision-making. ART-Express, St.Petersburg, 392p. (in Russian)
- Nielsen U.D. (2006) "Estimations of on-site directional wave spectra from measured ship responses". Marine Structure, v.19, i.1, pp.33-69
- Nielsen U.D. (2008) "Introducing two hyperparameters in Bayesian estimation of wave spectra". Probabilistic Engineering Mechanics, v.23, i.1, pp.84-94
- Nielsen U.D., Stredulinsky D.C. (2011) "Onboard Sea State Estimation Based on Measured Ship Motions", Proceedings of the 12th International Ship Stability Workshop, USA, pp.61-67
- On-board intelligent systems. (2006) Part 1. Aviation systems. Part 2. Ship systems – Radiotechnika, Moscow (in Russian)
- Pascoal R., C. Guedes Soares (2009) "Kalman filtering of vessel motion for ocean wave directional spectrum estimation", Ocean Engineering, v.36, i.6-7, pp.477-488
- Simons A.N., Tannuri E.A., Sparano J.V., Matos V.L.F. (2010) "Estimating wave spectra from the motions of moored vessels: Experimental Validation", Applied Ocean Research, v.32, i.2, pp.191-208

Capsizing and Sinking of the dredger Rozgwiadza

Zbigniew Szozda, *Maritime University of Szczecin, Poland*, z.szozda@am.szczecin.pl

ABSTRACT

Polish dredger Rozgwiadza capsized and sank while being towed. The paper shows chosen results of the accident investigation. The loading condition and stability characteristics on the departure are presented. Some of the deficiencies in ship construction and design are indicated. The sentenced reason of the capsizing was sea water inflow to one hold and locker through opening of the hawse hole which had not been closed and properly secured on departure. The most probable sequence of events is presented and stability calculations are performed for each major stage. The sequence of events (events' path) with the use of the TRIPOD method is presented.

Keywords: *stability accident investigation, capsizing, stability failure*

1. INTRODUCTION

Polish dredger Rozgwiadza capsized and sank in the Baltic Sea on 17th October 2008. The sea state at the time of the accident was 5-6[°]B with wind gusts to 7[°]B. The dredger was under tow. Two tugs were used for this purpose. All the crew (5 persons) lost their lives. Main particulars of the dredger are given in Table 1. The dredger was nearly 40 years old.

Table 1: Main particulars

Name	Value
Length over all	45,96 [m]
Breadth	12,05 [m]
Height	4,05 [m]
Draft fore (*)	3,97 [m]
Draft aft (*)	2,88 [m]
Displacement (*)	1266,46 [T]

(*) – on departure.

2. GENERAL ARRANGEMENT OF THE DREDGER ROZGWIAZDA

2.1 Locker, hold and hawse hole

The general arrangement of the dredger Rozgwiadza is shown in the Figure 1. From the accident point of view the most important are following features of the dredger:

- Two hulls in front part of the dredger in length about half of the overall length and one hull in aft part (see upper part of Figure 1).
- Boatswains lockers and holds located in left and right hull.
- Hoisting winch located in right (starboard side) hull - in the hold - used for the main anchor operations. The steel rope of the anchor went from the hold through the locker outside the hull (see figures 2 and 3).
- The hawse hole enabling the rope to go out the hold and the locker was located in front part of the right hull.

These particular arrangements caused that during dredging operations both right locker



and hold were opened to the outside environment.

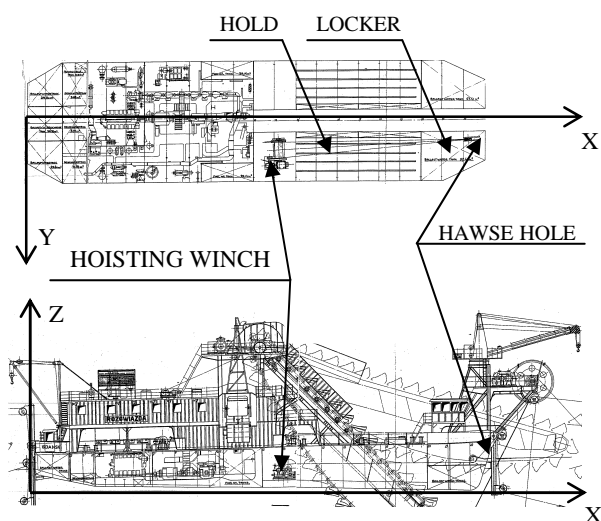


Figure 1: General Arrangement of Rozgwiązda

Figures 2, 3 and 4 show more details of these arrangements.

2.2 Latent failure

The arrangements described in section 2.1 are perceived as a “latent failure” of the dredger leading to the accident. The meaning of this term relates to the situation when the failure has been existing for relatively long time (from the launching of the dredger - in this case more than 30 years) but was not noticeable before the accident.

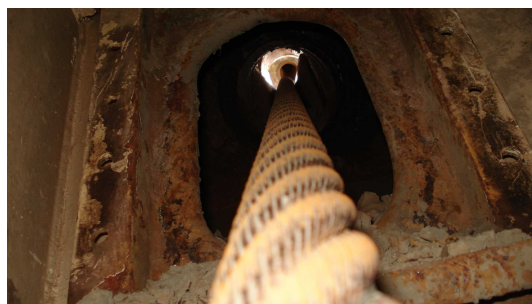


Figure 2: Hawse hole and anchor rope seen from inner side of the locker



Figure 3: Anchor rope going through the bulkhead from the locker to the hold



Figure 4: Anchor rope in the hold seen in the direction from hoisting winch to the locker

In a case when the anchor is fitted outside the dredger and consequently the rope goes from the winch through the hold, the locker and opened hawse hole - both spaces (the locker and the hold) are exposed to water ingress when the water level is above the hawse hole. The water ingress was not possible during usual dredger operation on river or lake but possible during towing of the dredger in waves at sea.

In this particular case the skipper left the anchor fitted prior to departure and endangered Rozgwiązda to water ingress at sea. As the result - the latent failure due to the design and construction became an active failure due to waves at sea and possibility of water inflow (see Figure 8).

3. STABILITY CHARACTERISTICS

3.1 Loading condition on departure

The drafts of the dredger were elaborated on the basis of a series of photos that were taken by crew members and others before and in time

of departure (not intentionally for this purpose – see Figure 5).



Figure 5: Departure of the dredger

Furthermore, the details of the loading condition were derived from the information on stability for the master (light ship etc.) and interviews with those who were responsible for the dredger operation in terms of ballast, fuel, stores and other components. This information was used for calculation of the displacement and centre of gravity co-ordinates. All weights and their positions were adjusted in that way that drafts calculated from the loading condition should correspond to that observed in the picture. The outcome was as follows:

$$D(x_G; y_G; KG) = 1266,46 (25,75; 0,00; 5,20).$$

Displacement force “D” is shown in Tonnes and the centre of gravity co-ordinates are shown in meters according to Figure 1.

3.2 Righting lever curve and GM on departure

The righting lever curve for this loading condition (on departure) is shown in the Figure 6.

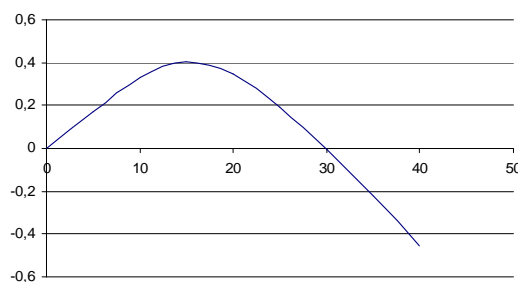


Figure 6: Righting lever curve

This is very important to note in the context of the accident the curve characteristics:

- the range of positive values is rather short – only about 30 [deg].
- The maximum righting lever occurs at the angle of heel only about 15 [deg] and its value is about 0,40 [m].

Initial metacentric height for this loading condition was: $GM = 1,98$ [m].

Additional information on the dredger’s stability might be obtained from the calculation of the angle of heel due to wind pressure. For observed at that time and place wind (up to 7[°]B in gusts) it was concluded that, taking into account windage area characteristics, the angle of heel due to perpendicular wind could amount to about 0,5 [deg].

The conclusions from these calculation:

- For small angles of heel the stability of the dredger was quite good and maybe sufficient for usual operation on rivers or lakes.
- The dredger was not sensitive to wind pressure in terms of the angle of heel.
- The stability could be questionable for sea towing operation in terms of angle of maximum GZ and the range of positive GZ values.

4. THE SEQUENCE OF EVENTS

At the time of departure the weather was calm but there was bad weather forecast. The dredger went to sea with hawse whole opened and the main anchor fitted outside the bow – ready to be dropped down. It was the decision of the skipper. It was not possible to operate the anchor when the hawse whole was closed. But actually there was no need to do so. Furthermore, the skipper had clear instructions to close the opening before going to the sea.

The dredger was towed by aft. In these circumstances sea water had free access to the locker and the hold placed on the starboard side



(fore part) if the water level was above the hawse hole.

The sequence of events leading to dredger's capsizing and sinking is summarised in Table 2. All the events were elaborated by the Marine Chamber's expert on the base of the reports of the witnesses of the accident – crew of two tugs and other employees of the ship-owner (Szozda, 2010).

Table 2: Sequence of events

Date, time	Probable events
16.10.08 Time: 08.00	Rozgwiazda is being towed by the tug Stefan (by aft). Boatswain locker (fore part of the vessel) on starboard side is dry. The hold on starboard side is dry. Fore draft $T_F=3.97$ [m], aft draft $T_A=2.88$ [m]; heel angle 0 [deg]. Due to deteriorating weather conditions, waves, heaving, pitching and rolling sea water starts to inflow into the locker through open hawse hole (see Figure 2). At this time water inflow could have form of „splashing” at the moment when sea level was above the opening.
16.10.08 Time: 19.00	The locker is filled up with sea water to the level about 0.4 [m], what corresponds to the weight of the water 10.4 [T]. Fore draft $T_F=4.02$ [m], aft draft $T_A=2.84$ [m]; heel angle to starboard 0.9 [deg]. The water starts to transfer (overflow) from the locker to the hold through the bulkhead between the locker and the hold (see Figure 3). Volume of the water in the locker does not increase.
16.10.08 Time: 23.00	Conversation between the skipper of Rozgwiazda and the master of the tug Stefan. Information on the Rozgwiazda's heel that was observed by the skipper. The skipper assumed the heel was caused by the wind. The tug is too weak to tow Rozgwiazda against the wind and waves. During the investigation the heel was estimated to 2.0-2.5 [deg]. It was found that due to small windage area and other characteristics this heel was caused by flooding of the locker (partly) and the hold (partly). The

	weight of the water at that time was estimated to 26.0 [T].
17.10.08 Time: 2.00- 2.30	The second tug Goliat starts to tow Rozgwiazda together with Stefan. The weight of the water in the locker and in the hold estimated to 44.0 [T]. The water in hold could not be seen above the level of the floor.
17.10.08 Time: 6.05- 6.10	The steel rope between Rozgwiazda and Stefan is broken. Rozgwiazda starts to drift towards the shore. The weight of the water in the locker and in the hold estimated to 62.0 [T]. The water in the hold could not be seen above the level of the floor. After about 10 minutes the skipper drops down the anchor. Rozgwiazda stopped on the anchor and turned exposing the hawse hole towards wind and waves what speeded up dramatically sea water inflow into the locker and the hold.
17.10.08 Time: 6.40- 6.45	The hold filled up with water over the level of the floor (0,8 [m]). The weight of the water estimated to 77.2 [T]. For draft $T_F=4.36$ [m], aft draft $T_A=2.79$ [m]; angle of heel 6.6 [deg].
17.10.08 Time: 6.54	The weight of the water estimated to 91.0 [T]. Fore draft $T_F=4.42$ [m], aft draft $T_A=2.78$ [m]; angle of heel 8.9 [deg]. Rozgwiazda capsizes through starboard side and fore.

Righting lever curves corresponding to main stages described in Table 2 are shown in the Figure 7.

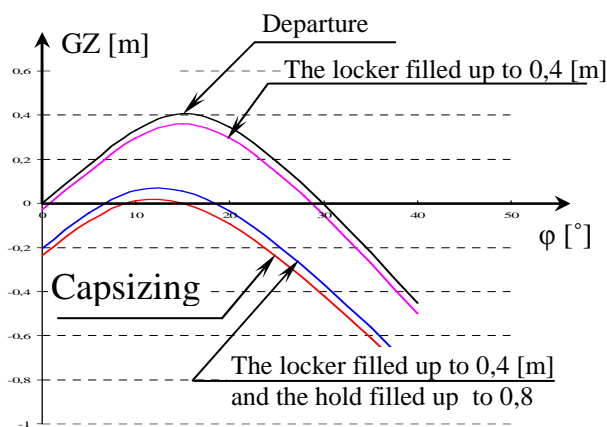


Figure 7: Righting lever curves corresponding to main stages described in Table 2

5. TRIPOD PATH AND BREACHED BARRIERS

TRIPOD is an approach to the analysis of accidents using the Tripod Theory of Accident Causation. The basic element consists of a “trio” Hazard, Target and Event (Gower-Jones, van der Graaf, 1998). A set of such “trios” may be used to describe the path that led to an accident. It also enables identification of different barriers which should stop the sequence of events provided the design and operation were free of human errors. This approach was used to describe capsizing of m/f Jan Heweliusz – Polish ro-ro passenger ferry that capsized in 1993 (Szozda, 2009).

The diagram containing a set of triple blocks (Hazard, Target and Event) identified during investigation of Rozgwiazda’s capsizing and sinking is presented in Figure 8. This figure exemplifies the TRIPOD path to this accident. It was assumed that in each step the vessel was a Target to a Hazard. The examination of the scenario identified six barriers that had been breached – five existing and one missing. If one of the first five barriers would not be breached – the accident (capsizing) probably would not have happened. Table 3 contains description of 6 breached barriers. All of them, except number 4, have been classified as human factor.

6. CONCLUSIONS

Most accidents at sea, especially capsizing and sinking of a ship in intact condition, are caused by a sequence of a number of events. TRIPOD method is suitable tool for accident analysis. In case of the dredger Rozgwiazda the main reason of the capsizing was latent failure that had been existing for a very long time – the main anchor system was designed in the way enabling the locker and the hold to be exposed to waves if certain preconditions (in this case human error) occur.

Table 3: Breached barriers

No	Type of a barrier	Description of a barrier
1	Existing	Departure in spite of bad weather forecast.
2	Existing	Hawse hole not closed. This is the main cause of the accident – a starter for the sequence of events at sea.
3	Existing	No action. The crew knowing that the hawse hole is opened did not check whether the flooding of the locker takes place.
4	Missing	A system for flooding detection. Such system in the locker or/and in the hold could provide the information on progressive flooding to the skipper
5	Existing	Misinterpretation of the observed angle of heel. The skipper was aware of the heel but thought that the heel was caused by the wind. Actually the heel was caused by lost buoyancy/ additional mass.
6	Existing	Skylights opened in bad weather. After capsizing the water flooded the machinery compartment and caused sinking.

The sentenced reason of the capsizing (from stability point of view) was sea water inflow to one hold and locker through opening of the hawse hole which had not been closed and properly secured on departure. The causes of Rozgwiazda’s capsizing are pure human error. The skipper:

- Should not go to sea due to bad weather forecast.
- If gone to sea – should not leave hawse hole opened.



- If gone to sea and hawse hole not closed and weather condition bad – should check frequently whether or not flooding of the locker and/or hold takes place.
- Should check with caution (preferably by calculation) and be aware what was actual reason of observed heel.

Having in mind present SLF efforts towards 2nd Generation Intact Stability Criteria the question appears: “how to avoid latent failures related to ship systems’ design and human failures of this type”? Accidents related to ships’ stability caused by relatively trivial factors still exist. How can it be addressed in the research and regulatory work?

7. REFERENCES

Gover-Jones, A.D., van der Graaf G.C., 1998, “Experience with Tripod Beta Incident Analysis”, SPE International Conference on Health, Safety and Environment in Oil and Gas Exploration and Production, Caracas, Venezuela, June 1998.

Szozda Z., 2009, “Application of the TRIPOD Method for Human Factor Analysis on the Example of m/f Jan Heweliusz Capsizing”, 10th International Conference on Stability of Ships and Ocean Vehicles, St. Petersburg, Russia, June 2009, pp. 493-499.

Szozda Z., 2010, *Opinia dotycząca stateczności w sprawie przewrócenia się i zatonięcia pogłębiarki Rozgwiadza na Morzu Bałtyckim w dniu 17.10.2008r.,(in Polish)*, (“Opinion on the stability concerning capsizing and sinking of the dredger Rozgwiadza in the Baltic Sea on 17th October 2008”), Maritime University of Szczecin, Maritime Chamber in Szczecin, May 2010.

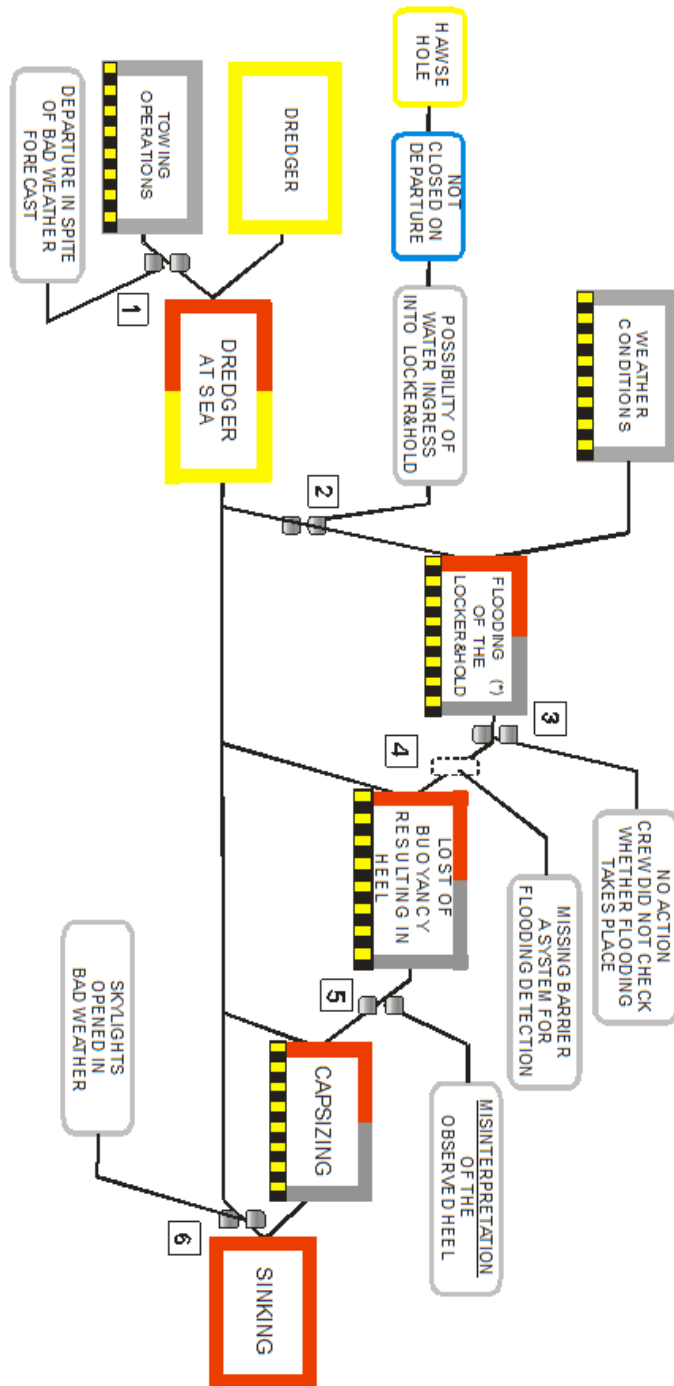


Figure 8: TRIPOD path for Rozgwiazda's capsizing and sinking (events' path)





Numerical Investigations of the Capsizing Sequence of SS HERAKLION

Stefan Krüger, *TU Hamburg Harburg*, krueger@tu-harburg.de

Hendrik Dankowski, *TU Hamburg-Harburg*, Dankowski@tu-harburg.de

Caroline Teuscher, *TU Hamburg-Harburg*, te@tu-harburg.de

ABSTRACT

The sinking of the RoRo- Passenger Ferry SS HERAKLION in 1966 was one of the most disastrous ferry accidents in modern Greek shipping. SS HERAKLION was originally built as combined freight and passenger vessel and was later converted into a RoRo- Passenger ship. Some technical aspects of the conversion were at least doubtful, however the ship started her final voyage on December 7 from Crete to Piraeus. The weather was rough, and the ship was travelling in a stern quartering sea condition with heavy beam winds. The rolling was strong, and after a course alteration into following seas the rolling increased. This caused cargo to shift and a side door was pushed open by a heavy truck which was not secured. Water entered into the car deck which resulted in a heavy list of the ship. When further water ingress took place, the ship finally sank. After the accident, investigations were carried out at NTUA (on behalf of the Hellenic authorities) and at the “Institut für Schiffbau”, Hamburg (on behalf of the insurance company). There are some interesting aspects of the accident which are worth to be studied again by more advanced methods compared to the late 60s.

Numerical evaluations of the accident (parts of this research were in close collaboration with NTUA, Ship Design Laboratory) have shown some interesting aspects of the earlier accident phase before and during the flooding of the main garage deck. The investigation has also shown options how the accident could have been avoided. The paper presents the treatment of complex full scale safety issues by numerical simulation methods. It shows that it is useful to apply different calculation methods for different phases of such accidents. The intact phase of the accident is treated by our sea keeping code E4ROLLS until water enters the car deck. The initial water ingress into the car deck is computed with Glim’s method until a certain list is reached, and some conclusions are drawn. The paper will also show that scientific advances in ship theory can help to better understand the accident roots of such complex accidents, and these methods can help to find new answers to old problems.

Keywords: *SS HERAKLION, capsizing, passenger ferry, flooding of the vehicle deck*

1. INTRODUCTION

Marine casualties are typically complex event chains, especially when the casualty leads to the total loss of a ship due to capsizing or sinking. Whenever such a casualty needs to be investigated, lots of computations need to be made to figure out the event chain which has lead to the final loss. During these

investigations, a variety of different computational methods is applied, which extends from simple hydrostatic calculations to complex dynamic simulations. The problem exists that all these methods require more or less sophisticated computational models, and both need to be validated. The validation of such methods can be performed by computing

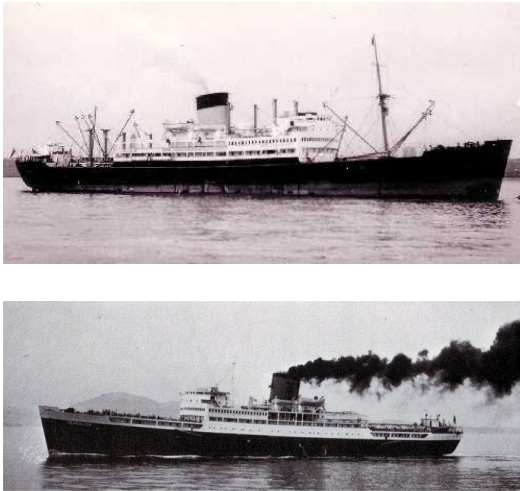


Figure 1: SS LEICESTERSHIRE (top) and SS HERAKLION (bottom) after the conversion

theoretical test cases, by the comparison with experiments or by full scale accidents. The validation by experiments has the advantage that all data and test conditions are well defined, which makes it quite easy to recompute these accidents. Further, any deviations between experiment and computation can in most cases be reasonably explained, and such deviations often result in the refinement of the computational procedure or in the model, or both. Therefore it is a condition sine qua non to validate numerical methods by experiments. However, with respect to marine casualties, experiments never reflect the full event chain as they can only focus on a small part of the problem, and they are always performed under ideal conditions. Therefore it seems plausible to also use full scale accidents of ships for validation purposes. But the problem exists that these accidents never happen under ideal conditions where all data is exactly known. Mostly the ship has sunk and it cannot be accessed, important data are not known with sufficient accuracy and the surviving witnesses often do not clearly remember important facts. This makes the analysis of full scale accidents always challenging, and often it is not clear whether a numerical model or a computational procedure is actually suitable for the analysis. Therefore, TUHH is actually running a research project

where we systematically collect data of full scale capsizing or sinking events, prepare the calculation models and figure out the relevant event chains. These data are collected in a database which will be used for the validation of other methods in the future. In the framework of these investigations, we came across the capsizing and sinking accident of SS HERAKLION, which took place in 1966. Although the accident was quite long ago and the ship has nothing in common with modern designs, the accident was characterized by a lot of interesting technical details which made the analysis quite challenging. Although no safety recommendations can be drawn from this accident, the technical analysis shows a variety of interesting details which allow the validation of a couple of computational methods. Our analysis of the accident, which was done in close collaboration with the National Technical University of Athens (NTUA) is presented in the following sections.

2. SHIP AND LOADING CONDITION

SS HERAKLION was originally built as SS LEICESTERSHIRE by Fairfield Shipbuilding and Engineering in 1949 as Hull No. 2562, call sign SZNO. The ship was a typical design of a combined freight and passenger vessel. 1964 the ship was bought by the Hellenic shipping company Typaldos Lines, and she was converted into a combined passenger and vehicle ferry, see Fig. 1. This major conversion showed already all later problems with RoRo-Passenger-ferries, which was a new ship type in those days and it was unclear for the authorities how to deal with this type of ship. Since 1949, additional safety requirements were put in place, and additional transversal bulkheads were retrofitted to meet a one compartment status. This was not consequently done, as Fig. 2 shows, because the additional transversal bulkheads did not extend down to the double bottom. An additional deck was fitted to serve as vehicle deck, which was accessed by side doors and ramps. As the watertight transversal bulkheads did for

obvious reasons not extent above the vehicle decks, the vehicle deck now was the freeboard deck, which made a complete set of safety relevant calculations necessary. An additional passenger deck was also retrofitted which resulted in a significant increase of the vertical centre of gravity.

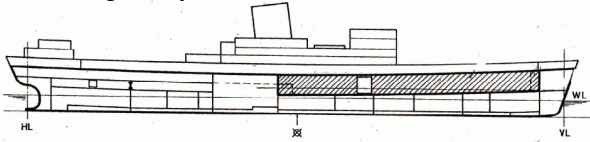


Figure 2: Sketch of SS HERAKLION after the conversion. The side door of the forward vehicle deck can also be seen.

However, during the conversion some existing regulations could not or only hardly be fulfilled, a fact which was later proven during the accident investigations. Therefore, the issuing of some certificates was doubtful, and was also later withdrawn by the Hellenic authorities.

The main dimensions of the ship after the conversion were the following: Length over all 146.50 m, moulded breadth 18.29 m, draft design 4.58m, depth to freeboard deck 5.35 m, depth to upper deck 10.851m, speed 17 knots.

During the accident investigations by the Hellenic authorities it was found quite challenging to figure out the stability condition of the vessel during her final voyage. An inclining experiment with SS HERAKLION was never performed, and the stability information on the vessel was extremely poor. During the accident investigations, the light ship weight of SS HEARKLION was determined by Fragoulis (Fragoulis 1967) and Georgiadis (Georgiadis 1967). They used the available data of the inclining experiment of sister vessel SS XANIA instead and considered some additional weights and also some that were not on board of SS HERAKLION. The loading condition of the final voyage was based on the available loading list and contained cars, trucks, passengers, ballast and bunker and stores. However, some information

was doubtful, also the inclining experiment performed with SS XANIA, which was based on level trim hydrostatics and small inclinations. Further, SS XANIA had a large amount of ballast water on board during the inclining experiment which also made the results doubtful. Some tank volumes were incorrect, too, and also the hydrostatic particulars were not fully available in the AEENA- accident reports. Therefore we had decided to recalculate all weight information, including a new evaluation of the inclining experiment (Teuscher 2011). This step was also necessary to generate the weight information for the mass moments of inertia computation for the dynamic analysis. It was found that due to the conversion, the centre of gravity was that high that the ship could only be operated when the complete double bottom fuel oil tanks were filled with ballast water. The loading condition during the final voyage resulted then in a total displacement of 7740 tons, draft at A.P. 6.35 m, Draft at F.P. 2.95 m, GM_c 0.94m, freeboard to vehicle deck of abt. 0.85 m. The tank fillings of the loading condition according to our investigation is plotted in Fig. 3 (Teuscher 2011).

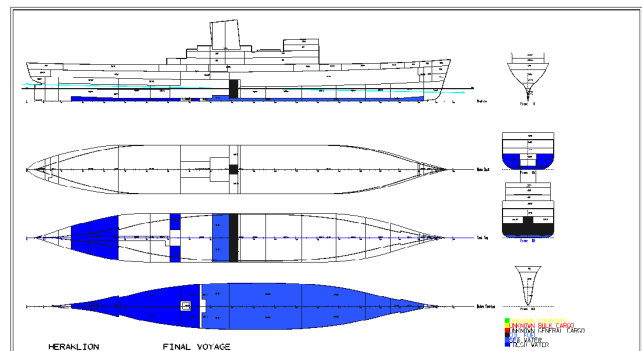


Figure 3: Loading Condition of the final voyage.

3. THE FINAL VOYAGE

On December 7th, 1966 SS HERAKLION departed from the port of Souda Bay, Crete to make her voyage to the port of Piraeus. The departure of the vessel was delayed due to the late arrival of a reefer truck, which was then



stowed unlashd in the forward garage deck rectangular to the ship's centre line. At about 22.00 hrs, the ship reached the open sea close to the island of Milos (see Fig. 4), steering a course of 352 degree. The wind was rough with 8 Bft (11 in gales). As the wind direction had changed overnight from about 180 degree to now 270 degree, the direction of the waves was still about 200 degree, bringing SS HERAKLION into the interesting situation of beam wind and stern quartering seas (see Fig. 4). The sea was rough with significant wave heights about 5-6 m, (significant) wave length between 80 and 120 m. The weather data were not recorded during the accident, but were later obtained from the German DWD (Wendel 1970).

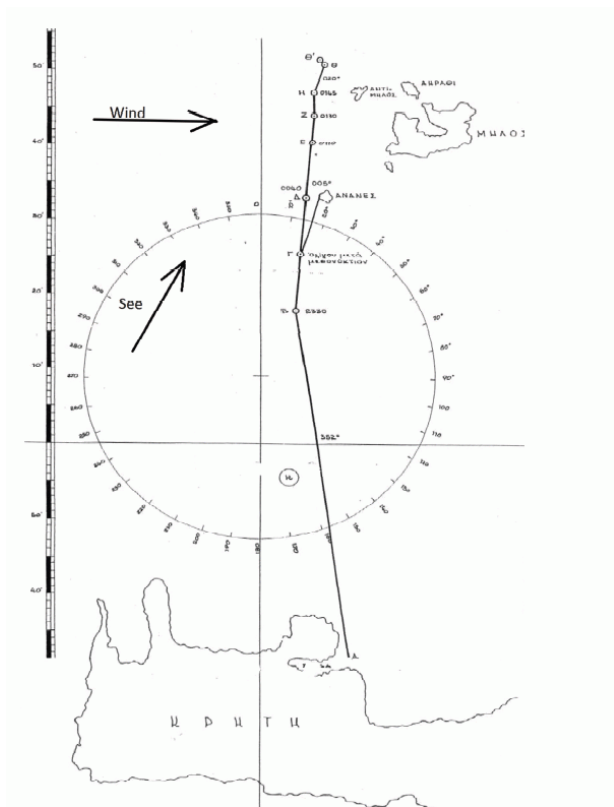


Figure 4: Accident scenario of SS HERAKLION. Source: AEENA.

Due to the beam wind, SS HERAKLION had a steady heel to starboard side of about 8 Degree. Due to the seastate, the ship was permanently rolling with amplitudes about 20 degree, as the surviving persons reported. This rolling motion caused the cargo to shift, and

some cars tipped over. This cargo shift increased the steady list of SS HERAKLION to about 11 degrees. The crew decided to alter the course to 20 Degree to bring SS HERAKLION directly before the seas. She was now travelling in following seas and beam wind. Despite the course alteration, the rolling motion increased, and due to the severe rolling, the unlashd reefer truck pushed against the starboard side door and forced the door open. Due to the steady list of about 11 Degree and the roll motion, water immediately entered the vehicle deck which caused a list of about 60 degree. Due to unsecured openings, further compartments were flooded, the vessel finally capsized and sank. Only 46 persons of 264 could be saved, this made the SS HERAKLION accident the most disastrous marine casualty in Modern Greek shipping.

4. ANALYSIS OF THE ROLL MOTION IN INTACT CONDITION

4.1 General Considerations

The accident of SS HEARKLION can be split into four different phases, which do all have some interesting technical challenges: The first phase is the intact rolling in a beam wind following sea scenario. The second phase took place after the alteration of the course, which made the rolling even worse and lead to the opening of the side door. The third phase is characterized by the flooding of the vehicle deck until the ship reaches a large list, and the fourth phase is the subsequent flooding of further compartments including the superstructure until the ship finally sinks. This paper deals with the first three phases of the accident: Because it is obvious that these phases are strongly influenced by dynamic effects, they can only be analyzed with methods which compute the roll motion in following seas with sufficient accuracy. Although many tanks were filled, free surface effects can be disregarded, as most tanks were completely filled. The flooding of the vehicle

deck can also be computed taking into account the relevant dynamics, as the fluid motion influences the ship motion and vice versa. The relative motion between the ship and the wavy surface triggers the in- and outflow of the water on deck and needs to be computed with sufficient accuracy. For these computations, we use the sea keeping code E4ROLLS which was originally developed by Söding and Kröger for the investigation of the ELMA- T.R.E.S. capsizing accident in 1986. E4ROLLS simulates all six degrees of freedom in time domain. The concept is that those degrees of freedom which are governed by hydrodynamic effects are computed linearly using RAOs (e.g. from a strip theory or panel code), whereas a non linear simulation is performed for those degree of freedom where the nonlinearities are the governing effects. The equation used for the roll motion reads (Petey 1988):

$$\ddot{\varphi} = \frac{M_{wind} + M_{gy} + M_{wave} + M_{Tank} - M_D - m(g - \zeta)h_s - I_{xz}[(\ddot{\theta} + 9\dot{\varphi}^2)\sin\varphi - (\ddot{\psi} + \psi\dot{\varphi}^2)\cos\varphi]}{I_{xx} - I_{xz}(\psi\sin\varphi + 9\cos\varphi)}$$

Here, M_{wave} denotes the direct roll moment obtained from the roll RAO, and h is the righting lever in waves computed by the concept of Grim's equivalent wave (Grim 1960). The latter makes the computation extremely fast and at the same time reliable. M_{wind} , M_{Tank} are external Moments from wind action or moving fluids, M_D is the (non linear) roll damping moment. I_{xx} and I_{xz} denote the mass moments of inertia including section added masses, m is the ship's mass (Petey 1988). E4ROLLS was intensively validated by model tests during German BMBF- funded research programs from 1998-2006.

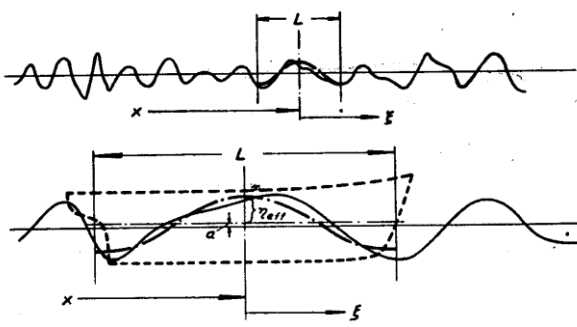


Figure 5: Principle of Grim's equivalent wave (Grim 1960).

4.2 Stability, roll motion and critical resonances

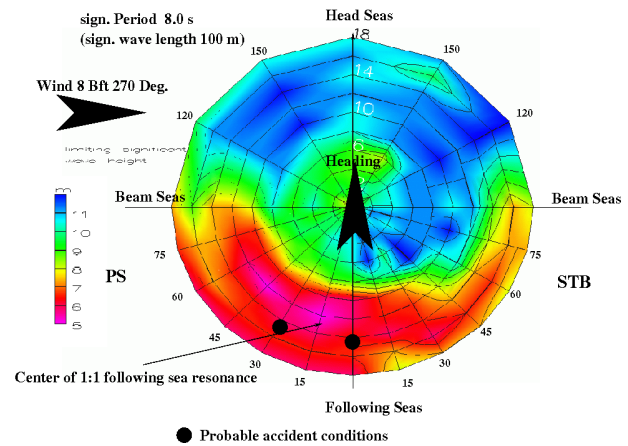


Figure 6: Polar Plot of significant wave heights required for a 25 Degree roll angle of SS HERAKLION in intact condition, 8s period

Figure 6 shows the results of an E4ROLLS-computation for the final voyage of SS HERAKLION, intact condition. The polar plot was computed for a significant period of 8 s, corresponding to a wave length of 100 m. The sea state is represented by a JONSWAP-spectrum, the radial energy distribution follows a \cos^2 - function. This leads to a short crested, natural seaway. The polar plot shows the required significant wave height which lead to a roll angle of 25 Degree (abt. 8 Degree STB static heel due to wind plus the roll amplitude). For each node of the polar, 10 simulations of 20000 s each have been performed for each significant wave height, and the wave height was varied in steps until 25 degree roll angle were reached. The radial rings show the ship speed, the circumferential axis shows the encounter angle. Beam wind was assumed from 270 Degree (90 degree PS), this is the reason why the polar plot is not symmetric. From these results, some interesting conclusions can be drawn. The computations show that in the accident situation of SS HEARKLION, roll amplitudes of about 20 degree - as reported - were likely to occur, as the required significant wave heights are about 5-6m. This value is typical for wave lengths of 100 m- 120 m, as reported by the German DWD for the day of the accident (Wendel 70 and AEENA-



Reports). Most interesting is the fact that SS HEARKLION was travelling close to the 1:1 roll resonance situation in following seas. Based on the Stillwater GM of 0.94 m and valid for small angles only, the natural roll period of SS HEARKLION amounts to 14.6 s. This results in a theoretical speed of 12.5 kn in following seas at an encounter angle of 30 degree, which is approximately the encounter angle of SS HEARKLION before her first change in course. The polar shows the well known fact that resonance situations in following seas are not distinct points - as a linear theory might suggest - but more or less broad banded resonance areas which extent over a range of speeds and encounter angles. This behaviour is a consequence of the fact that the natural roll period of a ship in following seas is not a fixed value, but is varies due to several nonlinearities. For the accident situation of SS HEARKLION, the following nonlinearities occur (see also Fig. 7):

- As the righting lever curve of SS HEARKLION is of progressive type (positive form stability), the natural roll period decreases with increasing roll angle or list. For the SS HEARKLION, the steady list due to wind and cargo shift plays a major role, and the larger the steady list becomes, the smaller becomes the roll period.
- For the roll period in waves, the still water righting lever curve is not relevant, but (as the two extremes) he crest and trough lever arm curve. The stability varies between these two situations, and the resulting roll period depends on how long these extreme phases occur during one cycle. The resulting roll period is longer compared to the computed Stillwater period.
- The roll angle itself has an influence on the roll period, especially when the crest and through curves are analyzed. For smaller roll angles up to approx. 15 degree, the roll period decreases, for larger roll angles

larger than 15 degree, the roll period increases.

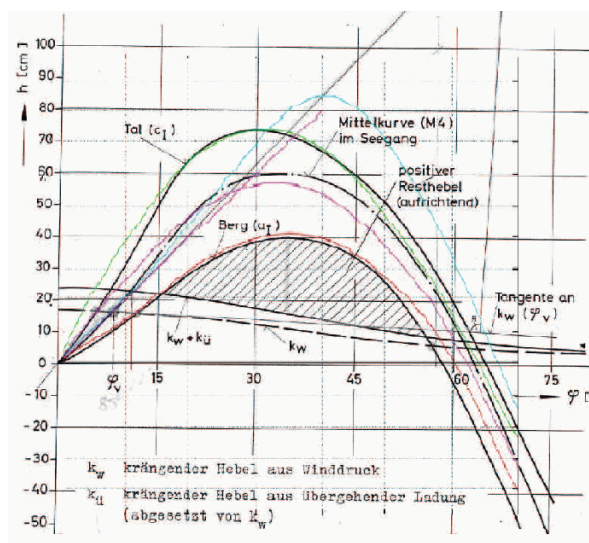


Figure 7: Righting levers of SS HEARKLION for Stillwater, crest and trough conditions. Computations by Wendel (Wendel 1970), coloured curves our computations.

This is underlined by Figure 7, where the righting lever curves in waves of SS HEARKLION have been computed by Wendel (Wendel 1970) for a 100 m wave, wave height 7 m. The mean value between crest and trough (used by Wendel for his analyses) differs significantly from the Stillwater curve (blue line), an indication for the fact that any conclusion from the Stillwater natural roll period (for small angles) is not valid for the SS HEARKLION accident.

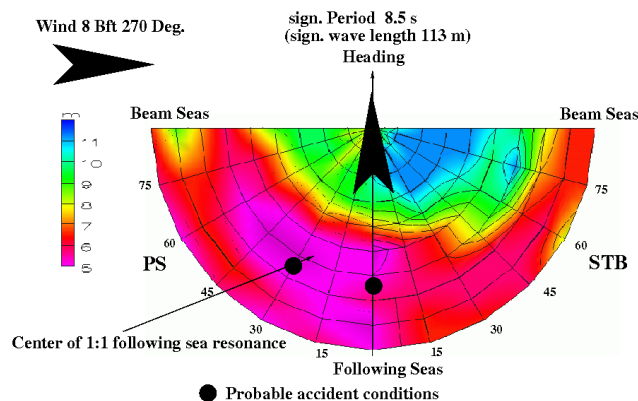


Figure 8: Polar Plot of significant wave heights required for a 25 Degree roll angle of SS HEARKLION in intact condition, 8.5s period.

All these findings are confirmed if the computation is repeated for another possible accident scenario. Fig. 8 shows the limiting significant wave height now for a significant period of 8.5s (113 m corresponding wave length). It can now even better be observed how close SS HERAKLION sails at the 1:1 resonance and that the alteration of the course did not improve the situation.

4.3 Conclusions for the first two phases

As shown, SS HERAKLION was travelling sufficiently close to the 1:1 following sea resonance situation, so that large rolling angles occurred. The polar also shows that changing the course was not a good choice, as the rolling motion was not reduced. The reason is that the ship was brought closer to the resonance at following seas, but the direct excitation (M_{Wave} in the roll angle equation) due to the waves was reduced slightly when SS HERAKLION took the waves exactly from abaft.

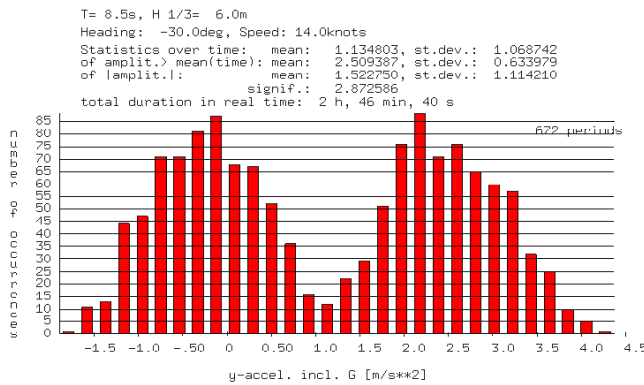


Figure 9: Horizontal accelerations computed for SS HERAKLION in the accident situation prior to the course alteration

From Fig. 6 and Fig. 8 the fact can be derived that the whole accident could have been avoided if the crew had decided to select another course or speed combination. At that course, SS HERAKLION was clearly safe below a speed of 10 knots, and if she had opted for a course with bow quartering wind (e.g. 60 or 75 Degree STB) she could have sailed nearly any speed without being endangered.

Even sailing at a higher speed than 15 knots would have improved the situation, but slightly. May be it was due the fact that SS HEARKLION was already delayed that the crew did not want to increase the delay by reducing speed or changing course. But had the crew done so, the accident could have been most probably avoided. In this respect, the SS HEARKLION accident is comparable to the loss of MV FINNBIRCH in 2005 and SS FIDAMUS in 1949, both ships capsized in following seas close to a 1:1 resonance (Kluwe and Krüger 2008). But there can be no doubt that SS HERAKLION was quite safe from the intact stability point of view, as our computations show. Fig 9 shows the horizontal acceleration computed for SS HERAKLION during the accident situation. It can be seen that accelerations of about 0.5 g occur to starboard side, this is sufficient to let the cargo tip over.

5. ANALYSIS OF THE WATER INGRESS INTO THE VEHICLE DECK

5.1 General considerations

The sinking of SS HERAKLION took place when the reefer truck struck against the STB-side door, pushed it open, which allowed water to enter the vehicle deck. It was shown in the accident investigations by Fragoulis, Georgiadis and Antoniou (Fragoulis 1967, Georgiadis and Antoniou 1967) and by Wendel (Wendel 1970) that the flooding of the vehicle deck resulted in such a loss of buoyancy that the ship irreversibly must have capsized. But a more precise stability computation (loss of buoyancy method, free trimming righting levers) gives a more complex picture, as Fig. 10 shows:

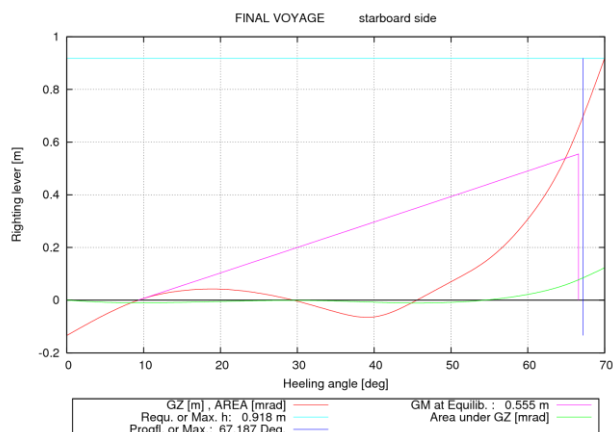


Figure 10: Righting levers computed for SS HERAKLION after the flooding of the forward car deck.

Figure 10 shows the computation of the righting levers of SS HERAKLION after the forward car deck is flooded. The computation assumes the complete superstructure to be watertight, as water will gradually enter these compartments. The heeling moment of the tipped cars has been taken into account, and also the heeling moment due to wind of 8 Bft, which must be added for the situation when the reefer truck struck the car deck open. From these calculations, it becomes obvious that after the flooding of the car deck, two equilibriums exist, where the first equilibrium is about 10 degree STB. This first equilibrium is only theoretically stable, because a larger wind heeling moment (gales were reported to be about 11 Bft) is sufficient to let the ship heel to about 45 degree STB. It is also possible that the wave moments from the sea state force sufficient water into the vehicle deck to overcome this first stability plateau. But this computation shows that SS HEARKLION was not necessarily lost when the STB side door was pushed open: If the crew had managed to turn her in such a way that the wind heeling moment would have acted from STB side on the vessel, she would have had chances to survive even the water ingress. This possible scenario will also be analyzed in the following sections. Further, even the equilibrium at about 45 degree is stable. Figure 11 shows the floating position of SS HERAKLION after the complete flooding of the car deck including the wind heeling moment from PS.

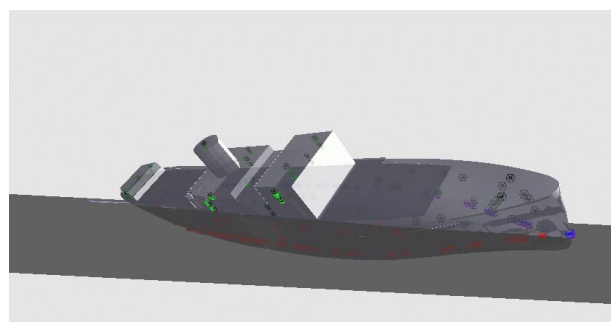


Figure 11: Floating position of SS HERAKLION after the flooding of the vehicle deck

Figure 11 shows that SS HERAKLION must not necessarily sink or capsize even after the most unfavourable combination of heeling moments (tipped cars at STB, wind from PS). If the crew had followed the relevant guidelines and kept all weather tight doors and openings closed, the ship could have stayed in that position. It was however unclear during the accident investigations if and how internal progressive flooding has taken place. Of course these computations depend on the assumptions made, where the largest uncertainty lies in the masses and centroids. If the stability of SS HERAKLION had been smaller than computed, the first stability plateau might become completely unstable, which forces the vessel to heel to about 50 Degree STB even without additional external moments. However, these computations indicate that based on our assumptions the ship had had a good chance to survive the accident if the crew had taken other operational decisions.

5.2 Numerical simulations of the water ingress with E4ROLLS

At present, we have two different methods to compute water ingress into vehicle decks: The first is E4ROLLS, which has been extended for water on deck problems by Petey (Petey 1988). The floodwater is modelled by Glim's method using shallow water equations. The inflow into the vehicle deck is computed by the net flux through the opening including the dynamics of the roll motion. This method gives good results (BSU 2010) when the

amount of water accumulated in the vehicle deck is small compared to the total mass of the ship and when the water inflow does not strongly influence the trim. Because in E4ROLLS only the additional roll moment (see M_{Tank} in Eqn. 1) is modelled, the mass increase and trim moment are neglected at present (we are currently improving this). Further, as the direct wave moment (see M_{Wave} in Eqn. 1) is obtained from the linear RAO, the results become less reliable when a certain static heel (typically 30 to 40 degree) is reached. From practical considerations, this is not a problem because the ship can be assumed as lost in case such large static heeling angles are reached. Further, we have developed a method for sinking computations E4SINKING (Dankowski 2011), which computes the static flux through the relevant openings and determines a hydrostatic equilibrium according to the added mass method. Dynamic effects can roughly be taken into account if the relative motion between ship and opening is computed (e.g. by E4ROLLS) and used for the flux computations. This method is of course more robust and for the desired purpose less precise, as the dynamics are underestimated. When analyzing the SS HERAKLION accident, Teuscher (Teuscher 2011) has checked both methods and found that they converged with respect to the most important results (flooding times and floodwater amount). We will in the following present the results obtained from E4ROLLS for the flooding of the vehicle deck.

Figure 12 shows the computed time series for SS HERAKLION after the STB side door was pushed open. The computation was made for a speed of 15 knots, encounter angle 0, wind 8Bft, significant period 8.5 s, significant wave height 5 m. The vehicle deck was modelled by two spaces to take into account the sheer (our code can at present handle only simple cuboids as spaces), therefore the total compartment volume is the sum of these two space volumes (see Fig. 12, bottom time series). Between these two spaces, the fluid can move freely. The hydrostatic computation resulted in about 1800t water accumulated in

the vehicle deck at the equilibrium of about 45 degree.

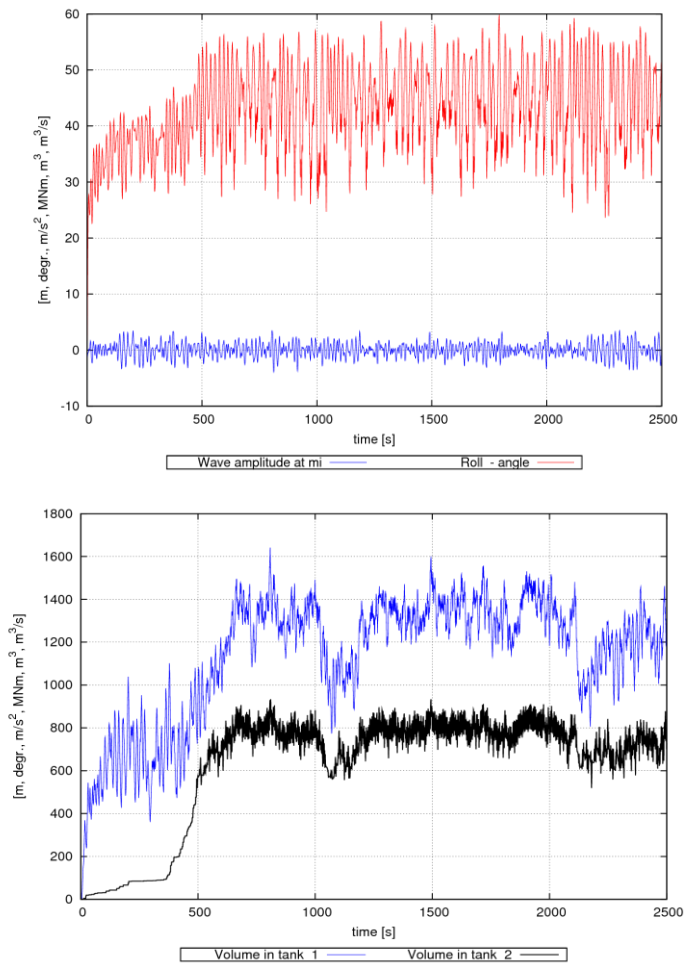


Figure 12: Time plot of the roll angle (top) and the volume in the vehicle compartment (sum of the space volume curves in the bottom plot), accident scenario

This coincides with the dynamic results obtained from E4ROLLS, where the static equilibrium is computed somewhat larger at slightly larger volumes in the vehicle deck. The first phase of the flooding shows that it takes approximately 500 s to flood the vehicle deck and to pass the first stability plateau, because the water inflow is forced into the ship by the motion. After this situation is reached, the vessel oscillates around this condition, but we have assumed that course and speed are kept during the simulation. It is now interesting to analyze alternative scenarios to check whether there had been additional possibilities to



prevent the accident. In his investigations, Wendel (Wendel 1970) has suggested that the ship should take the wind from abaft and the waves from STB stern quartering. The idea was to get rid of the wind heeling moment by a starboard turn. Unfortunately, numerical simulations by Teuscher (Teuscher 2011) have shown that SS HERAKLION would also have capsized during this manoeuvre. We have thought about another alternative which we present here for the first time, see Fig. 13. There, an alternative turn to STB is computed, but now in beam seas and stern quartering wind, both from STB. The open side door is now fully exposed to the sea.

that now, the water is entrapped in the vehicle deck, as the ship heels to PS due to the larger relative motion of the beam sea condition and the wind heeling moment. This heeling increases the freeboard further, and the situation converges into a condition where the amount of water on deck does not increase further. The ship remains stable at about 25 Degree heel to port side, where about 500 t of floodwater have now accumulated on the deck. It is quite probable that this manoeuvre - a turn to PS - would have saved the vehicle deck from being completely flooded.

5.3 Conclusions for the water ingress

The numerical simulations of the water ingress into the vehicle deck have shown reasonable results. The re computation of the accident scenario have shown that based on our assumptions, the vehicle deck is flooded and the ship takes a large heel. But the simulations have also shown that the ship was not necessarily lost when the refer truck opened the side door: The ship had some residual stability left even with the flooded vehicle deck, and if the heeling moment could have been reduced, the capsizing might have been prevented. The dynamics of the roll motion plus the wind heeling moment plus the moment of the tipped cars was too severe, and the residual stability was then lost. But the calculations have also shown that the ship could have been saved if the crew had turned her immediately and fully to starboard side into a beam sea, stern quartering wind scenario. In this situation, the open side door would have been directly exposed to the sea, which could have resulted in a PS heel. This PS heel would have led to a stable equilibrium floating condition with about 500 t of water entrapped in the vehicle deck, and the ship would have - according to our computations - survived.

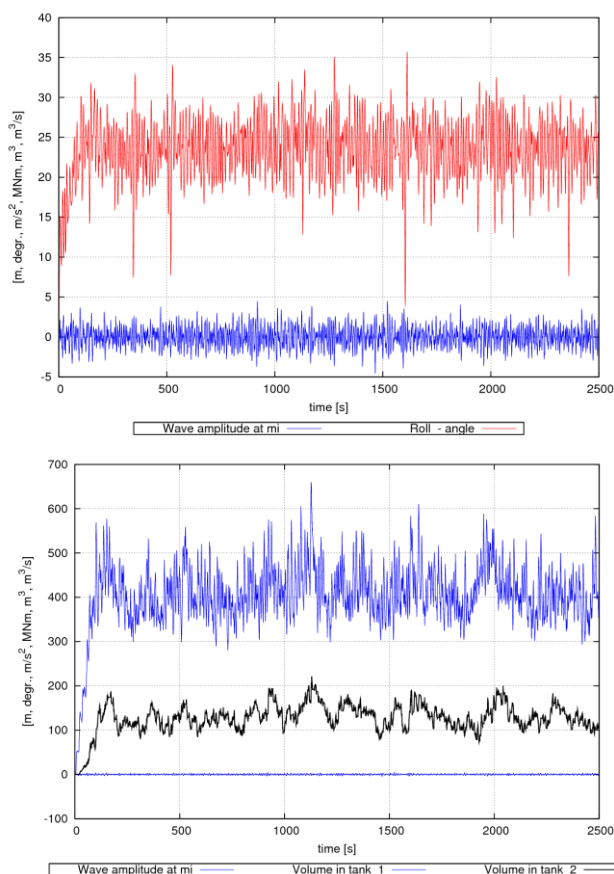


Figure 13: Time plot of the roll angle (top) and the volume in the vehicle compartment (sum of the curves in the bottom plot), alternative scenario

The ship is - like in the scenario suggested by Wendel - not exposed to the beam wind anymore, and the wind heeling moment increases the freeboard due do PS heel. The main difference between the two scenarios is



6. CONCLUSIONS

The capsizing accident of SS HERAKLION was analyzed with numerical methods. It could be shown that the application of such methods to marine casualties - even if they are some time ago - can show new facets of such accidents that are worth a scientific investigation. In the present case, the accident analysis came to a plausible event chain which is in line with the known facts and the observations of surviving witnesses. This is most important with respect to actual marine casualties, as it is important to use only validated methods and procedures for the evaluation of such accidents. The evaluation of the capsizing event of SS HERAKLION could plausibly show that it might have been possible to avoid the accident by operational measures, and this finding might be of some use with respect to the education of seafarers. However, the accident of SS HERAKLION has also shown that several safety rules were not followed, and it is most important that we obey all the existing rules strictly: All maritime casualties which we have investigated at our institute always showed a massive violation of existing safety regulations.

7. ACKNOWLEDGMENTS

The authors wish to thank Prof. Dr. Ing. S. Kastner, Univ. Bremen, for having initiated this work. We further thank Prof. Dr.- Ing. A. Papanikolaou, Ship Design Laboratory, NTUA for the excellent cooperation.

8. REFERENCES

- AEENA (Hellenic Maritime Accident Investigation Board) 1967 "Official Report HERAKLION", Original in Greece, 1967, Athens.
- BSU Bundesstelle für Seeunfalluntersuchung (Federal Bureau of Maritime Casualty Investigation) 2010, "Untergang des FK ORTGAL UNO am 13. Januar 2010 westlich von Irland (Foundering of FK ORTEGAL UNO 13th of January, 2010, west of Ireland). BSU Report 07/10, Hamburg, Germany.
- Dankowski, H. 2011 "Eine schnelle, direkte Methode zur Simulation von Flutungs- und Sinkvorgängen von Schiffen (A fast, direct method for the computation of flooding and sinking of ships)". Third Interdisciplinary Workshop Maritime Systems, TU Hamburg - Harburg, 2011.
- Georgiadis, S. and Antoniou A. 1967, "Expertise on the Sinking of SS HERAKLION". AEENA, Official Investigation Report, Athens 1967, Addendum No 5 (Original in Greece).
- Grim, O. 1960 "Beitrag zum Problem des Schiffes im Seegang". Schiffstechnik 1960.
- Fragoulis, 1967, "Expertise on the Sinking of SS HERAKLION". AEENA, Official Investigation Report, Athens 1967, Addendum No. 2, (Original in Greece).
- Kluwe, F. and Krüger, S. 2008, "Evaluation of Minimum Stability Requirements for Ships in Following Seas taking into account Dynamic Effects. PROC. JSTG 2008.
- Petey, F 1988, "Ermittlung der Kentersicherheit lecker Schiffe im Seegang aus Bewegungssimulationen." Rep. 487. Inst. F. Schiffbau, Univ.
- Teuscher, C 2011, "Technische Untersuchung des Seeunfalles von MS HERAKLION unter besonderer Berücksichtigung des dynamischen Verhaltens im Seegang", BSc Thesis, TU Hamburg Harburg, 2011.
- Wendel, K. 1970, "Gutachten über den Untergang des Fährschiffes HERAKLION (Expertise on the Foundering of the Ferry HERAKLION.", Inst. F. Schiffbau. TU Hamburg- Harburg, 1970.





Investigation into the Sinking of the RO-RO Passenger Ferry S.S HERAKLION

A. Papanikolaou, *National Technical University of Athens-Ship Design
Laboratory*, papa@deslab.ntua.gr

E. Boulougouris, *National Technical University of Athens-Ship Design
Laboratory*, yboulg@deslab.ntua.gr

A. Sklavenitis, *National Technical University of Athens-Ship Design Laboratory*

ABSTRACT

On December 8, 1966 the Ro-Pax ferry *S.S. Heraklion* capsized and sank in the Aegean Sea, resulting in the death of over 200 people. The present paper tries to shed some light into the various events that led to the largest tragedy of modern Greek maritime history. It re-constructs the accidental data based on a variety of original investigation reports, ship files and legal evidence. Ship's loading and damage stability behavior was re-investigated and the flooding/ sinking of the ship was simulated by use of a time simulation method. Results of our investigation are compared with available testimonies of survivors.

1. INTRODUCTION

In the night of December 8, 1966 the Ro-Pax ferry *S.S. Heraklion* capsized and sank in the Aegean Sea, resulting in the death of over 200 people.

SS Heraklion was originally built at Fairfield Shipbuilding and Engineering Company in Glasgow in 1949. Her first name was *SS Leicestershire* and she was owned by Bibby Line. She initially operated the UK to Burma route. She was also chartered to the British India Line for some time to supplement its London to East Africa service. Aegean Steam Navigation Co bought the ship in 1964 to operate her under their Typaldos Line. It was then renamed to *SS Heraklion*. In order to fit her new duties Typaldos Line converted the ship to a passenger/car ferry.

The ship sailed out from Souda Bay, Chania-Crete in the evening of December 7, 1966, under extreme weather conditions, for

the port of Piraeus. While sailing south of the rocky island of *Falkonera* a non-secured refrigerator truck moved transversely and hit the side loading door violently. The door opened and the truck plummeted into the sea. As result of that the car deck was flooded through the side door opening and this caused the capsize/sinking of the ship sometime after 2:00am on December 8, 1966.

Considering the significance of this accident for the modern Greek maritime history, the authors using state of the art methods and tools are revisiting this accident in order to assess the main reasons for this maritime tragedy, causing the lives to more than 200 people. The subject of the paper is part of the diploma thesis work of the 3rd author (Sklavenitis, 2012).

2. THE ACCIDENT

In the night of December 7, 1966, at about 7.30pm local time, the *S.S Heraklion* left Souda Bay in North-West Crete heading for



the port of Piraeus in mainland Greece. The ship was in regular service on the route Chania/Crete-Piraeus. There was a delay of about half an hour with the departure from Chania port due to the late arrival of an expected 34-ton reefer truck loaded with oranges. Upon arrival the truck entered in hurry the forward car deck of the ship from a side ramp/door. It was already late with ship's departure and the crew was under pressure to quickly load the truck so that the ship could leave; in view of this, the truck was unconventionally loaded *transversely* and without being lashed, noting that all other trucks and cars on the same deck were loaded longitudinally according to loading plan, but with no special means of lashing either.

At about midnight the already rough weather conditions worsened (winds of 8+ Beaufort scale and SW stern-quartering waves of 5 to 6m wave height) and the ship started to roll heavily, next to strong heave and pitch motions. According to testimonies of survivors, several trucks started moving and crashing against each other due to the extreme motions of the ship; at about 01:10am, a truck carrying soap and oil turned over; the released oily cargo made the car deck extremely slippery and dangerous to move on it.

Several minutes later, as the rolling motion was getting stronger, the heavy 34tons reefer truck started also moving transversely over the slippery deck and crashed against the side door of the garage, from which it entered the ship, several times. According to testimonies, this phase seems to have lasted for about fifteen minutes (01:30am-01:45am) and ended with the starboard side door giving in and getting open, with the truck plummeting into the sea (first, the trailer was disconnected from the tractor and did fall to the sea; shortly after the tractor followed).

With the ship moving heavily in strong seas, water started flooding the car deck, resulting in a heavy list. Despite the captain's efforts to restore the ship to her vertical position, the list

progressively increased and additional water entered ship's car deck from the open side door until the point of no return. The ship finally sank near the island of Milos (Fig.1, *Falkonera's Waters*), shortly after 2:00am on December 8, 1966.

An SOS signal from SS *Heraklion* was received at 02:06am from various stations and ships around the Aegean Sea. The SOS signal was repeated twice. The Greek Ministry of Mercantile Marine was underequipped to handle the necessary communications and SAR actions, while the port authorities of Piraeus, Syros and of other neighboring islands reported also unable to offer assistance due to lack of equipment. Unfortunately the ferry *Minos*, which was on the same route and some 15 miles away from the scene, did not receive the SOS.

At 4.30am the naval ship *RHS Syros* was ordered to get under way, while an hour later the Greek Air force was alerted. A C-47 sky-train took off from Elefsis airport followed shortly by two more. The first aircraft arrived at around 10:00am at the same time with the British *HMS Ashton*, which started picking up survivors aided from the three aircraft. This was about 8 hrs after ship's sinking!

Officially, out of 73 officers and crew and 191 passengers only 46 were rescued, (16 crew and 30 passengers), while 217 perished. The exact number remains however unknown (some speak of 247 lost lives), since at the time it was customary to board the ship without a ticket, which would be issued upon sailing.

The Greek government's investigation found the Typaldos Line guilty of negligence for several reasons; the company was also charged with manslaughter and faking documents. The owner of the company, the general manager and two officers were sentenced to jail in 1968 (5 to 7 years prison). In the aftermath, it was found that twelve of the company's fifteen ships failed inspections under international law. The company's remaining ships were taken over and sold either for scrap or sold off for other uses. The Typaldos line was dissolved.

Following the *S.S Heraklion* disaster, the Greek government released for all passenger ships leaving Greek ports the so-called ‘*suspension of sail-out in bad weather*’ decree. Based on this, passenger ships operating in Greek waters are prohibited from sailing out with winds blowing at 8 Beaufort scale or higher, depending on their size. At the time of accident, it was up to the captain to decide whether to sail out or not. The ‘*suspension of sail-out in bad weather*’ decree remains in force until today in Greece.

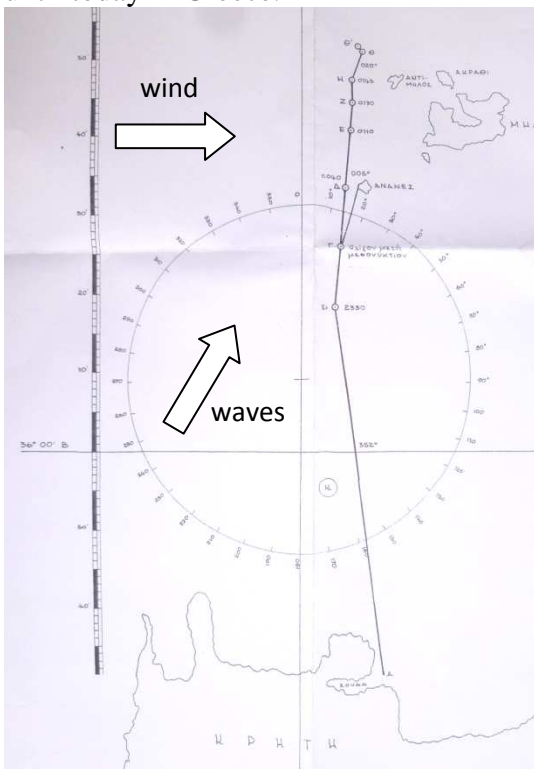


Figure 1: Ship's course

3. HISTORICAL BACKGROUND

The owner and operator of the tragic ship was the *Aegean Steam Navigation Co* of Typaldos brothers. The company was founded after WWII and started offering passenger transport and cruising services in the Greek coastal market. The company was quite successful and kept steadily growing, operating with more and more ships in the sixties. In 1964, *S.S Heraklion* was acquired by Typaldos brothers to provide passenger liner services between Piraeus and Chania-Crete. Once the ship arrived in Greece, the former

SS Leicestershire originally built by Fairfield Shipbuilding & Eng. Co. in Glasgow in 1949 for the UK Bibby line, was refitted as a passenger/car ferry. The ship had an overall length of 498 ft (152 m), a beam of 60 ft (18 m), gross tonnage of 8.922 tons, fitted with a single propeller and reaching a speed of close to 18 knots.

At that time, the Greek shipping industry was on the way to recover from the damages of WW II. Most ship-owners were looking for second hand and often unsuitable vessels that were converted to passenger ferries and completely refitted. Conversions took place at small Greek yards without experience in this type of work. Naval architects, in charge of the conversions, did also have little experience in the assigned work.

Next to them, the coast-guard authorities had also little experience in safety inspections of passenger ferries, thus could not properly monitor the condition of the growing fleet. Without appropriate staffing, the authorities were simply unable to meet the demands of their assigned tasks.

Even more, the political situation in Greece was at the time of the accident very unstable, if not chaotic, what was reflected in the performance of Greece's administration. In expectation of general elections, temporary governments were being appointed by the King of Greece, to be replaced by others within very short time. Notably, few months after the accident (April 21st, 1967) a military junta came into power in Greece.

According to a report of the chief of the coast guard's naval architecture department of December 12, 1966 (this report was released only 4 days after the accident...), only few passenger ships complied with the safety regulations in force. This is not surprising if we consider the following.

The naval architects in charge of the shipbuilding work rarely submitted any plans for approval to the authorities, though it was required; even more, when they submitted



plans, these plans and calculations usually did not correspond to the actual ship's condition. Incorrect gross & net tonnage calculations were often approved by incompetent authorities, as were freeboard and subdivision length calculations; inclining experiments were often not conducted, or accomplished incorrectly. Captains used to operate their ships without having proper instructions for the ballasting of the ship and vessels often disposed insufficient watertight subdivision after their conversion ("watertight" bulkheads were not truly watertight due to various non-watertight openings/ways in between subdivided spaces).

In this state of affairs of Greek coastal shipping business at the time of the accident, a fatal accident as that of *S.S Heraklion* could be expected to come.

Next to *S.S. Heraklion*, several other Typaldos Line's vessels, like *Lemnos*, *Ydra* and *Elli*, were often reported as operating without proper safety certificates, incorrect or no data at all in their files. According to the documentary files of the authorities, the *S.S. Heraklion* in particular encountered several problems during the period after her conversion and the commencement of operations in summer 1965 and up to December 1966, when she sank. This includes: improper fitting of watertight transverse bulkheads, with alleged 15 times 15cm holes, untrained crew in the proper use of the auxiliary systems of the ship (ballast pumps, etc), incorrect freeboard and subdivision studies submitted to the authorities, lack of inclining experiment and of related assessments of ship's stability, improper fitting of side ramp doors, with repeatedly broken mounting/hinges, etc. Given the additional fact that the ship had no proper class certificate as passenger ship, it is a miracle how the ship continued operating under temporary permit by the coast guard authorities for about 1.5 years!

It would be however improper to examine that time's state of affairs of Greece's Coast Guard by today's standards and rush to simple conclusions. Damage stability regulations for passenger ships were at the time of accident

insufficient, even at international level. SOLAS 48 came into force only in September 1961 (!) and its provisions were relevant strictly only for newbuildings. Only several years later, in October 1969, SOLAS 60 came into force, that more or less led the foundations for the later deterministic stability criteria of SOLAS 74 and SOLAS 90, which remained in use until quite recently.

4. "SS HERAKLION" - THE SHIP AFTER THE CONVERSION

SS Heraklion was originally built as a cargo liner by Fairfield in Glasgow in 1949 and named *SS Leicestershire*. After some years liner service between UK and Burma and later to East Africa, she was sold in 1964 to the *Aegean Steam Navigation Co -Typaldos Line*; she was then converted to a passenger/car ferry and renamed *SS Heraklion*.

She was equipped with a 4-cylinder steam turbine placed in an engine room amidships, like in most ships of that period. Powered by 7000HP and with a capacity of 1000 passengers and 400t of trucks & cars, she was one of the largest, fastest and most competitive ships operating in the Aegean at that time, achieving a speed of 18kn.

The main conversion works refer to the following:

- Four (4) additional transverse bulkheads were fitted, subdividing the existing holds of the ship and generating nine (9) new *void spaces* as shown in Figure 2 (encircled with blue colour).
- The original hatch coamings were covered in such a way so as to generate two car decks, namely one extending from the engine room to the forepeak ballast tank and another one extending from the engine room to the afterpeak ballast tank.
- The front part of the intermediate deck was totally removed (marked in red color in Fig. 2) in order to provide space for high trucks loaded on the forward car deck.

- Several compartments were refurbished as tourist class accommodation spaces (marked in grey color) while existing accommodation spaces on the main deck were extended/refitted.
- The original ship's winches, cranes and other equipment concerning the loading/unloading procedure were totally removed from the main deck while the hatch coamings were covered in such a way to form a continuous deck.
- The ship was equipped with four (4) side ramp-doors, two for the forward, larger car deck and two for the smaller car deck on the ship's stern.

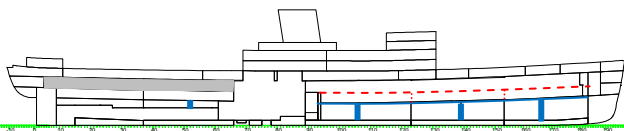


Figure 2: Main conversion's alterations

As shown in the side profile (Fig.2), the ship's watertight part, extending from the baseline to the car deck, was subdivided by eleven (11) transverse bulkheads. However, the four additional bulkheads fitted during the conversion works did not go through to the base of the double bottom, but reached only the double bottom's ceiling.

Table 1: SS HERAKLION main particulars

SHIP PARTICULARS	
Ship Name	SS HERAKLION
Ship Type	Passenger / Car Ferry
Builders	Fairfield Shipbuilding and Engineering Company
Year of built	1949
Area of Operation (last)	Aegean Sea
Service Speed, [kn]	18.0
Gross Register Tonnes	4407
Deadweight, in tonnes	1089
Passengers acc. to summer certificate	1375
Passengers acc. to winter certificate	625
Number of crew	95
SHIP DIMENSIONS	
Length over all, [m]	146.46
Breadth exteme, [m]	18.38
Depth to the main deck, [m]	5.334

It was definitely a major conversion in all respect that had a great impact on the ship's safety. It is notable that most of the conversion works were carried out at a local yard without experience in this type of conversion work and were completed without being supervised by the Greek Authorities and other authorities, as required. This may explain the numerous irregularities that were revealed later on, while the ship was in operation for a prolonged time without properly approved safety certificates.

5. SHIP MODEL RECONSTRUCTION

In an attempt to shed some light in this tragic accident, a reconstruction of the ship's hull has been attempted using various historical documents (Georgiadis and Antoniou 1967, Frangoulis 1967, AEENA 1967), the close cooperation with TUHH which provided us with an initial hullform data (Dankowski, 2011) and the available ship drawings. Based on the above, the geometry file of the hull was developed in NAPA (see Figure 3). The hydrostatics were verified at various loading conditions with those refered in the investigations reports. The ship model coloured according to the purpose of each room is shown in Figure 4.

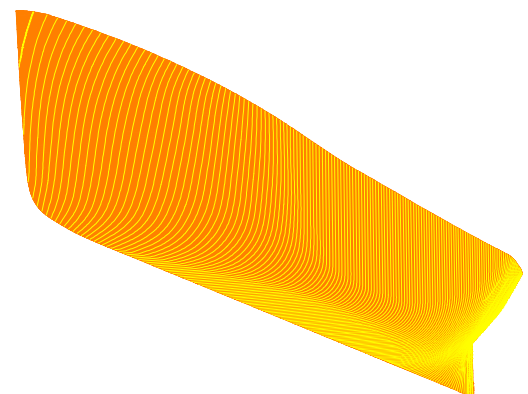


Figure 3: Hull lines in NAPA

A key issue in our study, but also in all the conducted investigations in relation to the accident, was the determination of ship's actual lightship weight and centroid's location. An inclining experiment was never properly conducted after ship's conversion and delivery,



thus the data of her sister vessel, namely SS CHANIA were used for extracting the SS HERAKLION's lightweight. Using the recorded data, the case was reconstructed in NAPA and the results are shown in Table 2. Both the lightship weight and VCG are in good agreement with the study of Georgiadis and Antoniou (1967). The displacement at the inclining test conditions was calculated to be 7444.5 tons, compared to 7447.62 given by the comparative study report. The VCG at the inclining experiment was estimated to have been 7.753 m, compared to 7.516 m in the comparative report.

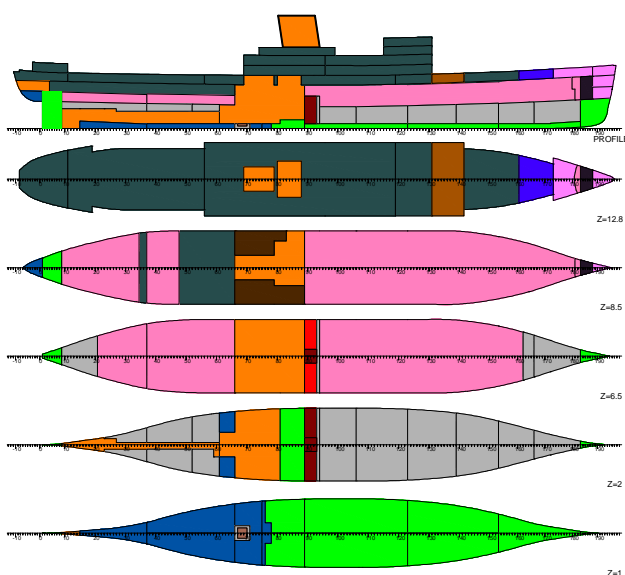


Figure 4: Napa model colours with room purposes

Table 2: SS HANIA inclining experiment results

Mean draught moulded	4.521	[m]
Trim (+fwd trim)	-3.687	[m]
Displacement	7444.5	[tons]
KM	8.771	[m]
GM	0.935	[m]
Free surface correction	0.083	[m]
GM ₀	1.018	[m]
KG	7.753	[m]
Lightweight	5722.3	[tons]
Lightweight-LCG	63.78	[m]
Lightweight-VCG	9.70	[m]

The geometric model gives a lightship of 5722.3 tons for SS CHANIA, 79.1 tons (1.3%) less than the lightship referred to in the accident investigation report. The main reason for the

increased difference between the inclining experiment and lightship weight data is the difference in the tank capacities used in the investigation report and those calculated by the model. Considering the lighter superstructure of SS HERAKLION due to the removal of the aft superstructure, her lightship was estimated as given in Table 3.

Table 3: Extracted SS HERAKLION lightship

Lightweight	5659.41	[tons]
Lightweight-LCG	64.19	[m]
Lightweight-VCG	9.641	[m]

In order to check the stability of the vessel, the reconstruction of the full load condition was made using the available data from Georgiadis and Antoniou (1967). The resulting floating conditions are shown in Figure 5 and the numerical results in Table 4.

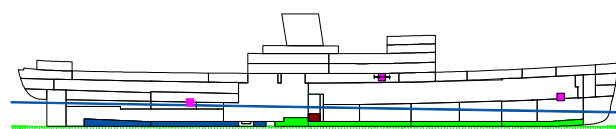


Figure 5: Full load floating condition

Table 4: Full load condition

Deadweight	2120.8	[tons]
Displacement-Full load	7780.2	[tons]
Full load-LCG	69.20	[m]
Full load -VCG	7.69	[m]
GM _{corr}	0.82	[m]

Table 5: Intact stability in full load condition

Criterion	REQ	ATTV	UNIT	STAT
AREA30	0.055	0.139	mrاد	OK
AREA40	0.090	0.257	mrاد	OK
AREA3040	0.030	0.118	mrاد	OK
GZ0.2	0.200	0.731	m	OK
MAXGZ25	25.000	40.331	deg	OK
GM0.15	0.150	0.822	m	OK

The results are in good agreement with those calculated in the Georgiadis and Antoniou (1967) report. The calculated displacement is 55.8 tons less (-0.7%) and the metacentric height 0.09 m less than the reported values. Surprisingly, the vessel fulfilled modern intact stability criteria as shown in

Table 5 (IMO Resolution A.749 (ES.IV)). The righting level at this loading condition is shown in Figure 6 and is in good agreement with comparative figures of other researchers (Dankowski, 2011).

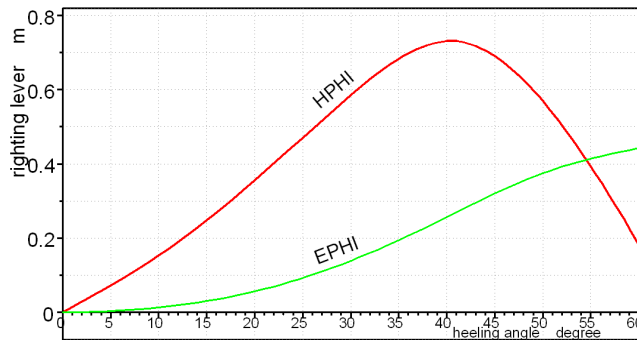


Figure 6: Stability in Full load condition

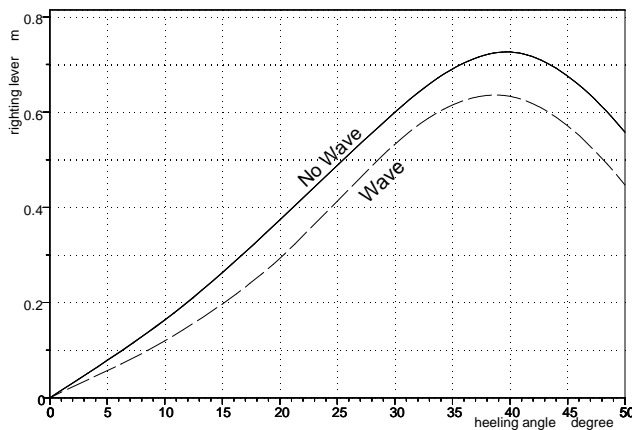


Figure 7: Ship's Stability in waves (hogging)

Based on the data from the official investigation, the loading condition at the time of the tragic accident was modeled. The vessel satisfied also at this condition the IMO intact stability standards. Additionally, the effect of the stern waves on stability was investigated, calculating the righting arm in waves. As can be seen in Figure 7 there is a reduction of the righting arm in the hogging condition ($h=4\text{m}$, $l=L_{wl}$) but not substantial.

6. FLOODING INVESTIGATION

The accident investigation has shown that the main cause of the accident was the shift of an unsecured reefer truck that struck several times against the starboard side door. This ended with the starboard side door giving in, with the truck plummeting into the sea (first,

the trailer was disconnected from the tractor and did fall to the sea; shortly after the tractor followed). The movement of the truck to the side created a significant heeling moment for the ship. The lower edge of the opened side door came closer to the wavy sea surface and considering ship's severe roll and heave motions the flooding of the vehicle deck was the due consequence. This resulted in loss of stability due to the significant free surface formed in the car deck space, while the floodwater account caused a reduction of freeboard and the additional increase of the water quantities entering the ship. Simultaneously, due to down-flooding openings on the car deck, amounts of water flooded the lower void spaces, rendering the capsizing of the vessel unavoidable.

The identified events that caused the rapid heeling of the ship at her starboard side were:

- The transverse shift of the reefer truck from the center line to the edge of the opened side door
- The flooding of the car deck
- The transverse shift of the rest of the cars
- The presence of following waves
- The beam winds blowing from the port side of the vessel

The heeling caused by the beam winds was calculated using the IMO weather criterion where the wind heeling moment that is generated when a pressure of 0.1 t/m^2 is applied on ship's profile area. This pressure would cause the heeling of the ship by 12.5 degrees in still water and more than 16 degrees at the hollow of the wave (hogging).

It should be mentioned here that due to the small freeboard the lower edge of the side door is submerged at an angle of about 10 degrees. The location of the side door at the middle of the forward car space combined with the sheer of the car deck and the large trim of the vessel permitted the accumulation of large quantities



of water in case of flooding and the developing of a large free surface. The calculation has shown that in its intact loading condition only 17 tons would be sufficient to diminish metacentric height of the vessel in still water condition and only 6 tons at hogging condition. For reference, the forward car deck space had a capacity according our NAPA model of more than 95 tons for a reference height of 0.5 meters at its lower aft end when the trim of the ship was 3 m (aft).

With the reefer truck hanging at the end of the opened side door, a significant heeling moment was imposed on the vessel. In still water the ship would heel about 4 degrees, reaching 15 degrees with the wind force. At hogging condition these values increase to 5 and 19 degrees respectively. Assuming a quantity of 50 tons of flood water on the car deck the static heel reaches 9 degrees and the wind heeling surpasses 21 degrees.

According to the testimonies, at the next stage the reefer plummeted into the sea removing its heeling moment, but at the same time the rest of the trucks in the car deck had shifted to the starboard side. Assuming a shift of 2 meters to the center of their weight and removing the reefer truck's weight creates a new loading condition with a static heel of 5 degrees and wind heeling of 19 degrees. It is obvious that at this condition significant quantities of water may enter the car deck. A quantity of 100 tons is sufficient to increase the static heel to 12 degrees and the wind heeling to 23 degrees. Increase of the flood volume would degrade further the stability of the ship.

6.1 Flooding simulation

In order to investigate more thoroughly the progressive flooding sequence a full geometric model was created in NAPA, modelling all spaces above the main deck as shown in *Figure 8*. A number of internal and external openings were modeled in order to create a full hydraulic model for the progressive flooding of the ship (Dankowski, 2011).

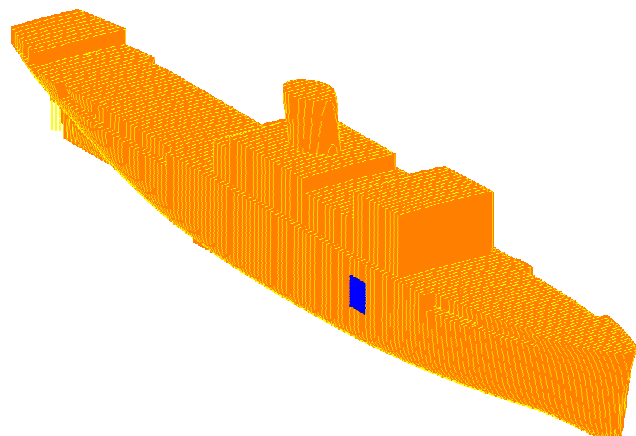


Figure 8: Geometric model with superstructure

6.2 The pressure-correction method

The NAPA dynamic flooding simulation tool was used for simulating the progressive flooding. The principles of the method were presented in Ruponen (2007). At each time step the conservation of mass is satisfied in each flooded room, both for water and air. The equation of continuity stipulates:

$$\int_{\Omega} \frac{\partial \rho}{\partial t} d\Omega = - \int_S \rho \mathbf{v} \cdot d\mathbf{S} \quad (1)$$

where ρ is the density of the fluid, \mathbf{v} the velocity vector and S the surface that bounds the control volume Ω . The velocities in the openings are calculated using Bernoulli's equation for a streamline from a point in the middle of a flooded room A to a point in the opening B:

$$\int_A^B \frac{dp}{\rho} + \frac{1}{2} (u_B^2 - u_A^2) + g(h_B - h_A) = 0 \quad (2)$$

where p is the air pressure, u the flow velocity and h the height for a reference level. The velocity at the center of the room is assumed zero. The flow is considered inviscid and irrotational, but semi-empirical discharge coefficients are used for the pressure losses in flooding openings and pipes. For the latter, the discharge coefficient is calculated according to the MSC.245(83) (IMO, 2007).



The flooding simulation uses the pressure-correction method. The ship is considered as an unstructured and staggered grid of volumes (cells). Each room is a single computational cell. The flux through a cell face is possible only with an opening that connects the room with another one or the sea (environment). The water is level in the room, thus sloshing effects are not taken into account. The volume in each room is calculated using the water depth in it and the heel and trim angles. Thus, the progress of floodwater is solved implicitly on the basis of the pressures in the rooms and the velocities in the openings (Metsa et. al., 2008). The underlying concept is that the equation of continuity and the linearization of the momentum equation (Bernoulli) are used for the correction of the pressures until the iteration is converged and both are satisfied at the same time.

The tool allows also the estimation of the dynamic roll motion of the ship. However, in contrast to the more accurate time domain simulation tools – e.g. CAPSIM (Papanikolaou et.al., 2000; Spanos, 2002), FREDYN (de Kat and Peters, 2002) or PROTEUS (Jiasionowski, 2002) - that allow the consideration of 6 degrees of freedom motions in seaways, the NAPA flooding simulation tool does account only in an approximate way for the roll motion and ship dynamics, whereas trim and draught are treated in a quasi-static way. Note that the simulated roll motion is also an approximation of the true response and is based on specified values for the natural roll period and roll damping, whereas incident wave's height and period are also restricted to moderate values (Metsa et. al., 2008).

The main advantage offered by this tool is its fast execution, allowing the assessment of many damage scenarios within reasonable time. Also, the impact of the intermediate stages of flooding can be systematically explored, while taking into account moderate motions of the ship in beam waves.

6.3 Simulation results

Given the uncertainties surrounding the condition of watertightness fitted bulkheads and of ship's outfitting during the conversion of the ship, a variety of different scenarios were examined.

In an initial scenario it was considered that after the refer truck was gone overboard, the remaining vehicles were also shifted transversely due to the severe rolling motions of the ship. This scenario results to a steady list of 3.7 degrees to starboard side (in still water and without considering wind heeling moment). For the simulation of ship's flooding and motion using NAPA's flooding module, we assumed for the natural roll period of the ship 14.9 seconds (corresponding to a $GM=0.902$) and a roll damping coefficient of 0.05. For the incident wave spectrum a typical JONSWAP spectrum was used with a period of 7.6 seconds, corresponding to wave lengths of 90 meters. It should be noted that the used NAPA model did not allow evaluating large incident wave heights, what would have probably accelerated the flooding of the internal spaces.

The simulations have shown that for the ultimate capsizing of the ship, the downflooding of the void spaces below the car deck proved essential. In those simulation cases in which the void spaces were kept dry, the ship was listing but it remained finally stable at a higher heeling angle. When downflooding occurred, the ship capsized. This is shown in the following figures. The rate of increase of heeling was proportional to the size of the openings connecting the forward car deck and the down-flooding rate. This is elaborated in the following.

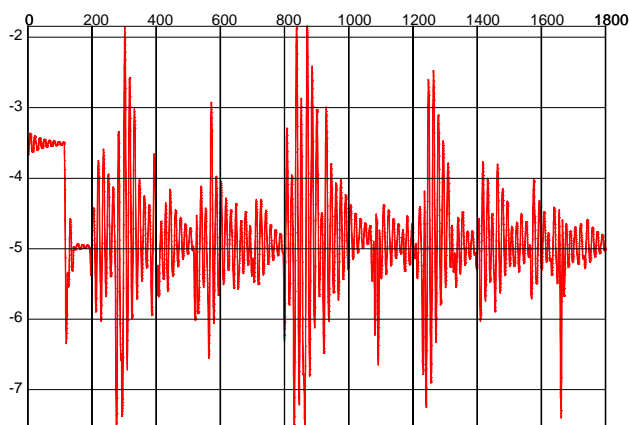


Figure 9: Heeling angle vs time [sec] for watertight cardeck

Initially the forward car deck was considered watertight with no downflooding points. In this case the ship would not capsize as can be seen in the Figure 9. As shown in Figure 10, an average quantity of about 30 tons of floodwater is entering the forward car-deck space though the side door opening. Ship's heeling increases from 3.7 degrees in still water due to the loading asymmetry to an average of about 5 degrees, rolling at times to more than 7 degrees; however, the ship is generally stable.

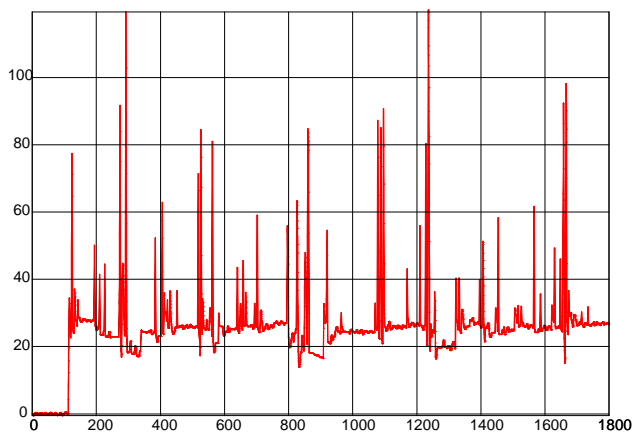


Figure 10: Floodwater versus time [sec] for watertight cardeck

Assuming that there are 6 down flooding openings on the car deck (for which there is evidence that it was not watertight), with an effective area of merely 0.1 sq.m., each connecting the cardeck space with the void spaces below, the situation changes dramatically. Now the list of the ship increases continuously and the ship capsizes after 340

seconds as can be seen in Figure 11. The floodwater is following the same trend as it is shown in Figure 12. The position of the ship just before capsizing is shown in Figure 13.



Figure 11: Heeling angle vs time [sec] for 0.1 sq.m. cardeck downflooding opening area each

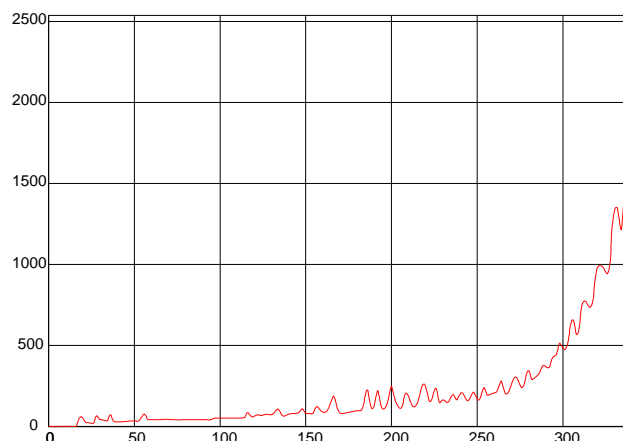


Figure 12: Floodwater versus time [sec] for 0.1 sq.m. cardeck downflooding opening area each

Doubling the size of the downflooding openings results in the capsize of the ship in almost half the time, from 340 seconds to 185 seconds. It is interesting to note that the floodwater quantity is about the same (around 2500 tons). The heeling angle time history for this case is illustrated in Figure 14 while the floodwater time history is depicted in Figure 15.

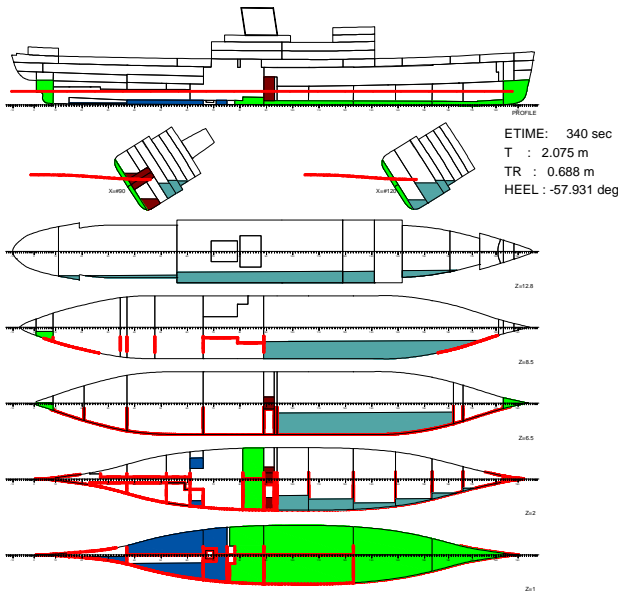


Figure 13: Intermediate stage of flooding just before capsizing for 0.1 sq.m. cardeck downflooding opening area each.

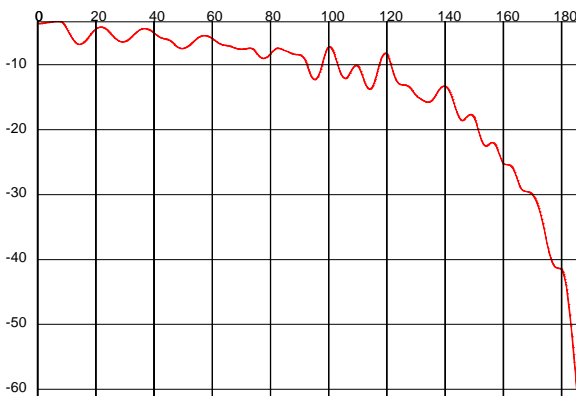


Figure 14: Heeling angle versus time [sec] for 0.2 sq.m. cardeck downflooding opening area each.

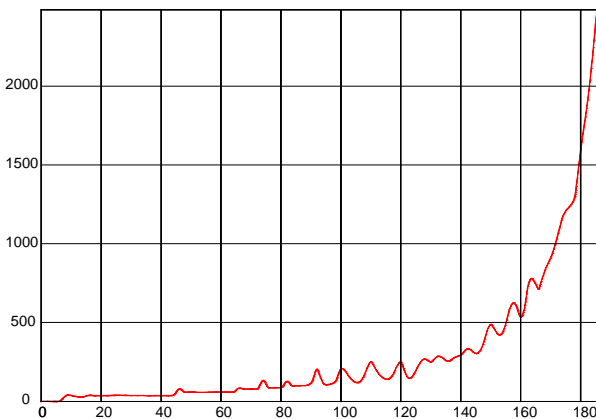


Figure 15: Floodwater versus time [sec] for 0.2 sq.m. cardeck downflooding opening area each

7. CONCLUSIONS

The results of the present stability analysis of SS HERAKLION using today's state-of-the-art tools support the findings of the original investigation report and agree with the eye witnesses. The capsizing of this ship was a typical RoRo ship accident with reduced freeboard, allowing the flooding of her car deck. Flooding of a RoRo ship's car deck was the cause of major marine accidents even in more recent years in Europe (e.g., *M/V Estonia* capsized in 1994 in a similar way almost 30 years after the SS HERAKLION). The risk of water-on-deck is considerable still today, even though current damage stability requirements are considerably more stringent. The present investigation suggests that the downflooding of large void spaces below the flooded car deck and the effect of multiple free surfaces was eventually the reason for ship's capsizing. Dynamic flooding simulation tools can provide significant insight and assist the work of both ship designers and the accident investigators.

8. ACKNOWLEDGEMENTS

The authors would like to thank Prof. S. Kruger and Dr. cand. H. Dankowski of TU Hamburg-Harburg for the excellent collaboration with NTUA-SDL in the collection of data and the analysis of this tragic marine disaster.

9. REFERENCES

- AEENA (Hellenic Maritime Accident Investigation Board) 1967, "Official Report HERAKLION", (in Greek), 1967, Athens.
- Dankowski H., "SS HERAKLION-Reconstruction of ship data model", TUHH report, December 5, 2011.
- deKat, J. O. and Peters, A.J., "Model Experiments and simulations of a damaged frigate", *Proceedings of the IMAM 2002 Congress*, No. 129, Crete, May 2002.
- Fragoulis, 1967, "Expertise on the Sinking of SS HERAKLION", (in Greek), AEENA,



Official Investigation Report, Athens 1967, Addendum No. 2.

Georgiadis, S. and Antoniou .A, “Expertise on the Sinking of SS HERAKLION”, (in Greek), AEENA, Official Investigation Report, Athens 1967, Addendum No. 5.

IMO, “Resolution MSC.245(83) Recommendation on a Standard Method for Evaluating Cross-Flooding Arrangements”, adopted on 12 October, 2007.

Jasionowski, A., “An Integrated Approach to Limit State Performance Assessment”, PhD thesis, University of Strathclyde, Glasgow, U.K, 2002.

Metsä, A., Ruponen, P., Ridgewell, C. and Mustonen, P., “Flooding Simulation as a Practical Design Tool”, Computer and IT Applications in the Maritime Industries (COMPIT), Liege, 21-23 April, 2008, pp. 135-147.

NAPA OY, Simulation tool, NAPA 2011, <http://www.napa.fi>.

Papanikolaou A., Zaraphonitis G., Spanos D., Boulougouris E. and Eliopoulou E., “Investigation into the capsizing of damaged Ro-Ro passenger Ships in Waves”, Proceedings of the 7th Inter. Conf. On Stability of Ships & Ocean Vehicles, STAB2000, Australia, Tasmania, 2000.

Ruponen, P., “Progressive Flooding of a Damaged Passenger Ship, Doctoral Dissertation”, Helsinki University of Technology, TKK Dissertations 94, 2007.

Sklavenitis, A., “Investigation into the sinking of SS Heraklion”, National Technical University of Athens, Ship Design Laboratory, Diploma Thesis, 2012.

Spanos, D., “Numerical Simulation of Flooded Ship Motions in Seaways and Investigation of the Behaviour of Passenger/Ro-Ro Ferries”, Doctoral thesis, National Technical University of Athens, Greece, 2002.



Influence of Lower Cargo Deck Longitudinal Subdivision of Solas 90/2004 on Ro-Pax Vessels over Attained Damage Stability Indices as 2006 Amendments Solas per MSC 216(82)

Fernando Junco, *PhD Naval Architect Professor Universidade da Coruña Spain*,
fjunco@cdf.udc.es

Juan M. Marcote, *PhD Naval Architect Maritime Safety Surveyor DGMM*, jmmarcote@fomento.es

Vicente Díaz, *PhD Naval Architect Professor Universidade da Coruña Spain*, vdiaz@udc.es

Marcos Míguez, *Naval Architect Professor Universidade da Coruña Spain*, mmiguez@udc.es

ABSTRACT

This paper presents the results of a study about the influence of the longitudinal subdivision in the lower cargo hold of a RO-PAX VESSEL in the attained subdivision index (A_s), according to MSC 216 (82). First the value of A_s has been computed based on a hypothetical and conventional compartment subdivision. Afterwards, we have analyzed the variation of the index (A_s) when the distance from the longitudinal lower hold cargo bulkheads to the side shell is increased. This study has shown that by applying the new regulations and by adjusting the ship subdivision, the hold cargo capacity could be increased.

Keywords: *Ferries, stability, probabilistic, ship design*

1. INTRODUCTION¹

The experience gained by the international maritime administration in the last 15 years, following the implementation of SOLAS 90 regulations, requires that all passenger ships must meet the damage stability criteria at large angles, taking into account the presence of additional heeling moments, such as those due to the distribution of passengers or boarding muster, wind or lowering of the survival craft. These criteria are complemented by the adoption of the Stockholm Agreement when the ship travels between states of the European Community. This Agreement also takes into account a residual heeling moment, considering a certain amount of water on the deck with a

certain height, depending on the wave height, the area of operation of the vessel and the residual freeboard after damage and its effect in the residual stability of the vessel. It is also applicable to the study of damage stability in vessels with longitudinal subdivision, which have a long cargo space below the bulkhead deck, which is quite usual in this type of Ferry vessels.

The need for unifying probabilistic damage stability criteria, which in general are applicable to the analysis of cargo ships since 1992, regardless of the type of cargo, forced the Maritime Safety Committee in 2006, considering the results of the HARDER project, (HARDER, 2006), to approve the proposed amendments to chapter II-1 of SOLAS, according to the MSC 216 (82) (IMO, 2006). The adoption of these amendments will affect the design of ships, both cargo and passenger ones, mainly Ferries (D. Vassalos et al., 2007),

¹ The naval architecture calculations of this research were carried out with the module Hydromax of Maxsurf program. All performances in the calculations are from MSC.194 (80), MSC.2161 (82) and MSC1 / Circ.1226 that can be modified in the future.



as originally did the entry into force of the SOLAS criteria, the A.265 Resolution (VIII) of 1973 (IMO, 1973), the Stockholm Agreement, the probabilistic criteria for cargo ships over 100 m long and the probabilistic criteria for cargo ships of length between 80 and 100 m.

The main objective of this work is to address the implementation of the new probabilistic method, with the specific purpose of analyzing how the partial attained subdivision index A_s varies when we alter the distance of the longitudinal bulkheads to the side shell in the area of the lower cargo hold of a Ro-Pax vessel.

2. VESSEL TYPE

In order to assess the effects on survival index, we have analyzed the behavior of a typical passenger ferry ship with five cargo decks.

Of these, the lowest, located on the double bottom, is situated between the double hull tanks; the possible variation in the size of this garage will be studied in this work.

The distance of the double hull bulkheads to the side shell is $B/5$, following the minimum requirements specified by SOLAS 90.

The longitudinal subdivision of that ship is composed of 19 zones, close to the value at which the influence of a new bulkhead in A index decreases (see Figure 1, G. Simopoulos et Al, 2008):

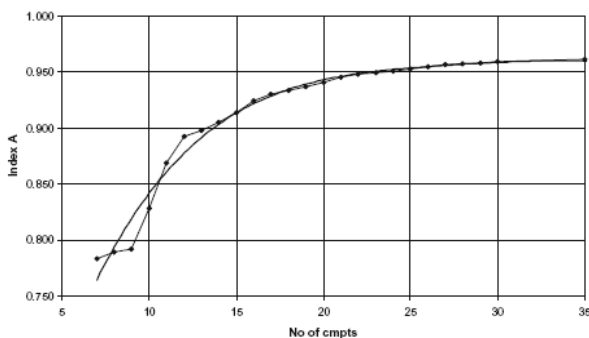


Figure 1: Influence of longitudinal subdivision on Index A.

For demonstration purposes, we have considered the following characteristics of the ship:

Subdivision length $L_s = 190$ m.

Beam $B = 26$ m.

Depth to bulkhead deck $D_{cp} = 9.20$ m.

Maximum draft $d_s = 6$ m.

Partial service draft $d_p = 5.50$ m.

Minimum draft (light weight condition) $d_l = 4.72$ m

N_1 (Number of people in boats) $N_1 = 300$ (2 lifeboats are considered, one on each side of 150 p. e.o.)

N_2 (No. remaining people on board) $N_2 = 600$

N_T Total number of persons on board) $N_1 + N_2 = 900$.

It is considered that the keel laying date is 2010 and hence is subject to the resolution requirements of the MSC 216 (82).

With these data the value of the required subdivision index R is 0.7391.

3. EVALUATION OF THE FACTOR A_s IN A STANDARD SHIP

The attained subdivision index A_s , expresses the probability of survival of the vessel after damage and must be greater than the required subdivision index R . To calculate the A_s index, it is necessary to include all possible failure scenarios for three loading conditions before the damage. Then, the results for each loading condition should be weighted as follows to obtain the total attained subdivision index.

$$A = 0,4 \cdot A_s + 0,4 \cdot A_p + 0,2 \cdot A_l$$

From this expression, it can be concluded that the most representative indexes, which provide a greater contribution to the attained subdivision index A , are A_S and A_p indexes. Hence, this research focuses primarily on the evolution of the attained partial subdivision index value A_S , at the maximum draft (d_s).

The general formula for the obtained index can be expressed as follows:

$$A = \sum p_i \cdot s_i$$

Where "i" represents the damage zone (group of compartments) under consideration, " p_i " represents the probability that only the zone "i" is flooded disregarding any horizontal subdivision, but taking into account the transverse one and the value of " s_i " represents the probability that the ship survives a flooding in the "i" zone under consideration.

The calculation of " p_i " depends on two parameters, p and r, where it is taken into account the transverse and longitudinal subdivision respectively.

As previously noted, in this work we assess compliance with regulatory requirements of different subdivision arrangements, in order to understand the relationship between the index A and the transversal distance from the longitudinal bulkheads to the side shell. To do that, an initial case corresponding to the longitudinal lower hold bulkheads at a distance of $B/5$ from the hull, will be compared with two other configurations in which the distance between the bulkheads and the external shell has been reduced, with the aim of increasing the capacity of the vessel.

Given that the modification of the position of the longitudinal bulkheads doesn't not affect the values of p, they have been computed and used in all the configurations.

To do this, it was decided to analyze the cases of one, two and three flooded compartments. The results are shown in Figures 2, 3 and 4:

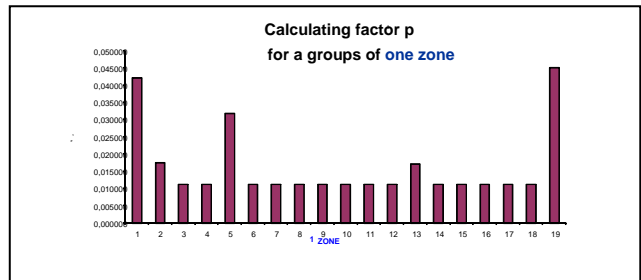


Figure 2: p factors. One zone computations.

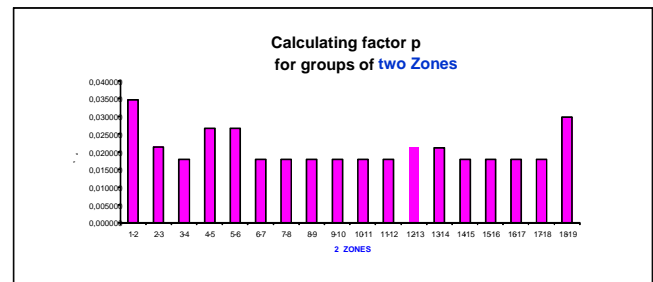


Figure 3: p factors. Two zones computations.

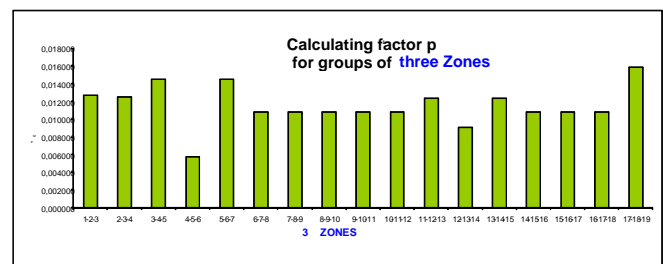


Figure 4: p factors. Three zones computations.

4. CALCULATION OF THE ATTAINED SUBDIVISION INDEX A_S

In order to evaluate the surviving probability of the ship after damage, some initial parameters have to be considered.

Moreover, if we want the results of this research to be a guide to future designers on



real projects, these data must somehow reflect certain plausibility.

Here is how this level of survivability varies if the ship subdivision is changed and where capacity would improve real Ro-Ro cargo capacity (mainly Ro-Ro lane meters).

It has been found in real cases for certain vessels of the type covered by this study, that the stability criteria of the intact vessel (especially at low drafts) are more determinant than those after damage. Evaluating separately the maximum theoretical KG available in the intact situation, we can consider that a margin of 0.8 m. in the KG would be sufficient for the purpose of this study. On the one hand we would calculate the value of A_s with sufficient margin to ensure an overall $A > R$ and moreover this would permit a future increase of the KG for real adjustments. Therefore in this study, the reference for calculations is $KG = 13.30$ m for the (ds) draft.

Studying damage of 1, 2 and 3 compartments, the following results have been obtained.

$$\sum p_i r_i s_i = 0,311(1c) + 0,3648(2c) + 0,1566(3c) = 0,8324$$

Regulation 6 of Chapter II-1 of SOLAS International Convention states that "the subdivision of a ship is considered sufficient, if the attained subdivision index A , determined in accordance with regulation 7, is not less than the required subdivision index R , and if, the indexes, A_s , A_p and A_l are not inferior to $0.9R$ for passenger ships and $0.5R$ for cargo ships."

The required value of the index $R=0.7391$. This value remains constant for any configuration of the subdivision of the ship, because it depends on the length (L_s) and the maximum number of persons (N). Multiplying this value R by the factor 0.9 would result in a value of $R' = 0.6651$

The value of the partial attained

subdivision index A_s for the initial configuration is 0.8324 , higher than the required subdivision index $R' = 0.6651$, so it can be concluded that the ship meets the second premise of rule number 6 of Chapter II-1 of SOLAS International Convention, which requires that the partial attained subdivision index $A_s > 0.9R$ for the condition of maximum depth of compartmentalized (ds).

Longitudinal bulkheads which limited the lower cargo hold were at a distance greater than $B/5$ (5.2 m) in most part of the hold, measured perpendicular to the side shell and at the deepest subdivision draft (ds). With this arrangement we could carry a total of eleven trucks.

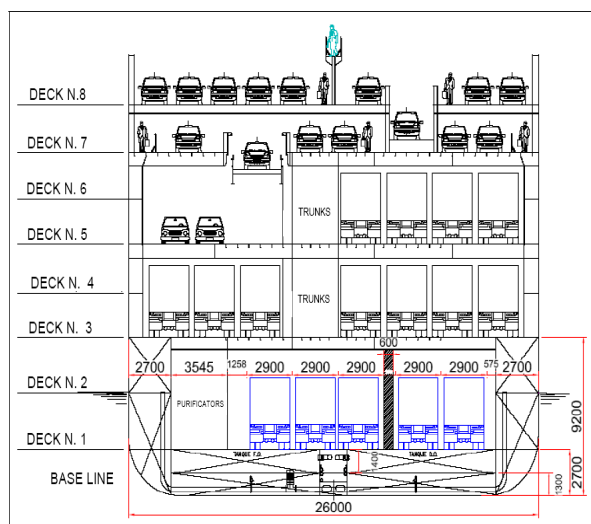


Figure 5: Ship transverse arrangement.

Then, the distance of the longitudinal bulkheads in lower hold area has been modified to 2.700 meters, as shown in Figure 5.

With this new arrangement and an appropriate modification of the access ramps to the lower cargo hold, the vessel could carry a total of up to seventeen trucks, as it is showed in the previous figure, if we can prove that the vessel meets the new probabilistic and deterministic criteria set forth in Chapter II-1 of SOLAS International Convention.

Calculation of p_i and r_i factors for this new subdivision.

P_i factor values will remain constant, because the distance between transverse bulkheads has not changed. The r_i values vary with respect to those obtained previously, because they depend on the transverse distance (b) from the side shell to the longitudinal bulkheads of the vessel.

Studying again the damages of 1, 2 and 3 compartments, we obtain the following:

$$\sum p_i r_i s_i = 0,2798(1c) + 0,2943(2c) + 0,1302(3c) = 0,7043$$

The partial attained index A_S for this new subdivision is **0,7043**, therefore higher than the required subdivision index $R' = 0.6651$. Thus it is proved that the ship meets the second premise of rule 6 of Chapter II-1 of SOLAS, which requires that the subdivision index obtained partial $A_S > 0.9 R$ for the condition of maximum subdivision draft (ds).

Since our intention in this paper is to analyze how the subdivision partial index A_S varies as a function of the distance to the longitudinal bulkheads limiting the lower cargo hold, we conducted a new study of the A_S index to take into account a third case, in which the longitudinal bulkheads of the cargo hold are placed at a distance of 4.10 meters, at an intermediate distance between the two arrangements discussed above. The result is as follows:

$$\sum p_i r_i s_i = 0,3104(1c) + 0,3176(2c) + 0,1344(3c) = 0,7624$$

The figure given below shows the relationship between the distance of the longitudinal bulkheads of the lowest cargo hold with respect to the molded breadth of the vessel (b/B) and the partial attained subdivision index

A_S , with respect to the required subdivision index R' (A_S/R').

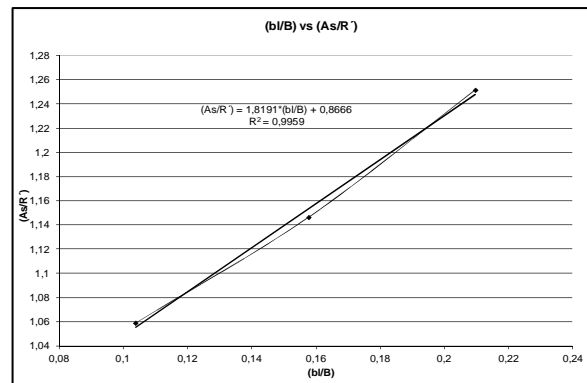


Figure 6: A_S index variation, depending on the distance of the longitudinal bulkheads of the lowest cargo hold to the side shell.

From Figure 6, we can conclude that the partial attained subdivision index A_S increases in a linear way when the distance from the longitudinal bulkheads of the lower cargo hold to the hull increases.

5. COMPLIANCE EVALUATION WITH OLDER CRITERIA

To make a comparison between the new and previous probabilistic methods, it is necessary to know the previous applicable rules to existing Ro-Pax vessels. These regulations are summarized in the Stockholm Agreement and Resolution A.265 (VIII).

The Stockholm agreement

The Stockholm Agreement applies to all passenger Ro-Ro ships operating from a port of a Member State in regular service, regardless of their flag, when engaged on international voyages. Under this agreement, the cases of water damage on deck are calculated according to Circular 1891 of the International Maritime Organization (IMO) of April 29, 1996 (Stockholm Agreement) in accordance with the requirements of the rule II-1/8 of SOLAS 90.

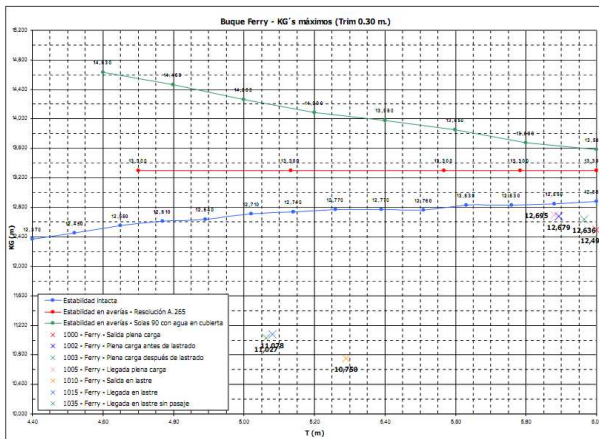


Figure 7: IMO A.265 and SOLAS 90 plus Stockholm Agreement maximum KG's.

Thus the ROPAX VESSELS must comply with paragraph 2 of this rule, given a hypothetical amount of water, which is assumed to accumulate on the Ro-Ro deck, which is the first deck of the garage above the splash cover. This amount of water on deck is calculated as a water surface of constant height above the deck, measured at the point where the minimum freeboard is produced locally (minimum freeboard in the damaged area). Once that point is submerged by the effect of the heel, said constant height of water is calculated on the floating line level. The height of water that must be considered depends on the residual freeboard (minimum freeboard in the damaged area), according to the following law:

- It will be taken a water height of 0.5 m. when the residual freeboard (fr) is ≤ 0.3 m.
- It will be taken a water depth of 0 m. when the residual freeboard (fr) is ≥ 2 m.
- For intermediate values of residual freeboard, the depth will be interpolated between these two values.

It is also necessary to take into account the significant wave height within the area where the ship will operate. Thus, the above values correspond to a significant wave height of 4 m. and may be reduced to zero in areas with

significant wave height less than or equal to 1.5 m.

Comparison of the new probabilistic method with the older regulations.

- Comparison of the probabilistic method with the Stockholm Agreement.

The main difference between the two regulations is the transverse extent of damage. While the maximum transverse extent of damage defined as the Stockholm Agreement, is $B/5$, the one defined under the new probabilistic method is $B/10$. Considering the new provision for subdivision of the ship, it is found that a transverse damage with an extension of $B/5$, would affect two side void/ballast tank spaces, the lower cargo hold and the garage.

Data from the initial state of equilibrium and stability at high angles to the above damaged indicate that the ship will not fulfill the criteria of the SA in relation to the maximum allowable angle of heel in case of unsymmetrical flooding or non-submergence of the margin line.

It must be stated that the reason why the longitudinal bulkheads in the area of the lower hold cargo were initially located at a distance of $B/5$, was precisely to meet the requirements demanded by the Regional Agreement and formerly Stockholm to meet the requirements imposed by SOLAS Regulation 90.

6. INFORMATION GENERATED AND CONCLUSIONS

The main conclusion obtained through this research, is that the new probabilistic calculation method for the case with the subdivision as amended, is less restrictive than previous standards (SOLAS 90, Stockholm Agreement). Therefore this new method gives us greater freedom in designing the ship, because we can modify the distance across the



longitudinal bulkheads of the lower cargo hold from a distance of $B/5$ up to $B/10$, allowing us to increase the capacity of the hold to carry more trucks, in this case 6 more.

The main restriction of new probabilistic method is imposed by the Rule 8.2, which requires that the A_s factor shall not be less than 0.9 for the three loading conditions that underpin the calculation of the subdivision.

It should be noted that to benefit from the greater design freedom offered by the new probabilistic approach, the vessel could not operate to or from a port of a Member State in regular service, for which the ship should comply the regional agreement would have to meet in Stockholm. Since the Stockholm Agreement, is the regulation that limits us more in terms of design, it is very important to make sure the area of the future operation of the ship.

implications of the new harmonised probabilistic damage stability regulations. International Shipbuilding Progress 54, pp 339-361.

7. REFERENCES

Harmonisation of Rules and Design Rationale. HARDER, 2004. Thematic Network SAFER EURORO II, Newsletter Issue No. 2.

International Maritime Organization, 2006. Resolution MSC.216(82). Adoption of Amendments to the International Convention for the Safety of Life at Sea, 1974, as Amended.

Internacional Maritime Organization, 1973. Assembly Resolution A.265 (VIII). Subdivision Rules and Stability of Passenger Ships, Equivalent to Part B of Chapter II of the International Convention for Safety of Life at Sea, 1960

G. Simopoulos, D. Konovessis. D. Vassalos, 2008. "Sensitivity analysis of the probabilistic damage stability regulations for RoPax vessels", Journal of Marine Science and Technology, 13, pp 164-177.

D. Vassalos, A. York, A. Jasionowski, M. Kanerva, A. Scott, 2007. Design





Damage Stability of Passenger Ships - Notions and Truths

Dracos Vassalos, *The Ship Stability Research Centre, Department of Naval Architecture and Marine Engineering, University of Strathclyde, Glasgow, Scotland, UK* d.vassalos@strath.ac.uk

ABSTRACT

A painstaking evolutionary development on damage stability of ships is giving way to unprecedented scientific and technological developments that has raised understanding on the subject as well as the capability to respond to the most demanding societal expectations on the safety of human life and to do so cost-effectively. Within less than half a century, damage stability calculations catapulted from **one** scenario per newbuilding (QE II, mid-1960s over a few months) **to tens of thousands of scenarios** (modern cruise liners in 2010s in a few weeks). Given the steepness of the learning curve and the pace of developments, it is understandable that certain notions were accepted as truths without due rigor and, as such, continue to shape contemporary thinking and developments. This paper draws attention to various issues that are emerging as knowledge grows and proposes a way forward for establishing a stronger foundation to safety assurance in the maritime sector and for future developments on the subject.

Keywords: *Damage Stability, Vulnerability, Emerging Issues with "Old" and "New" Ships and Rules, a Verification Framework for Maritime Safety*

1. INTRODUCTION

With artefacts on human endeavours at sea dated as far back as 6,500 B.C., it is mind boggling to think that it was not until 250 B.C. when the first recorded steps to establish the foundation of Naval Architecture, *floatability* and *stability*, were made by Archimedes. It is even more astonishing that it took nearly two millennia, after this, before the first attempts to convey the meaning of stability to the designers of the day took place in the 18th century by Hoste and Bouguer. Pertinent regulations, especially after accidents involving water ingress and flooding, were introduced even much later; notably, the first Merchant Shipping Act of 1854 addressing subdivision and leading eventually and after heavy loss of life to the adoption of the first internationally agreed system of subdivision in SOLAS 1929. Indeed, the first specific criterion on residual

static stability standards was introduced at the 1960 SOLAS Convention. This “tortoise” pace gave way to the steepest learning curve in the history of Naval Architecture with the introduction of the probabilistic damage stability rules in the late sixties as an alternative to the deterministic requirements. Prompting and motivating the adoption of a more rational approach to damage stability and survivability, probabilistic rules instigated the development of appropriate methods, tools and techniques capable of meaningfully addressing the physical phenomena involved. The ensuing improved technical capability virtually at worldwide has, in turn, been fuelling innovation in the shipping sector to meet the demand for larger, faster, more complex and specialised ships. Within 50 years, this new impetus has climaxed to the “zero tolerance” concept of Safe Return to Port in July 2009 and to an open proclamation by the Secretary General of the International Maritime Organization (IMO), stating that deterministic



regulations have no future. However, this is taking place in an industry that is fragmented, undermanned, intensely competitive and, above all, with a traditional deterministic and reactive mindset that sees all new developments as a hard-to-swallow "pill", likely to cause more ills than it can cure.

Deriving from this pace of developments and in the absence of a nurturing environment, the safety regime in the maritime industry is full of conceptual gaps that tend to undermine progress and safety at large. This paper draws attention to a few obvious issues, attempting to lay the foundation for a more concerted effort at international scale to "put things right". The best available means has always been legislation and, fortuitously or otherwise, the right instruments are in place to affect such change most effectively.

2. DAMAGE STABILITY LEGISLATION

2.1 Prevailing Regulatory System

The maritime regulatory system consists of internationally agreed standards at IMO, regionally agreed regulations, national standards, International Association of Classification Societies (IACS) Common Structural Rules and Unified Requirements, classification rules of individual Classification Societies and other technical standards. The regulatory system is a result of a continuous amendment process, mostly as a result of major accidents, tending to address the safety deficiencies resulting in the latest accident – in some cases only peripherally. Table 1 and Figure 1 tell the story!

Table 1: Modern Ferry Accidents in the Western World [VASSALOS 1999]

1953 Princess Victoria capsized and sank when large waves burst open the stern door in rough weather with the car deck and starboard engine room flooded (134 dead).

- 1974 Straitsman capsized and sank whilst approaching berth with the vehicle door partly open and, as a result of squat, flooding the vehicle deck (2 dead).
- 1987 Herald of Free Enterprise capsized when the bow wave and bow-trim combined to bring the open bow door underwater, leading to flooding of the vehicle deck (193 dead).
- 1987 Santa Margarita Dos capsized in port in Venezuela due to heeling while loading vehicles as a result of flooding of the vehicle deck (5 dead).
- 1994 Estonia capsized and sank due to flooding of the vehicle deck (852 dead).
- 2006 Al Salam Boccaccio '98 capsized and sank due to flooding of the vehicle deck, following fire (1,002 dead).

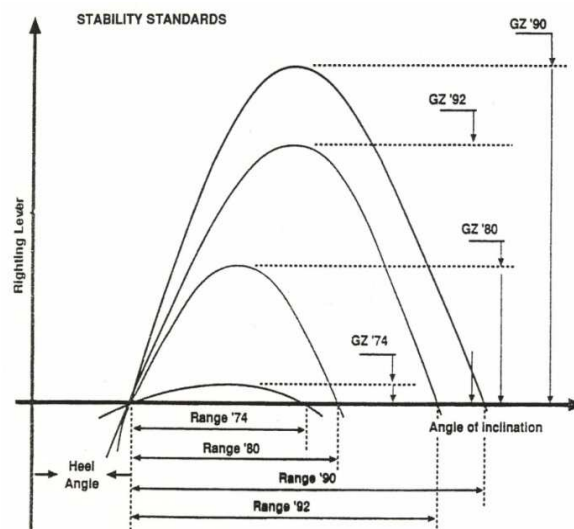


Figure 1: Deterministic Damage Stability Standards for Passenger Ships

The prevailing regulatory system is often referred to as prescriptive, implying that specific solutions are prescribed with little room for innovation. This may be cost-effective for standard ship designs like bulk carriers and oil tankers, resulting in very short delivery time, effective production and low costs. However, such regulations could inhibit innovation, as even designs that would increase ship safety may be violating existing prescriptive regulations.



2.2 Emerging Regulatory System

At IMO level, SOLAS-I.5 allows for equivalent design of "fitting, material, appliances or apparatus" provided "it is at least as effective as that required by the present regulations." This, in principle, facilitated equivalent safety and risk-based approaches but wide use is not documented. Today, the most widely used and known regulation SOLAS-II.2/17 addresses Alternative Design and Arrangements for fire safety. The associated guideline (IMO MSC 2001) advocates use of engineering analysis (i.e., risk analysis), a strategic goal adopted by IMO to "develop a regulatory framework for assessing alternative designs and arrangements so that new concepts and technologies may be permitted, which provide a level of safety at least equivalent to that provided by the prescriptive regulations." Other regulations in place that are, in principle, goal-based include: the new harmonised probabilistic rules for damage stability (this is implied but NOT explicit and has as a result not been utilised by the industry, with the exception of a few isolated cases on an informal basis), Safe Return to Port (Chapter II-2) and Regulation 38, Chapter III on Life Saving Appliances (IMO 2006). Assisting in this direction are regulations such as the Stockholm Agreement (IMO Resolution 14 1995), utilising a performance-based approach by means of numerical and physical model experiments.

However, legislation for "Alternative Design and Arrangements" and equivalent safety are now applicable to damage stability (albeit in principle only), fire safety, life saving appliances, ship systems and crashworthiness (again implicitly), thus offering probabilistic and risk-based approaches to safety for all these issues. As a result, safety equivalence will not be sufficient as an instrument to cater for innovative ships, which incorporate more than one risk-based design element. The safety implications between damage stability and fire safety on one hand and life saving appliances on the other are too complex to be handled in isolation and without the use of holistic risk

assessment and optimisation. In this context, optimisation should target not only optimum balance between safety and other design objectives but also between different safety objectives. The term to be used in this case is **risk balance**. As an example, even with very high survivability one would not eliminate the use of life saving appliances. On the other hand, efforts targeting safety enhancement could become much more effective. For example, with risk due to flooding-related accidents dominating the safety of passenger ships (some 90% of the risk), the focus on safety enhancement of passenger ships must clearly address damage stability as a priority. Ultimately, it is expected to see risk-based design being applied at ship / platform level as an holistic optimisation process. This will need to be supported by risk-based regulations (regulations justified by risk analysis based on agreed risk acceptance criteria) and approved Risk Control Options (design solutions or measures for risk prevention/mitigation).

2.3 Risk Acceptance Criteria

A common way of presenting risk graphically, in terms of fatalities, is by using the so-called F-N diagram, the plot of cumulative frequency of N or more fatalities, together with related risk acceptance criteria, Figure 2, (MSC 72/16, 14 Feb. 2000). In addition, some form of aggregate information is used, such as the expected number of fatalities $E(N)$, often referred to as the potential loss of life, PLL. This figure, innocent as a notion, hides **three** very important truths, as described next.

A cursory look at this diagram would reveal that tolerability drops by one order for every order of increase in fatalities. It is well-known that the public is much more averse to accidents, which kill many people at once than to others, which kill more people one at a time or in small "bunches". However, this has led to the situation where we have hundreds of people losing their lives in our industry every single day going unnoticed. For example, the total death toll at sea in the Philippines has been



estimated to be in the region of 20,000 - 40,000 per year if the small outriggers, pump boats and motor launches, which operate unscheduled services between islands, are to be included in the statistics [SPOUGE 1990].

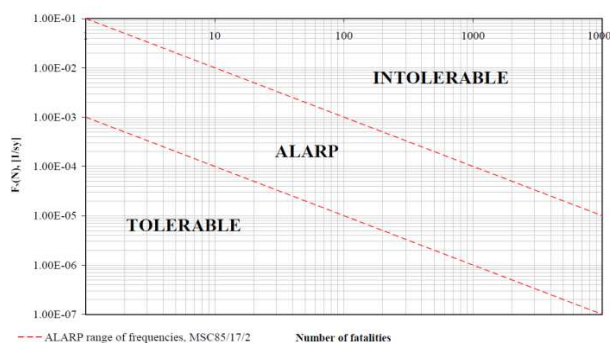


Figure 2: FSA - Decision Parameters and Risk Acceptance Criteria

This is not a problem specific to Philippines. The global fishing industry statistics from IMO, the International Labour Organization (ILO), and the Food and Agriculture Organization (FAO) of the United Nations, demonstrate a huge safety problem, as outlined next (Morall 2009):

- Each year there is an average of 24,000 fatalities and 24 million non-fatal accidents.
- The fishing fatality rate is estimated at 80 deaths/100,000 individuals per annum, which is 79 times higher than the overall occupational fatality rate.
- The risk of a fishing accident in EU waters is 2.4 times greater than the average of all EU industry sectors.

The principle that accidents involving large loss of life should be less likely than those involving a lesser loss was introduced by SOLAS 1929 and has not been addressed since. This notion, much as it sounds reasonable, is being severely challenged by a very different truth.

The second truth relates to the "value of life" as a currency for decision making in the risk assessment process. Risk acceptance implies two conditions: (a) the evaluated risk (profile) needs to be within the risk tolerability

region, referred to as ALARP and (b) it needs to be **As Low As Reasonably Practicable** within that region, the latter being decided on the basis of cost-effectiveness criteria, adopted by IMO [SKJONG 1998]. The basic principle on the latter relates to the cost society is prepared to invest for averting one fatality (CAF=\$3M adopted), which reflects some average value deriving from developed countries (SKJONG 2009), shown here as Figure 3.

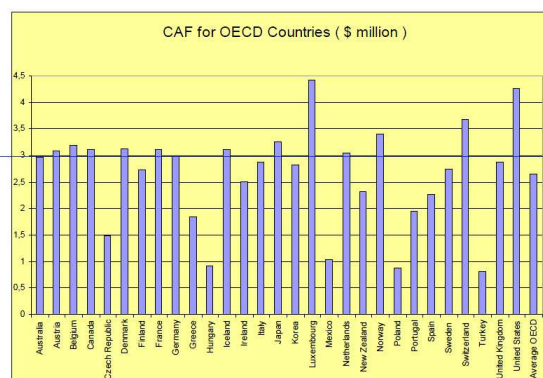


Figure 3: Societal Indicators (Risk-Based Regulation & Design in the Maritime Industry)

Notwithstanding the logic of this argument and the wisdom of this mechanism, there are side effects to it, namely: (a) a discriminatory incentive between developed and developing countries to invest on safety and (b) a discriminatory view on the value of life between developed and developing countries, which has nothing to do with propensity to invest for safety. The facts are clear to see. The world's worst shipping accident concerning loss of human life is that of the Philippine ferry Dona Paz in 1987, following a collision with an oil tanker. In the ensuing fire 4,400 people died (**who is** aware of this?). The same year, Herald of Free Enterprise capsized resulting in the loss of 193 lives (**who is not** aware of this?). Sulpicio Lines, the operator, offered compensation of £580 for passengers killed on the Dona Paz, which was the insurance required by the Philippine maritime authorities, (SPOUGE 1990). The corresponding compensation for the Herald of Free Enterprise was £500,000.



The third truth, still on risk acceptance criteria, relates directly to tolerability. On the basis that there are some 500 RoPax vessels worldwide carrying 1,000 persons or more, the proposed criterion of just below $1E-4$ in Figure 2 for accidents with 1,000 or more fatalities, implies that it is tolerable for such an accident to happen once every 20 years on average, assuming that RoPax population remains at current levels. To which extent this **truth** is understood widely is uncertain but this level, being considered tolerable by the maritime industry, deviates considerably from risk acceptance criteria of other comparable industries (JASIONOWSKI 2012).

3. DAMAGE STABILITY VERIFICATION

3.1 Validation and Verification

Safety legislation is one "thing" and safety verification an altogether different issue. Before elaborating further, it is important to elucidate the meaning of the two words: validation and verification. Validation ensures that the right model/method/formulation is being used whilst verification focuses on using the result right. This simple observation and understanding has, to date, eluded all of us working in maritime safety. This section will attempt to elucidate why verification is not receiving due attention by our industry.

Prescriptive safety legislation is, in principle, a risk control measure aimed primarily at risk mitigation post-accident for the specific hazard in question. The prevailing notion is that safety is ensured through compliance with pertinent regulations, which as we know only too well it has not worked all that well in the past. Key reason for this remains the fact that prescriptive rules are not risk informed. Prescriptive and performance-based instruments, described next, help illustrate this better:

- SOLAS 74: 1-compartment standard aimed at preventing ships from sinking / capsizing if any **one** compartment is breached in calm

water (static GZ curve characteristics). Little is known of the implied safety.

- SOLAS 90: 2-compartment standard aimed at preventing ships from sinking / capsizing if any **two** adjacent compartments are breached in calm water (static GZ curve characteristics). Little is known of the implied safety.
- Stockholm Agreement: as per SOLAS '90 but with a pre-defined level of water on deck depending on freeboard and in operational sea states of up to 4m significant wave height (IMO Resolution 14, 1995). This instrument represents a step change in damage stability verification in that the opted route for compliance is sought through performance-based assessment (model experiments). Still, because it is based on SOLAS '90, little is known of the implied safety.
- Harmonised Damage Stability Regulations, SOLAS Chapter II-1 (SOLAS 2009): in principle, assessment of all known damage cases, based on accident statistics, accounting for loading conditions and sea states at the time the accident occurred. Contrary to previous deterministic instruments, this is a goal-based regulation (Attained Index of Subdivision, $A >$ Required Index of Subdivision, R) and involves potentially thousands - rather than tens as in the first three - of damage cases. Adherence to the regulation is meant to ensure that the **majority** of cases are survivable (typically 80%).

All four instruments were validated using a specific data set of existing ships (this was aimed to ensure that the chosen GZ characteristics are the right ones). However, principally the same characteristics are used to date for completely new and very different ship designs. This trend climaxed with SOLAS 2009 when, in an attempt to harmonise the probabilistic rules for damage stability, cargo ships data was adopted as the basis for deriving the harmonised solution applicable to both cargo and passenger ships (i.e., the validated solution - formulae - are not being used right). Hence, verification of safety "went out of the



window" ...and it stayed there. There is more to this point as explained in the following.

3.2 Contemporary Developments

Over the recent past, knowledge on damage stability has been considerably enhanced with the development of advanced numerical simulation tools [JASIONOWSKI 2001], offering fast, accurate and reliable tools for performance-based evaluation and verification of damage stability (tens of thousands of damage cases in a few weeks). This capability has revealed two serious problems:

- Damage stability is the Achilles heel of passenger ships.
- The simple regression formulae used to assess damage stability of passenger ships (s-factors and Index-A) fail to capture the increasing complexity of the watertight arrangements of these ships (see Figure 4).

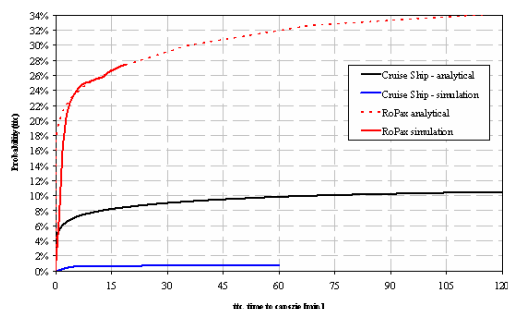


Figure 4: Cumulative probability distributions for time to capsize for a traditional RoPax and a large newbuilding cruise ship, (JASIONOWSKI 2007).

The cumulative probability distributions for time to capsize, for the two ships shown in Figure 4, are derived using two approaches: (a) an analytical expression based on the formulation of SOLAS 2009, (JASIONOWSKI 2006); and (b) numerical time-domain simulations using Monte Carlo sampling of pertinent statistical distributions of damage characteristics and sea states used in these rules (500 damage cases). Both ships comply with SOLAS 2009. Moreover, as explained in (VASSALOS 2004), the values of these

distributions tend to 1-A within a reasonable time period. Therefore, based on these results, the following observations can be made:

- For the RoPax, close agreement between calculation and performance-based assessment of damage stability is observed. However, approximately one in three collision and flooding events would lead to capsize within approximately half an hour. This is not a good standard.
- Application of SOLAS 2009 indicates that the cruise ship will follow a similar fate in approximately one in every 10 events whilst using first-principles time-domain simulation tools the rate becomes approximately 1:100. This is a big difference.

3.3 Project GOALDS

Based on these results and aiming to address the aforementioned "liberty" of using cargo ships characteristics as a basis for assessing damage stability of passenger ships, a large-scale EC Research Project was set up (GOALDS 2009-2012) to address these issues and to derive a verifiable goal-based (hence, performance-based) formulation for the damage stability of passenger ships. GOALDS helped produce the following revelations (more to the point, it helped reinforce some hard-learned truths):

New Formulation for Probability of Survival (s-factor)

As detailed in (CICHOWICZ 2011), the new s-factor formulation is as follows

$$H_{S\text{crit}} = \frac{A_{GZE}}{\frac{1}{2} GM_f \cdot Range} V_R^{1/3}$$

Where,

$H_{S\text{crit}}$: the critical significant wave height

A_{GZE} : an effective area under the GZ curve taken up to the heel angle corresponding to the submergence of the opening in question

$GM_f, Range, V_R$: residual GM, range and volume respectively

The much-awaited re-formulation of the s-factor has now taken place. The new formulation has all the characteristics that one would intuitively expect, in particular:

- The formulation is simple, rational and readily calculable.
- It is much along the lines of the SOLAS 2009 formulation but uses as a basis H_s critical for survivability, consistent with the Safe Return to Port philosophy.
- Water on deck is accounted for albeit not included explicitly in the formulation.
- It accounts for scale as we all suspected it should.
- It encourages use of a watertight envelop above the traditional bulkhead deck.
- Validation studies demonstrate a high degree of correlation with all available experimental data from HARDER, GOALDS and EMSA projects (Figure 5). The outcome expressed as a combination of linear, quadratic and interaction terms resulted in 0.99 correlation with the experimental data, which can be considered as a satisfactory test concerning completeness of the parameter set.

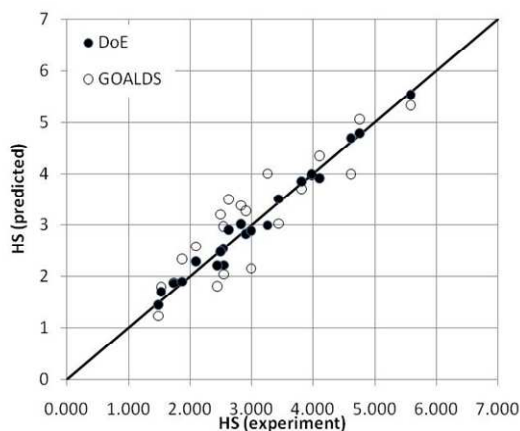


Figure 5: DoE applied to experimental data based on $A_{GZ}, GM_f, Range$ and V_R

Countering the aforementioned achievements are the following worrying observations:

- Comparison between A-Index calculations using SOLAS and GOALDS s-factor formulation revealed little difference. A cursory look of Figure 6 helps clarify this point (at least for RoPax vessels).

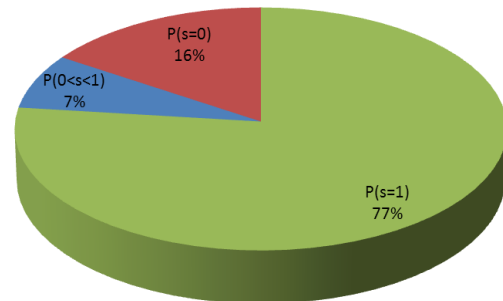


Figure 6: Typical outcome of damage stability calculations for a collision accident of a RoPax vessel

Figure 6 illustrates that 77% of damages are survivable, 16% non-survivable and the remaining 7% of ambiguous survivability. Thus, irrespective of the calculation error, known to be present in the s-factor for individual damage cases in the SOLAS formulation, a better formulation capable of resolving the inherent ambiguity will only improve the situation marginally. This is what was observed in GOALDS but the reasons were not quite appreciated. What is **worrying**, however, is that a large proportion of the feasible damages a RoPax vessel can suffer results in no stability, whatsoever. This is a design vulnerability in need of attention. (see next chapter).

- There are only two points in the data set representing cruise ships (one from HARDER and one from GOALDS). The rest is RoPax data.
 - Most RoPax ships are SOLAS '90 designs, hence not the best sample of ships to use as a basis for high survivability designs (see Section 5).
 - SOLAS '90 designs are of simple configuration, hence easy to predict their performance when flooding takes place following collision / grounding. None of the RoPax ships used include subdivided side casings or car decks, for example.
- As a result, calculations of Index-A alone,



using even the latest derived s-factors in Project GOALDS, does not constitute a sufficient means for damage stability verification of modern cruise ships and RoPax, particularly with complex watertight arrangement. This point is further elaborated in the following.

Comparison of Index-A with Performance-Based Assessment of Survivability (PBS)

PBS in this case entails numerical simulation "tools" using Monte Carlo sampling of pertinent probability distributions (damage characteristics, loading and sea states during collision). In the case studies considered, 300 damage cases (uncertainty 10%) were generated for the RoPax vessels and 500 for the cruise ships (uncertainty 4%). Each damage case was simulated for 30 minutes for RoPax and 60 minutes for cruise vessels. Index-A was calculated for the sample ships using NAPA. Unsurprisingly, the results of this study replicate Figure 4, namely, Index-A calculations show good agreement with PBS for traditional RoPax designs but not so in the case of cruise ships. A typical error distribution for RoPax is shown in Figure 7. The histogram is symmetrical around a mean value of approximately 5.0 with a standard deviation of 5.0. As indicated earlier, this error is expected to grow with complexity of watertight architecture, which is inevitable for the requisite higher survivability being sought.

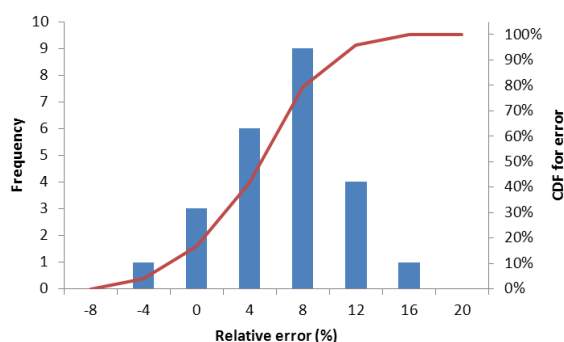


Figure 7: Typical error distribution of Index-A compared with PBS for RoPax

A similar comparison between Index-A calculations and numerical simulations for

cruise vessels is shown here in Figure 8. GOALDS results show a significant improvement over SOLAS (Figure 4) but the error is still large.

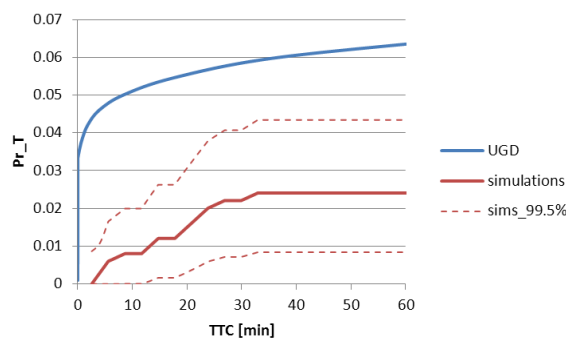


Figure 8: Comparison between Index-A and Simulations for a Typical Cruise Vessel

Having gained an increased understanding and made these observations, what can we do and what can we not do with the ensuing results/knowledge? It is clear that performance assessment of passenger ship survivability, using Index-A calculation, is far from perfect when compared with PBS, using modern "tools". Some reasons include the use of deterministic elements in the Index-A calculation, interpretation of the various elements involved in both calculations and simulations and so on but, ultimately, inability to deal with difficult physical phenomena, such as flooding of increasingly complex passenger ship watertight arrangements, constitutes the kernel of the problem. Notwithstanding this, the fact that results from Index-A calculations follow consistently the same trends as PBS results, renders Index-A a very attractive "tool" for survivability assessment and decision-making in concept design phase, including design optimisation.

However, before any passenger ship sets sail, damage stability needs to be verified by more rigorous means. The profession must realise that this is the only way forward and take action to develop and implement the right verification process and means to achieve this.

Can we imagine naval architects today using the Froude formula alone for resistance or the Watson formulae for powering calculations,

without the use of large scale model tests and extensive CFD (Computational Fluid Dynamics) studies for verification of power requirements and performance for any ship design? Why is shipping safety subjected to this degree of unwarranted and dangerous oversimplification?

Clearly we need to (and we can) do better!

4. PASSENGER SHIP VULNERABILITY

4.1 Basic Definition

"Vulnerability" is a word being used extensively in the naval sector but not so in the merchant shipping world. Hence, a definition here is in order. The way this term has been used by the Ship Stability Research Centre relates to "the probability that a ship may capsize within a certain time when subjected to any feasible flooding case." As such, vulnerability contains (and provides) information on every parameter that affects damage ship survivability. A simple example is provided next.

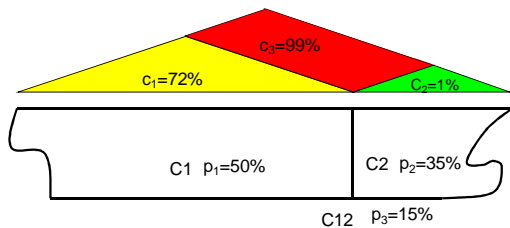


Figure 9: Vulnerability to Collision Flooding

Figure 9 indicates that there are 3 possible flooding cases of known (available statistics) frequency and calculable (available "tools") probability of surviving, say 3 hours, which is shown in the Figure. With this information at hand, Vulnerability to collision flooding of this simple example is:

$$0.5 * 0.72 + 0.35 * 0.01 + 0.15 * 0.99 = \mathbf{51.2\%}$$

4.2 Design Vulnerability

The vulnerability to collision / grounding damage of passenger ships is well documented through a number of accidents claiming many lives. Such vulnerability relates to **Water On Deck (WOD)**, leading to progressive flooding and rapid capsize of the ship. Whilst for Ro-Ro passenger vessels this design vulnerability is well understood, for cruise ships it has been brought to light as recently as the early 2000s. The latter case relates to the service corridor on the strength deck, which acts as conduit for floodwater to spread along the ship, leading to down flooding through deck openings / stairwells and ultimately to sinking / capsize of the ship. Figures 10 and 11, provide typical results demonstrating such vulnerability in the design of RoPax and Cruise vessels, respectively.

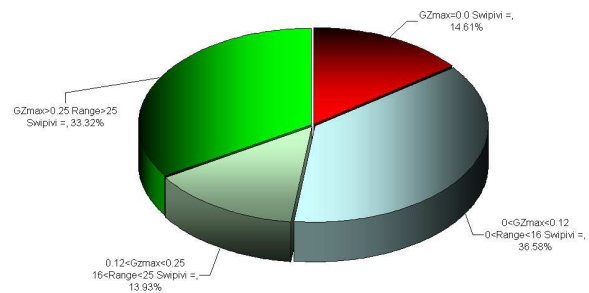


Figure 10: Design Vulnerability (Watertight Integrity - Typical RoPax)

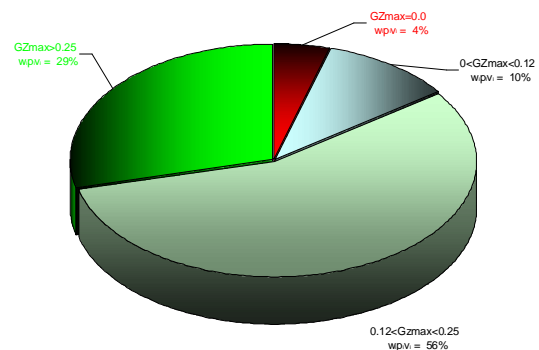


Figure 11: Design Vulnerability (Watertight Integrity - Typical Cruise Ship)



4.3 Vulnerability in Operation

A threat that exacerbates further the design vulnerability of passenger ships to collision / grounding damages, probably at the heart of many catastrophes is vulnerability in operation. This is an issue that has been attracting serious attention at IMO over the past few years and new legislation is now in place. It aims to address the fact that most passenger ships are operated with a number of Watertight (WT) doors open, thus exacerbating considerably the design vulnerability of these ships. Figures 12 and 13 demonstrate this rather emphatically by considering the well known Estonia case, as designed and at the time of her loss. In the latter case (because of open WT doors) the vulnerability of the vessel was at 68%; 3.5 times higher than her design vulnerability of 19%.

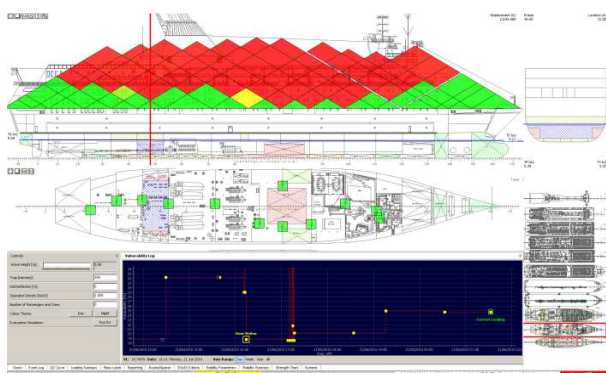


Figure 12: MV Estonia - Design Vulnerability

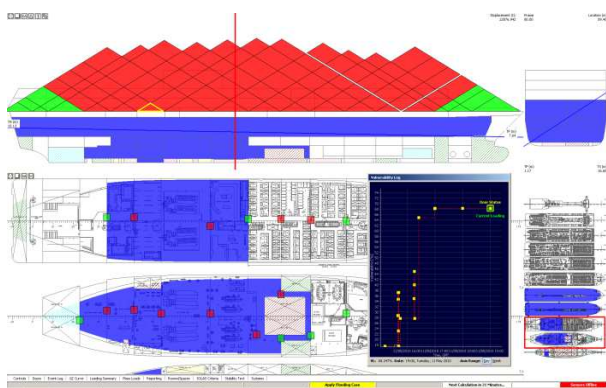


Figure 13: MV Estonia - As Operated at the Time of her Loss.

4.4 Watertight Doors - Current Legislation

SOLAS Regulation II-1/15.9.3: "Certain watertight doors may be permitted to remain open during navigation only if considered absolutely necessary; that is, being open is determined essential to the safe and effective operation of the ship's machinery or to permit passengers normally unrestricted access throughout the passenger area. Such determination shall be made by the Administration only after **careful consideration** of the impact on ship operations and survivability. A watertight door permitted to remain thus open shall be clearly indicated in the ship's stability information and shall always be ready to **be immediately closed.**"

However, careful consideration by an Administration would necessitate due ability by the Administration to address the impact on survivability of open watertight doors so as to ensure rational decision-making. The worst watertight door shown in Figure 14 increases ship vulnerability four-fold; yet it is Class-exempt. This is simply the result of the floatability assessment required by IMO. The requirement for a watertight door to be ready to be immediately closed is another myth. Measurements in the field indicated that such doors take on average 2.5 minutes to close (1 minute before "pressing the button" for obvious safety reasons and 1.5 minutes for the door to close) by which time the damage is done.

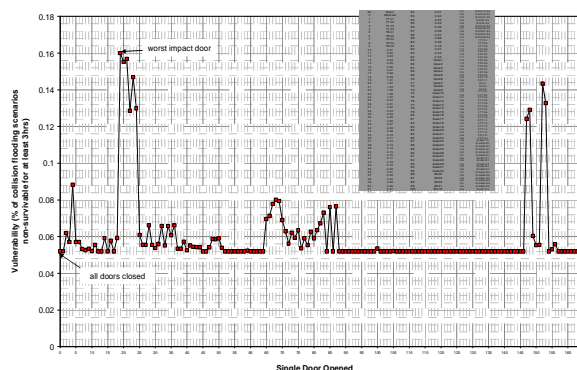


Figure 14: Watertight Door Exemptions - Cruise Ship Example.

5. NEW SHIPS VS EXISTING SHIPS

5.1 Regulatory Gaps

The Compartment "Currency" - Weakness in Old SOLAS

Adoption of probabilistic rules for damage stability and the use of damage statistics led to clearer understanding of the fact that high-energy impact collisions penetrate the ship's hull up to the centre line (in fact at a rate of 45%). Hence, side compartments (B/5, B/10 and so on) offer reduced protection from a survivability perspective. These different compartment "currencies" in old and new SOLAS (for example SOLAS '90 and SOLAS 2009, respectively) cause confusion when used to judge the level of damage survivability, making it imperative to use transparency in communicating compartment-based damage stability standards.

The "Compensation" Effect - Weakness in New SOLAS

Only survivable damage cases contribute to the value of Index-A (an *aggregate statistic*). As such, it is implied that even if a vessel achieved the required index of subdivision, there may be cases, which are likely and which have a low probability of survival – hence a high risk of sinking/capsize. The term introduced in the literature to describe this [VASSALOS 2008] is the "compensation effect" and as Figure 15 indicates, even vessels with very high index of subdivision, may fail to survive what is, in principle, one- and 2-compartment damages.

Safety Equivalence - Weakness in Knowledge

The safety standard in SOLAS 2009 was established by using a sample of SOLAS '90 ships as reference, aiming to ensure that the same damage stability standard is maintained in the new rules. However, evidence from performance-based assessment of damage survivability (recently gained knowledge) of existing and new ships demonstrates that this is hardly the case (Figure 16). The vulnerability of SOLAS '90 ships is considerably higher

than ships designed to SOLAS 2009 rules. Yet another reason for paying particular attention on the damage survivability of existing ships.

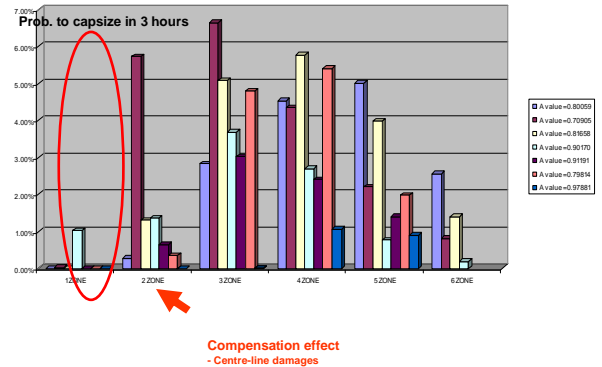


Figure 15: Compensation Effect - Newbuildings Experience (Passenger Ships).

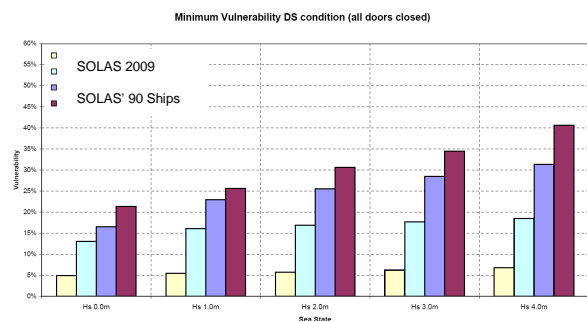


Figure 16: Comparative Assessment of Vulnerability between SOLAS '90 and SOLAS 2009 passenger ships; clearly the safety level is not the same.

Notwithstanding the dissimilarity in old and new SOLAS standards, striving for higher standards for passenger ships, one MUST NOT forget that if these were applied only to new ships and not to all existing ships (retrospectively as it was done, for example, with the Stockholm Agreement) we would only scratch the surface of the problem. Moreover, this would mean that we reinforce a **two-tier safety**, allowing the vast majority of ships to continue to operate, despite knowing that their safety standard is not good enough. This is a significant regulatory gap that needs attention! This is the focus of the next chapter.



6. A WAY FORWARD

6.1 Grandfather Clause¹

"International regulation would fall apart if the grandfather clauses were removed!!!"

This is the response of the former MSC Chairman (Tom Allan) when I made the suggestion to him of retrospective legislation, including the exclamation marks. I am certain, the same argument was made prior to the removal of the margin line, freeboard, factorial system of subdivision and other "grandfather concepts" but the world is still standing, financial problems apart.

What this paper tried to bring forward is many such concepts, which for lack of better knowledge at the time, they were adopted and most of these served our industry well. But the time has come for us to review critically the maritime safety system and lay the foundations for a modern, sustainable system. Key to this, particularly with reference to damage stability of passenger ships, is retrospectively applied legislation. There may be a need for a debate, at IMO level, to ensure that the time is ripe to rip the Grandfather clause apart but from a technical and practical perspective, if it can be done it should be done. This Chapter puts forward a workable framework to achieve this, which focuses on life-cycle risk management, as outlined next.

6.2 Life-Cycle Safety (Risk) Management

Safety Management is a life-cycle process, starting at the concept design stage and continuing throughout the life of the vessel. In this process, safety must be monitored and reviewed to ensure changes in design/operation are reflected in the way safety is managed. The safety management process must be formal and transparent to allow the operator to nurture a safety culture and to manage safety cost-effectively. More importantly, a formal process facilitates measurement of safety performance, which constitutes the basis for

continuous improvement, as indicated by the Virtuous Cycle in Figure 17.¹

This brings to the fore the role of ship operation in life-cycle safety management, which deserves special attention. This thinking is largely in line with the Safety Case approach (SAFETY CASE 2005) of Health and Safety Executive (HSE) and the IMO Guidelines on FSA and on Alternative Design and Arrangements (MSC\Circ.1002, 1212) with the focus clearly on safety performance verification. The Safety Case approach to safety management is more ship-specific rather than ship type specific as in the case of the FSA. As such, it is a "living instrument", starting with the first concept of design and spanning the whole life cycle of the vessel.

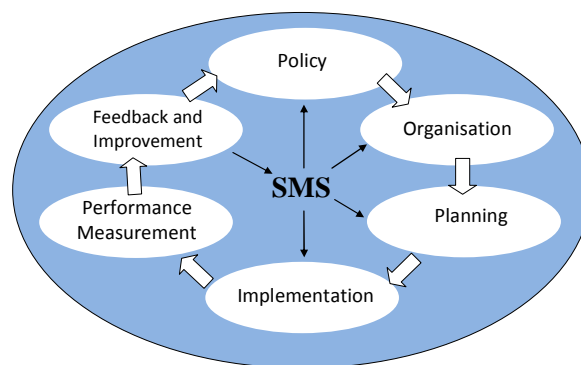


Figure 17: A Virtuous Life-Cycle Safety Management

The first 3 steps in Figure 17 point to the fact that safety management is an all-stakeholders affair. The next step (design phase) involves safety performance evaluation and verification activities (e.g., engineering

¹ **Grandfather clause** is a legal term used to describe a situation in which an old rule continues to apply to some existing situations, while a new rule will apply to all future situations. The term originated in late-19th-century legislation of U.S. Southern states, which created new literacy and property restrictions on voting, but exempted those whose ancestors (grandfathers) had the right to vote before the Civil War. The intent and effect of such rules was to prevent poor and illiterate African American former slaves and their descendants from voting, but without denying poor and illiterate whites the right to vote. The term *grandfather clause* remains in use but with no connotation regarding the justness of these provisions when applied in other areas.



analysis, model tests, etc.) aiming at minimising risk cost-effectively. The last 2 steps (operational phase) ensure that adequate measures are being taken, using safety performance measurement and feedback, to manage the residual risk, i.e., to render the residual risk acceptable.

The focus on dealing with residual risks, naturally leads to the need for a SMS (Safety Management System), outlining the organisation and procedures required to maintain an acceptable level of safety throughout the life of the vessel. This has to be aligned with the ISM (International Safety Management) Code implemented onboard. Pertinent activities include aspects of onboard and shore-based Safety Centres, monitoring systems and emergency Decision-Support for crisis management.

In conclusion, a formal process should address risk at the ship **design** stage (risk reduction/mitigation), in **operation** (managing residual risk) and, ultimately, in **emergencies** (crisis management), ensuring in all cases an acceptable level of risk (safety assurance). This constitutes the basis of the verification framework described in the next section.

6.3 A Damage Stability Verification Framework

Existing Ships

Deriving from the foregoing and with emphasis on existing ships, two main phases are envisaged:

1. Design Upgrade Phase: Recent knowledge, tools and experience has demonstrated that there is a great deal that can be achieved to improve the damage stability of existing passenger ships with minor modifications, addressing curtailment of progressive flooding by focusing on removing certain openings, introducing semi-watertight doors and such like. This will enhance survivability substantially. The outcome should be **verified** through performance-

based survivability assessment; first principles tools or model experiments.

2. Operational Phase: As it is more than likely that design measures alone will not be sufficient to raise the standard of existing ships to the requisite level, the next step should address management of the residual risk, along the lines discussed in the foregoing. Namely, the ship owner/operator will need to demonstrate, in a **verifiable** way, how residual risk is to be managed (rendered acceptable).
3. Emergencies: Preparedness is the key to handling emergencies with severe time constraints, such as accidents involving flooding, and limitations in human factor performance. This will require a **verifiable** emergency response system for crisis management along the lines described briefly in the previous section.

New Ships

The procedure outlined in section 6.2 will apply directly to newbuildings, subject to an appropriate verification framework.

For the design phase, we need to look no further than developing for damage stability the same framework as that already existing at IMO for fire, namely Alternative Design and Arrangements for Fire Safety and associated Guidelines. For the operational phase and for emergencies, a verification process needs to be established involving the instruments already in place as explained in section 6.2 (Safety Case, SMS, ISM Code). Possible actions would involve the following:

- Industry study to investigate feasibility of retrospective application of new rules for damage stability through (a) design upgrades, (b) operational measures and (c) focus on emergency response.
- Establish, through the IMO route of Alternative Design and Arrangements, a similar regulation for damage stability (as that for fire) for verification through performance-based assessment of typical cases from the industry study. This would



also enable setting in place a suitable framework for approval of damage survivability for newbuildings.

- Set in place through appropriate legislation at IMO and certification through Administration/Class a system for monitoring damage stability onboard (linked to SMS) to provide feedback for verification and management of residual risk, including crisis management.

7. CONCLUDING REMARKS

- A painstaking evolutionary development on ship stability is giving way to unprecedented scientific and technological developments that has raised understanding on the subject as well as the capability to address demanding societal expectations on human life safety and do so cost-effectively.
- This enhanced capability has brought with it knowledge on the level of safety ships are being designed to and on the way ship operation impacts on this.
- As a result, notions about ship stability and safety are also giving way to some important truths: ships are vulnerable platforms, particularly to flooding following collision/grounding accidents, a fact that is further exacerbated by accepted operational practices.
- This demands immediate action, led by industry, aiming to establish a workable framework and process for raising and upholding damage stability standards and to do so equitably across the whole fleet.
- More specifically, this paper is putting forward a strong case and means to argue that **the time is ripe to rip the Grandfather Clause apart** and to move on.
- In a wider sense this, in turn, necessitates raising awareness to stimulate and nurture a maritime industry safety culture and a safety regime that aims for and supports continuous safety improvement.

8. REFERENCES

- Vassalos, D., 1999, "Shaping Ship Safety: The Face of the Future", Journal of Marine Technology, Vol. 36, No. 4, 1999, pp. 1-20.
- IMO (2001), "Guidelines on alternative designs and arrangements for fire safety", MSC/Circ. 1002.
- IMO (2006), "Guideline on Alternative Designs and Arrangements for SOLAS chapter II-1 and III", MSC/Circ.1212.
- IMO Resolution 14, "Regional Agreements on Specific Stability Requirements for Ro-Ro Passenger Ships" – (Annex: Stability Requirements Pertaining to the Agreement), adopted on 29 November 1995.
- FSA, "Guidelines for Formal Safety Assessment for Use in the Rule-Making Process", MSC.1-Circ.1023 - MEPC.1-Circ.392, 2002.
- Spouge, J., 1990, "Passenger Ferry Safety in the Philippines", Transactions, RINA 1990.
- Morall, A. 2009, "Fishing Vessel Safety – How Can Safety Be Improved?", Report, RINA Safety Committee: Fishing Vessel Safety.
- Skjong, R. and Ronold, K., 1998, "Social Indicators and Risk Acceptance", Offshore Mechanics and Arctic Engineering Conference, OMAE, Lisbon 1998.
- Skjong, R., "Risk Based Regulation, Risk Based Design & SAFEDOR", Guest Lecture NTNU, 2009-10-21.
- Jasionowski, A., "Study on the Specific Damage Stability Parameters of RoRo Passenger Vessels according to SOLAS 2009, including Water on Deck Calculation", Project No EMSA / OP /08 / 2009, SSRC, University of Strathclyde, Glasgow, 2012.



Jasionowski, A., "An Integrated Approach to Damage Ship Survivability Assessment", PhD Thesis, University of Strathclyde, 2001, UK.

Jasionowksi, A., "Fast an accurate flooding prediction – analytical model", SAFEDOR, D2.1.3, November 2006.

Vassalos, D., "A risk-based approach to probabilistic damage stability", 7th International Workshop on the Stability and Operational Safety of Ships, November 2004, Shanghai, China.

Jassionowksi, A., YORK, A., "Investigation Into The Safety Of Ro-Ro Passenger Ships Fitted With Long Lower Hold", UK MCA RP564, 10 July 2007, Draft Report MCRP04-RE-001-AJ, Safety at Sea Ltd.

GOALDS 2009-2012, "Goal-Based Damage Stability", European Commission Project FP7 Project 233876, 3009-2012.

Cichowitz, J., Tsakalakis, N., and Vassalos, D., "Survivability of Passenger Vessels - Re-engineering of the s-Factor", Proceeding of the 12th International Ship Stability Workshop, 12 - 15, June 2011, Washington D.C., USA.

Vassalos, D., Jasionowski, A., Tsakalakis, N. and York, A., "SOLAS '90, Stockholm Agreement, SOLAS 2009 - The False Theory of Oranges and Lemons", 10th International Stability Workshop, Taejon, Korea, 2008.

SAFETY CASE, "The Offshore Installation (Safety Case) Regulations, UKSI 3117", 2005.





Effect of Revised Damage Survivability Formulation upon Ship Design

Romanas Puisa, r.puisa@strath.ac.uk

Przemek Zagorski, przemek.zagorski@strath.ac.uk

Dracos Vassalos, d.vassalos@strath.ac.uk

The Ship Stability Research Centre of University of Strathclyde

ABSTRACT

The presented study was undertaken in the aftermath of the recent revision of damage survivability, i.e. the s-factor, conducted under EU project GOALDS. It was hence of great interest to investigate the implications of the revision to one of the design qualities, namely the probabilistic index “A”, upon ship design. This paper specifically outlines the outcome of basic statistical analysis performed on data resulting for design exploration of passenger ship concepts. As a general conclusion, there is a clear difference between the SOLAS 2009 and GOALDS formulations and the nature of this difference is in line with expectations from the new s-factor formula. That is, the GOALDS formulation is more sensitive to variations in the watertight volume higher up the ship. However generally, this difference between the formulations is more of a trend than a rule, as far as our studied ship concepts are concerned.

Keywords: *Probabilistic subdivision index, sensitivity analysis, design exploration, optimisation, ropax, cruise*

1. INTRODUCTION

In view of recent findings in EU project GOALDS, a number of practical questions have arisen. Firstly, how different GOALDS and SOLAS 2009 (Chapter II-1 Regulations 5–9) formulations for probabilistic subdivision index “A” are, and if they are, what will be the implications to everyday design practice. Surely, the notion of “difference” in this context must also be settled. In this paper we exercise quantitative statistical methods in search for this difference, thereby focusing on quantitative dissimilarity. Qualitative aspects of the factual distinction (later alluded to in this section) are therefore outside the scope of this paper.

The second question of concern is whether the everyday use of the new formulation would bring about new, unconventional ship concepts,

for them being more safe and cost effective. In other words, would new design features, which are either “invisible” to or even penalised by SOLAS, be rewarded by the GOALDS formulation? On one hand, the answer to this question lays in the GOALDS formulation itself, as shown next, but on the other hand there has been some criticism towards the new formulation producing very similar values for the subdivision index “A”, and hence potentially having little effect upon design of ship subdivision. The latter criticism is addressed in this paper throughout the following sections.

So what does the new formulation for s-factor imply, as far as ship design is concerned? Taking a closer look at the GOALDS formulation¹ (Cichowicz, Tsakalakis

¹ Eq. 2 stands for a formulation based on the assumption that the shape of the GZ curve is triangular. This



et al. 2011) (see Eq. 1 and Eq. 2), it appears that

- (1) There must be a sufficient residual volume for a damaged ship to survive the damage. Apparently, the most reasonable location of this volume (in view of all plausible damage scenarios) is higher up in the ship, e.g. on the bulkhead deck and above. It also well agrees with the common sense.
- (2) The ratio GZ_{\max}/GM_f in Eq. (2) directly relates to the actual shape of the GZ curve, for this ratio is proportional to the heel angle at GZ_{\max} and hence the larger is the angle, the bigger is the GOALDS' s-factor. From design point of view, this can be achieved if the residual volume is again distributed higher up on the ship and seemingly as far from the centre line as possible. It is important to note that the SOLAS formulation is inherently incapable of rewarding (or penalising, for that matter) such design considerations, because of the prescribed limits for GZ_{\max} and the heel angle, not to mention that those limits are not relevant for passenger ships at all.

$$\forall(A_{GZ}, V_R, Range > 0) s = \exp(-\exp(0.16 - 1.2H_{Scrit})) \quad (1)$$

$$H_{Scrit} = \frac{\frac{1}{2}GZ_{\max} \cdot Range}{\frac{1}{2}GM_f \cdot Range} V_R^{1/3} \quad (2)$$

where,

H_{Scrit} : the critical significant wave height

$GM_f, Range, V_R$: residual GM , range and volume respectively

In project GOALDS, which is apparently featured in this paper, the effect of the new s-factor formulation upon design of ship subdivision was addressed through design optimisation studies. The studies focused on passenger ships, ROPAX and cruise ships of various sizes. The idea behind employing the formal design optimisation was twofold. Firstly, it was interesting to see whether the use of the new formulation would have any bias towards unconventional design solutions, i.e. the solutions that are unconventional within the SOLAS 2009 framework and perhaps general design practice. Secondly, some formal optimisation methods allow exhaustively exploring the design space of which statistical analysis can be then used to address the difference between the two formulations, in particular addressing the impact of the new formulation upon ship design. The latter undertaking formed the basis for this paper, which is organised as follows.

Section 2 describes aspects of the design space exploration, highlighting some general results. Section 3 focuses on the statistical analysis and its results, following by concise result interpretations which are then generalised in Section 4. Section 4 also concludes the paper.

2. DESIGN EXPLORATION

In this paper we deal with two passenger ships of which baseline characteristics are listed in Table 1 and Table 2. Two corresponding parametric ship models were developed, as described in Section 2.1.

2.1 Parametric ship models

Fig. 1 outlines the parametric model for the large ROPAX ship, which is controlled by 11 parameters listed in Table 3. The blue and green geometric elements in Fig. 1 are actually varied, whereas the red lines, which correspond to the main vertical fire (MVF) bulkheads and engine room bulkheads, indicate that these bulkheads were fixed. Thus for example, the parametric model could have the long lower

assumption is relaxed in the final formulation, as indicated in the reference.

hold or not, hence it is in blue, likewise could have side casings (longitudinal subdivision) on the car deck or not. The car deck could also subdivided transversely by two or three bulkheads and this transverse subdivision could be combined with the longitudinal subdivision (side casings).

Table 1: Main particulars for large ROPAX ship

Characteristic	Value
Yard	Meyer Werft
Length over all	~ 229 m
Length between perpendiculars	214.32 m
Subdivision length	227.97 m
Breadth	32 m
Subdivision draught	6.70 m
Height of bulkhead deck	9.70 m
Number of passengers	3300
Number of crew	200
Gross tonnage	70,000 m ³
Deadweight	6,900 tonne

Table 2: Main particulars for the cruise ship

Characteristic	Value
Yard	STX Finland
Length over all	~ 327m
Length between perpendiculars	300.70 m
Subdivision length	315.67 m
Breadth	37.40 m
Subdivision draught	8.80 m
Height of bulkhead deck	11.60 m
Number of passengers	4,200
Number of crew	1,400
Gross tonnage	125,000 m ³
Deadweight	10500 tonne
No of cabins	1,664

We also assumed a case that the side casings on the car deck could have, or not, passenger/crew cabins inside. As can be also seen from both Fig. 1 and Table 3, the number of transverse bulkheads between the MVF bulkheads could also vary. One of the key parameters introduced was the hull type. Three hull types were considered:

- Baseline hull, which has a fairly traditional shape
- Hull concept referred to as the UFO concept, which is the baseline hull widened by 6 meters on the car deck and above, as shown in Fig. 2
- Baseline hull widened by 3 meters

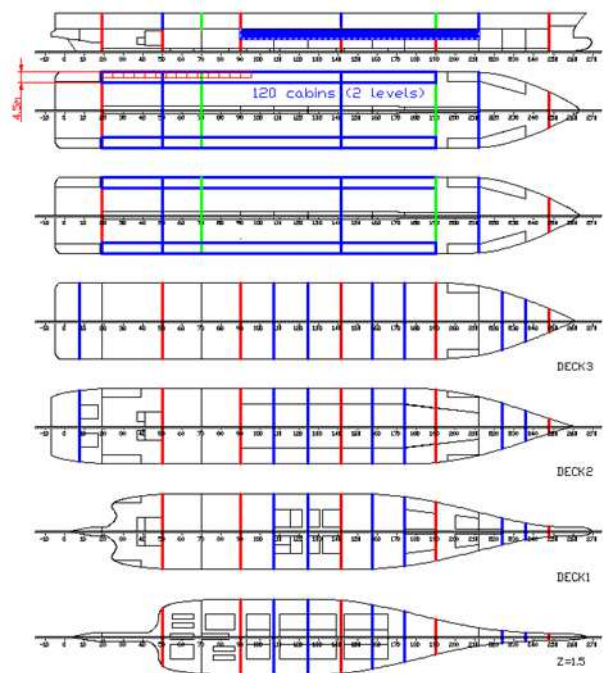


Figure 1: Outline of parametric model for the large ROPAX ship.

It is worth mentioning that the UFO hull concept is not at all new, and an experienced designer would be able to recall similar hull concepts that were under consideration in the past, e.g. in Finish design offices. Apparently, this hull concept may bring some difficulties during operation, but these difficulties can be overcome provided that ships with such a hull shape exhibits very high damage survivability and cargo capacity (if it is needed), as shown later. The main reason for introducing the UFO hull was to distribute the watertight volume higher up and wide in the ship, thereby increasing the damage survivability.



Table 3: List of parameters that control the configuration of the large ROPAX ship

Parameter	Values	Comments	Number of options
Presence of AFT TBH	0/1 (no/yes)		2
No. of TBH in Z1	0/1/2		3
No. of TBH in Z2	0/1/2		3
No. of TBH in Z3	0/1/2		3
No. of TBH on BHD	0/2/3		3
Side casings (SC)	0/1 (no/yes)	Transverse dist. = 4.5 m	2
Cabins in SC	0/1 (no/yes)	conditional on SC presence	2
Truck/trailer in SC	0/1 (no/yes)	conditional on SC presence	2
Presence of LLH	0/1 (no/yes)		2
BHD height	9 to 12 m	9.7 - baseline	5
Hull type	0/1/2 (baseline/UFO/+3m)		3
Number of combinations			38,880

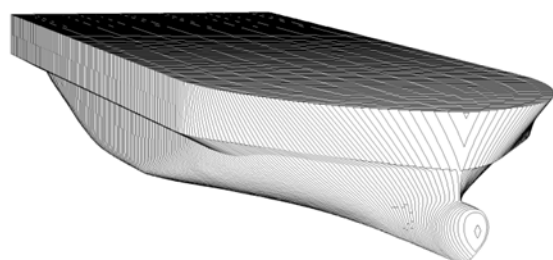


Figure 2: Alternative (UFO concept) hull for the large ROPAX ship.

This design strategy was alluded to in the previous section. However, in addition to increased damage survivability, this type of the hull allowed for extra cargo capacity or alternative/equivalent cargo placement when the long lower hold was absent and/or subdivision of the car deck was present. Note, any subdivision of the car deck inevitably reduces the cargo capacity.

It is important to emphasise that the design parameters in Table 3 are discrete and hence one can easily calculate the total number of combinations, i.e. distinct layout configurations for the large ROPAX, amounting above 38 thousands. As indicated in the previous paragraph, these combinations are basically design solutions with variable trade-offs

between damage survivability (safety) and economic performance (net revenues).

The parametric model for the cruise ship is outline in Fig. 3, whereas Table 4 lists categories of design parameters (the total number of design parameters was above 300) that could be altered.

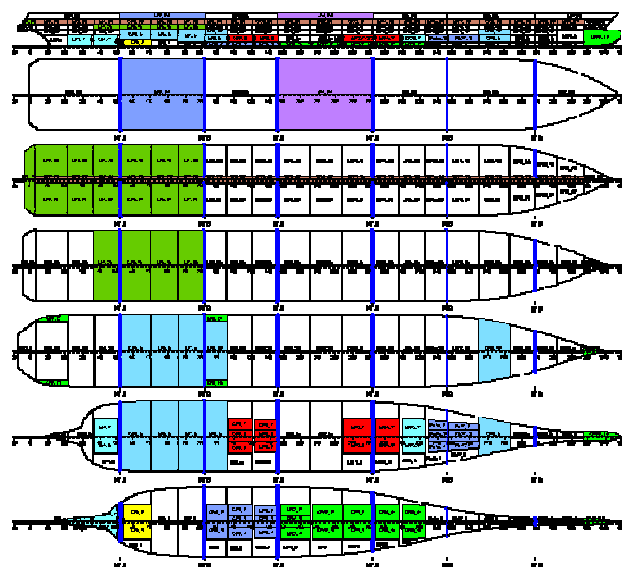


Figure 3: Outline of parametric model for the cruise ship.

Table 4: List of parameters that control the configuration and internal sizing of the cruise ship

Topological parameters
Number of transverse bulkheads within MFZ
Number of longitudinal bulkheads
Number of heeling tanks
Number of tanks within each category (potable water, diesel oil, heavy fuel oil etc.)
Number of watertight doors on the bulkhead deck
Purposes of tanks and spaces
Sizing parameters
Positions of transverse bulkheads within MFZ
Positions of longitudinal bulkheads
Sizes of tanks (transverse and longitudinal dimensions)
Deck heights

Note, the blue transverse bulkheads in Fig 3 refer to the main vertical fire bulkheads that

were kept untouched during the optimisation process, although they could also be varied as any other bulkhead.

The design parameters for the cruise ships (see Table 4) were split into two groups: (1) parameters controlling the topology (layout configuration) and (2) parameters controlling the sizes of volumes (compartments and tanks) that are defined by a specific topological configuration. Apparently, the both groups are geometrically dependent and this dependence is visualised in Fig. 4.

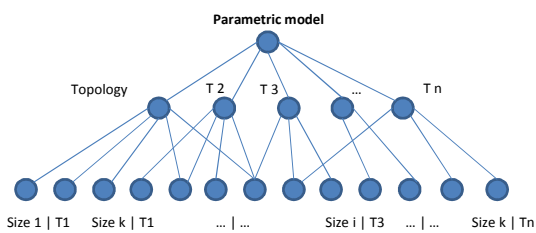


Figure 4: Graphical interpretation of the structure of the parametric cruise ship model, indicating dependencies between design parameter groups.

As shown in Fig. 4, there are a number of design solutions for a given topology, hence the sizing parameters are conditional on the topology parameters. This basically means that the two parameter groups should not be altered at the same time, but altered sequentially: topology first and the sizing next, keeping the topology fixed.

In the cruise parametric model, the number of design options in terms of topology was in the order of billions, whereas there was an infinite number of size variations for each given topology.

2.2 Sampling

Sampling represents another critical and also conventional step towards any statistical analysis. Although the role of parametric models in the sampling process may seem obvious, it is worth explaining to remove any doubts that less experienced readers may have.

Firstly, the purpose of sampling (sometimes referred to as design of experiments) is to produce distinct combinations of design parameters, so that the design space can be represented by those combinations. In our case, each such a combination is basically a distinct ship design solution. Because our design space is enormous, as highlighted in the previous subsection, we need to make sure it is covered as uniformly as possible, i.e. we should avoid “black holes” that would likely be left by random sampling.

Therefore, we employed deterministic sampling techniques to explore the design space uniformly, i.e. without any bias. Specifically, Improved Latin Hypercube sampling (ILHS) (Beachkofski and Grandhi 2002) and Latin Centroidal Voronoi tessellation (LCVT) (Romero, Burkardt et al. 2004; Saka, Gunzburger et al. 2007) were used. Fig. 5 illustrates an even distribution of 50 sample points produced through ILHS.

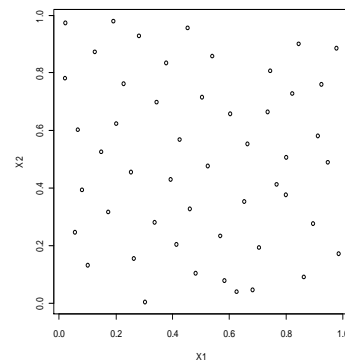


Figure 5: An illustrative distribution of sample points (i.e. combinations of design variables) over a hypothetical design space defined by two design variables X_1 and X_2 that vary within range $[0, 1]$.

Each combination of design parameters produced through the sampling process (see the previous section) had to be evaluated, assessing multidisciplinary performance of each design solution. Fig. 6 – 8 show sampling results for the both parametric models, plotting the results in the design performance space.

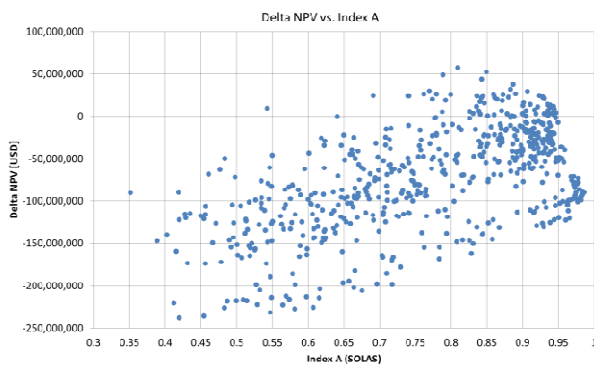


Figure 6: Sample points of the large ROPAX; 600 samples are displayed.

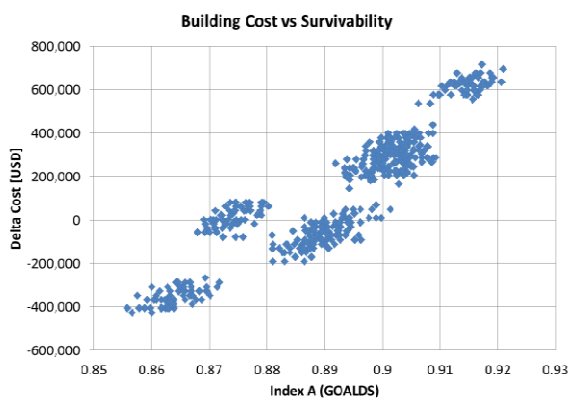


Figure 7: Sample points of the cruise ship, when only topology related parameters were sampled; 500 samples are displayed.

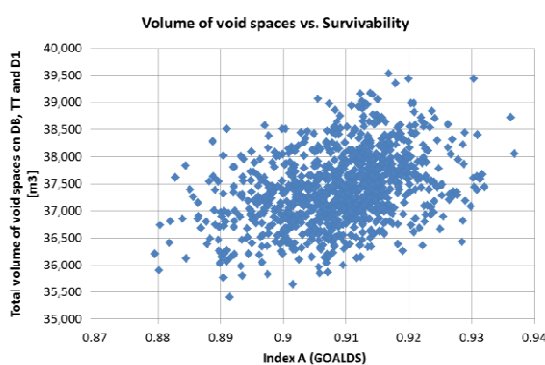


Figure 8: Sample points of the cruise ship, when only size related parameters were sampled, subject to a given topology (was selected from the topology samples); 1,000 samples are displayed.

It is not the purpose of this paper to go into detail, explaining the rationale behind each performance quality assessed, and therefore

only a brief reference to considered performance qualities is provided. That is, Fig. 6 plots the subdivision index “A” (SOLAS 2009) against the difference (compared to the baseline design) in the net present value, which is conventionally used as a measure of life-cycle economic performance of the vessel. The net present value was calculated as a function of changed building cost (the amount of still was affected), operational costs (the fuel consumption was affected) and operational earnings affected through changed cargo capacity. In Fig. 7 the change (compared to the baseline design) in the building cost is displayed. This change was brought about by primarily varying the number of bulkheads and the number of watertight doors. Fig. 8 shows that the total volume of void compartments in double bottom, tank top and deck 1 was affecting the index “A”.

The sampling for the both parametric models was performed in software *.spiral*TM (Puisa and Mohamed 2011; Puisa, Murphy et al. 2012), which represents a platform for software integration, process and data management, design exploration and optimisation.

3. STATISTICAL ANALYSIS

Note, for each design variation displayed in Fig. 6 – 8, the both GOALDS and SOLAS 2009 indices of subdivision were calculated. This enabled to perform the analysis performed next.

3.1 General trends (ROPAX ship)

In this section we make general observations concerning the difference between the two formulations. Thus, Fig. 9 – 10 shows distributions of indices “A” (600 sample points), highlighting the similarity between them. Apparently, the larger part of design variations has higher index “A” that of the baseline design. Another important observation which can be made from the histograms, is that it is possible to achieve very high survivability

($A > 0.98$) for large ROPAX ships. Surely, due to design modifications during the detailed design stage, the actual value of the index will drop by some 6%, but the ship would still exhibit very high damage survivability.

The third distribution of interest, Fig. 11, is basically the relative difference between the previous two, and the purpose of this distribution is to examine the deviation from the SOLAS formulation. Thus, it can be instantly observed that all GOALDS indices “A” are higher than corresponding SOLAS indices, although the best majority of GOALDS indices are close to their SOLAS counterparts. The observed maximum deviation is as much as 30%.

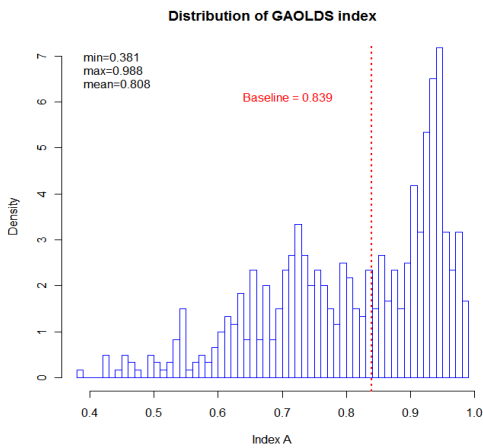


Figure 9: Histogram of sample points in terms of subdivision index “A” by GOALDS.

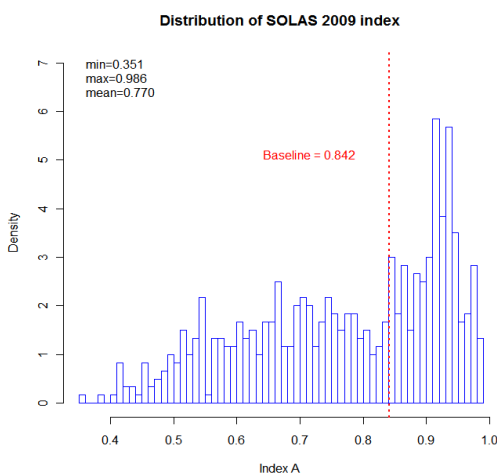


Figure 10: Histogram of sample points in terms of subdivision index “A” by SOLAS 2009.

As expected, the difference in the indices decreases as they approach their maximum value – unity, see Fig. 12. This means that for ship designs with high damage survivability the numerical difference between the indices may be negligible, but this is unlikely for designs with low index “A” (e.g., $A = 0.83$).

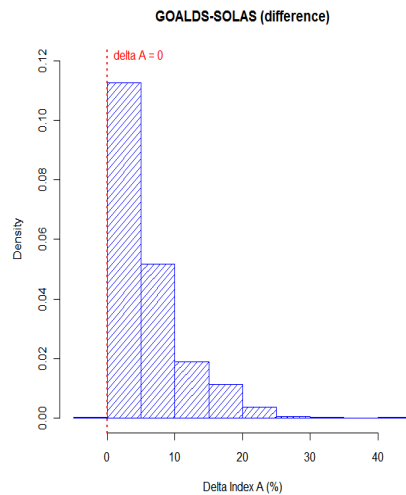


Figure 11: Histogram of sample points in terms of the relative difference between index “A” by GOALDS and SOLAS 2009.

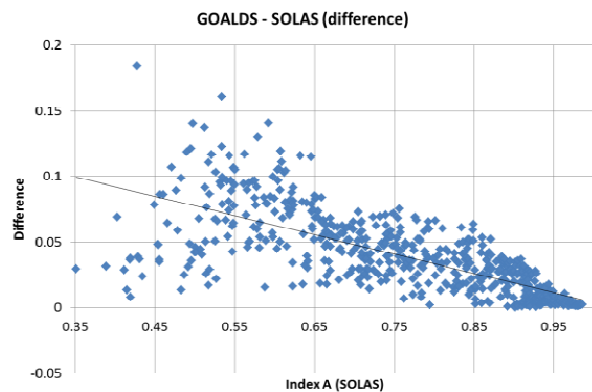


Figure 12: Decrease in the difference between index “A” by GOALDS and SOLAS 2009.

Consequently, we can observe a strong correlation between the two formulations, as shown in Fig. 13. However, if we were to consider low survivability designs only (e.g., $A < 0.75$), the correlation would not be strong at all. Therefore, the strength of correlation is apparently governed by the asymptotic



convergence of s-factor to unity in the both formulations.

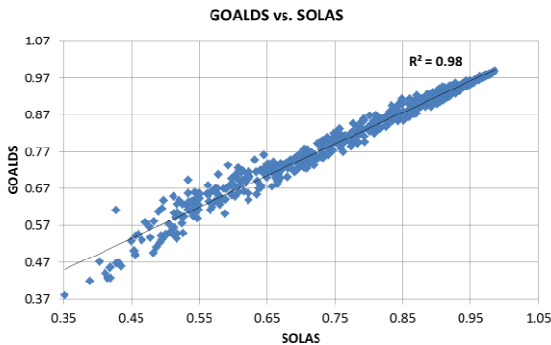


Figure 13: Correlation between index “A” by GOALDS and SOLAS 2009.

3.2 General trends (cruise ship)

Analogically to statistics on the ROPAX ship in the previous sub-section, statistical figures for the cruise vessel are provided. Thus, Fig. 14 – 15 show index “A” distributions for the sample points which were obtained through variation of topology related design parameters (see Table 4). The first observation is that, amongst the sample points, there is no ship design with GOALDS index “A” higher than the baseline GOALDS index.

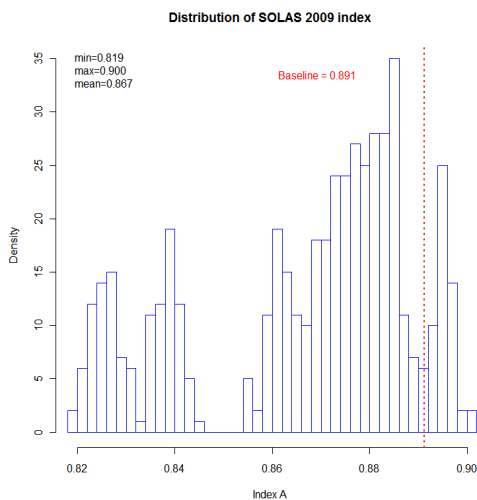


Figure 14: Histogram of topology sample points in terms of subdivision index “A” by SOLAS.

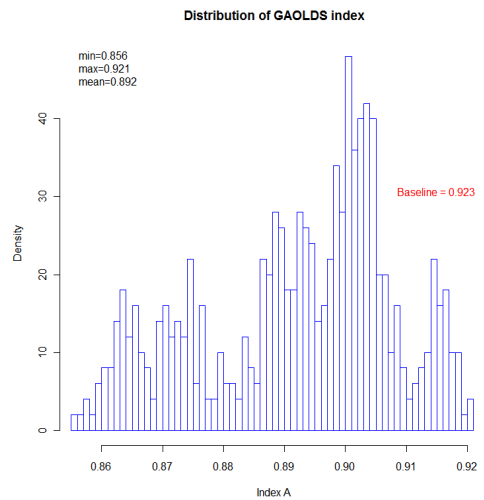


Figure 15: Histogram of topology sample points in terms of subdivision index “A” by GOALDS.

In Fig. 16 the relative difference between histograms in Fig. 14 and Fig. 15 is shown. It can be easily noticed that, likewise for the ROPAX ship, the GOALDS formulations yields higher indices of subdivision. This observation also applied to the sample designs produced through variation of size related parameters (see Table 4), as shown in Fig. 19.

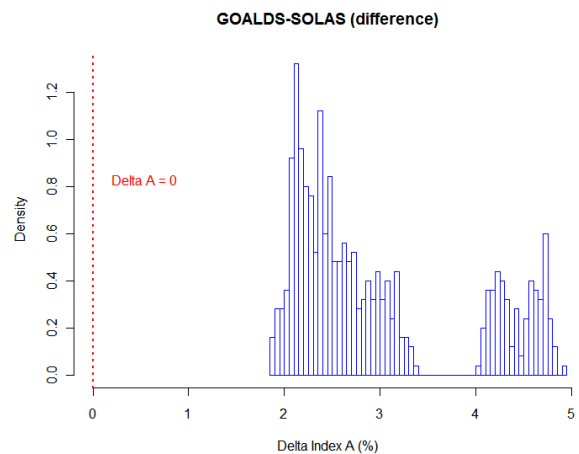


Figure 16: Histogram of topology sample points in terms of the relative difference between index “A” by GOALDS and SOLAS 2009.

The histograms in Fig. 17 – 18 are results of sampling the size related parameters (see Table 4) subject to a given topology (ship internal configuration) which was kept fixed.

Apparently, the sampling had some uncontrolled bias, which led to these Gaussian-like distributions. Interestingly, amongst the sample points there were many designs with higher indices of subdivision, compared to the one of the baseline.

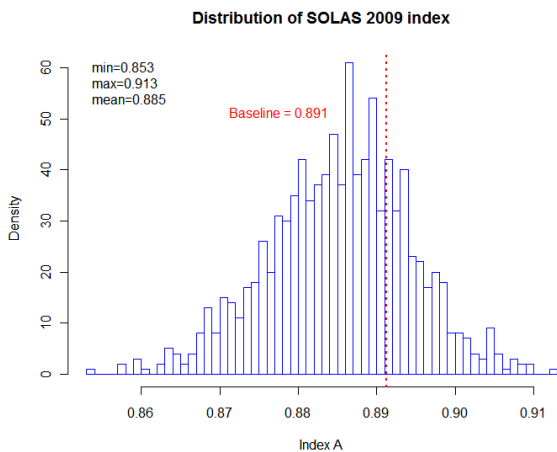


Figure 17: Histogram of sizing sample points in terms of subdivision index “A” by SOLAS.

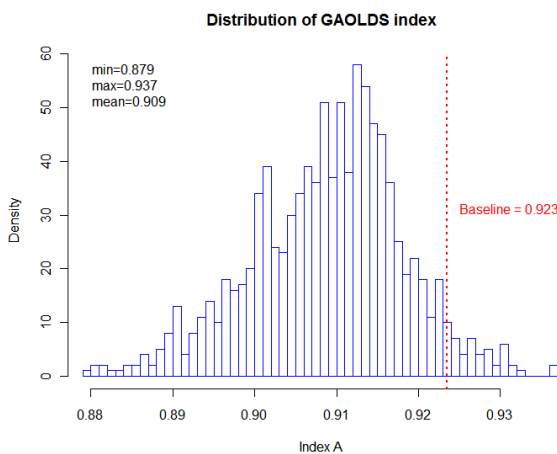


Figure 18: Histogram of sizing sample points in terms of subdivision index “A” by GOALDS.

The histograms in Fig. 17 – 18 also indicate that the maximum index of subdivision for the cruise ship parameterised as described in Section 2.1 can only reach ca. $A = 0.94$ (GOALDS), despite the fact that the bulkhead deck was raised by an entire deck. An intuitive conclusion, bearing in mind the reason for high survivability of the ROPAX ship, the lack of

residual buoyancy higher up in the ship is to blame. Perhaps, the bulkhead deck could be raised by at least two entire decks to secure the needed residual volume.

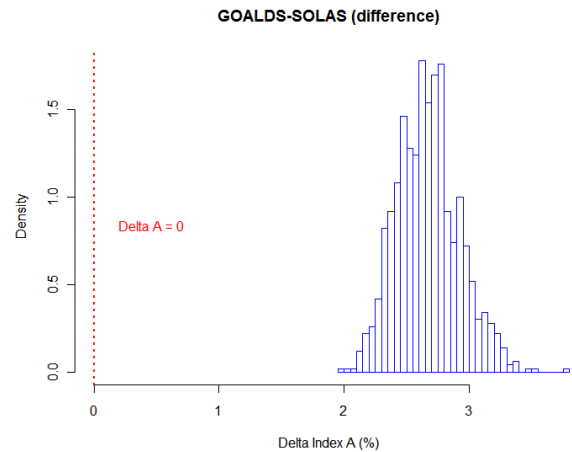


Figure 19: Histogram of sizing sample points in terms of the relative difference between index “A” by GOALDS and SOLAS 2009.

3.3 Sensitivity to design parameters in the ROPAX ship

In this section we draw reader’s attention to sensitivity analysis (SA) of the subdivision index “A” to design parameters, i.e. parameters that were varied through the process of sampling (see Section 2.2). Conventionally, and it also applies to this case, the purpose of SA is to

1. rank design parameters according to their importance (strength of influence the parameter under study, e.g. the index “A”) and
2. learn about the direction of that influence, i.e. whether a unit increase in a design parameter rises or reduces the dependent parameter such as index “A”

The second outcome of SA cannot be generally achieved for nonlinear relationships and when the global sensitivity, i.e. the effect of a design variable across its whole feasible range, is of



interest. As shown later in this section, the function of the index “A” is nonlinear and hence the property of SA is dropped from consideration in this paper.

There is a multitude of SA methods to choose from (Saltelli, Chan et al. 2000). In this work we found that so-called variance-based Monte Carlo methods are of most relevancy, specifically Sobol’ *first-order* and *total-effect* sensitivity indices (Sobol 1993; Saltelli 2002) were calculated. The indices vary within [0, 1] interval and the higher is the index value, the more sensitive output variable (e.g., index “A”) to the input variable. There are cases when the Sobol’s index may be negative, then is assumed to be zero (Saltelli, Chan et al. 2000). The first-order Sobol’s indices are related to the main effects (i.e. linear terms) in a mathematical model that maps input variables to an output variable. Such a model is also referred to as a statistical model, which is often created through response surface modelling. Total-effect Sobol’s indices are related to all term (e.g., linear and interaction etc.) in a statistical model and it is a sum of first-, second- (interaction) etc. order Sobol’s indices. Total-effect indices are much more reliable than the first-order indices, although might not be always computed successfully, and the first-order indices should be used instead.

Apparently, to perform the SA in our work, we needed to develop statistical models for index “A” of the ROPAX ship. Analogically, statistical models for the cruise ship were also developed, as shown in the next section. The accuracy of models is critical, for inaccurate models will not represent the reality adequately and hence cannot be used in any analysis. Thus, Fig. 20 and Fig. 21 show distributions of relative approximation error for the statistical/response surface models.

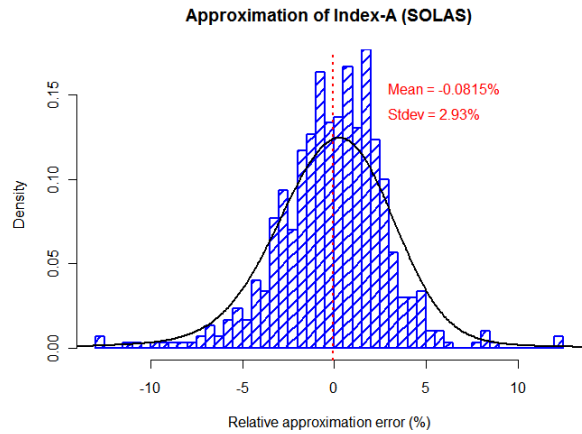


Figure 20: Approximation error for the response surface model of index “A” by SOLAS 2009. Coefficient of determination is $R^2 = 0.98$.

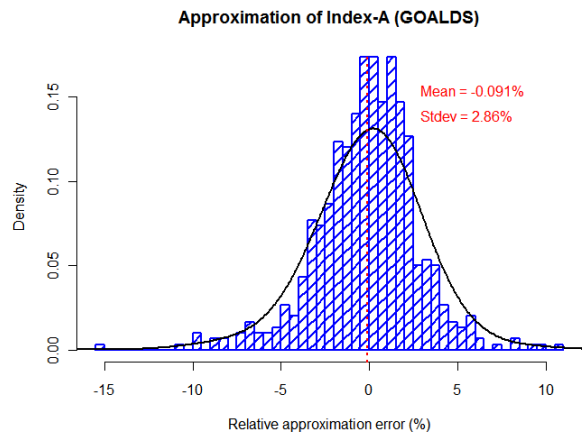


Figure 21: Approximation error for the response surface model of index “A” by GOALDS. Coefficient of determination is $R^2 = 0.97$.

As the histograms indicate, the accuracy of the response surface models is ca. $\pm 5\%$, which is very high. The developed response surface models included main effects, quadratic terms and two-way interaction terms, as shown in Eq. (3).

$$y = \beta_0 + \sum_{i=1}^n \beta_i x_i + \sum_{i=1}^n \beta_{ii} x_i^2 + \sum_{i=1}^n \sum_{i=1}^n \beta_{ij} x_i x_j \quad (3)$$

Results of SA is shown in Fig. 22, with the bars corresponding to Sobol’s indices enhanced with bootstrap confidence intervals (Varian

2005). The references to design parameters are explained in Table 5.

Table 5: Explanation of used references to design parameters in the ROPAX ship

Symbol	Explanation
VCG	Vertical centre of gravity of lightship
HULL	Hull type
N	Number of transverse bulkheads on the car deck
Z1	Number of transverse bulkheads in MFZ1
Z2	Number of transverse bulkheads in MFZ2
Z3	Number of transverse bulkheads in MFZ3
S	Presence of side casings on the car deck
LLH	Presence of long lower hold
BHDH	Bulkhead deck height
LWT	Lightship

- The most prominent design parameters are presence/absence of LLH, lightweight and hull type.
- S, i.e. the presence/absence of side casing on the car deck, seems to be more important to the SOLAS formulation. That is rather counterintuitive bearing in mind the GOALDS formulation, but perhaps the small difference and overlapping confidence intervals indicate the both regulations similarly react to presence/absence of side casings. However, the size of side casings in our parametric model (see Fig. 1) was relatively small, which could be the reason for the GOALDS formulation to “underperform”.
- Z1, Z2, Z3, and A are the number of transverse bulkheads in certain positions and they control the floodable

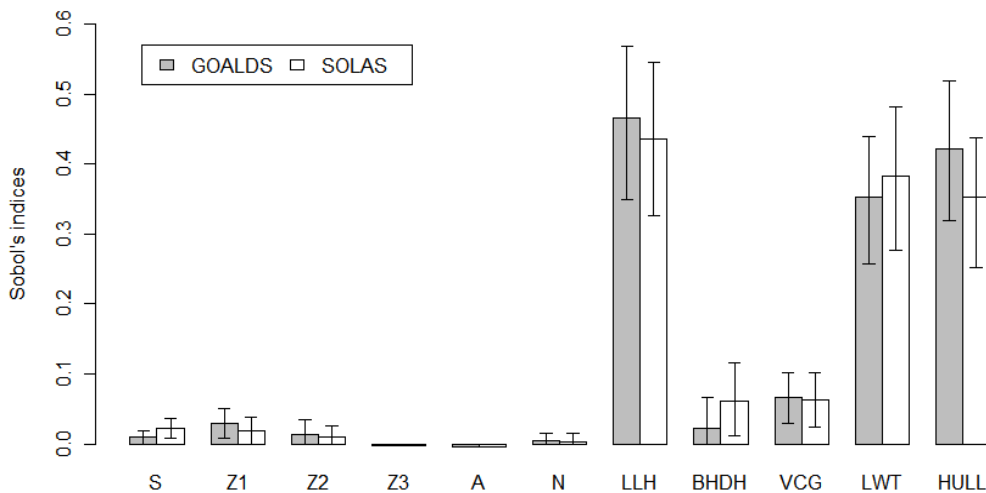


Figure 22: Sensitivity indices (Sobol's total-effect) for the both formulations.

Note that only design parameters which are showed to be statistically significant (level of $\alpha=5\%$ was used) are displayed in Fig. 22.

To this end, the following observations from Fig. 22 can be made.

volume of corresponding compartments. According to the sensitivity indices, the GOALDS formulation may be more sensitive to variations in the floodable volume, especially in MFZ1 and MFZ2.

- N seems to have a slightly stronger effect on the GOALDS formulation,



although the both formulations are relatively indifferent to the transverse subdivision of the car deck.

- LLH may have a generally stronger effect on the GOALDS formulation, although the difference is relatively small. The possible reason for the small difference is when the LLH is present, there is typically >10% of damage cases that are not physically survivable, i.e. regardless the formulation (see Fig. 23). These damage cases do not also contribute to the index “A” value. Provided that the share of damage cases with $s = 1$ is usually big and quite the same with the both formulations, then the only small share of damage cases with $0 < s < 1$ contributes to the difference. This share would be bigger, and hence the difference between the formulations as well, should the LLH not be present.
- BHDH or freeboard variations disturb the subdivision index “A” of SOLAS 2009 more than of the GOALDS formulation. However, the comparison is difficult without a more detailed analysis.
- VCG has a similar effect on the both formulations, although GOALDS seems to be more sensitive to variations in VCG. In our case, the VCG was mainly affected by subdividing the car deck or its widening.
- LWT should have generally a negative effect on the both formulations, leading to a smaller is the difference between them. The interpretation can follow a similar route as of the LLH interpretation, i.e. a heavier ship becomes more vulnerable to any damages, i.e. the share of damage cases with $s = 0$ increases, reducing the difference in the formulations. However, the GOALDS formulation may be somehow less sensitive to parameter variations and more research is needed to clarify the reason.
- HULL may have a stronger effect on the GOALDS formulation. The

parameter changed the conventional baseline hull to the UFO hull (Fig. 2) and the widened hull. For the UFO hull introduces extra buoyancy on the car deck, the GOALDS formulation seems to be more sensitive to it.

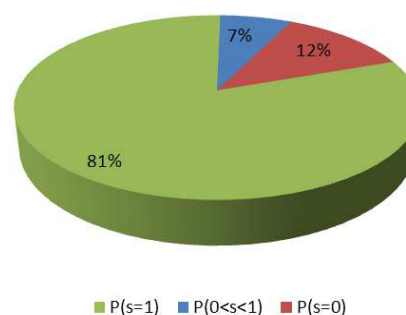


Figure 23: Typical distribution of s-factor probability across damage cases for a ROPAX ship equipped with LLH (adopted from (Puisa, Tsakalakis et al. 2012)).

It is important to note that Fig. 22 can only be used to highlight the trends (based on 500 design variations) in relation to the new formulation of the subdivision index. That is, on one hand it seems that the difference is small and even doubtful, but on the other hand the distinction between the two formulations is present when it is expected, e.g. migration from the conventional hull shape to the UFO shape that provides extra buoyancy higher up on the ship.

3.4 Sensitivity to topological design parameters in the cruise ship

The analogous SA procedure was applied to the cruise ship. Specifically, firstly we derived response surface models (see Eq. 3) for the both formulations of the probabilistic index “A”. Fig. 25 and Fig. 26 show the distributions of the approximation error, indicating that the models were highly accurate.

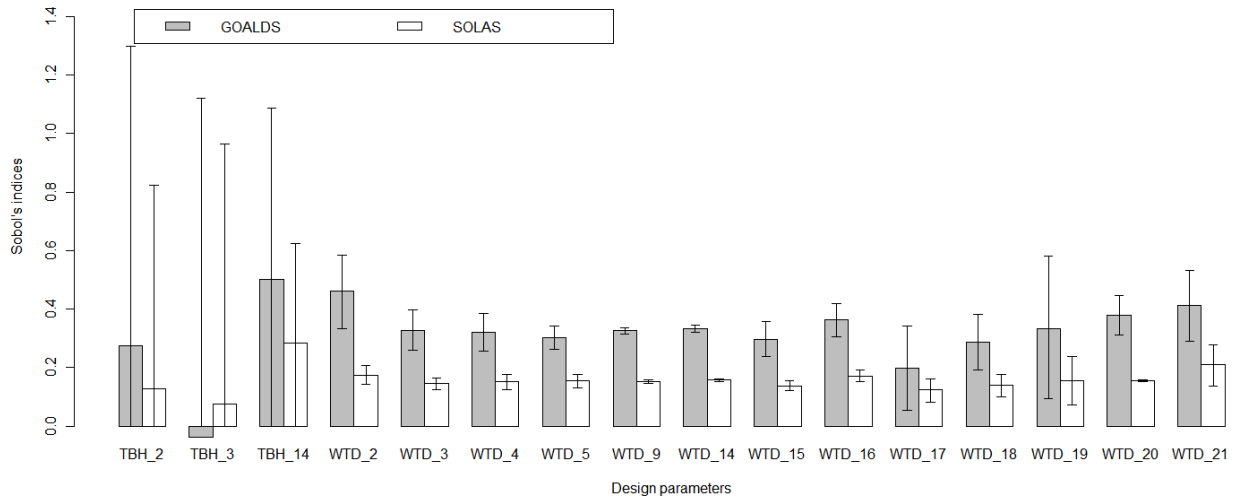


Figure 24: Sensitivity indices (Sobol's first-order) for the both formulations.

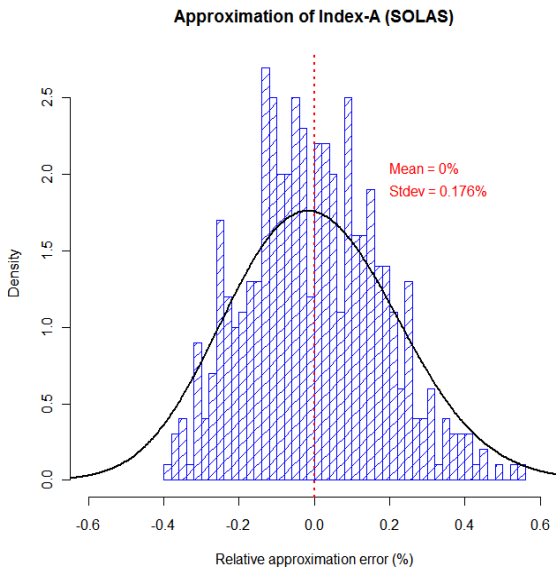


Figure 25: Approximation error for the response surface model of index “A” by SOLAS 2009. Coefficient of determination is $R^2 = 0.995$.

Following that, the sensitivity analysis was carried out, calculating the Sobol's sensitivity indices only. The majority of the total-effect indices appeared to be negative, which may be attributed to the numerical problems, as mentioned in (Saltelli, Chan et al. 2000), or the fact that none of the studied parameters does actually have any significant effect. We assumed that the latter is unlikely and therefore display the first-order indices, which were calculated correctly (see Fig. 24).

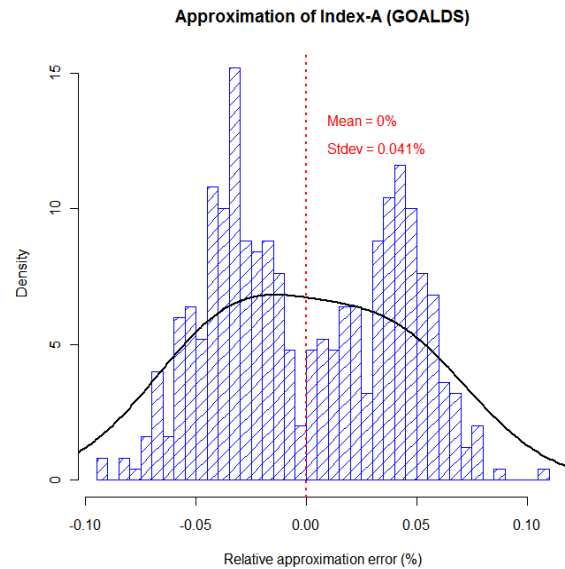


Figure 26: Approximation error for the response surface model of index “A” by GOALDS. Coefficient of determination is $R^2 = 0.99$.

Note that design variables used to vary the topology of the cruise ship and shown in Fig. 24 are explained in Table 6. Note, however, only statistically significant parameters are displayed in Fig. 24 (level of $\alpha=5\%$ was used).

Not going into much detail, the general observation is that the GOALDS formulation is significantly more sensitive to the raise of the bulkhead deck. This is in line with the expected difference between the formulations, as was indicated in Section 1.



Table 6: Explanation of used references to topological design parameters in the cruise ship

Symbol	Explanation
TBH_2	Presence/absence of transverse bulkhead at approx. frame 21 of the baseline design
TBH_3	... frame 36 ...
TBH_14	... frame 218 ...
WTD_2	Presence/absence of a watertight door on the bulkhead deck at approx. frame 21 the baseline design
WTD_3	... frame 36 ...
WTD_4	... frame 52 ...
WTD_5	... frame 71 ...
WTD_9	... frame 130 ...
WTD_14	... frame 218 ...
WTD_15	... frame 233 ...
WTD_16	... frame 246 ...
WTD_17	... frame 265 ...
WTD_18	... frame 283 ...
WTD_19	... frame 299 ...
WTD_20	... frame 312 ...
WTD_21	... frame 328 ...

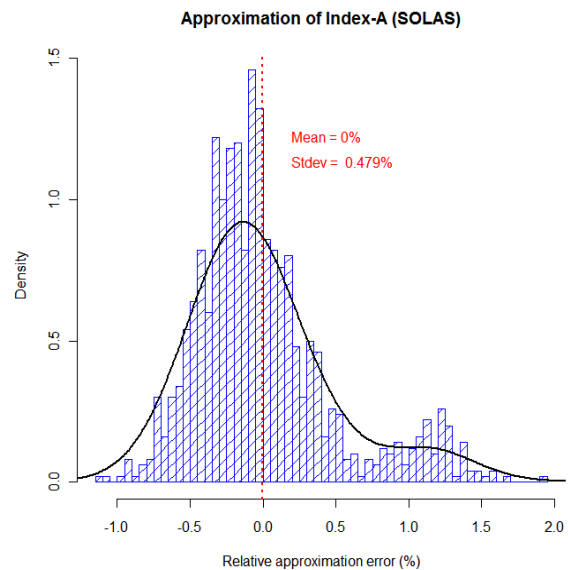


Figure 27: Approximation error for the response surface model of index “A” by SOLAS 2009. Coefficient of determination is $R^2 = 0.78$.

3.5 Sensitivity to sizing design parameters in the cruise ship

In this section the sensitivity to sizing parameters (the parameters that control the size of compartments and tanks) of the cruise ship is addressed. Thus, Fig. 27 and Fig. 28 depict distributions of the approximation error for the both response surface models. The models appeared to be less accurate than those in the previous sections, but the accuracy of is still quite high and hence acceptable for the analysis.

In contrast to the topology parameters in Section 3.4, the Sobol’s total-effect indices were successfully calculated and displayed in Fig. 29. The design parameters (again only statistically significant are shown) are explained in Table 7. The first observation from of Fig. 29 signals that there is no noticeable difference between the two formulations.

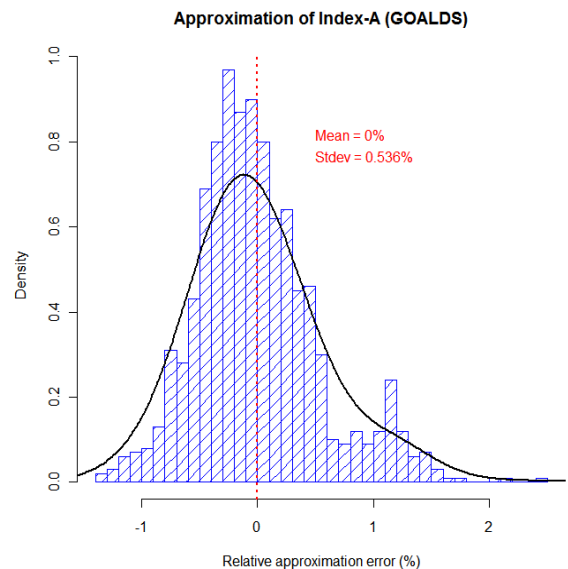


Figure 28: Approximation error for the response surface model of index “A” by GOALDS. Coefficient of determination is $R^2 = 0.71$.

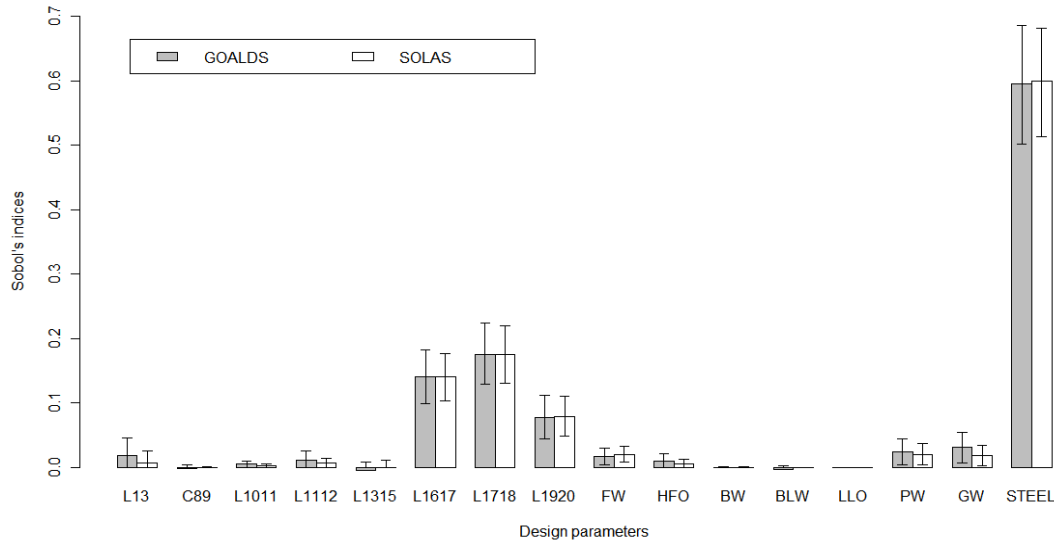


Figure 29: Sensitivity indices (Sobol's total-effect) for the both formulations.

Table 7: Explanation of used references to topological design parameters in the cruise ship

Symbol	Explanation
L13	Length of the wt. compartment being approx. between frame 3 and 36 of the baseline design
C89	Longitudinal position (to the mid length) of the wt. compartment being approx. between frame 115 and 130 of the baseline design
L1011	... between frame 146 and 165 ...
L1112	... between frame 165 and 183 ...
L1315	... between frame 202 and 218 ...
L1617	... between frame 233 and 246 ...
L1718	... between frame 265 and 283 ...
L1920	... between frame 299 and 312 ...
FW	Total volume of fresh water tanks, which are positioned on the tank top, mainly between frame 246 and 312. Because the tanks are not empty, the variation of FW volume affects the floodable volume in corresponding compartments, thereby affecting the index "A".
HFO	Total volume of heavy fuel oil tanks or the total floodable volume in compartments between frames 130-146 and 183-218 on the tank top.
BW	Total volume of ballast water tanks or the total floodable volume in compartments between frames 299-328, 133-146 and 3 in the double bottom.

BLW	Total volume of black water tanks or the total floodable volume in compartments between frames 146 and 165 in the double bottom.
LLO	Total volume of lubrication oil tanks the total floodable volume in compartments between frames 71 and 115 in the double bottom.
PW	Total volume of potable water tanks or the total floodable volume in compartments between frames 246 and 284 on the tank top.
GW	Total volume of grey water tanks or the total floodable volume in compartments between frames 21 – 71 165 -246 in the double bottom and 86 - 102 on the tank top.
STEEL	Steel weight of the ship

4. CONCLUSIONS

The paper has presented results of statistical analysis with the purpose to highlight implications of the new formulation of the s-factor by GOALDS on design of ROPAX and cruise ships. Specifically, the sensitivity of the subdivision index "A", calculated according to SOLAS 2009 and GOALDS formulations, to selected design variables have been of main interest. Additionally, general statistical metrics, e.g. maximum achievable values of index "A", have been presented.



Firstly, it has been shown that high indices for large ROPAX can be achieved through addition of extra buoyancy on the car deck and above. In our work, although not explicitly shown in this paper, the ROPAX design with high indices ($A > 0.98$) did not have the long lower hold, used the UFO hull (Fig. 2) and had the car deck subdivided either transversely or longitudinally. Surely, these are only concept design indices and they will drop by some 6% in the later design stages, but it is already very promising. In our work high indices for the cruise ship did not show up during the design exploration; max $A \approx 0.94$ was found. One of the possible reasons relates to the lack of the residual volume higher up the ship.

Secondly, it has been observed that in across all design variations the GOALDS index "A" has been always higher than its SOLAS counterpart. Perhaps the effect of ship size, which is explicitly taken into account in the GOALDS formulation through the residual volume, is the most likely reason.

Thirdly, the sensitivity analysis has indicated the difference between the SOLAS 2009 and GOALDS formulations and the nature of this difference is in line with expectations from the new s-factor formula. That is, the GOALDS formulation is more sensitive to variations in the watertight volume higher up the ship. However generally, this difference between the formulations is more of a trend than a rule, as far as our studied ship concepts are concerned. To prove the opposite, a more extended analysis would be necessary.

5. ACKNOWLEDGMENTS

The research work presented in this paper has been funded by the European Commission who is gratefully acknowledged.

6. REFERENCES

Beachkofski, B. and R. Grandhi (2002). "Improved Distributed Hypercube Sampling." American Institute of Aeronautics and Astronautics **1274**.

Cichowicz, J., N. Tsakalakis, et al. (2011). Survivability of Passenger Vessels - Re-engineering of the s-Factor. Proceeding of the 12th International Ship Stability Workshop, Washington D.C., USA.

Puisa, R. and K. Mohamed (2011). Prudent platform for multidisciplinary ship design exploration, analysis and optimisation. International Conference on Computer Applications in Shipbuilding (ICCAS 2011). Trieste, Italy, RINA.

Puisa, R., A. Murphy, et al. (2012). Design Customisation and Optimisation through Effective Design Space Exploration International Marine Design Conference 2012 (IMDC2012), Glasgow, Scotland, University of Strathclyde.

Puisa, R., N. Tsakalakis, et al. (2012). "A Critical Look at SOLAS CH II-1 with Respect to Floodable Length of Compartments in RoPax Ships." Journal of Marine Science and Technology (accepted).

Romero, V., J. Burkardt, et al. (2004). Initial Evaluation of Pure and "Latinized" Centroidal Voronoi Tessellation for Non-Uniform Statistical Sampling. Sensitivity Analysis of Model Output (SAMO 2004) Conference. Santa Fe.

Saka, Y., M. Gunzburger, et al. (2007). "Latinized, improved LHS, and CVT point sets in hypercubes." International Journal of Numerical Analysis and Modeling **4**(3-4): 729-743.

Saltelli, A. (2002). "Making best use of model evaluations to compute sensitivity indices." Computer Physics Communication **145**: 580-297.

Saltelli, A., K. Chan, et al. (2000). Sensitivity analysis, Wiley.

Sobol, I. M. (1993). "Sensitivity analysis for non-linear mathematical model." Math. Modelling Comput. Exp. **1**: 407-414.

Varian, H. (2005). "Bootstrap Tutorial." Mathematica Journal **9**: 768-775.



Coupling of Progressive Structural Failure and Loss of Stability in the Safe Return to Port Framework

Seungmin Kwon, *SSRC, University of Strathclyde*, seung.kwon@strath.ac.uk

Qi Chen, *SSRC, University of Strathclyde*, q.chen@strath.ac.uk

George Mermiris, *SSRC, University of Strathclyde*, g.mermiris@strath.ac.uk

Dracos Vassalos, *SSRC, University of Strathclyde*, d.vassalos@strath.ac.uk

ABSTRACT

This paper addresses the survivability assessment of damaged ships with respect to the coupled effects of structural degradation and damage stability in the context of the Safe Return to Port (SRtP) framework for passenger ship safety. The survivability is evaluated in the time domain with varying wave loads. The proposed methodology is demonstrated through application to two diverse but safety-critical ship types, namely a RoPax with side damage, and an Aframax tanker with asymmetric damage at the bottom, the latter for comparison purposes.

Keywords: *Safe Return to Port, Progressive structural failure, Damage stability*

1. INTRODUCTION

Although substantial effort has been spent in the design stage and operational procedures of ships towards prevention and mitigation of accidental events and their ensuing consequences, the residual risk remaining is sufficient to fuel progressively higher expectations on the acceptable level of safety at sea by the society at large. The recurrence of high profile accidents demonstrates this situation with little margin for dispute and stresses the urgency for more comprehensive understanding of the underlying phenomena of a ship in distress.

In response to this need, the SRtP framework for passenger ship safety has set the foundation for a series of developments by advocating zero tolerance to loss of life following an accident and allowing 100% survivability for a specified interval of time (3 hours recommended) if the casualty threshold criteria are exceeded, or indefinite survivability

otherwise. In the latter case, the ship should be able to return to port under its own power or remain upright, afloat and with sufficient functionality to support passengers and crew until help arrives (IMO, 2004).

In this context, the authors have developed a methodology for evaluating the coupled stability deterioration and progressive structural failure of a damaged ship for a succession of sea states until capsize or global structural failure occurs. The structural degradation of the hull girder is captured by parametric models of damage propagation developed on the basis of FE analyses (Kwon et al, 2011). The stability of the ship following initial damage is assessed with PROTEUS3, (Jasionowski, 2001).

The applicability of the developed methodology is demonstrated with two case studies, namely an Aframax tanker with asymmetric bottom damage, and a RoPax with side shell damage amidships. The two ship



types are selected on the basis of their robustness in stability and longitudinal strength respectively, and set the foundation for a comprehensive treatment of post-damage survivability of safety-critical ships. Obviously the SRtP legislation does not apply to tankers but it will be of interest to examine the two vessels comparatively.

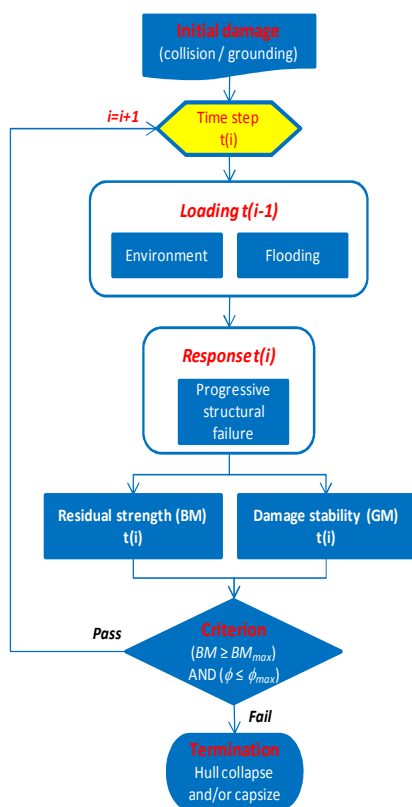


Figure 1: High level process of the proposed methodology.

2. METHODOLOGY FOR SURVIVABILITY ASSESSMENT

The key feature of this approach is the survivability assessment of ships with the coupling effect of damage evolution in the time domain. The progressive structural failure assessment of a damaged ship is achieved by crack propagation analysis under varying wave loading. In addition, when the damaged ship is flooded the water ingress and egress from the damaged compartment (due to the ship motion and the waves) constitutes a source of loading that deteriorates the structure locally and

induces further crack propagation. In turn, the damage extension will exacerbate flooding and the cycle repeats itself until either stability is lost or residual strength becomes insufficient to sustain the applied loads.

For every time step of the calculation, the crack propagation is analysed and the effect of damage evolution on the survivability of the damaged ship is assessed in terms of criteria pertaining to residual strength and damage stability. For example, such criteria may relate to the bending moment (BM) and the metacentric height (GM) respectively, and they should account for the dynamics of the situation by focusing on the time to break and the time to capsize respectively, (Vassalos, 2009). A high level description of the proposed methodology is shown in Figure 1.

2.1 Loading

Environmental loading

The load induced by the waves is the primary source for crack propagation and it is calculated either by an in-house 3D panel code with Green's function implementation, (Xie, 2011), or class guidelines, (DNV, 2012). The obtained wave and still water bending moments form direct input to the damage propagation analysis. On the other hand, the total bending moment will be compared with the residual strength of the damaged ship for every time step of the process. Finally, the calculated ship motions are used in flooding simulation.

Flooding loading

The flooding of the damaged ship will induce inflow and outflow of water as the ship moves in waves, and the ensuing pressure differential effect on the crack propagation needs to be taken into account in the progressive failure of the structure. Depending on the size and the location of the damage opening, the size of the compartment, and the ship motions, the induced flooding pressure

and its distribution is defined. In principle, this calculation should be based on CFD simulations and in particular the solution of the Navier-Stokes equations with the VOF method, (Gao, 2010). However, despite the increased resolution that this model could contribute to the overall methodology, its inherently complicated and computationally-intensive nature does not allow its direct integration in the methodology at the current stage of development and constitutes an item of future work.

2.2 Progressive Structural Failure

The crack growth modelling emanating from or near the damaged ship parts is based on the Linear Elastic Fracture Mechanics (LEFM) and Paris Law, in which ‘time’ is considered implicitly by the number of cycles, N , where ‘ N =time/period’. This approach has been adopted not only in the shipbuilding industry by Dexter & Pilarski (2000) and Dexter & Mahmoud (2004), but in the aviation industry by Farahmand et al. (2007) as well.

A crack growth model proposed by McEvily & Groeger (1977) has been modified to include the effective range of SIF and the material constants are chosen so as the linear region of the model fits with the original linear Paris Law, (Kwon et al, 2011). Also, instead of conducting FE analysis, the Stress Intensity Factor (SIF) has been obtained through knowledge-intensive models, in order to overcome cumbersome numerical FEA and to utilise exploitation of accumulated knowledge, (Tada et al, 2000). The benefit from the use of knowledge-intensive models is a fast and reliable analysis without preparing FE model while its application and accuracy is focused and depends on the ship type and size under consideration.

An example of validation result of the knowledge-intensive model of SIFs for circular opening in a stiffened panel is presented in

Figure 3, in which comparison with the result from FEA is shown to have good agreement.

A procedure for evaluating the progressive structural failure using the crack growth model is shown in Figure 2. The extended crack size in the time domain would be used to assess the residual hull girder strength, and to update the opening of the flooded compartment and the adjacent spaces if its boundaries are breached. In this manner, all the time-dependant information such as loading (and its resultant bending stress), damage and crack size is updated for each time step of the simulation.

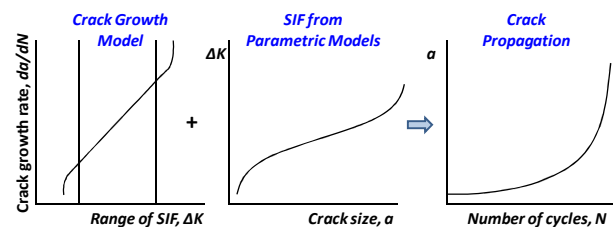


Figure 2: Procedure of progressive structural failure analysis.

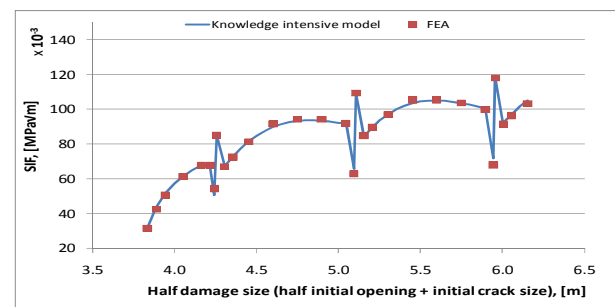


Figure 3: Comparison of SIF calculated by FEA and obtained by the model

2.3 Residual Strength

The residual strength assessment of a damaged ship is based on the moment-curvature relationship for stiffened panels known as Smith’s method, (Smith, 1977). The relationship is obtained by imposing a curvature from sagging to hogging on the hull girder, which is assumed to consist of several beam-column elements. For each curvature, the average strain of each element is calculated and the stress imposed on it is obtained from a corresponding load-end shortening curve. The



moment sustained by the whole section is obtained by summing up the moments of each element induced by axial force and distance of each element from the neutral axis of the section. The ultimate bending strength of the section is the maximum bending moment in hogging and sagging conditions.

The load-end shortening curve of each element is based on IACS rules (2008), in which the effect of plate induced failure, the flexural buckling failure of a column and the tripping failure of a stiffener are considered as failure modes.

Validation of this approach was made by Kwon et al, (2010), through comparison with FEA results. For each time step, the damage evolution reduces the effective width of plates and the number of effective stiffeners and results in reduction of the ultimate residual bending strength.

2.4 Damage Stability

The time to sink and/or capsize following damage is a critical factor in determining the level of safety of a damaged ship and constitutes one of the criteria in the Safe Return to Port Regulation for damage stability of passenger ships. In this case the dynamic response of the ship and the progressive flooding of its compartments in a random seaway form a highly non-linear dynamic system, the behaviour of which is modelled and simulated in the time domain by PROTEUS3, (Jasionowski, 2001). The main features of the software are:

- i) The ship hydrodynamics are derived from properties of the intact hull and they are based either on asymmetrical strip theory formulation with Rankine source distribution or a 3D panel code, both accounting for the non-linearities arising from the instantaneous variation of the mean ship position and large amplitude motions.

- ii) The effects of floodwater dynamics described by a full set of non-linear equations are derived from rigid-body dynamics.

- iii) The water ingress/egress is based on Bernoulli's equation and the floodwater motions are modelled as a Free Mass on Potential Surface (FMPS) de-coupled system in an acceleration field.

The ship geometry is defined in sections both for the hull and the internal compartments. The necessary environmental conditions for the simulations are generated according to JONSWAP or Pierson-Moskowitz spectra. The output of the calculation concerns ship motions, floodwater mass variation and motion, flow of floodwater through openings, environmental forces, etc.

2.5 Criteria

The survivability of damaged ships is assessed through comparison of the results from the residual strength analysis and the damage stability analysis with a set of criteria. That is, the damaged ship would be regarded as capsized if the roll angle exceeds 30 degrees instantaneously or if steady (average) heel is greater than 20 degrees for a period longer than three minutes according to EC (2003). On the other hand, the ship is considered to lose its structural integrity if the ultimate residual bending moment becomes lower than the applied one due to wave loading or when major structural elements are severed completely due to unstable crack propagation.

3. CASE STUDIES

The verification of the proposed approach is conducted by application of the methodology to an Aframax tanker with bottom damage, and a RoPax with damage on the side shell. In the analysis only the environmental loading (in deep water) is considered.

3.1 Tanker

The ship used in the analysis is an 112,700 DWT crude oil carrier fitted with double side structure. The ship has six cargo tanks on each side. Its principal dimensions are summarised in Table 1 and the midship section is shown in Figure 4.

Table 1: Principal dimensions of the tanker under consideration.

Type of dimension	Value
Length O. A.	250.17 m
Length B. P.	239.00 m
Breadth MLD.	44.00 m
Depth MLD.	21.00 m
Draught MLD. (Design)	14.60 m

The initial damage is located at the starboard side of the bottom structure close to mid length. The width of the initial damage is defined as 7.33 m as shown in Figure 4 according to ABS guidelines, (1995). A circular damage opening is assumed for convenience in the calculations.

A full load condition is considered for the wave loading analysis. The wave data is obtained from the BMA report, (2004). The resultant most probable wave bending moments within each observed time window for head sea conditions are shown in Figure 5.

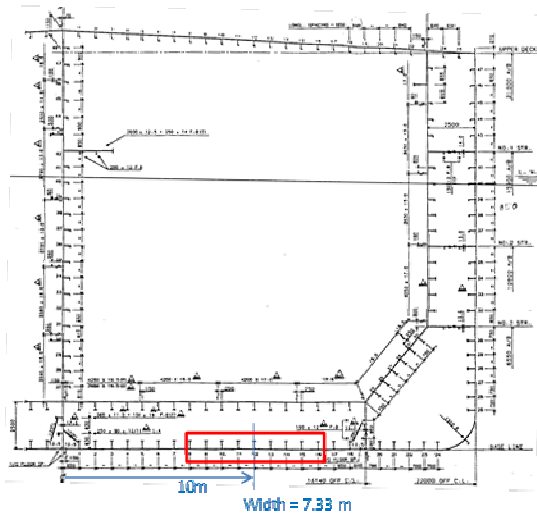


Figure 4: Midship section of the tanker with initial bottom damage.

The result of the asymmetric damage propagation is obtained from the progressive structural failure analysis and is shown in Figure 6. Accelerated propagation (unstable) starts at 68 hours and 73 hours for the port and starboard bottom damage, respectively. It is identified that the starboard bottom damage spreads to the starboard side inner bulkhead (bottom girder is included) and side shell in sequence, whilst the port damage propagates to the centre bulkhead and to the port side inner bulkhead (and bottom girder) gradually.

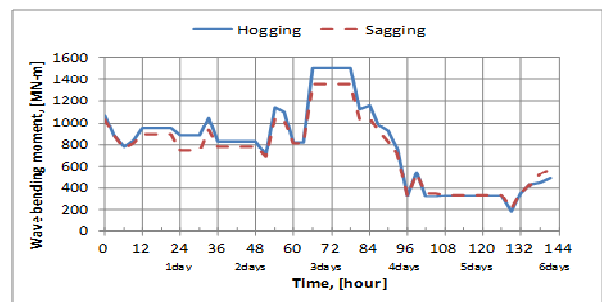


Figure 5: Wave bending moment based on the wave data from the *Prestige* accident report.

Considering that the crack propagation on the bulkheads exceeds the height of the inner bottom translates to the breach of the corresponding cargo tank. That is, oil outflow is expected to appear at 80 and 90 hours after the damage initiation from the starboard and port cargo tanks respectively.

Uncertainty analysis can be conducted with the developed parametric tool by taking into account the effect of various parameters.

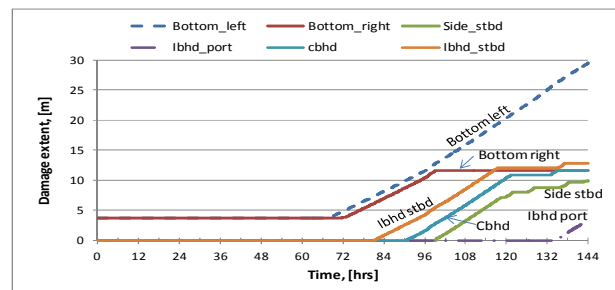


Figure 6: Asymmetric grounding damage propagation at the bottom of a tanker.

As damage propagates, the ultimate residual strength of the hull girder is calculated, as shown in Figure 7. Although it is advisable to



take the effect of heeling angles into account when calculating the ultimate residual strength, due to its small values during the simulation, the effect of heeling angle is not considered in the current analysis. The structural degradation starts at 72 hours after the initial damage occurred, and coincides with the unstable damage propagation of the bottom. From this point onwards, the ultimate hull girder strength is decreased by 53% and 23% for hogging and sagging respectively, compared to the bending moment capacity of the intact condition. The vessel is regarded as lost at 144 hours, i.e. when the bottom plate is severed.

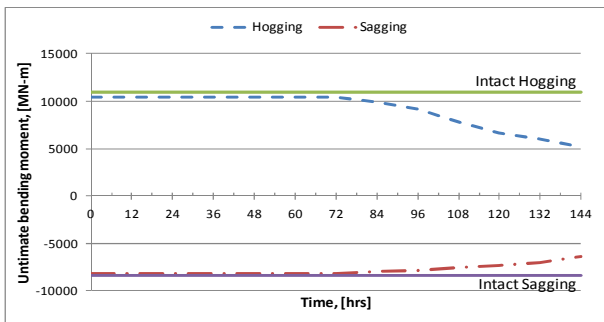


Figure 7: Degradation of the ultimate residual strength of the tanker.

The stability deterioration of a ship is measured by the time to capsize or sink after damage. For this calculation the permeability of the damaged compartment is assumed as 0.95. At 92 hours, i.e. when the damage size exceeds the centre bulkhead, the symmetrical compartment to the initially damaged compartment is considered flooded with identical permeability. Figure 8 shows the comparison of GZ curves for the fully loaded condition. The residual GZs for damage conditions prove that a wide safety margin is left following the damage occurrence, even after the flooding extends to the port side tank.

With respect to the time-domain numerical simulation, the initial transient flooding has been modelled by assuming that the water enters the compartments (after 92 hours) very fast. The survivability simulations are based on the same set of wave data as those used for the wave loading calculations, (BMA, 2004). Two headings of JONSWAP spectrum (90 degrees

and 180 degrees) are simulated to examine the influence of wave heading on damage stability. As expected no capsize occurs during the whole simulation time, regardless of the heading.

Table 2: Summary results for head seas conditions.

	H_s [m]	Cumulative simulation Time, [hrs]	$\phi_{max,180}$ [deg.]	Reduction of BM	
				BM _{hog}	BM _{sag}
Step1	5.5	3	3.13	4.8%	1.9%
Step2	5.1	6	3.27	4.8%	1.9%
Step3	4.5	36	3.23	4.8%	1.9%
Step4	4.0	54	3.12	4.8%	1.9%
Step5	5.0	66	3.08	4.8%	1.9%
Step6	6.5	81	2.93	8.1%	3.7%
Step7	4.7	92	3.20	13.5%	5.5%
Step8	3.25	102	0.01	24.0%	8.0%
Step9	2.5	132	0.03	45.3%	15.8%
Step10	3.5	144	-0.09	52.9%	23.3%

Table 2 presents the entire simulation process in ten consecutive steps. The output information (e.g. mode of motion, volume of flooded water) at the final stage in one step is accounted as the initial conditions for the successive step. The total simulation time is in line with the analysis for crack propagation, which lasts for 6 days (144 hours). Figure 9 provides snapshots of flooded compartments in the damage area of the ship. The maximum rolling during the simulation does not exceed 5 degrees. Because the flooding compartments concerned in this damage case are symmetric, capsize is highly unlikely during the long period of simulation time.

3.2 RoPax

The next application addresses a mid-sized RoPax vessel that has a vehicle deck at 9.0 m and a strength deck at 14.85 m above the baseline. The principal dimensions of the vessel are summarized in Table 3 while the cross section of interest and the general arrangement are illustrated in Figure 10 and Figure 11 respectively.

The initial damage is assumed to be located on the starboard side of the side shell near the

middle of the ship. The height and depth of the damage are defined as 5.88 m and 2.2 m, respectively according to ABS guidelines (1995). The damage length is chosen to be the same as the web frame spacing (4.8 m).

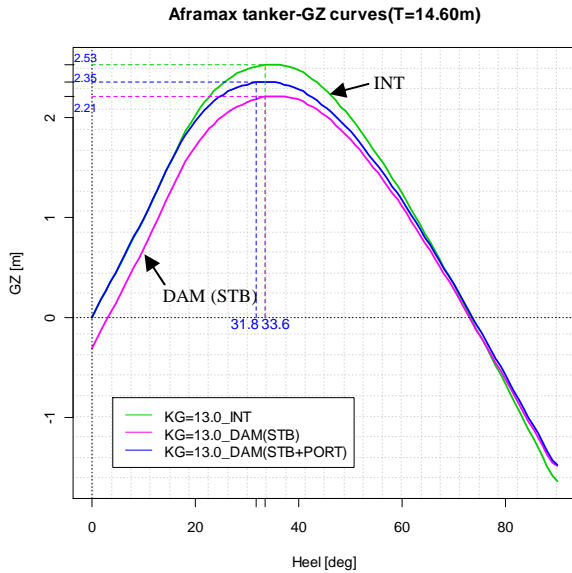


Figure 8: GZ curves calculated by PROTEUS3 for the tanker under consideration.

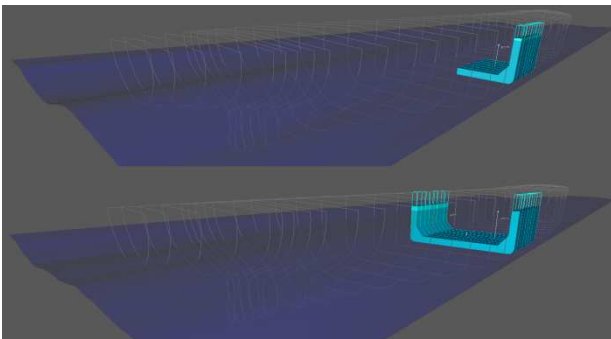


Figure 9: Numerical simulation of the bottom flooding before and after the 92 hours stage.

Table 3: Principal dimensions of the RoPax under investigation.

Type of dimension	Value
Length O. A.	194.30 m
Length B. P.	170.00 m
Breadth MLD.	27.80 m
Depth to strength deck	14.85 m
Depth to vehicle deck	9.00 m
Draught MLD. (Design)	6.25 m

Because of the sensitivity of the damage extent and the ensuing flooding conditions of the RoPax ship, two damage cases (of the same

size but different location) are investigated for comparison purposes as shown in Figure 10. In this manner, it will be demonstrated that uncertainty management is an inherent ingredient of the proposed methodology.

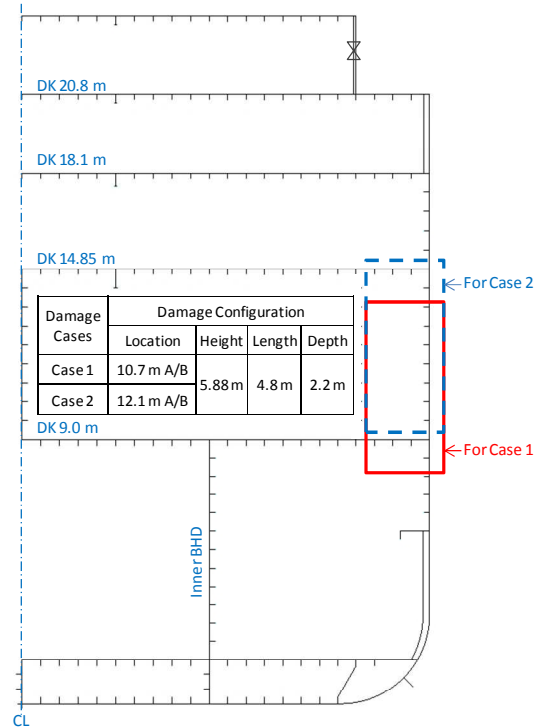


Figure 10: The cross section of the RoPax with the initial collision damage cases.

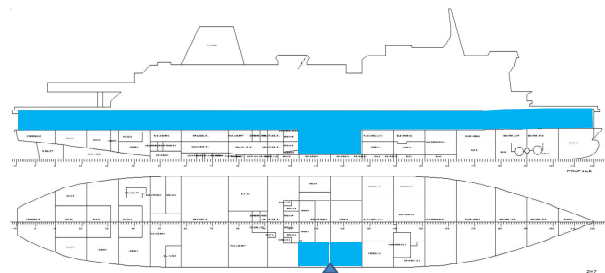


Figure 11: General arrangement of RoPax and the flooding compartments.

Table 4: Summary of the progressive structural failure results.

	Case 1	Case 2
Time, side upper unstable (hrs)	111.4	25.7
Time, Strength deck breach (hrs)	113.1	Initial
Time, deck 18.1m breach (hrs)	121.8	38.3
Time, deck 20.8m breach (hrs)	128.9	47.3
Time, vehicle deck breach (hrs)	Initial	130.7
Final damage size under vehicle deck (m)	1.26	1.89



The results of the progressive structural analysis are shown in Figure 12 and summarized in Table 4. The initial damage on the side shell is stable for the first 111 hours and 26 hours in Case 1 and 2 respectively, after which unstable propagation upwards starts causing sequential breach of the joints with the deck plates above the initial damage location. The cracks spreading to decks are found to sever the deck plates as the unstable propagation is fuelled by the high stress concentration levels.

In Case 1, the cracks on the vehicle deck and the lower part of the side shell propagate a negligible amount during the analysis. This is contributed to the fact that the initial location of the neutral axis of the damaged section is above the crack tips causing compressive bending stress on them during most of the analysis. Although a similar phenomenon happens to Case 2 at the initial stage, the elevated initial damage location causes earlier unstable damage propagation in deck plates, loss of which is sufficient to lower the neutral axis of the damaged section. As a result, the compressive bending stress on the lower side shell crack changes into tension at 45 hours. Consequently, the lower crack of the side shell will propagate below the vehicle deck at 131 hours causing extended flooding.

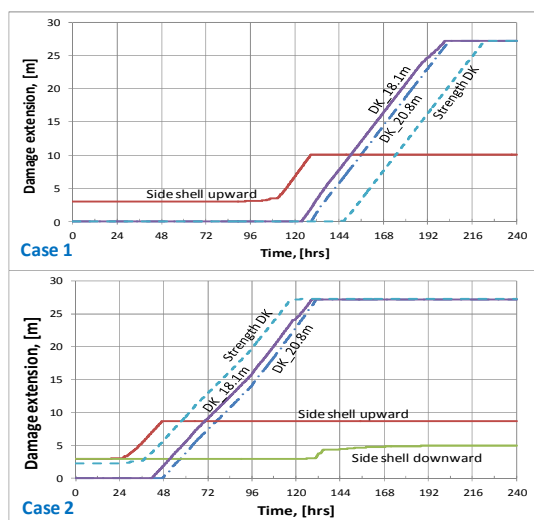


Figure 12: Damage propagation for collision damage on side shell of the RoPax.

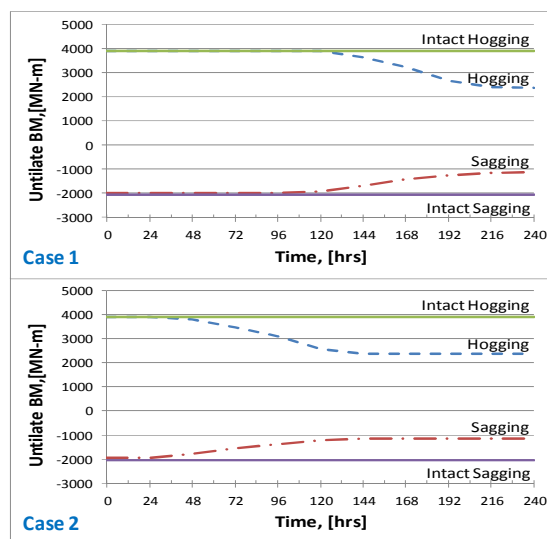


Figure 13: Decrease of the ultimate residual strength of the RoPax at the damaged section due to the progressive structural failure.

The ultimate residual strength of the vessel at the damaged section is reduced as shown in Figure 13. In general, as the unstable propagation of the upper side shell crack arises, the ultimate residual strength in sagging starts to decrease followed by similar deterioration of the ultimate bending capacity in hogging, which starts the damage propagation on deck plates becomes unstable. The rapid deterioration of the longitudinal strength continues until the cracks on the decks above the damage sever the entire deck plates across the hull breadth. In both cases, the damaged cross section loses its residual bending capacity by 39% and 45% for hogging and sagging respectively in comparison to the intact condition. The vessel is regarded as lost at 223 and 117 hours when the strength deck is totally severed for Case 1 and 2 respectively. The loss of multiple decks induces further reduction of strength in sagging by lowering the instantaneous neutral axis of the damaged section. It should be noted that the limitation of the damage propagation to the starboard side shell prevents further reduction of the residual strength and flooding extension. Although taking the heeling angles into account during the ultimate residual strength analysis is desirable, the upright condition is used. This assumption is reasonable for this analysis as

rapid capsizes takes place in Case 1 after the initial damage and Case 2 after 131 hours, prior to which the heeling angle is small (2 degrees).

With respect to flooding, the basic difference between Case 1 and 2 is the location of the initial opening. In Case 1 the side tanks below the vehicle deck are considered, whereas in Case 2 the lower vertical boundary of the damage opening ($Z = 9.16$ m) is above the water line ($T = 6.25$ m). The stability curves for the RoPax ship at the intact and damage conditions are presented in Figure 14.

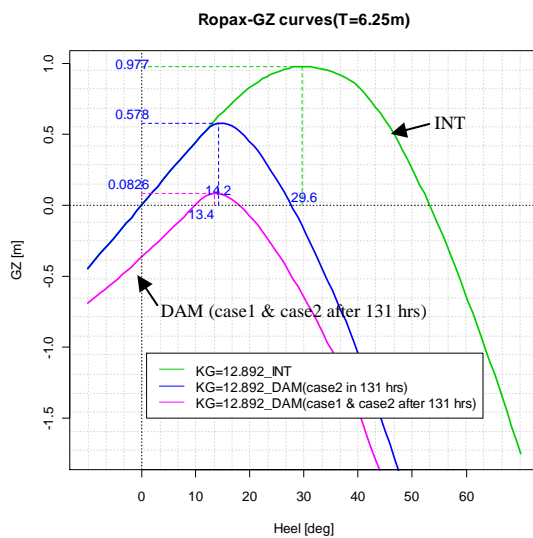


Figure 14: GZ curves for the RoPax ship.

According to the results of the damage propagation outlined in Table 4, it is assumed that the damaged RoPax has a fixed opening in Case 1 because crack propagations on the vehicle deck and the lower part of side shell are negligible. Contrary to this, an additional opening is required for Case 2 due to the breach of the vehicle deck at 131 hours after the initial damage. Transient flooding has been modelled for both cases.

The simulation results for Case 1 are presented in Table 5 (3-hour interval, $KG = 12.9$ m, $H_s = 2.0 \sim 4.0$ m, and 20 simulations per sea state). As expected the worst heading is the beam seas regardless of wave height. The $H_s = 2$ m is identified as the lower capsizes boundary, as no capsizes occurrence is observed below this threshold. Figure 15 shows an

example of a time series of the simulation with $H_s = 4.0$ m that results in capsizes after 4.6 minutes as the rolling angle exceeds 30 degrees.

Table 5: Numerical Simulation Matrix (Case 1).

H_s [m]	Heading [deg.]	No. of capsizes	No. of Runs	Probability of capsizes, P_{cap} ($t_{cap}=3hrs H_s$)
2.0	180	0	20	0
	270	0	20	0
2.5	180	0	20	0
	270	12	20	0.6
3.0	180	1	20	0.05
	270	20	20	1
3.5	180	17	20	0.85
	270	20	20	1
4.0	180	20	20	1
	270	20	20	1

The simulation results for Case 1 are illustrated in Figure 16, where the vulnerability to flooding against time is shown. In this case structural degradation is not of any concern for the survivability of the ship.

The results for Case 2 are presented in Table 6. This time only a small amount of floodwater accumulates on the vehicle deck in 131 hours' simulation even at $H_s = 4$ m in beam seas. The observed maximum list of the ship is close to 2 degrees (Step 1). Subsequently, further rectangular openings with a damage length of 4.8 m and the related heights, are added in order to reflect that the crack propagation reaches almost 1.0 m below the vehicle deck after 134 hours (Step 2) and 1.3m after 144 hours (Step 3), respectively.

The same range of wave heights as for Case 1 is applied for the survivability simulations. Based on the obtained capsizes probability, it appears that the ship's vulnerability in Case 2 is close to Case 1 from Step 2 onwards, where an enlargement of the flooding extent takes place.

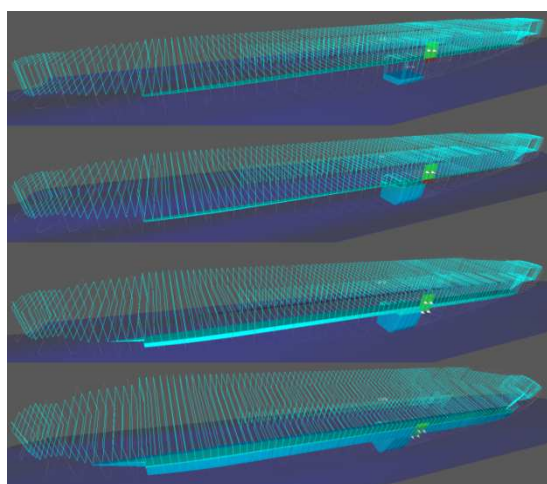
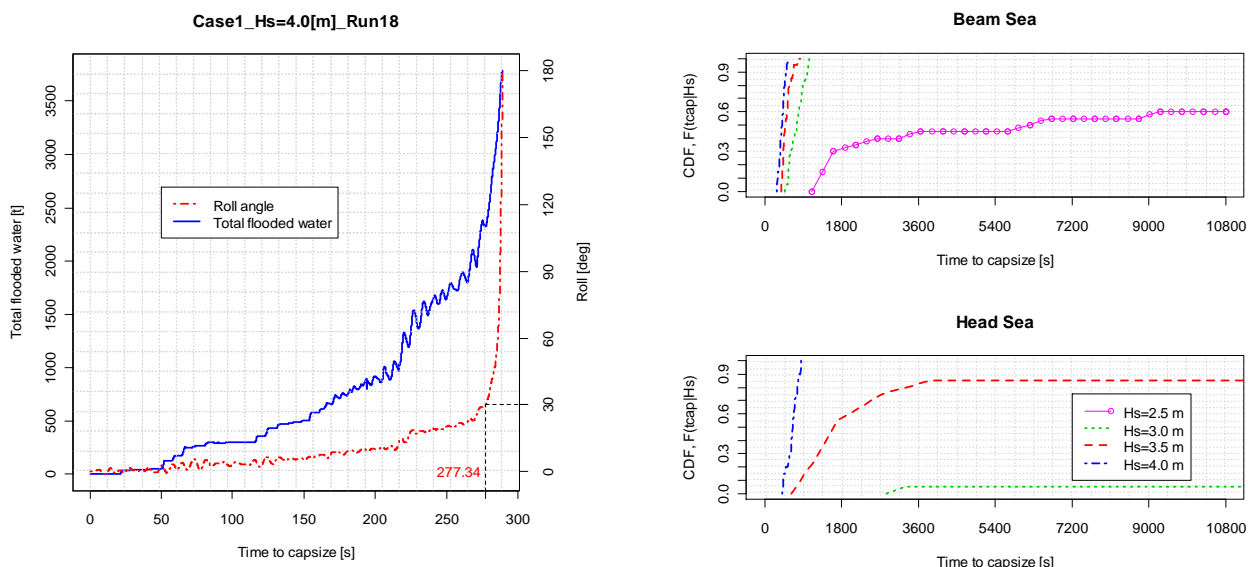


Figure 15: Time series of a typical capsize simulation in beam sea given $H_s = 4\text{m}$ (Case 1).

Table 6: Summary of results for beam seas (Case 2).

	Hs [m]	Simulation Time, [hrs]	Probability of capsize, $P_{\text{cap}}(\text{Time} H_s)$	Reduction of BM	
				BM _{hog}	BM _{sag}
Step1	2.0	131	0	38.9%	43.3%
	4.0				
Step2	2.0	134	0	38.9%	43.8%
	2.5		0.4		
	3.0		1		
	3.5				
4.0					
Step3	2.0	144	0	39.0%	44.1%
	2.5		0.9		

Figure 16: Cumulative probability distribution of time to capsize $F(t_{\text{cap}})$ given the specific loading, flooding extent, sea states, within the simulation time of 3 hours (Case 1).

4. CONCLUSIONS & FUTURE WORK

Based on the results of the two case studies of the developed methodology the following conclusions can be drawn:

- Survivability assessment following accidental damages is carried out in the *time domain* by taking into account the *coupling* of the progressive structural failure with the damage stability as well as the hull girder residual strength.

- For the tanker case, it is demonstrated that the degradation of the structural integrity becomes a priority over the stability deterioration due to the initial damage.

- On the other hand, the RoPax vessel is more susceptible to loss of stability, as it has been extensively documented in the literature. However, the geometry and location of the initial damage in combination with unfavourable environmental conditions can also threaten the structural capacity of the ship.



As discussed at the beginning of this paper, this methodology is still at its infancy, and the material presented here addresses only the main elements of it. Along these lines, the topics that will be addressed in the immediate future include:

- Investigating the effect of the various damage configurations (shapes, multiple openings) on the progressive structural failure analysis;
- Developing a platform that will embrace all the relevant tools (including analysis of systems availability) and will enable their consistent implementation in SRtP studies; and
- Coupling of structural FE models with CFD for flooding loading assessment.

5. REFERENCES

- ABS, 1995, "Guide for Assessing Hull Girder Residual Strength", American Bureau of Shipping.
- Bahamas Maritime Authority (BMA), 2004, "Report of the Investigation into the Loss of the Bahamian Registered Tanker 'Prestige' off the Northwest Coast of Spain on 19th November 2002", The Bahamas Maritime Authority.
- Dexter, R.J., Pilarski, P.J., 2000, "SSC-413: Effect of Welded Stiffeners on Fatigue Crack Growth Rate", Ship Structure Committee.
- Dexter, R.J. and Mahmoud, H.N., 2004, "SSC-435: Predicting Stable Fatigue Crack Propagation in Stiffened Panels", Ship Structure Committee.
- DNV, 2012, "Hull Structural Design, Ships with Length 100 metres and above", Rules for Classification of Ships, Part 3 Chapter 1, Det Norske Veritas.
- EC, 2003, "Directive 2003/25/EC of the European Parliament and of the Council on Specific Stability Requirements for Ro-Ro Passenger ships", European Commission.
- Farahmand, B., Saff, C., Xie, D. and Abdi, F., 2007, "Estimation of Fatigue and Fracture Allowables for Metallic Materials under Cyclic Loading", Proceedings of the 48th Conference of the American Institute of Aeronautics and Astronautics, AIAA-2007-2381.
- Gao, Z., Vassalos, D. and Gao, Q., 2010, "Numerical Simulation of Water Flooding into a Damaged Vessel's Compartment by the Volume of Fluid Method", Ocean Engineering, Vol. 37, pp. 1428-1442.
- IACS, 2008, "Common Structural Rules for Double Hull Oil Tankers", International Association of Classification Societies
- IMO, 2004, "Report of the Maritime Safety Committee on its Seventy-eighth Session", International Maritime Organization, MSC 78/26.
- Jasionowski, A., 2001, "An Integrated Approach to Damage Ship Survivability Assessment", PhD Thesis, University of Strathclyde, UK.
- Kwon, S., Vassalos, D., and Mermiris, G., 2010, "Understanding Potential Risk from a Coupled Problem of Flooding and Structural Degradation of a Damage Ship", Proceedings of the 4th International Maritime Conference on Design for Safety.
- Kwon, S., Vassalos, D. and Mermiris, G., 2011, "Progressive Structural Failure and Residual Strength of Damaged Ships", Proceedings of the International Conference on the Damaged Ship, The Royal Institution of Naval Architects, London, UK.
- McEvily, A.J. and Groeger, J., 1977, "On the Threshold for Fatigue-Crack Growth",



Proceedings of the 4th International Conference on Fracture, Vol. 2, pp. 1293-1298.

Smith, C.S., 1977, “Influence of Local Compression Failure on Ultimate Longitudinal Strength of a Ship’s Hull”, Proceedings of the International Symposium on Practical Design in Shipbuilding (PRADS), pp. 73-79.

Tada, H., Paris, P.C. and Irwin, G., 2000, “The Stress Analysis of Cracks Handbook”, Third Edition, ASME Press.

Vassalos, D., 2009, “Risk-Based Ship Design”, In: Papanikolaou, A. D. (ed.) Risk-Based Ship Design: Methods, Tools and Applications, Springer.

Xie, N., 2011, “A Numerical Prediction of Global Wave Loads for Intact and Damaged Ships”, Ship Stability Research Centre, Internal Report.



FLOODSTAND – Overview of Achievements

Risto Jalonen, *Aalto University*, risto.jalonen@aalto.fi,

Pekka Ruponen, *Napa Ltd*, pekka.ruponen@napa.fi,

Andrzej Jasionowski, *University of Strathclyde (SSRC)*, a.jasionowski@strath.ac.uk,

Pierre Maurier, *Bureau Veritas*, pierre.maurier@bureauveritas.com,

Markku Kajosaari, *STX Finland Oy*, markku.kajosaari@arctech.fi^{*},

Apostolos Papanikolaou, *National Technical University of Athens*, papa@deslab.ntua.gr

ABSTRACT

Project FLOODSTAND was targeted to develop and increase reliability of flooding simulations and assessments of passenger ship performance in safety-critical crises related to damage stability. Experimental tests and numerical studies, carried out in relation to the progress of flooding, are described. New approach to flooding simulation for onboard use has been developed. Some approaches to model the capsize as a stochastic process have also been studied, and uncertainties related to the “time-to-capsize” have been analysed. Mustering-Abandonment-Rescue process has been modelled using matrix-based obstacle model. Results of the project fill many gaps in previous knowledge related to flooding in passenger ships.

Keywords: *flooding, damage stability, leakage, collapse, capsize, time-to-flood, cross-flooding, evacuation, large passenger ship*

1. INTRODUCTION

FLOODSTAND, a collaborative 3-year EU-project coordinated by Aalto University (AALTO), was finished in February 2012. The project was focused on flooding in passenger cruise ships and ropax vessels. Emphasis has been put on topics like cross-flooding, leakage and collapse of non-watertight doors, effects of ship dynamics on flooding simulation, flooding progression modeling, sensitivity of the outcome of flooding on some selected parameters and flooding simulation and measurement onboard. Other main issues in the project are: time-to-capsize (ttc), uncertainty (related to the outcome of flooding) and rescue process modeling.

The project objectives and methodologies as well as the organizational structure applied were described in *Jalonen et al. (2010)*. Work

packages WP1-WP3¹ followed a deterministic, bottom-up approach, whereas in WP4-WP7¹ more stress was laid also on the probabilistic approach. The interplay between both outlooks, merged together in FLOODSTAND, turned out to be challenging, but important, too, in this research project. In the following, an extensive overview of the most important results and findings of the performed research is presented.

¹ Work Packages and WP-leaders of FLOODSTAND:
WP1: Design and application (STX Finland Oy);
WP2: Flooding Progression Modelling (AALTO)
WP3: Flooding Simulation and Measurement Onboard (NAPA)
WP4: Stochastic Ship Response Modeling (SSRC)
WP5: Rescue Process Modelling (BV)
WP6: Standard for Decision Making in Crises (SSRC)
WP7: Demonstration (NTUA)

* Present address: Arctech Helsinki Shipyard Oy, Helsinki, Finland



2. MODELLING OF FLOODING PROGRESSION (WP2)

2.1 Pressure Losses in Openings and Cross-Flooding Devices

One of the project objectives was to obtain new information on pressure losses in openings and cross-flooding ducts. For manholes the effective discharge coefficient in various flow conditions was evaluated both with full-scale experiments at Aalto University and CFD analyses by both CNRS² and CTO³.

The often applied discharge coefficient 0.6 was found to be a good approximation for the manhole in free flow conditions. The discharge coefficient of a full-scale manhole was mostly in the range between 0.58 and 0.59. In fully submerged flow, the discharge coefficients of the full-scale manhole were in the range between 0.67 and 0.70. The correspondence of CFD results and measurements was very good.

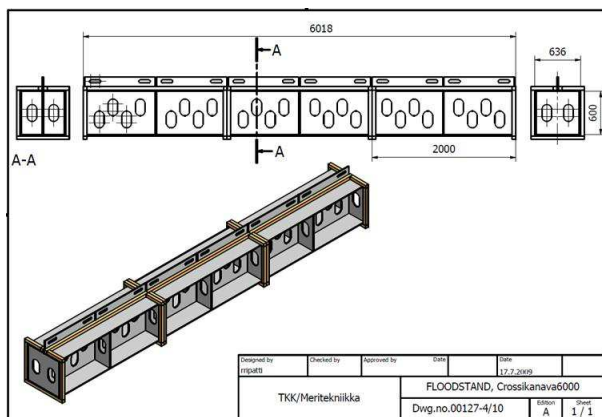


Figure 1: The 6 m long cross-flooding duct tested at Aalto University, Finland. Note! No stiffeners are marked here inside the duct.

Variations of a typical cross-flooding duct with two manholes in each girder were studied with large scale (1:3) model tests at Aalto University, Fig. 1. The test arrangement and the results are presented in *Stening et al.*

² In this project the “Centre National de la Recherche Scientifique” (CNRS) represented Lab Mecan Fluides, UMR 6598 CNRS, Ecole Centrale de Nantes (ECN).

³ CTO is the acronym for Centrum Techniki Okrętowej S.A. (Ship Design and Research Centre, in Poland).

(2011). Comparative CFD calculations were done both in model scale and in full-scale by CNRS. The scale-effects were shown to be minimal. Also the effect of inlet pressure height was found out to be very small.

Comparison to the current guidelines, *IMO Resolution MSC.245(83) (2007)*, showed that application of the suggested regression equations may result in significant underestimation (about 30%) of the pressure losses in the cross-duct.

In addition the pressure losses in two typical air pipe configurations were analysed with CFD tools at CTO. A summary of the research related to cross-flooding devices is presented in *Ruponen, et al. (2012a)*. The results have also been submitted to IMO for further consideration, *IMO SLF 54/4 (2011)*.

2.2 Effects of Non-Watertight Structures

Background for the research has been presented in *IMO SLF47/INF.6 (2004)*. The need to get better knowledge on leaking and collapsing of non-watertight structures has become more important as the time-domain flooding simulation tools have been taken into more frequent use.

A watertight tank to facilitate the tests with interchangeable structures under relevant water pressure and destructive loading was designed and built. It was fitted with a system for static water pressure adjustment and equipment for measurements and monitoring of the tested structure and for measurement of the leakage flow rate before the tested structure collapses.

Several different structures, such as both hinged and sliding fire doors, were tested, see Fig. 2. Many items were also tested to both directions. Comparative FEM analyses were also performed by MEC⁴, Fig. 3, to obtain further details on the failure mechanisms.

⁴ MEC is the acronym of MEC Insenerilahendus, a small Estonian engineering office concentrating on



Figure 2: Door tests in full scale at CTO's laboratory in Gdansk, Poland

Based on the test results, B-class structures do not significantly restrict flooding as the leakage was very significant even under small pressure heads. For A-class fire doors the critical collapsing pressure head ranged between 1.0 m and 2.5 m.

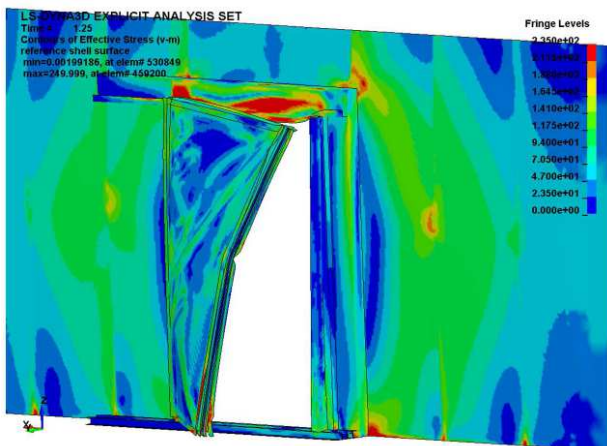


Figure 3: FEM analysis of the failure of a sliding fire door, MEC, Estonia

Based on the experimental and numerical research, guidelines for modelling leaking and collapsing structures in time-domain flooding analyses were developed. These have been presented in *IMO SLF54/INF.8/Rev.1 (2011)*.

2.3 Flooding Tests and Sensitivity Analysis

Dedicated mode tests on the detail level of modelling internal layout of the flooded compartments and the effects of air compression were studied by MARIN. Main outcomes and details of these tests are reported in *Ypma (2010)*. Furthermore, the sensitivity of flooding simulation results to the applied discharge coefficients and modelling of leaking and collapsing structures were studied, see *Karlberg et al. (2011)*.

3. FLOODING CONTROL AND DECISION SUPPORT (WP3)

3.1 Guidelines for Flooding Detection Sensors

For reliable flooding prediction the breach size and location need to be known. This is possible only if the ship is equipped with level sensors⁵. The flooding rates can be calculated based on the measurements, compartment geometry and floating position. And further the breach can be estimated based on the flow rates.

IMO has established some basic requirements for flooding detection systems on passenger ships, *IMO MSC.1/Circ.1291 (2008)*. A more comprehensive and detailed recommendation has been developed.

In summary the sensors should be placed so that the system can detect flooding before the stability of the ship is threatened. As parts of a decision support system, the sensors should detect flooding as early as possible. Moreover, the sensors should be placed so that the system is able to determine where the breach is located. In practice this means that normally each watertight compartment should have two level sensors in each watertight compartment on each deck below the bulkhead deck. The

advanced structural design and on (numerical) strength analysis.

⁵ Continuous measurement of floodwater level



complete guidelines are presented in the Deliverable D3.3, *Penttilä (2012)*.

Level sensors are necessary for obtaining the required data for flooding prediction onboard a damaged ship. On/off switches may only be installed to small spaces (i.e. sealed compartments in double bottom) from which the flooding cannot progress to other spaces. This is much more than current standards. Also level sensor and flooding detection system should be adjusted so that there are no false alarms. Periodical checks for level sensors are also recommended.

3.2 Breach Detection Based on Sensor Data

The first idea was to use an inverse method for prediction of the breach size and location on the basis of level sensor data and short simulations. This was described in *Penttilä and Ruponen (2010)*. The results were promising but the method was a little too time-consuming, especially when considering that the available input data is rather rough. Therefore, a simplified but faster method was developed. All rooms with detected flooding (soon after the accident) are considered to be breached. The breach location is in the outer shell, extending from the bottom of the room to the top of the room. If the room is not connected to the hull surface, a hole (connected to the sea) is modelled on the bottom of the room. The breach size (area) is determined from the flow rate on the basis of the measurement data. The accuracy of the fast method for estimating the breach opening is presented by Ruponen et al. (2012b).

3.3 Prediction of Progressive Flooding

When the hull of a ship is breached due to collision or grounding, the floodwater enters the damaged compartments. Open doors and various pipes may result in progressive flooding to undamaged compartments, thus making the situation even more critical. Also before the final floating position the ship may

pass through intermediate positions that are more dangerous than the final one. Thus for decision support it is necessary to check the whole process of progressive flooding. Within WP3 a completely new approach has been developed for prediction of progressive flooding. The details of the method are presented in *Ruponen et al. (2012b)*.

The developed method has been extensively tested against both experimental results from full-scale flooding of a decommissioned navy ship and dedicated simulations with the sample large cruise ship. This new approach is not time-accurate, but despite of this, the intermediate phases of flooding and time-to-flood are captured. As a part of demonstration work, the developed flooding prediction method was implemented into NAPA Loading Computer, Fig. 4. The flooding extent and the intermediate phases can be predicted in less than a minute for very extensive damage cases.

In addition, the effects of waves were studied by comparing fully quasi-stationary flooding simulation and combined approach with ship dynamics taken into account. The results have been presented in *Manderbacka et al. (2011)*.

4. TIME-TO-CAPSIZE (WP4)

A method for instantaneous classification of the severity of ship flooding casualty, was one of the issues covered. It was planned to be validated by a capsizing tests, with the model of a ropax (Estonia) at SSPA, Fig. 5, and numerical simulations conducted with the same ship by NTUA.

In both studies a two-compartment damage at aft bulkhead of the machinery room, aft amidships was selected as the damage case that included the vehicle space damaged and getting flooded. More details of the experimental and numerical studies with the selected ship can be found in *Rask (2011)* and in *Spanos & Papanikolaou (2011)*.

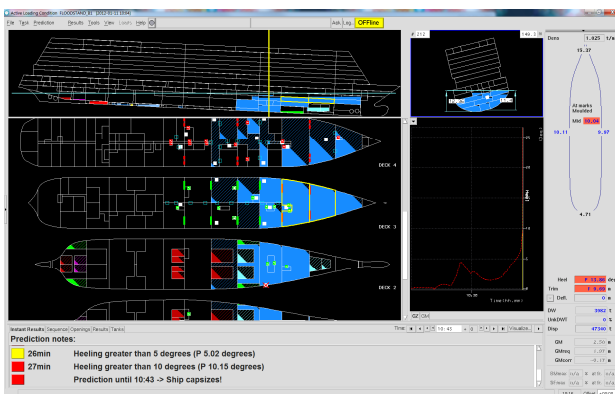


Figure 4: Flooding prediction tool for decision support, a schematic view on the user-interface with an example of a case, where open watertight doors (marked with red) lead to a rapid capsizes. (Note! This figure is in reduced scale of the full size of computer screen!)

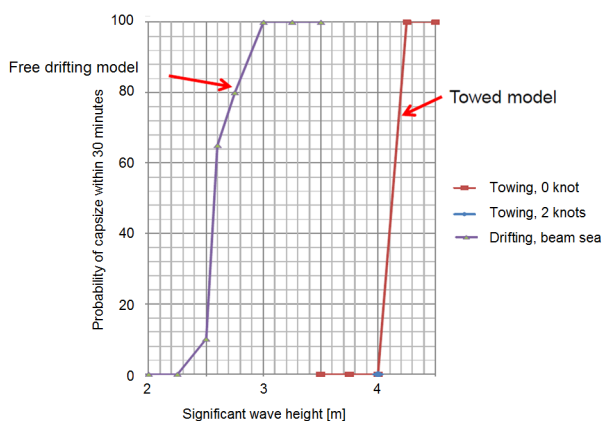


Figure 5: Probability of capsizing within 30 minutes vs. H_s . The change from 0% up to 100% occurred for the free drifting ropax model in beam seas between significant wave heights $H_s = 2.25\text{ m} - 3.0\text{ m}$. For the towed model in head sea it occurred at $H_s = 4.0\text{ m} - 4.25\text{ m}$. Results of the model tests at SSPA, Sweden, adopted from *Rask (2011)*.

The stochastic ship response modelling was developed on the basis of an analytical model and of a hybrid model as described by *Jasionowski (2012a, 2012b)*. Summaries of these reports include the following conclusions:

a) The case studies presented demonstrate that the extent of flooding, affecting parameters of

GZ_{max} ⁶ and Range⁷, seems to be one of the most critical information needed for confident assessment of criticality of flooding situation. The precision or lack thereof in estimating the extent of flooding experienced during crises seems to be an overriding uncertainty datum, on the basis of which the epistemic uncertainties of the modelling itself should be considered acceptable for engineering purposes of decision making during crises.

b) It was concluded based on a case study undertaken, involving nine hundred numerical simulations for three flooding cases and three sea state conditions, combined with statistical inference on heel angle development and further inference on projected time to capsize that *no enhancement of accuracy of prediction of the situation evolution can be attained through observing initially developing angles of heel*. This is to say, that development of angle of heel of up to about 8 to 10deg, (among the three study cases), does not influence probability that capsizes can occur over next say 30 minutes.

5. M-A-R MODEL (WP5)

Evacuating and abandoning a passenger ship implies a certain potential for hazardous situations, congestion issues, injuries and death of passengers. In order to assess the risk for passengers to abandon the ship this work package aims at studying the *Mustering, Abandonment and Rescue (M-A-R)* process.

5.1 Human Health Status

Health of passengers onboard the ship is modelled by a Human Health Status which is a continuous variable h , discretised into 4 states, Good Health, Minor Injuries, Severe Injuries and Deceased as described by *Nicholas et al (2010)*. The age of passengers is represented by

⁶ GZ_{max} : maximum positive righting lever (m)

⁷ Range: range of positive righting levers beyond the angle of equilibrium (degrees)



the variable a , discretised in 3 ranges, $[0; 50]$, $[50; 75]$, $]75, a_{\max}]$.

$f(h, a)$ is the probability density function providing the probability of having a passenger in health h for a given age a .

5.2 Obstacles

The M-A-R process is a sequence of actions to perform in order to evacuate safely the entire population onboard from the general emergency alarm signal to the shore. Several sequences as defined in the FLOODSTAND Deliverables D5.3, *Maurier et al (2011)*, and D5.4, *Maurier & Corrigan (2011)* depend on the means of escape (type of Life Saving Appliances, lifeboat or liferaft) and means of rescue.

For each potentially hazardous action an *obstacle* is defined that describes the probability of degradation of the human health status. The degradation of health associated to the obstacle k , D_k is defined as:

$$f_k(h, a) = D_k[f_{k-1}(h, a)]$$

D_k can be simplified after discretisation in three triangular matrices, one for each age range. Each Matrix can be found in the referenced FLOODSTAND Deliverables above.

5.3 Results

Fatality rate has been studied for several scenarios on two reference ships. Detailed results can be found in *Hifi (2012)*.

The Sea State is the main parameter influencing the fatality rate (see Figure 6). In severe sea states, the manoeuvrability performance of LSAs to clear off the vessel is predominant.

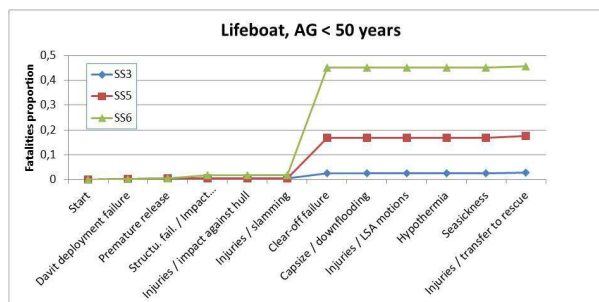


Figure 6: Influence of sea state

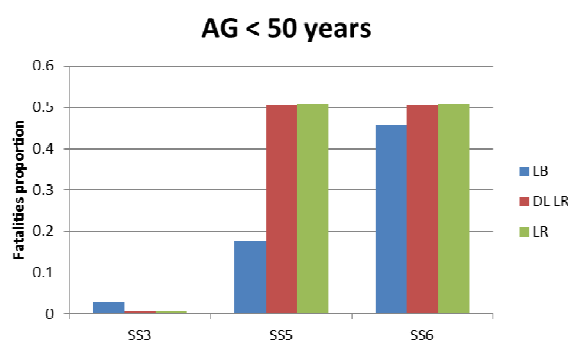


Figure 7: Comparison between LSAs (LB: Davit-launched Lifeboat, DL LR: Davit-Launched Liferaft, LR: Ladder boarded Liferaft)

6. DECISION MAKING (WP6)

The VulnerabilityLog, or VLog for short, is presented in *Jasionowski (2011)* as a functionality to inform the crew at all times on the instantaneous vulnerability to flooding of the vessel, considering its actual loading conditions, the environmental conditions and the actual watertight integrity architecture. The vulnerability is proposed to be measured in terms of the probability that a vessel might capsize within given time when subject to any feasible flooding scenario.

Models for loss function and likelihood functions have been developed and proposed, and an integrated format of decision making process addressing ship's residual stability, the abandonment and the rescue operations, as well as dominant inherent uncertainties have been proposed, see *Jasionowski (2012a, b)* and *Hifi (2012)*, as follows:

Step 1 - Order mustering and follow with situation assessment at the first sign of distress

Step 2 - If flooding extent not determinable or escalating then abandon

Step 3 - Else if $[\min(0,125 \cdot H_s, 1) \cdot F_{cap}(3hrs | H_s)]$
then abandon

Step 4 - Else stay onboard.

Note! In Step 3 above, the order to abandon the ship is tightly coupled to the significant wave height (H_s) and to the applied models of:

- expected losses in case of abandonment: $\min(0,125 \cdot H_s, 1)$

and

- expected losses in case of capsizing in 3 hours: $F_{cap}(3 \text{ hrs} | H_s)$

On the basis of a decision expected to lead to least expected casualties, Step 3, as given in *Jasionowski (2012c)*, simply suggests to abandon, if the latter value is higher.

Some fundamental uncertainties, described in the reports above concerning the various stochastic capsizing models, related to the assessment of the extent of flooding, do not seem resolvable at present according to *Jasionowski (2012c)*. Therefore, and given considerable level of typical ship vulnerability to flooding with possible rapid capsizing, it is recommended in the above process that the order to muster is an automatic and immediate crew reaction to first report or a sign that distress occurs. During the mustering time all efforts to assess the extent of flooding must be made, and in case doubts remain as to the scenario, or in case the flooding is escalating, an order to abandon should be given.

In case flooding situation is well established, a quantitative criterion is given to make judgement on the risk balance between decisions of abandonment and staying onboard. Naturally, the above process is susceptible to subjective interpretations as to what constitutes “doubt” or “well established” situation awareness, and these are proposed to remain discretionary judgements of the crew.

Technologies (better sensors, their denser distribution and good maintenance) and procedures for monitoring of all of ship spaces

should be, and have been, developed, so that this fundamental uncertainty can be resolved. However the proposed procedure above would seem competent and generic independent of the state of technology, see *Jasionowski (2012c)*.

The process highlights the important decision making elements, which when used in training may allow the crew to better understand importance of their preparedness for handling crises.

Assessment of the likelihood function is proposed to be adopted for any type and size of the vessel by *Jasionowski (2011)*, even though its key validation was performed for RoPax type ships only, as the formulation is based on generic parameters of residual stability, as well as generic assumptions on the impact of the process of floodwater progression (“GZ cut-off at down-flooding points”), with the latter mitigating the mentioned expected uncertainties of situation assessment.

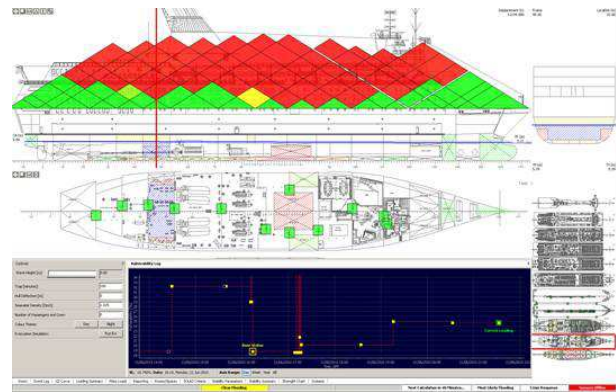


Figure 8: A schematic example of the view on computer screen with a sample information of the functionality VLog as shown by *Jasionowski (2012c)*.

Vulnerability due to open WT doors (between watertight compartments) was shown to be an important issue, to be clearly demonstrated for the crew members. The importance of the subdivision on the damage stability of the ship should be obvious to everyone involved. Floodwater that is allowed to progress freely, via an open WT door, from one compartment



to another may in some cases tip over the whole ship. The actions of the crew may have a big impact on the ship's vulnerability and operational risk related to flooding cases. Any functionality and training that can be used to raise the awareness of the crew about flooding risk, and the right actions to minimize the risk can have a notable impact on crew actions. Improvements in crew awareness and in support for decision-making, and training, can be used to promote a safety culture, where the aim is laid on a (continuous) improvement.

7. EFFECTS ON SHIP DESIGN (WP1&7)

Near the end of the project a comprehensive analysis of the obtained results and their effects and applications in the modern cruise ship design was carried out, Routi et al. (2012).

The results of the analysis did not reveal any major observations having significant influence on the general design of cruise vessels, but many of the assumption defined in the SOLAS explanatory notes could be confirmed.

The main focus was laid on the sustainability of non-watertight structures and how this may be used to enhance safety and to consider the physical behavior of the design. Here are the fire doors the main equipment, which – according to the current requirements – are regarded as non-watertight boundaries seriously restricting the flooding. According to the test results typical A-class fire doors are capable of withstanding a water pressure of app. 2.5 m before collapsing. The expected pressure head varies remarkably on different decks which subject to flooding. Based on this feature fire doors should be considered either as collapsing structures or an impermeable boundary, depending on the location. This effect can be used for restricting (or retarding) progressive flooding on the bulkhead deck, but on the tank top level the flooding through fire doors will take place in practice instantaneously.

Cold rooms and dry stores are currently subject to compliance with the same requirements to watertight integrity as fire doors. Considering both the typical location and construction of such rooms and the practice to keep the rooms normally closed, it is reasonable to assume that it may take a considerable time to flood these rooms.

Another important item is the effect of air pressure for cross flooding calculations. Here the obtained results provide the designer a more accurate method to consider and predict the effect of air pressure for the flooding scenario rather than using the 10% rule as proposed in the explanatory notes at the moment. The design of the tank and void spaces arrangement with air ducts and cross flooding ducts can be made in a more flexible way and the available space can be used more effectively.

Although the results do not lead us to the global design changes, some important details for the designer are explored and will influence the designs of cruise ships in the future. In addition, the findings of this project provide more precise input data for time-domain flooding simulations and thus improve the accuracy of the calculations and promote the acceptance of such calculations by the flag administrations.

The design changes can, however, only be applied, if the regulatory bodies consider the results of this project while developing new requirements for subdivision and stability within SOLAS. Some important details should be incorporated in SOLAS and the explanatory notes:

- flooding sequence through fire doors
- instantaneous flooding on tank top through fire doors
- restriction of flooding on bulkhead deck through fire doors
- new formulation for cross-flooding through ducts with restrictive effect of air pressure
- restriction of flooding in cold room area



The lay-out of spaces and the use of watertight doors in daily operation have an important influence on the vulnerability of a modern cruise ship. This may be affected by taking into account the operational needs at an early design stage. It has been shown, that the design of cruise ships can easily consider the operational needs, so that watertight doors are only used as secondary means of escape and need not to be opened during the daily service. These design changes may, however, require solutions and arrangements which lead to a lesser attained index and imply corresponding counter measures to comply with the rules, thus increasing the investment and life-cycle costs of the ships.

The analysis conducted and the experience collected in WP4-6 demonstrate that the loss, which is related to a damage with an extent of significance large enough to allow the progression of flooding in a quantity leading to the capsize of the ship, is a fast process. Thus, as addressed by *Spanos & Papanikolaou (2011, 2012)*, it is an urgent situation for the people onboard to timely evacuate the ship, maybe much more urgent compared to what may have been assumed before. If the time available for the mustering and abandonment of a passenger ship, in the rare severe damage cases that may cause an urgent need for it due to rapid capsize, is less than 30 minutes, as it was in many of the simulated cases, the sufficiency of the existing safety level, with all its components, seem to require careful reappraisal and improvements. An option for a reasonable strategic objective for the passenger ship design may be formulated out of this research, namely to establish even higher survivability requirements (sub-division required indices), so that the 'non-survival' cases could be limited to a minimum, and/or to pursue, where possible, even faster evacuation and abandonment procedure.

The question of reducing the vulnerability due to open watertight doors in operation depends strongly on the SOLAS requirements. Only if the regulatory bodies agree on clear

design requirements, future ship designs will be improved without economical disadvantages for the operators or shipbuilders.

8. CONCLUSIONS

The output of this research project is notable. It is considered to fill many gaps of information and lack of data to enhance more reliable flooding simulations. The results can be used for assessments of damage stability carried out due to various design purposes and, additionally, in onboard applications. They offer good prospects to improve timely support for designers and operators of passenger ships.

The work of project FLOODSTAND can be assumed to be valuable for the development of safety regulations concerning passenger ships, too. Most of the results can be further refined and will be submitted to the IMO SLF meetings, as already done in some cases. This work need to be done together with the member states.

Many of the results and general conclusions are related to intermediate stage flooding and progressive flooding. This information is presumed to be helpful in the work underway to refine the current intermediate stage flooding guidance. The flooding detection systems for passenger ships has been addressed, too. Information and results from the relevant part of the work could be used to update guidance for sensors and their arrangements, locations, types, etc.

The work in this research project has been carried out concentrating mainly on purely technical issues, therefore often focused on issues being more or less straightforward to be solved. However, the multitude of various interactions between the applied technology, human operators and the environment, should never be totally forgotten. It is assumed and hoped that the achievements and results obtained in project FLOODSTAND will foster better understanding and capabilities to cope



with a number of important parts within this huge framework and, especially, in relation to the development of the safety of passenger ships.

9. ACKNOWLEDGEMENT

The research leading to these results has received funding from the European Community's Seventh Framework Program (FP7/2007–2013) under grant agreement no. 218532 (project FLOODSTAND). The financial support is gratefully appreciated.

Although the opinions professed in this paper represent those of the individual authors, the team of which was selected from each WP leader organisation of FLOODSTAND, the paper strives to objectively describe the whole collaborative project.

Acknowledgement is naturally given to all members of the project Consortium and to all members of the Advisory Committee, too.

10. REFERENCES

Note! All the reports (deliverables) of this EU-funded project that are listed below are publicly available via the project webpage at http://floodstand.aalto.fi/Info/public_download.html.

IMO SLF47/INF.6 2004. Large Passenger Ship Safety: Survivability Investigation of Large Passenger Ships, submitted by Finland, 11. June 2004.

IMO Resolution MSC.245(83), 2007. Recommendation on a Standard Method for Evaluating Cross-Flooding Arrangements.

IMO MSC.1/Circ.1291 2008. Guidelines for Flooding Detection Systems on Passenger Ships, 8 December 2008.

IMO SLF54/INF.8/Rev.1 2011. Modelling of

leaking and collapsing of closed non-watertight doors, submitted by Finland, 28 October 2011.

IMO SLF54/4 2011. An analysis of the recommendation on a standard method for evaluation of cross-flooding arrangements as presented in resolution MSC.245(83), submitted by Finland, 14 October, 2011.

Hifi, Y. 2012 Report on the method for assigning of uncertainty bounds for methods for M-A-R assessment, FLOODSTAND Deliverable D5.5.

Jakubowski, P., Bieniek, N. (2010). Experiments with leaking and collapsing structures, FLOODSTAND Deliverable D2.1b.

Jalonen, R., Jasionowski, A., Ruponen, P., Mery, N., Papanikolaou, A., Routi, A-L. 2010. FLOODSTAND – Integrated Flooding Control and Standard for Stability and Crises Management, Proceedings of the 11th International Ship Stability Workshop, Wageningen, The Netherlands 21-23.6. 2010, pp. 159-165.

Jasionowski, A. 2011. Decision support for ship flooding crisis management, Ocean Engineering, Vol. 38, pp. 1568-1581.

Jasionowski, A. 2012a. Analytical model of stability deterioration process, FLOODSTAND Deliverable D4.2.

Jasionowski, A. 2012b. Hybrid model of stability deterioration process, FLOODSTAND Deliverable D4.4.

Jasionowski, A. 2012c. Standard for decision making in crises – loss and likelihood functions, FLOODSTAND Deliverable D6.2.

Karlberg, D., Jalonen, R., Ruponen, P. 2011. Sensitivity Analysis for the Input Data in flooding Simulation, FLOODSTAND Deliverable D2.6.

Manderbacka, T., Matusiak, J., Ruponen, P.



2011. Ship Motions Caused by Time-Varying Extra Mass on Board, Proceedings of the 12th International Ship Stability Workshop, Washington D.C., U.S.A. 12-15.6.2011, pp. 263-269.

Maurier, P., Hifi, Y., Corrigan, P. 2011. Report on validation and sensitivity testing of methods for assessing effectiveness of abandonment process, FLOODSTAND Deliverable 5.3.

Maurier, P., Corrigan, P. 2011. Report on validation and sensitivity testing of methods for assessing effectiveness of rescue process, FLOODSTAND Deliverable 5.4.

Nicholas, C., Mery, N., Hifi, Y. 2010. Benchmark data: Introduction to the Mustering, Abandonment and Rescue models”, FLOODSTAND Deliverable D5.1.

Penttilä, P., Ruponen, P. 2010. Use of Level Sensors in Breach Estimation for Damaged Ship, Proceedings of the 5th International Conference on Collision and Grounding of Ships ICCGS 2010, Espoo, Finland 14-16.6.2010, pp. 80-87.

Penttilä, P. 2012. Design Guidelines for Placement and Technical Requirements of Flooding Sensors in Passenger Ships, FLOODSTAND Deliverable D3.3.

Rask, I. 2011. Report on physical model experiments with ship model, FLOODSTAND Deliverable D4.1.

Routi, A.-L., Luhmann, H., Manderback, T., Seglem, I. 2012. Analysis and Applicability of Alternative Designs, FLOODSTAND Deliverable D1.2.

Ruponen, P., Routi, A.-L. 2011. Guidelines and criteria on leakage occurrence modeling, FLOODSTAND Deliverable D1.2.

Ruponen, P., Queutey, P., Kraskowski, M., Jalonen, R., Guilmineau, E. 2012a. On the calculation of cross-flooding time. Ocean

Engineering Vol. 40, 27-39

Ruponen, P., Larmela, M., Pennanen, P. 2012b. Flooding Prediction Onboard a Damaged Ship, accepted to STAB2012.

Spanos, D., Papanikolaou, A. 2011. On the time dependence of survivability of ROPAX ships, Journal of Marine Science and Technology, Published online, DOI: 10.1007/s00773-011-0143-0

Spanos, D., Papanikolaou, A. 2012. Report on the applicability of the standard for design practice, FLOODSTAND Deliverable D7.3.

Stening, M., Järvelä, J., Ruponen, P., Jalonen, R. 2011. Determination of discharge coefficients for a cross-flooding duct. Ocean Engineering Vol. 38, 570-578.

Ypma, E. 2010. Model tests in atmospheric and vacuum conditions, FLOODSTAND Deliverable D2.5b.





Multi-objective Optimization of ROPAX Ships Considering the SOLAS 2009 and GOALDS Damage Stability Formulations

George Zaraphonitis, *National Technical University of Athens* (NTUA), zar@deslab.ntua.gr

Sotiris Skoupas, *Lloyd's Register* (LR), sotiris.skoupas@lr.org

Apostolos Papanikolaou, *National Technical University of Athens* (NTUA), papa@deslab.ntua.gr

Mike Cardinale, *Fincantieri Cantieri Navali Italiani S.p.A.* (FC), Mike.Cardinale@fincantieri.it

ABSTRACT

The SOLAS 2009 probabilistic damaged stability regulation, which entered into force on January 1st, 2009 and applies to all dry cargo and passenger ship newbuildings, represents a major step towards the rationalization of the assessment of ship's survivability in damaged condition. There are, however, serious concerns regarding the same provisions for passenger ships of this new regulation, necessitating an in-depth review of the adopted formulation. The EU-funded research project GOALDS was launched in September 2009 with the aim to derive a new, risk-based formulation for the assessment of damaged stability of passenger ships. The investigation of the impact of the new formulation on the design and operational characteristics of ROPAX vessels is the main objective of this paper.

Keywords: *damaged stability, optimization, ROPAX ship*

1. INTRODUCTION

The safety of ships against sinking/capsize in case of loss of their watertight integrity is of prime interest to the international and national maritime regulatory bodies, the maritime industry the scientific community and to the entire society. The new probabilistic damaged stability regulation for dry cargo and passenger ships (SOLAS 2009), represents a major step towards the rationalization of the procedure for the assessment of ship's survivability in damaged condition. There are, however, serious concerns regarding certain aspects of this regulation, and in particular its impact on the level of safety of large passenger ships, necessitating an in-depth review of the adopted formulation. Great concerns were expressed by EU member states and the European Maritime

Safety Agency (EMSA) regarding the abolishment of the Stockholm Agreement provisions for ROPAX ships, when the new SOLAS 2009 entered in to force; in fact, there was strong evidence that SOLAS 2009 does not satisfactorily cover Water On Deck effects on ROPAX survivability (e.g., HSVA, 2009).

The EU-funded research project GOALDS (Goal Based Damage Stability) was launched in 2009 with the aim to address the open questions and to derive a new formulation for passenger ships based on updated accident statistics and state of the art scientific tools. As a result, a new formulation for the assessment of ship's survivability in damaged condition was developed. Validation studies demonstrated improved correlation of the proposed formulation with numerical



simulations as well as with an enhanced sample of experimental data, in comparison with the SOLAS 2009 regulation.

The investigation of the impact of the new damaged stability formulation on the design and operational characteristics of ROPAX vessels is the main objective of the present paper. A typical ROPAX design has been selected and redesigned. An integrated design optimization procedure, developed by the Ship Design Laboratory of NTUA with the collaboration of LR and FC, encompassing the parametric design and optimization of ROPAX vessels was adapted to the new formulation and applied for the optimization of the selected vessel for enhanced survivability, considering also building cost and efficiency in operation. Obtained results are presented and discussed.

2. DEVELOPMENT OF DAMAGED STABILITY FORMULATION

2.1 Damage Statistics

Among the main objectives of the GOALDS project was to develop updated collision damage statistics including as far as possible latest accident data, and to provide suitable probability distributions for damage characteristics pertinent to passenger ships. To this end, the existing HARDER database was updated with additional data coming from the project participants, as well as from other publicly available accident databases. Whereas previous damage statistics were limited to collision damages only, in the present project grounding damages were also considered. A total of 1587 casualties (collisions, groundings and contacts) were recorded in the updated database (349 GOALDS, 1238 HARDER). The analysis of the updated data in the GOALDS database did not lead to significant changes in the resulting probabilistic distributions for the collision damages, as laid down in SOLAS 2009. Results from the statistical analysis of data from collision and grounding damages are presented by Papanikolaou et al. (2011).

2.2 The s-factor

Deriving from the original HARDER project and the outcome of the EMSA studies EMSA/OP/08/2009 it has been decided to base the GOALDS s-factor formulation on the concept of critical significant wave height, H_{Scrit} . The analysis of available data indicated that existing formulations for the calculation of H_{Scrit} are insufficient to fully capture relations between sea-state and the damaged ship properties. Relevant studies within the GOALDS project showed that the following formula can be used to estimate the H_{Scrit} with satisfactory accuracy (Cichowicz et al., 2011):

$$H_{Scrit} = \frac{A_{GZ}}{\frac{1}{2} GM_f \cdot Range} V_R^{1/3} \quad (1)$$

where:

- A_{GZ} area under residual GZ curve up to the flooding angle [rad·m]
- GM_f metacentric height of flooded ship [m]
- V_R residual volume – volume of subdivided spaces not opened to sea [m³]
- $Range$ range of positive stability up to the flooding angle [rad]

The development of the formulation for the calculation of the critical significant wave height in damaged condition was supported by extensive numerical simulations along with experimental data, already available from previous studies, as well as from tank tests performed in the framework of the GOALDS project. Tank tests have been carried out by HSVA for two ROPAX ships and by Vienna Model Basin for two cruise ships. The ships have been tested for collision as well as for grounding damages. A brief description of the tank tests and of the obtained conclusions is presented by Papanikolaou et al. (2012).

The probability of surviving of a damaged ship is evaluated by mapping the H_{Scrit} by the IMO distribution of sea-states encountered during collision incidents:



$$s = \int_0^{H_{Scrit}} dH_s \cdot f_{H_s|coll}(H_s) = \exp(-\exp(0.16 - 1.2H_{Scrit})) \quad (2)$$

2.3 Risk-based Damage Stability Requirement

One of the main objectives of the GOALDS project was the development of a standard risk model for collision and grounding damages to passenger ships. The risk model consists of a collision/grounding frequency model, flooding frequency model, survivability model and a consequence model.

The collision/grounding frequency model is derived from accidents statistics. Accident data were deduced from IHS Fairplay Casualty database, LMIU and GISIS. Only collisions and groundings with 'serious' consequences were included in the study. Different flooding frequencies (i.e. the probability of water ingress) have been derived depending on the area of operation (en route, in limited waters or at terminal). The estimation of the damage extent in case of collisions is based on the SOLAS 2009 regulation. For grounding accidents, the damage extent estimation is based on probability distributions developed in GOALDS. The probability of capsizing or sinking is reflected through the attained index A .

Two different models have been applied for the calculation of consequents (i.e. fatalities in case of ship capsizing or sinking). Risk model A is based on an assumed fatality rate of 100% in case of capsizing/sinking. According to risk model B , the expected fatality rates are determined according to a more refined consideration of the accident scenario, namely considering the proximity to the shore and sinking velocity. For ROPAX ships it is assumed that the probability of slow/fast sinking is 50/50, while for passenger/cruise ships the corresponding distribution is 82/18. Fatality rates are assumed equal to 80% in case of fast sinking and 5% for the slow sinking

scenario. The above assumptions are still on the safe side, compared to historical data of relevant accident types.

The developed collision and grounding risk models have been applied to four sample ships; a medium ROPAX, a large ROPAX, a medium Cruise ship and a large Cruise ship. For each sample ship, Risk Control Options (RCO), i.e. design modifications intended to improve the survivability are proposed and evaluated. The proposed design modifications include increased breadth, increased freeboard, increased level of subdivision etc. By use of the generic risk model the improvement is quantified as a reduction of the Potential Loss of Lives (PLL) and Potential Loss of Ship (PLS). For the assessment of the ship's survivability the attained index A has been calculated using the GOALDS s -factor as well as by the current SOLAS 2009 formulation. The risk models developed in GOALDS have been used to assess the cost and benefits of several Risk Control Options (RCOs) for each sample ship. Based on the attained A indices for those RCOs found to be cost effective, a new level of the required index R has been proposed for discussion, expressed as a function of the number of Persons On Board (POB):

$$R_{GOALDS} = 1 - \frac{2300}{5POB + 20000} \quad (3)$$

The finalization of the GOALDS proposal for the new R index of passenger ships is still pending full validation for a larger range of sample ships and concluding discussions.

3. OPTIMIZATION OF A ROPAX SHIP

To investigate the impact of the GOALDS formulation on the design and operational characteristics of ROPAX and Cruise ships, a series of sample ships has been selected to be re-designed for enhanced survivability, considering also building cost, efficiency in operation and lifecycle cost, in addition to



safety. In the following, the results from the optimization of the design of a medium size ROPAX ship will be presented and discussed.

3.1 The original design

The selected vessel is a typical ROPAX ship, designed by FINCANTIERI Cantieri Navali Italiani S.p.A. for short international voyages. The vessel is twin screw with bulbous bow and an aft skeg. The General Arrangement Layout enables fast loading/unloading of passengers and vehicles, with good simultaneous flow of cargo, stores and necessary services. It is fitted with three trailer decks: a main and an upper trailer deck and a lower garage below the main deck. A hoistable car deck is arranged on the upper car deck; the aft panel is used as ramp. The vessel is fitted with side hinged bow doors and bow ramp and also fitted with two combined stern ramps. Access to the upper deck is arranged from the main deck via a tiltable ramp and to the lower garage deck via a fixed ramp with ramp cover. Deck 3 (main deck) is designated as the freeboard deck and it is considered to be watertight. The vessel is fitted with four diesel engines. Each set of two engines is coupled to one gear box with clutch couplings integrated in the gear for engaging/disengaging of the engines, connected to shaft line and propeller.

The vessel complies with the requirements of the SOLAS consolidated edition 2009 (all rules in force for keel laying at 31/12/2009), as well as with MARPOL 73/78 as amended (including addition to regulation 12A) and with the International Load Line Convention 1966 and following amendments. The ship is divided in 17 watertight zones, by 16 main transversal bulkheads. The lower hold extends from zone 8 to zone 13. Weathertight doors capable to sustain a head of 2.5m are fitted on the main deck (deck 3) providing access between the side casings and the garage space. The general arrangement of the original design up to deck 4 is presented in Figure 1, while its main characteristics are summarized in Table 1.

Table 1. Main Particulars of original vessel

Length OA	abt. 183m
Length BP	162.85 m
Subdivision length	182 m
Breadth	27.6 m
Subdivision draught	7.10 m
Height of bulkhead deck	9.80 m
Number of passengers	2080
Number of crew	120
Gross tonnage	abt. 36000
Deadweight	5000 t
Number of cabins	180
Lane meters	1950m
SOLAS required index	0.79804
A index (SOLAS/GOALDS)	0.8226/0.8267

3.2 Development of Parametric Model

A set of macros has been developed in *NAPA Basic* programming language, to facilitate the creation of a fully parametric model of the original design within the CASD software *NAPA*, based on a series of design variables. In total 32 design variables have been used to fully describe the model. They include the reference dimensions (length, beam and draught) along with 13 variables defying the deck heights and 16 variables defying the position of the watertight transverse bulkheads. The creation of the parametric model and the evaluation of the corresponding design consist of a series of major tasks:

1. Clear the *NAPA* database
2. Read variables
3. Create the hullform
4. Define the internal arrangement
5. Evaluate geometric constraints
6. Define openings and cross-connections
7. Calculate lanes length

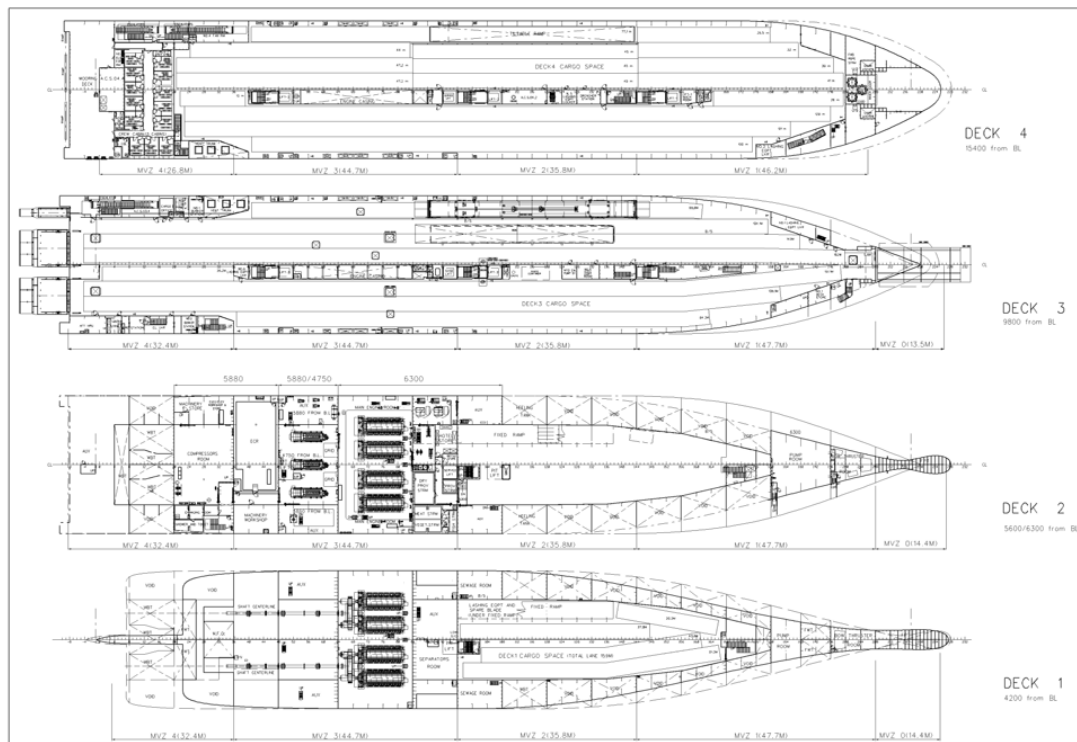


Figure 1: General Arrangement of original design

8. Define loading conditions
9. Calculate intact stability
10. Estimate resistance & propulsion power
11. Calculate A_S according to SOLAS 2009
12. Calculate A_G according to GOALDS
13. Calculate economic indicators
14. Print output files

The new hull is derived by a linear transformation of the original hullform. More complex transformations are also possible (e.g. piecewise linear transformations, or Lackenby transformations, allowing variations of the block coefficient and/or *LCB*), but they were not used in the present study. A detailed model of the internal arrangement up to deck 4, closely resembling the arrangement of the original design is created. The complete set of openings, cross connections and A-class bulkheads is also modelled to enable the accurate calculation of the attained index. A procedure developed by the shipyard, based on the analysis of available data, is applied for the

estimation of the resulting variations of lightship weight and weight centroid. The trailers carrying capacity in terms of lanes length is calculated, while the size of the superstructure and the number of passengers are assumed constant. The impact on building cost is estimated using unit costs and standard rates that have been proposed by the shipyards participating in the GOALDS project. All the loading conditions are subsequently redefined and compliance with intact stability requirements is assessed. The resistance and propulsion characteristics of each new design are estimated using the Holtrop 84 method (Holtrop, 1984). The resistance and propulsion data of the original design are used to calibrate the Holtrop results.

Finally, the attained subdivision indices according to SOLAS 2009 and the GOALDS proposal are calculated. The calculation of the GOALDS attained subdivision index is performed by a set of NAPA macros developed by Det Norske Veritas (Ribbe, 2012). The impact on risk associated with each design alternative is expressed in terms of the Potential Loss of Life (*PLL*). The calculation of



PLL is based on the following estimations, developed in GOALDS from the risk analysis of ROPAX ships accidents:

- Collision frequency: 7.778×10^{-3} (ROPAX ships larger than 1,000GT).
- Probability ship being struck: 0.689655.
- Area of operation at the time of the accident: en route (4%), in limited waters (23%), at the terminal (73%).
- Probability of water ingress: equal to 0.423077, while the ship is en route or in limited waters and equal to 0.117647 when the ship is at the terminal.
- Probability of capsizing/sinking: 1-A
- Probability of slow/fast sinking: 0.5/0.5.
- Fatalities in case of slow sinking: 5%
- Fatalities in case of fast sinking: 80%

In the analysis of consequences, the number of persons on board was estimated using an average annual utilization rate of 75% based on data from operators of ROPAX ships in European waters.

Finally the Gross and Net Cost of Averting a Fatality (*GCAF* and *NCAF*) are derived following IMO FSA guidelines (MSC 83/INF.2, 2007):

$$GCAF = \frac{\Delta C}{\Delta R} \quad (4)$$

$$NCAF = \frac{(\Delta C - \Delta B)}{\Delta R} \quad (5)$$

where ΔC and ΔB are the cost and the economic benefit variations per ship resulting from the implementation of the risk control option during the lifetime of the vessel and ΔR is the corresponding risk reduction, expressed by the reduction of the Potential Loss of Life ($\Delta R = \Delta PLL$).

3.3 Integration with Optimization Software

The developed parametric design software has been linked to a multi-objective optimisation software (i.e. modeFRONTIER) to form an integrated design and optimization environment. The method of Genetic Algorithms was selected as the most suitable optimisation method for the specific problem, in view of its inherent capability to deal with multi-objective optimisation problems with mixed continuous-discrete variables as well as with discontinuous and non-convex design spaces.

From the complete set of the design variables used for the definition of the parametric model, only ten were varied during the presented study; i.e. the variables corresponding to the ship's reference length, beam and draught and those defining the double bottom and the deck heights up to deck 4. More specifically, length was varied from 157m to 167m, beam from 27.5 to 28.2 and draught from 6.8 to 7.2. The relatively narrow range of beam variation was selected in order to avoid excessive *GM* values in the operational range of loading conditions.

Two objective functions were herein used: the minimization of the Potential Loss of Life (*PLL*) and the minimization of Gross Economic Impact resulting from an increase of construction and operational costs during a life time of 30 years. The calculation of *PLL* was based on the SOLAS 2009 and GOALDS subdivision indices. However, only the *PLL* value derived from the GOALDS subdivision index was used as an objective function.

The following constraints were introduced to distinguish the feasible from the unfeasible designs:

- $A_{SOLAS} > R_{SOLAS}$
- Obtained *PLL* is less than the original *PLL* (i.e. only the design alternatives leading to reduced risk are acceptable)

- The intact stability requirements are satisfied.
- Intact GM is less than 3.5m for all operational loading conditions, limiting excessive transverse acceleration in roll resonance conditions.

3.4 Discussion of results

The results derived from the optimization of the ROPAX ship are presented in the following. In total 547 alternative designs have been obtained, 423 of which complied with the applied constraints (feasible designs). The relationship between the Attained Indices calculated according to the SOLAS 2009 regulation (A_S) and the GOALDS formulation (A_G) is presented in Figure . As shown in this figure, A_G is generally larger than A_S . Their difference ranges from 0.0 to 0.0177 with an average of 0.00298. The larger differences are observed for the designs with relatively low attained index.

Figure presents a diagram of A_G versus the beam of the ship. As expected, the maximum attained index is exhibited by the designs at the upper limit of the beam range. The original design is marked by a red triangle at the lower left quadrant of the diagram. Figure presents the corresponding plot of A_G versus the ship's reference length. The effect of freeboard on A_G is presented in Figure . A maximum is reached for a freeboard value of 3.4m, above which a very small decrease of the attained index may be observed.

Figure presents A_G versus the metacentric height at the subdivision draught. According to the results, the maximum obtained A_G values, ranging from 0.882 to 0.884 are obtained in a GM range from 2.18m to 2.63m. For higher GM values, most designs are marked as unfeasible, since at lighter draughts they exhibit GM values larger than the maximum permissible limit of 3.5m, as specified by the shipyard. The corresponding diagrams for the

partial and lightest draughts are presented in Figure and Figure respectively.

A plot of A_G versus the difference of building cost from the cost of the original design (in mUSD) is presented in Figure . According to these results, the design maximising the attained index with $A_G=0.8841$ and $A_S=0.8824$ (whereas the corresponding indices for the original design are 0.8267 and 0.8227 respectively) would have a building cost increased by 2.18mUSD above the cost of the original design.

Figure presents a plot of A_G versus the gross economic impact, calculated over a lifetime of 30 years. The gross economic impact is calculated considering the differences from the original design in building cost, fuel expenses and other operational costs. The differences in annual revenues are considered only in case of reduced trailers capacity, while in case the trailers capacity is increase no extra revenue is considered, assuming that there is no additional cargo available to be transported. Additional revenue in case of increased transport capacity is considered in the calculation of the net economic impact, presented in Figure . According to this plot, the design maximizing A_G and A_S exhibits a negative net economic impact of -36mUSD. This is because, assuming that the extra lanes length will be fully exploited, the additional annual revenues are prevailing over the increased building and operating costs. In a more realistic situation, assuming for example that only 20% of the extra lanes length will be exploited on an annual basis, this particular design, with a significantly improved survivability, in the assumed lifetime of 30 years would not only be able to break-even but to obtain a profit of around 1.5mUSD. The Gross Cost of Averting a Fatality, calculated according to GOALDS and SOLAS formulations versus the A index is presented in Figures 12 and 13. In the GOALDS project, a design modification aiming to reduce risk is considered cost effective if the corresponding $GCAF$ does not exceed 7.45mUSD.

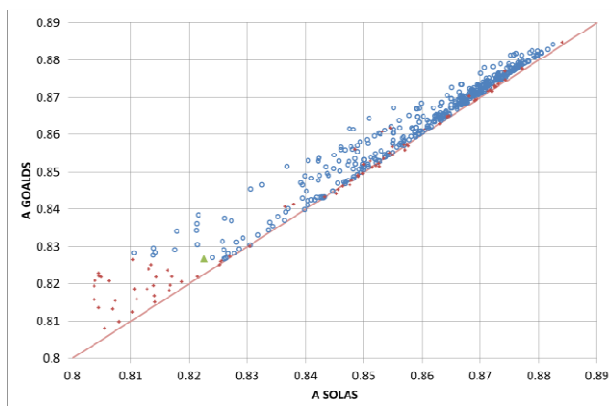


Figure 2: A_G vs. A_S Index

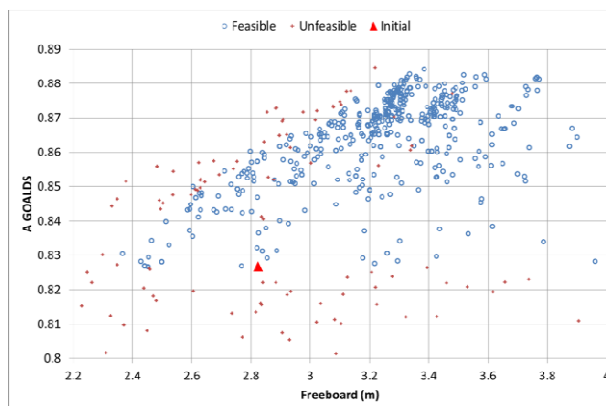


Figure 5: A_G vs. Freeboard

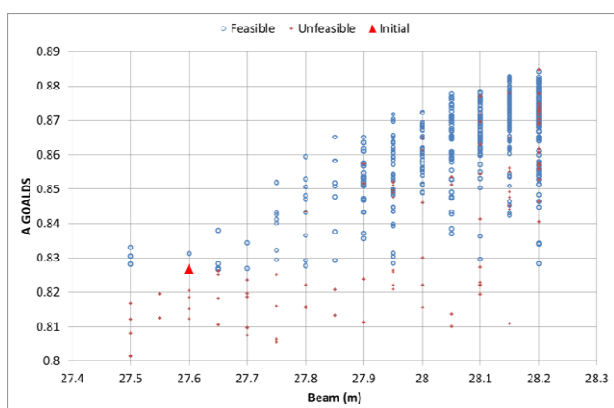


Figure 3: A_G vs. Beam

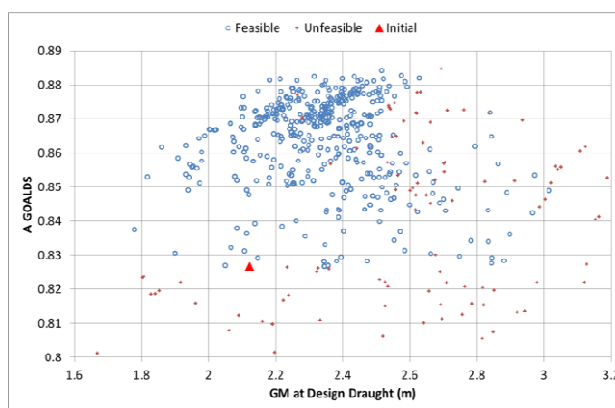


Figure 6: A_G vs. GM at subdivision draught

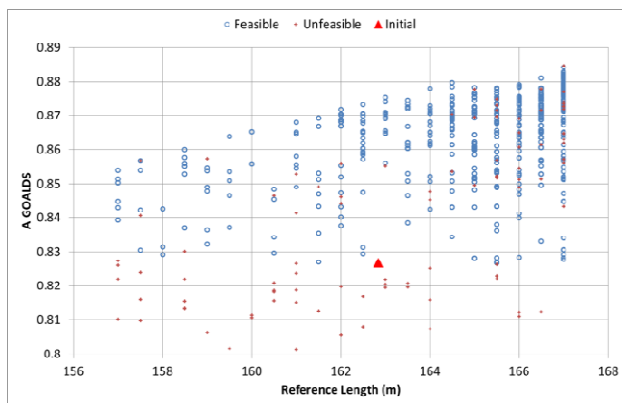


Figure 4: A_G vs. Reference Length

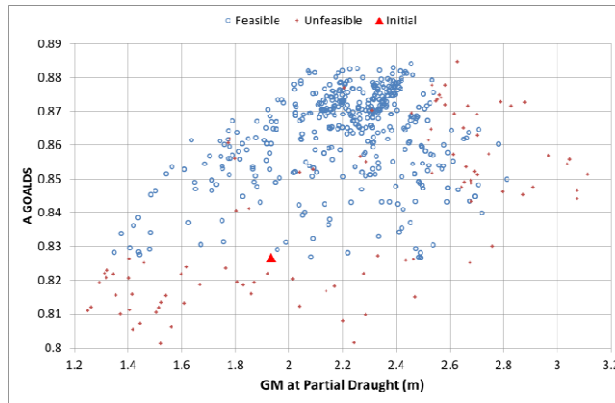


Figure 7: A_G vs. GM at partial draught

As may be observed from the presented results, a large number of designs meeting the above criterion have been obtained.

4. CONCLUSIONS

The results from the optimization of the design of a typical ROPAX ship based on the new GOALDS damage stability formulation as

well as on the existing SOLAS 2009 regulation were presented, indicating that there is room for a significant improvement of current survivability levels of ROPAX ships, without compromising the operational and economic potential of the resulting designs.

The attained index A according to GOALDS is slightly higher than that of SOLAS 2009 (0% to 2.2% for the tested ship cases). The presented results indicate that an



increase of main dimensions (and hence of building cost and light ship weight) leads to an increase of A -index. This is particularly true in case of beam; however an upper beam limit was herein set in order to avoid excessive GM values, resulting in problematic seakeeping. Increased freeboard leads in general to an increase of A ; a saturation effect is visible above a limiting freeboard value. Increase of GM leads also to an increase of A , however, limits on GM have been set to ensure

acceptable seakeeping behaviour; a saturation effect above certain GM value is also observed.

Although increased A -index is associated in general with increased building cost and/or lifecycle cost, several designs were obtained *with an increased A but with reduced building cost or lifecycle cost* (particularly when assuming additional income from increased capacity). $GCAF$ converges to a value of 4.55mUSD for an attained index A_G of 0.884.

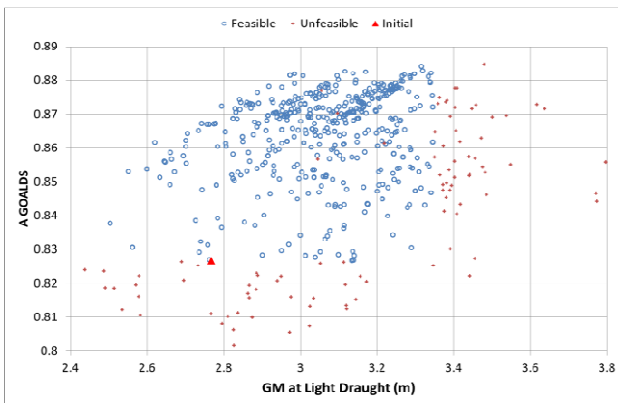


Figure 8: A_G vs. GM at lightest draught

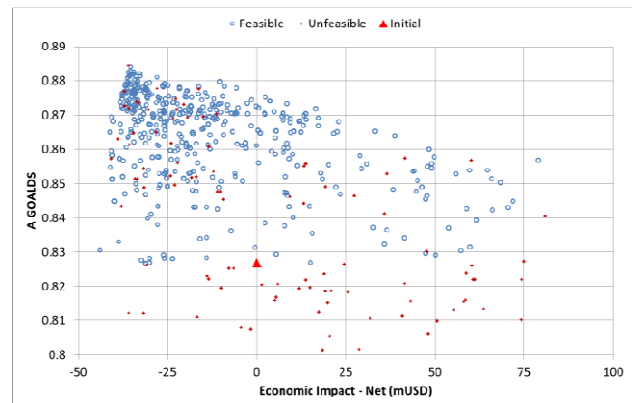


Figure 11: A_G vs. net economic impact

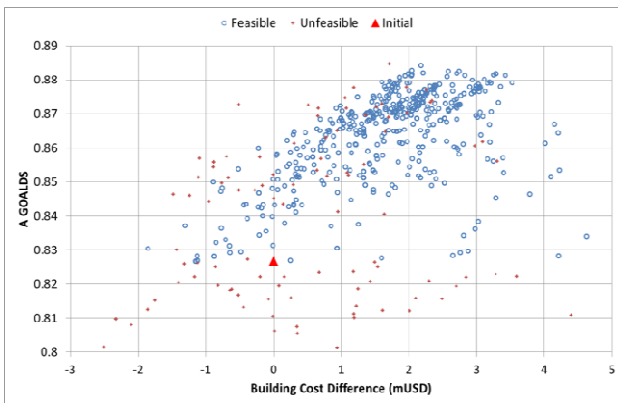


Figure 9: A_G vs. building cost difference

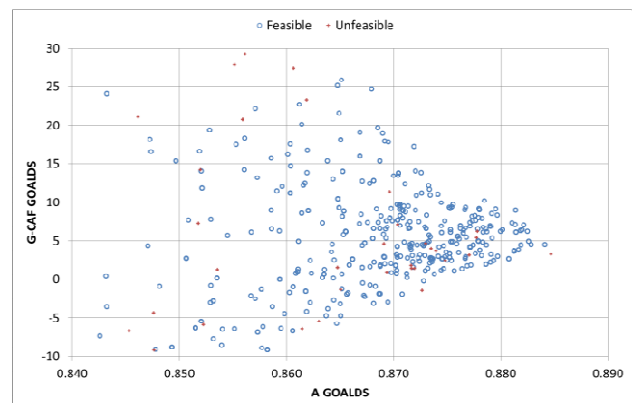


Figure 12: $GCAF$ acc. to GOALDS vs. A_G

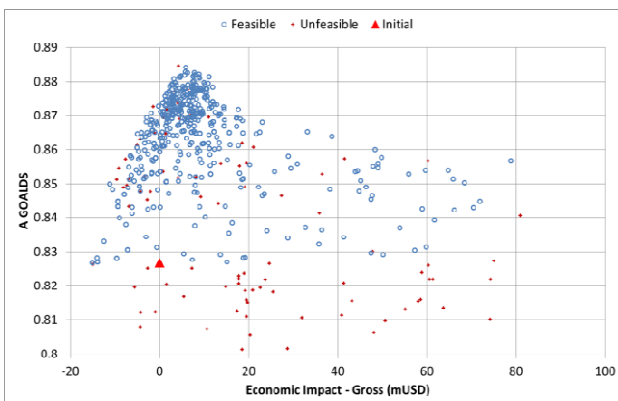


Figure 10: A_G vs. gross economic impact

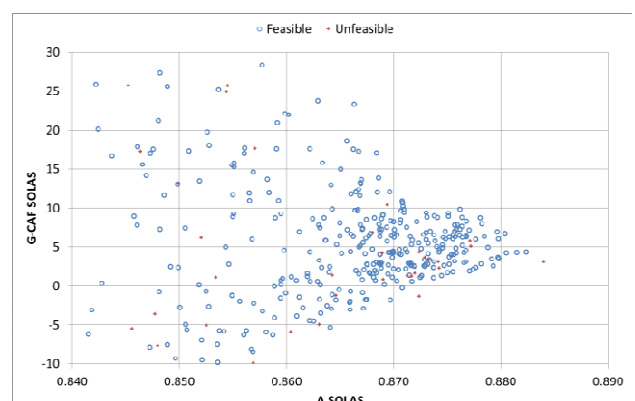


Figure 13: $GCAF$ acc. to SOLAS vs. A_S



Based on the presented results, it is the opinion of the authors that formal multi-objective optimization procedures, addressing both safety and economy (construction and operational cost and income) are powerful tools in assisting designer's daily work and in defining rational, reasonably practical and societally acceptable safety levels.

5. ACKNOWLEDGMENTS

The authors acknowledge the financial support by the European Union's Seventh Framework Programme (FP7/2007-2013) under grant agreement n° 233876. Dr. S. Skoupas acknowledges the support of Lloyd's Register Strategic Research.

"Lloyd's Register, its affiliates and subsidiaries and their respective officers, employees or agents are, individually and collectively, referred to in this clause as the "Lloyd's Register Group". The Lloyd's Register Group assumes no responsibility and shall not be liable to any person for any loss, damage or expense caused by reliance on the information or advice in this document or howsoever provided, unless that person has signed a contract with the relevant Lloyd's Register Group entity for the provision of this information or advice and that in this case any responsibility or liability is exclusively on the terms and conditions set out in that contract".

6. REFERENCES

- Cichowicz, J., Tsakalakis, N., Vassalos, D. and Jasionowski, A., 2011, "Survivability of passenger vessels – re-engineering of the s-factor", Proceedings of the 12th International Ship Stability Workshop, Washington D.C.
- HARDER, 1999-2003, "Harmonisation of Rules and Design Rationale". EC funded project, DG XIIBRITE.
- Holtrop, J., 1984, "A statistical re-analysis of resistance and propulsion data". International Shipbuilding Progress, vol. 31, No. 363, pp.272–276.
- Papanikolaou, A. Bulian, G. and Mains, C., 2011, "GOALDS – Goal Based Ship Stability: Collision and Grounding Damages", Proceedings of the 12th International Ship Stability Workshop, Washington D.C.
- Papanikolaou, A., Byung Suk Lee, Mains, C., Olufsen, O., Vassalos, D. and Zaraphonitis, G., 2012, "GOALDS – Goal Based Ship Stability & Safety Standards", Transport Research Arena, Athens.
- Ribbe, G., 2012, "Development of software for damage stability calculations based on the new formulation", Deliverable D3.6, GOALDS project.
- GOALDS, 2009-2012, "Goal Based Damage Stability", <http://www.goalds.org>
- HSVA, 2009, "Research for the Parameters of the Damage Stability Rules including the Calculation of Water on Deck of Ro-Ro Passenger Vessels, for the amendment of the Directives 2003/25/EC and 98/18/EC", Final Report Part I-II, funded by EMSA, July 2009, <http://www.emsa.europa.eu>.
- MSC 83/INF.2, 2007, "Consolidated Text of the Guidelines for Formal Safety Assessment (FSA) for Use in the IMO Rule-Making Process" (MSC/Circ.1023-MEPC/Circ.392)



Evaluation of Hydrodynamic Pressures for Autoregression Model of Irregular Waves

Alexander Degtyarev, *Saint-Petersburg State University, Faculty of Applied Mathematics and Control Processes, Russia, deg@csa.ru*

Ivan Gankevich, *Saint-Petersburg State University, Faculty of Applied Mathematics and Control Processes, Russia, gig.spb@gmail.com*

ABSTRACT

In the paper a new way of simulating hydrodynamic pressure near ship's hull is proposed. This approach is based on autoregressive model (ARM) which is used for wave surface generation. ARM is good for long-term direct simulations. This model retains all hydrodynamic characteristics of sea waves. These features allow you to accurately solve the potential problem and to calculate the hydrodynamic pressure at the surface. The paper shows the solution of two-dimensional problem. In the paper calculation scheme and complete problem solution as well as test results are provided.

Keywords: *autoregressive model, ship dynamics, hydrodynamic pressure, virtual testbed, OpenCL, OpenMP, MPI.*

1. INTRODUCTION

Direct stability assessment of ship stability in irregular waves may require numerical simulation using advanced hydrodynamic codes, (e.g. see Beck & Reed 2001). The length of record needs to be long enough that nonlinear behavior of dynamical system can be revealed. If the volume of sample is insufficient, even qualitative conclusions may not be possible, see for example (Degtyarev & Reed 2011). This reference describes benchmarking of parametric roll (numerical simulations against model test) and shows that one 20 min record does not contain sufficient information to pass a judgment.

The reason for these difficulties is a nonlinear character of ship roll in waves; as it was shown by (Belenky, *et al* 1998), nonlinearity may lead to practical non-ergodicity if the length of the record is not long enough. Using a set of independent records resolves the problem;

however, the length of each record still needs to be sufficient. This length may be not small, especially for large speeds in following waves where the number of waves encounters is small. Numerical simulation of long records bears large computational cost, because Longuet-Higgins model requires an increase of frequency component with length (Belenky, 2011)

Autoregression model of wave elevations (Degtyarev, 2011) holds a promise to decrease computational costs of long records. This model offers certain advantages over existing wave wind models. First of all, it enables efficient computation of sea wave elevation compared to linear Longuet-Higgins model. Secondly, it can be used to produce wave fields with arbitrary chosen distribution function via nonlinear inertialess transformation of generated surface. It is important property because investigations show that real waves are characterized by a non-Gaussian distribution



law of wave elevation. Degtyarev & Reed (2011) have shown that dispersion relation is kept in the autoregressive model.

However, autoregressive model is not limited only to generating wave fields and, when extended, this model can also produce pressures and/or velocity potentials within the fluid domain, so that it can be easily used to predict the Froude-Krylov forces on a ship's hull in a seaway. Such autoregressive approach can substantially reduce complexity of computations required for producing pressures. Knowing pressures is important when solving problem of vessel dynamics in rough sea. So, the described approach can be employed to solve a variety of simulation problems inside a virtual testbed, such as simulation of marine object behavior in irregular waves. Problems of that kind frequently involve large-scale or long-term simulation, that is why it is important to use autoregressive model to reduce computation time.

Application of ARM to a moving wavy surface in three dimensions (2-D space + 1-D temporal) can be defined as

$$\zeta_{(x,y,t)} = \sum_{i=0}^{N_x} \sum_{j=0}^{N_y} \sum_{k=0}^{N_t} \Phi_{(i,j,k)} \zeta_{(x-i,y-j,t-k)} + \varepsilon_{(x,y,t)} \quad (1)$$

where $\Phi_{(i,j,k)}$ is the generalized coefficients of ARM, and $\varepsilon_{(x,y,t)}$ a field of white noise.

Autoregressive coefficients can be estimated from the autocovariate function (ACF) using Yule-Walker equations. Theoretically the number of autoregressive coefficients tends to infinity. In practice we have such an ACF that high order of autoregressive coefficients tend to zero, and we can neglect them. So really the order in one direction is from 3 to 10.

In simplest case of one dimensional stochastic process we have the following ARM

$$\zeta_t = \sum_{i=1}^N \Phi_i \zeta_{t-i} + \varepsilon_t; \quad (2)$$

with the system of linear equations for ARM coefficients determination (Yule-Walker equations for one dimensional case)

$$K_{\zeta}(n) = \sum_{i=1}^N \Phi_i K_{\zeta}(k-n)$$

where $k,n=1,\dots,N$; $K_{\zeta}(i)$ – value of ACF at the moment $\tau = i \Delta t$ (Δt is the value of time discretization).

The advantages and features of ARM are described in detail in several previous articles: Degtyarev & Reed (2011), Degtyarev (2011), Boukhanovsky & Degtyarev (1996), etc. Computational efficiency in long-term wind waves simulations is shown in Degtyarev & Gankevich (2011). Initial statement of the problem is described in Degtyarev & Boukhanovsky (1997), Degtyarev & Podolyakin (1998), Degtyarev & Mareev (2010).

2. STATEMENT OF PROBLEM OF HYDRODYNAMIC PRESSURE DETERMINATION UNDER THE WAVE SURFACE

To determine the evolution of the hydrodynamic pressure at the rough wave surface we consider the classical problem of the wave theory. For simplicity we consider two-dimensional problem.

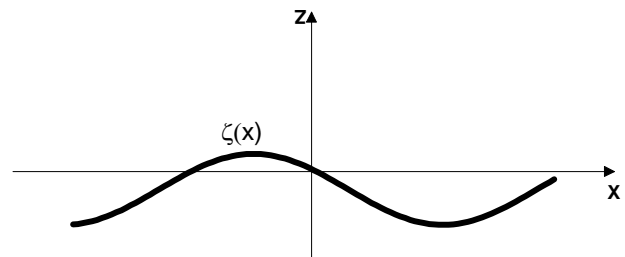


Figure 1: The coordinate system.

Traditional formulation is reduced to finding the wave potential (Kochin, et al., 1964). Solution to this problem provides a complete



definition of the hydrodynamic pressure at the wave surface.

$$\Delta\varphi = 0$$

$$\frac{\partial\varphi}{\partial t} + \frac{1}{2}\left(\left(\frac{\partial\varphi}{\partial x}\right)^2 + \left(\frac{\partial\varphi}{\partial z}\right)^2\right) + g\zeta = p_0 \quad (3)$$

$$\frac{\partial\zeta}{\partial t} + \frac{\partial\zeta}{\partial x} \frac{\partial\varphi}{\partial x} = \frac{\partial\varphi}{\partial z} \quad \text{at } z = \zeta(x)$$

The Laplace equation for the potential $\varphi(x,z,t)$ in the coordinate system shown in Fig.1 is supplemented by two boundary conditions on the wave surface. These are conditions that the pressure at the surface equals to atmospheric pressure p_0 (dynamic boundary condition) and the continuity of fluid motion (kinematic condition). The last condition says that a fluid particle belonging to the surface can not go into the liquid and remains on the surface.

The complexity of Problem (3) consists first of all in that the boundary conditions are nonlinear, and secondly, they satisfy in every moment at the unknown free surface. Problem (3) can be reduced to Laplace's equation with one combined boundary condition by eliminating the unknown elevation of free surface (Kochin, 1964; Newman, 1977). It is known that this formulation assumes the transfer of boundary conditions on the well-known in advance and the unperturbed surface $z=0$.

Our assumption in the modification of the problem statement (1) is related with the fact that we know the free surface $\zeta(x,t)$ at any time. The assumption of knowledge of the wave surface at any time makes it possible to give up one of the boundary condition. This is exactly that condition which defines variation of free surface. Of course, in general this approach is incorrect because prescribed free surface has to correspond to the described physical phenomenon. In other words, we need to "guess" the correct decision.

The validity of the decision to use the free surface $\zeta(x,t)$ obtained using the AR model is the fact that the adequacy of this model to the hydrodynamic reality was earlier proved (Boukhanovsky & Degtyarev, 1996; Degtyarev & Reed, 2011, etc.). In other words, the wave surface resulting AR model correctly "guesses" the evolution of real sea waves under some initial conditions. As for the ship motion calculations we are interesting in any realization of a stationary sea wave, the choice of initial conditions can be made arbitrarily. As a result of the solution of (3), we obtain a realization of a stationary field of the hydrodynamic potential evolution.

Since at any given time the surface on which the boundary conditions is known, one of them may be excluded from consideration. It is logical to exclude the first (dynamic) condition, since only it has a derivative of the hydrodynamic potential over time. Laplace equation itself and the second boundary condition do not contain derivatives of the unknown function of time. It should be noted that it is the first boundary condition is used in the process of linearization to find the free surface $\zeta(x,t) = -\frac{1}{g} \frac{\partial\varphi(x,t)}{\partial t}$. Since the surface in this formulation is already known, you can use the first boundary condition for finding the derivative of the potential over time.

$$\frac{\partial\varphi}{\partial t} = -p_0/\rho - \frac{1}{2}\left(\left(\frac{\partial\varphi}{\partial x}\right)^2 + \left(\frac{\partial\varphi}{\partial z}\right)^2\right) - g\zeta \quad (4)$$

In addition, you must understand that in order to determine the hydrodynamic pressure is necessary the determination of derivatives of the potential in time and space coordinates. Potential itself for further calculations is not involved.

Thus, Problem (3) reduces to successive solution of Laplace's equations with the second boundary condition at any particular time.



$$\Delta\varphi = 0$$

$$\frac{\partial\varphi}{\partial z} - \alpha(x)\frac{\partial\varphi}{\partial x} = g(x), \quad (5)$$

where $\alpha(x) = \frac{\partial\zeta}{\partial x}$; $g(x) = \frac{\partial\zeta}{\partial t}$ are known functions (wave slope and velocity of points at the surface), which we can easily determine with the help of AR model. Boundary conditions are defined at the surface that is known in any time moment.

Notable in the formulation of Problem (5) is its linearity and definiteness of the border. Thus, a complex nonlinear problem with an unknown boundary is replaced by a sequence of simple linear problems with known boundary.

3. SOLUTION OF 2D PROBLEM

Let us represent the components of the velocity of the fluid particles as they follow $u = \frac{\partial\varphi}{\partial x}$, $w = \frac{\partial\varphi}{\partial z}$. Then Laplace equation and boundary condition (5) will

$$\frac{\partial u}{\partial x} + \frac{\partial w}{\partial z} = 0$$

$$w - \alpha(x)u = g(x) \quad (6)$$

In this case condition of the Cauchy-Riemann (7) for the velocity components u and w is also true:

$$\frac{\partial u}{\partial z} - \frac{\partial w}{\partial x} = 0 \quad (7)$$

From the Laplace equation (6) and the Cauchy-Riemann condition (7) we can get two of the Laplace equations for the velocity components: $\Delta u = 0$; $\Delta w = 0$. As a result of transformations (see Appendix 1) we obtain for the velocity components u the following linear problem.

$$\Delta u = 0$$

$$\frac{\partial u}{\partial z} - \alpha(x)\frac{\partial u}{\partial x} - \alpha_x(x)u = \alpha_t(x) \quad (8)$$

Equation (8) is a mixed boundary value problem for the Laplace equation or the other problem of Robin (Zachmanoglou & Thoe, 1976).

3.1 Exact solution of the Robin's problem at the wave surface

Solutions of the Laplace equation with respect to the vertical velocity component at the surface is not required, because, if we find u on the surface, then according to the initial boundary condition (6) and (4) we find

$$w = g(x) + \alpha(x)u$$

$$\frac{\partial\varphi}{\partial t} = -g\zeta - \frac{1}{2}(u^2 + w^2) \quad (9)$$

Knowing these three components on the surface, you can find the hydrodynamic pressure at any point below the surface (Degtyarev & Boukhanovsky, 1997; Degtyarev & Podolyakin, 1998). Thus Problem reduces to solving only the equation (8).

The Robin's problem (reduction of the general problem to it) is good because it is a standard model problem. The problem itself is linear, the boundary condition is also linear. This simplifies the solution by standard methods. Let us apply Fourier method for solution of equation (8) (see Appendix 2). As a result, we obtain the following integral formula (Kochin, 1964).

$$u(x, z) = \int_0^{\infty} e^{\lambda z} (E_1(\lambda) \sin \lambda x + E_2(\lambda) \cos \lambda x) d\lambda \quad (10)$$

Finding the coefficients of the $E_{1,2}$ is determined by the mixed boundary condition (8).

In the practical solution of the problem integral in (10) is replaced by a sum of λ as well as in finding the coefficients $E_{1,2}$

$$u(x, z) = \sum_{\lambda} e^{\lambda z} (E_1(\lambda) \sin \lambda x + E_2(\lambda) \cos \lambda x) \quad (11)$$

This makes it possible to determine all the derivatives of the potential on the surface at any one time. To do this, let us use the following expressions $u = \partial\varphi/\partial x - (11)$, $w = \partial\varphi/\partial z, \partial\varphi/\partial t - (9)$.

3.2 Approximate solution of the Robin's problem at the wave surface

However, Problem (8) can be solved by an approximate method. For this we use the assumption of slow decay of the coherence function of wind waves. It is analogous to the assumption of weak changes in the local wave number in time and space in comparison with the process. The possibility of such a assumption is quite justifiable. Figure 2 illustrates the difference of time scales of these two processes.

As mentioned, Degtyarev & Reed (2011) showed that the AR model keeps the dispersion relation. In this case it corresponds to the real waves, and not the dispersion relation corresponding to waves of very small amplitude. It should be noted that this theory is the basis for the majority of expressions for the hydrodynamic exiting forces and moments. In Boukhanovsky & Degtyarev (1995) it is shown how to obtain a smooth realization of the local wave number in dynamic, as well as to avoid some rare computer problems.

Under this assumption, we can approximately put

$$\frac{\partial \zeta(x, t)}{\partial z} = k(x, t) \zeta(x, t) \quad (12)$$

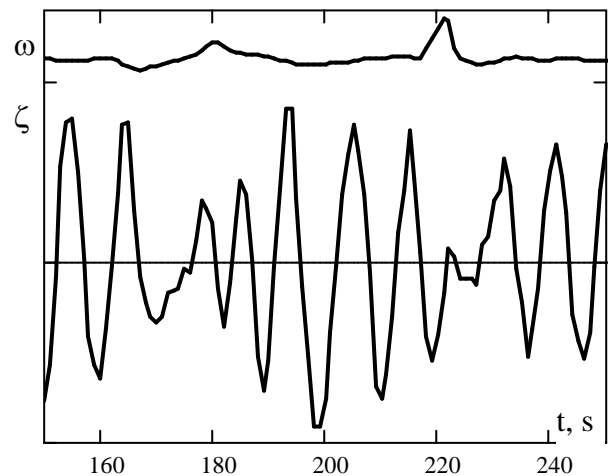


Figure 2: Fragment of synchronous realizations of wind waves and instantaneous frequency generated by AR model.

This approach from a mathematical point of view is totally incorrect, but to study a class of considered processes (sea waves) may be quite adequate. It allows you to simplify (5), reducing it to solution of isolated ordinary differential equation of second order with variable coefficients. The solution is given in Appendix 3.

3.3 Pressure determining under the water surface

Determination of derivatives of the potential on the surface of wavy fluid, as already mentioned, makes it possible to determine the hydrodynamic pressure at any point below the surface. For this we consider the concept of the complex potential:

$$W = \varphi + i\psi, \quad (13)$$

where ψ is stream function.

In accordance with Cauchy-Riemann condition



$$\frac{\partial \varphi}{\partial x} = \frac{\partial \psi}{\partial z}; \quad \frac{\partial \varphi}{\partial z} = -\frac{\partial \psi}{\partial x}, \quad (14)$$

Let us $\xi = x_0 + i z_0$. Then in accordance with integral Cauchy formula

$$W(\xi) = \frac{1}{2\pi i} \oint_C \frac{W(\eta)}{\eta - \xi} d\eta, \quad (15)$$

Here C is boundary of region D, carried out in such a way that D is always on the left (bypass is counter-clockwise – see Fig. 3).

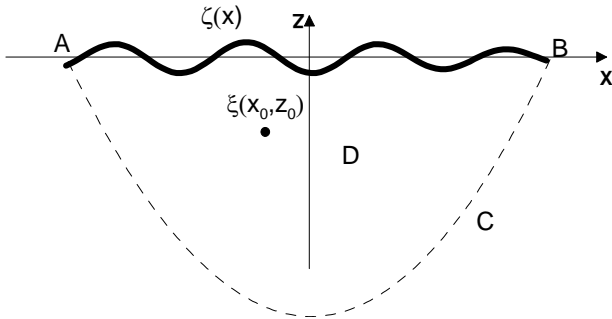


Figure 3: The domain of integration.

Let us divide contour C on two parts: (1) BA – free surface; (2) AB – semicircle lying in the lower half-plane (with radius R)

$$\oint_C = \int_{BA} + \int_{AB}, \quad (16)$$

Based on Jordan's lemma the second integral tends to 0 as $R \rightarrow \infty$.

Thus, to find the potential at any point below the surface it is sufficient to integrate only on the free surface. Meanwhile the points A and B must be sufficiently distant from the point of ξ (in this case we can substitute infinity limits on finite limits).

Since we are mostly interested in the value of not the potential and its derivatives, we differentiate expression (15)

$$\begin{aligned} W'(\xi) &= \frac{\partial \varphi}{\partial x} + i \frac{\partial \psi}{\partial x} = \frac{\partial \psi}{\partial z} - i \frac{\partial \varphi}{\partial z} = \\ &= \frac{\partial \varphi}{\partial x} - i \frac{\partial \varphi}{\partial z} \end{aligned} \quad (17)$$

From the other side in accordance with integral Cauchy formula (and Jordan's lemma)

$$\begin{aligned} W'(\xi) &= \frac{1}{2\pi i} \int_{BA} \frac{W(\eta)}{(\eta - \xi)^2} d\eta = \\ &= \frac{1}{2\pi i} \int_{BA} \frac{W'(\eta)}{\eta - \xi} d\eta \end{aligned} \quad (18)$$

Because we bypass the counter-clockwise, we obtain

$$\begin{aligned} \frac{\partial \varphi}{\partial x} - i \frac{\partial \varphi}{\partial z} &= \\ &= -\frac{1}{2\pi i} \int_{AB} \left(\frac{\partial \varphi}{\partial x}(\eta) - i \frac{\partial \varphi}{\partial z}(\eta) \right) / (\eta - \xi) d\eta \end{aligned} \quad (19)$$

In calculating the integral we can operate in accordance with the definition of the integral along the contour C:

$$\lim_{n \rightarrow \infty} \sum_{k=0}^{n-1} f(\zeta_k) (\eta_{k+1} - \eta_k) = \int_C f(\eta) d\eta, \quad (20)$$

where $\eta_0 = a, \eta_1, \eta_2, \dots, \eta_{n-1} = b$ – consecutive points, dividing the contour C into n sections, through a and b the ends of the C are denoted. ζ_k is arbitrary point lying on the interval $[\eta_k, \eta_{k+1}]$ of curve C. The limit is taken under the assumption that $\max(\eta_{k+1} - \eta_k) \rightarrow 0$. Since the wave profile is piecewise smooth curve for non-braking waves, and the integrand is piecewise, continuous and bounded function when ξ is not on the surface, the integral exists. Let us $\eta = x + iz$. Then we can represent contour of integration C and point ξ (fig.3) by the following view

$$\begin{aligned} \eta_C &= x_\zeta + iz_\zeta, \\ \xi &= x_0 + iz_0 \end{aligned}, \quad (21)$$



where index ζ means that coordinates of points are taken on the free surface $\zeta(x)$ in the coordinate system $0xz$ (fig.3).

Using (21) in the formal definition of the integral along the contour (20), we find the values of the velocity components u and v at the point ξ in terms of quadratures

$$\begin{aligned} \frac{\partial \varphi}{\partial x} &= -\frac{1}{2\pi} \sum_{k=0}^{n-1} \frac{u_k \Delta z_k + v_k \Delta x_k}{(x_{\zeta_k} - x_0)^2 + (z_{\zeta_k} - z_0)^2}, \\ \frac{\partial \varphi}{\partial z} &= -\frac{1}{2\pi} \sum_{k=0}^{n-1} \frac{u_k \Delta x_k + v_k \Delta z_k}{(x_{\zeta_k} - x_0)^2 + (z_{\zeta_k} - z_0)^2} \end{aligned} \quad (22)$$

where

$$u_k = \frac{\partial \varphi}{\partial x} \Big|_{(x_{\zeta_k}, z_{\zeta_k})} (x_{\zeta_k} - x_0) - \frac{\partial \varphi}{\partial z} \Big|_{(x_{\zeta_k}, z_{\zeta_k})} (z_{\zeta_k} - z_0)$$

$$v_k = -\frac{\partial \varphi}{\partial x} \Big|_{(x_{\zeta_k}, z_{\zeta_k})} (z_{\zeta_k} - z_0) - \frac{\partial \varphi}{\partial z} \Big|_{(x_{\zeta_k}, z_{\zeta_k})} (x_{\zeta_k} - x_0)$$

$$\Delta x_k = x_{\zeta_{k+1}} - x_{\zeta_k}; \quad \Delta z_k = z_{\zeta_{k+1}} - z_{\zeta_k}$$

Similar to the previous reasoning derivative of the complex potential over time is calculated. The peculiarity of these calculations is the need for knowledge of the stream function and the derivative (13) on the free wave surface. It is separate problem, but it could be solved correctly also.

In the issue for the time derivative of the potential at the point ξ we get a similar (22) expression in quadratures.

Now we can obtain hydrodynamic pressure in any point ξ under the free surface

$$p(x_0, z_0) = -\rho \frac{\partial \varphi}{\partial t} - \frac{\rho}{2} \left(\left(\frac{\partial \varphi}{\partial x} \right)^2 + \left(\frac{\partial \varphi}{\partial z} \right)^2 \right) - \rho g z_0 \quad (23)$$

4. COMPUTATIONAL ASPECTS

The computational efficiency of the proposed approach is based on fast algorithms of AR model. These algorithms are simple, require the use of a small number of elementary operations (addition and multiplication). These algorithms are very favorable with those of the Fourier series like models of St.Denis & Pearson, Rosenblatt, Sveshnikov, or Longuet-Higgins. However, Degtyarev & Gankevich (2011) have shown that these algorithms can be efficiently parallelized for long implementations. The multithread character of the considered algorithms makes it possible to increase the speed of computing through the use of graphics accelerators.

Thus, the first step in calculating the excitation forces acting on the vessel is to generate wind wave fields and kinematic characteristics of the wave surface. The size of the area that is being generated depends on the size of the vessel, the nature of waves and should be so large that it would have been achieved the convergence of the integrals (18) (19).

The second step is to calculate the derivatives of the potential on the surface of the water. This step has a maximum degree of parallelism, because we have independent problems (8) at each time moment. Any of described methods for solution of problem (8) (Sections 3.1, 3.2) or the direct method of solving the elliptic problem (8), such as multigrid method (Mijalkovic & Joppich, 1993), can be expressed by an efficient parallelizable algorithm.

The third step is to find the pressure at a given set of points under the free surface (the points of the hull). The pressure at each point is calculated independently of each other.

5. CONCLUSIONS

It can be concluded that the autoregression model gives an accurate, hydrodynamically valid description of wind waves



(Boukhanovsky & Degtyarev, 1996; Degtyarev & Reed, 2011). This means that we can use the model to solve the problem of predicting the velocity potential in the fluid below the wave surface. In this case we can reduce this complicated nonlinear hydrodynamic problem with an unknown boundary to linear problem with a known boundary and linear boundary conditions. It is proposed several approaches for problem solving.

From a computational point of view, the algorithm of problem solving consists in three major steps, each of which has a high degree of parallelism, a well-balanced and scalable.

6. ACKNOWLEDGMENTS

The authors are very grateful to Dr. Vadim Belenky and Dr. Arthur Reed for discussions and review of materials of the paper.

7. REFERENCES

- Anderson D.A., Tannehill J.C., Pletcher R.H. (1984) Computational fluid mechanics and heat transfer. – New York, Hemisphere Publishing Corporation
- Beck, R.F. and Reed, A.M. (2001). “Modern Computational Methods for Ships in Seaway”, Trans. SNAME, Vol. 109 pp. 1–48.
- Belenky, V.L., Degtyarev, A.B., Boukhanovsky A.V. (1998) Probabilistic qualities of nonlinear stochastic rolling, Ocean Engineering, Vol. 25, No 1, pp. 1-25.
- Belenky V.L., Sevastianov N.B. (2007) Stability and Safety of Ships. Risk of Capsizing. Second Edition, SNAME, Jersey City
- Belenky, V.L. (2011) “On Self-Repeating Effect in Reconstruction of Irregular Waves” Chapter 33 of “Contemporary Ideas on Ship Stability”, Neves, M.A.S., et al. (eds), Springer, ISBN 978-94-007-1481-6 pp. 589-598
- Boukhanovsky, A., Degtyarev A. (1995) On the Estimation of the Motion Stability in Real Seas. Proc. Int’l Symp. Ship Safety in a Seaway: Stability, Maneuverability, Nonlinear Approach, Kaliningrad, Vol. 2, Paper 8, 10 p.
- Boukhanovsky A.V., Degtyarev A.B. (1996) The instrumental tool of wave generation modelling in ship-borne intelligence systems. Trans. of the 3d Intern. Conf. CRF-96, St.Petersburg, vol.1, pp 464-469
- Boukhanovsky A. V., Degtyarev A. B. (1996) Probabilistic modelling of storm waves fields. Proc. of International Conference "Navy and Shipbuilding Nowadays", St. Petersburg, Vol. 2, A2–29, 10 p. (in Russian)
- Degtyarev A.B., Reed A.M. (2011) Modeling of Incident Waves near the Ship's Hull (Application of Autoregressive Approach in Problems of Simulation of Rough Seas). Proceedings of the 12th International Ship Stability Workshop, June 2011, Washington, D.C. USA, pp.175-187
- Degtyarev A.B., Mareev V.V. (2010) “Climatic Spectra and Long-Term Risk Assessment”, Proceedings of the 11th International Ship Stability Workshop, June 2010, Wageningen, The Netherlands, pp.108-114
- Degtyarev A.B., Podolyakin A.V. (1998) “Simulation of ship behaviour in real sea”, Proceedings of II International shipbuilding conference – ISC’98, St.Petersburg, Russia, vol. B pp.416-423. (in Russian)
- Degtyarev A., Boukhanovsky A. (1997) “Analysis of Peculiarities of Ship-Environmental Interaction”, Technical Report of Ship Stability Research Center, Strathclyde University, Glasgow, Sep-97 1



of 1 09-97-1AB-1VA

Degtyarev A. (2011) “New Approach to Wave Weather Scenarios Modeling”, In book “Contemporary Ideas on Ship Stability and Capsizing in Waves”, Fluid Mechanics and Its Applications, M.A.S.Neves et al. (eds.), Springer, ISBN 978-94-007-1481-6, pp.599-617

Degtyarev A., Gankevich I. (2011) “Efficiency Comparison of Wave Surface Generation Using OpenCL, OpenMP and MPI”, Proceedings of 8th International Conference «Computer Science & Information Technologies», Yerevan, Armenia, pp.248-251

Kochin, N. E., Kibel, I. A. & Roze N. V. (1964) Theoretical Hydromechanics. Wiley-Interscience, 577 p. (Translated from Russian)

Mijalkovic S., Joppich W. (1993) Multigrid method for Process Simulation. – Series “Computational Microelectronics” ed. by S. Selberherr, Springer Verlag, New York, Vienna.

Newman J.N. (1977) Marine Hydrodynamics. – Massachusetts, The MIT Press

Zachmanoglou E.C., Thoe D.W. (1976) Introduction to Partial Differential Equations with Applications. – Baltimore: Williams & Wilkins

8. APPENDIX 1. DERIVATION OF EQUATION FOR THE VELOCITY COMPONENT U

Indeed from equation (4) and the Cauchy-Riemann condition (5) Laplace equations for two velocity components can be obtained. Let us derivate Laplace equation (4) on x :

$$\begin{aligned} \frac{\partial}{\partial x} \left(\frac{\partial u}{\partial x} - \frac{\partial w}{\partial z} \right) &= \frac{\partial^2 u}{\partial x^2} + \frac{\partial^2 w}{\partial x \partial z} = \\ \frac{\partial^2 u}{\partial x^2} + \frac{\partial}{\partial z} \left(\frac{\partial u}{\partial z} \right) &= \frac{\partial^2 u}{\partial x^2} + \frac{\partial^2 u}{\partial z^2} = 0 \end{aligned} \quad (\text{A1.1})$$

In the third terms, replacing w by u carried out in compliance with the condition of the Cauchy-Riemann condition.

Similarly, the second Laplace equation for the vertical velocity component can be obtained.

Now let us differentiate the boundary condition on the coordinate x . To do this we have the right, because differentiation is carried out along the border, and not by the normal.

$$\frac{\partial w}{\partial x} - \frac{\partial \alpha}{\partial x} u - \frac{\partial u}{\partial x} \alpha = \frac{\partial g}{\partial x} \quad (\text{A1.2})$$

The first term can also be replaced, based on the Cauchy-Riemann condition. As a result, we obtain the following boundary condition

$$\frac{\partial u}{\partial z} - \alpha \frac{\partial u}{\partial x} - \alpha_x u = \alpha_t, \quad (\text{A1.3})$$

where the last term is the time differentiation of the wave slope angle. We can easily calculate this derivative using AR model:

$$\frac{\partial g}{\partial x} = \frac{\partial}{\partial x} \frac{\partial \zeta}{\partial t} = \frac{\partial}{\partial t} \frac{\partial \zeta}{\partial x} = \frac{\partial}{\partial t} \alpha = \alpha_t,$$

9. APPENDIX 2. SOLUTION OF MIXED BOUNDARY VALUE PROBLEM FOR VELOCITY COMPONENT U

Since Problem (6) is linear, we apply the standard Fourier method of separation of variables to solve it.

$$\begin{aligned} u(x, z) &= A(x)B(z) \\ A''(x)B(z) + A(x)B''(z) &= 0 \Rightarrow \\ -\frac{A''(x)}{A(x)} &= \frac{B''(z)}{B(z)} = \lambda^2 \end{aligned} \quad (\text{A2.1})$$



Let us also take into account boundary condition at infinity: $\nabla\varphi \rightarrow 0$ at $z \rightarrow -\infty$ for deep water. This condition is equivalent to condition of absence of disturbance at great depth: $\lim_{z \rightarrow -\infty} u = 0$. Solution (A2.1) has the following view

$$\begin{aligned} A''(x) + \lambda^2 A(x) = 0 &\Rightarrow A(x) = C e^{i\lambda x} + \bar{C} e^{-i\lambda x} \\ B''(z) - \lambda^2 B(z) = 0 &\Rightarrow \\ B(z) = D_1 e^{-\lambda z} + D_2 e^{\lambda z} &= D_2 e^{\lambda z} \end{aligned} \quad (\text{A2.2})$$

$D_1=0$ in accordance with boundary condition at infinity. Then

$$\begin{aligned} u(x, z) = e^{\lambda z} (E(\lambda) e^{i\lambda x} + \bar{E}(\lambda) e^{-i\lambda x}) = \\ e^{\lambda z} (E_1(\lambda) \sin \lambda x + E_2(\lambda) \cos \lambda x) \end{aligned} \quad (\text{A2.3})$$

Due to the linearity of (6), its solution will also be solutions of any sum (A2.3). Thus, the general solution of (6) is

$$\begin{aligned} u(x, z) = \int_0^\infty e^{\lambda z} (E_1(\lambda) \sin \lambda x + E_2(\lambda) \cos \lambda x) d\lambda \\ = \int_0^\infty E(\lambda) e^{\lambda(z+ix)} d\lambda + cc \end{aligned} \quad (\text{A2.4})$$

Where cc is complex conjugation term. To find the complex amplitudes E should be replaced with a solution of (A2.4) into the boundary condition (6).

$$\begin{aligned} \int_0^\infty E(\lambda) e^{\lambda(\zeta(x)+ix)} (\lambda(1-i\alpha(x)) - \alpha_x(x)) d\lambda + cc \\ = \alpha_t(x) \end{aligned} \quad (\text{A2.5})$$

Let us simplify this expression taking the integral $\int_0^\infty E(\lambda) \lambda e^{\lambda(\zeta(x)+ix)} d\lambda$ by parts. Use the property that $E(\lambda) \lambda e^{\lambda(\zeta(x)+ix)} \Big|_{\lambda=\infty} = 0$. In this case we can simplify (A2.5) by the following

$$(i\alpha - 1 + \alpha_x) \int_0^\infty E(\lambda) e^{\lambda(\zeta(x)+ix)} d\lambda + cc = \alpha_t \quad (\text{A2.6})$$

10. APPENDIX 3. SOLUTION OF APPROXIMATE PROBLEM FOR VELOCITY COMPONENT U

Let us solve the Laplace equation with the second boundary condition at a known position of the free surface (3), using the assumptions of validity of the relation (10). To do this we formally differentiate the boundary condition in z .

$$\begin{aligned} \frac{\partial^2 \varphi}{\partial z^2} = \frac{\partial}{\partial z} \left(\frac{\partial \zeta}{\partial t} - \alpha \frac{\partial \varphi}{\partial x} \right) = \\ \dot{\zeta}_z - \alpha_z \frac{\partial \varphi}{\partial x} - \alpha \frac{\partial^2 \varphi}{\partial z \partial x} = \\ \dot{\zeta}_z - \alpha_z \frac{\partial \varphi}{\partial x} - \alpha \dot{\alpha} + \alpha \alpha_x \frac{\partial \varphi}{\partial x} + \alpha^2 \frac{\partial^2 \varphi}{\partial x^2} \end{aligned} \quad (\text{A3.1})$$

Here ζ is a process of wave ordinate variation, α is a process of wave slope variation, the dot at above is differentiation with respect to time, lower indexes x or z are differentiation with respect to corresponding coordinate.

Substituting this result into the Laplace equation results in the ordinary differential equation of first order with variable coefficients with respect to the velocity component $u = \partial\varphi/\partial x$.

$$u' + \frac{\alpha \alpha_x - \alpha_z}{1 + \alpha^2} u + \frac{\dot{\zeta}_z - \alpha \dot{\alpha}}{1 + \alpha^2} = 0 \quad (\text{A3.2})$$

Here the derivative is considered as a derivation of the variable x .

Taking into account the relation (10) we can represent derivations with respect to z as follows



$$\begin{aligned}\dot{\zeta}_z &= \frac{\partial}{\partial t}(k\zeta) = \dot{k}\zeta + k\dot{\zeta} \\ \alpha_z &= \frac{\partial^2 \zeta}{\partial x \partial z} = \frac{\partial}{\partial x}(k\zeta) = k_x \zeta + k\alpha\end{aligned}\quad (\text{A3.3})$$

Synchronous processes $\zeta, \alpha, \dot{\zeta}, \dot{\alpha}, \alpha_x, k, \dot{k}, k_x$ can be easily reproduced using the AR model.

In result we have the following equation

$$u' + f(x)u + g(x) = 0 \quad (\text{A3.4})$$

where

$$\begin{aligned}f(x) &= \frac{\alpha\alpha_x - k_x\zeta - k\alpha}{1 + \alpha^2} \\ g(x) &= \frac{\dot{k}\zeta + k\dot{\zeta} - \alpha\dot{\alpha}}{1 + \alpha^2}\end{aligned}\quad (\text{A3.5})$$

General solution of equation (A3.4) is

$$u(x) = e^{-F(x)} \left(\eta + \int_{\xi}^x g(y) e^{F(y)} dy \right) \quad (\text{A3.6})$$

Here (ξ, η) are initial conditions of differential equation (A3.4);

$$F(x) = \int_{\xi}^x f(y) dy \quad (\text{A3.7})$$

We are free to choose the origin. Let us choose a point with zero initial conditions $(0, 0)$. In this case we have

$$F(x) = \ln \sqrt{1 + \alpha(x)^2} - \int_0^x \frac{k_x \zeta + k\alpha}{1 + \alpha^2} dy \quad (\text{A3.8})$$

Denote the second integral in (A3.8) through $I(x)$. Then the final solution can be found in the following way

$$u(x) = \frac{1}{\sqrt{1 + \alpha^2}} e^{I(x)} \int_0^x \frac{\dot{k}\zeta + k\dot{\zeta} - \alpha\dot{\alpha}}{\sqrt{1 + \alpha^2}} e^{-I(y)} dy \quad (\text{A3.9})$$





Application of Computing Hydrodynamic Forces and Moments on a Vessel without Bernoulli's Equation

Arthur M. Reed

David Taylor Model Basin, Carderock Division, Naval Surface Warfare Center

`arthur.reed@navy.mil`

ABSTRACT

Reed & Telste (2011) presented a methodology for computing the forces and moments on a vessel that converts the traditional integration of the pressure over the hull surface into an impulse, which is the time derivative of several integrals of the velocity potential over the surface of the vessel and possibly over the free surface near the vessel. This eliminates the need to evaluate Φ_t , Φ_x , Φ_y , Φ_z at every instant in time, which results when Bernoulli's equation is used to compute the pressures. The present work presents some examples of applying the impulsive theory to 2- and 3-dimensional bodies.

KEYWORDS

Hydrodynamic forces; Momentum theory; Hydrodynamic impulse

INTRODUCTION

Reed & Telste (2011), Scлавounos (2012) and Scлавounos & Lee (2012) have presented a nonlinear model for the treatment of the potential flow problem governing the responses of a vessel in steep random waves. Boundary value problems were derived for the disturbance radiation and diffraction velocity potentials relative to the ship-fixed coordinate system. A sectional force method treats as unknown the sectional force distribution along the ship length as opposed to the local pressure.

The derivation of correct sectional force distributions has played a central role in the theory of aerodynamics and hydrodynamics. The direct application of Bernoulli's equation is complicated by a number of facts. The first is the need to evaluate gradients of the velocity

potential, which may be a delicate computational task within a panel method. The second is the proper treatment of the longitudinal gradients of the ambient and disturbance potentials. A third fact which arises in connection with the present nonlinear time-domain theory is the proper interpretation of time derivatives with respect to the ship-fixed coordinate system and the careful treatment of time derivatives in the vicinity of the free-surface ship-hull intersection.

These complications with the direct application of Bernoulli's equation are mitigated if the integrated sectional forces are instead evaluated by the proper application of the momentum conservation theorem. Expressions have been derived for the sectional force distributions which are simple functions of the sectional integrals of the velocity potential. This impor-



tant result circumvents in an elegant and robust manner the need to interpret the longitudinal convective terms in Bernoulli's equation. Moreover, the presence of a sectional integral of the velocity potential in the force expression suggests that this is the fundamental quantity needed for the evaluation of the sectional and total forces, as opposed to the local values of the pressure or velocity potential. Finally, this sectional force formulation allows for a simple and robust interpretation of time derivatives when the sectional wetted surface is time dependent as the vessel sections move in and out of the free surface.

SUMMARY OF MOMENTUM THEORY

Assume as an earth-fixed reference a right-handed coordinate system (X, Y, Z) and a ship-fixed right-handed coordinate system (x, y, z) centered at an arbitrary point B with the xy -plane parallel to the calm-water surface, $Z = 0$, when the ship is at rest (Figure 1). The ship position in space is completely defined by the rectilinear displacement vector $\Xi_B(t) = \xi_1(t)\mathbf{i} + \xi_2(t)\mathbf{j} + \xi_3(t)\mathbf{k}$ from the origin of the earth-fixed coordinate system to the origin of the ship-fixed coordinate system and the Euler angles defined in the order $[\xi_6(t), \xi_5(t), \xi_4(t)]$.

The Boundary Value Problem and Its Decomposition

The free surface is assumed to be a single-valued function of the horizontal coordinates X and Y . Surface tension is negligible. The fluid is assumed to be homogeneous, incompressible, and frictionless. The fluid flow is assumed to be irrotational. These conditions are sufficient to guarantee the existence of a velocity potential.

The Total Velocity Potential

In the fluid surrounding the ship, the total velocity potential is Φ . It satisfies the Laplace equation,

$$\nabla^2 \Phi = 0,$$

within the fluid domain bounded by the free-surface, $Z = \zeta(X, Y, t)$, and the hull of the ship. The total potential satisfies at least a linear free-surface boundary condition on $Z = \zeta(X, Y, t)$.¹

Velocity of Points on the Hull

To obtain the hull boundary condition satisfied by Φ , we first consider a point fixed on the hull (fixed in the ship-fixed frame of reference). The vectors \mathbf{x} and \mathbf{X} from the origins of the ship-fixed and earth-fixed coordinate systems to the point, respectively, satisfy the equations

$$\begin{aligned} \mathbf{X} &= X\mathbf{i} + Y\mathbf{j} + Z\mathbf{k} \\ \mathbf{x} &= x\bar{\mathbf{i}} + y\bar{\mathbf{j}} + z\bar{\mathbf{k}} \\ \mathbf{x} &= \mathbf{X} - \Xi_B(t) \end{aligned}$$

where $\Xi_B(t) = \xi_1\mathbf{i} + \xi_2\mathbf{j} + \xi_3\mathbf{k}$ is the vector from the origin of the earth-fixed coordinate system to the origin of the ship-fixed coordinate system. Since the point is fixed on the hull, x , y , and z are independent of time. Consequently, the ship-fixed time derivative of \mathbf{x} vanishes. We have

$$\mathbf{0} = \frac{d^*\mathbf{x}}{dt} = \frac{d\mathbf{X}}{dt} - \frac{d\Xi_B}{dt} - \boldsymbol{\Omega} \times \mathbf{x}$$

where d^*/dt and d/dt operating on a vector obtain the ship-fixed and earth-fixed time derivatives of the vector, respectively. The velocity \mathbf{v}_{SHIP} of the point on the hull is then

$$\mathbf{v}_{SHIP} = \frac{d\mathbf{X}}{dt} = \frac{d\Xi_B}{dt} + \boldsymbol{\Omega} \times \mathbf{x}. \quad (1)$$

Hull Boundary Condition

The hull-surface-boundary condition requires that the normal velocity of a fluid particle on the hull surface match the normal velocity of the hull:

$$\mathbf{n} \cdot \nabla \Phi = \mathbf{n} \cdot \left(\frac{d\Xi_B}{dt} + \boldsymbol{\Omega} \times \mathbf{x} \right) \mathbf{n} \cdot \mathbf{v}_{SHIP}$$

where \mathbf{v}_{SHIP} is given by (1).

¹As the free-surface boundary condition is not used in the development of the momentum theory for the force, the specific free-surface boundary condition chosen is not important.

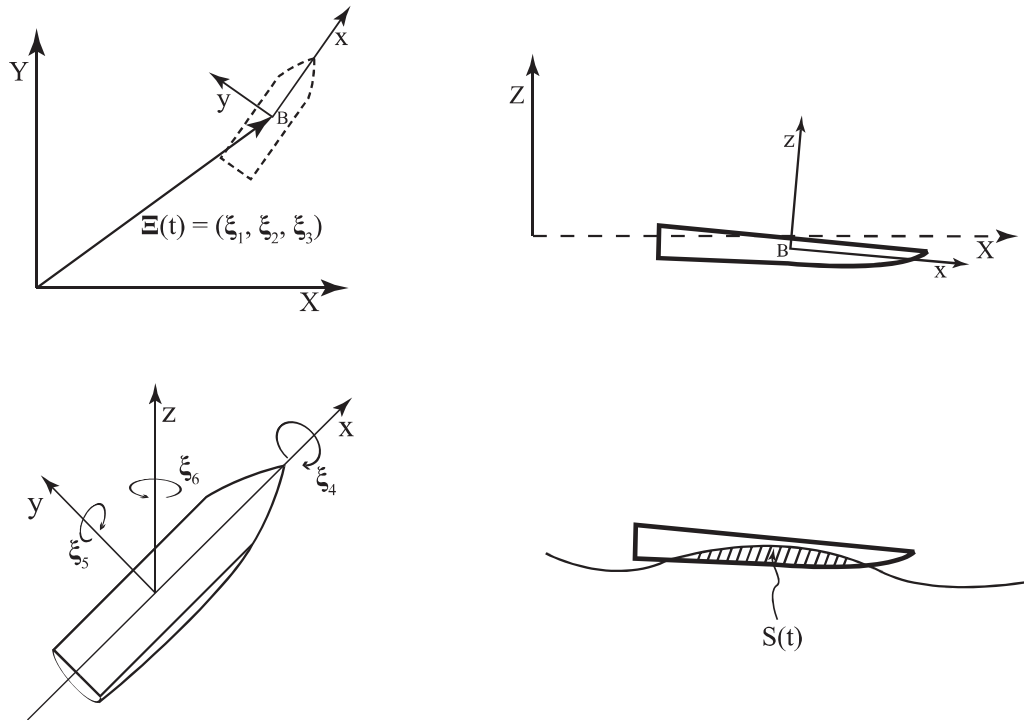


Fig. 1 Coordinate systems for the nonlinear ship response problem.

Incident Wave Potential

In the absence of a body, the velocity potential would have been the ambient velocity potential ϕ_I , which satisfies the Laplace equation,

$$\nabla^2 \phi_I = 0,$$

in the fluid below the free-surface elevation $Z = \zeta_I(X, Y, t)$.

The ambient wave velocity potential, ϕ_I , is assumed to satisfy the same free-surface boundary condition as the total velocity potential, but on $Z = \zeta_I(X, Y, t)$.

The Disturbance Velocity Potential

A disturbance potential, ϕ_D , is defined everywhere in the fluid domain according to the equation

$$\phi_D = \Phi - \phi_I.$$

The difference in wave elevation between the total wave elevation around the hull and the ambient wave potential that would have existed in the absence of the ship is ζ_D . It obviously

satisfies the equation

$$\zeta_D = \zeta - \zeta_I.$$

The free-surface boundary condition for the disturbance potential is derived from that of the total velocity potential, substituting $\phi_I + \phi_D$ and $\zeta_I + \zeta_D$ for Φ and ζ in the total velocity potential free-surface boundary condition and linearizing in ϕ_D and ζ_D .

Hull Boundary Condition for the Disturbance Potential

Using the decomposition of the total potential as the sum of the incident-wave potential and a disturbance potential, we obtain as the body boundary condition the equation,

$$\mathbf{n} \cdot \nabla \phi_D = \mathbf{n} \cdot \mathbf{v}_{SHIP} - \mathbf{n} \cdot \nabla \phi_I,$$

where \mathbf{v}_{SHIP} is given by (1).

The Fluid Force on the Vessel

The purely three-dimensional case of a vessel oscillating in six degrees of freedom in steep ambient waves is considered. The sectional force is

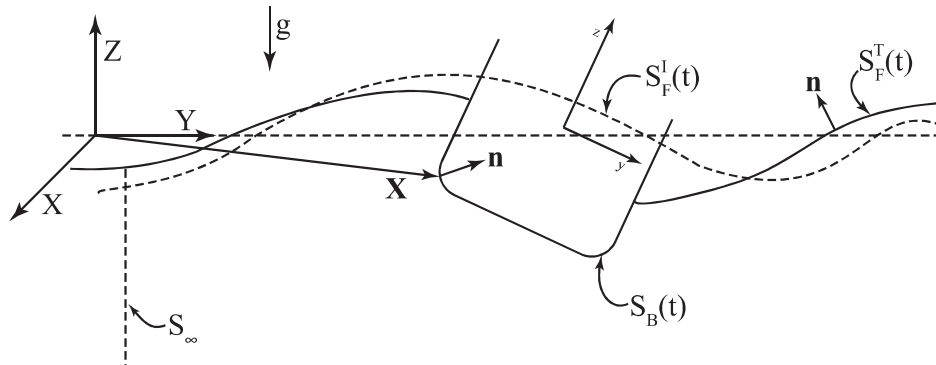


Fig. 2 Coordinate system for vessel undergoing rectilinear and rotational displacement in steep ambient waves

presented relative to the ship-fixed coordinate system.

Figure 2 illustrates a 3D vessel undergoing rectilinear and rotational displacements in steep ambient waves. The fully nonlinear free-surface elevation is $\zeta(t)$ and the corresponding total free surface is denoted by $S_F^T(t)$. The nonlinear wave elevation of the ambient wave alone is $\zeta_I(t)$ and the corresponding free-surface elevation is denoted by $S_F^I(t)$. The difference between the two free-surface elevations is assumed to be finite. Yet, this difference is expected to be small, except possibly near the vessel. This assumption is essential for the derivation of an approximate form of the three-dimensional force acting on the vessel using the momentum theorem. The fluid in the volume V bounded by the wetted surface S_B^T of the hull, the free surface S_F^T , and a control surface S_∞^T is considered:

$$S^T = S_B^T + S_F^T + S_\infty^T.$$

The control surface is fixed with respect to the earth-fixed coordinate system.

Starting with the momentum theorem applied over the control volume bounded by S^T , the fluid force is given by

$$\mathbf{F}_{\text{FLUID}} = \rho \frac{d}{dt} \iiint_V dV \nabla \Phi = \rho \frac{d}{dt} \iint_{S^T} dS \Phi \mathbf{n}.$$

Applying Gauss' theorem to convert the volume integral to an integral over the surface of the control volume (which includes the in-

stantaneous wetted surface of the vessel) and employing the transport theorem (Serrin, 1959; Smirnov, 1964, §120),

$$\frac{d}{dt} \iiint_{V_C} dV f(\mathbf{x}, t) = \iiint_{V_C} dV \frac{\partial f}{\partial t} + \iint_{\partial V_C} dS f V_n,$$

where V_C is a control volume and ∂V_C is the boundary of the control surface; Newman's identity (Newman, 1977),

$$\iint_{\partial V_C} dS \left[\nabla \varphi \frac{\partial \varphi}{\partial n} - \frac{1}{2} \nabla \varphi \cdot \nabla \varphi \mathbf{n} \right] = 0,$$

which holds for any velocity potential φ within a volume enclosed by the surface ∂V_C ; and the fact that the disturbance velocity generated by the vessel approaches zero at infinity to derive the total force on the vessel, with no approximations, the total force acting on the vessel is given by

$$\begin{aligned} \mathbf{F}_{\text{TOT}} &= -\rho \iint_{S_B^T} dS \left(\frac{\partial \Phi}{\partial t} + \frac{1}{2} \nabla \Phi \cdot \nabla \Phi + gZ \right) \mathbf{n} \\ &= -\rho \frac{d}{dt} \iint_{S_B^T} dS \Phi \mathbf{n} - \rho g \iint_{S_B^T} dS Z \mathbf{n} \\ &\quad - \rho \frac{d}{dt} \left[\iint_{S_F^T} dS \Phi \mathbf{n} - \iint_{S_F^I} dS \phi_I \mathbf{n} \right] \\ &\quad - \rho g \left[\iint_{S_F^T} dS Z \mathbf{n} - \iint_{S_F^I} dS Z \mathbf{n} \right], \end{aligned}$$



where S_B^I , S_F^I and S_E^I are defined above.

Invoking the weak-scatter approximation, whereby it is assumed that the wave due to the disturbance (radiation and diffraction disturbances) caused by the presence of the vessel are small relative to the incident wave, and expanding the disturbance wave in a Taylor series about the incident wave results in the approximate total force acting on the vessel,

$$\begin{aligned} \mathbf{F}_{\text{TOT}} \simeq & -\rho \frac{d}{dt} \iint_{S_B^I} dS \phi_D \mathbf{n} - \rho \frac{d}{dt} \iint_{S_B^I + S_W^I} dS \phi_I \mathbf{n}' \\ & - \rho g \iint_{S_B^I + S_W^I} dS Z \mathbf{n}' \\ & - \rho \frac{d}{dt} \iint_{S_E^I} dS \phi_D \mathbf{n} - \rho g \iint_{S_E^I} dS \zeta_D \mathbf{n}, \end{aligned} \quad (2)$$

where S_B^I is the surface of the vessel up to the undisturbed incident wave, S_W^I is the waterplane of the vessel cut by the incident wave, S_E^I is the surface of the incident wave exterior to the waterplane of the vessel, and \mathbf{n}' points downward on S_W^I and into the body on S_B^I .

Three force components may be identified in (2): the buoyancy force, Froude-Krylov force, and disturbance force. The buoyancy force is

$$\mathbf{F}_B \simeq -\rho g \iint_{S_B^I} dS Z \mathbf{n}.$$

where we have used the ‘‘approximately equal’’ relation because we are integrating up to the incident wave height along the hull rather than the ‘‘disturbed’’ wave height.

In defining the traditional Froude-Krylov and disturbance forces, we add

$$-\rho \iint_{S_B^I} dS \left(\frac{\partial \phi_I}{\partial n} - U_n \right) \nabla \phi_I,$$

to the Froude-Krylov force (and subtract this

term from the disturbance force), yielding

$$\begin{aligned} \mathbf{F}_{F-K} = & -\rho \frac{d}{dt} \iint_{S_B^I} dS \phi_I \mathbf{n} + \rho \frac{d}{dt} \iint_{S_W^I} dS \phi_I \mathbf{n} \\ & - \rho \iint_{S_B^I} dS \left(\frac{\partial \phi_I}{\partial n} - U_n \right) \nabla \phi_I \\ & + \rho g \iint_{S_W^I} dS Z \mathbf{n} \end{aligned}$$

where U_n denotes the normal velocity of the hull which is a known function of the vessel’s kinematics. The disturbance (radiation and diffraction) force is

$$\begin{aligned} \mathbf{F}_D \simeq & -\rho \frac{d}{dt} \iint_{S_B^I} dS \phi_D \mathbf{n} - \rho \frac{d}{dt} \iint_{S_E^I} dS \phi_D \mathbf{n} \\ & - \rho g \iint_{S_E^I} dS \zeta_D \mathbf{n} \\ & + \rho \iint_{S_B^I} dS \left(\frac{\partial \phi_I}{\partial n} - U_n \right) \nabla \phi_I. \end{aligned}$$

APPLICATION OF MOMENTUM THEORY

In order to investigate the validity of the momentum theory based impulsive forces derived in Reed & Telste (2011), Scлавounos (2012) and Scлавounos & Lee (2012); and summarized above, the results of two studies will be presented. First there will be response-amplitude operators (RAO’s) for a containership, and second there will be the results from a nonlinearity study for a two-dimensional circular cylinder that is compared with linear experimental results.

For these computations, a linearized version of the momentum theory is employed, where it is assumed the $-\rho \frac{d}{dt} \iint_{S_E^I} dS \phi_D \mathbf{n}$ in

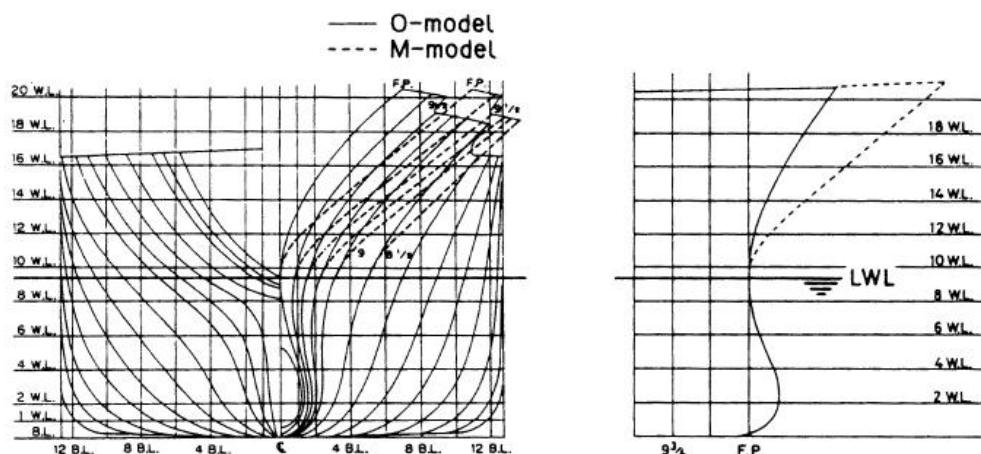


Fig. 3 Body Plan and Bow Profile for S-175 Containership (O-Model). (Watanabe, *et al.*, 1989)

(2) is negligible, resulting in

$$\begin{aligned}
 \mathbf{F}_{\text{LIN}} \approx & -\rho \frac{d}{dt} \iint_{S_B^I} dS \phi_D \mathbf{n} - \rho \frac{d}{dt} \iint_{S_B^I + S_W^I} dS \phi_I \mathbf{n}' \\
 & - \rho g \iint_{S_B^I + S_W^I} dS Z \mathbf{n}' - \rho g \iint_{S_E^I} dS \zeta_D \mathbf{n} \\
 \approx & \iint_{z=0} dS \left(\frac{\partial \phi}{\partial t} + g \zeta \right) \mathbf{k},
 \end{aligned} \tag{3}$$

where the latter form of the equation represents the linear dynamic free-surface condition.

RAO's for S-175 Containership

To understand the general applicability of the impulse theory for the forces and moments on a ship, the linear motions of the S-175 containership are predicted in head and stern-quartering seas at two Froude numbers, $F_n = 0.0$ and 0.2 . The S-175 containership (Watanabe, *et al.*, 1989) is a 175.0 m vessel, with a beam of 25.4 m and a draft of 9.5 m; it displaces 24,742 t. The body plan and bow profile of the vessel are shown in Fig. 3. This vessel has been used as a standard geometry for many seakeeping studies by the International Towing Tank Conference (ITTC), (*cf.*, O'Dea, *et al.*, 1992).

The motions of the S-175 are predicted using three or four different methods, three using pressure integration over the hull surface with Bernoulli's equation; the fourth being

momentum-theory based impulse method. The first pressure integration method is a conventional strip theory, similar to that of Salvesen, *et al.* (1970), implemented in the University of Michigan code SHIPMO; the second is the conventional strip theory with the Ogilvie-Tuck corrections (Ogilvie & Tuck, 1969); and the third is the University of Michigan nonlinear strip theory (UMBest)² (*cf.*, Bandyk, 2009).

Starting with the traditional head-seas case, the heave and pitch response amplitude operators (RAO's) and phase angles of the responses of S-175 are predicted at $F_n = 0.0$ and 0.2 . The heave and pitch RAO's and phase angles of the containership are presented in Figs. 4 and 5, respectively, as a function of wave length over ship length, L/λ .

At $F_n = 0.0$ the heave and pitch RAO's and phase angles from predictions by all four methods are in very close agreement over the entire range of L/λ 's. However, at $F_n = 0.2$, there is a distinct increase in the RAO's at the peaks of the responses for both UMBest and momentum-theory results relative to the conventional strip theory and Ogilvie-Tuck predictions—the conventional strip theory and Ogilvie-Tuck results agree with each other, as do UMBest and momentum theory results. The phase angles for all four methods agree.

As a consequence of this simplest linear

²In the plots that follow, the UMBest results are labeled "Current Method".

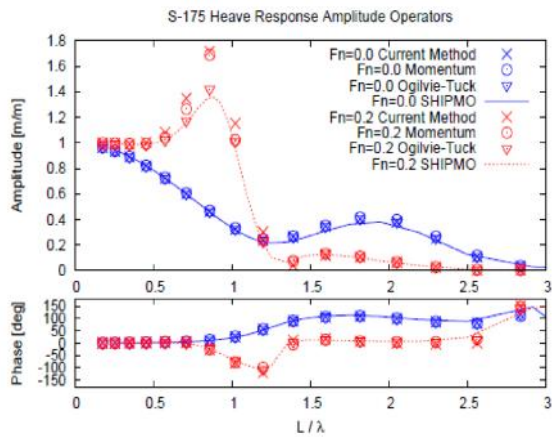


Fig. 4 Heave Response-amplitude Operator and Phase Angle as a Function of L/λ for S-175 at $F_n = 0.0$ & 0.2 in Head Seas ($\beta = 180^\circ$). (Courtesy of R. F. Beck, *et al.*; U. Mich.)

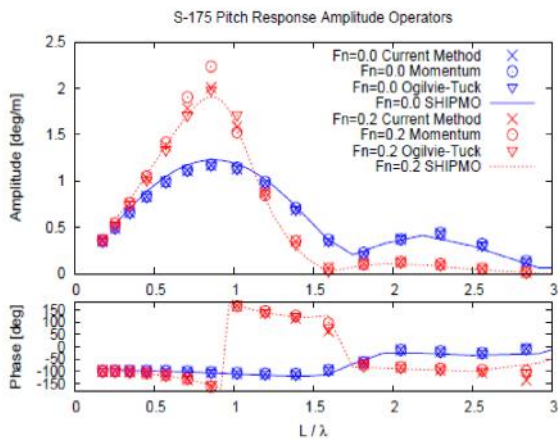


Fig. 5 Pitch Response-amplitude Operator and Phase Angle as a Function of L/λ for S-175 at $F_n = 0.0$ & 0.2 in Head Seas ($\beta = 180^\circ$). (Courtesy of R. F. Beck, *et al.*; U. Mich.)

ship-motion prediction case, it can be concluded that the momentum formulation is correct. We shall now examine its performance in a full six-degrees-of-motion case.

The next comparison of the theories is for S-175 in stern-quartering seas at two Froude numbers, where motion responses in all six-degrees-of-freedom are expected. In this case, we only have results for conventional strip theory and the nonlinear strip theory—no Ogilvie-Tuck predictions to compare with the momentum theory results. These results are pre-

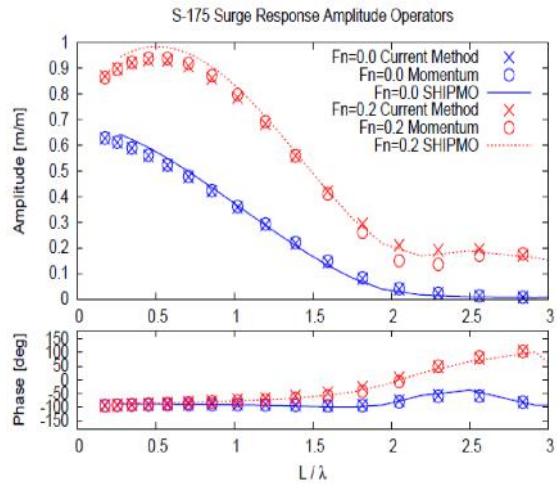


Fig. 6 Surge Response-amplitude Operator and Phase Angle as a Function of L/λ for S-175 at $F_n = 0.0$ & 0.2 in Stern-quartering Seas ($\beta = 45^\circ$). (Courtesy of R. F. Beck, *et al.*; U. Mich.)

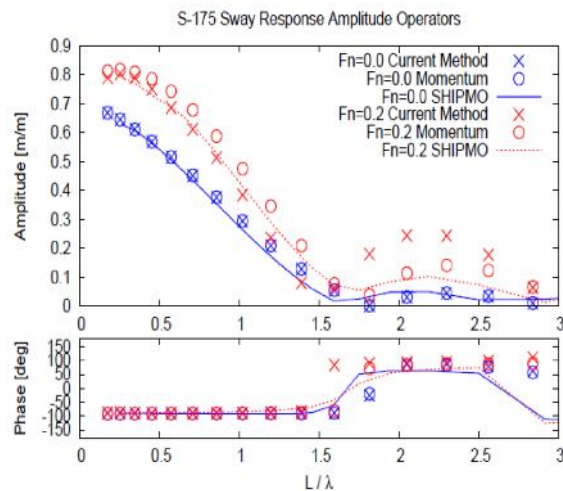


Fig. 7 Sway Response-amplitude Operator and Phase Angle as a Function of L/λ for S-175 at $F_n = 0.0$ & 0.2 in Stern-quartering Seas ($\beta = 45^\circ$). (Courtesy of R. F. Beck, *et al.*; U. Mich.)

sented as RAO's and phase angles versus L/λ in Figs. 6–11 for each mode of motion—surge, sway, heave, roll, pitch and yaw, respectively.

As was the case for head seas, at $F_n = 0.0$ the predictions in all modes of motion agree substantially for all three methods. Where

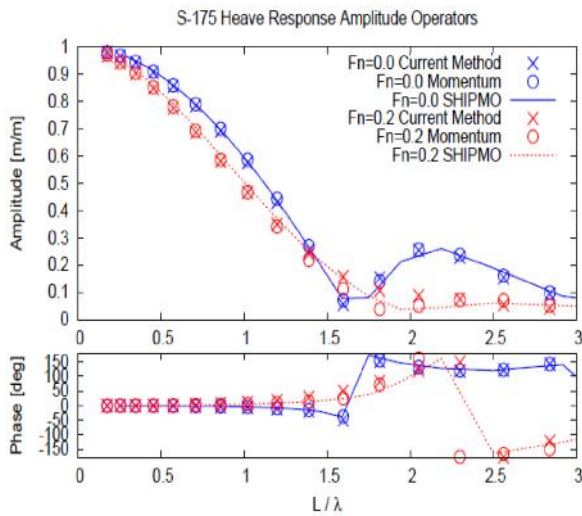


Fig. 8 Heave Response-amplitude Operator and Phase Angle as a Function of L/λ for S-175 at $F_n = 0.0$ & 0.2 in Stern-quartering Seas ($\beta = 45^\circ$). (Courtesy of R. F. Beck, *et al.*; U. Mich.)

there are slight deviations, the results from the nonlinear strip theory and the momentum formulation agree quite well.

For $F_n = 0.2$, there are significant differences in the results from the three prediction methods, particularly for sway and yaw—this is likely due to the effect of the method in which the “controller” is implemented and operates to keep the ship at speed and on heading, the results for each mode of motion will be discussed in order.

The $F_n = 0.2$ surge results (Fig. 6) agree well across the entire range of L/λ , except for a slight spread between all three methods of prediction for a short interval around $L/\lambda = 2.0$ – 2.25 , where the surge response is relatively small anyway. The surge phases agree between all three prediction methods.

For smaller L/λ 's, the sway results (Fig. 7) agree reasonably well, with the momentum method, the RAO being slightly higher than those of the conventional and nonlinear strip theories. However, for $L/\lambda > 1.5$, the RAO from the nonlinear strip theory increases relative to the other two methods, to exceed the conventional strip theory by a factor of roughly

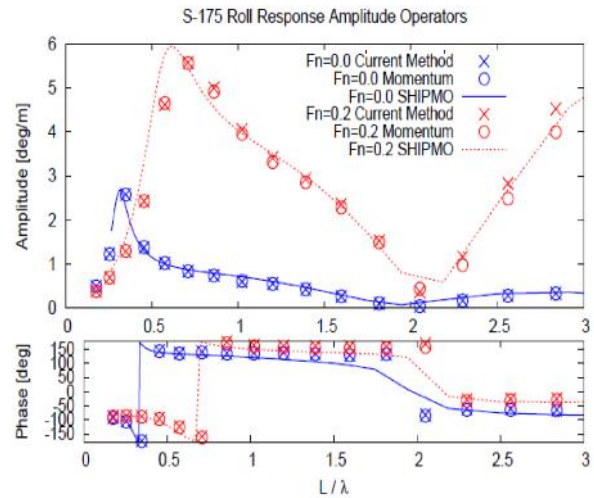


Fig. 9 Roll Response-amplitude Operator and Phase Angle as a Function of L/λ for S-175 at $F_n = 0.0$ & 0.2 in Stern-quartering Seas ($\beta = 45^\circ$). (Courtesy of R. F. Beck, *et al.*; U. Mich.)

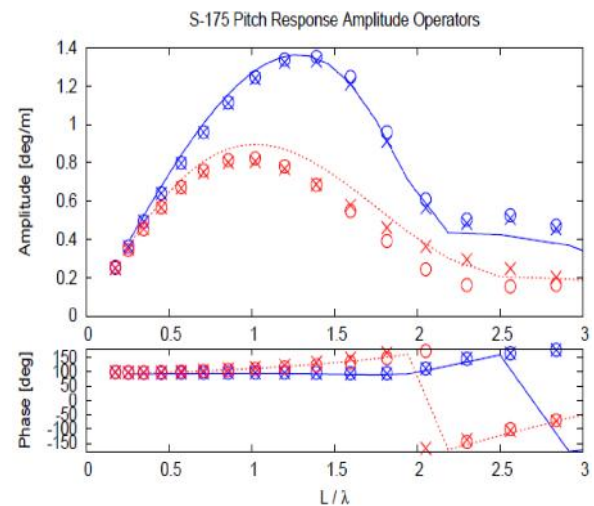


Fig. 10 Pitch Response-amplitude Operator and Phase Angle as a Function of L/λ for S-175 at $F_n = 0.0$ & 0.2 in Stern-quartering Seas ($\beta = 45^\circ$) — Legend is as Given in Fig. 9. (Courtesy of R. F. Beck, *et al.*; U. Mich.)

2.5 times, but by $L/\lambda \sim 3$, all three methods are back in agreement. Except at the highest L/λ 's, the phases agree. However, the L/λ at which the phase of the nonlinear strip theory jumps is lower than that of both conventional strip theory and momentum theory.

Examination of the predicted heave RAO's

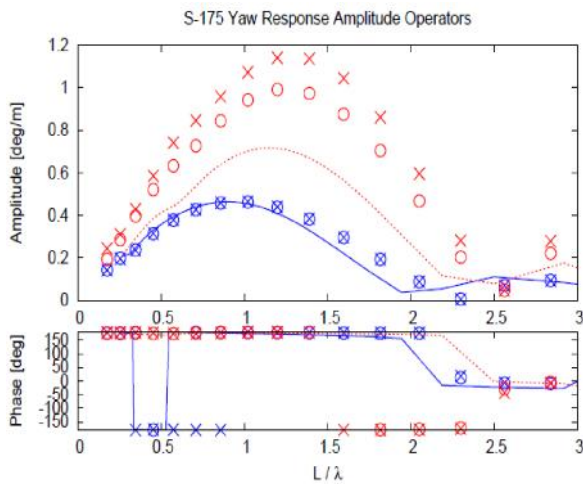


Fig. 11 Yaw Response-amplitude Operator and Phase Angle as a Function of L/λ for S-175 at $F_n = 0.0$ & 0.2 in Stern-quartering Seas ($\beta = 45^\circ$) — Legend is as Given in Fig. 9. (Courtesy of R. F. Beck, *et al.*; U. Mich.)

(Fig. 8) shows results that are very similar to those for surge, but with even smaller differences. Accounting for the wraparound in the phase angle, at $F_n = 0.2$ the phase for heave is very similar to that of surge, which is not the case for $F_n = 0.0$.

The comparison of the roll results (Fig. 9) is also similar to those of surge and heave. However, there is a slight shift to the right (higher L/λ) in the location of the peak of the RAO for the nonlinear strip theory and the momentum theory results relative to the location of the peak for conventional strip theory. It is noted that after achieving a minimum at around $L/\lambda = 2.0$, the RAO starts to increase again. This increase in RAO is probably a consequence of the roll moment created by the rudder's activation as a consequence of the controller that keeps the vessel on heading.

Through the resonant peak of the pitch RAO (Fig. 10), the momentum theory and the nonlinear strip theory agree quite well, and are slightly below the conventional strip theory results. However, for $L/\lambda > 1.75$, the nonlinear strip theory and momentum theory results start to separate, with the momentum theory results staying below the conventional strip theory re-

sults, while the nonlinear strip theory RAO increases to slightly above that of the conventional strip theory. By $L/\lambda = 2.75$, all three sets of predictions have converged to the same result.

At $F_n = 0.2$ the yaw results (Fig. 11) show the greatest differences in RAO responses of all the modes of motion across the three computational models. At the lowest and highest L/λ values, the three methods agree reasonably well. But in between the three sets of predictions show a resonant-like natural frequency peak, with the conventional strip theory having the smallest response and the nonlinear strip theory having the highest response by almost a factor of 2. The momentum theory results are in between, but closer to the nonlinear strip theory than to the conventional strip theory. Consistent with the sway observations, the peaks of the RAO for nonlinear strip theory and momentum theory are slightly to the right of the peak for the conventional strip theory. Again, this resonant like peak is probably a consequence of the heading controller. The reason that the deviations in the yaw responses are largest of all the modes of motion is because the rudder is most efficient at generating yaw responses, much more so than for sway or roll.

The momentum theory has now been tested in a much more challenging case than the head-seas case first tested—stern-quartering seas. Although the lateral-plane motions show some differences between the three prediction methods, it seems likely that these deviations are a result of the effects of the controller used to keep the vessel on course at this heading.

Nonlinearity Effects for 2-D Circular Cylinder

The previous RAO predictions have all been made for small-amplitude waves that result in small-amplitude motions. To test the large-amplitude aspects, and thus nonlinear aspects, the momentum theory was used to predict the added mass and damping of a two-dimensional semicircular cylinder that was forced in heave of varying amplitudes. The results of this ex-

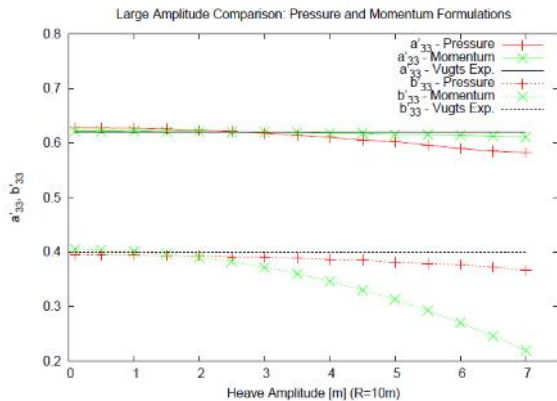


Fig. 12 Added Mass & Damping of Heaving 2-Dimensional Circular Cylinder as a Function of Heave Amplitude, $\omega\sqrt{r/g} = 1.0$. (Courtesy of R. F. Beck, *et al.*; U. Mich.)

ercise are shown in Fig. 12 for a single non-dimensional frequency, $\omega\sqrt{r/g} = 1.0$.

Figure 12 presents the non-dimensional added mass ($a'_{33} = a_{33}/\rho A$, where ρ is the mass density of the fluid and A is the immersed area of the section) and damping ($b'_{33} = b_{33}/\rho A\sqrt{r/g}$, where r is the radius and g is the acceleration due to gravity) as a function of the motion amplitude which varies from 0.1 m to 7 m for a 20 m diameter cylinder ($\xi_3/r = 0.01$ to 0.7). These results are predicted by both momentum theory and nonlinear strip theory with Bernoulli's equation for pressure integration. For reference, the added mass and damping measured by Vugts for small amplitude motions is also provided (Vugts, 1968). For small heave amplitude, the added masses by the two computational methods are in full agreement and agree with Vugts' experiments. As the heave amplitude increases, the added mass by nonlinear strip theory decreases slightly relative to the experimental result, while the added mass by momentum theory agrees substantially with Vugts' experimental results. For small amplitude, the damping from the two prediction methods agree and are in agreement with Vugts' experimental results. However, as the heave amplitude increases, the damping by the nonlinear strip theory decreases slightly (by an amount comparable to the decrease in the added mass), while the damping by momentum

theory decreases substantially.

It is hypothesized that the significant decrease in damping by the momentum theory is a result of using the linearized form (3) which neglects the integral of the potential over the free surface. Although this is only an untested hypothesis, it is consistent with the damping being a function of the waves being radiated away from the cylinder.

CONCLUSIONS

The new nonlinear momentum formulation presented in Reed & Telste (2011), Sclavounos (2012) and Sclavounos & Lee (2012) has been used to predict response-amplitude operators for the S-175 containership in head and stern-quartering seas. The momentum theory predictions are found to be in substantial agreement with those by a nonlinear strip theory. The nonlinear aspects of the theory are tested against large-amplitude forced heave of a semi-circular cylinder. The added mass computations are found to be in agreement with the results by Bernoulli's equation in conjunction with the nonlinear strip theory and experiments by Vugts. However, it is found that there is an unexpected decrease in the damping for increasing heave amplitude. It is hypothesized that this is a consequence of having employed a linearized form of the momentum theory for the calculations. This bears further investigation.

ACKNOWLEDGMENTS

The efforts of Prof. Robert F. Beck of the University of Michigan and his graduate students Xinshu Zhang, Jim Bretl, Piotr Bandyk and Rahul Subramanian who provided the computational results reported herein are very much appreciated.

This work was supported by Drs. L. Patrick Purtell and Paul Hess of the Office of Naval Research (ONR).



REFERENCES

- Bandyk, P. J. (2009) A Body-Exact Strip Theory Approach to Ship Motion Computations. Ph.D. Dissertation, Univ. Mich., Ann Arbor, MI, xii+122 p.
- Newman, J. N. (1977) *Marine Hydrodynamics*. MIT Press, xiii+402 p., Cambridge, MA.
- O'Dea, J. F., E. J. Powers & J. Zselecsky (1992) Experimental Determination of Nonlinearities in Vertical Plane Ship Motions. *Proc. 19th Symp. Naval Hydro.*, Seoul, Korea, pp. 73–91.
- Ogilvie, T. F. & E. O. Tuck (1969) A rational strip theory of ship motions: Part I. Dept. of Nav. Arch. and Marine Eng., College of Eng., Univ. Michigan, Report No. 013, ix+92 p.
- Reed, A. M. & J. G. Telste (2011) Computing Hydrodynamic Forces and Moments on a Vessel without Bernoulli's Equation. *Proc. 12th Int'l Ship Stability Workshop*, Washington, D.C., pp. 341–51.
- Salvesen, N., E. O. Tuck & O. Faltinsen (1970) Ship motions and sea loads. *Trans. SNAME*, 78:250–87.
- Sclavounos, P. D. (2012) Nonlinear Impulse of Ocean Waves on Floating Bodies. *J. Fluid Mech.*, 697:316–35.
- Sclavounos, P. D. & S. Lee (2012) A Fluid Impulse Nonlinear Theory of Ship Motions and Sea Loads. *Proc. 29th Symp. Naval Hydro.*, Gothenburg, Sweden, 14 p.
- Serrin, J. (1959) Mathematical principles of classical fluid mechanics. *Encyclopedia of Physics*, Vol. VIII/I, pp. 125–263, Springer-Verlag, Berlin.
- Smirnov, V. I. (1964) *A Course of Higher Mathematics, Vol. II: Advanced Calculus*. Pergamon Press, 630 p., Oxford.
- Vugts, J. H. (1968) The hydrodynamic coefficients for swaying, heaving and rolling cylinders in a free surface, *Int'l Shipbuilding Prog.*, 15(167):251–76.
- Watanabe, I., M. Ueno, H. Sawada (1989) Effects of Bow Flare Shape to the Wave Loads of a container ship. *J. Society Naval Architects of Japan*, 166:259–66





Captive Model Test and Numerical Simulation on the Manoeuvring Forces in Waves

Young Jae Sung, *Hyundai Heavy Industries Co., Ltd.*, ojae@hhi.co.kr

Hyun-ho Lee, *Hyundai Heavy Industries Co., Ltd.*, hhlee@hhi.co.kr

Tae-il Lee, *Hyundai Heavy Industries Co., Ltd.*, tilee@hhi.co.kr

Sungeun Kim, *American Bureau of Shipping*, sungeunkim@eagle.org

ABSTRACT

For a validation of numerically simulated manoeuvring forces in waves, a series of captive model tests by using a Planar Motion Mechanism (PMM) were conducted in waves. The simulated surge force, sway force and yaw moment of an obliquely moving KCS in regular following waves were compared with the measured ones. Satisfactory agreements between measurements and simulations could confirm that the developed program can make reliable estimates not only on the manoeuvring forces in waves but also on the variation of dynamic stability of a ship with its relative position in waves.

Keywords: *manoeuvring forces, waves, captive model test, numerical simulation*

1. INTRODUCTION

The manoeuvrability of a ship has been evaluated by the size of turning trajectories or the overshoot angles in calm water or relatively mild sea trial conditions. However, the ship manoeuvrability in waves is of vital importance for navigational safety of seagoing ships, and there have been many researches on this subject (ITTC, 2008, IMO SLF 53/WP.4, 2011).

A traditional approach on manoeuvring in waves is the system based simulation using 4-DOF or 6-DOF mathematical models. Two major groups of mathematical models have been used; one is the unified theory model and the other is the two time scale model (Skejic & Faltinsen, 2008). The unified theory model utilises the linear convolution integral formulation by Cummins to account for the unsteady wave memory effects. Ankudinov (1983), Bailey et al. (1998), and Fossen (2005)

developed this approach. Although this model is capable of estimating some of the mean second-order wave effects by integrating linear forces on the time dependent wetted body surface, it does not account for all the terms presented in the expression for the mean second-order wave loads (Skejic & Faltinsen, 2008). Similar way of pressure integration on the instantaneous wetted surface has been used by the two time scale method. However, by accounting for the second-order effects in association with the linearization of boundary value problem, a more accurate estimation on the drifting forces becomes possible. The name “two time scale” comes from that it separates the high frequency dependent wave induced motions from the low frequency dependent manoeuvring motions. The hydrodynamic forces due to wave-body interactions are calculated by sea-keeping theories such as strip method, slender-body theory or 3-D panel method in frequency or in time domain. Then,



the simulation of manoeuvring motions is conducted by using manoeuvring theory.

Experimental methods also have played important roles to investigate the manoeuvring in waves. Free sailing model tests in waves (Hirano et al., 1980, Ueno et al., 2003, Yasukawa, 2006) or full scale trials in following waves have been conducted to observe the manoeuvring behaviours in waves. Forces in waves, especially the nonlinear wave drift forces, have been investigated by the captive model tests (Ueno et al., 2000, Yasukawa & Adnan, 2006, Xu et al., 2007, Lee et al., 2009). Variation of manoeuvring coefficients and dynamic stability of a ship with its relative position in following waves have been investigated by the tests in waves which are generated by the fixed wave making board on the carriage or on the circulating water channel (Hamamoto, 1971, 1973, Renilson & Driscoll, 1981, Son & Nomoto, 1982) or by the actuating wave maker (Matora et al., 1981, Fujino et al., 1982).

These previous researches have found that there are two major concerns for the manoeuvring in waves; one is the wave drift forces or nonlinear wave loads at low frequency which would affect the manoeuvring motions significantly, and the other is the course keeping in astern seas. When a ship is travelling in following waves, it may be liable to unpleasant and even frightening behaviour called broaching. Several causes of this phenomenon have been proposed; (a) the wave exciting yaw moment becomes remarkably higher than the hydrodynamic course keeping moment by the helm of rudder (Motor et al., 1981), (b) reduction of rudder effectiveness in the following seas (Renilson & Driscoll, 1981), (c) instability of course keeping of a ship travelling on the downhill slope of wave (Wahab & Swaan, 1964, Hamamoto, 1971, 1973, Son & Nomoto, 1982), (d) the action of turning moment due to the cross flow component of the orbital motion of water particle.

Based on these previous researches, we would like to develop a numerical simulation procedure which can give reliable estimates on the manoeuvring performances of a ship in waves. The developed procedure determines the effects of radiation, diffraction and forward speed by 3-D panel method. Viscous effects on the manoeuvring related horizontal plane forces and moment were taken into account by including supplementary viscous damping coefficients. For the validation of the estimated horizontal plane forces and moment in waves, the simulated forces and moment were compared with the measurements of captive model tests in regular waves. Satisfactory agreements between measurements and simulations could confirm that the developed program give reliable estimate not only on the manoeuvring forces in waves but also on the variation of dynamic stability of a ship in its relative position in waves

2. NUMERICAL SIMULATION

The nonlinear wave-body hydrodynamics interaction forces and the ship motions in the time domain were numerically simulated by using the ABS NLOAD3D program. Numerical solutions of the problem were based on an approximate nonlinear time domain approach, which combines the body-nonlinear hydrostatic and Froude-Krylov forces with a 3-D body-linear solution of the wave body disturbance potential and nonlinear models for viscous and appendage forces (see Figure 1).

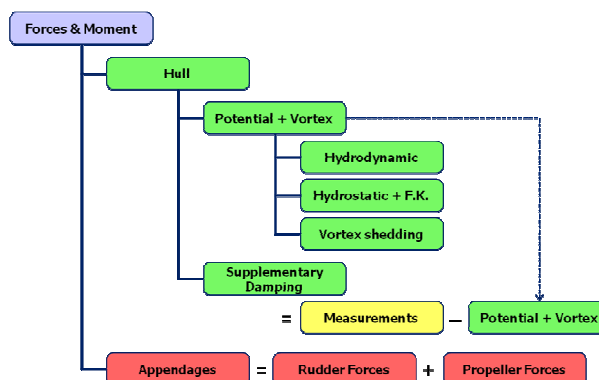


Figure 1: Calculation of forces and moment.

Effects of radiation, diffraction and steady forward speed were predicted by solving the unsteady 3-D velocity potential of a ship moving through the incident wave field. Hydrostatic restoring and incident wave forces were computed by integrating the hydrostatic and Froude-Krylov pressure on the portion of the hull beneath the instantaneous incident wave surface. Viscous effects on the manoeuvring related horizontal plane forces and moment were taken into account by including supplementary damping coefficients, which are analogous to the manoeuvring derivatives used in the system based manoeuvring simulation. These supplementary damping coefficients were determined from captive model tests in calm water, so that the predicted hull forces and moment match the measured data. Rudder lift curve and propeller open water characteristics were used to determine the rudder and the propeller forces respectively. Details of the calculation method are described by Kim & Sung (2012).

3. CAPTIVE MODEL TEST

3.1 Model Ship and Arrangement

For the validation of the simulated manoeuvring forces and moment in waves, captive model tests were conducted at the towing tank of Hyundai Maritime Research Institute. A KCS model of 1/40 scale was used in the tests. KCS is a 3,600 TEU class container carrier designed by MOERI. It is one of the hulls chosen by the 24th ITTC for the benchmark study of ship manoeuvrability (Stern & Agdrup, 2008). Principal dimensions of KCS are listed in Table 1.

Table 1: Principal dimensions of KCS.

	Full scale	Model
$L_{PP} / B / T$ [m]	230/32.2/10.8	5.75/0.805/0.27
Disp. (∇) [m^3]	52030	0.8130
Prop. Dia. [m]	7.9	0.198
Rudder Height [m]	9.9	0.248
Speed	24.0 knot	1.952 m/s
$\dot{\delta}_{Rudder}$ [$^{\circ}/s$]	2.32	14.7

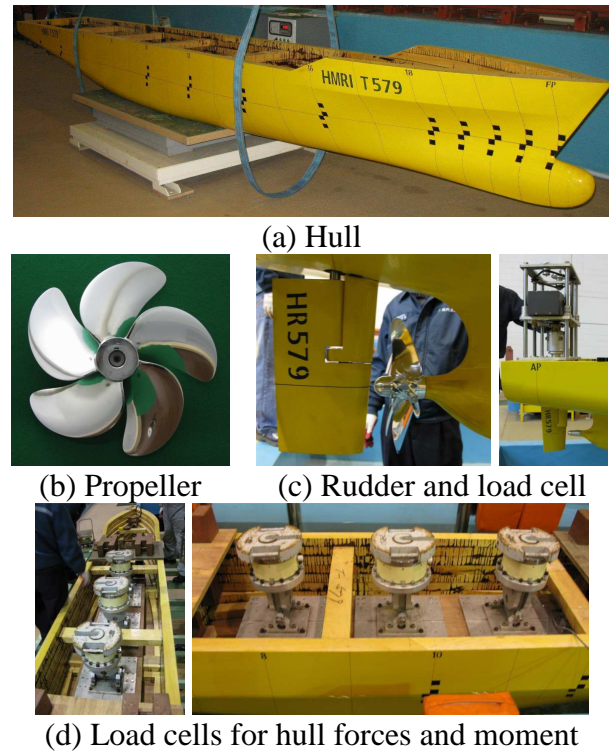


Figure 2: Photographs of KCS model.

An arrangement of the model ship is shown in Figure 2. The surge load cell, located at LCG, measured the longitudinal forces. Transverse forces and yaw moments were measured by two load cells that were equally spaced from LCG. These load cells were connected with PMM through the gimbal pistons. Hence, heave and pitch motions are free. All the measurements were done for more than 20 seconds at the 100 Hz. Coordinate systems for the measurements are shown in Figure 3.

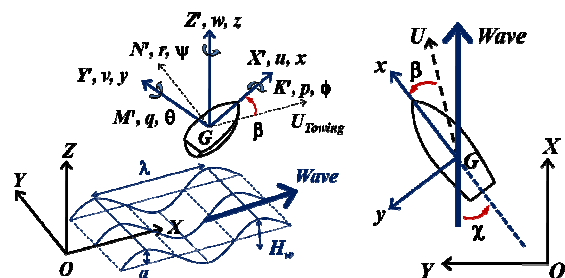


Figure 3: Coordinate systems.

3.2 Test Conditions

Captive model tests in calm water (Table 2 and 3) and in following regular waves (Table 4) were conducted. Calm water tests were



necessary to estimate the manoeuvring derivatives in modular type equations of manoeuvring motion. Details of the modular type equations of motion are described in Sung et al. (2009). The estimated derivatives were used to generate a set of tuning data for the determination of supplementary damping coefficients. The results from static drift tests in waves were used for the validation of simulated forces and moment.

Table 2: Bare hull test conditions in calm water.

Type of test (variable)	Range of variable
Static drift (β)	$0^\circ, \pm 2^\circ, \dots, \pm 24^\circ$
Pure sway (\dot{v}'_{\max})	0.05, 0.10, ..., 0.30
Yaw and drift (r'_{\max}, β)	$r'_{\max}: 0.1, 0.2, \dots, 0.6$ $\beta: 0^\circ, 3^\circ, \dots, 12^\circ$

Table 3: Fully equipped test conditions in calm water.

Type of test (variable)	Range of variable
Speed and rudder ($U/U_0, \delta$)	$U/U_0: 1.00, \dots, 0.50$ $\delta: 0^\circ, \pm 5^\circ, \dots, \pm 30^\circ$
Drift and rudder (β, δ)	$\beta: 0^\circ, 3^\circ, \dots, 12^\circ$ $\delta: 0^\circ$ and nonzero

Table 4: Bare hull test conditions in following waves.

Wave 1: $\lambda/L = 0.5, H_w/L = 0.013, \chi = 0^\circ$	
Type of test (variable)	Range of variable
Static drift (β)	$0^\circ, \pm 6^\circ, \dots, \pm 24^\circ$
Pure sway (\dot{v}'_{\max})	0.10, 0.20, 0.30
Yaw and drift (r'_{\max} & β)	$r'_{\max}: 0.1, 0.3, 0.5$ $\beta: 0^\circ, 9.0^\circ$
Wave 2: $\lambda/L = 1.0, H_w/L = 0.013 (0.026), \chi = 0^\circ$	
Type of test (variable)	Range of variable
Static drift (β)	$0^\circ, \pm 3^\circ, \dots, \pm 24^\circ$
Pure sway (\dot{v}'_{\max})	0.10, 0.20, 0.30
Yaw and drift (r'_{\max} & β)	$r'_{\max}: 0.1, 0.3, 0.5$ $\beta: 0^\circ, 3.0^\circ, 6.0^\circ, 9.0^\circ$
Wave 3: $\lambda/L = 1.5, H_w/L = 0.013 (0.026), \chi = 0^\circ$	
Type of test (variable)	Range of variable
Static drift (β)	$0^\circ, \pm 3^\circ, \dots, \pm 24^\circ$
Pure sway (\dot{v}'_{\max})	0.10, 0.20, 0.30
Yaw and drift (r'_{\max} & β)	$r'_{\max}: 0.1, 0.3, 0.5$ $\beta: 0^\circ, 4.5^\circ, 9.0^\circ$

4. MANOEUVRING IN CALM WATER

4.1 Manoeuvring Derivatives and Supplementary Damping Coefficients

The estimated manoeuvring derivatives in modular type equations of motion are listed at Table 5. These derivatives were used to generate a set of tuning data for the various combinations of drift angles and yawing rates. Diamond symbols in Figure 4 represent the generated tuning data. After a series of simulations at the same combinations of tuning data, the supplementary damping coefficients were determined to minimize the differences between the tuning data and the simulated forces and moment. Dotted lines in Figure 4 represent the calculated forces and moment by using the determined supplementary damping coefficients. The manoeuvring related hull forces and moment by the program show a good agreement with the tuning data.

Table 5: Manoeuvring derivatives for KCS.

$X'_H (\times 10^3)$ $= X_H / (0.5\rho L T U^2)$	X'_{vv}	-73.003
	X'_{rr}	-17.240
	$X'_{vr} + (m' + m'_y)$	296.015
$Y'_H (\times 10^3)$ $= Y_H / (0.5\rho L T U^2)$	$m' + m'_y$	371.582
	Y'_r	-23.357
	Y'_v	-249.073
	Y'_{vvv}	-1747.365
	Y'_{vrr}	-468.528
	$(m' + m'_x) - Y'_r$	172.686
	Y'_{rrr}	-26.864
$N'_H (\times 10^3)$ $= N_H / (0.5\rho L^2 T U^2)$	Y'_{rvv}	-423.637
	$N'_\dot{v}$	-10.374
	$I'_{zz} + J'_{zz}$	23.575
	N'_v	-143.366
	N'_{vvv}	-252.977
	N'_{vrr}	-49.808
	N'_r	-48.601
<i>Interaction coefficients</i>	N'_{rrr}	-30.995
	N'_{rvv}	-694.343
	$(1 - t_R)$	0.671
	$(1 + a_H)$	1.230
	$(x'_R + a_H x'_H)$	-0.617
ε	0.986	
	$\gamma (\beta_R \geq 0 / \beta_R < 0)$	0.522 / 0.315

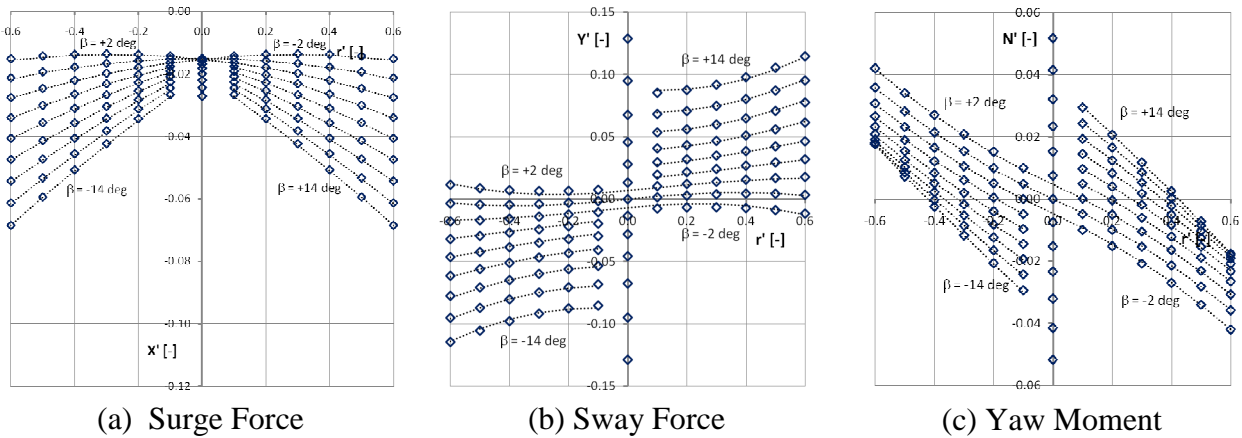


Figure 4: Determination of supplementary damping coefficients (\diamond : tuning data, dotted line: calculated by using the determined supplementary damping coefficients).

4.2 Propeller Force and Rudder Forces

Open water characteristics of geometrically similar propeller were used to calculate the thrust force by propeller (Figure 5).

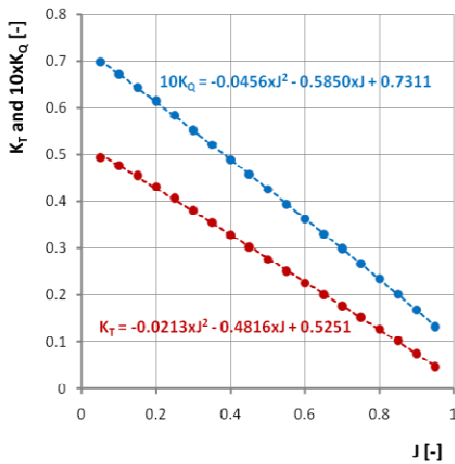


Figure 5: Propeller open water characteristics of KCS model propeller (Kim et al., 2006).

Lift and drag forces generated by rudder were estimated by using the following equations;

$$\text{Lift} = C_L \cdot (1/2) \cdot \rho U^2 \cdot A_R \quad (1)$$

$$\text{Drag} = C_D \cdot (1/2) \cdot \rho U^2 \cdot A_R \quad (2)$$

$$U^2 = u_R^2 + v_R^2 \quad (3)$$

where, A_R is rudder area. C_L and C_D are the lift and drag coefficients which were determined from the well known Fujii's prediction formula as shown in Figure 6 (Fujii & Tuda, 1961). U is the rudder inflow velocity which takes into account the effects of propeller stream. In the modular type equations of motion, the effects of propeller stream were accounted for by the longitudinal inflow velocity of rudder, u_R as the equation (4) (Yoshimura, 2005). Hence, the propeller loading condition can affect the rudder inflow velocity.

$$u_R = \varepsilon(1-w)u \sqrt{\eta \left\{ 1 + \kappa \left(\sqrt{1 + 8K_T / \pi J^2} - 1 \right) \right\} + (1-\eta)} \quad (4)$$

In the developing program, however, a fixed increment, Δu was added as a constant input to the surge speed ($u_R = u + \Delta u$)

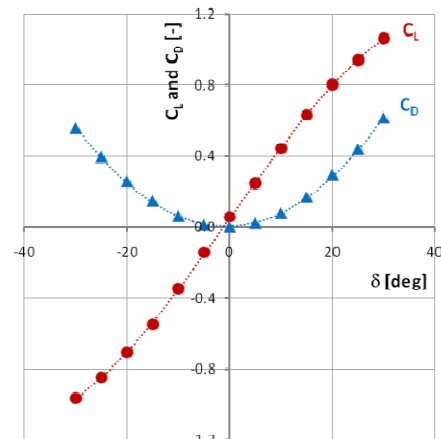


Figure 6: C_L and C_D of KCS rudder.



4.3 Manoeuvring Simulations in Calm Water

Simulated turning trajectories and heading angles in calm water from the present approach are compared with those from the modular type equations of motion in Figure 7. The approach speed is 1.952 m/s ($F_n=0.26$) and the rudder inflow velocity increment is 0.225 m/s. In case of zigzag manoeuvres, during which the speed of a ship doesn't change significantly, the estimated heading angles from the program show a good agreement with those from the modular type model simulation. In case of turning trajectories, however, steady turning diameters estimated by the program are quite larger than those by the modular type model simulations.

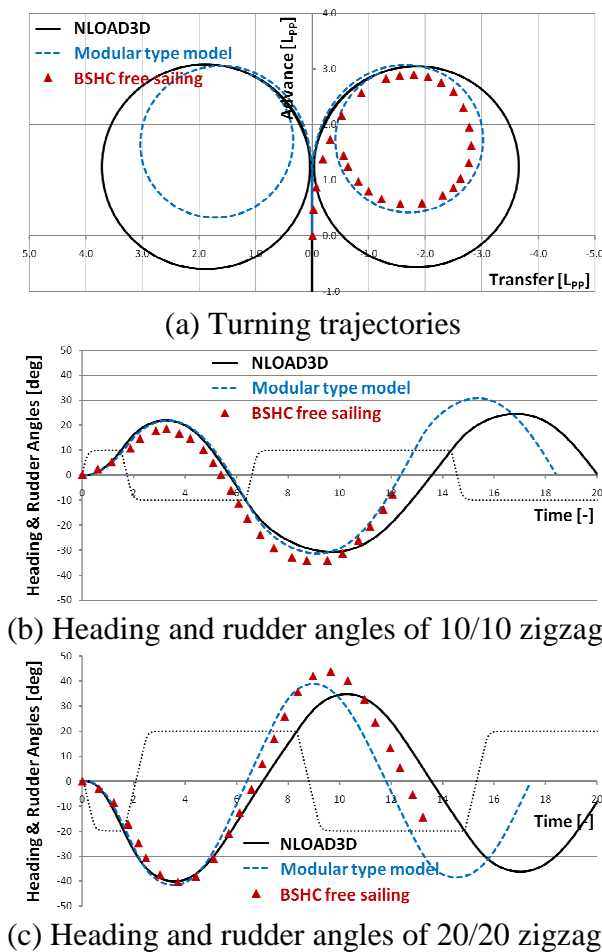


Figure 7: Simulated manoeuvring motions of KCS in calm water.

The adopted simple inflow speed model may be a cause of this disagreement. During the turning manoeuvre, a ship experiences significant increases in drift angle and decreases in speed. This causes the increase of propeller loading, $8K_T/\pi J$, and the rudder inflow velocity, u_R . In the modular type model simulation, the dependence of rudder inflow speed on propeller loading was taken into account by the equation (4). But the developed program assumed a fixed increment of rudder inflow velocity throughout the manoeuvring motions. The estimated surge speed and the rudder inflow speed are shown in Figure 8. During the turning motion, the rudder inflow speed by the developed program is quite smaller than that by the modular type model simulation, and this may cause the smaller rudder forces and the larger turning circles during steady turning state.

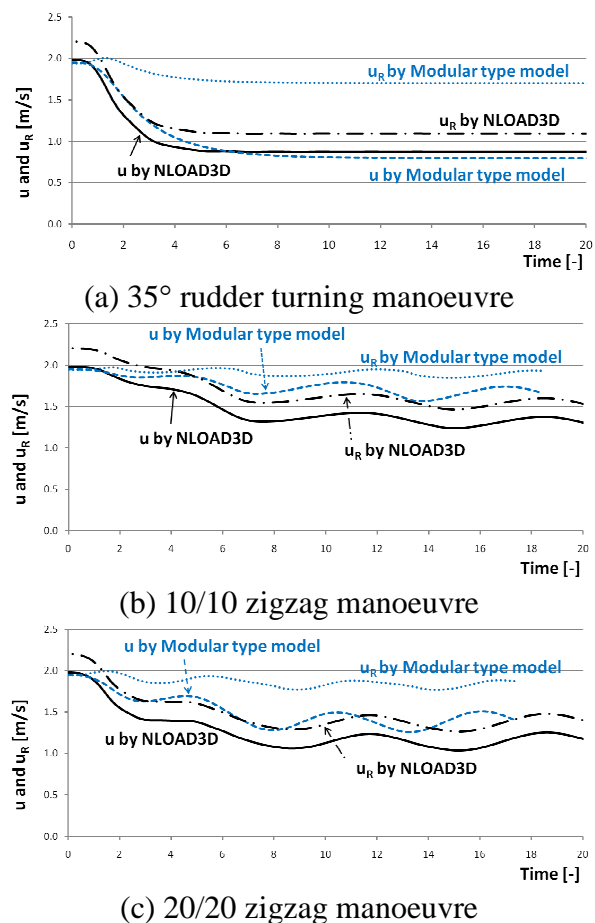


Figure 8: Simulated surge speed, u , and rudder inflow speed, u_R , of KCS in calm water.

5. MANOEUVRING IN WAVES

5.1 Forces and Moment from Drift Test

A typical variation of forces, moment and pitch angle with a ship's relative position in following waves are shown in Figure 9. In this figure, the hull is towed with 12° drift angle in the regular following waves of length ratio, λ/L of 1.5 and steepness ratio, H_w/λ of $1/57.5$. The relative phase velocity of wave, U_w/U_0 , is 1.879, hence the waves overtake the ship. Red diamonds are the measurements and blue solid lines are the simulated results. The simulation results show a good agreement with the measurements.

When the wave crest proceeds from LCG to bow, a ship experiences negative surge force. The opposite situation happens when the wave crest approaches from stern and proceeds to LCG. These variations of surge force, X are dominated by the hydrostatic and Froude-Krylov force component (red dotted line). The variations of sway force, Y , and yaw moment, N , are not as clear as those of surge force. However, we can find a relationship between the moment arm, N/Y , and the relative location of a ship in waves. The moment arm becomes shorter when a ship is on the rear slope of waves, while it becomes longer when a ship is on the front slope of waves. The longer moment arm is one of the well known characteristics of a directionally unstable ship. Hence, the measured and the simulated moment arms show a good agreement with the previous observations that a ship becomes directionally more unstable on the front slope of following waves. (Wahab & Swaan (1964), Renilson & Driscoll (1981) and Son & Nomoto (1982))

Forces and moments at the other conditions are compared in Figure 10. Except the slightly overestimated yaw moment at $\pm 24^\circ$ drift, the simulated forces and moment show a good agreement with the measurements.

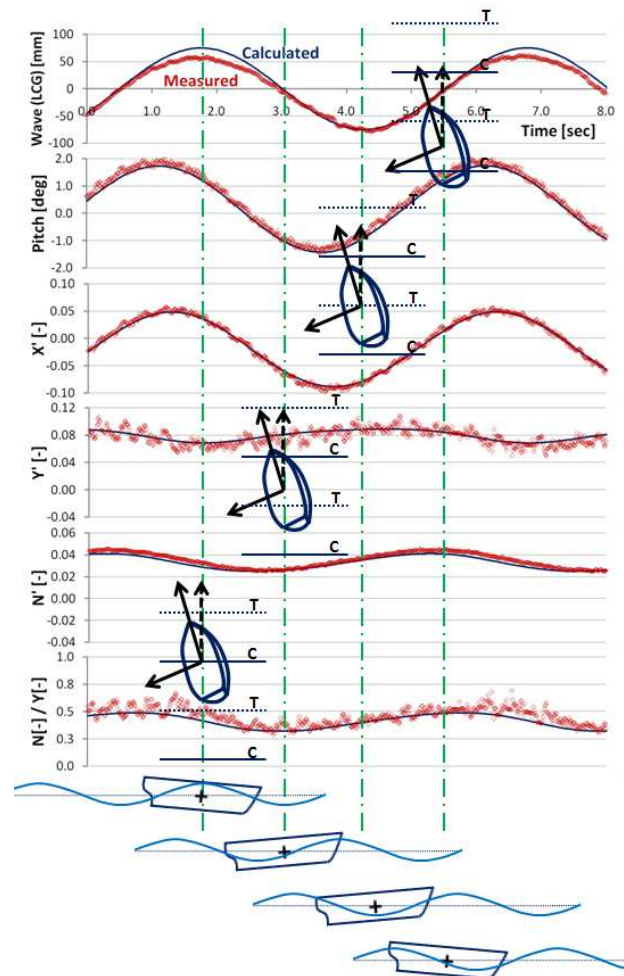


Figure 9: Surge and sway forces, yaw moment and pitch angle of KCS during a drift test in wave of $\lambda/L = 1.5$, $H_w/L = 0.026$, $\chi = 12^\circ$.

5.2 Forces and Moment from Harmonic Oscillation Tests

Typical time series and FFT spectrums of measured forces and moment from the harmonic oscillation tests are shown in Figure 11 and 12. Figure 11 shows the results from the pure sway test with the oscillating frequency of 0.058 Hz. At this frequency the maximum non-dimensional sway acceleration, \dot{v}'_{\max} is 0.2. Figure 12 shows the results from the pure yaw test with the oscillating frequency of 0.071 Hz. Each test was performed in following waves of different wave lengths; $\lambda/L = 0.5, 1.0$ and 1.5 . The phases of measurements were adjusted so that they have the same sway phase. In case of surge force, X' , clear oscillations at the wave encounter frequencies can be found.

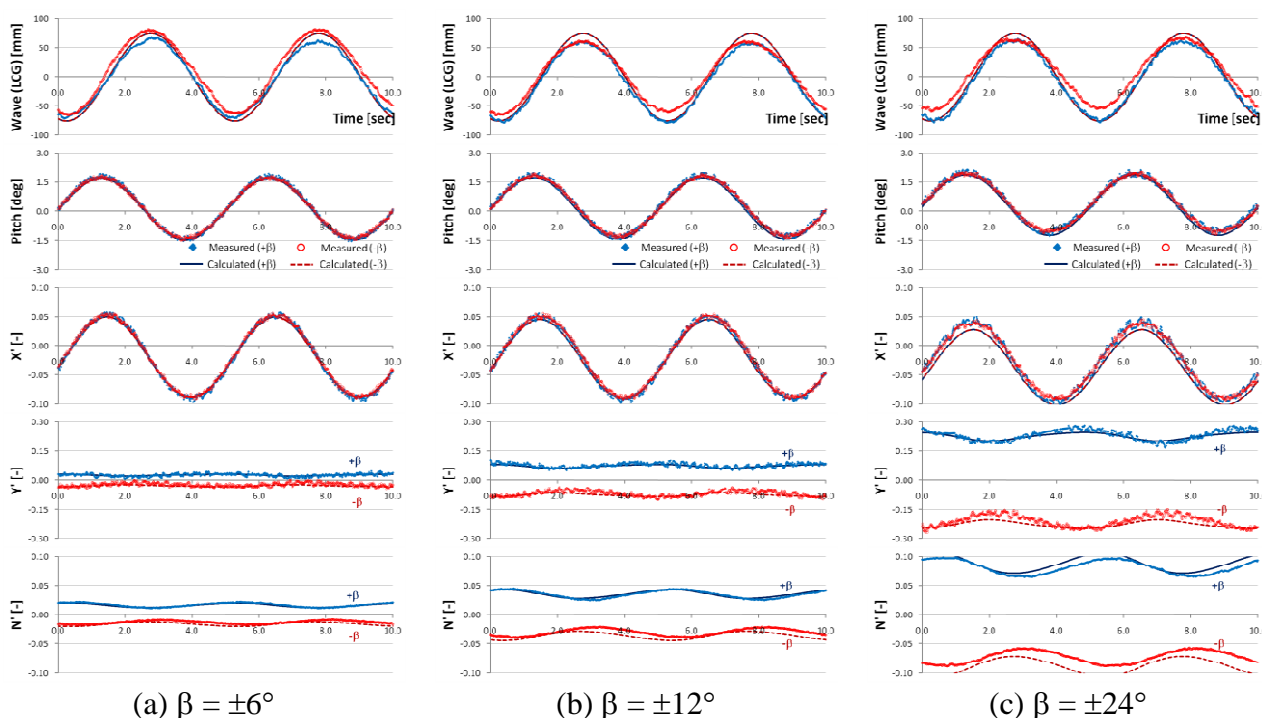


Figure 10: Surge and sway forces, yaw moment and pitch angle of KCS during a drift test in wave of $\lambda/L = 1.5$, $H_w/L = 0.026$, $\chi = 0^\circ$.

This means that the hydrostatic and Froude-Krylov component play a dominant role as it does in the oblique towing tests. In case of sway force and yaw moment, only the oscillations at PMM frequency can be clearly found. This means that the hull lift component is dominant in the sway force and yaw moment at the given test conditions. Hence, it was not easy to observe the effects of mean second order wave drift forces from the measurements. To observe such effects on the sway forces and yaw moments, low speed model test seems to be necessary in the future works.

5.3 Manoeuvring Simulations in Waves

Simulated turning and zigzag manoeuvring motions of KCS in waves are simulated as Figure 13 and 14 respectively. The approach speed and the rudder inflow velocity are the same as the calm water simulations. Variations of starboard turning trajectories in waves are shown in Figure 13. The tendencies of variation agree with those of previous

researches that the trajectories are drifted in both horizontal and perpendicular directions with respect to the wave progress directions and the shorter waves result in the larger drifted trajectories (Yasukawa, 2006, Yen et al., 2010, Seo & Kim, 2011).

Variations of heading angles of $10^\circ/10^\circ$ zigzag manoeuvre are shown in Figure 14. When the waves are coming from the starboard side, the shorter wave generates the larger variations on the heading angle. However, when the waves are coming from the bow, the wave of $\lambda/L=1.0$ generates the largest variation. This can be explained by the effects of relative wave directions on the wave drift forces. Yasukawa & Adnan (2006) observed that, in case of beam sea, the wave drift forces becomes larger for the shorter waves, and, in case of head sea, they becomes the largest near $\lambda/L=1.0$. These tendencies of wave drift forces agree with the variations of overshoot angles in different wave directions.

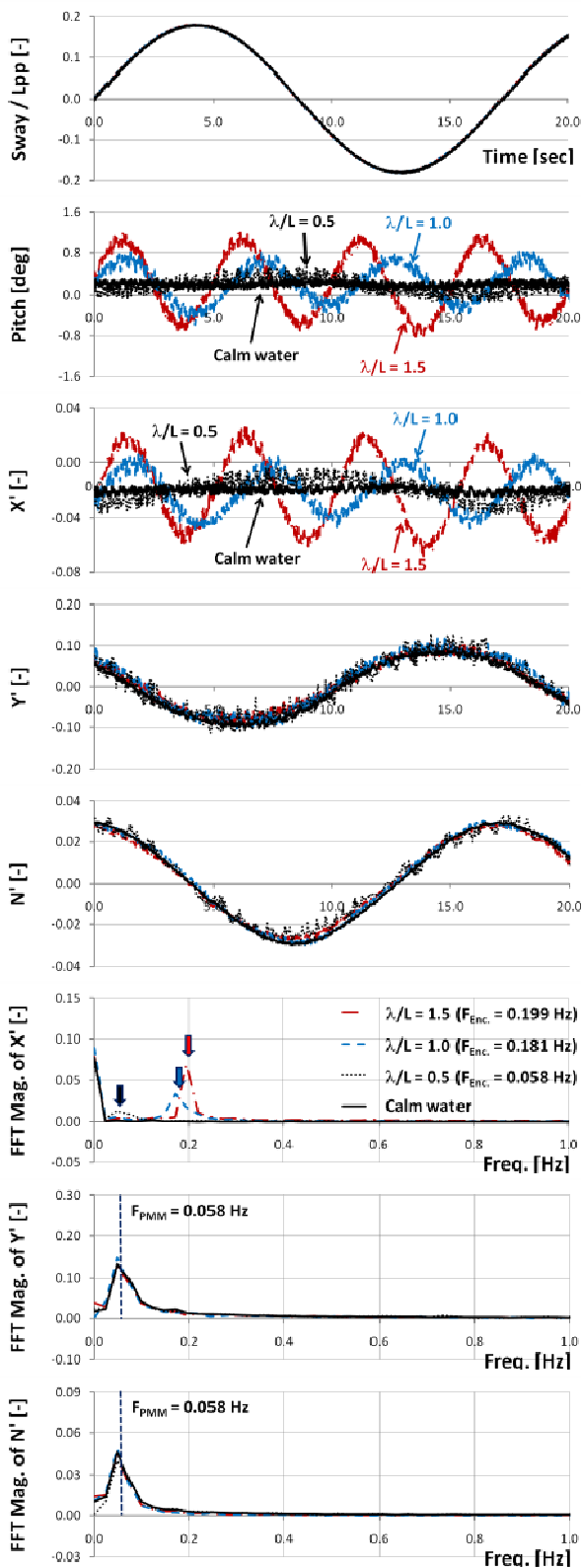


Figure 11: Surge and sway forces, yaw moment and pitch angle of KCS during pure sway tests of $\dot{v}'_{\max} = 0.2$ ($f_{\text{PMM}} = 0.058$ Hz) in regular following waves.

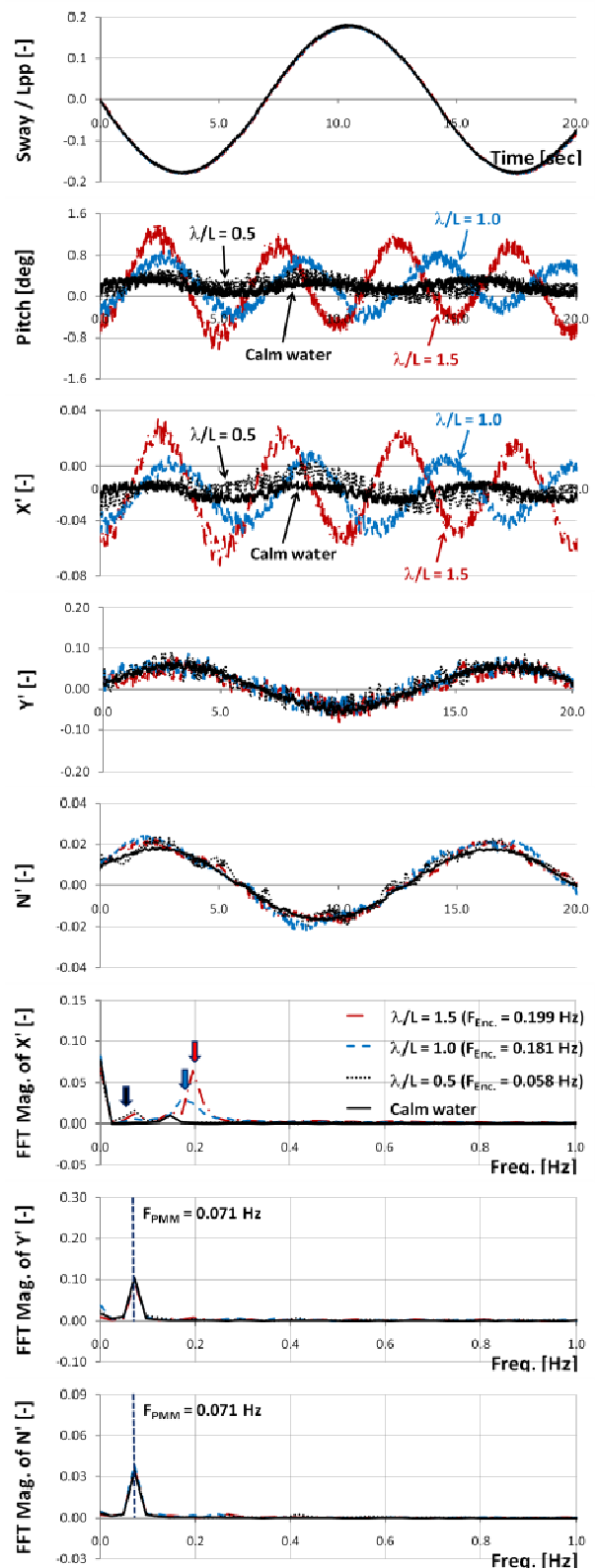
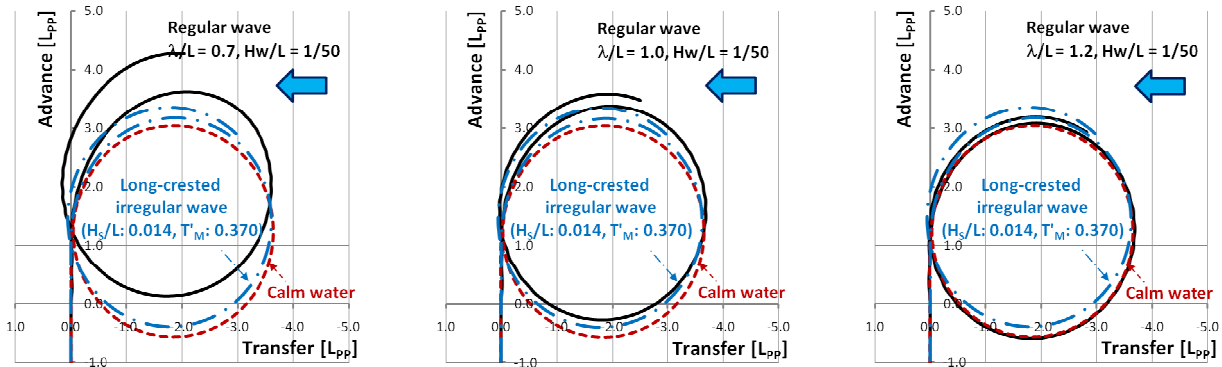
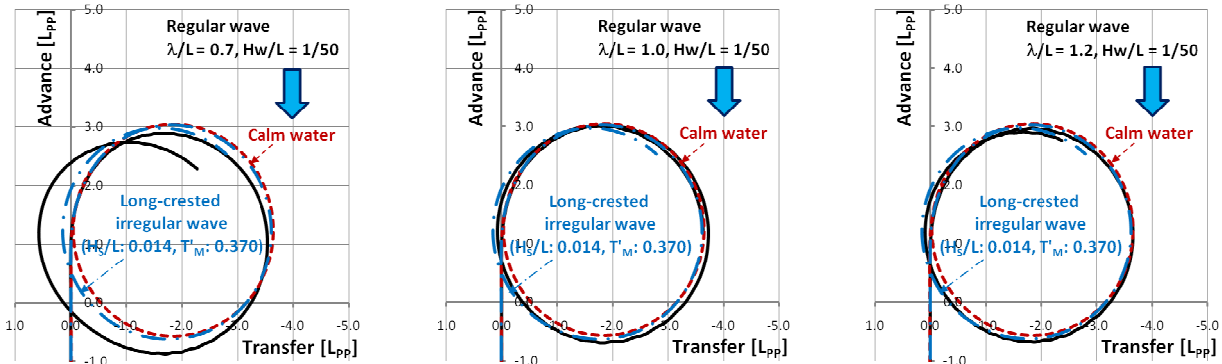


Figure 12: Surge and sway forces, yaw moment and pitch angle of KCS during pure yaw tests of $r'_{\max} = 0.3$ ($f_{\text{PMM}} = 0.071$ Hz) in regular following waves.

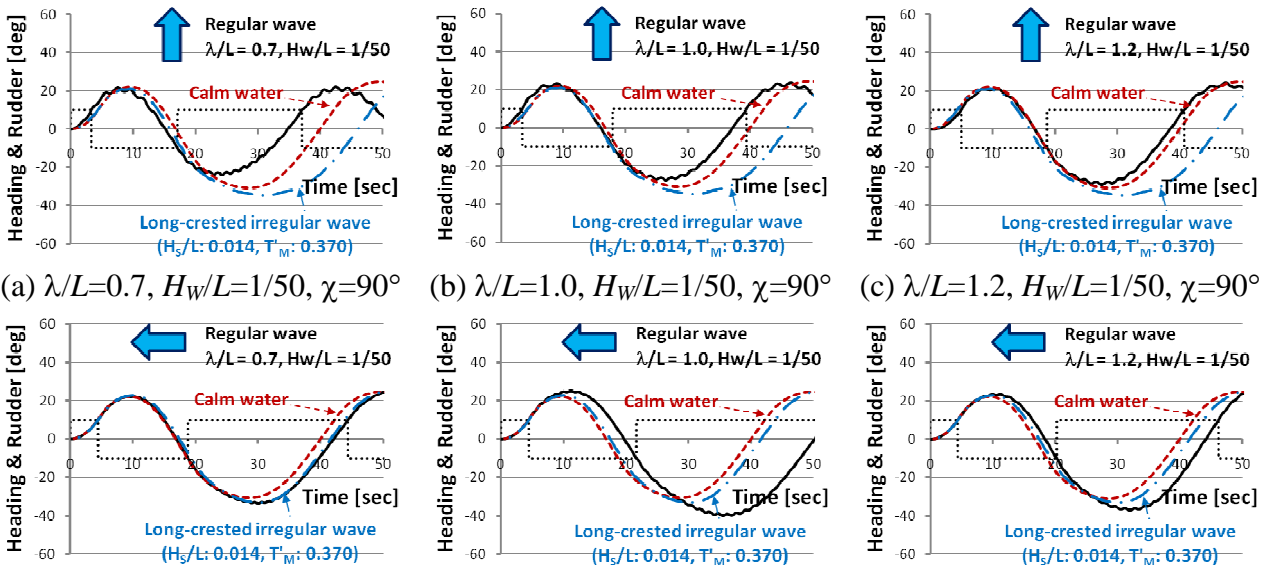


(a) $\lambda/L=0.7, H_w/L=1/50, \chi=90^\circ$ (b) $\lambda/L=1.0, H_w/L=1/50, \chi=90^\circ$ (c) $\lambda/L=1.2, H_w/L=1/50, \chi=90^\circ$



(d) $\lambda/L=0.7, H_w/L=1/50, \chi=180^\circ$ (e) $\lambda/L=1.0, H_w/L=1/50, \chi=180^\circ$ (f) $\lambda/L=1.2, H_w/L=1/50, \chi=180^\circ$

Figure 13: Starboard turning trajectories of KCS in waves.



(a) $\lambda/L=0.7, H_w/L=1/50, \chi=90^\circ$ (b) $\lambda/L=1.0, H_w/L=1/50, \chi=90^\circ$ (c) $\lambda/L=1.2, H_w/L=1/50, \chi=90^\circ$
(d) $\lambda/L=0.7, H_w/L=1/50, \chi=180^\circ$ (e) $\lambda/L=1.0, H_w/L=1/50, \chi=180^\circ$ (f) $\lambda/L=1.2, H_w/L=1/50, \chi=180^\circ$

Figure 14: Heading angles of 10/10 zigzag manoeuvres of KCS in waves.



6. CONCLUSIONS

In this study, a brief description about the numerical simulation approaches used in developing a numerical simulation tool which can estimate the manoeuvring performances of a ship in waves was introduced and some validation results were shown.

As a first step of the validation process, the manoeuvring forces in regular following waves calculated by the program were compared with the captive model test results. The calculated manoeuvring forces showed a good agreement with the measurements and the dominant role of hydrostatic and Froude-Krylov forces could be observed. Turning and zigzag manoeuvring motions calculated in regular waves showed well known drifting behaviours. These promising results from the comparison could give a more confidence in using the proposed approach. However, the rudder inflow velocity model needs to be updated to improve the accuracy of simulation.

7. REFERENCES

- Ankudinov, V., 1983, "Simulation Analysis of Ship Motions", Proceedings of International Workshop on Ship and Platform Motions, Berkeley, CA, USA, pp.384-403.
- Asai, S., 1981, "A Study on Check Helms for Course Keeping of a Ship under Steady External Forces", Journal of the Society of Naval Architects of Japan, No.150, pp.245~253.
- Bailey, P.A., Price W.G., and Temarel, P., 1998, "A Unified Mathematical Model Describing the Manoeuvring of a Ship Travelling in a Seaway", Transactions of RINA, Vol.140, pp.131-149.
- Fossen, T.I., 2005, "A Nonlinear Unified State-Space Model for Ship Maneuvering and Control in a Seaway", International Journal of Bifurcation and Chaos, Vol.15, pp.2717-2746.
- Fujii, H. and Tuda, T., 1961, "Experimental Research on Rudder Performance (2)" (in Japanese), Journal of the Society of Naval Architects of Japan, No.110, pp.31-42.
- Fujino, M., Yamasaki, K. and Ishii, Y., 1982, "On the Stability Derivatives of a Ship Travelling in the Following Waves" (in Japanese), Journal of the Society of Naval Architects of Japan, No.152, pp.167-179.
- Hamamoto, M., 1971, "On the Hydrodynamic Derivatives for the Directional Stability of Ships in Following Seas (1)", (in Japanese), Journal of the Society of Naval Architects of Japan, No.130, pp.83-94.
- Hamamoto, M., 1973, "On the Hydrodynamic Derivatives for the Directional Stability of Ships in Following Seas (2)", (in Japanese), Journal of the Society of Naval Architects of Japan, No.133, pp.133-142.
- Hirano, M., Takashina, J., Takaishi Y. and Saruta, T., 1980, "Ship Turning Trajectory in Regular Waves", Transactions of the West-Japan Society of Naval Architects, No.40, pp.17-31.
- IMO SLF 53/WP.4, 2011, "Report of the Working Group", London.
- ITTC, 2008, Proceedings of 25th ITTC, Vol. I, pp. 171-175.
- Kim, J., Kim, K.S., Kim, G.D., Park, I.R. and Van, S.H., 2006, "Hybrid RANS and Potential Based Numerical Simulation for Self-Propulsion Performances of the Practical Container Ship", Journal of Ship and Ocean Technology, Vol.10, No.4, pp.1-11
- Kim, S. and Sung, Y.J., 2012, "Numerical Simulations of Maneuvering and Dynamic Stability of a Containership in Waves", Proceedings of STAB 2012, Athens, Greece.
- Lee, S.K., Hwang, S.H., Yun S.W., Rhee, K.P.



- and Sung, W.J., 2009 “An Experimental Study of a Ship Manoeuvrability in Regular Waves”, Proceedings of MARSIM 2009, Panama City, Panama.
- Motora, S., Fujino, M., Koyanagi M., Ishida, S., Shimada, K. and Maki, T., 1981, “A Consideration on the Mechanism of Occurrence of the Broaching-to Phenomenon” (in Japanese), Journal of the Society of Naval Architects of Japan, No.150, pp.211-222.
- Renilson, M.R. and Driscoll, A., 1981, “Broaching-An Investigation into the Loss of Directional Control in Severe Following Seas”, Transactions of RINA, pp.253-273.
- Seo, M.K. and Kim, Y., 2011, “Numerical Analysis on Ship Maneuvering Coupled with Ship Motion in Waves”, Ocean Engineering, Vol.38, pp.1934-1945
- Skejic, R. and Faltinsen, O.M., 2008, “A Unified Seakeeping and Maneuvering Analysis of Ships in Regular Waves”, Journal of Marine Science and Technology, Vol.13, pp.371-394.
- Son, K.H. and Nomoto, K., 1982, “On the Coupled Motion of Steering and Rolling of a Ship in Following Seas”, (in Japanese), Journal of the Society of Naval Architects of Japan, No.152, pp.180-191.
- Stern, F. and Agdrup, K. (editors), 2009, “Proceedings of the Workshop on Verification and Validation of Ship Manoeuvring Simulation Methods, SIMMAN 2008”, FORCE Technology, September 2009, Lyngby, Denmark
- Sung, Y.J., Ahn, K.S., Lee, T.I. and Rhee, K.P., 2009, “Effects of the Self-Propulsion Point during PMM Test on the Prediction of Ship Manoeuvrability”, Proceedings of MARSIM 2009, Panama City, Panama.
- Ueno, M., Nimura, T., Miyazaki, H. and Nonaka K., 2000, “Steady Wave Forces and Moment Acting on Ships in Manoeuvring Motion in Short Waves”, Journal of the Society of Naval Architects of Japan, No.188, pp.163-172.
- Ueno, M., Nimura, T. and Miyazaki, H., 2003, “Experimental Study on Manoeuvring Motion of a Ship in Waves”, Proceedings of MARSIM 2003, Kanazawa, Japan.
- Wahab, R., and Swaan, W.A., 1964, “Course-keeping and Broaching of Ships in Following Seas”, Journal of Ship Research, Vol.7, No.4, pp.1-15.
- Xu, Y., Kinoshita, T. and Itakura, H., 2007, “A PMM Experimental Research on Ship Maneuverability in Waves”, Proceedings of the 26th Inter-national Conference on Offshore Mechanics and Arctic Engineering, OMAE2007-29521, San Diego, CA, USA.
- Yasukawa, H., 2006, “Simulations of Ship Maneuvering in Waves (1st report: turning motion)” (in Japanese), Journal of the Society of Naval Architects and Ocean Engineers, Vol.4, pp.127-136.
- Yasukawa, H. and Adnan, F.A., 2006, “Experimental Study on Wave-Induced Motions and Steady Drift Forces of an Oblique Moving Ship” (in Japanese), Journal of the Society of Naval Architects and Ocean Engineers of Japan, Vol.3, pp.133-138.
- Yen, T.G., Zhang, S., Weems, K. and Lin, W.M., 2010 “Development and Validation of Numerical Simulations for Ship Maneuvering in Calm Water and in Waves”, Proceedings of 28th Symposium on Naval Hydrodynamics, Pasadena, CA, USA.
- Yoshimura, Y., 2005 “Mathematical Model for Manoeuvring Ship Motion”, Proceedings of Workshop on Mathematical Models for Operations involving Ship-Ship Interaction, August 2005, Tokyo, Japan.



Assessment of Ship Roll Damping Through Full Scale and Model Scale Experiments and Semi-Empirical Methods

Carl-Johan Söder, *Wallenius Marine AB / KTH Royal Institute of Technology*, cjsoder@kth.se

Anders Rosén, *KTH Royal Institute of Technology* aro@kth.se

Sofia Werner, *SSPA Sweden AB*, sofia.werner@sspa.se

Mikael Huss, *Wallenius Marine AB*, mikael.huss@walleniusmarine.com

Jakob Kutteneuler, *KTH Royal Institute of Technology*, jakob@kth.se

ABSTRACT

This paper presents unique experimental set-ups in model scale and full scale for evaluating roll damping properties of a Panamax Pure Car and Truck Carrier at speed. The purpose of this study is to develop a method for the assessment of roll damping based on full scale trials and to validate the use of roll damping derived from model tests for full scale vessels. Experimental data are also used to assess a semi-empirical method that today provides input for the prediction of critical rolling events such as parametric rolling and severe rolling motions in general.

Keywords: *Roll damping, Parametric roll, Roll decay, Ikeda's method, Full-scale, Model-scale*

1. INTRODUCTION

With ever increasing focus on maximizing payload and minimizing fuel consumption, modern Panamax Pure Car and Truck Carriers (PCTC) have evolved into highly optimized designs, incorporating very high centre of gravity for maximum cargo volume, combined with slender hulls for minimum resistance. High centre of gravity requires hull forms that provide high form stability, which is partially achieved by largely flared aft body sections with large water plane area. With slender and very form stable hulls PCTC's are very efficient volume carriers but also more

vulnerable for events such as parametric rolling caused by stability variations in waves. In recent years several severe cases have been reported with modern PCTC designs, e.g. Palmquist & Nygren (2004) and Rosén et al. (2012), with extreme roll amplitudes causing significant risks to the crew and cargo on board.

The onset of parametric rolling requires that the stability varies in resonance with the natural roll period of the vessel as the waves travel along the hull and the vessel is pitching. In case of parametric resonance the roll damping is decisive for the roll amplitude. If the damping is sufficiently high parametric rolling will



never develop, but if the damping is low relative to the stability variation large roll angles can develop rapidly.

To avoid incidents as those referred to in the previous, parametric rolling needs to be properly accounted for in design as well as in operation. In ABS (2008) a guide for parametric roll susceptibility assessment is provided. If a design is found susceptible the guide requires operational guidance or anti rolling devices to assign for an optional, "parametrical roll under control", class notation. In the second generation intact stability criteria, which are under development within the IMO, parametric rolling and other dynamic stability failure modes are addressed with a multi-level approach including simple vulnerability criteria, direct stability assessment, and formulation of ship specific operational guidance (e.g. IMO 2012, Francescutto & Umeda 2010). In particular for the direct assessment level and for formulation of ship specific operational guidance, proper assessment of a ship's vulnerability to parametrical rolling is depending on accurate description of the roll damping.

Roll damping properties can either be estimated using semi-empirical formulations or by experiments. Direct calculations using RANS-CFD can, as shown by van't Veer & Fathi (2011), be used for investigating the flow around the hull and appendices due to rolling motions, but is not yet widely used for quantitative estimates of the damping.

The most established semi-empirical method for roll damping prediction is Ikeda's method (1978) which is recommended by ITTC (2011). This method is derived based on a mixture of theory and systematic model testing using different kind of hull shapes and 2D sections. As to experiments roll damping properties can be derived using forced roll motions or free roll decay model tests, for the actual hull with appendices as described in

IMO (2006). According to Himeno (1981) scale effects of roll damping are mainly associated with skin friction related damping which however often constitute a negligible part of the total damping. Therefore, damping derived from model tests are normally transferred directly to full scale using a non-dimensional formulation expressed as the ratio between the actual damping and the critical damping of the rolling motion.

Little work has however been done for assessing the validity of model scale test results in full scale for large ships. In fact, Valle & Pérez-Rojas (1997) and Valle et al. (2000) claimed considerable scale effects in roll damping for a fishing vessel when comparing full scale results with results from model tests. Furthermore; in Kawahara et al. (2009) it was found that the accuracy of Ikeda's method decreased for vessels with high centre of gravity and large flared stern sections – characteristics that are typical for modern PCTC's. Consequently, there appear to be a need for addressing the validity of current approaches, and possibly also a room for improvements.

This paper presents new approaches for assessing ship's roll damping at speed. Unique experimental set-ups in model scale in towing tank as well as in full scale with a Panamax PCTC, as seen in figure 1, are presented. Data generated is evaluated and the results are also used to benchmarking Ikeda's method for roll damping prediction.



Figure 1: The Panamax Pure Car and Truck Carrier that serves as case vessel in this paper.



2. ROLL DECAY TESTS

Full-scale and model-scale roll decay tests have been performed on a Panamax PCTC, the Wallenius vessel m/v Faust with vessel particulars according to table 1.

Table 1: Main particulars of m/v Faust

Length	[m]	220
Beam	[m]	32.3
Draft	[m]	9.5
Displacement	[m ³]	41000
Bilge keel dimension	[m x m]	0.4 x 66
Block Coefficient	[-]	0.66
Midship Coefficient	[-]	0.93
Scale factor, model	[-]	29.6

2.1 Model Scale Roll Decay Tests

The model tests were performed in the towing tank at SSPA Sweden AB in Gothenburg. The tank measures 260m x 10m and is 5m deep. The model hull was produced in plastic foam and equipped with rudder and bilge keels but no propeller. The model was ballasted to the design draft condition as described in table 1, with a metacentric height, GM, corresponding to 1.1m for the full scale ship and a roll period corresponding to about 28s. Draughts at the forward and aft perpendiculars were measured with rulers and GM was verified with inclination tests.

The roll decay tests were carried out by inclining the model to a heel angle of around 5°-10°, keeping it heeled for a moment and then releasing it. This was done at no speed as well as in speed, by towing the model in Froude numbers corresponding to full scale speeds of 12, 14 and 16 knots. The roll angle was measured with a gyro at a sampling frequency of 100Hz. The accuracy of the gyro is 0.1° and the resolution 0.0023°.

During the tests at speed, the model was towed by the carriage through a solid rod attached amidships. The model was kept on course by attaching a connection fore and aft leaving the model free in heave and pitch but restrained in sway and yaw. The towing rod and the connection were located at a height corresponding to the assumed roll axis, and attached using joints that are free in rotation. Under the condition that the joints are placed exactly along the model's roll centre axis, the model can be considered as free in roll.

There is of course a risk that the roll motion is affected by the yaw restraint if the assumed roll centre deviates from the true roll centre. In order to investigate the effect of this yaw restraint, roll decay tests at zero speed were carried out with the model totally free. By comparing these tests with the corresponding tests of the restrained model, it was found that the influence of the yaw restraint on the roll damping is negligible at zero speed.

The connection joint locations were kept constant for all speeds. However, it is likely that the roll centre moves as the model sinks and trims with increasing speed. If the true roll centre deviates from the connections, forces will be transferred between the model and the connection and this may have some effect on the roll damping. Therefore, force transducers were mounted on the connections and the side forces were recorded throughout all tests. At 12 knots the side forces were of the same magnitude as at 0 knots. At the higher speeds, the side forces were larger than at 0 knots, which may indicate an effect on the decays. Even though the sizes of these forces were measured it is difficult to quantify their effect on the roll damping. A consequence of this is that the data for tests carried out at 0 and 12knots should be considered more reliable than the data from the 14 and 16knots runs.

In figure 2 time series of roll motions can be seen from a selection of the model scale roll



decay tests. The figure shows two different tests performed in Froude number corresponding to full scale speeds 0 and 16 knots. As can be seen the damping is very low at zero speed but increases significantly at speed.

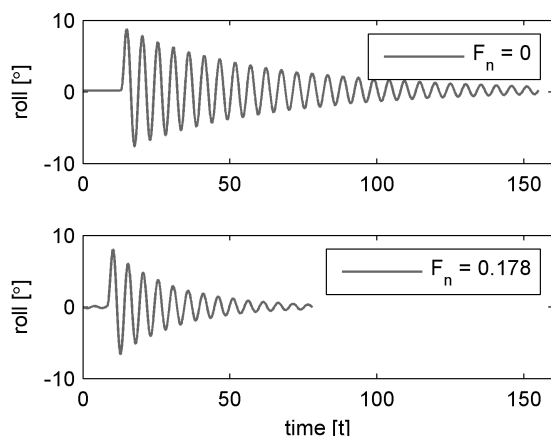


Figure 2: Time series from model scale roll decay tests at speed corresponding to full scale speeds of 0kn and 16kn.

2.2 Full Scale Roll Decay Tests

Full scale roll-decay tests were performed by inducing roll motion using controlled rudder impulses. For normal load cases, the vertical centre of gravity of PCTC's is high – as well as for most vessel that are sensitive for parametrical rolling – giving a good lever for the rudder and distinct rudder-roll coupling as a consequence. Since the inertia of yaw is much larger than the inertia of roll, short rudder impulses can produce a roll motion without generating large yaw motion. In figure 3 a roll decay test conducted on board m/v Faust can be seen. The figure shows the rudder angle, the roll motion as measured by the gyro compass and the heading.

Figure 3 shows how two rudder impulses in opposite direction causes the vessel to roll with an initial amplitude of about 3° but only initiates a very limited change of heading. The

duration of each rudder impulse was around half the natural roll period so the total duration of two rudder impulses was to be equal to the ships natural period of roll. The roll motion can be considered as freely oscillating as soon as the rudder is stationary in or near midships position. Tests were performed at three different speeds, around 14, 16 and 18 knots. During the tests the vessel was loaded to design draft. According to the on board loading computer GM was 1.7m which was higher than the model test condition. The natural period of roll was measured to about 23s. Roll motions, water speed, rudder angle and heading were measured with a rate of 1Hz with a resolution of 0.1°. All tests were performed in smooth weather conditions.

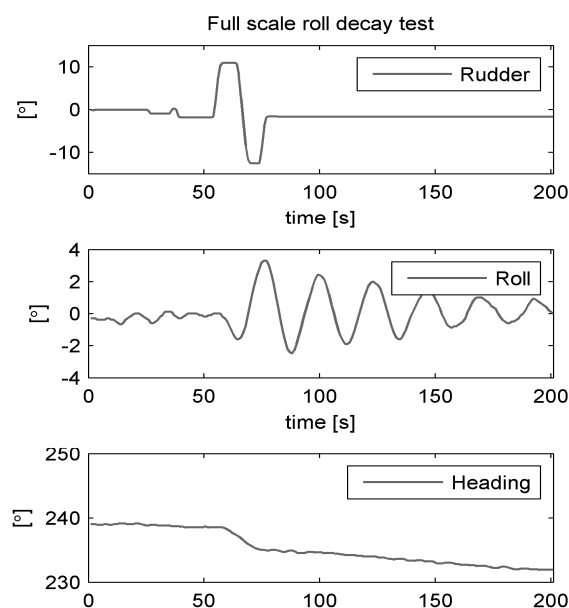


Figure 3: Time series of rudder angle, roll angle and the heading during a full scale roll decay test onboard m/v Faust.

3. ROLL DAMPING EVALUATION

From roll decay tests roll damping coefficients are normally derived based on the

logarithmic decrement of the roll peaks. However, this approach is sensitive to low-frequency disturbances and noise, which does not have to be a problem in controlled model test environment, but is difficult to avoid during full scale tests. An alternative and more robust approach, which utilizes full time series of roll decay tests and not only the peaks, is the numerical Parameter Identification Technique (PIT) as described in IMO (2006) and also used in Bulian (2004). In this approach a numerical solution to a one degree of freedom roll equation is fitted to the roll decay time series by tuning the parameters in the roll equation.

To evaluate the performed tests, a modified version of the PIT approach is developed. This modified approach adds a time-dependent second-degree polynomial to the fitting, that later can be separated from the solution to account for low frequency disturbances. The roll equation that is used for the evaluation has a linear-quadratic damping dependence and a linear restoring term. It should be noted that even though the approach could well handle roll equations with higher order of non-linearities in the damping term as well as a non-linear restoring term, the limited amplitudes at which the roll decay tests was conducted cannot motivate advantages of higher order models.

The equation of a freely oscillating roll motion with linear-quadratic damping can in non-dimensional form be expressed as

$$\ddot{\varphi} + 2\zeta\omega_0\dot{\varphi} + d|\dot{\varphi}|\dot{\varphi} + \omega_0^2\varphi = 0 \quad (1)$$

where φ is the roll angle, ω_0 is the non-damped natural frequency of roll, ζ is the linear damping coefficient and d is the quadratic damping coefficient. For convenience the equation is rewritten as a system of coupled first-order differential equations by introducing $y_1 = \varphi$ and $y_2 = \dot{\varphi}$ according to

$$\begin{cases} \dot{y}_1 = y_2 \\ \dot{y}_2 = -2\zeta\omega_0 y_2 - d|y_2|y_2 - \omega_0^2 y_1 \end{cases} \quad (2)$$

which can be solved in the time domain t using numerical integration if the initial values $\varphi(0)$ and $\dot{\varphi}(0)$ are given.

Roll decay tests are evaluated by tuning $\bar{k} = [\zeta, \omega_0, d, \varphi(0), \dot{\varphi}(0)]$ for best fit between the numerical solution and sampled roll decay data. This can be expressed as an unconstrained nonlinear optimization problem, by minimizing the sum square residual between the time samples from the decays φ_{m_i} and the numerical solution $\varphi_{n_i}(\bar{k}, t_i)$, according to

$$\min_{\bar{k}, p(t)} f(\bar{k}, p(t)) \quad (3)$$

where $p(t)$ is the previously mentioned second degree polynomial that is added in order to account for low frequency disturbances and

$$f = \sum_{i=0}^t (\varphi_{m_i} - \varphi_{n_i}(\bar{k}, t_i) - p(t_i))^2 \quad (4)$$

For comparative purpose it is convenient to express the linear-quadratic damping as equivalent linear damping ζ_e . At a certain roll amplitude φ_a this linear equivalent damping constitutes the same damping over one period as the non-linear damping over the same period. In line with Himeno (1981) this equivalent linear damping is calculated as

$$\zeta_e = \zeta + \frac{4}{3\pi} d\varphi_a \quad (5)$$

In figure 4 evaluations of full scale as well as model scale decays are exemplified. The derived linear-quadratic as well as linear equivalent damping for $\varphi_a = 2^\circ$ are given in the diagram titles.

When comparing the linear damping term ζ with the linear equivalent damping term ζ_e in figure 4 it can be seen that the non-linearities are weak at amplitudes of 2° . Damping derived from all model tests and full scale tests are compared in figure 5 in terms of linear



equivalent damping at 2° has been evaluated for all the conducted tests. For equally premised comparison the data in figure 5 comes from evaluations of test data with amplitudes in the range 4° to 1° (as in figure 4).

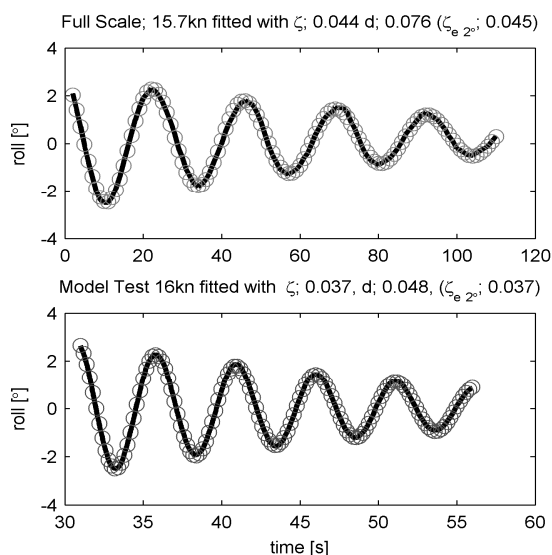


Figure 4: Full scale and model scale roll decay tests evaluated with the linear-quadratic damping model. For comparative purpose the linear equivalent damping is displayed, calculated according to equation (5).

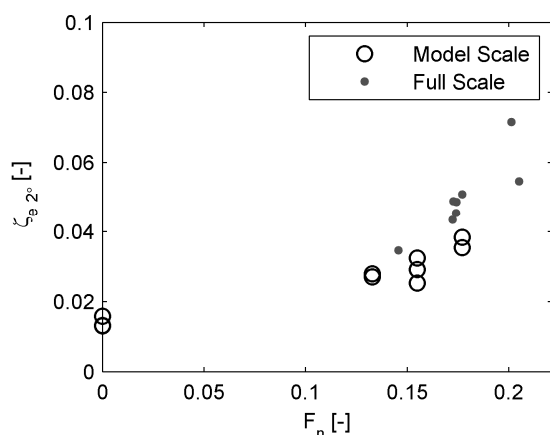


Figure 5: Linear equivalent damping for $\varphi_a = 2^\circ$ from model tests and full scale tests at different Froude numbers

As seen the evaluated damping from model tests and full scale tests show quite good agreement. This indicates a good potential for the full scale approach as such and also builds confidence in the procedure of applying roll damping evaluated based on model tests on full scale vessels. There is a trend though that the full scale evaluations give slightly higher damping results than the model tests.

4. DISCUSSION

The model was fitted with continuous bilge keels while the real bilge keels on the ship are divided into five successive parts. The later configuration may have a positive effect on the damping at speed as discussed by Segal & Segal (2011). Additionally the profiles of the full scale bilge keels are L-profiles (400x100mm) which are likely to be slightly more efficient than the flat plate profiles (400mm) of the model.

As previously mentioned, it is difficult to quantify the influence of the yaw restraint of the model in the towing tank for the higher speeds. In a similar manner slight yawing motions may have affected the full scale tests even though the tests were performed in such a manner that large yaw motions could be avoided.

There is of course scatter in the data associated to full scale measurements which have to be considered. As an effect of that the damping is very low small differences in input can have a large relative effect on the evaluations. However, in absolute figures the repeatability of the full scale tests appears to be quite good with a standard deviation of ~0.003 (0.3% of the critical damping) which actually is in the same magnitude as the standard deviation of the model tests.

According to IMO (2006) scale models with appendices shall have a minimum length



of 2m, the bilge keel height shall exceed 7mm and the scale factor shall not be less than 1:75 to avoid viscous scale effects. These requirements are well fulfilled here. The requirement on bilge keel size is likely there to avoid that the boundary layer around the hull reduces the efficiency of the bilge keels in model scale. However, when considering the solution to Blasius equation it appears that the boundary layer thickness due to forward speed could be considerable during the model tests performed at speed. The boundary layer thickness t_b can be estimated based on the local Reynolds number Re_x at a longitudinal position x according to

$$t_b \approx 4.91x/\sqrt{Re_x} \quad (6)$$

For the model tests performed at speed this gives a thickness up to, and for some cases more than, half the bilge keel height (depending on speed and position). This could have a negative impact on the bilge keel efficiency. In full scale the boundary layer is in the magnitude of some percentages of the bilge keel height.

Even though the full-scale vessel and model had the same draughts during the tests, the vertical centre of gravity was different, and as a consequence GM and the natural frequency was different which could have an influence on the damping.

In heavy weather it is common practice that captains on Wallenius PCTC's prefers bow heading wind to expose much lateral wind area while at the same time make use of the stabilizing forces of the strong apparent wind towards the hull to reduce the rolling motions. Considering that the lateral wind area of PCTC's are very high, aerodynamical damping may have a slight impact on the damping during the full scale trials, even though they were performed in calm weather.

As discussed by van't Veer & Fathi (2011), memory effects may play an important role when evaluating roll damping from roll decays. Roll damping may be overestimated during the initial phase of a roll decay test in the absence of the memory of previous rolling motions. In an attempt to investigate this effect the roll damping was evaluated for two different roll decay tests, the first with an initial amplitude of 9° and the second with an initial amplitude of 6°. Both tests were performed at the same speed (corresponding to 12kn in full scale) and the roll damping was evaluated from time series when the amplitude was between 6° and 3°. No significant difference in evaluated damping could be observed between the two cases.

Water temperature differences affecting the viscous forces, increased hull surface roughness due to fouling and external forces disturbing the tests are other factors that may have an effect on the results.

5. IKEDA'S METHOD VS. EXPERIMENTAL DATA

Even though first published in the late 1970s, Ikeda's method is still commonly used for roll damping prediction. In this method, roll damping in dimensional form B is calculated for a given amplitude, corresponding to linear equivalent damping, due to five different components; friction, wave generation, eddy making, linear-lift and bilge keel. For comparative purpose these components will here be presented non-dimensionalized according to

$$\zeta_e = \frac{1}{2\omega_0} \frac{B}{A} \quad (7)$$

where A is the inertia term that is estimated as $\rho g \nabla GM \omega_0^{-2}$, ρ is the water density, g is the constant of gravity and ∇ is the displacement of the vessel.



The method as described in Ikeda (1978) and Journee (2003) has been implemented and applied on the here studied ship. In figure 6 all components can be seen exemplified for $\varphi_a = 10^\circ$, $T = 27.6$ s and $GM = 1.1$ m.

As seen in the figure the bilge keel damping is the dominating component at low speeds for the given condition. The contribution from bilge keels is caused by three different components: a pure drag normal force component, a bilge keel generated hull pressure component and bilge keel generated lift. At higher speeds the hull lift component becomes dominant. This component is created when the submerged hull, periodically, has an angle of attack due to sway motions caused by rolling. With the magnitude of these sway motions being dependent on the distance of the roll centre above the water line, this component becomes particularly large for vessels with high centre of gravity. The lift component in Ikeda's method has been derived based on maneuvering experiments. The frictional component, which constitutes a small contribution, was derived from experiments with rotating cylinders where the viscous damping is dependent on the Reynolds number. This component also incorporates a small semi-theoretical correction for forward speed. The wave damping is the linear potential damping which typically is calculated using strip theory for zero forward speed and is modified with an empirical formula to incorporate forward speed effects. The eddy-making component represents damping due to vortex separation, and is almost negligible at forward speed.

In Kawahara et al. (2009) the validity of Ikeda's method was found questionable for vessels with high centre of gravity combined with buttock flow stern (largely flared stern sections), especially for small roll angles. With Faust being a buttock flow stern type PCTC with high centre of gravity, and with roll damping tests being conducted at small roll

amplitudes, Ikeda's method should not be expected to have very good agreement with the tests.

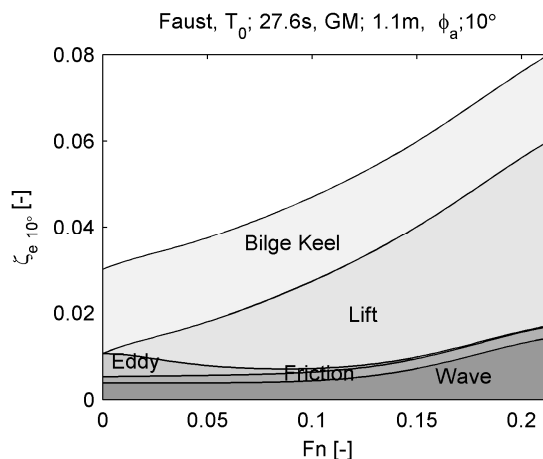


Figure 6: Results from Ikeda's method for m/v Faust with the five different damping components; friction, wave, eddy, linear lift and bilge keel.

In figure 7 the roll damping derived from the model tests are compared with Ikeda's method for the corresponding loading condition and scale. As previously stated it is important to keep in mind that the accuracy of the model tests performed at 14 and 16 knots may have been affected by the yaw constraint and should be considered with care. However the general observation is that Ikeda's method seems to overestimate the damping except for the smallest roll amplitudes at zero speed. As seen, the speed dependence according to Ikeda's method is stronger than what is shown by the model tests, indicating that the lift damping component, which constitutes the dominant part of the speed dependence, probably is overestimated for this ship. Furthermore, Ikeda's method seems to overestimate the non-linearities (amplitude dependence) that essentially are caused by the bilge keel component.

Both the lift damping and the bilge keel damping are strongly dependent on the location

of the roll centre. In accordance with the prediction formula this is assumed to be located in the vertical centre of gravity. Recorded sway and yaw motions however indicate that the roll centre normally is located lower than the centre of gravity. If the height of the assumed centre of roll in the prediction formula is reduced, better agreement is achieved, thus indicating a potential for improvement of the method.

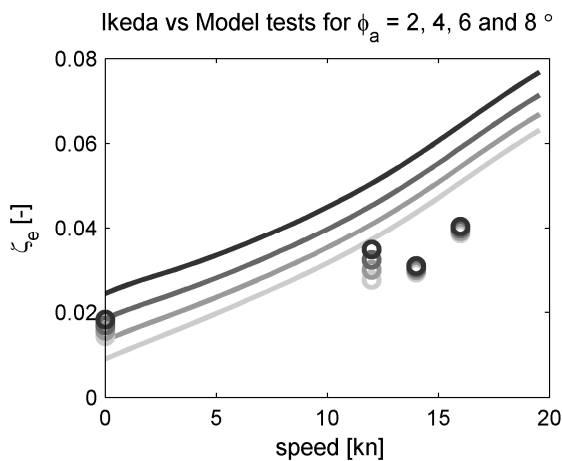


Figure 7: Predicted damping for m/v Faust in model scale using Ikeda's method and model tests for roll amplitudes of 2, 4, 6 and 8°.

6. CONCLUSIONS

A method for assessing roll damping properties based on full scale roll decay tests has been developed. Evaluated roll damping from full scale tests shows good agreement with model tests for a Panamax Pure Car and Truck Carrier. This indicates a good potential for the approach as such and also builds confidence in the procedure of applying roll damping evaluated from model tests on full scale vessels. The tests presented here though indicate that the full scale damping is slightly higher than the model test damping. This should be further investigated.

The presented full scale tests have been performed in-service with the vessel loaded to the design condition. Alternatively, tests could be performed during the sea trial from the ship yard. However, as roll damping is dependent on the loading condition and speed, results will always be limited to specific cases. And as required test matrices to cover all possible operational conditions is practically impossible to perform, semi-empirical methods appear as an attractive option for inter- and extrapolation of test results to various conditions. Ikeda's semi-empirical method implemented for the studied vessel give physically relevant predictions of the roll damping. However, speed dependence and amplitude dependence was significantly overestimated by the method, likely as a consequence of that the method not has been adopted for modern volume carriers with very high centre of gravity such as PCTC's. Future work could therefore preferably aim at assessing the centre of gravity dependence of the lift damping and the bilge keel damping which are the two damping components in Ikeda's method that constitutes the major part of the non-linearities and the speed dependence.

An accurate description of the roll damping is crucial when predicting the risk of severe rolling events, such as parametric rolling. The here presented full-scale approach is well suited for providing roll damping input to methods for operational guidance (e.g. as presented in Ovegård et al 2012) for accurate on-board decision support with respect to parametric rolling.

7. ACKNOWLEDGMENTS

This research has been financially supported by the Swedish Mercantile Marine Foundation (Stiftelsen Sveriges Sjömanshus) and the Swedish Maritime Administration (Sjöfartsverket) which are both gratefully acknowledged.



8. REFERENCES

ABS, 2008, "Guide for the Assessment of Parametric Roll Resonance in the Design of Container Carriers

Bulian G., 2004, "Estimation Of Nonlinear Roll Decay Parameters Using An Analytical Approximate Solution Of The Decay Time History", International Shipbuilding Progress 51, no. 1, pp. 5-32.

Francescutto A., Umeda N., 2010, "Current Status of New Generation Intact Stability Criteria Development", 11th Intl Ship Stability Workshop (ISSW2010), Wageningen, The Netherlands.

Himeno Y., 1981, "Prediction of Ship Roll Damping- State of the Art", The University of Michigan College of Engineering, No.239.

IMO 2006, Interim Guidelines For Alternative Assessment Of The Weather Criterion, MSC.1/Circ.1200.

IMO, 2012, "Development of Second Generation Intact Stability Criteria, Report of the Working Group", SLF 54/WP.3.

Ikeda, Y., Himeno, Y. & Tanaka, N., 1978, "Components of roll damping of ship at forward speed", Journal of the Society of Naval Architects of Japan, Vol. 143.

ITTC, 2011, "ITTC Recommended Procedures Numerical Estimation of Roll Damping", International Towing Tank Conference, Report 7.5-02-07-04.5.

Journée J.M.J. and Adegeest L.J.M., 2003, Theoretical Manual of "SEAWAY for Windows, TUD Report No. 1370 Revision: 14-12-2003.

Kawahara et al., 2009, "A Simple Prediction Formula of Roll Damping of

Conventional Cargo Ships on the Basis of Ikeda's Method and Its Limitation", Proceedings of the 10th International Conference on Stability of Ships and Ocean Vehicles, Saint Petersburg, Russia.

Ovegård E., Rosén A., Palmquist M., Huss M., 2012, "Operational Guidance with Respect to Pure Loss of Stability and Parametric Rolling", 11th Intl Conf on the Stability of Ships and Ocean Vehicles (STAB 2012), Greece.

Palmquist M., Nygren C., 2004, "Recordings of Head-Sea Parametric Rolling on a PCTC", Annex in IMO SLF 47/INF.5.

Rosén A., Huss M., Palmquist M., 2012, "Experience from Parametric Rolling of Ships", chapter in the book Fossen T.I., Nijmeijer H., Parametric Resonance in Dynamical Systems, Springer.

Segal Z. and Segal A., 2011, "Roll Stabilization with Short Wings", American Society of Naval Engineers, Naval Engineers Journal, pp. 45-54.

J. Valle, L. Pérez-Rojas, 1997, "Study of ship roll decrement tests in calm water", Proceedings of the 6th International Conference on Stability of Ships and Ocean Vehicles international Conference, Varna, Bulgaria, p 121-128.

Valle J., Pérez-Rojas L., Carrillo E.J., 2000, "Influences of Test Parameters on Roll Damping Coefficients", Proceedings of the 7th International Conference on Stability of Ships and Ocean Vehicles, Launceston, Tasmania, Australia, vol B, p 751-766.

van 't Veer R., Fathi F., 2011, "On the Roll Damping of an FPSO with Riser Balcony and Bilge Keels", 30th International Conference on Ocean, Offshore and Arctic Engineering, Rotterdam, The Netherlands.



Roll Damping of Twin-Screw Vessels: Comparison of RANSE with Established Methods

Sven Handschel, Nikolai Köllisch, Moustafa Abdel-Maksoud, *Hamburg University of Technology,
Institute for Fluid Dynamics and Ship Theory, Germany*

ABSTRACT

A RANSE method is applied to estimate the roll damping of a RoPax ship. The simulations are carried out in full scale and with a free water surface. The influence of the roll amplitude up to 35 degrees, three ship speeds and the vertical position of the roll axis are investigated. The interaction between the bilge keels and the ship hull are analyzed. The damping effect of the rudder is studied. All simulation results are compared with established methods developed by Ikeda and Blume.

Keywords: RANSE, Roll Damping, Twin-Screw Vessel

NOMENCLATURE

b_{BK} [m]	bilge keel breadth
d [m]	ship draft
k [-]	velocity increment factor
l_{BK} [m]	bilge keel length
r, r_{BK} [m]	distance from roll axis - to center of effort, - to bilge keel
v, v_A [m/s]	transverse velocity component (ampl.)
x, x_A [m]	relative motion (amplitude) of water in crosswise direction to bilge keel
A_{BK} [m ²]	bilge keel area
B [Nms], \hat{B} [-]	roll damping coefficient, dimensionless roll damping coefficient
B_{WL} [m]	ship breadth of the waterline
$C_{D,BK}, C_P$ [-]	drag coefficient for bilge keel, hull-bilge keel pressure coefficient
C_B, C_W [-]	block and waterplane coefficient
KC_{BK} [-]	local Keulagan-Carpenter-Number for bilge keel
L_{OA}, L_{WL} [m]	length over all, length of waterline
RA [m]	dist. to roll axis over undisturbed water surface
S [m ²]	wetted surface area of the ship
U [m/s]	ship speed
α [rad]	angle between an orthogonal line to the normal force and line of the lever (Fig. 6)
σ [-]	section area coefficient
$\varphi, \dot{\varphi}, \varphi_A, \dot{\varphi}_A$	roll angle, roll velocity (amplitude)
φ_H [rad]	heel angle
ρ [kg/m ³]	density of water
ω [rad/s]	roll frequency

1. INTRODUCTION

Calculating ship motions in natural waves with potential theory-based simulation methods has been a well-known practice for several decades. However, the accuracy of the calculated results for roll motion is strongly influenced by viscous damping. While potential theory-based methods are able to predict main energy dissipation in all other degrees of freedom, estimating damping for the roll motion is still a weak point in the simulations. The reason for this is that the magnitude of dissipation caused by viscous effects compared with wave damping may be of similar orders of magnitude.

Extensive investigations (Ikeda, 1976-78 and Himeno, 1981) on roll damping were carried out, in the mid-70s, which resulted in a division of the phenomena into a wave, friction, eddy and lift part. A semi-empirical method, also known as the Ikeda method, was developed based on these assumptions. It has become one of the most popular methods to correct the calculated energy dissipation using potential theory. The empirical coefficients included in



the method are based on former typical ship geometries.

Based upon simpler measurements, Blume (1979) published roll damping coefficients that continue to be used. The applicability of both methods to today's modern RoPax ferry is investigated in this paper. RANSE-based simulations with various roll parameters have been carried out and the obtained results are compared with those of the Ikeda and Blume method.

2. NUMERICAL SIMULATIONS

2.1 Geometry

The investigated RoPax ferry with a length over all of $L_{OA} = 185.0[m]$ was designed by SVA Potsdam. The ferry is a twin-screw vessel, arranged with two shafts, propellers, two rudders and a large deadwood (see Figure 2). The main dimensions are summarized in Table 1, and the section plan is shown in Figure 1.

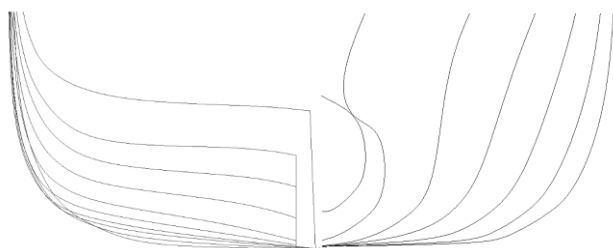


Figure 1: Section plan of the RoPax ferry

2.2 Numerical method

The RANS-solver STAR-CCM+ is used to simulate the incompressible flow around the ship with and without forward speed at different roll amplitudes. The volume of fluid method (VOF) is applied to calculate the free water surface flow. The $k - \omega - SST$ turbulence model was used in all computations. The conservation equations for mass and

momentum in integral form, the equations of the turbulence model and the volume fraction equation (the mixture of water and air) are solved using an iterative manner based on the finite volume method in combination with SIMPLE-algorithm (see Enger, 2010). First-order Euler implicit scheme is used for time integration.

Table 1: Main specification of the RoPax ferry

length waterline L_{WL}	[m]	176.0
breadth waterline B_{WL}	[m]	26.0
draft d	[m]	6.0
waterplane coefficient C_W	[-]	0.75
block coefficient C_B	[-]	0.53
wetted surface area S	[m ²]	4678

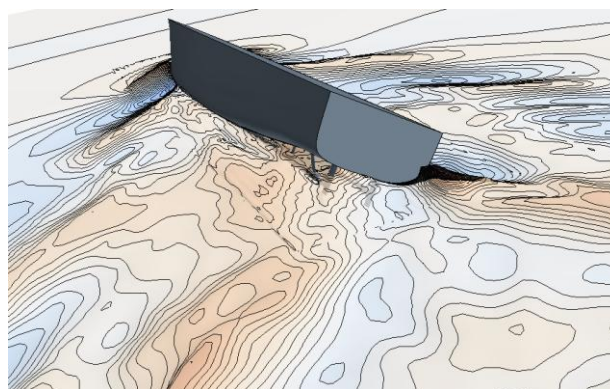


Figure 2: Calculated wave system of the RoPax ferry with forward velocity $Fn = 0.26$ and $\varphi_A = 35 [^\circ]$

The flow field is divided into a rotating and a stationary region. The rotating region has a cylindrical shape. The roll axis of the ship is fixed and coincident with the cylinder axis. The stationary region has a rectangular shape. A sliding interface boundary condition is applied on the common surface between both regions. The whole domain has a length of $6.6 \cdot L_{WL}$, a breadth of $2.4 \cdot L_{WL}$ and a height of $3 \cdot L_{WL}$. The inflow boundary condition is a velocity

inlet, the outlet a hydrostatic pressure condition. Except the geometry which is a regular wall, all other boundaries are slip walls.

Unstructured trimmed hexahedral grid with prism layer and local refinements near the hull and the appendages surface is applied (see Figure 3). The grid size depends on the roll amplitude. For a amplitude of 25 [deg] usually 4 M. cells are used. The ship motion is realized by a sinusoidal forced roll motion.

A detailed description and a validation of the numerical method with respect to the estimation of roll damping can be found in Handschel et al. (2012).

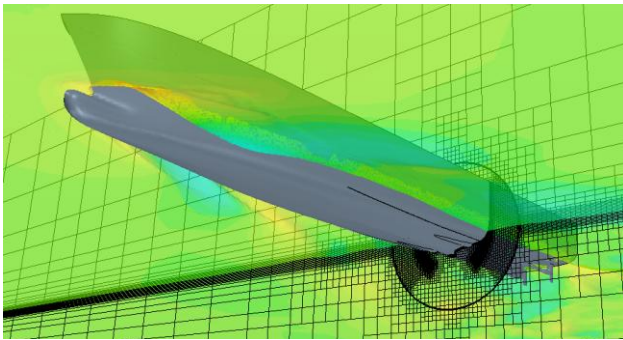


Figure 3: RoPax ferry hull enclosed by cylindrical mesh domain. Mesh refinements are applied at the free water surface and near bilge keels. The sliding interface is shown as a circle; investigated roll amplitude $\varphi_A = 35$ [°].

3. COMPARISON WITH ESTABLISHED METHODS

Ikeda divided the roll damping phenomena into the following parts: wave, friction, eddy and lift damping of the bare hull. The bilge keel effect was investigated separately and divided into three components. The first one is the normal-force acting on the keels; the second component is caused by the interaction between the bare hull and the bilge keel, and is acting on the hull; the interaction with the free surface as the third component is assumed to be small and is neglected.

Due to the semi-empirical character of the Ikeda method, the application of this method should be done with care. Straight forward solutions are often favored (Kawahara, 2009). Further, the results of a systematic experimental investigation carried out by Blume (1979) for three different bare hull forms are often used to estimate the roll damping part in numerical ship motion simulations. Based on sinusoidal exciting roll motion measurements, Blume determined damping coefficient over a wide range of ship speeds and roll angles up to 20 degrees. The measured results are summarized in a parametric form to be used in numerical simulations and will be referred to as the Blume method. To estimate the roll moment of the bilge keel, Blume recommended the approach developed by Gadd, which corresponds to the normal-force bilge keel part of Ikeda.

The results of the numerical simulations are compared with these two well-established methods. Both were developed in the 1970s.

Due to comparability, all results are presented as dimensionless roll damping coefficients

$$\hat{B} = \frac{B}{\rho \nabla B_{WL}^2} \sqrt{\frac{B_{WL}}{2g}} \quad (1)$$

3.1 Bare hull roll damping

The Blume Method. Blume measured the roll damping moment for three single-screw ship models (A, B – two series 60 ships, C – typical container ship) up to a roll angle of 20 degrees including rudder and propeller.

The simulations of the investigated hull geometry are compared with results of 5 and 15 degrees (Figure 4) using Blume's model C (see Table 2). Model C does not have a flat stern, a second rudder or a large transom. It should be noted that all of these components increase damping. For 5 degrees the Blume method

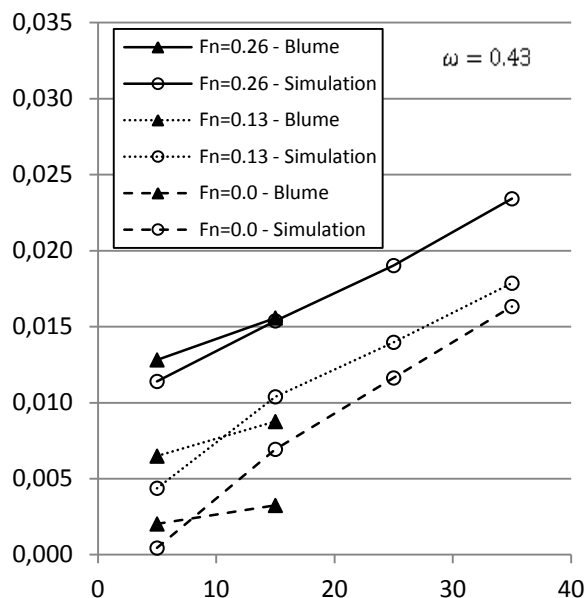


Figure 4 Roll damping coefficients estimated by the Blume method and CFD simulations for RoPax without bilge keels

over-estimates the roll damping for all investigated Froude numbers.

In contrast, for 15 degrees the roll damping, according to measured data by Blume, is smaller, whereas the differences decrease for higher Froude numbers. This effect may be caused by the dominated lift damping effect at high Froude numbers. Both Blume's experiments and the simulations indicate a weak nonlinear character over ship speed. In addition to the geometrical influence, one reason for the difference could be that the Blume method does not consider the correction of the scale effect included in the friction part.

Table 2 Ship form data and roll frequency parameter

	Model C	RoPax
L_{WL}/B_{WL}	6.37	6.77
B_{WL}/d	3.46	4.33
C_B	0.503	0.53
$\omega^2 B_{WL}/2g$	0.202	0.245

The Ikeda Method. The CFD simulation results were compared with the Ikeda method for bare hull roll damping in the form, which was published by Himeno (1981). For the wave damping part B_W for zero velocity, an approach from Zhou (1987), based on a strip method that, considers the damping of several heel angles with

$$B_W(\varphi) \approx B_{W,\varphi_H=0} + \frac{1}{2} B_W'' \varphi^2 \quad (2)$$

is applied. In addition to the zero heel wave roll damping $B_{W,\varphi_H=0}$, B_W'' considers the energy dissipation due to submerged hull form with higher amplitudes. Figure 5 shows the damping components over ship speed. For full scale ships, the frictional part is vanishing. The small lift damping is caused by the fact that the roll axis RA is located in the undisturbed water surface. The estimated wave damping part is relatively large compared to other ship hull forms, which could be caused by a large beam-draught ratio.

3.2 Damping of bilge keel

Normal-Force Damping. Both Ikeda (1976) and Blume recommend an approach which is based on the simple formula

$$F_{NBK} = \frac{1}{2} \rho A_{BK} C_{D,BK} v^2(t) \quad (3)$$

to estimate the normal drag force of the bilge keel. The velocity v is the relative transversal velocity component between hull and the surrounding water when the influence of bilge keel on the flow is neglected.

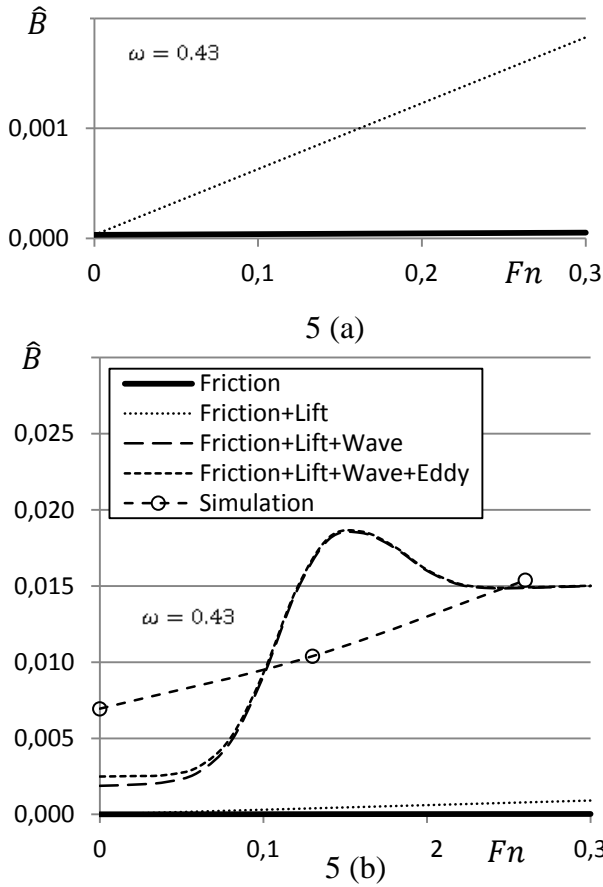


Figure 5: (a)/(b) Roll damping components of the Ikeda method compared with simulation results of $\varphi_A = 15$ [°]

$$v(t) = r_{BK} k \dot{\varphi}(t) \quad (4)$$

The factor k is a velocity increment factor to take into account the local effect of the hull shape on the velocity field. Ikeda has suggested a sectional area coefficient formulation which is applied for sections with small bilge radii ($\sigma > 0.975$). Blume formulates k as a function of ship breadth and bilge radius.

Using Equations (3) and (4), the roll moment for one bilge keel follows to

$$M_{NBK}(t) = F_{BK}(t) \cdot r_{BK} \cos \alpha \quad (5)$$

$$= \frac{1}{2} \rho A_{BK} C_{D,BK} r_{BK}^3 k^2 \dot{\varphi}^2(t) \cdot \cos \alpha.$$

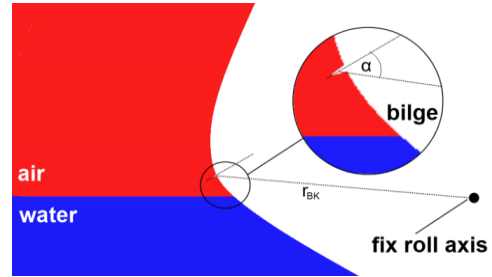


Figure 6: Emerging bilge keel, main section, $\varphi = 25$ [°]

After a linearization with the energy equivalence principle, a linear damping moment for both bilge keels can be written as:

$$B_{NBK} = \frac{8}{3\pi} \rho A_{BK} C_{D,BK} r_{BK}^3 k^2 \omega \varphi_A \cdot \cos \alpha \quad (6)$$

Compared to Blume, Ikeda recommends the calculation of the bilge keel damping coefficient in integral form over the bilge keel length l_{BK} .

Both authors give formulations for the drag coefficient $C_{D,BK}$ that depend on the velocity increment factor k , the relative motion of the water orthogonal to the bilge keel $x(t) = v(t)/\omega$ and the bilge keel breadth b_{BK} . On closer consideration, a connection to a local Keulegan-Carpenter-Number (here for both bilge keels) becomes obvious.

$$KC_{BK} = \frac{v_A T}{2b_{BK}} = \frac{r_{BK} k \omega \varphi_A 2\pi}{2b_{BK} \omega} = \pi \frac{x_A}{b_{BK}} \quad (7)$$

The parameters k and $C_{D,BK}$ are based on experimental measurements in towing tanks, partly with simple geometrical bodies (Ikeda, 1976). The factor k_{sim} represents the estimated value in the numerical simulation.



$$k_{Sim} = \frac{v_{A,Sim}}{r_{BK}\omega\varphi_A} \quad (8)$$

Thus, the relative velocity amplitude $v_{A,Sim}$ between the fluid and the bilge keel around the bilge is normalized by the velocity amplitude of the bilge keel (see Figure 7). This is done at 12 sections along the keel for a simulation without bilge keel. In the position $\varphi = 0$ [°], k_{Sim} is different for portside and starboard. Because of harmonic rotating motion, a mean value can be calculated (see Figure 8).

The mean velocity increment factors in the simulation $\bar{k}_{Sim} \approx 1$ coincide well with Ikeda's suggestion regarding cases that with section area coefficients of $\sigma < 0.975$. Estimating k for the investigated shape of the section according to the definition of Blume's method is difficult to perform because of the failing distinctive bilge radius.

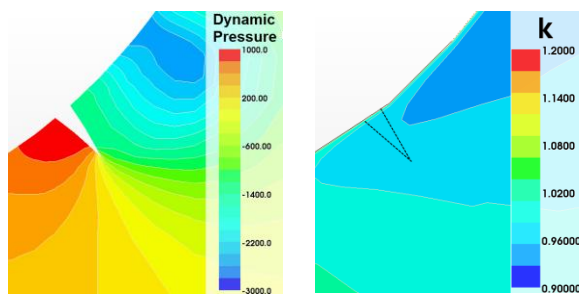


Figure 7: Simulation with and without bilge keel: dynamic pressure [Pa] (left), k (right) - $T = 14.6$ [s], $\varphi_A = 15$ [°], $Fn = 0.13$ -

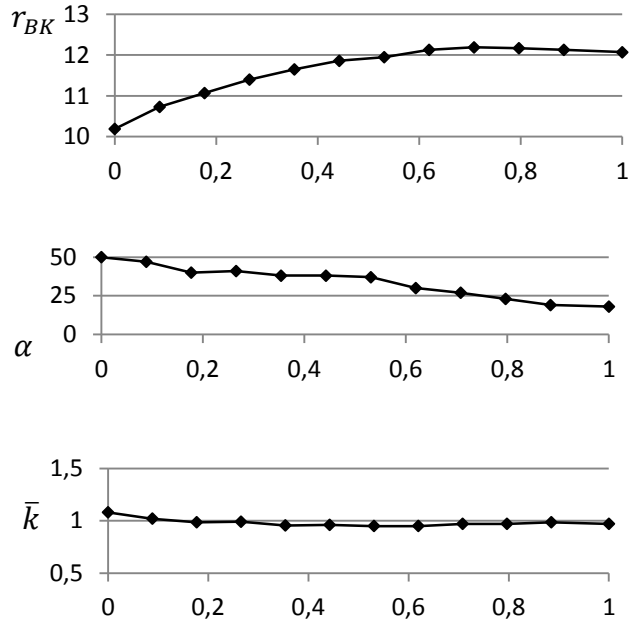


Figure 8: Variation of radius r_{BK} , angle α , velocity increment factor \bar{k} in the simulation over non-dimensional bilge keel length $\frac{x}{l_{BK}}$

The average drag coefficient $C_{D,BK,Sim}$ over one period for the normal-forced damping at bilge keel (Figure 9) can be estimated by the following formulation of the linear damping coefficient $B_{NBK,Sim}$, which is defined as

$$C_{D,BK,Sim} = \frac{3\pi B_{NBK,Sim}}{8\rho b_{BK}\omega\varphi_A \int_{l_{BK}} k_{Sim}^2 r_{BK}^3 \cos\alpha dl_{BK}} \quad (9)$$

Blume assumed that the forward speed is a negligible factor because the additional lifting effect due to the increasing of the forward speed is compensated by the decreasing normal-force damping. A very small correction for forward speed effects which has been introduced by Himeno (1981) and more recently by Ikeda (2004) will be not considered; it is assumed that the forward speed effect is less than 5.25% of the normal-force bilge keel damping.

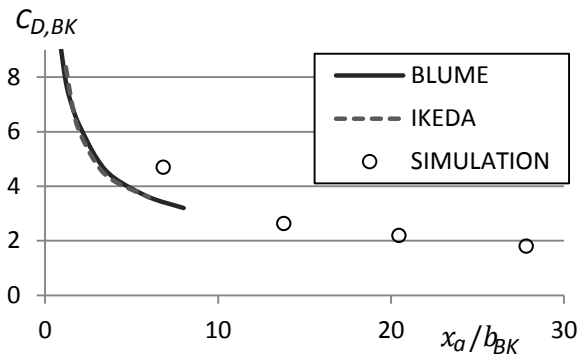


Figure 9: Comparison drag coefficient $C_{D,BK}$ of bilge keel ($Fn = 0.13$)

Whereas Blume uses only $C_{D,BK}$ to consider the bilge keel effect, Ikeda divides the bilge keel damping into three parts: the normal-force, the hull-pressure damping- as well as the wave-interacting bilge keel damping. The wave interacting part is neglected in the original method.

Hull-Pressure Damping Due To Bilge Keels.

Ikeda analyzed the effect of eddies, produced by the bilge keels, which interact with the flow of the ship hull. An approach based on surface pressure measurement on two-dimensional ship section is presented by Ikeda (1977b). The induced damping by the surface pressure on the hull due to the bilge keels,

$$B_{SBK} = \frac{4}{3\pi} \rho \omega \varphi_A \cdot \int_S r_{BK}^2 k^2 C_{P,BK} r ds \quad (10)$$

can be determined in a similar manner to Equation (6). $B_{SBK,Sim}$ is estimated based on two simulations, one with and the other without bilge keel. The normal-force part of the bilge keel was subtracted from the estimated difference between the linear roll damping moment of the two simulations which results in $B_{SBK,Sim}$.

The damping due to the bilge-keel-hull-pressure distribution in the simulation shows a similar tendency in comparison with the results

obtained by the Ikeda method; even so, the Ikeda method gives higher values of the bilge-keel-hull interaction component (see Figure 10).

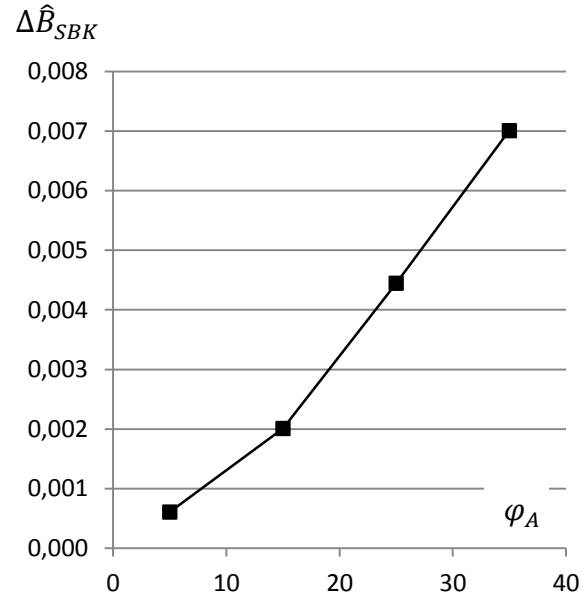


Figure 10: Differences between results of CFD and Ikeda's method concerning hull interaction damping with bilge keel ($Fn = 0.13$)

Bilge Keel Damping Due To Water Surface Interaction.

The systematic investigations carried out by Ikeda for bilge keel damping coefficient do not include roll angles higher than 17.2 degrees ($\varphi_A = 0.3 [rad]$). No explicit limitations for applying the method were given. Nevertheless, there is an angle for each ship where the bilge keel emerges. For the RoPax, this angle is $\varphi \approx 20[^\circ]$. An emerging or re-entering of bilge keels seems to be dominated by nonlinear effects (see Bassler, 2010).

The effect of bilge keels emergence was not considered in the Ikeda investigations, and, therefore, the results should be carefully analyzed using the present simulations of 25 [°] and 35 [°] roll angle (Figure 11).

Himeno (1981) presented results for investigations on increasing the wave radiation damping due to the interaction of the bilge keel with the free surface. Comparisons of the



measured and calculated results obtained by the linear theory showed that the additional damping underlie nonlinear effects of wave damping for higher roll angle. He noted that for ordinary ship hulls of that time (the 1970s), a wave-bilge keel effect can be safely neglected for a bilge keel breadth of $b_{BK} = B/60$ to $b_{BK} = B/80$. The ratio of ship breadth and breath of the bilge keel for the present RoPax is $B/b_{BK} > 140$.



Figure 11: Entrapped air in the simulation due to emerging and re-entering bilge keel - $T = 14.6$ [s], $\varphi_A = 35$ [°], $Fn = 0.13$ -

3.3 Rudders

Blume (1979) measured the damping coefficients of hull forms equipped with rudders. The dimensions of the rudders were not specified in the published results. Based on the approach of dividing the roll damping coefficient into different components, Ikeda did not investigate ship models with appendages, except bilge keels. Recommendations for rudder treatment were not published.

Two CFD simulations, one with and one without rudders are carried out. With a roll amplitude $\varphi_A = 35$ [°], a roll frequency $\omega = 0.43$ [rad/s] and a ship velocity of $U = 11.06$ [m/s], the contribution of the rudders is 0.81 % of the total linear roll damping. The rudder component is considered

to be independent from roll frequency and only depends linearly on the roll angle (described by Bertram, 2011). It should be mentioned that the rudder emerges. The result of the simulation will be added as a correction of the Ikeda method in order to be able to compare the results with Blume and the simulations.

3.4 Shaft Brackets and Shafting Line

In Ikeda's and Blume's investigations only single-screw hull shapes were studied. Therefore, no investigations of shaft brackets and shafting line were carried out. The results of the CFD simulations of the estimated roll damping coefficients did not show distinctive differences between the simulation with and without shaft brackets and shafting line.

The flow on the house of the shafting line does not show any large separation areas. The interaction between shaft brackets and shafting line with the rudder was not studied in the investigation.

4. SUMMARY OF THE RESULTS

Blume (1979) measured the damping coefficients with rotating propeller. The propeller was not included in the Ikeda method or in the CFD. In the comparison it is assumed that the propeller has no significant contribution to the roll damping. The simulations were varied over ship velocity and roll amplitude (Figure 12, 13, 14 and 15) for a roll period $T = 14.6$ [s]. The roll axis is situated in the undisturbed free water surface plane.

The roll damping coefficients of the Blume method show similar characteristics to CFD results for moderate roll angles and are in good agreement, especially for higher Froude numbers.

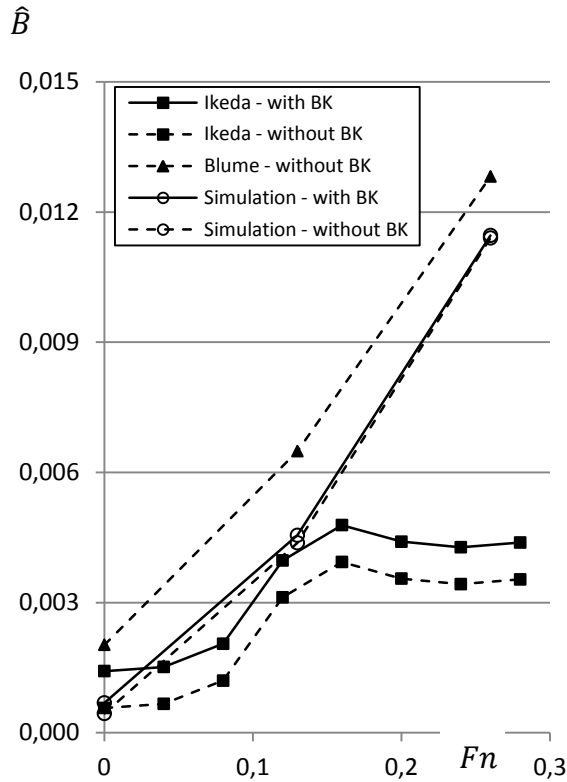


Figure 12: Comparison of Blume and Ikeda methods with simulations for $\varphi_A = 5 [^\circ]$

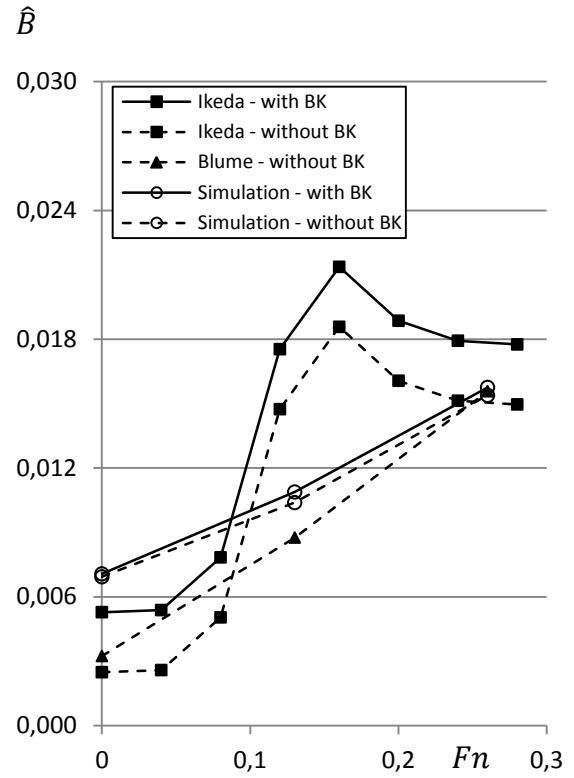


Figure 13: Comparison of Blume and Ikeda methods with simulations for $\varphi_A = 15 [^\circ]$

Figure 14: Comparison of the Ikeda method with simulations for $\varphi_A = 25 [^\circ]$

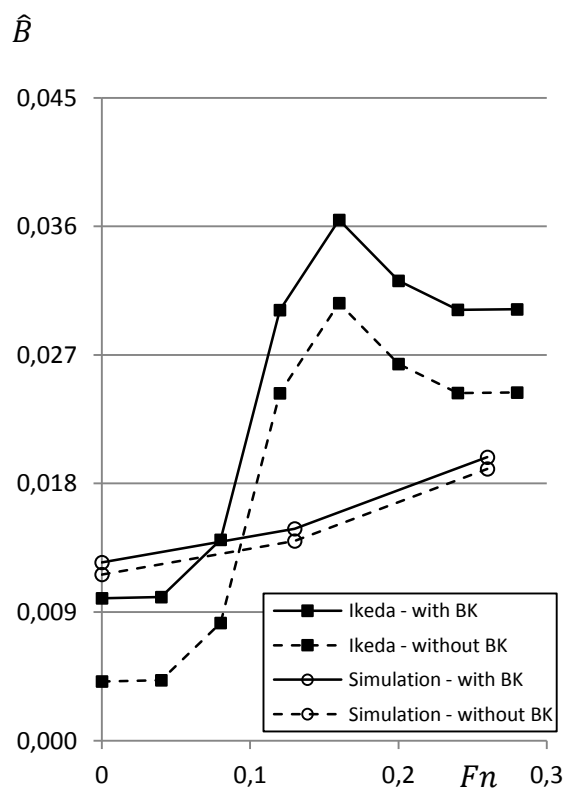
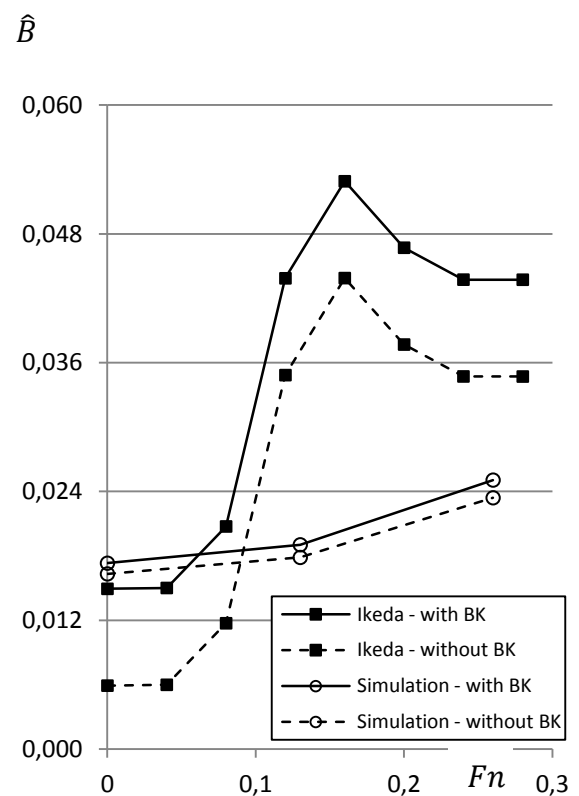


Figure 15: Comparison of the Ikeda method with simulations for $\varphi_A = 35 [^\circ]$



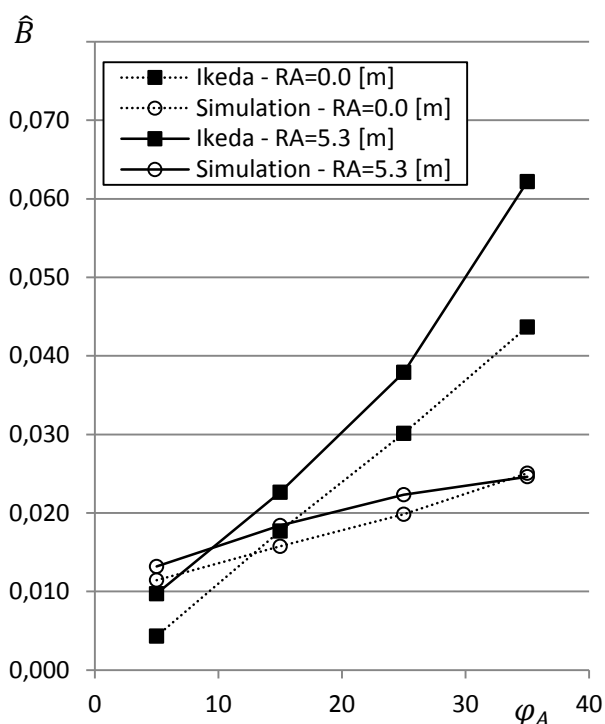


Figure 16: Roll axis variation

For 5 [°] and 15 [°] the Ikeda method results also estimates roll damping coefficients similar to CFD simulations, especially for $Fn = 0.0$ and $Fn = 0.13$. For the design speed of the ferry, the Ikeda method shows lower damping values for small roll angles for the investigated ship geometry. The bilge keel damping is relatively large compared to CFD, possibly because Ikeda is neglecting the angle α and use simple treatments of estimation of geometrical parameters, such as r_{BK} . Even so, the normal-force coefficient $C_{D,BK}$ based on CFD simulations agrees with the established methods (see Figure 9). A further reason may be the large bilge-keel-hull interaction component in the Ikeda method. The calculated characteristic of the wave damping component over the ship forward speed can neither be confirmed by the Blume method nor the CFD simulations.

For large roll angles the Ikeda method in the present configuration overpredicts the roll damping compared to the simulation.

As expected, the roll damping raises with increasing the height of roll axis of

$RA = 5.3$ [m] above the water surface (see Figure 16). Compared with the Ikeda method, the calculated influence of the height of the roll axis on the roll damping coefficient is smaller.

It should be noted that the method was compared with towing tank model tests for a container ship (see Handschel et al., 2012). Detailed validation data for a RoPax ship was not available.

5. CONCLUSION

CFD simulations allow calculating roll damping coefficients effectively. The present numerical approach enables the detailed analysis of roll damping components.

Although the established methods have been developed for single-screw ships, they are able to give an acceptable approximation of the roll damping for twin-screw vessels. Results from the Ikeda method for moderate roll angles and zero ship velocity are fairly good compared with the simulation results. For high Froude numbers, the Blume method can be used for a wide range of operational conditions. For large roll angles, the present Ikeda method does not provide sufficient results for the investigated case. The numerical investigations are carried out for one ship form. Therefore, further investigations are needed to be able to capture general tendencies.

When single components of roll damping are focused, a good agreement with the established methods and the simulation results can be found. Even so, for more complex geometrical parts like twisted rudders and curved bilge keels as well as section lines, which have no typical bilge radius, the usage of established methods is difficult. Further, emerging ship appendages are not considered in the classical approaches. Such effects can be calculated using CFD simulations.

For large roll amplitude simulations using potential flow theory in time domain extensive



considerations seems to be important in improving the accuracy of the simulations, especially for the ship interaction with the free surface. In this case, using linear or quadratic damping coefficients constant over one roll period should not be applied in the simulation.

6. ACKNOWLEDGEMENT

This project is funded by the German Federal Ministry of Economics and Technology under the aegis of the BMWi-project *Best Rolldämpfung* (<http://www.tu-harburg.de/roll-damping>) within the framework program *Schiffahrt und Meerestechnik für das 21. Jahrhundert*. The authors would like to thank the project partners: Prof. Dr. B. el Moctar, Henry Piehl and Rainer Kaiser from the University Duisburg-Essen, Dr. Fröhlich of the SVA-Potsdam and Dr. Shigunov from the Germanischer Lloyd.

7. REFERENCES

- Bassler, C.C. and Reed, A.M., 2009, "An Analysis of the Bilge Keel Roll Damping Component Model", Proc. 10th International Conference on Stability of Ships and Ocean Vehicles, St. Petersburg, Russia.
- Bassler, C.C., Reed, A.M., and Brown, A.J., 2010, "Characterization of Physical Phenomena for Large Amplitude Ship Roll Motion", The 29th American Towing Tank Conference, Annapolis, Maryland, USA.
- Bertram, V., 2011, "Practical Ship Hydrodynamics", Butterworth Heinemann, 2nd revised edition.
- Blume, P., 1979, "Experimentelle Bestimmung von Koeffizienten der wirksamen Rolldaempfung und ihre Anwendung zur Abschaetzung extremer Rollwinkel", Bericht Nr. 1511, Hamburgische Schiffbau-Versuchsanstalt, Hamburg, Germany (*in German*).
- Enger, S., Peric, M. and Peric R., 2010, "Simulation of flow around KCS-hull", A Workshop on Numerical Ship Hydrodynamics, Proceedings, Vol. II, Gothenburg, Sweden.
- Handschel, S., Köllisch, N., Soproni, J. P. and Abdel-Maksoud, M., 2012, "A numerical method for estimation of ship roll damping for large amplitudes", (*to be published in 29th Symposium on Naval Hydrodynamics, Gothenburg, Sweden*).
- Himeno, Y., 1981, "Prediction of Ship Roll Damping – A State of the Art", Report 239, Dept. Of Naval Architecture and Marine Engineering University of Michigan, Ann Arbor, Michigan, USA.
- Ikeda, Y., Himeno, Y. and Tanaka, N., 1976, "Ship Roll Damping – Frictional Component and Normal Pressure on Bilge Keel", J Kansai SNA, Vol. 161 (*in Japanese, English translation available*).
- Ikeda, Y., Himeno, Y. and Tanaka, N., 1977a, "On eddy-making component of roll damping force on naked hull", J Japan SNA, Vol. 142 (*in Japanese*).
- Ikeda, Y., Komatsu, K., Himeno, Y. and Tanaka, N., 1977b, "On Roll Damping Force of Ship – Effect of Hull Surface Pressure Created by Bilge Keels", J Kansai SNA, Vol. 165 (*in Japanese, English translation available*).
- Ikeda, Y., Himeno, Y. and Tanaka, N., 1978, "Components of roll damping of ship at forward speed", J Japan SNA, Vol. 143 (*in Japanese, English translation available*).
- Ikeda, Y., 2004, "Prediction Methods of Roll Damping of Ships and Their Application to Determine Optimum Stabilization Devices", Marine Technology, Vol. 41.



Kawahara, Y., Maekawa, K., Ikeda, Y., 2009, “A Simple Prediction Formula of Roll damping of Conventional Cargo Ships on the Basis of Ikeda’s Method and Its Limitations”, Proc. 10th. International Conference on Stability of Ships and Ocean Vehicles, St. Petersburg, Russia.

Zhou, Y.-Z., 1987, “Die Berechnung der Rolldaempfung von Schiffen”, Bericht 474, Institut für Schiffbau der Universität Hamburg, Germany (*in German*).



Improvement of Ship Safety through Stability Research and Innovations

Fai Cheng, Lloyd's Register, fai.cheng@lr.org

Spyros Hirdaris, Lloyd's Register, spyros.hirdaris@lr.org

ABSTRACT

Design of a safe ship is by far the most fundamental goal of a naval architect; the corner stone of ship safety is intact and damage stability. Determination of what is safe, however, has been the subject of continuous and relentless endeavours by the profession as well as regulators and Class Societies. For more than two centuries the maritime industry has relied on the technical rules developed by Classification Societies as the basis for safe design as well as standards supported by the regulations set down by the International Maritime Organization (IMO) and by national government. This keynote reviews past lessons, discusses the relationships between Class and Statutory Regulations and the general approach to maritime technology and innovation for ship safety with particular reference to stability through the exploitation of the outcomes from research. It also outlines some thoughts on the potential pull through of the results from research on naval architecture and ship operations.

KEYWORDS: *Safety; stability ; classification; regulation; shipping; technology; research; innovation; design*

1. INTRODUCTION

The safety of a ship depends on its structure, equipment, shape, disposition and its specific purpose, which varies from one ship to another; the purpose of one ship may be the carriage of persons or goods, the purpose of another may be fishing, towing, the rendering of assistance or any other purpose. The safety of a ship also depends on the nature of the cargo (which determines the danger inherent in its carriage), the composition of its crew, labour conditions and the education and level of communication between its members, on the use of signals and the proper function of telecommunications, as well as on other related factors. As a principle, every State, after taking into consideration all the above factors, is entitled and also obliged to ensure the safe navigation of ships flying its flag by implementing all the measures imposed especially by international rules, processes and

generally accepted practices in accordance to the United Nations Convention on the Law of the Sea (UNCLOS), developed through the International Maritime Organisation (IMO). However, the Flag State itself, in view of the inflexibility and the lack of vigilance that dominates the administration and management of its affairs, is not always in a position to secure effective control of the ships flying its flag, especially in the case of a State having developed a significant merchant fleet and the international nature of shipping. In such case the Flag State may delegate such responsibilities, selectively, to a Recognised Organisation (RO), such as a Classification Society.

However, Recognised Organisations such as Classification Societies are not guarantors of safety of life or property at sea or the seaworthiness of a vessel in the sense that they do not have full control over how the vessel is



operated and maintained in between the periodic surveys. Further, proper and effective construction of the ship lies in the hands of the designer and shipbuilder. Safe operation of a ship for its intended service depends principally upon the shipowner, the shipowner's representatives and the crew who operate and maintain the ship on its daily business.

IMO Conventions concentrate on principal safety and environmental issues relating to operation and statutory matters, such as the computation of load lines and conditions of assignment, stability, security, fire safety, life-saving appliances, navigation lights and equipment and radio communication. IMO, as a specialized agency of the UN, enables Member States to meet collectively for the purpose of producing International Conventions, instead of producing their own safety and pollution prevention requirements individually and in isolation. However Class Rules and IMO Conventions are interlinked as shown in Figure 1.

one of the major drivers for IMO developing increasingly sophisticated standards to ensure a safe design. This has been complimented by the introduction of ever more advanced structural rules and calculation methods to ensure structural integrity since the arrival of digital computers. This collection of safety standards must be continually improved through innovation that takes into account service experience, research and new concepts.

Therefore while Class Societies do not address stability explicitly in their Class Rules, or treat stability as a Class matter, they nevertheless have an important role to play in assisting in the implementation of regulations when so authorised as it has important impact on ship structural integrity and vice versa. Where stability matters are delegated by a flag state, Class Societies are obliged to demonstrate their competence, knowledge and expertise by investing in technology and human resources on a continual basis. This paper will discuss a general approach to maritime technology and innovation for ship safety with particular reference to stability through the exploitation of the outcomes from experience and research. It will outline some thoughts on the potential pull through of the results from research on naval architecture and ship operations.

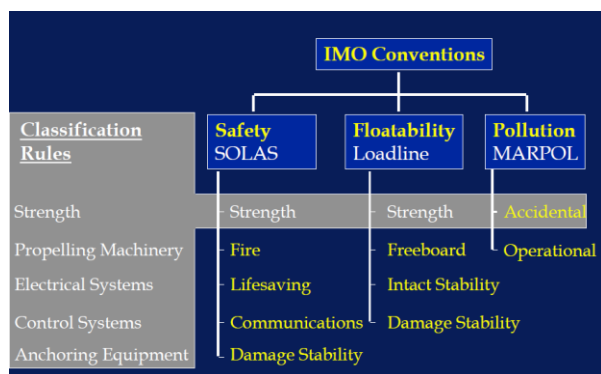


Figure 1: Interlink between Class Rules and IMO Conventions

In naval architecture terms, the preoccupation of Class Rules has always been concentrating on structural integrity to ensure the ship is not endangered by the ingress of water. IMO regulations primarily focused on regulating a ship's intact and damage stability to ensure both floatability and survivability. Flooding of ship as the result of the ingress of water with the consequential loss of stability initially and of the ship ultimately have been

2. IMPROVEMENT THROUGH INNOVATIONS

Given the pivotal role of the Classification Societies within the maritime industry and the interlink between Class Rules and statutory instruments, it is important to ensure that the regulatory processes do not constrain the take up of innovation other than by providing effective safeguards in any technology development. The latter offers the potential to develop products and services which take better account of the technology advances.

The approach taken to strategic research by Lloyd's Register is well balanced by considering the imperative that the rules,



regulations and their supporting knowledge, which form the basis of Classification or implementation of IMO led development, reflect current technology, design assurance methodologies and analysis methods.

Lloyd's Register works with principal academic institutions in the UK and around the world as well as industry visionaries to research into novel ideas, and to facilitate the development and implementation of results through collaborative projects and trial applications with ship owners and operators. The captured knowledge and know-how will eventually find their way to Lloyd's Register Rules and Procedures to enable their widespread use throughout the industry. Whereas the academic institutions are primarily associated with the so called bleeding edge low cost/investment initiatives; the industry collaborators facilitate the innovation spectrum where decisions are made on which technologies will be adopted and offered to the marine industry for marine application. While the focus of our research and development programme is primarily safety; the results also help us to improve our skills and technology base which maintains the value of the human capital and enhances service delivery.

2.1 Strategic Research Approach

Lloyd's Register strategic research approach in relation to technology and innovations comprises of three levels. At the top level we are tracking scientific and technological research around the world and regulatory changes at IMO that may enable us to develop future technology investment plans and to prepare briefings to inform marine stakeholders on technology and regulatory trends to assist them in their preparedness for current and future business needs in new ship ordering, operational efficiency improvement and regulatory compliance.

At the intermediate level we carry out or support collaborative projects to evaluate new technologies for their potential usefulness; to

monitor and transfer cross-sector technologies for marine applications. We also carry out and support projects that help to develop an understanding of fundamental concepts and methods that have potential for marine applications.

The fundamental level of activities involves the translation of the captured knowledge to useful products for the marine industry such as:

- Development of revised Rules and survey procedures for Classification for all types of marine vehicles;
- Development of new or revised services for analysis or other processes;
- Preparation and maintenance of guidance documents for customers and surveyors;
- Development of new capabilities for specialist services that form part of the portfolio of services and products.

These three levels of approach compliment each other in delivering our Strategic Research Agenda to the marine community and fulfil Lloyd's Register's constitutional objective in adding value to society.

2.2 Strategic Research Agenda

In the medium to long term, our Strategic Research Agenda for ship safety with particular reference to stability will be focused in the following areas:

- Performance and goal based safety regulations with particular emphasis on alternative designs and arrangements;
- Risk assessment and mitigation including flooding risk assessment and procedure development;
- On board decision support systems with the provision of artificial intelligence systems;
- Better description of sea conditions for development of better stability criteria for both intact and damage stability with special emphasis for emergency preparedness and dynamic intact



stability;

- In case of damage, we would need to research into different flooding scenarios with particular emphasis on the use of risk and probability approaches;
- Human reliability and ship stability.

It is also important to research into the integration of ship strength and stability design methodologies.

2.3 Collaborative Approach

The availability of research funding has become scarce as the cost of research projects has rocketed by a factor of 20 in the last thirty years. Consequently, in recent years the competition for funding has resulted in a strong focus on collaborative projects with support from industry through Joint Industry Projects, support from UK government agencies such as UK Engineering Research Council and Technology Strategy Board working with academes; and support from EU Strategic Research funding mechanisms such as EU Framework 7 Programmes working with industry partners.

3. INTACT STABILITY

It is no coincidence that stability considerations during design often concentrate on limiting ship motions experienced in service. The sea can be an inhospitable place and heavy weather is still the cause of damages to ships and in some cases to the loss of the ship due to excess motions. Heavy weather has also been instrumental in the loss of life and cargo at sea, notably lost containers from container ships due to parametric roll, and sudden capsizing of fishing boats due to broaching.

Most of our efforts have been investing in the hydrodynamic response of ships in wave environment for design hull structures and appendages. However considerable efforts have also been spent on the subject of stability,

especially in relation to its effect on operations and survivability.

The following sections discuss some of these topics by bringing together experiential and research focused lessons highlighting the importance of excitation on ship dynamics.

3.1 Unexcited Instability

While most accidents occurred in open seas, there are plenty of examples of failures in sheltered waters, particularly in harbour and dockside during ship launch, outfitting and passenger embarkation. A few examples are outlined below.

At around 16:00 hours on August 10, 1628 the warship *Vasa* set sail in Stockholm harbour on its maiden voyage as the newest ship in the Royal Swedish Navy. After sailing about 1300 meters, a light gust of wind caused the *Vasa* to heel over on its side and the ship sank with the loss of 53 lives. There were then no known methods for calculating factors such as stability, stiffness, and sailing characteristics of ships. A stability test was conducted during outfitting of the *Vasa*; the test consisted of having 30 men run from side-to-side amidship (a "lurch" test). After three traversals by the men, the test was halted because the ship was rocking so violently it was feared it would heel over. The ship *Vasa*, pride and joy of the Swedish Navy, never went to the sea.

The SS *Daphne* was a ship which sank moments after her Ship naming and launching at a shipyard in Govan, Glasgow, Scotland, on July 3, 1883. Around 200 workmen were on board the ship, ready to begin working fitting it out as soon as it was properly afloat, at the time it was launched. As per the usual practice, anchors were attached by cable to each side of the ship before launching. As the *Daphne* moved into the river, the anchors failed to stop the ship's forward progress. The starboard anchor moved only 6-7 meters but the port anchor was dragged 60 meters. The current of the river caught the *Daphne* and flipped it over

onto its port side, sinking it in deep water. Around 70 lives were saved, but 124 died (some sources say 195 died), including many young boys, some of whose relatives watched the ceremony from shore. The cause of the disaster was reported to be little initial stability combined with too much loose gear and too many people aboard. This happened two centuries after Paul Hoste introduced the concept of stability in 1698!

Principessa Jolanda was a ship built by Societa Esercizio Bacini at Riva Trigoso for Navigazione Generale Italiana and intended for the South American service. She was launched on September 22, 1907 and was 141 meters in length and 9,200 tons. She capsized and sank immediately after launching for undetermined reasons. Many suspected the ship stability was questionable.

The S.S. Eastland was a passenger ship based in Chicago and used for tours. On July 24, 1915, the Eastland was chartered to take passengers for a picnic. The ship was packed with 2,752 passengers, many standing on the open upper decks when the ship began to list slightly to the port side away from the wharf. During the next 15 minutes a number of passengers rushed to the port side, and the ship lurched sharply to port and then rolled completely onto its side, coming to rest on the river bottom which was only 6 meters below the surface. This resulted in a total of 841 fatalities with many being young women and children.



Figure 2: Launch accident still happened

Nowadays ship launching, outfitting and passenger embarkation are much safer affairs, though accidents still happen, see Figure 2. They are governed by statutory conventions and national legislations; for ship in service, they are sometimes delegated to a Classification Society to ensure their compliance by the examination of the stability booklets and loading manuals, witnessing its launch and sea trials to ensure safety after delivery before acceptance by owners and the issuance of safety certificates by the Flag State.

Today there are various launch methods deployed depending on the circumstance. One fairly novel method is using airbags such as the one developed by Evergreen. The basic body of the Evergreen airbags consists of four synthetic-cord-reinforced rubber layers, and they are cylindrical airbags with hemispherical heads at the both ends. All of these bags are vulcanized together, and then inflated with compressed air to enable them to roll (Evergreen 2009).

3.2 Excited Instability

‘When a ship is subjected to the effect of large waves it may capsize according to a number of different scenarios, depending on the magnitude and direction of the wave excitation and the ship’s own capability to resist such excitations’ (Spyrou 2000). There are essentially three types of effects as the result of wave excitation: pure loss of stability, parametric roll and broaching.

The first one is the pure loss of stability. As defined by Spyrou this is ‘a sudden, non-oscillatory type capsize taking place around a wave crest due to slow passage from a region of the wave where roll restoring has become negative’ (Spyrou 2000). Sometimes it could be caused by what is termed “rogue waves”.

The second one is the parametric instability. According to Spyrou this is ‘the gradual build-up of excessively large rolling created by a mechanism of internal forcing, the



result of a fluctuating restoring that depends on where the ship lies in relation to the wave' (Spyrou 2000).

In October 1988, a post-Panamax C11 class containership encountered extreme weather and sustained extensive loss and damage to deck stowed containers. Later investigations confirmed that parametric roll was the most likely cause of the accident. It is now widely recognised that any large container ships, given the right combinations of hull form, loading pattern, speed and wave conditions can encounter very large roll angles due to parametric roll. This could cause the loss of stability of cargoes on-board, and in severe cases, could endanger the ship and the lives of the crew, Figure 3.



Figure 3: Example of container losses

Lloyd's Register has been working with the MARIN led CRS groups (Peters A.J. 2008) and in association with the University of Southampton (Ahmet et al 2006, Ballard, 2006) seeking to develop methods by which an assessment of parametric roll effect might be carried out. This is done by firstly examining the physical characteristics of the parametric roll phenomenon. Armed with an understanding of what might cause parametric roll, methods are initially sought for identifying the combination of vessel and wave characteristics in which parametric roll is able to occur. This understanding allows the development of a susceptibility check methodology, which offers a simplified but fast

means for performing an initial check of the conditions which, for a particular vessel, are suitable for the development of parametric rolling.

We have also been working with industry to develop guidelines on container stowage and lashing based on the technologies developed from these research projects (A Master's Guide to Container Securing, 2010).

Recently we have provided support for further research into parametric roll of container ships with particular emphasis on ship operations and human elements undertaken by the University of Strathclyde.

The third distinctively identified, yet until recently not fully understood, type of excitation is broaching. Spyrou defines broaching as 'an unintentional change in the horizontal-plane kinematics of a ship. Broadly speaking, it may be described as the - loss of heading - by an actively steered ship that is accompanied by an uncontrollable build up of large deviation from the desired course' (Spyrou 2002). Broaching is more commonly the cause of casualties amongst smaller ships such as fishing boats. These smaller ships are usually less than 500 gross tonnes and they are not subject to IMO regulations but national legislation. Attempts have been made by national authorities to increase awareness amongst fishermen of the danger of such a mode of instability with disappointing results. Much research work remains to be done to understand fully the broaching phenomenon before solution can be found in design and construction of such boats (Atua, 2003).

3.3 Cargo Shift and Liquefaction

SOLAS Chapter VI Part B, Resolution 6.2 states that "concentrates or other cargoes which may liquefy shall only be accepted for loading when the actual moisture content of the cargo is less than its Transportable Moisture Limit". The results of cargo shift or liquefaction can

have detrimental effects on a ship stability and structural integrity (Wang 2011).

In a fine grain, moisture laden cargo the spaces between cargo grains are filled with both air and water. Whilst at sea the cargo is subject to forces due to the vibration and rolling of the vessel. These forces cause the inter-grain spaces to contract. The water in the spaces between grains is subject to a compressive force but as it is a liquid it cannot be compressed. This has the effect of reducing the inter-grain frictional force that holds the cargo in a solid state. Where enough moisture is present the reduction in inter-grain friction due to the ship's motion and vibration can be sufficient to cause the cargo flow like a liquid i.e. to liquefy, Figure 4.



Figure 4: Example of liquefaction

The most significant consequence for the vessel resulting from liquefaction is cargo shift leading to loss of stability. This may produce dangerous angles of list and in some instances the sudden resulting loss of stability can be such that the vessel is lost. It is therefore imperative that seafarers are aware of the types and condition of cargo that may give rise to liquefaction.

Between late October and December 2010, there were three significant bulk carrier casualties (M/V Jian Fu Star, M/V Nasco Diamond and MV Hong Wei), which lead to a combined loss of more than 40 seafarers together with around 150, 000 tons of nickel ore cargo. It is believed that the primary cause

of these accidents is the liquefaction of the nickel ore loaded in the bulk carriers.

On Christmas Day 2011, the nickel-ore carrier, Vinalines Queen together with her crew of 22 seafarers went missing in the western Pacific Ocean. No trace of the ship was ever found. Investigations into the ship's disappearance attributed her loss to cargo liquefaction, and a resultant loss of ship's stability.

This has obvious implication for structural integrity and downstream impact on intact ship stability. We are monitoring the development in order to formulate a research project to develop solution or guidelines to ensure ship safety.

3.4 Ballast Water Exchange

The ballast water exchange is focused on minimizing the introduction of unwanted organisms from the discharge of ballast water. Ballast water exchange in deep water is the most practical approach to minimize aquatic species in the ballast to be discharged. Ballast water exchange can be accomplished by either the sequential empty-refill method or by flow through method. These methods are around 95% effective in eliminating aquatic organisms.

However these methods need to be carefully considered in relation to intact stability at the design stage to ensure compliance with the criteria of IMO Resolutions. Additionally these two methods could introduce complications in ballast management; excess trim could cause propeller emergence and stern slamming causing damages to hull structures and appendices.

We have published guidelines for ballast water management and the checking of impact of such systems on local structural strength and hull girder strength remains a priority to ensure compliance with Class Rules (Lloyds Register 2011).



3.5 Structural Arrangement

Transverse and longitudinal watertight bulkheads were introduced in ironclad designs between 1860 and the 1880s, anti-collision bulkheads having been made compulsory in British steam merchant ships before 1860. Prior to this, a hull breach in any part of a vessel could flood the entire length of the ship.

Transverse bulkheads increase the likelihood of ship survival in the event of damage to the hull by limiting flooding to breached compartments separated by bulkheads from undamaged ones. Longitudinal bulkheads have a similar purpose, but damage stability effects must be taken into account to eliminate excessive heeling.

Today, most ships have means to equalize the water in sections port and starboard (cross flooding), which helps to limit the stresses experienced by the structure and also to alter the heel and/or trim of the ship.

Structural arrangements are mandated in various International Conventions interlinked with Class Rules most visibly in terms of the MARPOL, Load Line and SOLAS Conventions. Class Rules stipulate extensive requirements for ship structures.

In the early 1990s, due to the loss of bulk carriers, bulkheads of new and existing ships were required to be strengthened and an enhanced survey programme introduced to ensure that ships are properly maintained. As a result of the Derbyshire Inquiry further investigations, a forecastle was required to be fitted to minimize the green water on deck and protect the cargo holds in heavy seas.

A large amount of effort has also been spent on ensuring structural integrity as a result of collisions and groundings (Zhu et al 2002).

3.6 Add-on Stability Systems

These systems are designed to reduce the effects of waves or wind gusts. They do not increase the stability of the vessel in a calm sea. The International Convention on Load Lines does not mention active stability systems as a method of ensuring stability. The hull must be stable without active systems. However sometimes passive systems are fitted depending on the hull form.

A bilge keel is a long fin of metal, often in a "V" shape, welded along the length of the ship at the turn of the bilge. Bilge keels increase the hydrodynamic resistance when a vessel rolls, thus limiting the amount of roll a vessel has to endure. Failures were recorded with potential damage to the ship hull and the rules provide detailed requirements for their implementation (Lloyd's Register Rules for Ships 2012).

Outriggers may be employed on certain vessels to reduce rolling. Rolling is reduced either by the force required to submerge buoyant floats or by hydrodynamic foils. Generally outriggers are more common for smaller ships. Bigger ships tend to have large "outriggers" which are in general treated as a multi-hulled ship with specific requirement detailed in the Class Rules (Lloyd's Register SSC Rules 2012).

Anti-roll tanks are tanks within the vessel fitted with baffles intended to slow the rate of water transfer from the port side of the tank to the starboard side. This is intended to have an effect completely opposite to that of the free surface effect. However these systems would need to be carefully checked for their potential impact on local structural strength.

The Anti-Rolling System type MOCON has been developed to reduce the roll motions of vessels at sea. MOCON is based on a U-shape tank system which is equipped with monitoring and control equipment. All



electronic components are type approved by Lloyd's Register and other Class Societies (Hoppe anti-rolling system).

Many vessels are fitted with active stability systems. These systems include stabilizer fins attached to the side of the vessel or tanks in which fluid is pumped to counteract the motion of the vessel. Cruise ships and yachts frequently use this type of stabilizer system. When fins are not retractable, they constitute fixed appendages to the hull, possibly extending the beam or draft envelope, requiring attention for additional hull clearances.

Again, whilst such installations are not "Class" items, their attachment to the hull structures would be required to be checked to ensure there would be no impact on hull structures in case of failures.

4. DAMAGE STABILITY

Since Paul Hoste introduced the concept of ship stability measure in 1698, the metacentric height, or GM as it is known today, great strides have been made in the next three centuries in ship design to ensure its stability at launch and during operation. Nowadays accidents due to intact stability tend to be rare and most serious fatalities are mainly caused by human fallibilities, acts of God or acts of wars.

The wartime sinking of the Wilhelm Gustloff in January 1945 during World War II by a Soviet Navy submarine, with an estimated loss of about 9,500 people remains the greatest maritime disaster ever. In peacetime, the loss of the Doña Paz with an estimated 4,386 dead is the largest non-military loss recorded involving a single ship as a result of collision.

Indeed, amongst the top ten worst peacetime maritime disasters in terms of fatality in the last two centuries, five were caused by collision and grounding (HMS Birkenhead, RMS Empress of Ireland, RMS Titanic, Norwegian Ship Imo and Doña Paz), two were caused by overloading (SS Eastland

and MV Le Joola), one by boiler explosion (SS Sultana) and one was caused by structural failure as a result of severe weather (MV Estonia).

4.1 Collision and Grounding

The sinking of RMS Titanic in 1912, with 1,523 fatalities, is probably the most famous shipwreck in history. This led to the development of the Safety of Life at Sea (SOLAS) Convention in 1914, one of the most important international marine Conventions. However the sinking of the Titaic was not the world's worst.

The worst peacetime maritime disaster in terms of fatalities as a result of collision was the sinking of Doña Paz.

The Doña Paz was a passenger ferry that sank after colliding with the oil tanker Vector on December 20, 1987. The Vector's cargo ignited and caused a fire that rapidly spread onto the Doña Paz, which sank within minutes. Some reports claim that the ferry was overcrowded and that the true death toll was at least 4,386.

One hundred years after the sinking of the Titanic, on January 13, 2012 at about 09:45 hours, in calm seas and overcast weather, Costa Concordia struck a rock in the Tyrrhenian Sea just off the eastern shore of Isola del Giglio. This tore a 50 meter gash on the port side of her hull, with water flooding in and listing, the ship drifted back to Giglio Island, where she grounded just 500 meters north of the village of Giglio Porto resulting in 32 fatalities.

The reasons for the above casualties can be blamed on human fallibility. This illustrates again the need to research into the relationship between human reliability and stability, and evacuation technology and procedure post damage (Webb, R.D.G. 2003).



4.2 Damage Survivability Improvement

Lloyd's Register is a partner of the EU FP7 research project entitled "Goal-Based Damage Stability (GOALDS)" which aims to contribute to IMO regulatory work supported by a consortium of industry partners and academics. The key objectives of the project are to develop an enhanced formulation accounting for key design parameters of passenger ships and for the time evolution of flooding scenarios; to develop a new survivability formulation for flooding following grounding accidents and to integrate and validate collision and grounding survivability formulations into a single framework.

Lloyd's Register has provided support to research into survivability systems such as airbags system after damage. Whether this is a practical solution remains to be proven, but certainly one must not dismiss it outright, Figure 5.



Figure 5: Airbags system

4.3 Ship Emergency Responses

Lloyd's Register has developed "Ship Emergency Response" services to provide real-time assistance to ships in distress as a result of collision, grounding and stability loss to minimise the impact to the environment and lives. Today we have nearly 3,000 ships in the system and are the largest provider of such services.

We are also partner to the EU Project "People Localization for safe ship evacuation

during Emergency (LYNCEUS)". The aim of the LYNCEUS project is to develop a distributed wireless sensor network system that will enable the ship safety officer and team to monitor the location of each passenger for safe evacuation, to monitor in real time the status and spread of the emergency (flood, fire etc) and also provide the engineers with vital information for proper maintenance and optimization of the ship operation procedures. The LYNCEUS project is timely in view of the recent sinking of Costa Concordia.

5. CONCLUSION

The International Conference on Stability of Ship and Ocean Vehicles (STAB) was started in 1975 at the initiative of Professor Chengi Kuo from Strathclyde University. It has since become the most representative professional meeting in the stability safety field in the world. The achievement of scientific research in intact and damage stability since the Conference's inception has been incredible. This is reflected in the parallel development in IMO regulatory drives to improve safety with continuous amendment of statutory legislation in relation to ship intact and damage stability. However it is obvious as science, technology and regulation progress through the ages, incidents and accidents still, and will, occur.

We must not be complacent and we have to invest more in research in this critical area of safety, not just in terms of science, technology and regulations, but also in safety culture, human elements, especially crew training needs.

There is also a need to look at the interplay between structural integrity and stability. In this respect, the methodology and philosophy adopted by naval ships should be examined carefully to see if there is any potential for cross-fertilization. Damage stability and survivability are high on the agenda of naval ship design philosophy. It is required to conduct residual and damage strength



calculations for different scenarios as a result of enemy actions causing damage to the ship structures and systems (Lloyd's Register Rules for Naval Ships 2012).

6. ACKNOWLEDGEMENT

The authors wish to thank Lloyd's Register Group Limited for its permission to publish this paper. The views expressed are those of the authors and do not necessarily represent the policy or the view of Lloyd's Register. Lloyd's Register assumes no responsibility and shall not be liable to any person for any loss, damage or expense caused by reliance on the information or advice in this document or howsoever provided, unless that person has signed a contract with the relevant Lloyd's Register Group Limited entity for the provision of this information or advice and in that case any responsibility or liability is exclusively on the terms and conditions set out in that contract.

To demonstrate various technologies and methodologies, some of the figures used herein are taken from the public domain using internet search. This is gratefully acknowledged.

7. REFERENCES

A Master's Guide to Container Securing, 2010.

Atua, K.I. "Critical review of transverse stability criteria of fishing vessels", *Alexandria Engineering Journal*, 42(5)627-535 (2003).

Ahmed, T.M., Hudson, D.A., Temarel, P. and Ballard, E.J., "Prediction of Parametric Roll Resonance in Longitudinal Regular Waves Using a Non-Linear Method", *Proceedings of 9th International Conference on the Stability of Ships and Ocean Vehicles (STAB'06)*, Rio de Janeiro.

Ballard E.J. "Assessment of the Susceptibility of Vessels to Parametric Rolling", Lloyd's

Register Research and Development, Internal Report (2006).

Evergreen, "Product & information guide 2009."

GOALDS (2009-2012). "Goal-based Damage Stability", Project funded by the European Commission, FP7- DG Research, Grant Agreement 233876 (www.goalds.org).

Hoppe Bordmesstechnik, "MOCON - Anti Rolling System".

Lloyd's Register "Ballast water treatment technology", June 2011.

Lloyd's Register Rules and Regulations for the Classification of Ships 2012.

Lloyd's Register Rules and Regulations for the Classification of Special Service Craft (SSC) 2012.

Lloyd's Register Rules and Regulations for the Classification of Naval Ships 2012.

LYNCEUS (2012) "People Localization for safe ship evacuation during Emergency", Project funded by the European Commission, FP7 DG Research Grant Agreement Number 286148.

Peters A.J Damage simulation assessment methodology for damage ship modelling with time domain simulation, CRS programme report by QinetiQ/11/01676 (2008).

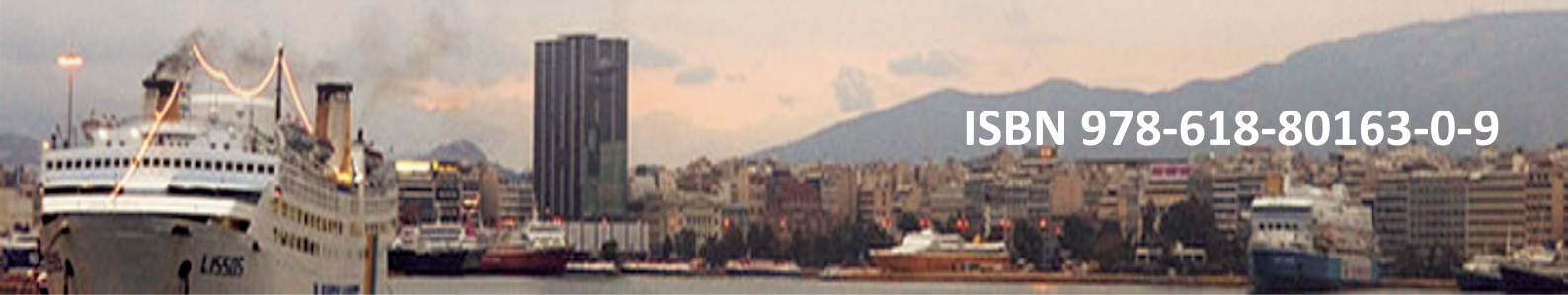
Spyrou K.J. "The nonlinear dynamics of ships in broaching". *The Annals of Marie-Curie Fellowships*. Published by the European Commission, 1:62-69, www.mariecurie.org/annals/volume1/spyrou.pdf (2000).

Wang, J.P "A Study on Safe Operation of Nickel Ore Cargo", International Conference IMLA 19, Otapija (2011).



Webb, R.D.G. "Human reliability and ship stability", Canada DND Report No: PWGSC-W7711-017747/001/TOR, 2003.

Zhu, L., James, P. and Zhang, S. "Statistics and damage assessment of ship grounding", Marine Structures 15, 2002.



ISBN 978-618-80163-0-9